Türk Fizik Derneği
1950
Turkish Physical Society

e-BOOK of FULL TEXT PROCEEDINGS

Turkish Physical Society 35th International Physics Congress (TPS35)

04-08 September 2019

Bodrum-Muğla / TURKEY

Editors

Baki AKKUŞ
Feyza GÜZELÇİMEN
Barış KINACI
Yeşim YALÇIN
Doğukan BİNGÖL
Çağlar ÇETİNKAYA
Merve SİRKECİ
Erman ÇOKDUYGULULAR

ISBN:978-605-83516-6-0

Contents

01.Applied Physics ……...…**1**

Producing of CuS Thin Films by Different Coating Methods and Investigation of Optical Properties…….2

Investigation of Physical Properties and Antibacterial Activity of Ce-Doped Chitosan Nanofibers Obtained by Electrospinning Process…….....10

Assessment of Acoustic Performance of Stratified Composites Prepared from Recycled Paper and Polyurethane Foam……17

Nanostructured TiO2 Layer Thickness Dependence of the Surface Morphology and Acoustic Impedance…….…...23

Generation of Programmable Diffractive Lenses with Multiple or Multi-Optical Axes, Multi–Focus, Dynamic Distance Control of Focal Lengths and Energy Intensities at Foci…….…….....27

Preparation of PAN/PMMA-Based Antibacterial Carbon Nanofiber by Electrospinning Method…….31

Preparation of Eu/Dy-doped ZnO Thin Films by Sol-Gel Process……37

Fully 3D Printed Bead-Pull Measurement of an Elliptical Cavity…….42

Femtosecond Laser-Induced Filamentation Control in Liquids……...…….50

Design of an Ultra-Sensitive Optical Sensor for Atmospheric Level Methane Measurement……..54

Developing Miniaturized Orthogonal Fluxgate Sensors……...59

Piezoelectric Based Acoustics Frequency Converter……67

Investigations for Increasing the Accuracy of Dielectric Constant Measurements……..74

The Study on Noise Reduction Analysis of Untreated Leaves of Plants in Urban Areas……...82

02. Astrophysics and Cosmology……..**87**

Analysis of Some Semi-Detached Systems Observed by TESS……...88

Could the CF Tuc Contain the Black Hole Closest to The Earth?.....92

Analysis of Apsidal Motion in Eclipsing Binaries: V919 Cep and V957 Cep……..98

Light Curve Analysis of Very Short-Period Binary System KIC 11494583…….....102

String Cloud Solutions in $\boldsymbol{f(R, T)}$ Gravity……..…….106

T100 Observation of Selected Magnetic Cataclysmic Variables……....114

Orbital Period Change of UU Leo……...……119

Searches for Uniform Metal Distributions in Galaxy Clusters……...…….123

The Short-Period Eclipsing Binary 1SWASPJ173327.97+265547.9:
Photometric Solution and Period Investigation……...127

Eclipse Timing Study of a Quadruple System: KIC 7177553…….……134

A Study for KIC 5621294 and Its Component…….……...139

Light Curve and Period Analysis of The Beta Lyrae Type System V359 Cas……....145

New Transit Observation for HAT-P-36 b and HAT-P-37 b……..……....152

The First Orbital Solutions of Two Eccentric Eclipsing Binary Stars From
Southern: V881 Sco and GV Nor…….....157

A Comparison of the Supernovae Ratios Between the Nearby and Distant
Galaxy Clusters…….……...161

03. Atomic and Molecular Physics…….……..……...**167**

Circular Polarization Effect Dependence of High Harmonic Generation by
Excited Argon Atom……168

Investigation of Structural, Geometric and Radical Properties of N-Propyl
Alcohol by DFT Calculations……...173

Molecular Structure and Conformational Analysis of "Phenacetin"……178

Molecular Structure and Conformational Analysis of "(R)-2-Methylamino-1-
Phenylethanol"……..184

Theoretical Calculations of Electron Paramagnetic Resonance Parameters of
Liquid Phase Isopropyl Alcohol……...188

In Silico Analysis of Hair Growth Peptide……...193

DNA Interaction of Some Hydantoin-Based Drugs with Molecular Docking
Calculation……203

Isotope Effect on Molecular Dissociation by Intense Laser Fields in The Vicinity of Metallic Nanotip……...210

Controlling Electron Localization in the Dissociation of H_2^+ and HD^+……217

Theoretical Calculations of Electron Paramagnetic Resonance Parameters of Acetamide in Water……..221

A DFT Study on Molecular Structure and EPR Parameters of N, N-Dimethylformamide in Acetone and Water……..225

Structural, Vibrational and Quantum Chemical Studies on C_{2N} (N: 0, 4, 6 and 8) Fullerenes……..230

Quantum Chemical Investigations on C_{30}, C_{32}, C_{34}, C_{36} and C_{38} Fullerenes……...235

Structural Correlations in Partly Quenched Two and Three Component Ionic Systems and Detecting the Structural Holes……241

The Life Times of Hydrogen Like Neptunium……244

04. Condensed Matter Physics…….……..…….....……...**250**

Characterization of Electrical Properties of PMMA/PbO Structures……...251

Analyses of Diode Parameters Using C–V Characteristics of Al/PMMA/PbO/P-Si Structures……..255

Janus Monolayers of MXenes: A DFT Study…….....261

Smectic Phase Transition of Ferroelectric Liquid Crystals under Influence Electric Field……..266

The Optical and Morphological Properties of Gd doped CuO Film Using Spin Coating Method……274

The Structural and Electrical Properties of Cu2O/ZnO Nanostructure Growth on n-type Porous Si……280

Investigation of Some Physical Properties of Tungsten Trioxide Thin Films Deposited via Thermionic Vacuum Arc Technique……..285

Electrical and Morphological Properties of CuO:In Thin Films……...293

Characterization of DLC Thin Films Deposited on Glass and Si Substrates under The Influence of Electric Field with ECR-MP Method……...298

Enhancing Tribological Characteristics of Piston Rings of Internal Combustion Engines Using ECR-CVD Coating Method…….304

Graphene Oxide Assembled Au-based Nanocomposite for Temperature Dependent InP Heterojunction Devices……307

Preparation and Characterization of Fe Doping CoO Thin Films……317

Optical and Morphological Studies of CoO:Ni Thin Films Grown by Ultrasonic Spray Pyrolysis……322

Experimental Investigation of Some Thermal Properties of Al-1,9Sc Alloy……...327

Experimental Investigation of Some Thermal Properties of Al-6Mg-1,9Sc Alloy……..332

The Theorical Investigation of Antiperovskite $ANTi_3$ (A=A1l, In, Tl) Compounds with DFT Calculations……..337

Anisotropic, Elastic and Lattice Dynamical Properties of Mo_2AB (A=Al, P, Si) MAX Phase Compounds……..345

05. Energy……..……..……..……...……...**354**

Comparative Performance Analysis of Two-Bed Adsorption Cooling System Using Water Vapor Adsorption on Different Types of Silica Gel……355

06. High Energy and Plasma Physics…….…….**364**

Demirci-Pro: A Single Software Interface for RFQ, Ion Source and LEBT Line Design……...……365

Investigating Magnetic Properties of YIG Thin Film Grown on Si Substrates……369

Investigating Magnetic Properties of NiFe Dot/Antidot Structure……...372

Associated Production of Higgs Boson at an Electron-Photon Collision in The Two Higgs Doublet Model……....376

Neutral Higgs Boson Pair Production via Photon-Photon Collision in The Two Higgs Doublet Model……...381

Searching for the Dark Photon with the PADME Experiment…….387

Review of The Nucleon to Delta Transition Axial Form Factors……395

07. Mathematical Physics……...…..……..……...**399**

LRS Bianchi-Type I Space-Time in κ(R,T) Gravity……400

Bianchi-Type I Universe With Dust Matter in κ(R,T) Gravity……406

Cosmological Evolution and Constraint Equations in f(G,T) Gravıty…….411

Power-Law Solution in f(G,T) Gravity……420

Bianchi Type-V Cosmology with Gamma Law EoS in F(R,T) Gravity……..427

The Purity and Entropy of a Multi-Site Dissipative System Driven by Random Telegraph Noise……432

String Cloud with Perfect Fluid Matter Distribution for Homogenous and Anisotropic Space-Time in $\boldsymbol{f}(\boldsymbol{R}, \boldsymbol{T})$ Gravity……437

Space-Time Geometry of Perfect Fluid Distribution in $\boldsymbol{f}(\boldsymbol{R}, \boldsymbol{T})$ Gravitation Theory…...447

Bianchi V Universe Model for String Cloud with Perfect Fluid in Lyra Manifold…….456

Solutions for Some DarkEnergyModels inKaluza-Klein Space-Time…….463

Examination of Bianchi Type -VI0- for Dark Energy in Ƒ(R,T)=R+Λt Gravity…….469

08. Medical Physics……..……...…..……..……...**474**

CSDA Range Calculation of Proton Beam and Water Equivalent Ratio (WER) Value of Lucite ($C_5O_2H_8$)……..…475

09. Nuclear Physics……..……...…..……..……...**481**

A Study on TL Properties of Natural Dolomite Mineral Irradiated with Beta Particles……482

Nucleon Densities of Chrome Isotopes Calculation by Skyrme Interactions……...491

Calculation of The Photomultiplier Output Voltage by FLUKA Monte Carlo Program……497

Energy Resolution Improvement Using Timing Method…….503

Radiogenic Heat Productions Caused by Volcanic Tuffs Collected from Quarries in Turkey……...511

The Excess Lifetime Cancer Risk Caused by Ingestion of Some Bottled Waters Consumed in Turkey…….515

Electric Dipole (E1) Strength in ^{139}La Nucleus below The Neutron-Separation Energy……...519

Radon Exhalation Rate and Effective Radium Content of the Soil Samples Collected from Orhaneli District of Bursa,Turkey……...524

The Investigation of the Giant Dipole Resonance (GDR) Characteristics for ^{141}Pr Nucleus*……...532

10. Statistical Physics……..……...…….……...**539**

Phase Diagrams of Generalized Spin-S Magnetic Binary Alloys…….540

11. Condensed Matter Physics II…….…..……..……...**547**

Zinc Molar Concentration Induced Structural and Optical Properties of Chemically Derived ZnS Thin Films…… ……...548

12. Mathematical Physics II…….…….....……...**553**

Investigation of Bianchi Type-V Dark Energy Cosmological Models in F(R,T) Gravity.....554

01. Applied Physics



BOOK OF FULL TEXT PROCEEDINGS TURKISH PHYSICAL
SOCIETY 35th INTERNATIONAL PHYSICS CONGRESS (TPS35)
TPS35, Vol.01, No.01, pp.2-9.
ISBN:978-605-83516-6-0

15 December 2019

Producing of CuS Thin Films by Different Coating Methods and Investigation of Optical Properties

Namık AKÇAY[1, a)] and Ozan KUŞ[1, b)]

[1]*Department of Physics, Faculty of Science, Istanbul University, Istanbul,*

[a)]Corresponding author: akcay@istanbul.edu.tr
[b)] ozan_kus@hotmail.com.

Abstract. Copper sulfide is a good prospective opto-electronic p-type material. It is potentially used in solar cells, IR-detectors, optical filters and other low cost devices owing to its narrow band gap (2.1– 2.5 eV). In this study CuS nanostructures produced by sol-gel route and coated on glass substrate. As coating technique spin coating and spray pyrolysis were used. Absorption and transmittance measurements of thin films were done. According to absorption result bang gaps of thin films were calculated by using Tauc formula. CuS nano structured thin films band gaps were calculated 2.11eV to 2.56 eV. Nanostructures were examined by Scanning Electron Microscopy (SEM). SEM analysis showed particles size around 20 nm. Energy Dispersive Spectroscopy (EDS) analysis of the same compounds was performed. Cu and S were dominant in the EDS analysis.

INTRODUCTION

Nanostructures and their applications have been widely studying last few decades. Nano structure especially such as CuS has many application areas. In this areas great variability in functional properties makes copper sulfide attractive for applications in Energy conversion and storage, photovoltaic cells, optoelectronic devices, sensors or photocatalysis[1].

In recent years, there is increasing interest in transition metals due to their novel physical, chemical and non-toxic properties. Covellite copper sulfide has been used in applications such as solar cells [2,3], light emitting diodes thermal infrared dedectors, gas sensors, temperature control of satellites and Li-ion batteries [4,5,6].

In production of CuS nano structures have many different methods. Xiao-Sai Hu at al. were prepared flower-like CuS by solvothermal method [7] and Qing-Li Huang at al. were prepared CuS nanostructures by hydrothermal method [8]. Sol-gel method is low-coast and easy production method among of production methods of CuS nanostructures.

In this study, we have produced CuS nanostructured thin films. CuS nanostructures were produced by using low-cost sol-gel method and 1:2 and 2:4 molarity ratios copper sulfide nanostructured were produced. The CuS nanostructured solutions were coated on microscope glass substrate as thin films. As thin films coating technique we have used spin coating and spray pyrolysis technique.

ISBN:978-605-83516-6-0

EXPERIMENT

Materials

Copper Acetate monohydrate (Cu(CO2CH3)2), Thiourea (NH2CSNH2) were commercially purchased from Merck. 2-Methoxyethanol (CH3OCH2CH2OH) reagent used were of analytical grade and purchased from Sigma-Aldrich which were all of analytical grade and used directly without any further treatment. Microscope glass slides were as substrate materials.

Synthesis of CuS Nano Structures

Synthesis of CuS nanostructure by sol-gel method was carried out as follows: 0.1 M of Copper Acetate Monohydrate and 0.2 M of Thiourea dissolved each in 20 ml of 2-methoxyethanol. Ratio of Copper and Sulfide were determined as 1:2 and 2:4 in this study. Copper Acetate and Thiourea dissolved different pots. Stirring in different pots were carried 30 minutes, 500 rpm of stirred at room temperature (298 K). After that stirring 30 minutes, Thiourea solution were mixed with Copper solution drop by drop. Then solution was stirred 90 minutes at room temperature. The same procedures were repeated for other ratios to prepare CuS nano structures.

Thin Film Coating

CuS thin films production two different methods were used. Spin coating and spray pyrolysis methods were used as thin film coating. Before coating, microscope glass slides were cleaned. glass substrates were first cleaned in detergent water. After that, glasses were cleaned 10 minutes long at 80°C in Ammonia, hydrogen peroxide and deionize water solution. After 10 minutes substrates rinsed with deionize water. The thin films prepared with spin coating technique coating were made in 2000 rpm and 20 seconds. Coatings were made 20 layer and after each layer were heated 1 minute at 200°C.

Spray pyrolysis technique were performed as thin films coating. Glass substrate were heated up to 200°C. Then solution was sprayed on substrate 20 cm distance and 0.5ml.min-1 conditions.

RESULTS AND DISCUSSION

Optical Characterizations

To characterize the optical properties, UV-Visible spectrum analysis is performed by Varian 634S UV- Visible Spectrophotometer. Absorption spectrums were taken in the wavelength range from 300 to 800 nm.

Absorption spectrum of thin film coated by spin coating method CuS with 1:2 ratios is shown in Fig.1. Thin films of CuS with 2:4 ratios and coated by spin coating and spray pyrolysis are shown in Fig.2 and Fig.3.

ISBN:978-605-83516-6-0

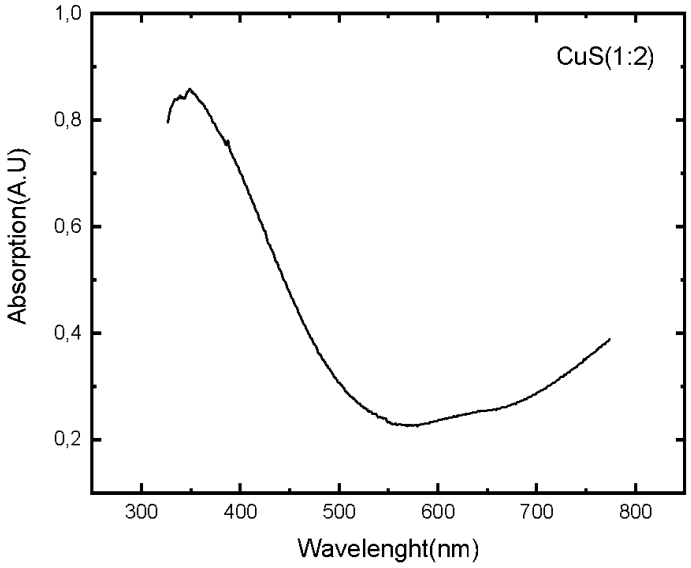


FIGURE 1. CuS(1:2) nanostructured thin films coated by spin coating technique.

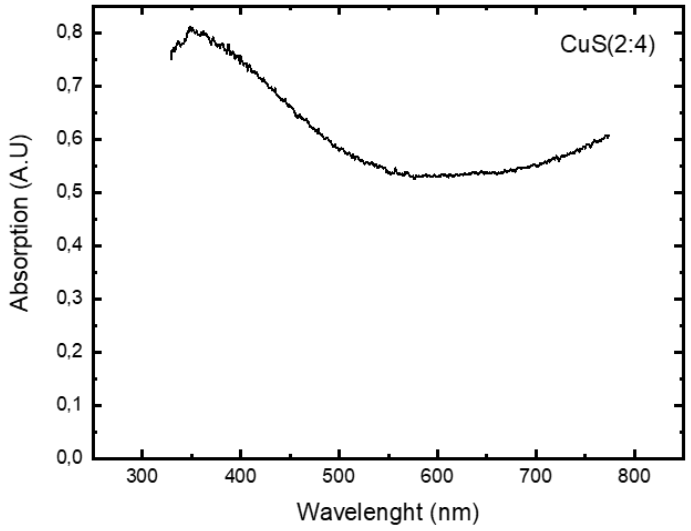


FIGURE 2. CuS(2:4) nanostructured thin films coated by spin coating technique.

ISBN:978-605-83516-6-0

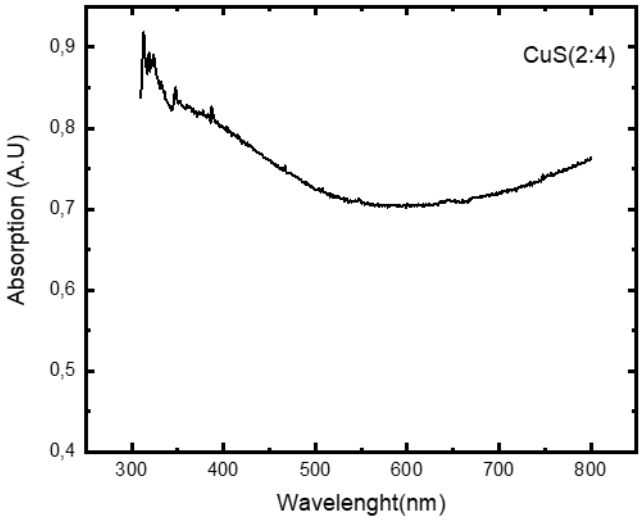


FIGURE 3. CuS(2:4) nanostructured thin films coated by spray pyrolysis technique.

Calculated band gaps of CuS nanostructure thin films respectively 2.56eV, 2.16 eV and for spray pyrolysis coated thin film CuS 2.11 eV respectively. Band gaps were calculated by using Tauc formula [9].

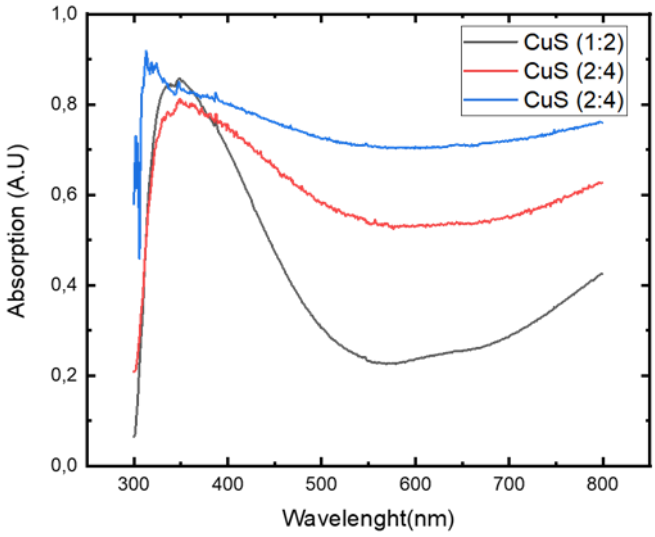


FIGURE 4. Absorptions measurements of CuS thin films.

As shown in the absorption graphics, absorption of spin coated thin films have low absorptions in range of Visible light at 400-700nm. Band gaps and optical properties of CuS thin films have similarities with literature [10,11].

ISBN:978-605-83516-6-0

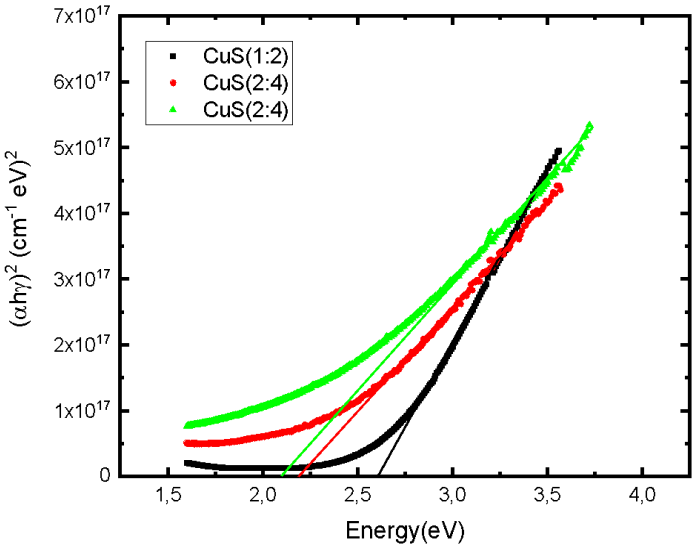


FIGURE 5. Band gap graphs of CuS nanostructures.

SEM Analysis

The morphology of the sample was observed by SEM. SEM images of the CuS nanostructures are shown in the following figures at different magnification. SEM images of spin coated CuS(2:4) nanostructure is shown in Fig.6. As shown in Fig. 6 particle distribution is homogeneous. Particle size of CuS thin films are about less than 20 nm observed.

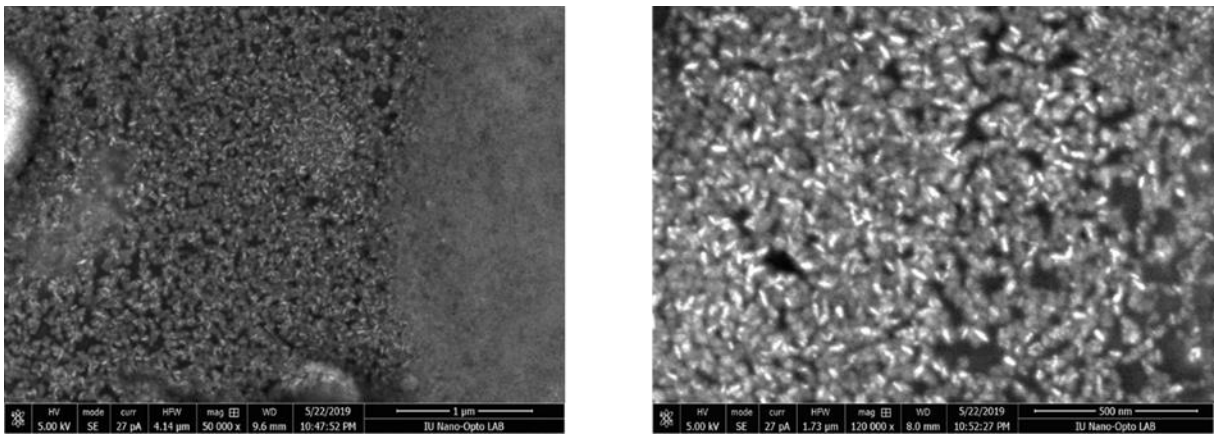


FIGURE 6. SEM images of spin coated CuS(2:4) a) 50000X and b)120000X magnifications

The morphology analyses of the CuS nanostructured thin films were done employing scanning electron microscopy (SEM) (model Zeiss EVO LS 10).

ISBN:978-605-83516-6-0

EDS Analysis

The elemental analysis was performed by Energy-dispersive Spectroscopy(EDS). EDS spectrum is shown in Fig.7 and the EDS spectrum confirms presence of copper(Cu) and sulphur(S). Also EDS spectrum of CuS thin film showed that there is little amount of nitrogen (N), carbon(C) and oxygen (O) which there are residues from solvent 2-methoxyethanol. Oxygen may also come from oxidation of thin films.

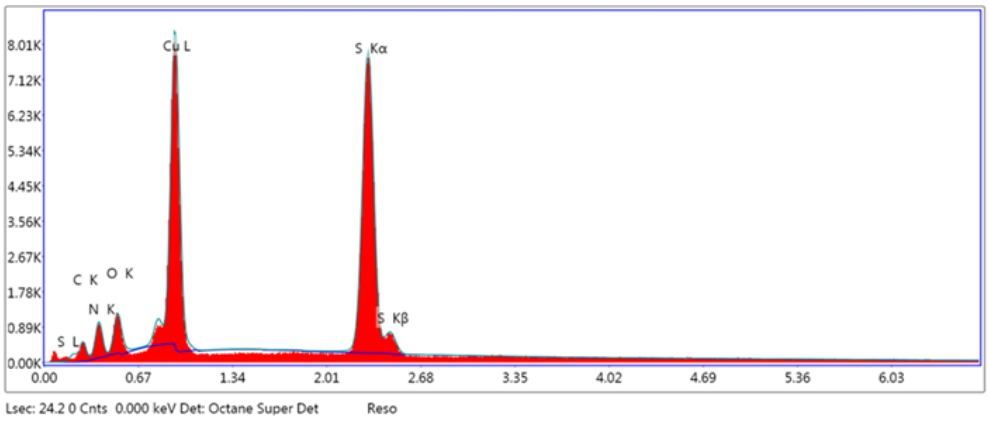


FIGURE 7. EDS spectrum of Spin Coated CuS nanostructure with 2:4 ratios.

Structural Analysis (XRD)

The structural analysis was performed by using an X-ray diffractometer. The XRD patterns were measured by a Rigaku D/Max-2200/PC powder diffractometer with Cu Kα radiation (1.5418 Å) in the 2θ range of 20° – 80° by steps of 0.02 °/min for full scan. The scanning regions of the diffraction angle (2θ) were 20°—60°and Cu K radiation were used to collect the spectrum. The XRD pattern of CuS nanostructures is shown below which can be indexed to hexagonal CuS structure as compared to the JCPDS database no 79-2321. XRD analysis of CuS(2:4) spin coated thin film shown Fig.7.

ISBN:978-605-83516-6-0

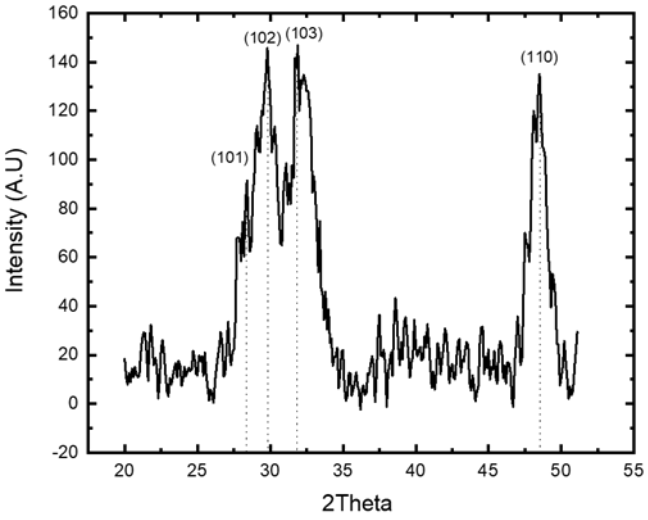


FIGURE 7. XRD pattern of CuS(2:4) thin film nanostructure.

Average particle size were calculated from the XRD analysis using the Debye-Scherrer formula [12].

$$D = \frac{k\lambda}{\beta \cos\theta} \tag{1}$$

where K is the shape factor, β is full width at half maxima (FWHM) of the highest peak in radian.

λ=1.5404 Å , β=0.499, 2θ=28,088° then the calculated particle sizes D=25.73 nm.

XRD pattern of CuS thin film show nanostructure has hexagonal copper sulfide crystallite structure [13]. The characteristic peaks of as-obtained CuS at 2θ= 28.08°, 29.81°, 32.06°, 48.59° can be corresponding to the (101), (102), (103), (110) reflections with lattice parameters (a = 3.78 Å and c = 16.48 Å) respectively.

CONCLUSION

By using low- cost sol-gel method and 1:2 and 2:4 molarity ratios copper sulfide nanostructured thin films were produced. Two different coating methods were used as coating method which are spin coating and spray pyrolysis methods. Band gaps of thin films were calculated between 2.56 eV and 2.11 eV. Particle size were found about 20 nm in SEM analysis. Crystallite size calculated by using Debye-Scherrer formula from XRD pattern and found 25 nm. Found that copper sulfide nanostructure thin films have hexagonal copper sulfide crystal structure.

ACKNOWLEDGMENTS

This work was supported by Scientific Research Center Coordination Unit of Istanbul University. Project Number are FYL-2017-24168.

ISBN:978-605-83516-6-0

REFERENCES

1. M. Milan, U. Michal, U. Pavel, M. Zuzana, M. Jan, R. S. Yadav, D. Skoda, M. Michal, and K. Ivo, Mater. Chem. Phys., **237**,121823 (2019).
2. K. D. Yuan, J. J. Wu, M. L. Liu, L. L. Zhang, F. F. Xu, L. D. Chen, and F. Q. Huang, Appl. Phys. Lett. **93**, 132106 (2008).
3. M. Dhanasekar, G. Bakiyaraj, K. Rammurthi, International Journal of ChemTech Research, **Vol.7**, No.3, pp 1057-1064 (2015).
4. H. Qi, J. F. Huang, L.Y. Cao, J.P. Wu, D.Q. Wang, Ceramics International **38**, 2195–2200 (2012).
5. F. A. Sabah, N. M. Ahmed, Z. Hassan, H. S. Rasheed, Sensors and Actuators A **249**, 68–76 (2016.)
6. C. Feng, L. Zhang, M. Yang, X. Song, H. Zhao, Z. Jia, K. Sun, G. Liu, ACS Appl. Mater. Interfaces. **29**, 7, 15726-34 (2015).
7. X.S. Hu, Y. Shen, L.H. Xu, L.M. Wang, Y.J. Xing, Journal of Alloys and Compounds **674**, 289-294 (2016).
8. Q.L. Huang, H. Chen, Y. C. Zhang, C. L. Wu, Journal of Alloys and Compounds **509**, 6382–6387 (2011).
9. K.R. Nemade, S.A. Waghuley, Materials Science in Semiconductor Processing **39**, 781-785 (2015).
10. X. Xu, J. Bullock, L. T. Schelhas, E. Z. Stutz, J. J. Fonseca, M. Hettick, V. L. Pool, K. F. Tai, M. F. Toney, X. Fang, A. Javey, L. H. Wong, J.W. Ager, Nano Lett. **16**, 1925−1932 (2016).
11. M. Saranya, R. Ramachandran, E. James J. Samuel, S. K. Jeong, A. N. Grace, Powder Technology **279**, 209–220 (2015).
12. S. Riyaz, A. Parveen, A. Azam, Perspectives in Science **8**, 632—635 (2016).
13. X.S. Hu, Y. Shen, L.H. Xu, L.M. Wang, L.S. Lu, Y.-T. Zhang, Applied Surface Science **385**, 162–170 (2016).

BOOK OF FULL TEXT PROCEEDINGS TURKISH PHYSICAL
SOCIETY 35th INTERNATIONAL PHYSICS CONGRESS (TPS35)
TPS35, Vol.01, No.01, pp.10-16.
ISBN:978-605-83516-6-0

15 December 2019

Investigation of Physical Properties and Antibacterial Activity of Ce-Doped Chitosan Nanofibers Obtained by Electrospinning Process

Nalan ÇİÇEK BEZİR[1a], Atilla EVCİN[2b], Emine ŞENOL[1], Burcu ÖZCAN[3], Esengül KIR[3], Gökhan AKARCA[4] and Ozan CEYLAN [5]

[1]*Süleyman Demirel University, Physics Department, ISPARTA*
[2]*Afyon Kocatepe University, Materials Science and Engineering Department, AFYON*
[3] *Süleyman Demirel University, Chemistry Department, ISPARTA*
[4]*Afyon Kocatepe University, Food Engineering Department, AFYON*
[5]*Akdeniz University, Elmalı Vocational School, ANTALYA*

[a)]Corresponding author: cicekn@gmail.com
[b)] evcin@aku.edu.tr

Abstract. In this study, pure and Ce-doped Chitosan nanofibers were prepared by sol-gel assisted electrospinning process at the different conditions. Chitosan solution was prepared by dissolving chitosan in acetic acid following by stirring for 24 h at room temperature. Cerium nitrate solution was prepared by dissolving required amount of absolute ethanol and stirred at 70 °C for 90 min, leading to the formation of a clear and homogeneous solution. Then two solutions were mixed and loaded into syringe equipped with the stainless steel needle. The filled syringe was placed into the electrospinning device and nanofibers were produced. Prepared nanofibers was characterized by X-ray diffraction (XRD), scanning electron microscopy (SEM), the differential scanning calorimetry/the thermal gravimetric analysis (DSC/TGA), and energy dispersive X-ray spectrometer (EDX). Obtained results showed that nanofibers were produced succesfully with uniform morphologies.

INTRODUCTION

Nowadays, the field of nanotechnology is one of the most popular fields for studies in all technical disciplines [1]. Nanotechnology has a wide range of applications as it works with materials that are in nanometer scale length (1-100 nm) sizes. Therefore, it is used for the production of various nano materials and devices [2]. Generally, nanofibers with a diameter of less than 1 micron have a few surprising properties compared to other known forms of the material. These are properties such as very large surface area at volumetric rate, flexibility in surface functions and superior mechanical performance [3]. Many methods are used to produce nanofibers. Among these methods, electrospinning is widely used as the simplest and cheapest method for producing nanofibers from a variety of synthetic or natural polymers [4]. Polyvinyl alcohol (PVA) is a synthetic polymer that has water solubility, hydrophilic structure, bio-compatibility, chemical resistance and natural adhesion properties that can be obtained by polymerization of alcohol [5]. Besides, some researchers have noted that polyvinyl alcohol (PVA) increases the nanofiber-forming property [6-8]. Many researchers have used chitosan in their studies due to its antibacterial properties [9,10]. On the other hand, some researchers have observed the effect on the antibacterial properties of chitosan nanofibers doped with cerium(Ce) [11,12].

In this study, Ce was used by adding chitosan because it increased the antibacterial property. In addition, Ce-doped chitosan nanofibers were prepared by electrospinning method. Structure and morphology were investigated by X-ray diffraction (XRD), scanning electron microscopy (SEM) and differential thermal (DTA) methods. In

ISBN:978-605-83516-6-0

experimental studies, the parameters analyzed are; Solution feed rate, needle-to-collector distance, electrostatic potential difference between the needle and the collector, and concentration in solution. The antibacterial properties of Ce-added CS nanofiber containing different amounts of Ce were tested on selected S. *aureus* bacteria.

MATERIALS AND METHOD

The chemical precursors used in the experiments are given in Table 1. The chemical precursors were used directly without any treatment.

TABLE 1. Chemical substances and formulas used in the study

Precursors	Formulas
Polyvinyl alcohol	PVA
Chitosan	CS
Cerium nitrate	Ce(NO3)2
Asetik asit	CH3COOH
Dimethylformamide (DMF)	C3H7NO
Dietanoleamin	C4H11NO2
Polyethylene glycol	HO(C2H4O)nH

Production of pure Chitosan nanofibers:

PVA was dissolved in distiled water. Chitosan was dissolved in acetic acid solution in a separate beaker. PVA solution and chitosan solution were mixed homogeneously. This prepared solution was drawn into a syringe and placed in the electrospinning setup.

Production of Ce - Chitosan nanofibers:

PVA solution was prepared same way. Its concentration was 10 wt%. Chitosan was also prepared same way.Its concentration was 3 wt%. Both solutions were mixed homogeneously. Cerium doping was changed from 1 wt% to 5wt%. Cerium nitrate was dissolved in ethanol. Then it was added main solution. Its composition was as follows

1. 14 mL PVA + 3 mL CS + 0,17 g Ce (%1)
2. 14 mL PVA + 3 mL CS + 0,34 g Ce (%2)
3. 14 mL PVA + 3 mL CS + 0,51 g Ce (%3)
4. 14 mL PVA + 3 mL CS + 0,68 g Ce (%4)
5. 14 mL PVA + 3 mL CS + 0,85 g Ce (%5)

Nanofibers were produced constant voltage (25 kV,) distance (8 cm), time (10 min) and flowrate (0.1 mL/h)

Baird Parker Agar Plate were applied to see the antibacterial effects of nanofiber samples on S. aureus bacteria. Baird Parker Agar Plate method was applied for Ce-doped nanofibers. S. aureus bacteria were counted using Baird Parker agar by spreading plate method.

Morphology of undoped and 1%, 2%, 3%, 4% and 5% by weight Ce-doped chitosan nanofibers in pure, were measured by LEO 1430 VP model SEM. XRD measurements of 1%, 2%, 3%, 4% and 5% Ce-doped chitosan nanofibers were measured using Shimadzu XRD-6000 model device. TGA and DTA analyzes were carried out using the NETZSCH model device between 25-800 °C.

ISBN:978-605-83516-6-0

RESULTS

SEM images and measured average thicknesses of Ce-doped chitosan nanofibers are given in Fig. 1 and Table 2, respectively.

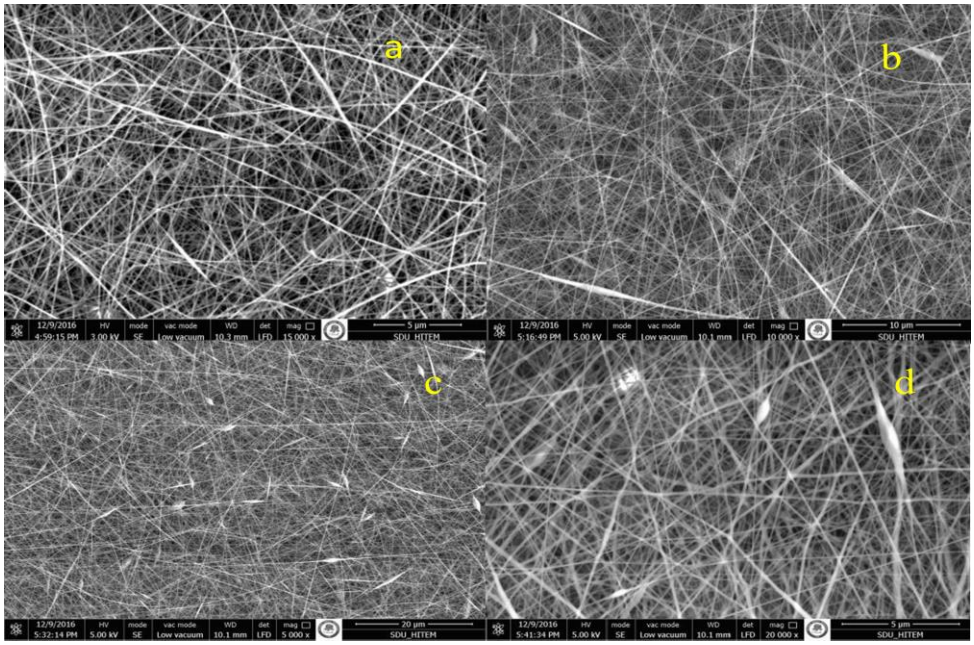


FIGURE 1. SEM images of pure chitosan nanofibers (1) 20 kv, 0,5 mL/h, 8 cm (2) 20 kv, 0,1 mL/h, 8 cm, (3) 15kv, 0,1 mL/h, 8 cm, (4) 25 kv, 0,1 mL/h, 8 cm

TABLE 2. Diameter of produced nanofibers

Sample ID	Fiber Diameter (µm)			# of Measurements	Image Area Analyzed (%)
	Average	Std Dev	Median		
a	1,043	0,603	0,939	239	100%
b	0,160	0,081	0,149	1103	100%
c	0,297	0,166	0,266	1120	100%
d	0,151	0,074	0,135	919	100%

ISBN:978-605-83516-6-0

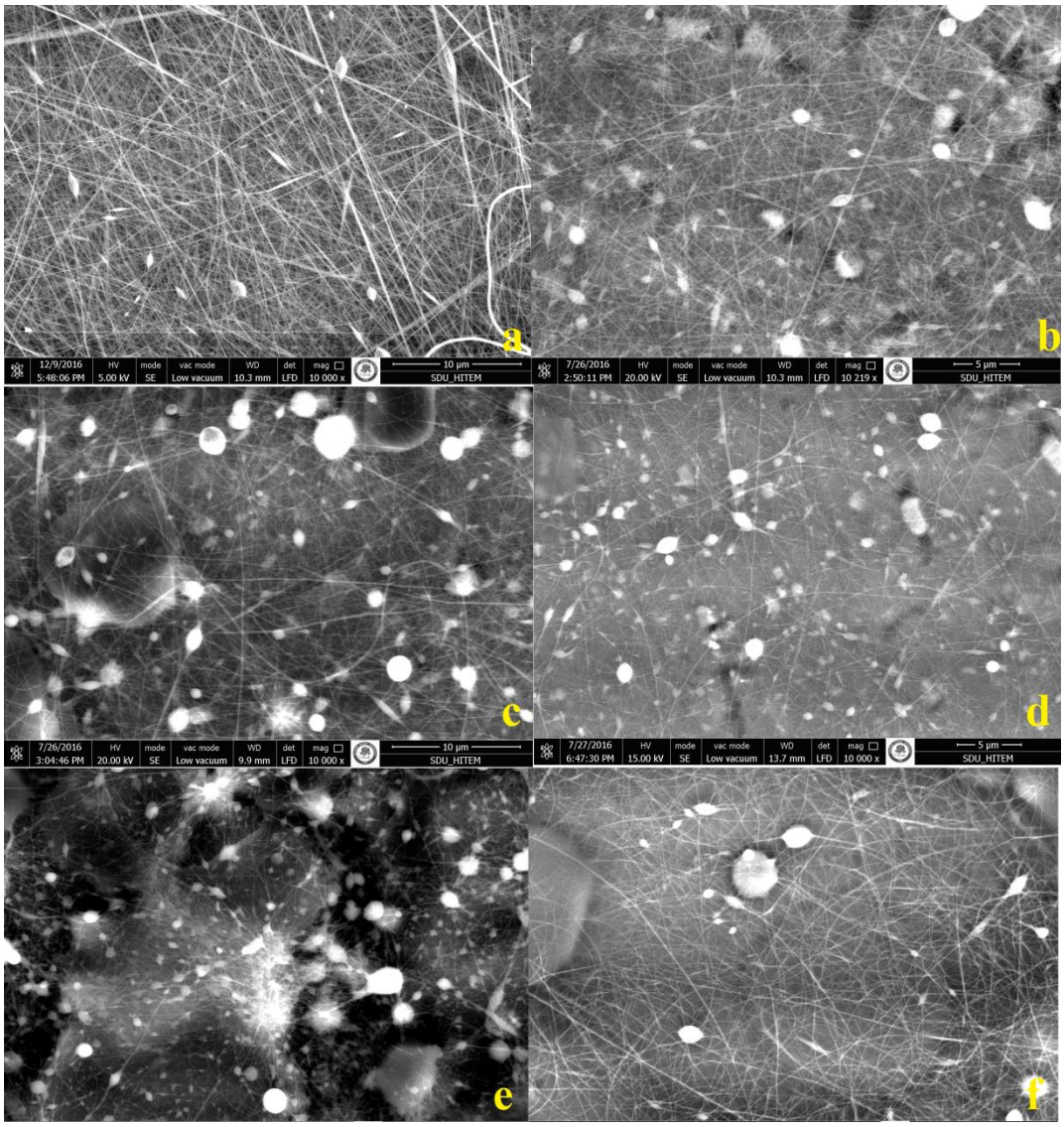


FIGURE 2. SEM images of Ce-CS nanofibers (25 kv,0,1 mL/h, 8 cm), (a) Pure chitosan (b) %1 Ce, (c) %2 Ce, (d) %3 Ce, (e) %4 Ce, (f) %5 Ce

TABLE 3. Diameter of produced nanofibers

Sample ID	Fiber Diameter (µm)			# of Measurements	Image Area Analyzed (%)
	Average	Std Dev	Median		
Pure.tif	0,670	0,491	0,614	125	100%
1%.tif	0,478	0,289	0,436	351	100%
2%.tif	0,332	0,330	0,242	102	100%
3%.tif	0,288	0,155	0,248	1015	100%
4%.tif	0,345	0,232	0,296	181	100%
5%.tif	0,310	0,235	0,246	614	100%

ISBN:978-605-83516-6-0

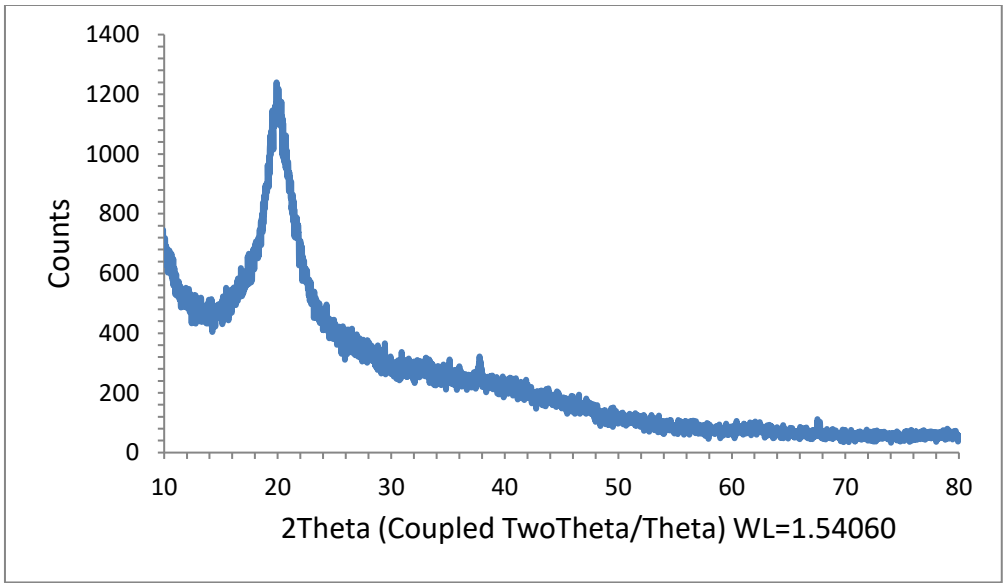


FIGURE 3. 5% Ce doped chitosan nanofibers

XRD patterns of 5% Ce doped chitosan nanofibers thermally treated at 500 ° C are shown in Fig. 3. Similar peaks were obtained in the literature [13-15].

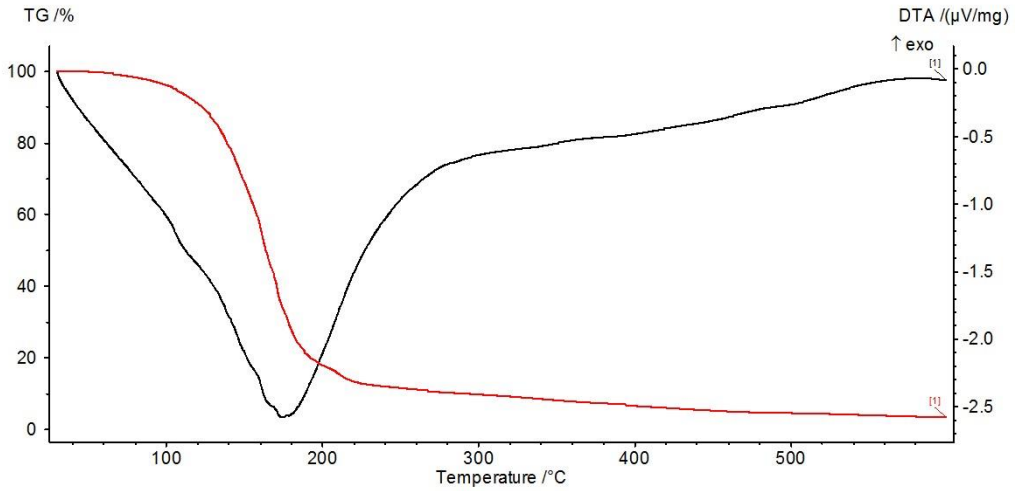


FIGURE 4. DTA and TG analysis of Ce doped chitosan nanofibers

DTA and TGA analysis of 5% Ce doped chitosan nanofibers are shown in Fig. 4. DTA/TGA analysis of the chitosan was conducted in the temperature ranges from the room temperature to 500℃ (Fig.4). The chitosan weight loss curves in the range of 200°C to 400℃ can be associated with decomposition of the chitosan [15]. The test results of 1%, 2%, 3%, 4% and 5% of the Baird Parker Agar Plate method of Ce doped CS nanofibers are given in Tables 4. As can be seen in Tables 4, the number of bacteria decreases with increasing cerium content under UV, sunlight and darkness and becomes completely zero. In conclusion, Ce-doped chitosan nanofibers have very good antibacterial effect on S. *aureus* bacteria.

ISBN:978-605-83516-6-0

TABLE 4. Bacteria Amount (kob / cm^2) (Ce-Cs)

% Ce-Cs	Bacteria Amount (kob/cm^2)		
	Darkness	UV	Sunlight
Pure		1.10^6	
1% ce	$2,5.10^4$	$1,0.10^3$	$1,23.10^4$
2% Ce	$4,7.10^3$	$1,2.10^2$	$3,14.10^3$
3% Ce	$3,3.10^3$	$0,5.10^2$	$1,84.10^3$
4% Ce	$1,4.10^3$	0	$1,65.10^3$
5% Ce	$1,07.10^2$	0	$1,10^2$

CONCLUSION

Using electrospinning method, pure and doped chitosan nanofibers were successfully produced. The results obtained from the characterization measurements of the samples are given as follows;

- Antibacterial properties of produced nanofibers were investigated by using Baird Parker agar plate.
- S. *aerus* (ATCC 6538) strain was used as Baird Parker agar plate method.
- Almost all bacteria disappeared under UV, darkness and sunlight, while the cerium concentration increased.
- Good antibacterial effects were achieved according to the results.
- The morphology and structure of pure and Ce doped chitosan nanofibers were confirmed by SEM, XRD and DTA / TGA techniques.

ACKNOWLEDGMENTS

This work was supported by Suleyman Demirel University via Research Project Coordination Unit [BAP PROJECT-4688YL1-16].

REFERENCES

1. Paul, D. R., & Robeson, L. M. (2008). Polymer nanotechnology: Nanocomposites. Polymer, 49(15), 3187–3204
2. Nikalje, A. P. (2015). Nanotechnology and its applications in medicine. Med chem, 5(2), 081-089.
3. Huang, Z. M., Zhang, Y. Z., Kotaki, M., & Ramakrishna, S. (2003). A review on polymer nanofibers by electrospinning and their applications in nanocomposites. Composites science and technology, 63(15), 2223-2253.
4. Bhattarai, N., Edmondson, D., Veiseh, O., Matsen, F. A., & Zhang, M. (2005). Electrospun chitosan-based nanofibers and their cellular compatibility. *Biomaterials*, *26*(31), 6176-6184.
5. İkiz Y., (2009). Elektro çekim yöntemi işlem parametrelerinin PVA nanolif morfolojisine etkileri, Pamukkale Üniversitesi, Mühendislik Bilimleri Dergisi, Cilt 15, Sayı 3, Sayfa 363-369.
6. Yang, D., Li, Y., & Nie, J. (2007). Preparation of gelatin/PVA nanofibers and their potential application in controlled release of drugs. Carbohydrate Polymers, 69(3), 538-543.
7. Zeytuncu, B. (2014). Elektrospinning Tekniği ve Uv Işımasının Eşzamanlı Olarak Uygulanması ile Nanofiber Membranların Hazırlanması ve Kıymetli Metallerin Adsorpsiyonunda Uygulanması (Doctoral dissertation, Fen Bilimleri Enstitüsü).

ISBN:978-605-83516-6-0

8. Sasipriya, K., Suriyaprabha, R., Prabu, P. Rajendran, V. (2013). Synthesis and characterisation of polymeric nanofibers poly (vinyl alcohol) and poly (vinyl alcohol)/silica using indigenous electrospinning set up. Materials Research, 16 (4), 824-830.
9. Perelshtein, I., Ruderman, E., Perkas, N., Tzanov, T., Beddow, J., Joyce, E., ... & Frenkel, A. I. (2013). Chitosan and chitosan–ZnO-based complex nanoparticles: formation, characterization, and antibacterial activity. Journal of Materials Chemistry B, 1(14), 1968-1976.
10. Krajewska, B., Wydro, P., & Jańczyk, A. (2011). Probing the modes of antibacterial activity of chitosan. Effects of pH and molecular weight on chitosan interactions with membrane lipids in Langmuir films. Biomacromolecules, 12(11), 4144-4152.
11. Kaygusuz, H., Torlak, E., Akın-Evingür, G., Özen, İ., von Klitzing, R., & Erim, F. B. (2017). Antimicrobial cerium ion-chitosan crosslinked alginate biopolymer films: a novel and potential wound dressing. International journal of biological macromolecules, 105, 1161-1165.
12. Goh, Y. F., Akram, M., Alshemary, A., & Hussain, R. (2016). Antibacterial polylactic acid/chitosan nanofibers decorated with bioactive glass. Applied Surface Science, 387, 1-7.
13. Kumar S. and Koh J., (2012). Physiochemical, Optical and Biological Activity of Chitosan-Chromone Derivative for Biomedical Applications, *Int. J. Mol. Sci.*, *13*, 6102-6116.
14. Gokila S., Gomathi T., Sudha P.N., Anil S.,, (2017). Removal of the heavy metal ion chromiuim(VI) using Chitosan and Alginate nanocomposites, Int J Biol Macromol. Nov;104(Pt B):1459-1468.
15. Annaduzzaman, M., (2015). Chitosan biopolymer as an adsorbent for drinking water treatment – Investigation on arsenic and uranium. TRITA-LWR LIC-2015-02, 26p.

BOOK OF FULL TEXT PROCEEDINGS TURKISH PHYSICAL
SOCIETY 35th INTERNATIONAL PHYSICS CONGRESS (TPS35)
TPS35, Vol.01, No.01, pp.17-22.
ISBN:978-605-83516-6-0

15 December 2019

Assessment of Acoustic Performance of Stratified Composites Prepared from Recycled Paper and Polyurethane Foam

Doğukan BİNGÖL[1], Merve SİRKECİ[1], Burak ÖZYÜREK[2], Erhan SANCAK[3], Feyza GÜZELÇİMEN[4,a]

[1] *Graduate School of Engineering and Sciences, Istanbul University, TR-34116, Beyazıt, Istanbul, Turkey*
[2] *YÖK Fundamental Sciences Program, Faculty of Science, Istanbul University, 34134, Vezneciler, Istanbul, Turkey*
[3] *Department of Textile Engineering, Technical Education Faculty, Marmara University, TR-34722, Kuyubaşı, Istanbul, Turkey*
[4] *Istanbul University, Faculty of Science, Physics Department, TR-34134, Vezneciler, Istanbul, Turkey*

[a)] Corresponding author: feyzag@istanbul.edu.tr

Abstract. Sound absorbing materials with porous structure are effective on reducing noise pollution. For acoustic performance of the materials, sound absorption is a characteristic parameter. In the present study, a part of samples was obtained from recyclable paper waste with melted wax by turning into a slurry. The other samples were formed in layers; medium one is well-mixed and pressed paper waste, the top-bottom ones are polyurethane foam. The acoustic measurements were performed on two-microphone transfer-function method in accordance with the ISO 10534-2 standard. Frequency-dependent sound absorption coefficient values have been determined for all samples. By using these numerical data, the noise reduction coefficients have been calculated. The compared results with each other have been presented.

INTRODUCTION

Natural materials are becoming attractive for use in several applications due to acoustic properties. However, studies have been mostly dedicated to understanding their Carbon retention and Oxygen production properties, but few are focusing on their sound attenuation behaviour [1].

Polyurethane foam included large number of cells in a polymer is also a prominent material. Foam can have an open, partially open, or a closed cell structure [2]. Polyurethane foams that can have an open, partially open, or a closed cell structure are used due to their mechanical, electrical, thermal and acoustic properties [3]. Polyurethane foam and the combination of foam with different materials are utilized in most of the thermal and acoustic insulations [4].

Nowadays the problem of noise has become much more serious; the demands for a better environment are increased. Therefore, the thin, lightweight, low-cost, natural and recyclable materials that will absorb sound waves in a region of wide frequencies are highly desirable [5].

ISBN:978-605-83516-6-0

The reduction and recycling of wastes is significantly preferred in current environmental studies. In addition, the basis of recycling has been form by means of segregation, decomposition and stabilization of organic wastes [6, 7].

The goals of the study are to investigate the impact on the reduction of noise pollution of composite made from recycled paper and to determine sound absorption coefficient, noise reduction coefficient of composite formed by recycled paper and polyurethane.

MATERIAL AND METHOD

A five-step process have been followed to obtain composite materials made from recycled paper:

- Designation and manufacturing of molds suitable for measurement,
- Preparation of recycled paper,
- Mixing wax with paper,
- Preparation of polyurethane foam,
- Combination the wax+paper with polyurethane foam.

The composites have a certain fluidity in preparation and become irregular as time passes. However, experimental set-up is allow us to measure materials with a diameter of 29 and 100mm, thus the materials should be formed in molds suitable for the test tube. Polyacetal (POM) material with high mechanical strength, rigidity (rockwell hardness: M94, R 120) and temperature resistance (-500, +1600) was used for the raw material of mold [8]. Technical drawings of the molds are given in Fig. 1 a-b.

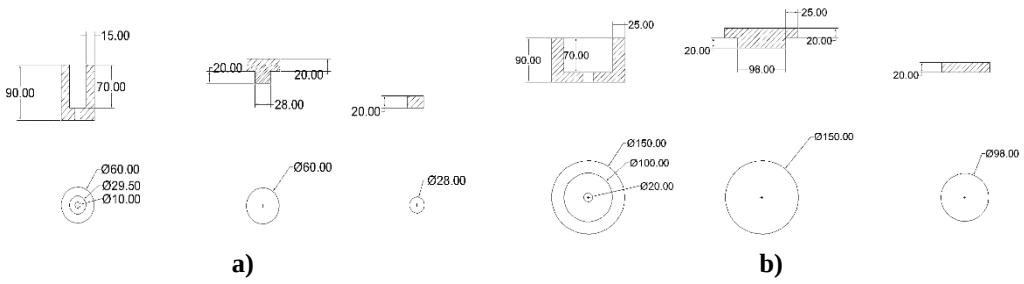


Fig. 1: Technical drawings of the molds with diameters of a) 29 and b)100 mm.

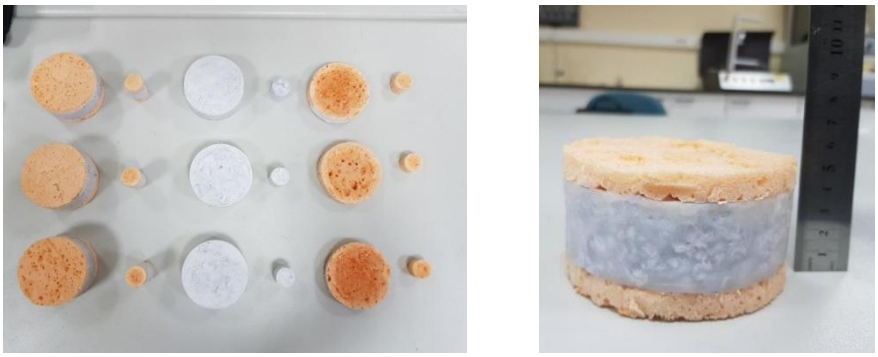
The further steps for forming composite are: Recycled papers were kept in hot water for two hoursa and then the excess water is removed from paper pulp. After waiting for about 1 hour, the pulp was divided into small pieces and mixed with melted wax. The prepared material was poured into molds and samples were formed with diameters of 29-100 mm (Fig. 2a-b).



Fig. 2: Wax+paper mixed composites with diameter of a) 29 mm, b) 100 mm.

ISBN:978-605-83516-6-0

Polyurethane foam layer was placed in front of and behind the paper-wax composite to prevent easy flammability. Three samples have been created for each form with 29 mm and 100 mm diameters of polyurethane foam, wax-paper mix and composite (Fig. 3a). The foam and composite are 1 cm and 3 cm thick, respectively (Fig. 3b).



(a) **(b)**

Fig. 3: a) All composites, b) the side view of one composite example.

The experiment is based on two microphone transfer function method. A sample of material to be measured is placed in a sample holder and mounted to one end of a straight tube. There is a rigid plunger with an adjustable depth behind the sample to provide a reflecting surface. A sound-source is connected at the opposite end of the tube. A pair of microphones is mounted in the tube [9].



Fig. 4: Impedance tube kit (4206) used in experimental set-up.

The measurement is on the ability to determine the sound reflection factor r from the transfer function H_{12} measured between the two microphone positions in front of the test-material. The sound pressures of incoming wave p_I and reflected wave p_R are;

$$p_I = \hat{p}_I e^{jk_0 x} \tag{1}$$

$$p_R = \hat{p}_R e^{-jk_0 x} \tag{2}$$

where $\hat{p}_I$ and $\hat{p}_R$ are the amplitudes of p_I and p_R in the reference plane (x = 0), respectively; $k_0 = k_0' - jk_0''$ is the number of complex waves. Sound pressures at two microphone positions p_1 and p_2 are;

$$p_1 = \hat{p}_I e^{jk_0 x_1} + \hat{p}_R e^{-jk_0 x_1} \tag{3}$$

ISBN:978-605-83516-6-0

$$p_2 = \hat{p}_I e^{jk_0x_2} + \hat{p}_R e^{-jk_0x_2} \quad (4)$$

Transfer function only for incoming wave $H_1$is;

$$H_1 = \frac{p_{2I}}{p_{1I}} = e^{jk_0(x_1 - x_2)} = e^{-jk_0s} \quad (5)$$

where $s = (x_1 - x_2)$, refers to the distance between the two microphones. Similarly, transfer function only for the reflected wave H_R is;

$$H_R = \frac{p_{2R}}{p_{1R}} = e^{jk_0(x_1 - x_2)} = e^{-jk_0s} \quad (6)$$

If the transfer function for the entire sound field H_{12} is (considering $\hat{p}_R = r\hat{p}_I$);

$$H_{12} = \frac{p_2}{p_1} = \frac{e^{jk_0x_2} + re^{-jk_0x_2}}{e^{jk_0x_1} + re^{-jk_0x_1}} \quad (7)$$

With the help of (5) and (6) equations, r is; defined as;

$$r = \frac{H_{12} - H_I}{H_R - H_{12}} e^{2jk_0x_1} \quad (8)$$

Thus, the sound reflection factor r at the reference plane (x = 0), the transfer functions, the distance of x_1 and the wave number k_0, which may include the pipe attenuation constant k_0'', can be determined. The sound absorption coefficient is calculated using the sound reflection coefficient as;

$$\propto = 1 - |r|^2 = 1 - r_r^2 - r_i^2 \quad (9)$$

where r_r represents the real component of the sound reflection factor and r_i represents the virtual component. A sound absorption coefficient value could calculate for each frequency from measurements.

For any particular material, the absorption properties are a function of the frequency. In order to rate the overall absorbent property of the material, the noise reduction coefficient (NRC) is used as a measure of the arithmetic average ratio of coefficients in certain frequency range [9, 10]:

$$NRC = \frac{1}{4}(\propto_{125} + \propto_{250} + \propto_{500} + \propto_{1000} + \propto_{2000} + \propto_{4000}) \quad (10)$$

In this study, the impedance tube (Brüel & Kjaer 4206) in the Textile Engineering Department of Marmara University, Faculty of Technology was utilized for acoustic measurements. The following conditions were taken into consideration in terms of the accuracy of the measurement:

- Environmental setting of ambient air temperature, relative humidity and atmospheric pressure,
- Microphone calibration,
- Thickness of sample,
- Signal-to-noise ratio evaluation: background noise measurement and signal measurement.

Considering these conditions, the atmospheric pressure of the test medium is 100.7 - 101.5hPa, the temperature of the medium is 24.5 - 27.5 ^{0}C and the humidity is 64.6 - 69.2% during the experiment.

ISBN:978-605-83516-6-0

RESULTS

Linearly increasing sound level in the frequency range was performed in impedance tube experiment for polyurethane, wax+paper mix and composite. Fig. 5 shows the graph of sound absorption coefficient versus sound frequency in the range of 50-6400 Hz. There are three frequency-sound absorption coefficient spectra based on 2 Hz frequency change for each sample type (wax+paper, foam, composite).The average spectrum of each one is shown in Fig. 5.

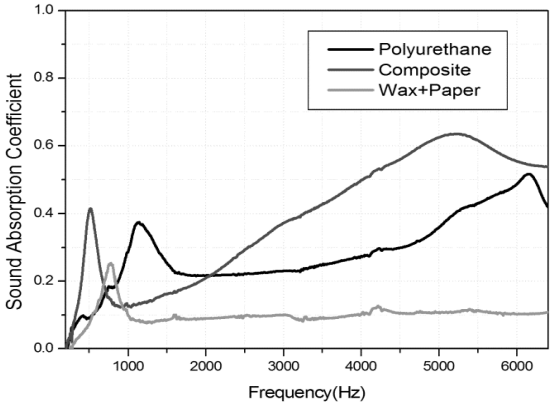


Fig. 5: Sound absorption coefficient values of polyurethane, wax+paper mix and composite.

Indicating the sound absorbing properties of materials by using the absorption coefficient values at different frequency ranges might be too complex. Thus for all samples, the noise reduction coefficient (NRC) values are calculated and the results are given in Fig. 6. The composite material has the maximum NRC value of 0.196, which is higher than rigid polyurethane foam. Noteworthy results have been observed that the noise reduction coefficient increased an average value of 0.196 for composite prepared in this study comparing with polyurethane foam. The composite material have better acoustic properties compared to polyurethane foam. However, we can also comment that with the increase of paper waste percentage, the value of noise reduction coefficient (NRC) also increases.

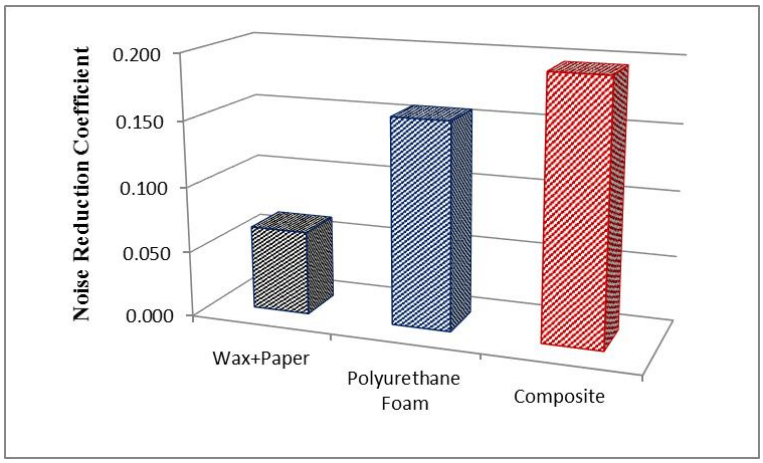


Fig. 6: Noise reduction coefficient values of wax+paper, polyurethane foam and composite.

Properties of materials obtained in this study are of a great importance for improving and for developing new materials with better acoustical properties. Alternative composite materials can be cost beneficial as well as useful in

ISBN:978-605-83516-6-0

developing materials from natural and recycled resources. The developed composite with different percentage of recycled paper can be used both in the outdoor and in the indoor environment.

REFERENCES

1. Lee HP., Pun Ng BM., Rammohan AV., and Tran LQN., An Investigation of the Sound Absorption Properties of Flax/Epoxy Composites Compared with Glass/Epoxy Composites, Journal of Natural Fibers, 2017, 14(1), 71–77.
2. Niaounakis, M., Biopolymers: Processing and Products, Chapter 9–Foaming and Foamed Products, Elsevier, 2015.
3. Verdejo, R., Stampfli, R., Alvarez–Lainez, M., Mourad, S., Rodriguez–Perez, MA., Bruhwiler, PA., et.al. Enhanced acoustic damping in flexible polyurethane foams filled with carbon nanotubes. Compos Sci Technol 2009;69:1564–9.
4. Kapps, M., Buschkamp, S., The production of rigid polyurethane foam, Insulation Technical Information, Bayer Material Science; 2004, http://virtualpu.com/uploads/user_doc_attachment/0-2015-04-16%2018:32:05-T_The-production-of-rigid-polyurethane-foam.pdf
5. Hong, Z., Bo, L., Gungsu, H. and Jia, H., A novel composite sound absorber with recycled rubber particles, Journal of Sound and Vibration, 2007, 304, 400–406.
6. Bahrami, B. and Jafari, P., Paper recycling, directions to sustainable landscape, International Journal of Environmental Science and Technology, 2019, 1-12.
7. Amritha PK. and Anilkumar PP. Development of Landscaped Landfills Using Organic Waste for Sustainable Urban Waste Management, National Institute Of Technology, Calicut, India. Procedia Environ. Sci., 2016, 35, 368–376.
8. Bashford, D., Polyoxymethylene; Polyacetals (POM). In: Thermoplasticis, Springer, Dordrecht, 1997 pp 255-267.
9. Simpson, MA., Noise Barrier Design Handbook, U.S. Department of Transportation Federal Highway Administration Office of Research, Washington DC., 1976.
10. Zhang H., Building Materials In Civil Engineering, Woodhead Publishing Limited and Science Press, UK, 2011.

BOOK OF FULL TEXT PROCEEDINGS TURKISH PHYSICAL
SOCIETY 35th INTERNATIONAL PHYSICS CONGRESS (TPS35)
TPS35, Vol.01, No.01, pp.23-26.
ISBN:978-605-83516-6-0

15 December 2019

Nanostructured TiO_2 Layer Thickness Dependence of the Surface Morphology and Acoustic Impedance

Doğukan BİNGÖL[1], Merve SİRKECİ[1], Halil İbrahim EFKERE[2], Yunus ÖZEN[2], Meltem DÖNMEZ KAYA[2], Bükem TANÖREN[3], Barış KINACI[4], Feyza GÜZELÇİMEN[4,a]

[1] *Graduate School of Engineering and Sciences, Istanbul University, TR-34116, Beyazıt, Istanbul, Turkey*
[2] *Photonics Application and ResearchCenter, Gazi University, TR-06500, Ankara, Turkey*
[3] *Department of Physics, Faculty of Science and Arts, Boğaziçi University, TR-34342, Istanbul, Turkey*
[4] *Istanbul University, Faculty of Science, Physics Department, TR-34134, Vezneciler, Istanbul, Turkey*

[a)] Corresponding author: feyzag@istanbul.edu.tr

Abstract. We report that the effect of layer thickness of TiO_2 thin films on the morphological and acoustical properties is evaluated in this study. TiO_2 layers with five different thicknesses at 50 nm, 75 nm, 100 nm, 125 nm, 150 nm were grown on p-type Si substrate using sputtering system. Atomic force microscopy (AFM) was performed as one part of the present study and was used to obtain the surface morphological analysis of the grown layers. The other part was assessment of acoustic impedance values that were determined by measurements carried out scanning acoustic microscopy (SAM). The study have presented that the acoustic impedance values depends obviously on the thickness considering the roughness of the films.

INTRODUCTION

In recent years, TiO_2 is one of the most interesting and usable materials. TiO_2 thin films have attracted the attention of the physicists, material scientists, physical chemists, and engineers due to its semiconductor and catalytic properties [1]. It is utilized as a desiccant, brightener, layer or reactive mediator in several fields such as drugs, cosmetics, paints, pharmaceuticals, sunscreens, solar cells, gas sensors. TiO_2 film is a major component of next-generation solar cells [2, 3]. Several strides solar cells have been significantly made to achieve efficiencies by designing in different shapes with TiO_2 nanostructure layer due to optical and electronic properties. Nowadays, the practical uses of shape- and size-controlled TiO_2 nanostructures is common in areas such as energy conversion and storage.

In this study, it is aimed to determine whether the roughness, thickness and acoustic impedance parameters of thin films are correlated with each other. We have studied investigation of the morphological and acoustical properties of TiO_2 thin films with different thicknesses of 50 nm, 75 nm, 100 nm, 125 nm and 150 nm prepared by sputtering system (Nanovak, NVTS-500). The surface morphology and acoustical measurements were examined by atomic force microscopy (AFM) and scanning acoustic microscopy (SAM), respectively.

ISBN:978-605-83516-6-0

EXPERIMENTAL METHODS

Sputtering System:

The TiO_2 nanostructure layers was prepared by radio-frequency sputtering system (Nanovak, NVTS-500) placed at Photonics Application and Research Center, Gazi University.

The nano-layers with five different thicknesses were grown on p-type Silisium (Si) substrate in the argon (Ar) gas atmosphere with the base pressure about 10^{-6} Torr [4]. The distance between the target which is a TiO_2 ceramic disk with 0.125 thickness and 99.9% purity and substrate was about 8 cm. The rotation speed and pressure were kept at 5 rpm and 10^{-3} mTorr, respectively during the deposition. Then the thickness of the films was measured with a stylus type profile meter as 50 nm, 75 nm, 100 nm, 125 nm, 150 nm.

Atomic Force Microscopy (AFM):

The topology of film surfaces was examined by atomic force microscope (AFM) at Photonics Application and Research Center, Gazi University. Three-dimensional (3D) AFM images have been identified on 10×10 μm^2 scan area. The root mean square (RMS) values of the surface roughness have been measured for comprehending the surface uniformity.

Scanning Acoustic Microscopy (SAM):

SAM is an easy and quickly measuring technique without any operation on the material capable of detecting variations in elastic features of samples. SAM can measure and map micro-structure of the sample with variations in sound speed and acoustic impedance profiles [5].

In our study, SAM (Honda/AMS-50SI) device at Medical and Biological Physics Laboratory, Boğaziçi University was performed for identifying elasticity factor. The difference in acoustic impedance values is due to the variation of elasticity.

Fig. 1 shows the schematic of acoustic impedance measurement by scanning acoustic microscope.

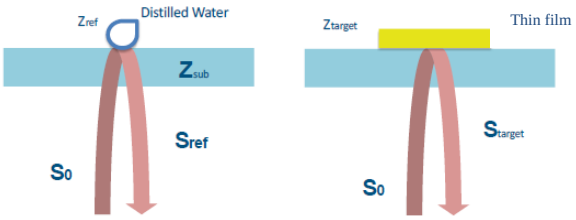


Fig. 1: Schematic for the principle of acoustic impedance measurement by SAM.

Reflected ultrasound signals from surfaces of water and sample are collected. The acoustic impedance of the sample is obtained from comparing the signals mentioned above. The same transducer radiates and receives the acoustic wave. The target-signal $\boldsymbol{S_{target}}$ is described as:

$$s_{target} = \frac{Z_{target}-Z_{sub}}{Z_{target}+Z_{sub}} S_0 \qquad (1)$$

where S_0 is the signal transmitted by the transducer, Z_{target} and Z_{sub} are the acoustic impedance of target and of substrate (2.37 MRayl), respectively. The reflected-signal $\boldsymbol{S}_{\text{ref}}$ is described as:

ISBN:978-605-83516-6-0

$$S_{ref} = \frac{Z_{ref}-Z_{sub}}{Z_{ref}+Z_{sub}} S_0 \quad (2)$$

where Z_{ref} is the acoustic impedance of reference material. The acoustic impedance of target is subsequently calculated as:

$$Z_{target} = \frac{1+\frac{S_{target}}{S_0}}{1-\frac{S_{target}}{S_0}} Z_{sub} = \frac{1-\frac{S_{target}}{S_{ref}}\left[\frac{Z_{sub}-Z_{ref}}{Z_{sub}+Z_{ref}}\right]}{1+\frac{S_{target}}{S_{ref}}\left[\frac{Z_{sub}-Z_{ref}}{Z_{sub}+Z_{ref}}\right]} Z_{sub} \quad (3)$$

where S_0 is assumed to be a constant during the observation process [6, 7].

RESULTS

We have investigated the morphological and acoustical properties of TiO_2 thin films with different thicknesses of 50 nm, 75 nm, 100 nm, 125 nm and 150 nm prepared by sputtering system. Atomic force microscopy (AFM) and scanning acoustic microscopy (SAM) were performed in order to analyse the surface morphology and acoustical measurements, respectively. Fig. 2 shows the 3D AFM images of TiO_2 samples produced in different thickness.

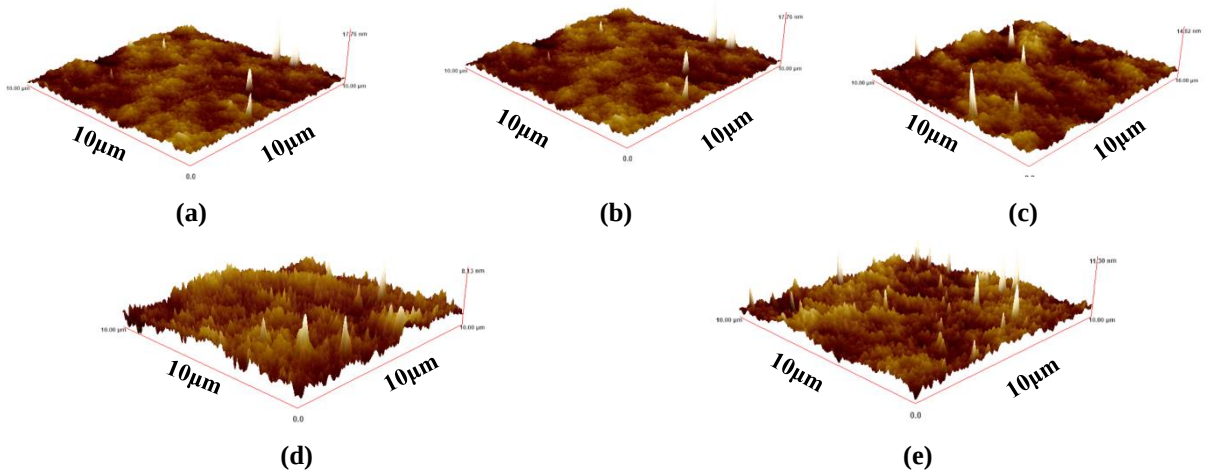
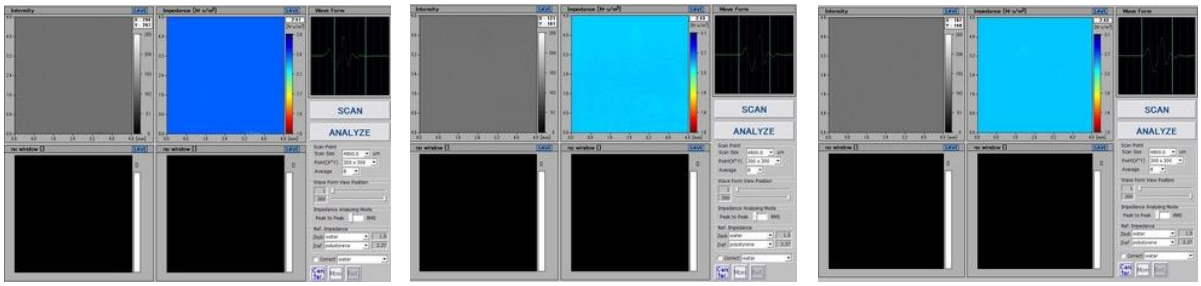
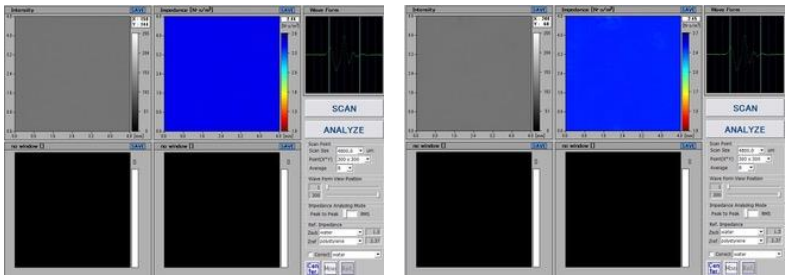


Fig. 2: 3D AFM images of thin films: a) 50 nm, b) 75 nm, c) 100 nm, d) 125 nm, e) 150 nm. The scan area is 10×10 µm^2.

Fig. 3 shows the cross-sectional view of SAM. Left top image is the intensity map and right top image is the acoustic impedance map of the sample. The samples scanned an area of about 16 µm^2 in 2D.



ISBN:978-605-83516-6-0



d) **e)**

Fig. 3: PC window of SAM showing cross-sectional view of thin films with thickness of a) 50nm, b) 75 nm, c) 100nm, d) 125 nm, e) 150nm. Scan area is 4.8 × 4.8 mm^2.

The root mean square (RMS) values are achieved from data by AFM and acoustic impedance values are calculated from data by SAM. The comparison between those values are given in Table 1.

Table 1. The root mean square (RMS) and acoustic impedance values of TiO_2 films with different thickness.

Thickness (nm)	RMS (nm)	Acoustic Impedance (μRal)
50	0.68	2.41
75	0.69	2.43
100	0.70	2.43
125	0.77	2.44
150	0.78	2.45

As a result, the study have presented that the acoustic impedance values depends obviously on the thickness and surface roughness of the films. In this study, we have determined a correlation between the surface roughness, thickness and elasticity of the investigated samples.

REFERENCES

1. Kamat, PV., TiO2 Nanostructures: Recent Phys. Chem. Adv., J. Phys. Chem. C, 2012, 116, 11849−11851.
2. Peter, LM., The Gratzel Cell: Where Next?, J. Phys. Chem. Lett., 2011, 2, 1861−1867.
3. Miyasaka, T., Toward Printable Sensitized Mesoscopic Solar Cells: Light-Harvesting Management with Thin TiO_2 Films. J. Phys. Chem. Lett., 2011, 2, 262−269.
4. Comert, B., Akin, N., Donmez, M., Saglam, S. and Ozcelik, S., Titanium Dioxide Thin Films as Methane Gas Sensors, IEEE Sensors Journal, 2016, 16(24).
5. Bilen, B., Kafa, Ü., Ünlü, MB., Characterization of Carotid Atherosclerotic Plaques by Measurement of Acoustic Impedance, Celal Bayar University Journal of Science, 2018, 14(3), 321-325.
6. Kobayashi, K, Yoshida, S, Saijo, Y, Hozumi, N, Acoustic impedance microscopy for biological tissue characterization, Ultrasonics, 2014, 54, 1922–1928.
7. Hozumi, N., Nakano, A., Terauchi, S., Nagao, M., Yoshida, S., Kobayashi, K., Yamamoto, S. and Saijo, Y., In IEEE International Ultrasonics Symposium, New Yorkz, NY, USA, 2007, 1051-0117/07.

BOOK OF FULL TEXT PROCEEDINGS TURKISH PHYSICAL
SOCIETY 35th INTERNATIONAL PHYSICS CONGRESS (TPS35)
TPS35, Vol.01, No.01, pp.27-30.
ISBN:978-605-83516-6-0

15 December 2019

Generation of Programmable Diffractive Lenses with Multiple or Multi-Optical Axes, Multi–Focus, Dynamic Distance Control of Focal Lengths and Energy Intensities at Foci

Gurkan Celik[1, a)], Gamze Kaya[2], Mustafa Kurt[3] and Necati Kaya[1,4]

[1]*Department of Physics, Graduate School of Natural and Applied Sciences, Canakkale 18 Mart University, Canakkale, Turkey*
[2]*Electric and Energy Programs, Canakkale Vocational School of Technical Sciences, Canakkale 18 Mart University, Canakkale, Turkey*
[3]*Department of Physics, Faculty of Arts and Sciences, Canakkale 18 Mart University, Canakkale, Turkey*
[4]*Department of Energy Management, Canakkale School of Applied Sciences, Canakkale 18 Mart University, Canakkale, Turkey*

[a)] Corresponding author: gurkancelik91@gmail.com

Abstract. In this study, we aimed to develop programmable diffractive lenses with coaxial multi-focus by generating holographically programmable Fresnel diffractive lenses. The focal distances and energy densities in the foci can be dynamically controlled by computer generated holographic codes. These holographic lenses with multi-transverse focus phases can be used in application areas such as creating image systems by performing multiple focus manipulations fast enough by creating axial copies of the transverse foci very easily and quickly. Since the holographic Fresnel lens is producible in the light intensity of 10^{11}W/cm^2 level, they find applications in the nonlinear optics such as the high harmonic generation from the laser and molecules interaction.

INTRODUCTION

Diffractive optical elements reproduced by spatial light modulators (SLM) provide solutions for applications that require complex phase profiles. Those are difficult to construct with the conventional optics [1, 2]. Currently, liquid crystal displays operating as phase modulators are widely used in processing optical information for the reproduction of diffractive optical elements which provides the additional advantage of being programmable and computer controllable [3]. There are several studies of the combination of different diffractive lenses in the same device [4-9]. The diffractive lenses are now widely used optical elements in a wide range of applications, so the simple and predictive design of diffractive lenses will be of great interest. It is possible to change the distance between the focal points and the energy densities in the foci of the multifocal diffractive lenses by only changing the modulation depth and the grating period of the grating but, for each targeted optical arrangement, new grating structures are needed to be fabricated. These grating structures are very difficult to form and contain certain technological constraints. There are some efforts in the literature to solve this problem. For example, the approaches to design a variable focal length in grayscale photolithography by using supercontinuum and specific wavelength light [10] or lenses with extended focal length with focal modulation using rotating phase filters were applied [11]. However, in these diffractive lens designs, it is not possible to provide a real-time dynamic energy distribution and focal point control between foci.

ISBN:978-605-83516-6-0

In this study, it is aimed to develop programmable diffractive lenses with multi-focus, dynamically control focal distance and energy densities in the foci by generating holographically programmable Fresnel diffractive lenses. Since holographic codes can be easily optimized by computer generated hologram of Fresnel diffractive lenses, the intensity distribution and distance between the foci can be easily obtained. The advantages of using fewer optical elements in multi-directional applications have a widespread effect in interdisciplinary and multidisciplinary scientific studies and application areas.

SPATIAL PIXELATION OF CONTINUOUS FRESNEL LENS FUNCTIONS

We consider the second order phase pattern of a lens with a focal length f given by $\varphi(x_0, f)$. The second order phase distribution of the convergent lens placed in the plane of (x, y) rectangular coordinates as a continuous function can be expressed as

$$\varphi\left(x,\mathrm{y},f\right)=e^{-j\frac{\pi}{\lambda f}(x^2+y^2)} \tag{1}$$

where f is the focal length and λ is the wavelength of light. Suppose this lens function is represented by a sampling period given by pixel area (or pixel pitch). The lens should be represented in the light modulator by the $M \times M$ pixel matrix with a squared pixel pitch and a gradation factor smaller than the unit. We assume that the lens pattern mostly reaches the circular contour of the aperture and therefore no secondary lenses form. This means that the focal length f must be equal to or longer than the reference focal length f_r, which is the critical distance. The repeat period (Δ) must be dependent on the pixel (M_i) and wavelength. The focal length depending on the repeat period Δ, the pixels (M_i) and wavelength λ must be

$$f \geq f_r\left(\lambda\right)=\frac{M_i\Delta^2}{\lambda} \tag{2}$$

The maximum diameter R is in the circular range across the screen of the light modulator as $R = M_i\Delta/2$. Thus, the discrete phase distribution can be written in one dimension for simpler expression as

$$\varphi\left(\Lambda,f\right)=exp(-j\frac{\pi}{\lambda f}\frac{R^2}{M_i}\Lambda) \tag{3}$$

where R is the diameter of the lens corresponding to the given number of pixels and Λ values are between $\left(-\frac{M_i}{2}+1\right)$ and $\left(\frac{M_i}{2}\right)$.

EXPERIMENTAL DETAILS

Firstly, the light modulator is calibrated according to the laser phase modulation of [0, 2π] in 256 grayscales. For the wavelength of the laser source, the yield graphs are obtained in different grating periods for different grayscales as we did before in Ref [12]. Then, the holograms are created in MATLAB codes using Fresnel lenses in grayscale at 0-255 scale due to diffraction of light intensity. We present an example hologram of 600x800 pixels to focus the

ISBN:978-605-83516-6-0

beam on three coaxial focal points in Fig.1. In the Fig. 1, the modulation depth and repetition period are exaggerated in order to better see the phase transitions at 256 depth in grayscale.

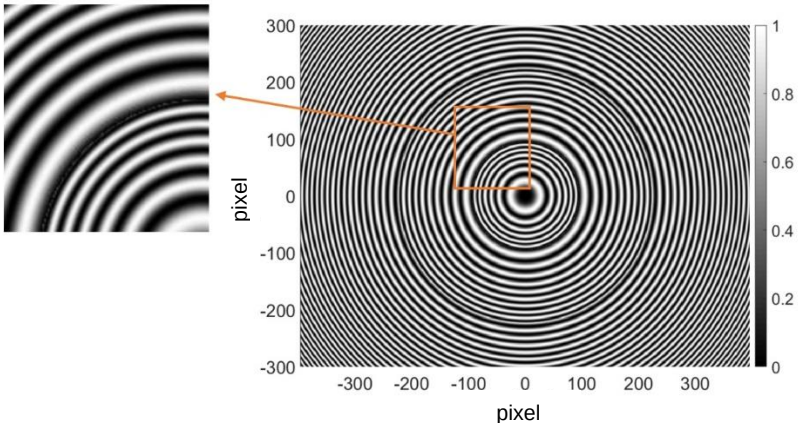


FIGURE 1. 600x800 pixels size hologram to focus the beam on three coaxial focal points.

The experimental setup is shown in Fig. 2. The holograms are produced on the computer and reflected on the screen of the light modulator. The incident laser beam is modulated according to the phase mask of the generated programmable holograms and reflected in different diffraction orders. By optimizing the grating structure of the holograms, the beam intensity is obtained by maximizing the light intensity for the +1 order of diffraction. After input parameters is determined according to the light modulator, dynamic holograms can be obtained by changing the hologram parameters by computer control. Therefore, the focal length and energy density values at the foci can be controlled.

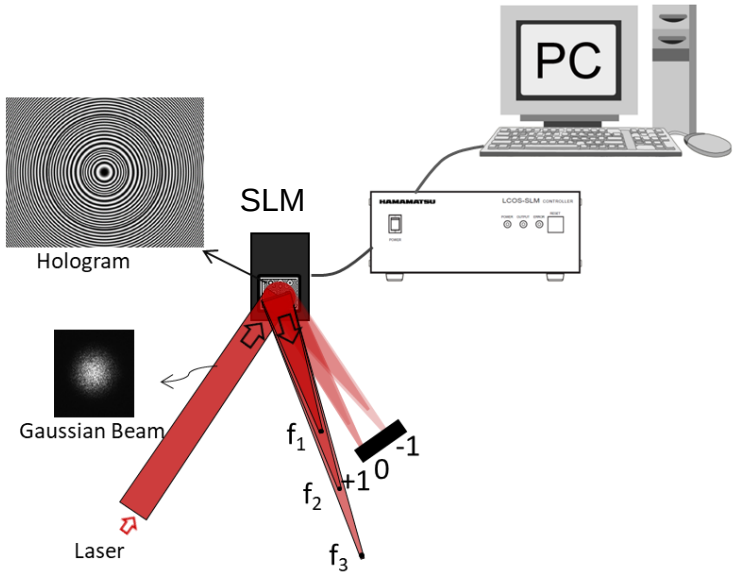


FIGURE 2. Experimental setup for coaxial multifocal holographic lens.

CONCLUSIONS

The aim of this study is to develop programmable diffractive multifocal coaxial lenses by producing holographically programmable Fresnel lenses. Since holographic codes can be easily optimized for the hologram of computer-

ISBN:978-605-83516-6-0

generated Fresnel diffractive lenses, the energy density distribution and distance between foci can be easily obtained. The advantages of using fewer optical elements in multi-directional applications will have a widespread effect in interdisciplinary and multidisciplinary scientific studies and application areas. With the holographically programmable Fresnel lenses, the ability to focus the laser energy on very small (micron scale) points, control dynamically the distance between the focal lengths and the distribution of the energy between the foci let us to have a high-aspect-ratio blind micro holes in high-precision cutting surface and laser drilling operations. These lenses with multi-transverse focus phases can be used in application areas such as creating image systems by performing multiple focus manipulations fast enough by creating axial copies of the transverse foci very easily and quickly. We can also produce the holographic Fresnel lenses up to the laser intensity of $10^{11}W/cm^2$ level, so one can use them in the nonadiabatic molecular alignment in the nonlinear optics with the pump-probe experiments. By creating proper orientations of molecules, one can be able to study on the high harmonic generation from the laser and molecules interaction.

REFERENCES

1. Laude, V., *Twisted-nematic liquid-crystal pixelated active lens.* Optics Communications, 1998. 153(1): p. 134-152.
2. Davis, J.A., et al., *Multiplexed phase-encoded lenses written on spatial light modulators.* Optics Letters, 1989. 14(9): p. 420-422.
3. Ambs, P., L. Bigue, and E. Hueber, *Implementation of diffractive optical elements onto liquid crystal devices*. Optical Science and Technology, the SPIE 49th Annual Meeting. Vol. 5518. 2004: SPIE.
4. Iemmi, C., et al., *Depth of focus increase by multiplexing programmable diffractive lenses.* Optics Express, 2006. 14(22): p. 10207-10219.
5. Márquez, A., et al., *Achromatic diffractive lens written onto a liquid crystal display.* Optics Letters, 2006. 31(3): p. 392-394.
6. Vázquez-Villa, A., et al., *Aspheric lens to increase the depth of focus.* Optics Letters, 2015. 40(12): p. 2842-2845.
7. Marin, P., et al., *Labeling technique for nonplanar surfaces based on the combination of a diffractive axilens with digital holography methods.* Optical Engineering, 2015. 54(5): p. 1-8, 8.
8. Pérez-Cabré, E. and M.S. Millán, *Liquid Crystal Spatial Light Modulator with Optimized Phase Modulation Ranges to Display Multiorder Diffractive Elements.* Applied Sciences, 2019. 9(13): p. 2592.
9. Millán, M.S., J. Otón, and E. Pérez-Cabré, *Chromatic compensation of programmable Fresnel lenses.* Optics Express, 2006. 14(13): p. 6226-6242.
10. García, J.A., et al., *Imaging with extended focal depth by means of the refractive light sword optical element.* Optics Express, 2008. 16(22): p. 18371-18378.
11. Valle, P.J., V.F. Canales, and M.P. Cagigal, *Focal modulation using rotating phase filters.* Optics Express, 2010. 18(8): p. 7820-7826.
12. Strohaber, J., et al., *In situ tomography of femtosecond optical beams with a holographic knife-edge.* Optics Express, 2011. 19(15): p. 14321-14334.

BOOK OF FULL TEXT PROCEEDINGS TURKISH PHYSICAL
SOCIETY 35th INTERNATIONAL PHYSICS CONGRESS (TPS35)
TPS35, Vol.01, No.01, pp.31-36.
ISBN:978-605-83516-6-0

15 December 2019

Preparation of PAN/PMMA-Based Antibacterial Carbon Nanofiber by Electrospinning Method

Atilla Evcin[1, a)] and Nalan Çiçek Bezir[2,b)]

[1]*Afyon Kocatepe University, Materials Science and Engineering Department, 03200, Afyonkarahisar, Turkey*
[2]*Süleyman Demirel University, Physics Department, 32260, Isparta, Turkey*

[a)]Corresponding author: evcin@aku.edu.tr
[b)] cicekn@gmail.com

Abstract. In this study, carbon nanofibers have been synthesized from solutions of polyacrylonitrile/Poly(methyl methacrylate) (PAN/PMMA) by electrospinning method. Production of antibacterial carbon nanofiber (CNF) with silver doping was investigated. The antibacterial properties of pure and Ag doped CNF were tested on Staphylococcus aureus bacteria. The antibacterial effect of these fabricated nanofibers has been determined by disc diffusion and Baird parker methods. Three different electric fields were applied to investigate effect on carbon nanofiber structure. The carbon nanofibers have been first stabilized by oxidation at 250 °C for 2 h in air and then carbonized at 750 °C for 1 h in H2/N2. Morphological properties of carbon nanofibers have been examined by scanning electron microscopy (SEM). The images have been analyzed to study the fiber morphology and to determine the distribution of the fiber diameter using FibraQuant 1.3 software. The antibacterial activity of CNFs was evaluated against S. aureus. At result, homogeneous carbon nanofibers were obtained with optimized electrospinning conditions.

INTRODUCTION

Over the last ten years, the development of advanced nanomaterials based on Carbon Nanofiber (CNF) has shown a special interest in many technological and industrial areas [1]. Carbon nanofibers are one dimensional nanomaterial for polymer composites because of their specific properties. Typical methods used to fabricate CNFs involve electrospinning, chemical vapor deposition (CVD), solid-state reaction et al [1-4]. Its precursors are generally polyacrylonitrile (PAN), polyimide, PMMA, polyvinyl alcohol (PVA), polybenzimidazole, phenolic resins, Polyvinylidene fluoride (PVDF), cellulose and pitch [5]. In Figure 1, electrospinning is a technological method commonly used to produce nanosized fiber from polymer solutions [6-9]. Many nanofibers such as ceramic, polymer and composite are nowadays begun to be utilized in many applications in our daily life. Nanofibers have gained a lot of attention among scientists. Many properties change at the nanometer size. Nanofibers have a large surface area and unique mechanic, optical, magnetic, electronic and chemical properties [7,8].

Türk Fizik Derneği
1950
Turkish Physical Society

ISBN:978-605-83516-6-0

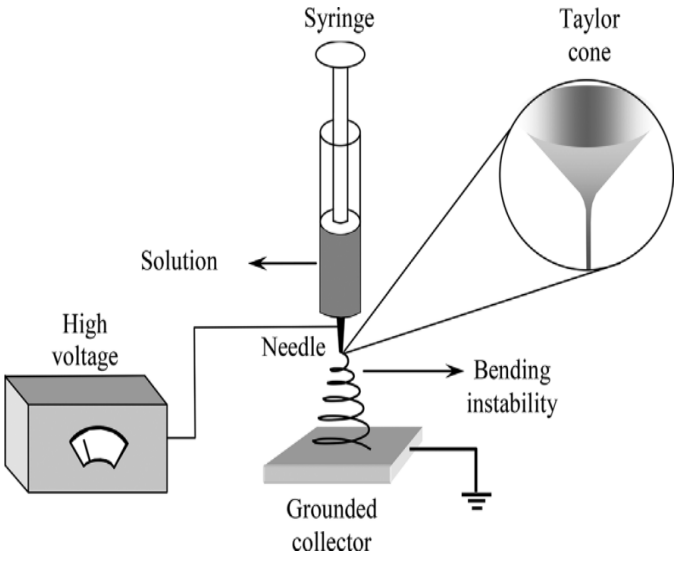


FIGURE 1. Electrospinning process [9]

MATERIALS AND METHOD

Polyacrylonitrile [(C3H3N]x , Mw=150,000 g/mol), Poly(methyl methacrylate) [CH2C(CH3)(CO2CH3)]n, Mw=100,000 g/mol), N,N-dimethylformamide (N,N DMF, HCON(CH3)2 , Mw=73.09 g/mol), and silver nitrate (AgNO3, >99% Mw= 169.87 g/mol) is used as the starting polymer reagents, solvent and antibacterial agent source respectively.

Pure and Ag doped PAN/PMMA solutions were prepared by dissolving in N,N DMF as described in detail elsewhere [7,8]. Amount of silver was 0.01wt% of PAN/PMMA solutions. 8wt% solutions of PAN and PMMA in N,N DMF were mixed. Nanofibers were produced by means of the homemade electrospinning experimental set-up in the Advanced Technology Materials Laboratory at Afyon Kocatepe University (Fig 2).



FIGURE 2. Home-made electrospinning setup

The first group CNFs samples were produced applying a constant heights of the needle (10 cm) and constant flow rate (0.5 mL/h) at different voltages (20, 25 and 30 kV). Then stabilization and carbonization treatments were applied. The detailed methods for stabilization and carbonization treatments is described elsewhere [7,8]. The

ISBN:978-605-83516-6-0

diameter distribution, mineralogical and morphological properties of the pure and Ag doped CNFs were evaluated by FibraQuant 1.3 software, X-ray diffraction (XRD 6000-Shimadzu) and SEM analysis (Leo 1430 VP).

RESULTS

As seen from Figure 3 the formation of silver NPs was proved using XRD.

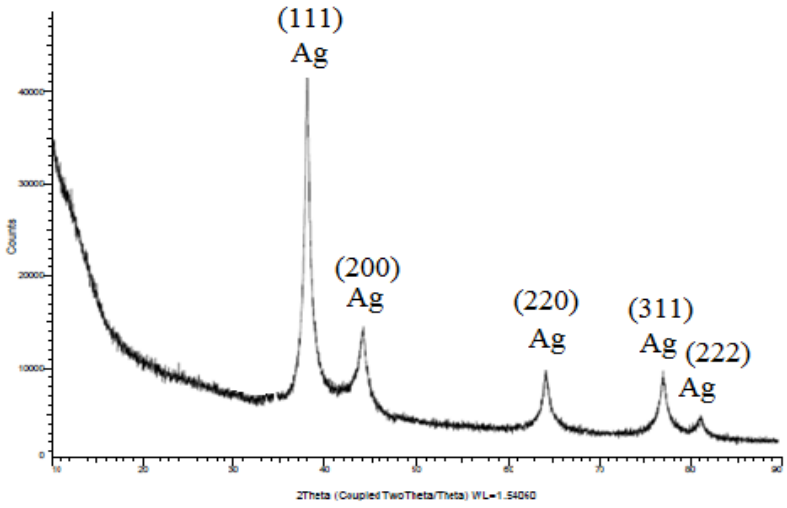


FIGURE 3. XRD analysis of Ag doped antibacterial carbon nanofibers

Figure 3 displays five major peaks at 27, 32, 46, 54, 57° diffraction angles corresponding to (111), (200), (220), (311) and (222) orientation planes respectively. This confirms that the prepared Ag doped antibacterial carbon nanofibers have the face centered cubic (FCC) structure [10-11].

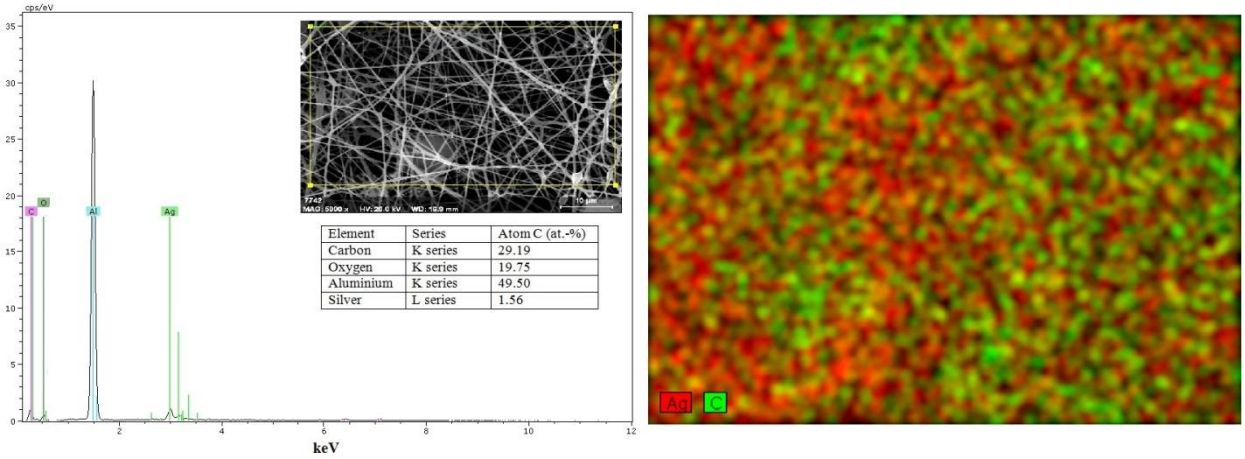


FIGURE 4. SEM-EDX results of CNFs.

Figure 4 shows SEM-EDX analysis and elemental mapping. The SEM-EDX elemental mapping images of Ag doped antibacterial carbon nanofibers confirm the arrangements of C (green) and Ag (red) nanoparticles [12]. It shows that C and Ag elements were homogeneously distributed.

Figure 5 shows SEM photos of pure and Ag doped CNFs produced at different voltage (20, 25, 30 kV). The effect of applied voltage on mean nanofiber diameter is shown in Figure 5. The mean nanofiber diameter is decreased as the applied voltage enhanced from 20 to 30 kV. In stabilization and carbonization step, non-carbon

ISBN:978-605-83516-6-0

elements were removed in form of various gases such as NH_3, HCN and H_2O which cause to shrinkage of nanofibers diameter [13].

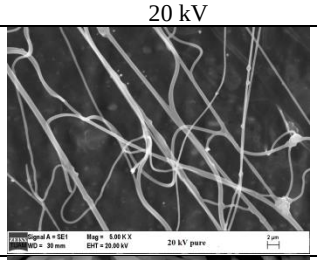
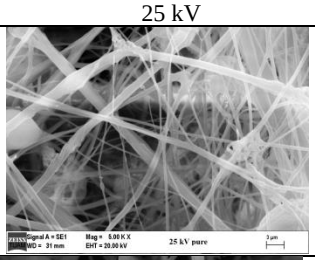
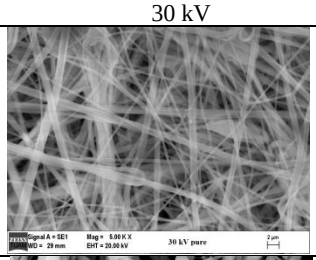
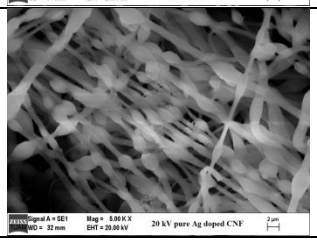
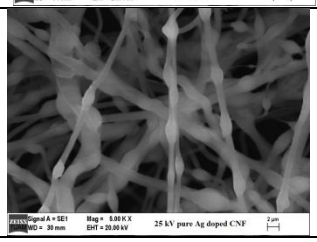
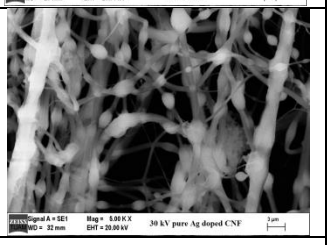
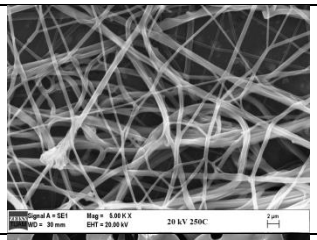
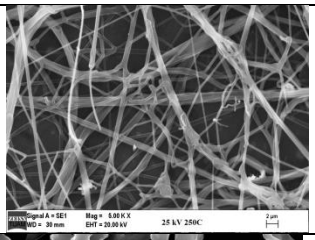
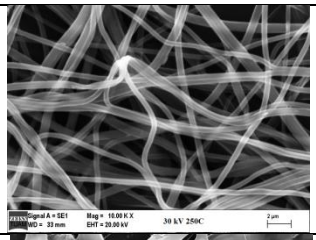
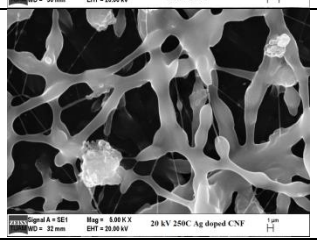
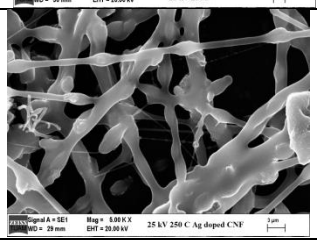
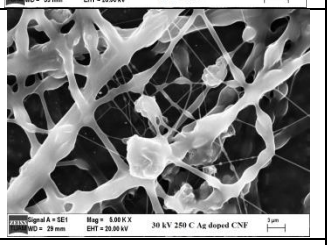
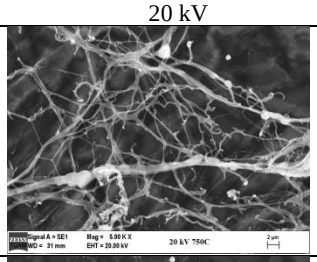
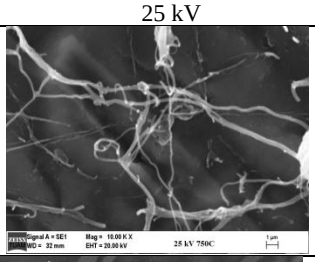
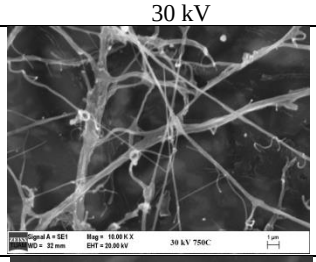
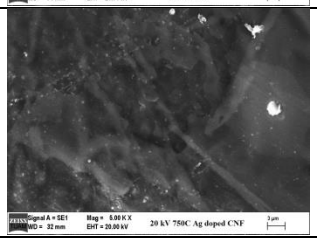
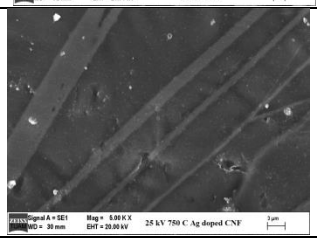
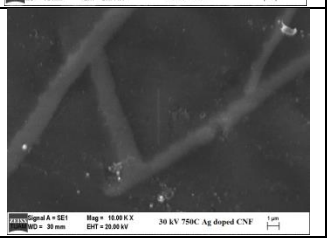
	Before heat treatment		
	20 kV	25 kV	30 kV
Pure CNFs			
Ag doped CNFs			
	After stabilization at 250°C		
	20 kV	25 kV	30 kV
Pure CNFs			
Ag doped CNFs			
	After carbonization at 750 °C		
	20 kV	25 kV	30 kV
Pure CNFs			
Ag doped CNFs			

FIGURE 5. SEM images of CNFs after carbonization

ISBN:978-605-83516-6-0

TABLE 1. Distribution of CNFs diameters (nm) calculated by FibraQuant 1.3 software

	20 kV		**25 kV**		**30 kV**	
	Before heat treatment					
	Diameter	Std. Dev.	Diameter	Std. Dev.	Diameter	Std. Dev.
Pure CNFs	528	400	404	356	352	223
Ag doped CNFs	906	733	790	521	602	577
	After stabilization at 250 °C					
Pure CNFs	297	169	218	172	167	118
Ag doped CNFs	714	553	699	488	507	405
	After carbonization at 750 °C					
Pure CNFs	177	131	169	129	126	107
Ag doped CNFs	548	385	406	265	326	215

The average diameters of these pure and Ag doped CNFs depending on thermal treatments are shown in Table 1. As given in Table 1 diameter of both pure and Ag doped CNFs is bigger than that for the stabilized and carbonized CNFs. CNFs diameters decrease when the heat treatment temperature from 25° to 750°C increases. The effect of applied voltage on mean nanofiber diameter is clear for all samples. Decrease in nanofibers diameter can be described that by increasing applied voltage, the solution move faster from tip of nozzle to collector and polymer jet is stretched in less time, resulting in smaller nanofibers diameter. It is also seen that fiber diameters increase with the addition of silver [14].

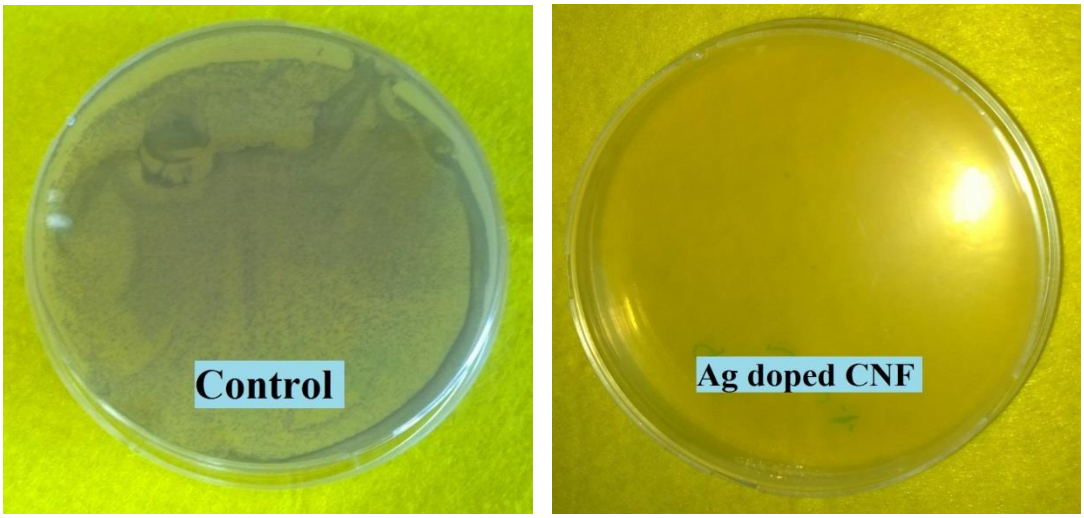


FIGURE 6. Antibacterial effect of Ag doped CNF against S. Aureus.

The antibacterial effect for control (pure) and Ag doped CNF samples can be seen in Figure 6. According to the results, good antibacterial effects were obtained against St. aureus. Antibacterial test showed that Ag doped CNFs had pronounced antibacterial activity against St. aureus [15].

ACKNOWLEDGMENTS

This work was supported by Afyon Kocatepe University via Scientific Research Projects (No: 16.KARİYER.17)

ISBN:978-605-83516-6-0

REFERENCES

1. A. Evcin and F. Ekşi, "SiO_2 doped carbon nanofiber by electrospinning process", AIP Conference Proceedings 2042, 020002 (2018); https://doi.org/10.1063/1.5078874
2. G.G. Tibbetts, C.A. Bernardo, D.W. Gorkiewicz, R.L. Alig, Carbon **32** 569–576 (1994).
3. T. Hyeon, S.J. Han, Y.E. Sung, K.W. Park, Y.W. Kim., Angewandte Chemie **42**, 36 4352-4356 (2003) https://doi.org/10.1002/anie.200250856.
4. S. Amelinckx, X.B. Zhang, D. Bernaerts, X.F. Zahng, V. Lvanov, J.B. Nagy, Science **265** 635-639 (1994).
5. S. Ma., Y. Wang, Z. Liu, M. Huang, H. Yang, Z. Xu, Chemical Engineering Science, **205**, 181-189 (2019), https://doi.org/10.1016/j.ces.2019.05.001
6. A.A. Almetwally, E. Mohamed, M.H. Elshakankery, M.H. Kasem, Journal of the Textile Association **78**, 5-14 (2017).
7. A. Evcin, N. Çiçek Bezir, R. Duman, N. Duman, "UV Resistibility of a Carbon Nanofiber Reinforced Polymer Composite". World Academy of Science, Engineering and Technology, International Science Index 142, International Journal of Chemical, Molecular, Nuclear, Materials and Metallurgical Engineering, (2018), 12 (10), pp. 575-578., https://doi.org/10.5281/zenodo.1474769
8. A. Evcin, B. Ersoy, S. Akpınar, İ.S. Atlı "Characterization of Electrospun Carbon Nanofiber Doped Polymer Composites", World Academy of Science, Engineering and Technology, International Science Index 142, International Journal of Chemical, Molecular, Nuclear, Materials and Metallurgical Engineering, (2018), 12(10), pp. 509-513., https://doi.org/10.5281/zenodo.1474978
9. A. Evcin, N. Çiçek Bezir, R. Kayalı, M. Arı, and D.B. Kepekçi, Cryst. Res. Technol., **49**, 5, 303-308 (2014). https://doi.org/10.1002/crat.201300424
10. P. Senthilkumar, G. Yaswant, S. Kavitha, E. Chandramohan, G. Kowsalya, R. Vijay, B. Sudhagar, D.S. Ranjith, S. Kumar, International Journal of Biological Macromolecules, **141**, 290-297 (2019). https://doi.org/10.1016/j.ijbiomac.2019.08.234.
11. A.S. Hassanien, U.T. Khatoon, Physica B: Condensed Matter, **554**, 21-30, (2019). https://doi.org/10.1016/j.physb.2018.11.004.
12. R. Praveen, R. Ramaraj, Materials Chemistry and Physics, **238**, 121915, (2019). https://doi.org/10.1016/j.matchemphys.2019.121915.
13. M. Adabi, R. Saber, R. Faridi-Majidi, F. Faridbod, Materials Science and Engineering: C, **48**, 673-678, (2015). https://doi.org/10.1016/j.msec.2014.12.051.
14. S.J. Park, S.H. Im,Bulletin of the Korean Chemical Society. **29** 777–781 (2008). https://doi.org/10.5012/bkcs.2008.29.4.777
15. T.G. Volova, A.A. Shumilova, I.P. Shidlovskiy, E.D. Nikolaeva, A.G. Sukovatiy, A.D. Vasiliev, E.I. Shishatskaya, Polymer Testing, **65**, 54-68 (2018). https://doi.org/10.1016/j.polymertesting.2017.10.023.

BOOK OF FULL TEXT PROCEEDINGS TURKISH PHYSICAL
SOCIETY 35th INTERNATIONAL PHYSICS CONGRESS (TPS35)
TPS35, Vol.01, No.01, pp.37-41.
ISBN:978-605-83516-6-0

15 December 2019

Preparation of Eu/Dy-doped ZnO Thin Films by Sol-Gel Process

Atilla Evcin[1, a)] and Nalan Çiçek Bezir[2,b)]

[1]*Afyon Kocatepe University, Materials Science and Engineering Department, 03200, Afyonkarahisar, Turkey*
[2]*Süleyman Demirel University, Physics Department, 32260, Isparta, Turkey*

[a)]Corresponding author: evcin@aku.edu.tr
[b)] cicekn@gmail.com

Abstract. In this study, we first, produced Eu/Dy-doped ZnO thin films by sol-gel dip coating method on glass substrates. To prepare the solutions of the pure and Eu and Dy doped ZnO thin films, zinc acetate dihydrate [$Zn(CH_3COO)_2.2H_2O$] and Dy nitrate [$Dy(NO_3)_3.xH_2O$], Eu nitrate [$Eu(NO_3)_3.5H_2O$] were used as starting reagents and the absolute ethanol (CH_3CH_2OH) was used as a solvent. For both doped and undoped ZnO thin film were prepared on glass surface. The precursor solutions were prepared by dissolving in absolute ethanol, Triton X-100, PEG400 and stirred at 50 °C for 60 min, leading to the formation of a homogeneous solution. ZnO thin films were prepared by dip-coating method on the glass substrates. Crystal structure, surface morphology, thermal properties and optical properties of ZnO thin films were characterized by means of X-ray diffraction (XRD), scanning electron microscopy (SEM), ultraviolet/visible (UV/VIS) absorption spectrometry and Contact Angle Goniometer respectively.

INTRODUCTION

Zinc oxide (ZnO) is a multifunctional semiconductor material having a broad energy band gap (3.37 eV) [1-2]. It can be used in many technological applications like light emitting diodes [4], chemical and biological gas sensors [5], solar cells [6], piezoelectric devices [7], lasers [8], thin-film transistors [9], photodetectors solar cells [10], UV detectors [11]. ZnO is produced in variety form of particle, powder, thin film, bulk materials and they have been synthesized with different synthesis methods[12]. Many researchers have studied effect of rare elements (RE) on the structural, optical and electrical properties of ZnO [1,3,13].

MATERIALS AND METHOD

[$Zn(CH_3COO)_2.2H_2O$], [$Dy(NO_3)_3.xH_2O$], [$Eu(NO_3)_3.5H_2O$], Triton X-100, PEG400 were used as starting reagents. All reagents were purchased from Sigma Aldrich and were used without further purification. Soda lime glass slides were cleaned by soaking them in HCI and NaOH solutions for 5 min followed by thorough deionized water cleaning. They were then rinsed with acetone and dried at room temperature. ZnO-based ceramic thin films were deposited on glass substrates by novel sol-gel process. The flowchart that shows the procedure used for preparing ZnO thin films is given in Fig. 1. The sols were prepared by zinc acetate dehydrate, surfactant such as Triton X-100 and PEG 400, dopants such as Dy nitrate and Eu nitrate at 50 °C. The molar ratio of Dy and Eu nitrate to zinc acetate was maintained at 0.01 (Table 1). The resultant solutions typically became clear within an hour of preparation; once cooled to room temperature. The glass substrates were then dipped into the solution and

Türk Fizik Derneği
1950
Turkish Physical Society

ISBN:978-605-83516-6-0

withdrawn at a rate of 2.0 cm min^{-1}. The coated substrate was dried at 80°C for 10 min in heater of dip coater (Fig.2) and then repeated 4 times dipping procedure.

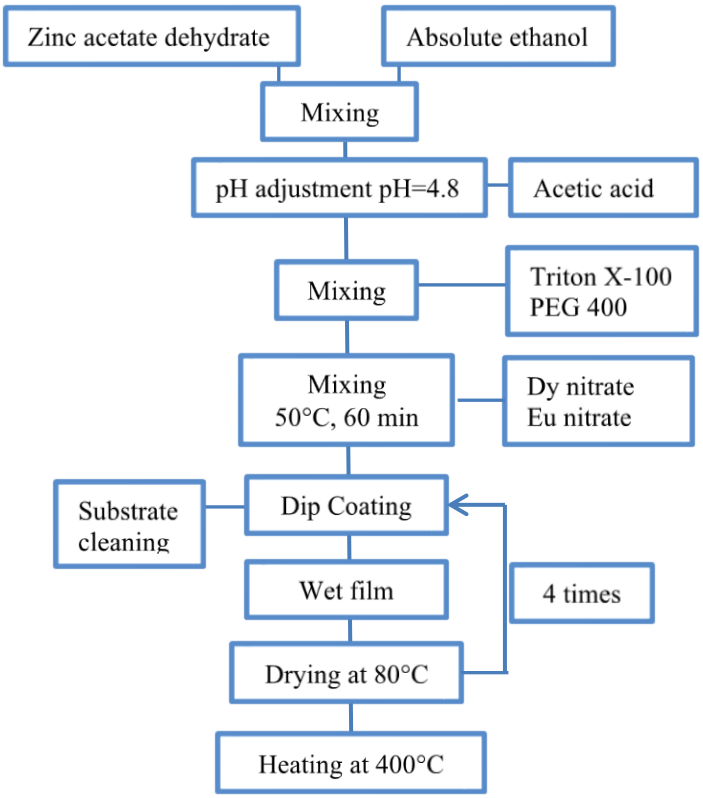


FIGURE 1. Flowchart of experimental method.



FIGURE 2. Homemade dip coater.

TABLE 1. Composition of solutions.

Composition	C1	C2	C3	C4
Zinc acetate dehydrate	5.49 g	5.49 g	5.49 g	5.49 g
Absolute ethanol	100 mL	100 mL	100 mL	100 mL
Triton X-100	1 mL	1 mL	1 mL	1 mL
PEG 400	1 mL	1 mL	1 mL	1 mL
Dy nitrate	-	0.104 g	-	0.104 g
Eu nitrate	-	-	0.128 g	0.128 g

Thin films were produced by means of the homemade dip coater with heater in the Advanced Technology Materials Laboratory at Afyon Kocatepe University. The morphologies of film were evaluated by SEM analysis (Leo 1430 VP). The optical properties of the ZnO thin films were measured using Perkin Elmer lambda 20 UV spectrometer. Contact angles of thin films were measured by Attension theta lite tensiometer.

RESULTS

In Fig. 3 the SEM analysis shows photos of coated glass surfaces. Pure ZnO film is very homogeneous and smooth. But surface of Dy and Eu doped ZnO films aren't homogeneous.

ISBN:978-605-83516-6-0

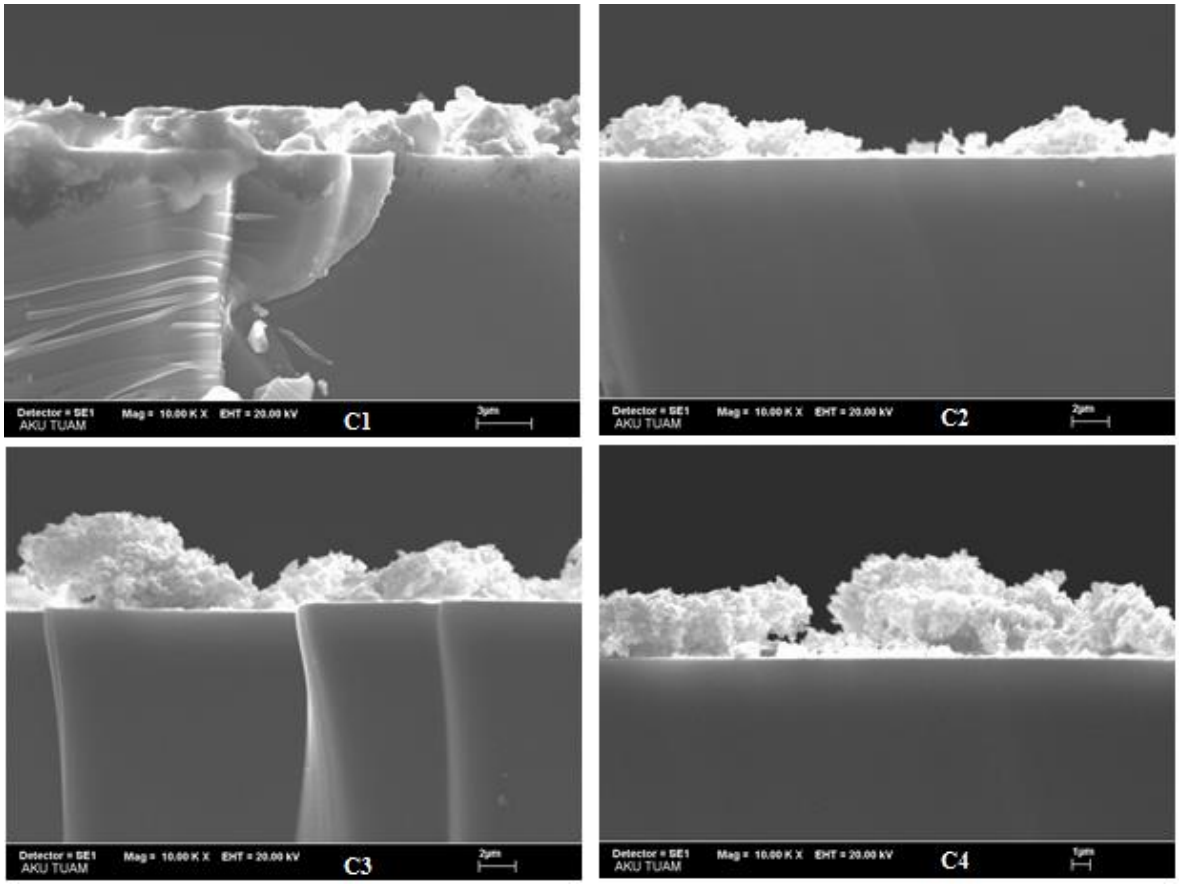


FIGURE 4. SEM images of thin films; C1:ZnO, C2: Dy-ZnO, C3: Eu-ZnO, C4: Eu/Dy-ZnO

The optical band gap of the ZnO thin film as a direct bandgap semiconductor was determined using Tauc method. The optical band gaps are given in Table 2. Optical band gaps decreases with Eu-Dy doping.

TABLE 2. Optical band gap values.

Composition	C1	C2	C3	C4
Band gap (eV)	3.22	3.04	3.18	3.13

Contact angle (CA) measurements are shown in Fig.5. All film surface have hydrophilic chara cter because of CA<90°. CA of surface decreases with Eu-Dy doping. Doped ZnO films are more hydrophilic.

ISBN:978-605-83516-6-0

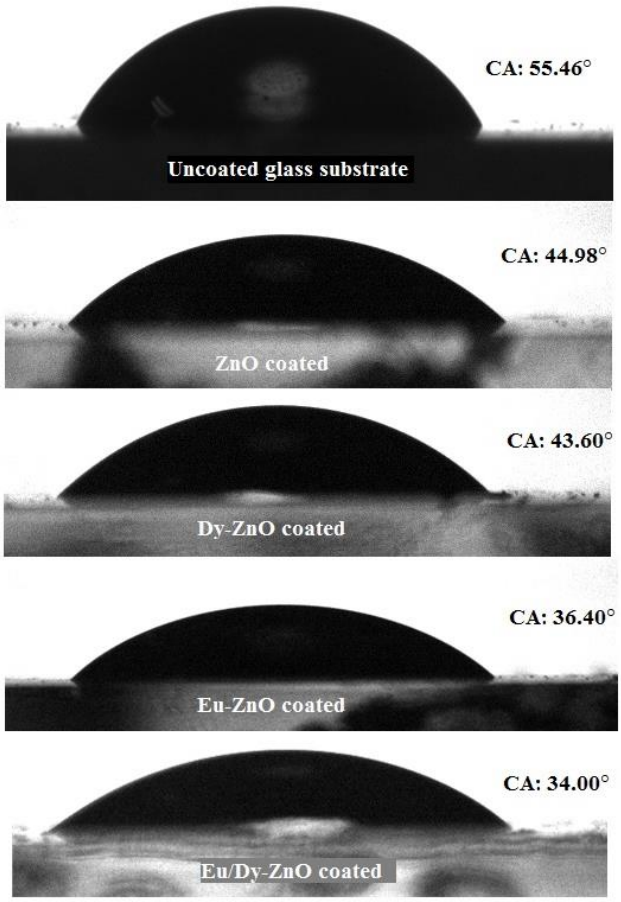


FIGURE 5. Contact angles of coated glass surface

CONCLUSION

Rare element doped ZnO thin films were produced successfully by sol-gel dip coating. Optic band gap decreases with doping Eu and Dy elements. Film thickness of coating was average 150 μm. Doping of Eu and Dy wasn't affected from film thickness. But it was affected from homogeneity of surface negatively. Contact angle of surface decreases with doping rare elements.

ACKNOWLEDGMENTS

This work was supported by Afyon Kocatepe University via Scientific Research Projects (No: 17.KARİYER.87)

ISBN:978-605-83516-6-0

REFERENCES

1. E. Hasabeldaim, O.M. Ntwaeaborwa, R.E. Kroon, H.C. Swart, Journal of Molecular Structure **1192** 105-114 (2019). https://doi.org/10.1016/j.molstruc.2019.04.128
2. H. Wang, X. Mo, Z. Chen, S. Li, H. Huang, Y. Liu, G. Fang, Mater. Res. Express **2**, 035005 (2015). https://doi.org/10.1088/2053-1591/2/3/035005
3. C.L. Henga, W. Xiang, W.Y. Su, Y.K. Gao, P.G. Yin, T.G. Finstad, Journal of Luminescence **210** 363–370 (2019). https://doi.org/10.1016/j.jlumin.2019.02.062
4. D. Chen, S. Chen, S. Yue, B. Lu, X. Pan, H. He, Z. Ye, Journal of Luminescence, **216** 116719, (2019). https://doi.org/10.1016/j.jlumin.2019.116719.
5. V. S. Bhati, M. Hojamberdiev, M. Kumar, Energy Reports, 2019 https://doi.org/10.1016/j.egyr.2019.08.070
6. Z. Pang, Y. Sun, Y. Gao, X. Zhang, Y. Sun, J. Yang, F. Wang, L. Yang, Journal of Power Sources, **438**, 226957, (2019) https://doi.org/10.1016/j.jpowsour.2019.226957
7. R.S. Sabry, A.D. Hussein, Polymer Testing, **79**, 2019, 106001 https://doi.org/10.1016/j.polymertesting.2019.106001
8. G. Jo, J.H. Koh, Ceramics International, **45**, 5, 6190-6197 (2019). https://doi.org/10.1016/j.ceramint.2018.12.096
9. J. Meza-Arroyo, M.G. Syamala Rao, I. Mejia, M.A. Quevedo- López, R. Ramírez-Bon, Applied Surface Science, **467–468**, 456-461 (2019). https://doi.org/10.1016/j.apsusc.2018.10.170
10. J.Y. Kim, P. Vincent, J. Jang, M.S. Jang, M. Choi, J.H. Bae, C.L., H. Kim, Journal of Alloys and Compounds, **813**, 152202 (2020). https://doi.org/10.1016/j.jallcom.2019.152202
11. S. Alamdari, M.S. Ghamsari, H. Afarideh, A. Mohammadi, S. Geranmayeh, M.J. Tafreshi, M.H. Ehsani, M.H. Majles ara, Optical Materials, **92**, 243-250 (2019). https://doi.org/10.1016/j.optmat.2019.04.041
12. D. Ponnamma, J.J. Cabibihan, M. Rajan, S.S. Pethaiah, K. Deshmukh, J.P. Gogoi, S.K.K. Pasha, M. B. Ahamed, J. Krishnegowda, B.N. Chandrashekar, A.R. Polu, C. Cheng, Materials Science and Engineering: C, **98**, 1210-1240 (2019). https://doi.org/10.1016/j.msec.2019.01.081
13. F. Jia, Q.Y. Hou, Z.C. Xu, L.F. Qu, Journal of Magnetism and Magnetic Materials, **465**, 128-135 (2018). https://doi.org/10.1016/j.jmmm.2018.05.037

BOOK OF FULL TEXT PROCEEDINGS TURKISH PHYSICAL
SOCIETY 35th INTERNATIONAL PHYSICS CONGRESS (TPS35)
TPS35, Vol.01, No.01, pp.42-49.
ISBN:978-605-83516-6-0

15 December 2019

Fully 3D Printed Bead-Pull Measurement of an Elliptical Cavity

Anıl Karatay [1, a)] and Fatih Yaman [1, b)]

[1] *İzmir Institute of Technology, Dept. of Electrical & Electronics Eng. 35430 Urla, İzmir, Turkey*

[a)] Corresponding author: anilkaratay@iyte.edu.tr
[b)] fatihyaman@iyte.edu.tr

Abstract. In this study, the feasibility of a low-cost bead-pull measurement setup to investigate cell misalignment defects for an elliptical cavity produced via 3D printing technology is presented. Surfaces of the cavity and bead are plated with sufficiently thick nickel and copper layers. The bead-pull experiment based on the reflection coefficient measurements with a vector network analyzer at certain time steps during the longitudinal movement of the metallic bead at the center of the cavity region is illustrated in details. The setup is simulated with a general-purpose electromagnetic field solver as well. The effects of the cell alignment error on field flatness are determined numerically and experimentally such that both results well agree in terms of changes in the parameters to be observed.

INTRODUCTION

Microwave cavities which may have various shapes, e.g. rectangular, cylindrical, spherical, elliptical, can be used in many areas such as dielectric constant measurements, heating applications, frequency measurements and in particle acceleration. Particularly, elliptical cavities are one of the most important components of particle accelerators and their fabrication from bulk niobium, copper or stainless steel are very expensive and time consuming. Although careful efforts have been made to produce these structures in a perfect manner, flaws are unavoidable in the process. On the other hand, fabrication of a defected elliptical cavity would heavily increase the budget of the research whose aim is only to examine electromagnetic effects of the geometrical defects, experimentally. Therefore, 3D printing technology may be a good alternative when the effect of these defects on material independent parameters is to be investigated.

In the literature, 3D printers are used in different fields of electromagnetic and microwave applications such as in the production of antenna [1], waveguide [2] and cavity [3] etc. Some of those components are employed as prototypes and the others are used in a real applications having the advantage of being light and cheap. For this study an elliptical cavity structure has been designed to observe cell alignment errors experimentally with the aid of bead-pull measurement. The superconducting elliptical cavities are produced as half cells and dumbbells which are then welded to each other [4] in the fabrication. This study illustrates the experimental procedures to investigate the effects of errors during welding of these cavities on the electric field distribution. For this aim a 3-cell elliptical cavity whose π-mode resonates at 3.9 GHz is designed and manufactured in a way that misalignments could be adjusted easily.

Organization of paper is as follows. Firstly, fabrication of the elliptical cavity, conversion of the dielectric cavity to the conductive one are explained. Afterwards, we describe how to increase the conductivity value of the cavity which is necessary for the sufficiently accurate measurements. Next, an experimental setup for the bead-pull measurement of this cavity and the comparison of simulation and measurement results are presented. Finally, the measurement results and the future works are discussed.

ISBN:978-605-83516-6-0

DESIGN AND FABRICATION

Our main aim is to fabricate 3-cell elliptical cavity whose π-mode is at 3.9 GHz with the aid of a 3D printer, and make it conductive. Cell-to-cell coupling should be increased to reduce the negative effects of possible manufacturing errors, so the iris radius is kept large (i.e. r_{iris} = 2.5 cm while $r_{equator}$ = 3.5 cm). After that, 2 dumbbells and 2 end half cells were fabricated with acrylonitrile butadiene styrene and polylactic acid filaments while these materials can be easily melted and formed when exposed to temperature, but they are electrically insulating. On the other hand, the necessity to make the cavity conductive was realized with nickel plating in the first step. Each part of the cavity was covered three times in total and let them to dry for one day after each coating. We note that it is absolutely necessary not to touch the cavity at least for 10 min. after the coating process and to take safety precautions against chemical exposure during the coating. The relation between the number of coatings and the surface thickness can be seen in Fig. 1 which shows the second and third coating thicknesses are sufficiently close to each other due to the exponential-type variation of the curve. Accordingly, the fourth coating is not considered in this study.

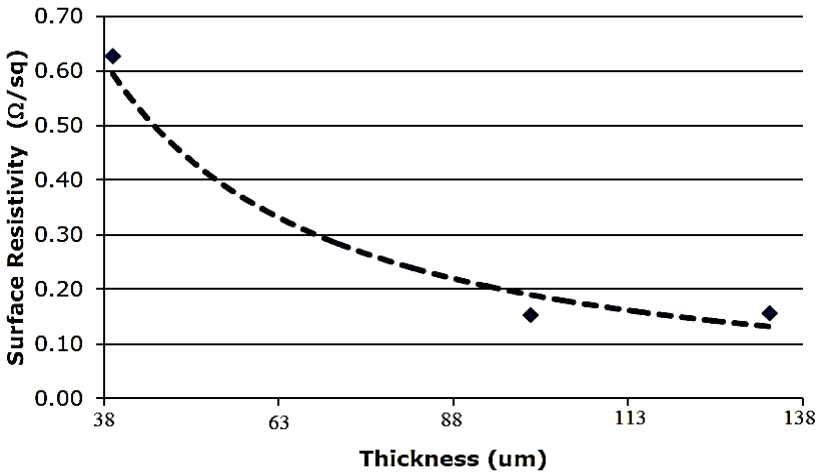
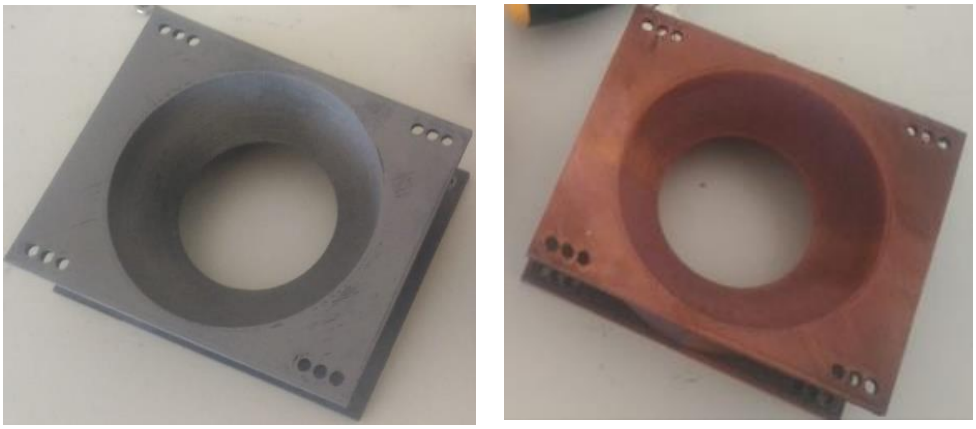


FIGURE 1. Surface resistivity of 1, 2, and 3 coats [5]

Inner and outer surfaces of the cavity were coated with the help of a nickel spray though the nickel could not provide sufficiently high conductivity to observe resonances separately via VNA. Therefore, the inner walls of the cavity were additionally plated with copper on nickel. We remind that, nickel plating was carried out by aerosol while the copper plating was achieved by electrolysis. The copper plate was used as the anode since the cathode had a nickel-plated structure and the solution was the salt of copper. After two layers of copper coating the effective conductivity of the walls increased approximately 5 times more than its former value.

ISBN:978-605-83516-6-0



(a) (b)

FIGURE 2. Coated Dumbbells (a) Nickel (b) Copper

As it can be seen from Fig. 2, three holes are prepared for each corner of the structure to adjust an intentional misalignment error when they are attached to each other with the help of screws and nuts, i.e. the first hole of one part can be attached to the second hole of the other part. The distance between the centers of the screw holes is 0.46 cm.

RESULTS

Metallic bead-pull method is based on the shape perturbation theory [6]. The corresponding mode of the hollow cavity has a certain resonant frequency, and the incoming perturber brings additional boundary conditions to the former problem definition, hence the resonant frequency shifts. The frequency may increase or decrease depending on whether the perturber stays in the electric field or magnetic field region of the cavity. In other words, if we know the amount of frequency shift, we can obtain information on the amplitude of the electric field or the magnetic field in the related region. It should also be noted that the magnetic field is approximately zero at the center of the cavity where our bead moves. For further information, we recommend the references to the reader [7,8].

After the coating process, the bead-pull measurement setup was designed, see Fig. 3. The rope in the figure is fixed to the circular object on the motor while it is passing through the cavity and the bead. Each step of the motor is controlled by an Arduino Mega, allows the bead to move $\approx$3 mm in the cavity. In the meantime, the frequency of the π-mode of the cavity is measured by the vector network analyzer (VNA) and the frequency shift is calculated. The region where the cavity is excited by an N-type coupler and a loop antenna was not originally manufactured with a 3D printer, but covers compatible with the iris radius of the cavity are attached to both sides of the cavity. In this way, a certain amount of possible RF leakage is prevented. In addition, such excitation is more appropriate, since exciting the cavity from the electric field region would interfere with the axis of the bead.

It should also be emphasized that not only the cavity, but also the bead, having 0.6 cm radius, is manufactured by the 3D printer and coated with nickel. Since the conductivity of the bead is not as important as that of the cavity, it does not need to be further plated with copper.

ISBN:978-605-83516-6-0

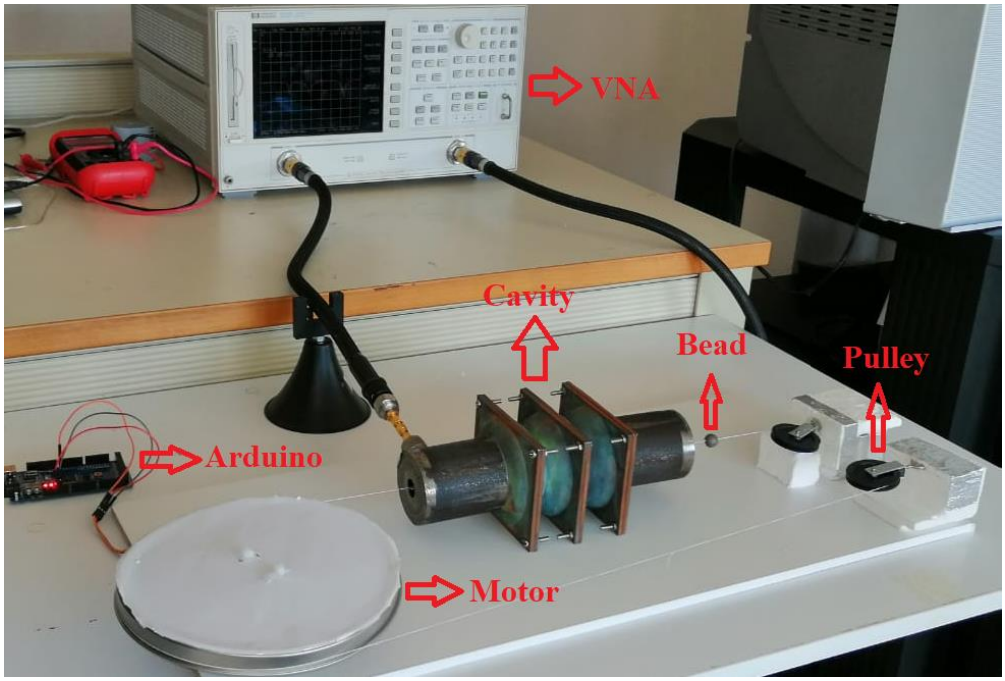


FIGURE 3. Experimental Setup

Simulation results were obtained by using eigenmode solver of CST-MWS. This solver treats the electromagnetic problem as a homogenous eigenvalue problem hence does not need a source for the solution. In this way, the electromagnetic field pattern of the desired mode can be obtained. The screenshot of CST program, in which the 3-cell cavity with dimensions in mm is modeled with screw holes and additional covers, can be seen in Fig. 4. The background was set to vacuum and the holes through which the bead will pass were also added to the simulation to observe the electromagnetic effect. Although the conductivity value for resonant pattern has no direct effect, the conductivity values were also chosen according to the measurement results.

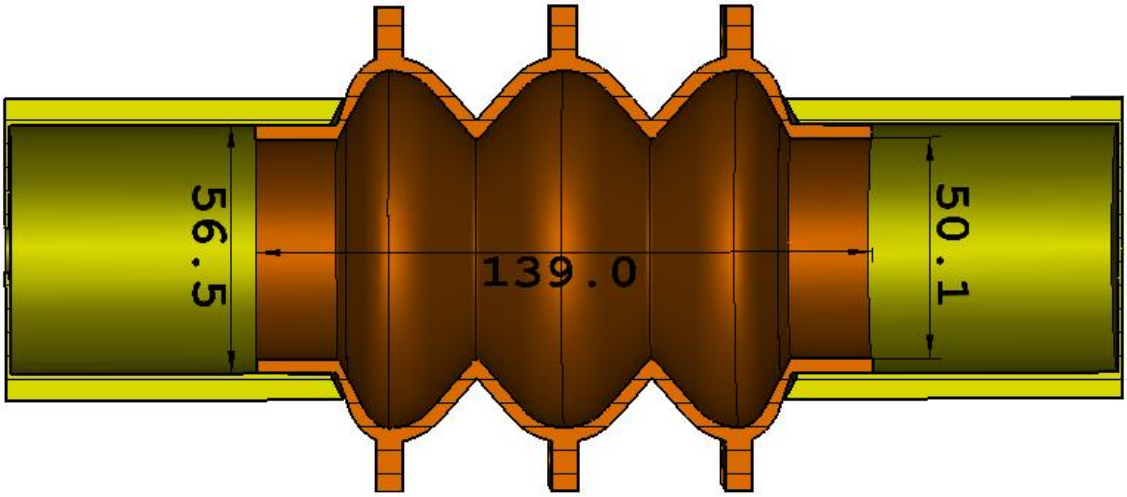


FIGURE 4. A screenshot for the cavity model in CST-MWS eigenmode solver [9]

ISBN:978-605-83516-6-0

The first bead-pull measurement result in Fig. 5 belongs to the case where all the cells are correctly aligned. A good agreement between simulation and measurement result has been obtained except for a slight field drop on the second cell in the measurement result. Note that, the average peak frequency shifts are normalized to unity and simulation results are obtained at 1300 equidistant points while the measurements are collected at 47 sampling points in Fig. 5 - 7. Therefore the curves belonging to simulation results are smoother than those curves obtained from measurements.

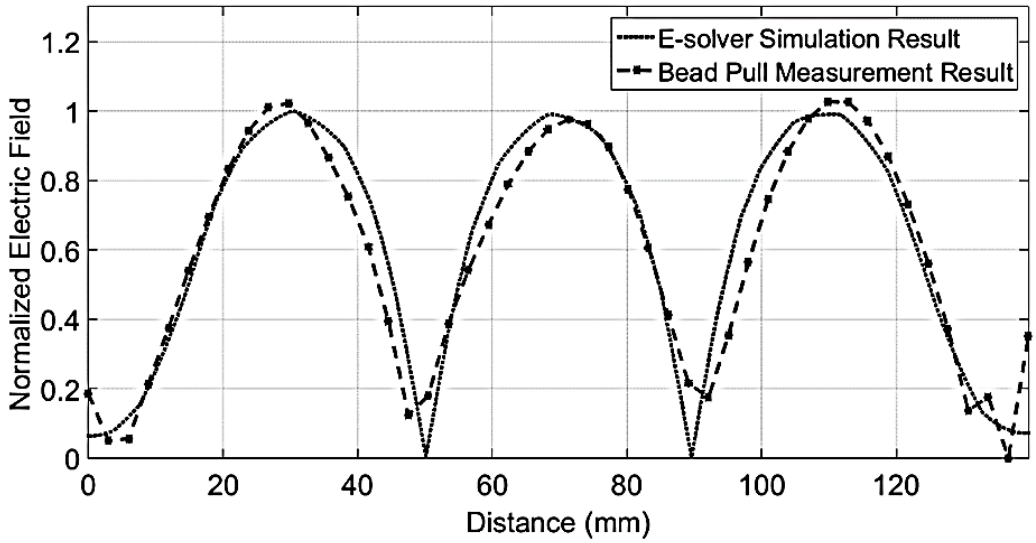


FIGURE 5. No misalignment case

Assume, equator region of the first cell cannot be correctly aligned during fabrication. This case can be realized with the aid of the screw holes, see Fig. 2. In Fig. 6 electric field magnitude on the first cell is decreasing while the magnitude of the furthest cell increasing. Similarly, if the equator region cannot be correctly aligned in the second cell, the electric field magnitude on the misaligned cell decreases while other two peaks increases, see Fig. 7. It can be seen that these results are quite compatible with paper [10].

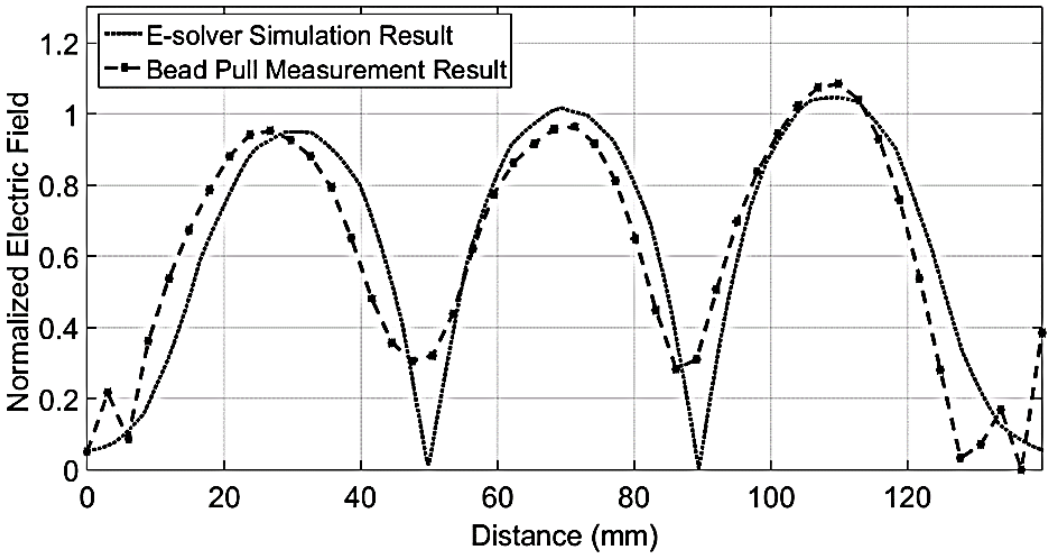


FIGURE 6. Misalignment on the first cell

ISBN:978-605-83516-6-0

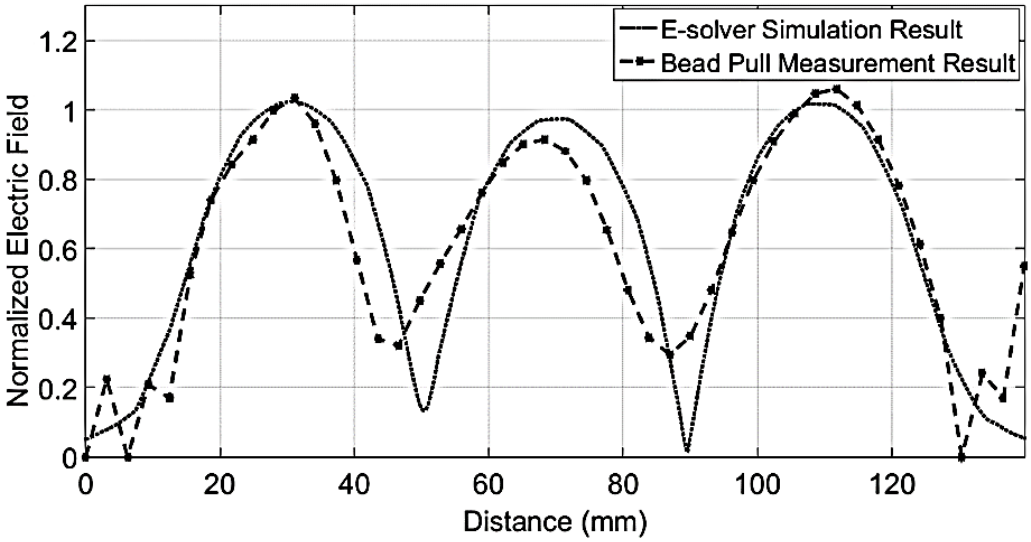


FIGURE 7. Misalignment on the second cell

Table 1 shows the relationship between field flatness, see equation 1, and cell alignment error. According to the simulation results, when there is no alignment error, the amplitude of the field within the cells is approximately equal to each other, and this equality starts to deteriorate when misalignment occurs. It is possible to say that the misalignment in the first cell is affecting field flatness more significantly than the second cell. Likewise, the results show that the first cell has a stronger impact than the second cell, and this effect can be observed even if the electric field magnitude held in the second cell in aligned case is lower than it should be. If the aligned field flatness were closer to 100% in the experiment, it would be more obvious that the effect of cell 1 was greater than cell 2, as in the simulation. The fact that the second cell has a lower amplitude in the experiment than the simulation is due to errors in manufacturing.

$$Field\ Flatness = \frac{E_{peak,\min}}{E_{peak,\max}}\ x\ 100\% \tag{1}$$

TABLE 1. Field flatness comparison

Case	Measurement (%)	Simulation (%)
No Misalignment	95.0	99.8
Cell 1	87.7	90.1
Cell 2	88.5	95.0

On the other hand, if the resonance region of the structure is considered, the change of the electric field during the bead passes through the structure can be seen in Fig. 8. In the region around the bead, the electric field reaches peaks and even exceeds the electric field values in the equator region.

ISBN:978-605-83516-6-0

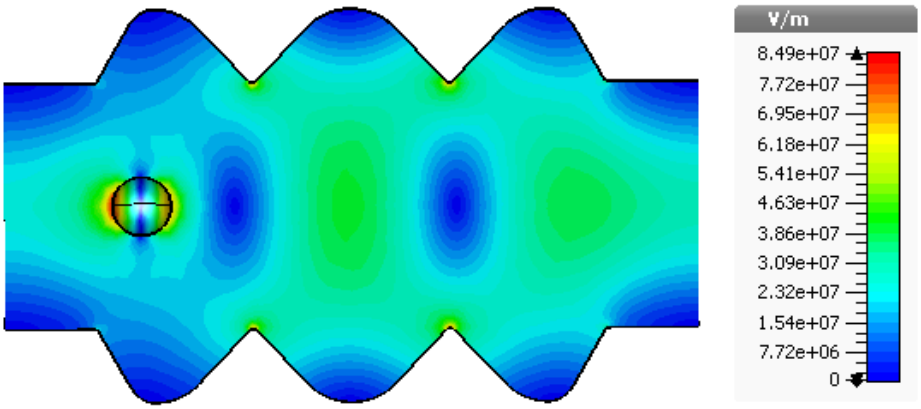


FIGURE 8. Electric field distribution during the bead-pull measurement

CONCLUSION

In this study, it was shown that an elliptical cavity prototype which is produced via 3D printing technology and coated according to the illustrated processes is feasible for bead-pull measurements to investigate cell misalignment effects at the desired level of accuracy. This prototype with π-mode at 3.9 GHz was designed to have a high cell-to-cell coupling due to large production errors. As a result, field values are obtained approximately equal for each cell. We report based on our observations from the practice that the copper coating via electrolysis increases the effective conductivity of the printing material approximately 5 times as compared to the nickel spray coating. We expect the conductivity value could be increased more if one can achieve an equal level of thickness on the surfaces of the cavity walls for the initial nickel coating. According to our measurements using the prototype cavity and from the simulation results which models the complete experimental setup we initially conclude that if the alignment error occurs in the first cell the electric field distribution is deteriorated at most inside the end cell. Therefore, one can remark the shunt impedance of the cavity should decrease due to the defect. This mechanism can be expressed via computations more clearly since we can ignore the unavoidable measurement errors in the simulations even though the same behavior is seen in our experiments. As a future work, the electromagnetic effects of the similar misalignment errors will be investigated by using a highly conducting cavity such that this study can be extended for different number cells and frequencies.

ACKNOWLEDGMENTS

This work is supported by Izmir Institute of Technology Scientific Research Program (BAP) IYTE0299.

REFERENCES

1. V. Kyovtorov, I. Georgiev, S. Margenov, D. Stoychev, F. Oliveri, and D. Tarchi, Int. J. Electron. Commun **73**, 119–128 (2017).
2. A. Bal, D. Carey, F. Espinal, and G. Huff, Electronics Letters **55**, 100–102 (2019).
3. D. L. Creedon, M. Goryachev, N. Kostylev, T. B. Sercombe, and M. E. Tobar, Appl. Phys. Lett. **109**, 032601 (2016).
4. T. Saha, J. Mondal, K. C. Mittal, K. G. Bhushan, and A. V. Bapat, "Fabrication of niobium superconducting accelerator cavity by electron beam welded joints" in International Symposium on Vacuum Science Technology and Its Application for Accelerators, (Calcutta, India, 2012), pp. 1-8.

ISBN:978-605-83516-6-0

5. MG Chemicals, Nickel 841 technical data sheet, (2013).
6. S. Som, S. Seth, A. Mandal and S. Ghosh, "Bead-pull Measurement using phase-shift technique in multi-cell elliptical cavity" in Proceedings of IPAC2011, (San Sebastian, Spain, 2011), pp. 280-282.
7. D. A. Hill, "Deterministic Theories" in *Electromagnetic Fields in Cavities: Deterministic and Statistical Theories,* edited by A. Cangellaris (Wiley, New Jersey, 2012), pp. 20-23.
8. D. M. Pozar, "Microwave Resonators*",* in *Microwave Engineering 4th ed.,* edited by A. Cangellaris (Wiley, New Jersey, 2009), pp. 309-312.
9. CST MICROWAVE STUDIO, CST AG – Computer Simulation Technology, Darmstadt, Germany [online] Available: http://www.cst.com (2018).
10. A. Karatay and F. Yaman, IEEE Transactions on Nuclear Science. Early Access 1-1, DOI: 10.1109/TNS.2019.2945138, (2019).

BOOK OF FULL TEXT PROCEEDINGS TURKISH PHYSICAL
SOCIETY 35th INTERNATIONAL PHYSICS CONGRESS (TPS35)
TPS35, Vol.01, No.01, pp.50-53.
ISBN:978-605-83516-6-0

15 December 2019

Femtosecond Laser-Induced Filamentation Control in Liquids

Alpgiray Keskin[1, a)], Gamze Kaya[2,3] and Necati Kaya[3,4]

[1]*Energy Resources and Management, Graduate School of Natural and Applied Sciences, Canakkale 18 Mart University, Canakkale, Turkey*
[2]*Electric and Energy Programs, Canakkale Vocational School of Technical Sciences, Canakkale 18 Mart University, Canakkale, Turkey*
[3]*Department of Physics, Science, Texas A&M University, College Station, TX, USA*
[4]*Department of Energy Management, Canakkale School of Applied Sciences, Canakkale 18 Mart University, Canakkale, Turkey*

[a)] Corresponding author: alpgiray_keskin@yahoo.com

Abstract. We studied the controlling and organizing of laser-induced filamentation in liquids by generating a spatial phase change into the initial laser beam. Multi-filament formations can be caused by localized inhomogeneities in the medium and irregularities in the incident laser profile. In order to overcome these random small-scale multiple filament formations, we applied more stronger controllable disturbers using the spatial light modulator (SLM) to redistribute laser intensity in certain locations where the peak intensity exceeded the critical threshold. By depending on phase switching on the SLM through the computer-controlled phase mask, we observed that the filament formations could be controlled and organized.

INTRODUCTION

Femtosecond (fs) laser filamentation is a rapidly growing field of modern optics interconnected with many aspects of the propagation of intense and ultrafast laser pulses in transparent media (see [1, 2] for comprehensive reviews) since it was discovered for the first time in 1995 [3]. Main physical properties of femtosecond laser filamentation were reviewed in various transparent media, such as air (gases), transparent solids, and liquids [2]. When the laser power exceeds a certain threshold value, filamentation can be observed experimentally due to intensity fluctuation or changes refractive index. [4-6]. Experiments verify that the self-focusing triggers filament formations [7]. When a certain threshold power for filamentation corresponds to the calculated critical power for self-focusing [8-11].

Many efforts aimed to control the single and multiple filamentation processes in greater details and the distribution of filaments in the medium. Aperture control of the filament parameters was studied by scaling the beam diameter [12]. The critical power for self-focusing for an elliptical beam was found to be greater than a beam with cylindrical symmetry, and the role of the elliptical intensity distribution was discussed in details [13-17]. Studies also show that controlling and organizing filament formations are possible by inserting slits and meshes into the beam path of an intense laser pulse [18], creating Fresnel diffraction from a circular aperture [19], applying amplitude [20, 21] and phase [22, 23] modulation of the beam field, combining the phase plates [24], producing high order Hermite Gaussian beams, and crossing two femtosecond laser beams [25] etc.

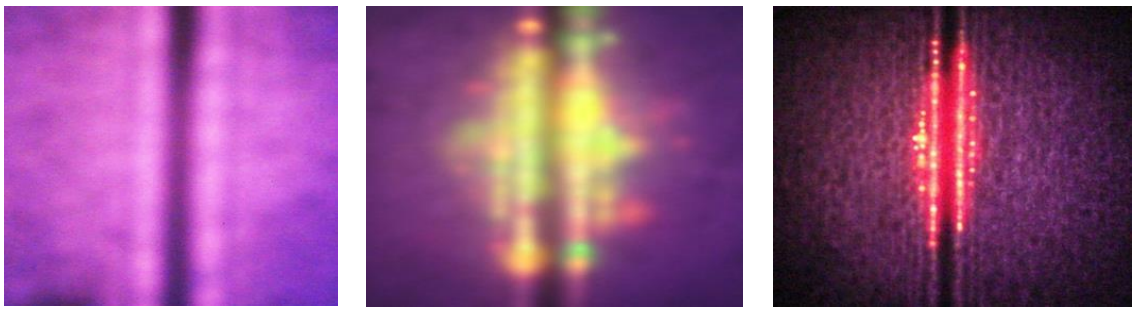
The aim of this study is to overcome random small-scale multiple filament formations caused by localized inhomogeneities in the medium and irregularities in the incident laser profile and to control and organize the filament formations in liquids. So, we applied more stronger controllable disturbers using the SLM to redistribute

ISBN:978-605-83516-6-0

laser intensity in certain locations where the peak intensity exceeded the critical threshold. By depending on phase switching on and off on the SLM through the computer-controlled phase mask, we showed that filament formations can be controlled and organized.

RESULTS AND DISCUSSIONS

The laser beam from Ti:Sapphire laser system was used in the experiment. With Spitfire system the laser average power was $P_{ave} = 940\,\text{mW}$. For the repetition rate 1kHz and the pulse duration $t = 50\,\text{fs}$ we obtain the peak power $P_{peak} = 1.8 \times 10^{10}\,\text{W}$. The oscillating intensity distribution was formed by using a Spatial Light Modulator (SLM) with a liquid crystal phase mask by shifting the phase of half of the wave front in the beam cross section by $180°$ relative to the other half. Consequently, an intensity modulation across the beam appears as seen in Fig.1 (a). One can see dark area in the middle due to intensity suppression resulting from the π-phase step. Fig. 1 (b) presents image of the distribution of the laser intensity in a laser beam with a π phase step in the cross section at higher laser intensity, when filament formation takes place in liquid benzene. One can see the distribution of filaments along the laser intensity distribution. We also imaged the light scattered at the exit wall of the cell, projected on a white screen with a lens f=10 cm and taken through a red filter blocking light with λ<640nm as seen in Fig.1(c). Notice the coincidence of the lines of intense laser field with alignment of filaments.

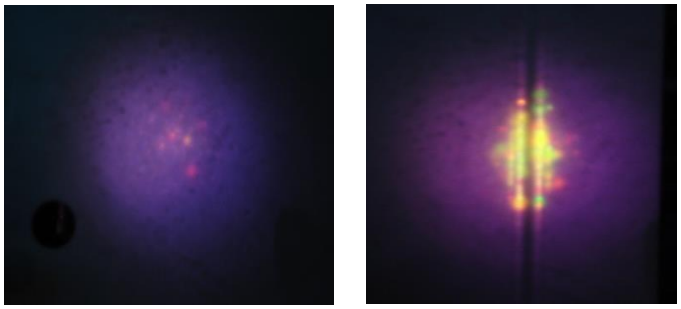


(a) (b) (c)

FIGURE 1. (a) Image of the distribution of the laser intensity in a laser beam with a π phase step in the cross section, (b) same as in (a) at higher laser intensity, when filament formation takes place in liquid benzene.

Then we examined the distribution of the laser intensity in a laser beam after it passes through liquid benzene as seen in Fig 2 (a) in case of few filaments just start forming. These filament formations are random scale formations due to both beam irregularities and inhomogeneities of the transparent medium, and avoidable and uncontrollable at higher laser intensities. However, when we introduced a π-phase step in the middle of the beam, one can see that laser intensity is distributed non-uniformly and in certain locations the peak intensity exceeds the threshold, and filaments are formed in the peaks of the intensity in seen Fig.2 (b). This means that we can overcome random small-scale multiple filament formation due to both beam irregularities and inhomogeneities of the transparent medium by applying more stronger controllable disturbers and we control and organize filament formation in certain locations where the distributed peak intensity exceeded the critical threshold.

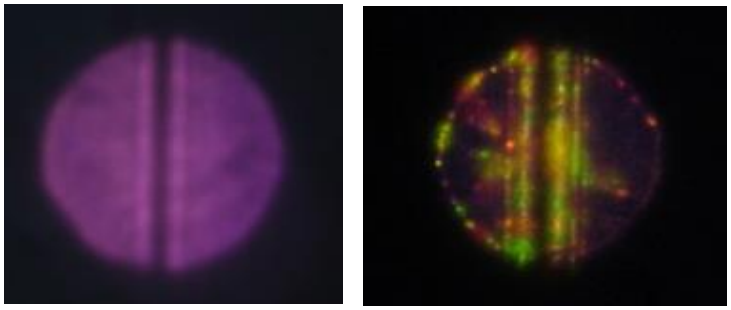
ISBN:978-605-83516-6-0



(a) (b)

FIGURE 2. (a) Image of the distribution of the laser intensity in a laser beam after it passes through benzene. Few filaments just start forming. (b) A π-phase step in the middle of the beam is introduced. In this case peak intensity exceeds the threshold in certain locations, and filaments are formed in the peaks of the intensity.

The distribution of the laser intensity of the beam with π-phase step in the middle of the beam going though an aperture is used as incident beam in liquid benzene (Fig. 3). The filament formation at somewhat higher intensity is presented in Fig.3 (b) where the light around 800 nm is filtered out. One can see filament formation takes place along the lines of intense laser field with the phase step in the middle and hard aperture edges. Knowing intensity one can infer the dependence of the filament formation length on the intensity.



(a) (b)

FIGURE 3. (a) Image of the distribution of the laser intensity of the beam with π-phase step in the middle of the beam going though an aperture. (b) The same at somewhat higher intensity, light around 800 nm is filtered out.

CONCLUSIONS

We experimentally report the controlling and organizing of laser filaments in liquid through inserting a phase step into incident laser beam. We introduced a spatial phase shape into the incident beam, providing a π phase shift in one half of the beam profile with respect to the other half. We observed a higher density of filament formations, when creating a strong spatial intensity modulation of the beam profile with the phase shift. This controlling and organizing effect derived from the redistributed laser intensity can overcome localized inhomogeneities of laser field and the inhomogeneities of the transparent medium. The research is significant for ultrafast physics.

ACKNOWLEDGMENTS

We are thankful to our colleagues, J Strohaber, A Kolomenskii, and H Schuessler, who shared their knowledge and expertise that greatly assisted in this work. This work was partially supported by Çanakkale Onsekiz Mart University, The Scientific Research Coordination Unit, Project number: FYL-2019-2985.

ISBN:978-605-83516-6-0

REFERENCES

1. Chin, S.L., et al., *The propagation of powerful femtosecond laser pulses in opticalmedia: physics, applications, and new challenges.* Canadian Journal of Physics, 2005. **83**(9): p. 863-905.
2. Couairon, A. and A. Mysyrowicz, *Femtosecond filamentation in transparent media.* Phys. Rep. , 2007. **441**: p. 47-189.
3. Braun, A., et al., *Self-channeling of high-peak-power femtosecond laser pulses in air.* Optics Letters, 1995. **20**(1): p. 73-75.
4. Chin, S.L., et al., *Filamentation of femtosecond laser pulses in turbulent air.* Applied Physics B, 2002. **74**(1): p. 67-76.
5. Xi, T.-T., X. Lu, and J. Zhang, *Interaction of Light Filaments Generated by Femtosecond Laser Pulses in Air.* Physical Review Letters, 2006. **96**(2): p. 025003.
6. Kaya, N., et al., *White-light generation using spatially-structured beams of femtosecond radiation.* Optics Express, 2012. **20**(12): p. 13337-13346.
7. Brodeur, A. and S.L. Chin, *Ultrafast white-light continuum generation and self-focusing in transparent condensed media.* J. Opt. Soc. Am. B 1999. **16**: p. 637-650
8. Smith, W.L., P. Liu, and N. Bloembergen, *Superbroadening in H2O and D2O by self-focused picosecond pulses from a YAlG: Nd laser.* Phys. Rev. A 1977. **15**: p. 2396-2403.
9. Corkum, P.B., C. Rolland, and T. Srinivasan-Rao, *Supercontinuum Generation in Gases.* Phys. Rev. Lett., 1986. **57**: p. 2268-2271.
10. Ilkov, F.A., L.S. Ilkova, and S.L. Chin, *Supercontinuum generation versus optical breakdown in CO2 gas.* Opt. Lett. , 1993. **18**: p. 681-683.
11. François, V., F.A. Ilkov, and S.L. Chin, *Experimental study of the supercontinuum spectral evolution in CO2 gas.* Opt. Commun., 1993. **99**: p. 241-246.
12. Kosareva, O.G., et al., *Controlling a bunch of multiple filaments by means of a beam diameter.* Applied Physics B, 2006. **82**(1): p. 111-122.
13. Fibich, G. and B. Ilan, *Self-focusing of elliptic beams: an example of the failure of the aberrationless approximation.* Journal of the Optical Society of America B, 2000. **17**(10): p. 1749-1758.
14. Kandidov, V.P. and V.Y. Fedorov, *Properties of self-focusing of elliptic beams.* Quantum Electronics, 2004. **34**(12): p. 1163-1168.
15. Dubietis, A., et al., *Multiple filamentation induced by input-beam ellipticity.* Optics Letters, 2004. **29**(10): p. 1126-1128.
16. Jin, Z., et al., *Control of filamentation induced by femtosecond laser pulses propagating in air.* Optics Express, 2005. **13**(25): p. 10424-10430.
17. Fibich, G., et al., *Control of the collapse distance in atmospheric propagation.* Optics Express, 2006. **14**(12): p. 4946-4957.
18. Schroeder, H., J. Liu, and S.L. Chin, *From random to controlled small-scale filamentation in water.* Optics Express, 2004. **12**(20): p. 4768-4774.
19. Cook, K., A.K. Kar, and R.A. Lamb, *White-light filaments induced by diffraction effects.* Optics Express, 2005. **13**(6): p. 2025-2031.
20. Kandidov, V.P., et al., *A method for spatial regularisation of a bunch of filaments in a femtosecond laser pulse.* Quantum Electronics, 2004. **34**(10): p. 879-880.
21. Kandidov, V.P., et al., *Towards a control of multiple filamentation by spatial regularization of a high-power femtosecond laser pulse.* Applied Physics B, 2005. **80**(2): p. 267-275.
22. Luo, Q., et al., *Effect of beam diameter on the propagation of intense femtosecond laser pulses.* Applied Physics B, 2005. **80**(1): p. 35-38.
23. Rohwetter, P., et al., *Laser multiple filamentation control in air using a smooth phase mask.* Physical Review A, 2008. **77**(1): p. 013812.
24. Liu, L., et al., *Fine control of multiple femtosecond filamentation using a combination of phase plates.* Journal of Physics B: Atomic, Molecular and Optical Physics, 2011. **44**(21): p. 215404.
25. Kolomenskii, A.A., et al., *White-light generation control with crossing beams of femtosecond laser pulses.* Optics Express, 2016. **24**(1): p. 282-293.

BOOK OF FULL TEXT PROCEEDINGS TURKISH PHYSICAL
SOCIETY 35th INTERNATIONAL PHYSICS CONGRESS (TPS35)
TPS35, Vol.01, No.01, pp.54-58.
ISBN:978-605-83516-6-0

15 December 2019

Design of an Ultra-Sensitive Optical Sensor for Atmospheric Level Methane Measurement

Alpgiray Keskin[1, a)], Gamze Kaya[2,3] and Necati Kaya[3,4]

[1]*Energy Resources and Management, Graduate School of Natural and Applied Sciences, Canakkale 18 Mart University, Canakkale, Turkey*
[2]*Electric and Energy Programs, Canakkale Vocational School of Technical Sciences, Canakkale 18 Mart University, Canakkale, Turkey*
[3]*Department of Physics, Science, Texas A&M University, College Station, TX, USA*
[4]*Department of Energy Management, Canakkale School of Applied Sciences, Canakkale 18 Mart University, Canakkale, Turkey*

[a)]Corresponding author: alpgiray_keskin@yahoo.com

Abstract. It is aimed to design a novel ultra-sensitive (ppb-level) portable optical sensor for methane gas detection. A circular multi-pass optical cell is designed to obtain a very long effective absorption path. The absorption signal is subjected to secondary harmonic wavelength modulation. The noise ratio of optical absorption signals is minimized by the dual-beam schematic method in order to produce a complete ppb-level optical sensor with a suitable selection of methane absorption bands in the near-infrared region. The optical platform is designed in a compact and portable way to be suitable for effective use in a wide application in fields such as physical, atmospheric, environmental and analytical chemistry, in the fields of combustion science, physics, medical diagnosis, biology, and process technology. The laser source can be also selected according to the target trace gas absorption band so that other trace gases can be measured in the field.

INTRODUCTION

Methane (CH_4) is a hydrocarbon and primary component of natural gas. Due to its greenhouse gas properties, its presence in the atmosphere affects the world's temperature and climate system. The atmospheric methane concentration has risen by about 150% since 1750 and accounts for 20% of all long-lived and globally generated greenhouse gases [1]. The heat capacity of methane is much higher than carbon dioxide. As a chemically active gas, methane strongly influences the chemical composition of the atmosphere. Taking into account the atmospheric life span of carbon dioxide and methane, scientists calculated that the global warming potential of methane gas was 28 times higher than carbon dioxide in a 100-year period [2]. Methane has a shorter life span compared to carbon dioxide. Therefore a significant reduction of methane gas concentration has a rapid and significant effect on global warming potential. Precise detection of changes in methane concentration is important for studies on climate change. For this reason an optically stable and precise measurement of atmospheric methane at the level of ppb will have a widespread impact on the studies in atmospheric science.

The aim of this study is to develop a new sensing method by considering the different sensitivities and detection limits of the specific optical approaches. The optical platform is designed as compact and portable for field applications and can perform very precise measurements. The wavelength modulation approach is adopted to have high sensitivity for field applications. The sensitivity of the sensor is improved by using near IR laser. By selection of appropriate methane absorption bands, the high detection limit is intended to achieve by combining the wavelength modulation approach with a circular multi-pass optical cell. In order to eliminate the effects of laser power fluctuations, we include the double-beam scheme in the optical setup.

ISBN:978-605-83516-6-0

SELECTION OF SUITABLE METHANE ABSORPTION BANDS

The absorption band is selected by considering minimal interference from other gases in the air. We calculated absorption spectrum from 6045 cm^{-1} to 6060 cm^{-1} for typical atmospheric air using the HITRAN database [3] and shown in Fig. 1. It is noticed that CH_4 (R4=6056.94 cm^{-1}) absorption band overlaps less with H_2O and CO_2 absorption bands (see inset of Fig.1).

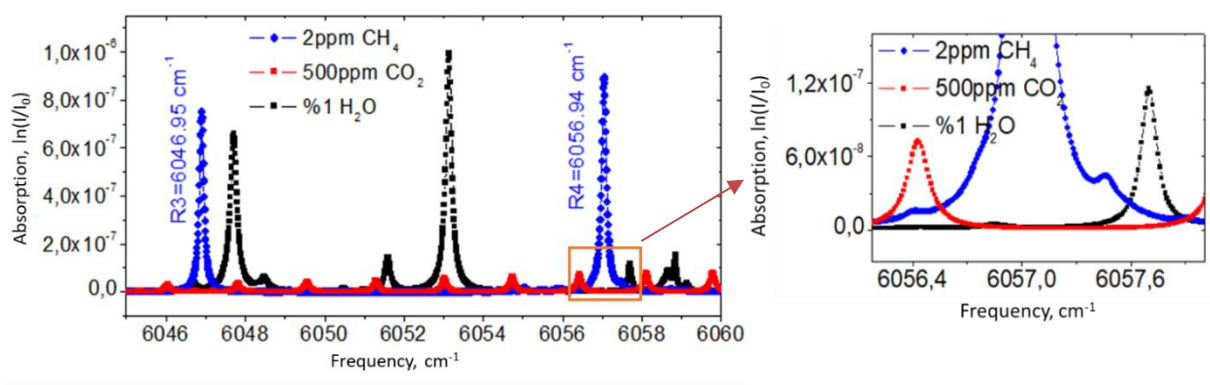


FIGURE 1. Simulated absorption spectral profiles of H_2O, CO_2 and CH_4 obtained with HITRAN data for 1 cm optical path with 296 K, 1 atm pressure and 1% H_2O, 500 ppm CO_2 and 2 ppm CH_4 cross-sectional volumes.

CIRCULAR MULTI-PASS OPTICAL CELL DESIGN AND ANALYTICAL EXAMINATION

The circular multi-pass cell is designed such that the laser beam enters at a certain angle into a single circular mirror whose inner surface is coated with a high reflectivity coating. After the beam enters the cell, the mirror reflects on the surface of the mirror until it exits from the hole which the beam enters. The spherical equations are useful for monitoring successive reflections of the beam and the main beam in a circular multi-pass cell. The top view of the successive reflections within the cell is as shown in Fig. 2.

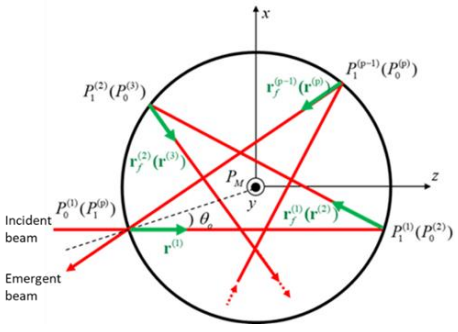


FIGURE 2. Top view of successive reflections on spherical mirrors within a conventional circular multi-pass cell.

ISBN:978-605-83516-6-0

The beam path can be determined by the spherical equations: $z^{(i)} = -r^{(i)}\left(P_0^{(i)} - P_C^{(i)}\right) + \left(\left[r^{(i)}\left(P_0^{(i)} - P_C^{(i)}\right)\right]^2 - \left(P_0^{(i)} - P_C^{(i)}\right)\left(P_0^{(i)} - P_C^{(i)}\right) + R^2\right)^{1/2}$ [4] where $P_1^{(i)} = P_0^{(i)} + z^{(i)} r^{(i)}$, $r_N^{(i)} = \left(P_1^{(i)} - P_C^{(i)}\right)/R$, and $r_f^{(i)} = r^{(i)} - \left(2r^{(i)} \cdot r_N^{(i)}\right) r_N^{(i)}$. $z^{(i)}$ is the optical path length of the ith reflection; $r^{(i)}$, $r_f^{(i)}$ and $r_N^{(i)}$ are the direction vectors related to incidence, reflectance and surface normal, respectively; $P_0^{(i)}$, $P_1^{(i)}$ and $P_C^{(i)}$ coordinate points related to incidence, reflection and the center of curvature, respectively and R is the radius of curvature related to the inner spherical surface. Each reflection point and direction vector of the reflected beam are the incidence point and direction vector of incident beam for the next reflection. $P_0^{(i+1)} = P_1^{(i)}$ and $r^{(i+1)} = r_f^{(i)}$. The center of curvature of arbitrary reflections on the inner spherical surface of the circular mirror is always $P_C^{(i)} = (0,0,0)$. The first reflection, the reflection point and direction vector of the reflected beam can be $P_1^{(1)} = \left(-R\sin\theta_0, 0, R\cos\theta_0\right)$ and $r_f^{(1)} = \left(\sin 2\theta_0, 0, -\cos 2\theta_0\right)$. The direction vector and incidence point of the second reflection are $r^{(2)} = \left(\sin 2\theta_0, 0, -\cos 2\theta_0\right)$ and $P_0^{(2)} = \left(-R\sin\theta_0, 0, -R\cos\theta_0\right)$ respectively. By repeating equations, beam tracing of the following reflections is obtained. The general expression of the reflection point of the nth reflection in a circular multi-pass cell is $P_1^{(n)} = \left(\left(-1\right)^n R\sin\left(2n-1\right)\theta_0, 0, \left(-1\right)^n R\cos\left(2n-1\right)\theta_0\right)$.

To validate the general expressions, we utilized this equation to verify the result of the relationship between the number of passes p and incident angle $\theta_0 = (p-2q)\pi/2p$ [4, 5]. Here p denotes the total number of edges in a regular star polygon pattern, and q indicates circlar segments where the arc corresponding to an edge on the circle drawn outside the regular star polygon pattern is divided by other vertexes. Also, p and q are relative prime integers. Therefore, the results of polygonal geometry correspond to the analytical beam tracing results obtained using spherical equations. An example of a 10-pass (p = 10, q = 3) of the circular multi-pass cell is shown in Fig. 3. The circular multi-pass cell can be fully identified by the parameters set R, p, q, and θ. The incoming beam angle is determined only by the parameters p and q of the normal star polygon pattern.

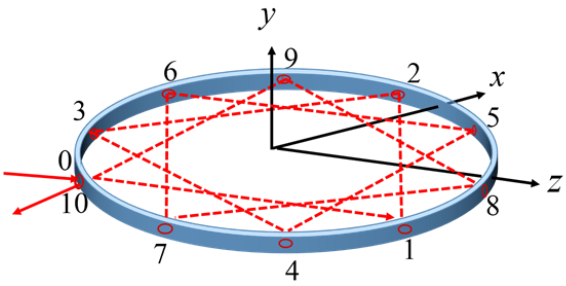


FIGURE 3. Three-dimensional view of a 10-pass sample (the number of passes p = 10 and beam density of the p-sided star polygon pattern q = 3). Straight / dashed arrows indicate the beam path within the circular multi-pass cell; the numbers on the circle indicate the order in which the rays reach the mirror surface; 0 (incident) and 10 (exit) indicate the position of the incident/exit holes.

WAVELENGTH MODULATION

Absorption occurs when light interacts with gas molecules and is described by the Beer-Lambert Law. The disadvantage of this simple technique is that its sensitivity is usually limited to low-frequency noise in the signal. This low frequency noise can be mainly due to laser intensity noise, mechanical and other external fluctuations. This noise is often called 1/f-noise, because the power spectrum is roughly scaled with inverse frequencies [6]. By modulation techniques, the effect of 1/f noise can be greatly reduced by shifting the detection to higher frequencies.

ISBN:978-605-83516-6-0

The most common of these techniques is the wavelength modulation method. In this technique, the laser wavelength and intensity are modulated by applying a sine wave signal via the injection current, resulting in deviations from the high frequencies of the measuring bandwidth where the laser intensity noise is reduced [6, 7]. A simple experimental setup for wavelength modulation is shown in Fig. 4.

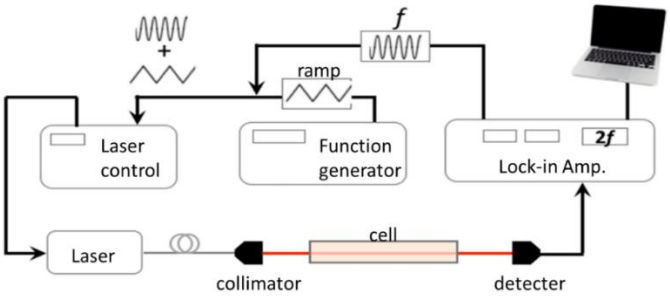


FIGURE 4. Simple experimental setup for wavelength modulation technique

DIAGRAM OF THE OPTICAL SENSOR

The diagram of the sensor is shown in Fig. 5. For the laser in the sensor design, a DFB diode laser with a commercial laser control permits an external modulation frequency of up to 15 kHz. The modulated laser output is split into two channels by the fiber coupler. One of the arm is directed to the circular multi-pass optical cell as the signal beam. The other arm is used as the reference beam. The laser beam passing through the optical arrangements is sent into the circular multi-pass optical cell. After beam path optimizations it is reflected back through the window where the beam enters. In circular multi-pass optical cell design, the number of internal reflections is determined by circular multi-pass cell parameters. The effective path length is calculated. The output signal is collected by the fiber collimator. The signal and reference beams is measured with a balance detector. The balance detector effectively serves to reduce laser intensity noise. Then the signals is modulated and run in the LabVIEW program.

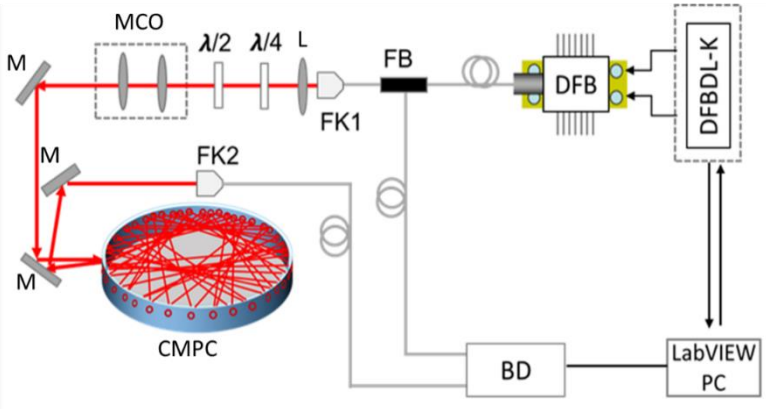


FIGURE 5. Experimental setup of the optical sensor: DFB: Diode Laser Source, DFBDL-K: DFB Diode Laser Controller, FB: 99/1 Fiber Connector, FK1-2: Fiber Collimators, MCO: Mode Coupling Optics, BD: Balance Detector, L: Lens, M: Mirror, CMPC: Circular Multi-Pass Cell.

ISBN:978-605-83516-6-0

CONCLUSIONS

In the study it is aimed to achieve high precision and methane detection at ppb limit in atmospheric level with a new optical spectroscopy method. The near IR band is selected as the absorption band instead of the mid IR. This minimizes interference caused by other gases in the air. The precision is increased by using wavelength modulation method and long effective absorption path is obtained by using a multi-pass optical cell design. Double beam optical assembly is used to reduce laser power fluctuations and the effect of unwanted laser intensity modulations. Due to our novel design, wide selectivity can be achieved by integrating many different laser diode sources.

ACKNOWLEDGMENTS

This work was partially supported by Çanakkale Onsekiz Mart University, The Scientific Research Coordination Unit, Project number: FYL-2019-2985.

REFERENCES

1. Castelvecchi, D. and A. Witze. *Einstein's gravitational waves found at last*. 2016 2016/11/02; Available from: https://www.nature.com/news/einstein-s-gravitational-waves-found-at-last-1.19361.
2. Griggs, H.D., *Climate Change 2001: Working Group I: The Scientific Basis*. 2001: The Pitt Building, Trumpington Street, Cambridge, United Kingdom.
3. Rothman, L.S., et al., *The HITRAN2012 molecular spectroscopic database.* Journal of Quantitative Spectroscopy and Radiative Transfer, 2013. **130**: p. 4-50.
4. Yang, Z., et al., *Generalized Optical Design of the Double-Row Circular Multi-Pass Cell.* Sensors, 2018. **18**(8): p. 2680.
5. Tuzson, B., et al., *Compact multipass optical cell for laser spectroscopy.* Optics Letters, 2013. **38**(3): p. 257-259.
6. Jane, H. and P.T. Ralph, *Optical gas sensing: a review.* Measurement Science and Technology, 2013. **24**(1): p. 012004.
7. Liu, X., et al., *A Survey on Gas Sensing Technology.* Sensors, 2012. **12**(7): p. 9635.

BOOK OF FULL TEXT PROCEEDINGS TURKISH PHYSICAL
SOCIETY 35th INTERNATIONAL PHYSICS CONGRESS (TPS35)
TPS35, Vol.01, No.01, pp.59-66.
ISBN:978-605-83516-6-0

15 December 2019

Developing Miniaturized Orthogonal Fluxgate Sensors

Fatmanur Kocaman[1,a)], Hava Can[2,b)], Uğur Topal[2,c)], Fikret Yıldız[3,d)]

[1] *Department of Electrical-Electronics Engineering, Erzurum Technical University, Erzurum, TURKEY*
[2]*TÜBITAK-UME National Metrology Institute, Gebze – Kocaeli, TURKEY*
[3]*Department of Physics, Gebze Technical University, Gebze – Kocaeli, TURKEY*

[a)]Corresponding author: fatmanur.kocaman@erzurum.edu.tr
[b)]hava.can@tubitak.gov.tr
[c)]ugur.topal@tubitak.gov.tr
[d)]fyildiz@gtu.edu.tr

Abstract. In this study, we designed miniaturized orthogonal fluxgate sensors capable of detecting very small magnetic fields. Within the scope of this study, amorphous cobalt-based METGLAS 2714A ribbon and annealed form of this magnetic material were used because it has soft property as magnetic core material. The core materials were formed on the silicon substrate using lithography and chemical etching techniques. Sensors were characterized for two different core materials. The sensors were investigated as a function of excitation current and effect of heat treatment on core materials. The measurements of sensor parameters showed that both heat treatment and current affect strongly the efficiency of sensor.

INTRODUCTION

With the development of technology, it is seen that the interest in the production of small sized devices is increasing day by day. In this study, fluxgate sensors capable of detecting small DC magnetic fields were fabricated and characterized. The aim of this study is to develop fluxgate sensors with high sensitivity and low noise. The sensors we produce have a magnetic core material and a pick-up coil wrapped around the core. Fluxgate sensors can be parallel or orthogonal configuration. In order to obtain smaller structures, we chose orthogonal configuration which does not need excitation coil in its structure. When the sensor core is excited by an excitation signal, the permeability of the core material changes with the magnetic field generated. The pick-up coil detects this change and induces a voltage. This voltage is the second harmonic voltage which is twice the excitation frequency. The magnetic core material is of great importance in the operation of fluxgate sensors. It is particularly desirable for the core material to have high permeability, low coercivity and low saturation magnetization [1].

In this work cobalt-based amorphous METGLAS 2714A ribbon and its annealed form under certain conditions were preferred as magnetic core material. The effect of these two core materials as well as the excitation current applied to the sensor on the sensitivity and noise of the sensor were investigated. The results showed that the second harmonic signals changed linearly with the DC magnetic field to be measured. The sensitivity and noise levels were obtained 387 V/T and 4.3 nT/√Hz@1Hz respectively. After some optimization studies, the sensitivity and noise levels were further improved.

ISBN:978-605-83516-6-0

EXPERIMENTAL

Firstly, the VSM device was used to compare the magnetic properties of two different magnetic films. M-H curves showing the magnetization of the ferromagnetic material against the applied magnetic field were observed. Fig. 1 shows the comparison of the M-H curves of the annealed core material and the non-annealed core material. When ferromagnetic materials are annealed, grain size increases, and lattice tension and surface defects reduce [2]. As a result, the coercivity of the material is decreased. As shown in Fig. 1, the annealed METGLAS 2714A ribbon film has lower coercivity.

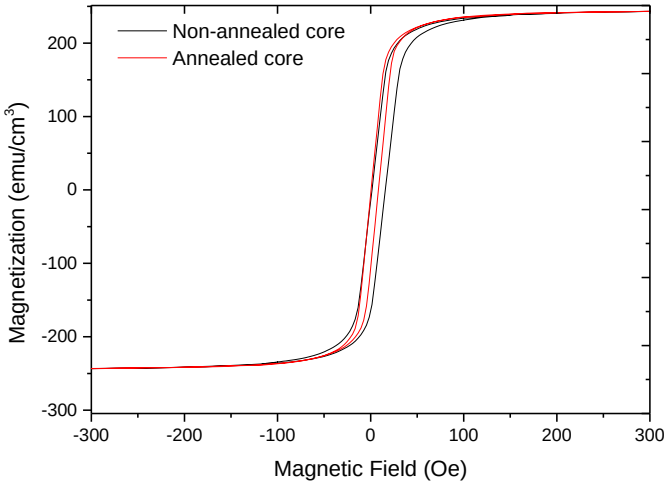


FIGURE 1. In-plane M-H curves of the non-annealed and annealed core material.

The design of the core material used in the sensor and the schematic view after adding the pick-up coil to the sensor were shown in Fig. 2. When determining the shape and size of the core material, a study in the literature was used as a reference [3]. The meander shape is given to the core to improve cross sectional area using photolithography and chemical etching methods. The width of each strip is 250 microns and the distance between the strips is 150 microns. Meander shape consists of 8 turns. The thickness of the METGLAS 2714A ribbon was 23 microns. Silicon wafer was preferred as substrate for the ribbon. Before starting photolithography process, METGLAS 2714A ribbon was cut and glued onto the silicon substrate. The photoresist of the suitable thickness was then coated on the magnetic ribbon using spin coater. After UV exposure process, a mixture of H_2O, HNO_3, HCl, H_2O_2 chemicals was prepared and the surface without photoresist was etched. The final form of the meander shaped core material after fabrication processes is shown in Fig. 3.

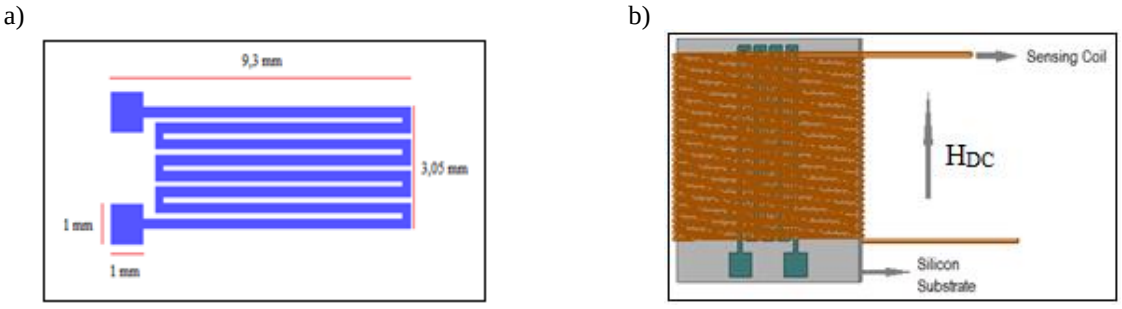


FIGURE 2. Schematic view of the (a) core design (b) miniaturized fluxgate sensor.

ISBN:978-605-83516-6-0

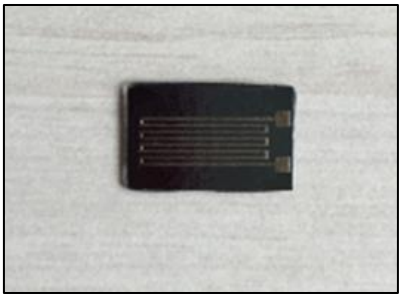


FIGURE 3. Final image of the core of the fluxgate sensor

Copper wire with a diameter of 0.11 mm was used for the pick-up coils. The pick-up coil had 52 turns. In all studies, the effect of core material on sensor performance was investigated by changing the properties of the core material used, provided that the pick-up coil assembly was the same. After the fabricated core material was inserted into the pick-up coil, the production of the miniaturized fluxgate sensor was completed as shown in Fig. 4.

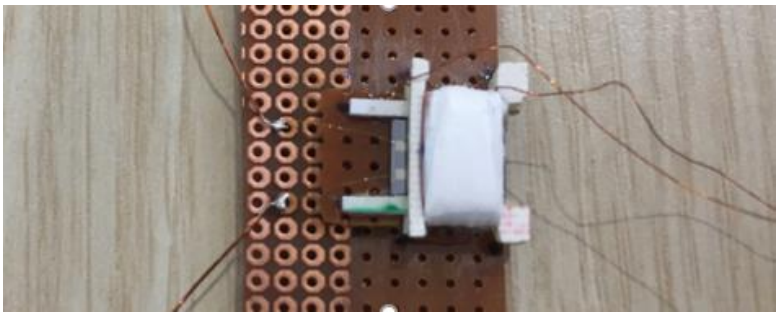


FIGURE 4. Final image of the miniaturized fluxgate sensor

Helmholtz coil was used to create the uniform DC field to be measured. Keitley 220 programmable current source was used as the current source. Noise measurements of the sensors were made with a dynamic spectrum analyzer Agilent 35670A in a three-layer mu-metal shields. SR844 RF lock-in amplifier was used for the second harmonic measurements.

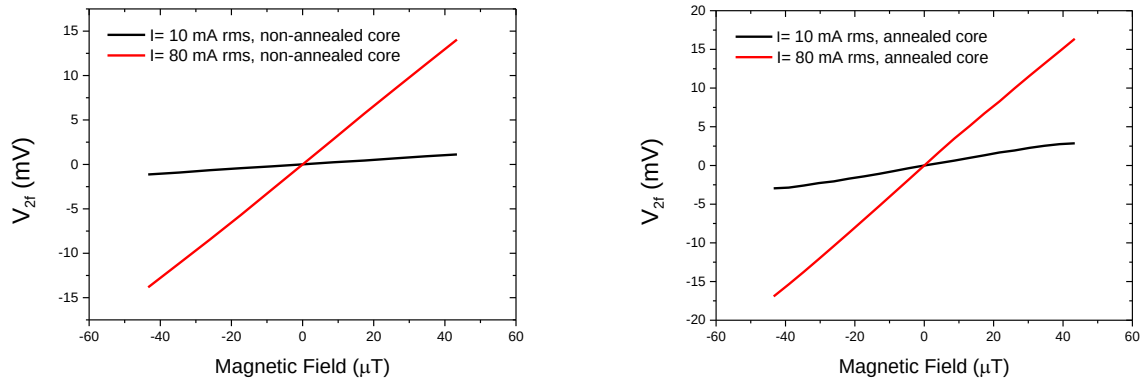
RESULTS AND DISCUSSION

In order to determine the sensitivity of the sensor, f-V measurements were performed showing the working frequency at which the sensor gives higher output voltage. The frequency range of 250 kHz and 900 kHz was scanned to determine the second harmonic signal values at the output of the lock-in amplifier corresponding to these frequencies. This frequency scanning process and the sensitivity of the sensors were analyzed with the LABVIEW program. The working frequency of our sensors was 550 kHz.

The sensitivity of the sensor is expressed by the slope of the second harmonic voltage corresponding to the DC magnetic field curves. Fig. 5a and Fig. 5b shows the sensitivity curves for the sensors with annealed and non-annealed core which were excited with excitation currents of 10 mA rms and 80 mA rms. In fluxgate sensors, the excitation current must be large enough to saturate the sensor core sufficiently [4]. As seen in the slope of curves in Fig. 5a and Fig. 5b increasing the current from 10 mA rms to 80 mA rms greatly improved the sensitivity of the sensors. Furthermore, when these two graphs are examined, it is seen that the sensor with the annealed core has higher sensitivity. Fig. 6a and Fig. 6b shows the noise levels of the sensors having annealed and non-annealed core

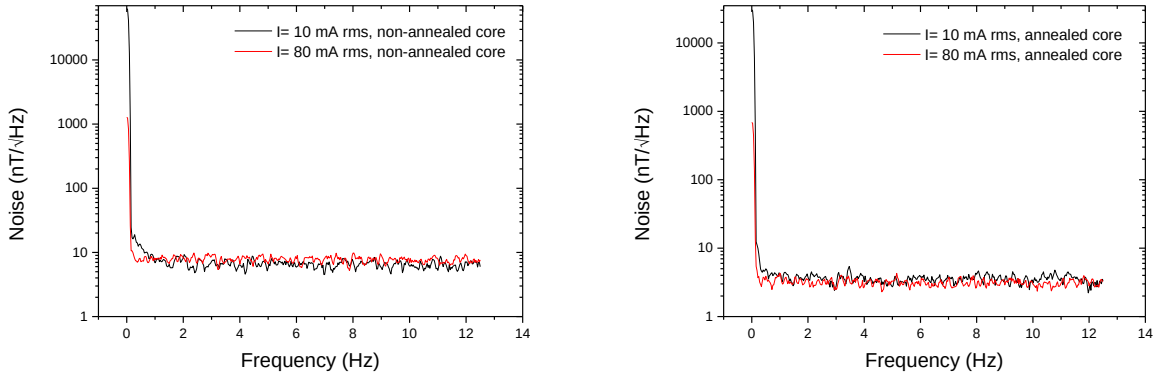
for two different excitation current values. No significant effect of increasing current on the noise level was observed. It was seen that the sensor with annealed core has a slightly lower noise level at 1 Hz frequency.

Looking at the results obtained for these two current values, it is seen that the sensor having annealed core performs better. Therefore, the current value was slightly increased to see if the sensor with annealed core can achieve better sensitivity and noise level. Since there is no current source that can give higher current at 550 kHz, this process was performed at 200 kHz. As shown in Fig. 7a and Fig. 7b, compared to the results when 80 mA rms current was applied at 550 kHz, there has been no improvement in the sensitivity and noise level of the sensor in this current and frequency value.



(a) (b)

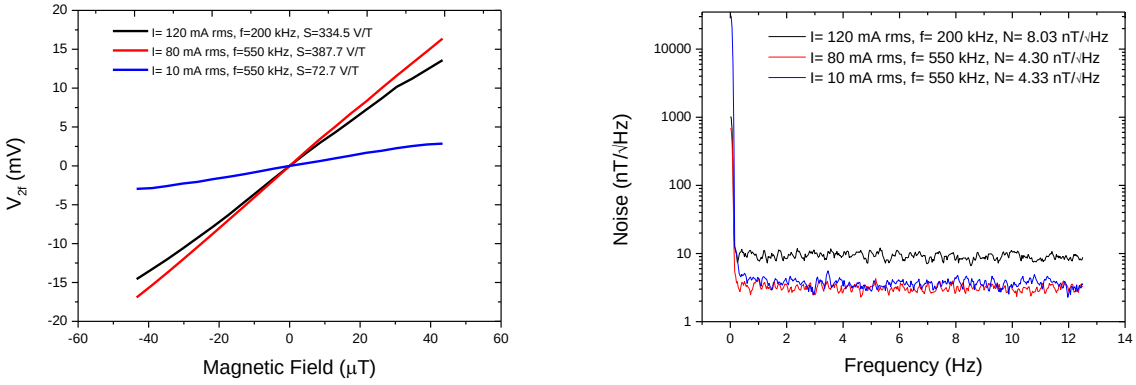
FIGURE 5. Sensitivity measurement results for the sensors with (a) non-annealed core (b) annealed core



(a) (b)

FIGURE 6. Noise measurements of sensors (a) with non-annealed core (b) annealed core

ISBN:978-605-83516-6-0



(a) (b)

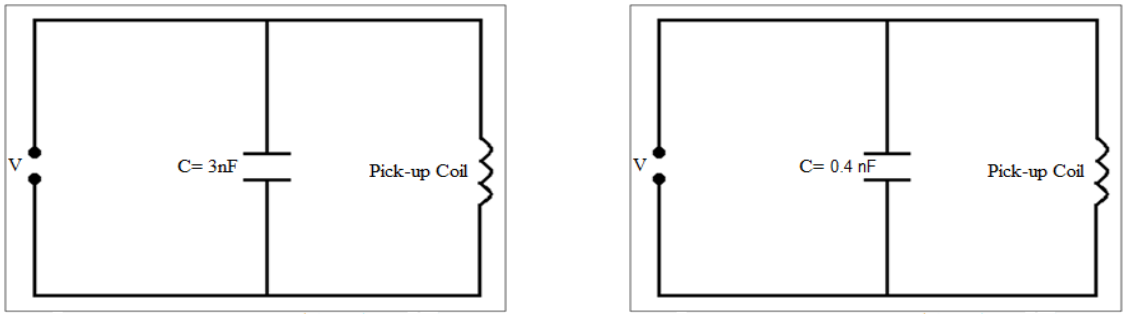
FIGURE 7. Comparison of (a) sensitivity values and (b) noise levels of sensors with annealed core

Table 1 shows the sensitivity and noise values for the sensors with different excitation currents and core materials. The highest sensitivity and the lowest noise values were obtained as 387 V/T and 4.30 nT/√Hz respectively.

TABLE 1. Sensitivity and noise values for sensors with different excitation current and core materials

Excitation Current	Frequency	Core Material	Sensitivity	Noise
10 mA rms	550 kHz	Non-annealed	25.9 V/T	6.89 nT/√Hz
10 mA rms	550 kHz	Annealed	72.7 V/T	4.33 nT/√Hz
80 mA rms	550 kHz	Non-annealed	323 V/T	7.66 nT/√Hz
80 mA rms	550 kHz	Annealed	387 V/T	4.30 nT/√Hz
120 mA rms	200 kHz	Annealed	334 V/T	8.03 nT/√Hz

When the sensitivity and noise values obtained are considered, it is thought that these results should be improved. In order to improve the performance of the sensor, suitable capacitor values that will resonate the pick-up coils have been determined and added in parallel to the coils as shown in Fig. 8. For 10 mA rms and 80 mA rms excitation currents, the capacitor values to resonate the winding systems were 3 nF and 0.4 nF respectively.



(a) (b)

FIGURE 8. Addition of capacitor to the pick-up coils of the sensors with annealed and non-annealed core for (a) 10 mA rms excitation current (b) 80 mA rms excitation current

ISBN:978-605-83516-6-0

After adding the capacitor values, an increase in sensor sensitivity was observed for 10 mA rms current value since the signal strength increases when the winding system is resonated as shown in Fig. 9a and Fig. 9b.

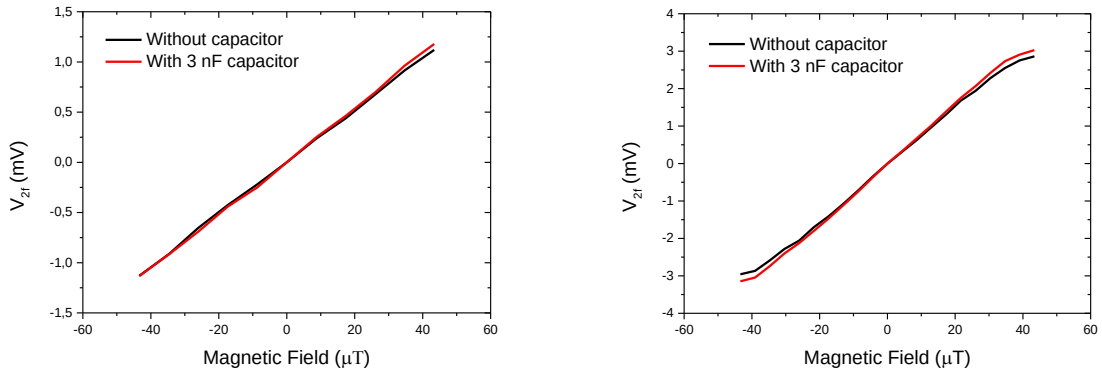


FIGURE 9. Sensitivity measurement results of sensors with capacitor and without capacitor for the sensor with (a) non-annealed core (b) annealed core for 10 mA rms excitation current

Noise levels at 1 Hz decreased after adding capacitors in sensors with both annealed and non-annealed core for 10 mA rms excitation current (see Fig. 10a and Fig. 10b).

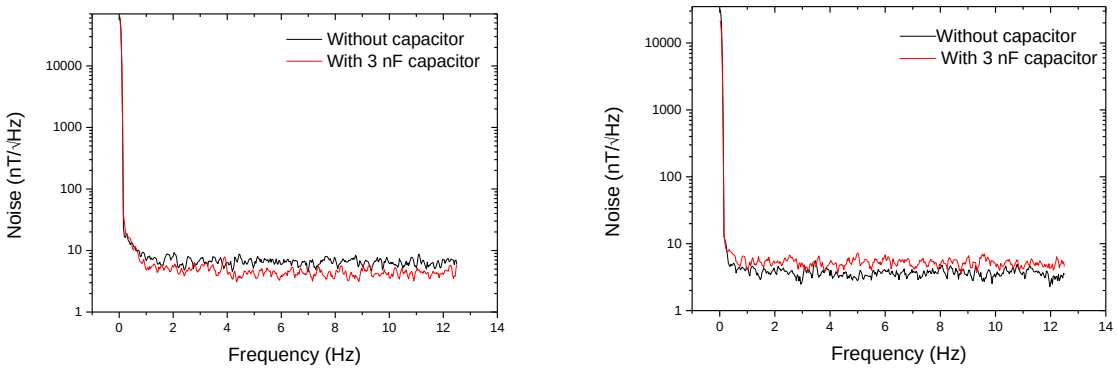


FIGURE 10. Noise levels of sensors with capacitor and without capacitor for the sensor with (a) non-annealed core (b) annealed core for 10 mA rms excitation current

For 80 mA rms excitation current, adding the capacitor to the system has helped improve the sensitivity as seen in the slope of the curves in Fig. 11a and Fig. 11b. For this current value the capacitor reduced the noise level of the sensor with non-annealed core. However, the capacitor slightly increased the noise level of the sensor with annealed core (see Fig. 12a and Fig. 12b).

ISBN:978-605-83516-6-0

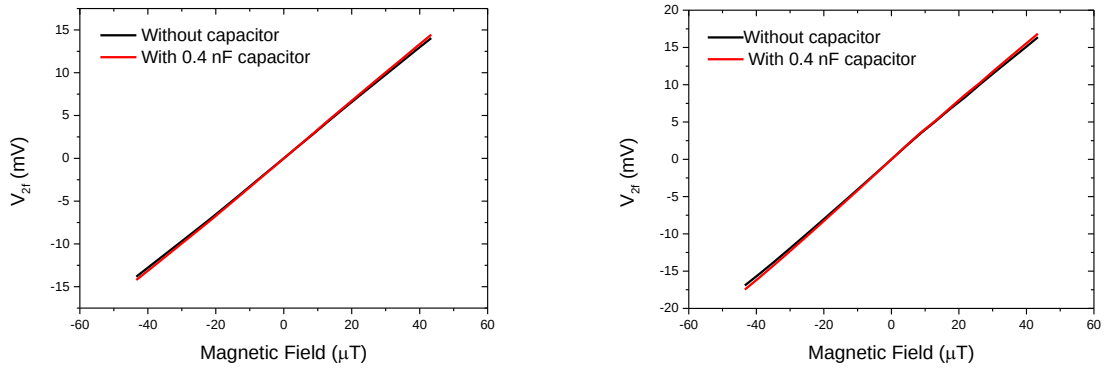


FIGURE 11 . Sensitivity measurement results of sensors with capacitor and without capacitor for the sensor with (a) non-annealed core (b) annealed core for 80 mA rms excitation current

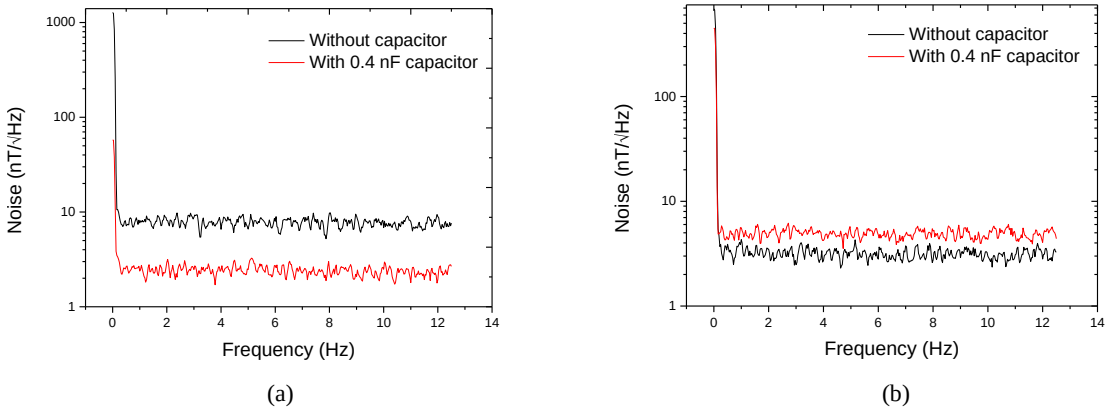
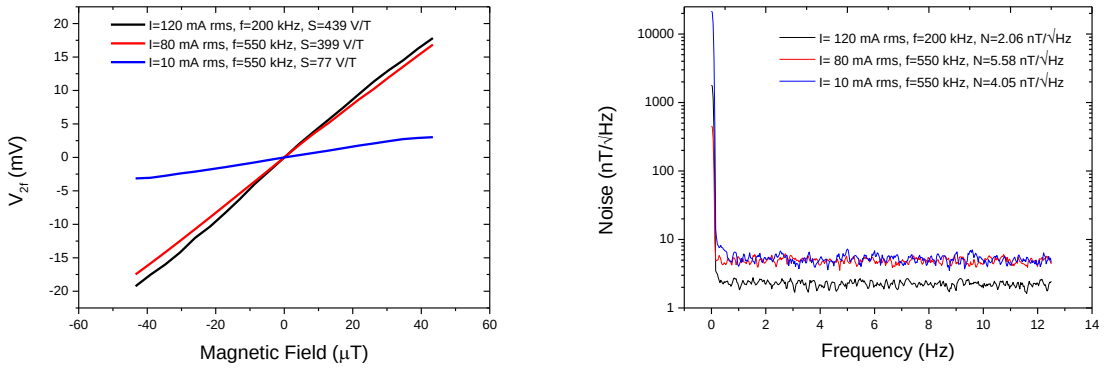


FIGURE 12. Noise levels of sensors with capacitor and without capacitor for the sensor with (a) non-annealed core (b) annealed core for 80 mA rms excitation current

When the excitation current is 120 mA rms, the capacitor value to resonate the winding system was 5.6 nF. As shown in Fig. 13a, when the excitation current was 120 mA rms at 200 kHz, the sensor with the annealed core has reached a better sensitivity value compared to other excitation current values. In addition, Fig. 13b shows that the noise level was quite low.

ISBN:978-605-83516-6-0



(a) (b)

FIGURE 13. For the sensors having annealed core with different capacitors connected comparison of (a) sensitivities (b) noise levels

Table 2 shows the sensitivity and noise values for the sensors with different excitation currents and core materials after adding proper capacitors. The highest sensitivity and the lowest noise level were obtained in the sensor with annealed core for 120 mA rms excitation current value at 200 kHz.

TABLE 2. Sensitivity and noise values for sensors with different excitation current and core materials after adding proper capacitors

Excitation Current	Frequency	Core Material	Sensitivity	Noise
10 mA rms	550 kHz	Non-annealed	26.7 V/T	4.77 nT/√Hz
10 mA rms	550 kHz	Annealed	76.9 V/T	4.05 nT/√Hz
80 mA rms	550 kHz	Non-annealed	332 V/T	2.38 nT/√Hz
80 mA rms	550 kHz	Annealed	399 V/T	5.58 nT/√Hz
120 mA rms	200 kHz	Annealed	439 V/T	2.06 nT/√Hz

CONCLUSION

In this study, we investigated the effect of current and heat treatment applied to the sensor core on the performance of the sensor. We have prepared two sensors consisting of two different core materials, keeping the pick-up coil assembly fixed. It has been observed that increasing the excitation current to a certain value improves the sensitivity of the sensor. We also observed that heat treatment applied to the core material was highly effective on the performance of the sensor. In addition, the sensor sensitivity was improved by adding suitable circuit element like capacitor to the pick-up coil system. In this work, after some improvement studies we obtained a miniaturized fluxgate sensor with maximum sensitivity of 439 V/T and 2.06 nT/√Hz noise level.

REFERENCES

1. P. Ripka, "Magnetic Sensors and Magnetometers", 1st Edition, Boston: Artech House (2001)
2. A. Sarkar, S. Hembram, S. Chatterjee, A. B. Mallick, "Effect of Annealing Treatments on the Magnetic Properties of FeCo/Cu Core Shell Nanostructures", Materials Today: Proceedings, 5, 745–751 (2018)
3. S. Zhi, Z. Feng, L. Guo, C. Lei, Y. Zhou, "Investigation of a Novel MEMS Orthogonal Fluxgate Sensor Fabricated with Co-based Amorphous Ribbon Core", Sensors and Actuators A, 267, 121–126 (2017)
4. L. Guo, C. Wang, S. Zhi, Z. Feng, C. Lei, Y. Zhou, "Wide Linearity Range and Highly Sensitive MEMS-based Micro-Fluxgate Sensor with Double-Layer Magnetic Core made of Fe-Co-B Amorphous Alloy", Micromachines, 8 (12), 352 (2017)

BOOK OF FULL TEXT PROCEEDINGS TURKISH PHYSICAL
SOCIETY 35th INTERNATIONAL PHYSICS CONGRESS (TPS35)
TPS35, Vol.01, No.01, pp.67-73.
ISBN:978-605-83516-6-0

15 December 2019

Piezoelectric Based Acoustics Frequency Converter

Mustafa Kurt [1, a)], Çiğdem Bilge Çiftçi [1]

[1]*Department of Physics, Çanakkale18Mart University, 17100 Çanakkale, Turkey*

[a)]Corresponding author: mkurt@comu.edu.tr

Abstract Acoustic transducers use piezoelectric materials to produce sound waves. When exposed to a harmonically variable electric field, a vibrating piezoelectric material creates a compression and causing noise to be generated in the surrounding environment. Likewise, when the piezoelectric material is exposed to pressure from the acoustic energy, it generates an electrical signal. Since acoustic waves with different energies exhibit different pressure values on the piezoelectricity, the amplitude of the wave causing the effect can be determined from the potential voltage on the piezoelectric. However, the identification of the amplitude is only insufficient to determine the sound source frequency, in this study we determined the acoustic frequency produced by piezoelectric sensor by using FFT method.

INTRODUCTION

The piezoelectric effect was discovered in the 18th century by French physicists Jacques and Pierre Curie. If pressure is applied to the ribbon shape piezoelectric material, the load accumulation on the surface ends increases depending on the pressure level simultaneously. So a voltage difference between the two ends of the ribbon occur with the depending on strain level. Thus, the mechanical effect is transformed into the finite electrical voltage. As a result of the applied vibration, polarization occurs when the positive and negative charges in the ribbon shape piezoelectric material are collected on opposite sides. This polarization results in a potential difference between the ends. When the band-shaped piezoelectric structure is vibrated at certain frequencies, it generates an electrical potential oscillation that is dependent on the vibration frequency. Piezoelectric materials were firstly used in the ultrasonic submarine detector during World War I. In this application, ultrasonic sound waves frequency 20 kHz and above were generated, and directed to bottom surface of the sea. By using returned sound waves from submarine, rocks or any other object, the distance and shape of object could be determined. Due to its wide frequency response and the physical properties of piezo materials, it has become a preferred material for some medical probes and test applications. In addition, film sensors are used in applications in ultrasonic-based detection devices. It is found in liquid level sensors, such as air gap ultrasound for distance measurement, and in-flow measuring devices that use the doppler shift of sound velocity distortions proportional to the liquid flow.

Piezoelectric based sensors is widely used in many fields to determine the source of the sound and the location of the sound source. For example, ultrasonic transducers produced from piezoelectric materials can be used to determine the material properties. In addition to ultrasonic transducers, many piezoelectric applications such as accelerometers and microphones have been developed. Zhenyu Li, and Xiaoming Zhang (2017) studied the design of a kind of identifiable piezoelectric security system based on piezoelectric cable. This system collects the vibration signals of different moving objects such as human, vehicle and animal with piezoelectric cable buried in the ground and differentiates different moving objects with the recognition algorithm. Based on the piezoelectric cable, the mobile body identification device has transformed the vibration signal of three kinds of mobile body (human, bicycle, small truck) into electrical signal by means of piezoelectric cable carrier base, and has processed the data with the system matching algorithm, and has finally achieved the target of detecting three kinds of moving object [1]. In this study, piezoelectric signal is however produced by physical contact instead of direct acoustic signal.

ISBN:978-605-83516-6-0

Alexander Ekimov and James M. Sabatier (2006) by the force sensor and human footsteps sound responses from vibration and two characteristic frequency bands in vibration were investigated in a building experimentally. The first frequency band is observed as a normal force to the surface in the low frequency range below 500 Hz, the second frequency band is observed as the tangential force to the ground and ground reaction or friction force in the high frequency range. Three different gait styles with regular, smooth and the same movement speed were defined and investigated with different vibration amplitudes in the low frequency range below 500 Hz. Sound vibrations in the ground and in the air produced by human footsteps have weakened the distance with loss of energy due to dissipation and loss of energy due to absorption [2]. In other studies by Alexander Ekimov and James M. Sabatier (2006), high frequency responses were not detected in the outdoor test, but only low frequency vibration responses (below 1 kHz) to the footsteps of the ground were observed [3].

It is a disadvantage of acoustic systems to detect acoustic signals generated by the human step from noise sources and is a difficult problem to solve. Environmental noise reduces the maximum distance to the target from which the acoustic signal can be received. In this study, acoustic signals generated by human steps were conceptually detected by using piezoelectric sensors with ribbon structure. For the identification of complex and noise-containing acoustic signals, signature frequencies were derived by performing FFT analysis of the signals. The frequency range of the detected signal was analyzed using MATLAB programing. The frequency range is limited to differentiate the step signal from environmental noise. In the theory part of the article, piezoelectric working principles and FFT transformations are explained and the calculations and results are presented in the calculations and results section.

THEORY

Piezoelectric effect is the change in the electrical polarization produced in certain materials as a result of exposure to mechanical stresses. In the simplest mode, the piezo film acts as a dynamic voltage meter, except that it does not require an external power source, and generates signals larger than the signals from conventional voltage meters after amplification. The frequency response cannot be limited due to the need for high gains and extends to the frequency limit of the given converter. The potential output energy of the piezoelectric ribbon is proportional to the volume of the stretched film. The film thickness can be selected by optimizing the electrical signal or considering mechanical strength considerations. Thick films produce higher voltages, but produce smaller capacitors; thus , instead of a single thick film, a laminate of a thinner film having a compatible material may be preferred. Piezo ceramic transducers do not offer a wide dynamic range, but piezo film transducers are evaluated over a wide bandwidth range. (About 2 Hz to about 2 GHz).

Piezoelectric voltage constant g refers to the electric field formed in a piezoelectric material to which mechanical pressure is applied, also known as piezoelectric potential difference coefficient. The size of the electric field to be obtained in the piezoelectric material depends on the value of the applied pressure and the g parameter. In the case of using of piezoelectric material as sensors, g value getting importance. Unit of g parameter is Volt. Meter / Newton (Vm / N) [4].

$$g = \frac{Electric\ Field}{Applied\ Strain} \tag{1}$$

In Fig. 1, deflection of ribbon piezoelectric vs produced electric potential is shown. Slope of this graph is correspond to g parameter. It is demanded in the most of application that g parameter is high, because small force produce small deflection. If and only if g parameter enough greater, we can resolve small effects as being sound wave pressure.

ISBN:978-605-83516-6-0

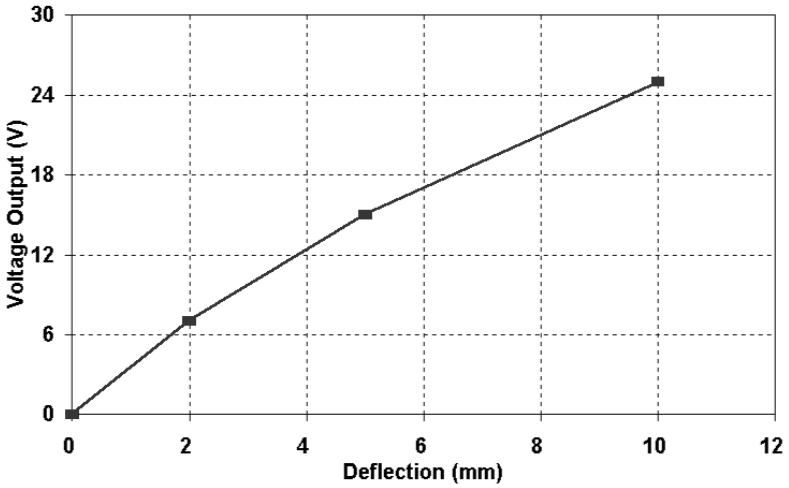


FIGURE 1. Electrical potential generated by deflection in a piezoelectric film.

Sound is longitudinal wave of a certain energy, emitted from pulsating sources at certain frequencies. The sound energy per unit surface per unit time is defined as the intensity of the sound. The propagation of sound cause the vibration of the surrounding particles and transmit of these vibrations to the neighboring particles. Each different frequency sound wave have a specific sound pressure value, shown in Table 1. The definition of sound wave pressure value is different from atmospheric pressure. Waves caused by the vibration of particles in the environment create pressure changes in the air and solids. This pressure change produces deformations on the surface it acts. The distortion on the surface of ribbon shape piezoelectric sensor is directly proportional to the volume and frequency. The dB unit is used to define the sound intensity, the dB unit being the logarithmic ratio of the minimum pressure value of the human ear and the pressure value generated by the ambient sound wave.

$$dB_{SPL} = 10\log\left(\frac{P}{P_0}\right) \tag{2}$$

P represents the measured power Po reference power.

$$dB_{SPL} = 20\log\left(\frac{p}{p_0}\right) \tag{3}$$

p represent the measured pressure, p_0 reference pressure. The amount of pressure produced by sound is called sound pressure. Pressure levels unit is pascal (Pa). The logarithmic scale of the root mean square of sound pressure calculates the Sound Pressure Level (SPL) and is expressed in decibels (dB).The base of the 0 dB SPL is equal to the human hearing threshold of 20 μPa for the sound pressure level. The value sound pressure level (dB_{SPL}) vs sound intensity are shown in Table 1.

ISBN:978-605-83516-6-0

TABLE 1. Sound pressure level depending on dB SPL.

Sound Source	**Intensity**	**dB SPL**	**Pressure**
Threshold severity	1.10^{-12} W/m^2	0	0.00002 Pa
Whisper	1.10^{-10} W/m^2	20	0.0002 Pa
Normal conversation	1.10^{-6} W/m^2	60	0.02 Pa
Heavy traffic on the street	1.10^{-5} W/m^2	70	0.063245553 Pa
Takeoff of the jet plane	1.10^{2} W/m^2	140	200 Pa
Eardrum damage	1.10^{4} W/m^2	160	2000 Pa

The sounds we hear has not always single frequency consist of overlapping of several frequencies.Interference of waves is called superposition. According to the superposition principle, the waves pass without disturbing each other. The current displacement at any given time is the sum of the individual displacements of the waves. This applies to waves with finite length wave pulses or continuous sine waves. In addition, the wave formed by combining multiple waves can be analyzed using various methods. As a result of this analysis, each wave constituting the event wave is analyzed. The most widely used of these methods is the Fourier Transform method.

Signals detected in any system are usually measured as a function of time. However, the most basic information about the system, this signal is obtained by making frequency space solutions. For most events, information about the signal is expressed in the frequency definition range. By using Fourier analysis, a signal is transferred from time domain to frequency domain. In the Fourier approximation, it is assumed that all sub-waves that make up the event wave consist of sinus and cosine functions. The Fourier transform function is shown below [5].

$$f(x)=a_0+\sum_{n=1}^{\infty}(a_n\cos nx+b_n\sin nx)$$

The sum of cosine and sine represents the function f(x).

$$f(t)=f\left(\frac{2\pi t}{T}\right)\qquad a_0=\frac{1}{2\pi}\int_{-\pi}^{\pi}f(x)dx$$

The Fourier series is written as follows.

$$f(x)=\frac{1}{2}a_0+\sum_{n=1}^{\infty}a_n\cos\left(\frac{2\pi nt}{T}\right)+\sum_{n=1}^{\infty}b_n\sin\left(\frac{2\pi nt}{T}\right)$$

coefficients are expressed as follows.

$$a_n=\frac{1}{\pi}\int_{-\pi}^{\pi}f(x)\cos(nx)dx\qquad a_n=\frac{2}{T}\int_{-T/2}^{T/2}f(t)\cos\left(\frac{2\pi nt}{T}\right)dt$$

$$b_n=\frac{1}{\pi}\int_{-\pi}^{\pi}f(x)\sin(nx)dx\qquad b_n=\frac{2}{T}\int_{-T/2}^{T/2}f(t)\sin\left(\frac{2\pi nt}{T}\right)dt$$

the equation changes as stated above.

$$f(t)=\frac{1}{2\pi}\int_{-\infty}^{+\infty}F(\omega)e^{-i\omega t}d\omega$$

$$F(\omega)=\int_{-\infty}^{+\infty}f(t)e^{i\omega t}dt$$

With Euler equation f (t) is obtained from a time-dependent function F (ω) transformation function. ω is frequency. The frequency function is obtained from the time function.FFT analysis of the received signal can be performed with MATLAB application for human step detection.

ISBN:978-605-83516-6-0

CALCULATIONS AND RESULTS

The piezoelectric ribbon is deformed proportional to the frequency of acoustic signals, thus there are a direct relationship between the electrical signal detected from the piezoelectric ribbon and the acoustic signal. From low frequency signals, high amplitude responses are obtained. In this way, the low frequency acoustic signal produced by the human footstep can be perceived as a higher amplitude electrical signal. The acoustic signals sensed by the piezoelectric ribbon is taken as analog data at the output of the piezoelectric sensor and converted into digital signals via DAQ (Data Acquisition Systems). The general form of acoustic signal generated by the human footstep is shown in Fig. 2. We assume that the signal is being measured directly at the output of the piezoelectric ribbon sensor. Then, FFT analysis is performed for this signal.

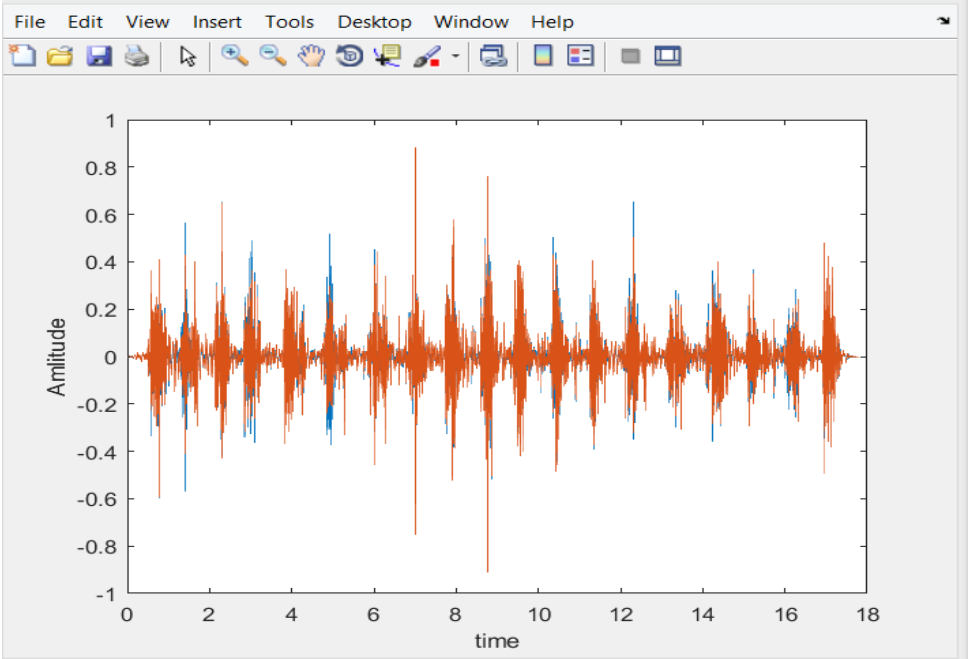


FIGURE 2. Acoustic signal of the human foot step.

In this study, a signal processing tool is designed using the MATLAB Graphical User Interface (GUI), in order to process real time signal. Real-time signals are obtained and analyzed in the frequency domain. By this way, the incoming audio signal can be analyzed simultaneously. The data digitized by the DAQ (Data acquisition) can be displayed on the computer screen in real time. The digital data was used for input data of our software. The GUI signal was designed to be stopped, resumed and recorded in frequency domain analysis. The sampling frequency and Nyquist frequency of the signal were determined. The frequncy response is shown in Fig.5.

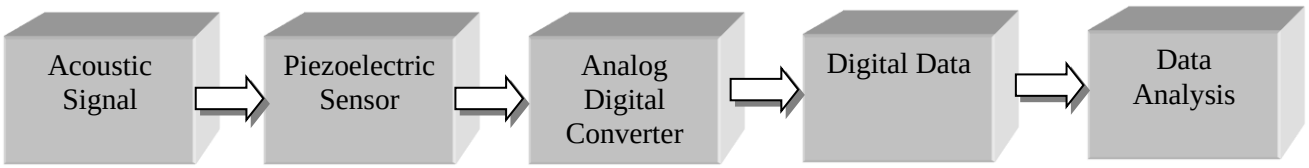


FIGURE 3. Digital data acquisition system.

ISBN:978-605-83516-6-0

Flow chart of our algorithm for data processes is shown in Fig.3. In the process of listening to the audio data of the human footstep on the computer, the digital audio data is read on the storage devices, transferred to the microprocessor and transmitted to the DSP (Digital Signal Processor) on the sound card. DSP decodes the data. The decoded data is converted to analog audio signals by the digital analog converter (DAC) of the sound card and transmitted to the output of the sound card and then to the speaker. In this way, the audio signal present or produced in the computer is transferred to the speaker via the sound card. Audio signals that are digitally present in the computer are transmitted to the speakers by converting them into analog form by sound cards, and the vibrating speaker diaphragm converts electrical signals into sound waves. The sound waves from the loudspeaker are received by the piezoelectric structure. The piezoelectric ribbon structure is deformed harmonically with acoustic signals of different frequencies. Acoustic signals coming to the piezoelectric material are taken as analog data at the output of the piezoelectric material and converted to digital signal by means of Data Acquisition Systems (DAQ).

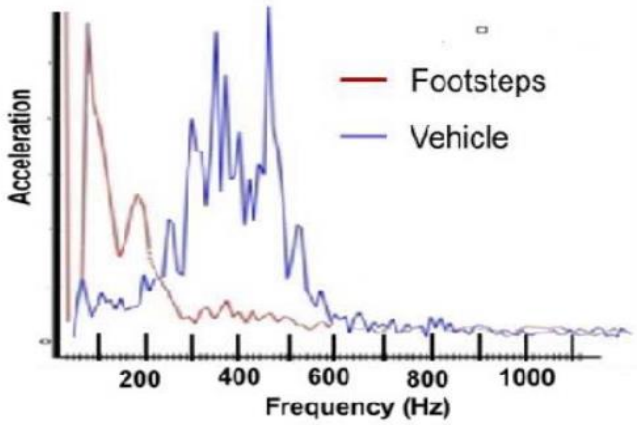


FIGURE 4. Seismic signal bandwidth for footsteps and vehicles [6].

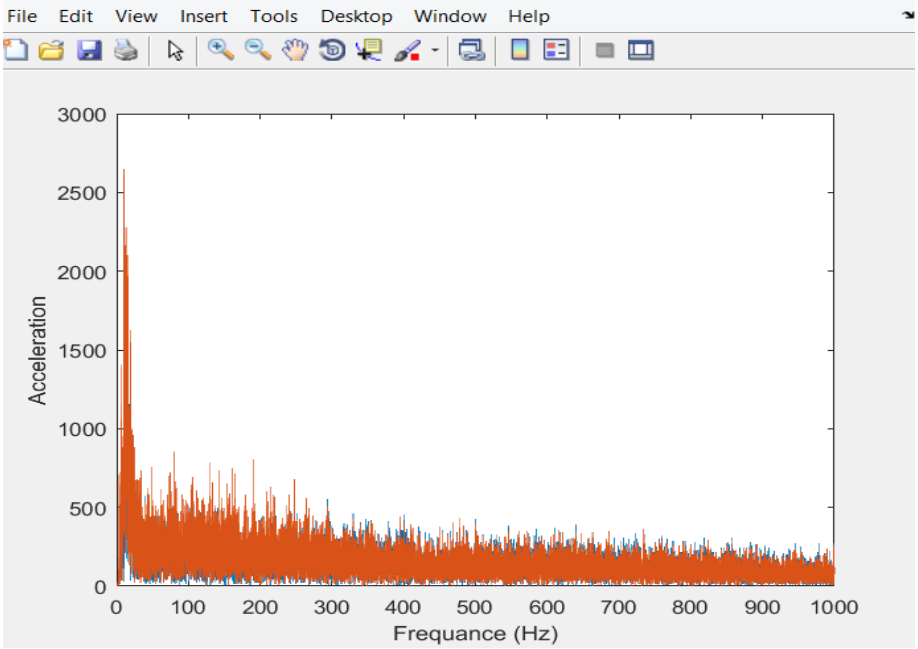


FIGURE 5. Acoustic signal of the human footstep.

The frequency distribution analyzed for human and vehicle by Levy et al. is shown in Fig. 4. In these study, Levy et al. used a seismometer to detect footstep and vehicle acoustic signal. They modified the seismometer's amplitude bandwidth for the different kind of grounds. After measuring of the seismic vibration with seismometer, they made the Fourier transformations and published the results in 2017 articles. In our study, assuming that the acoustic signal data is taken by piezoelectric signal which is exactly match to the acoustic signal, Fourier transforms are performed. The frequency distribution of our results which is consistent with found by Levy et al are presented in Fig. 5.This study shows that our method can be used to detect and analyze acoustic signals.

CONCLUSION

Acoustic signal conversion of any undefined sound source is taken interest in the literature. In this study, assuming that the electric output voltage of piezoelectric sensor is completely coincide with the frequency of acoustic signals, the acoustic signal data is analyzed by performing FFT method. It was seen that our results in the sense of frequency distributions is compatible with the literature. In this study, it is shown that the proposed approach method can be applied to identify undefined acoustic sound sources.

ACKNOWLEDGMENTS

This study is supported by Çanakkale Onsekiz Mart University The Scientific Research Coordination Unit, (Project number: FYL-2019-2912).

REFERENCES

1. Zhenyu Li and Xiaoming Zhang, *Identifiable piezoelectric security system design*., AIP Conference Proceedings 1890, 040016, 2017
2. Alexander Ekimov and James M. Sabatier, *Vibration and sound signatures of human footsteps in buildings*, The Journal of the Acoustical Society of America 120, 762, 2006
3. A.Ekimov and J. M. Sabatier,*Broad frequency acoustic response of ground/floor to human footsteps*.Proceedings Volume 6241, Data Mining, Intrusion Detection, Information Assurance, and Data Networks Security 2006; 62410L, 2006
4. YunusUzun, *Periyodik Manyetik Alanlar Etkisinde Doğrusal Olmayan Titreşimlerden Elektrik Enerjisi Üretimi*, Gazi ÜniversitesiFen Bilimleri Enstitüsü, Aralık2012
5. Alper Ermiş, *İzinsiz girişlerin zemin titreşimlerinin ölçümü ve analizi ile tespiti*, Gazi Üniversitesi Fen Bilimleri Enstitüsü, 2012
6. Raphaël Levy, Julien Moras and Benjamin Pannetier, *Vibrating Beam MEMS Seismometer for Footstep and Vehicle Detection*,IEEE Sensors Journal, Vol. 17, No. 22, November 15, 2017

BOOK OF FULL TEXT PROCEEDINGS TURKISH PHYSICAL
SOCIETY 35th INTERNATIONAL PHYSICS CONGRESS (TPS35)
TPS35, Vol.01, No.01, pp.74-81.
ISBN:978-605-83516-6-0

15 December 2019

Investigations for Increasing the Accuracy of Dielectric Constant Measurements

Ceren Özkal[1, a)] and Fatih Yaman[1, b)]

[1] *İzmir Institute of Technology, Dept. of Electrical & Electronics Eng. 35430 Urla, İzmir, Turkey*

[a)] Corresponding author: cerenozkal@iyte.edu.tr
[b)] fatihyaman@iyte.edu.tr

Abstract. In this study, the results obtained via the cavity perturbation method are investigated to find the most accurate dielectric constant measurement setup parameters. The rectangular and cylindrical cavities are modelled via CST-MWS where the modes of the cavities are determined such that the maximum electric field occurs in the middle of the cavities for high precision. Simulation setups are prepared with different material volumes and different dielectric constants in the S-band. The most reliable results are achieved for materials with low dielectric constants. It is observed that the error rate between the exact and analytically calculated dielectric constant values decrease for small volumes of the samples which is the case for high frequencies. Moreover, the effect of the cavity shapes on the dielectric measurements is illustrated numerically.

INTRODUCTION

Permittivity is a measure of the resistance of a material against to increment in charge when the material to be polarized under an electric field [1]. It is a complex value and the ratio of the real part of it to the free space permittivity is called the dielectric constant. The information on the value of the dielectric constant has a significant importance to understand the electrical characteristics of the material. For instance, identification of the electrical characteristics plays a vital role for the detection of water hardness in the cooling systems [2], the specification of the electrical properties of printed circuit substrates [3], the determination of moisture content of seeds used in agriculture [4], the assignment of heating time in microwave processing of foods [5].

There are several techniques to measure the dielectric constant of materials, which can be classified into two broad groups: transmission line/free space methods and resonance methods [6]. The first group is proper for ferrites and measurements for a wide frequency band, while the second group provides the highest accuracy which has weak assumptions on the sample shape or size. Microwave resonator cavities are used for solid and liquid materials in the resonance method. The dielectric constant is calculated from the frequency shift caused by the sample located inside the cavity according to the principles of the material perturbation theory [7].

In literature, examinations to increase the accuracy of the measurements associated with the volume and shape of the sample can be found in [8]. However, the aim of this study to investigate which of the rectangular and cylindrical cavity geometries commonly used in cavity perturbation method gives more reliable results. For the numerical results a full wave electromagnetic simulator CST-MWS [9] is employed in 2-4 GHz frequency range for the materials with different dielectric constants and various sample volumes.

ISBN:978-605-83516-6-0 15 December 2019

METHOD

The method used in this study can be explained based on the analogy with the inverse problems. Here, the aim of the direct problem is the calculation of the desired mode's resonant frequency by employing a full-wave electromagnetic simulator CST-MWS for the empty cavity and for the dielectric loaded cavity by using the given permittivity value ε_{exact}. The inverse problem whose aim is to reconstruct the relative dielectric constant ε_r, from the knowledge of the cavity volume V_c, the sample volume V_s, the resonant frequency for the perturbed cavity f_s and the resonant frequency for the unperturbed cavity $f_{0,}$ is solved analytically via the resonator cavity technique which utilizes the material perturbation approach. The formulation starts with Helmholtz equations for the isotropic material in the source-free domain such that the following equation is achieved [10]:

$$\frac{f_S - f_0}{f_0} \approx \frac{-\int_{V_0} (\Delta\varepsilon \left|\vec{E}_0\right|^2 + \Delta\mu \left|\vec{H}_0\right|^2) dV}{\int_{V_0} (\varepsilon \left|\vec{E}_0\right|^2 + \mu \left|\vec{H}_0\right|^2) dV} \tag{1}$$

where $\vec{E}_0$ indicates the electric field and $\vec{H}_0$ denotes the magnetic field vectors of the empty cavity. In this equation $\Delta\varepsilon$ and $\Delta\mu$ represent the change in the permittivity and in the permeability, respectively. The expressions are integrated over the whole volume of the cavity, V_0.

Equation 1 represents the relation between the shift in the resonant frequency and the change in permittivity or permeability. If the sample under test is non-magnetic, as in our study, the permeability change $\Delta\mu$ vanishes. Furthermore, we can assume the initial and perturbed fields are approximately equal since the volume of the sample is quite small as compared to the volume of the cavity. Additionally, the electric field value at each point on the sample can be considered as constant when the sample volume is chosen sufficiently small. Finally, it is necessary to note that the electric field expression according to the cavity geometry should be used. Dielectric constant equations for rectangular and cylindrical cavities respectively are given for the stated assumptions in the following form [11] – [12]:

$$\varepsilon_r = 1 + 0{,}5 \frac{V_c}{V_s} \frac{f_0 - f_s}{f_0} \tag{2.a}$$

$$\varepsilon_r = 1 + 0{,}539 \frac{V_c}{V_s} \frac{f_0 - f_s}{f_0} \tag{2.b}$$

We note that the constant '0,539' in equation 2.b is written for the cylindrical cavity obtained from the roots of the Bessel functions [12].

TE_{101} mode for the rectangular cavity and TM_{010} mode for the cylindrical cavity are modelled since these modes have no electric field variation along the vertical y-axis. A tube containing the sample is inserted in the centre of the cavity where the magnitude of the electric field is maximum, see Fig. 1.

ISBN:978-605-83516-6-0

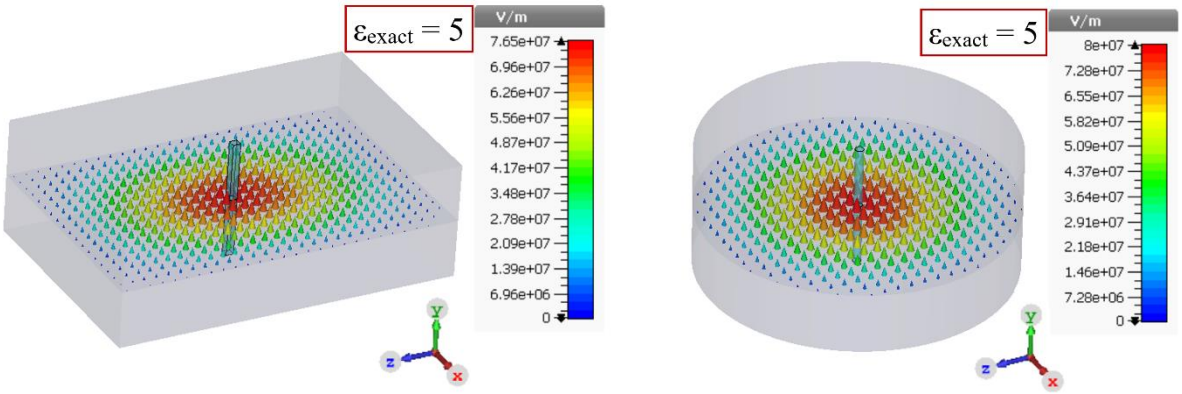


FIGURE 1. Rectangular TE_{101} cavity and cylindrical TM_{010} cavity with dielectric samples in CST-MWS.

Two investigations were performed for this study. The first one focus on how the error rate is affected by any increment at the dielectric constant value. The resonator cavities are designed such that their selected modes operate at 3 GHz frequency and the cavity volumes are adjusted as approximately equal. Similarly, the sample volumes are also fixed to nearly the same value for each setup, so that the ratio of the cavity volume to the sample volume in equations 2.a and 2.b is kept constant. While the dielectric constant value of the sample ε_{exact}, used in the direct problem computations is increased from 2 to 20, the percentage error rate is determined as follows

$$error\ rate\ \% = \frac{|\varepsilon_{exact} - \varepsilon_r|}{\varepsilon_{exact}} \times 100 \tag{3}$$

using the ε_r which is obtained from the corresponding equations (2), analytically.

For the second investigation, a comparison of rectangular and cylindrical cavities is carried out and it is examined how the increment in the dielectric constant, the sample volume and the resonant frequency would affect the reconstructed dielectric constant values. At each step, the volumes of the cavities are kept at similar values. In this case, all simulations are done for two different materials with dielectric constants 5 and 10. Besides, the volumes of the samples are decided as 50, 200 and 800 mm^3 and thus, it is observed how the change in sample volume will affect the perturbation approach. The frequency range of 2-4 GHz is chosen. The frequency of the TM_{010} cylindrical cavity can be simply found via the radius of the cavity. If the frequency of the TE_{101} rectangular cavity is to be adjusted on only one axis for realization, the limitation is encountered. Even if the length on the z-axis reaches very large values, the frequency change is insignificant. Therefore, the rectangular cavity was analysed in the frequency range of 2-3 GHz and 3-4 GHz.

RESULTS

At first, the accuracy of the permittivity reconstructions obtained from the analytical formulations for two different types of cavities were studied. For this aim, the volume of the cavity, the volume of the sample and the resonant frequency in equations 2-a and 2-b were kept constant. Simulations were prepared at 3 GHz where the dielectric constant was changed from 2 to 20. Afterwards, dielectric constant values were calculated. The exact dielectric constant values and the reconstructed ones are illustrated for rectangular and cylindrical cavities in Fig. 2. The Y values inside the yellow coloured boxes which are located over the curves represent the numerical results for the rectangular cavities while the boxes under the curves correspond the results of the cylindrical cavities.

ISBN:978-605-83516-6-0

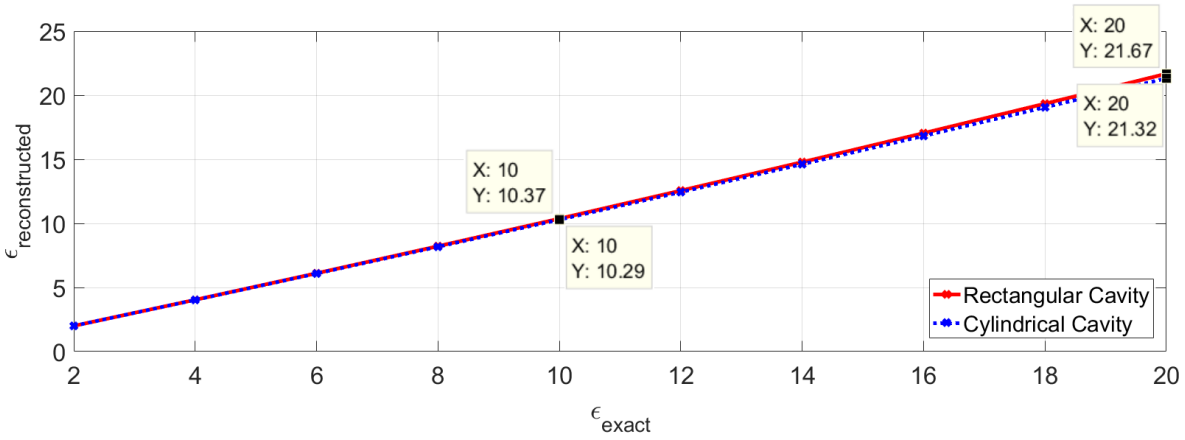


FIGURE 2. Comparison of the reconstructed dielectric constant values for rectangular and cylindrical cavities

As can be seen from Fig. 2 that the accuracy of the inversion formulas is satisfactory even though the precision decreases when the value of the dielectric constant increases. Furthermore, the results obtained by using cylindrical cavities are slightly more accurate and to observe the difference between rectangular and cylindrical cavities more clearly, we present Fig. 3 by considering percentage error calculations. Here we can conclude that since perturbation approach holds the problems based on the small quantities effectively, the error rate reaches to higher values with the increment in the volume of the sample and the value of the dielectric permittivity.

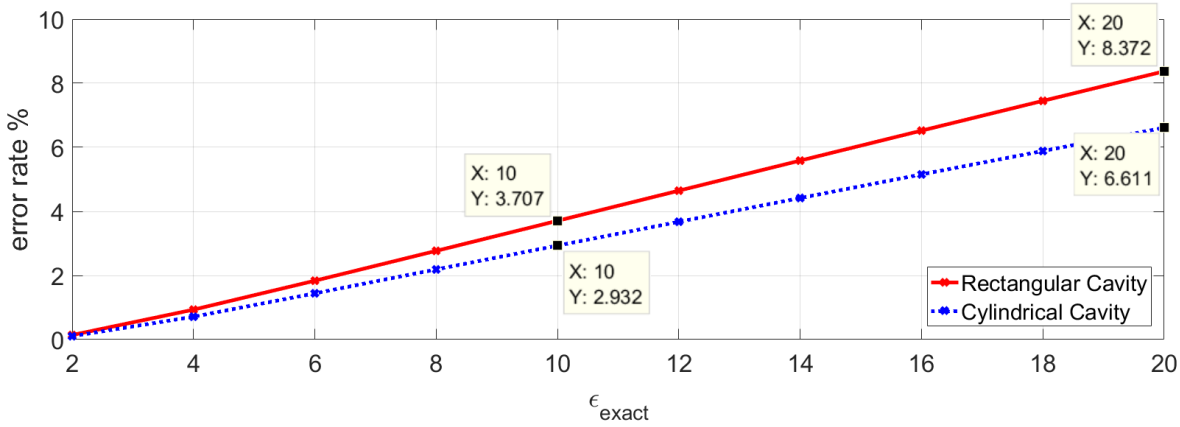
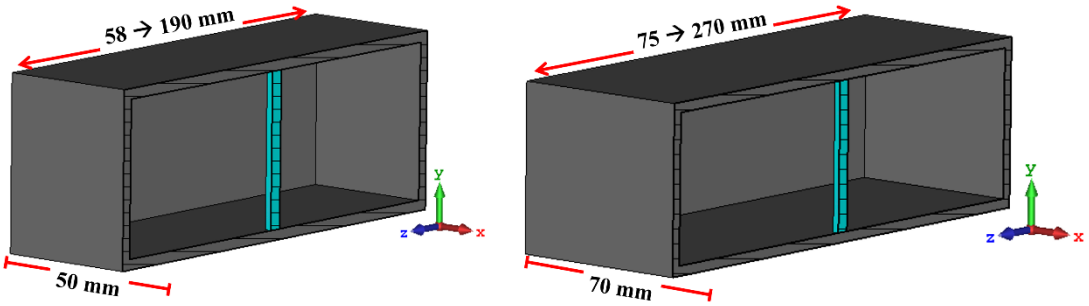


FIGURE 3. Comparison of the error rates for rectangular and cylindrical cavities

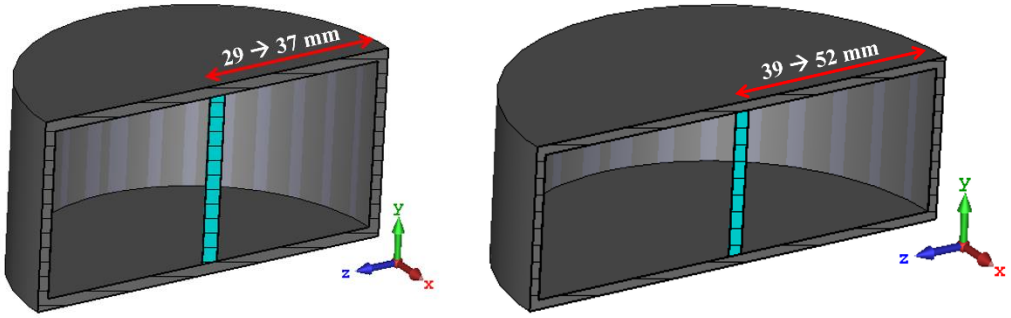
In the second investigation, the impacts of changes in the dielectric constant, the sample volume and the resonant frequency were observed. The volumes of the empty cavities were increased step by step to reduce the resonant frequency values for the considered modes as shown in Fig. 4 and 5. The volumes of the cavities were kept close to each other at every step. Accordingly, 4 figures were obtained for two different substances with dielectric constants 5 and 10 in the two frequency ranges, 2-3 GHz and 3-4 GHz. Moreover, each plot shows the results of 3 different sample volumes for 50, 200 and 800 mm^3.

ISBN:978-605-83516-6-0



(a) (b)

FIGURE 4. Rectangular cavity dimensions for different frequency ranges (a) 3-4 GHz; (b) 2-3 GHz



(a) (b)

FIGURE 5. Cylindrical cavity dimensions for different frequency range (a) 3-4 GHz and (b) 2-3 GHz

The reconstructed results for the material whose exact dielectric constant 5 in the frequency range of 2-3 GHz and 3-4 GHz are shown in Fig. 6 and 7, respectively. The errors in the reconstructions decreased as the frequency increased for the rectangular cavity while the reconstruction curves for the cylindrical cavity changed slightly. For the rectangular cavity, the most accurate result was obtained as the frequency increased, i.e. as the cavity volume was reduced and the sample volume was reduced as well. Unexpectedly the opposite behaviour for the reconstructions are observed since the most accurate results via cylindrical cavities are obtained as the frequency decreases. We also report that the error rate is less than 1% for both cavities if we use the smallest volume of the sample. As can be seen in the first figures of Fig. 6 and 7 there is a jump at around 3 GHz for the rectangular cavities. This sudden increment is related to the new dimensions chosen for the rectangular cavity (i.e. 70 mm along x-axis, 75 mm along z-axis lengths, respectively) to sweep frequencies 2-3 GHz with ~100 MHz steps by changing the length of the cavity along the z-axis.

ISBN:978-605-83516-6-0

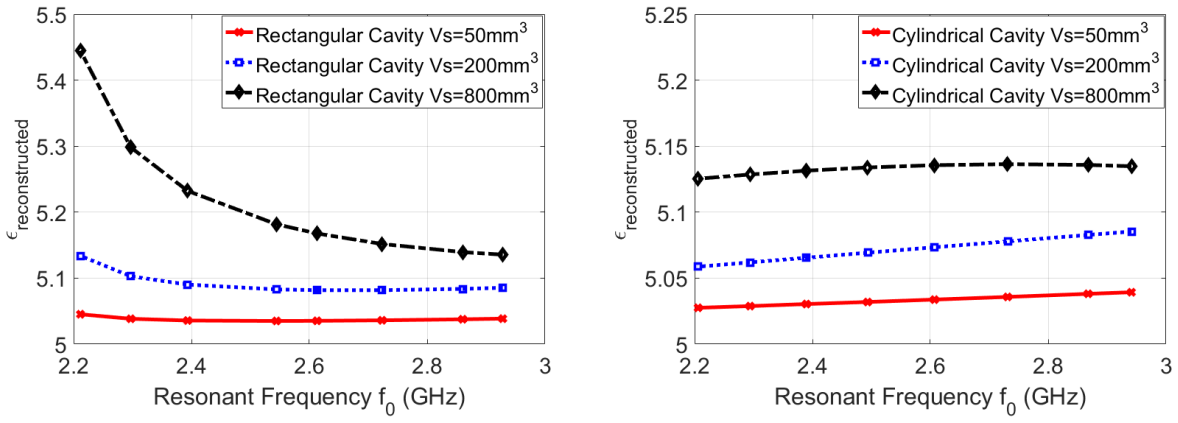


FIGURE 6. Comparison of reconstructed dielectric constant values for different volumes of material with dielectric constant 5 in the frequency range 2-3 GHz

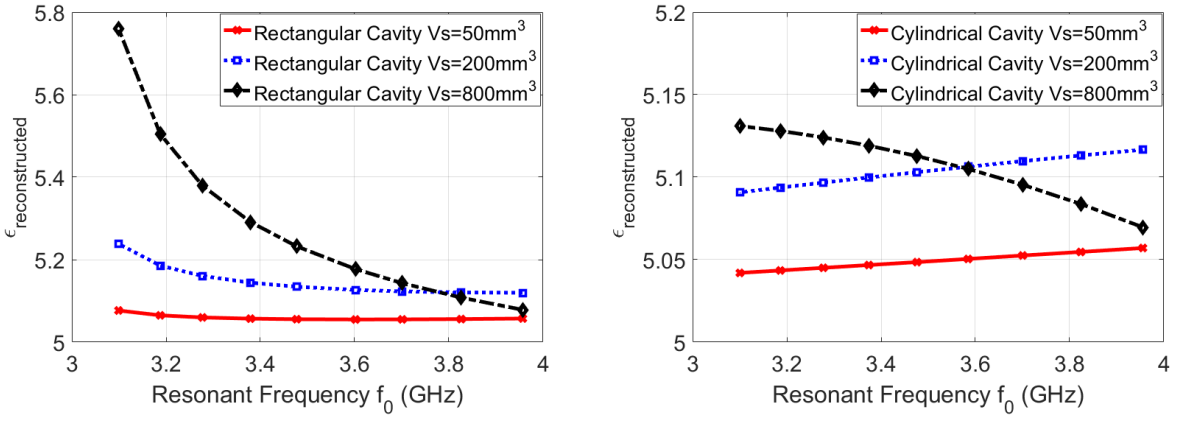


FIGURE 7. Comparison of reconstructed dielectric constant values for different volumes of material with dielectric constant 5 in the frequency range 3-4 GHz

Fig. 8 and 9 show analytically calculated dielectric permittivity results for the material having exact relative dielectric constant value 10 in the frequency range of 2-3 GHz and 3-4 GHz. Reconstructions behave similar to the former ε_{exact}=5 investigations however as a worst-case scenario the error rate reached to 40% at 3.1 GHz for ε_{exact}=10 using rectangular cavity. For the cylindrical cavity, the least accurate result was obtained at the highest frequency of our frequency spectrum for V_s=200mm^3 where the error rate was approximately 6%. In general, we observe larger sample volumes increase the error rate in all cases. At this point, we note that, the black curves for the cylindrical cavities illustrated in Fig. 7 and 9 have unexpected variations even though the same procedures for the all simulations were followed. To understand the behaviours of these results we suggest experimental verifications.

ISBN:978-605-83516-6-0

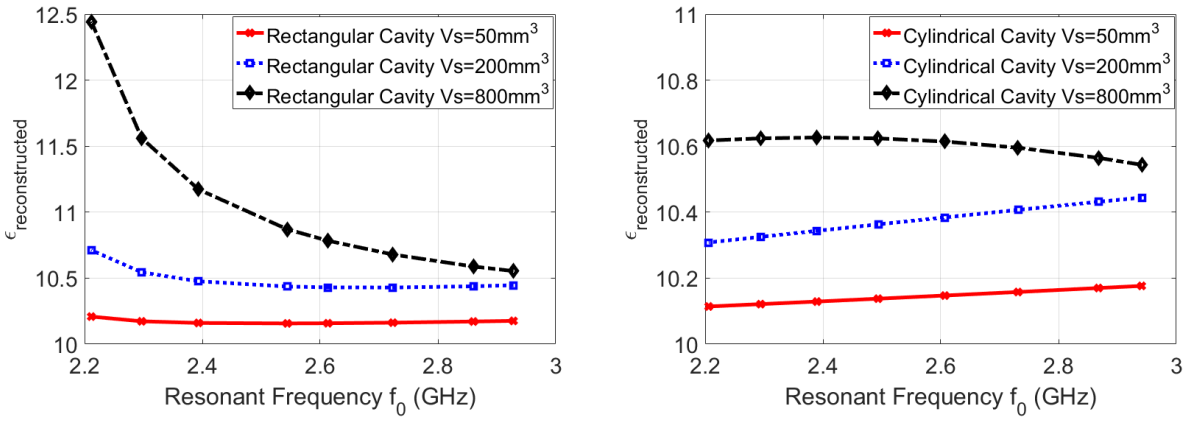


FIGURE 8. Comparison of reconstructed dielectric constant values for different volumes of material with dielectric constant 10 in the frequency range 2-3 GHz

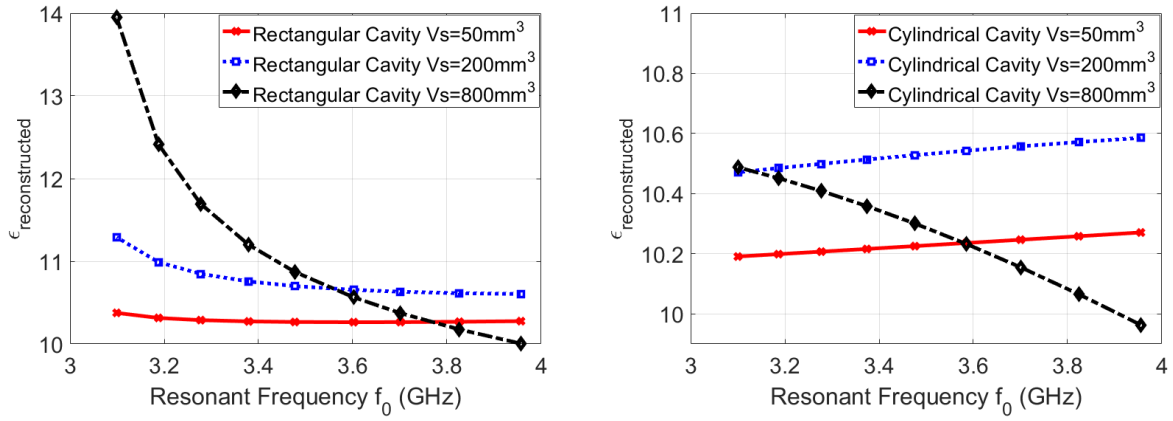


FIGURE 9. Comparison of reconstructed dielectric constant values for different volumes of material with dielectric constant 10 in the frequency range 3-4 GHz

CONCLUSIONS

In this study, the accuracy of dielectric constant measurements for rectangular and cylindrical cavities using different cavity dimensions were compared. Simulations were performed to obtain resonant frequencies of the selected modes in the 2-4 GHz frequency range for different dielectric constants and different sample volumes. We note that the ratio of the cavity volume to the sample volume was kept constant. Dielectric constant values were reconstructed from the knowledge of the cavity volume, sample volume and resonant frequency by using the approximate analytical expressions which were obtained via the perturbation method.

Firstly, it was shown that the error rate in the reconstructions increases for the larger dielectric constants due to the limitations of the perturbation approach. We also observe cylindrical cavities could provide more accurate results than rectangular cavities in all cases. Generally speaking, the accuracy of the results obtained via the rectangular cavity increased when the frequency increased, i.e. the cavity volume decreased. However, we cannot generalize the same behaviour for the cylindrical cavities even though the results in this type of cavity are closer to the exact values. The accuracy of the results deteriorated as the sample volume raised due to the perturbation theory for both cavities. Our investigations suggest that in the S-band, a rectangular cavity setup at the higher frequencies or cylindrical cavity setup at lower frequencies should be preferred for a more accurate dielectric constant measurement of the same sample with the procedure presented in this study.

ISBN:978-605-83516-6-0

REFERENCES

1. C. A. Balanis, *Advanced Engineering Electromagnetics*, 2nd Ed., John Wiley, New York, 2012, pp. 41-47
2. K. H. Teng, M. Ateeq, Shaw A., Al-Shamma'a A., S. N. Kazi, B. T. Chew and Kot P., International Journal of Electromagnetics and Applications, 7(2):38-47 (2017).
3. C. H. Riedell, M. B. Steer, M. R. Kay, J. S. Kasten and M. S. Basel, IEEE Transactions on Instrumentation and Measurement, vol. 39, no. 2, 1990.
4. M. S. Venkatesh, "Cavity perturbation technique for measurement of dielectric properties of some agri-food materials", Ms.thesis, McGill University,1996.
5. S. O. Nelson, Transactions of the ASAE, vol. 42(2): 523 – 529, 1999.
6. J. Krupka, Meas.Sci. Technol. 17, R55-R70, 2006.
7. R. A. Waldron, Institution Monograph, no. 373 E, 1960.
8. Z. Peng, J. Y. Hwang and M. Andriese, IEEE Transactions on Instrumentation and Measurement, vol. 63, no. 2, 2014.
9. CST AG - Computer Simulation Technology, Darmstadt, Germany. *CST MICROWAVE STUDIO*. (2018). [Online]. Available: http://www.cst.com.
10. D. M. Pozar, *Microwave Engineering*, 4th Ed., John Wiley, New York, 2012, pp. 306-309.
11. A. Verma and D. C. Dube, IEEE Transactions on Instrumentation and Measurement, vol. 54, no. 5, 2005.
12. R. G. Carter, IEEE Transactions on Microwave Theory and Techniques, vol.49, no. 5, 2001.

BOOK OF FULL TEXT PROCEEDINGS TURKISH PHYSICAL
SOCIETY 35th INTERNATIONAL PHYSICS CONGRESS (TPS35)
TPS35, Vol.01, No.01, pp.82-86.
ISBN:978-605-83516-6-0

15 December 2019

The Study on Noise Reduction Analysis of Untreated Leaves of Plants in Urban Areas

Serhun SAĞLAM[1, a)], Doğukan BİNGÖL[2], Ulaş Yunus ÖZKAN[1], Bülent EKİCİ [3], Feyza GÜZELÇİMEN[4]

[1] *Department of Forest Management and Planning, Faculty of Forestry, Istanbul University-Cerrahpasa, TR-34473, Bahçeköy, Istanbul, Turkey.*
[2] *Graduate School of Engineering and Sciences, Istanbul University, TR-34116, Beyazıt, Istanbul, Turkey*
[3] *Department of Mechanical Engineering, Faculty of Engineering, Marmara University, TR-34722, Kuyubaşı, Istanbul, Turkey*
[4] *Istanbul University, Faculty of Science, Physics Department, TR-34134, Vezneciler, Istanbul, Turkey*

[a)]*Corresponding author: nuhres@istanbul.edu.tr*

Abstract. The noise pollution, nowadays, increases in parallel with rapid urbanization. Noise that should be controlled is a serious problem for both life and ecological environment in urban. Urban plants are of the natural sound-absorbent materials. The aim of this study is to find out the effect of acoustic characteristics of various plants on noise reduction. The measurements of sound absorption have been obtained by using impedance tube (Brüel & Kjaer 4206) which provides ISO 10534-2 standard for leaves of investigated plants. Three samples have been taken for each leaf type and frequency dependent sound absorption coefficient data have been determined. The noise reduction coefficient values have been calculated by using the data.

This work was supported by TUBITAK with the project no 118O494.

INTRODUCTION

In recent years, the world has been polluted by factors such as pollution, global warming and some human practices. The noise pollution, one of the most important factors affecting human quality of life, is examined in the present article. In many studies on outdoor noise reduction, natural fibers have been considered in order to optimize the sound absorption capacity rather than synthetic sound barriers [1–3].

These materials are generally identified by natural or renewable sources for emitting low level of environmental pollution during production [4]. There is particularly increasing interest in natural fiber materials for acoustic uses. [5-7]. The tree leaves which is one of the natural materials could ecologically and aesthetically be popular with the aspects of cheap cost, easy processing in environmental area [8].

The purpose of this study is to obtain the sound absorption coefficient with an impedance tube involving the two-microphone transfer-function method and to realize the effect of one-layer and three-layer leaves on reducing noise pollution.

Türk Fizik Derneği
1950
Turkish Physical Society

ISBN:978-605-83516-6-0

MATERIAL AND EXPERIMENT

The entire leaves were collected from the healthy trees in the same climate and soil conditions from the Education and Research Forest of Istanbul University Cerrahpaşa. According to Greenwich, the Research Forest located on the Thrace side of the Marmara Region is located between the eastern longitudes of 28° 59' 17" – 29° 32' 25" and the northern latitudes of 41° 09' 15" – 41° 11' 01" (Fig. 1).

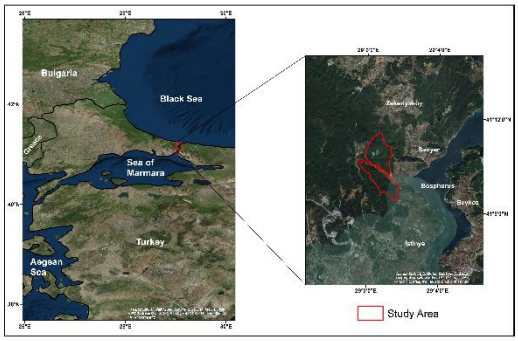


Fig. 1: Location of Education and Research Forest of Istanbul University Cerrahpaşa in Istanbul, Turkey.

We have chosen different tree species which are common in the urban area of Turkey. These are Sycamore (*Platanus orientalis*), Laurus (*Laurus Nobilis*), Linden (*Tilia tomentosa*), Chestnut (*Castanea sativa*), Ligustrum (*Ligustrum japonicum*), Prunus (*Prunus laurocerasus*), Magnolia (*Magnolia grandiflora L.*), Hortensia (*Hydrangea macrophylla*), Osmanthus (*Osmanthus heterophyllus*), Hedera Helix (*Hedera sp.*).

As shown in Figure 2, the preparation process of one leaf sample (Osmanthus) is shown for our experiment. In total, three samples were at least formed with a diameter of 29 mm from leaves of each tree species.



Fig. 2: (a) Osmanthus leaf (b, c) Leaf formed with diameter of 29 mm.

An impedance tube (Brüel & Kjaer 4206 [9], with ASTM E1050 and ISO 10534-2 standarts) equipment based on two microphone transfer function method in the Textile Engineering Department of Marmara University, Faculty of Technology was performed to realize the acoustic behavior of selected leaves (Fig. 3).

ISBN:978-605-83516-6-0



Fig. 3: Impedance tube kit (4206) used in experimental set-up.

In this experiment set-up, a pair of microphones is mounted flush with the inner wall of the tube. Any sample to be tested is firstly mounted to straight tube with appropriate diameter. A high-output acoustic sound source is connected at the opposite end of the tube [10].

A multi-channel spectrum analyzer obtains the transfer function (H_{12}) between the microphones. The pressure reflection coefficient R of the material is determined by:

$$R = \frac{H_{12} - e^{-jks}}{e^{jks} - H_{12}} e^{j2k(L+s)} \quad (1)$$

where L is the distance from the sample face to the first microphone and s is the distance between the microphones, $k = 2\pi f/c$, f is the frequency, and c is the speed of sound. The ratio of the energy absorbed by a material to the total incident sound energy is known as the sound absorption coefficient ($\propto$). The absorption coefficient α of the sample could be determined by [10]:

$$\propto = 1 - |R|^2 \quad (2)$$

For any particular material, the absorption properties are a function of the frequency. In order to rate the overall absorbent property of the material, the noise reduction coefficient (NRC) is used as a measure of the arithmetic average ratio of coefficients in certain frequency range [11,12]:

$$NRC = \frac{1}{6}(\propto_{125} + \propto_{250} + \propto_{500} + \propto_{1000} + \propto_{2000} + \propto_{4000}) \quad (3)$$

During the measurement, the conditions such as environmental setting of ambient air temperature, relative humidity and atmospheric pressure, microphone calibration, thickness of sample, signal-to-noise ratio evaluation (background noise measurement and signal measurement) could be taken into consideration to increase the accuracy of the measurement. In our experiment, these conditions are the atmospheric pressure of the test medium is 100.7-101.5hPa, the temperature of the medium during the measurement is 24.5-27.5 ^{0}C and the humidity is 64.6-69.2%.

To increase the accuracy of the measurements, the experiments were repeated under the same conditions for at least three samples per each tree species. The sound absorption coefficients dependent to frequency of each sample with a diameter of 29 mm in the range of 50-6400 Hz and NRC values calculated by Eq. 3.

RESULTS

Linearly increasing sound level in the frequency range of 50-6400 Hz was performed for leaf samples collected from ten different tree species. Figure 4-a shows the graph of sound absorption coefficient versus frequency for each

ISBN:978-605-83516-6-0

investigated leaves with one-layer. Similarly, Figure 4-b shows the graph of sound absorption coefficient versus frequency for each investigated leaves with three-layer (with five-layer for only linden and chestnut).

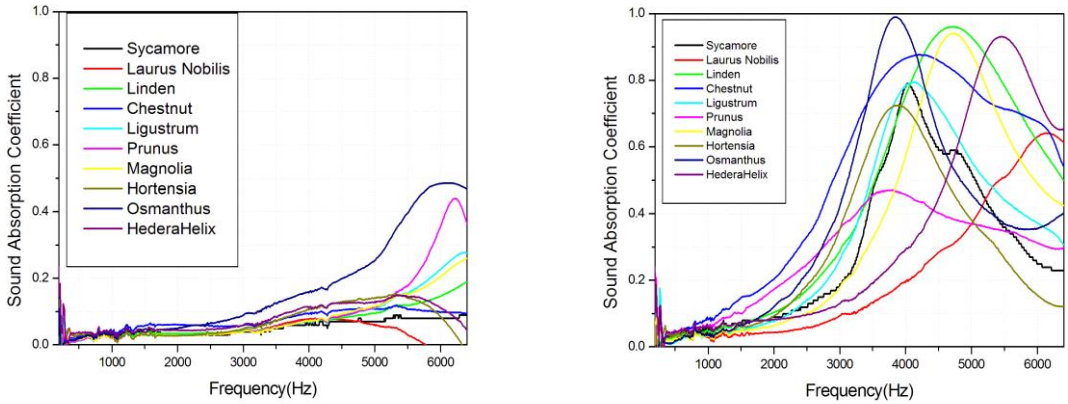


Fig. 4. The sound absorption coefficient versus frequency; (a) for one-layer leaves, (b) for three-layer leaves (with five-layer for only linden and chestnut).

For all samples, the calculated NRC values are given in Table 1.

Table 1. Noise reduction coefficients (NRC)

Species	NRC (One Leaf)	NRC (There Leaves)
Sycamore	0.023	0.160
Laurus Nobilis	0.027	0.059
Linden	0.024	0.156*
Chestnut	0.037	0.083*
Ligustrum	0.022	0.157
Prunus	0.026	0.139
Magnolia	0.024	0.116
Hortensia	0.032	0.148
Osmanthus	0.043	0.197
Hedera Helix	0.053	0.084

* five leaves

The sound absorbability depends significantly on density parameter that affects the acoustic properties of materials except from thickness of leaf, leaf roughness, tree age. The density values of investigated ten species are calculated between 0.9-2.8 g/cm^3. The results show that tree leaves with one-layer considered in the present work have low sound absorption values between 0.02-0.05 and leaves with three-layer have higher values between 0.06-0.2. Considering the whole leaf population and leaf density of a tree, it can be concluded that trees can be used as sound barriers in urban areas and outside laboratory environment.

ACKNOWLEDGMENTS

The present study has supported by TUBITAK Project no. 118O494. We would like to thank to Assoc. Prof. Erhan Sancak and his team for contributions during experiments.

REFERENCES

1. Glé, P., Gourdon, E., Arnaud, L., Acoustical properties of materials made of vegetable particles with several scales of porosity, Appl Acoust., 2011, 72:249–59.

ISBN:978-605-83516-6-0

2. Asdrubali, F., Schiavoni, S., Horoshenkov, KV., A review of sustainable materials for acoustic applications, Build Acoust, 2012, 19(4):283–312.
3. Iannace, G., Maffei, L., Trematerra P., On the use of green materials for the acoustic correction of classrooms, In: Proceedings of EuroNoise, Prague, 2012, 89–94.
4. Arenas, JP., Crocker, MJ., Recent trends in porous sound absorbing materials for noise control, Sound Vib., 2010, 44(7):12–7.
5. Berardi, U., Iannace G., Acoustic characterization of natural fibers for sound absorption applications, Build Environ., 2015, 94(2):840–52.
6. Fatima, S., Mohanty AR., Acoustical and fire-retardant properties of jute composite materials, Appl. Acoust., 2011, 72:108–14.
7. Fouladi, MH., Ayub, M., Nor, MJM., Analysis of coir fiber acoustical characteristics, Appl. Acoust., 2011, 72:35–42.
8. Berardi, U., Iannace, G., Predicting the sound absorption of natural materials: Best-fit inverse laws for the acoustic impedance and the propagation constant, Appl. Acoust., 2017, 131-138.
9. Brueel and Kjaer, Brochure using 4- microphones with impedance tube, Brueel and Kjaer Sound and Vibration Measurement, Denmark, Brueel and Kjær Application Note BO 0113-11. https://www.bksv.com/en/Applications/product-noise/Acoustic-material-testing (Date of access:31.05.2019)
10. Seybert, AF., Notes on absorption and impedance measurements, Astm E1050, 2010, 1-6.
11. Simpson, MA., Noise Barrier Design Handbook, U.S. Department of Transportation Federal Highway Administration Office of Research, Washington DC., 1976.
12. Zhang H., Building Materials In Civil Engineering, Woodhead Publishing Limited and Science Press, UK, 2011.

02. Astrophysics and Cosmology



BOOK OF FULL TEXT PROCEEDINGS TURKISH PHYSICAL
SOCIETY 35th INTERNATIONAL PHYSICS CONGRESS (TPS35)
TPS35, Vol.01, No.02, pp.88-91.
ISBN:978-605-83516-6-0

15 December 2019

Analysis of Some Semi-Detached Systems Observed by TESS

Fahri Aliçavuş[1, a)]

[1]*Canakkale Onsekiz Mart University, Faculty of Sciences and Arts, Physics Department, 17100, Canakkale, Turkey*.

[a)]Corresponding author: fahrilcvs@gmail.com

Abstract. Semi-Detached binary stars are very important systems for the precise determination of astrophysical parameters and the analysis of mass transfer and loss mechanisms between the components. In this study, the light curve analysis of some semi-detached systems whose light changes are obtained by the Transiting Exoplanet Survey Satellite (TESS) was performed. The astrophysical parameters of the systems were obtained. In addition, oscillational properties of the systems were investigated, and the mass transfer and the loss amount of such stars are discussed and compared with observational data.

INTRODUCTION

Semi-detached binary systems are very remarkable objects considering the evolutionary conditions. Interactions between components are important in terms of their effects on stellar evolution and testing of models. In addition, the effects of the components on each other and if one of the components contains oscillation, such objects come into prominence in terms of the nature of oscillations, the examination and understanding of physical processes. Accurate data obtained through the recent satellite observations increase the effect of such studies.

In this study, two semi-detached binary systems RV Pic and AS Eri are discussed. These stars have been observed by TESS and they are located inside the classical instability strip. RV Pic (HD 32011, V=9m.67, P=1.812604 day) is a neglected binary system. The most detailed study of the binary was made by Mendez (1975). In the study, RV Pic was observed in UBV bands, but a complete light curve was not obtained. Furthermore, in the same study, the radial velocities of the system were measured and only the velocities of the hot component were obtained, but no measurements of the second component were found.

The other selected semi-detached binary system is AS Eri (HD 21985, V=8m.30, P=2.664152 day) it was was first discovered by Hoffmeister (1934). In the following years, a lot of studies have been done and the absolute parameters have been determined quite well (Popper (1973), Refsdal et. al. (1974), Van Hamme and Wilson (1984)). Gamarova et al. (2000) showed that the hot component showed pulsation with a period of 24.39 minutes. Subsequently, Mkrtichian et al. (2004) revealed the existence of three different frequencies and obtained the star's oscillation modes. Finally, Narusawa (2013) conducted an abundance analysis of the primary component and discussed the relationship between pulsational characteristics and metallicity.

In this study, TESS light curves analyzes were performed for RV Pic and AS Eri and absolute parameters were calculated. In addition, oscillational properties were investigated for AS Eri.

LIGHT CURVE SOLUTIONS AND ABSOLUTE PARAMETERS

The light curves produced by the sensitive observation data of TESS were taken over the MAST portal (https://mast.stsci.edu/portal/Mashup/Clients/Mast/Portal.html) and made ready for solution. The Wilson-Devinney

Türk Fizik Derneği
1950
Turkish Physical Society

ISBN:978-605-83516-6-0

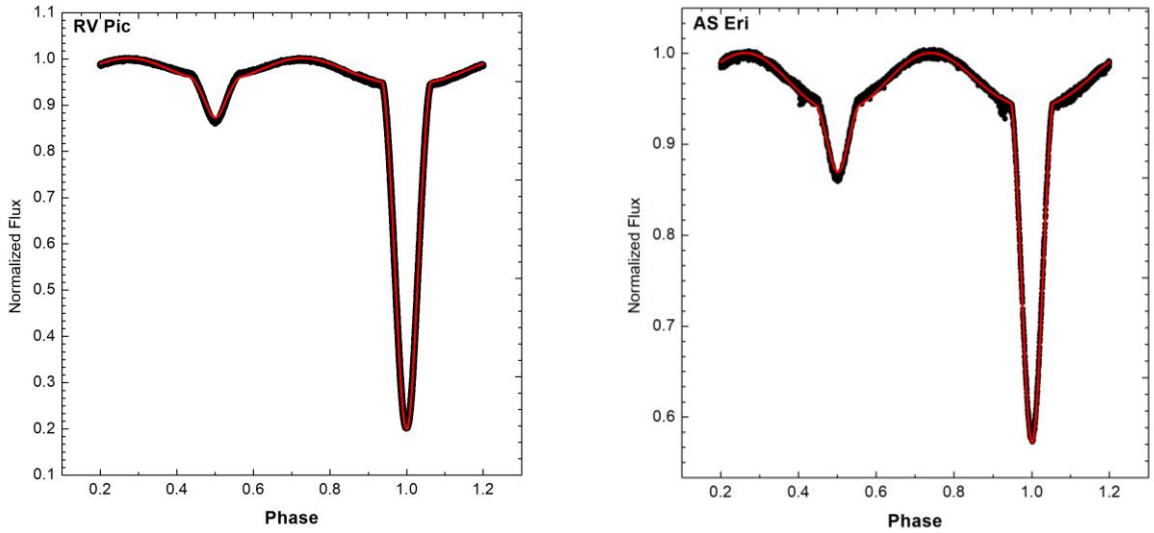
(WD) (Wilson and Devinney 1971) code's MOD 5 was used for the light curve solution. Interstellar reddening was taken into account when calculating the primary components temperatures using with GAIA distances and Galactic extinction from Schlafly and Douglas (2011). The temperatures of the primary components were kept constant during the analyzes. The temperatures according to Eker et. al. (2018) were used using the calculated $(B-V)_0$ values. A detailed description of the light curve solution method is described by Soydugan et al. (2016) and Kahraman Aliçavuş and Aliçavuş (2019). Possible third-light contributions were also considered in the solutions. There was no third light effect for RV Pic, and a third light contribution of about 13% was found for AS Eri. The obtain results from the light curve solution are given in Table 1. Also, the agreement of observations with the theoretical light curves obtained from the solution is shown in Figure 1.

In addition, the basic properties of the components were determined using the parameters detemined from the light curve solutions of both binary systems. The absolute parameters for AS Eri were calculated using with radial velocities measured by Popper (1973). For RV Pic, absolute parameters were estimated using the mass corresponding to the temperature of the primary component (from Eker et al. 2018), since we do not have enough radial velocity measurement. The calculated absolute parameters are given in Table 1.

TABLE 1. Photometric solutions of TESS light curves and absolute parameters of the RV Pic and AS Eri

Parameter	RV Pic	AS Eri
P (day)	3.97178	2.664148
T_1 (K)	8200(150)	8750(100)
T_2 (K)	4221(155)	5099(108)
i (deg)	84.83(14)	81.30(6)
a ($R_\odot$)	14.24(26)	10.35(10)
Ω_1	6.3821(48)	6.4231(79)
Ω_2	2.1666	1.9834
q	0.174(2)	0.108*
Phase Shift	0.0000(1)	-0.0037(3)
$l_1/(l_1+l_2)$	0.806(7)	0.729(14)
$l_1/(l_1+l_2)$	0.194(7)	0.271(14)
l_3	-	0.126(13)
e	0	0
w	90	90
A_1-A_2	1.00-0.50	1.00-0.50
g_1-g_2	1.00-0.32	1.00-032
f_1	34	31
f_2	100	100
$r_{1(mean)}$	0.1609(2)	0.1582(2)
$r_{2(mean)}$	0.2404(2)	0.2096(2)
M_1 ($M_\odot$)	1.95(12)	1.895(49)
M_2 ($M_\odot$)	0.34(2)	0.204(10)
R_1 ($R_\odot$)	2.30(1)	1.642(17)
R_2 ($R_\odot$)	3.27(1)	2.038(19)
L_1 ($L_\odot$)	21.4(1.6)	14.1(7)
L_1 ($L_\odot$)	2.96(42)	2.5(2)
$\mathrm{Log}g_1$	4.01(3)	4.285(14)
$\mathrm{Log}g_2$	2.95(3)	3.13(2)

ISBN:978-605-83516-6-0



(a) (b)

FIGURE 1. TESS (black) and synthetic (red) light curves of RV Pic (a) and AS Eri (b)

PULSATION PROPERTIES

When the TESS data were analyzed, no evidence of pulsation for RV Pic was found. For AS Eri, in which pulsations were determined in previous studies, the effects caused by the orbital motion of the binary star were subtracted from the light curve and oscillational properties were examined using with TESS data. Frequency analysis was performed by using Period04 software. Significant frequency limit was taken as four sigma and analyzes were performed. As a result of the analysis, the dominant frequency was found to be 59.036 c/d which agrees with previous studies. The frequencies and amplitudes obtained from the analyzes are listed in Table 2. In addition, the model representing the frequencies and the compatibility of the observation points are given in Figure 2.

TABLE 2. Frequency analysis parameters for AS Eri.

	Frequency (c/d)	**Amplitude (Flux)**
F_1	59.036	0.00134
F_2	65.385	0.00069
F_3	65.156	0.00041
F_4	58.184	0.00046
F_5	61.937	0.00038
F_6	61.405	0.00037
F_7	58.795	0.00020

ISBN:978-605-83516-6-0

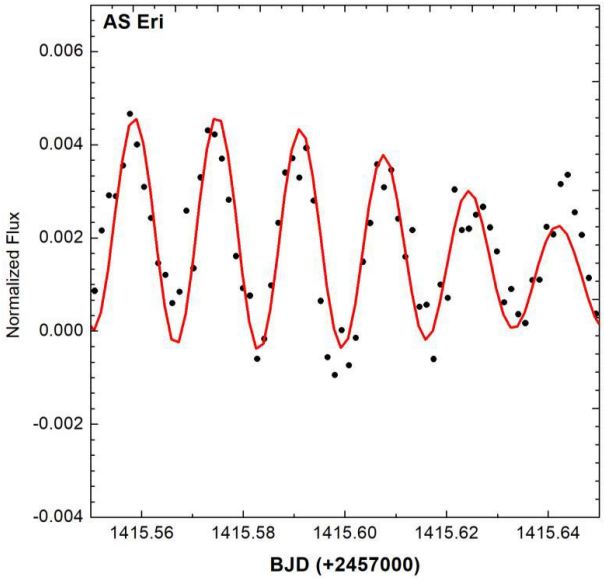


FIGURE 2. Out of eclipse, light variations of AS Eri. (TESS data (black) and synthetic (red) light curve)

DISCUSSION AND CONCLUSION

In this study, TESS light curves of RV Pic and AS Eri were examined for the first time. The absolute parameters of AS Eri have been updated more sensitively. RV Pic was studied in detail for the first time and the masses of the primary and secondary components were calculated as $1.95M_{\odot}$ and $0.34M_{\odot}$, respectively. In addition, considering the fact that both binary stars are semi-detached, the orbital period changes were examined. However, no significant changes were observed in O-C diagrams. Considering the produced binary star evolution models, it is expected that the mass transfer and loss rates of stars with similar mass ratios will be low. The situation in the O-C diagrams in AS Eri and RV Pic indicates this.

When the pulsation frequencies of AS Eri were examined, in addition to the three frequencies Mkrtichian et. al. (2004) found, four new frequencies were found and a total of seven frequencies were determined for the hot component.

Such stars are important for understanding the evolution of stars and studying the dynamics of orbits in binary stars. Therefore, the increase of sensitive observational data is critical. Obtaining new high-resolution spectral data for RV Pic is crucial for testing our approaches to the nature of the binary system.

REFERENCES

1. Eker et. al., 2018, MNRAS, 479, 5491.
2. Gamarova, A. Yu., Mkrtichian, D. E., Kusakın, A. V., 2000, IBVS, 4837.
3. Hoffmeister, C., 1934, AN, 235, 195.
4. Kahraman Alicavus, F., Alicavus, F., 2019, MNRAS, 488, 5279.
5. Mendez, R. H., 1975, IBVS, 1000.
6. Mkrtichian, D. E., et. al., 2004, A&A, 419, 1015.
7. Narusawa, S., 2013, PASJ, 65, 105.
8. Popper, D. M., 1973, ApJ, 185, 265.
9. Refsdal, S., Roth, M. L., Weigert A., 1974, A&A, 36, 113.
10. Schlafly, E. F., Douglas, F. P., 2011, ApJ, 737, 103.
11. Soydugan, E., Soydugan, F., Aliçavuş, F., Erdem, A., NewA, 2016, 46, 40.
12. van Hamme, W., Wilson, R. E., 1984, A&A, 141, 1.
13. Wilson, R.E., Devinney, RJ., 1971. ApJ, 166, 605.

BOOK OF FULL TEXT PROCEEDINGS TURKISH PHYSICAL
SOCIETY 35th INTERNATIONAL PHYSICS CONGRESS (TPS35)
TPS35, Vol.01, No.02, pp.92-97.
ISBN:978-605-83516-6-0

15 December 2019

Could the CF Tuc Contain the Black Hole Closest to The Earth?

Fahri Aliçavuş[1,2,a], Faruk Soydugan[1,2], Filiz Kahraman Aliçavuş[1,2] and Esin Soydugan[1,2]

[1]*Astrophysics Research Centre and Observatory, Çanakkale Onsekiz Mart University Terzioğlu Campus, TR-17020, Çanakkale, Turkey.*
[2]*Department of Physics, Faculty of Arts and Sciences, Çanakkale Onsekiz Mart University, Terzioğlu Campus, TR-17020, Çanakkale, Turkey.*

[a)] Corresponding author: fahrilcvs@gmail.com

Abstract. In this study, we present a detailed analysis of a RS CVn type binary star CF Tuc which has high quality data of Transiting Exoplanet Survey Satellite (TESS). During the photometric analysis, spot mobility was examined. Sensitive absolute parameters (e.g. M, R) of the binary components were obtained by modelling the light changes caused by eclipsing by eliminating the spots effect. Using the obtained parameters parameters, and considering different effects (magnetic activity, rotation, angular momentum evolution, etc.), binary star evolution models were produced, and the initial evolutionary parameters of the binary star were calculated. In addition, taking into account the possibility of hosting the closest black hole to Earth (Doğru et al. 2009), the new minimum data observed by TESS has been added and the orbital period changes have been examined. The results obtained were evaluated together with X-ray observations and evolutionary models. We discussed the existence of the possible black hole component.

Keywords: stars:binaries: eclipsing – orbital period change – stars: fundamental parameters: evolution models – individuals: CF Tuc

INTRODUCTION

The eclipsing binary stars are important in terms of obtaining the basic parameters accurately and understanding the dynamics of the galaxy. The obtained precise parameters from eclipsing binaries have a particular importance to make comparison between evolution models and observational findings. They are also useful for examining the minimum time of such stars to reveal the properties of possible extra components and to make better galaxy population syntheses. Nowadays, due to the satellite observations on such stars, the increased sensitivity enables the discussions on the subject to be made better. Over the past year, the basic parameters of the reconstituted precise light curve of this type of star can be reached with the TESS data which is expected to reach more consistent results on the effects of spots and possible third body movements.

In this context, CF Tuc (HD 5303, V=7^m .90), is a chromospheric active binary star, which was found from the TESS data was selected within the scope of the study. CF Tuc has been studied in detail for years. The first detailed light curve and radial velocity solution was published by Collier et al. (1981). Afterwards, there are studies on the magnetic activity of the system and the change of the orbital period (Budding and Zeilik (1995), Anders et. al. (1999)). The most recent detailed study of CF Tuc was done by Doğru et. al. (2009). In the study, spectral and photometric properties of the star were investigated. As a result, models containing two spots on the cooler component were derived and the basic parameters were calculated with good sensitivity. As a result of their analysis of the change of the orbital period, they concluded that CF Tuc may be a member of a triple system with a blackhole. In the following years, Yamamoto et. al. (2012) and Iwakiri et. al. (2018) observed X-ray flux activity in the 2-20 keV band for 3 and 2.5 hours, respectively.

In spite of many studies, the light curves of the star were observed with quite scattering. In this study, the basic parameters were updated, and spot structure was examined by using TESS light curves with high accuracy. Then, the O-C (Observed-Calculated) analysis was renewed by including the minimum times obtained from the TESS. In addition, with the help of the obtained parameters, binary star evolution models of the system were produced and compared with the observation results.

Türk Fizik Derneği
1950
Turkish Physical Society

ISBN:978-605-83516-6-0

LIGHT CURVE ANALYSIS

The sensitive TESS light curves of the system were taken over the MAST portal (https://mast.stsci.edu/portal/Mashup/Clients/Mast/Portal.html) and made ready for solution. The Wilson-Devinney (WD) code (Wilson and Devinney 1971) was used for the light curve solution. Considering the presence of spots, spotted models were produced. The mass ratio (q) was taken as 1.117 (Doğru et. al. 2009) during the solutions. A detailed explanation for the path and error analysis in the light curve solution can be found Kahraman Aliçavuş and Aliçavuş (2019). The determined results from the light curve solution are given in Table 1. In addition, the theoretical fit to the observation points is given in Figure 1a. The Roche geometry of the system and the distribution of the spots on the component stars are given in Figure 1b.

TABLE 1. Photometric solutions of TESS light curve of CF Tuc

Parameter	CF Tuc
P (day)	2.7975004
T_1 (K)	6100*
T_2 (K)	4416(35)
i (deg)	70.55(4)
Ω_1	8.222(39)
Ω_2	4.540(8)
q	0.117*
Phase Shift	0.0061(1)
$l_1/(l_1+l_2)$	0.395(5)
$l_1/(l_1+l_2)$	0.605(5)
l_3	-
e	0
w	90
A_1-A_2	0.50-0.50
g_1-g_2	0.32-0.32
f_1 (%)	50
f_2 (%)	88
$r_{1(mean)}$	0.1406(6)
$r_{2(mean)}$	0.3159(6)

ISBN:978-605-83516-6-0

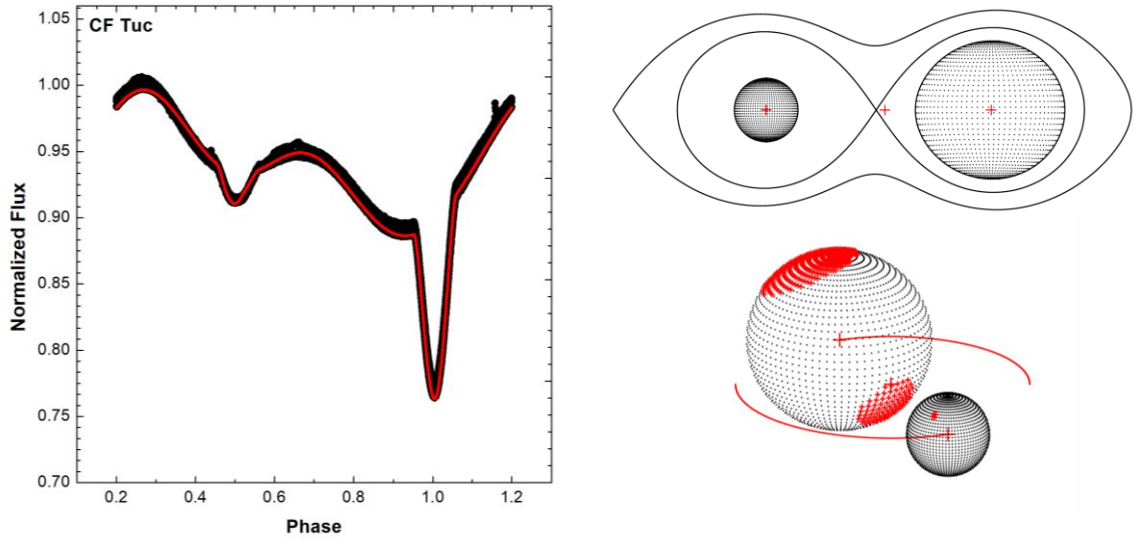


Figure 1. a) TESS light curve of CF Tuc and teoretical fit to the observational data (left panel). b) Roche geometry of the system and locations of spots on the surface of the components (right panel).

ORBITAL PERIOD VARIATIONS

In this study, all the minimum times published in the literature between 1980-2019 were collected in order to examine the change of orbital period. When the O-C diagram created with the minimum time is examined, it was found that the system shows a periodic orbital period change (Figure 2). As Doğru et. al. (2009) and Jableka et. al. (2012) also mentioned, considering that the light-time effect (LITE) caused by the movement of the binary system around the common center of mass of the triple system can lead to this periodic change. In this context, the methods described by Zasche et. al. (2009) and Soydugan et. al. (2011) were applied to represent the observed changes and to obtain the physical parameters. Unlike other studies, the period decrease was considered to be zero because it was quite small. It is understood that the change from the third body is the result of an orbital movement of e = 0.38 and a period of 34.9 years. The results of O-C analysis are shown in Table 2 and the comparison of the theoretical fit representing the solution with the observation data is shown in Figure 2.

TABLE 2. Parameters found as a result of O-C analysis for CF Tuc.

Parameter	CF Tuc
T_0 (HJD) + 2400000	48922.1509(34)
P_{orb} (day)	2.7976159(24)
a_{12}sini' (AU)	17.49(42)
A_s (day)	0.101(3)
e'	0.38(4)
ω' (deg.)	103(7)
T' (HJD) +2400000	11907 (667)
P_3 (year)	34.9(6)
$f(M_3)$ ($M_\odot$)	4.39(3)
M_3 $(i=90)$	7.54 (38)

ISBN:978-605-83516-6-0

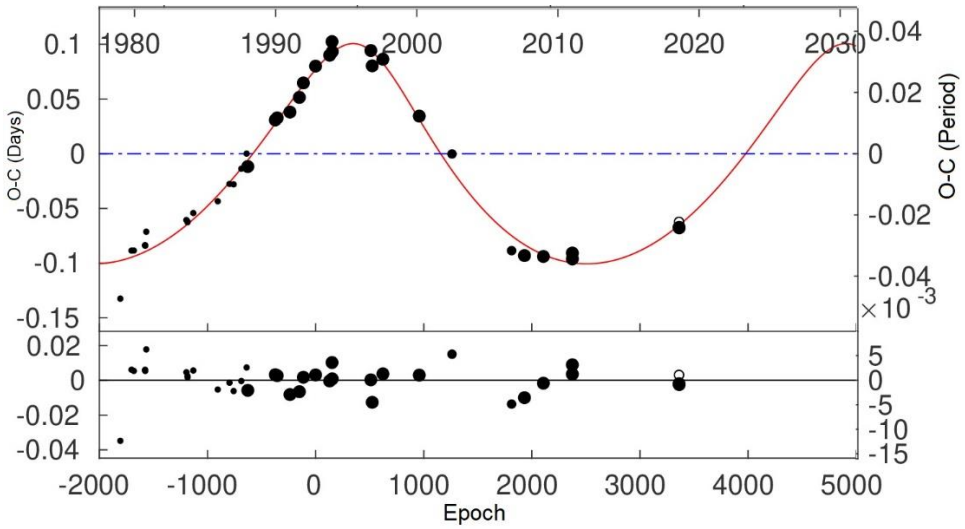


Figure. 2. O-C diagram for CF Tuc. The black dots on the top panel show the observed minimum times, the blue dashed line shows the parabolic change and the red line shows the cyclic change. The lower panel shows residuals between the fit and the observation points.

ABSOLUTE PARAMETERS AND EVOLUTIONARY STATUS

The light curve analysis of CF Tuc given in the previous section allows the calculation of the physical properties and absolute parameters of the components in a very sensitive way. These parameters are obtained by the help of the parameters calculated to the components of basic parameters and their errors are given in Table 3. As a result of the calculations, the masses of the components of CF Tuc were found to be 1.11 and 1.23 $M_\odot$ for the primary and secondary components, respectively. The radii were obtained as 1.56 and 3.51 $R_\odot$, for the primary and secondary components, respectively.

The evolution of CF Tuc was investigated by using the calculated basic parameters. The evolutionary study was carried out using the binary module of MESA (Paxton et. al. 2011,2013,2015), which also takes into account the angular momentum evolution of binary stars. When producing binary star evolution models, considering the fact that both components have convective envelopes, the effect of magnetic braking is taken into account in the calculations for both components. The most suitable solution was selected from the model pool created by considering different initial parameters (Z=0.017). As a result of the solutions, the CF Tuc system was found to have an age of 4.7 billion years. In addition, it was found that the initial period of the binary system should be P_{int} = 4.265 days. The models produced for CF Tuc and Age-log R diagrams that best represent the observational findings are given in Figure 3.

TABLE 3. Absolute parameters for CF Tuc

Parameter	CF Tuc
T_1 (K)	6100 (150)
T_2 (K)	4416 (185)
M_1 ($M_\odot$)	1.11(1)
M_2 ($M_\odot$)	1.23(1)
R_1 ($R_\odot$)	1.56(1)
R_2 ($R_\odot$)	3.51(1)
Logg_1	4.09(1)
Logg_2	3.44(1)

ISBN:978-605-83516-6-0

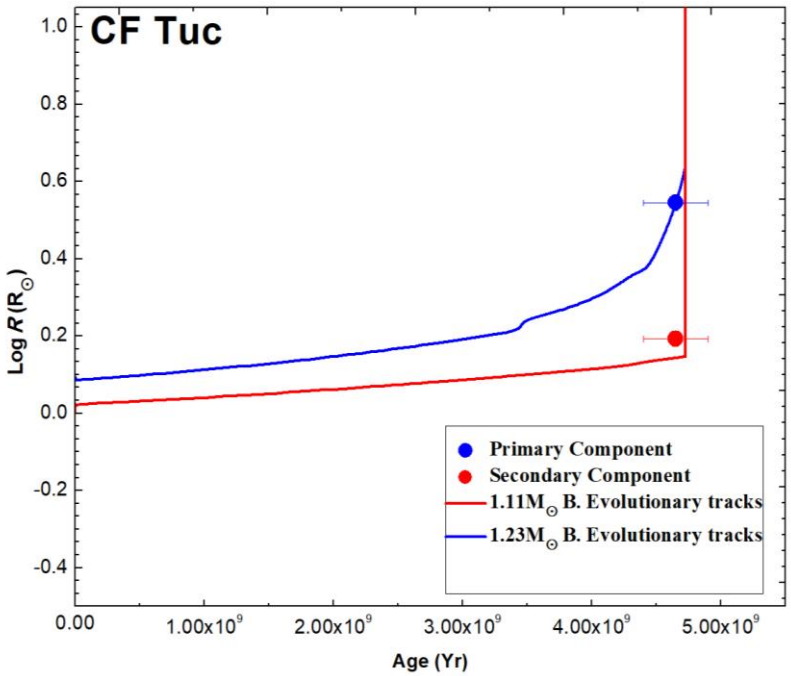


Figure. 3. Age-Log R diagram from binary evolution models for CF Tuc and locations of the system's components.

DISCUSSIONS AND CONCLUSIONS

In this study, the basic parameters of CF Tuc were updated by solving the TESS light curve. When the Roche geometry of the components was examined, it was obtained that the massive component has a filling rate of 88% and the small mass component has a filling rate of 50%. Due to the stellar activity, spot activity was observed on both components. As Doğru et. al. (2009) pointed out in the models, two large spots on the cooler component show its presence with its changing position. In addition, the presence of spots on the hotter component was also found in this study. This is a clear indication of the presence of activity in both components. Yamamoto et. al. (2012) and Iwakiri et. al. (2018) observed that X-ray emission of flux levels and when the durations are taken into account that it is clear that the release of the stars can be associated with the flare.

When the evolution models are examined, it is seen that the initial orbital period is around P_{int} = 4.265 days and decreases with time. In models, the radii found for the small mass, hotter component remain smaller than the observed radius. This is likely to be due to magnetic activity for late type stars as noted in previous studies.

When the orbital period change is examined, it was found that the information about the triple system changes with the new minimum times added. When the analyzes in this study are compared with the previous ones, it is seen that the orbital period (P_3) has increased from 15 to 35 years and has an eccentricity of 0.38. In addition, the decrease in the orbital period has changed considerably according to Doğru et. al. (2009) finding, which seems to be more compatible with the detached structure of the CF Tuc. As a result of the new solutions, the minimum possible black hole mass was calculated as 7.54 $M_{\odot}$. This mass value has almost doubled compared to previous studies. For more precise evidence of the existence of the black hole, new minimum times and observations of possible high energy X-ray emissions are needed. As a result, we may conclude that in order to better understand the nature of the system, the orbital period evolution needs to be simulated and examined with triple dynamic models.

ACKNOWLEDGMENTS

This work was supported by Çanakkale Onsekiz Mart University The Scientific Research Coordination Unit, Project number: FBA-2019-2966.

ISBN:978-605-83516-6-0

REFERENCES

1. Anders, G. L., Coates, D. W., Thompson, K., Innis, J. L., 1999, MNRAS, 310, 377.
2. Budding, E., Zeilik, M., 1995, Ap&SS, 232, 355.
3. Collier, A. C., Hearnshaw, J. B., Austin, R. R. D., 1981, MNRAS 197, 769.
4. Doğru, D., Erdem, A., Doğru, S. S., Zola, S., 2009, MNRAS, 397, 1647.
5. Iwakiri et. al., 2018, ATel, 2009.
6. Jableka et. al., 2012, AASP, 2, 128.
7. Paxton et al., 2011, ApJS, 192, 3.
8. Paxton et al., 2013, ApJS, 208, 4.
9. Paxton et al., 2015, ApJS, 220, 15.
10. Soydugan, F., Erdem, A., Doğru, S. S., Aliçavuş, F., Soydugan, E., Çiçek, C., Demircan, O., 2011, 16, 4, 253.
11. Wilson, R.E., Devinney, RJ., 1971. ApJ, 166, 605.
12. Yamamoto et. al., 2012, ATel, 3897.
13. Zasche, P., Liakos, A., Niarchos, P., Wolf, M., Manimanis, V., Gazeas, K., 2009 New Astronomy, 14, 121.

BOOK OF FULL TEXT PROCEEDINGS TURKISH PHYSICAL
SOCIETY 35th INTERNATIONAL PHYSICS CONGRESS (TPS35)
TPS35, Vol.01, No.02, pp.98-101.
ISBN:978-605-83516-6-0 15 December 2019

Analysis of Apsidal Motion in Eclipsing Binaries: V919 Cep and V957 Cep

Ahmet Bulut[1, a)] and İbrahim Bulut[2, b)]

[1]*Department of Physics, Faculty of Art and Science, Çanakkale Onsekiz Mart University, Çanakkale, TURKEY*

[2]*Department of Space Sciences and Technologies, Faculty of Art and Science, Çanakkale Onsekiz Mart University, Çanakkale, TURKEY*

[a)]Corresponding author: abulut@comu.edu.tr
[b)]ibulut@comu.edu.tr

Abstract. In this study, we were presented the apsidal motion analysis in the eccentric eclipsing binaries: V919 Cep and V957 Cep. The method proposed by Giménez and Garcia-Pelayo (1983) were used for the apsidal motion analysis. The apsidal motion periods were found to be 65 ± 1 and 172 ± 10 years for V919 Cep and V957 Cep, respectively.

Keywords: *Eclipsing binary stars, Apsidal motion, Individual: V919 Cep and V957 Cep*

INTRODUCTION

The study of apsidal motion of eccentric eclipsing binaries is an important source in order to understand stellar structure. There is a direct relationship between the apsidal motion and internal density concentration in eclipsing binary stars. These studies provide observational testing of theoretical models of stellar structure and evolution

In this work, we presented an analysis of apsidal motion of V919 Cep and V957 Cep. They are eclipsing binary systems with eccentric orbit. These systems are included in the catalog of elliptical orbital pairs given by Bulut and Demircan (2007).

APSIDAL MOTION ANALYSIS

A well-known method for analysing the apsidal motion in eclipsing binaries is to use their eclipse times. We used for apsidal motion analyses of V919 Cep and V957 Cep the mathematical method presented by Gimenez & Bastero (1995).

For the apsidal motion analysis in the systems were gathered all minima time from the literature. In addition, the photometric observations of V919 Cep were made at the Çanakkale Onsekiz Mart University Observatory. During these observations, we obtained one primary time of minima. This was calculated by means of using Kwee and van Woerden Method (1956). The new minima time is 2458745.3961 ± 0.012 (HJD) for V919 Cep.

Türk Fizik Derneği
1950
Turkish Physical Society

ISBN:978-605-83516-6-0

V919 CEP

V919 Cep (BD+64 1740, GSC 04286-00049, TYC 4286-49-1, Gaia DR2 2208837461981821056, Gaia DR1 2208837461981821056; R.A. = $22^h\ 59^m\ 40^s.8084$, DEC = $+65^o\ 12'\ 40".114$, V_{max} = $10^m.48$, (Simbad) 10.62 – 10.92 (10.86), P = 1.85197 days) is a detached eclipsing binary systems. It discovered to be an eclipsing binary system by Otero et al. (2004) in the NSVS database. Otero reported a relatively apsidal motion and obtained the light elements for V919 Cep.

We used the times of minimum light published in the last several years by Otero et al. (2004), Diethelm (2010, 2011, 2012, 2013, 2014), Lampens et al. (2017), Hubscher (2015, 2016), Ogloza et al. (2017), Kim et al. (2018), and Pagel (2018). A total of 20 (10 primary and 10 secondary) minima times of V919 Cep were used in this analysis. The *O - C* residuals were calculated using the following linear light elements:

$$HJD\ (MinI) = 2452501.4214 + 1^d.851982 \times E \qquad (1)$$

The parameters of V919 Cep derived from apsidal motion analysis are listed in Table 1. The diagram of the period variation is also given in Figure 1.

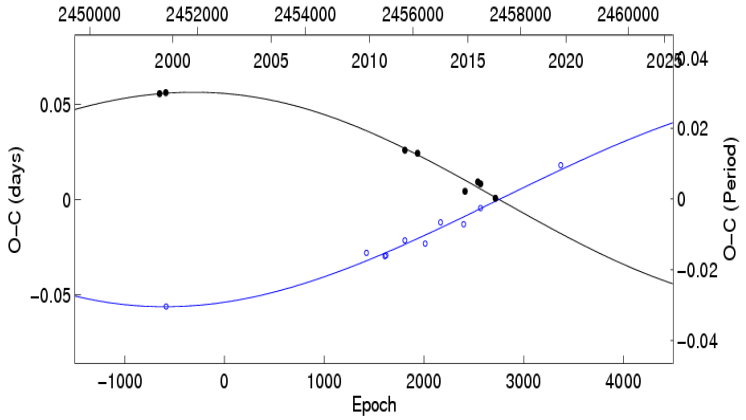


FIGURE 1. The period variation of V919 Cep. The filled symbols show the primary minima, and the open symbols show the secondary minima.

V957 CEP

V957 Cep (GSC 04487-00347, 2MASS J23461047+7129554, PPMX J234610.4+712955, TYC 4487-347-1, Gaia DR2 2215718450566544512, Gaia DR1 2215718446267286144; R.A. = $23^h\ 46^m\ 10^s.47$, DEC = $+71^o\ 29'\ 55".308$, V_{max} = $11^m.26$ (Simbad) is a fairly neglected binary system with eccentric orbit. It was discovered to be an eclipsing binary by Otero et al. (2006) in the ASAS, HIPPARCOS NSVS database. We used the times of minimum light published in the last several years by Otero et al. (2006), Brat et al. (2008), Lampens et al. (2010), Brat et al. (2011), Kozyreva et al. (2012), Diethelm (2013), Kozyreva and Kusakin (2014), and Lampens et al. (2017). A total of 24 (9 primery and 15 secondry) photometric minima time were used in this anlaysis. The *O - C* residuals were calculated using the following linear light elements:

$$HJD\ (MinI) = \text{HJD } 2451504.7308 + 1^d.9887333 \times E \qquad (2)$$

The derived apsidal motion parameters for V957 Cep are listed in Table 1. The diagram of its period variation is also given in Figure 2.

ISBN:978-605-83516-6-0

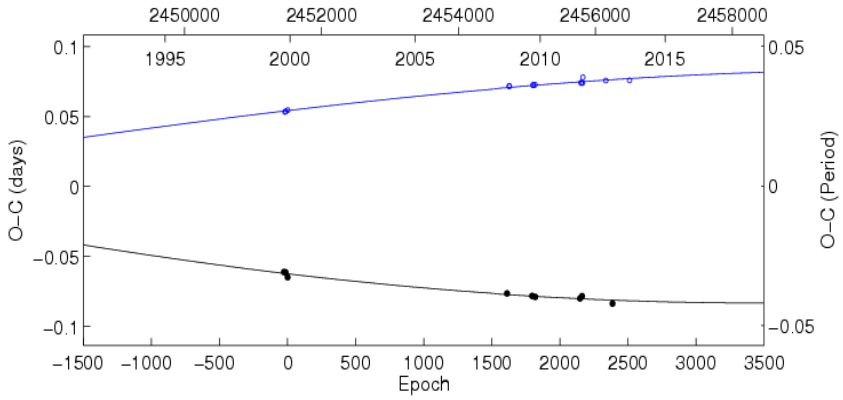


FIGURE 2. As per Fig. 1 but for V957 Cep

TABLE 1. Apsidal motion elements for V919 Cep and V957 Cep

Parametres	**V919 Cep**	**V957 Cep**
T_o (HJD)	2452501.4215 ± 0.0131	2451504.7308 ± 0.0296
Ps [days]	1.851982 ± 0.000006	1.988733 ± 0.000017
Pa [days]	1.852126 ± 0.000006	1.988796 ± 0.000017
e	0.095 ± 0.015	0.131 ± 0.024
ώ [deg/cycle]	0.0281 ± 0.0005	0.0114 ± 0.0006
ω [deg]	192.7 ± 0.7	314.7 ± 1.1
U [yr]	65 ± 1	172 ± 10

CONCLUSIONS AND REMARKS

In this study, the apsidal motion parameters of two eccentric eclipsing binary systems were estimated. The Apsidal motion periods of V919 Cep and V957 Cep were achieved to be 65 ± 1 years and 172 ± 10 years respectively. This shows that the apsidal motion in V919 Cep is rapid. The orbital eccentricity of V919 Cep and V957 Cep were calculated as 0.095 ± 0.015 and 0.131 ± 0.024, respectively.

REFERENCES

1. L. Brát, L. Šmelcer, H. Kuèáková, R. Ehrenberger, R. Kocián, F. Lomoz, L. Urbanèok, P. Svoboda, J. Trnka, P. Marek, R. Døevini, R. Uhláø, S. Poddanı, P. Zasche and M. Skarka, Open European Journal on Variable Stars, **94**, 1, 1 (2008).
2. L. Brat, J. Trnka, L. Smelcer, M. Lehky, H. Kucakova, F. Lomoz, D. Hanzl, M. Vrastak, G. Corfini, V. Pribik, R. Dreveny, R. Ehrenberger, R. Kocian, M. Masek, J. Polak, J. Starzomski, F. Marchi, S. Poddany, M. Zejda and P. Cagas, Open European Journal on Variable stars, **137**, 1 (2011).
3. İ. Bulut and O. Demircan, Monthly Notices of the Royal Astronomical Society, **378**, 1, pp. 179-181 (2007).
4. R. Diethelm, Information Bulletin on Variable Stars, 5920 (2010).
5. R. Diethelm, Information Bulletin on Variable Stars, 5960 (2011).

ISBN:978-605-83516-6-0

6. R. Diethelm, Information Bulletin on Variable Stars, 6011 (2011).
7. R. Diethelm, *Information Bulletin on Variable Stars*, 6029 (2012).
8. R. Diethelm, *Information Bulletin on Variable Stars*, 6042 (2013).
9. R. Diethelm, *Information Bulletin on Variable Stars*, 6093 (2014).
10. A. Giménez and M. Bastero, *Astrophysics and Space Science*, **226**, 1, pp. 99-107 (1995).
11. A. Gimenez and J. M. Garcia-Pelayo, *Astrophysics and Space Science*, **92**, 1, pp. 203-222 (1983).
12. J. Hubscher, *Information Bulletin on Variable Stars*, 6152 (2015).
13. J. Hubscher, *Information Bulletin on Variable Stars*, 6157 (2016).
14. C. H. Kim, J. M. Kreiner, B. Zakrzewski, W. Ogloza, H. W. Kim, and M. J. Jeong, *The Astrophysical Journal Supplement Series*, **235,** 41, pp. 27 (2018).
15. K. K. Kwee and H. van Woerden, *Bulletin of the Astronomical Institutes of the Netherlands*, **12**, pp. 327-330 (1956).
16. V. S. Kozyreva and A. V. Kusakin, *Astrophysics*, **57**, 2 (2014).
17. V. S. Kozyreva, A. V. Kusakin and J. Menke, *Information Bulletin on Variable Stars*, 6020 (2012).
18. P. Lampens, S. Kleidis, P. Van Cauteren, F. J. Hambsch, M. Vanleenhove and S. Dufoer, *Information Bulletin on Variable Stars*, 5933 (2010).
19. P. Lampens, P. Van Cauteren, A. Ayiomamitis, S. Kleidis, K. Panagiotopoulos, M. Vanleenhove, J. Hambsch, H. Hautecler, J. Van Wassenhove and L. Vermeylen, *Information Bulletin on Variable Stars*, 6230 (2017).
20. W. Ogloza, M. Drozdz, J. M. Kreiner, G. Stachowski, M. Winiarski and B. Zakrzewski, *Information Bulletin on Variable Stars*, 6193 (2017).
21. S. A. Otero, P. Wils and P. A. Dubovsky, *Information Bulletin on Variable Stars*, 5570 (2004).
22. S. A. Otero, P. Wils, G. Hoogeveen and P. A. Dubovsky, *Information Bulletin on Variable Stars*, 5681 (2006).
23. L. Pagel, *Information Bulletin on Variable Stars*, 6244 (2018).

BOOK OF FULL TEXT PROCEEDINGS TURKISH PHYSICAL
SOCIETY 35th INTERNATIONAL PHYSICS CONGRESS (TPS35)
TPS35, Vol.01, No.02, pp.102-105.
ISBN:978-605-83516-6-0

15 December 2019

Light Curve Analysis of Very Short-Period Binary System KIC 11494583

Ahmet Bulut[1,2, a)] and İbrahim Bulut[1,3, b)]

[1]*Astrophysics Research Centre and Observatory, Canakkale Onsekiz Mart University, Terzioglu Campus, TR-17020, Canakkale, Turkey*
[2] *Department of Physics, Faculty of Arts and Sciences, Canakkale Onsekiz Mart University, Terzioglu Campus, TR-17020, Canakkale, Turkey*
[3] *Department of Space Sciences and Technologies, Faculty of Arts and Sciences, Canakkale Onsekiz Mart University, Terzioglu Campus, TR-17020 Canakkale, Turkey*

[a)]*Corresponding author:abulut@comu.edu.tr*
[b)]*ibulut@comu.edu.tr*

Abstract. The preliminary results of an analysis of the Kepler photometric data of KIC 11494583 (2MASS J18572818+4927518, R.A.(2000) = 18 57 28.19, DEC.(2000) = +49 27 51.82, K = 15.43 mag) are presented. KIC 11494583 is a W UMa-type eclipsing binary system with an orbital period of 0.2483419 days. The Kepler light curve of KIC 11494583 was analyzed using the PHOEBE program to determine the photometric parameters of the system. The analysis results show that the best fit was obtained at photometric mass ratio (q = 2.454) and inclination (i = 40 deg). We calculated the effective temperatures of the primary and the secondary components at 4385 K and 3904 K, respectively. The preliminary absolute dimensions were also calculated for KIC 11494583.

INTRODUCTION

Eclipsing binary stars are very important objects in astrophysics. The star parameters such as mass, radius can be determined directly by observational studies on them. The orbit periods of very short-period eclipsing binary systems are less than 0.2 days.

KIC 11494583 (2MASS J18572818+4927518, R.A.(2000) = 18 57 28.19, DEC.(2000) = +49 27 51.82, K = 15.43 mag) is a W UMa-type eclipsing binary system in the Kepler Field. The orbital period is 0.2483419 days that is below the short-period limit for contact binaries.

In this work, we analyzed the Kepler photometric data of KIC 11494583 for the geometric and physical parameters of the system.

LIGHT CURVE ANALYSIS

The phometric observatinal date of KIC 11494583 were taken from Kepler Database (http://keplerEBs.villanova.edu). In order to determine the geometric and physical parameters of KIC 11494583, Kepler data were analyzed using the PHOEBE program (Prsa and Zwitter, 2005) which is based on the Wilson–Devinney method (Wilson and Devinney, 1971). We used MODE 3 in Wilson–Devinney code. This MODE is for contact binaries.

For modelling the observatinal light curve of KIC 11494583, the effective temperature (T_1) of the primary companent was assumed to be 4385 K from the Kepler Catalogue. The limb-darkening coefficients ($x_{1,2}$) were given

Türk Fizik Derneği
1950
Turkish Physical Society

ISBN:978-605-83516-6-0

from the tables of van Hamme (1993). The gravity-darkening coefficients ($g_{1,2}$ = 0.32) and the bolometric albedos ($A_{1,2}$ = 0.5) were fixed.

The adjustable parameters were the mass ratio (q), the orbital inclination (i), the temperature (T_2) of the secondary component, the surface potentials ($\Omega_1 = \Omega_2$), and the luminosity (L_1) of the primary companent. The results of light curve analysis are given in Table 1. In this table, ($r_{1,2}$) are the fractional radii of the componets. The teoretical and observatical light curves were graphed in Figure 1. The accord between observed and final synthetic light curves is quite good. The Roche surface geometry of KIC 5621294 is represented in the orbital plane in Fig. 2.

CONCLUSIONS AND RESULTS

The photometric light curve of the short-period W UMa-type binary, KIC 11494583 has been analysed by using PHOEBE program. The solitions of the light-curve analysis represents that the eclipsing pair of the system is a W-type W UMa system with a mass ratio of q = 2.454 ± 0.011. Its orbital inclination is i = 38.81 ± 0.05 deg. The temperature difference between the hotter and cooler components ((T_1–T_2) is 481 K. The observed light curves of KIC 11494583 is almost symmetrical. Therefore during the solutions, no spots were modeled on the component stars.

The preliminary values of stellar parameters of KIC 11494583 were derived in Table 1 and the emprical relations between temperature and stellar mass. Depending on the temperature of the primary star, its main sequence mass would be 0.70 $M_\odot$ (Eker et al. 2015). Other parameters of the components were determined using the Third Law of Kepler. The calculted absolude parameters for KIC 11494583 are given in Table 2. The fill-out factor (*f*) was calculated about 100%. This shows that KIC 11494583 is a over-contact system.

TABLE 1. Parameters derived from light curve analysis of KIC 5621294

Parameter	**KIC 11494583 Value**
T_0 (HJD)	2454964.6852
P (days)	0.2483419
i (deg)	38.81 ± 0.05
T_1 (K)	4385
T_2 (K)	3904 ± 2
$\Omega_1 = \Omega_2$	5.6384
q (M_2/M_1)	2.454 ± 0.011
x_1	0.797
x_2	0.796
$A_1 = A_2$	0.5
$g_1 = g_2$	0.32
$L_1 / (L_1+L_2)$	0.455 ± 0.010
$L_2 / (L_1+L_2)$	0.545
$r_{1, pole}$	0.303778 ± 0.000012
$r_{1, side}$	0.319944 ± 0.000013
$r_{1, back}$	0.369969± 0.000015
$r_{2, pole}$	0.450280 ± 0.000014
$r_{2, side}$	0.485410 ± 0.000015
$r_{2, back}$	0.520184 ± 0.000017
$r_{1, mean}$	0.331233 ± 0.000014
$r_{2, mean}$	0.485291 ± 0.000016

ISBN:978-605-83516-6-0

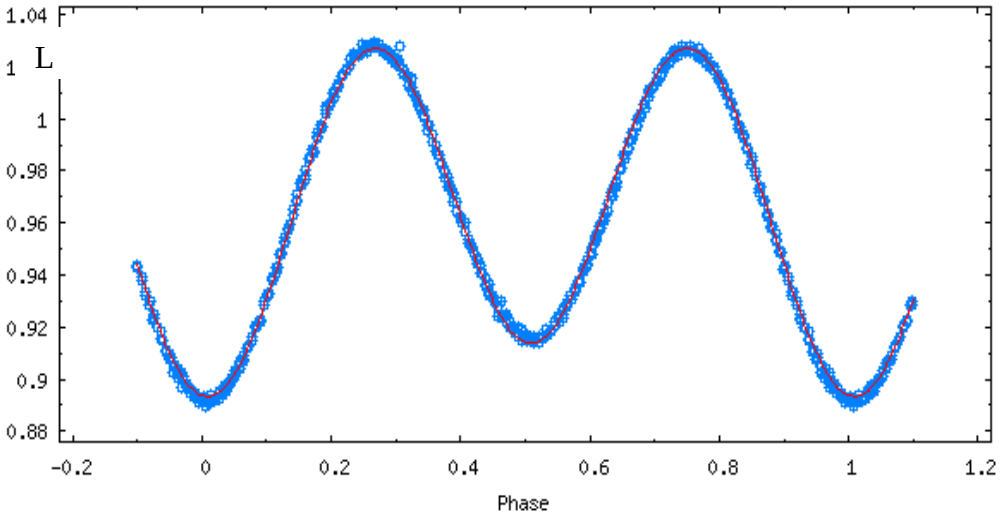


FIGURE 1. The light curves of KIC 11494583. Points showed the observations. Solid lines are the final synthetic light curve.

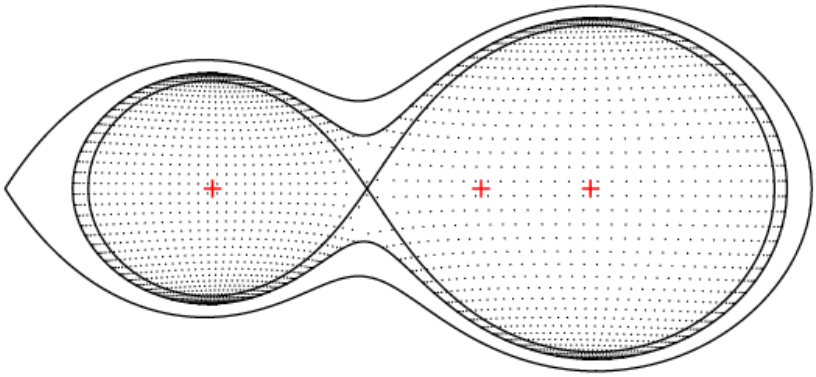


FIGURE 2. The Roche geometry on the orbital plane for KIC 5621294.

TABLE 2. Fundamental parameters of KIC 11494583

Parameter	**Primary**	**Secondary**
M ($M_\odot$)	0.70	1.72
R ($R_\odot$)	0.74	0.85
log g (cgs)	4.55	4.82
T_1(K)	4385	3904
L ($L_\odot$)	0.18	0.15
a **($R_\odot$)**	2.23	

ISBN:978-605-83516-6-0

REFERENCES

1. Z. Eker, F. Soydugan, E. Soydugan E, et al. *Astron. J.*, **149**, 131 (2015).
2. A. Prsa and T. Zwitter, *Astrophys. J*., **628**, 426 (2005).
3. W. van Hamme, *Astronomical Journal*, 1**06**, pp. 2096-2117 (1993).
4. R. E. Wilson and E. J. Devinney, *Astrophys. J*., **166**, 605 (1971).

BOOK OF FULL TEXT PROCEEDINGS TURKISH PHYSICAL
SOCIETY 35th INTERNATIONAL PHYSICS CONGRESS (TPS35)
TPS35, Vol.01, No.02, pp.106-113.
ISBN:978-605-83516-6-0 15 December 2019

String Cloud Solutions in $f(R,T)$ Gravity

Halife ÇAĞLAR[1, a)] and Sezgin AYGÜN[2, b)]

[1] *Çanakkale Onsekiz Mart University, Institute for Natural and Applied Sciences, Terzioğlu Campus, Çanakkale, 17020, Turkey.*
[2] *Çanakkale Onsekiz Mart University, Arts and Sciences Faculty, Department of Physics, Terzioğlu Campus, Çanakkale, 17020, Turkey.*

[a)] Corresponding author: hlfcglr@gmail.com
[b)] saygun@comu.edu.tr

Abstract. In this study, we have investigated homogeneous and anisotropic Marder type universe model for string cloud matter distribution in the framework $f(R,T)$ theory with the cosmological term (Λ). We have obtained solutions of this model by using anisotropy future of the universe. Also, we have obtained string density and cosmological term values non-zero and time depended for Marder universe in $f(R,T)$ gravity. However, we have transformed our results into General Relativity theory. And the obtained results have been discussed in gravitation theories.

INTRODUCTION

Over the years, many observations and studies have been done to explain features of the universe. Some researchers have found out expanding in an accelerating phase of the Universe according to recent observations like supernovae type Ia (SNe Ia) [1,2], Planck data [3], the cosmic microwave background radiation (CMBR) [4], Large-Scale Structure (LSS) [5], Wilkinson Microwave Anisotropy Probe (WMAP) [6]. Since Einstein General Relativity (GR) theory alone is not sufficient to clarify the expansion, researchers have proposed modifications of general relativity named alternative gravitation theories such as Lyra manifold [7], Brans-Dicke theory [8], Barber's theory [9], Saez-Ballester theory [10], *f(R)* theory [11]. After proposing *f(R)* theory from modification of Einstein Hilbert action, some theories have been suggested like *f(T)* [12], *f(G)* [13] and *f(R,T)* [14]. Here *T*, *G* and *R* respectively are the torsion scalar, the Gauss Bonnet scalar and the scalar curvature. The *f(R,T)* theory could be a significant alternative theory to describe the late time cosmic accelerated expansion of the Universe [15]. The study of Harko et.al. [14] has given motivation to many scientists to work about the accelerating. And in recent years, *f(R,T)* theory has been investigated for several universe models with several matter distributions. Adhav [16] has obtained exact solutions of the field equations of LRS Bianchi type-I universe for *f(R,T)* gravity in presence of perfect fluid. Reddy et.al. [17] have studied perfect fluid for a five-dimensional Kaluza-Klein space-time in a scalar-tensor theory of gravitation proposed by Harko et.al [14]. Rao and Nelima [18] have solved field equations of Einstein-Rosen space-time filled with perfect fluid for *f(R, T)* modified theory by using anisotropy features. Higher dimensional spherical symmetric metric with perfect fluid in *f(R,T)* gravity has been studied by Samanta and Dhal [19]. Mahanta [20] has studied bulk viscous in *f(R,T)* theory for LRS Bianchi-I space time and obtained the model degenerates into effective stiff fluid model of the universe. Singh and Singh [21] have investigated behaviors of scalar field in Friedmann-Robertson-Walker space-time for modified theory of gravitation formulated by Harko et al [14]. Also *f(R,T)* gravitation theory with time depending cosmological constant has been studied for Bianchi type-I universe in presence of scalar field by Singh et al. [22]. Chaubey and Shukla [23] have analyzed anisotropic universe in *f(R,T)* theory with $\Lambda(T)$. Nagpal et.al. [24] have studied the Friedmann-Lemaître-Robertson-Walker (FLRW) metric in the presence of the magnetized quark matter (QM) and strange quark matter (SQM) distributions for *f(R,T)* gravity proposed by Harko et al. [14]. However, Aygün et al. [25] have investigated homogenous and isotropic FRW space-

Türk Fizik Derneği
1950
Turkish Physical Society

ISBN:978-605-83516-6-0

time in *f(R,T)* theory with massive and massless scalar field. LRS Bianchi type-I universe has been perused in frame work *f(R,T)* modified theory by Güdekli and Çalışkan [26]. Aktaş [27] has studied Kaluza-Klein universe in *f(R,T)* gravity with massive and massless scalar fields.

Also, it is important that studying on cosmic string because of spontaneously symmetry breakings at the initial stage of the universe cause topological defects such as domain walls, monopoles, cosmic string etc. [28]. Also It is said that cosmic strings couples to gravitational field and are responsible for density perturbations which leads to formation of galaxies [29], [30]. Kiran and Reddy [31] have studied cosmic string in a spatially homogeneous and anisotropic Bianchi type-III space-time for *f(R,T)* theory suggested by Harko et al. [14]. Reddy et al. [32] have analyzed a spatially homogenous and anisotropic Kantowski-Sachs universe for *f(R,T)* gravity with bulk viscous fluid containing one-dimensional cosmic string. Kanakavalli and Rao [33] have investigated LRS Bianchi type-I universe in *f(R,T)* modified theory with cosmic strings. Kaluza-Klein universe have been examined in frame work *f(R,T)* theory by Pawar et al. [34]. In recent years, studying on cosmic string with quark matter distribution has come into question. The phase transitions named quark-hadron phase transition (QGP) has occurred when cosmic temperature was T ≈ 200 MeV [35]. Bodmer [36], Witten [37] and Itoh [38] have suggested generation of the quark matter in two ways. These two ways respectively are QGP transition in the early age and conversion of neutron stars into SQM at ultrahigh densities. The quarks have been assumed as massless and non-interacting in primitive bag model and explained with equation of state (EOS) based on bag model of quark matter [39]. Thus we have quark matter pressure as

$$p_q = \frac{\rho_q}{3} \tag{1}$$

where ρ_q represents quark energy density. And the total energy density is given as

$$\rho = \rho_q + B_c \tag{2}$$

here B_c is called bag constant of quark matter. Also total pressure is written as follow [40]-[42].

$$p = p_q - B_c \tag{3}$$

Mahanta et al. [43] have investigated Self Creation cosmological theory for Bianchi type-III space-time with strange quark matter attached to string cloud. Rao and Sireesha [44] have discussed strange quark matter coupled with string cloud in Bran-Dicke modify theory in frame work Bianchi type-II, VII and IX universes. Also Kink space-time with strange quark matter attached to string cloud has been studied in GR by Sahoo and Mishra [45]. Çağlar and Aygün [46] have analyzed homogenous and isotropic higher dimensional flat FRW universe with strange quark matter and normal matter attached to string cloud and domain walls in Barber's second theory. Also the second stage of earlier phase of the Universe has been described as anisotropic and homogenous geometry. And this geometric structure could be defined with Bianchi type space-times [47] or Marder type universe model [48].

Motivated by above discussion, we have analyzed anisotropic and homogenous Marder universe with quark matter attached to string cloud in *f(R,T)* modified gravitational theory suggested by Harko et al. [14]. In this study, firstly we have given *f(R,T)* theory and line element of Marder space time. And then, we have obtained and solved field equations of our model. Finally, we have discussed our results.

$f(R,T)$ MODIFY THEORY WITH COSMOLOGICAL TERM

Harko et al. [14] have suggested the action function of $f(R,T)$ gravity as follows

$$S = \frac{1}{16\pi G}\int f(R,T)\sqrt{-g}d^4x + \int L_m\sqrt{-g}d^4x \tag{4}$$

here $f(R,T)$ is the arbitrary of Ricci scalar and L_m is the matter Lagrangian density. Also *R* represents Ricci scalar curvature, *T* shows the trace of energy-momentum tensor and g is the determinant of g_{ik} [14], [15]. The energy momentum tensor of matter is written as

$$T_{ik} = -\frac{2}{\sqrt{-g}}\frac{\delta(\sqrt{-g}L_m)}{\delta g^{ik}} \tag{5}$$

ISBN:978-605-83516-6-0

By assuming L_m to be depending only g_{ik}, we obtain

$$T_{ik} = g_{ik}L_m - \frac{2\partial L_m}{\partial g^{ik}} \tag{6}$$

And when we get variation eq. (4) with respect to the metric tensor components g_{ik}, the gravitational field equations of $f(R,T)$ modified theory is get as

$$f_R(R,T)R_{ik} - \frac{1}{2}f(R,T)g_{ik} + (g_{ik}\Box - \nabla_i\nabla_k)f_R(R,T) = 8\pi T_{ik} - f_T(R,T)T_{ik} - f_T(R,T)\Xi_{ik} \tag{7}$$

where $f_R(R,T)$ and $f_T(R,T)$ indicate of $f(R,T)$ with respect to R and T. ∇_i represents covariant derivative; $\Box = \nabla_i\nabla_i$ [14], [24]. Here Ξ_{ik} is written by

$$\Xi_{ik} = -2T_{ik} + g_{ik}L_m - 2g^{\alpha\beta}\frac{\partial^2 L_m}{\partial g^{ik}g^{\alpha\beta}} \tag{8}$$

If eq. (4) contracted, we get connection between R and T as follows;

$$f_R(R,T)R + 3\Box f_R(R,T) - 2f(R,T) = 8\pi T - f_T(R,T)T - f_T(R,T)\Xi. \tag{9}$$

Taking eq. (7) and eq. (9) together, we obtained gravitational field equations [14]

$$f_R(R,T)\left(R_{ik} - \frac{1}{3}Rg_{ik}\right) + \frac{1}{6}f(R,T)g_{ik} = \left(8\pi - f_T(R,T)\right)\left(T_{ik} - \frac{1}{3}Tg_{ik}\right) - f_T(R,T)\left(\Xi_{ik} - \frac{1}{3}\Xi g_{ik}\right) + \nabla_i\nabla_k f_R(R,T) \tag{10}$$

And, energy momentum tensor is given as follow

$$T_{ik} = (\rho + p)u_i u_k - pg_{ik} \tag{11}$$

here, ρ is energy density and p is matter pressure. Also, u_i represents four-velocity and satisfies the relation $u_i u^i = 1$ [14]. Also we obtained from eq. (8)

$$\Xi = -2T_{ik} - pg_{ik}\,. \tag{12}$$

$f(R,T)$ gravity could be solved by using three different $f(R,T)$ models as follows [14]

$$f(R,T) = \begin{cases} R + 2f(T) \\ f_1(R) + f_2(T) \\ f_1(R) + f_2(R)f_3(T) \end{cases} \tag{13}$$

In this paper we have used first model of Harko et al. i.e. $f(R,T) = R + 2f(T)$. With cosmological term, we get $f(R,T)$ gravitation theory equation as follows [14]

$$G_{ik} = \left[8\pi + 2\acute{f}(T)\right]T_{ik} + \left[2p\acute{f}(T) + f(T) + \Lambda\right]g_{ik} \tag{14}$$

here the prime represents differentiation with respect to the argument. When we chose $f(T) = \mu T$ (μ is a constant) we obtained eq. (14) as follows

$$G_{ik} = [8\pi + 2\mu]T_{ik} + [\mu\rho - \mu p + \Lambda]g_{ik} \tag{15}$$

ISBN:978-605-83516-6-0

SOLUTIONS OF FIELD EQUATIONS FOR MARDER UNIVERSE

For homogenous and cylindrical symmetric Marder universe, the line element has given as

$$ds^2 = A^2(dt^2 - dx^2) - B^2dy^2 - C^2dz^2 \tag{16}$$

here *A*, *B* and *C* are functions respect to cosmic time *t* [49]. Also we have calculated kinematic quantities such as 4-velocity u_i, spatial volume a^3, deceleration parameter *q*, expansion scalar θ, Hubble parameter *H* and shear scalar components for Marder space-time as follows θ

$$u_i = (0,0,0,A) \tag{17}$$

$$a^3 = ABC \tag{18}$$

$$q = -\frac{a\ddot{a}}{\dot{a}^2} \tag{19}$$

$$\theta = \frac{1}{A}\left(\frac{\dot{A}}{A} + \frac{\dot{B}}{B} + \frac{\dot{C}}{C}\right) \tag{20}$$

$$H = \frac{1}{3}\left(\frac{\dot{A}}{A} + \frac{\dot{B}}{B} + \frac{\dot{C}}{C}\right) \tag{21}$$

$$\sigma_X^X = \frac{1}{3A}\left(\frac{2\dot{A}}{A} - \frac{\dot{B}}{B} - \frac{\dot{C}}{C}\right) \tag{22}$$

$$\sigma_Y^Y = \frac{1}{3A}\left(\frac{2\dot{B}}{B} - \frac{\dot{A}}{A} - \frac{\dot{C}}{C}\right) \tag{23}$$

$$\sigma_Z^Z = \frac{1}{3A}\left(\frac{2\dot{C}}{C} - \frac{\dot{A}}{A} - \frac{\dot{B}}{B}\right) \tag{24}$$

The energy momentum tensor of string cloud matter distributions is written as [50]-[51]

$$T_{ik} = \rho u_i u_k - \rho_s X_i X_k \tag{25}$$

here u_i is the four velocity of the particles and X_i represents the direction of string and they have following equalities,

$$u_i u^i = -x_i x^i = 1 \text{ and } u^i X_i = 0 \tag{26}$$

Also in eq. (25), ρ shows the rest energy density of the string cloud with particles attached to them, ρ_s gives the string tension density and they are related by

$$\rho = \rho_p + \rho_s \tag{27}$$

here ρ_p is represent particle energy density [51]. In this study, we will attach quark matter to string cloud. The particle energy density from eq. (2) with eq. (27) can be written as follow

$$\rho = \rho_q + \rho_s + B_c \tag{28}$$

By using eq. (28) in eq. (25), we have obtained energy momentum of quark matter attached to string cloud as follows

$$T_{ik} = (\rho_q + \rho_s + B_c)u_i u_k - \rho_s X_i X_k \tag{29}$$

ISBN:978-605-83516-6-0

Using eq. (10), (15), (16) and (29), we get modified field equations of Marder universe for *f(R, T)* theory with cosmological term and quark matter distribution attached to string cloud as follows

$$\frac{\ddot{C}}{A^2C}+\frac{\ddot{B}}{A^2B}+\frac{\dot{B}\dot{C}}{A^2BC}-\frac{\dot{A}\dot{B}}{A^3B}-\frac{\dot{A}\dot{C}}{A^3C}=8\pi\rho_s+3\mu\rho_s+\mu\rho_q+\mu B_c+\Lambda \tag{30}$$

$$\frac{\ddot{A}}{A^3}-\frac{\dot{A}^2}{A^4}+\frac{\ddot{C}}{A^2C}=2\mu\rho_s+\mu\rho_q+\mu B_c+\Lambda \tag{31}$$

$$\frac{\ddot{A}}{A^3}-\frac{\dot{A}^2}{A^4}+\frac{\ddot{B}}{A^2B}=2\mu\rho_s+\mu\rho_q+\mu B_c+\Lambda \tag{32}$$

$$\frac{\dot{B}\dot{C}}{A^2BC}+\frac{\dot{A}\dot{B}}{A^3B}+\frac{\dot{A}\dot{C}}{A^3C}=8\pi(\rho_s+\rho_q+B_c)+3\mu\rho_q+4\mu\rho_s+3\mu B_c+\Lambda \tag{33}$$

Here, we have six unknowns and four field equations. For the solutions of field equations, firstly, we assume relation between shear scalar and expansion scalar as follows

$$\frac{\sigma_X^X}{\theta}=\xi=constant. \tag{34}$$

From eq. (34), we have calculated metric potential *A* respect to metric potentials *B* and *C* as

$$A=BC^{-\frac{3\xi+1}{3\xi-2}} \tag{35}$$

here ξ is an arbitrary constant. Secondly, we will use deceleration parameter. From eq. (19), we use constant deceleration parameter. Using $q=Q$=const., we get metric potential *B* as follows,

$$B=\frac{(at+b)^{-\frac{3\xi+2}{Q+1}}}{C} \tag{36}$$

By using eq. (31) and eq. (32) with eq. (35) and (36), we have obtained metric potential *C* as follows

$$C=\left((at+b)(Q+1)^2\right)^{-\frac{3\xi+2}{2Q+2}}e^{\frac{-2c_1(Q+1)(at+b)\left(\frac{at+b}{a}\right)^{-\frac{3\xi-2}{Q+1}}+2c_2(Q+1)-a(3\xi-2)}{a(Q+3\xi-1)}} \tag{37}$$

Using eqs. (36) and (37), we get metric potential *B* as follows

$$B=(at+b)^{-\frac{3\xi+2}{2Q+2}}(Q+1)^{-\frac{6\xi+4}{2Q+2}}e^{\frac{2c_1(Q+1)(at+b)\left(\frac{at+b}{a}\right)^{\frac{3\xi-2}{Q+1}}-2c_2(Q+1)+a(3\xi-2)}{2a(Q+3\xi-1)}} \tag{38}$$

Also we have calculated metric potential *A* from eq. (35) with eqs. (37) and (38) as follows

$$A=(at+b)^{\frac{3\xi+1}{Q+1}} \tag{39}$$

After obtained metric potentials, eq. (31) and eq. (32) became same equations. Thus we have three field equations given from eqs. (30), (31) and (33) and three unknowns as string energy density ρ_s, particle energy density ρ_q and cosmological term Λ. When we solved the three field equations (30), (31) and (33) we have obtained, quark energy density ρ_q, string energy density ρ_s and cosmological term Λ respectively as

$$\rho_q=\frac{\left\{(15\xi+2Q+4)(2-3\xi)a^2-4c_1^2(at+b)^2(Q+1)^2\left(\frac{at+b}{a}\right)^{\frac{6\xi-4}{Q+1}}\right\}}{4(4\pi+\mu)(Q+1)^2(at+b)^2}(at+b)^{-\frac{6\xi+2}{Q+1}}-B_c \tag{40}$$

ISBN:978-605-83516-6-0

$$\rho_s = \frac{9\xi a^2(Q+3\xi-1)(at+b)^{-\frac{6\xi+2}{Q+1}}}{4(4\pi+\mu)(Q+1)^2(at+b)^2} \tag{41}$$

$$\Lambda = \frac{\left\{c_1^2(at+b)^2(Q+1)^2(4\pi+2\mu)\left(\frac{at+b}{a}\right)^{\frac{6\xi-4}{Q+1}} - a^2\left[6\xi\pi\,(Q+3)+4\pi(2Q+1)+\frac{3}{2}\mu(Q+1)(3\xi+2)-9\pi\xi^2\right]\right\}}{(4\pi+\mu)(Q+1)^2(at+b)^2}(at+b)^{-\frac{6\xi+2}{Q+1}} \tag{42}$$

Also we have obtained quark pressure by using eq. (1) and eq. (40) as follows

$$p_q = \frac{\left\{(15\xi+2Q+4)(2-3\xi)a^2 - 4c_1^2(at+b)^2(Q+1)^2\left(\frac{at+b}{a}\right)^{\frac{6\xi-4}{Q+1}}\right\}}{12(4\pi+\mu)(Q+1)^2(at+b)^2}(at+b)^{-\frac{6\xi+2}{Q+1}} - \frac{1}{3}B_c \tag{43}$$

and we have calculated total pressure with help of eqs. (3) and (43) as

$$p = \frac{\left\{(15\xi+2Q+4)(2-3\xi)a^2 - 4c_1^2(at+b)^2(Q+1)^2\left(\frac{at+b}{a}\right)^{\frac{6\xi-4}{Q+1}}\right\}}{12(4\pi+\mu)(Q+1)^2(at+b)^2}(at+b)^{-\frac{6\xi+2}{Q+1}} - \frac{4}{3}B_c \tag{44}$$

Also particle energy density has been obtained from eqs. (2) and (40) as follow

$$\rho_p = \frac{\left\{(15\xi+2Q+4)(2-3\xi)a^2 - 4c_1^2(at+b)^2(Q+1)^2\left(\frac{at+b}{a}\right)^{\frac{6\xi-4}{Q+1}}\right\}}{4(4\pi+\mu)(Q+1)^2(at+b)^2}(at+b)^{-\frac{6\xi+2}{Q+1}} \tag{45}$$

and we have obtained total energy density by using eqs. (28), (40) and (41) as follows

$$\rho = \frac{\left\{(15\xi+2Q+4)(2-3\xi)a^2 - 4c_1^2(at+b)^2(Q+1)^2\left(\frac{at+b}{a}\right)^{\frac{6\xi-4}{Q+1}} + 9\xi a^2(Q+3\xi-1)\right\}(at+b)^{-\frac{6\xi+2}{Q+1}}}{4(4\pi+\mu)(Q+1)^2(at+b)^2} \tag{46}$$

DISCUSSIONS

In this study, we have solved field equations of *f(R,T)* modified theory suggested by Harko et al. [14] with Λ for homogenous and anisotropic Marder type universe. We have used quark matter distribution attached to string cloud in our model. It can be say that metric potentials *A* and *B* are increase but metric potential *C* is decrease by the time from eqs. (37)-(39). It is clearly seeing from eqs. (37) and (38) that Q must be $Q \neq -1$ to make metric potentials *C* and *B* different from zero. Also, arbitrary constant *a* is important parameter and must be $a \neq -b/t$ for our solutions. If we choose $a = 0$, metric potential *A* are become constant. Since quark matter energy density is increase when string energy density is decrease. For these results, we can say that string matter forms turn into quark matters form by the cosmic time. However, we have calculated cosmological term Λ is time variable. Also, arbitrary constant μ must be $\mu \neq -4\pi$ for meaningful solutions about matter distribution and cosmological term.

In addition, if $\mu = 0$ is chosen, we get General Relativity solutions for our model. By this way we have obtained quark energy density ρ_q, string energy density ρ_s and cosmological term Λ in GR respectively as

ISBN:978-605-83516-6-0

$$\rho_q = \frac{\left\{(15\xi+2Q+4)(2-3\xi)a^2-4c_1^2(at+b)^2(Q+1)^2\left(\frac{at+b}{a}\right)^{\frac{6\xi-4}{Q+1}}\right\}}{16\pi(Q+1)^2(at+b)^2}(at+b)^{-\frac{6\xi+2}{Q+1}} - B_c \tag{47}$$

$$\rho_s = \frac{9\xi a^2(Q+3\xi-1)(at+b)^{-\frac{6\xi+2}{Q+1}}}{16\pi(Q+1)^2(at+b)^2} \tag{48}$$

$$\Lambda = \frac{\left\{4\pi c_1^2(at+b)^2(Q+1)^2\left(\frac{at+b}{a}\right)^{\frac{6\xi-4}{Q+1}} - a^2\left[6\xi\pi\,(Q+3)+4\pi(2Q+1)-9\pi\xi^2\right]\right\}}{16\pi(Q+1)^2(at+b)^2}(at+b)^{-\frac{6\xi+2}{Q+1}} \tag{49}$$

And we have get quark pressure by using eq. (1) and eq. (47) for GR as

$$p_q = \frac{\left\{(15\xi+2Q+4)(2-3\xi)a^2-4c_1^2(at+b)^2(Q+1)^2\left(\frac{at+b}{a}\right)^{\frac{6\xi-4}{Q+1}}\right\}}{48\pi(Q+1)^2(at+b)^2}(at+b)^{-\frac{6\xi+2}{Q+1}} - \frac{1}{3}B_c \tag{50}$$

Total pressure in GR has been calculated with help of eqs. (3) and (50) as

$$p = \frac{\left\{(15\xi+2Q+4)(2-3\xi)a^2-4c_1^2(at+b)^2(Q+1)^2\left(\frac{at+b}{a}\right)^{\frac{6\xi-4}{Q+1}}\right\}}{48\pi(Q+1)^2(at+b)^2}(at+b)^{-\frac{6\xi+2}{Q+1}} - \frac{4}{3}B_c \tag{51}$$

Also particle energy density has been obtained in GR from eqs. (2) and (47) as follow

$$\rho_p = \frac{\left\{(15\xi+2Q+4)(2-3\xi)a^2-4c_1^2(at+b)^2(Q+1)^2\left(\frac{at+b}{a}\right)^{\frac{6\xi-4}{Q+1}}\right\}}{16\pi(Q+1)^2(at+b)^2}(at+b)^{-\frac{6\xi+2}{Q+1}} \tag{52}$$

We have get total energy density for GR by using eqs. (28), (47) and (48)

$$\rho = \frac{\left\{(15\xi+2Q+4)(2-3\xi)a^2-4c_1^2(at+b)^2(Q+1)^2\left(\frac{at+b}{a}\right)^{\frac{6\xi-4}{Q+1}}+9\xi a^2(Q+3\xi-1)\right\}(at+b)^{-\frac{6\xi+2}{Q+1}}}{16\pi(Q+1)^2(at+b)^2} \tag{53}$$

REFERENCES

1. S. Perlmutter et al., Astrophys. J. **565**, 565 (1999).
2. A. G. Riess et al., Astron. J. **116**, 1009 (1998).
3. Planck Collaboration (P.A.E. Ade et al.), Astron. Astrophys. **571**, A16 (2014).
4. D.N. Spergel et al., Astrophys. J. Suppl. 170, 377 (2007).
5. A.G. Riess et al., Astron. J. **117**, 707 (1999).
6. S. Perlmutter et al., Astrophys. J. **598**, 102 (2003).
7. G. Lyra, Mathematische Zeitschrift **54**, 52 (1951).
8. C. Brans and R. H. Dicke, Phys. Rev. **124**, 925 (1961).
9. G. A. Barber, Gen. Relativ. Gravit. **14**, 117-136 (1982).
10. D. Saez and V. J. Ballester, Phys. Lett. A **113**, 467-470 (1986).
11. S. M. Carroll, V. Duvvuri, M. Trodden, M. S. Turner, Phys. Rev. D **70**(4), 043528 (2004).
12. G. R. Bengochea and R. Ferraro, Phys. Rev. D **79**, 124019 (2008)
13. K. Bamba, C.Q. Geng, S. Nojiri and S. D. Odintsov, Europhys. Lett. **89**: 50003(7) (2010).
14. T. Harko, F. S N. Lobo, S. Nojiri and S. D. Odintsov, Phys. Rev D **84**, 024020-0240230 (2011).
15. N. Ahmed and A. Pradhan, Int. J. Theor. Phys. **53**, 289 (2014).

16. K. S. Adhav, Astrophysics and Space Science **339**, Issue 2, 365-369 (2012).
17. D. R. K. Reddy, R. L. Naidu and B. Satyanarayana, Int. J. of Theo. Physics **51**, Issue 10, 3222-3227 (2012)
18. V. U. M. Rao and D. Neelima, The European Physical Journal Plus **128**, 35-42 (2013)
19. G. C. Samantha and S. N. Dhal, International Journal of Theoretical Physics **52** (4), 1334-1344 (2013).
20. K. L. Mahanta, Astrophysics and Space Science **353**, Issue 2, pp.683-689 (2014).
21. V. Singh and C. P. Singh, Astrophysics and Space Science **356**, Issue 1, 153-162 (2015).
22. G. P. Singh, B. K. Bishi and P. K. Sahoo, Chinese Journal of Physics **54**, issue 2, 244-255 (2016).
23. R. Chaubey and A. K. Shukla, Pramana **88**, 65-77 (2017).
24. R. Nagpal, J. K. Singh and S. Aygün, Astrophys. Space Sci. **363**, 114-125 (2018).
25. S. Aygün, C. Aktaş, P. K. Sahoo and B. K. Bishi, Gravitation and Cosmology **24**, Issue 3, 302-307 (2018).
26. E. Güdekli and A. Çalışkan, AIP Conference Proceeding **2042**, Issue 1, id.020052 (2018).
27. C. Aktaş, Modern Physics Letters A **34**, Issue 11, id. 1950066 (2019)
28. T. W. B. Kibbe, Phys. J. A **9**, 1387-1398 (1976).
29. P.S. Letelier, Phys. Rev. D **28**, 2414 (1983).
30. Ya. B. Zeldovich, Mon. Not. R. Astron. Soc. **192**, 663 (1980).
31. M. Kiran, D. R. K. Reddy, Astrophysics and Space Science **346**, Issue 2, 521-524 (2013).
32. D. R. K. Reddy, S. Anitha, and S. Umadevi, The European Physical Journal Plus **129**, 96 (2014).
33. T. Kanakavalli, A. G. Rao, Astrophysics and Space Science **361**, Issue 7, 206-211 (2016).
34. D. D. Pawar, G. G. Bhuttampalle, P. K. Agrawal, New Astronomy **65**, 1-6 (2018).1
35. İ. Yılmaz, Gen Relativ Gravit **38**, 1397–1406 (2006).
36. A. R. Bodmer, Phys. Rev. D **4**, 1601 (1971).
37. E. Witten, Phys. Rev. D **30**, 272 (1984).
38. N. Itoh, Prog. Theor. Phys. **44**, 291 (1970).
39. K.S. Adhav, A.S. Nimkar and M.V. Dawande, Int. J. Theor. Phys. **47**, 2002 (2008).
40. H. Çağlar and S. Aygün, Chinese Physics C **40**, No. 4, 045103(2016).
41. A. Pradhan, V. K. Yadav and I. Chakraborty, Int. J. Mod. Phys. D. **10**, 339-349 (2001).
42. K. S. Adhav, V. B. Raut, A. S. Nimkar and R. S. Thakar, Astrophys. Space Sci. **319**, 81-84 (2009).
43. K. L. Mahanta, S. K. Biswal, P. K. Sahoo and M. C. Adhikary, IJTP **51**, Issue 5, 1538-1544 (2012).
44. V. U. M. Rao and K. V. S. Sireesha, IJTP **52**, Issue 4, 1240-1249 (2013).
45. P. K. Sahoo and B. Mishra, Journal of Theoretical and Applied Physics **7**, article id.62 (2013).
46. H. Çağlar and S. Aygün, Chinese Physics C **40**, Issue 4, article id. 045103 (2016).
47. Jr. P. R. Michael, Journal of Mathematical Physics **10**, 1724-1728 (1969). 35
48. D. R. K. Reddy, R. S. Kumar and R. L. Naidu, Astrophysics and Space Science **342**, Issue 1, 249-252 (2012).
49. L. Marder, Proc. Royal Society London Ser. **A246**, 133–143 (1958).
50. P. S. Letelier, Phys. Rev. D **28**, 2414 (1983).
51. İ. Yılmaz, İ. Yavuz, H. Baysal, İ. Tarhan and U. Camcı, IJMP D **8**, Issue 05, 659-668 (1999).

BOOK OF FULL TEXT PROCEEDINGS TURKISH PHYSICAL
SOCIETY 35th INTERNATIONAL PHYSICS CONGRESS (TPS35)
TPS35, Vol.01, No.02, pp.114-118.
ISBN:978-605-83516-6-0

15 December 2019

T100 Observation of Selected Magnetic Cataclysmic Variables

Dicle Zengin Çamurdan[1, a)]

[1]*University of Ege, Faculty of Science, Department of Astronomy & Space Sciences, Bornova, 35100, Izmir, Turkey*
[a)] *Corresponding author: dicle.zengincamurdan@ege.edu.tr*

Abstract. We present the observations of selected magnetic cataclysmic variables observed by T100 telescopes at the TÜBİTAK National Observatory (TNO). The aim of this study is to obtain photometry of short-period, faint magnetic cataclysmic variables and to search orbital variability due to accretion-spot modulation, flickering structures, occurring on short time scales. The results obtained from the light variation analysis of the system are presented.

INTRODUCTION

Cataclysmic Variables (CVs) are close binary star systems consisting of a white dwarf (WD) and a low mass main-sequence star. The mass accretion on this systems releases large amounts of gravitational energy which makes CVs powerful emitters of radiation from infrared to X-ray wavelength. The magnetic systems (MCVs) where the WD is strongly magnetic (10–230 MG) the accretion is magnetically funnelled directly onto the magnetic poles of the WD (Warner, 2003).

Emission in accreting objects arises from different parts of the system. In the case of the harder X-rays the emission arises directly from the shocked material. The soft X-rays, however originate both near the base of the accretion column, where the material is cooler (Cropper et al. 2000) and from the reprocessing of the hard X-rays intercepted by the primary. The optical brightness observations are coming from the accretion region on WD and also are mostly modulated with orbital period of the systems. The multiwavelength observations will enhance our understanding of accretion physics in MCVs and the understanding of X-ray emission mechanisms in accreting objects in general.

The aim of the optical observations is to obtain photometry of short-period, faint MCVs and to search orbital variability occurring on short time scales and periodicities related to eclipsing other components and compare these data with X-ray observations. Most of the MCVs are too faint for spectroscopic studies by using moderate-sized telescopes, therefore, the most used way to determine their orbital periods is the timing of photometric variations. In this study we will give the preliminary results of optical observations of three MCVs which were observed by TNO T100 telescope and compare the results with X-ray archival observations.

OBSERVATIONS

The photometric observations of these objects were performed by 1-m telescope T100 at the TNO (Turkey) using ANDOR CCD (2048×2048 pixels at 0.24 arc s pixel^{-1} resolution). We used standard routines for bias subtraction and flat-fielding of the CCD frames using the APPHOT package in IRAF. Differential magnitudes were measured relative to one or more nearby comparison stars on the CCD frame.

ISBN:978-605-83516-6-0

In order to study of the variation of the X-ray light curves over the orbital period, the archival X-ray observations of EP Dra and GG Leo were reanalyzed. The X-ray observation of EP Dra was performed by the *XMM-Newton* on 18 October, 2002 (OBS-ID: 0109464501) with a 18 ksec of exposure time, while the observation of GG Leo was performed on 13 May 2002 (OBS-ID:0109461401) with a 7 ks of exposure time. The standard SAS analysis tasks SAS, version 14.0, were used to extract the light curves from the data set for the X-ray CCDs with a bin time of 100 sec and FTOOLS analysis tasks were used to fold the light curve over the orbital period.

RESULTS

EP Dra

EP Dra which has an orbital period of 104.8 min is an eclipsing MCV. Bridge et al. (2003) attributed the varying eclipse profile to a variation in the amount and location of bright material in the accretion stream. Ramsay et al. (2004) had also presented X-ray energy-resolved and optical/UV light curves of EP Dra using *XMM-Newton*. They showed a prominent dip in X-rays and in the UV, which was thought to be the accretion stream obscuring the accretion region. Our dataset consists of one observing run using 60 sec exposures in the *V*-filter. Along with the X-ray data, we present *V* light curve of the source. The *V* light curve show a faint minimum phase at 1.0 coinciding with X-ray minimum phase which means the origin of the variation in both wavelenghts is same. The optical brigntness is also diminished at phase 0.3. We folded the light curves of EP Dra over the orbital period (Fig.1). The phases of the mean light curves are locked to the ephemerides reported by Schwope & Mengel (1997) from optical spectroscopy which is given below:

$$HJD = 2447681.72918 + 0^d.07265625(5) \times E \quad (1)$$

In order to further investigate the behaviour of the orbital modulation in X-rays and to account for the energy dependence of the modulation, we extracted light curves from two different energy ranges. EPIC-pn light curve split into the soft component *S* (E ≤ 0.5 keV), the hard component *H* (E ≥ 0.5 keV), and the associated hardness ratio *HR*=(*H*−*S*)/(*H*+*S*). We confirmed that the source obviously shows hardening during the orbital bright phases which means soft X-rays are absorbed and during minimum phases, no flux was observed for *HR* variation as reported by before.

GG Leo

The soft X-ray source GG Leo (RX J1015.6+0904) was detected during the ROSAT All-Sky Survey and identified as an AM Herculis binary candidate. A preliminary analysis of optical and X-ray photometry of GG Leo have been presented in Burwitz et al. (1995). Burwitz et al. (1998) determined that it shows strong modulations of the X-ray and optical fluxes repeating about every 80 min, which is close the orbital period of the system. The optical light curve can be characterized by a double-hump structured bright phase coinciding with the X-ray bright phase.

The photometric observations of GG Leo were obtained on one nights in May 2015 using the T100 telescope during the low accretion state. Fig. 2 shows the EPIC/pn and the photometric data folded with the orbital period according to the ephemeris derived by Burwitz et al. (1998) given in below (Eq. 2),

$$HJD = 2449488.0237036 + 0^d.05547184(4) \times E \quad (2)$$

The mentioned prominent dip during the bright phases in previous studies is obtained in X-ray light curve. The *V*-light curve shows an asymmetric and a wider minimum phase. A strong orbital modulation can be seen in optical light curve of GG Leo.

ISBN:978-605-83516-6-0

GG Leo was in a high accretion state during these *XMM-Newton* observations. There is an increase of hard X-rays (hardening) in *HR* ratio during the minimum phase at 0.95-1.0 (Fig. 2). The soft X-rays are significantly absorbed at these phases.

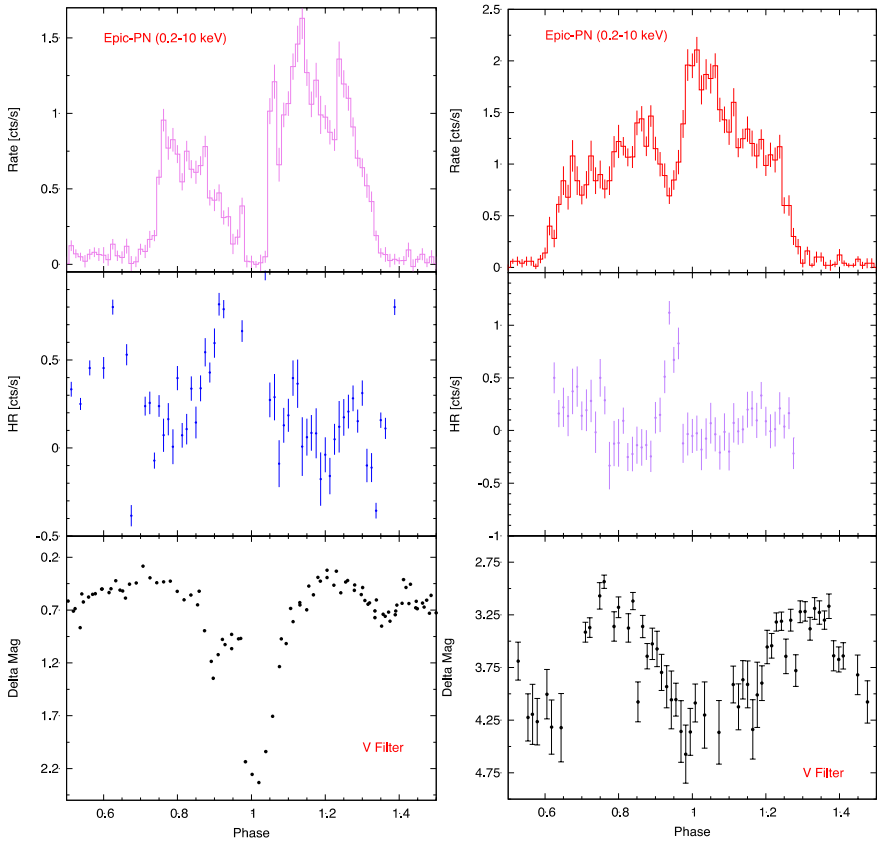


FIGURE 1. In the left, the Epic-pn light curve of EP Dra in time bins of 100 s folded on the orbital period using Eq.1 and shown in upper panel. Corresponding hardness ratio between the counts in the 0.1-0.5 keV and in the 0.5-10 keV shown in the middle panel. Optical *V* light curve obtained at 2014/08/22 during a high state of accretion and plotted in the bottom panel. In the right, the phased and binned X-ray (upper) and optical (bottom) light curves of GG Leo are shown. We have folded the data on the ephemeris given in Eq.2. Energy band of Epic-pn light curve in 0.2–10 keV which have bin widths of 50 sec. Corresponding hardness ratio is shown in the middle panel. Optical *V* light curve obtained at 2015/05/14 during a low state of accretion.

V1189 Her

The only optical observation of V1189 Her was published by Szkody et al. (2005). In this study this object identified as a polar. They obtained a large (0.6 mag) modulation with a period of 122 minutes in the photometric observations. The spectroscopic observation independently determined a period of 120 minutes from the radial velocities and they concluded the large K amplitudes imply a polar nature for this object and that further observations are required to find out true nature of V1189 Her. Gansicke et al. (2009) determined a new orbital period (134±2) for V1189 Her using the optical data, which were obtained by Szkody et al. (2005). No ephemeris time estimate currently exists for this object and also no X-ray observations of V1189 Her have been published to date.

ISBN:978-605-83516-6-0

The unfiltered photometry was performed during the nights of June 28th to 30th 2014 using the 100 cm TNO Telescope in Turkey. We obtained over 140 exposures, each 150 s long. The signal-to-noise ratio is typically 40-50 on each frame. The brightness of these stars was constant within the error of the differential photometry of the two objects ($\Delta m \sim 0.25$ mag).

During three nights in June 2014, we observed the 18th magnitude polar V1189 Her spanning over 4 h in each night. The lightcurve of those observations clearly shows the shape of the variation is asymetric and the peak-to-peak amplitude of the modulation is ~1.5 mag. A less steep rising to bright phase than the faint phase is prominent in the light curve. Also some fluctuations can be seen during the faint and bright phase of V1189 Her. Details of the light curves, i.e. light fluctuations in short time intervals, could not be revealed due to the long exposure times we used.

Two optical minima and four maxima have been observed in three subsequent nights in our observations. The period analysis was performed using PERIOD04 (Lenz & Breger, 2005) based on the Discrete Fourier Transform method, which was applied to all the data obtained. We searched for the fundamental frequency in the range 0 to 50 1/day and the resulted of the period can be seen in Eq.3. We derive the following ephemeris,

$$HJD = 2456837.5553625 + 0^d.09284285(2) \times E \qquad 3.$$

The light curve folded with this period is shown in Fig. 2. The analyzing of X-ray observation of V1189 Her is still not completed.

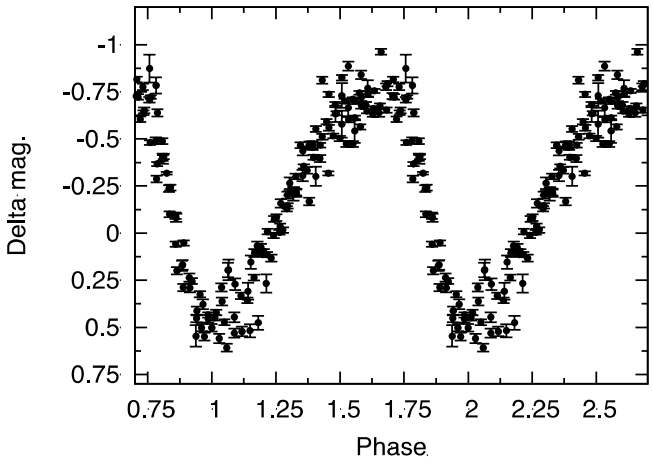


FIGURE 2. Phase-folded optical light curve of V1189 Her is shown which was obtained by T100 telescope.

CONCLUSIONS

We present the preliminary study of the light variations of polar EP Dra, GG Leo and V1189 Her. To fully understand the structure of the post-shock region both the visible and the X-ray bands, need to be studied more comprehensively. Although the obtained data of the two magnetic CVs are insufficient to study their photometric variation in details, the photometric observation will continue in next observing seasons. A more detailed study will be presented in Zengin Çamurdan et al. (2019).

ISBN:978-605-83516-6-0

ACKNOWLEDGMENTS

We thank to TUBITAK for a partial support in using T100 telescope with project number 654.

REFERENCES

1. B.Warner, “Cataclysmic Variable Stars”, pp. 592. ISBN 052154209X, Cambridge, UK, Cambridge University Press, 2003.
2. M. Cropper, K. Wu, and G. Ramsay, “The emission from post-shock flows in mCVs,” 44, 57–62 (2000), arXiv:astro-ph/9907285 [astro-ph].
3. C. M. Bridge, Cropper, G. Ramsay, et al., “Variability of the accretion stream in eclipsing polar EP Dra,” 341, 863-869 (2003).
4. G. Ramsay and M. Cropper, “The energy balance of polars revisited,” 347, 497–507 (2004), arXiv:astro-ph/0309527 [astro-ph].
5. A.D.SchwopeandS.Mengel,“Phase-resolved spectroscopy and photometry of the eclipsing polar EPDraconis (=H1907+690), ”Astronomische Nachrichten 318, 25 (1997), arXiv:astro-ph/9701086 [astro-ph].
6. V. Burwitz, K. Reinsch, A. D. Schwope, K. Beuermann, S. Mengel, P. Notni, A. van Teeseling, and H. C. Thomas, “RX J1015.5+0904: a new polar at the lower period limit.” in *Astronomische Gesellschaft Abstract Series*, Vol. 11 (1995) p. 148.
7. V. Burwitz, K. Reinsch, A. D. Schwope, P. J. Hakala, K. Beuermann, T. Rousseau, H. C. Thomas, B. T. Gänsicke, V. Piirola, and O. Vilhu, “A new ROSAT discovered polar near the lower period limit: RX J1015.5+0904 in Leonis,” 331, 262–270 (1998).
8. P.Szkody, A.Henden, O.J.Fraser, N.M.Silvestri, G.D.Schmidt, J.J.Bochanski, M.A.Wolfe, M.Agüeros, S.F.Anderson, L.Mannikko, R. A. Downes, D. P. Schneider, and J. Brinkmann, “Cataclysmic Variables from Sloan Digital Sky Survey. IV. The Fourth Year (2003),” 129, 2386–2399 (2005).
9. B. T. Gänsicke, M. Dillon, J. Southworth, J. R. Thorstensen, P. Rodríguez-Gil, A. Aungwerojwit, T. R. Marsh, P. Szkody, S. C. C. Barros, J. Casares, D. de Martino, P. J. Groot, P. Hakala, U. Kolb, S. P. Littlefair, I. G. Martínez-Pais, G. Nelemans, and M. R. Schreiber, “SDSS unveils a population of intrinsically faint cataclysmic variables at the minimum orbital period,” 397, 2170–2188 (2009), arXiv:0905.3476 [astro-ph.SR].
10. P.Lenzand, M.Breger,“Period 04 User Guide,”Communications in Asteroseismology,146,53–136(2005).
11. D. Z. Çamurdan, (2019), in preparation.

BOOK OF FULL TEXT PROCEEDINGS TURKISH PHYSICAL
SOCIETY 35th INTERNATIONAL PHYSICS CONGRESS (TPS35)
TPS35, Vol.01, No.02, pp.119-122.
ISBN:978-605-83516-6-0

15 December 2019

Orbital Period Change of UU Leo

C. Çicek[1, a)], A. Bulut[1, b)] and İ. Bulut[2, c)]

[1]*Department of Physics, Faculty of Art and Science, Çanakkale Onsekiz Mart University, Çanakkale, TURKEY*

[2]*Department of Space Sciences and Technologies, Faculty of Art and Science, Çanakkale Onsekiz Mart University, Çanakkale, TURKEY*

[a)] Corresponding author: ccicek@comu.edu.tr
[b)]abulut@comu.edu.tr

Abstract. We present the study of the orbital period variations of the Algol-type eclipsing binary star UU Leo (AN 351.1934, TYC 834-1297-1), using its (*O – C)* diagram gathered from all available times of eclipse minima. Its (*O − C*) diagram exhibits a long-term period increase (caused by the mass transfer between the two components) and a periodic (LITE term due to the existence of a unseen low-mass third body). Our analysis indicates a period increase of 3.88×10^{-7} day/yr. This period increment of UU Leo can be explained as mass transfer of rate 2.14×10^{-8} $M_{\odot}$ / yr, from the less to the more massive component. We found the third body period about 59.98 ± 0.01 years for UU Leo.

Keywords: *stars: binaries: eclipsing; stars: period analysis: individual: UU Leo*

INTRODUCTION

UU Leo (TYC 834-1297-1, AN 351.1934, 2MASS J09474968+1259024, Gaia DR1 614345937267033728, Gaia DR2 614345937267033728; R.A. = 09^h 47^m $49^s.6957$, DEC = $+12^o$ $59'$ 02".537, V_{max} = $11^m.75$, (Simbad), *P* = 1. 6797 days) and *e* = 0.4550 at 2000.0) was discovered by Hoffmeister (1934). The system's apparent brightness changes from $11^m.4$ to $12^m.7$ (Malkov et al. 2006). UU Leo displays a spectral type of A2. The mentioned value was proposed by Brancewicz and Dworak (1980). Budding (1984) classified this star as "Algol-type eclipsing binary". The period analysis of this star was studied by different authors. Jensch (1935) calculation for the orbital period was 1.67975 days. Whitney (1959) revised this value as 1.6797459 days. Later orbital period was calculated to be 1.6797366 days (Mallama 1980) and 1.67974627 days (Kreiner 2004).

Erdem et al. (2007) also studied the system. According to Erdem et al. (2007) there were "changes in orbital period and obtained a secular period increase superimposed on a quasi-cyclic oscillation with a period of P_3 = 62 year and a high eccentricity of *e* = 0.77, which was commented by mass transfer and magnetic activity", individually. Recently, Liakos et al. (2011) studied the *O* - *C* curve of UU Leo and obtained a light-time orbit with A = 0.48 day and P_3 = 72 year. Therefore, Liakos et al. (2011) also gathered a photometric solution that included a third light (i.e., l_3 = 11.5%) from their observations. The outcome of their study indicate that UU Leo may be a detached eclipsing binary with a mass ratio of *q* = 0.286.

Türk Fizik Derneği
1950
Turkish Physical Society

ISBN:978-605-83516-6-0

PERIOD VARIATION

All minima times of UU Leo were collected from the literature to analysis the period variation in the system. We used total 122 times of minima of UU Leo in our analysis. The following linear ephemerides were used to calculate the *O* - *C* values;

$$\text{Min I} = \text{HJD } 2456309.2083 + 1^{d}.\,6797668 \times E \qquad (1)$$

($O - C$) diagram exhibits a long-term period increase (triggered by the mass transfer between the two components) and a periodic (LITE term due to the existence of an unseen low-mass third body). Zasche (2009)'s program was applied to these *O*-*C* values. The *O* - *C* diagrams of the system are presented in Figure 1 and Figure 2, and the resulting parameters are given in Table 1.

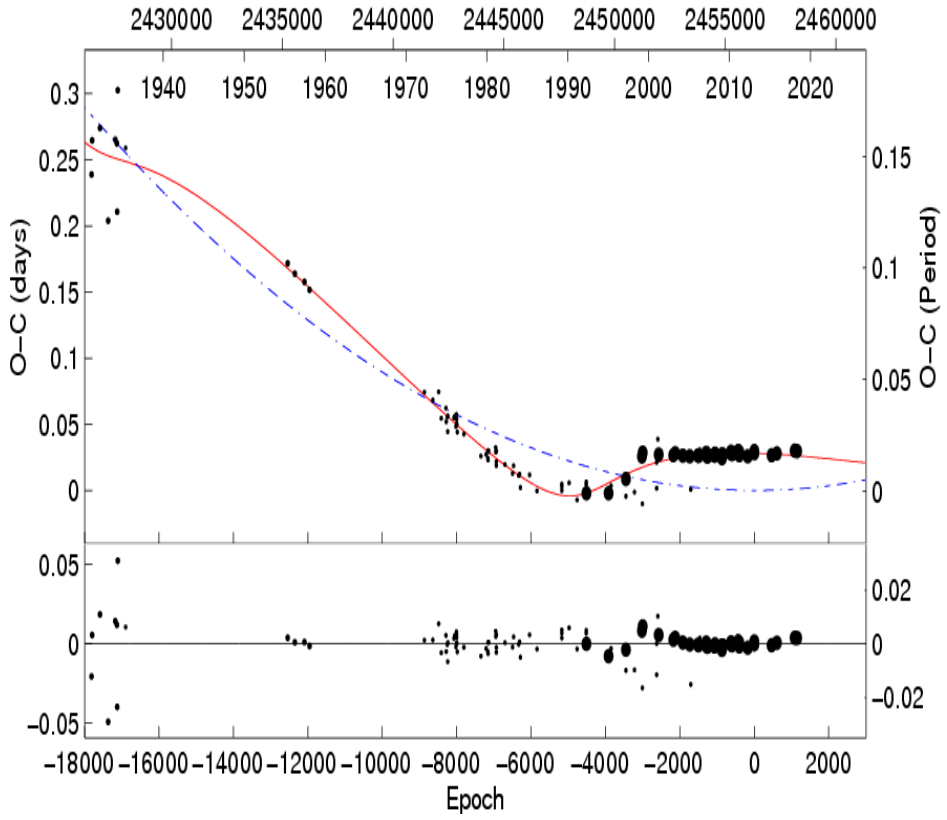


FIGURE 1. Period analysis of UU Leo. (included all effects)

ISBN:978-605-83516-6-0

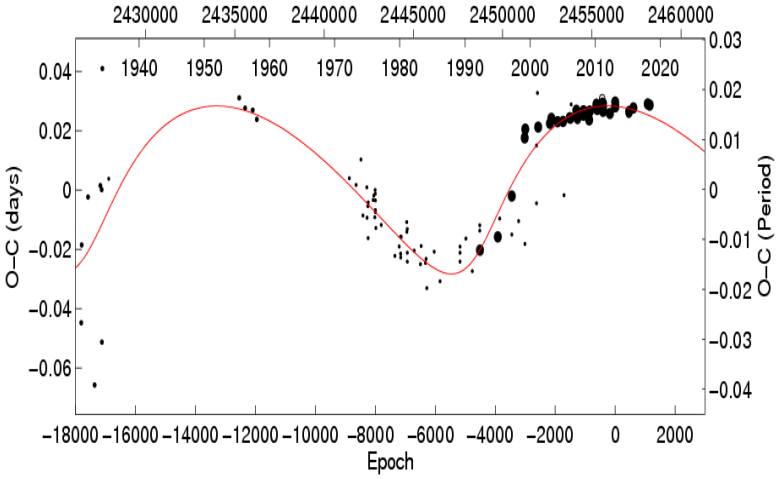


FIGURE 2. Period analysis of UU Leo. (Not included third-body LITE term)

TABLE 1. Obtained Parameters of the LITE Orbits Parameter of UU Leo

Parameter	**UU Leo**
T_o (HJD)	2456309.2083 ± 0.0097
P_{orb} (day)	1.6797668 ± 0.0000016
Q (day)	$(8.9368 \pm 0.0008)\times10^{-10}$
A_s (day)	0.02833 ± 0.0034
a12 sin i [AU]	5.21 ± 0.65
e'	0.4550 ± 0.2496
ω' (deg)	317.4 ± 33.6
T_3 (HJD)	2623984 ± 1668
P_3 (yr)	59.98 ± 0.01
$f(M_3)$ ($M_\odot$)	0.0392 ± 0.0002
M_3 ($M_\odot$) (i = 90 °)	0.6508 ± 0.0019
M_3 ($M_\odot$) (i = 60 °)	0.7747 ± 0.0024
M_3 ($M_\odot$) (i = 30°)	1.5947 ± 0.0056

CONCLUSIONS AND REMARKS

In this review, we restudied the orbital period analysis of eclipsing binary UU Leo. We found out that this binary system shows light-time effects because of third body. That's why, binary system has evident variations of its orbital period. The mass function of third body for UU Leo was computed to be 0.6508 ± 0.0019 $M_\odot$. According to our calculation, the orbital period of the third body for UU Leo was 59.98 ± 0.01 years.

ISBN:978-605-83516-6-0

REFERENCES

1. H. K. Brancewicz and T. Z. Dworak, *Acta Astron*, **30**, pp. 501-524 (1980).
2. E. Budding, *Bulletin d'Information du Centre de Donnees Stellaires*, **27**, pp. 91-129 (1984).
3. A. Erdem, S. S. Doğru, V. Bakış, O. Demircan, *Astronomische Nachrichten*, **328**, 6, pp.543-550 (2007).
4. C. Hoffmeister, *Astronomische Nachrichten*, **253**, pp.195 (1934).
5. A. Jensch, *Astronomische Nachrichten*, **257**, pp.139 (1935).
6. J. M. Kreiner, *Acta Astronomica*, **54**, pp.207-210 (2004).
7. A. Liakos, P. Zasche and P. Niarchos, *New Astronomy*, **16**, 8, pp. 530-538 (2011).
8. O. Y. Malkov, E. Oblak, E. A. Snegireva and J. Torra, *Astronomy and Astrophysics*, **446**, 2, pp. 785-789 (2006).
9. A. D. Mallama, *Astrophysical Journal*, **44**, pp. 241-272 (1980).
10. B. S. Whitney, *Astronomical Journal*, **64**, pp. 258-265 (1959).
11. P. Zasche, A. Liakos, P. Niarchos, M. Wolf, V. Manimanis and K. Gazeas, *New Astronomy*, **14**, 2, pp. 121-128 (2009).

BOOK OF FULL TEXT PROCEEDINGS TURKISH PHYSICAL
SOCIETY 35th INTERNATIONAL PHYSICS CONGRESS (TPS35)
TPS35, Vol.01, No.02, pp.123-126.
ISBN:978-605-83516-6-0

15 December 2019

Searches for Uniform Metal Distributions in Galaxy Clusters

Murat Hüdaverdi[1,a)], Cemile Ezer[1,b)] and M. Kıyami Erdim[1,2,c)]

[1]*Yildiz Teknik University, Faculty of Science and Art, Department of Physics, İstanbul, 34220, Turkey.*
[2]*Yildiz Teknik University, Graduate School of Natural and Applied Sciences, İstanbul, 34220, Turkey.*

[a)]Corresponding author: hudaverd@yildiz.edu.tr
[b)]cemile.ezer@boun.edu.tr
[c)]mkiyami@yildiz.edu.tr

Abstract. The presence of gravitational potential well is of a great help in preserving all metals synthesized by star formation and supernova explosions within the intra-cluster medium (ICM) of the galaxy cluster and hence recording the chemical enrichment history. Measuring these metal abundances from low signal to noise regions, namely clusters outskirts, is possible with current X-ray missions. In this work, we review the searches on the metal abundances which were detected in the clusters outskirts and strong evidences on the possible early enrichment scenario where the mixing and dispersion of these metals into the ICM took place before the clusters formation (z > 2-3). We also present our latest joint Suzaku and XMM-Newton analysis on intermediate redshift Abell 2667 (z ~ 0.23) galaxy cluster and compare these results with our current study.

INTRODUCTION

The dominant fraction of baryonic matter of a galaxy cluster resides in the intra-cluster medium (ICM) form of hot ($10^7 - 10^8$ K) and tenous ($10^{-4} - 10^{-2}$ cm^{-3}) gas. The hot gas emits its energy via thermal bremsstrahlung process in the X-ray band. The X-ray spectra of the ICM have revealed that the gas is enriched by metals, where iron is being the most promising one. Since all metals through the stellar populations in member galaxies are trapped inside the deep potential wells of the clusters , metal measurements have great importance on manifesting the chemical enrichment scenario.

There are many possible processes responsible for the distribution of metals from cluster's center to outskirts. Measuring spatial distributions of these metals out to virial radius is a powerful diagnostic to reveal the chemical enrichment history of the cluster. In this study, we concentrate on robust studies of iron distributions out to R_{200}, where the average density is 200 times the critical density of the Universe. In 2013, *Suzaku Key Project* deep data with 1 Ms exposure time were analyzed [1]. They reported the measurements on spatial and azimuthal distributions of iron abundance out to R_{200} by using 8 different pointings of nearby cool-core Perseus galaxy cluster. The iron abundance was found to be constant as a function of radius and azimuth and reported as $Z_{Fe} = 0.314 \pm 0.012$ Solar (abundances adopted from [2]). Another work from ten massive clusters ($1.4 - 14 \times 10^{14}$ M$\odot$) was done by [3] and their results are quite similar with Perseus cluster. In this work, they showed that these clusters have uniform iron distribution after exclusion of up to central $0.25R_{200}$ region and the value is $Z_{Fe} = 0.316 \pm 0.012$ Solar (abundances adopted from [2]).

In this study, we will give results on Abell 2667 (A2667) as being one of the distant luminous galaxy cluster located at redshift $\simeq 0.23$, [4]. It is a cool-core cluster, regular X-ray morphology and so different from the majority of similar X-ray luminous clusters at this distance [5, 6].

It is the first time measurement extending out to R_{200} for this cluster. We will give results of Suzaku-XIS analysis of four different observations together with ~30 ks XMM-Newton EPIC observation for point source detection.

Observations and Data Reduction

We used ~ 31 ks XMM-Newton EPIC and ~ 167 ks Suzaku XIS archival observations belonging to A2667 galaxy cluster. The details of the observations are listed in Table 1. For XMM-Newton data, we used ESAS (SAS version

Türk Fizik Derneği
1950
Turkish Physical Society

ISBN:978-605-83516-6-0

TABLE 1. Suzaku and XMM-Newton Archival Observations

Observatory	Obs ID	Ra (J2000)	Dec (J2000)	Obs Date	Pointing	Cleaned Exposure (ks)
						XIS0/XIS1/XIS3
Suzaku	806029010	357.9715	-25.9262	2011-06-09	Offset	38.9/38.9/38.9
	806029020	357.7341	-26.0226	2011-06-10	Offset	44.2/44.2/44.2
	806029030	357.8478	-26.2362	2011-06-12	Offset	41.2/41.2/41.2
	806029040	358.0843	-26.1324	2011-06-13	Offset	42.1/42.1/42.1
						MOS1/MOS2/PN
XMM-Newton	0148990101	357.91	-26.08	2003-06-21	Onaxis	19.2/19.9/13.9

18.0.0) software and the latest calibration files for our analysis procedure. *emchain* and *epchain* tools were used to create calibrated EPIC-MOS and EPIC-PN data respectively. This procedure is followed by the use of *mos-filter* and *pn-filter* scripts to handle soft proton contamination. The point sources were detected by using *cheese* task and the location of these sources were used in our Suzaku data.

For Suzaku data, we used HEASOFT (version 6.24) with the latest calibration files. The data were reprocessed and screened by using *aepipeline* tool and all the standard filters listed in Suzaku ABC guide were applied. Clean event files were created by merging 3x3 and 5x5 modes. Following this procedure, additional filter to one-eighth of XIS0 CCD segment is forced due to the meteorite hit at June 2009. We filtered all the point sources detected by XMM-Newton with 35" extraction radius, since Suzaku-XIS point-source resolution is much larger. For more details of Suzaku-XIS analysis procedure, one can refer [7, 8, 9].

Spectral Analysis

Cluster's emission was investigated by using Suzaku-XIS regions (shown in Figure 1) extracted via *xselect* command. Due to large point-spread function (PSF) of Suzaku, we determined our extraction radius at least $120''$ to minimize scatter from neighbouring regions. During our fits, we require to have at least 1000 counts. We examined total four regions from center to outskirts (0-120 arcsec, 120-240 arcsec, 240-400 arcsec and 400-660 arcsec). In all regions, we performed our spectral analysis by summing two front illuminated (FI) spectra (XIS0 and XIS3) and fitted with back illuminated (BI) spectra (XIS1) simultaneously.

Except for the non X-ray background generated by *xisnxbgen* and extracted prior to fitting on XSPEC (version 12.10.0), all other background components (Cosmic X-Ray Background, Galactic Halo, Local Hot Bubble) were taken into account by the following procedure. First, we extracted local background outside from R_{200} (660-900 arcsec) where one assumes almost no cluster emission and then fit these spectra with Rosat All Sky Survey (RASS) data simultaneously. Our results lead 15276.20/13794 (Cstat/dof). Finally, we fixed all background parameters during our fits.

We modelled our source spectra with single thermal apec model ([10]) with solar abundance table adopted from [11]. Errors are quoted at 68% confidence for each parameter. The best-fit apec temperature and abundance profiles can be found in Figure 2.

ISBN:978-605-83516-6-0

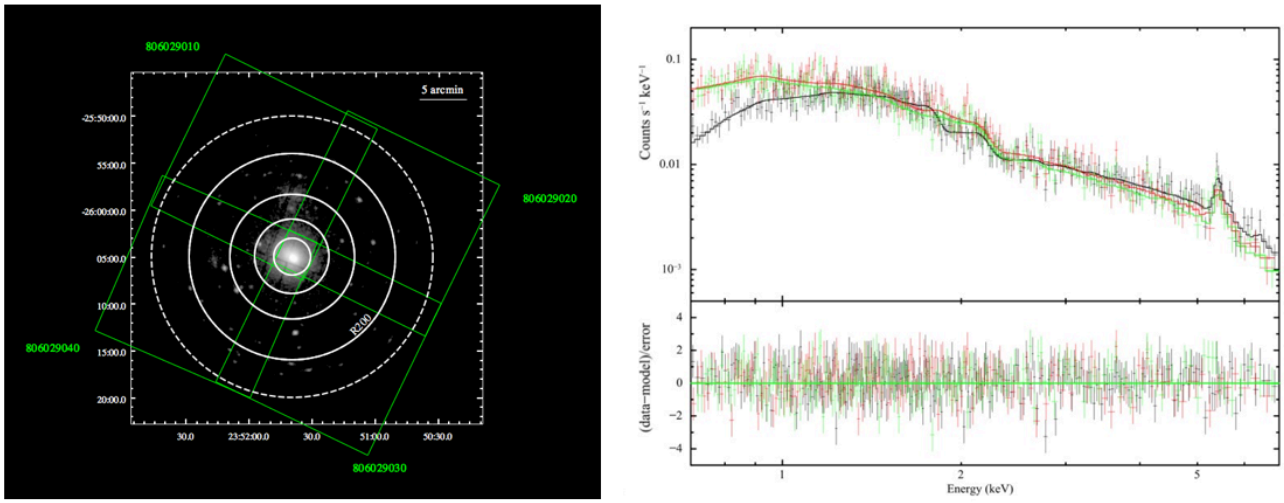


FIGURE 1. *Left-panel*: Exposure corrected, background subtracted XMM-Newton image of A2667 galaxy cluster. The green squares represent Suzaku XIS field-of-view (FOV), whereas the white solid annular regions used for cluster spectra. We should note that local background was extracted from white dashed annulus as the outer-most region. *Right-panel*: The Suzaku-XIS spectral fit for the central region.

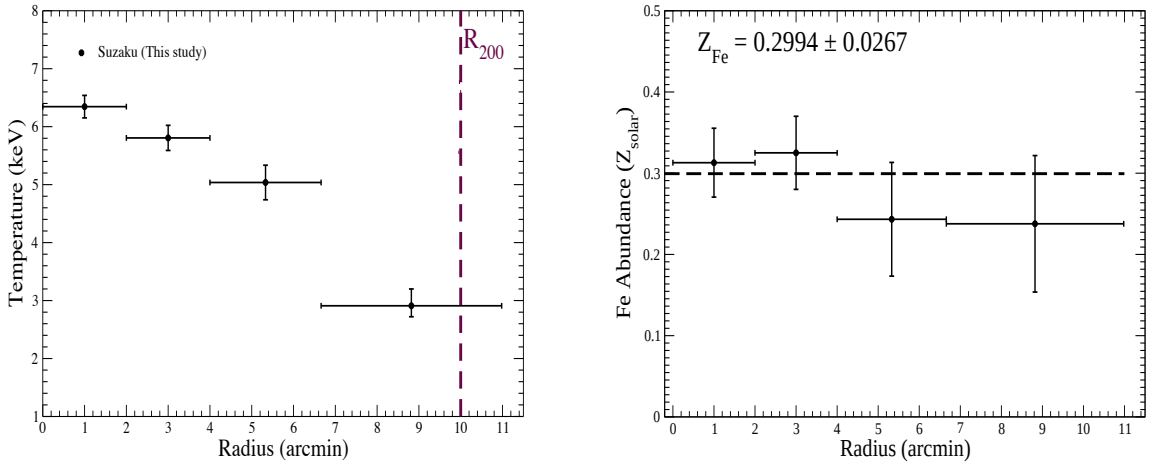


FIGURE 2. Temperature and Iron Abundance of galaxy cluster A2667's ICM as a function of radius.

Conclusion

Measuring iron abundance in the ICM has great importance, since this information shed light on to the cluster and so galaxy formation. In this work, we performed a joint analysis which aims to reveal iron abundance distribution of A2667 galaxy cluster. We found that iron distribution is best represented by a constant fit giving a value 0.2994 ± 0.02667 with χ^2/dof = 1.16/3. When the effect of ram-pressure stripping as being efficient metal transport mechanism in low redshifts is considered, one expects to observe central excess. Our observation approves more homogenous

ISBN:978-605-83516-6-0

distribution from center to virial radius. The uniform distribution of metals supports the early enrichment scenario, which can be achieved by including the effects of AGN feedback and supernova driven galactic outflows. This scenario predicts that the iron abundance is the result of forming and accreting at early epoch, as earlier as the member galaxies or just after. Therefore, the metals that we observed today were already at proto-cluster region, $z > 2 - 3$.

ACKNOWLEDGEMENTS

This work is a part of M.K.E.s PhD research. We would like to acknowledge financial support from the Scientific and Technological Research Council of Turkey (TÜBİTAK) project number 118F035. While this full-text proceeding focuses on the preliminary analysis results of A2667, a manuscript discussing the detailed structural analysis of the cluster is currently in preparation.

REFERENCES

[1] N. Werner, O. Urban, A. Simionescu, and S. A. Allen, Nature. **502**, 656–658 (2013).
[2] M. Asplund, N. Grevesse, A. J. Sauval, and P. Scott, Ann. Rev. Astr. Astrophys. **47** (2009).
[3] O. Urban, N. Werner, S. W. Allen, A. Simionescu, and A. Mantz, MNRAS **470** (2017).
[4] M. F. Struble and H. J., ApJ. **125**, 35–71 (1999).
[5] S. W. Allen, R. W. Schmidt, A. C. Fabian, and H. Ebeling, MNRAS. **342**, p. 287298 (2003).
[6] M. Rossetti, D. Eckert, B. M. Cavalleri, S. Molendi, F. Gastaldello, and S. Ghizzardi, A&A. **532** (2011).
[7] M. W. Bautz, E. D. Miller, J. S. Sanders, K. Hayashida, J. P. Henry, H. J. P., and T. Tamura, PASJ. **61**, p. 11171133 (2009).
[8] E. Bulbul, S. W. Randall, M.Bayliss, E. Miller, R. J. F. Andrade-Santos, M. Bautz, E. L. Blanton, W. R. Forman, C. Jones, R. Paterno-Mahler, S. S. Murray, C. L. Sarazin, R. K. Smith, and C. Ezer, ApJ. **818** (2016b).
[9] C. Ezer, E. N. Ercan, R. K. Smith, M. W. Bautz, M. Loewenstein, M. McDonald, and E. D. Miller, ApJ. **836** (2017).
[10] R. K. Smith, N. S. Brickhouse, D. A. Liedahl, and J. C. Raymond, ApJ. **556** (2001).
[11] E. Anders and N. Grevesse, Geochim. Cosmochim. Acta. **53**, 197–214 (1989).

BOOK OF FULL TEXT PROCEEDINGS TURKISH PHYSICAL
SOCIETY 35th INTERNATIONAL PHYSICS CONGRESS (TPS35)
TPS35, Vol.01, No.02, pp.127-133.
ISBN:978-605-83516-6-0

15 December 2019

The Short-Period Eclipsing Binary 1SWASPJ173327.97+265547.9: Photometric Solution and Period Investigation

Seda Kaptan[1, a)] and Burcu Özkardeş[2, 3, b)]

[1]*Department of Astronomy and Space Sciences, Institute of Graduate Studies in Science and Engineering, İstanbul University, İstanbul, TURKEY.*
[2] *Department of Space Sciences and Technologies, Faculty of Art and Science, Çanakkale Onsekiz Mart University, Çanakkale, TURKEY.*
[3] *Çanakkale Onsekiz Mart University Astrophysics Research Center and Ulupınar Observatory, Çanakkale, TURKEY.*

[a)] sedakaptan@gmail.com
[b)] Corresponding author: burcu@comu.edu.tr

Abstract. The first period analysis and light curve modeling for the short period eclipsing binary 1SWASP J173327.97+265547.9 (V1097 Her=GSC 02083-01870=NSVS 8002361) is presented in this study. The SuperWASP light curve of the binary system was modeled by applying the Wilson-Devinney method. The photometric mass ratio of the system is obtained. The physical parameters of the components of the target system, namely the masses and radii, are estimated. Using all the public data, the orbital period change of the eclipsing binary is studied, and the mechanisms that are responsible for the period variation are discussed.

INTRODUCTION

Some observational studies (Hoffman et al. (2009), Avvakumova et al. (2013)) show that the short-period (P=0.3608 days) eclipsing binary 1SWASP J173327.97+265547.9 (V1097 Her=GSC 02083-01870=NSVS 8002361) is a W UMa type binary star. W UMa type binaries, also called to be contact/over-contact binaries, consist of late type components which have a nearly equal temperatures. These type binaries' orbits are a circular, and the components rotate synchronously. Considering the evolutionary status of W UMa type binaries, the hotter component could be the less massive one due to the energy transfer between each component. Binnendijk (1970) divided the W UMa type eclipsing binary stars to two subtype as A and W (for A subtype: $M_1 > M_2$; $T_1 > T_2$—for W subtype: $M_1 < M_2$; $T_1 > T_2$).

The motivation of the present work is that there is no a photometric and/or spectroscopic study for V1097 Her in the literature. By analyzing the light curve and period variation of V1097 Her it is aimed to get some fundamental informations about the nature of the system. Basic features of V1097 Her are given in Table 1.

TABLE 1. Basic features of V1097 Her.

Star Name	Variability Type	Coordinates	B (mag)	V (mag)	Parallax (mas)	Reference
V1097 Her	EW	α: $17^h33'27''$ δ: $+26^\circ55'47''$	11.69±0.07	11.04±0.06	3.9955±0.0231	Simbad Database[1]

[1] https://simbad.u-strasbg.fr/simbad

Türk Fizik Derneği
1950
Turkish Physical Society

ISBN:978-605-83516-6-0

PERIOD ANALYSIS

To analyze the orbital period variation of V1097 Her, it was picked available light minimum times of the system up from the *O-C* Gateway (OCG) archive[2]. In the current study, 53 primary minimum (Min I) and 44 secondary minimum (Min II) were obtained from the archive light curve in SuperWASP of V1097 Her. In Table 2 the eclipse timings and their properties are tabulated. Abbreviations used in the table are: HJD: Heliocentric Julian Day – p/s: primary/secondary – c/BVRI: clear/BlueVisualRedInfrared.

TABLE 2. Minimum light times and their properties for V1097 Her.

HJD Min	Min Type	Filter	Reference	HJD Min	Min Type	Filter	Reference	HJD Min	Min Type	Filter	References
2451306.8926	p	c	OCG	2453178.6054	p	V	SWASP	2453834.4476	s	V	OCG
2452411.4455	p	c	OCG	2453179.5085	s	V	SWASP	2453923.3951	p	I	OCG
2452415.4139	p	c	OCG	2453180.5912	s	V	SWASP	2453991.4154	s	R	OCG
2452426.4205	s	c	OCG	2453181.4927	p	V	SWASP	2454002.4182	p	R	OCG
2452442.4772	p	c	OCG	2453182.5751	p	V	SWASP	2454210.4505	s	c	OCG
2452463.4064	p	c	OCG	2453184.5603	s	V	SWASP	2454240.4001	s	V	OCG
2452463.5857	s	c	OCG	2453185.4619	p	R	OCG	2454240.4003	s	I	OCG
2452475.4953	s	c	OCG	2453185.4622	p	V	SWASP	2454240.4003	s	R	OCG
2452483.4344	s	c	OCG	2453188.5308	s	V	SWASP	2454591.8665	s	c	OCG
2452746.4914	s	c	OCG	2453189.6121	s	V	SWASP	2454946.3996	p	I	OCG
2453096.5127	s	c	OCG	2453190.5134	p	V	SWASP	2454946.3996	p	V	OCG
2453128.6294	s	V	SWASP	2453191.5953	p	V	SWASP	2454946.4002	p	R	OCG
2453129.5315	p	V	SWASP	2453192.4987	s	V	SWASP	2455003.7746	p	V	OCG
2453129.7125	s	V	SWASP	2453194.4825	p	V	SWASP	2455059.3463	p	c	OCG
2453130.6137	p	V	SWASP	2453194.4825	s	V	SWASP	2455059.5273	s	c	OCG
2453132.5989	s	V	SWASP	2453195.5657	p	V	SWASP	2455311.2184	p	V	OCG
2453137.6504	s	V	SWASP	2453196.4684	s	V	SWASP	2455315.0072	s	Rc	OCG
2453138.5523	p	V	SWASP	2453197.5516	s	V	SWASP	2455316.0905	s	Rc	OCG
2453139.6346	p	V	SWASP	2453199.5350	p	V	SWASP	2455350.0106	s	Rc	OCG
2453141.6199	s	V	SWASP	2453200.4383	s	V	SWASP	2455350.1900	p	Rc	OCG
2453142.5211	p	V	SWASP	2453201.5200	s	V	SWASP	2455351.0922	s	V	OCG
2453142.7022	s	V	SWASP	2453203.5041	p	V	SWASP	2455687.5825	p	R	OCG
2453143.6035	p	V	SWASP	2453205.4886	s	V	SWASP	2455727.8163	s	V	OCG
2453144.6858	p	V	SWASP	2453207.4738	p	V	SWASP	2455740.4471	s	R	OCG
2453146.6798	s	V	SWASP	2453212.5227	p	V	SWASP	2456024.9749	p	c	OCG
2453149.5592	s	V	SWASP	2453215.4085	p	V	SWASP	2456061.7807	p	VRI	OCG
2453151.5438	p	V	SWASP	2453218.4808	s	V	SWASP	2456072.7903	s	VRI	OCG
2453152.4457	s	V	SWASP	2453220.4646	p	V	SWASP	2456096.4229	p	R	OCG
2453152.6244	p	V	SWASP	2453222.4474	s	V	SWASP	2456111.3994	s	BVRI	OCG
2453153.5268	s	V	SWASP	2453223.5331	s	V	SWASP	2456112.3004	p	BVRI	OCG
2453154.6096	s	V	SWASP	2453224.4333	p	V	SWASP	2456112.4819	s	BVRI	OCG
2453155.5109	p	V	SWASP	2453226.4186	s	V	SWASP	2456113.3827	p	BVRI	OCG
2453155.6926	s	V	SWASP	2453229.4858	p	V	SWASP	2456114.4646	p	BVRI	OCG
2453156.5942	p	V	SWASP	2453230.3880	s	V	SWASP	2456167.3315	s	R	OCG
2453157.4953	s	V	SWASP	2453231.4714	s	V	SWASP	2456411.0818	p	Rc	OCG
2453157.6752	p	V	SWASP	2453233.4525	p	V	OCG	2456411.2637	s	Rc	OCG
2453158.5785	s	V	SWASP	2453235.4404	s	V	SWASP	2456460.5191	p	R	OCG
2453159.6616	s	V	SWASP	2453237.4238	p	I	OCG	2456522.4057	s	R	OCG
2453160.5634	p	V	SWASP	2453237.4248	p	V	SWASP	2456777.5265	s	R	OCG
2453161.4645	s	V	SWASP	2453239.4093	s	V	SWASP	2456810.5413	p	I	OCG
2453162.5490	s	V	SWASP	2453241.3934	p	V	SWASP	2456817.3984	p	R	OCG
2453163.6306	s	V	SWASP	2453242.4756	p	V	SWASP	2456831.4728	p	I	OCG
2453164.5312	p	V	SWASP	2453243.3790	s	V	SWASP	2457158.4023	p	I	OCG
2453165.6154	p	V	SWASP	2453246.4455	p	V	SWASP	2457160.5661	p	R	OCG
2453166.5184	s	V	SWASP	2453250.4153	p	V	SWASP	2457179.5118	s	R	OCG
2453167.6001	s	V	SWASP	2453250.4154	s	V	SWASP	2457207.4774	p	c	OCG
2453168.5016	p	V	SWASP	2453252.3999	s	V	SWASP	2457546.4975	s	I	OCG
2453168.6827	s	V	SWASP	2453254.3860	p	V	SWASP	2457571.3959	s	R	OCG
2453169.5844	p	V	SWASP	2453256.3697	s	V	SWASP	2457868.5538	p	R	OCG
2453170.4871	s	V	SWASP	2453261.4220	s	V	SWASP	2457868.5538	p	V	OCG
2453170.6669	p	V	SWASP	2453263.4059	p	V	SWASP	2457868.5541	p	I	OCG
2453171.5694	s	V	SWASP	2453510.4048	s	I	OCG	2457884.4324	p	Ir	OCG
2453172.4717	p	V	SWASP	2453512.3889	p	I	OCG	2457918.7120	p	c	OCG
2453172.6525	s	V	SWASP	2453516.3591	p	I	OCG	2457920.6983	s	BVRI	OCG
2453173.5538	p	V	SWASP	2453612.3452	p	c	OCG	2457920.8779	p	BVRI	OCG

[2] http://var2.astro.cz/ocgate/index.php?lang=en

2453174.4558	s	V	SWASP	2453612.5256	s	c	OCG	2457922.6822	p	BVRI	OCG
2453174.6365	p	V	SWASP	2453636.3412	s	I	OCG	2457922.8639	s	BVRI	OCG
2453175.5386	s	V	SWASP	2453638.3258	p	V	OCG	2457973.3811	s	I	OCG
2453176.6220	s	V	SWASP	2453815.5014	p	I	OCG	2457973.3819	s	V	OCG
2453177.5251	p	V	SWASP	2453832.4613	p	R	OCG	2457973.3825	s	R	OCG

To examine the period variation of V1097 Her, a well-known *O-C* method was applied to the eclipse timings listed in Table 2. The *O-C* values were computed by the Equation 1., which is covered the linear ephemeris provided by Kreiner et al. (2004):

$$Min.I = 2452463.4057 + 0^d.36084796xE \quad (1)$$

The distribution of *O-C* values is shown in Figure 1. As seen in this figure, the distribution has an upward parabolic form. The LITE code developed by Zasche et al. (2009) was applied to the *O-C* data of V1097 Her, and the mode "only quadratic fit" was selected in the analysis. The *O-C* diagram of V1097 Her and the residuals from the final model are shown in Figure 2. The final parameters are given in Table 4.

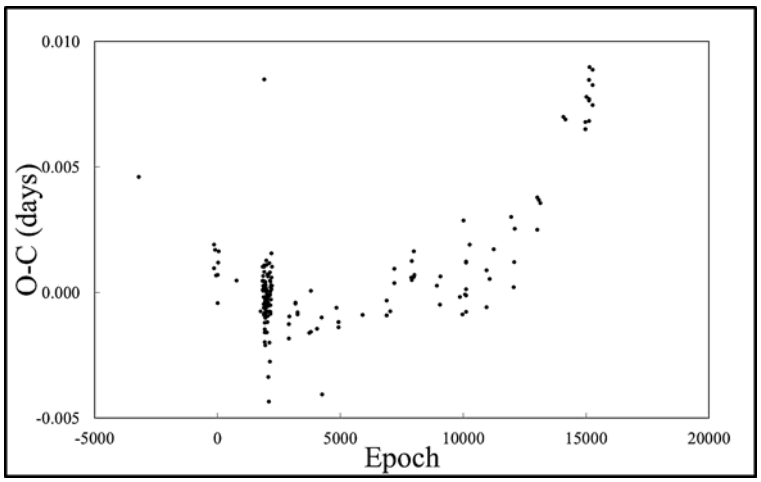


FIGURE 1. *O-C* values' distribution of V1097 Her.

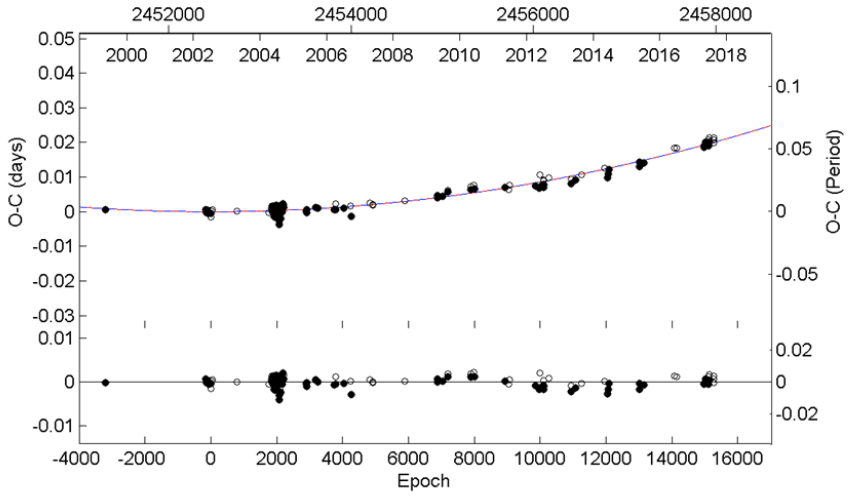


FIGURE 2. *O-C* diagram of V1097 Her. Top: *O-C* data's distribution and parabolic representation (solid line); bottom: residuals from the best fit.

ISBN:978-605-83516-6-0

LIGHT CURVE ANALYSIS

For analyzing the light curve of V1097 Her, the photometric data were taken from The SuperWASP (Wide Angle Search for Planets) database[3]. In the SuperWASP project two robotic telescopes (placed in Northern and Southern hemisphere) are used that the telescopes have 8 CCD cameras taken images in 4000-7000ÅÅ. In this study, observational data of the CCD camera 104 were used by taking into account the abundance and low scattering in the data.

The archive light curve of the system was solved by using the Wilson–Devinney (WD) method (Wilson and Devinney, 1971, vers. 1996). There are seven modes in the WD code. MOD 3 was selected corresponding to W UMa type binaries. The primary component's effective temperature was determined to be 5945 K corresponding to the intrinsic colour indice $(B\text{-}V)_0$=0.579 given by Terrel et al. (2012), of the system using the MK spectral type calibration table published by Drilling and Landolt (2000). Gravity darkening coefficients and albedos were set to be $g_{1,2}$=0.32 and $A_{1,2}$=0.5 according to the theory given by Rucinski (1969) and Lucy (1968), respectively, for stars with convective envelopes. The limb darkening coefficients were gotten from van Hamme (1993). It was assumed that both the components of V1097 Her rotate synchronously and the system move in a circular orbit. q-search method was used for determination of the mass ratio of the system. The initial value of the parameter q was found to be 3.31 (see Figure 3). The results of the solution are given in Table 3 with the errors corresponding to the last digit. Comparison of the observational data with the best model is plotted in Figure 4.

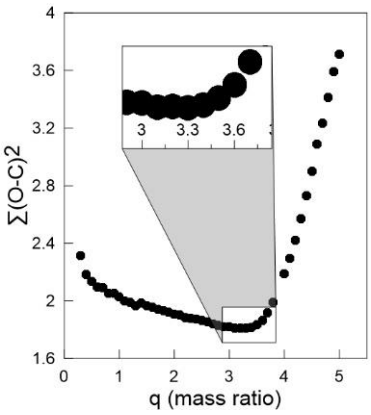


FIGURE 3. q versus $\Sigma(O\text{-}C)^2$ for V1097 Her.

TABLE 3. Final solution of the SWASP light curve of V1097 Her.

Parameter	Value	Parameter	Value
T_1 (K)	5945	$A_1 = A_2$	0.5
T_2 (K)	5748±46	$g_1 = g_2$	0.32
$\Omega_1 = \Omega_2$	6.9439±0.0090	$r_{1(pole)}$	0.2671
$q = M_2/M_1$	3.3120±0.0065	$r_{1(side)}$	0.2789
f (fillout)	0.13	$r_{1(back)}$	0.3159
Phase shift	0.0005 ± 0.0001	$r_{1(aver)}$	0.2866
i (°)	77.8 ± 0.1	$r_{2(pole)}$	0.4605
$L_1/(L_1+L_2)$	0.28 ± 0.01	$r_{2(side)}$	0.4963
X_1, X_2	0.292	$r_{2(back)}$	0.5232
Y_1, Y_2	0.539	$r_{2(aver)}$	0.4927
$\Sigma(O\text{-}C)^2$	0.7596		

[3] https://wasp.cerit-sc.cz/form

ISBN:978-605-83516-6-0

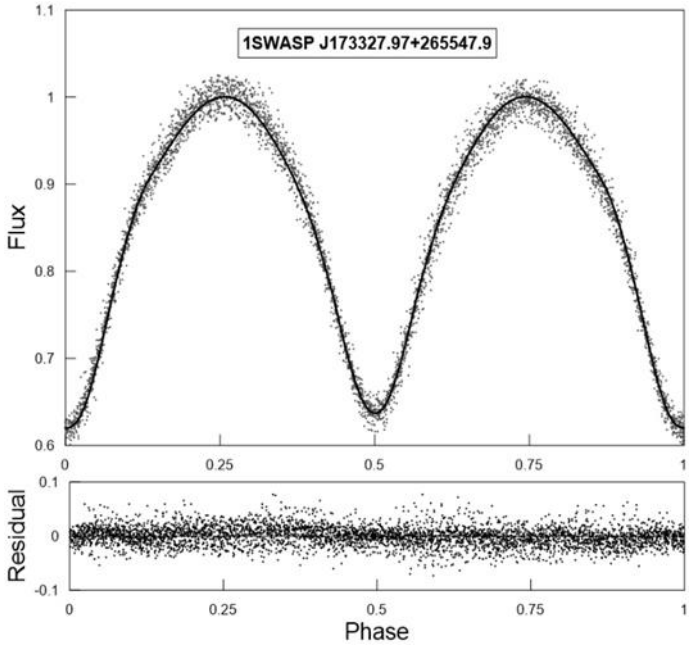


FIGURE 4. Comparison of the observed (filling circle) and model (solid line) light curve of V1097 Her (top) and residuals (bottom).

RESULTS

The following results are obtained from the analysis of the SuperWASP light curve and period variation of V1097 Her:

- The upward parabolic form in the period variation of V1097 Her shows the mass transfer from the primary component to secondary one. The results from the analysis are given in Table 4.

TABLE 4. Parameters obtained from the period analysis of V1097 Her.

Parameter	Value
T_0 (HJD)	2452463.4068 ± 0.0005
$P_{orbital}$ (days)	0.3608471 ± 0.0000001
Q (days)	$(8.58 \pm 0.07)10^{-11}$
dP/dt (s/year)	0.015 ± 0.001
dm/dt ($M_\odot$/year)	$0.32x10^{-7}$
χ^2	0.0015

- The system is a contact eclipsing binary according to the photometric solution, and the filling factor of the components are 113%. The surface geometries of the primary and secondary components are given in Figure 5. at four different phases (BM3 program, Bradstreet and Steelman, 2002).

ISBN:978-605-83516-6-0

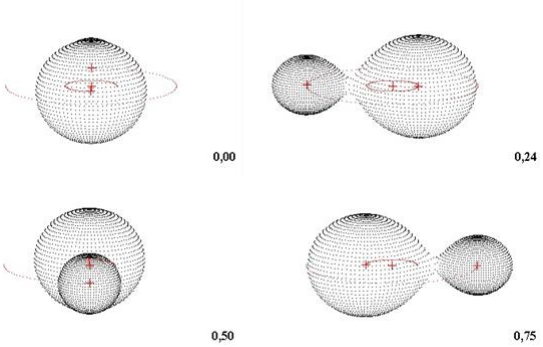


FIGURE 5. Surface geometry of the system at four different phases.

- Due to the absence of the spectroscopic observations of the contact binary, the absolute dimensions of both components of V1097 Her were estimated. The semi-major axis of the system was determined by using the a—$P_{orbital}$ relation given by Kaptan and Özkan (2019). The mass of the primary component was adopted as 0.394 $M_{\odot}$ using the MK spectral type calibration given by Drilling and Landolt (2000). Solar values of T_{eff}, M_{bol}, g were taken from Pecaut and Mamajek (2013). The resulting parameters are given in Table 5 ($\odot$: solar unit). The parallax provided by the GAIA Data Release 2 gives the distance of the eclipsing pair as ~250±1 pc. The distance of the contact binary V1097 Her found in this study (see Table 5.) is in agreement with the GAIA's one. For more precise determination of the absolute parameters and discussion of the evolutionary state of V1097 Her both spectroscopic observations and multi-band photometric data are needed.

TABLE 5. Estimated absolute parameters of V1097 Her.

Parameter	Value	Parameter	Value
a ($R_{\odot}$)	2.545 ± 0.260	L_2 ($L_{\odot}$)	1.516 ± 0.016
M_1 ($M_{\odot}$)	0.394 ± 0.001	$M_{bol,1}$	5.31 ± 0.15
M_2 ($M_{\odot}$)	1.306 ± 0.002	$M_{bol,2}$	4.29 ± 0.42
R_1 ($R_{\odot}$)	0.729 ± 0.074	M_v	3.94 ± 0.13
R_2 ($R_{\odot}$)	1.254 ± 0.128	d (pc)	244 ± 15
L_1 ($L_{\odot}$)	0.587 ± 0.006		

ACKNOWLEDGMENTS

The authors would like to thank Prof. S. Zola for making use of version 96 of the Wilson-Devinney code. This work has made use of the SIMBAD database, NASA's Astrophysics Data System Abstract Service and data from the first public release of the WASP data (Butters et al. 2010). Also, this work was supported by Çanakkale Onsekiz Mart University The Scientific Research Coordination Unit, Project number: FBA-2019-2930.

REFERENCES

1. D. I. Hoffman, T. E. Harrison, B. J. McNamara, AJ **138**, 466 – 477 (2009).
2. E. A. Avvakumova, O. Yu. Malkov, A.Yu. Kniazev, AN **334**, 860 (2013).
3. L. Binnendijk, VA **12**, 217 – 256 (1970).
4. J. M. Kreiner, Aca **54**, 207–210 (2004).
5. P. Zasche, A. Liakos, P. Niarchos, M. Wolf, V. Manimanis, K. Gazeas, NewA **14**, 121–128 (2009).
6. R. E. Wilson and E. J. Devinney, The Astronomical Journal, **166**, 605–619, (1971).
7. D. Terrell, J. Gross, W.R. Cooney, AJ **143**, 99 (2012).

ISBN:978-605-83516-6-0

8. J. S. Drilling and A. U. Landolt, Allens Astrophysical Quantities, 4th. Edition, AIP Press., Springer NY, (2000).
9. S. M. Rucinski, AcA **19**, 245 (1969).
10. L. B. Lucy, ApJ **151**,1123 (1968).
11. W. van Hamme, AJ **106**, 2096 – 2117 (1993).
12. D. H. Bradstreet and D. P. Steelman, AAS **201**, 7502 (2002).
13. S. Kaptan and T. Özkan, "Bazı W UMa Tipi Çift Yıldızların Fotometrik Analizi", MSc thesis, Istanbul University, 2019.
14. M. J. Pecaut and E. E. Mamajek, ApJS **208**, 9 (2013).
15. O. W. Butters, R. G. West, D. R. Anderson, A. Collier Cameron, W. I. Clarkson, B. Enoch, C. A. Haswell, C. Hellier, K. Horne, Y. Joshi, S. R. Kane, T. A. Lister, P. F. L. Maxted, N. Parley, D. Pollacco, B. Smalley, R. A. Street, I. Todd, P. J. Wheatley, D. M. Wilson, A&A **520**, 4 (2010).

BOOK OF FULL TEXT PROCEEDINGS TURKISH PHYSICAL
SOCIETY 35th INTERNATIONAL PHYSICS CONGRESS (TPS35)
TPS35, Vol.01, No.02, pp.134-138.
ISBN:978-605-83516-6-0

15 December 2019

Eclipse Timing Study of a Quadruple System: KIC 7177553

Çağlayan Nehir[1,2, a)] and İbrahim Bulut[1,3, b)]

[1]*Astrophysics Research Centre and Observatory, Canakkale Onsekiz Mart University, Terzioglu Campus, TR-17020, Canakkale, Turkey*
[2] *Department of Physics, Faculty of Arts and Sciences, Canakkale Onsekiz Mart University, Terzioglu Campus, TR-17020, Canakkale, Turkey*
[3] *Department of Space Sciences and Technologies, Faculty of Arts and Sciences, Canakkale Onsekiz Mart University, Terzioglu Campus, TR-17020 Canakkale, Turkey*

[a)]*Corresponding author:caglayannehir@gmail.com*
[b)]*ibulut@comu.edu.tr*

Abstract. Eclipse timing variation of KIC 7177553 quadruple binary system with approximately 18-day orbital period which observed by Kepler space telescope was analysed in this work. It is shown that this orbital variation of KIC 7177553 is due to light travel time and dynamical effect from gravitational influence of third body. Our results show that KIC 7177553 binary system has a giant planet with 4 M_j mass.

INTRODUCTION

KIC 7177553 is an eccentric detached-type (Slawson et al. 2011) eclipsing binary system with an approximately 18-day period which was observed by Kepler space telescope. It was mentioned in Lehmann et al. (2016) the light curve and spectroscopic analyses of the system that KIC 7177553 is a quadruple system and at least one of the components is an eclipsing binary. Moreover, the radial velocity analyses were also conducted for all four components in the said study. It was determined that KIC 7177553 has dynamical effect and the mass of third body is 2.5 M_j in a study by Borkovits et al. (2016) along with the light time effect (LTE) which was shown in the study published by Irwin (1952, 1959).

OBSERVATIONAL DATA AND METHOD

A Python based code was written to determine the eclipse times precisely with the Gauss-fitting method from Kepler long-cadence data. 74 primary minima times were calculated from all quarters. Nested-sampling algorithm 'MultiNest' (Feroz et al. 2009) and its Python based version 'PyMultiNest' (Buchner et al. 2014) were used for the eclipse timing variation (ETV) analysis. The results of this analysis were obtained using a Python based code which takes into account the dynamical effect shown by Borkovits et al. (2007, 2011, 2015) and LTE.

ETV ANALYSIS

The LTE and third body orbital parameters which arise from the existence of additional were explained by Irwin (1952, 1959). The components of the system may interact with each other. The change in orbital period which is caused by this interaction was named dynamical effect and was mathematically formalized by Borkovits et al (2007, 2011, 2015). In our study, the analyses were conducted taking LTE and the dynamical effect into account. The masses

Türk Fizik Derneği
1950
Turkish Physical Society

ISBN:978-605-83516-6-0

of the first and the second component were attained by Lehmann et al. (2016) and were taken as constants in this analysis. The results are shown here in Table 1 along with the results from Borkovits et al. (2016). The following linear light elements were used to determine the ETV of KIC 7177553.

$$\text{Min I= BJD } 2454954.545842 + 17^{d}.9464667 \times E \quad (1)$$

The Parameters derived from the ETV analysis of KIC 7177553 are given in Table 1. The ETV diagrams are plotted in Figures 1-3. The posterior distribution is shown in Figure 4.

TABLE 1. Parameters derived from the ETV analysis of KIC 7177553

		This Work	
Parameter	**Borkovits et al. (2015)**	**Posterior**	**Prior**
T_0 (BJD)		$54954.5468\ ^{+6.01e-5}_{-6.00e-5}$	$54954.544, 54954.547$
P_{bin} (day)	17.99628 ± 0.00006	$17.99645763\ ^{+3.58e-6}_{-3.64e-6}$	$17.996, 17.997$
Q (day)		$3.3310e-8\ ^{+4.56e-8}_{-4.52e-8}$	$(-1e-4), (1e-4)$
T_s (BJD)	55124 ± 6	$55234.1389\ ^{+4.2242}_{-4.1019}$	$55000, 55500$
P_3 (day)	529 ± 2	$527.4481\ ^{+3.6310}_{-4.0716}$	$300, 700$
e_3	0.46 ± 0.02	$0.3725\ ^{+0.0281}_{-0.0272}$	$0, 0.95$
ω_3 (deg)	201 ± 5	$135.5389\ ^{+4.2482}_{-4.4186}$	$100, 150$
a_3 ($R_\odot$)	339 ± 50	$348.3707\ ^{+26.7122}_{-26.7294}$	–
ETV_{jitter}		$0.00016\ ^{+1.74e-5}_{-1.54e-5}$	$5e-6, 5e-4$
cos i_3	0.1564	$0.0004\ ^{+0.2108}_{-0.2115}$	$-0.6, 0.6$
$\Delta\Omega$ (deg)	26 ± 3	$180.2270\ ^{+9.2431}_{-9.6251}$	$0, 360$
M_{12} ($M_\odot$)	1.9 ± 0.8	2.029*	–
M_3 (M_j)	2.5 ± 0.3	$4.0160\ ^{+0.3613}_{-0.3448}$	$1e-3, 0.1$

ISBN:978-605-83516-6-0

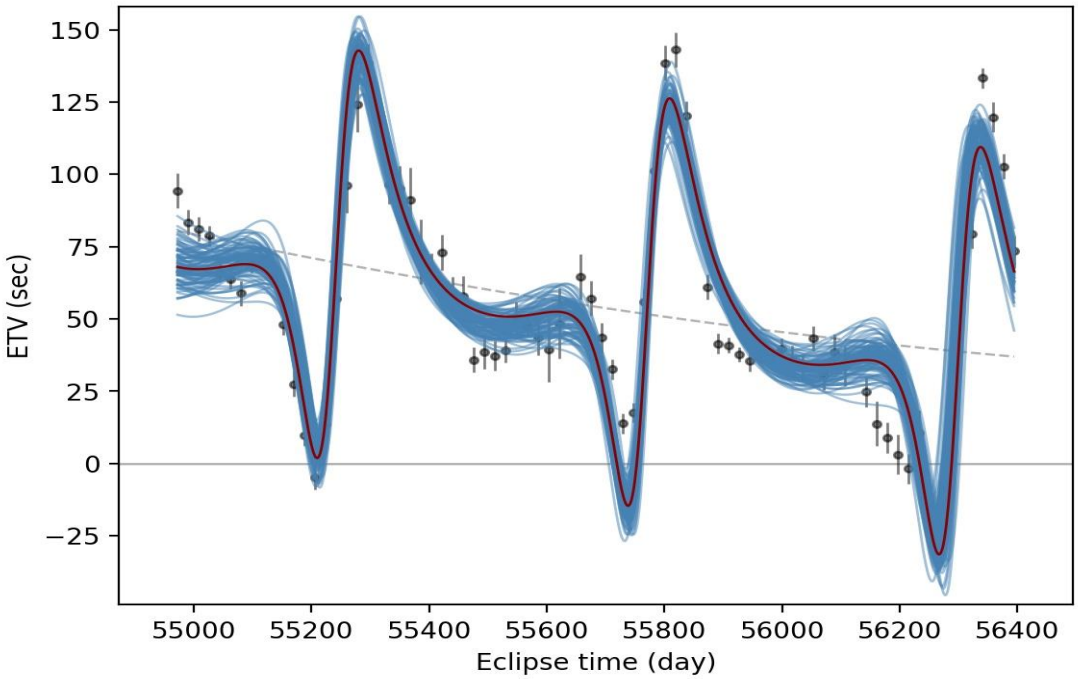


FIGURE 1. ETV diagram (LTE + dynamical effect and parabola) of KIC 7177553. Red line represents the best model and blue lines shows a random hundred solutions from the whole solution space. Dashed line depicts the parabola.

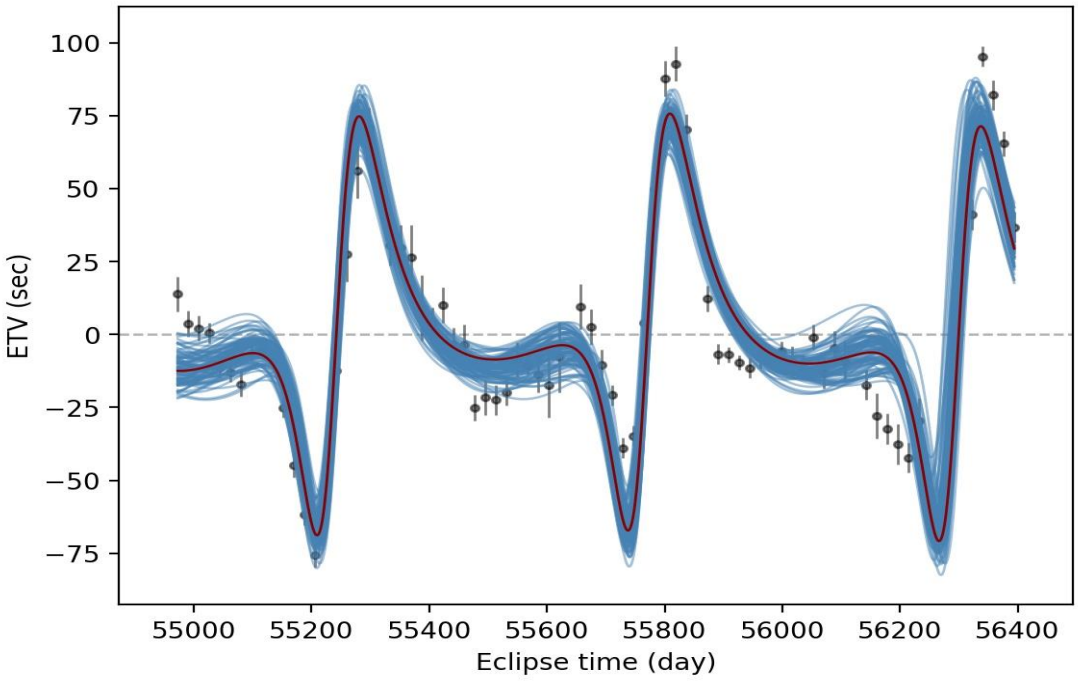


FIGURE 2. Diagram obtained after parabola was subtracted this is only contains LTE and dynamical effect.

ISBN:978-605-83516-6-0

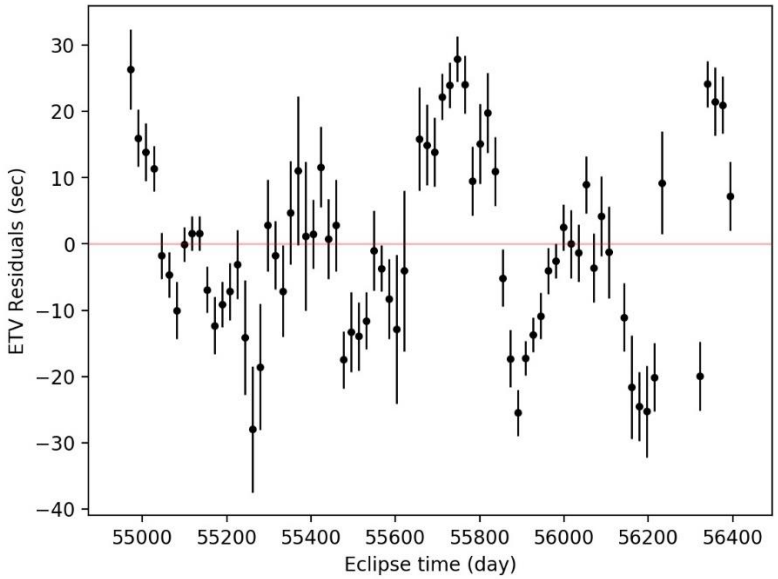


FIGURE 3. Residuals from all models.

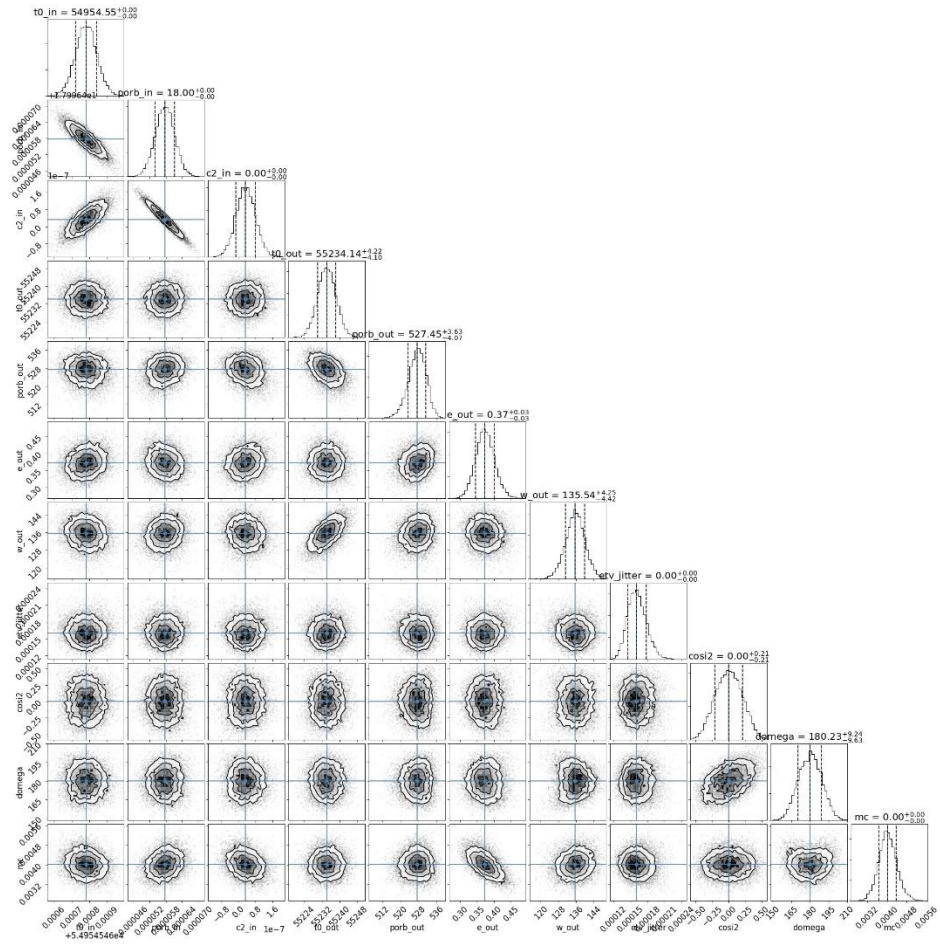


FIGURE 4. Posterior distribution from the LTE and dynamical effect analysis

ISBN:978-605-83516-6-0

RESULTS AND CONCLUSIONS

ETV analysis of KIC 7177553 binary system is given in this work. According to our ETV results, the system shows apparent changes periodically. This periodic change can be explained by the existence of third body. The orbital period and the mass of the third body are calculated to be as 527 days and 4 M_j respectively. It is inferred that this additional body can be a giant planet bounded to KIC 7177553 system gravitationally.

Acknowledgements: This work has been produced from the PhD thesis research of Çağlayan NEHİR.

REFERENCES

1. T. Borkovits, S. Csizmadia, E. Forgács-Dajka, and T. Hegedüs, Astron. Astrophys. (2011).
2. T. Borkovits, E. Forgács-Dajka, and Z. Regály, Astron. Astrophys. (2007).
3. T. Borkovits, T. Hajdu, J. Sztakovics, S. Rappaport, A. Levine, I.B. Bíró, and P. Klagyivik, Mon. Not. R. Astron. Soc. 455, 4136 (2016).
4. T. Borkovits, S. Rappaport, T. Hajdu, and J. Sztakovics, Mon. Not. R. Astron. Soc. (2015).
5. J. Buchner, A. Georgakakis, K. Nandra, L. Hsu, C. Rangel, M. Brightman, A. Merloni, M. Salvato, J. Donley, and D. Kocevski, Astron. Astrophys. 564, A125 (2014).
6. F. Feroz, M.P. Hobson, and M. Bridges, Mon. Not. R. Astron. Soc. 398, 1601 (2009).
7. H. Lehmann, T. Borkovits, S.A. Rappaport, H. Ngo, D. Mawet, S. Csizmadia, and E. Forgács-Dajka, Astrophys. J. 819, 33 (2016).
8. J.B. Irwin, Astrophys. J. 116, 211 (1952).
9. J.B. Irwin, Astron. J. 64, 149 (1959).
10. R.W. Slawson, A. Prša, W.F. Welsh, J.A. Orosz, M. Rucker, N. Batalha, L.R. Doyle, S.G. Engle, K. Conroy, J. Coughlin, T.A. Gregg, T. Fetherolf, D.R. Short, G. Windmiller, D.C. Fabrycky, S.B. Howell, J.M. Jenkins, K. Uddin, F. Mullally, S.E. Seader, S.E. Thompson, D.T. Sanderfer, W. Borucki, and D. Koch, Astron. J. 142, 160 (2011).

BOOK OF FULL TEXT PROCEEDINGS TURKISH PHYSICAL
SOCIETY 35th INTERNATIONAL PHYSICS CONGRESS (TPS35)
TPS35, Vol.01, No.02, pp.139-144.
ISBN:978-605-83516-6-0

15 December 2019

A Study for KIC 5621294 and Its Component

Çağlayan Nehir[1,2, a)] and İbrahim Bulut[1,3, b)]

[1]*Astrophysics Research Centre and Observatory, Canakkale Onsekiz Mart University, Terzioglu Campus, TR-17020, Canakkale, Turkey*
[2] *Department of Physics, Faculty of Arts and Sciences, Canakkale Onsekiz Mart University, Terzioglu Campus, TR-17020, Canakkale, Turkey*
[3] *Department of Space Sciences and Technologies, Faculty of Arts and Sciences, Canakkale Onsekiz Mart University, Terzioglu Campus, TR-17020 Canakkale, Turkey*

[a)]*Corresponding author:caglayannehir@gmail.com*
[b)]*ibulut@comu.edu.tr*

Abstract. In this paper, we present the photometric and the eclipse timing variation analyses of KIC 5621294 that was observed by the Kepler space telescope. We used Wilson and Devinney code's 2015 version (Wilson & Devinney 1971) for the light curve and radial velocity curve analyses simultaneously. A custom code written in Python to determine minima times from Kepler long-cadence data and nested-sampling algorithm 'MultiNest' (Feroz et al. 2009) and its Python based version 'PyMultiNest' (Buchner et al. 2014) were used for the eclipse timing variation analysis.

INTRODUCTION

KIC 5621294 is an algol-type eclipsing binary system that was observed by the Kepler satellite with approximately 0.93-day period (Prsa et al. 2011, Slawson et al. 2011, Kirk et al. 2016). In Kepler team's work, possible third body effect that bounded the system gravitationally was dwelled on (Gies et al. 2012, 2015, Conroy et al. 2014). The light curve and the orbital period variations of the system were analysed by Lee et al. (2015) and the mass of the third body was given as 44 M_j. By Zasche et al. (2015) and Borkovits et al (2016), the mass of the said third body was found to be as 39 Mj and 21 M_j respectively.

The temperature of the first component of the system is given as T_1=10828K by Armstrong et al. (2013) that estimates the temperatures of the components for Kepler eclipsing binary stars. The spectroscopic observations of the system were obtained by Matson et al. (2017) and mass ratio of the system was given as q=0.24.

OBSERVATIONAL DATA AND METHOD

Kepler long-cadence data series of KIC 5621294 are taken from Kepler Eclipsing Binary Catalog (Kirk et al. 2016) which is available on the Villanova's site (http://keplerebs.villanova.edu/). This approximately 4 years long light curve data is folded, binned and averaged for light curve analysis. The radial velocities of the components of the system were obtained by Matson et al. (2017) and used for the light curve analysis simultaneously.

The minima times were calculated using the 4-year data which was later used for the analyses of the eclipse timing variation (ETV). For this purpose, a python code has been written which uses Gauss fitting method to determine the eclipse times.1261 primary eclipse times were calculated to be used in the ETV analysis.

ISBN:978-605-83516-6-0

LIGHT CURVE ANALYSIS

The 2015 version of the Wilson and Devinney code (1971) has been used the analyses of the light curve and radial velocities simultaneously. The mod 5 which is very suitable for Algol-type binary systems was selected for these analyses. The Heliocentric Julian Dates (HJD) of radial velocities of components are converted into Barycentric Julian Dates (BJD) using the code published by Eastman et al. (2010). The constant parameters used in the analyses are as follows: systemic velocity V_{gam}=19km/s and mass ratio q=0.24 (Matson et al. 2017), the temperature of the first component T_1=10828K (Armstrong et al. 2013), the bolometric albedos A_1=1.0, A_2=0.5 (Rucinski, 1969), the gravity darkenings g_1=1.0, g_2=0.32 (Lucy, 1967) and the eccentricity e=0 for a circular orbit. Cool spot modelling has been applied on the second component during the light curve analysis. The spot parameters along with other parameters are given in Table 1. The light curve solution for KIC 5621294 can be shown in Figure 1. The orbital solution is presented in Figure 2.

TABLE 1. Parameters derived from light curve analysis of KIC 5621294

Parameters	**Value**
T_0 (BJD)	2454954.510518
P (day)	0.9389049
a ($R_\odot$)	5.895 ± 0.059
Pshift	0.0029 ± 0.0001
V_{gam} (km/s)	19
i (º)	76.619 ± 0.018
T_1 (K)	10828
T_2 (K)	5055 ± 214
Ω_1	3.0355 ± 0.0037
Ω_2	2.3295
q	0.24
A_1 - A_2	1.00 – 0.50
g_1 - g_2	1.00 – 0.32
$L_1/(L_1+L_2)$	0.9653 ± 0.0012
$L_2/(L_1+L_2)$	0.0347
ℓ_3	-
r_1 (pole)	0.3559 ± 0.0005
r_1 (point)	0.3770 ± 0.0006
r_1 (side)	0.3667 ± 0.0005
r_1 (back)	0.3724 ± 0.0006
r_2 (pole)	0.2453 ± 0.0005
r_2 (point)	0.3581 ± 0.0006
r_2 (side)	0.2553 ± 0.0005
r_2 (back)	0.2878 ± 0.0006
Spot	
Colatitude (deg)	74.5 ± 2.4
Longitude (deg)	341.2 ± 1.7
Radius (deg)	23.1 ± 0.5
T_{spot}/T_{local}	0.90 ± 0.01

ISBN:978-605-83516-6-0

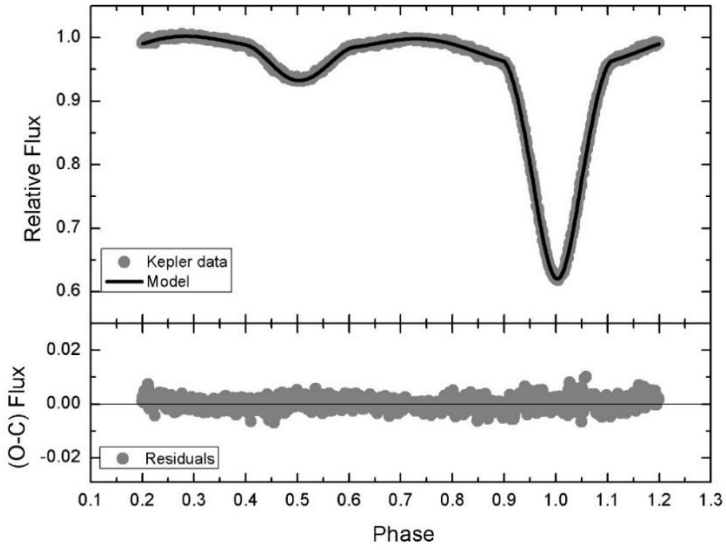


FIGURE 1. Kepler light curve of KIC 5621294 and model (solid line). Bottom panel shows residuals from the model.

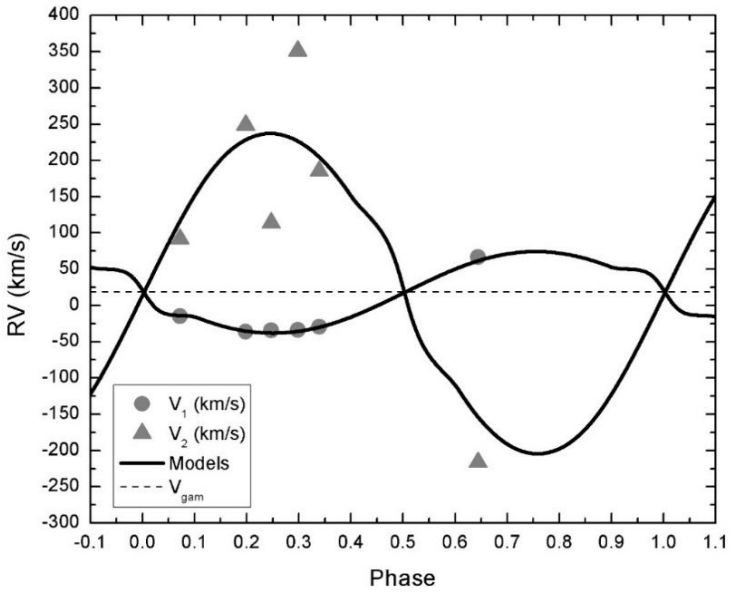


FIGURE 2. Radial velocitie curves of KIC 5621294. Solid lines represent results from analysis. Dashed line shows systemic velocity (V_{gam} =19km/s).

ETV ANALYSIS

The light time effect which originate from the existence of additional body and its orbital parameters are published by Irwin (1952, 1959). To determine these orbital parameters a python code has been written which uses nested-sampling algorithm 'MultiNest' (Feroz et al. 2009) and its Python based version 'PyMultiNest' (Buchner et al. 2014). The following linear light elements were used to determine ETV of KIC 5621264.

$$\text{Min I= BJD } 2454954.510518 + 0^{d}.9389049 \text{ x E} \quad (1)$$

The Parameters derived from the ETV analysis of KIC 5621294 are listed in Table 2. The ETV diagrams are shown in Figures 3-4.

ISBN:978-605-83516-6-0

TABLE 2. Parameters derived from ETV analysis of KIC 5621294

			This work	
Parameters	**Borkovits et al. (2016)**	**Lee et al. (2015)**	**Posterior**	**Prior**
T_0 (BJD)		55672.77655 (5)	$54954.5120\ ^{+1.47e-5}_{-1.51e-5}$	55954.509, 55954.514
P_{bin} (day)	0.93890979 (5)	0.93890525 (2)	$0.93891027\ ^{+3.71e-8}_{-3.91e-8}$	0.937, 0.940
Q (day)		$-8.0\ (1)e-9$	$-3.3492e-9\ ^{+2.02e-11}_{-1.97e-11}$	(-1e-4), (1e-4)
T_s (BJD)	55143 (22)	57355 (40)	$55159.2617\ ^{+5.6952}_{-5.4913}$	54500, 55500
P_3 (day)	1083 (15)	970 (11)	$1028.3207\ ^{+5.6085}_{-5.8379}$	500, 1500
e_3	0.43 (5)	0.47 (6)	$0.6572\ ^{+0.0330}_{-0.0326}$	0, 0.95
ω_3 (deg)	323 (7)	303 (10)	$148.8403\ ^{+2.7835}_{-2.7962}$	-180, 180
a_3 ($R_\odot$)		547 (4)	$598.7825\ ^{+38.8459}_{-39.2191}$	-
ETV_{jitter}			$8.1296e-5\ ^{+2.02e-6}_{-1.98e-6}$	(1e-8), (1e-6)
M_3 (M_j)	21	46.9	$44.9156\ ^{+1.5046}_{-1.3425}$	(1e-6), 0.1

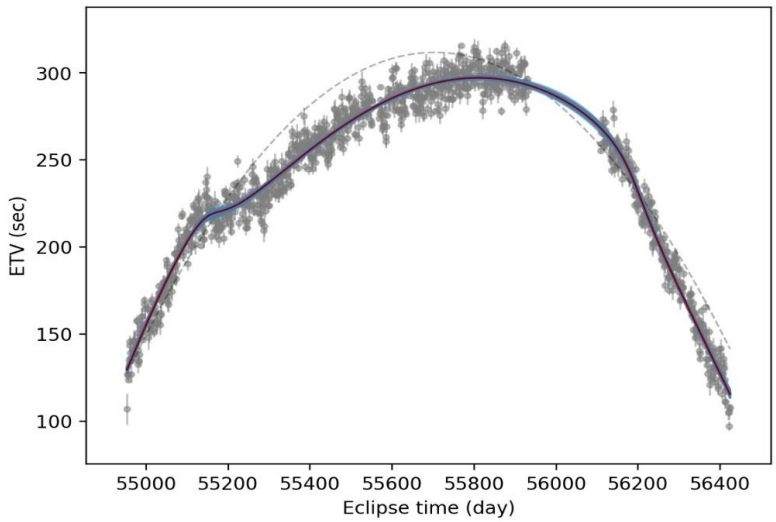


FIGURE 3. ETV diagram (LTE and parabola) for KIC 5621294. Red line represents the best model and blue lines shows random hundred solutions from the whole solution space. Dashed line shows the parabola.

ISBN:978-605-83516-6-0

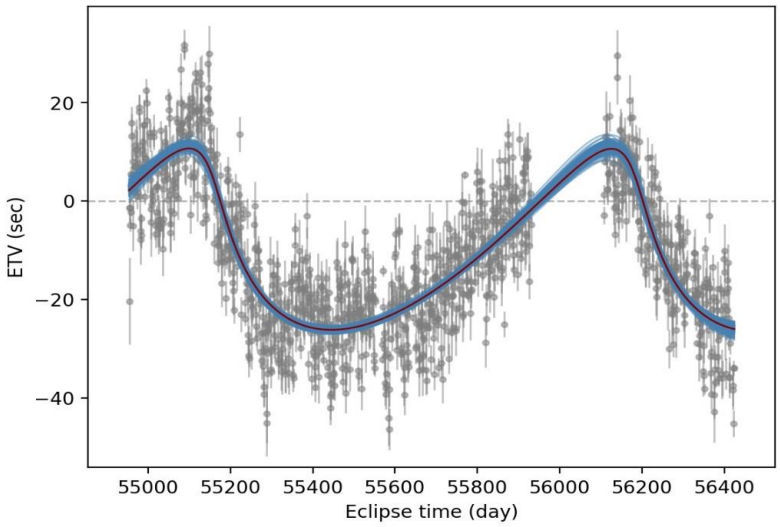


FIGURE 4. The residuals from the parabola in ETV diagram of KIC 5621294.

RESULTS AND CONCLUSIONS

The light curve and ETV analyses of KIC 5621294 binary system are presented in this study. According to our ETV results, the system shows apparent changes periodically. This periodic variation can be explained by the existence of a third body which is bounded to the system gravitationally. The third body orbital parameters are given in Table 2 along with their respective published results. The period and the mass of the third body are calculated as approximately 1028 days and 45 Mj, respectively. The absolute parameters calculated using the results of the light curve analysis are given in Table 3.

TABLE 3. Absolute parameters of KIC 5621294

Absolute Parameters	
M_1 ($M_\odot$)	2.20*
M_2 ($M_\odot$)	0.53 ± 0.11
R_1 ($R_\odot$)	2.07 ± 0.14
R_2 ($R_\odot$)	1.60 ± 0.11
$logg_1$ (cm/s^2)	4.15 ± 0.04
$logg_2$ (cm/s^2)	3.75 ± 0.02
L_1 ($L_\odot$)	53.03 ± 1.17
L_2 ($L_\odot$)	1.50 ± 0.75
M_{bol1} (mag)	0.44 ± 0.16
M_{bol2} (mag)	4.31 ± 0.24
d (pc)	2518 ± 250

Acknowledgements: This work has been produced from the PhD thesis research of Çağlayan NEHİR.

ISBN:978-605-83516-6-0

REFERENCES

1. D.J. Armstrong, Y. Gómez Maqueo Chew, F. Faedi, and D. Pollacco, Mon. Not. R. Astron. Soc. 437, 3473 (2013).
2. T. Borkovits, T. Hajdu, J. Sztakovics, S. Rappaport, A. Levine, I.B. Bíró, and P. Klagyivik, Mon. Not. R. Astron. Soc. 455, 4136 (2016).
3. J. Buchner, A. Georgakakis, K. Nandra, L. Hsu, C. Rangel, M. Brightman, A. Merloni, M. Salvato, J. Donley, and D. Kocevski, Astron. Astrophys. 564, A125 (2014).
4. K.E. Conroy, A. Prša, K.G. Stassun, J.A. Orosz, D.C. Fabrycky, and W.F. Welsh, Astron. J. 147, 45 (2014).
5. J. Eastman, R. Siverd, and B.S. Gaudi, Publ. Astron. Soc. Pacific 122, 935 (2010).
6. F. Feroz, M.P. Hobson, and M. Bridges, Mon. Not. R. Astron. Soc. 398, 1601 (2009).
7. D.R. Gies, R.A. Matson, Z. Guo, K. V. Lester, J.A. Orosz, and G.J. Peters, Astron. J. 150, 178 (2015).
8. D.R. Gies, S.J. Williams, R.A. Matson, Z. Guo, S.M. Thomas, J.A. Orosz, and G.J. Peters, Astron. J. 143, 137 (2012).
9. J.B. Irwin, Astrophys. J. 116, 211 (1952).
10. J.B. Irwin, Astron. J. 64, 149 (1959).
11. B. Kirk, K. Conroy, A. Prša, M. Abdul-Masih, A. Kochoska, G. Matijevič, K. Hambleton, T. Barclay, S. Bloemen, T. Boyajian, L.R. Doyle, B.J. Fulton, A.J. Hoekstra, K. Jek, S.R. Kane, V. Kostov, D. Latham, T. Mazeh, J.A. Orosz, J. Pepper, B. Quarles, D. Ragozzine, A. Shporer, J. Southworth, K. Stassun, S.E. Thompson, W.F. Welsh, E. Agol, A. Derekas, J. Devor, D. Fischer, G. Green, J. Gropp, T. Jacobs, C. Johnston, D.M. LaCourse, K. Saetre, H. Schwengeler, J. Toczyski, G. Werner, M. Garrett, J. Gore, A.O. Martinez, I. Spitzer, J. Stevick, P.C. Thomadis, E.H. Vrijmoet, M. Yenawine, N. Batalha, and W. Borucki, Astron. J. 151, 68 (2016).
12. J.W. Lee, K. Hong, and T.C. Hinse, Astron. J. 149, 93 (2015).
13. L. B. Lucy, ZA 65, 89-92 (1967).
14. R.A. Matson, D.R. Gies, Z. Guo, and S.J. Williams, Astron. J. 154, 216 (2017).
15. A. Prša, N. Batalha, R.W. Slawson, L.R. Doyle, W.F. Welsh, J.A. Orosz, S. Seager, M. Rucker, K. Mjaseth, S.G. Engle, K. Conroy, J. Jenkins, D. Caldwell, D. Koch, and W. Borucki, Astron. J. 141, 83 (2011).
16. S. M. Rucinski, AcA 19, 245-255 (1969).
17. R.W. Slawson, A. Prša, W.F. Welsh, J.A. Orosz, M. Rucker, N. Batalha, L.R. Doyle, S.G. Engle, K. Conroy, J. Coughlin, T.A. Gregg, T. Fetherolf, D.R. Short, G. Windmiller, D.C. Fabrycky, S.B. Howell, J.M. Jenkins, K. Uddin, F. Mullally, S.E. Seader, S.E. Thompson, D.T. Sanderfer, W. Borucki, and D. Koch, Astron. J. 142, 160 (2011).
18. R.E. Wilson and E.J. Devinney, Astrophys. J. 166, 605 (1971).
19. P. Zasche, M. Wolf, H. Kučáková, J. Vraštil, J. Juryšek, M. Mašek, and M. Jelínek, Astron. J. 149, 197 (2015).

BOOK OF FULL TEXT PROCEEDINGS TURKISH PHYSICAL
SOCIETY 35th INTERNATIONAL PHYSICS CONGRESS (TPS35)
TPS35, Vol.01, No.02, pp.145-151.
ISBN:978-605-83516-6-0

15 December 2019

Light Curve and Period Analysis of The Beta Lyrae Type System V359 Cas

Burcu Özkardeş[1, 2, a)]

[1]*Department of Space Sciences and Technologies, Faculty of Art and Science, Çanakkale Onsekiz Mart University, Çanakkale, TURKEY.*
[2]*Çanakkale Onsekiz Mart University Astrophysics Research Center and Ulupınar Observatory, Çanakkale, TURKEY.*

[a)]Corresponding author: burcu@comu.edu.tr

Abstract. In the present work, it has been focused on the analysis of the light curve and period behaviour of the β Lyr type eclipsing binary V359 Cas. Literature light curve (SWASP) of the eclipsing binary was modelled by applying the Wilson-Devinney method. The absolute parameters of the components, namely masses and radii, were estimated, and the distance to V359 Cas is calculated. Using all available minima found in the literature the orbital period change of V359 Cas was examined.

INTRODUCTION

The eclipsing binary V359 Cas is one of the less studied systems in the literature. The variability of V359 Cas was first described by Hoffmeister (1949). Kinnunen and Skiff (2000) listed accurate positions and identifications for 274 variable stars including V359 Cas. Malkov et al. (2006) presented the catalogue of 6330 eclipsing binary stars categorized from observations and gave the light curve type, period and spectral type of V359 Cas as EB, 1.3039 days and A0, respectively. Avvakumova et al. (2013) represented a new version catalogue for 7200 eclipsing binaries, which contains parameters and morphological type of light curves for the catalogued stars. The authors determined the evolutionary class of the system to be a classical algol. The eclipsing timings of V359 Cas were obtained by many authors: Agerer and Huebscher (1997), Agerer and Huebscher (2001, 2003), Diethelm (2005), Huebscher et al. (2005, 2006), Huebscher (2007, 2011), Brat et al. (2007), Huebscher et al. (2010) and Huebscher et al. (2012). Basic properties of V359 Cas are given in Table 1.

TABLE 1. Basic properties of V359 Cas.

Star Name	Eclipsing Binary Type	Coordinates	B (mag)	V (mag)	Parallax (mas)	Reference
V359 Cas	Beta Lyrae	α: $23^h34'27''$ δ: $+56^\circ19'17''$	12.44±0.18	12.47±0.21	0.5204±0.0300	Simbad Database[1]

PERIOD ANALYSIS

For studying the orbital period change of V359 Cas, all public light minimum times of the system were collected from the *O-C* Gateway archive[2]. In the present study, 3 primary minimum (Min I) and 1 secondary minimum (Min

[1] https://simbad.u-strasbg.fr/simbad

Türk Fizik Derneği
1950
Turkish Physical Society

ISBN:978-605-83516-6-0

II) were obtained from the SuperWASP light curve of V359 Cas. These eclipse timings and their informations are tabulated in Table 2. Abbreviations used in this table are defined as follows: HJD: Heliocentric Julian Day – p/s: primary/secondary – pg/vis/CCD: photographic/visual/Charge Couple Device.

TABLE 2. Minima timings and their informations of V359 Cas.

HJD (2400000+)	Min. Type (p/s)	Method (pg/vis/CCD)	Reference	HJD (2400000+)	Min. Type (p/s)	Method (pg/vis/CCD)	Reference
27955.5060	p	pg	OC	51766.4568	s	CCD	OC
29079.4630	p	pg	OC	52122.4144	s	CCD	OC
29109.4940	p	pg	OC	52146.5333	p	CCD	OC
29130.4120	p	pg	OC	52146.5351	p	CCD	OC
29160.3530	p	pg	OC	52180.4351	p	CCD	OC
30173.4950	p	pg	OC	52180.4361	p	CCD	OC
30259.5100	p	pg	OC	53283.5076	p	CCD	OC
30576.4090	p	pg	OC	53349.3561	s	CCD	OC
31001.4390	p	pg	OC	53656.4147	p	CCD	OC
31267.4630	p	pg	OC	54017.5906	p	CCD	OC
31344.3880	p	pg	OC	54360.5050	p	CCD	This study
31353.4130	p	pg	OC	54362.4810	s	CCD	This study
31413.4280	p	pg	OC	54373.5310	p	CCD	This study
31645.4550	p	pg	OC	54394.4000	p	CCD	This study
33914.3130	p	pg	OC	55072.4352	p	CCD	OC
33923.3730	p	pg	OC	55074.3880	s	CCD	OC
33928.5840	p	pg	OC	55076.3472	p	CCD	OC
47139.6050	p	vis	OC	55098.5146	p	CCD	OC
48503.5010	p	vis	OC	55409.4955	s	CCD	OC
48539.3870	s	vis	OC	55495.5532	s	CCD	OC
49615.7120	p	CCD	OC	55502.7235	p	CCD	OC
49627.4502	p	CCD	OC	55838.4792	s	CCD	OC
49644.3991	p	CCD	OC	55849.5615	p	CCD	OC
50344.5852	p	CCD	OC	55874.3362	p	CCD	OC
50636.5960	p	vis	OC	55874.3363	p	CCD	OC
50717.4750	p	vis	OC	56132.5120	p	CCD	OC
51323.7860	p	CCD	OC	57646.3473	p	CCD	OC

To examine the period variation of V359 Cas, a well-known *O-C* method was applied to all eclipse timings listed in Table 2. The *O-C* values were computed by the Equation 1., which is covered the linear ephemeris provided by Kreiner (2004):

$$Min.I = 2429079.4990 + 1^{d}.30388506xE \quad (1)$$

The distribution of *O-C* values is shown in Figure 1. As seen in this figure, the distribution before 10000 cycles is highly scattered. For this reason, these data were excluded in the analysis. Other light minimum times not considered are 2450636.5960, 2454373.5307 and 2454362.4809. Because of a sinusoidal variation it was considered only light time effect, and the LITE code developed by Zasche et al. (2009) was applied to the *O-C* data for 10600-22000 epoches interval. The *O-C* diagram of V359 Cas and the residuals from the final model are shown in Figure 2. The resulting parameters are given in Table 4.

[2] http://var2.astro.cz/ocgate/index.php?lang=en

ISBN:978-605-83516-6-0

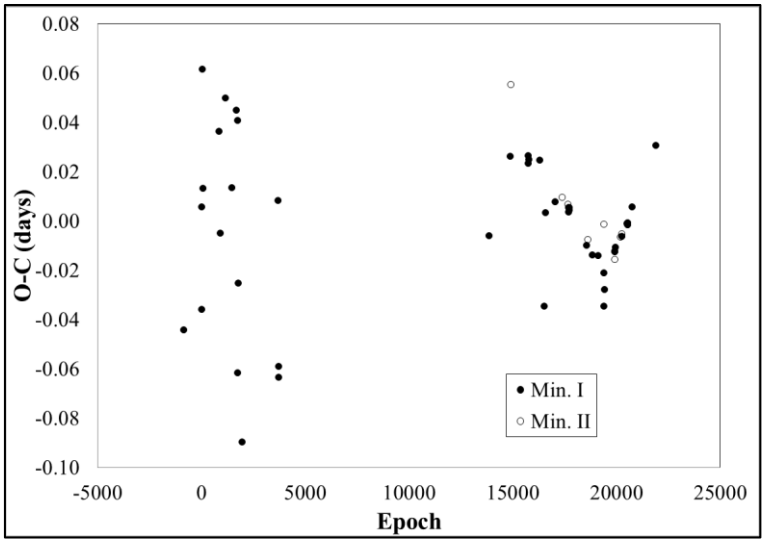


FIGURE 1. *O-C* values' distribution of V359 Cas.

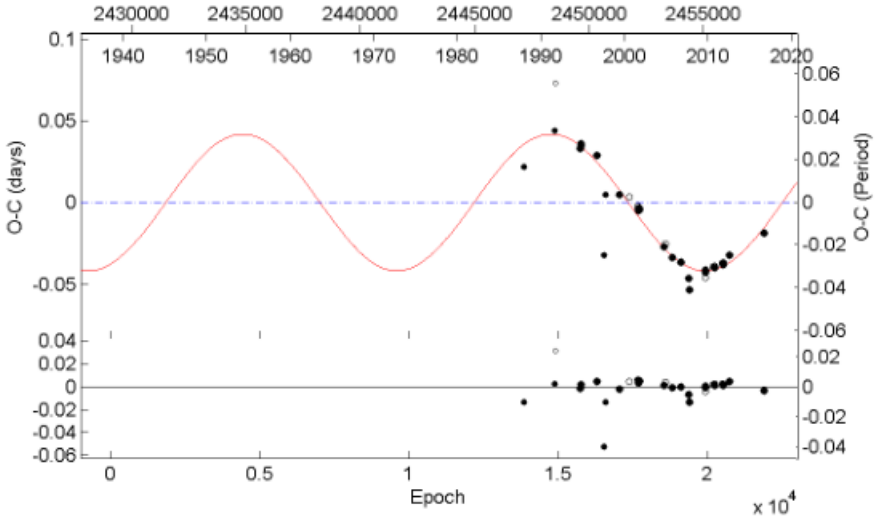


FIGURE 2. *O-C* diagram of V359 Cas. Top: *O-C* data's distribution and sinusoidal representation (solid line with red colored); bottom: residuals from the best fit.

LIGHT CURVE ANALYSIS

The SuperWASP (Wide Angle Search for Planets) light curve, which is available online at https://wasp.cerit-sc.cz/form, of V359 Cas was solved by using the Wilson–Devinney method (Wilson and Devinney, 1971). To get the physical parameters of the system, the Monte Carlo (MC) search algorithm (Kreiner et al., 2003, Baran et al., 2004) was used instead of the Differantial Correction (DC) code.

In the MC procedure, the best solution is searched within chosen ranges for the free parameters. The adjusted parameters and their search intervals are given in Figure 3.

ISBN:978-605-83516-6-0

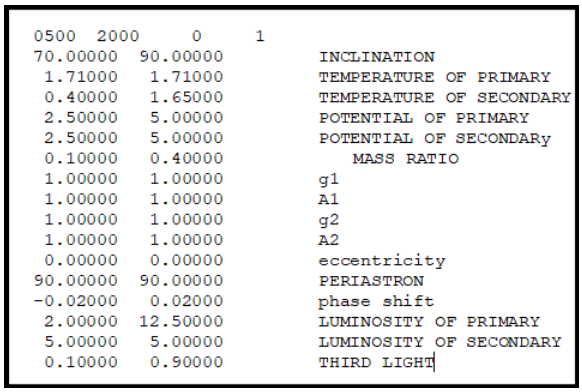


FIGURE 3. Search intervals of the parameters used in the MC algorithm.

The primary component's effective temperature was determined to be 17100 K corresponding to the intrinsic colour indice $(B\text{-}V)_0$=-0.19, from absolute calibrations for detached binaries given by Bilir et al. (2008), of the system using the MK spectral type calibration table published by Drilling and Landolt (2000). Gravity darkening coefficients and albedos were set to be $g_{1,2}$=1.0 and $A_{1,2}$=1.0 according to the theory given by Rucinski (1969) and Lucy (1967), respectively, for stars with radiative envelopes. The square-root limb darkening law was used, and the coefficients were gotten from Claret and Bloemen (2011) and Claret et al. (2013). It was accepted both the components of V359 Cas rotate synchronously and the system move in a circular orbit. The MC search results are given in Table 3, where the errors given in parenthesis correspond to the 90% confidence level in MC computations. In Figure 4., the observational data are compared with the best fit achieved for the system.

TABLE 3. Final solution of the SWASP light curve of V359 Cas.

Parameter	Value
i (°)	87.6(±0.5)
Phase shift	0.0063(±0.0002)
T_1 (Kelvin)	17100
T_2 (Kelvin)	8194(±35)
Q	0.334(±0.010)
Ω_1	3.2300(±0.0189)
Ω_2	2.5392(±0.0207)
r_{1mean}	0.351(±0.005)
r_{2mean}	0.288(±0.009)
l_1/l_{total}	0.32(± 0.02)
l_3/l_{total}	0.62(±0.02)
$\Sigma W(O\text{-}C)^2$	0.2514

ISBN:978-605-83516-6-0

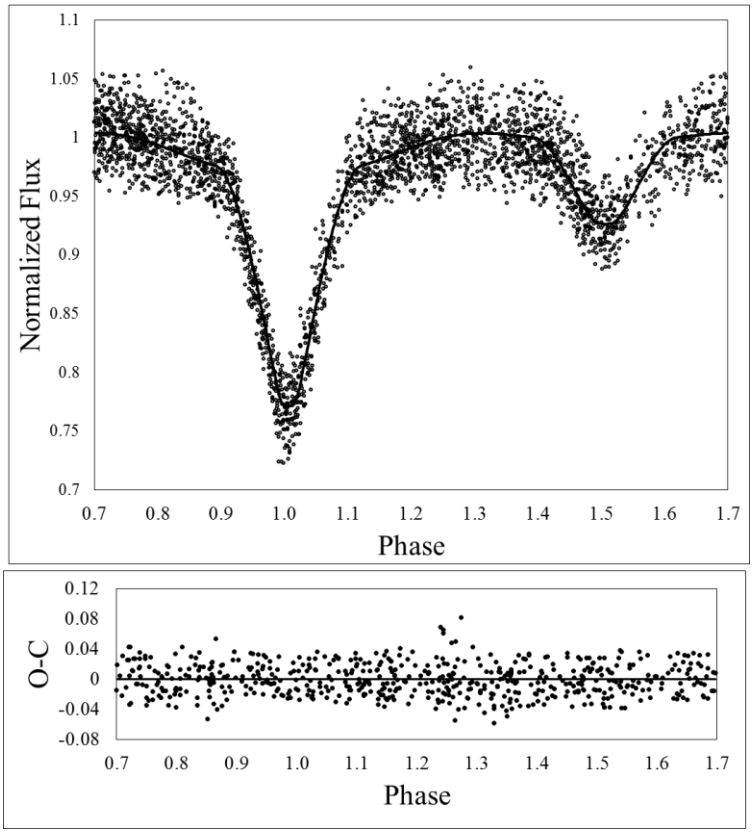


FIGURE 4. Comparison of the observed and theoretical light curve of V359 Cas (upper panel) and residuals (lower panel).

CONCLUSIONS

In this work, preliminary results obtained from the analysis of the SuperWASP light curve and period variation of V359 Cas are as follows:

- With respect to the period analysis, the cyclic variation in the system's orbital period can be interpreted as the third component which is gravitationally bounded to V359 Cas. The results from the analysis are given in Table 4.

TABLE 4. Parameters obtained from the period analysis of V359 Cas.

Parameter	Value
T_0 (HJD)	2429079.3384(±0.0558)
$P_{orbital}$ (days)	1.30389464(±0.00000347)
P_3 (year)	37(±9)
T_3 (HJD)	2421396(±416)
A (days)	0.042(±0.022)
e	0*
w (deg)	90*
$f(m_3)$	0.28(±0.06)
m_3 ($M_\odot$) (i=90°)	3.67(±0.55)
$\Sigma W(O-C)^2$	0.0256

*assumed.

ISBN:978-605-83516-6-0

- To the photometric solution, the system is a semi-detached eclipsing binary, and the filling rates of the Roche lobes of the components are 79% and 100%, respectively. Accordingly, it can be said that the system is a new classical-Algol type binary.
- The absolute dimensions of both components of V359 Cas were estimated because there are no spectroscopic observations of the binary in the literature so far. Firstly, the mass of the primary component was adopted as 6.75 $M_\odot$ using the MK spectral type calibration given by Drilling and Landolt (2000). In order to compute the remaining parameters, it was used the photometric mass ratio, the Kepler's third law and the Stefan-Boltzman law. Solar values ($T_{\rm eff}$ = 5771±0.7 K, $M_{\rm bol}$ = 4.755±0.000 mag and g = 27423.2±7.9 cm/s^2) of Pecaut and Mamajek (2013) were considered in the computations. To estimate the uncertainties in the absolute parameters it was assumed a ten-percent error in the mass of the primary one. The resulting parameters are given in Table 5., where the symbol ⊙ in the second column indicates the solar unit, and the values in parenthesis show the errors in the last digits. According to the parallax provided by the GAIA Data Release 2, the distance of V359 Cas is about 2000±200 pc. The distance of the eclipsing binary V359 Cas obtained from this study (see Table 5.) was found to be slightly different from the GAIA's one. For more precise determination of the distance and the absolute parameters both spectroscopic observations and multi-band photometric data are needed.

TABLE 5. Estimated absolute parameters of V359 Cas.

Parameter	Unit	Value	
		Primary	**Secondary**
Separation	$R_\odot$	10.44(±0.06)	
Mass	$M_\odot$	6.75(±0.68)	2.25(±0.47)
Radius	$R_\odot$	3.60(±0.06)	3.01(±0.08)
Luminosity	$L_\odot$	1032(±106)	37(±10)
log g	cm/s^2	4.14(±0.14)	3.83(±0.14)
Distance	pc	4389(±100)	

ACKNOWLEDGMENTS

I would like to thank Prof. S. Zola for allowing the use of Tel50 Computer to run the Wilson-Devinney FORTRAN code. This work has made use of the SIMBAD database, NASA's Astrophysics Data System Abstract Service and data from the first public release of the WASP data (Butters et al. 2010). Also, this work was supported by Çanakkale Onsekiz Mart University The Scientific Research Coordination Unit, Project number: FHD-2019-2853.

REFERENCES

1. C. Hoffmeister, Astron. Abh. Erganzungshefte z.d. Astron. Nach., **12**, No. 1, A3 (1949).
2. T. Kinnunen and B. A. Skiff, IBVS **4906**, 1–8 (2000).
3. O. Yu. Malkov, E. Oblak, E. A. Snegireva and J. Torra, A&A **446**, 785–789 (2006).
4. E. A. Avvakumova, O. Yu. Malkov and A. Yu. Kniazev, AN **334**, 860 (2013).
5. F. Agerer and J. Huebscher, IBVS **4472**, 1–4 (1997).
6. F. Agerer and J. Huebscher, IBVS **5016**, 1–4 (2001).
7. R. Diethelm, IBVS **5653**, 1–5 (2005).
8. J. Huebscher, P. Anton and F. Walter, IBVS **5657**, 1–24 (2005).
9. J. Huebscher, P. Anton and F. Walter, IBVS **5731**, 1–31 (2006).
10. J. Huebscher and F. Walter, IBVS **5761**, 1–12 (2007).
11. L. Brat, M. Zejda and P. Svoboda, OEJV **74**, 1–75 (2007).
12. J. Huebscher, P. B. Lehmann, G. Monninger, IBVS **5941**, 1–16 (2010).
13. J. Huebscher, IBVS **5984**, 1–16 (2011).
14. J. Huebscher, IBVS **6010**, 1–22 (2012).
15. J. M. Kreiner, Aca **54**, 207–210 (2004).
16. P Zasche, A. Liakos, P. Niarchos, M. Wolf, V. Manimanis, K. Gazeas, NewA **14**, 121–128 (2009).

17. J. M. Kreiner, S. M. Rucinski, S. Zola, P. Niarchos, W. Ogloza et al., A&A **412**, 465–471 (2003).
18. A. Baran, S. Zola, S. M. Rucinski, J. M. Kreiner, M. Siwak, M. Drozdz, AcA **54**, 195–206 (2004).
19. R. E. Wilson and E. J. Devinney, The Astronomical Journal, **166**, 605–619, (1971).
20. S. Bilir, T. Ak, E. Soydugan, F. Soydugan, E. Yaz, F. N. Ak, Z. Eker, O. Demircan and M. Helvacı, AN **329**, 835 (2008).
21. J. S. Drilling and A. U. Landolt, Allens Astrophysical Quantities, 4th. Edition, AIP Press., Springer NY, (2000).
22. L. B. Lucy, ZA **65**,89 (1967).
23. S. M. Rucinski, AcA **19**, 245 (1969).
24. A. Claret and S. Bloemen, A&A **529**, 75 (2011).
25. A. Claret, P. H. Hauschildt and S. Witte, A&A **552**, 16 (2013).
26. M. J. Pecaut and E. E. Mamajek, ApJS **208**, 9 (2013).
27. O. W. Butters, R. G. West, D. R. Anderson, A. Collier Cameron, W. I. Clarkson, B. Enoch, C. A. Haswell, C. Hellier, K. Horne, Y. Joshi, S. R. Kane, T. A. Lister, P. F. L. Maxted, N. Parley, D. Pollacco, B. Smalley, R. A. Street, I. Todd, P. J. Wheatley, D. M. Wilson, A&A **520**, 4 (2010).

BOOK OF FULL TEXT PROCEEDINGS TURKISH PHYSICAL
SOCIETY 35th INTERNATIONAL PHYSICS CONGRESS (TPS35)
TPS35, Vol.01, No.02, pp.152-156.
ISBN:978-605-83516-6-0

15 December 2019

New Transit Observation for HAT-P-36 b and HAT-P-37 b

R. K. Seyhan [1,a] , Ö. Baştürk [2], N. Aksaker [3]

[1]*Cukurova University, Astronomy & Astrophysics Dept., Uzaymer Adana / Turkey*
[2]*Ankara University, Faculty of Science, Astronomy & Space Sciences Dept., TR-06100 Ankara / Turkey*
[1]*Cukurova University, Vocational School of Technical Sciences, Uzaymer Adana / Turkey*

[a)] Corresponding author: rvdsyhn@gmail.com

Abstract. Transiting planets HAT-P-36b and HAT-P-37b have been discovered by The Hungarian-made Automated Telescope Network (HATNet) Exoplanet Survey in 2012 (Bakos et al. 2012). We have observed the transits of these planets with the 1 m Turkish telescope T100 in TUBITAK National Observatory of Turkey (TUG) and 0.5 m telescope UT50 in Çukurova University Observatory (UZAYMER). We have analyzed our transit light curves and determined the mid-transit timings from these observations. We have also collected transit light curves from the literature, constituted and analyzed the so- called Transit Timing Variation (TTV) diagram based on these observations. Finally, we have corrected the ephemeris information for these two systems. We present our results within this contribution.

INTRODUCTION

Exoplanet are planets outside our solar system orbiting stars other than our Sun. The first confirmed extrasolar planets were found in 1992, orbiting an unlikely stellar candidate a pulsar, which is the dense core of an exploded star. Shortly after, in 1995, Michel Mayor and Dider Queloz (University of Geneva) discovered the first exoplanet around a sun-like star, 51 Pegasi b, for which they have been rewarded with a Nobel Prize in Physics very recently. The planet has a mass of about half that of the gas giant Jupiter, but it orbits at a strikingly small orbit,only 8 million kms away from the star on average in 4.2 days. Exoplanet names are normally formed by taking the name of their parent stars and adding lowercase letters; the first planet discovered in a system is given the designation "b" (the parent star is considered to be "a") and later planets are given subsequent letters.

The Extrasolar Planets Encyclopedia (http://www.exoplanet.eu/research/) lists web-sites of 39 planet search projects currently that indicate 'transits' as a principal observing method. These projects include finished ones, currently operating ones, projects that are in various preparation stages, as well as projects or proposals that have never moved beyond some design phase. The Hungarian-made Automated Telescope Network (HATNet; Bakos et al. 2004) survey, has been one of the main contributors to the discovery of transiting exoplanets (TEPs), being responsible for approximately a quarter of the ∼ 100 confirmed TEPs discovered to date. It is a wide-field transit survey, similar to other projects such as Super-WASP (Pollaco et al. 2006), XO (McCullough et al. 2005), and TrES (Alonso et al. 2004).

The Hungarian Telescope Network (HATNet) has been in operation since 2003 and has discovered 70 exoplanets since then HATNet telescopes are located at the Fred Lawrence Whipple Observatory (FLWO) on Mount Hopkins (5 telescopes) in the US state of Arizona, and at the Mauna Kea Observatory (2 telescopes) in Hawaii, USA. The various methods that have been employed for the detection of exoplanets are; the Radial Velocity, or Doppler method, Transits, Astrometry, Direct imaging, Microlensing, and Timing variations. To date, all of these techniques have been successful at detecting extrasolar planets.

A transit occurs when an exoplanet passes across the face of its host star and blocks out some of the star's light. Upon studying the light curve of the star, a plot of brightness vs time, a dip in the brightness of the star can be observed. If these dips in brightness occur periodically, it can be indicative of the possible presence of an exoplanet orbiting the star.

Transit light curves can be used to measure the planetary orbital period, the planet-star radius ratio and the orientation of the planet's orbit. Transit timing variations (TTV) occur when an exoplanet's orbit is perturbed by gravitational interactions with additional exoplanets in the stellar system or when the observed system has an orbital motion around a common center-of-mass with such additional bodies causing the arrival time of light to the observer

Türk Fizik Derneği
1950
Turkish Physical Society

ISBN:978-605-83516-6-0

change continuously, which is called the Light Time Effect (LiTE) or Roemer delay. Therefore, TTVs can be used to infer the presence of unseen bodies gravitationally bound to a transiting planet. TTV's can also be used as a tool to empirically determine the absolute masses of additional planets when they also transit their stars .

We have selected two transiting planets HAT-P-36b and HAT-P-37b, discovered by Bakos et al. (2012) to investigate if they display variations in their transit timings. We have observed the systems reduced their raw data and obtained their transit light curves. We then calculated the mid-transit times from our own light curves. We also collected the mid-transit times reported by professional and amateur observers from the literature and Exoplanet Transit Database (ETD).We then constructed the so-called TTV diagrams, refined the ephemeris information and looked for periodicities in the residuals from the linear fits to remove the linear trend caused by the accumulation of observational errors on the light elements that we have made use of in the estimation of transit timings.

OBSERVATIONS and DATA ACQUISITION

In this section we present new photometric follow-up observations of HAT-P-36 and HAT-P-37. For both the planetary systems, two complete transit light curves were acquired with two different telescopes.

HAT-P-36 b and HAT-P-37 b

HAT-P-36 planetary system, discovered by the HAT-Net survey (Bakos et al. 2012), is composed of a V = $12^m.5$, G5V star (Bakos et al. 2012), similar to our Sun, and a hot Jupiter (M∼ 1.8 M_{Jup} and R ∼ 1.3 R_{Jup}), which revolves around its parent star in nearly 1.3 days.

We used the 0.5 m Ritchey Chretien telescope (UT50) at the observatory of the Cukurova University Space Sciences and Solar Energy Research and Application Center (UZAYMER), to observe a complete transit of HAT-P-36 b on 2019 March 07. The instrument was equipped with an Orion Parsec 8300C CCD camera, which had 5.4×5.4-µm size pixels. Observations began at 22:37 UT, 45 min before the ingress, and ended at 01:36 UT, 50 min after the egress. The camera can take images in 1x1 normal mode (3326x2504), but also in 2x2 binning mode (1663x1252) to further increase sensitivity by increasing the signal-to-noise ratio (SNR). The binning mode of 2×2 was used for fast readout. The exposure time was 60 s. R filter was used for observation.

HAT-P-37 b orbits the G-type dwarf (V = $13^m.23$) with a period of 2.80 days (Bakos et al. 2012). According to the discovery paper, it has a mass of M ~1.17±0.10 Mjup a radius of R ~ 1.18 ± 0.08 Rjup.

We used the 1 m Ritchey Chretien telescope at the observatory of the TÜBİTAK National Observation (TUG), to observe a complete transit of HAT-P-37 b on 2019 May 17. The instrument was equipped with an SBIG ST402M CCD camera, which 9x9 microns size pixels. Observations began at 01:46 UT, 1.5 hours before the ingress, and ended at 06:55 UT, 1.5 hours after the egress. The binning mode of 2×2 was used for fast readout. The exposure time was 115s in the R filter.

TABLE 1. Log of our observations with UT50 and T100.

Planet	Date of Obs.	Telescope	Band	Exp. Time [s]
HAT-P-36b	2019-03-07	UT50	Bessel R	60
HAT-P-37b	2019-05-17	T100	Bessel R	115

We used AstroImagej (AIJ) (Collins et al. 2017), or the reduction of our CCD frames, aperture differential photometry, and airmass detrending. After having reduced the observations with AIJ, we modeled the resultant light curves with the online of the EXOFAST software package (Eastman 2013). (http://astroutils.astronomy.ohio-state.edu/exofast/exofast.shtml)

ISBN:978-605-83516-6-0

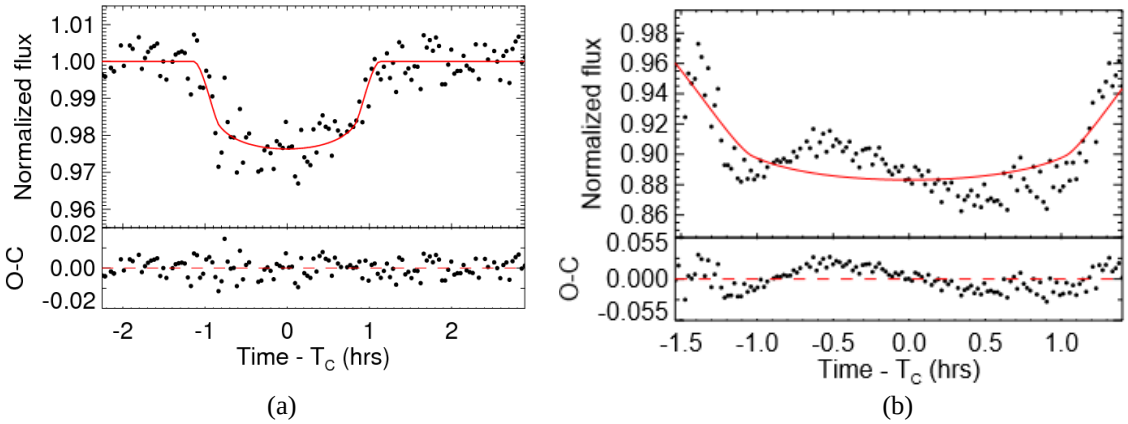


FIGURE 1. (a) The transit light curve of HAT-P-37 b obtained with T100 on 17 May 2019.The resulting best-fitting model is shown by the red line. (b) The transit light curve of HAT-P-36 b obtained with UT50 on 7 March 2019. The resulting best-fitting is shown by the red line. Lower panels are the residuals from the fit on both light curves.

We collected the transit timings of HAT-P-36 b and HAT-P-37 b exoplanets determined by amateur and professional observers and published in the literature and the Exoplanet Transit Database (ETD) website (Poddany et al. 2010), which we have converted to Dynamic Barycentric Julian Days (BJD_{TDB}) based on the geographical coordinates of the observatory and the time reference in which the observations were recorded. By combining these converted mid-transit times to BJD_{TDB} with a Python code written by us for the purpose, which include ETD data, with our own mid-transit times in the same time reference we then aimed at constructing the so-called O-C diagrams In order to reach the goal, we calculated the differences between these observed mid-transit timings (O: observed) and that calculated (C) with respect to reference light elements (a mid-transit time T_0, and an orbital period P), which are given in

TABLE 2. Reference Ephemeris Information For HAT-P-36b and HAT-P-37b (Bakos et al. 2012).

Planet	T_0 [BJD-TDB]	σ_T [s]	Period [days]	σ_P [s]
HAT-P-36b	2455565.18144	17.28	1.327347	0.26
HAT-P-37b	2455642.14318	25.06	2.797436	0.60

We obtained the T_o values for the stars from the first discovery paper. A refined ephemeris for each target is using the following equation:

$$T_c = T_0 + P \times E \quad (1)$$

where T_0 is the mid-transit time at the discovery epoch measured in BJD-TDB P is the orbital period of the target also taken from the discovery paper and expressed in days and E is the integer number of cycles after their discovery paper. In the O-C diagrams of transiting planets and eclipsing binaries, a linear trend is expected due to the accumulation of uncertainties on the reference light elements (T_0 and P) with time. This linear trend should be removed and this procedure is often known as the refinement of the ephemeris information. We used the new photometric data to refine the transit ephemeris of HAT-P-36b and HAT-P-37b.

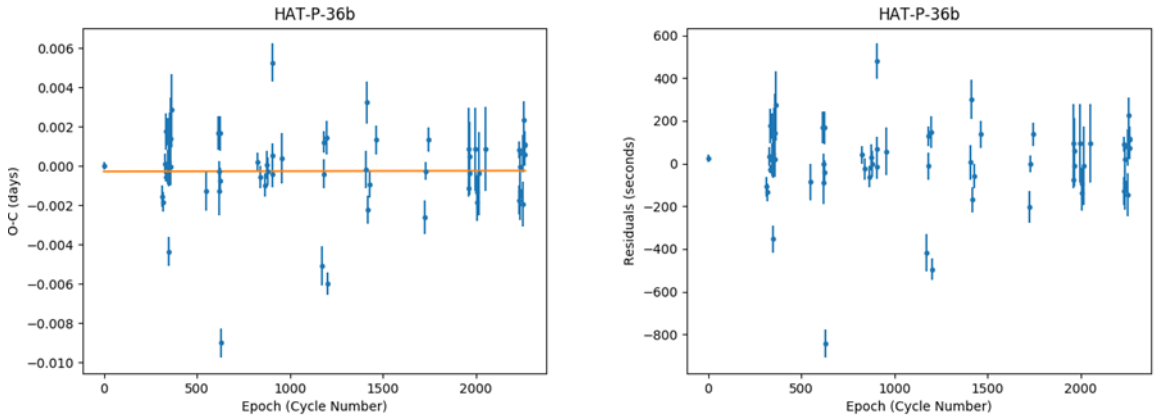
Long-term transit timing variations may reveal a departure from a linear ephemeris due to an orbital decay caused by planet-star tidal interactions (e.g. Murgas et al. 2014) or due to gravitational perturbations induced by an unseen planetary companion (e.g. Ballard et al. 2011) or Light Time Effect (LiTE) (e.g. Agol et al. 2005). New mid-transit times, together with those redetermined from literature data, were used to refine the transit ephemeris for each

ISBN:978-605-83516-6-0

transiting planet. The orbital period P and the time of the reference epoch for cycle zero T_0 were determined in the result of a least-square linear fit, in which timing uncertainties were taken as weights.

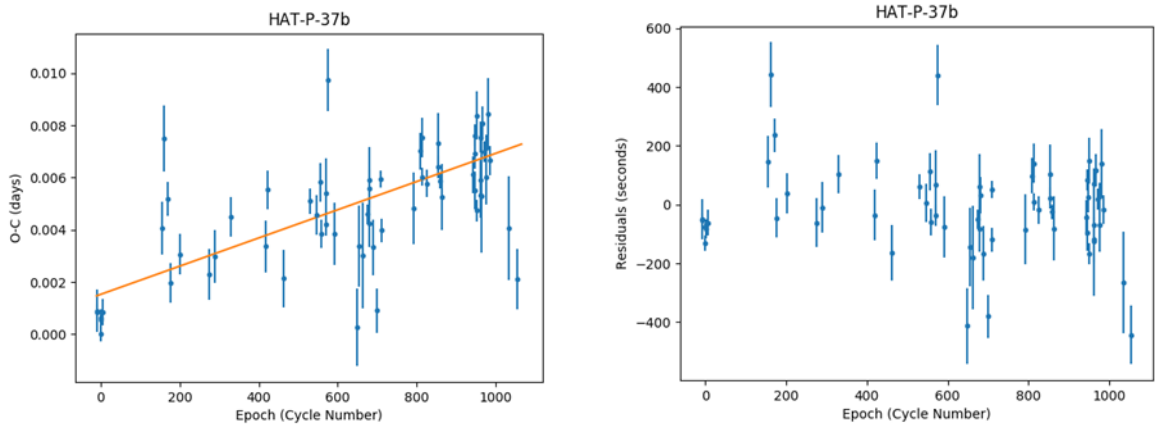
CONCLUSIONS

We observed a transit of each of the exoplanets, HAT-P-36 b and HAT-P-37 b with UT50 Telescope in UZAYMER and T100 in TUG, respectively. Based on these observations we obtained precise transit light curves, which we modeled in EXOFAST-v1 (Eastman 2013) to get the mid-transit times and their errors presented in Table-2. With these mid-transit times in hand, we refined the orbital ephemeris for each system as a result of linear fitting with the least squares technique. In comparison to the published results, our ephemerides are more precise and reliable as result of sufficiently precise transit observations, which we collected from the literature and open databases based on their photometric quality and our own. The constructed O-C diagrams (Figs. 2 & 3) greatly expand the total time span of observations, which further increases the precision and accuracy of the derived ephemerides, which are presented in Table-4 together with their uncertainties.



(a) (b)

FIGURE 7. (a) O-C Diagram for HAT-P-36b. Continous line is the linear fit to data points (in blue with their errors) (b) Residuals from the linear fit.



(a) (b)

FIGURE 8. O-C diagram and its residuals from the linear fit for HAT-P-37b. The same as in Figure 2, only for HAT-P-37b

Acknowledgments

ISBN:978-605-83516-6-0

TABLE 3. Refined Ephemeris Information For HAT-P-36b and HAT-P-37b as a result of this study.

Planet	T_0 [BJD-TDB]	σ_T [s]	Period [days]	σ_P [s]
HAT-P-36b	2455565.181157	45.30	1.327347	0.03
HAT-P-37b	2455642.145026	43.15	2.797436	0.06

ACKNOWLEDGMENTS

Ravide Kezban SEYHAN would like to thank TÜBİTAK for the support with the research project number 118F042 and Şeyma Torun for her help with the analysis. Özgür Baştürk thanks for their partial support in using T100 with the project 19AT100-1417. We also acknowledge all the amateur and professional observers, who reported their observations to Exoplanet Transit Database (ETD).

REFERENCES

1. Bakos, G., et al., *Publications of the Astronomical Society of the Pacific*, Volume 116, pp.266–277 (2004)
2. Roi Alonso., et al., *The Astrophysical Journal Letters*, Volume 613, pp. 2 (2004)
3. E. Agol., et al., *Monthly Notices of the Royal Astronomical Society, Volume 359, pp. 2 (2005)*
4. P. R. McCullough., *Publications of the Astronomical Society of the Pacific*, Volume 117, pp. 783–795 (2005)
5. D. L. Pollacco., *The Astronomical Society of the Pacific*,Volume 118, pp.848 (2006)
6. Stanislav Poddany., et al., *New Astronomy*, Volume 15 pp. 3 (2010)
7. Bakos, G., et al., *The Astronomical Journal*, Volume 144,19 pp. 14 (2012)
8. Jason Eastman.,*Publications of the Astronomical Society of the Pacific*, Volume 125 (2012)
9. Collins, Karen A, et al., *The Astrophysical Journal,* Volume 153, id. A 77,. (2012)
10. Eastman, J., et al., *Publications of the Astronomical Society of the Pacific*, Volume 125,88 (2013).
11. F. Murgas., *Astronomy & Astrophysics*, Volume 563, pp. 14 (2014)
12. Mancini, L., et al., *Astronomy & Astrophysics*, Volume 579,136 (2015)
13. Karen A. Collins., *The Astronomical Journary*, Volume 153 pp. 2 (20017)
14. Yong-Hao Wang et al., *The Astronomical Journal*, Volume 157,82 (20019)

BOOK OF FULL TEXT PROCEEDINGS TURKISH PHYSICAL
SOCIETY 35th INTERNATIONAL PHYSICS CONGRESS (TPS35)
TPS35, Vol.01, No.02, pp.157-160.
ISBN:978-605-83516-6-0

15 December 2019

The First Orbital Solutions of Two Eccentric Eclipsing Binary Stars From Southern: V881 Sco and GV Nor

D. Sürgit[1,2, a)], A. Erdem[2,3,b)] and C. A. Engelbrecht[4,c)]

[1] *Department of Space Sciences and Technologies, Faculty of Arts and Sciences, Çanakkale Onsekiz Mart University, Terzioğlu Kampüsü, TR-17020 Çanakkale, Turkey*

[2] *Astrophysics Research Centre and Observatory, Çanakkale Onsekiz Mart University, Terzioğlu Kampüsü, TR-17020 Çanakkale, Turkey*

[3] *Department of Physics, Faculty of Arts and Sciences, Çanakkale Onsekiz Mart University, Terzioğlu Kampüsü, TR-17020 Çanakkale, Turkey*

[4]*Department of Physics, University of Johannesburg, PO Box 524, Auckland Park 2006, South Africa*

[a)]Corresponding author: dsurgit@comu.edu.tr
[b)]aerdem@comu.edu.tr
[c)] engelbrecht.chris@gmail.com

Abstract. We present the first analysis of spectroscopic observations of the two Southern eclipsing binary stars V881 Sco and GV Nor. Spectroscopic observations of V881 Sco and GV Nor were taken with the Cassegrain-focus-mounted "SpUpNIC" spectrograph mounted on the 1.9-m telescope at the Sutherland station of the South African Astronomical Observatory (SAAO) in 2018. The radial velocities (RVs) of the components of V881 Sco and GV Nor were determined using the cross-correlation technique (CCT), and the first orbital solutions of V881 Sco and GV Nor are obtained in this study.

INTRODUCTION

V881 Sco (CPD-33 4099 = HD 150384 = GSC 07354-00071 = Gaia DR2 6021188323863057920, *V*=9.27 mag) was classified as a variable star by Kukarkin et al. (1975). Then the system was listed by Houk (1982), and the spectral type was given as A1/2IV. The photometric period of the system was determined as 2.49157 days by Pojmanski (2002). The photometric period of the system was updated by Dvorak (2004). V881 Sco was also listed as an eclipsing system in catalogues by Malkov et al. (2006) and Avvakumova et al. (2013). Zasche (2010) included V881 Sco in his analysis of the light curves and apsidal motion analysis of 13 eccentric eclipsing binaries, deriving the basic physical properties of these systems.
GV Nor (CPD-53 7685 = HD 146375 = GSC 08711-00192 = Gaia DR2 5932204435609715584, *V*=10.55 mag) was classified as a variable star by Kruytbosch (1932). The system was also listed by Houk and Cowley (1975). They assigned a spectral type of B5/8 to GV Nor. GV Nor was also listed as a Algol-type eclipsing binary by Budding et al. (2004). Thehe system was confirmed as an eclipsing binary star in catalogues by Malkov et al. (2006) and Avvakumova et al. (2013). The photometric period of the system was determined as 2.971924 days by Pojmanski (2002). Zasche (2010) included GV Nor in his analysis of the light curves and apsidal motion analysis of 13 eccentric eclipsing binaries. He derived the basic physical properties of this system.

Türk Fizik Derneği
1950
Turkish Physical Society

ISBN:978-605-83516-6-0

SPECTROSCOPIC OBSERVATIONS AND DATA REDUCTIONS

Spectroscopic observations of V881 Sco and GV Nor were made with the SpUpNIC spectrograph mounted at the Cassegrain focus of the 1.9-m telescope at the South African Astronomical Observatory (SAAO). We used grating 4 of the spectrograph - which has a wavelength coverage of 400 – 525 nm with a blaze peak at 510 nm. The resolution of 0.13 nm in binned mode (giving R = 3600 for the chosen wavelength range) - and a slit width of 1.35 arcsec for all spectroscopic observations of the two target stars. In our all observations, using a Cu/Ar lamp, arc spectra were taken as comparison spectra for each stellar image. A set of Quartz-Iodine lamp images was also taken every night for flat-field calibrations. IRAF was used for the spectral data reductions and calibrations.

ORBITAL SOLUTIONS

Radial velocities (RVs) of the components of V881 Sco and GV Nor were obtained by the cross-correlation technique (CCT, (Tonry and Davis, 1979; Popper and Jeong, 1994). He I 4713, 4921, and 5015, Mg I 4703, and Mg II 4481 lines of the components were used as the most suitable lines in RV measurements. The ELEMDR77 program (https://www.astro.sk/~pribulla/soft.html) was used to determine the orbital parameters of V881 Sco and GV Nor, using the determined radial velocities of the components. The final parameters of spectroscopic solutions for V881 Sco and GV Nor are presented in Table 1. The best theoretical fits for the radial velocity curves of both stars are also plotted in Figures 1 and 2, respectively.

Table 1. Spectroscopic orbital parameters of V881 Sco and GV Nor.

Parameter	V881 Sco	GV Nor
P_{orb} (day)	2.49157(fixed)	2.971876(fixed)
T_o (HJD)	52126.6791(±0.069)	54994.2467(±0.091)
K_1 (km s^{-1})	116.81(±3.09)	131.23(±5.26)
K_2 (km s^{-1})	136.68(±2.83)	98.50(±4.41)
e	0.12(±0.02)	0.19(±0.04)
V_γ (km s^{-1})	-27.59(±1.72)	-8.68(±2.70)
$a_1 \sin i$ (AU)	0.0266(±0.0007)	0.0352(±0.0014)
$a_2 \sin i$ (AU)	0.0311(±0.0007)	0.0264(±0.0012)
$M_1 \sin^3 i$ ($M_\odot$)	2.216(±0.192)	1.518(±0.223)
$M_2 \sin^3 i$ ($M_\odot$)	1.894(±0.171)	2.023(±0.296)

ISBN:978-605-83516-6-0

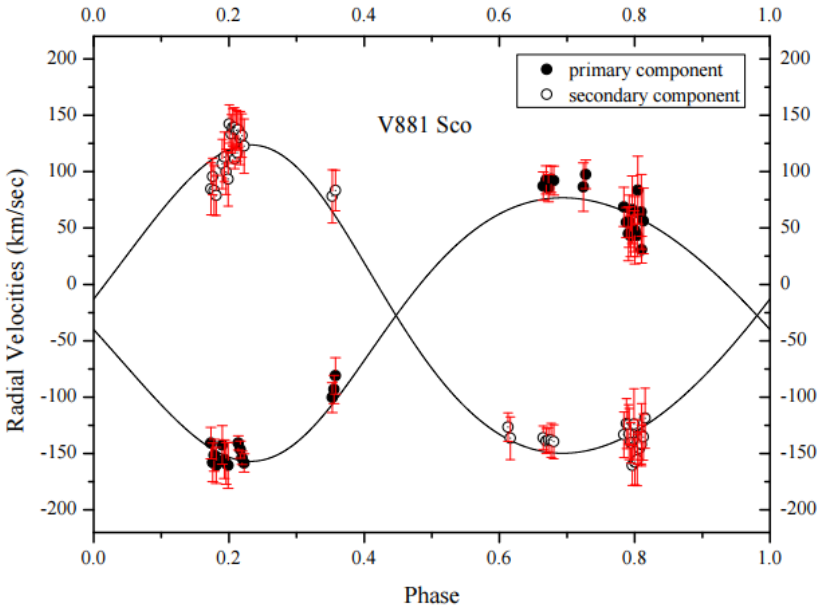


Figure 1: Best theoretical fits to radial velocity curves of components of V881 Sco.

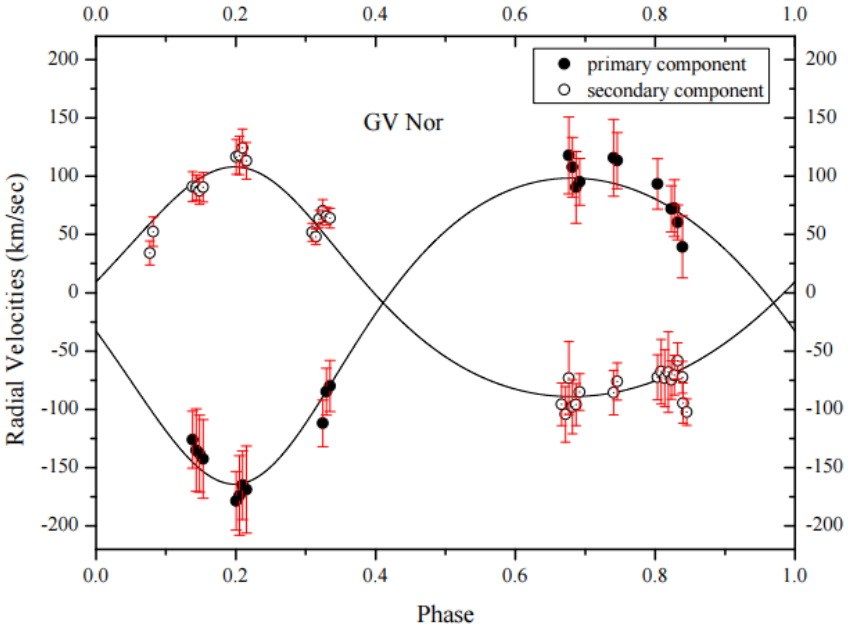


Figure 2: Best theoretical fits to radial velocity curves of components of GV Nor.

ISBN:978-605-83516-6-0

CONCLUSION

The radial velocities (RVs) of the components of V881 Sco and GV Nor were determined by the cross-correlation technique (CCT), and the first orbital solutions of V881 Sco and GV Nor are obtained. The mass ratio of the systems are estimated as 0.85 and 1.3, respectively. The spectroscopic observations of the systems are continuing. Our next step will be to re-analyze the orbital solutions with additional spectral data for both systems. Then, the physical parameters of our targets will be examined, together with available light curves of the two systems published in the literature.

ACKNOWLEDGMENTS

C.A. Engelbrecht thanks the South African National Research Foundation and UJ for financial support. All the authors thank the SAAO for observing time.

REFERENCES

1. Avvakumova, E. A., Malkov, O. Yu., Kniazev, A. Yu., AN, 3364, 860 (2013).
2. Budding, E., et al. A&A, 417, 263 (2004).
3. Dvorak, S. W., IBVS 5542 (2004).
4. Houk, N. 1982mcts.book.....H.(1982).
5. Houk, N. and Cowley, A. P. 1975mcts.book.....H.(1975).
6. Kruytbosch, W. E., BAN, Vol. 6, p.233 (1932).
7. Kukarkin, B. V. et al. , IBVS 961 (1975).
8. Malkov, O. Yu. et al. A&A, 446, 785-789 (2006).
9. G. Pojmanski, AcA, v.52, pp.397-427, (2002).
10. Popper, D.M. and Jeong, Y.-C. PASP, 106,189 (1994).
11. Tonry, J., Davis, M. AJ, 84, 1511-1525 (1979).
12. Zasche, P. NewA, 15, 150 (2010).

BOOK OF FULL TEXT PROCEEDINGS TURKISH PHYSICAL
SOCIETY 35th INTERNATIONAL PHYSICS CONGRESS (TPS35)
TPS35, Vol.01, No.02, pp.161-166.
ISBN:978-605-83516-6-0

15 December 2019

A Comparison of the Supernovae Ratios Between the Nearby and Distant Galaxy Clusters

Onur Ünver[a)] and Murat Hudaverdi[b)]

Yıldız Technical University, Faculty of Science and Art, Department of Physics, Istanbul 34220, Turkey

[a)]*Corresponding author: onrunver@gmail.com*
[b)]*Electronic mail: hudaverd@yildiz.edu.tr*

Abstract. Galaxy clusters are the most massive, dark matter dominated and gravitationally collapsed objects in the known universe. The enrichment and the metallicity of the Intra Cluster Medium (ICM) is directly related to the supernova types that occur in the galaxies. Hence, those supernovae and their ratios in the galaxy clusters with different redshifts play a crucial role to understand the enrichment history and the galaxy evolution. The X-ray analysis of the galaxy clusters is based on the archival data of $XMM-Newton$ X-ray Observatory. In this study we present the results of the supernovae Type Ia and Type II core collapse ratios in the galaxy clusters with different redshifts.

INTRODUCTION

The chemical elements, which are listed in the periodic table, are synthesized in a long course of cosmic time line. Nucleosynthesis is the process of creating new atomic nuclei from pre-existing nuclear particles such as protons and neutrons. The first atomic nuclei formed about three minutes after the Big Bang, or so called Big Bang nucleosynthesis. Hydrogen and helium form the components of the first stars and the current hydrogen / helium ratio of the universe is based on those times. The abundance in the universe of some light elements such as lithium, beryllium, helium-3, and boron are thought to be created by cosmic ray decay [1].

The further formation of the elements is closely related to the life history of the stars. The stars are born, live and die for a while. In the meantime, they synthesize the elements responsible for vitality. Different type of stars at different morphological states contribute to different chemical synthesis. Stars are composed of clouds of gas and dust collapsing under their own gravitational pull. As the matter continues to collapse, the pressure of the gas that begins to compress in a smaller volume increases. It is reached that the pressure force at the end, equal to the gravitational force, prevents the gas from settling further on itself. This condition, in which the gravitational force and the pressure force are balanced, is called hydrostatic equilibrium. Small and large stars have different physical dynamics and thus creates light and heavy elements at different quantities.

When a massive star (>8-10 $M_{\odot}$) burns out its fuel or an additional material accretion from a close star occurs, hydrostatic equilibrium breaks. After this point heavier elements (C, Ne, O, Si) are created and the density reaches the Chandrasekhar limit (1.4 $M_{\odot}$). The star quickly collapses on to itself by blasting the all the elements into the interstellar medium. For a detailed review see Refs. [2, 3]). This energetic processes produce majority of the chemical elements in the periodic table. Fig. 1 shows the synthesis origin of each element briefly, including the artificial (man-made) elements at the right-bottom.

Enrichment of the Inter Galactic Medium

Galaxy clusters are the largest gravitational structures. They are formed by the gathering of galaxies and smaller groups. They are great cosmic laboratories to study chemical enrichment of the Universe. All the galaxies, stars and the synthesized elements are trapped into the gravitational potential well of the cluster. Therefore, clusters of galaxies possess all the materials produced at different stars, and ejected by different types of supernovae. This makes them unique astro-archaeological sites to explore chemical origins.

The early observatories were not good enough to resolve all the emission lines from intra cluster medium (ICM). Based on the early studies of Perseus, Coma and Virgo clusters it is understood that abundant with metals. The first information that we know was ICM is rich in Fe-K line emission at about 0.3-0.5 solar abundance [4, 5]. After ASCA mission, we could detect not only Fe but also many elements in the ICM including O, Ne, Mg, Si, S, Ar, Ca, and Ni (e.g. 6, 7, and 8). With the advent of the detector technologies used in latest observatories like *Chandra*,

Türk Fizik Derneği
1950
Turkish Physical Society

ISBN:978-605-83516-6-0

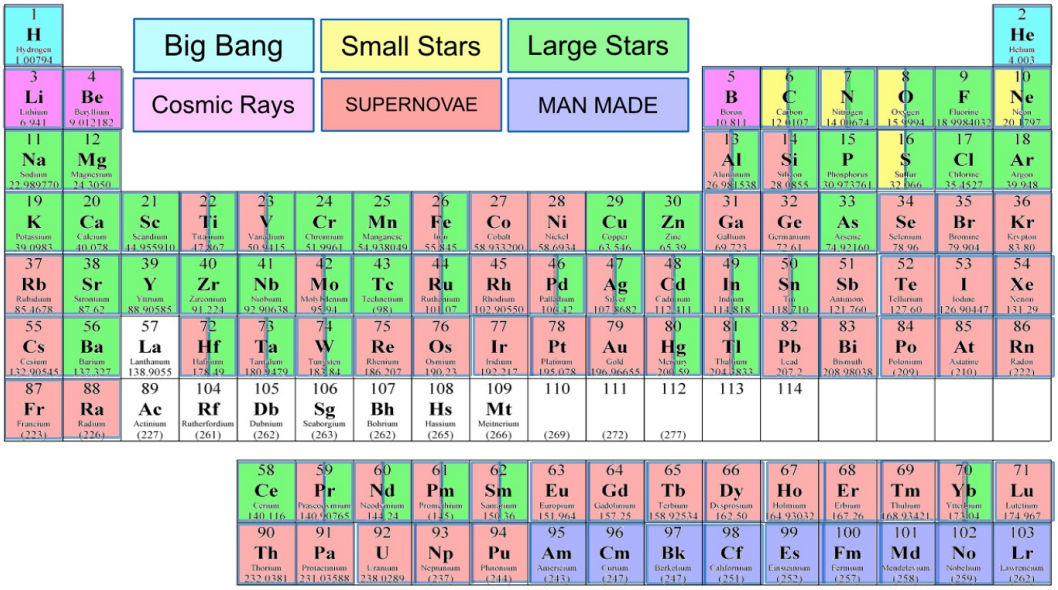


FIGURE 1. Periodic table showing the synthesis origin of each element.

XMM − Newton, and *Suzaku*, We can now detect the most of the elements in the ICM with an unprecedented accuracy. And it opened up a new era for studying chemical origins of the elements.

The Role of Supernova: SNIa and SNcc

Supernovae are divided into various groups by considering the undergoing physical processes. When a massive star (>8-10 $M_{\odot}$) burns out its fuel, the equilibrium breaks. After this point heavier elements (C, Ne, O, Si) are created. If the density reaches the Chandrasekhar limit (1.4 $M_{\odot}$), star quickly collapses. The mechanism is called as core-collapse supernova, SNcc. Type Ia supernovae (SNIa) are not formed by gravitational collapse. They are binary systems composed of a white dwarf (<8 $M_{\odot}$) and its companion object, from which a mass accretion occurs [9] . Violent explosion kicks out its material into the interstellar medium. SNIa are dominantly produce Ar, Ca, Cr, Mn, Fe, and Ni. It is also thought That about 50% of the Si and S in the Universe is synthesized by SNIa. For reviews on supernova mechanisms the readers can see recent papers [9, 10].

A galaxy is composed of different types of SNe, intra galactic medium is polluted with the metals that are ejected by SNcc and SNIa. Consequently, galaxy clusters and intra cluster medium is filled with metal abundances originating from integrated synthesis of all the past SNe within the potential well.

Sample Selection

Since it is pretty much known, which of the SNe mechanism produce with of the metal abundances, one can estimate the total number of SNe within a cluster to produce estimated amount of the elements. By going one step further, we estimate the fraction of SNcc and SNIa for that particular source. And if a quality of data is provided we can even understand if these mechanism change, or one of them dominates the other at different time lines of the cosmos.

In order to address these questions and contribute to our understanding of how to differ the SNe types and ratios over redshift and cluster mass, we have selected two clusters from archival *XMM − Newton* data with different redshifts and masses: nearby source Abell 2717 ($z = 0.049$) and distant source MACS J0429.6-0253 ($z = 0.399$).

A2717: The southern galaxy cluster A2717 has a cD galaxy which is associated with a Wide angle tail (WAT) source. It is has been studied in very detail in the optical band [11]. *ROSAT* data reveals a plasma luminosity of L_x = 7.8×10^{43} erg s^{-1} and a temperature of $kT = 1.9^{+0.3}_{-0.2}$ keV [12].

ISBN:978-605-83516-6-0

TABLE I. *XMM − Newton* EPIC Observations.

Cluster	Coordinates	Obs. ID	Redshift	EPIC	Exposure (s)
Abell 2717	$00^h03^m12.1^s, -35^d55^m38^s$	0145020201	0.049	MOS1 - MOS2	54258
MACS J0429.6-0253	$04^h29^m36.0^s, -02^d53^m08^s$	0720700101	0.399	MOS1 - MOS2	134599

MACS J0429.6-0253: Structural properties and metal abundance of this cluster have been reported and the Chandra observations of the cluster at the radius $R_{500} = 1.12$ Mpc, reveals the plasma luminosity of $L_x = 23.1 \pm 0.6 \times 10^{44}$ erg s^{-1}, the ICM temperature $kT = 5.4^{+0.4}_{-0.2}$ keV and metal abundance $Z = 0.51^{+0.10}_{-0.09}\ Z_\odot$ [13].

We are totally aware that two sources are insufficient to get a clear conclusion, but the results help us to understand a step further the problem of chemical synthesis evolution in the universe.

ANALYSIS AND RESULTS

Our X-ray analysis uses *XMM − Newton* observatory [14] archival data. Abell 2717 was observed on 2002 December 26 (Obs.ID 0145020201) for a total exposure of 54.2 ksec. And the distant cluster MACS J0429.6-0253 was observed on 2013 August 22, (Obs.ID 0720700101) for a total exposure of 134.6 ksec. Table I shows the log of *XMM − Newton* observations for both clusters.

Observations and Data Reduction

The observations were performed with the European Photon Imaging Camera (EPIC) MOSs (MOS1 and MOS2) [15] and Pn [16] cameras operating in the 0.2 - 15 keV energy range. Due to the high soft proton background effects on the EPIC Pn CCDs, in this study we only considered front illuminated EPIC MOS data. Since the performance of the each CCD on EPIC is slightly time dependant, we carefully examined data for a potential anomaly. A2717 data, which was observed on December 2002, was fine and all the CCDs were operating smoothly. Since 2012 EPIC-MOS1 two CCDs (CCD-3 and CCD-6) stopped operating and registering photon counts, for MACS J0429.6-0253 data we excluded MOS1 CCD-3 and CCD-6, which was observed in 2013.

The EPIC-MOS data were processed with the *XMM − Newton* Science Analysis System (SAS) version 16.1.0 with the Current Calibration Files (CCF). For filtering the data and preparing the spectral files we used ESAS tools integrated into SAS. In order to obtain clean event files cleaning and filtering routines are applied. We processed the MOS raw data with CCFs, by using ESAS tools `emchain` and `mos_filter`, respectively. The spectral files of the considered regions were created in the 0.3 - 7.0 keV energy band, with the `mos_spectra` and `mos_back` tasks. These tools are using `evselect` V3.62, `rmfgen` V2.5.1 and `arfgen` V1.93.1 to generate final spectra and response files. The X-ray point like features were detected by `cheese` tool which uses SAS task `edetect_chain`. We also visually correct and reorganize any potential false detection, before proceeding the masking of point sources.

Fig. 2 shows 0.3-10 keV energy band MOS images of A2717 (*top*) and MACS J0429.6-0253 (*bottom*). The white circles represents the R_{500}, which is defined to be the radius at which the mean density of the cluster is 500 times the critical density of the Universe at the cluster's redshift.

Throughout this paper, we used $H_0 = 70 kms^{-1}Mpc^{-1}$, $\Omega_M = 0.3$ and $\Omega_\Lambda = 0.7$. Otherwise stated, all errors are at the 1σ confidence level.

Spectral Analysis

For the spectral analysis of the ICM we used X-Ray Spectral Fitting Package (Xspec) version 12.9 [17]. Both MOSs' spectra were modeled in 0.3 - 7.0 keV energy range using *C*-statistic. Photon counts are collected from within the R_{500} circles, which is shown in Fig. 2 with white circles. The values of R_{500} and $M_{(gas,R_{500})}$ for the clusters were adopted from the previous works [13, 18, 19]. Fig. 2 right-panel shows the best fit spectral modelling of photon counts from the R_{500} circles.

ISBN:978-605-83516-6-0

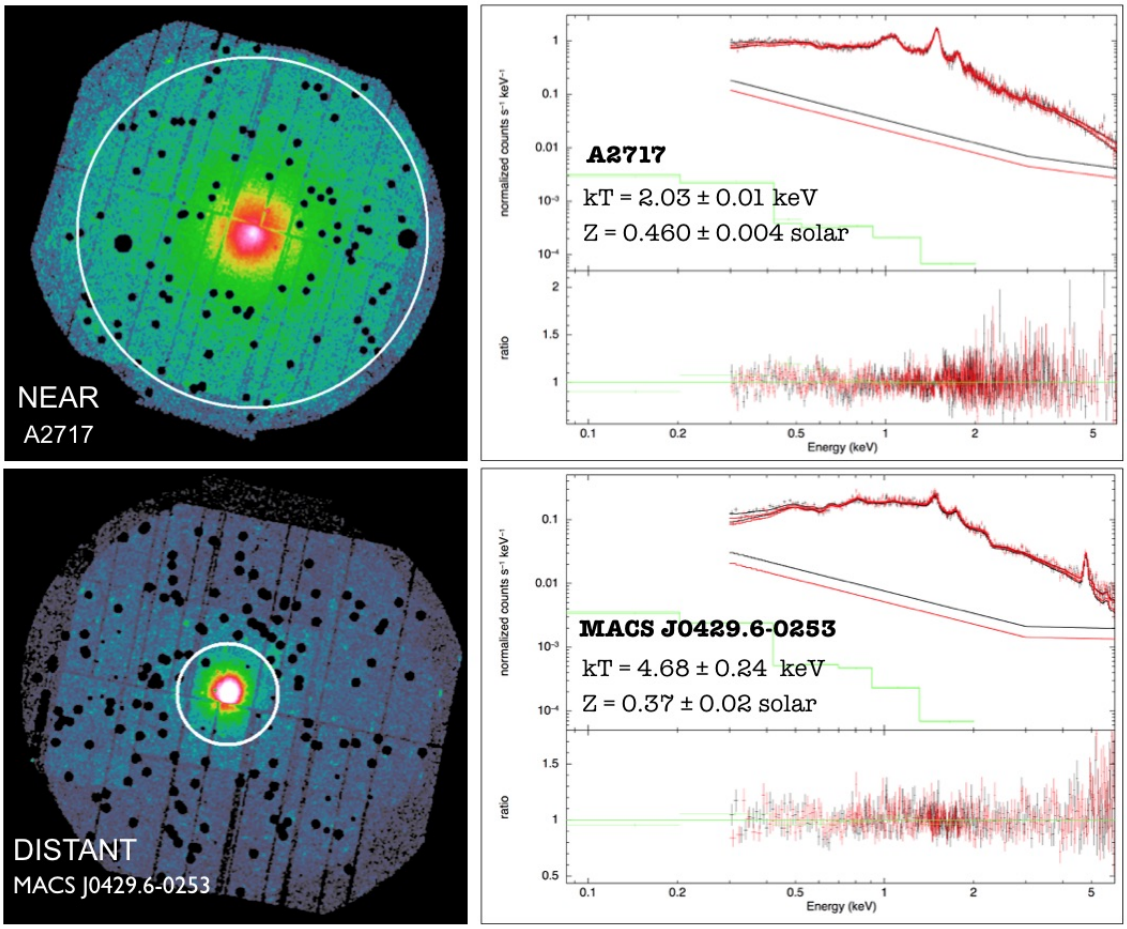


FIGURE 2. *Top-left*: Exposure corrected, background subtracted, point sources filtered XMM-Newton image of nearby galaxy cluster A2717. *Top-right*: The spectral fit for the R_{500} regions. *Bottom-left* and *Bottom-right* are the similar images for distant cluster MACS J0429.6-0253, respectively.

In the spectral analysis of diffuse objects such as galaxy clusters, background treatment become crucial. Incorrect modeling of background effects may cause nonphysical results. There are several background analysis methods in the literature which are successfully applied: (i) modelling the background, (ii) using blank sky event files, and (iii) using local background. In our work, we modeled background as described by [20]. We modeled both MOS spectra simultaneously with ROSAT All-Sky Survey (RASS) data for constraining the Cosmic X-ray Background (CXB). The RASS data for the clusters are obtained and pre-processed by using `X-Ray Background Tool` of `Heasarc` [21]. Both MOS1 and MOS2 *broken power law* models are added as separate component with their related diagonal response files for the Soft Proton contamination. We added two Gaussian lines to represent the fluorescent emission lines of Si-K_α and Al–K_α at the energies of 1.49 keV and 1.75 keV.

In order to obtain total supernova number and the ratio of the source region, we used absorbed *snapec* plasma model [22]. The model has seven parameters, and during the spectral analysis gas temperature (kT), total number of SNe, SN ratio, redshift and the normalization were set to free. However, SNIa and SNcc parameters are fixed to their own table values. Galactic column density was taken from HI4PI Collaboration [23] and fixed the value at the cluster's redshift.

The clusters' gas masses within R_{500} are in the units of 10^{12} $M_\odot$ was applied as conversion factor to obtain the total number of SNe. The conversion factors of Abell 2717 and MACS J0429.6-0253 are 10.2 and 70.2, respectively. For the SNIa yield model parameter, we used W7 [24], W70, WDD and CDD [25]. W7 and W70 represents Convective Deflagration Models. WDD and CDD express the Delayed – Detonation (Explosion) Models. For SNcc yields we used the table of I99 [25] Salpeter-IMF-average yields which cover 10 - 50 $M_\odot$ progenitor masses with metallicities

ISBN:978-605-83516-6-0

TABLE II. Best-fit Parameters of the *snapec* model to the MOS spectrum of the clusters

Source	SN Ia	kT (keV)	N^{SNe} ($\times 10^9$)	R	R^{Ia} (%)	χ^2 (dof)
A2717	*W7*	2.03±0.01	17.03±0.20	0.31±0.01	23.70±0.58	4457.04(5788)
	W70	2.04±0.01	17.03±0.10	0.31±0.01	23.70±0.58	4443.18(5788)
	WDD	2.03±0.01	11.53±0.51	0.89±0.11	47.10±3.07	4426.33(5788)
	CDD	2.02±0.01	12.51±0.51	0.85±0.10	45.95±2.92	4428.36(5788)
MACS J0429.6-0253	*W7*	4.65±0.21	169.50±28.70	0.11±0.04	9.90±3.20	1969.25(2267)
	W70	4.63±0.22	167.30±31.50	0.11±0.05	9.90±4.10	1669.08(2267)
	WDD	4.62±0.25	158.96±35.01	0.12±0.06	10.71±4.78	1596.15(2267)
	CDD	4.67±0.23	149.93±38.51	0.19±0.11	15.96±7.76	1969.74(2267)

0 - 1 $Z_\odot$. A similar method and *snapec* application is explained in detail in [26] and references therein. The best-fit parameters of *snapec* model are given in Table. II for both nearby and distant galaxy clusters, respectively.

A2717 spectrum is well defined with a thermal plasma model with a temperature of kT = 2.04±0.01 keV, which is perfectly consistent with the *ROSAT* result of $kT = 1.9^{+0.3}_{-0.2}$ keV [12].

CONCLUSION

In this study, we analysed $XMM-Newton$ the archival data of the galaxy clusters Abell 2717 and MACS J0429.6-0253 up to R_{500} outskirts. In order to determine the SNIa and SNcc ratios and their chemical contribution to the ICM, we fitted the X-ray data with the absorbed *snapec* model.

The best fit parameters are shown in Table II; among the SNIa models for Abell 2717 W7 and W70 models with the ratio of 23.70±0.58 % and for MACS J0429.6-0253 WDD model with the ratio of 10.71±4.78 % show significant consistency. For Abell 3112, it is reported that the SNe ratios are between 12-16% [26]. Results of the X-ray analysis of Virgo Cluster reveal that the SNe ratios are 12-37% [27]. Based on the analysis, we report that our preliminary results are perfectly consistent with the previous studies in the literature [26, 27].

We also estimate a total SNe number of 17.03±0.10 $\times 10^9$ for A2717 and 158.96±35.01 $\times 10^9$ for MACS J0429.6-0253. Since the gas mass for MACS J0429.6-0253 (7.02×10^{13} $M_\odot$) is about 7 times larger than A2717 (1.02×10^{13} $M_\odot$), an elevated total number or SNe is quite expected and reasonable.

Unfortunately, the analysis results of two clusters are not sufficient to make a general and powerful conclusion, but the acquired results clearly show that SNcc is the dominant enrichment mechanisms for the both galaxy clusters.

ACKNOWLEDGMENTS

This work is a part of O.Ü.'s PhD research. M.H. would like to acknowledge financial support from the Scientific and Technological Research Council of Turkey (TÜBİTAK) project number 118F035. While this full-text proceeding focuses on the preliminary analysis results, a paper discussing the further details is currently in preparation.

REFERENCES

1. D. L. Heiserman, *Exploring Chemical Elements and Their Compounds* (Tab Books, 1991).
2. H. Y. Janka, Annual Rev. of Nuc. and Part. Sci. **62**, 407 (2012).
3. A. Burrows, Rev.of Mod. Phys. **85**, 245 (2013).
4. R. F. Mushotzky, P. J. Serlemitsos, E. A. Boldt, S. S. Holt, and B. W. Smith, Ap. J. **225**, 21 (1978).
5. R. F. Mushotzky, Physica Scripta Volume T **7**, 157 (1984).
6. R. Mushotzky, M. Loewenstein, and K. A. Arnaud, Ap. J. **466**, 686 (1996).
7. Y. Fukazawa, K. Makishima, and T. Tamura, PASJ **50**, 187 (1998).
8. A. Finoguenov, L. P. David, and T. J. Ponman, Ap. J. **544**, 188 (2000).
9. W. Hillebrandt, M. Kromer, F. K. Röpke, and A. J. Ruiter, Frontiers of Physics **8**, 116 (2013).

10. W. Hillebrandt and J. C. Niemeyer, ARA&A **38**, 191 (2000).
11. C. M.M., *A Dynamical Study of Rich Clusters*, PhD dissertation, University of Cambridge (1987).
12. H. Liang, M. Pierre1, A. Unewisse, and R. Hunstead, Astron. Astrophys. **321**, 64–70 (1997).
13. B. Maughan, C. Jones, W. Forman, and L. Van Speybroeck, The Astrophysical Journal Supplement Series **174**, 117 (2008).
14. F. Jansen, D. Lumb, B. Altieri, J. Clavel, M. Ehle, C. Erd, C. Gabriel, M. Guainazzi, P. Gondoin, R. Much, *et al.*, Astronomy & Astrophysics **365**, L1–L6 (2001).
15. M. J. Turner, A. Abbey, M. Arnaud, M. Balasini, M. Barbera, E. Belsole, P. Bennie, J. Bernard, G. Bignami, M. Boer, *et al.*, Astronomy & Astrophysics **365**, L27–L35 (2001).
16. L. Strüder, U. Briel, K. Dennerl, R. Hartmann, E. Kendziorra, N. Meidinger, E. Pfeffermann, C. Reppin, B. Aschenbach, W. Bornemann, *et al.*, Astronomy & Astrophysics **365**, L18–L26 (2001).
17. K. Arnaud, B. Dorman, and C. Gordon, Astrophysics Source Code Library (1999).
18. M. Arnaud, E. Pointecouteau, and G. Pratt, Astronomy & Astrophysics **474**, L37–L40 (2007).
19. E. Pointecouteau, M. Arnaud, and G. Pratt, Astronomy & Astrophysics **435**, 1–7 (2005).
20. S. Snowden, R. Mushotzky, K. Kuntz, and D. S. Davis, Astronomy & Astrophysics **478**, 615–658 (2008).
21. E. J. Sabol and S. L. Snowden, Astrophysics Source Code Library (2019).
22. E. Bulbul, R. K. Smith, and M. Loewenstein, The Astrophysical Journal **753**, 54 (2012).
23. H. Collaboration, N. B. Bekhti, L. Flöer, R. Keller, J. Kerp, D. Lenz, B. Winkel, J. Bailin, M. Calabretta, L. Dedes, *et al.*, Astron. & Astrophys **594**, A116 (2016).
24. T. Tsujimoto, K. Nomoto, Y. Yoshii, M. Hashimoto, S. Yanagida, and F.-K. Thielemann, Monthly Notices of the Royal Astronomical Society **277**, 945–958 (1995).
25. K. Iwamoto, F. Brachwitz, K. Nomoto, N. Kishimoto, H. Umeda, W. R. Hix, and F.-K. Thielemann, The Astrophysical Journal Supplement Series **125**, 439 (1999).
26. C. Ezer, E. Bulbul, E. N. Ercan, R. K. Smith, M. W. Bautz, M. Loewenstein, M. McDonald, and E. D. Miller, The Astrophysical Journal **836**, 110 (2017).
27. A. Simionescu, N. Werner, O. Urban, S. Allen, Y. Ichinohe, and I. Zhuravleva, The Astrophysical Journal Letters **811**, L25 (2015).

03. Atomic and Molecular Physics



BOOK OF FULL TEXT PROCEEDINGS TURKISH PHYSICAL
SOCIETY 35th INTERNATIONAL PHYSICS CONGRESS (TPS35)
TPS35, Vol.01, No.03, pp.168-172.
ISBN:978-605-83516-6-0

15 December 2019

Circular Polarization Effect Dependence of High Harmonic Generation by Excited Argon Atom

Dilan ALP[1,a], Ilhan CANDAN[2]

[1]*Sirnak University, Dept. of Energy Systems Engineering, 73000, Sirnak, Turkey.*
[2]*Dicle University, Dept. of Physics, Diyarbakir, Turkey*

[a)] Corresponding author: dalp@sirnak.edu.tr

Abstract. The interaction of the intense laser pulse, which forms the basis of the strong laser field and non-linear optical physics, with atoms, molecules and solids leads to the High Order Harmonic Generation (HHG). There are many theoretical and experimental research related to this process defined by the Semi-Classic Model which is called Three Step Model. In this paper, the Argon atom interacting with the strong circular laser field (800nm) and the resulting non-dipole effects in the theoretical Lewenstein model to be used in the production of the higher order harmonic spectrum will be investigated.

INTRODUCTION

The most recent advances in ultrafast spectroscopy technology used in various applications over the last 25 years are sources of high harmonic production and high-resolution imaging of molecules, atoms and nanostructures [1-5].

Higher Order Harmonic Generation (HHG), as one of the subjects of nonlinear optical science that is one of the fastest developing research areas in atom-intense laser interaction. In many theoretical and experimental studies, the most basic principle understanding the origin of high-order harmonics is defined as semi-classical three-step model. This model has been particularly useful description for the 'cut-off and plateau region' in the HHG spectrum [6]. In addition to this model, the electron is firstly tunneled from the ground state of the atom passing through the barrier formed by the Coulomb potential in intense laser field. The next motion is considered classically and consists primarily of free charge oscillation which may come back near the core and return to the ground state in the laser field. If it returns the photon energy that is defined where $E_{kin} + I_p$ is kinetic energy, and I_p is ionization potential which may be emitted. The harmonic photon energy $E_C = 3.2U_p + I_p$ is given by the cutoff law where U_p is ponderomotive energy $\left(U_p\left[eV\right] = E_0^2/4\omega_0^2\right)$ [6]. The cutoff region occurs in the harmonic spectrum at harmonics order which is given $N_{\max} = \left(3.2U_p + I_p\right)/\hbar\omega$.

As a result of intense research using linear polarization, it has been observed that some classical trajectories of the electron pass through the nucleus periodically, therefore allowing for recombination radiatively and generation of harmonics. Although a great progress has been done in the use of linearly polarized beams that have been made in the high harmonic generation, until recently it was not possible to directly obtain circularly polarized HHG pulses. In contrast, elliptically polarized driving lasers (or circularly polarized lasers) are strongly suppressed by the possibility of electron recollision and therefore do not emit harmonics [7,8]. Recent studies have indicated the synthesis of circular polarized high harmonic attosecond pulse train which is modified by the deeper physical insight of HHG with the combination of collinear counter-rotating light of different degrees and macroscopic phase matching [10-13].

Polarization is a fundamental feature of electromagnetic waves and often plays an important role in the interaction of light with matter. It is particularly investigated that using circularly polarized short EUV pulses for generating harmonics which are ultra-fast spin dynamics, circular dichroism, chirality allocation magnetic

ISBN:978-605-83516-6-0

microscopy, and so forth. Various theoretical approaches have been proposed for generating circular polarized harmonics [14-16]. For instance, recent studies on the very strong dependence on polarization ellipticity in high harmonic generation require that numerical approximation to intense field ionization to go beyond the current models based on linear polarization [17-19].

The polarization is not only important to study the basic optical views of light-matter interactions, but also a time-varying polarization state, which forms the basis of numerous spectroscopic and harmonics control techniques related to HHG in soft X-ray and XUV spectrum in Attoscience [20,21]. There are many experimental and theoretical scientific studies used in the generation of harmonics obtained by circular polarization laser field interacting with the matter, for instance non-adiabatic tunneling by spin polarized electrons, producing vortex-shaped photoelectron momentum distributions, attosecond control by spin-dissolved recoil dynamics, and examining atto-clock techniques via angular streaking using cold target recoil ion momentum spectroscopy form [22-26].

In this study, consequently the event of interacted circular polarized beam with atom that is defined cut-off region in the conventional harmonic spectrum will be shown by reference [27] to a different numerical method for generate harmonics. Here, a proposed simple method will be used to obtain forward ellipticity in the presence of magnetic fields that can move in the same direction as the Lorentz force, so that in the harmonic emission allowed to equal intensity and wavelength using two non-collinear opposite circular polarized beams.

THEORETICAL METHODS

Here we consider the harmonics generated in Argon gas by two opposite circular polarization beams within x, z propagating plane.

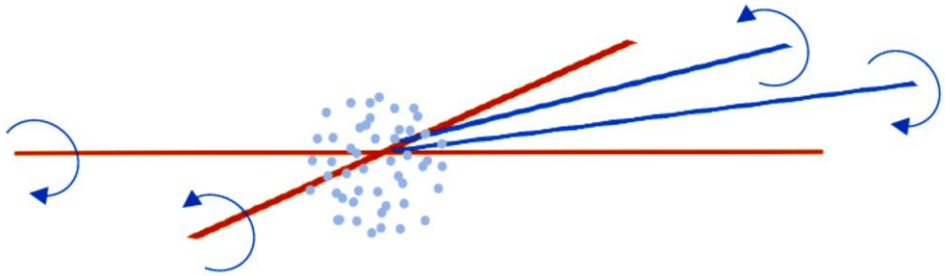


FIGURE 1. Scheme for two co-linear circular polarized beams generating high harmonics [28].

Using Strong Field Approximation with Lewenstein Model

In this paper, we use non-dipole and non-relativistic Strong Field Approximation (SFA) model within Lorentz force $\vec{F} = \vec{V}/c \times \vec{B}$ which is reduced photon emission [29,30]. Firstly, we noted that the Hamiltonian is

$$H = \left(\frac{1}{2}\left[-i\nabla + \vec{A}\left(\vec{r},t\right)\right]^2 + V_0 \right). \tag{1}$$

Considering the HHG in noble gas by two opposite circular polarized propagation wave vectors are

$$\vec{k} = k\left(\sin\left(\theta\right), 0, \cos\left(\theta\right)\right). \tag{2}$$

Then, defined vector potential and determined initial conditions $\left(z{=}0, kx\sin(\theta){=}\pi/2\right)$ [27].

$$\vec{A}\left(\vec{r},t\right) = \sum_{\pm} \frac{F}{2\omega} \begin{pmatrix} \cos\left(\theta\right)\cos\left(\vec{k}\cdot\vec{r}-\omega t\right) \\ \pm\sin\left(\vec{k}\cdot\vec{r}-\omega t\right) \\ \sin\left(\theta\right)\cos\left(\vec{k}\cdot\vec{r}-\omega t\right) \end{pmatrix} = \frac{F}{\omega} \begin{pmatrix} \cos\left(\theta\right)\cos\left(kz\cos\left(\theta\right)-\omega t\right)\cos\left(kx\sin\left(\theta\right)\right) \\ \cos\left(kz\cos\left(\theta\right)-\omega t\right)\sin\left(kx\sin\left(\theta\right)\right) \\ -\sin\left(\theta\right)\sin\left(kz\cos\left(\theta\right)-\omega t\right)\sin\left(kx\sin\left(\theta\right)\right) \end{pmatrix} \tag{3}$$

ISBN:978-605-83516-6-0

$$\vec{A}(\vec{r},t) \approx \frac{F}{\omega}\begin{pmatrix} \cos(kx\sin(\theta)) \\ \sin(kx\sin(\theta)) \\ 0 \end{pmatrix}\cos(\omega t) \tag{4}$$

$$\vec{A}(\vec{r},t) = \frac{F}{2\omega}\begin{pmatrix} 0 \\ \cos(\omega t) \\ \sin(\theta)\sin(\omega t) \end{pmatrix} \tag{5}$$

Transforming length gauge $(\vec{\nabla}\cdot\vec{A}=0)$ and here define Hamiltonian

$$H = \frac{1}{2}\left[-i\nabla + \vec{A}(0,t)\right]^2 + \frac{1}{c}\hat{k}\cdot\hat{r}\left[-i\nabla + \vec{A}(0,t)\right]\cdot\vec{F}(t) + V_0 \tag{6}$$

$$H = \frac{1}{2}\left[\hat{p} + (\hat{r}\cdot\vec{\nabla})\vec{A}(0,t)\right]^2 + \hat{r}\cdot\vec{F}(t) + V_0 \tag{7}$$

Then neglected $\left[(\hat{r}\cdot\vec{\nabla})\vec{A}(0,t)\right]^2$ terms in Equation (7), yields final Hamiltonian [27]

$$H = \frac{\hat{p}^2}{2} + \hat{r}\cdot\vec{\nabla}\vec{A}(t)\cdot\hat{p} + \hat{r}\cdot\vec{F}(t) + V_0 \tag{8}$$

The calculation of the harmonic emission caused by the above Hamiltonian is as conventional as in the case of dipole and the continuous wave function must be changed to express the non-dipole term. The solution of Equation (9) can be expressed as a time-dependent Lippmann-Schwinger equation containing the Green function $G_V^+(r,t;r',t')$ associated with $H(t)$ [31,32]. Lewenstein and co-workers using the SFA approach neglecting dipole moment and the full Green function is replaced by the non-dipole and non-relativistic Volkov state with the Hamiltonian which is described that free electron laser field interacted with ionic core [33,34].

The SFA approach definition of dipole moment in the strong laser field is

$$d(t) \propto \int_{-\infty}^{t} dt' \int dr dr' \phi_0^*(r,t)\, r G_V^+(r,t;r',t')\, H(t)\, \phi(r',t') + c.c \tag{9}$$

where the $\phi(r,t) = \phi_0(r)\exp(I_p t)$ is initial eigenstate of Hamiltonian, (I_p) is ionization potential and $G_V^+(r,t;r',t')$ is green function. In the dipole approximation Equation (9) has been neglected the ground state depletion [34,35]in order to take into account, the magnetic field component generalized easily Volkov state is

$$\left|\psi_p^V(t)\right\rangle = e^{-\frac{1}{2}\int \pi(\vec{p},\tau)^2 d\tau}\left|\pi(\vec{p},t)\right\rangle \tag{10}$$

where $\pi(\vec{p},t)$ momentum at the plane wave

$$\pi(\vec{p},t) = p + A(t) + \frac{1}{c}\left|\vec{p}\cdot\vec{A}(t) + \frac{1}{2}A^2(t)\right|\hat{k}\,. \tag{11}$$

Equation (11) modified monochromatic field and using $\int \vec{\nabla}\vec{A}d\tau \propto \frac{k}{\omega}A = \frac{1}{c}A$,

$$\pi(\vec{p},t) = p + A(t) + \int \vec{\nabla}\vec{A}(\tau)\cdot\left(\vec{p} + \vec{A}(\tau)\right)d\tau\,. \tag{12}$$

Then harmonic emission can be calculated with SFA approach by using non-dipole Volkov state wave function that gives dipole form

$$d(t) \propto \int_{t_0}^{t} dt' \int dp d\left(\pi(p,t)\right) e^{iS(p,t,t')} F(t') d\left(\pi(p,t')\right) + c.c. \tag{13}$$

where $S(p,t,t')$ is

$$S(p,t,t') = I_p(t-t') + \frac{1}{2}\int_{t'}^{t} \pi(p,t)^2\, d\tau\,. \tag{14}$$

ISBN:978-605-83516-6-0

In practical terms from the theoretical perspective the non-dipole Volkov states we use the basis of solution of Schrödinger equation by choosing circular polarization which tends to act in opposite direction intense laser field. Calculating the harmonic generation by this method is known as 'bicircular' laser field that is superposed of two opposite circular polarization [9-13,36-39].

In addition to here we show how to use non-collinear beams with opposite circular polarization with Mathematica program codes. The program run into non-dipole approximation in non-collinear strong magnetic field that its implementation is available at references 40 and 41. Fig. 2 shows that harmonic spectrum in non-dipole regime at 800 nm drivers for Argon atom and proposed $\sim 10^{15}\,W/cm^2$ [28] intensities with ionization potential $15.7eV$ [16] using $\theta = 4°$ half-angle beam. Finally, z-polarized harmonics eliminated because the region is arbitrary.

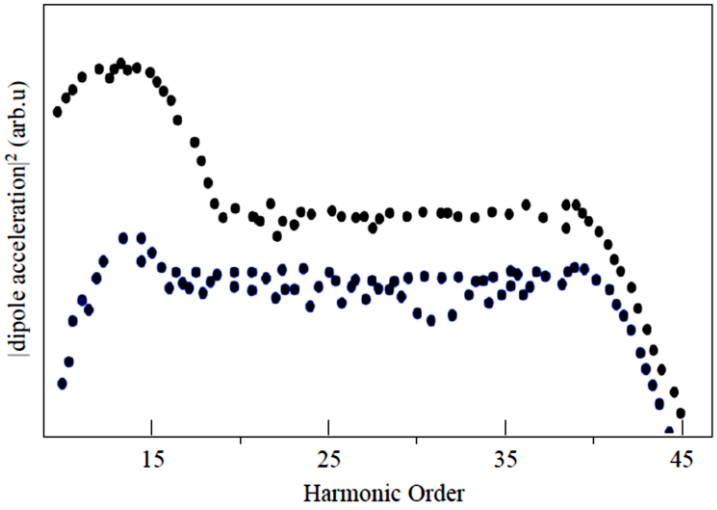


FIGURE 2. Harmonic spectrum (black dot is odd, and blue is even harmonics) produced in Argon atom at 800 nm in non-dipole regime for monochromatic laser field.

CONCLUSION

In recent breakthrough HHG techniques offers a lot of methods containing that are most commonly used non-collinear beams in which are opposite circularly polarized extreme ultraviolet driving laser light. Furthermore, all techniques proposed in the literature for the production of HHG based on Attosecond science. We summarize the mechanisms of non-collinear HHG and evaluate HHG spectrum for Argon atom interacted with 800 nm circular intense laser field. It is clear that the plateau and cutoff regions change dependence on the non-dipole effect. In the plateau regions, polarization calculation remains more smoothly connected to the field intensity of the harmonic phase, while the cutoff region maintaining perfectly in HHG spectrum. To conclude, we note that results of numerical calculation propose and analyze different schemes of HHG.

ACKNOWLEDGMENTS

This research has been supported by Sirnak University Scientific Research Projects Coordination Unit. Project Number: 2019.FNAP.06.03.01, 2019.

REFERENCES

1. E. Goulielmakis et al., Nature **466**, 739–43 (2010).
2. S. Baker, J.S. Robinson, C.A. Haworth et al., Science **31,** 424–7 (2006)
3. W. Li, X. Zhou, R. Lock, S. Patchkovskii et al., Science **322,** 1207–11(2008).
4. J. Itatani, J. Levesque, D. Zeidler et al., Nature **432**, 867–71 (2004).
5. A. L. Cavalieri et al., Nature **449** 1029–32 (2007).
6. J. L. Krause, K. J. Schafer, and K. C. Kulander, Phys. Rev. Lett. **68**, 3535 (1992).
7. P. Dietrich, N. H. Burnett, M. Ivanov, & P. B. Corkum, Phys. Rev. A **50**, R3585–R3588 (1994).

8. F. A. Weihe, et al. Phys. Rev. A **51**, R3433–R3436 (1995).
9. H. Eichmann, A. Egbert, S. Nolte, C. Momma & B. Wellegehausen, Phys. Rev. A **51,** R3414–R3417 (1995),
10. A. Fleischer, O. Kfir, T. Diskin, P. Sidorenko & O. Cohen, Nat. Photon. **8**, 543–549 (2014)
11. T. Fan et al., Natl Acad. Sci. USA **112**, 14206–14211 (2015).
12. O. Kfir et al., Nat. Photon. **9**, 99–105 (2015).
13. L. Medišauskas, J. Wragg, H. van der Hart & M. Y. Ivanov, Phys. Rev. Lett. **115**, 153001 (2015).
14. A. Husakou, F. Kelkensberg, J. Herrmann & M. J. J. Vrakking, Opt. Express **19**, 25346–25354 (2011).
15. K. J. Yuan and A.D. Bandrauk, Phys. Rev. A **83**, 063422 (2011).
16. D.B. Milošević, W. Becker & R. Kopold, Phys. Rev. A **61**, 063403 (2000).
17. K. Budil et al., Phys. Rev. A **48**, R3437 (1993).
18. Y. Liang et al., J. Phys. B **27**, 1296 (1994).
19. Y. Liang, et al., J. Phys. B **28**, 2757 (1995).
20. T. Brixner, et al., Phys. Rev. Lett. **92**, 208301 (2004).
21. S. Kerbstadt, L. Englert, T. Bayer & M. Wollenhaupt, J. Mod. Opt. **64**, 1010–1025 (2017).
22. I. Barth, & O. Smirnova, Phys. Rev. A **84**, 063415 (2011).
23. T. Herath, L. Yan, S. K. Lee, & W. Li, Phys. Rev. Lett. **109**, 043004 (2012).
24. A. Hartung, et al., Nat. Photon. **10**, 526–528 (2016).
25. D. Ayuso, et al., New J. Phys. **19**, 073007 (2017).
26. D. B. Milošević, Phys. Rev. A **93**, 051402(R) (2016).
27. E. Pisanty, D. D. Hickstein, B. R. Galloway, et al., arXiv:1606.01931v1, 1-6, (2016).
28. C. Hernandez-Garcıa, C. G. Durfee, et al., Phys. Rev. A, **93,** 043855 (2016).
29. D. B. Miloševic, S. Hu, and W. Becker, Phys. Rev. A **63**, 011403(R) (2000).
30. S. Brennecke and M. Lein, Phys. Rev. A **98**, 063414 (2018)
31. Bethe, H.A., Salpeter, E.E., 1957. Quantum mechanics of one and two electron atoms., In: Atoms I/Atome I. Encyclopedia of Physics, Handbuch der Physik, 7
32. Springer, Berlin, Heidelberg, H. R. Reiss, Physical Review A, **22**, 1786(1980).
33. M. Lewenstein, P. Balcou, et al., Phys. Rev. A, **49**(3), 2117-2132 (1994).
34. P. Salières, A. L'Huillier, P. Antoine, and M. Lewenstein, Adv. At. Mol. Opt. Phys., **41**, 83-142 (1999).
35. G. Tempea, M. Geissler and T. Brabec, J. Opt. Soc. Am. B **16**, 669 (1999).
36. S. Long, W. Becker and J. K. McIver. Phys. Rev. A **52** no. 3, 2262-2278 (1995).
37. D. B. Milosevic, W. Becker and R. Kopold, Phys. Rev. A **61** no. 6, 063 403 (2000).
38. E. Pisanty, S. Sukiasyan and M. Ivanov. Phys. Rev. A **90** no. 4, 043 829 (2014).
39. D. B. Milosevic, Phys. Rev. A **92** no. 4, 043 827 (2015).
40. E. Pisanty. RB-SFA: High Harmonic Generation in the Strong Field Approximation via Mathematica. https://github.com/episanty/RB-SFA (2016).
41. E. Pisanty. Figure-maker code and data for High harmonic interferometry of the Lorentz force in strong mid-infrared laser fields. Zenodo (2016).

BOOK OF FULL TEXT PROCEEDINGS TURKISH PHYSICAL
SOCIETY 35th INTERNATIONAL PHYSICS CONGRESS (TPS35)
TPS35, Vol.01, No.03, pp.173-177.
ISBN:978-605-83516-6-0

15 December 2019

Investigation of Structural, Geometric and Radical Properties of N-Propyl Alcohol by DFT Calculations

Ömer DERELİ[1,a], Ebru KARAKAŞ SARIKAYA[1]

[1] Konya Necmettin Erbakan University, A. Keleşoğlu Education Faculty, Department of Physics, Konya, Turkey

[a)] Corresponding author: odereli@erbakan.edu.tr

Abstract. The structural, geometric and radical properties of the N-Propyl alcohol ($CH_3CH_2CH_2OH$) were investigated using computational methods. This molecule is colorless and liquid. As a result of detailed conformational search of the N-Propyl alcohol, five different conformers of molecule have been obtained. For the most stable conformation, fourteen possible radicals were modelled by using DFT computations with respect to molecular structure. The geometry optimization of the title molecule and Electron Paramagnetic Resonance parameters of these model radicals were computed using the Gaussian 03W program package. A visualization of the calculated results was carried out via the Gaussview 5.0 program. And then calculated EPR parameters were compared with the experimental ones. In all computations, we used the Becke's three parameter exact exchange-functional combined with the gradient-corrected correlation functional of Lee, Yang, Parr in the DFT method with the 6-311++G(d,p) basis set.

INTRODUCTION

N-Propyl Alcohol (NPA) was obtained by fractional distillation of fuel oil. Indeed, NPA is a major constituent of fuel oil, a by-product formed from certain amino acids when potatoes or grains are fermented to produce ethanol[1]. NPA has high octane numbers and it is suitable for engine fuel usage. However, the production of propanol has been too expensive to make it a common fuel[2].

Structures of many molecules have not been determined or could not be determined using experimental techniques; it can be determined by molecular modeling techniques as in this study. Firstly conformational analysis was done in our paper, because the structure has not been determined experimentally yet. After conformational analysis, geometry optimization calculations were done. And then energies of molecules were compared and the stable conformer was detected. Using this conformer, model radicals were formed and EPR parameters of model radicals were determined. Consequently, theoretical and experimental values were compared.

EXPERIMENTAL

Experimental EPR study of NPA was taken from Livingston and Zeldes study[3]. In their article, the liquid sample was flowed through the microwave cavity of the spectrometer and was photolysis as it passed the sensitive region of the cavity. They have observed the steady-state concentration of short lived radicals. They were studied NPA containing up to 1 % H_20_2. They claimed that the radicals formed by abstraction of a hydrogen from the position alpha to the hydroxyl group. The experimental spectrum taken from article was shown in Fig. 1.

Türk Fizik Derneği
1950
Turkish Physical Society

ISBN:978-605-83516-6-0



FIGURE 1. The experimental spectrum of N-Propyl alcohol was taken from literature [3]**.**

COMPUTATIONAL DETAILS

The molecular structure was determined by scan the potential energy surfaces. This technique is known as conformational analysis. Conformational space of NPA was scanned by Spartan 08 program[4]. As a result of literature research, NPA molecule has two rotational isomers trans and gauche[5]. In our theoretical calculations results show us that five conformations were obtained. Conformational energies of molecule were seen from the Table 1. And geometry parameters of stable conformer 1 were given Table 2.

TABLE 1. Conformational energy of NPA in **water**

Conformation	Energies (kcal/mol)	Dipol Moment (Debye)
Conf1	-122003.675	2.3653
Conf2	-122003.551	2.1376
Conf3	-122003.436	2.3487
Conf4	-122003.340	2.3416
Conf5	-122003.284	2.1512

Then, geometry optimizations of these conformations were performed in liquid phase. The calculations of geometrical parameters in the ground state were performed by using the Gaussian 03W[6] Program. The output files were visualized via GaussView[7] software. The structural properties were determined through performing DFT/B3LYP method 6-311++G(d,p) basis set in water.

Table 2. The calculated geometry parameters of N-Propyl Alcohol by B3LYP/6-311++G(d,p) method in **water**

Bond lengths(A°)	Teo.	Bond angles (^{0})	Teo.	Dihedral angles (^{0})	Teo.
O1,C3	1.436	C3,O1,H12	108.2	H12,O1,C3,C2	-62.4
O1,H12	0.964	C3,C2,C4	112.4	H12,O1,C3,H7	177.0
C2,C3	1.526	C3,C2,H5	108.8	H12,O1,C3,H8	61.3
C2,C4	1.532	C3,C2,H6	108.9	C4,C2,C3,O1	178.4
C2,H5	1.095	C4,C2,H5	110.1	C4,C2,C3,H7	-60.7
C2,H6	1.097	C4,C2,H6	109.6	C4,C2,C3,H8	58.0
C3,H7	1.093	H5,C2,H6	106.8	H5,C2,C3,O1	-56.2
C3,H8	1.098	O1,C3,C2	113.0	H5,C2,C3,H7	61.5
C4,H9	1.093	O1,C3,H7	105.4	H5,C2,C3,H8	179.8
C4,H10	1.094	O1,C3,H8	110.0	H6,C2,C3,O1	59.9
C4,H11	1.094	C2,C3,H7	110.4	H6,C2,C3,H7	177.6
		C2,C3,H8	110.2	H6,C2,C3,H8	-63.7
		H7,C3,H8	107.6	C3,C2,C4,H9	179.7
		C2,C4,H9	111.0	C3,C2,C4,H10	-59.8
		C2,C4,H10	111.3	C3,C2,C4,H11	60.4
		C2,C4,H11	111.2	H5,C2,C4,H9	58.9
		H9,C4,H10	107.7	H5,C2,C4,H10	178.8
		H9,C4,H11	107.7	H5,C2,C4,H11	-61.0
		H10,C4,H11	107.8	H6,C2,C4,H9	-58.4
				H6,C2,C4,H10	61.5
				H6,C2,C4,H11	178.3

ISBN:978-605-83516-6-0

Energy, dipole moment, bond lengths, bond angles and dihedral angles for all conformers were calculated with DFT/B3LYP level of the theory 6-311++G (d, p) basis set in water. Energy values obtained from geometry optimization for each molecule were compared. The most stable conformer of NPA is the conformer 1 which has that a minimum energy value is -122003.675 kcal/mol. The most stable conformer's dipol moment is 2.3653 Debye. In Fig. 2, conformations are given.

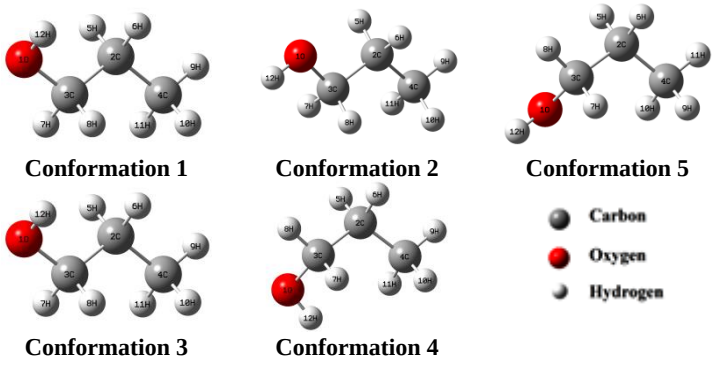


FIGURE 2. Stable conformers of the N-Propyl Alcohol molecule in water.

For the calculations of hyperfine coupling constants (hfccs) and g-values, the most stable conformation was used. Fourteen possible radicals were modelled for NPA, using this conformer. Model radicals were shown in Fig. 3. First two radicals; Model Radical 1 (MR1) and MR2 were modelled as the cation and anion of the NPA molecule, respectively. MR3 is a neutral radical formed by abstraction of H5 atom from the molecule. MR4 is cation form of MR3 and MR5 is anion form of MR3. MR6 is a neutral radical formed by abstraction of H7 atom from the molecule. MR7 and MR8 is cation and anion form of MR6, respectively. MR9 is a neutral radical formed by abstraction of H9 atom from the molecule. MR10 is cation form of MR9 and MR11 is anion form of MR9. MR12 is a neutral radical formed by abstraction of H12 atom from the molecule. MR13 is cation form of MR12 and MR14 is anion form of MR12.

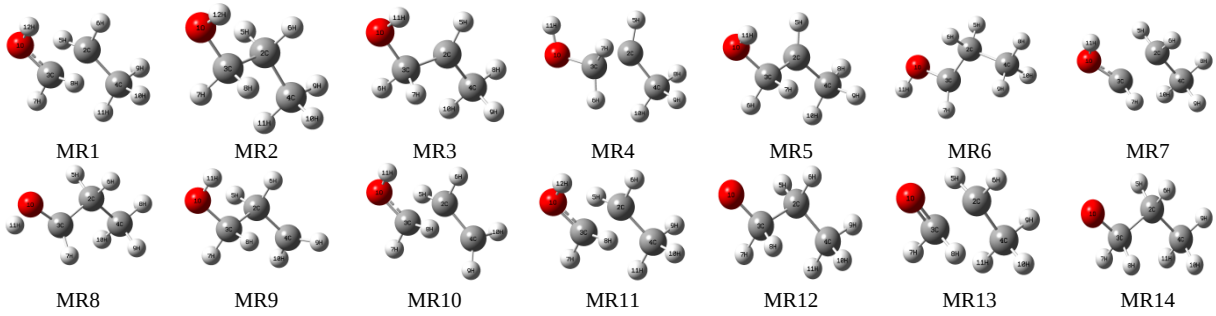


FIGURE 3. Model radicals of N-Propyl Alcohol molecule in water.

Hfccs and g-values of model radicals were computed within NMR /GIAO approach which is the most common method used to calculate EPR parameters and also we used that method previous study[8-12]. Hfccs and g-factors of modelled radicals were found by B3LYP method TZVP basis set obtained from Basis Set Exchange (BSE) software and the EMSL Basis Set Library of DFT after accomplished geometry optimization calculations.

ISBN:978-605-83516-6-0

RESULT and DISCUSSION

The spectrum for NPA taken from literature is shown in Fig.1. They suggested that two equivalent protons accused a 1-2-1 splitting with 21.4-G spacing and also a third proton accused a further splitting of 15.1 G in the spectrum. They said that the most reasonable radical in this spectrum was $CH_3CH_2\dot{C}HOH$. There were six lines with relative intensities 1-1-2-2-1-1 in spectrum like shown in figure 1. Theoretically modeled radicals MR6 is experimentally modeled radical. MR7 and MR8 is cation and anion form of MR6, respectively.

In combined experimental and theoretical EPR studies, similar to this study in the literature, as a comparison criterion, a deviation of 500 ppm between theory and experiment usually falls within the experimental error and even an agreement with theory within 1000 ppm (1 ppt) is considered satisfactory [13, 14]. Therefore difference between experimental and calculated g values of radical must lie within 1000 ppm. As seen as Table 3, MR2, MR3, MR5, MR6, MR9 and MR11 are in this area. Similarly, a criterion is used when comparing experimental and theoretical hfccs values. 20% deviations in experimental and theoretical calculations include intrinsically the errors originating from environmental effects. For most purposes of interpretation and assignment, 20% deviations would be quite acceptable for calculated isotropic hyperfine splitting values of experimentally isolated radicals[15].

Table 3. The theoretical and experimental hyperfine-splitting parameters (G) and g-values of model radicals in water

a_{iso}	MR1	MR2	MR3	MR4	MR5	MR6	MR7	Exp.[a]
5H	0.43	0.50	-	-	-	15.76	3.69	
6H	1.59	-0.76	-18.93	-1.00	-7.11	39.74	9.54	
7H	17.77	-3.55	23.16	6.32	12.34	-	-	
8H	17.17	-4.21	42.58	23.11	19.74	-8.57	44.82	
9H	49.91	-0.29	8.13	23.67	2.68	-0.73	30.10	
10H	4.15	-0.38	49.84	28.06	23.24	-0.51	0.26	
11H	3.97	-0.51	16.57	16.49	9.86	-0.64	3.05	
12H	-8.43	34.74	-0.28	-6.18	19.69	-3.55	23.84	g = 2.00319
g_{iso}	2.00502	2.00212	2.00267	2.00909	2.00269	2.00327	2.00656	a_H=21.46 G
a_{iso}	**MR8**	**MR9**	**MR10**	**MR11**	**MR12**	**MR13**	**MR14**	a_H=21.46 G
5H	8.63	13.42	20.75	6.00	0.71	1.11	-0.22	a_H=15.1 G
6H	18.07	11.70	19.94	5.80	0.77	1.15	-0.19	a_H=15.1 G
7H	-	-1.57	10.18	-2.57	76.07	68.89	38.02	
8H	-5.95	-1.46	9.05	-2.71	71.96	68.85	36.43	
9H	-0.47	-	-	-	-0.20	21.57	-1.99	
10H	-0.40	-20.53	-4.32	-10.09	0.18	1.33	-1.75	
11H	-0.46	-20.48	9.37	-10.13	0.16	1.34	-1.75	
12H	22.99	-0.29	-4.45	17.67	-	-	-	
g_{iso}	2.00430	2.00269	2.00872	2.00263	2.02220	2.01115	2.04382	

[a]Experimental values are taken from Ref[3]

Deviations from the experimental values of MR9 are less than 20%. When the theoretical and experimental values are compared using criteria, the proposed experimentally radical is not accurate. Radical was not correctly dedected in experimental study. In this study, different from the experimental study, MR9 ($\dot{C}H_2CH_2CH_2OH$) was suggested. This situation shows that theoretical studies are important.

ACKNOWLEDGMENT

This work was financially supported by the Bap, Necmettin Erbakan University in Turkey.

ISBN:978-605-83516-6-0

REFERENCES

1. M. James L. Unmack, CIH, Health-Base Assessment and Recommendation for HEAC (2011).
2. Bioalcohols, (2010), pp. Retrieved 16 Apr 2014.
3. R. Livingston and H. Zeldes, The Journal of Chemical Physics **44** (3), 1245-1259 (1966).
4. Irvine, (Wavefunction Inc., CA 92612, USA, 2008).
5. R. Alexander, G. Dearnaley, D. Morgan and J. Poate, PHYSICS LETTERS (1970).
6. M. J. Frisch and e. t. al., (Gaussian, Inc., Wallingford CT, 2003).
7. R. Dennington, T. Keith and J. Millam, Semichem Inc.: Shawnee Mission, KS (2009).
8. E. K. Sarikaya and Ö. Dereli, AIP Conference Proceedings **1815** (1), 030006 (2017).
9. E. K. Sarikaya and Ö. Dereli, AIP Conference Proceedings **1815** (1), 030005 (2017).
10. E. K. Sarikaya, Y. Erdoğdu and Ö. Derelı, AIP Publishing **2042** (1), 020019 (2018).
11. L. Ateş, Y. Erdoğdu, E. K. Sarıkaya, F. P. Özturan and Ö. Dereli, Selçuk-Teknik Dergisi, 15(3), 253-263 (2016).
12. Ö. Dereli, Y. Erdoğdu, L. Ateş, E. K. Sarıkaya and F. P. Özturan, Gazi University Journal of Science **30** (1), 161-165 (2017).
13. F. Neese, Journal of Chemical Physics **115** (24), 11080-11096 (2001).
14. L. Ates, O. Dereli, E. Turkkan, U. Sayin, F. Sevgi, R. Tapramaz and M. Birey, Journal of Molecular Structure **1005** (1-3), 8-11 (2011).
15. D. M. Chipman, in *Quantum mechanical electronic structure calculations with chemical accuracy* (Kluwer Academic Publishers, CANADA, 1994).

BOOK OF FULL TEXT PROCEEDINGS TURKISH PHYSICAL
SOCIETY 35th INTERNATIONAL PHYSICS CONGRESS (TPS35)
TPS35, Vol.01, No.03, pp.178-183.
ISBN:978-605-83516-6-0

15 December 2019

Molecular Structure and Conformational Analysis of "Phenacetin"

Ömer DERELİ[1,a], Ebru KARAKAŞ SARIKAYA[1]

[1] *Konya Necmettin Erbakan University, A. Keleşoğlu Education Faculty, Department of Physics, Konya, Turkey*

[a)] Corresponding author: odereli@erbakan.edu.tr

Abstract. Some spectral properties of "Phenacetin" were studied in advance without conformational analysis. In order to investigate the conformational distribution of the title compound, potential energy surface was scanned by molecular mechanic calculation. 43 different structures were obtained from this calculation. Then, these structures were optimized by high level B3LYP method and 6-311++G(d,p) basis set. At the last stage, after determination of the structures and energies of conformers, it was observed that structures and energies of some conformers overlapped. Extracting these overlapping conformers, 8 different conformers of the title compound were determined.

INTRODUCTION

In this study, our main aim is to emphasize the importance of conformational analysis used in molecular calculations, For this purpose, the phenacatin molecule was chosen as a useful example, Because both computational[1] and crystal structure [2] of this molecule have been studied before, useful data are available in the literature,

In molecular calculations, the reliability of the calculated physical or chemical property is directly related to initial geometry, Like the first button on a shirt, If the first button is incorrectly buttoned, all the other buttons will be incorrectly buttoned, Just like this, if the calculations start with the wrong geometry, all the other calculations will be wrong, Therefore, calculations can be started using experimental geometries, if available in the literature. Experimental geometry parameters are used as an initial geometry, and geometry optimization is done using appropriate method and basis set according to the desired sensitivity,

While working on molecules whose experimental geometry parameters have been unknown, it should be better to start calculations with conformational analysis instead of geometry optimizations.

There are two different techniques of conformational analysis in literatüre. The first of these, which is the most known and applied one, is manual technique. In this technique, dihedral angles, which provide rotation around single bonds, are determined and energy is calculated by rotating these dihedrals at the specified angles. During the scan, all the other geometrical parameters are simultaneously relaxed. This technique is the most known and applied one, but it is annoying if molecule has more than one single bond.

The latter, which is less known and applied one, is automatic technique. An easy and effective way of performing conformational analysis is searching conformational distrubition using Spartan 08. Computations using this technique can be performed in two different ways, depending on the molecular size, the calculation method, the desired sensitivity and the computer on which the calculations are made.

If the molecule being studied has a reasonable number of single bonds, the computational space of the molecule can be scanned and possible conformations can be determined automatically by calculations made with many functionals of DFT.

ISBN:978-605-83516-6-0

If the molecule being studied contains a large number of single bonds, calculations are started with molecular mechanic methods and then possible conformers are determined. Then these conformers are optimized by high level methods using Gaussian 03 program package. At the last stage, after determination of the structures and energies of conformers, it can be observed that structures and energies of some conformers overlap. After extracting these overlapping conformers, remaining conformers are real conformers which span the conformational space of studied structure.

While we were studying on the phenacatin molecule, we noticed that both calculated and experimental geometry parameters of the molecule were found in the literature. Computational structural study [1] was performed by Madanagopal et al. (This work is named as "example study" in the rest of the text) and experimental crystal structure [2] was studied by Hansen et al. However, the results of these two studies did not match. Therefore, in this study, the conformation analysis of the molecule was repeated with the above mentioned methods and the results were compared with the experimental data.

COMPUTATIONAL DETAILS

In this study, two different automatic techniques were used for conformational analysis. In both, all single bonds were rotated from 0 to 360 degrees by ten-degrees. In the first one, all calculations were made directly by B3LYP / 6-311 ++ G (d, p) method in Spartan14 program and 8 conformers obtained.

In the second one, calculations were started with molecular mechanic MMFF method and then 43 possible conformers were determined. Then, these conformers were optimized by B3LYP / 6-311 ++ G (d,p) method using Gaussian 03 program package. At the last stage, after determination of the structures and energies of these conformers, it was observed that structures and energies of some conformers overlapped. After extracting these overlapping conformers, remaining 8 conformers were determined.

RESULT AND DISCUSSION

The molecular structure obtained from the experimental study, and atomic numbering scheme of the phenacetin molecule is given in the following Fig. 1

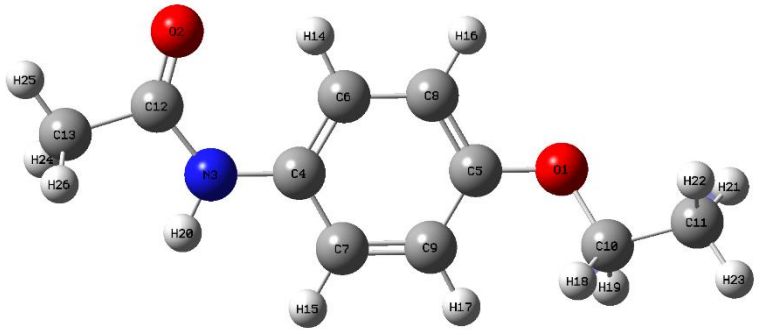


FIGURE 1. Molecular Structure and Atom numbering scheme of Phenacetin

In the example study, conformational analysis was performed by varying only one torsional angle C4-N3-C12-O2 and two conformers were found. However, the molecule contains six different single bonds (C13-C12, C12-N3, N3-C4, C5-O1, O1-C10, C10-C11) which may result in different conformational configurations. As it can be seen from that study, the authors used the manual technique and they considered turning only around a bond.

In this study, two different automatic techniques were used. The results obtained from these both techniques are the same. The energies, dipole moments and Boltzmann distributions of the obtained conformations are given in Table 1. Conformers are ordered from the lowest energy to the highest energy in this table.

ISBN:978-605-83516-6-0

TABLE 1. Energetics of the conformers calculated at the B3LYP/6311++G(d,p) level

Conformers	Energy (Hartree)	Relative Energy (kcal/mol)	Boltzman Distribution	Dipol Moment
Conformer 1	-594,27633629	0,0000	57,11%	2,3270
Conformer 2	-594,27589098	0,0004	35,63%	4,7399
Conformer 3	-594,27379013	0,0025	3,85%	2,2198
Conformer 4	-594,27325124	0,0031	2,18%	4,8633
Conformer 5	-594,27256243	0,0038	1,05%	5,3939
Conformer 6	-594,27000252	0,0063	0,07%	5,3461
Conf0rmer 7	-594,26997122	0,0064	0,07%	5,4071
Conformer 8	-594,26966263	0,0067	0,05%	4,6625

Results of computations have indicated that the title compound has 8 conformers as shown in Fig, 2. As it is seen in Table 1, conformer 1 is the most stable one. Therefore, the discussion will be based on this conformer, further in this paper.

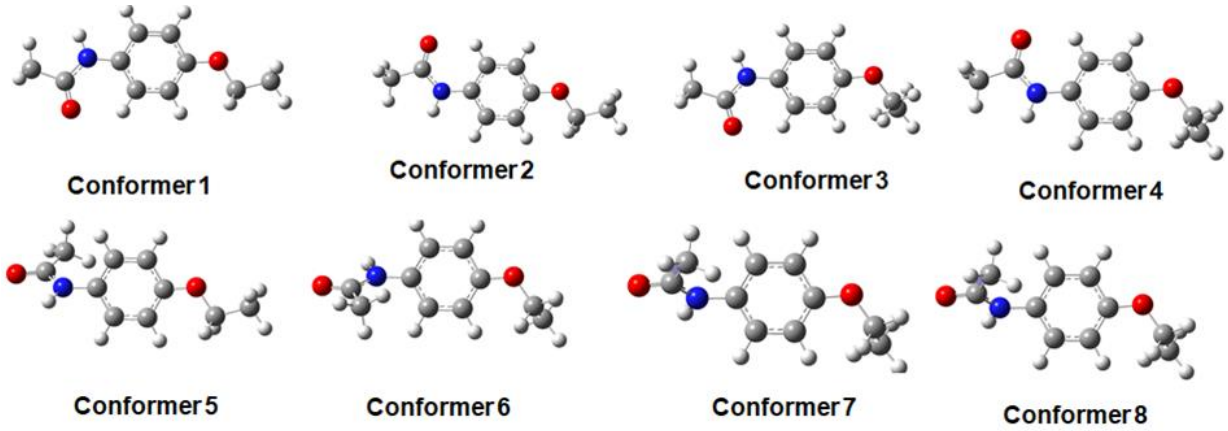


FIGURE 2. Stable conformers of Phenacetin

The calculated geometry parameters of conformer1 are given in Table 2. Comparison of these geometry parameters with literature values are also given in this table.

The first and second columns of Table 2 are filled with the values taken from the example study performed before. These belong to the results of HF/6-311++G(d,p) and B3LYP/6-311++G(d,p) computations, respectively. The values in the third column are the values of conformer 1 calculated in this study. The values in the fourth column are taken from the experimental crystal structure study.

ISBN:978-605-83516-6-0

TABLE 2, Geometric parameters of Phenacetin, bond lengths (Å) and angles (degrees)

	Literature[a]	Literature[b]	B3LYP/6311++G(d,p)[c]	Experimental[d]
Bond Lenghts (Å)				
C(13)-C(12)	1,511	1,516	1,52	1,50
C(12)-N(3)	1,363	1,378	1,374	1,34
C(12)-O(2)	1,202	1,220	1,22	1,23
C(11)-C(10)	1,513	1,516	1,517	1,51
C(10)-O(1)	1,416	1,431	1,429	1,422
C(9)-C(5)	1,387	1,401	1,395	1,479
C(9)-C(7)	1,386	1,386	1,397	1,386
C(8)-C(5)	1,387	1,397	1,4	1,377
C(8)-C(6)	1,386	1,395	1,384	1,374
C(7)-C(4)	1,388	1,400	1,396	1,374
C(6)-C(4)	1,388	1,393	1,404	1,385
C(5)-O(1)	1,358	1,362	1,366	1,374
C(4)-N(3)	1,423	1,425	1,416	1,421
Bond Angles (^{0})				
O(2)-C(12)-N(3)	120,44	120,23	123,948	122,797
O(2)-C(12)-C(13)	122,08	121,95	121,392	121,755
N(3)-C(12)-C(13)	117,46	117,81	114,66	115,448
O(1)-C(10)-C(11)	108,15	107,72	107,741	107,274
C(5)-C(9)-C(7)	119,85	120,39	120,768	120,060
C(5)-C(8)-C(6)	119,85	119,72	120,223	120,028
C(9)-C(7)-C(4)	120,57	120,68	120,193	120,753
C(8)-C(6)-C(4)	120,57	121,15	121,054	121,162
O(1)-C(5)-C(9)	119,99	115,88	125,042	125,085
O(1)-C(5)-C(8)	119,99	124,76	115,942	115,417
C(9)-C(5)-C(8)	119,97	119,35	119,015	119,497
N(3)-C(4)-C(7)	120,41	121,34	123,858	123,613
N(3)-C(4)-C(6)	120,41	119,96	117,395	117,883
C(7)-C(4)-C(6)	119,16	118,65	118,747	114,494
C(4)-N(3)-C(12)	127,63	129,25	129,152	127,317
C(5)-O(1)-C(10)	116,29	119,12	118,847	118,533
Dihedrals (^{0})				
C(13)-C(12)-N(3)-C(4)	0,007	1,002	-179,995	-178,702
O(2)-C(12)-N(3)-C(4)	-179,989	-179,163	0,007	1,214
C(11)-C(10)-O(1)-C(5)	-180	-179,163	-179,988	-171,656
C(7)-C(9)-C(5)-C(8)	0,191	0,419	-0,001	-0,299
C(7)-C(9)-C(5)-O(1)	178,306	-179,300	179,999	179,658
C(5)-C(9)-C(7)-C(4)	-0,274	-1,534	0	-0,378
C(6)-C(8)-C(5)-C(9)	-0,191	0,858	0,001	0,520
C(6)-C(8)-C(5)-O(1)	-178,306	-179,450	180	179,440
C(5)-C(8)-C(6)-C(4)	0,275	-1,049	-0,001	-0,074
C(9)-C(7)-C(4)-C(6)	0,354	1,3378	0	0,812
C(9)-C(7)-C(4)-N(3)	178,947	179,059	-179,998	-178,018
C(8)-C(6)-C(4)-C(7)	-0,354	-0,045	0	-0,591
C(8)-C(6)-C(4)-N(3)	178,947	-177,798	179,999	178,307
C(8)-C(5)-O(1)-C(10)	-90,934	-0,491	179,986	173,201
C(9)-C(5)-O(1)-C(10)	90,951	179,209	-0,015	-6,757

a:Results of HF/6-311++G(d,p) computation, taken from Ref. [1]
b: Results of B3LYP/6-311++G(d,p) computation, taken from Ref. [2]
c: Results of B3LYP/6311++G(d,p) computations of conformer1
d:Taken from Ref [2]

ISBN:978-605-83516-6-0

When the values given in this table were compared for bond lengths and bond angles, significant differences were not observed. But the same cannot be said for dihedral angles. While the values we obtained in this study for conformer 1 are in good agreement with the experimental values, the results of the example study are not in agreement with neither experimental values nor each other. The most important differences are observed in the dihedral angles C(13)-C(12)-N(3)-C(4), O(2)-C(12)-N(3)-C(4), C(8)-C(5)-O(1)-C(10) and C(13)-C(12)-N(3)-C(4). Fig. 2 shows the comparison between calculated (structure of this study and structures of example study are shown by tube model) and experimental (shown by ball-bond model) structures of phenacatin.

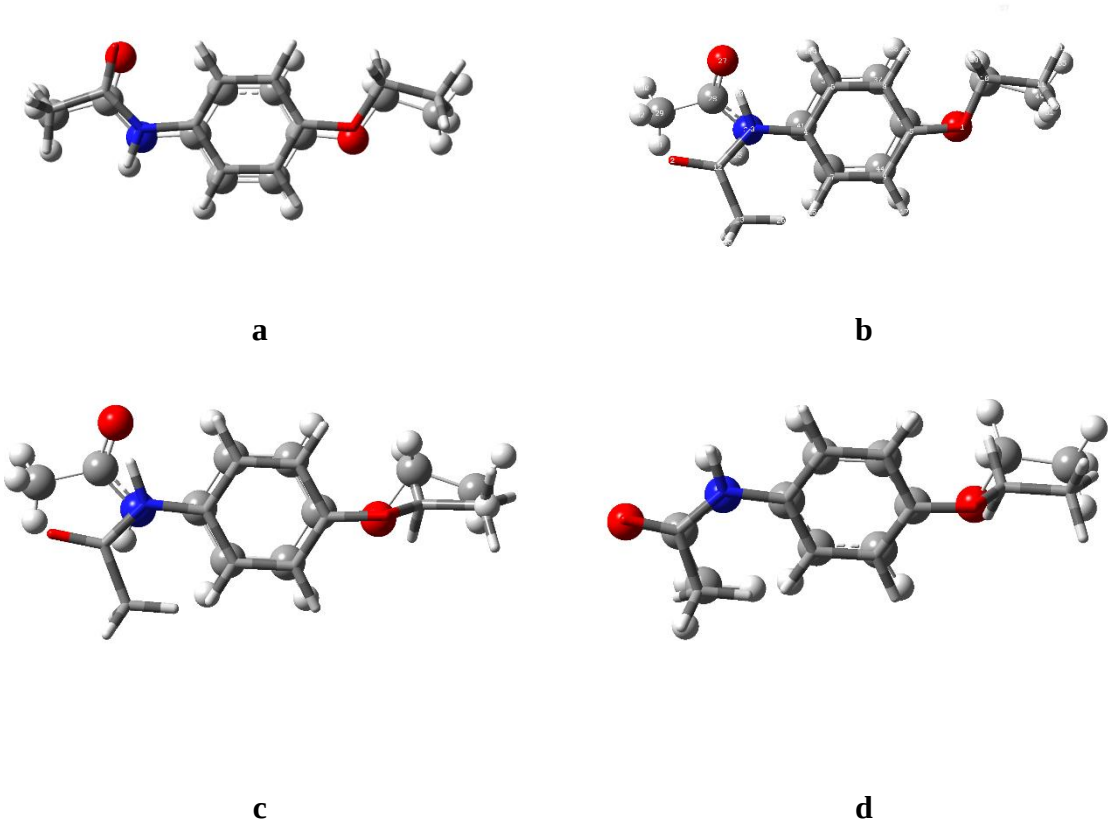


FIGURE 3: a Comparison of our structure with experimental structure, **b** Comparison of B3LYP/6-311++G(d,p) structure of example study with experimental structure, **c** Comparison of HF/6-311++G(d,p) structure of example study with experimental structure, **d** Comparison of structures taken from example structure

As seen in Fig. 3a, the structure obtained in this study coincides very well with the experimental structure. Many different methods were used in the example study. We took their B3LYP/6-311++G(d,p) and HF/6-311++G(d,p).results, because the results of the other calculations were almost the same as B3LYP/6-311++G(d,p), whereas HF/6-311++G(d,p) were different from them. This difference is clearly seen in Fig. 3d. We do not think that the change in the calculation method will cause such a big change in the molecular geometry. This difference is probably due to the selection of two different initial geometries. Conformational analysis by automatic techniques is not so dependent on initial geometry.

ISBN:978-605-83516-6-0

CONCLUSION

As it can be seen from this study, automatic conformation analysis methods are working quite successfully. There are many studies in the literature[3-7] that have been performed with this technique and have yielded good results. However, since it is not widely used, in studies where conformation analysis is performed with this technique, the referees persistently demand manual conformation analysis. Nevertheless, it is very difficult and sometimes impossible to perform conformal analysis by manual method for molecules containing too many single bonds. Sometimes the referees criticize the start of calculations by means of molecular mechanical methods in very large molecules. However, the aim of scanning potential energy surfaces by molecular mechanical methods is only to determine the location of the minimum. Scanning of the conformation space using ab-initio methods in large molecules containing a large number of single bonds is difficult and laborious.

Referees express concerns about the sensitivity of calculations made by molecular mechanical methods. They may seem justified in their concern, but this relates to the depth of the minimums on the potential energy surface. After the location of the minimum is determined by molecular mechanic methods, the depth of the minimum can be found more sensitively through ab -initio geometry optimizations. This is exactly what was done in this study. In the example study, conformation analysis was performed by manual technique and stable structure was found. However, the structure in the example study did not coincide with the experimental structure. In this study, conformational analysis was performed using both of the automatic techniques, and it was observed that the results of the computations performed with both techniques overlap both each other and the experimental structure.

ACKNOWLEDGMENT

This work was financially supported by the Bap, Necmettin Erbakan University in Turkey.

REFERENCES

1. A.Madanagopala, S.Periandy, P. Gayathri, S.Ramalingam, S.Xavier, Journal of Molecular Structure, **1127**, 611-625 (2017)
2. L. Kr. Hansen, G. L. Perlovich, A. Bauer-Brandl, Acta Crystallographica Section E, **E62**, o2712–o2713, (2006)
3. Ö. Dereli, Optics And Spectroscopy, 120(5), 690–700 (2016).
4. E. K. Sarıkaya, Ö. Dereli, Y. Erdoğdu, M.T. Güllüoğlu, Journal of Molecular Structure, 1049, 220–226 (2013).
5. M. Yilmaz, B. Aydin, O. Dogan, Ö. Dereli, Journal of Molecular Structure, 1128, 345–354 (2017).
6. Ö. Dereli, Y. Erdogdu, M.T. Gulluoglu, Journal of Molecular Structure, 1012, 105–112 (2012).
7. S. Kalaichelvan, N. Sundaraganesan, Ö. Dereli, U. Sayin, Spectrochimica Acta Part A: Molecular and Biomolecular Spectroscopy, 85(1), 198–209 (2012).

BOOK OF FULL TEXT PROCEEDINGS TURKISH PHYSICAL
SOCIETY 35th INTERNATIONAL PHYSICS CONGRESS (TPS35) 15 December 2019
TPS35, Vol.01, No.03, pp.184-187.
ISBN:978-605-83516-6-0

Molecular Structure and Conformational Analysis of "(R)-2-Methylamino-1-Phenylethanol"

Ersin DURGUT[1,a], Ebru KARAKAŞ SARIKAYA[1], Ömer DERELİ[1]

[1] *Konya Necmettin Erbakan University, A. Keleşoğlu Education Faculty, Department of Physics, Konya, Turkey*

[a)] Corresponding author: erdurgut@gmail.com

Abstract. "(R)-2-Methylamino-1-Phenylethanol" was synthesized and some spectroscopic properties studied in advance. Conformational analysis of the tittle compound was performed by Spartan 14 program automatically, and 61 different structures were obtained. B3LYP functionals of Density Functional Theory and B3LYP/6-311++G(d,p) basis sets were used for geometry optimizations of all these structures. All these calculations were performed by Gaussian 03 program. As a results of calculations, 19 stable conformers of the tittle compound were determined. Molecular structure and some molecular properties of the most stable conformer were calculated.

INTRODUCTION

Molecular structure, conformational analysis and some spectroscopic properties of 2-Methylamino-1-Phenylethanol (MAPE) were studied before[1]. In that study, conformatiolal analysis was performed by manuel techniques. It is difficult to perform manuel conformational analysis for the molecules that have more than one single bonds. MAPE has five single bonds which can be cause different conformations.

In this study conformational analysis of MAPE was performed by automatic technique of Spartan 14 program. Obtained structure was compared with the structure of the study[1] which conformational analysis was performed by manuel technique.

COMPUTATIONAL DETAILS

In this study Conformational analysis was performed in the same way as in the previous study of 3-Aminocoumarin[2].

RESULT AND DISCUSSION

Sixty one different conformers of MAPE were obtained from MMFF computations. It is known that sensitivity of MMFF computations lover than ab-initio. For that reason, B3LYP/6-311++G(d,p) geomety optimizations were performed for all these 61 conformers. Results of geometry optimizations shown that energies and structures of some conformers overlapped. When these overlapped conformers were extracted, 19 different conformers were obtained. These conformers are stable conformers which are span the conformational space of MAPE. Some energy parameters of these conformers are given in Table 1. Because zero point energies did not show significant difference, zero point corrections were not given in this table. Molecular shapes of these conformers were given in Fig. 1

ISBN:978-605-83516-6-0

TABLE 1. Conformational energy parameters and dipol moment of MAPE

Conformers	Energy (Hartree)	Boltzman Distibution	Relative	Dipol
Conf01	-480,88844063	60,3204%	0,000	3,0943
Conf02	-480,88762689	25,4785%	0,001	2,8056
Conf03	-480,88703273	13,5794%	0,001	1,0751
Conf04	-480,88294771	0,1794%	0,005	2,3532
Conf05	-480,88263792	0,1292%	0,006	1,0374
Conf06	-480,88226770	0,0873%	0,006	0,9055
Conf07	-480,88210070	0,0732%	0,006	2,0505
Conf08	-480,88147664	0,0378%	0,007	2,0480
Conf09	-480,88139639	0,0347%	0,007	1,0530
Conf10	-480,88082252	0,0189%	0,008	1,4436
Conf11	-480,88081501	0,0187%	0,008	1,3182
Conf12	-480,88063782	0,0155%	0,008	2,2397
Conf13	-480,88025844	0,0104%	0,008	2,7608
Conf14	-480,87969407	0,0057%	0,009	2,3959
Conf15	-480,87946404	0,0045%	0,009	1,0051
Conf16	-480,87905998	0,0029%	0,009	1,6637
Conf17	-480,87854227	0,0017%	0,010	0,6991
Conf18	-480,87803887	0,0010%	0,010	2,6513
Conf19	-480,87769617	0,0007%	0,011	1,3785

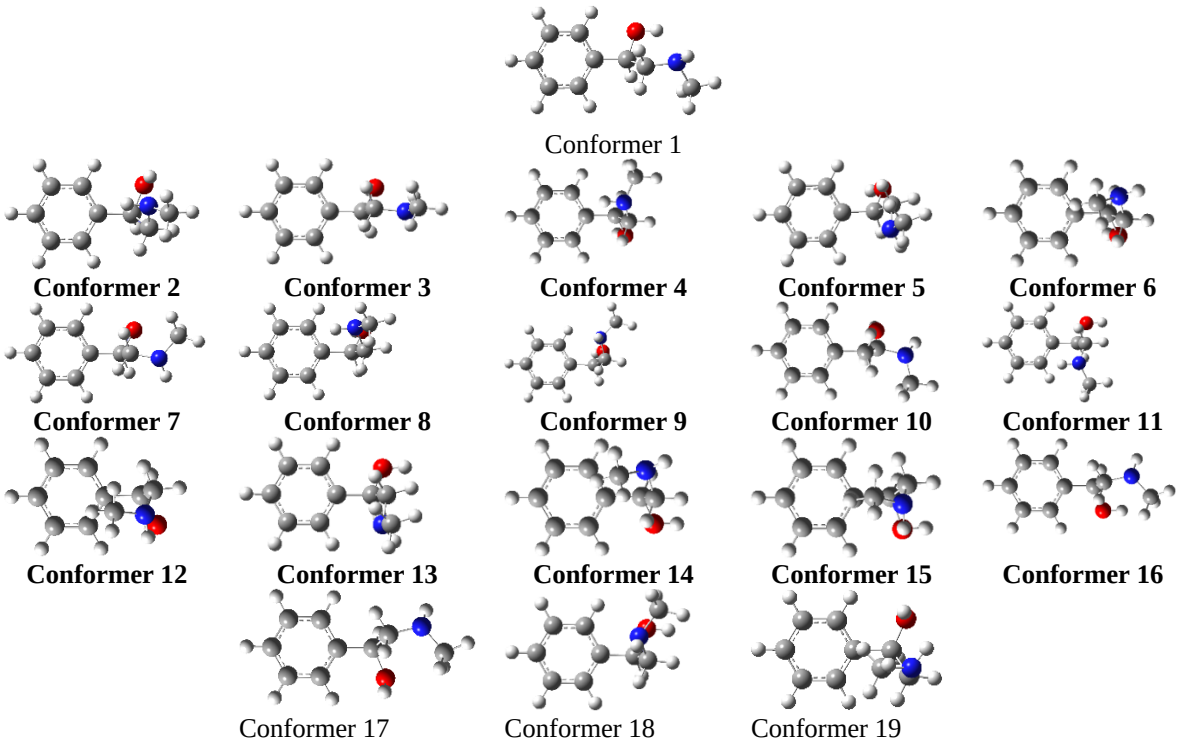


FIGURE 1. Stable conformers of MAPE

As it is seen in Table 1, the most stable conformer of MAPE is conformer 1. So, from this point all discussions will be based on this conformer, further in this manuscript. Molecular shapes of conformer 1 and the structure taken from literature were compared in Fig. 2. Structural parameters of them were compared in Table 2.

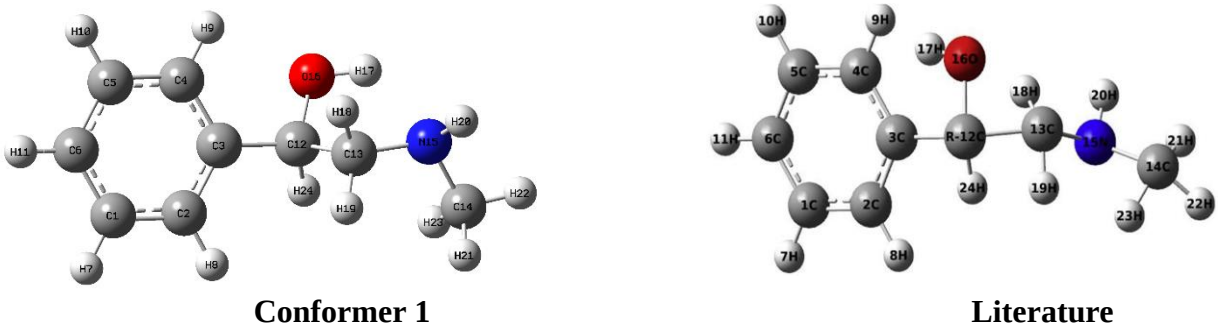


FIGURE 2. Comparison of Molecular structure of MAPE obtained in this study and Literature

TABLE 2. Comparison of geometry parameters of MAPE with literatüre

Parameters	Conf1	Literature[a]	Parameters	Conf1	Literature[a]	Parameters	Conf1	Literature[a]
Bond Lenght			***Bond Angles***			***Dihedral Angles***		
H(24)-C(12)	1.101	1.1001	H(18)-C(13)-H(19)	107.929	107.0736	C(14)-N(15)-C(13)-C(12)	-84.530	88.9731
H(23)-C(14)	1.093	1.0984	C(3)-C(12)-C(13)	111.213	115.3299	H(19)-C(13)-C(12)-H(24)	-55.648	-58.7111
H(22)-C(14)	1.092	1.0947	C(3)-C(12)-O(16)	110.607	112.4593	H(19)-C(13)-C(12)-O(16)	-174.707	-174.6324
H(21)-C(14)	1.101	1.0931	C(3)-C(12)-H(24)	108.061	107.9274	H(19)-C(13)-C(12)-C(3)	63.142	60.7314
H(20)-N(15)	1.012	1.0125	C(13)-C(12)-O(16)	108.919	105.362	H(18)-C(13)-C(12)-H(24)	-172.957	55.8623
H(19)-C(13)	1.101	1.0941	C(13)-C(12)-H(24)	108.610	106.1442	H(18)-C(13)-C(12)-O(16)	67.984	-60.0589
H(18)-C(13)	1.093	1.0963	O(16)-C(12)-H(24)	109.388	109.3436	H(18)-C(13)-C(12)-C(3)	-54.167	175.3049
H(17)-O(16)	0.971	0.963	H(11)-C(6)-C(5)	120.268	120.2876	N(15)-C(13)-C(12)-H(24)	69.103	177.267
O(16)-C(12)	1.419	1.4324	H(11)-C(6)-C(1)	120.184	120.219	N(15)-C(13)-C(12)-O(16)	-49.956	61.3457
N(15)-C(14)	1.463	1.4596	C(5)-C(6)-C(1)	119.545	119.4918	N(15)-C(13)-C(12)-C(3)	-172.107	-63.2905
N(15)-C(13)	1.465	1.452	H(10)-C(5)-C(6)	119.950	120.0146	H(24)-C(12)-C(3)-C(2)	36.426	36.253
C(13)-C(12)	1.546	1.548	H(10)-C(5)-C(4)	119.658	119.6818	H(24)-C(12)-C(3)-C(4)	-145.423	-144.257
C(12)-C(3)	1.514	1.5194	C(6)-C(5)-C(4)	120.390	120.3035	O(16)-C(12)-C(3)-C(2)	156.139	156.9465
H(11)-C(6)	1.084	1.0842	H(9)-C(4)-C(5)	120.660	119.9583	O(16)-C(12)-C(3)-C(4)	-25.710	-23.5634
H(10)-C(5)	1.085	1.0846	H(9)-C(4)-C(3)	118.952	119.403	C(13)-C(12)-C(3)-C(2)	-82.694	-82.2017
H(9)-C(4)	1.083	1.0836	C(5)-C(4)-C(3)	120.377	120.6365	C(13)-C(12)-C(3)-C(4)	95.457	97.2883
H(8)-C(2)	1.086	1.0861	C(12)-C(3)-C(4)	121.123	121.7987	C(1)-C(6)-C(5)-C(4)	-0.400	-0.3878
H(7)-C(1)	1.085	1.0845	C(12)-C(3)-C(2)	119.933	119.6111	C(1)-C(6)-C(5)-H(10)	179.248	179.6807
C(6)-C(5)	1.394	1.3931	C(4)-C(3)-C(2)	118.919	118.5883	H(11)-C(6)-C(5)-C(4)	-179.838	-179.9296
C(6)-C(1)	1.394	1.3951	H(8)-C(2)-C(3)	119.698	119.5871	H(11)-C(6)-C(5)-H(10)	-0.190	0.1389
C(5)-C(4)	1.394	1.3948	H(8)-C(2)-C(1)	119.555	119.532	C(5)-C(6)-C(1)-C(2)	0.113	0.1901
C(4)-C(3)	1.397	1.3982	C(3)-C(2)-C(1)	120.744	120.8806	C(5)-C(6)-C(1)-H(7)	-179.265	-179.2926
C(3)-C(2)	1.399	1.3998	H(7)-C(1)-C(6)	120.135	120.0665	H(11)-C(6)-C(1)-C(2)	179.552	179.7322
C(2)-C(1)	1.393	1.3923	H(7)-C(1)-C(2)	119.841	119.8391	H(11)-C(6)-C(1)-H(7)	0.173	0.2495
Bond Angles			C(6)-C(1)-C(2)	120.021	120.0923	C(6)-C(5)-C(4)-C(3)	0.111	-0.0999
C(12)-O(16)-H(17)	104.826	108.8097	***Dihedral Angles***			C(6)-C(5)-C(4)-H(9)	178.896	-179.5665
C(13)-N(15)-C(14)	115.077	117.5138	H(17)-O(16)-C(12)-H(24)	-84.617	64.4389	H(10)-C(5)-C(4)-C(3)	-179.538	179.8318
C(13)-N(15)-H(20)	110.249	110.8301	H(17)-O(16)-C(12)-C(13)	33.955	178.1456	H(10)-C(5)-C(4)-H(9)	-0.753	0.3652
C(14)-N(15)-H(20)	110.227	112.4263	H(17)-O(16)-C(12)-C(3)	156.472	-55.4368	C(5)-C(4)-C(3)-C(2)	0.459	0.7713
N(15)-C(14)-H(21)	113.265	108.7996	H(20)-N(15)-C(14)-H(23)	-168.855	69.72	C(5)-C(4)-C(3)-C(12)	-177.711	-178.7238
N(15)-C(14)-H(22)	109.434	109.0825	H(20)-N(15)-C(14)-H(22)	-51.014	-168.6599	H(9)-C(4)-C(3)-C(2)	-178.346	-179.7592
N(15)-C(14)-H(23)	110.086	115.4341	H(20)-N(15)-C(14)-H(21)	70.276	-52.0743	H(9)-C(4)-C(3)-C(12)	3.484	0.7457
H(21)-C(14)-H(22)	108.575	107.1589	C(13)-N(15)-C(14)-H(23)	65.718	-60.725	C(4)-C(3)-C(2)-C(1)	-0.748	-0.972
H(21)-C(14)-H(23)	107.881	108.1811	C(13)-N(15)-C(14)-H(22)	-176.441	60.8952	C(4)-C(3)-C(2)-H(8)	178.595	178.8361
H(22)-C(14)-H(23)	107.419	107.8814	C(13)-N(15)-C(14)-H(21)	-55.151	177.4808	C(12)-C(3)-C(2)-C(1)	177.444	178.5344
C(12)-C(13)-N(15)	110.046	117.5908	H(20)-N(15)-C(13)-H(19)	-87.082	-166.2444	C(12)-C(3)-C(2)-H(8)	-3.214	-1.6575
C(12)-C(13)-H(18)	107.898	105.5012	H(20)-N(15)-C(13)-H(18)	32.346	77.5111	C(3)-C(2)-C(1)-C(6)	0.466	0.4991
C(12)-C(13)-H(19)	109.648	108.7437	H(20)-N(15)-C(13)-C(12)	150.055	-42.2048	C(3)-C(2)-C(1)-H(7)	179.846	179.983
N(15)-C(13)-H(18)	108.271	108.7379	C(14)-N(15)-C(13)-H(19)	38.333	-35.0664	H(8)-C(2)-C(1)-C(6)	-178.878	-179.3091
N(15)-C(13)-H(19)	112.895	108.7086	C(14)-N(15)-C(13)-H(18)	157.761	-151.311	H(8)-C(2)-C(1)-H(7)	0.503	0.1748

[a]Taken from ref1

As it can be seen in Table 2, there is no significant difference between the bond lengths and bond angles of the two structures. The difference between these two structures is easily seen in terms of dihedral angles and Fig. 2.

CONCLUSION

There are two different conformational analysis technique in the literature. One of them can be named as manual technique and the other can be named as automatic technique. It is difficult to perform manuel conformational analysis for the molecules that have more than one single bonds. However, conformational analysis of MAPE was performed by manual technique in a literature study[1].

Conformational analysis, performed by automatic technique, of molecules containing more than one single bond yielded quite successful results [3-6]. In these studies, the structures of the most stable conformations were compared with the experimental structures and very good fit was obtained.

In this study, conformational analysis of MAPE was performed by automatic technique and different structure from literature was obtained.

REFERENCES

[1]. K. Subashini, R. Govindarajan, R. Surendran, K. Mukund, S. Periandy, Journal of Molecular Structure, **1125**, 576–591 (2016).

[2].Ö. Dereli, Optics And Spectroscopy, **120(5)**, 690–700 (2016).

[3] E. K. Sarıkaya, Ö. Dereli, Y. Erdoğdu, M.T. Güllüoğlu, Journal of Molecular Structure, **1049**, 220–226 (2013).

[4] M. Yilmaz, B. Aydin, O. Dogan, Ö. Dereli, Journal of Molecular Structure, **1128,** 345–354 (2017).

[5] Ö. Dereli, Y. Erdogdu, M.T. Gulluoglu, Journal of Molecular Structure, **1012**, 105–112 (2012).

[6] S. Kalaichelvan, N. Sundaraganesan, Ö. Dereli, U. Sayin, Spectrochimica Acta Part A: Molecular and Biomolecular Spectroscopy, **85(1)**, 198–209 (2012).

BOOK OF FULL TEXT PROCEEDINGS TURKISH PHYSICAL
SOCIETY 35th INTERNATIONAL PHYSICS CONGRESS (TPS35) 15 December 2019
TPS35, Vol.01, No.03, pp.188-192.
ISBN:978-605-83516-6-0

Theoretical Calculations of Electron Paramagnetic Resonance Parameters of Liquid Phase Isopropyl Alcohol

Ersin DURGUT[1,a], Ebru KARAKAŞ SARIKAYA[1], Ömer DERELİ[1]

[1] *Konya Necmettin Erbakan University, A. Keleşoğlu Education Faculty, Department of Physics, Konya, Turkey*

[a)] Corresponding author: erdurgut@gmail.com

Abstract. Isopropyl Alcohol is a compound with the chemical formula $CH_3CHOHCH_3$. It is a colorless, flammable chemical compound with a strong odor. As a first step of the molecular structure calculation of Isopropyl Alcohol, the conformational analysis were done by using the Spartan14 program and two conformers were determined. And then geometry optimizations were performed with Becke's three-parameter hybrid-exchange functional combined with the Lee–Yang–Parr correlation functional (B3LYP) method and the standard 6-311++G(d,p) basis sets in liquid phase using Gaussian03 program. The most stable conformation energy is -194.43035 a.u. Including recommended radical in experimental study, total fourteen radicals were modeled. Hfccs and g-factors of the modeled radicals were calculated by the B3LYP method using the TZVP basis set and compared with the experimental counterparts. Small differences between experimental and calculated parameters may come from the environment of the compound.

INTRODUCTION

Isopropyl Alcohol (IPA) which has antibacterial properties is an isomer of propyl alcohol. Though the exact mechanism of isopropanol's disinfecting action is not known, it might kill cells by denaturing cell proteins and DNA, interfering with cellular metabolism, and dissolving cell lipo-protein membranes[1]. IPA is used in making cosmetics, skin and hair preparations, pharmaceuticals, perfumes, lacquer formulations, dye solutions, antifreezes, soaps, window cleaners[2]. Electron Paramagnetic Resonance (EPR) spectroscopy is a technique for the study of species containing one or more unpaired electrons. In essence, the technique is not only a very sensitive one but also provides a wealth of further detail about the radicals. However, it is not possible to determine the radical formed in the structure by the experimental method alone. Therefore, theoretical calculation techniques should be used.

Since there is no experimental structure, we started our study by conducting conformation analysis. And geometry optimization calculations were done. And then energies of molecules were compared, the stable conformer was detected. Using this conformer, model radicals were form. EPR parameters of model radicals were determined. Consequently, theoretical and experimental values were compared.

EXPERIMENTAL

Livingston and Zeldes[3] in their study observed the steady-state concentration of short-lived radicals. They studied IPA containing up to 0.4% H_2O_2. The radical which formed by abstraction of a hydrogen from the position alpha to the hydroxyl group is caused by the addition of hydrogen peroxide. They recommend that the radical was $(CH_3)_2\dot{C}OH$ and seven lines in spectrum with relative intensities 1-6-15-20--15-6-1 arise from the six equivalent

Türk Fizik Derneği
1950
Turkish Physical Society

ISBN:978-605-83516-6-0

protons, and each of these lines was split into a doublet by the hydroxyl-proton interaction at room temperature. The experimental spectrum taken from article was shown in Fig. 1.



FIGURE 1. The experimental spectrum of IPA at 26^0C was taken from Livingston and Zeldes study[3].

COMPUTATIONAL DETAILS

In first place, the calculations were started with the conformational analysis. Conformational analysis of IPA was performed by Spartan 08 program[4]. In our study, we identified two conformations.

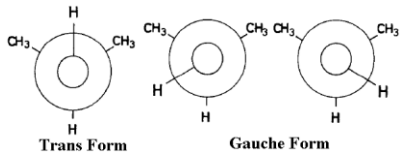


FIGURE 2. Schematic diagram of rotational isomers of IPA[5]

When searching in the literature experimental structure parameters, two rotational isomers (Trans and Gauche) were detected for the IPA molecule from the analysis of the microwave spectrum as shown in Fig.2. Isomers are that each of two or more compounds with the same formula but a different arrangement of atoms in the molecule and different properties. Fig. 3 shows that the conformation 1 is the gauche form of molecule and the conformation 2 is the Trans form of molecule. As a result of our calculations, conformation 1 is more stable than conformation 2.

TABLE 1. Conformational energy of IPA in water

Conformation	Energies (a.u.)	Dipol Moment (Debye)
Conf1	-194.43035	2.3185
Conf2	-194.38630	2.3504

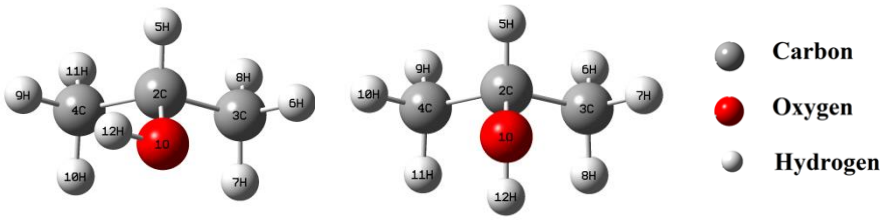


FIGURE 3. Stable conformers of the IPA molecule in water and acetone

Then, geometry optimizations of these conformations were performed in liquid phase. Conformational energies of molecule were seen from the Table 1. And geometry parameters of stable conformer were given Table 2. The structural properties were determined through performing DFT/B3LYP method 6-311++G(d,p) basis set in water.

ISBN:978-605-83516-6-0

Table 2. The calculated geometry parameters of IPA by B3LYP/6-311++G(d,p) method in water

Bond lengths(A°)	Teo.	Bond angles (^{0})	Teo.	Dihedral angles (^{0})	Teo.
O1,C2	1.44	C2,O1,H12	108.3	H12,O1,C2,C3	179.2
O1,H12	0.96	O1,C2,C3	106.6	H12,O1,C2,C4	-57.6
C2,C3	1.52	O1,C2,C4	110.9	H12,O1,C2,H5	62.0
C2,C4	1.53	O1,C2,H5	108.4	O1,C2,C3,H6	-57.6
C2,H5	1.10	C3,C2,C4	112.8	O1,C2,C3,H7	62.6
C3,H6	1.09	C3,C2,H5	109.0	O1,C2,C3,H8	177.5
C3,H7	1.09	C4,C2,H5	109.0	C4,C2,C3,H6	179.7
C3,H8	1.09	C2,C3,H6	110.7	C4,C2,C3,H7	-59.4
C4,H9	1.09	C2,C3,H7	110.5	C4,C2,C3,H8	60.4
C4,H10	1.09	C2,C3,H8	110.4	H5,C2,C3,H6	59.2
C4,H11	1.09	H6,C3,H7	108.5	H5,C2,C3,H7	179.4
		H6,C3,H8	108.3	H5,C2,C3,H8	-60.7
		H7,C3,H8	108.4	O1,C2,C4,H9	59.4
		C2,C4,H9	111.0	O1,C2,C4,H10	-61.0
		C2,C4,H10	110.5	O1,C2,C4,H11	178.9
		C2,C4,H11	110.5	C3,C2,C4,H9	178.9
		H9,C4,H10	108.4	C3,C2,C4,H10	58.6
		H9,C4,H11	107.7	C3,C2,C4,H11	-61.6
		H10,C4,H11	108.5	H5,C2,C4,H9	-59.9
				H5,C2,C4,H10	179.8
				H5,C2,C4,H11	59.6

To provide accurate calculations for hyperfine-splitting and g-values, precise geometric structures of possible radicals were needed. After the most stable conformer of the title compound was determined, the possible radicals were modeled by *ab-initio* computations. Including recommended radical in experimental study, all possible radicals were modeled in this study. Fourteen possible radicals were modelled for IPA using this conformer and model radicals were shown in Fig. 4. Model Radical 1 **(MR1)** is a radical **cation** and MR2 is radical **anion** of molecule. MR3 is a neutral radical formed by abstraction of **H5** atom from the molecule. MR4 is cation form of MR3 and MR5 is anion form of MR3. MR6 is a neutral radical formed by abstraction of **H6** atom from the molecule. MR7 and MR8 is cation and anion form of MR6, respectively. MR9 is a neutral radical formed by abstraction of **H9** atom from the molecule. MR10 is cation form of MR9 and MR11 is anion form of MR9. MR12 is a neutral radical formed by abstraction of **H12** atom from the molecule. MR13 is cation form of MR12 and MR14 is anion form of MR12.

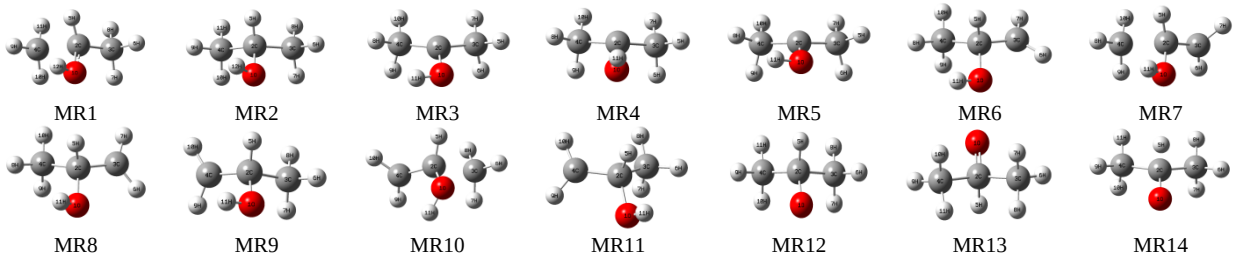


FIGURE 4. Model radicals of IPA molecule in water

Hfccs and g-values of model radicals were computed within NMR /GIAO approach. Hfccs and g-factors of modelled radicals were found by B3LYP method TZVP basis set obtained from Basis Set Exchange (BSE) software and the EMSL Basis Set Library of DFT after accomplished geometry optimization calculations.

ISBN:978-605-83516-6-0

RESULT AND DISCUSSION

The spectrum for IPA taken from literature is shown in Fig.1. They suggested that seven lines in spectrum arise from the six equivalent protons and their relative intensities were 1-6-15-20-15-6-1 and then each of these lines was split. However, our calculations showed that the calculated radicals had no six equivalent protons. Furthermore, if the spectrum is examined, there may be four identical protons of relative intensities 1-4-6-4-1. In combined experimental and theoretical EPR studies, as a comparison criterion, a deviation of 500 ppm between theory and experiment usually falls within the experimental error and even an agreement with theory within 1000 ppm (1 ppt) is considered satisfactory[6-11]. Therefore difference between experimental and calculated g values of radical must lie within 1000 ppm. As seen as Table 3, MR3, MR5, MR6, MR8, MR9 and MR11 are in this area. Similarly, a criterion is used when comparing experimental and theoretical hfccs values. 20% deviations in experimental and theoretical calculations include intrinsically the errors originating from environmental effects. For most purposes of interpretation and assignment, 20% deviations would be quite acceptable for calculated isotropic hyperfine splitting values of experimentally isolated radicals[12].

Table 3. The theoretical and experimental hyperfine-splitting parameters (G) and g-values of model radicals in water

a_{iso}	**MR1**	**MR2**	**MR3**	**MR4**	**MR5**	**MR6**	**MR7**	**Exp.**[a]
5H	39.63	-5.20	-	-	-	45.21	20.56	
6H	26.70	-0.13	11.38	10.79	5.42	-	-	
7H	6.00	3.55	40.72	13.41	19.63	-19.76	-8.34	
8H	-1.22	6.69	4.84	1.94	5.05	-20.60	-1.35	
9H	-5.32	-1.52	11.54	9.84	4.70	0.27	-0.82	
10H	-1.95	-0.47	41.10	13.65	19.04	-1.00	-1.50	
11H	6.81	5.04	3.98	2.77	6.10	-0.77	7.28	
12H	-9.33	31.72	-2.63	9.90	22.81	-0.07	-3.34	
g_{iso}	2.00544	2.00202	2.00316	2.00692	2.00377	2.00265	2.00924	g =2.00317
a_{iso}	**MR8**	**MR9**	**MR10**	**MR11**	**MR12**	**MR13**	**MR14**	a_{β}=19.66 G,
5H	14.95	8.87	26.48	16.75	26.28	82.43	65.44	a_{OH}=0.70 G
6H	-	8.54	-1.29	1.55	-2.78	-0.58	-0.07	
7H	-8.20	-1.10	-0.02	-0.15	-2.87	1.83	1.08	
8H	-7.18	0.59	6.09	2.91	12.91	5.18	1.62	
9H	1.76	-	-	-	-0.24	-0.17	-0.07	
10H	-0.68	-19.38	-7.61	-8.24	0.30	1.38	1.08	
11H	2.95	-20.91	-0.91	-7.67	0.76	5.22	1.62	
12H	18.65	-1.29	-6.78	20.15	-	-	-	
g_{iso}	2.00230	2.00250	2.00896	2.00229	2.02154	2.00983	2.02939	

[a]Experimental values are taken from Ref[3]

But their hfccs values not agreement with each other. The reason for this is the complexity of the spectrum shown in Figure 1. In the experimental study, the researchers stated that they could not completely solve the spectrum. Theoretical calculations show that the theoretically suggested MR5 may be the experimental observed radical. Repeating the experiment in better conditions would be appropriate.

ACKNOWLEDGMENT

This work was financially supported by the Bap, Necmettin Erbakan University in Turkey.

ISBN:978-605-83516-6-0

REFERENCES

1.https://ncit.nci.nih.gov/ncitbrowser/ConceptReport.jsp?dictionary=NCI_Thesaurus&ns=NCI_Thesaurus&code =C 602.
2. https://cameochemicals.noaa.gov/chemical/946.
3. R. Livingston and H. Zeldes, The Journal of Chemical Physics **44** (3), 1245-1259 (1966).
4. Irvine, (Wavefunction Inc., CA 92612, USA, 2008).
5. S. Kondo and E. Hirota, Journal of Molecular Spectroscopy **34** (1), 97-107 (1970).
6. F. Neese, Journal of Chemical Physics **115** (24), 11080-11096 (2001).
7. Ö. Dereli, Y. Erdoğdu, L. Ateş, E. K. Sarıkaya and F. P. Özturan, Gazi University Journal of Science **30** (1), 161- 165 (2017).
8.Ö. Derelı, E. K. Sarikaya and Y. Erdoğdu, presented at the AIP Conference Proceedings, 2018 (unpublished).
9. E. K. Sarikaya and Ö. Dereli, AIP Conference Proceedings **1815** (1), 030006 (2017).
10. E. K. Sarikaya and Ö. Dereli, AIP Conference Proceedings **1815** (1), 030005 (2017).
11. E. K. Sarikaya, Y. Erdoğdu and Ö. Derelı, AIP Publishing **2042** (1), 020019 (2018).
12. D. M. Chipman, in *Quantum mechanical electronic structure calculations with chemical accuracy* (Kluwer Academic Publishers, CANADA, 1994).

BOOK OF FULL TEXT PROCEEDINGS TURKISH PHYSICAL
SOCIETY 35th INTERNATIONAL PHYSICS CONGRESS (TPS35) 15 December 2019
TPS35, Vol.01, No.03, pp.193-202.
ISBN:978-605-83516-6-0

In Silico Analysis of Hair Growth Peptide

Serda Kecel-Gunduz,[1] Esra Koc,[2] Bilge Bicak,[1, 2] Yagmur Kokcu,[2]
Aysen E. Ozel,[1] and Sevim Akyuz[3]

[1)] *Istanbul University, Faculty of Science, Physics Department, 34134, Istanbul, Turkey*
[2)] *Institute of Graduate Studies in Sciences, Istanbul University,34452, Istanbul, Turkey*
[3)] *Physics Department, Science and Letters Faculty, Istanbul Kultur University, Atakoy Campus, Bakirkoy 34156, Istanbul, Turkey*

Abstract. AHK (Alanine-Histidine-Lysine) tripeptide, known as an antioxidant because of its amino acid properties, has been clinically developed for the treatment of hair loss and skin rash. The copper complex of this tripeptide (AHK-Cu) is an analog with a stronger effect than the Gly-His-Lys (GHK-Cu) tripeptide which is used for hair growth. The effects of AHK-Cu on human hair growth were evaluated by in vitro studies [1] and the results showed that AHK-Cu promotes the growth of human hair follicles. In addition, Vitamin C conjugated AHK has been developed to increase collagen synthesis and promote human dermal fibroblast growth. These results provided important data for the development of peptide-based bone regenerative agents for the treatment of bone-related disorders [2]. The aim of this study is to determine the most stable geometric structure of AHK tripeptide by using theoretical methods with different approaches to determine the binding properties with proteins that can act in the body. Firstly, the most stable molecular structure of tripeptide was determined with the help of quantum mechanical method, which included electronic interactions in the calculation. Then, the most efficient structure of the tripeptide in the water medium such as the human body was determined using Molecular Dynamic (MD) analysis. In addition; the binding properties of title tripeptide was investigated by molecular docking technique. The discovery and improvement of the structure and activity of cosmetic peptide is an active field of study, particularly in biochemistry and pharmacology.

Keywords: AHK, L-Alanine-L-Histidine-L-Lysine, tripeptide-copper complex, DFT, MD, Molecular Docking

INTRODUCTION

Drugs are a very important factor that affect human life and health. Unfortunately, the discovery of molecules result in safe and effective drugs involves a process that has high cost, production, development and testing stages; they must go through certain stages as a result of the experiments performed in the laboratory, and then include clinical research. Designing and developing the most effective drug in a short time and with lower costs attracts the attention of many scientists working in different fields. In the process of designing the most effective drug, in silico methods are preferred because it minimizes time and cost. The appropriate drug structures obtained in accordance with the calculations made with in silico methods also allow more rational drug designs by reducing the processes of organic synthesis with high budget. The aim of molecular modeling methods that define molecular systems at the atomistic level is to show how atoms and molecules can interact with a three-dimensional image and simulation, and to determine the structure of these interaction mechanisms. These models can also be used to interpret existing observations or to predict new chemical behaviors. In the drug design process, in silico methods have become a valuable and necessary tool for the modeling of molecular structures that have been nominated for drugs, for increasing the effectiveness of drugs, and for the design of new drug molecules with unknown molecular structure. With these methods, it is possible to examine the relationship between chemical structure and function from small systems to large biologic molecules and material groups. The contribution of modern computer-aided drug design to the discovery of drugs is an indisputable fact and is understood to have been used by large pharmaceutical companies in many commercially available drugs. Modern computer-aided drug design has contributed to the discovery and development of many medicines such as Captopril, Dorzolamide, Saquinavir, Zanamivir, Oseltamivir, Aliskiren, Boceprevir, Nolatrexed, Rupintrivir, and NVP-AUY922.

AHK (Alanine-Histidine-Lysine) tripeptide which shows antioxidant effect because of its amino acid properties, has been clinically developed for the treatment of hair loss and skin rash [3, 4]. It is claimed that copper peptides can increase hair follicle size and create a healthier environment for the growth of scalp hairs. AHK copper complex (AHK-Cu) is an analog of Gly-His-Lys copper complex (GHK-Cu), which has antioxidant and anti-inflammatory effects, is recommended for wound healing, enhancing the effect of immune cells, stimulating collagen synthesis, skin fibroblasts and the growth of blood vessels. The effects of AHK-Cu on human hair growth were evaluated many in-vitro and ex-vivo studies [1] and it also promotes the growth of human hair follicles [5]. It provides an increase dermal cell multiplication and viability to help to production of collagen [6]. It has also stronger effect than GHK-Cu for hair growth. Vitamin C conjugated AHK has been developed to increase collagen synthesis and promote

Türk Fizik Derneği
1950
Turkish Physical Society

human dermal fibroblast growth. These results provided important data for the development of peptide-based bone regenerative agents and for the treatment of bone-related disorders [2]. The aim of this study is to determine the most stable molecular structure of AHK tripeptide, which is a very effective field of cosmetic use, and to identify the binding mechanisms by proteins with which it acts.

MATERIALS AND METHODS

Molecular Dynamic Method

Molecular Dynamic Simulation was performed using the GROMACS software (version 5.1.2) [7] to determine the conformational change in the water medium on the optimized geometry, calculated at DFT/B3LYP level of theory with the 6-311++ G (d,p) basis set, of the AHK in the vacuum medium obtained by the Gaussian 09 software program [8]. Initially, the GROMOS96 54a7 force field [9] was chosen where the topology file would be created to perform molecular dynamic simulation. AHK tripeptide was placed at the center, a distance of 1.0 nm between the outside of the molecule and the edge of the solvent box, and simulated with water medium. The cubic box was filled with 978 moles of SPC (simple point charge) water [10] mediums and two Na+ and three Cl- ions were added in the cubic box to neutralize the system. The steepest descent method was chosen for the energy minimization at 200 ps for water medium. To equilibrate the temperature and pressure of the systems, NVT (50 ps) and NPT (500 ps) ensembles were carried out for 310 K temperature using a V-rescale thermostat [11] and 1 bar pressure using the isotropic Parrinello-Rahman barostat [12]. To obtain the trajectory files during 5 ns for analysis the systems behaviors', Molecular dynamics (MD) simulations were performed by applying periodic boundary conditions in all three directions. Leap-frog algorithm was used in equation of motion was united in order to generate time-dependent trajectories. All bond lengths were constrained with the LINCS (linear constraint solver) algorithm [13]. The Particle Mesh Ewald (PME) method [14] was used to calculate the long-range electrostatic interaction with a grid width of 0.16 nm and a fourth order cubic interpolation. Verlet cut-off scheme [15] was used with a 0.8 nm cut-off radius for identified the cut-off distances, the van der Waals and the short-range electrostatic interactions. The atom coordinates, velocities and energies were saved every step and obtained the trajectory files. The resulting of trajectory files were viewed and analyzed with the VMD software [16].

Molecular Docking Method and ADME Analysis

The molecular structure of the AHK tripeptide, which was subjected to molecular dynamics simulation in the water medium for 5 ns at GROMACS program introduced to Schrödinger Maestro program for use as a ligand in the calculation of docking. Schrödinger Lig Prep module was used to prepare ligand to docking analysis. AHK was prepared for docking calculations using the OPLS3 force field [17]. A maximum of 24 stereoisomers were produced for the ligand after the ionization states at pH 7.0±2.0 were selected. The tripeptide-copper complex, defined as a growth factor, stimulates the proliferation of dermal fibroblasts and increases vascular endothelial growth factor production, while at the same time decreasing the secretion of transformed growth factor-beta1 by dermal fibroblasts. For this reason, transforming growth factor-β (TGFβ) receptor kinase inhibitors have a great therapeutic potential. The TGFBR1 gene provides instructions for making a protein called transforming growth factor-beta (TGF-β) receptor type 1. This receptor transmits signals from the cell surface into the cell through a process called signal transduction. Through this type of signaling, the environment outside the cell affects activities inside the cell such as stimulation of cell growth and division. The docking analysis of AHK tripeptide onto a Transforming growth factor-β (TGFβ) (3TZM) was also conducted [18] and prefered as a receptor and was prepared with Protein preparation wizard tool [19] in Schrödinger software. The receptor was obtained from the PDB database but due to the lack of residues in the protein structure, the crystal structure was obtained using the SWISS-MODEL server [20]. All waters, metals and ions except protein were deleted from the data file. The polar hydrogens were added to the heavy atoms in the protein. The bond orders were assigned, charges were defined at pH 7.0 and the selected receptor was optimized using PROPKA [21]. The heavy atoms in the receptor were converged by preferring 0.3Å RMSD and the OPLS3 force field. After the grid was generated using glide grid generation tool, drug candidate molecule was docked to the receptors using Glide SP (standard precision) module of the Maestro version 11.4 [22, 23, 24]. Determination of the pharmacokinetic properties of drug candidate molecules is very important for the design and synthesis of drugs with better bioavailability. The drug

candidate compounds which easily absorbed orally, easily transported to the target region (skin, stomach, blood brain barrier) in the body and easily removed from the body are determined by ADME profiles which are required by the FDA in the drug approval process [25]. The Qik-Prop module was used to determine the ADME profile of the AHK tripeptide.

RESULTS AND DISCUSSIONS

Molecular Dynamics Results

Molecular Dynamic Simulation was performed using the GROMACS software (version 5.1.2) to determine the conformational change in the water medium on the optimized geometry, calculated at DFT/B3LYP level of theory with the 6-311++ G (d,p) basis set, of the AHK in the vacuum medium obtained by the Gaussian 09 software program. The AHK tripeptide was trapped in 978 moles of water molecule and two Na+ and three Cl- ions were added to ensure system neutralization in Fig. 1. For the energy minimization, the steepest descent method was chosen at 200 ps for water medium in Fig. 2. Using the NVT (50 ps) and NPT (500 ps) assemblies, the temperature and pressure of the system were brought to 310 K and 1 bar, respectively, and a 5 ns Molecular dynamic (MD) simulation was performed, thereby examining the conformational change of the peptide in a similar environment to the human body. During the simulation, the RMSD value of AHK tripeptide in water medium was found to be in the range of 0.02 - 0.1 nm in Fig. 3. A rmsd of about 0.2 nm or less indicates that the peptide is in its original crystal form. The Rg change graph was also plotted for 5 ns. According to this graph, the constant Rg value to a relatively constant mean tells us that the peptide has stable structure in the water medium in Fig. 4.

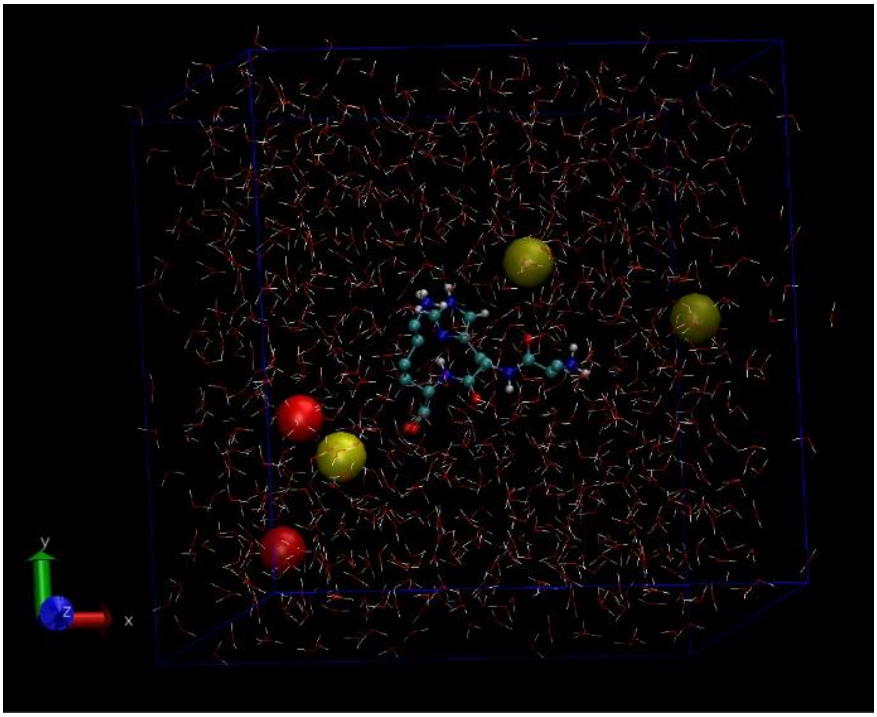


FIGURE 1. AHK tripeptide in a cubic box solvated with 978 SPC water molecules with two Na^+ and three Cl^- ions.

ISBN:978-605-83516-6-0

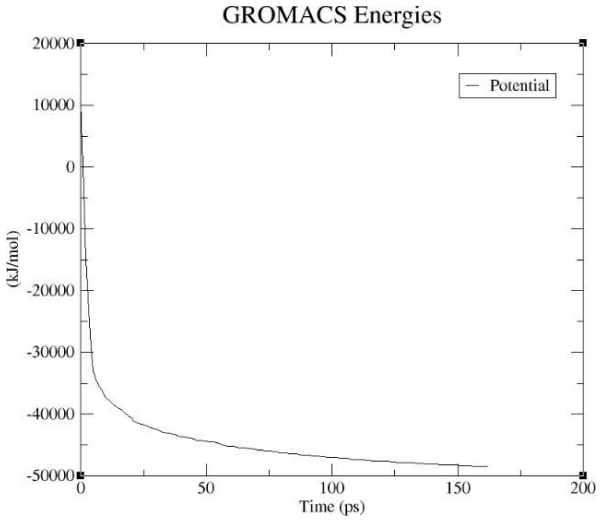


FIGURE 2. The potential energy minimization of the system using the Steepest Descent algorithm for water medium system of AHK tripeptide.

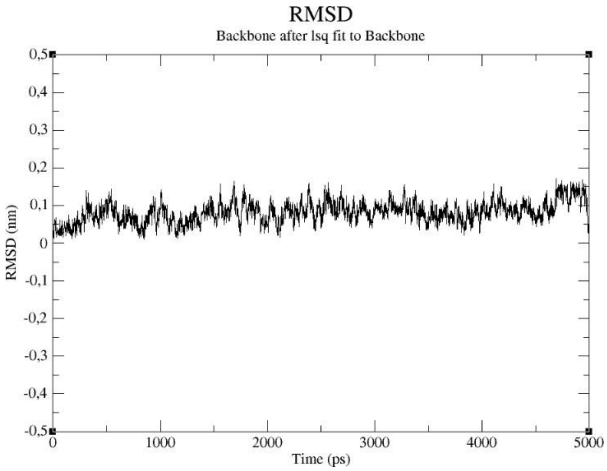


FIGURE 3. The RMSD values of the water medium system of AHK tripeptide.

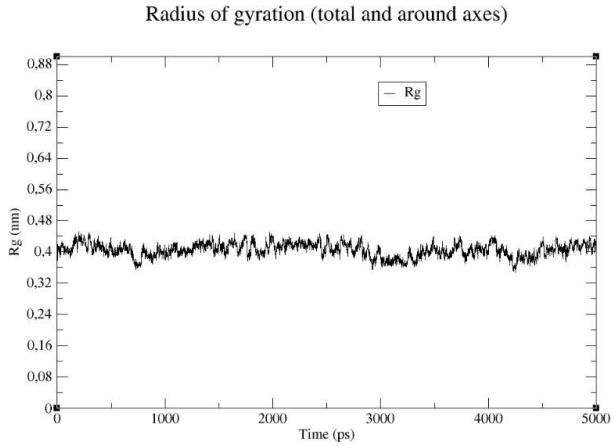


FIGURE 4. The Radius of gyration valuesof the water medium system of AHK tripeptide.

Molecular Docking and ADME Results

The docking analysis of AHK tripeptide onto a Transforming growth factor-β (TGFβ) (pdb code: 3TZM) was performed and the most possible binding energies were calculated at -8.640 kcal / mol in Fig. 5. and Fig. 6. In the active region of the protein in which the AHK tripeptide interacts with, the green, blue, dark blue and orange colored parts represent regions of hydrophobic, polar, positively charged and negatively charged amino acids, respectively in Fig. 7. The strong hydrogen bonds formed resulted in the formation of stable binding poses between AHK tripeptide and protein. As shown in Fig. 7 and Fig. 8, the hydrogen bonds formed with LEU-84 (2.29 Å), SER-86 (1.80 Å and 1.93 Å), ASP-96 (1.55 Å) and two salt bridges LYS-38 and ASP-96 residues for Transforming growth factor-β (TGFβ) receptor kinase inhibitors were revealed. The electrostatic potential of the Transforming growth factor-β (TGFβ) and the docked pose of the AHK was shown in Fig. 9. The ADME profile, in which the pharmacokinetic properties of AHK was determined by Qikprop tool of the Maestro software in Table I). Pharmacokinetic parameters which are required for predicting the drug-like properties of molecules were defined based on Lipinski 5s rule. According to this rule; the molecular weight should not be greater than 500Mw, no more than 5 hydrogen bond donors, no more than 10 hydrogen bond acceptors, and the octanol / water partition coefficient should not be greater than 5. AHK tripeptide has 354 g/mol molecular weight, 6.5 hydrogen bond donors and 9 hydrogen bond acceptors, and the calculated value of octanol / water partition coefficient was-3.393. The rate of skin permeability (SP) is a very important pharmacokinetic property for the transdermal effect of drugs and cosmetics, especially in the fields of medicine and cosmetics. The calculated QP log Kp for skin permeability (Kp in cm/hr) value of AHK tripeptide was -9.435. It is also important to know the ability to cross the blood brain barrier. The calculated brain/blood partition coefficient (QPlogBB) is -2.398 and is within the recommended range of value (-3.0 – 1. 2).

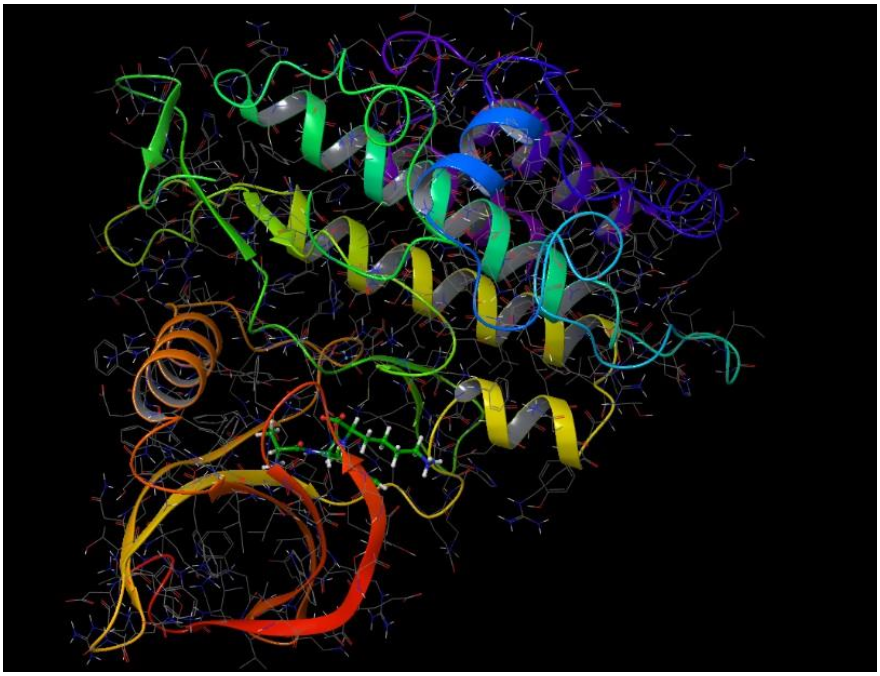


FIGURE 5. The binding poses between the active site of the Transforming growth factor-β (TGFβ) receptor kinase inhibitor and AHK tripeptide.

ISBN:978-605-83516-6-0

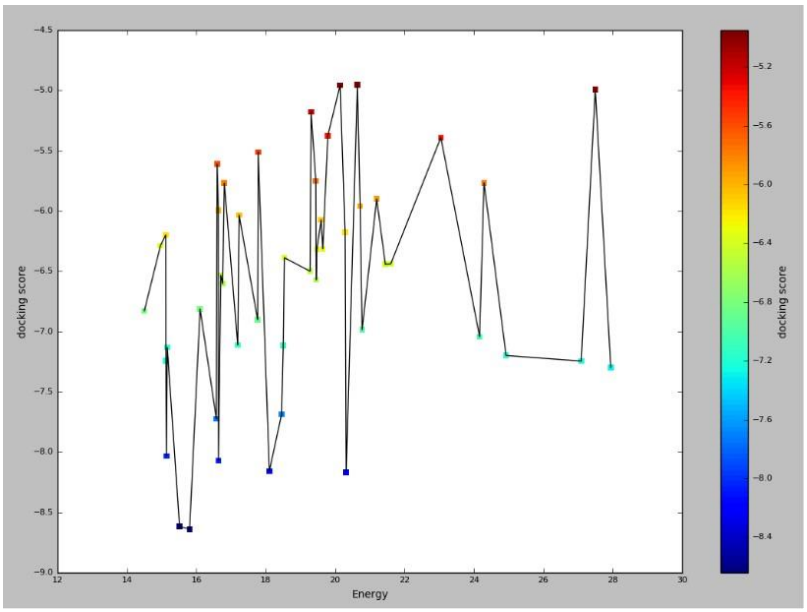


FIGURE 6. The possible docking score values and their energies between the Transforming growth factor-β (TGFβ) and AHK tripeptide.

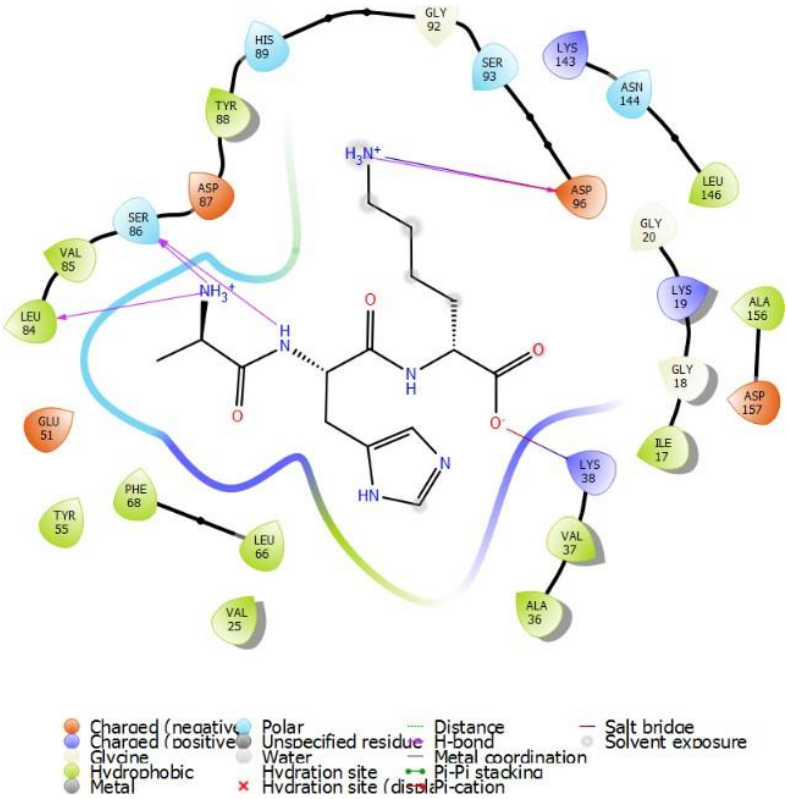


FIGURE 7. 2D ligand interaction of AHK tripeptide in the active side of the Transforming growth factor-β (TGFβ).

ISBN:978-605-83516-6-0

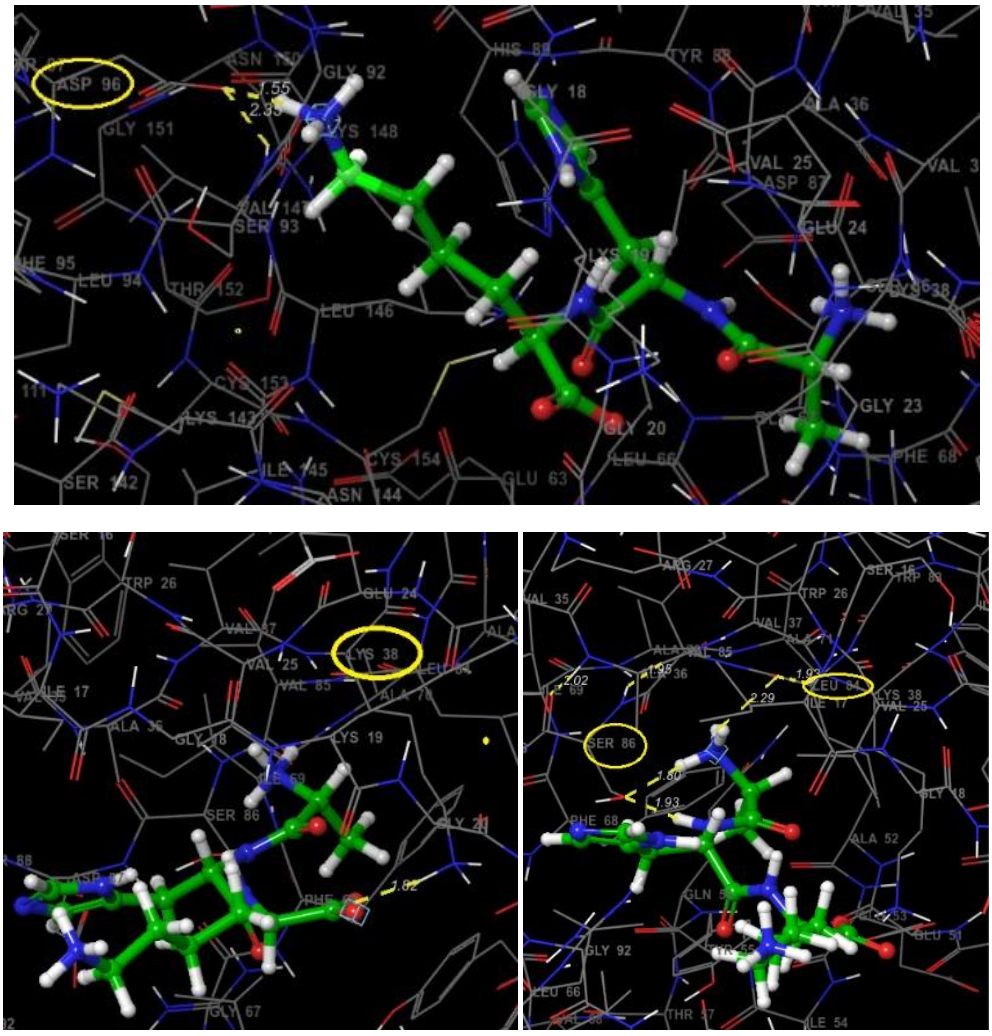


FIGURE 8. The hydrogen binding interactions of AHK with LEU-84 (2.29 Å), SER-86 (1.80 Å and 1.93 Å), ASP-96 (1.55 Å) and two salt bridges LYS-38 and ASP-96 residues for Transforming growth factor-β (TGFβ) receptor.

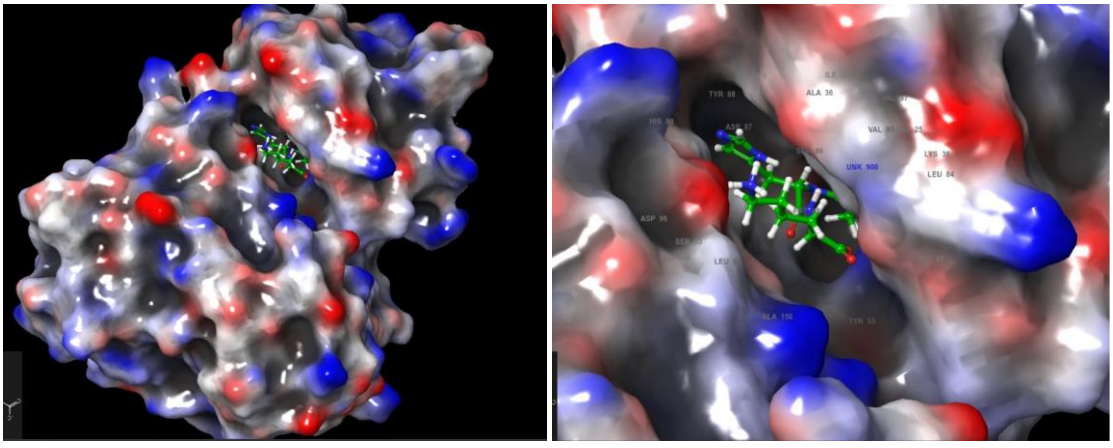


FIGURE 9. The electrostatic potential of the Transforming growth factor-β (TGFβ) receptor and the docked pose of the AHK.

ISBN:978-605-83516-6-0

TABLE I. The calculated ADME properties of AHK tripeptide.

Principal Descriptors:		**Values**	**Recommended Values**
Solute Molecular Weight	=	354.408	(130.0 / 725.0)
Solute Dipole Moment (D)	=	5.530	(1.0 / 12.5)
Solute Total SASA	=	668.280	(300.0 /1000.0)
Solute Hydrophobic SASA	=	284.839	(0.0 / 750.0)
Solute Hydrophilic SASA	=	291.063	(7.0 / 330.0)
Solute Carbon Pi SASA	=	92.378	(0.0 / 450.0)
Solute Weakly Polar SASA	=	0	(0.0 / 175.0)
Solute Molecular Volume (A^3)	=	1178.842	(500.0 /2000.0)
Solute vdW Polar SA (PSA)	=	193.036	(7.0 / 200.0)
Solute No. of Rotatable Bonds	=	13	(0.0 / 15.0)
Solute as Donor - Hydrogen Bonds	=	6.5	(0.0 / 6.0)*
Solute as Acceptor - Hydrogen Bonds	=	9.0	(2.0 / 20.0)
Solute Globularity (Sphere = 1)	=	0.808	(0.75 / 0.95)
Solute Ionization Potential (eV)	=	9.672	(7.9 / 10.5)
Solute Electron Affinity (eV)	=	-0.189	(-0.9 / 1.7)
Predictions for Properties:			
QP Polarizability (Angstroms^3)	=	33.558M	(13.0 / 70.0)
QP log P for hexadecane/gas	=	13.355M	(4.0 / 18.0)
QP log P for octanol/gas	=	25.788M	(8.0 / 35.0)
QP log P for water/gas	=	22.173M	(4.0 / 45.0)
QP log P for octanol/water	=	-3.393	(-2.0 / 6.5)*
QP log S for aqueous solubility	=	0.117	(-6.5 / 0.5)*
QP log S - conformation independent	=	0.404	(-6.5 / 0.5)
QP log K hsa Serum Protein Binding	=	-1.436	(-1.5 / 1.5)
QP log BB for brain/blood	=	-2.398	(-3.0 / 1.2)
No. of Primary Metabolites	=	8	(1.0 / 8.0)
Predicted CNS Activity (– to ++)	=	–	
HERG K+ Channel Blockage: log IC50	=	-1.982	(concern below -5)
Apparent Caco-2 Permeability (nm/sec)	=	0	(<25 poor. >500 great)
Apparent MDCK Permeability (nm/sec)	=	0	(<25 poor. >500 great)
QP log Kp for skin permeability	=	-9.435	(Kp in cm/hr)
Jm. max transdermal transport rate	=	0	(micrograms/cm^2-hr)
Lipinski Rule of 5 Violations	=	1	(maximum is 4)
Jorgensen Rule of 3 Violations	=	2	(maximum is 3)
% Human Oral Absorption in GI (+-20%)	=	0	(<25% is poor)
Qual. Model for Human Oral Absorption	=	low	(>80% is high)

CONCLUSION

Along with its high antioxidant properties, AHK tripeptide is used in the treatment of hair loss and skin rashes, and it also has an important potential in cosmetics because it helps collagen production and increases dermal cell proliferation and viability. AHK tripeptide which has such important fields of application has been modeled for the first time using in silico methods, the most stable geometric structure has been determined, the conformational variations tripeptide in body conditions (water medium) has been examined and also the mechanism of interaction of AHK tripeptide with possible receptor that can effect in the body has been revealed. The discovery and development of peptide structures with a more active and improved mechanism of action is an active field of study, particularly in biochemistry and pharmacology and cosmetic. This study, which reveals the molecular structure, conformational change and mechanism of action of AHK tripeptide, is an original study.

ACKNOWLEDGMENTS

This study consists of the results of the master thesis study and was supported by the Scientific Research Project Coordination Unit of Istanbul University [FYL-26314]. Authors are very thankful to Rita Podzuna for allowing to use the docking program with Schrödinger's Small-Molecule Drug Discovery Suite.

REFERENCES

1. H. K. Pyo, H. G. Yoo, C. H. Won, S. H. Lee, Y. J. Kang, H. C. Eun, K. H. Cho, and K. H. Kim, "The effect of tripeptide-copper complex on human hair growth in vitro," Archives of pharmacal research **30**, 834–839 (2007).
2. J.-I. Jung, K.-Y. Park, Y. Lee, M. Park, and J. Kim, "Vitamin c-linker–conjugated tripeptide ahk stimulates bmp-2-induced osteogenic differ- entiation of mouse myoblast c2c12 cells," Differentiation **101**, 1–7 (2018).
3. D. Rushton, "Nutritional factors and hair loss," Clinical and Experimental Dermatology: Clinical dermatology **27**, 396–404 (2002).
4. H. Shimura, R. Tanaka, Y. Shimada, K. Yamashiro, N. Hattori, and T. Urabe, "Glycyl-alanyl-histidine protects pc12 cells against hydrogen peroxide toxicity," BMC biochemistry **18**, 14 (2017).
5. L. M. Patt and A. Procyte, "Neova R advanced essential eyelash™ conditioner renews health and restores vitality to natural lashes," skin **1**, 2 (2009).
6. L. M. Patt and A. Procyte, "Neova R : refining eye lift reduces the appearance of periorbital wrinkles with dna repair and copper peptide technologies," skin **1**, 2 (2010).
7. D. Van Der Spoel, E. Lindahl, B. Hess, G. Groenhof, A. E. Mark, and H. J. Berendsen, "Gromacs: fast, flexible, and free," Journal of computational chemistry **26**, 1701–1718 (2005).
8. M. Frisch, G. Trucks, H. B. Schlegel, G. Scuseria, M. Robb, J. Cheeseman, G. Scalmani, V. Barone, B. Mennucci, G. Petersson, *et al.*, "Gaussian 09, revision a. 02, gaussian," Inc., Wallingford, CT **200**, 28 (2009).
9. W. F. van Gunsteren, S. Billeter, A. Eising, P. Hünenberger, P. Krüger, A. Mark, W. Scott, and I. Tironi, "Biomolecular simulation: the gromos96 manual and user guide," Vdf Hochschulverlag AG an der ETH Zürich, Zürich **86** (1996).
10. P. E. Smith and W. F. van Gunsteren, "The viscosity of spc and spc/e water at 277 and 300 k," Chemical physics letters **215**, 315–318 (1993).
11. G. Bussi, D. Donadio, and M. Parrinello, "Canonical sampling through velocity rescaling," The Journal of chemical physics **126**, 014101 (2007).
12. M. Parrinello and A. Rahman, "Polymorphic transitions in single crystals: A new molecular dynamics method," Journal of Applied physics **52**, 7182–7190 (1981).
13. B. Hess, H. Bekker, H. J. Berendsen, and J. G. Fraaije, "Lincs: a linear constraint solver for molecular simulations," Journal of computational chemistry **18**, 1463–1472 (1997).
14. T. Darden, D. York, and L. Pedersen, "Particle mesh ewald: An n log (n) method for ewald sums in large systems," The Journal of chemical physics **98**, 10089–10092 (1993).
15. L. Verlet, "Computer" experiments" on classical fluids. i. thermodynamical properties of lennard-jones molecules," Physical review **159**, 98 (1967).
16. W. Humphrey, A. Dalke, and K. Schulten, "Vmd: visual molecular dynamics," Journal of molecular graphics **14**, 33–38 (1996).
17. E. Harder, W. Damm, J. Maple, C. Wu, M. Reboul, J. Y. Xiang, L. Wang, D. Lupyan, M. K. Dahlgren, J. L. Knight, *et al.*, "Opls3: a force field providing broad coverage of drug-like small molecules and proteins," Journal of chemical theory and computation **12**, 281–296 (2015).
18. A. A. Ogunjimi, E. Zeqiraj, D. F. Ceccarelli, F. Sicheri, J. L. Wrana, and L. David, "Structural basis for specificity of tgfβ family receptor small molecule inhibitors," Cellular signalling **24**, 476–483 (2012).
19. G. M. Sastry, M. Adzhigirey, T. Day, R. Annabhimoju, and W. Sherman, "Protein and ligand preparation: parameters, protocols, and influence on virtual screening enrichments," Journal of computer-aided molecular design **27**, 221–234 (2013).

ISBN:978-605-83516-6-0

20. S. Bienert, A. Waterhouse, T. A. de Beer, G. Tauriello, G. Studer, L. Bordoli, and T. Schwede, "The swiss-model repository—new features and functionality," Nucleic acids research **45**, D313–D319 (2016).
21. C. R. Søndergaard, M. H. Olsson, M. Rostkowski, and J. H. Jensen, "Improved treatment of ligands and coupling effects in empirical calculation and rationalization of p k a values," Journal of chemical theory and computation **7**, 2284–2295 (2011).
22. R. A. Friesner, R. B. Murphy, M. P. Repasky, L. L. Frye, J. R. Greenwood, T. A. Halgren, P. C. Sanschagrin, and D. T. Mainz, "Extra precision glide: Docking and scoring incorporating a model of hydrophobic enclosure for protein- ligand complexes," Journal of medicinal chemistry **49**, 6177–6196 (2006).
23. R. A. Friesner, J. L. Banks, R. B. Murphy, T. A. Halgren, J. J. Klicic, D. T. Mainz, M. P. Repasky, E. H. Knoll, M. Shelley, J. K. Perry, *et al.*, "Glide: a new approach for rapid, accurate docking and scoring. 1. method and assessment of docking accuracy," Journal of medicinal chemistry **47**, 1739–1749 (2004).
24. T. A. Halgren, R. B. Murphy, R. A. Friesner, H. S. Beard, L. L. Frye, W. T. Pollard, and J. L. Banks, "Glide: a new approach for rapid, accurate docking and scoring. 2. enrichment factors in database screening," Journal of medicinal chemistry **47**, 1750–1759 (2004).
25. F. Ntie-Kang, L. L. Lifongo, J. A. Mbah, L. C. O. Owono, E. Megnassan, L. M. Mbaze, P. N. Judson, W. Sippl, and S. M. Efange, "In silico drug metabolism and pharmacokinetic profiles of natural products from medicinal plants in the congo basin," In silico pharmacology **1**, 12 (2013).

BOOK OF FULL TEXT PROCEEDINGS TURKISH PHYSICAL
SOCIETY 35th INTERNATIONAL PHYSICS CONGRESS (TPS35) 15 December 2019
TPS35, Vol.01, No.03, pp.203-209.
ISBN:978-605-83516-6-0

DNA Interaction of Some Hydantoin-Based Drugs with Molecular Docking Calculation

M. Can Kandemir[1], Bilge Bıçak[1,2] and Serda Kecel-Gündüz[1,a)]

[1)]Istanbul University, Faculty of Science, Physics Department, 34134, Istanbul, Turkey.
[2)]Institute of Graduate Studies in Sciences, Istanbul University,34452, Istanbul, Turkey.
[a)]Corresponding author: skecel@istanbul.edu.tr

Abstract. Epilepsy is one of the most common neurological disorders in the worldwide. Hydantoin based anti-epileptic drugs, such as Phenytoin, Mephenytoin and Ethotoin are widely used as anticonvulsant in the treatment of epilepsy. Drug-DNA non-binding interactions are more preferred comparing to covalent binding because of drug metabolism and potential toxic effects. Non-binding interactions (such as electrostatic, hydrogen bonds and dipole-dipole) can affect DNA structure. The stability of DNA-drug complex relates to the intensity of these interactions. Cytochrome P450 (CYP) 3A4 is a "heme" containing isoform of CYP family, is responsible for the metabolism of most of the currently known drugs, which is very important in drug-protein studies. In this study, we investigated DNA and CYP3A4's binding interactions with Phenytoin, Mephenytoin and Ethotoin by using molecular docking method. As a result of molecular docking calculations, we determined the interaction areas, binding distances and binding affinities of three drugs with DNA and CYP3A4.

Keywords: Epilepsy, Docking, Cytochrome P450 3A4, DNA, hydantoin-based drugs

INTRODUCTION

Epilepsy is the one of the most common neurological disorders in the worldwide affecting all ages people. Epilepsy cause seizure types varying from person-to-person and can trigger other health problems. The seizures associated with epilepsy cause repetitive and unpredictable deductions of normal brain function [1,2]. Antiepileptic drugs (AEDs) can be used to reduce or eliminate seizures, to avoid the side effects arising from long-term treatment. At the same time, AEDs purpose to help the people with epilepsy maintaining a normal lifestyle [3,4]. At the treatment of epilepsy, AEDs are used as pharmacological agents for treating of epileptic seizures. When a seizure occurs, AEDs aim at preventing the extreme fast discharge of neurons and seizure from spreading inwards the brain [5,6].

Phenytoin, whose trade name is known as *dilantin* is widely used as an antiepileptic drug. It is formed imidazolidine-2,4-dione that consists of hydantoin. Phenytoin is effectively used in the treatment of partial-onset and generalized tonic–clonic seizures and it's effective on the sodium channels [7]. Mephenytoin marketed as *mesantoin* is one of the hydantoins and used in epilepsy treatment [8]. It potentially supports sodium efflux from neurons in motor cortex. This drug molecule decreases the membrane sodium gradient and forecloses cortical seizure signal spreading [9]. Ethotoin commercially known as *Peganone* has also antiepileptic effect like phenytoin and mephenytoin. Ethotoin affects the influx of sodium and calcium ions and calcium uptake. Thus, it helps to ensure the stailization of neuronal membranes and prevents the spread of seizure activity in the motor cortex [10].

Deoxyribonucleic acid, DNA, has four different nucleotide subunits. These nucleotides consist of deoxyribose that is a five-carbon sugar. Most drug molecule are able to interact with these nucleotids (adenine,guanine, cytosine and thymine) forming DNA. These drug molecules can change DNA conformation, torsional tension and can disconnect protein–DNA interaction [11]. The crystal structure of the synthetic DNA dodecamer d(CpGpCpGpApApTpTpCpGpCpG) has been refined to a residual error of R = 17.8% at 1.9-A resolution (two-sigma data). The molecule forms slightly more than one complete turn of right-handed double-stranded B helix [12].

The cytochrome P450 (CYP) found in human body is the most abundant and sophisticated isoform of CYP and responsible for the metabolism of most drugs [13]. Undesired drug-drug interactions during multi-drug treatments can be prevent by understanding of CYP3A4 which an enzyme is belong to cytochrome P450 family of oxidizing enzymes. CYPs also found at central nervous system (CNS), therefore hydantoin-based drug interaction is important while epilepsy treatment [14]. CYP3A4 is also directly correlated with epilepsy seizures [15]. Studies have shown that transcript levels of several P450 enzymes (CYPs) are elevated in brain endothelial cells derived from temporal lobe resections of drug resistant patients with epilepsy. Among these enzymes, CYP3A4 was further explored in non-CNS organs [14].

Molecular docking is an important tool in computer-assisted drug design. The molecular docking approach is able to provide prediction of the interaction between a small molecule and a receptor at the atomic level, which allow us to characterize the behavior of small molecules in the binding site of target proteins as well as to elucidate fundamental biochemical processes.

In this study the interactions, the binding distances and binding affinity values of the best docking poses were determined for hydantoin based drugs with using CYP3A4 and DNA.

MATERIALS AND METHODS

In the docking studies, the 3D structure of a B-DNA dodecamer containing 486 nucleic acid atoms with the 1.9 Å resolution (PDB: 1BNA) [12] and Cytochrome P450 3A4 molecule (PDB:4K9T) [16] with 487 sequence length and 2.5 Å resolution were obtained from PDB DataBank and SwissModel (code P08684) [17], respectively. All waters, heavy metals and ligands were removed to prepare this protein and polar hydrogens are added to the protein for molecular docking analysis using AutoDockTools1.5.6. Phenytoin with 1665626 ZINC database code, mephenytoin with 453 ZINC database code, ethotoin with 271 ZINC database code [18] were used as the ligands at the molecular docking studies. The grid box for all ligands (Phenytoin, Mephenytoin, Ethotoin) set to 20 × 20 × 30 Å and 40 × 40 × 40 Å, with 0.375 Å grid spacing was set around where the ligand can interact for ligand-DNA and ligand- CYP3A4 docking studies, respectively. All pdb files were converted to pdbqt file formats for docking analysis. Docking studies were carried out using AutoDock Vina 1.1.2 [19] program. This program was used to define the binding affinities and root mean square deviation (RMSD) values for each ligand. The pose with best binding affinity was visualized using AutoDockTools1.5.6 [20], Pymol [21] and Discovery Studio [22].

RESULTS

According to the first of molecular docking calculations, the binding affinity value has -5.8 kcal/mol energy value as a result of the ligand phenytoin- B-DNA dodecamer binding work, as shown in Table 1. Phenytoin had close interaction with deoxy guanosine (DG4 and DG22) and deoxy adenosine (DA5 and DA6) shown in Fig. 1. As a result of phenytoin docking study, the first hydrogen bond was occurred between O2 atom of phenytoin and H21 atom of deoxy guanosine (H21 of DG22) on B-Chain of B-DNA with 2.2 Å bond length. The second hydrogen bond was observed between O2 atom of phenytoin and H22 atom of deoxy guanosine (H22 of DG4) on A-Chain of B-DNA with 2.3 Å bond length, shown in Fig. 1 and Table 2. The other hydrogen bond was determined between O2 atoms of phenytoin and H3 atoms of deoxy guanosine (H3 of DG4) on A-Chain of B-DNA with 3.2 Å bond length, shown in Table 2. Beside of these hydrogen bonds, phenytoin has also close interaction with deoxy guanosine (DG4 and DG22) and deoxy adenosine (DA5 and DA6).

The best binding affinity value between B-DNA dodecamer and mephenytoin was found as -6.0 kcal/mol, as show in Table 1. Mephenytoin had also close interaction with deoxy guanosine (DG4 and DG22) and deoxy adenosine (DA5 and DA6) shown in Fig. 2. It is found that mephenytoin has two hydrogen bonds in this work. The first hydrogen bond was determined between O2 atom of mephenytoin and H21 atom of deoxy guanosine (H21 of DG22) on B-Chain of B-DNA dodecamer with 2.1 Å bond length. The other hydrogen bond was observed between O2 atom of mephenytoin and H3 atom of deoxy guanosine (H3 of DG22) on B-Chain of B-DNA dodecamer with 2.3 Å bond length, shown in Figure 2 and Table 2. Mephenytoin has also close interaction with deoxy guanosine (DG4 and DG22) and deoxy adenosine (DA5 and DA6).

Results showed that ethotoin has -5.8 kcal/mol binding affinity value, as shown in Table 1. Ethotoin had also close interaction with deoxy guanosine (DG4 and DG22) and deoxy adenosine (DA5) and deoxy cytosine (DC21) shown in Fig. 3. In this molecular docking calculation, the first of the three-hydrogen bond was determined between O2 atom of ethotoin and H22 atom of deoxy guanosine (H22 of DG4) on A-Chain of B-DNA dodecamer with 2.8 Å bond length. The second hydrogen bond was observed between O2 atom of ethotoin and H21 atom of deoxy guanosine (H21 of DG4) on A-Chain of B-DNA dodecamer with 3.2 Å bond length. The third hydrogen bond was observed between O2 atom of ethotoin and H3 atom of deoxy adenosine (H3 of DA5) on A-Chain of B-DNA dodecamer with 1.9 Å bond length, shown in Fig. 3 and Table 2. Besides the interactions mentioned above, ethotoin interacted with deoxy guanosine deoxy adenosine and deoxy cytosine (DG4, DG22 and DA5 and DC21). In the second of molecular docking calculations, the interactions and the binding distances and binding affinity values of

the obtained best docking poses were determined for hydantoin based drugs (Phenytoin, Mephenytoin, Ethotoin) with CYP3A4.

According to the docking results, the phenytoin and the **CYP3A4 enzyme** had a binding affinity value with -8.6 kcal/mol, as shown in Table 3. Phenytoin had close interaction with more CYP3A4 residues than the other ligands. These interactions were **Arg352, Asp56, Gly460, Gly461, Ile30, Leu196, Leu201, Phe195, Phe200, Phe37, Phe88, Thr204, and Tyr33 residues** of the CYP3A4, as shown in Fig. 4. The Pi-Pi T-shaped interaction between **Phe88** and benzene ring of phenytoin and carbon-hydrogen bond between **Leu201** and **O2** atom in the imidazolidine2,4-dione of phenytoin were determined with 3.3 Å bond length. **Leu201** had also Pi-Alkyl interaction with benzene ring of phenytoin, shown in Fig. 4.

The binding affinity value of mephenytoin and CYP3A4 were determined -7.6 kcal/mol, as shown in Table 3. Mephenytoin had close interaction with **Gly461, Leu201, Leu462, Phe193, Phe195, Phe200, Phe37, Phe88,** and **Thr204** residues, as shown in Fig. 5. Mephenytoin had more interaction diversity than phenytoin and ethotoin. The first interaction of mephenytoin was Pi-Pi Stacked interaction between **Phe200** and benzene ring of mephenytoin. Second interaction was Pi-Pi T-Shaped interaction, **Phe37** and **Phe88** both bound to benzene ring with Pi-Pi T-Shaped interaction. The C6 of mephenytoin and **Phe200** was also interacted with Pi-Sigma interaction, as well as Pi-Pi Stacked interaction. The other one interaction was conventional hydrogen bond with **2.37 Å** bond length (cf. Figure 5 and Tablo 2), observed between **Phe195** residue of **CYP3A4** and H1 atom in the HN group of imidazolidine-2,4-dione of mephenytoin. It was also observed that Phe195 and C6 atom of mephenytoin interact with Pi-Alkyl bond.

Ethotoin has -7.7 binding affinity value, as shown in Table 3. Ethotoin had close interaction with **Ile30, Leu201, Phe195, Phe200, Phe37, Phe88, Thr204,** and **Tyr33** residues of **CYP3A4**, as shown in Fig. 6. The ethotoin had alkyl bond between **Leu201** and its C7 atom. It also had Pi-Pi Stacked bond between its benzene ring and **Phe88**. The last interaction of ethotoin was conventional hydrogen bond between **Thr204** and H1 atom in the HN group of its imidazolidine-2,4-dione with **2.27 Å** bond length, shown in Fig. 6 and Tablo 2.

CONCLUSIONS

Phenytoin, Mephenytoin and Ethotoin are molecules used as antiepileptic drug known as anticonvulsants. In the drug discovery, molecular docking methods are one of the preferred methods. The calculations using molecular docking methods provide to predict the binding conformations and binding affinity values of ligands in the ligand-receptor system. In this study, the interactions of these antiepileptic drugs with DNA and Cytochrome P450 3A4 were investigated using molecular docking method. In the DNA study, the antiepileptic drugs (Phenytoin, Mephenytoin and Ethotoin) was linked to B-DNA dodecamer and revealed the locations of the hydrogen bonds that provided stable binding. According to molecular docking results, the lowest docking score was determined as -6.0 kcal/mol for Mephenytoin. When we investigated Cytochrome P450 3A4 study, the lowest docking score was determined as -8.6 kcal/mol for Phenytoin.

ISBN:978-605-83516-6-0

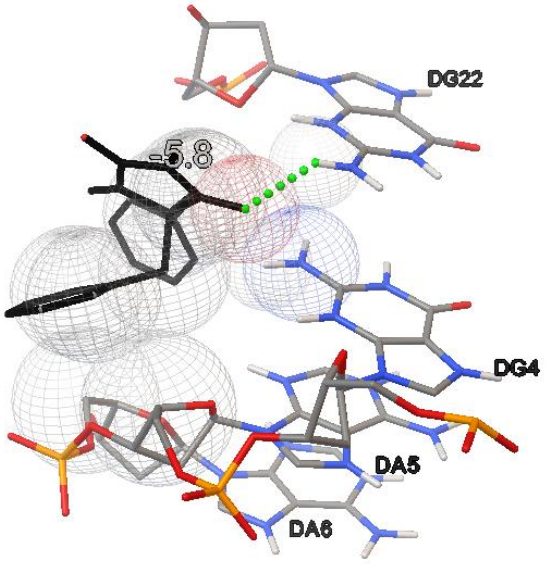


FIGURE 1.

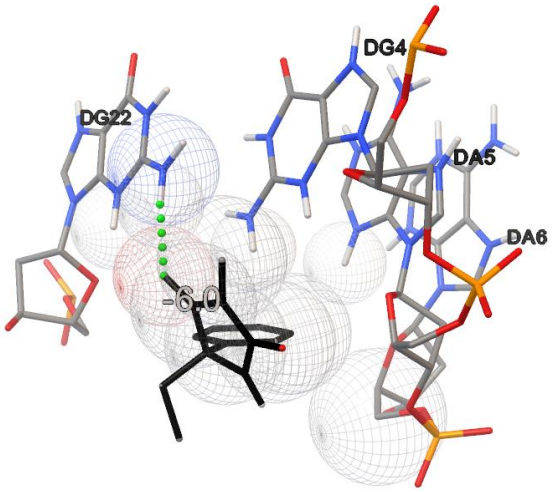


FIGURE 2.

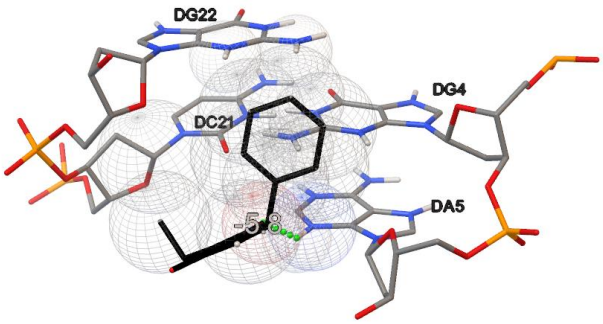


FIGURE 3.

ISBN:978-605-83516-6-0

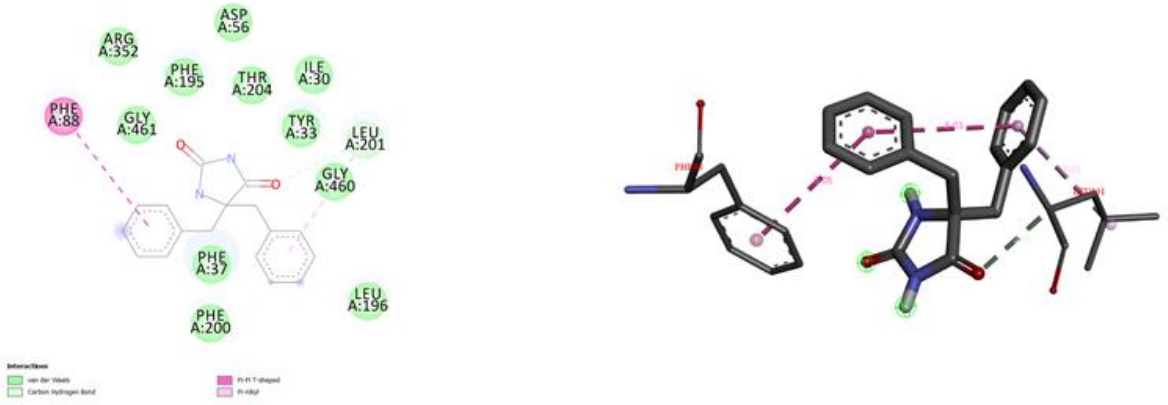


FIGURE 4.

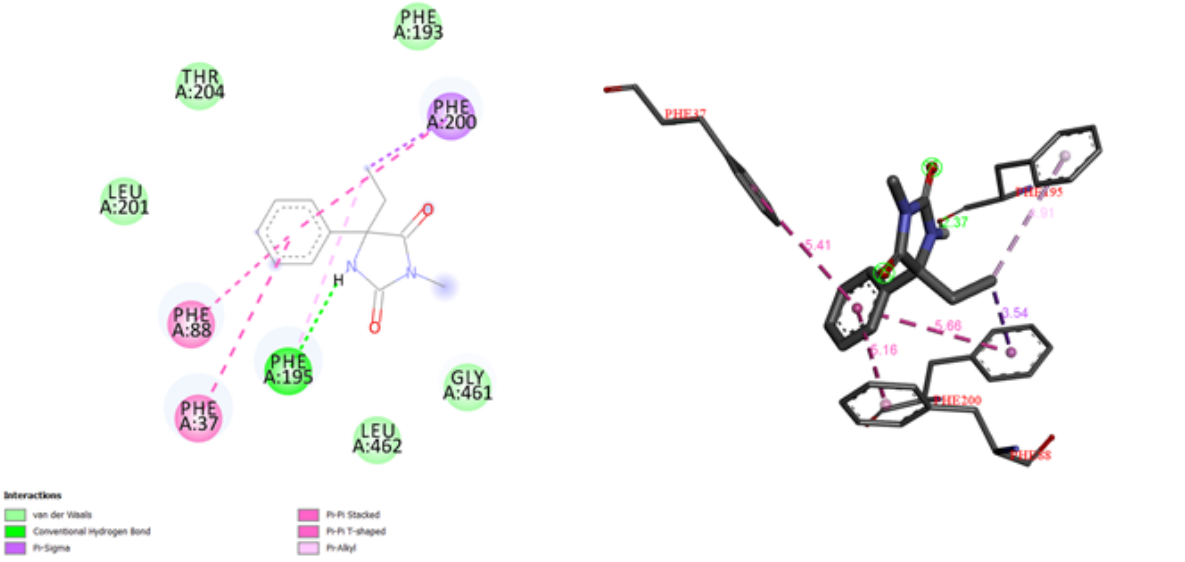


FIGURE 5.

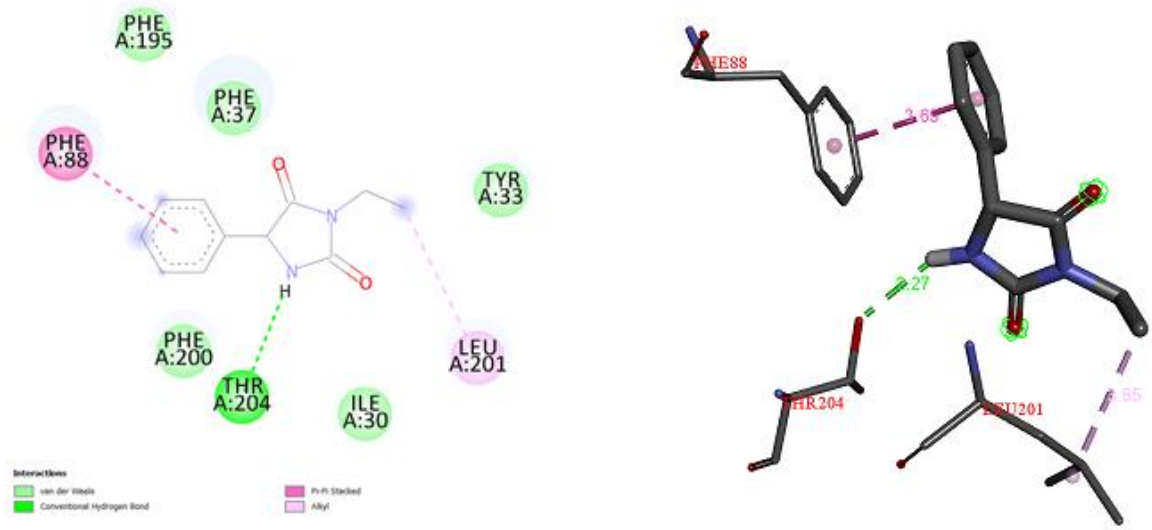


FIGURE 6.

TABLE 1. The binding affinities and RMSD values between B-DNA dodecamer and hydantoin-based drugs.

Mode	Phenytoin			Mephenytoin			Ethotoin		
	Affinity	Distance from best mode		Affinity	Distance from best mode		Affinity	Distance from best mode	
	(kcal/mol)	rmsd l.b.	rmsd u.b.	(kcal/mol)	rmsd l.b.	rmsd u.b.	(kcal/mol)	rmsd l.b.	rmsd u.b.
1	-5.8	0.000	0.000	-6.0	0.000	0.000	-5.8	0.000	0.000
2	-5.7	2.433	3.604	-6.0	0.225	1.217	-5.7	2.861	5.332
3	-5.7	2.081	5.276	-5.9	2.588	4.660	-5.7	2.603	4.023
4	-5.7	2.863	4.281	-5.6	1.942	2.857	-5.7	1.849	5.310
5	-5.5	2.633	3.968	-5.4	1.453	1.985	-5.7	1.750	5.199
6	-5.5	2.360	3.522	-5.3	2.002	4.710	-5.6	2.236	5.225
7	-5.4	1.717	2.503	-5.2	1.916	5.436	-5.4	2.600	4.039
8	-5.4	2.296	4.480	-5.1	2.079	4.524	-5.4	3.081	5.706
9	-5.3	2.010	3.798	-5.0	2.357	3.786	-5.3	1.431	2.061

TABLE 2. Hydrogen bond values hydantoin-based drugs with B-DNA dodecamer and CYP3A4.

Donor Atom	Acceptor Atom	Bond Length (Å)
H21 of DG22 (Chain B) of DNA	O2 of Phenytoin	2.2
H22 of DG4 (Chain A) of DNA	O2 of Phenytoin	2.3
H3 of DG4 (Chain A) of DNA	O2 of Phenytoin	3.2
H21 of DG22 (Chain B) of DNA	O2 of Mephenytoin	2.1
H3 of DG22 (Chain B) of DNA	O2 of Mephenytoin	2.3
H22 of DG4 (Chain A) of DNA	O2 of Ethotoin	2.8
H21 of DG4 (Chain A) of DNA	O2 of Ethotoin	3.2
H3 of DA5 (Chain A) of DNA	O2 of Ethotoin	1.9
H1 of Mephenytoin	Phe 195 residue of CYP3A4	2.37
H1 of Ethotoin	Thr204 residue of CYP3A4	2.27

TABLE 3. The binding affinities and RMSD values between CYP3A4 and hydantoin-based drugs.

Mode	Phenytoin			Mephenytoin			Ethotoin		
	Affinity	Distance from best mode		Affinity	Distance from best mode		Affinity	Distance from best mode	
	(kcal/mol)	rmsd l.b.	rmsd u.b.	(kcal/mol)	rmsd l.b.	rmsd u.b.	(kcal/mol)	rmsd l.b.	rmsd u.b.
1	-8.6	0.000	0.000	-7.6	0.000	0.000	-7.7	0.000	0.000
2	-8.5	3.477	6.561	-7.1	2.389	3.407	-7.5	0.244	1.260
3	-8.4	2.333	5.298	-7.1	1.221	1.590	-7.0	2.052	3.323
4	-8.3	2.750	4.285	-7.0	2.375	3.575	-7.0	3.004	4.331
5	-8.2	5.242	7.242	-6.9	1.997	4.333	-6.9	2.319	3.350
6	-8.2	1.240	4.842	-6.9	1.586	4.259	-6.9	3.298	4.700
7	-8.1	4.348	7.212	-6.5	2.336	3.124	-6.9	1.701	2.247
8	-8.0	2.574	3.844	-6.5	2.652	3.917	-6.7	1.629	5.523
9	-7.9	2.432	5.487	-6.5	1.738	2.845	-6.7	2.570	5.333

REFERENCES

1. R. S. Fisher, W. V. E. Boas, W. Blume, C. Elger, P. Genton, P. Lee, and J. Engel Jr, "Epileptic seizures and epilepsy: definitions proposed by the international league against epilepsy (ilae) and the international bureau for epilepsy (ibe)," Epilepsia 46 , 470–472 (2005).
2. Y. H. Yin, N. Ahmad, and M. Makmor-Bakry, "Pathogenesis of epilepsy: challenges in animal models," Iranian journal of basic medical sciences 16 , 1119 (2013).
3. L. P. Rowland, T. A. Pedley, et al. , Merritt's neurology , Vol. 11 (Lippincott Williams & Wilkins Philadelphia, 2005).
4. M. M. Goldenberg, "Overview of drugs used for epilepsy and seizures: etiology, diagnosis, and treatment," Pharmacy and Therapeutics 35 , 392 (2010).
5. M. J. McLEAN and R. L. Macdonald, "Sodium valproate, but not ethosuximide, produces use-and voltage-dependent limitation of high fre- quency repetitive firing of action potentials of mouse central neurons in cell culture." Journal of Pharmacology and Experimental therapeutics 237 , 1001–1011 (1986).
6. C. L. Harden, "New antiepileptic drugs," Neurology 44 , 787–787 (1994).
7. B. Guldiken, J. Rémi, and S. Noachtar, "Cardiovascular adverse effects of phenytoin," Journal of neurology 263 , 861–870 (2016).
8. S. Patel, G. Mukherji, J. Patil, and S. Mate, "Pharmaceutical composition for extended release of phenytoin sodium," (2006), uS Patent App. 11/199,169.
9. NCI Thesaurus, "Definition of Mephenytoin," https://ncit.nci.nih.gov/ncitbrowser/ConceptReport.jsp?dictionary=NCI_Thesaurus&ns=NCI_Thesaurus&code=C66091 (2019), accessed: 14 October 2019.
10. NCI Thesaurus, "Definition of Ethotoin," https://ncit.nci.nih.gov/ncitbrowser/ConceptReport.jsp?dictionary=NCI_Thesaurus&ns=NCI_Thesaurus&code=C47524 (2019), accessed: 14 October 2019.
11. M. M. Aleksic and V. Kapetanovic, "An overview of the optical and electrochemical methods for detection of dna–drug interactions," Acta Chimica Slovenica 61 , 555–573 (2014).
12. H. R. Drew, R. M. Wing, T. Takano, C. Broka, S. Tanaka, K. Itakura, and R. E. Dickerson, "Structure of a b-dna dodecamer: conformation and dynamics," Proceedings of the National Academy of Sciences 78 , 2179–2183 (1981).
13. F. P. Guengerich, "Cytochrome p-450 3a4: regulation and role in drug metabolism," Annual review of pharmacology and toxicology 39 , 1–17 (1999).
14. C. Ghosh, N. Marchi, N. K. Desai, V. Puvenna, M. Hossain, J. Gonzalez-Martinez, A. V. Alexopoulos, and D. Janigro, "Cellular localization and functional significance of cyp3a4 in the human epileptic brain," Epilepsia 52 , 562–571 (2011).
15. S. Williams, M. Hossain, L. Ferguson, R. M. Busch, N. Marchi, J. Gonzalez-Martinez, E. Perucca, I. M. Najm, and C. Ghosh, "Neurovascular drug biotransformation machinery in focal human epilepsies: Brain cyp3a4 correlates with seizure frequency and antiepileptic drug therapy," Molecular Neurobiology , 1–16 (2019).
16. I. F. Sevrioukova and T. L. Poulos, "Dissecting cytochrome p450 3a4–ligand interactions using ritonavir analogues," Biochemistry 52 , 4474– 4481 (2013).
17. F. Kiefer, K. Arnold, M. Künzli, L. Bordoli, and T. Schwede, "The swiss-model repository and associated resources," Nucleic acids research 37 , D387–D392 (2008).
18. J. J. Irwin, T. Sterling, M. M. Mysinger, E. S. Bolstad, and R. G. Coleman, "Zinc: a free tool to discover chemistry for biology," Journal of chemical information and modeling 52 , 1757–1768 (2012).
19. O. Trott and A. J. Olson, "Autodock vina: improving the speed and accuracy of docking with a new scoring function, efficient optimization, and multithreading," Journal of computational chemistry 31 , 455–461 (2010).
20. R. Huey, G. M. Morris, and S. Forli, "Using autodock 4 and autodock vina with autodocktools: A tutorial," The Scripps Research Institute Molecular Graphics Laboratory (2012).
21. PyMOL, "The pymol molecular graphics system, version 2.0," (2017).
22. D. S. Biovia, "Discovery studio modeling environment," (2017).

BOOK OF FULL TEXT PROCEEDINGS TURKISH PHYSICAL
SOCIETY 35th INTERNATIONAL PHYSICS CONGRESS (TPS35)
TPS35, Vol.01, No.03, pp.210-216.
ISBN:978-605-83516-6-0

15 December 2019

Isotope Effect on Molecular Dissociation by Intense Laser Fields in The Vicinity of Metallic Nanotip

Saba Arife Karakas[1,a),b)], Muratcan Oner[1,c)] and Ilhan Yavuz[1,d)]

[1]*Marmara University Goztepe Campus Faculty of Arts and Science Physics Department*

[a)]Corresponding author: saba.bozpolat@marmara.edu.tr, OrcID: 0000-0002-2166-6464
[b)]URL: http://www.simulab.net
[c)]muratcan.oner@marun.edu.tr, OrcID: 0000-0003-4095-6835
[d)]ilhan.yavuz@marmara.edu.tr, OrcID: 0000-0002-3268-6268

Abstract. We study the isotope effect on the interaction between ultrashort femtosecond laser pulse with the Hydrogen molecular cation near metallic nanotips with different sharpness values. We only consider Deuterium as the isotope of Hydrogen. We operated the MO-ADK calculations to find the ionization times and ionization rates of neutral molecules. Then we solved Time Dependent Schrödinger Equation to describe the interaction with laser pulse. We calculated the Kinetic Energy Release of dissociation and the asymmetry in Kinetic Energy Release distribution. We observed a less powerful dissociation rate for Deuterium and the asymmetry for Deuterium is less apparent. We also checked on the contrast parameter and observed varying characteristic in different KER regimes, attributed to the paths.

INTRODUCTION

Recently two different field of physics, attosecond physics and nanoscale physics, begin to join together [1]. This merge of two different main field yields interesting phenomena such as, laser induced near fields [2], above-threshold and strong-field ionization [3, 4, 5, 6, 7, 8, 9, 10, 11, 12], electron acceleration [13, 14] and recollision [15, 16, 17, 18, 19, 20], near-field effect on dissociation [21, 22]. In attosecond physics, researchers investigate the interactions between lasers and atoms or molecules. For such interactions, the timescale of electron's motion is relatively small than the period of driven laser field. Therefore it is safe to neglect the spatial dependence of laser field to explain the physics behind the electron motion. At the same time, when a metallic nanostructure interacts with laser fields, the field can resonant the plasmon frequency within the structure which induces a local, strong electrical field of order of a small molecule. This way the local electrical field in which the molecule is located can be modified spatially and the neglection of spatial dependence of the electrical field is no longer valid. This spatial dependence of local electrical field reveals interesting physics to study [23, 24, 25, 26, 27, 28, 29, 30, 31, 32, 33, 34, 35, 36, 37].

In this work, we study the isotope effect on molecular dissociation of H_2^+ near metallic nanotips with different apex sharpness values. We pay attention to Deuterium molecular cation as the isotope. We assume that the cations are created during the interaction with laser field. We use MO-ADK calculations [38] to obtain ionization times and rates of neutral Hydrogen and Deuterium molecules. Then we numerically solved Time Dependent Schrödinger Equation (TDSE) to obtain Kinetic Energy Release (KER) of dissociation. We make use of binning mechanism to calculate the asymmetry of electron localization after dissociation. Our results showed that the dissociation rate is smaller for the isotope than that of the essential molecule. The asymmetry occurs in lower energy regimes for Deuterium and it is more pale than the asymmetry for Hydrogen. To place a nanotip near molecule introduces a phenomenon called "contrast" which is the asymmtry of the asymmetry. The contrast showed different behaviour for different molecules in different energy regimes.

METHOD

We investigate the influence of a metallic nanotip on the asymmetry of dissociation of Hydrogen cation, H_2^+ and its first isotope Deuterium cation, D_2^+, by ultrashort laser pulse by solving TDSE. We simulate the influence of the nanotip via an approximation for near fields [39, 40, 41] as,

$$E(z,t) = E(t)\exp(-z/d), \tag{1}$$

where $E(t)$ is the laser field, z is the relative position of the molecule's center to the nanotip and d is the decay length which is inversely proportional to the nanotip sharpness, R_0. As d goes to infinity, or likewise R_0 goes to zero, ordinary homogeneous field is recovered. In the calculations, we use a linear polarized ultrashort laser pulse which is 5.4 fs at Full-Width at Half-Maximum (FWHM) defined as,

$$E(t) = E_0\exp(-t^2/\tau^2)\cos(\omega_0 t + \phi), \tag{2}$$

where E_0 is the intensity, τ is the duration at FWHM, ω_0 is the frequency and ϕ is the Carrier-Envelope Phase (CEP). This is an emulation of 780 nm Ti-Sapphire laser. In the simulations H_2^+ is assumed to be created during the interaction with the laser pulse. For the ionization times and rates, we use the MO-ADK calculations [38], namely,

$$\omega_{ion}(t) = Q\sqrt{\frac{3|E(t)|}{\pi\kappa^3}}\frac{1}{\kappa^{2Z_c/\kappa-1}}\left(\frac{2\kappa^3}{|E(t)|}\right)^{2Z_c/\kappa-1}e^{-2\kappa^3/3|E(t)|}, \tag{3}$$

where, $Q = 3.5$, $\kappa = \sqrt{2I_p}$, I_p is the ionization potential of the molecule, Z_c is effective charge. w_{ion} is the ionization rate for H_2 at specific time t which determines the amount of ionization in an ensemble of Hydrogen molecules under the laser influence. In Figure 1 one can see that the main peak of ionization rate occurs at $t = 0$ which corresponds to the peak of the laser field. There are two satellite peaks in ionization rate of H_2 occurs at the second-most powerful times of the laser field. This means that the ionization of neutral molecule is emanated at three powerful times of laser pulse. Since there is no mass-related term in Equation 3, the MO-ADK rate for both Hydrogen and Deuterium is of the same form shown in Figure 1.

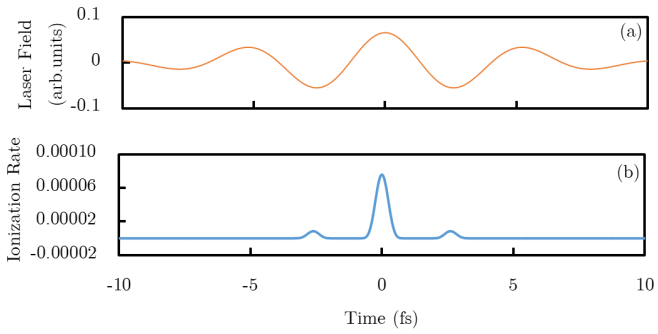


FIGURE 1. (color online) (a) Laser field. (b) Ionization rate of H_2 as a function of time. There are two satellite peaks in ionization which corresponds to the second-most powerful times of the laser field.

We then numericcally solved TDSE,

$$i\frac{d}{dt}\Psi(t,z,R) = H(t,z,R)\Psi(t,z,R), \tag{4}$$

where $\Psi(t,z,R)$ is the wavefunction, $H(t,z,R)$ is the hamiltonian of the interaction defined as,

$$H(t,z,R) = T_e + T_n + V_e(z,R) + V_n(R) + zE(z,t), \tag{5}$$

where T_e and T_n are kinetic energy terms for electron and nuclei, V_e and V_n potential energy terms for electron-nuclei and nucleus-nucleus interactions, respectively, and the last term is the molecule-field interaction term. We started the

simulations at the ionization times determined by the peaks of Equation 3 and propagate the wave-function in time under the influence of the laser pulse. At the end of each time-step, we calculated the flux-density, $j(R_d,t)$ and the wave-function probability, $\rho(R_d,t)$ at $R = R_d$ which is the place of the "virtual detector" [42],

$$j(R_d,t) = \frac{1}{m} Re[\langle\Psi(t)|\hat{p}|\Psi(t)\rangle]|_{R=R_d}, \quad (6)$$

$$\rho(R_d,t) = Re[\langle\Psi(t)|\Psi(t)\rangle]|_{R=R_d}. \quad (7)$$

R_d is a distance beyond which the dissociation occurs. With use of the flux density and the wave-function probability, the momentum of the wave-packet can be calculated as,

$$k(R_d,t) = m\frac{j(R_d,t)}{\rho(R_d,t)}. \quad (8)$$

After the simulations, a binning/histogramming mechanism is employed to obtain the dissociation probability as a KER distribution. The total KER distribution after dissociation of H_2^+ is then determined by MO-ADK ionization rates via,

$$P_{total}(E) \propto \int \omega_{ion}(t)P(t,E)dt. \quad (9)$$

Here $P(t,E)$ is the KER distribution for the dissociation of H_2^+ born at time t. We only pick the rates and the times on the main peak and satellite peaks to converge the integral in Equation (9) and we employ a finite sum over these times as,

$$P_{total}(E) \propto \sum_{peaks} \omega_{ion}(t_{peak})P(t_{peak},E). \quad (10)$$

We have defined the asymmetry as $(P_R - P_L)/(P_R + P_L)$, where $P_{R/L}$ is right/left going wave-packet which is calculated through right/left virtual detectors. Then we investigate the "asymmetry in asymmetry" which is the contrast, defined as,

$$C = \frac{max(A(\phi)) - |min(A(\phi))|}{max(A(\phi)) + |min(A(\phi))|}, \quad (11)$$

where $A(\phi)$ is averaged-asymmetry within different energy ranges, therefore, only depends on ϕ, the phase angle.

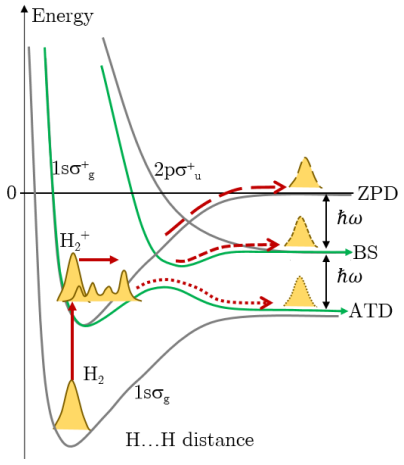


FIGURE 2. (color online) Potential Energy Surfaces (PES) and dissociation paths for Hydrogen. Dissociation paths for Deuterium have same definitions. After the ionization of neutral Hydrogen (or Deuterium), the dissociation occurs different paths which is ATD, BS and ZPD. See the text for more information.

The reactions we have simulated can be summed up as follows,

$$H_2 + \gamma \rightarrow H_2^+ + e + \gamma \rightarrow H + p + e,$$
$$D_2 + \gamma \rightarrow D_2^+ + e + \gamma \rightarrow D + D^+ + e, \quad (12)$$

where γ is the ultrashort femtosecond laser pulse. These reactions occur from different reaction paths. In this work, we consider three of them, namely, Above Threshold Dissociation (ATD), Bond-Softening (BS) and Zero-Photon Dissociation (ZPD) shown in Figure 2. In ATD path, the molecule first absorbs three-photon and is stimulated to the first, repulsive state in Potential Energy Surface (PES) diagram then emits one photon back to the ground state at more-widely-spaced point in the diagram and dissociates through the ground state. In BS path, the molecule only absorbs one-photon and is stimulated to the repulsive state then dissociates. In ZPD path, as the name implies, the molecule absorbs no photon and dissociates through the ground state.

RESULTS & DISCUSSIONS

In this proceeding we have investigated the isotope effect on dissociation of Hydrogen molecule near a metallic nanotip. We have numerically solved TDSE for laser-matter interaction near a metallic nanotip and by use of the virtual detector method, we have calculated the dissociation rates and asymmetry in dissociation. The dissociation rates are given in Figure 3. For Hydrogen has a peak around 1.3 eV and Deuterium has a peak near 0.9 eV which is the overlap energy ranges for ATD and BS. We have observed the weakening of the dissociation signal under isotope effect. On the other hand, the peak is wider for Hydrogen than the peak of Deuterium which indicates the shortened of ATD energy gap for Deuterium. At the same time, the peak of dissociation shifts to the slightly less energy values with nanotip sharpness for both Hydrogen and Deuterium. But the shift is relatively more dramatic for Hydrogen.

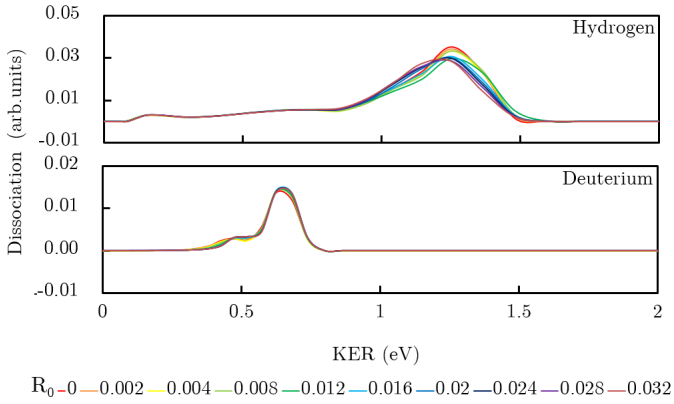


FIGURE 3. (color online) Dissociation rates for Hydrogen and Deuterium. In both cases the dissociation has a peak near different energy values which shifts to the lower energy values with rising sharpness parameter.

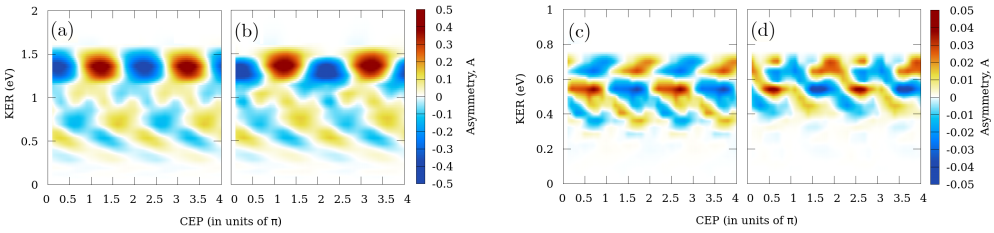


FIGURE 4. (color online) Asymmetry maps for Hydrogen and Deuterium with and without nanotip. Asymmetry for (a) Hydrogen molecule, without nanotip, (b) Hydrogen molecule, with nanotip, (c) Deuterium, without nanotip and (d) Deuterium, with nanotip.

To obtain asymmetries for both Hydrogen and Deuterium, we make use of the difference between right-going and left-going wave-packets through virtual detectors placed on the right and the left. Asymmetry maps obtained this way are given in Figure 4. We report that the asymmetry for Deuterium is ten times less than the asymmetry for Hydrogen [43]. Then we took averages of asymmetry over two different energy ranges for each molecule given in Figure 5, a process which lefts the asymmetry to depend on only the CEP. In Figure 5, it is easier to see the sinuos behaviour of asymmetry with CEP. This behaviour is similar for both Hydrogen and Deuterium in both energy regions but it is the

most blotless for Hydrogen in high energy region. At the same time, while the maximum points of asymmetries is not changing, the minimum points of them become different from each other with nanotip sharpness. This change is the origin of the "asymmetry of asymmetry", the contrast.

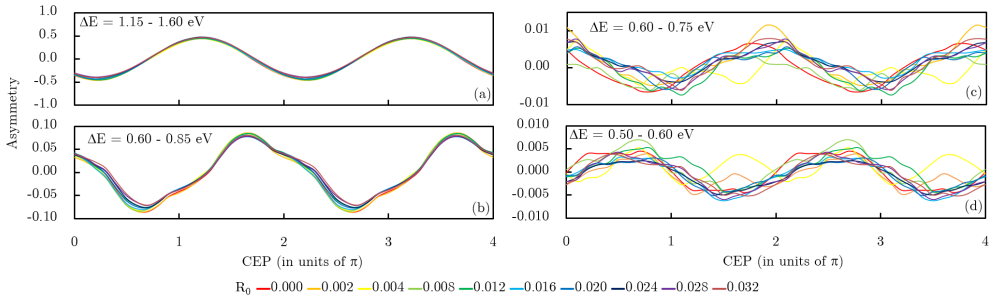


FIGURE 5. (color online) Asymmetry dependence on CEP for (a) Hydrogen in high energy range, (b) Hydrogen in low energy range, (c) Deuterium in high energy range, (d) Deuterium in low energy range. R_0 is the nanotip sharpness parameter.

Once the nanotip is introduced into the system, the contrast is generated which is shown visually in Figure 6. Different sharpness values cause different contrasts. It tends to be growing with sharpness for Hydrogen apart from the sudden decrease around $R_0 \sim 0.02$ alu^{-1} for low energy range whereas it is tumultuous between 0.0 and 0.4 for Deuterium in both energy regions. Contrast for Deuterium is stronger than that of Hydrogen.

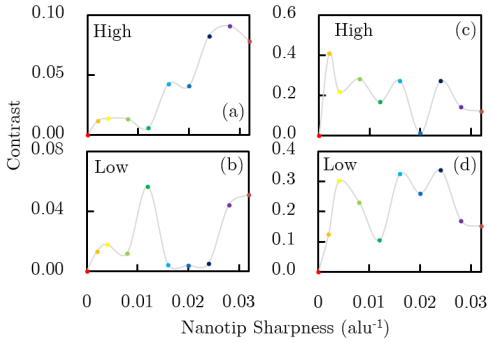


FIGURE 6. (color online) Contrast in different energy ranges for Hydrogen (left-panel) and Deuterium (right-panel).

CONCLUSION

We have simulated the interaction between an ultrashort laser pulse and Hydrogen cation molecule and we have investigated the isotope effect on this interaction. We only consider the first isotope, Deuterium, in this work. We reckoned for the cations are created during the interaction with laser pulse. For this purpose, we used MO-ADK method to gain the ionization times and ionization rates for neutral molecules. Then we solved the TDSE for interactions with different CEP values. We started the simulations at the ionization times and we calculated the momenta via virtual detector method at each time step. After the simulations, we employed the binning/histogramming mechanism to obtain dissociation rates as a function of KER. Using the dissociation distributions obtained for different ionization times, we calculated the total dissociation rate per molecule. We have investigated the asymmetry in dissociation and through the average of asymmetry, we obtained the contrast parameters.

Dissociation rates have a peak around 1.3 eV for both Hydrogen and Deuterium. The peak is narrower for the isotope which is evident for a shorter ATD channel. Dissociation rates for Deuterium is weaker than that of Hydrogen and so as the Asymmetries in different energy regions. But the contrast for Deuterium is stronger than the contrast for Hydrogen.

ACKNOWLEDGMENTS

Authors are supported by Marmara University Scientifical Research Projects Unit, BAPKO, under project number FEN-C-DRP-230119-0005. SAK is grateful for the partial support of Turkish Funding Agency, TUBITAK, by 2211 Graduate Bursary Program. Simulations are performed on super computers located in Istanbul Technical University National Center for High Performance Computing of Turkey (ITU-UHeM) under project number 1006582019. Post-processing is done in the workstations at Simulab@MU (www.simulab.org).

REFERENCES

[1] M. F. Ciappina, J. A. Pérez-Hernández, A. S. Landsman, W. A. Okell, S. Zherebtsov, B. Frg, J. Schtz, L. Seiffert, T. Fennel, T. Shaaran, T. Zimmermann, A. Chacón, R. Guichard, A. Zar, J. W. G. Tisch, J. P. Marangos, T. Witting, A. Braun, S. A. Maier, L. Roso, M. Krger, P. Hommelhoff, M. F. Kling, F. Krausz, and M. Lewenstein, Reports on Progress in Physics **80**, p. 054401mar (2017).

[2] S. Kim, J. Jin, Y.-J. Kim, I.-Y. Park, Y. Kim, and S.-W. Kim, Nature **453**, p. 757760 (2008).

[3] P. Hommelhoff, Y. Sortais, A. Aghajani-Talesh, and M. A. Kasevich, Phys. Rev. Lett. **96**, p. 077401Feb (2006).

[4] C. Ropers, D. R. Solli, C. P. Schulz, C. Lienau, and T. Elsaesser, Phys. Rev. Lett. **98**, p. 043907Jan (2007).

[5] R. Bormann, M. Gulde, A. Weismann, S. V. Yalunin, and C. Ropers, Phys. Rev. Lett. **105**, p. 147601Sep (2010).

[6] M. Schenk, M. Krüger, and P. Hommelhoff, Phys. Rev. Lett. **105**, p. 257601Dec (2010).

[7] H. Yanagisawa, M. Hengsberger, D. Leuenberger, M. Klöckner, C. Hafner, T. Greber, and J. Osterwalder, Phys. Rev. Lett. **107**, p. 087601Aug (2011).

[8] D. J. Park, B. Piglosiewicz, S. Schmidt, H. Kollmann, M. Mascheck, and C. Lienau, Phys. Rev. Lett. **109**, p. 244803Dec (2012).

[9] P. Dombi, A. Hrl, P. Rcz, I. Mrton, A. Trgler, J. R. Krenn, and U. Hohenester, Nano Letters **13**, 674–678 (2013).

[10] J. Vogelsang, J. Robin, B. J. Nagy, P. Dombi, D. Rosenkranz, M. Schiek, P. Gro, and C. Lienau, Nano Letters **15**, 4685–4691 (2015).

[11] K. E. Echternkamp, G. Herink, S. V. Yalunin, K. Rademann, S. Schäfer, and C. Ropers, Applied Physics B **122**, p. 80 (2016).

[12] S. Li and R. R. Jones, Nature Communications **7**, p. 13405 (2016).

[13] E. A. Peralta, K. Soong, R. J. England, E. R. Colby, Z. Wu, B. Montazeri, C. McGuinness, J. McNeur, K. J. Leedle, D. Walz, E. B. Sozer, B. Cowan, B. Schwartz, G. Travish, and R. L. Byer, Nature **503**, p. 91 (2013).

[14] J. Breuer and P. Hommelhoff, Phys. Rev. Lett. **111**, p. 134803Sep (2013).

[15] M. Krger, M. Schenk, and P. Hommelhoff, Nature **475**, p. 78 (2011).

[16] G. Wachter, C. Lemell, J. Burgdörfer, M. Schenk, M. Krüger, and P. Hommelhoff, Phys. Rev. B **86**, p. 035402Jul (2012).

[17] S. Zherebtsov, F. Sßmann, C. Peltz, J. Plenge, K. J. Betsch, I. Znakovskaya, A. S. Alnaser, N. G. Johnson, M. Kbel, A. Horn, V. Mondes, C. Graf, S. A. Trushin, A. Azzeer, M. J. J. Vrakking, G. G. Paulus, F. Krausz, E. Rhl, T. Fennel, and M. F. Kling, New Journal of Physics **14**, p. 075010jul (2012).

[18] L. Seiffert, P. Henning, P. Rupp, S. Zherebtsov, P. Hommelhoff, M. F. Kling, and T. Fennel, Journal of Modern Optics **64**, 1096–1103 (2017).

[19] P. Rupp, L. Seiffert, Q. Liu, F. Smann, B. Ahn, B. Frg, C. G. Schfer, M. Gallei, V. Mondes, A. Kessel, S. Trushin, C. Graf, E. Rhl, J. Lee, M. S. Kim, D. E. Kim, T. Fennel, M. F. Kling, and S. Zherebtsov, Journal of Modern Optics **64**, 995–1003 (2017).

[20] F. Süssmann, L. Seiffert, S. Zherebtsov, V. Mondes, J. Stierle, M. Arbeiter, J. Plenge, P. Rupp, C. Peltz, A. Kessel, S. A. Trushin, B. Ahn, D. Kim, C. Graf, E. Rühl, M. F. Kling, and T. Fennel, Nature Communications **6**, p. 7944 (2015).

[21] I. Yavuz, J. Schötz, M. F. Ciappina, P. Rosenberger, Z. Altun, M. Lewenstein, and M. F. Kling, Phys. Rev. A **98**, p. 043413Oct (2018).

[22] E. Kazuma, J. Jung, H. Ueba, M. Trenary, and Y. Kim, Science **360**, 521–526 (2018).

[23] Q. Zhang, E. Uchaker, S. L. Candelaria, and G. Cao, Chem. Soc. Rev. **42**, 3127–3171 (2013).

[24] Y.-F. Huang, H.-P. Zhu, G.-K. Liu, D.-Y. Wu, B. Ren, and Z.-Q. Tian, Journal of the American Chemical Society **132**, 9244–9246 (2010).
[25] H. Zhu, X. Ke, X. Yang, S. Sarina, and H. Liu, Angewandte Chemie International Edition **49**, 9657–9661 (2010).
[26] L. Kang, P. Xu, B. Zhang, H. Tsai, X. Han, and H.-L. Wang, Chem. Commun. **49**, 3389–3391 (2013).
[27] Z. Zhang, T. Deckert-Gaudig, P. Singh, and V. Deckert, Chem. Commun. **51**, 3069–3072 (2015).
[28] S. Mukherjee, F. Libisch, N. Large, O. Neumann, L. V. Brown, J. Cheng, J. B. Lassiter, E. A. Carter, P. Nordlander, and N. J. Halas, Nano Letters **13**, 240–247 (2013).
[29] Z. Zhang, S. Sheng, H. Zheng, H. Xu, and M. Sun, Nanoscale **6**, 4903–4908 (2014).
[30] A. M. Brown, R. Sundararaman, P. Narang, W. A. Goddard, and H. A. Atwater, ACS Nano **10**, 957–966 (2016).
[31] H. A. Atwater and A. Polman, Nature Materials **9**, 205–213 (2010).
[32] C. Clavero, Nature Photonics **8**, 95–103 (2014).
[33] M. L. Brongersma, N. J. Halas, and P. Nordlander, Nature Nanotechnology **10**, 25–34 (2015).
[34] S. Linic, U. Aslam, C. Boerigter, and M. Morabito, Nature Materials **14**, 567–576 (2015).
[35] E. M. van Schrojenstein Lantman, T. Tanja Deckert-Gaudig, A. J. G. Mank, V. Volker Deckert, and B. M. Weckhuysen, Nature Nanotechnology **7**, 583–586 (2012).
[36] P. Christopher, H. Xin, and S. Linic, Nature Chemistry **3**, 467–472 (2011).
[37] R. Sundararaman, P. Narang, A. S. Jermyn, W. A. Goddard III, and H. A. Atwater, Nature Communications **5** (2014).
[38] X. M. Tong, Z. X. Zhao, and C. D. Lin, Phys. Rev. A **66**, p. 033402Sep (2002).
[39] J. Schötz, B. Förg, M. Förster, W. A. Okell, M. I. Stockman, F. Krausz, P. Hommelhoff, and M. F. Kling, IEEE Journal of Selected Topics in Quantum Electronics **23**, 77–87May (2017).
[40] S. Thomas, G. Wachter, C. Lemell, J. Burgdrfer, and P. Hommelhoff, New Journal of Physics **17**, p. 063010jun (2015).
[41] L. Novotny and B. Hecht, *Principles of Nano-Optics* (Cambridge University Press, Cambridge, 2012).
[42] B. Feuerstein and U. Thumm, Phys. Rev. A **67**, p. 043405Apr (2003).
[43] J. J. Hua and B. D. Esry, Journal of Physics B: Atomic, Molecular and Optical Physics **42**, p. 085601mar (2009).

BOOK OF FULL TEXT PROCEEDINGS TURKISH PHYSICAL
SOCIETY 35th INTERNATIONAL PHYSICS CONGRESS (TPS35)
TPS35, Vol.01, No.03, pp.217-220.
ISBN:978-605-83516-6-0

15 December 2019

Controlling Electron Localization in the Dissociation of H_2^+ and HD^+

Muratcan Oner[1,b)], Saba Arife Karakas[1,c)] and Ilhan Yavuz[1,a)]

[1]*Department of Physics, Faculty of Arts & Science, Marmara University, Goztepe, Istanbul, Turkey*

[a)]Corresponding author: ilhan.yavuz@marmara.edu.tr, OrcID: 0000-0002-3268-6268
[b)]muratcanoner@marun.edu.tr, OrcID: 0000-0003-4095-6835
[c)]saba.bozpolat@marmara.edu.tr, OrcID: 0000-0002-2166-6464

Abstract. We demonstrate a theoretical study of molecular ions dynamics in plasmon-enhanced laser fields and study the effects on the asymmetric molecular ion. Nuclei dissociate due to the strong laser pulse targeted to the molecule and after dissociation, probability of localization of the electron can be deliberately changed by moderating the phase angle of the laser pulse and the sharpness of the nanostructure. We present dissociation of both H_2^+ and HD^+ and the asymmetries of the electron localization probabilities in the vicinity of a nanostructure.

INTRODUCTION

Understanding of the behavior of electrons and using the information we get from such processes to control electron dynamics is one of the most intriguing topics of molecular science. One such way is exposing an intense and coherent electromagnetic radiation to the molecular systems. As a result of this molecule-laser interactions, some interesting phenomena occur such as High Harmonic Generation (HHG) [1], Above Treshold Ionization (ATI) [2], recombination [3, 4, 5], bond softening and bond hardening [6, 7, 8, 9]. Here, we develop an understanding of the dynamics of Hydrogen based molecular ions in the presence of a metallic structure, called nanotip. Carrier Envelope Phase (CEP) controlled laser pulse defined as,

$$E(t) = E_0 exp(-t^2/\tau^2) cos(w_0 t + \phi), \tag{1}$$

where E_0 is the strength, τ is the duration, w_0 is the frequency and ϕ is the CEP, is targetted to the symmetric H_2^+ and asymmetric HD^+ molecular ions in order to gain a preliminary understanding about molecular dynamics of asymmetric molecules. Other works show that the CEP parameter has a controlling effect on the electron localization [10]. We present theoretical electron-proton coupled dynamic simulations on the, $HD^+ \rightarrow H + D^+$ by a strong laser pulse. In this study, nanotip is another tool that has an effect on electron localization. In the vicinity of the sharp edge of the nanotip, intensity of the laser field is varied. Because there are two parameters in this theoretical model, a second order asymmetry in the localization occurs, and the purpose of this study is to observe the contrast between these cases for both symmetric H_2^+ and asymmetric HD^+ molecular ions.

METHODS

A. Numerical Solution Of The Time-Dependent Schrodinger Equation (TDSE)

TDSE for the both H_2^+ and HD^+ molecular ions with the laser field in atomic units is numerically solved under Born-Oppenheimer (BO) approximation and the equation is considered as,

$$[-\frac{1}{2}\frac{\partial^2}{\partial z^2} - \frac{1}{2\mu_p}\frac{\partial^2}{\partial R^2} + V_e(z,R) + V_n(R) + V_L(z,t)]\Psi(z,R,t) = i\frac{\partial}{\partial t}\Psi(z,R,t), \tag{2}$$

Türk Fizik Derneği
1950
Turkish Physical Society

where $\mu_p = \frac{m_p}{2}$ is the reduced mass of the two nuclei and the contributions from the potential energies , $V_e(z,R)$, $V_n(R)$ and $V_L(z,t)$ are electron-nuclei attraction, nucleus-nucleus repulsion and laser field respectively. Explicit forms of the potentials in atomic units considered as,

$$V_e(z,R) = -\frac{a}{\sqrt{(z+R/2)^2+b(R)}} - \frac{a}{\sqrt{(z-R/2)^2+b(R)}}, \tag{3}$$

$$V_n(R) = \frac{1}{R}, \tag{4}$$

$$V_L(z,t) = -zE(z,t), \tag{5}$$

where a and $b(R)$ are parametrized as to match the exact potential energy curves of the H_2^+ and HD^+.

B. Metallical Structure and Field Enhancement

A metallic nanotip is placed close to the H_2^+ and HD^+ molecular ions in the setup so that the laser pulse can affect both the nanotip and the molecular ion. The interaction between laser pulse and the nanotip causes plasma oscillations which creates a spatial inhomogeneous electric field in the local area. Due to this spatial inhomogeneity in electric field, symmetric dissociation of the electron being with a nucleus changes and the asymmetric dissociation occur. Spatial form of the enhanced field can be determined by the Finite-difference time-domain (FDTD) method [11]. In a typical theoretical modeling of laser and matter interaction, basic assumption is that the electric field is spatially homogeneous and only time dependent. On the other hand, electric field produced by the plasma oscillations on the surface of the metallic nanotip, as in our case, is dependent of the position. Therefore, we modified laser-matter interaction as to include this field inhomogenity [12].

RESULTS

In this section, we show the dissociation dynamics and the electron localization obtained from the simulations due to the nanotip and the CEP controlled laser interactions.

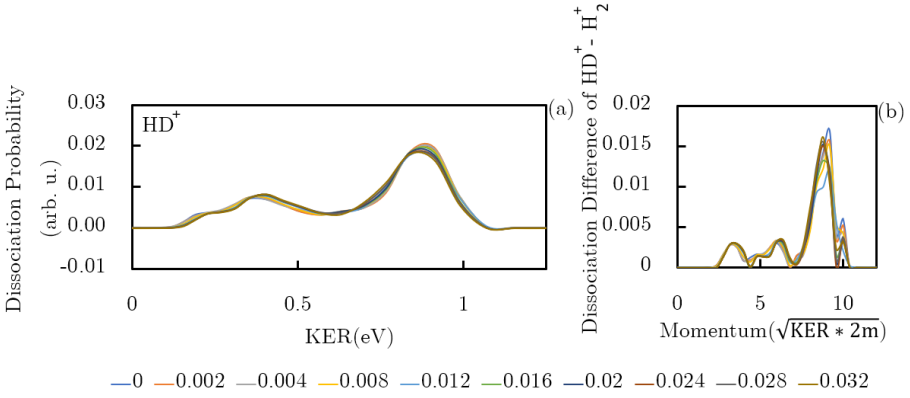


FIGURE 1. (Color online) (a) show, dissociation probability as a function of the Kinetic Energy Release (KER). Colours respectively show the increase of the nanotip sharpness. (b) shows the absolute difference in dissociation between H_2^+ and HD^+.

In Figure 1 (a), around the values 0.4 and 0.9 eV, dissociation probabilities make peaks and those are the KER values where the dissociation takes place for the nuclei. From Figure 1 (b), we have an understanding that there is a variation in dissociation between H_2^+ and HD^+ for various nanotips as the momentum differs.

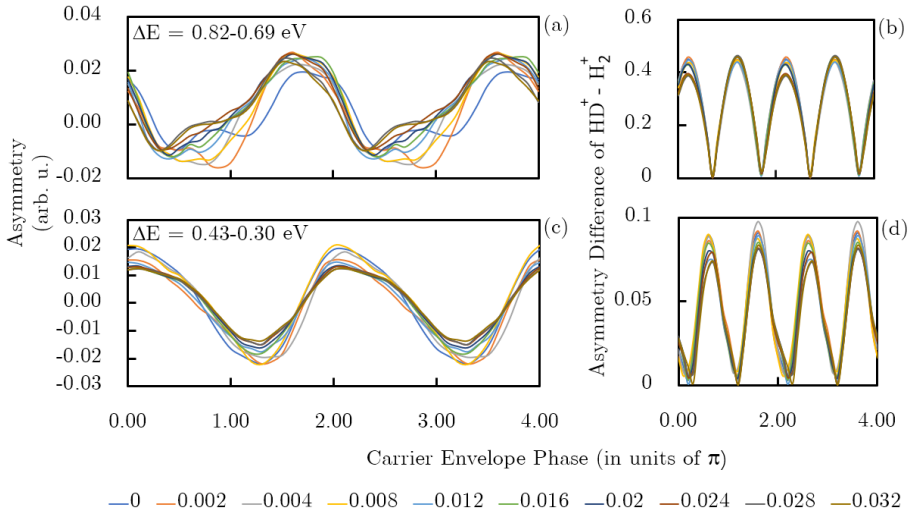


FIGURE 2. (Color online) (a) and (c) are KER integrated asymmetries of electron localization for various Carrier Envelope Phase (CEP) for high energy region and low energy region, respectively. Colours respectively show the increase of the nanotip sharpness. (b) and (d) represent the absolute asymmetry difference between H_2^+ and HD^+ corresponding to (a) and (c), respectively.

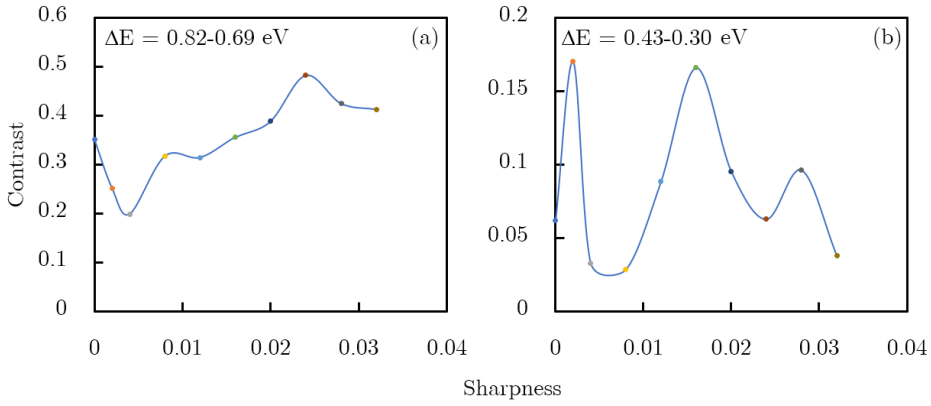


FIGURE 3. (Color online) Contrast between the asymmetric probabilities of electron localization in arbitrary units for different sharpness values of the nanotip. Dots in the graph has the same colours with the sharpness values from Figure 2.

From Figure 2 (a) and (c), we can assume that there is a sinusoidal pattern of asymmetry for different sharpness values of the nanotip as the CEP parameter changes. For instance, in Figure 2 (a) which consist the asymmetry information in the high energy region, there is a significant variation in asymmetry, between 0 and $\frac{\pi}{2}$. As the CEP goes to $\frac{\pi}{2}$, first, asymmetry goes to zero and continuing to increase in the negative direction. For every different sharpness values for the nanotip, relatively similar asymmetry patterns has been detected even though the asymmetries differ for various sharpness values. Figure 2 (b) and (d) show that there are also periodic differences between H_2^+ and HD^+ for the asymmetry values in electron localization for high and low energy regions, respectively.

Both for the high and low energy regions for several CEP values, there are peak asymmetry values as can be seen in Figure 2 (a) and (c). When we look at where the asymmetries make peak in magnitude for maximum values, there is a difference. This difference we call here is “contrast”. It can be said that there is also a asymmetry between the asymmetric probabilities of electron localization for both right and left protons. Figure 3 (a) shows this contrast with an increasing pattern for the high energy region and Figure 3 (b), with a wavy behaviour for the low energy region.

CONCLUSION

We have studied the electron localization of HD^+, which is an asymmetric molecular ion, and H_2^+, which is a symmetric molecular ion when a strong laser pulse is subjected in the presence of a nanotip in order to understand the molecular dynamics of these systems. Asymmetries in the electron localization occured as we manipulate the carrier envelope phase and changed the sharpness of the nanotip in order to induce spatially inhomogeneous electric field in a local area near the sharp edge of the nanotip. Because there are two different types of parameters in the system, asymmetric probabilities of the electron localization becomes also asymmetric, and the contrast between these has been explained. This study gives us an understanding how atomic and molecular particles behave in different situations.

ACKNOWLEDGMENTS

This study is supported by Marmara University Scientifical Research Projects Unit, BAPKO, under project number FEN-C-DRP-230119-0005. SAK is grateful for the partial support of Turkish Funding Agency, TUBITAK, by 2211 Graduate Bursary Program. Simulations are performed on super computers located in Istanbul Technical University National Center for High Performance Computing of Turkey (ITU-UHeM) under project number 1006582019. Post-processing is done in the workstations at Simulab@MU (www.simulab.org).

REFERENCES

[1] P. B. Corkum and F. Krausz, Nature Physics **3**, 381–387 (2007).
[2] F. Krausz and M. Ivanov, Rev. Mod. Phys. **81**, p. 163 (2009).
[3] G. Wachter, C. Lemell, J. Burgdörfer, M. Schenk, M. Krüger, and P. Hommelhoff, Phys. Rev. B **86** (2012).
[4] V. R. Bhardwaj, P. B. Corkum, and D. M. Rayner, Phys Rev Lett **93** (2012).
[5] F. Sussmann, L. Seiffert, S. Zherebtsov, V. Mondes, J. Stierle, M. Arbeiter, J. Plenge, P. Rupp, C. Peltz, A. Kessel, S. A. Trushin, B. Ahn, D. Kim, C. Graf, E. Ruhl, M. F. Kling, and T. Fennel, Nature Communications **6**, p. 7944 (2015).
[6] P. H. Bucksbaum, A. Zavriyev, H. G. Muller, and D. W. Schumacher, Phys. Rev. Lett. **64**, p. 1883 (1990).
[7] A. Zavriyev, P. H. Bucksbaum, J. Squier, and F. Saline, Phys. Rev. Lett. **70**, p. 1077 (1993).
[8] L. J. Frasinski, J. H. Posthumus, J. Plumridge, K. Codling, P. F. Taday, and A. J. Langley, Phys. Rev. Lett. **83**, p. 3625 (1999).
[9] H. Abou-Rachid, T. Tung Nguyen-Dang, and O. Atabek, J. Chem. Phys **110**, p. 4737 (1999).
[10] M. F. Kling, C. Siedschlag, A. J. Verhoef, J. I. Khan, M. Schultze, T. Uphues, Y. Ni, M. Uiberacker, M. Drescher, F. Krausz, and M. J. J. Vrakking, Science **312**, p. 246 (2006).
[11] A. F. Oskooi, D. Roundy, M. Ibanescu, P. Bermel, J. D. Joannopoulos, and S. G. Johnson, Computer Physics Communications **181**, 687–702 (2009).
[12] I. Yavuz, J. Schötz, M. F. Ciappina, P. Rosenberger, Z. Altun, M. Lewenstein, and M. F. Kling, Phys. Rev. A **98** (2018).

BOOK OF FULL TEXT PROCEEDINGS TURKISH PHYSICAL
SOCIETY 35th INTERNATIONAL PHYSICS CONGRESS (TPS35) 15 December 2019
TPS35, Vol.01, No.03, pp.221-224.
ISBN:978-605-83516-6-0

Theoretical Calculations of Electron Paramagnetic Resonance Parameters of Acetamide in Water

Ebru KARAKAŞ SARIKAYA[1,a], Ömer DERELİ[1]

[1] *Konya Necmettin Erbakan University, A. Keleşoğlu Education Faculty, Department of Physics, Konya, Turkey*

[a)] Corresponding author: ebrukarakas_84@hotmail.com

Abstract. Acetamide (CH_3CONH_2) is a member of the class of acetamides that results from the formal condensation of acetic acid with ammonia. This molecule is a colorless crystal with a mousy odor. To obtain molecular structure, conformational analysis of Acetamide was performed. Geometry optimizations were performed with DFT/B3LYP method and the standard 6-311++G(d,p) basis set in water. Dipole moment and energy of the molecule calculated as 3.9734 Debye and -131330.6475 kcal/mol, respectively. From our assumptions made on the basis of the experimental spectra and suggested radical form in the literature, a total of eight radicals were modeled by DFT computations (in water). Theoretically modeled Rad3 is an experimentally proposed radical. Hfccs and g-factors of the modeled radicals were calculated by the B3LYP method using the TZVP basis set and compared with the experimental counterparts.

INTRODUCTION

Acetamide is used as a solvent, stabilizer, plasticizer, wetting agent and to make other chemicals and it is very soluble in water. Investigators that use acetamide may breathe in vapors or have direct skin contact, however; the people may be exposed by smoking cigarettes or through skin contact with products containing acetamide. Acetamide is a mild skin and eye irritant[1]. Data on the potential for acetamide to produce additional toxic effects in humans is not available. Researchers reported that acetamide has low acute toxicity in laboratory animals and decreased body weight was the only toxic effect associated with a single exposure to a very high oral dose. Moreover, they reported that liver tumors and lymphoma were observed in laboratory animals following repeated oral exposure to acetamide over time[1].

Because of these important properties obtained by searching literature, in this study conformation of acetamide was determined and stable structure of molecule was revealed. All physical and chemical properties of a molecule are related to molecular structure. DFT technique is used to determine energy, dipole moment, bond lengths, bond angles and dihedral angles of molecular and radical structure. Considering the experimental results obtained from the literature, eight radical structures were modeled from the stable structure obtained. DFT has also been used for the determination of Electron Paramagnetic Resonance (EPR) parameters. In this article, the experimental results obtained from the literature are compared with the results of the theoretical study conducted by us.

COMPUTATIONAL DETAILS

To determine the correct radical structure, it is necessary to determine the correct molecular structure primarily. For this purpose, the calculations were started with the conformational analysis. So as to obtain stable conformer, initially conformational analysis was done. Spartan 08 program[2] was used for conformational analysis and the conformational space of Acetamide was scanned with Merck Molecular Force Field (MMFF) method. As a result of

Türk Fizik Derneği
1950
Turkish Physical Society

this calculation, only one conformation was obtained and it is not a flexible molecule. Then, geometry optimization of this conformation was performed in water. The calculations of geometrical parameters in the ground state were performed by using the Gaussian 03W[3] Program. The output files were visualized via GaussView[4] software. For the purpose that obtain accurate geometric parameters, the structural properties were determined through performing B3LYP method 6-311++G (d,p) basis set. This method has been used many times in our study[5-9], on the grounds that the calculations results are more accurate. Energy, dipole moment, bond lengths, bond angles and dihedral angles for acetamide in water were calculated with the same level of the theory.

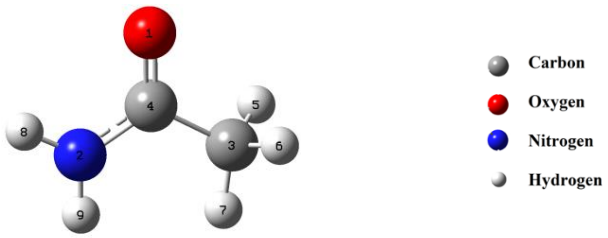


FIGURE 1. Stable conformer of the Acetamide molecule in liquid phase (water).

Energy value obtained as a result of geometry optimization calculation is **-131330.6475 kcal/mol** and dipole moment is **3.9734 Debye**. By the way, conformer has been obtained as shown in Fig. 1. And geometry parameters of stable conformer and crystal structure parameters were given Table 1. The structural parameters of the studied molecule compared with data in the literature.

Table 1. The calculated geometry parameters of Acetamide by B3LYP/6-311++G(d,p) method in water and Experimental values

Bond lengths(A°)	Teo.	Exp.*	Bond angles (^{0})	Teo.	Exp.*	Dihedral angles (^{0})	Teo.	Exp.*
O1,C4	1.23	1.22	C4,N2,H8	119.4	-	H8,N2,C4,O1	0.0	-
N2,C4	1.35	1.38	C4,N2,H9	122.3	-	H8,N2,C4,C3	-180.0	-
N2,H8	1.01	1.02	H8,N2,H9	118.3	-	H9,N2,C4,O1	180.0	-
N2,H9	1.01	1.02	C4,C3,H5	108.7	109.8	H9,N2,C4,C3	0.0	-
C3,C4	1.51	1.51	C4,C3,H6	108.7	109.8	H5,C3,C4,O1	-58.4	-
C3,H5	1.09	1.12	C4,C3,H7	113.4	109.8	H5,C3,C4,N2	121.6	-
C3,H6	1.09	1.12	H5,C3,H6	107.7	-	H6,C3,C4,O1	58.5	-
C3,H7	1.09	1.12	H5,C3,H7	109.1	-	H6,C3,C4,N2	-121.5	-
			H6,C3,H7	109.1	-	H7,C3,C4,O1	180.0	-
			O1,C4,N2	122.0	122.0	H7,C3,C4,N2	0.0	-
			O1,C4,C3	121.6	123.0			
			N2,C4,C3	116.4	115.1			

*Values are taken from Ref[10].

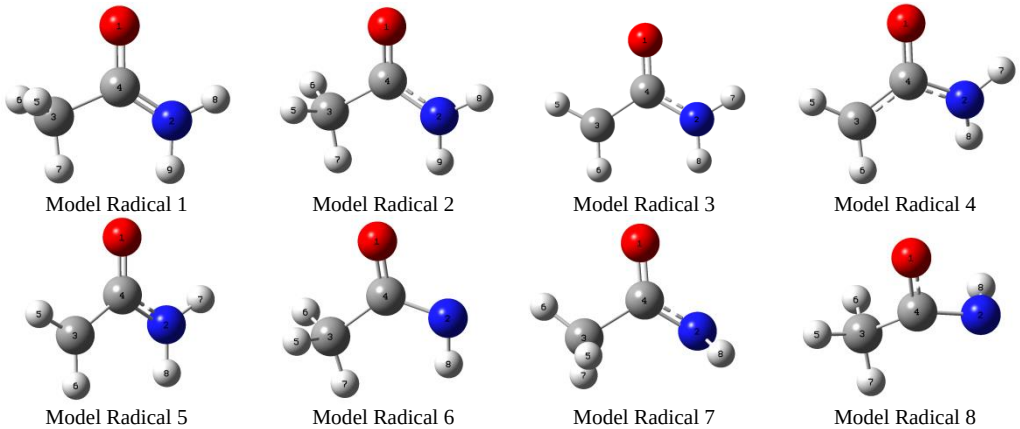


FIGURE 2. Model radicals of Acetamide molecule in water

According to the geometry optimizations results, obtained stable structure were used for eight different radicals were modeled. Model radicals were shown in Fig. 2. Model Radical 1 (MR1) and MR2 were modelled as the cation and anion of the Acetamide molecule, respectively. MR3 is a neutral radical formed by abstraction of **H5** atom from the molecule. MR4 is cation form of MR3 and MR5 is anion form of MR3. MR6 is a neutral radical formed by abstraction of **H8** atom from the molecule. MR7 and MR8 is cation and anion form of MR6, respectively.

Table 2. The theoretical and experimental hyperfine-splitting parameters (a) and g-values of model radicals Acetamide in water

a_{iso}	MR1	MR2	MR3	MR4	MR5	MR6	MR7	MR8	Experimental[a]
N2	6.94	-0.56	0.62	4.06	-0.89	9.04	6.84	14.40	g = 2,00298
H5	-3.09	31.59	-	-	-	-3.64	0.12	4.29	A_N=1,72G
H6	-3.07	31.60	-19.30	-8.89	-10.20	-3.63	3.43	14.23	A_H=2,04G
H7	24.11	0.58	-18.97	-6.32	-10.17	-0.43	6.07	2.67	A_H=2,43 G
H8	-0.44	-3.91	-2.43	-6.75	-2.20	-	-	-	A_H=21,34 G
H9	2.25	-4.05	-1.71	-5.33	-2.18	-17.58	-11.26	12.48	
g_{iso}	2.00848	2.00341	2.00372	2.02629	2.00698	2.00607	2.00909	2.00885	

[a]Experimental values are taken from Ref[11].

Hfccs and g-values of model radicals were computed within NMR /GIAO approach which is the most common method used to calculate EPR parameters. Hfccs and g-factors of modelled radicals were found by B3LYP functional TZVP basis set obtained from Basis Set Exchange (BSE) software and the EMSL Basis Set Library of DFT after accomplished geometry optimization calculations. The theoretical and experimental hfccs and g-values of model radicals were shown in Table 2.

RESULT AND DISCUSSION

With only experimental techniques, the analysis of the EPR spectra having hyperfine splittings is very difficult. So we calculated EPR parameters of these model radicals which are shown in Fig.2. And then the obtained values were compared to the corresponding experimental data reported in the literature.

Experimental EPR study of Acetamide was reported by "Paramagnetic Resonance Study of Liquids during Photolysis. V. Acid Amides and an Imide"[11]. The experimental spectrum taken from article was shown in Fig. 3. The researchers reported that they had prepared free radicals resulting from abstraction of hydrogen form acetamide by irradiation of solutions (a water solution of 200 g/liter of acetamide) containing 1%H_2O_2 with ultraviolet light[11]. They suggested that $\dot{C}H_2CONH_2$ radical was present in their spectrum.

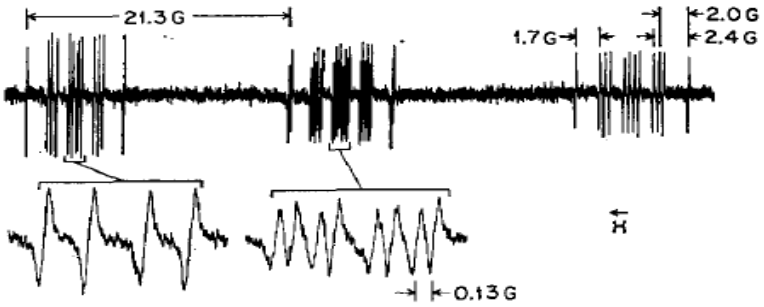


FIGURE 3. The experimental spectrum of Acetamide was taken from Exp. study[11].

It is difficult to measure g-values more accurately than by 10^{-3}. Thus, a deviation of 500 ppm between theory and experiment usually falls within the experimental error, and even an agreement with theory within 1000 ppm (1ppt) is considered satisfactory[12]. Consequently, difference between experimental and calculated g values of radical must lie within 1000 ppm. In our study, MR2 and MR3 are in this area. The results have demonstrated that the experimentally observed EPR parameters match the theoretical EPR values obtained for MR3. The model MR3 is a neutral radical formed by abstraction of H5 atom from the molecule. 20% deviations would be quite acceptable for calculated isotropic hyperfine splitting values of experimentally isolated radicals[13]. As seen as Table 2, the

ISBN:978-605-83516-6-0

calculated hyperfine constants of MR3 are a_N: 0.62, a_H: 19.30, a_H: 18.97, a_H: 2.43, a_H: 1.71 and the experimental counterparts are a_N: 1.72, a_H: 21.34, a_H: 21.34, a_H: 2.43, a_H: 2.04. These results showed that experimentally and theoretically proposed radical is correct.

ACKNOWLEDGMENT

This work was financially supported by the Bap, Necmettin Erbakan University in Turkey.

REFERENCES

1. R. P. Pohanish, *Sittig's Handbook of Toxic and Hazardous Chemicals and Carcinogens*. (Elsevier Science, 2011).
2. Irvine, (Wavefunction Inc., CA 92612, USA, 2008).
3. M. J. T. Frisch, G. W.; Schlegel, H. B.; Scuseria, G. E.; Robb, M. A.; Cheeseman, J. R.; Montgomery, Jr., J. A.; Vreven, T.; Kudin, K. N.; Burant, J. C.; Millam, J. M.; Iyengar, S. S.; Tomasi, J.; Barone, V.; Mennucci, B.; Cossi, M.; Scalmani, G.; , N. P. Rega, G. A.; Nakatsuji, H.; Hada, M.; Ehara, M.; Toyota, K.; Fukuda, R.; Hasegawa, J.; Ishida, M.; Nakajima, T.; Honda, Y.; Kitao, O.; Nakai, H.; Klene, M.; Li, X.; Knox, J. E.; Hratchian, H. P.; Cross, J. B.; Bakken, V.; Adamo, C.;, J. G. Jaramillo, R.; Stratmann, R. E.; Yazyev, O.; Austin, A. J.; Cammi, R.; Pomelli, C.; Ochterski, J. W.; Ayala, P. Y.; Morokuma, K.; Voth, G. A.; Salvador, P.; Dannenberg, J. J.; Zakrzewski, V. G.; Dapprich, S.; Daniels, A. D.;Strain, M. C.; , O. M. Farkas, D. K.; Rabuck, A. D.; Raghavachari, K.; Foresman, J. B.; Ortiz, J. V.; Cui, Q.; Baboul, A. G.; Clifford, S.; Cioslowski, J.; Stefanov, B. B.; Liu, G.; Liashenko, A.; Piskorz, P.; Komaromi, I.; Martin, R. L.; Fox, D. J.; Keith, T.; and M. A. P. Al-Laham, C. Y.; Nanayakkara, A.; Challacombe, M.; Gill, P. M. W.; Johnson, B.; Chen, W.; Wong, M. W.; Gonzalez, C.; and Pople, J. A, (Gaussian, Inc., Wallingford CT, 2003).
4. R. Dennington, T. Keith and J. Millam, Semichem Inc.: Shawnee Mission, KS (2009).
5. L. Ateş, Y. Erdoğdu, E. K. Sarıkaya, F. P. Özturan and Ö. Dereli, Selçuk-Teknik Dergisi, 15(3), 253-263 (2016).
6. Ö. Dereli, Y. Erdoğdu, L. Ateş, E. K. Sarıkaya and F. P. Özturan, Gazi University Journal of Science **30** (1), 161-165 (2017).
7. E. K. Sarıkaya, S. Bahçeli, D. Varkal and Ö. Dereli, Journal of Molecular Structure **1141**, 44-52 (2017).
8. E. K. Sarıkaya and Ö. Dereli, Journal of Molecular Structure **1052**, 214-220 (2013).
9. E. K. Sarıkaya, Ö. Dereli, Y. Erdoğdu and M. Güllüoğlu, Journal of Molecular Structure **1049**, 220-226 (2013).
10. M. Kitano and K. Kuchitsu, Bulletin of the Chemical Society of Japan **46** (10), 3048-3051 (1973).
11. R. Livingston and H. Zeldes, The Journal of Chemical Physics **47** (10), 4173-4180 (1967).
12. F. Neese, Journal of Chemical Physics **115** (24), 11080-11096 (2001).
13. D. M. Chipman, in *Quantum mechanical electronic structure calculations with chemical accuracy*, edited by P. G. Mezey (Kluwer Academic Publishers, CANADA, 1994).

BOOK OF FULL TEXT PROCEEDINGS TURKISH PHYSICAL
SOCIETY 35th INTERNATIONAL PHYSICS CONGRESS (TPS35)
TPS35, Vol.01, No.03, pp.225-229.
ISBN:978-605-83516-6-0

15 December 2019

A DFT Study on Molecular Structure and EPR Parameters of N, N-Dimethylformamide in Acetone and Water

Ebru KARAKAŞ SARIKAYA[1, a], Ömer DERELİ[1]

[1] *Konya Necmettin Erbakan University, A. Keleşoğlu Education Faculty, Department of Physics, Konya, Turkey*
[a)] *Corresponding author: ebrukarakas_84@hotmail.com*

Abstract. N, N-Dimethylformamide ($HCON(CH_3)_2$) is an organic compound. This colorless liquid is a water-white liquid with a faint fishy odor which is miscible with water and the majority of organic liquids. This study was started by determining the molecular structure in the liquid phase (in acetone and water). For this purpose, conformation analysis was performed by using spartan14 program. One conformer was determined. In this study only the theoretical calculation was performed experimental results were taken from a previous study. In experimental study, researchers suggested that the radicals resulted from abstraction of methyl hydrogen and that two isomers were present. Theoretically eleven radicals were modeled. Rad3 and Rad6 are isomeric radicals. As suggested in the experiment, it was established that also theoretically found together for these radicals in radical structure.

INTRODUCTION

N,N-dimethylformamide (DMF) is a member of the class of formamides that is formamide in which the amino hydrogens are replaced by methyl groups. It has a role as a polar aprotic solvent and a hepatotoxic agent. It is a volatile organic compound and a member of formamides[1-3]. Shih-Min Wang et al. in their study reported that "Major adverse health effects associated with DMF exposures include alcohol intolerance, hepatotoxicity, male reproductive cancers, possible embryo toxicity, teratogenicity in human and animals and sperm mortality perturbation in humans. In 2000, DMF was selected as one of four chemicals needed for conducting human field study"[4]. So there many study about DMF in literature. However, the originality of this study is that the radical properties of DMF in two solutions (in acetone and water) are calculated.

EXPERIMENTAL

Experimental Electron Paramagnetic Resonance (EPR) study of DMF was reported by R. Livingston and H. Zeldes study[5]. Experimental parameters used in this study were taken from their study. In their study, they investigated the paramagnetic resonance spectra of free radicals formed by abstracting hydrogen from DMF. Radicals were prepared by photolysis solutions of DMF and acetone (10% of each and 20% of each were tried) in water solution. Moreover, the hydrogen abstraction was brought about by ultraviolet irradiation of a solution of DMF containing **water** and **acetone**. They have claimed that while the radical formation, methyl hydrogen is abstracted from DMF and that two isomers were present. The experimental spectrum taken from article was shown
in Fig. 1.

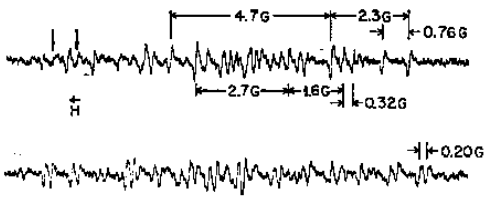


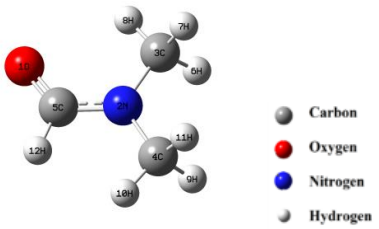
FIGURE 1. The experimental spectrum of DMF was taken from Literature[5].

Türk Fizik Derneği
1950
Turkish Physical Society

ISBN:978-605-83516-6-0

COMPUTATIONAL DETAILS

A conformational analysis of title compound was performed by considering the O_1-C_5-N_2-C_3 and H_{12}-C_5-N_2-C_4 dihedral angles. For the dihedral angles were carried out around the bond C_5-N_2 by changing of torsion angle at10^0 steps from 0^0 to 360^0. The conformational analysis of DMF was performed by conformational distribution option of Spartan14 program[6], as a consequence one conformer of molecule has been obtained as shown in Fig. 2.



Conformation 1

FIGURE 2. Stable conformer of the DMF molecule in water and acetone

Geometry optimization calculation of conformer was carried out with the GaussView05 program and Gaussian03W[7] program package. This calculation was calculated by using DFT/B3LYP methods with 6-311++G(d,p)[8-10] in **water** and **acetone**. As a result, conformational energy of molecule was seen from the Table 1. And geometry parameters of stable conformer and crystal structure parameters were given Table 2.

TABLE 1. Conformational energy of DMF in **water** and **acetone**

Conformation	Energies (Hartree)	Dipol Moment (Debye)
Conf1	-248.61152	5.6798

TABLE 2. The calculated geometry parameters of DMF by B3LYP/6-311++G(d,p) method (in water and acetone) and Experimental values bond lengths (Å) and angles (degrees)

Bond lengths	Teo	Exp.*	Bond angles	Teo	Exp.*	Dihedral angles	Conf1 Teo	Exp.*
O1,C5	1.230	1.230	C3,N2,C4	117.1	117.5	C4,N2,C3,H6	55.8	-
N2,C3	1.455	1.452	C3,N2,C5	121.6	120.8	C4,N2,C3,H7	-64.0	-
N2,C4	1.455	1.453	C4,N2,C5	121.3	121.6	C4,N2,C3,H8	175.8	-
N2,C5	1.348	1.340	N2,C3,H6	110.1	113.1	C5,N2,C3,H6	-125.6	-
C3,H6	1.094	0.949	N2,C3,H7	110.5	109.5	C5,N2,C3,H7	114.6	-
C3,H7	1.096	0.971	N2,C3,H8	109.5	108.9	C5,N2,C3,H8	-5.6	-
C3,H8	1.089	0.942	H6,C3,H7	108.5	109.3	C3,N2,C4,H9	-60.2	-
C4,H9	1.095	0.962	H6,C3,H8	109.1	108.7	C3,N2,C4,H10	179.8	-
C4,H10	1.091	0.985	H7,C3,H8	109.1	107.0	C3,N2,C4,H11	59.9	-
C4,H11	1.095	0.965	N2,C4,H9	110.5	111.1	C5,N2,C4,H9	121.2	-
C5,H12	1.102	0.984	N2,C4,H10	109.9	109.5	C5,N2,C4,H10	1.2	-
			N2,C4,H11	110.6	109.7	C5,N2,C4,H11	-118.7	-
			H9,C4,H10	108.7	108.0	C3,N2,C5,O1	0.3	-
			H9,C4,H11	108.5	109.4	C3,N2,C5,H12	-179.8	-
			H10,C4,H11	108.6	109.1	C4,N2,C5,O1	178.8	-
			O1,C5,N2	126.1	125.2	C4,N2,C5,H12	-1.3	-
			O1,C5,H12	121.4	122.1			
			N2,C5,H12	112.4	112.7			

*Values are taken from Ref[11, 12]

ISBN:978-605-83516-6-0

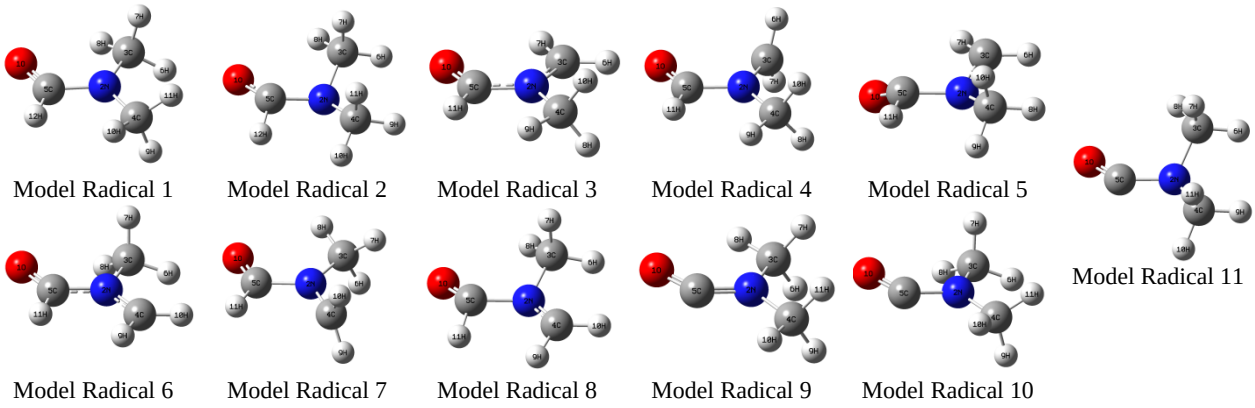


FIGURE 3. Model radicals of DMF molecule in water and acetone.

Considering the geometric structure, eleven possible radicals were modelled and model radicals were shown in Fig. 3. Model Radical 1 (MR1) is a radical cation and MR2 is radical anion of molecule. MR3 is a neutral radical formed by abstraction of H6 atom from the molecule. MR4 is cation form of MR3 and MR5 is anion form of MR3. MR6 is a neutral radical formed by abstraction of H9 atom from the molecule. MR7 and MR8 is cation and anion form of MR6, respectively. MR9 is a neutral radical formed by abstraction of H12 atom from the molecule. MR10 is cation form of MR9 and MR11 is anion form of MR9.

Conformational analyze and geometry optimization were performed again for all of model radicals because experiment done in the liquid phase. It is clear that molecule can return easily after photolisation in liquid phase. These calculations were performed by the same level of DFT. Hyperfine coupling constants (hfccs) and g-values of model radicals were calculated with NMR/GIAO method by using Gaussian03W[7] program. Hfccs and g-values of modelled radicals were found by B3LYP/6-311++G(d,p) level of DFT in water and acetone after accomplished geometry optimization calculations.

RESULT AND DISCUSSION

Researchers who carried out the experiment have suggested that the spectrum consisted of three clusters of lines. Clusters what they talk about in their study are shown in Fig. 1. Also, they said that more than one radical was present and most of the lines of Fig. 1 are the stronger lines of 1-3-3-1 groups. Because a methyl radical has 3 equivalent protons interacting with the unpaired electron, each with I=1/2 as their nuclear state yielding 4 peaks. They claimed that the radicals resulted from abstraction of methyl hydrogen and that two isomers were present. They suggest the radical shown in Fig.4.

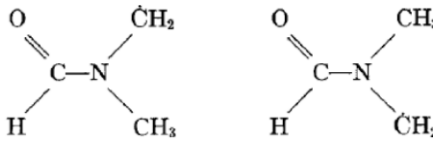


FIGURE 4. Suggested radical isomers in experimental study[5]

According to Neese[13], measuring g values more accurately than by $\sim 10^{-3}$ is difficult; thus, a deviation of 500 ppm between theory and experiment usually falls within the experimental error, and even an agreement with theory within 1000 ppm is considered satisfactory. As a result of theoretical results, calculated g_{iso} value of the MR2, MR3, MR6, MR10 and MR11 are closer to the experimental g_{iso} value than that of other model radicals. Besides MR3 and MR6 are isomer I and isomer II, respectively as can be seen from Fig.3 and Fig 4. Moreover, g values of MR3 and MR6 are

ISBN:978-605-83516-6-0

too close to the experimental equivalent. For these reasons, we identified MR3 and MR6 as a radical produced in DMF molecule in liquid phase.

TABLE 3. The theoretical and experimental hyperfine-splitting parameters (a)(G) and g-values of model radicals DMF in acetone and water

a_{iso}	MR1	MR2	MR3	MR4	MR5	MR6	MR7	MR8	MR9	MR10	MR11	Experimental[a]	
N2	10.58	-1.26	-1.90	3.38	2.02	-1.43	3.37	2.48	21.35	18.12	6.62	İsomer 1	İsomer 2
H6	22.34	-0.75	-	-	-	0.17	33.79	0.97	-0.54	5.85	2.15	$g_=$2.00284	$g_=$ 2.00296
H7	62.12	1.76	-18.93	8.70	-4.74	0.89	14.78	5.37	-0.53	32.19	-0.15	a_N=2.25	a_N=1.58
H8	8.48	0.21	-18.62	8.66	-5.02	-0.17	5.83	0.34	-1.04	11.59	0.06	a_H=4.72	a_H=2.72
H9	68.06	-1.12	1.86	25.27	1.30	-	-	-	-0.83	38.77	-0.43	a_H=18.37	a_H=18.33
H10	6.22	-0.16	-0.34	2.93	0.17	-18.88	11.87	-5.33	-0.39	3.12	-0.19	a_H =18.54	a_H=18.46
H11	29.16	-0.96	1.86	31.44	4.85	-19.52	11.65	-4.60	-0.83	16.20	-0.13	a_H=0.76	a_H=0.32
H12	0.08	13.04	-4.33	1.13	7.46	-2.75	-0.12	7.66	-	-	-		
g_{iso}	**2.00485**	**2.00356**	**2.00306**	**2.00772**	**2.00649**	**2.00320**	**2.00715**	**2.00654**	**2.00177**	**2.00347**	**2.00321**		

[a]Experimental values are taken from Ref[5]

Chipman said that anisotropic hfccs on isolated molecules deviations of about 20% from the experimental values are quite acceptable[14]. The calculated hfccs of model radical (MR3) are a_N=1.90, a_H=18.93, a_H=18.62, a_H =1.86, a_H=0.34 a_H =1.86 and a_H=4.33 G. And also, the calculated hfccs of model radical (MR6) are a_N=1.43, a_H=0.17, a_H=0.89, a_H =0.17, a_H=18.88 a_H =19.52 and a_H=2.75G. The experimental counterparts are a_N=2.25, a_H=4.72, a_H=18.37, a_H =18.54 and a_H=0.76 for isomer I and a_N=1.58, a_H=2.72, a_H=18.33, a_H=18.46 and a_H=0.32 for isomer II as seen as Table 3. For these reasons, we identified MR3 and MR6 as radicals produced from DMF in acetone and water. These results are good agreement with the experimentally proposed radical. These results were also consistent with our previous studies[15-17].

ACKNOWLEDGMENT

THIS WORK WAS FINANCIALLY SUPPORTED BY THE BAP, NECMETTIN ERBAKAN UNIVERSITY IN TURKEY.

REFERENCES

1. H. A. Favre and W. H. Powell, *Nomenclature of organic chemistry: IUPAC recommendations and preferred names 2013*. (Royal Society of Chemistry, 2013).
2. M. E. Barsan, NIOSH pocket guide to chemical hazards (2007).
3. "Dimethylformamide", in *Immediately Dangerous to Life and Health Concentrations (IDLH).* edited by N. I. f. O. S. a. H. (NIOSH). (December 4, 2014).
4. S.-M. Wang, H.-Y. Chang, J.-C. Tsai, W.-C. Lin, T.-S. Shih and P.-J. Tsai, Science of the total environment **407** (19), 5229-5234 (2009).
5. R. Livingston and H. Zeldes, The Journal of Chemical Physics **47** (10), 4173-4180 (1967).
6. Irvine, (Wavefunction Inc., CA 92612, USA, 2008).
7. M. J. Frisch and e. t. al., (Gaussian, Inc., Wallingford CT, 2003).
8. E. K. Sarıkaya, S. Bahçeli, D. Varkal and Ö. Dereli, Journal of Molecular Structure **1141**, 44-52 (2017).
9. E. K. Sarıkaya and Ö. Dereli, Journal of Molecular Structure **1052**, 214-220 (2013).
10. E. K. Sarıkaya, Ö. Dereli, Y. Erdoğdu and M. Güllüoğlu, Journal of Molecular Structure **1049**, 220-226 (2013).

ISBN:978-605-83516-6-0

11. H. Borrmann, I. Persson, M. Sandström and C. M. Stålhandske, Journal of the Chemical Society, Perkin Transactions 2 (2), 393-402 (2000).
12. H. Ohtaki, S. Itoh, T. Yamaguchi, S.-i. Ishiguro and B. Rode, Bulletin of the Chemical Society of Japan **56** (11), 3406-3409 (1983).
13. F. Neese, Journal of Chemical Physics **115** (24), 11080-11096 (2001).
14. D. M. Chipman, in *Quantum mechanical electronic structure calculations with chemical accuracy*, edited by P. G. Mezey (Kluwer Academic Publishers, CANADA, 1994).
15. L. Ateş, Y. Erdoğdu, E. K. Sarıkaya, F. P. Özturan and Ö. Dereli, Selçuk-Teknik Dergisi, 15(3), 253-263 (2016).
16. Ö. Dereli, Y. Erdoğdu, L. Ateş, E. K. Sarıkaya and F. P. Özturan, Gazi University Journal of Science **30** (1), 161-165 (2017).
17. E. Karakaş Sarıkaya, L. Ateş, U. Sayin, A. Ozmen and Ö. Dereli, Radiation Effects and Defects in Solids, 1-11 (2018).

BOOK OF FULL TEXT PROCEEDINGS TURKISH PHYSICAL
SOCIETY 35th INTERNATIONAL PHYSICS CONGRESS (TPS35)
TPS35, Vol.01, No.03, pp.230-234.
ISBN:978-605-83516-6-0

15 December 2019

Structural, Vibrational and Quantum Chemical Studies on C_{2N} (N: 0, 4, 6 and 8) Fullerenes

Kamil Soyarslan[1], Yusuf Erdogdu[a1]

[1]*Gazi University, Science Faculty, Department of Physics, Ankara, Turkey*
[a)]Corresponding author: yusuferdogdu@gmail.com

Abstract. A systematic study of the C_{2N} (N=0, 4, 6 and 8) fullerenes with various spin multiplicities have been performed by using Density Functional Theory calculations at the B3LYP/6-311G(d,p) level. Several properties including equilibrium geometries, electronic states and relative energy have been investigated. The HOMO, LUMO and HOMO–LUMO energy gap are also computed for the most stable isomer of each fullerene.

INTRODUCTION

Recently, the nanotechnology and the discovery of fullerenes have been very useful in several scientific areas [1–5]. This discovery leads to a rapid increase in carbon research as an elementary atom in fullerenes. This helps researches to prepare a good way to find other carbon nanomaterials, including nanotubes, graphene and other exotic structures. Nowadays, these structures have become important molecules in science and industrial research. They have very practical and extraordinary properties. Indeed, the most recent and outstanding works focus on these nanostructures to study their magnetic properties. Otherwise, they and their derivatives are building blocks of potential high performance organic devices.

Fullerene [6] are carbon cages which appear in the vaporization of graphite. They are similar in structure to graphite, which is composed of stacked graphene sheets of linked hexagonal rings, but they may also contain pentagonal or heptagonal rings. A fullerene is any molecule composed entirely by carbon atoms, in the form of a hollow sphere, ellipsoid or tubicle. Spherical fullerenes are also Buckyballs, and nanotubes or Buckytubes. The σ skeleton defines a polyhedral network, consisting of 12 pentagons and m hexagons, where m, according to Euler's law, is any number, other than one (including zero). Carbon cages in which the pentagons are isolated are more stable than structures in which they about (isolated pentagon rule). Using this rule, a family of closed carbon cages with (20+2n) atoms (n=0, 2, 3, 4, …) is predicted to exist. The smallest member is fullerene-20. Such fullerene has been intensively studied after its first successful production by Prinzbach et al. [8] The C20 as the smallest carbon-based fullerene with a dodecahedral cage structure [7].

We have carried out a detailed systematic study of the equilibrium structure and various electronic-structure related properties of C_{2N} (N=0, 4, 6 and 8) fullerenes. Here, we study the evolution of their geometric structure, electronic structure and HOMO–LUMO gap for C_{2N} (N=0, 4, 6 and 8) fullerenes.

Computational Details

All the theoretical process and calculations were performed with the Gauss View 5.0 [9] and Gaussian 09W [10] quantum chemistry package programs by used DFT/B3LYP [11] functional and 6-311G(d,p) [12] basis set. The fullerene geometries are based on structures in the Fullerene Library that has been created by M. Yoshida [13]. Calculations are carried out without any symmetry restrictions for different starting geometries. Starting with the spin singlet configurations of even electron system, the calculation procedure was repeated for various spin multiplicities for given fullerenes. The calculations are continued until the minimum energy is reached. Frequency analysis is performed at the B3LYP/6-311G(d,p) level to check whether the optimized structures are transition states or true

Türk Fizik Derneği
1950
Turkish Physical Society

ISBN:978-605-83516-6-0

minima on the potential energy surfaces of corresponding clusters. The ground-state structures are obtained as actually equilibrium states without imaginary frequencies.

RESULTS AND DISCUSSIONS

In this work, we are concerned with the stability and properties of neutral C_{2N} (N=0, 4, 6 and 8) fullerenes. Geometry optimization for neutral states and different spin multiplicities were carried out for each of C_{2N} (N=0, 4, 6 and 8) fullerenes. The lowest-energy structures of the C_{2N} (N=0, 4, 6 and 8) fullerenes are shown in Figs. 1-4. The optimized energies and relative energies of C_{2N} (N=0, 4, 6 and 8) fullerenes for various spin multiplicities are given in Tables 1-4.

C20 Fullerene

TABLE 1. Optimized energy of C20 fullerene

Symmetry	Multiplicity	Optimized Energy (a.u)	Relative Energy (k. cal/mol)
I_H	Singlet	-761.59280003	0.000
	Triplet	-761.59197346	0.519

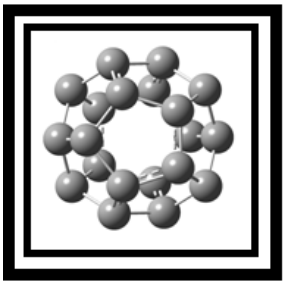


FIGURE 1. The optimized geometry of C20 fullerene

C24 Fullerene

TABLE 2. Optimized energy of C24fullerene

Symmetry	Multiplicity	Optimized Energy (a.u)	Relative Energy (k. cal/mol)
D_{6D}	Singlet	-914.00089641	5.048
	Triplet	-914.00894067	0.000
	Quintet	-913.98961591	12.12

ISBN:978-605-83516-6-0

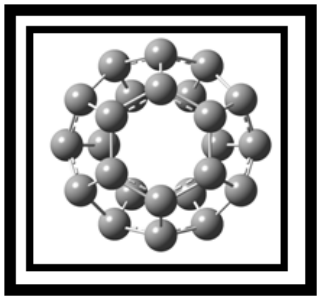


FIGURE 2. The optimized geometry of C24 fullerene

C26 Fullerene

TABLE 3. Optimized energy of C26fullerene

Symmetry	Multiplicity	Optimized Energy (a.u)	Relative Energy (k. cal/mol)
D_{3H}	Singlet	-990.22775763	20.88
	Triplet	-990.23862398	14.06
	Quintet	-990.26103602	0.000
	Septet	-990.21484669	28.98

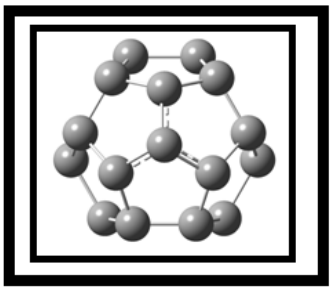


FIGURE 3. The optimized geometry of C24 fullerene

C28 Fullerene

TABLE 4. Optimized energy of C28fullerene

Symmetry	Multiplicity	Optimized Energy (a.u)	Relative Energy (k. cal/mol)	Relative Energy (k. cal/mol)
D_2	Singlet	-1066.49407671	0.000	27.89
	Triplet	-1066.48517587	5.585	33.48
T_D	Singlet	-1066.50391816	21.71	21.71
	Triplet	-1066.51690226	13.57	13.57
	Quintet	-1066.53852935	0.000	0.000
	Septet	-1066.44268455	60.14	60.14

ISBN:978-605-83516-6-0

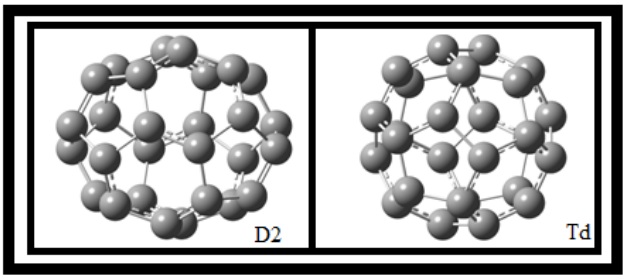


FIGURE 4. The optimized geometry of C24 fullerene

Frontier Molecular Orbital Analysis

The evolution of the electronic structure can be probed by calculating the highest occupied molecular orbital (HOMO) as well as the energy gap (E_{GAP}) between HOMO and the lowest unoccupied molecular orbital (LUMO). The energy gap is a characteristic quantity of electronic structure. HOMO, LUMO and HOMO-LUMO gap energy values for C_{2N} (N=0, 4, 6 and 8) fullerenes are gathered in Table 5. HOMO and LUMO PLOT of C_{2N} (N=0, 4, 6 and 8) fullerenes are shown in Fig.5.

TABLE 5. HOMO, LUMO and HOMO-LUMO gap energy values for C_{2N} (N=0, 4, 6 and 8) fullerenes

	C20	C24	C26	C28
E_{HOMO}	-7.709	-6.153	-6.469	-6.683
E_{LUMO}	-3.526	-3.628	-2.930	-2.295
$E_{H\text{-}L}$ gap	4.183	2.525	3.539	4.388

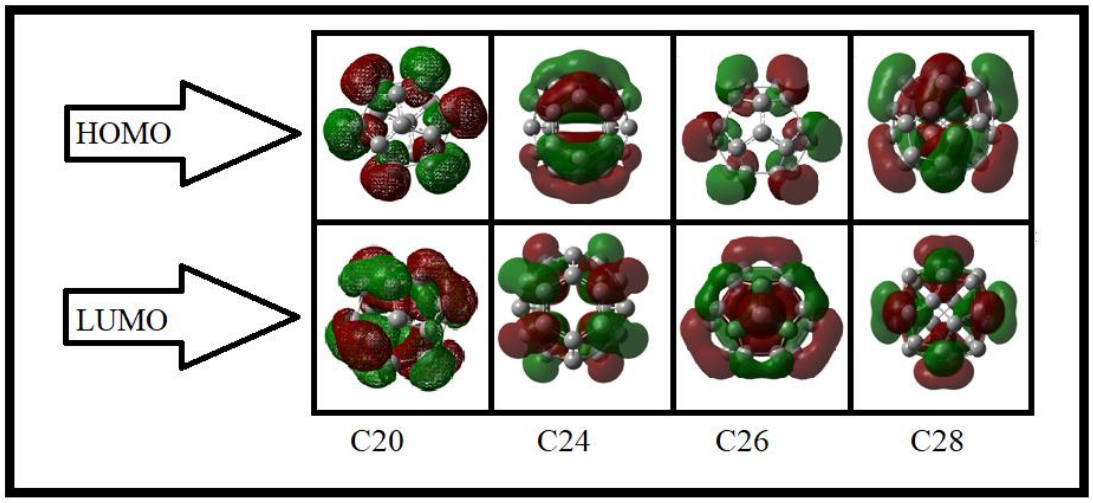


FIGURE 5. HOMO and LUMO PLOT of C_{2N} (N=0, 4, 6 and 8) fullerenes

ISBN:978-605-83516-6-0

REFERENCES

1. R.E. Camley, J. Barnaś, Phys. Rev. Lett. 63 (1989) 664.
2. M.H. Phan, S.C. Yu, J. Magn. Magn. Mater. 308 (2007) 325 I J L Diaz, N S Branco, Physica A 468, (2017), 158–170.
3. P.M. Levy, S. Zhang, A. Fert, Phys. Rev. Lett. 65 (1990) 1643.
4. R. Skomski, J. Phys. Condens. Matter 15 (2003) 841.
5. H. Schlorb, V. Haehnel, M.S. Khatri, A. Srivastav, A. Kumar, L. Schultz, S. Fahler, Phys. Status Solidi B 247 (2010) 2364.
6. H.W. Kroto, J.R. Heath, S.C. O'Brien, R.F. Curl, R.E. Smalley, Nature 318 (1985) 162.
7. S. Aouini, A.Mhirech, A. A. Ismaili, L. Bahmad, Chinese Journal of Physics, 56, 2018, 1640-1647
8. H. Prinzbach, A. Weiler, P. Landenberger, F. Wahl, J. Wörth, L.T. Scott, M. Gelmont, D. Olevano, B. Issendorff, Nat. London 407 (2000) 60.
9. A B Frisch, A J H Nielson, Gaussview User Manual, Gaussian Inc., Pittsburgh, PA, 2000.
10. M. J. Frisch, et al. Gaussian 09, Revision B.01, Gaussian Inc., Wallingford CT, 2010.
11. A D Becke, Phys. Rev. A 38(1988) 3098-3100.
12. R. Krishnan, J.S. Binkley, R. Seeger, J. A. Pople, The Journal of Chemical Physics 72 (1980) 650.
13. http://www.nanotube.msu.edu/fullerene/fullerene-isomers.html

BOOK OF FULL TEXT PROCEEDINGS TURKISH PHYSICAL
SOCIETY 35th INTERNATIONAL PHYSICS CONGRESS (TPS35)
TPS35, Vol.01, No.03, pp.235-240.
ISBN:978-605-83516-6-0

15 December 2019

Quantum Chemical Investigations on C_{30}, C_{32}, C_{34}, C_{36} and C_{38} Fullerenes

Kamil Soyarslan[1], Yusuf Erdogdu[a1]

[1]*Gazi University, Science Faculty, Department of Physics, Ankara, Turkey*
[a)]Corresponding author: yusuferdogdu@gmail.com

Abstract. This study focuses on C_{30}, C_{32}, C_{34}, C_{36} and C_{38} fullerenes optimized with various spin multiplicities with the computational Gaussian 09 package using the ab initio calculations and the density functional theory (DFT) with the hybrid functional B3LYP and the basis set 6-311G(d,p). The paper presents the calculations of the following the most stable geometry, relative energy and the difference between the highest occupied molecular orbital (HOMO) energy and the lowest unoccupied molecular orbital (LUMO) energy.

INTRODUCTION

A fullerene is an allotrope of carbon whose molecule consists of carbon atoms connected by single and double bonds so as to form a closed or partially closed mesh, with fused rings of five to seven atoms. All fullerenes have an even number of carbon atoms arranged over the surface of a closed hollow cage. Structurally fullerenes are identical to graphite and are composed of irregular stacked graphene sheets, and form hexagonal or pentagonal rings. Each atom is trigonally linked to three near neighbors, with three of the four valence electrons involved in *sp*2 σ-bonding. The remaining *p* electrons are delocalized in π-molecular orbitals covering the outside and inside surfaces of the molecule. Fullerenes are wealth of interesting phenomena due to their π-electron nature that can be easily manipulated by chemical means [1-3].

The unique physical, chemical, electrical, and optical properties of fullerenes and their derivatives have led to their incorporation into new or improved devices and materials, and to advancements in engineering, industry, and science. The exploration for the biomedical applications of fullerenes started in 1993 when Friedman et al. discovered that the hydrophobic gap in HIV-1 protease could be tightly packed with C60 molecules, and through the formation of protease-fullerene complex, lead to enzyme inactivation and elimination of the viral activities. The biological and medical applications of fullerene derivatives reported during the last 3 years, which include anti-viral, PDT, antioxidant, anticancer, immunological, MRI contrast agents and tumor therapy. Remarkable progress has been made in the biological applications of fullerenes since the first report in 1993. Given the fast growth of these compounds for different biological applications combined with low toxicity, it is anticipated that many more biomedical applications will be forthcoming for these interesting compounds [4-6].

We have carried out a detailed systematic study of the equilibrium structure and various electronic-structure related properties of C_{30}, C_{32}, C_{34}, C_{36} and C_{38} fullerenes. Here, we study the evolution of their geometric structure, electronic structure and HOMO–LUMO gap for C_{30}, C_{32}, C_{34}, C_{36} and C_{38} fullerenes.

Computational Details

All the theoretical process and calculations were performed with the Gauss View 5.0 [7] and Gaussian 09W [8] quantum chemistry package programs by used DFT/B3LYP [9] functional and 6-311G(d,p) [10] basis set. The fullerene geometries are based on structures in the Fullerene Library that has been created by M. Yoshida [11]. Calculations are carried out without any symmetry restrictions for different starting geometries. Starting with the spin singlet configurations of even electron system, the calculation procedure was repeated for various spin multiplicities for given fullerenes. The calculations are continued until the minimum energy is reached. Frequency

ISBN:978-605-83516-6-0

analysis is performed at the B3LYP/6-311G(d,p) level to check whether the optimized structures are transition states or true minima on the potential energy surfaces of corresponding clusters. The ground-state structures are obtained as actually equilibrium states without imaginary frequencies.

RESULTS AND DISCUSSIONS

In this work, we are concerned with the stability and properties of neutral C_{30}, C_{32}, C_{34}, C_{36} and C_{38} fullerenes. Geometry optimization for neutral states and different spin multiplicities were carried out for each of C_{30}, C_{32}, C_{34}, C_{36} and C_{38} fullerenes. The lowest-energy structures of the C_{30}, C_{32}, C_{34}, C_{36} and C_{38} fullerenes are shown in Figs. 1-5. The optimized energies and relative energies of C_{30}, C_{32}, C_{34}, C_{36} and C_{38} fullerenes for various spin multiplicities are given in Tables 1-5.

C30 Fullerene

TABLE 1. Optimized energy of C30 fullerene

1	D5H	Singlet	-1142.68661671	0.000	55.818	3	C2V	-1142.77329993	1.423	1.423
		Triplet	-1142.68338900	2.025	57.843			-1142.77556826	0.000	0.000
		Quintet						-1142.73456300	25.731	25.731
2	C2V	Singlet	-1142.76714208	0.000	5.288					
		Triplet	-1142.74033678	16.821	22.108					
		Quintet								

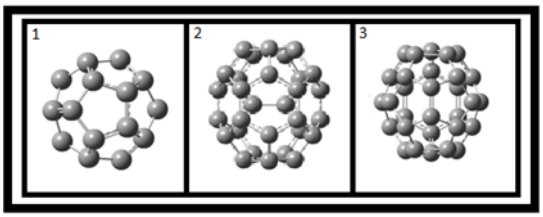


FIGURE 1. The optimized geometry of C30 fullerene

C32 Fullerene

TABLE 2. Optimized energy of C32 fullerene

1	C2	Singlet	-1218.97653261	0.000	54.596	4	C2	Singlet	-1219.02251592	0.000	25.741
		Triplet	-1218.97517418	0.852	55.448			Triplet	-1219.00146252	13.21	38.952
2	D2	Singlet	-1218.95901242	0.000	65.590	5	D3H	Singlet	-1218.93884942	0.000	78.243
		Triplet	-1218.95071300	5.208	70.798			Triplet	-1218.89209592	29.33	107.58
3	D3D	Singlet	-1218.94522008	0.000	74.245	6	D3	Singlet	-1219.06353687	0.000	0.000
		Triplet	-1218.93837565	4.295	78.540			Triplet	-1219.01991849	27.37	27.371

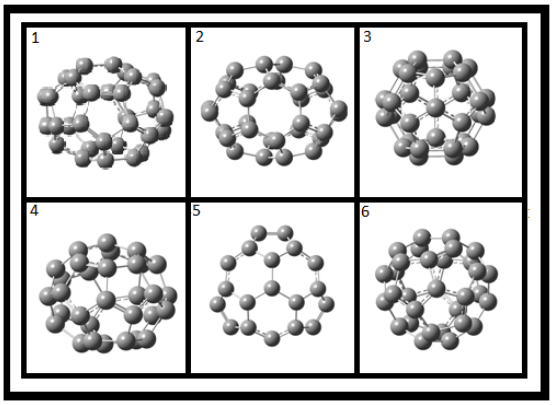


FIGURE 2. The optimized geometry of C32 fullerene

C34 Fullerene

TABLE 3. Optimized energy of C34 fullerene

1	C_2	Singlet	-1295.25734143	46.56	73.364	4	C_S	Singlet	-1295.21709231	74.44	98.620
		Triplet	-1295.33154274	0.000	26.802			Triplet	-1295.33572233	0.000	24.179
		Quintet	-1295.27027000	38.44	65.251			Quintet	-1295.22499100	69.48	93.664
2	C_2	Singlet	-1295.24849989	78.91	78.912	5	C_{3V}	Singlet	-1295.21656627	79.70	98.951
		Triplet	-1295.37425385	0.000	0.000			Triplet	-1295.34358001	0.000	19.248
		Quintet	-1295.23782800	85.60	85.609			Quintet	-1295.2209990	76.92	96.169
3	C_S	Singlet	-1295.22354998	82.56	94.568	6	C_2	Singlet	-1295.15244632	69.48	139.18
		Triplet	-1295.35512283	0.000	12.005			Triplet	-1295.26317654	0.000	69.702
		Quintet	-1295.22147100	83.86	95.873			Quintet	-1295.14537342	73.92	143.62

ISBN:978-605-83516-6-0

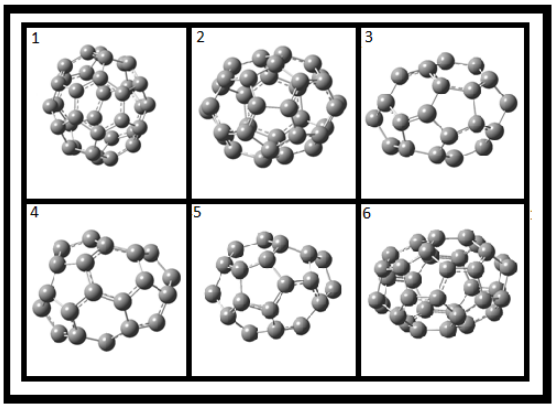


FIGURE 3. The optimized geometry of C34 fullerene

C36 Fullerene

TABLE 4. Optimized energy of C36 fullerene

Singlet			-1371.37921052	3.302	87.716			-1371.50756305	0.000	7.173
Triplet	1	C2	-1371.38447219	0.000	84.414	9	C2V	-1371.50339270	2.617	9.790
Quintet			-1371.37693594	4.729	89.143					
Singlet			-1371.34322711	0.000	110.296			-1371.44211576	0.373	48.242
Triplet	2	D2	-1371.33167320	7.250	117.546	10-	C2	-1371.44270968	0.000	47.869
Quintet								-1371.43068846	7.543	55.413
Singlet			-1371.42372598	0.755	59.782			-1371.49799941	0.000	13.175
Triplet	3	C1	-1371.42492853	0.000	59.027	11	C2	-1371.49627672	1.081	14.256
Quintet			-1371.41346696	7.192	66.219					
Singlet			-1371.39495343	1.562	77.837			-1371.50827452	0.000	6.727
Triplet	4	C2	-1371.39744268	0.000	76.275	12	C2	-1371.50696255	0.823	7.550
Quintet			-1371.37509289	14.025	90.300					
Singlet			-1371.37450366	0.000	90.669			-1371.45426904	0.000	40.616
Triplet	5	D2	-1371.36282390	7.329	97.999	13	D3H	-1371.44987918	2.755	43.370
Quintet										
Singlet			-1371.46801640	0.000	31.989			-1371.50211233	8.794	10.594
Triplet	6	D2D	-1371.45425193	8.637	40.627	14	D2D	-1371.51612630	0.000	1.800
Quintet								-1371.49275653	14.665	16.464
Singlet			-1371.45943847	0.362	37.372			-1371.51474954	2.664	2.664
Triplet	7	C1	-1371.46001463	0.000	37.010	15	D6H	-1371.51899435	0.000	0.000
Quintet			-1371.43228920	17.398	54.408			-1371.48784602	19.546	19.546
Singlet			-1371.48007237	0.000	24.424					
Triplet	8	CS	-1371.46928588	6.769	31.193					
Quintet										

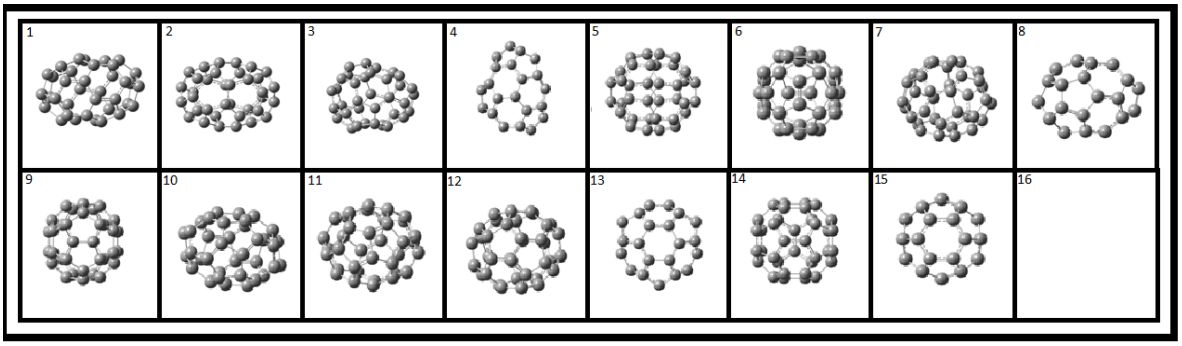


FIGURE 4. The optimized geometry of C36 fullerene

ISBN:978-605-83516-6-0

C38 Fullerene

TABLE 5. Optimized energy of C38 fullerene

Singlet			-1447.60233477	0.000	102.601			-1447.72167745	4.374	27.712
Triplet	1	C2	-1447.59856881	2.363	104.964	10	C2	-1447.72864739	0.000	23.339
Quintet								-144769510500	21048	44386
Singlet			-1447.55470289	0.183	132.490			-1447.69256101	0.000	45.983
Triplet	2	D3H	-1447.55499448	0.000	132.307	11	C1	-1447.68866502	2.445	48.428
Quintet			-1447.52905989	16275	148582					
Singlet			-1447.66551219	0.000	62.956			-1447.60459198	13.648	101.185
Triplet	3	C1	-1447.66400765	0.944	63.901	12	C2V	-1447.62634092	0.000	87.537
Quintet								-1447.60156200	15.549	103.086
Singlet			-1447.64226581	0.000	77.544			-1447.73590378	0.000	18.785
Triplet	4	C1	-1447.62952521	7.995	85.539	13	C2	-1447.73114799	2.984	21.769
Quintet										
Singlet			-1447.69988597	0.000	41.387			-1447.72322978	0.000	26.738
Triplet	5	C1	-1447.69583425	2.542	43.929	14	C1	-1447.72198896	0.779	27.517
Quintet										
Singlet			-1447.67916336	0.000	54.390			-1447.67562348	6.126	56.612
Triplet	6	C2	-1447.66621957	8.122	62.513	15	C2V	-1447.68538558	0.000	50.486
Quintet								-1447.67909400	3.948	54.434
Singlet			-1447.65557812	0.076	69.190			-1447.70717454	10.835	36.813
Triplet	7	C1	-1447.65569935	0.000	69.114	16	C3V	-1447.72444084	0.000	25.978
Quintet			-144762519000	19145	88259			-144769415400	19005	44983
Singlet			-1447.70520579	0.000	38.048			-1447.76583967	0.000	0.000
Triplet	8	C1	-1447.69784565	4.619	42.667	17	C2	-1447.74670360	12.008	12.008
Quintet										
Singlet			-1447.65284576	0.000	70.905					
Triplet	9	D3	-1447.63547393	10.901	81.806					
Quintet										

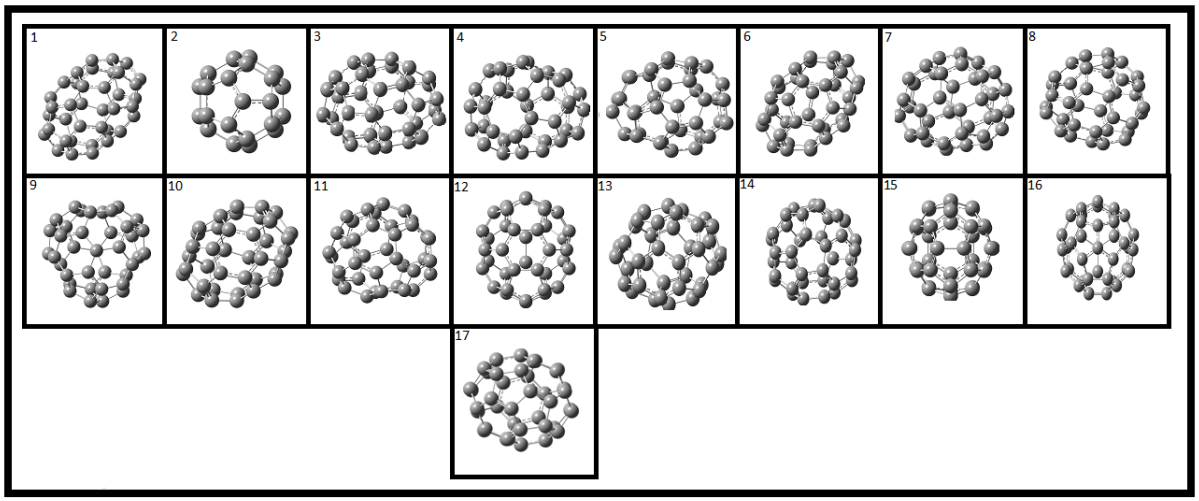


FIGURE 5. The optimized geometry of C38 fullerene

ISBN:978-605-83516-6-0

Frontier Molecular Orbital Analysis

The evolution of the electronic structure can be probed by calculating the highest occupied molecular orbital (HOMO) as well as the energy gap (E_{GAP}) between HOMO and the lowest unoccupied molecular orbital (LUMO). The energy gap is a characteristic quantity of electronic structure. HOMO, LUMO and HOMO-LUMO gap energy values for C_{30}, C_{32}, C_{34}, C_{36} and C_{38} fullerenes are gathered in Table 6. HOMO and LUMO PLOT of C_{30}, C_{32}, C_{34}, C_{36} and C_{38} fullerenes are shown in Figure 6.

TABLE 6. HOMO, LUMO and HOMO-LUMO gap energy values for C_{30}, C_{32}, C_{34}, C_{36} and C_{38} fullerenes

	C30	C32	C34	C36	C38
E_{HOMO}	-6.831	-6.628	-6.776	-6.196	-5.836
E_{LUMO}	-4.131	-4.016	-3.868	-3.904	-4.067
$E_{H\text{-}L}$ gap	2.700	2.612	2.908	2.291	1.769

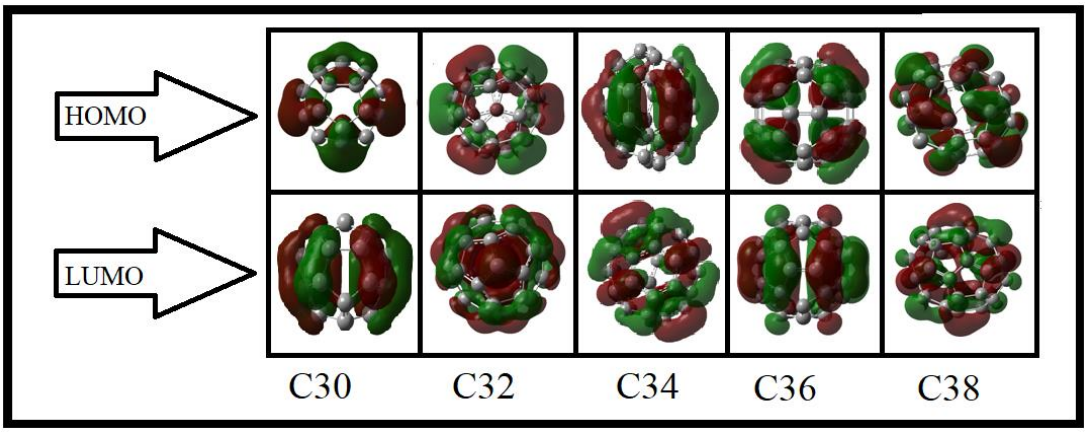


FIGURE 6. HOMO and LUMO PLOT of C_{30}, C_{32}, C_{34}, C_{36} and C_{38} fullerenes

REFERENCES

1. https://en.wikipedia.org/wiki/Fullerene
2. M. Nasrollahzadeh, Z. Issaabadi, M. Sajjadi, S. M. Sajjadi, M.Atarod, Interface Science and Technology, 28 (2019) 29-80
3. B. D. Malhotra, Md. A. Ali Functionalized Carbon Nanomaterials for Biosensors, Nanomaterials for Biosensors, Fundamentals and Applications, Micro and Nano Technologies (2018)75-103
4. S. H. Friedman, D. L. DeCamp, R. P. Sijbesma, G. Srdanov, F. Wudl and G. L. Kenyon, J. Am. Chem. Soc., 1993, 115, 6506–6509.
5. Katsuhiko Ariga Masakazu Aono, Advanced Supramolecular Nanoarchitectonics
6. E. Castro, A. H. Garcia, G. Zavala and L. Echegoyen, Fullerenes in biology and medicine Journal of Materials Chemistry B
7. A B Frisch, A J H Nielson, Gaussview User Manual, Gaussian Inc., Pittsburgh, PA, 2000.
8. M. J. Frisch, et al. Gaussian 09, Revision B.01, Gaussian Inc., Wallingford CT, 2010.
9. A D Becke, Phys. Rev. A 38(1988) 3098-3100.
10. R. Krishnan, J.S. Binkley, R. Seeger, J. A. Pople, The Journal of Chemical Physics 72 (1980) 650.
11. http://www.nanotube.msu.edu/fullerene/fullerene-isomers.html

BOOK OF FULL TEXT PROCEEDINGS TURKISH PHYSICAL
SOCIETY 35th INTERNATIONAL PHYSICS CONGRESS (TPS35)
TPS35, Vol.01, No.03, pp.241-243.
ISBN:978-605-83516-6-0

15 December 2019

Structural Correlations in Partly Quenched Two and Three Component Ionic Systems and Detecting the Structural Holes

Hasan TATLIPINAR

Yildiz Technical University, Physics Department, 34220, Esenler, Istanbul-TURKEY
htatli@yildiz.edu.tr

Abstract. In recent years, developments in statistical mechanics have allowed to obtain distribution and correlation functions for non-equilibrium systems which have important applications in various fields. Some of these non-equilibrium systems can be considered as a partly quenched system, where one component is quenched or frozen, the other components are allowed to equilibrate with quenched component and itself. In this study by using Ornstein-Zernike integral equations correlation functions for the partly quenched two and three component ionic systems are evaluated. Pair correlation functions for the two component systems were obtained both for the liquids in fully equilibrium state and for the partly quenched state. From the distribution functions the structural holes of the quenched component were also analyzed by choosing different fluid density. The theory also extended the three component partly quenched ionic systems. The model can also be used to study the transport properties of the fluid component in matrix fluid systems.

INTRODUCTION

Statistical mechanics of equilibrium liquid state theory recently extended to some non-equilibrium systems such as partly quenched liquid, spin glasses, sequential adsorption processes. Such systems have applications in engineering composites, porous materials, spin glasses, electrolyte mixtures [1,2]. This study consider a partly quenched ionic liquid systems. Partly quenched means one component (or some components) is quenched or frozen and other components are allowed to equilibrate with quenched component. It is well known from equilibrium liquid state theory that with appropriate pair interactions and related closure relations Ornstein-Zernike(O-Z) integral equation gives pair correlation and distribution functions of liquid structure[3].

METHOD

For the multi component liquid at the full equilibrium O-Z integral equations are defined as fallows

$$h_{ij}(\boldsymbol{r}) = c_{ij}(\boldsymbol{r}) + n\sum_l x_l \int d\boldsymbol{r}' h_{il}(\boldsymbol{r}')c_{lj}(\boldsymbol{r}-\boldsymbol{r}') \quad (1)$$

Where the first term at right hand side is direct correlation function, it gives a direct correlation of a particle to other all particles by direct interactions. The second term is indirect correlation term and takes into account all of the indirect interactions. Left hand side is total correlation function and related to pair distribution function

$$h_{ij}(\boldsymbol{r}) = g_{ij}(\boldsymbol{r}) + 1 \quad (2)$$

In equation (1) n is particle density and x_l is partial concentrations.

Türk Fizik Derneği
1950
Turkish Physical Society

ISBN:978-605-83516-6-0

O-Z equation give connections between, direct correlation function $c(\boldsymbol{r})$, pair correlation $g(\boldsymbol{r})$ function and density function $\rho(\boldsymbol{r})$. For homogenous system $\rho(\boldsymbol{r}) = \rho$. To obtain solution of O-Z equations one needs convenient closure relations depending $u(\boldsymbol{r})$ pair interactions. For the long range interactions the convenient closure relation is Hypernetted- Chain Closure (HNC).

$$\frac{u(\boldsymbol{r})}{k_B T} = -\ln[1 + h(\boldsymbol{r})] + \rho \int c(\boldsymbol{r} - \boldsymbol{r}')h(\boldsymbol{r}')\boldsymbol{dr}' \tag{3}$$

For the short range interactions case Percus-Yevick Closure (P-Y) is useful and given as

$$\frac{u(\boldsymbol{r})}{k_B T} = -\ln[1 + h(\boldsymbol{r})] + \ln[1 + h(\boldsymbol{r}) - c(\boldsymbol{r})] \tag{4}$$

There are relations between pair correlation function g(r) and measureble thermodynamic quantities for example for isotermal compresibility and structure factor is given respectively:

$$\rho\int_0^\infty (g(r)-1)4\pi r^2 dr = \rho k_B T\chi_T - 1 \tag{5}$$

$$S(k) = 1 + \frac{4\pi}{k}(n)\int (g(r)-1)\sin(kr)rdr \tag{6}$$

O-Z integral equation has analytical solutions for some simple model such as mean spherical pair interactions model. For more realistic pair interactions numerical solutions are possible to obtain pair correlation function $g(\boldsymbol{r})$. $g(\boldsymbol{r})$ gives connections to all measurable thermodynamic quantities. For the numerical solutions of this integral equations it is convenient to write Fourier transform which have a linear equations form. Accordingly we can write O-Z equations for partly quenched liquid structure in Fourier space as follows, The quenched (or matrix) component is given as equation (7).

$$h_{11}(k) = c_{11}(k)[1 + n_1 h_{11}(k)] \tag{7}$$

Where suffix $i = 1$ and n_i is partial ionic number densities.

For the annealed or fluid component,

$$\begin{aligned} h_{21}(k) &= h_{12}(k) = c_{12}(k) + n_1 c_{11}(k)h_{12}(k) + n_2 c_{12}(k)h_c(k) \\ h_{22}(k) &= c_{22}(k) + n_1 c_{12}(k)h_{12}(k) + n_2 c_c(k)h_{22}(k) + n_2 c_b(k)h_c(k) \end{aligned} \tag{8}$$

Where

$$h_{22}(k) = h_b(k) + h_c(k)\ ,\ c_{22}(k) = c_b(k) + c_c(k)\ h_c(k) = c_c(k) + n_c c_c(k)h_c(k)$$

In equation (8) index b refer to blocked and c refer to connected contributions [1,2]. Choosing $c_b = 0$ is consistent with the Percus-Yevich closure, in this approximation connected correlations are come from in the same layer interactions. For the HNC closure blocked contribution should take into account and in this case all layer correlations of the annealed particle also take into account. With the same notation in k space (O-Z) equations can be written for the partly quenched three component system. For the short range interacting systems, we can write nine algebraic linear equations for the nine correlation functions. In matrix notation these equations are as follows.

ISBN:978-605-83516-6-0

$$\begin{matrix} c_{11} \\ c_{12} \\ c_{13} \\ c_{22} \\ c_{22}^c \\ c_{23} \\ c_{23}^c \\ c_{33} \\ c_{33}^c \end{matrix} = \begin{bmatrix} (1-n_1c_{11}) & 0 & 0 & 0 & 0 & 0 & 0 & 0 & 0 \\ 0 & (1-n_1c_{11}) & 0 & 0 & -n_2c_{12} & -n_3c_{13} & 0 & 0 & 0 \\ 0 & 0 & (1-n_1c_{11}) & 0 & 0 & 0 & -n_2c_{12} & 0 & -n_3c_{13} \\ 0 & -n_2c_{12} & 0 & (1-n_2c_{22}^c) & 0 & -n_3c_{23}^c & 0 & 0 & 0 \\ 0 & 0 & 0 & 0 & (1-n_2c_{22}^c) & 0 & -n_3c_{23}^c & 0 & 0 \\ 0 & 0 & -n_1c_{12} & 0 & 0 & (1-n_2c_{22}^c) & 0 & -n_3c_{23}^c & 0 \\ 0 & 0 & 0 & 0 & 0 & 0 & (1-n_2c_{23}^c) & 0 & -n_3c_{23}^c \\ 0 & 0 & -n_1c_{13} & 0 & 0 & -n_2c_{23}^c & 0 & (1-n_3c_{33}^c) & 0 \\ 0 & 0 & 0 & 0 & 0 & 0 & -n_2c_{23}^c & 0 & (1-n_3c_{33}^c) \end{bmatrix} \begin{matrix} h_{11} \\ h_{12} \\ h_{13} \\ h_{22} \\ h_{22}^c \\ h_{23} \\ h_{23}^c \\ h_{33} \\ h_{33}^c \end{matrix} \quad (9)$$

By solving these linear algebraic equations $h_{11}, h_{12}, h_{13}, h_{22}, h_{22}^c, h_{23}, h_{23}^c, h_{33}, h_{33}^c$ can obtained.

RESULTS AND CONCLUSION

In equation (9) $h_{11}(k)$ refer the matrix component total correlation function and given by equation (7). The algebraic form of the other total correlation functions are not that much simple. By using appropriate pair interactions and with careful numerical calculation it is possible to calculate partial structure factors and partial radial distribution functions.

We have studied partly quenched two component MCl and MCl_3 ($M = Na, Cu, Al$) molten salt systems with both $c_b = 0$ and $c_b \neq 0$ case[4,5,6]. Molten trivalent metal halogens are known to have a short range local structure as well as a medium range local structure. Quenching the chlorine component disrupts the intermediate-range order and as a result the metal component settles in the selective structural holes of the quenched structure [6]. Three component systems given in equation (9) corresponds to $c_b = 0$ case. For given realistic pair interactions, the solution of these linear algebraic equations numerically possible. Although it is not easy to obtain pair distribution functions from the equations (5), but once it done it promise very rich applications in many physical systems such as ionic glasses, flow in porous media, electrolyte systems.

REFERENCES

1. Fanti, L.A., Glandt, T.E. and Madden W.G. 1990, J. Chem. Phys., 93, 5945.
2. Given, W.G., and Stell G., J. Chem. Phys., 97, 1992,4573
3. Tatlipinar, Hasan, PROCEEDINGS OF THE TURKISH PHYSICAL SOCIETY 32ND INTERNATIONAL PHYSICS CONGRESS (TPS32) Book Series: AIP Conference Proceedings Volume: 1815 Article Number: 030016 Published: 2017.
4. Pastore G, Tatlipinar H. and Tosi M.P. Phys. Chem. Liq. 31,(1996),89.
5. Pastore G, Tatlipinar H. and Tosi M.P. Phys. Chem. Liq. 31,(1996),189-200.
6. Pastore G, Tatlipinar H. and Tosi M.P., NUOVO CIMENTO DELLA SOCIETA ITALIANA DI FISICA D-CONDENSED MATTER ATOMIC MOLECULAR AND CHEMICAL PHYSICS FLUIDS PLASMAS BIOPHYSICS Volume: 20 Issue: 9 Pages: 1337-1344 Published: SEP 1998.

BOOK OF FULL TEXT PROCEEDINGS TURKISH PHYSICAL
SOCIETY 35th INTERNATIONAL PHYSICS CONGRESS (TPS35)
TPS35, Vol.01, No.03, pp.244-249.
ISBN:978-605-83516-6-0

15 December 2019

The Life Times of Hydrogen Like Neptunium

Güldem ÜRER

Fundamental Science of Engineering, Sakarya University of Applied Science, 54140, Sakarya, Türkiye

gurer@subu.edu.tr

Abstract. Neptunium is the fifth element of actinides (Z=89-103). Although hydrogen like ion have the simplest structure of neptunium, theoretical works on it have still some difficulties. The information and data about SHE (Super Heavy Elements) and highly ionized SHE is almost nonexistent. Due to lack of in this subject, a multi-configuration Dirac-Fock (MCDF) calculation with GRASP code has performed for highly ionized actinides. The calculation has performed as a part of a large scale studies about highly ionized (hydrogen, helium and lithium like) actinides. The investigation for the life times of hydrogen like neptunium, Np^{92+} (Z=93), has contained quantum electrodynamic effects besides Breit correction and correlation effects. One theoretical work is in available literature and there is no experimental one for Np^{92+}. The MCDF results and the theoretical work have been evaluated together and interpreted. The lifetimes of 8g and 9g states have been presented for the first time, additionally.

INTRODUCTION

There is an increasing interest in detailed data for wavelengths, oscillator strengths, transition probabilities and life times for highly charged ions. The data has been needed in interpretation of astrophysical spectra and atomic collision, the diagnostics of fusion plasmas, and the development of x-ray lasers studies. Furthermore, theoretical works of transition parameters for with high Z of few electronic systems has been also challenged experimental levels structures studies [1]. The calculating parameters in high accuracy has begins with sensitively determining level structure for ion. There are large lists in NIST atomic data base [2] contains theoretical and experimental papers for neutral and all ions of atoms. There is so scarce data has had for Np^{92+}.

The works of Johnson and Soff [3] and Yerokhin and Shabaev [4] have presented energies just for 4 levels belongs to $1s_{1/2}$, $2s_{1/2}$, $2p_{1/2}$, $2p_{3/2}$ levels. Jitrik and Bunge [5, 6] have performed more complicated calculations for *nl* (up to n=25, l=25) levels of atoms with $1\leq Z\leq 118$ by using point nucleus Dirac eigenfunctions. In the same time, they represented their data on their web site on a web site [7] as two sets. As the Jitric and Bunge's data have been detailed investigated, it has been seen it is not sufficiently sensitive. Thus, it has been performed a MCDF calculation for transition parameters of Np^{92+}. This work has been enlarging for hydrogen, helium and lithium-like all actinides.

It is a need the supporting theoretically works with experimental ones to increase the trustworthiness of its. Unfortunately, there is not any experiment for Np^{92+} yet. The radioactivity and so sort life times of actinides obstructs the experiments.

The MCDF calculating has been performed for *nl* (n=1-9, l=0-4) levels of Np^{92+}. First, the levels structures have been determined then electric dipole (E1), electric quadrupole (E2) and magnetic dipole (M1) transition parameters and life times have been obtained. To support the MCDF calculation with GRASP code [8], a multiconfiguration Hartree-Fock approximation calculation using MCHF atomic structure package has been performed in the same way. In the both methods, the correlation effects have been contained the calculations. Furthermore, MCDF method covers quantum electrodynamic effects and the transverse Breit correction as the MCHF approximation involves the Breit-Pauli contributions. It has been performing an extensive study about hydrogen helium and lithium like actinides ($89\leq Z\leq 103$) [10-15]. The data in this paper is small part of extensive investigation mentioned above.

Türk Fizik Derneği
1950
Turkish Physical Society

ISBN:978-605-83516-6-0

METHOD OF CALCULATION

The transition parameters are so useful in many branches for example astrophysics, plasma physics, atomic physics, laser spectroscopy and quantum electronic. One of the parameters for transitions is life time.

It is defined the life time of *i* level as

$$\tau_i = \frac{1}{\sum_i A_{if}} . \tag{1}$$

Here, A_{if} is rate (or probability) from the upper level to the lower level transition and it is given by

$$A^{\pi k}\left(\gamma' J', \gamma J\right) = 2C_k \left[\alpha\left(E_{\gamma' J'} - E_{\gamma J}\right)\right]^{2k+1} \frac{S^{\pi k}(\gamma' J', \gamma J)}{g_{J'}} . \tag{2}$$

The photon of absorption or emission with angular momentum, *k*, and parity, $\pi = (-1)^k$, the transition is defined as electric multipole transition (*Ek*). If the parity is $\pi = (-1)^{k+1}$, the transition is called magnetic multipole transition (*Mk*).

It has briefly mentioned the theory of the both MCHF and MCDF methods used in this work. The methods have been detailed in [9, 16] and [8, 17-20], respectively even [10 and 11].

A wave function, $\Psi(\gamma LS)$, in the MCHF method, has been linear combinated of configuration state functions (CSFs) $\Phi(\gamma_i LS)$,

$$\Psi(\gamma LS) = \sum_{i=1}^{M} c_i \Phi(\gamma_i LS) , \qquad \sum_{i=1}^{M} c_i^2 = 1 . \tag{3}$$

The energy functional of non-relativistic Hamiltonian of an atom or ion, is based on,

$$H_{NR} = \sum_{j=1}^{N} \left(\frac{1}{2}\nabla_j^2 - \frac{Z}{r_j} \right) + \sum_{j<k} \frac{1}{r_{jk}} . \tag{4}$$

The equation 1 is changed by 3 in the fully relativistic MCDF method.

$$\Psi_\alpha\left(PJM\right) = \sum_r^{n_c} c_r(\alpha) \left| \gamma_r PJM \right\rangle \tag{5}$$

The energy functional is based on the Dirac-Coulomb Hamiltonian in the MCDF method,

$$H_{DC} = \sum_{j=1}^{N} \left(c\vec{\alpha}_j . \vec{p}_j + (\beta_j - 1)c^2 + V\left(r_j\right) \right) + \sum_{j<k}^{N} \frac{1}{r_{jk}} . \tag{6}$$

The nuclear charge distribution is used by the two-component Fermi function in the both methods. The relativistic effects in the MCHF method are perturbated as a first-order correction using Breit-Pauli operators in CI proses. The transverse Breit interaction at the low-frequency limit and the vacuum polarization and self-energy, QED corrections, are considered in the MCDF method. The both methods are also included correlation effects.

ISBN:978-605-83516-6-0

RESULTS AND DISCUSSION

The heaviest and simplest ion of neptunium is Np^{92+}. There is just one and only electron moves in the strong field of heavy nucleus (Z=93). The study has focused on lifetimes of Np^{92+}. It is performed with GRASP code [8]. For the life times calculations *nl* (*n*=1-9, *l*=0-5) configurations have been used.

It has been computed energy levels and allowed and forbidden transition parameters, first. Then, it has been calculated life times for the selected levels from electric dipole, E1, quadrupole, E2, magnetic dipole, M1, and quadrupole, M2, transitions. It is indisputable truth that taking into account quantum electrodynamic, QED, contribution is obligation for atoms with high Z. The calculation in this study has been contained QED and Breit contributions. The Breit contributions in this calculation are almost zero.

For the accuracy of the life times, first, it is necessary to ensure the energy levels are in high accuracy. It has been also performed multiconfiguration Hartree-Fock, MCHF, calculation to support each other. The only work with available comparative value for the life times belongs to Jitrik and Bunge [7] have been checked in the Fig.1. The both methods have yielded so good agreement with Jitrik and Bunge's work. Because MCHF and MCDF calculations involves different contributions (MCHF contains just Breit-Pauli, the other comprises the transverse photon and QED), very small difference has been arisen.

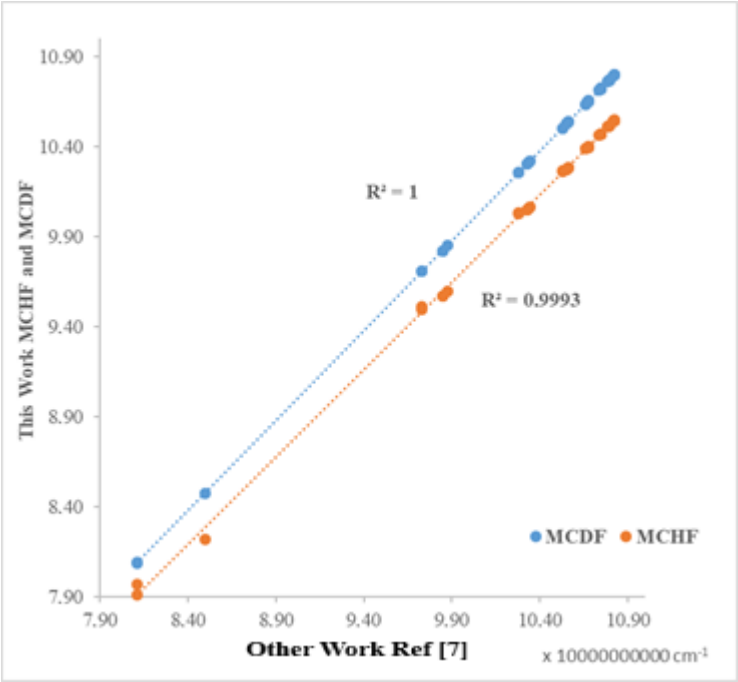


FIGURE 1. The graphical comparison for energy levels Np^{92+}

It can be an evidence of reliability of methods in this figure. On the other hand, Energy value of nl_j levels are same with $n(l+1)_j$ levels in reference [7]. For example, $2s_{1/2}$ and $2p_{1/2}$ states, $3p_{3/2}$ and $3d_{3/2}$ states, and $4d_{5/2}$ and $4f_{5/2}$ states are in same value. Thus, it is thought that MCDF study has given the most sensible and reliable results ever. Since the MCDF results have been considered to be better, life times have been calculated only by MCDF method.

The calculated life time values have been given in the Table 1. The levels are arranged increasing energy values which is subject of another paper. The life time values have been computed in Coulomb (velocity) and Babushkin (length) gauge because of ratio of gauges points the accuracy of calculation [16]. In tables and graphics, the gauges have been indicated "C" and "B" abbreviations according to their first letters. There is a great agreement in the presented data between other work data.

ISBN:978-605-83516-6-0

TABLE 1. The life time values calculated with MCDF method of Np^{92+}

Level	MCDF^{C}	MCDF^{B}	Other Work [7]
$2p_{1/2}$	1.2380994E-17	1.3298831E-17	1.33468E-17
$2s_{1/2}$	1.3968649E-15	1.3968950E-15	1.34876E-15
$2p_{3/2}$	2.3283480E-17	1.7028215E-17	1.67852E-17
$3p_{1/2}$	4.2684300E-17	5.2061481E-17	5.09123E-17
$3s_{1/2}$	4.4993297E-16	4.5453440E-16	4.41574E-16
$3p_{3/2}$	6.7421481E-17	5.3492180E-17	5.21857E-17
$3d_{3/2}$	1.0736287E-16	1.1105260E-16	1.05562E-16
$3d_{5/2}$	1.3142126E-16	1.3157757E-16	1.31029E-16
$4p_{1/2}$	1.0338472E-16	1.2906968E-16	1.26083E-16
$4s_{1/2}$	7.3025822E-16	7.4171901E-16	7.27630E-16
$4d_{3/2}$	2.3681687E-16	2.4429433E-16	2.36221E-16
$4p_{3/2}$	1.5100681E-16	1.2313317E-16	1.19857E-16
$4f_{5/2}$	5.7808268E-16	5.7846488E-16	5.75392E-16
$4d_{5/2}$	2.9138845E-16	2.9747704E-16	2.96439E-16
$4f_{7/2}$	6.2002930E-16	6.1986279E-16	6.18106E-16
$5p_{1/2}$	2.0320747E-16	2.6026338E-16	2.52253E-16
$5s_{1/2}$	1.2355651E-15	1.2533162E-15	1.23081E-15
$5d_{3/2}$	4.4883754E-16	4.6234402E-16	4.47905E-16
$5p_{3/2}$	2.9791667E-16	2.3878053E-16	2.30805E-16
$5f_{5/2}$	1.0968118E-15	1.0968201E-15	1.08742E-15
$5d_{5/2}$	5.4918172E-16	5.6735937E-16	5.63789E-16
$5g_{7/2}$	1.9710311E-15	1.9700886E-15	1.96711E-15
$5f_{7/2}$	1.1807330E-15	1.1796237E-15	1.17348E-15
$5g_{9/2}$	2.0339722E-15	2.0329657E-15	2.03002E-15
$6p_{1/2}$	3.6271998E-16	4.6662026E-16	4.43047E-16
$6s_{1/2}$	2.0241406E-15	2.0326822E-15	1.97960E-15
$6d_{3/2}$	7.7002278E-16	7.9331179E-16	7.61071E-16
$6p_{3/2}$	5.1365699E-16	4.1719604E-16	3.96076E-16
$6f_{5/2}$	1.8706588E-15	1.8646023E-15	1.84345E-15
$6d_{5/2}$	9.3818516E-16	9.7348126E-16	9.58259E-16
$6g_{7/2}$	3.3550700E-15	3.3478926E-15	3.33419E-15
$6f_{7/2}$	2.0185609E-15	2.0086829E-15	1.99350E-15
$6g_{9/2}$	3.4677847E-15	3.4603306E-15	3.44680E-15
$7p_{1/2}$	6.0366493E-16	7.7319113E-16	7.12147E-16
$7s_{1/2}$	3.1486239E-15	3.1579619E-15	3.01867E-15
$7d_{3/2}$	1.2430398E-15	1.2729910E-15	1.19622E-15
$7p_{3/2}$	8.2947495E-16	6.7887057E-16	6.26741E-16
$7f_{5/2}$	2.9752327E-15	2.9520406E-15	2.89212E-15
$7d_{5/2}$	1.5080868E-15	1.5583638E-15	1.50513E-15
$7g_{7/2}$	5.3136373E-15	5.2853844E-15	5.21266E-15
$7f_{7/2}$	3.2134114E-15	3.1822610E-15	3.13065E-15
$7g_{9/2}$	5.4966188E-15	5.4666619E-15	5.39423E-15
$8p_{1/2}$	9.5671950E-16	1.2255712E-15	1.07326E-15
$8s_{1/2}$	4.7619295E-15	4.7697531E-15	4.39576E-15
$8d_{3/2}$	1.9158683E-15	1.9637226E-15	1.77391E-15
$8p_{3/2}$	1.2909383E-15	1.0599092E-15	9.33885E-16
$8f_{5/2}$	4.5377587E-15	4.4846721E-15	4.28220E-15
$8d_{5/2}$	2.3118887E-15	2.3939809E-15	2.22973E-15
$8g_{7/2,}$	8.0579507E-15	7.9786064E-15	-
$8f_{7/2}$	4.9041165E-15	4.8308155E-15	4.63752E-15
$8g_{9/2,}$	8.3379437E-15	8.2520536E-15	-
$9p_{1/2}$	1.5291843E-15	1.9523520E-15	1.54012E-15

ISBN:978-605-83516-6-0

TABLE 1. Continued

Level	MCDF^{C}	MCDF^{B}	Other Work [7]
$9s_{1/2}$	7.3479580E-15	7.2833857E-15	6.15956E-15
$9p_{3/2}$	2.0193822E-15	1.6649071E-15	1.32860E-15
$9d_{3/2}$	2.9900358E-15	3.0599541E-15	2.51470E-15
$9f_{5/2}$	6.9664642E-15	6.8654310E-15	6.06255E-15
$9d_{5/2}$	3.5823096E-15	3.7066550E-15	3.15745E-15
$9g_{7/2}$	1.2270949E-14	1.2093221E-14	-
$9f_{7/2}$	7.5201349E-15	7.3805387E-15	6.56681E-15
$9g_{9/2}$	1.2692818E-14	1.2494893E-14	-

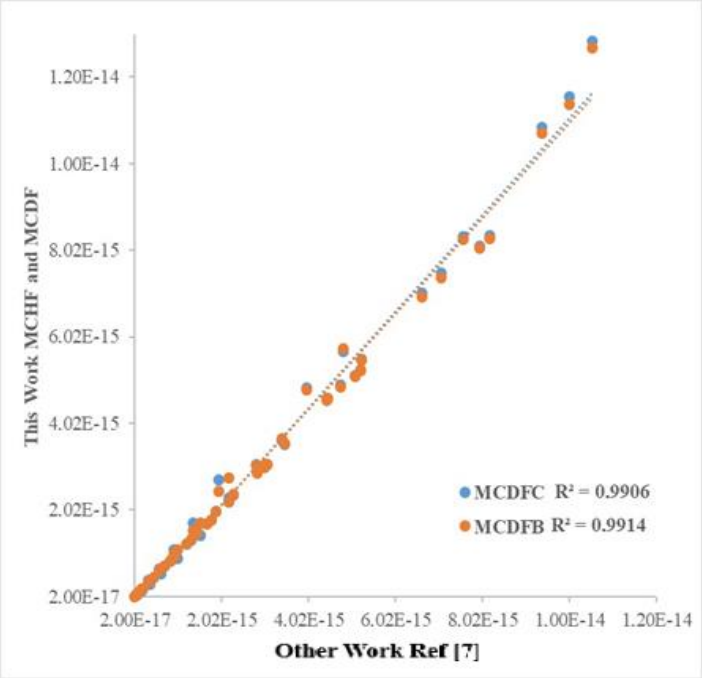


FIGURE 2. (a) The life times crosscheck of Np^{92+}

The life time's comparisons have been presented in Figure 2. This figure has shown Coulomb and Babushkin gauges comparison of MCDF calculation and other work [7]. The R^2 coefficient of determination of gauges is 0.9906 and 0.9914 for Coulomb and Babuskin, respectively. Moreover, the linear correlation coefficient between Coulomb and Babushkin is 0.9988. The ratio between the scales to be 1 is an indication of the accuracy of the calculation [16]. Unluckily, there is not any experimental comparison value for the values presented in this study neither energy levels nor life times in the accessible literature.

In addition to all this, the life time of $8g_{7/2}$, $8g_{9/2}$, $9g_{7/2}$, $9g_{9/2}$ levels have been represented for the first time.

CONCLUSION

The paper has been performed as a small part of a large scale calculation works applying both MCHF and MCDF methods for carry out the structure and spectroscopic data in high accuracy for highly ionized actinide atoms. It is a fact that one of the fundamental of atomic theory is the relativistic and radiative effects all. The excitation or level energy, life time, and other transition parameters for E1, E2 and M1 between several levels of Np^{92+} have investigated in high precision. For the brevity just life times presented here. As computing values, the Breit-Pauli, Breit and QED contributions have considered. It is thought that the present paper will lead to other workers in theoretical and experimental way also in the field of technology in future.

ISBN:978-605-83516-6-0

REFERENCES

1. V. G. Pal'chikov, Phys. Scr. **57**, 581 (1998).
2. https://www.nist.gov/pml/atomic-spectra-database.
3. W. R. Johnson and G. Soff, At. Data and Nuc. Data Tables **33**, 405 (1985).
4. V. A. Yerokhin and V. M. Shabaev, J. Phys. Chem. Data **44** 033103 (2015).
5. O. Jitrik and C.F. Bunge, J. Phys. Chem. Ref. Data **33**,1059 (2004).
6. O. Jitrik and C.F. Bunge, Phys. Scripta **69**,196 (2004).
7. http://www.fisica.unam.mx/research/tables/spectra/1el/index.shtml
8. K. G. Dyall, I. P. Grant, C. T. Johnson, F. A. Parpia and E. P. Plummer, Comp. Phys. Commun. **55**, 425 (1989).
9. C.F. Fischer, Com. Phys. Commun. **64**, 369 (1991).
10. G. Ürer, Can. J. Phys. **94**, 1138 (2016).
11. G. Ürer, Can. J. Phys. **96**, 1359 (2018).
12. G. Ürer, M. Arslan, A. Keçeli, and E. Balkaya, AIP Conference Proceedings, **1722**, 190002 (2016)
13. G. Ürer, Sakarya Üniversitesi Fen Bilimleri Enstitüsü Dergisi, **22**(3), 970 (2018).
14. G. Ürer, Bilecik Şeyh Edebali Üniversitesi Fen Bilimleri Dergisi, **5**(1), 18 (2018).
15. G. Ürer, Beykent Üniversitesi Fen ve Mühendislik Bilimleri Dergisi, **11**(1), 63 (2018).
16. C.F. Fischer, T. Brage and P. Jönsson, *Computational Atomic Structure-an MCHF approach*, (Bristol and Philadelphia: Institute of Physics Publishing, 1997).
17. I. P. Grant, Advan. Phys. **19** ,747 (1970).
18. I. P. Grant, J. Phys. B, **7**, 1458 (1974).
19. I. P. Grant, *Computational Chemistry* (Vol 2) ed. Wilson S (Plenum, New York, USA, 1988).
20. I. P. Grant, *Relativistic Quantum Theory of Atoms and Molecules* (Springer, New York, USA, 2007).

04. Condensed Matter Physics



BOOK OF FULL TEXT PROCEEDINGS TURKISH PHYSICAL
SOCIETY 35th INTERNATIONAL PHYSICS CONGRESS (TPS35)
TPS35, Vol.01, No.04, pp.251-254.
ISBN:978-605-83516-6-0

15 December 2019

Characterization of Electrical Properties of PMMA/PbO Structures

D. Akay[1], U. Gökmen[2] and S. Bilge Ocak[2, a)]

[1] *Ankara University, Faculty of Science, Department of Physics, 06100 Tandogan, Ankara, Turkey*
[2] *Gazi University, Graduate School of Natural and Applied Sciences, Department of Advanced Technologies, 06500 Ankara, Turkey*

[a)]Corresponding author: sbocak@gazi.edu.tr

Abstract. Al/PMMA/ PbO /p-Si structures were fabricated using thermal evaporation technique and spin coating method. Interface states density, series resistance and ideality factor using I–V characteristics in Al/PMMA/ PbO /p-Si structures have been reported for four structures using different techniques.

INTRODUCTION

Organic semiconductors are attractive for the perspective of exciting applications [1]. In particular, great advances have been made in the area of transistors, LEDs and high resolution with power consumption and even on the flexible textile substrate because of having the electrical properties of semiconductors [2]. So, organic materials have become an appealing class of semiconductor and good candidate for developing electronic and optoelectronic flexible components. Additionally, to using organic polymers or organic molecules have many advantages [3].
Organic materials and devices are mostly inexpensive (low-cost), the preparation at low process temperatures, environment friendly, homogeneity and variety of means by which the materials can be deposited. Moreover, optical and electronic features can be ordered in a wide range such as luminescence and high absorption offers the possibility to use flexible substrates [4,5]. It is intriguing that organic semiconductor materials also give an opportunity for allow to keep active layers very thin. Besides all the advantages, semiconductors have also some disadvantages. The semiconductors possess an electrical conductivity that is between that of inorganic semi-conductors and that of insulators. The reason for this drawback can be depend on the relatively an inefficient hopping process which are primarily bound by van der Waals interaction. Because of this low carrier mobility in semiconductor organic materials, long term stability problems have occurred. However, the main problem is that organic semiconductors are low efficiency devices. To enhance the efficiency of organic electronic devices, it is crucial to investigate the coupling between the molecules. Thus, optical and electronic properties can be managed more efficiently and accurately.

To convert metal-semiconductor (MS) structures into metal / polymer / oxide structure, polymer and oxide layer are used as insulator layer. These structures contain a semiconductor substrate cloaked by a layer of insulation upon placed a metal electrode [5]

Polymer/Oxide used as interfacial layer perform significant role for determination of electrical properties such as dielectric and electrical parameters of organic structures. The investigation of optical, dielectric and electrical characteristics of organic semiconductors show their widespread andincreasing use inorganic–organic hybrid structures [6]. To obtained new design organic semiconductors with high mobility is great interest subject for many years.

PbO films are effective inorganic compounds occurring in two polymorphs. They can be induced, reproductive system and blood, gum tissue, kidneys, affects central nervous system, respiratory tract and eyes. They are used nuclear and space industries pharmaceutical, medical. To form PMMA/PbO composite structure, the most usually used polymer (polymer poly methyl methacrylate) PMMA with PbO is incorporated [7-9]

In this study, to obtain a high performance Metal/Polymer/Oxide structures PMMA/PbO composite structure as thin interfacial polymer layer was formed on p-Si. Interface states density, series resistance and ideality factor using

Türk Fizik Derneği
1950
Turkish Physical Society

ISBN:978-605-83516-6-0

I–V characteristics in Al/PMMA/ PbO /p-Si structures have been reported for four structures using different techniques.

EXPERIMENTAL PROCEDURE

P-type Si (111) wafer used resistivity of 1-10 Ω.cm and thickness of 380 μm is cleaned to eliminate organic waste using Radio Corporation of America (RCA) [6]. The fabricated Al / PMMA / PbO/P-Si structure are defined at Defne et al [10].

RESULTS AND DISCUSSION

Al/PMMA/ PbO /p-Si structures have been analysed by using the $I-V$ measurements technique. As known that the Scottky structures appropriate with the thermionic emission theory [11]

$$I = I_0\, exp\left(\frac{qV_d}{nkT}\right)\left[1 - exp\left(-\frac{qV_d}{nkT}\right)\right] \quad (1)$$

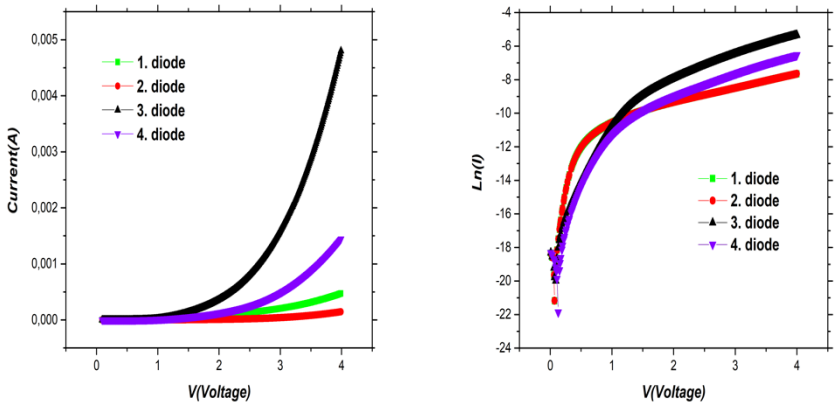
where the term $I_0 = AA^*T^2\exp\left(\frac{-q\Phi_b}{kT}\right)$ is saturation current that can be provided by the $lnI-V$ graph from y-intercept of the figure at the zero voltage. In the description of the saturation current, $A^*$is the Richardson constant which corresponds to $32\ A/cm^2K^2$ for p-type Si. q is the electronic charge, k described as a Boltzmann constant and T absolute temperature in K. As similar the saturation current, an ideality factor $\left[n = q/kT\,\frac{dV}{dLn(I)}\right]$ can be obtained from the $lnI-V$ graph but by using the inverse slope of the linear part. The $\Phi_b = \frac{kT}{q}\ln\left(\frac{A\,A^*\,T^2}{I_0}\right)$ represents zero bias barrier height which can be calculated from the forward $I-V$ characteristics. Figure 1a and b show $I-V$ and $lnI-V$ characteristics. As known that by using figure 1a and 1b, barrier height and ideality factor has been found and its values can be seen from the table1. But a major disadvantage of the thermionic emission theory is the lack of account for the influence of series resistance. We have extended the study with the Cheung method both to detect the parameter of series resistance (R_s), which is a really important parameter for electrical and dialectical characteristics of the structure, and to improve the accuracy values of the barrier height (Φ_B) and ideality factor (n) in the calculation process. To determine the barrier height according to the Cheung method [12], we have plotted the dependence as a relation

$$H(I) = V - \frac{nkT}{q}ln\left(\frac{I}{AA^*T^2}\right) \quad (2)$$

But we have to in to account that the applicability of the method only at the voltages $V > 3kT/q$. The Eq.(2) can expressed by the electrical parameters of barrier height and series resistance by a relation,

$$H(I) = n\Phi_B + IR_s \quad (3)$$

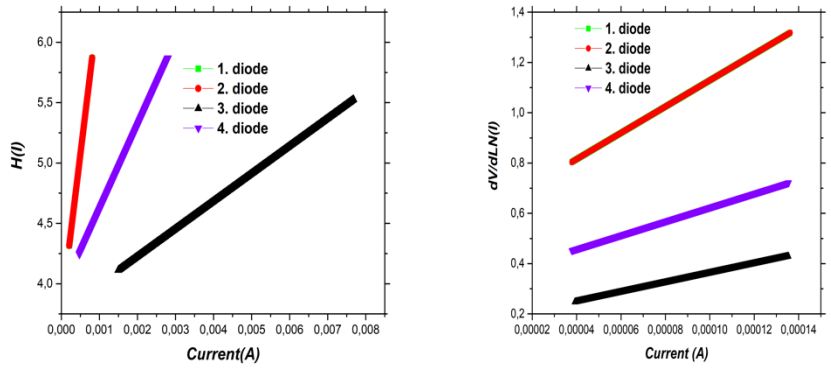
ISBN:978-605-83516-6-0



(a) (b)

FIGURE 1. a) I-V behaviors of Al/PMMA/Pbo/P-Si b) Semi-logarithmic I-V behaviors of Al/PMMA/Pbo/P-Si.

approximating the line part with straight line$y = a + bx$, the coefficients $b = R_s$and $a = n\Phi_B$, have been obtained, and knowing these coefficients it is easy to find Φ_B and n .



(a) (b)

FIGURE 2. a) *H(I)-I* characteristics of Al/PMMA/Pbo/P-Si structures b) *dV/dln(I)-I* behaviors of Al/PMMA/Pbo/P-Si structures. (The values of 1. and 2. diode overlap in the graph)

TABLE 1. Electrical characteristics of Al/PMMA/Pbo/P-Si structures

	I – V parameters							
	Standard Method				**Cheung Method**			
	$\Phi_b(eV)$	n	R_s	$I_0\ (A)$	$\Phi_b(eV)$	n	$R_s(\Omega)$	$I_0(A)$
1. diode	0.822	1.439	-	5,877E-10	0.851	1.085	25.147	1,928E-10
2. diode	0.758	1.085	-	6,976E-09	0.713	3.551	42.237	4,079E-08
3. diode	0.747	1.086	-	1,090E-08	0.745	4.460	28.193	1,180E-08
4. diode	0.739	3.355	-	1,508E-08	0.741	3.555	62.257	1,377E-08

ISBN:978-605-83516-6-0

To evaluate the other substantial characteristic properties of four structures, we have computed in other parameters as well as series resistance. n and Φ_B have been obtained by the Thermionic emission theory and Cheung method. As can be seen from the table 1 that n and Φ_B values for four structures calculated from Cheung method are larger than those calculated from standard method.

CONCLUSION

I-V characteristics for Al / PMMA/ PbO / P-Si structures were studied at room temperature. It is shown that these characteristics are sensitive voltage. n, Φ_B and R_s values were calculated by using Thermionic emission theory and Cheung method for four structures. This study recommends that PMMA/ PbO layer can be considered as a potential thin film.

REFERENCES

1. Podzorov, V,Loginova, *S E*, Pudalov, *V M*, Gershenson, M E. App. Phys. Lett. 83, 17 (2003).
2. G.D. Sharma, S.K. Sharma, M.S. Roy, Thin Solid Films 468, (1–2) 208(2004).
3. T.S. Shafai, Thin Solid Films 517 (3), 1200 (2008).
4. M.S. Roy, G.D. Sharma, S.K. Gupta, Thin Solid Films 310 (1–2), 279 (1997).
5. T. Kilicoglu, M. E. Aydin, Y. S. Ocak, Physica B **388** (1,2), 244 (2007).
6. A B Selçuk, S Bilge Ocak, G Kahraman and A H Selçuk, Bull. Mater. Sci., 37 1717 (2014).
7. A. Sayed, A.El, M:A:M. Ali, M.R.Ismail, Radiat. Phys. Chem. 66, 185(2003).
8. W.H. Zhong, G.Sui, S.Jana, J. Miller, J. Compos.Sci.Technol. 69, 2093 (2009).
9. N.Erdem, O. Baykara, M. Dogru, F. Kuluozturk, Radiat. Phys. Chem. 79, 917 (2010).
10. D Akay, U Gokmen and S B Ocak, Physica Scripta, 94, 115302 (2019).
11. Z. L. Wang J. Phys-Condens. Mat. 16, 829–58 (2004).
12. S.K. Cheung and N. W. Cheung Appl. Phys. 49 85 (1986).

BOOK OF FULL TEXT PROCEEDINGS TURKISH PHYSICAL
SOCIETY 35th INTERNATIONAL PHYSICS CONGRESS (TPS35)
TPS35, Vol.01, No.04, pp.255-260.
ISBN:978-605-83516-6-0

15 December 2019

Analyses of Diode Parameters Using C–V Characteristics of Al/PMMA/PbO/P-Si Structures

D. Akay[1], U. Gökmen[2], S. Bilge Ocak[2a]

[1] *Ankara University, Faculty of Science, Department of Physics, 06100 Tandogan, Ankara, Turkey*
[2]*Gazi University, Graduate School of Natural and Applied Sciences, Department of Advanced Technologies, 06500 Ankara, Turkey*

[a)]Corresponding author: sbocak@gazi.edu.tr

Abstract. Al/PMMA/ PbO /p-Si structures were fabricated using thermal evaporation technique and spin coating method. Interface states density and series resistance using G–V and C–V characteristics in Al/PMMA/ PbO /p-Si structures at 500 kHz and 1MHz have been reported for four structures. Due to trapping states, the capacitance is dependent on frequency. The barrier height, diffusion voltage, Fermi energy, space charge layer width and donor carrier concentration for these devices have been obtained at 500 kHz and 1MHz. It is shown that the G–V and C–V characteristics are dependent on the electrical parameters in these structures such as barrier Height, interface state density and series resistance.

INTRODUCTION

Electronic technology uses organic semiconductor devices in recent years. Due to attractive features of these materials such as all of which offer the prospect of cheaper photovoltaic energy, low material consumption for ultra thin molecular films, they have a wide application in this technology [1-4]

To convert metal-semiconductor (MS) structures into metal / polymer / oxide structure, polymer and oxide layer are used as insulator layer. These structures contain a semiconductor substrate cloaked by a layer of insulation upon placed a metal electrode. Because of dielectric property of insulation layers, what they generate in the end is a sort of capacitor capable of storing electronic charges. A very thin insulator film for these structures is used to permit the tunneling carriers [5]

Polymer/Oxide used as interfacial layer perform significant role for determination of electrical properties such as dielectric and electrical parameters of organic structures. The investigation of optical, dielectric and electrical characteristics of organic semiconductors show their widespread and increasing use inorganic–organic hybrid structures [6]. To obtained new design organic semiconductors with high mobility is great interest subject for many years.

PbO films are effective inorganic compounds occurring in two polymorphs. They can be induced, reproductive system and blood, gum tissue, kidneys, affects central nervous system, respiratory tract and eyes. They are used nuclear and space industries pharmaceutical, medical. To form PMMA/PbO composite structure, the most usually used polymer (polymer poly methyl methacrylate) PMMA with PbO is incorporated [7-9]

In this study, to obtain a high performance Metal/Polymer/Oxide structures PMMA/PbO composite structure as thin interfacial polymer layer was formed on p-Si. The capacitance-voltage (C-V) and conductance-voltage (G-V) characteristics of these structures were measured at 500 kHz and 1 MHz room temperature. It is obtained that the C–V and G–V characteristics are dependent on electrical parameters as barrier Height, interface state density and series resistance in these structures.

Türk Fizik Derneği
1950
Turkish Physical Society

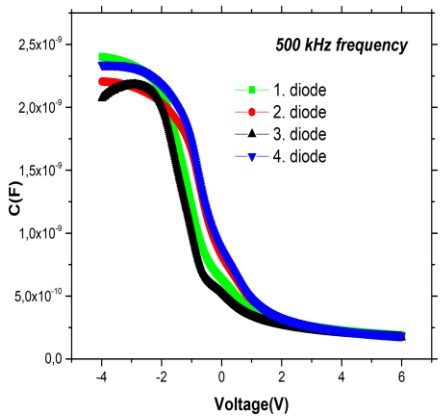
ISBN:978-605-83516-6-0

EXPERIMENTAL PROCEDURE

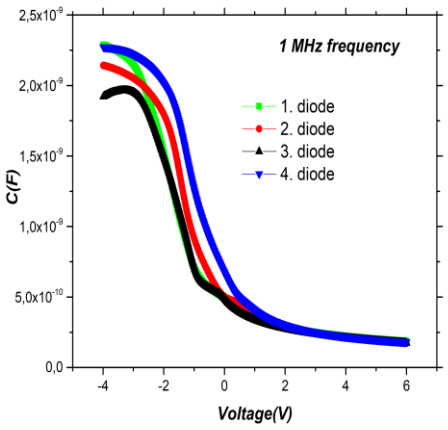
P-type Si (111) wafer used resistivity of 1-10 Ω.cm and thickness of 380 µm is cleaned to eliminate organic waste using Radio Corporation of America (RCA) [6]. The fabricated Al / PMMA / PbO/P-Si structure are defined at Defne et al [10].

RESULTS AND DISCUSSION

The used C-V method is the most popular technique to characterize electrical measurement for Schottky structures Fig. 1a and 1b, Fig 2a and 2b show voltage dependence of C–*V* and *G*–*V* characteristics for 1D, 2D, 3D and 4D formed Al / PMMA / PbO/P-Si at 500 kHz and 1MHz and the bias voltage was applied between -4 and +6 VDC for four structures. These curves composed three regimes have defined as inversion–depletion–accumulation regions. Capacitance and conductance values depend on energy distribution, interface states, series resistance and thickness formation of polymer and oxide layers. When G–V and C–V curves are measured at adequately high frequencies ($f \geq 500$kHz) [6] the effect interface state density can be omitted, because charges at interface states could not track an A.C. signal [6]. So, the semiconductors are in equilibrium with the interface states.



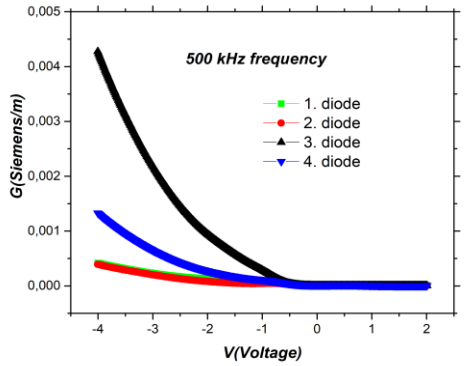
(a)



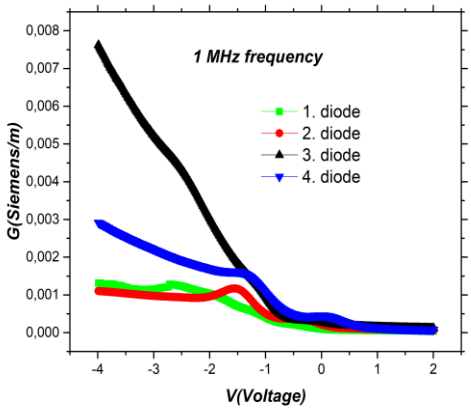
(b)

Figure. 1. C–V characteristics for Al/PMMA/Pbo/P-Si a) 500kHz b) 1MHz.

ISBN:978-605-83516-6-0



(a)



(b)

Figure. 2. G–V characteristics for Al/PMMA/Pbo/P-Si a) 500kHz b) 1MHz

G and C values forward voltage is attributed to interfacial polymer layer, distribution of D_{it} and effect of series resistance (R_s). R_s is really major parameter which has been influenced from the electrical and dielectrical properties of the device. The R_s values of the material has been calculated to Eq.1

$$R_s = \frac{G_m}{{G_m}^2 + (\omega C_m)^2} \quad (1)$$

where G_m and C_m are the measured conductance and capacitance values and ω is the angular frequency. R_s values have evaluated in strong accumulation region and at f≥500kHz As seen figure 3, R_s values increase by increasing voltage and vary from 4.15 to 24.95 at 500 kHz as seen table1 and from 13.94 to 35.84 at 1 MHz for four structures as seen table 2.

ISBN:978-605-83516-6-0

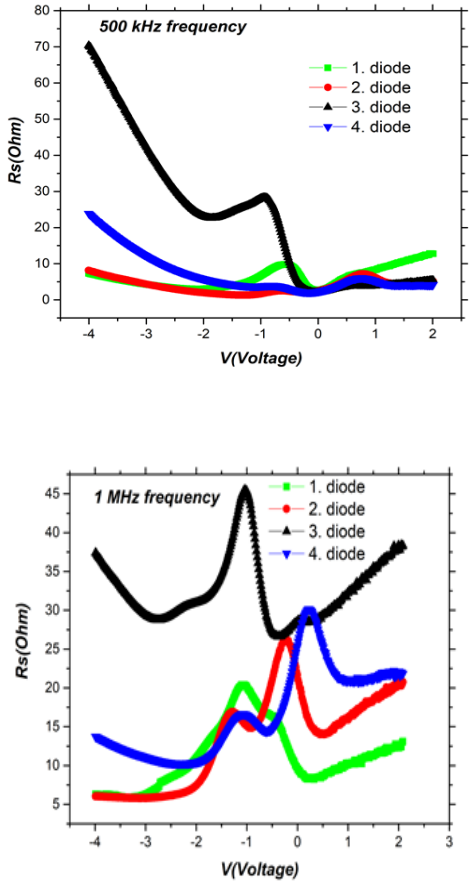


Figure 3.Series resistance (R_s)-Voltage characteristics of Al/PMMA/Pbo/P-Si at a) 500kHz b) 1MHz

In the depletion region, doping concentration in a *p*-type s can be defined

$$\frac{\partial(1/C^2)}{\partial V} = \frac{2}{A^2 \varepsilon_s \varepsilon_0 q N_A} \tag{2}$$

Where C, A, N_A, ε_s, ε_0 and V are defined the capacitance, area of structure, ionized traps like-acceptor, semiconductor permittivity (ε_S = 11.8ε_0 for Si), vacuum permittivity (ε_0 = 8.85×10^{-12} F/m) and gate voltage respectively [6].

$\phi_b(C-V)$, $\Delta\phi_b$ and E_m defined as barrier height, image force lowering and maximum electric field, respectively can be formulated as below

$$\phi_b(C-V) = V_{bi} + E_F - \Delta\phi_b \tag{3}$$

ISBN:978-605-83516-6-0

$$\Delta\phi_b = \left(\frac{qE_m}{4\pi\varepsilon_s\varepsilon_0}\right)^{1/2} \quad (4)$$

$$E_m = \frac{2qV_{bi}N_A}{\varepsilon_s\varepsilon_0} \quad (5)$$

When $\phi_b(C-V)$ and N_A increase, frequency increases. Density distribution of interface states and interfacial layer are affected behavior of $\phi_b(C-V)$ and N_A.

Besides, to understand frequency dependence of interface states density as defined D_{it} , Hill–Coleman method is used. It is can be computed [11]

$$D_{it} = \frac{2}{qA}\frac{G_{cMax}/\omega}{\left(\frac{G_{cMax}/\omega}{\omega C_i}\right)^2 + \left(1-\frac{C_c}{C_i}\right)^2} \quad (6)$$

where G_{cMax} , $C_c and\ C_i$ are defined as maximum in the corrected *G–V* curve and capacitance to G_c and capacitance of interfacial layer respectively [6]. As seen table 1 and 2, when frequency increases D_{it} and R_s values are decrease due to distribution of interface states between semiconductor interface and interfacial layer [6].

Table 1. Diode parameters of Al/PMMA/ PbO /p-Si structures at 500 kHz.

500 kHz	$V_d(V)$	$E_F(eV)$	$N_A\ (cm^{-3})$ 10^{16}	$R_s(\Omega)$	$\Phi_b(eV)$	$W_d(cm)$	$\Phi_b-\Delta\Phi_b(eV)$	$D_{it}(eV^{-1}cm^{-2})$ 10^{12}
1. diode	0.4810	0.1357	4.56	4.15	0.6168	1173.87	0.5852	0.1652
2. diode	0.2227	0.1422	3.51	1.36	0.3650	910.56	0.3405	0.2377
3. diode	0.7110	0.1400	3.83	24.95	0.8511	1556.47	0.8177	0.5913
4. diode	0.2156	0.1394	3.93	4.15	0.2394	576.46	0.2188	0.8389

Table2. Diode parameters of Al/PMMA/ PbO /p-Si structures at 1 MHz.

1 MHz	$V_d(V)$	$E_F(eV)$	$N_A\ (cm^{-3})$ 10^{16}	$R_s(\Omega)$	$\Phi_b(eV)$	$W_d(cm)$	$\Phi_b-\Delta\Phi_b(eV)$	$D_{it}(eV^{-1}cm^{-2})$ 10^{12}
1. diode	0.94099	0.1346	4.76	16.08	1.07565	1606.48	1.03785	0.01195
2. diode	0.39285	0.1406	3.75	15.88	0.53350	1170.18	0.5048	0.0216
3. diode	0.81713	0.1383	4.10	35.84	0.955	1612.55	0.9203	0.5357
4. diode	0.2845	0.1391	3.98	13.94	0.4237	966.20	0.3969	0.8304

ISBN:978-605-83516-6-0

CONCLUSION

C–V and *G–V* characteristics for Al / PMMA/ PbO / P-Si structures were examined at 500 kHz and 1 MHz at room temperature. It is shown that these characteristics are sensitive voltage and frequency. D_{it} and R_s values using these characteristics have been calculated for four structures. It is deduced that D_{it} values decrease with increasing frequency and R_s values are increase with increasing frequency. This study recommends that PMMA/ PbO layer can be considered as a potential thin film.

REFERENCES

1. Podzorov, V,Loginova, *S E*, Pudalov, *V M*, Gershenson, M E. App. Phys. Lett. 83, 17 (2003).
2. G.D. Sharma, S.K. Sharma, M.S. Roy, Thin Solid Films 468, (1–2) 208(2004).
3. T.S. Shafai, Thin Solid Films 517 (3), 1200 (2008).
4. M.S. Roy, G.D. Sharma, S.K. Gupta, Thin Solid Films 310 (1–2), 279 (1997).
5. T. Kilicoglu, M. E. Aydin, Y. S. Ocak, Physica B **388** (1,2), 244 (2007).
6. A B Selçuk, S Bilge Ocak, G Kahraman and A H Selçuk, Bull. Mater. Sci., 37 1717 (2014).
7. A. Sayed, A.El, M:A:M. Ali, M.R.Ismail, Radiat. Phys. Chem. 66, 185(2003).
8. W.H. Zhong, G.Sui, S.Jana, J. Miller, J. Compos.Sci.Technol. 69, 2093 (2009).
9. N.Erdem, O. Baykara, M. Dogru, F. Kuluozturk, Radiat. Phys. Chem. 79, 917 (2010).
10. D Akay, U Gokmen and S B Ocak, Physica Scripta, 94, 115302 (2019).
11. Hill, W A, Coleman, AA. Sol. Stat. Electronics, 23, 987 (1980).

BOOK OF FULL TEXT PROCEEDINGS TURKISH PHYSICAL
SOCIETY 35th INTERNATIONAL PHYSICS CONGRESS (TPS35)
TPS35, Vol.01, No.04, pp.261-265.
ISBN:978-605-83516-6-0

15 December 2019

Janus Monolayers of MXenes: A DFT Study

Berna Akgenc[1, a)]

[1]*Department of Physics, Kirklareli University, Kirklareli, Turkey*

[a)]Corresponding author: berna.akgenc@klu.edu.tr

Abstract. Two-dimensional (2D) transition metal carbides and nitrides, which called as "MXenes" displaying astonishing properties are emerged as a new class of 2D layered materials. We have investigated the structural, electronic and magnetic properties of Janus structure of pristine MXene by means of first-principles calculations. The ground state structures of Janus monolayers of MXenes are found in different magnetic configurations. Our calculated electronic band structures indicate that the Janus monolayers MXenes are half-metallic, metallic and semiconductor behaviors upon compounds. Janus monolayers of MXenes suggest that they are promising candidates for future spintronic applications, which should stimulate interest in their synthesis.

INTRODUCTION

Spintronic is one of the new emerging fields of promising technologies for next-generation devices due to their spin degree of freedom of electrons [1-3]. With the discovery of superior graphene in the last decade [4,5], two-dimensional (2D) materials have extensively attracted due to their many intriguing physical and chemical properties. The following question is raised as natural: Is there any 2D materials can be used in spintronic applications? Magnetic order and high spin-polarization at room temperature are great advantage for spintronic applications. Nevertheless, many of 2D materials are naturally non-magnetic and their applications are limited in spintronics [6]. The current efforts in designing and manufacturing spintronic devices involve introducing specific defects, depositing magnetic adatoms on the material, applying external electric field or tensile strain. Although these effects produce high spin polarization, it is still challenge to prepare/control materials for experiments with ordered spin structure at room temperature. For instance, asymmetrical chemical modifications to graphene nanoribbons result in very weak spin-spin interactions resulting from the magnetism of the p-electrons.

The development of spintronics depends on finding new materials which have specific magnetic properties. The early transition metal carbides and/or nitrides, which are known as "MXenes", just recently entered the research area as a new member of 2D materials following the synthesis of Ti_3C_2 [7]. Depending on their constituent elements, MXenes have unique properties such as unique electronic, magnetic, mechanical and optical properties were dedicated as being tapological insulator, metal-to-insulator transition and superconductivity.

Their general formula consist of $M_{n+1}AX_n$ (n=1,2,3), M, A and X represent early transition metal, A-group elements and C and/or N, respectively. More than 70 MAX phases have been realized experimentally. MXenes were produced by selectively etching "A" layers out of this MAX bulk.

Desirable magnetic properties of 2D materials may show in these MXenes have intrinsic magnetism and high spin-polarization stemmed from d-electrons. There are exists rapidly increasing theoretical research activity focused on this area. For instance, Cr_2C MXene exhibits intrinsic half-metallic ferromagnetic (8.0 μ_B per unit cell) behavior with the half-metallic gap as large as 2.85 eV due to itinerant Cr d-electrons. Ferromagnetic-antiferromagnetic transitions accompanied by a metal to insulator by terminal groups have been demonstrated [8]. He *et al.* have found that asymmetrical functionalized ternary MXenes (example: Cr_2TiC_2FCl) shows a novel bipolar antiferromagnetic semiconductor streaming from vanishing magnetism. The mixed functionalization with F/Cl show bipolar AFM semiconductor [9]. Stable monolayers of Ti_2C and Ti_2N have also been reported and it is found that they have ferromagnetic ground states [10]. There are several studies that can be cited as examples: Bare V_2C monolayers MXene have shown metallic with antiferromagnetic configuration. As an semiconductor MXenes, Sc_2C monolayer have been predicted and have shown tunable band gap with OH, F, or O chemical groups. After surface terminations, electronic properties of Sc_2C MXene transforms from metallic to semiconductor [11].

Structural symmetry breaking is crucial for tunable electronic properties. We have motivated with Cr_2C have intrinsic magnetism; we have created janus monolayers of MXenes as Cr-based. The other transition metal atoms

Türk Fizik Derneği
1950
Turkish Physical Society

ISBN:978-605-83516-6-0

have selected from same column in the periodic table (Ti, Sc and V). According to our knowledge, there are few reports on the electronic and magnetic properties of Janus MXenes up to date. With this motivation, we have investigated the electronic and magnetic properties of Janus monolayers of MXenes and they are promising candidates for spintronic applications, which should stimulate interest in their synthesis.

COMPUTATIONAL DETAILS

All calculations are performed based on density functional theory (DFT) as implemented in the Vienna *ab-initio* simulation package (VASP) [12,13] within the generalized gradient approximation (GGA) employing Perdew-Burke-Ernzerhof (PBE) [14] exchange-correlation functional. The projector augmented wave (PAW) potential is used with the plane-wave cutoff energy set as 550 eV. van der Waals (vdW) correction DFT-D2 proposed by Grimme to describe the long-range vdW interactions [15]. We consider a vacuum layer of about 20 Å to avoid interaction between neighboring slabs. The Brillouin zone is sampled $12x12x1$ Monkhorst-Pack *k*-point mesh for the structural properties. The electronic band structure calculations were presented more sensitive; the BZ integration was increased to twofold. The convergence of energy criteria were set to 10^{-5} eV between two ionic steps, and the maximum force allowed on each atom was 0.005 eV/Å . Gaussian smearing factor was used and the pressures on the unit cell were decreased to a value of less than 1.0 kBar in all three directions.

Considering the strong correlation effects between *d*-orbitals of transition metal atoms, electronic structure calculations and structural relaxation are performed by using Dudarev's GGA+U approach [6]. It is important note that the structural relaxation of the transition metal atoms strongly dependent on the whether the plus U parameter is included or not. In our calculations, Hubbard on-site Coulomb parameter (U) was taken into consideration. Here, the U value of Cr, Sc, Ti atoms are set to be 4 eV.

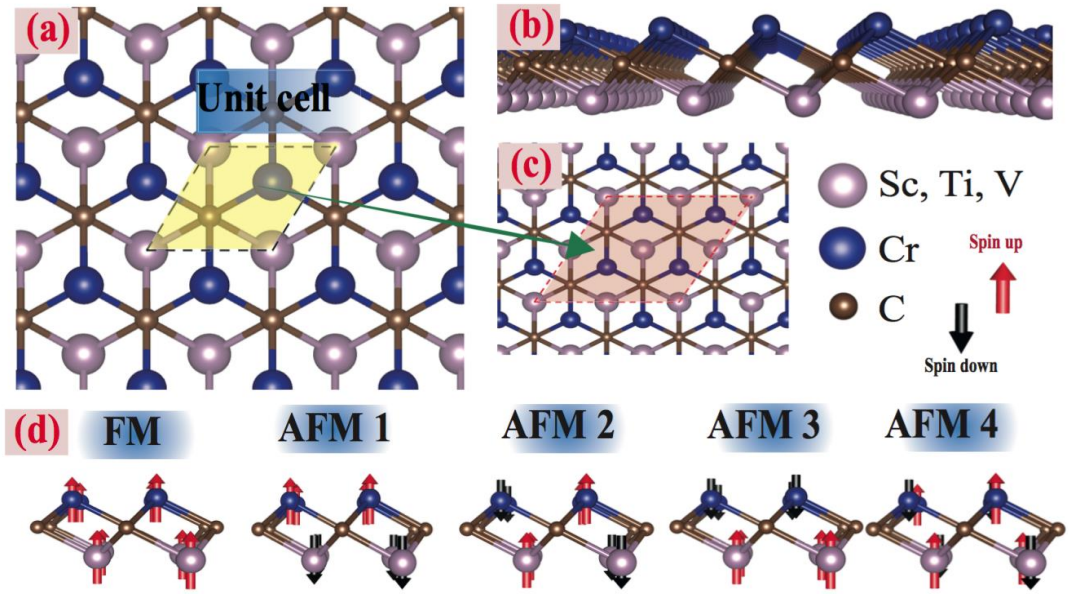


FIGURE 1. Atomic structure of pristine and Janus 2D MXenes. Dark blue spheres represent Cr atom, purple sphere represents Sc,Ti and V atoms: (a) top view of the atomic structure; (b) side view of Janus 2D MXenes. (c) 2x2x1 supercell used for magnetic configurations. (d) Schematics of five different magnetic structures: FM, AFM1- AFM4.

RESULTS AND DISCUSSION

Figure 1(a-b) shows the lattice structure of M_2C type MXene. It basically defines as C atom is sandwiched between transition atoms. From its top view showed that atoms are layered hexagonally. Because of MXenes are magnetic material, we have continued with determination of ground state of pristine monoloyers of MXenes Cr_2C,

ISBN:978-605-83516-6-0

V_2C, Ti_2C, Sc_2C and their janus structures. In order to find the magnetic ground state, we increased unit cell size from one unit to 2x2x1 supercell which contains eight transition metal atoms in Figure 1(c). Ferromagnetic (FM), antiferromagnetic (AFM1-AFM4) five different magnetic configurations are considered. These ferromagnetic configurations shall not be considered as realistic ordering in Figure 1(d). We have also considered spin-unpolarized case in our calcilation as NM (non-magnetic). The total energy calculations reveal that in Table 1. According to our results, Cr_2C, V_2C, Sc_2C have FM ground state. Ti_2C have antiferromagnetic (AFM3) magnetic ground state. We have continued with their janus structure and our calculations shows that CrVC, CrScC and CrTiC have FM ground state. Among the MXenes, Cr_2C shows strong ferromagnetism stream from itinerant Cr d electrons. Cr-based Janus monolayers are also effect from intrinsic magnetism, and they can be showed as strong magnetism. We have considered FM states are ground state in janus monolayer of MXenes in the rest of the paper.

TABLE 1. Magnetic configuration and Total Energy (in eV) for pristine and Janus MXenes

Type	Cr_2C	V_2C	Ti_2C	Sc_2C	CrVC	CrScC	CrTiC
FM	-82.99	-74.10	-70.74	-69.62	-78.51	-76.01	-77.39
AFM1	-81.00	-73.54	-70.26	-69.54	-76.26	-71.35	-76.42
AFM2	-80.48	-73.42	-70.54	-69.55	-72.58	-71.86	-74.80
AFM3	-80.72	-73.20	-71.29	-69.61	-76.36	-71.68	-72.38
AFM4	-81.02	-73.60	-70.52	-69.54	-77.50	-72.47	-73.03
NM	-67.37	-69.00	-69.72	-69.10	-67.75	-66.17	-67.63

Electronic band structure of janus monolayers of MXenes are also calculated with GGA including U-Hubbard term because of GGA+U method extends the functional approach to deal with the self-interacting electron correlation sand it is strongly suggested to be used to examine spintronic materials. Researchers have proposed various concepts in spintronic materials to address; including half-metals (HM), sem-metal (SM) and Dirac half metallic (DHM) beside metallic (M) behavior. In Figure 2, several densities of states (DOS) of M, HM, SM, DHM are dramatically described.

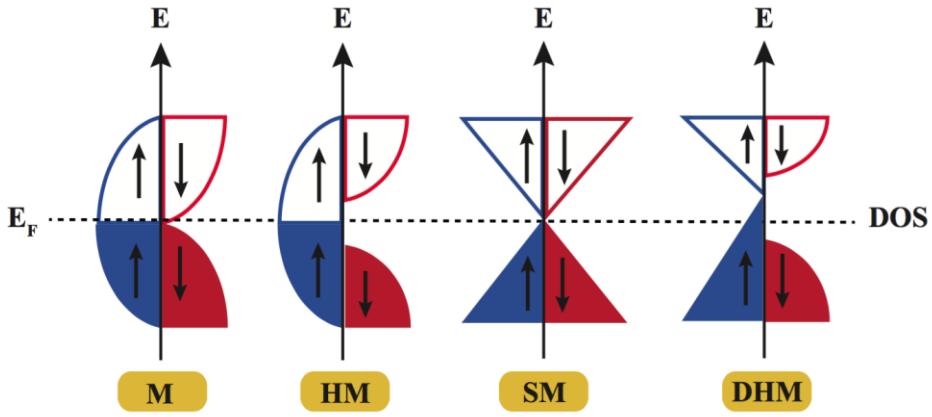


FIGURE 2. Schematic density of states of metal (M), half-metal (HM), semi-metal (SM) and Dirac half-metal (DHM). "↑" and "↓" indicate spin-up and spin-down channel, respectively.

As shown in Figure 3, the electronic band dispersion is comprehensively investigated for magnetic ground state of (a) Cr2C, (b) CrScC (c) CrTiC and (d) CrVC. Figure 3 (a) show that pristine Cr_2C MXene exhibits half-metallic behavior with a gap of 2.24 eV and it is consistent with previous study [8].

ISBN:978-605-83516-6-0

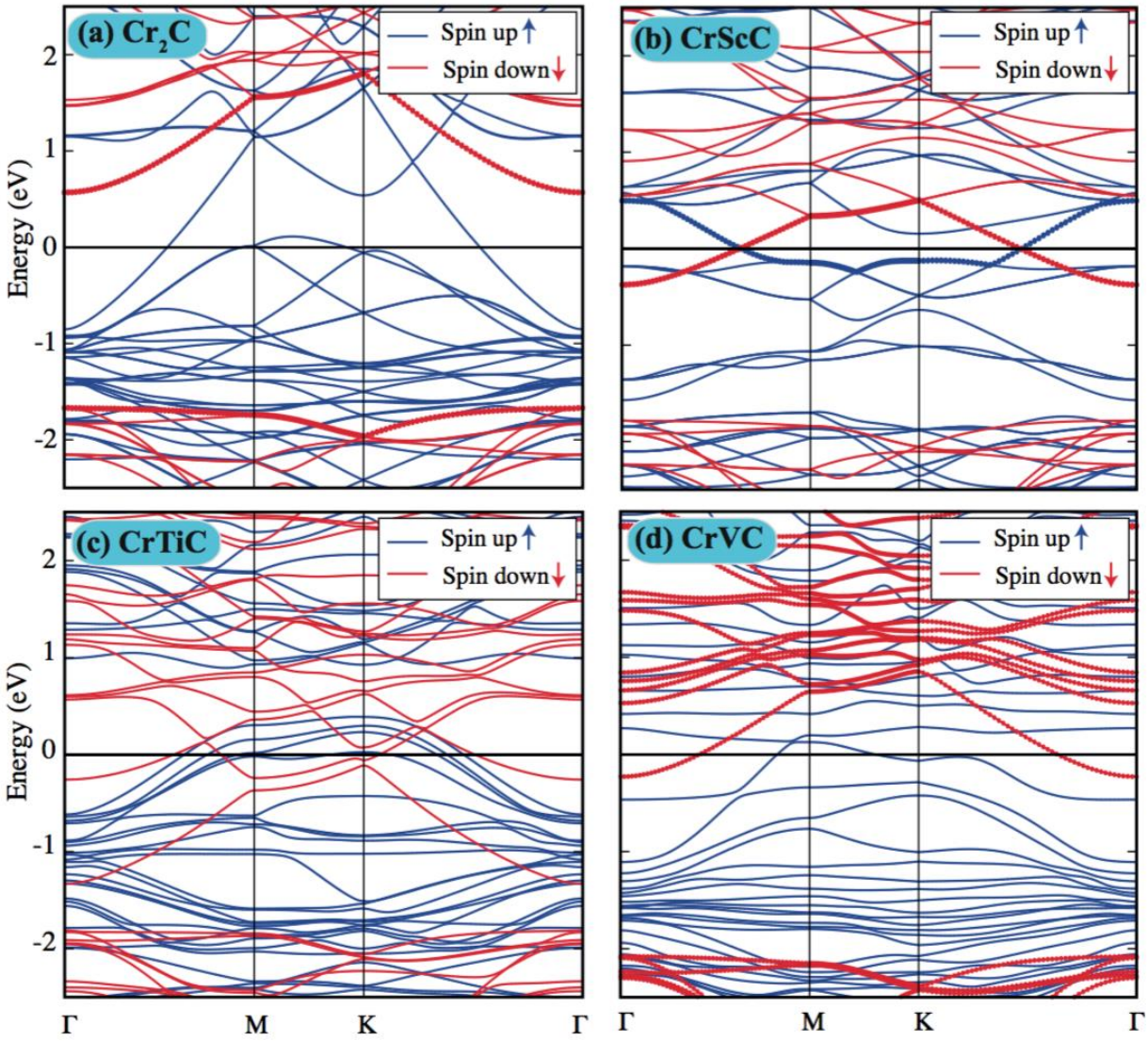


FIGURE 3. The electronic band structure of (a) Cr_2C, (b) CrScC, (c) CrTiC (d) CrVC Janus monolayers of MXene calculated at the level of PBE+U. Spin up and spin down bands are shown with blue and red lines, respectively. Fermi level is set to zero and shown with black line.

CONCLUSION

In this study, we have systematically investigated the structural, electronic and magnetic properties of Janus structure of pristine MXene by means of first-principles calculations based on GGA+U method. The results show that CrScC, CrTiC, and CrVC janus monolayers of MXene are found ferromagnetic ground state. We show that CrC, CrScC, CrTiC and CrVC MXenes exhibits half-metallic, semi-metal, metal and Dirac half-metallic behavior. Our results demonstrated that Cr-based janus monolayers of MXene is very promising material for nanoscale electronic and spintronic applications.

ISBN:978-605-83516-6-0

ACKNOWLEDGMENTS

Computational resources were provided by TUBITAK ULAKBIM, High Performance and Grid Computing Center (TR-Grid e-Infrastructure). The author acknowledges the support from KLU-BAP under 189 project number.

REFERENCES

1. S. Wolf, D. Awschalom, R. Buhrman, J. Daughton, S. Von Molnar,M. Roukes, A. Y. Chtchelkanova and D. Treger, Science **294**, 1488–1495 (2001).
2. W. Han, R. K. Kawakami, M. Gmitra and J. Fabian, Nature nanotechnology **9**, 794 (2014).
3. L. Dong, H. Kumar, B. Anasori, Y. Gogotsi and V. B. Shenoy, The journal of physical chemistry letters **8**, 422–428 (2017).
4. K. S. Novoselov, A. K. Geim, S. V. Morozov, D. Jiang, Y. Zhang, S. V.Dubonos, I. V. Grigorieva and A. A. Firsov, Science **306**, 666–669 (2004).
5. K. Geim and K. S. Novoselov, World Scientific, 11–19 (2010).
6. W. Han, APL Materials **4**, 032401 (2016).
7. P. Urbankowski, B. Anasori, T. Makaryan, D. Er, S. Kota, P. L. Walsh,M. Zhao, V. B. Shenoy, M. W. Barsoum and Y. Gogotsi, Nanoscale **8**, 11385–11391(2016).
8. Si, J. Zhou and Z. Sun, ACS Applied Materials & Interfaces, **7**, 17510-17515 (2015).
9. He, G. Ding, C. Zhong, S. Li, D. Li, and G. Zhang, Nanoscale, **11**, 356-364 (2019).
10. G. Gao, G. Ding, J. Li, K. Yao, M. Wu, and M. Qian, Nanoscale, **8**, 8986-8994 (2016).
11. S. Wang, Y.L. Du, and W.H. Liao, Chinese Physics B, **26**, 017806 (2017).
12. G. Kresse, J. Hafner, Physical Review B **47**, 558 (1993).
13. G. Kresse, J. Furthmuller, Physical Review B **54**, 11169 (1996).
14. J. P. Perdew, K. Burke, M. Ernzerhof, Physical Review Letters **77**, 3865 (1996).
15. S. Grimme, Journal of Computational Chemistry, **27**, 1787–1799 (2006).

BOOK OF FULL TEXT PROCEEDINGS TURKISH PHYSICAL
SOCIETY 35th INTERNATIONAL PHYSICS CONGRESS (TPS35)
TPS35, Vol.01, No.04, pp.266-273.
ISBN:978-605-83516-6-0

15 December 2019

Smectic Phase Transition of Ferroelectric Liquid Crystals under Influence Electric Field

Sedat Avcı[1,a], Mustafa Kurt[1]

[1]Department of Physics, Çanakkale18 Mart University, 17100 Çanakkale, Turkey

[a)]Corresponding author: sdtvc@hotmail.com

Abstract. Smectic phase transitions (Sm A-Sm C) of C7 and the binary mixture of C7+10.O.4 have been indicated as a function of an applied electric field depending on temperature. By modifying of Landau free energy equation, we determined the phase transitions conditions of these liquid crystals with respect to electric field strength and temperature. Also, we calculate the entropy changes of these ferroelectric liquid crystals by using Clausius-Clapeyron equation. Constants of the modified Landau free energy equation were determined by iterating of the experimental data. The results show that our modified model is so satisfactory for modeling of smectic phase transitions of the ferroelectric liquid crystals.

INTRODUCTION

In nature, substances are generally present in solid, liquid and gaseous form. Some of substances cannot directly switch from solid to liquid when heat treated. A gradual transition takes place through one or more intermediate phases. Molecules in solids can stop by making lattice vibrations but cannot make rotational motion. In liquids, molecules can do both translational and rotational motion. As a result of the melting of solids, regular molecular structure is disrupted. Thus, molecules of the material can rotate by becoming liquid. At the intermediate phase values in the transition from solid to liquid, molecules are similar to solids with their orientation and arrangement, and to liquids because of their fluidity. This condition, in which both states are observed, is called liquid crystal. Liquid crystals firstly founded in 1888 by the Austrian botanist Friedrich Reinitzer. Immediately after this invention, German physicist Lehman's work on the turbid liquid seen during the transition from solid to liquid has shown that some liquid molecules have a molecular-like molecular structure. Although Lehman looks like a liquid at first glance, he called them “liquid crystal” because of its crystal-like structure. Due to their anisotropic properties, liquid crystal materials have found many applications, especially liquid crystal display (LCD) and LED display. Smectic A- Chiral Smectic C phase transition behaviors were first proposed by Gennes in cartesian coordinates. In Landau's theory of mean fields, the free energy expression slope angle for these behaviors θ and self-polarization are obtained as the expansion of P order parameter terms. Landau's proposal was accepted as the most basic model in the literature. However, this model did not meet the requirements over time. Thus, it is seen in the literature that phase transition behaviors are determined more clearly by adding some terms to Landau's most basic model.

In 1850, Rudolf Virchow showed that nerve fibers became fluid in water. The liquid crystal was first observed in this way but its structure was not understood. This was not called a new phase transition at that time. In 1888, the Australian botanist Friedrich Reinitzer stated that cholesteryl benzoate had two boiling points. In 1916, Max Born proposed a dipolar theory for such substances. However, it was stated that this proposition failed. In 1922, the French crystallography expert Georges Friedel proposed that the liquid crystal molecules be classified as oriented. Thus, the definition of the liquid crystal phase is obtained. In 1935, Vsevolod Freedericksz observed that liquid crystals can be directed under electric field. As a result of these studies, interest in liquid crystals increased, but the start of the Second World War caused most of the research on liquid crystals to stop. After the Second World War, in 1948, George Gray

ISBN:978-605-83516-6-0

synthesized liquid crystal materials. With all these studies, it has been stated that interest in liquid crystals has increased again [1].

Sm A- Sm C (or Sm C *) phase transitions show first order or second order phase transition. As a result of experimental studies until 1986, Sm A- Sm C (or Sm C *) phase transitions were reported as second order phase transitions. HOBACPC, 2M45OBC, 70.6, AMC-11, MBRA8 crystals are some crystals showing second order phase transition. Theoretically, Sm A- Sm C second order phase transitions were first defined by Gennes in cartesian coordinates. This model is based on the helium-like critical behavior of phase transition. Later theoretical studies have shown that Sm A- Sm C (or Sm C *) phase transitions exhibit average field-like behavior. After 1986, new ferroelectric liquid crystals with first order Sm A- Sm C * phase transition were discovered. These liquid crystals showed high self-polarization. A7, C7, A7 + C7 mixture, R-1M7 (14) OPPBC are some liquid crystals showing first order Sm A- Sm C * phase transition [2].

Bahr and Heppke (1990) experimentally studied the Sm A- Sm C * transitions of 10.O.4 crystals with varying molar concentrations in C7. 10.O.4 crystal is said to show second order Sm A-Sm C phase transition. The slope angle and self-polarization values under the influence of electric field were measured for both first order and second order phase transitions near the triple point [3].

Salihoglu et al. (1998a) by using the average area model with the terms of the first order Sm A- Sm C * phase transitions in the behavior of C7 were investigated. The expression of free energy is expressed using the mean fields model $P^2\Theta^2$, which expresses the overlap between the inclination angle and polarization. Using this form of free energy, the angle of inclination and polarization values were calculated depending on the temperature. Obtained slope angle and polarization values were compared with the experimental values given in the literature. It was seen that the calculated polarization values and the experimental data were very well adapted to the temperatures far from the critical transition temperature which is the experimental transition temperature and deviation occurred when the critical temperature approached [4].

In previous studies to describe the nature of the transition from Sm A phase to Sm C * phase in liquid crystals, in the absence of the electric field effect, Landau was solved using the mean fields model [5-10]. In this study, the slope angle and slope angle sensitivity of the C7 liquid crystals were investigated under the influence of electric field and temperature, and the phase transition was investigated using Landau Model with bilinear coupling of slope angle. Then, the dielectric constant of the liquid crystal mixture formed with C7 and 10.O.4 was investigated depending on the electric field strength and temperature. C7 and C7 + 10.O.4 mixtures were shown to provide Clausis-Clapyron equilibrium and E-T phase transition diagrams were obtained.

CALCULATIONS AND RESULTS

In order to investigate the phase transition of Sm A - Sm C * in liquid crystals, the Landau Mean Field Model developed by adding the electric field effect to the serial angle formed using the terms of Gibbs Free Energy inclination angle and polarization P is used.

$$g = \frac{1}{2}a(T - T_0)\theta^2 + \frac{1}{4}b\theta^4 + \frac{1}{6}c\theta^6 + \frac{1}{2\chi_0\varepsilon_0}P^2 - CP\theta \quad (1)$$

When derivative is taken according to Θ and equal to zero;

$$\frac{dg}{d\theta} = a(T - T_0)\theta + b\theta^3 + c\theta^5 - CP = 0 \quad (2)$$

$$P = \frac{\theta}{C}\{a(T - T_0) + b\theta^2 + c\theta^4\} \quad (3)$$

When derivative is taken according to P and equal to zero;

$$\frac{dg}{dP} = \frac{1}{\chi_0\varepsilon_0}P - C\theta = 0 \quad (4)$$

ISBN:978-605-83516-6-0

$$P = C\chi_0\varepsilon_0\theta \tag{5}$$

The equation (1) can be rewritten using equation (5),

$$g = \frac{1}{2}\{a(T-T_0) - C^2\chi_0\varepsilon_0\}\theta^2 + \frac{1}{4}b\theta^4 + \frac{1}{6}c\theta^6 \tag{6}$$

Using equation (6), equation (7) is obtained,

$$T = T_0 + \frac{3b^2}{16ac} + \frac{C^2\chi_0\varepsilon_0}{a} \tag{7}$$

T=T_{SmA} for Sm A phase. Within the framework of the Landau model, the first order transition temperature of the chiral ferroelectric compounds is given by,

$$T_{SmA} = T_0 + \frac{3b^2}{16ac} + \frac{C^2\chi_0\varepsilon_0}{a} \tag{8}$$

C=0 T=T_{SmC} for Sm C. In the racemic non-ferroelectric versions of the compounds the coupling constant **C** is zero,

$$T_{SmA} = T_0 + \frac{3b^2}{16ac} \tag{9}$$

Phase transition temperature,

$$T_{SmC} - T_{SmA} = \frac{C^2\chi_0\varepsilon_0}{a} \tag{10}$$

Then, ΔP is obtained,

$$\Delta P = C\chi_0\varepsilon_0\left(-\frac{3b}{4c}\right)^{1/2} \tag{11}$$

Gibbs free energy,

$$dG = -SdT + VdP \tag{12}$$

S: entropy, V volume, T temperature, P pressure,

$$\left(\frac{dG}{dT}\right)_P = -S \qquad \left(\frac{dG}{dP}\right)_T = V \tag{13}$$

ΔS is obtained,

$$\Delta S = -\frac{dg}{dT} = \frac{3ab}{8c} \tag{14}$$

the electric field-induced temperature shift **ΔT/E** which we observe for the chiral compounds can be described by a Clausius-Clapeyron type of equation,

$$\frac{\Delta T}{E} = \frac{\Delta P}{\Delta S} \tag{15}$$

Finally obtained,

$$\frac{\Delta T}{E} = \left\{2\chi_0\varepsilon_0\frac{(T_{SmC}-T_{SmA})}{\Delta S}\right\}^{1/2} \tag{16}$$

Landau Free Energy Density,

$$g = g_0 + \frac{1}{2}a(T-T_0)\theta^2 + \frac{1}{4}b\theta^4 + \frac{1}{6}c\theta^6 + \frac{1}{2\chi_0\varepsilon_0}P^2 - CP\theta - EP \tag{17}$$

T_0 is the temperature of the stability limit of the high-temperature phase for the system with $C=0$ and $E=0$. $c>0$ and $b<0$ describes first order transition and linear coupling between polarization and tilt angle.

ISBN:978-605-83516-6-0

$$E = \frac{1}{C\chi_0\varepsilon_0}\{[a(T-T_0) - C^2\chi_0\varepsilon_0]\theta + b\theta^3 + c\theta^5\} \quad \rightarrow \begin{matrix} b<0 & first\ order\ transition \\ b>0 & second\ order\ transition \end{matrix} \tag{18}$$

DISCUSSION

In this study, the data obtained from Bahr and Heppke experiments were used. Bahr and Heppke used two different liquid crystals in their studies. These crystals are C7 and 10.O.4 liquid crystals with ferroelectric properties. The experimental apparatus they have used is shown in Figure 1 [11].

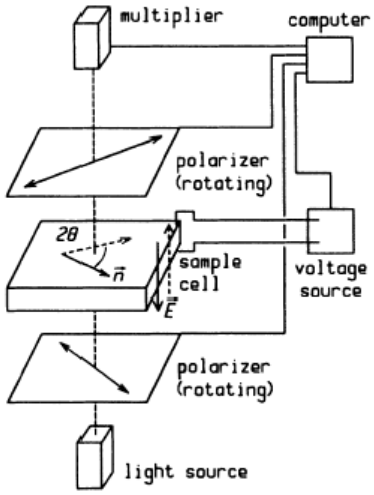


Figure 1. Experimental setup for the tilt angle measurements [11].

Using Bahr and Heppke experimental devices, they measured the electrical properties of C7 and C7 + 10.O.4 crystal mixtures using LCR meters. The variation of C7 crystal in dielectric coefficient with respect to temperature under different bias voltage is shown in Figure 2. In the S_A phase, ε shows an increase with decreasing temperature corresponding to the usual electroclinic soft mode behavior of the S_C, phase of chiral molecules [12]. In Figure 2, the peaks of the curves correspond to the phase transition temperatures, from which the peak of each curve is determined and the phase transition curve is generated according to the applied electric field. The electrical field versus phase transition temperatures of the C7 crystal are shown in Figure 3. The slope of this curve corresponds to the **ΔT / E** value in the Clausius-Clapeyron equation. As a result of the linear fit to the data in Figure 3, the slope of the curve was found to be 0.01628. The result of the calculation with equation 16 is close to this value.

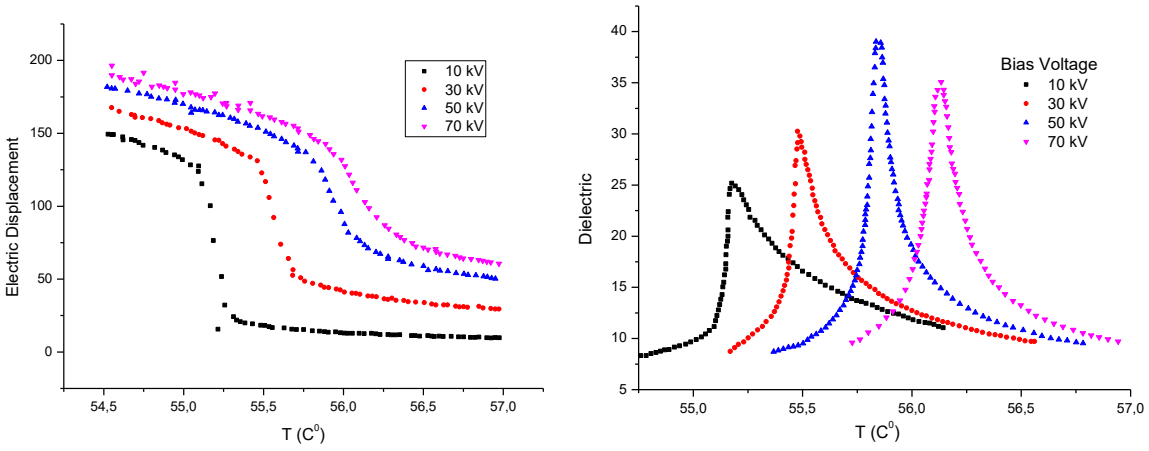


Figure 2. Temperature dependence of the static dielectric constant of C7 at various bias field strengths.

ISBN:978-605-83516-6-0

Table 1. Phase transition temperatures under the electric field for C7 crystal.

E (kV)	Tc
10	55.173
30	55.476
50	55.864
70	56.129

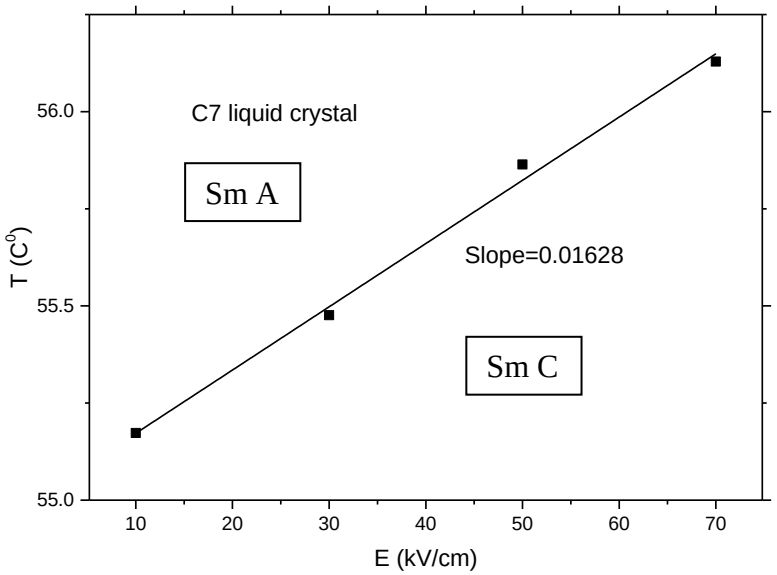


Figure 3. Electric field strength dependence of the S_A-S_C transition temperature of compound C7.

The variation of the dielectric coefficient of the C7 + 10.O.4 crystal mixture according to temperature under different bias voltage is shown in Figure 4. In Figure 4, the peaks of the curves correspond to the phase transition temperatures, from which the peak of each curve is determined and the phase transition curve is generated according to the applied electric field. The electric field versus phase transition temperatures of the C7 + 10.O.4 crystal mixture are shown in Figure 5. The slope of this curve corresponds to the **ΔT / E** value in the Clausius-Clapeyron equation. The linear fit to the data in Figure 5 shows that the slope of the curve is 0.0275. The result of the calculation with equation 16 is close to this value. To calculate the Clausius-Clapeyron equation for the phase transition of Sm A – Sm C of the base mixture of C7 + 10.O.4, the data of the fits constructed in equation 10 are presented in Table 2 for the below critical temperature and in Table 3 for the above critical temperature.

ISBN:978-605-83516-6-0

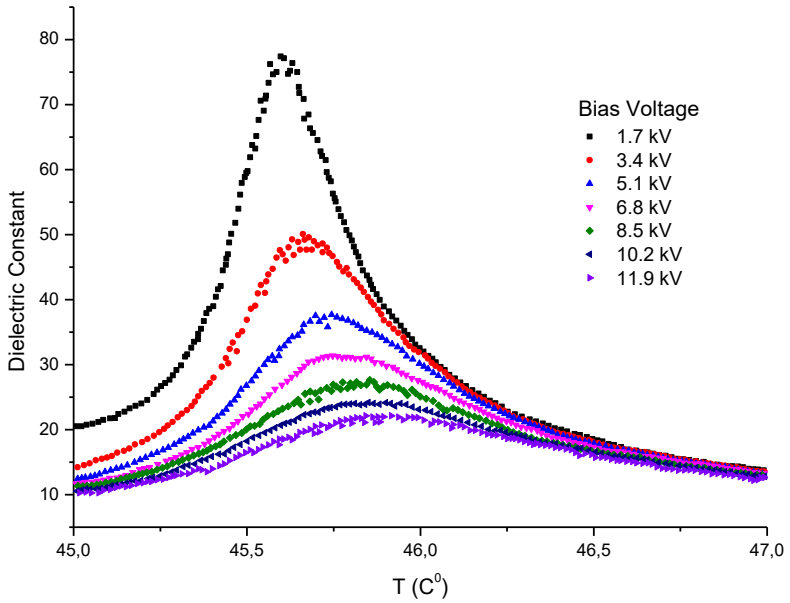


Figure 4. Temperature dependence of the static dielectric constant of C7+10.O.4 binary mixture at various bias field strengths.

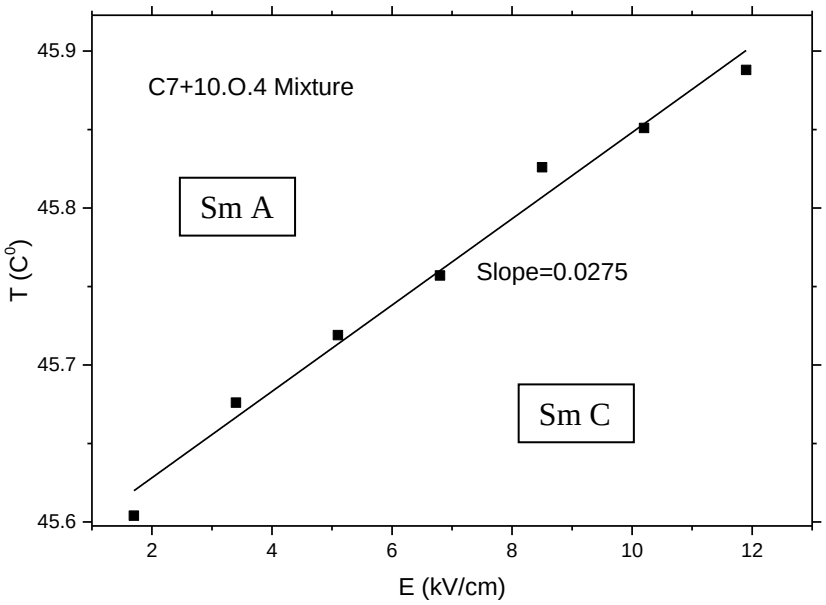


Figure 5. Electric field strength dependence of the S_A-S_C transition temperature of compound C7+10.O.4.

ISBN:978-605-83516-6-0

Table 2. Equation 10 coefficients for the subcritical temperature

Below Tc				
E (kV)	Tc	a	C	Temp interval
1,7	45,604	0,695	0,907	45,0125-45,50
3,4	45,676	0,699	0,739	45,00-45,610
5,1	45,719	0,638	0,860	45,006-45,563
	45,719	0,173	11,246	45,576-45,726
6,8	45,757	0,662	0,709	45,006-45,557
8,5	45,826	0,696	0,628	45,006-45,710
10,2	45,851	0,653	0,724	45,006-45,644
11,9	45,888	0,594	0,894	45,006-45,701

Table 3. Equation 10 coefficients for above critical temperature

Above Tc				
E (kV)	Tc	a	C	Temp interval
1,7	45,604	0,637	1,479	45,676-46,987
3,4	45,676	0,586	1,644	45,751-46,993
5,1	45,719	0,521	2,017	45,807-47,000
6,8	45,757	0,495	2,122	45,901-46,618
8,5	45,826	0,405	2,841	45,973-46,774
10,2	45,851	0,320	4,031	45,898-46,658
11,9	45,888	0,389	2,818	46,107-47,000

CONCLUSION

Sm A –Sm C ferroelectric phase transitions of C7 liquid crystal and C7 + 10.O.4 liquid crystal mixture were studied under the external electric field. The experimental data made by Bahr and Heppke were examined using the Landau Mean Field Model. The dielectric coefficient changes due to the temperature under different external electric field and the phase transition states depending on the electric field and temperature were determined. Clausius-Clapeyron equality. C7 liquid crystal and C7 + 10.O.4 liquid crystal mixture connected to the external electric field phase transition temperature graphs were created. The results showed a linear relationship between the external electric field and the phase transition temperature.

ISBN:978-605-83516-6-0

REFERENCES

1. Palffy-Muhoray P., 2007. Orientationally Ordered Soft Matter: The Diverse World of Liquid Crystals, Electronic-Liquid Crystal Communications August 26.
2. De Gennes P.G., 1973. Some Remarks on The Polymorphism of Smectics, Molecular Crystals and Liquid Crystals, 21:49-76.
3. Bahr C., Heppke G., 1990. Behaviour of Susceptibility and Polarization Near a Smectic A – Ferroelectric Smectic C Tricritical Point, Physical Review A, 44: 3669-3672.
4. Salihoglu S., Yurtseven H., Giz A., Kayisoglu D., Konu A., 1988a. The Mean Field Model with P2Θ2 Coupling fort the Smectic A – Smectic C* Phase Transition in Liquid Crystals, Phase Transitions, 66: 259-270.
5. K. Denolf, B. Van Roie, G. Pitsi and J. Thoen, Mol. Cryst. Liq. Cryst., 449(2006)47.
6. D.P. Ojha, H. Yurtseven, A.K. Prajapati and M.I.N.M. Mohan, Liquid Crystal Research: Current Trends and Future Perspectives, Adv. In Condensed Matter Phys., 2013. (Hindawi Publishing Corporation).
7. C.C. Huang and S.C. Lien, Phys. Rev.,A31(1985)2621.
8. K. Denolf, B. Van Roie, G. Pitsi and J. Thoen, Mol. Cryst. Liq. Cryst., 449(2006)47.
9. Ch. Bahr and G. Heppke, Mol. Cryst. Liq. Cryst., 150b(1987)313.
10. B.R. Ratna, R. Shashidhar, G.G. Nair, S.K. Prasad, Ch. Bahr and G. Heppke, Phys. Rev. A, 37(1988)1824.
11. Bahr Ch. And Heppke G., *Infiuence of electric field on a first-order smectic-A ferroelectric-smectic-C liquid-crystal phase transition: A field-induced critical point*, Physical Review A, Vol.41, Number 8, 4335-4342, 1990.
12. Garoff S., and Meyer R. B., Phys. Rev. Lett., 38, 848, 1977.

BOOK OF FULL TEXT PROCEEDINGS TURKISH PHYSICAL
SOCIETY 35th INTERNATIONAL PHYSICS CONGRESS (TPS35)
TPS35, Vol.01, No.04, pp.274-279.
ISBN:978-605-83516-6-0

15 December 2019

The Optical and Morphological Properties of Gd doped CuO Film Using Spin Coating Method

Ilhan CANDAN [1, a)] and Silan BATURAY[1]

[1]*Dicle University, Faculty of Science, Dept. of Physics, Diyarbakır, Turkey*
[a)]Corresponding author: ilhan.candan@dicle.edu.tr

Abstract. In recent years, Metal oxide nanostructures such as CuO, FeO and ZnO have attracted much attention due to their important properties in different fields including optics, optoelectronics. Nanostructured CuO have been comprehensively investigated due to their potential applications in chemical, photochemical and electrochemical fields, particularly in windows for solar energy conversion and electrochromic applications. The purpose of the present work is to grow and characterize 0, 2, 4 and 6% Gd doped CuO film. Nanostructured CuO films were prepared by spin coating method, copper acetate as a starting material, a gadolinium (III) chloride as dopant source and soda lime glass as substrate. The structural and optical properties of the films were characterized by X-Ray Diffraction (XRD) and Uv-vis spectrophotometer, respectively. The structural properties of the films were investigated by XRD Rigaku Ultimata III. Ultraviolet–visible spectroscopy measurements of the Gd doped film indicated that transmittance value and energy band gap of thin films changed for 0, 2, 4 and 6 % Gd incorporation.

Key Words: Thin film; Transmittance; Energy band gap; XRD, Gd, CuO

INTRODUCTION

Transition metal oxides films are a family of nanomaterials, and they are very important component for the improvement of different advanced functional materials. These studies have been attracted extensive interest owing to their physical properties, chemical properties, its favorable capacitive properties, environmental friendliness and potential applications in various scientific research fields and different scientific applications[1-10]. These properties of the films are vigorously bound to the particle size and shape which controls surface morphologies of the nanomaterials. In addition, the physical and chemical properties of nanomaterials can be improved when several elements used as doping elements. Interesting phenomena such as noticeable enhancement in large surface-to-volume ratio which supplies further surface field for physical and chemical interactions, important alteration in surface energy that afford tuning, and quantum confinement influences occur when transition metal oxides are decreased to the dimensions of nanoscale[11-13]. These phenomena can exchange differently with unique properties such as physical and chemical ones that are not applicable for functional materials with their bulk dimensionality. Thus, the manipulation of well-controlled deposition of nanoscale transition metal oxide films with different particle size, shape, electrical properties and structures is very important in the improvement in nanotechnology. Consequently, in comparison to their nano counterparts, nanostructured transition metal oxides films show unique structural properties and particle size confinement impact as well as novel physical characterization.

Among the studies of different transition metal oxides materials in the nanoscale area for both theoretical exercises and practical implementation in nanodevices, Cupric oxide (CuO) has been a very important hot topic owing to its interesting properties including non-toxicity, excellent performance as a catalyst, the sufficient present of copper, effect of potential particle size and a solar cell performance of 18 % [14]. CuO is an important monoclinic p–type semiconductor with band gap between 1.2 - 1.9 eV [15-17] and has promising applications in many areas including solar cell techonology [18], chemical sensor [19], gas sensor [20], application in lithium ion batteries [21, 22], catalytic [23], glucose sensing [24], photocatalytic [25], diodes [26] and sufide sensing [27]. CuO performance in such applications can be improved when the particle size effects are well controlled to vary within the nanoscale field. Although there have been several studies on doping of nanostructured metal oxide films, it is still continued to be a challenge to gain high quality crystalline films with unique physical and

ISBN:978-605-83516-6-0

chemical properties of doped CuO nanocrystalline thin films. Many different methods have been employed for the fabrication of nanocrystalline CuO thin films, such as sol–gel dip coating method [28], SILAR method [29], hydrothermal method [30], domestic hydrothermal microwave [31], pulsed laser deposition [32] and spin coating method [33]. Among these methods or techniques, spin coating method is a very effective method in transition metal oxides films because it has the advantages like adjustable high deposition rate, fabrication at high oxygen pressure, oriented crystalline growth of the films and easily controlled substrate temperature. In the present work, we have a different approach to deposit Gd doped CuO thin films on sodalime glass substrates with various doping concentrations of Gd using the spin coating method for the first time. The structural and optical properties of undoped and Gd doped CuO films have been studied by X-ray diffraction (XRD) and UV–vis spectrophotometry.

EXPERIMENTAL DETAILS

Pure and Gd doped CuO films were deposited on soda lime glass substrates by spin coating technique at 450 ºC. For the weight quantities of pure copper (II) acetate (Cu $(CH_3COO)_2 \cdot H_2O$), copper precursor solution was first dissolved in the solution of ethanol to gain 0.1 M concentration. Gd (gadolinium (III) chloride) was also dissolve in the solution of ethanol to obtain 0.01 M concentration to prepare Gd doped CuO thin film. All solution was stirred in magnetic stirrer for 12h. After this process, two solutions have been used to obtain pure and Gd doped CuO nanostructure with 0, 2, 4, and 6 at wt% of Gd and this mixed solutions were stirred at room temperature for 3 hours to gain clear and homogenous blue solution. Before deposition process, soda lime glass substrates firstly washed with detergent. Then, these substrates boiled in the mixture of 5:1:1 H_2O, NH_3 and H_2O_2 for 15 min at 90 ºC and in the mixture of 5:1:1 H_2O, H_2O_2 and HCL for 15 min at 90 ˚C, respectively. Substrates cleaning process has been explaıned elsewhere [34]. The crystalline properties of the obtained pure and Gd doped CuO thin films were characterized by X ray Diffractometer (XRD) with the range of θ-2θ for structural and phase purity analysis. The conclusion of the absorbance, transmittance and energy band gap value of the pure and Gd doped CuO films were analyzed using UV-Vis spectrophotometer in the 300-1100 nm wavelength.

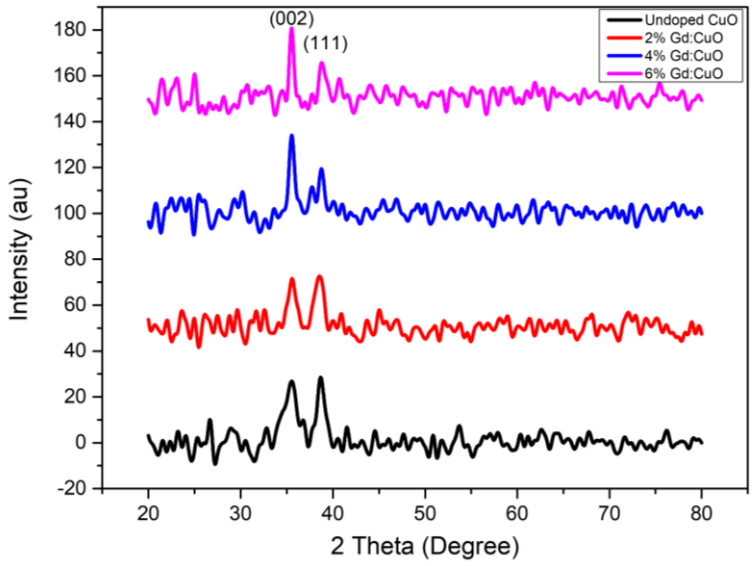


FIGURE 1: XRD spectrum of undoped and Gd doped CuO thin films.

ISBN:978-605-83516-6-0

RESULTS and DISCUSSION

Structural Analysis

For structural and phase purity analysis of pure and Gd doped CuO thin films were prepared on soda lime glass substrate via spin coating method, the XRD spectrum of all the films was investigated by a X-ray diffractometer (XRD: Cu Kα radiation, λ = 1.540056 Å) and the results are shown in Fig 1. It is seen in the Fig 1. that the films exhibit polycrystalline nature, giving the formation of monoclinic structure. The peak positions of the XRD pattern were located at 2θ = 35.5 and 38.7 corresponding to (002), and (111) planes, respectively. Furthermore, we can see from the XRD data that there are no clear change in the peaks position and additional peaks, which may be attributed to the peaks of Gd atoms were weak and vanished in the noise signal region. Additionally, it is said that the substitution of Cu atoms by Gd atoms has not altered the structure of the parent CuO films. It is seen that the intensities of the (002) diffraction peak is much stronger than (111) peak which shows that all the films have preferred crystal planes of nanostructures. It was seen in our previous study that XRD spectra of Ni doped CuO film had a polycrystalline nature, with preferential plane of (002) and (111) [35]. Increasing the Gd doping caused a radical change in the intensity of (002) and (111) peaks. The intensity of (111) observed to slowly decrease while (002) peak radically increase with Gd doping. It is important to note here that the intensities of (002) peak increased as Gd was doped in CuO and increasing Gd doping in CuO thin films caused the crystalline quality to improve. An exchange of Cu and Gd ions change the crystal structure owing to the fact that the atomic radius of the Gd ion is different from that of the Cu+2 ion. For the 2, 4 and 6 % Gd doped CuO thin film, the intensity of (111) peak is increased compared with that of undoped CuO thin film. This implies that the crystalline quality of Gd doped CuO films are improved by 2, 4, and 6 % Gd doping in CuO films.

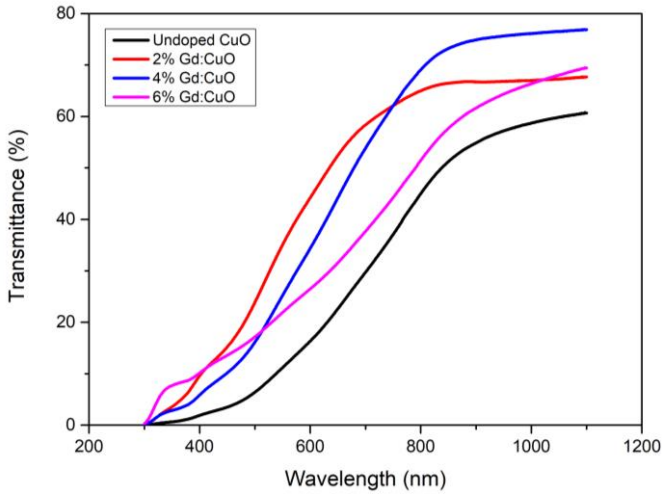


FIGURE 2: Transmission values of undoped and Gd doped CuO thin films.

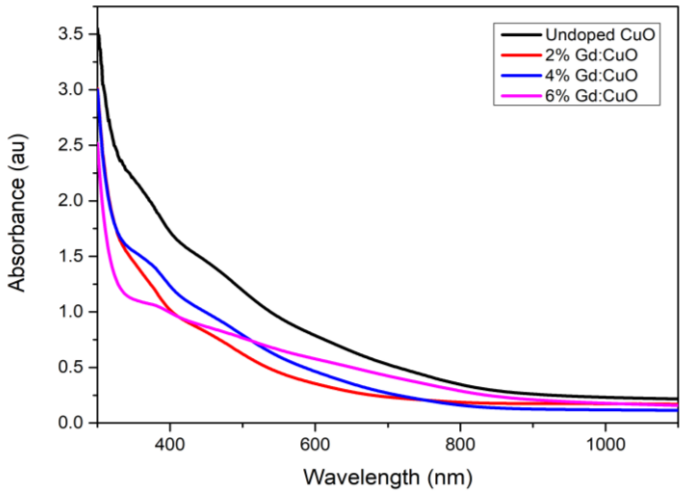


FIGURE 3: Absorption values of undoped and Gd doped CuO thin films.

ISBN:978-605-83516-6-0

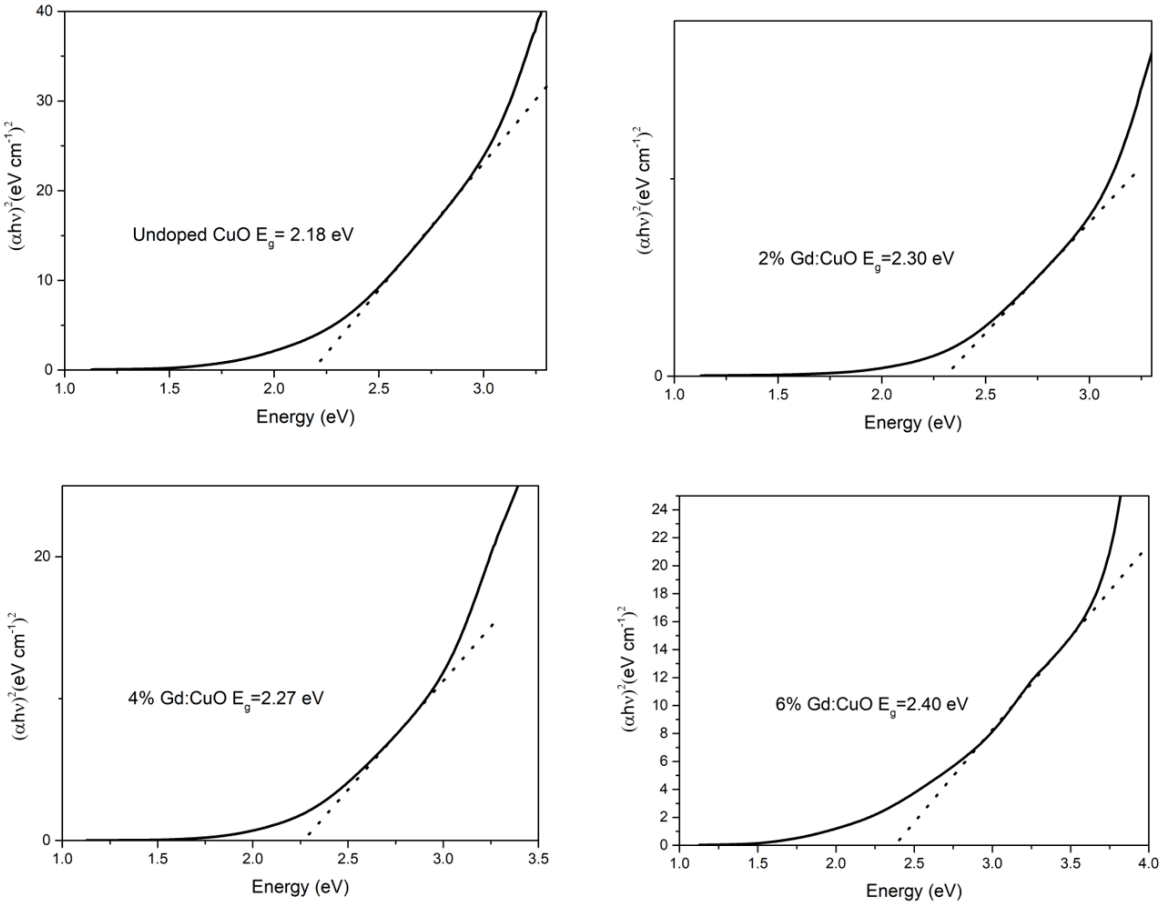


FIGURE 4: Energy band gap values of undoped and Gd doped CuO thin films.

Optical Studies

The optical properties of undoped and Gd doped CuO films prepared onto soda lime glass substrate are analyzed to observe the effect of doping on the band gap energy Eg(λ), the transmittance T(λ) and reflectance R(λ) by using UV–visible spectroscopy in the wavelength range from 300 to1100 nm at room temperature. There was not seen any other peak in the UV-vis area because all the thin films were in a good quality, clear and homogenous. Fig. 2 indicates that the transmission spectra of undoped and Gd doped CuO thin film for various concentrations. Undoped CuO nanostructure film has minimum transmit value compared to the other films for all wavelength region. As seen from Fig.2 that the transmission value of Gd doping in the solution increases with increasing incorporation concentrations and the highest transmittance value for films was obtained above 75 % at 4 % doping as compared to others. The optical absorption value of undoped and Gd doped CuO nanostrucrure films was investigated and indicated in the Fig. 3. It gives that Gd doped CuO thin films have very low absorbance in the visible region of the spectra. The highest absorbance for wavelengths below 350 nm. The energy band gap of pure and Gd doped CuO nanostrucrure films in the wavelength range of 300–1100 nm was investigated and illustrated in the inset of Fig. 4. For such materials, optical absorption theory shows the absorption coefficient (α) and incident photon energy (hν) behaves as follows:

$$\alpha h\nu = K(h\nu - Eg)^n \quad (1)$$

where K is an energy-independent constant depending on the material, hv is the energy of photon and E_g is the optical band gap energy. A graph of $(\alpha h\nu)^2$ vs. photon energy (hv) for the Gd doped CuO films as shown in Fig. 4 demonstrates the dependence of concentration on the band gap energies (E_g). The calculated energy band gaps of the films found from this graph were 2.18, 2.30, 2.27 and 2.40 eV for 0, 2, 4 and 6 % Gd doped CuO films, respectively. Gd doping in solution has changed the energy band gap, which indicates that Gd could be

ISBN:978-605-83516-6-0

used to regulate the optical band gap of CuO films. Joseph and Venkateswaran reported that The values of E_g for the CuO thin films on doping with Fe increased [36].

CONCLUSIONS

In summary, we have studied the optical and structural properties of undoped and Gd doped CuO nanostructure thin films via spin coating technique. The X-ray diffraction (XRD) pattern study show that undoped and Gd doped CuO thin films have polycrystalline nature with the formation of monoclinic structure. The transmission value of Gd doping in the solution increases with increasing incorporation concentrations Absorption value of undoped and Gd doped CuO indicated that all thin films have very low absorbance in the visible region of the spectra. A slightly increase in optical band gap is observed from 2.18 to 2.40 eV with an increase of Gd concentration in solution from 0 to 6%.

REFERENCES

1. M. J. S. Spencer, Progress in Materials Science **57** (3), 437-486 (2012).
2. S. Barth, F. Hernandez-Ramirez, J. D. Holmes and A. Romano-Rodriguez, Progress in Materials Science **55** (6), 563-627 (2010).
3. E. Comini, C. Baratto, G. Faglia, M. Ferroni, A. Vomiero and G. Sberveglieri, Progress in Materials Science **54** (1), 1-67 (2009).
4. H. Zhang, Z. Wu, D. Yan, X. Xu and Y. Jiang, Thin Solid Films **552** (0), 218-224 (2014).
5. X.-Y. Yu, Z.-G. Liu and X.-J. Huang, Trends in Environmental Analytical Chemistry **3–4** (0), 28-35 (2014).
6. E. Polydorou, E. Makarona, A. Soultati, D. G. Georgiadou, T. Kyrasta, T. Speliotis, C. Tsamis, N. Papanikolaou, P. Argitis, I. Kostis, A. Kokkosis, D. Davazoglou and M. Vasilopoulou, Microelectronic Engineering **119** (0), 100-104 (2014).
7. V. M. Nair, R. Jose, K. Raju and P. R. S. Wariar, Journal of Alloys and Compounds **552** (0), 180-185 (2013).
8. D. W. Liu, G. Z. Cao and Y. Wang, in *Encyclopedia of Electrochemical Power Sources*, edited by J. Garche (Elsevier, Amsterdam, 2009), pp. 337-355.
9. W. Gao and Z. Li, in *Physical Properties and Applications of Polymer Nanocomposites*, edited by S. C. Tjong and Y. W. Mai (Woodhead Publishing, 2010), pp. 723-742.
10. Q. Zhang, K. Zhang, D. Xu, G. Yang, H. Huang, F. Nie, C. Liu and S. Yang, Progress in Materials Science **60** (0), 208-337 (2014).
11. J. Park, J. Joo, S. G. Kwon, Y. Jang and T. Hyeon, Angewandte Chemie International Edition **46** (25), 4630-4660 (2007).
12. H. Zheng, J. Z. Ou, M. S. Strano, R. B. Kaner, A. Mitchell and K. Kalantar-zadeh, Advanced Functional Materials **21** (12), 2175-2196 (2011).
13. X. Chen and S. S. Mao, Chemical Reviews **107** (7), 2891-2959 (2007).
14. S. S. Jeong, A. Mittiga, E. Salza, A. Masci and S. Passerini, Electrochimica Acta **53** (5), 2226-2231 (2008).
15. I. Singh and R. K. Bedi, Applied Surface Science **257** (17), 7592-7599 (2011).
16. R. Sahay, J. Sundaramurthy, P. Suresh Kumar, V. Thavasi, S. G. Mhaisalkar and S. Ramakrishna, Journal of Solid State Chemistry **186** (0), 261-267 (2012).
17. L. Zheng and X. Liu, Materials Letters **61** (11–12), 2222-2226 (2007).
18. H. Kidowaki, T. Oku and T. Akiyama, presented at the Journal of Physics: Conference Series, 2012 (unpublished).
19. R. Vasiliev, M. Rumyantseva, N. Yakovlev and A. Gaskov, Sensors and Actuators B: Chemical **50** (3), 186-193 (1998).
20. A. Chowdhuri, V. Gupta, K. Sreenivas, R. Kumar, S. Mozumdar and P. Patanjali, Applied physics letters **84** (7), 1180-1182 (2004).
21. W. Zhang, H. Wang, Y. Zhang, Z. Yang, Q. Wang, J. Xia and X. Yang, Electrochimica Acta **113** (0), 63-68 (2013).
22. H. Wang, Q. Pan, J. Zhao and W. Chen, Journal of Alloys and Compounds **476** (1–2), 408-413 (2009).
23. N. K. Renuka, A. V. Shijina, A. K. Praveen and C. U. Aniz, Journal of Colloid and Interface Science **434** (0), 195-200 (2014).
24. X. Zhang, G. Wang, X. Liu, J. Wu, M. Li, J. Gu, H. Liu and B. Fang, The Journal of Physical Chemistry C **112** (43), 16845-16849 (2008).

25. Y. Wang, T. Jiang, D. Meng, J. Yang, Y. Li, Q. Ma and J. Han, Applied Surface Science **317** (0), 414-421 (2014).
26. İ. Y. Erdoğan and Ö. Güllü, Journal of Alloys and Compounds **492** (1–2), 378-383 (2010).
27. J. Tamaki, K. Shimanoe, Y. Yamada, Y. Yamamoto, N. Miura and N. Yamazoe, Sensors and Actuators B: Chemical **49** (1-2), 121-125 (1998).
28. A. Yildiz, Ş. Horzum, N. Serin and T. Serin, Applied Surface Science **318** (0), 105-107 (2014).
29. Y. Gülen, F. Bayansal, B. Şahin, H. A. Çetinkara and H. S. Güder, Ceramics International **39** (6), 6475-6480 (2013).
30. A. Zainelabdin, G. Amin, S. Zaman, O. Nur, J. Lu, L. Hultman and M. Willander, Journal of Materials Chemistry **22** (23), 11583-11590 (2012).
31. D. Volanti, D. Keyson, L. Cavalcante, A. Z. Simões, M. Joya, E. Longo, J. A. Varela, P. Pizani and A. Souza, Journal of Alloys and Compounds **459** (1-2), 537-542 (2008).
32. P. Chand, A. Gaur, A. Kumar and U. Kumar Gaur, Applied Surface Science **307** (0), 280-286 (2014).
33. J. S. Shaikh, R. C. Pawar, R. S. Devan, Y. R. Ma, P. P. Salvi, S. S. Kolekar and P. S. Patil, Electrochimica Acta **56** (5), 2127-2134 (2011).
34. Ş. Baturay, A. Tombak, D. Batibay and Y. S. Ocak, Applied Surface Science (2017).
35. S. Baturay, A. Tombak, D. Kaya, Y. S. Ocak, M. Tokus, M. Aydemir and T. Kilicoglu, Journal of sol-gel science and technology **78** (2), 422-429 (2016).
36. D. P. Joseph, C. Venkateswaran, S. Sambasivam and B. C. Choi, Journal of the Korean Physical Society **61** (3), 449-454 (2012).

BOOK OF FULL TEXT PROCEEDINGS TURKISH PHYSICAL
SOCIETY 35th INTERNATIONAL PHYSICS CONGRESS (TPS35)
TPS35, Vol.01, No.04, pp.280-284.
ISBN:978-605-83516-6-0

15 December 2019

The Structural and Electrical Properties of Cu_2O/ZnO Nanostructure Growth on n-type Porous Si

Alper ÇETİNEL[1, a)] and Gökhan UTLU[1, b)]

[1]*Department of Physics, Ege University, Bornova, 35030, Izmir, Turkey*

[a)]Corresponding author: alper.cetinel@ege.edu.tr
[b)]gokhan.utlu@ege.edu.tr

Abstract. Cu_2O/ZnO nanostructures were deposited by electrochemical deposition method onto n-type porous silicon (PSi) at 0.8 mA/cm^2 constant current density in different deposition times (15, 30, 60 and 90 min). The effect of deposition time on the structural and electrical properties of PSi/Cu_2O/ZnO nanostructures was analyzed by FE-SEM, XRD and current-voltage (I-V) measurement. The FE-SEM images have clearly revealed that with increasing deposition time, two types of structures (nanoparticles and nanowires) were successfully grown by electrochemical deposition method on PSi surface. XRD analysis has indicated that Cu_2O/ZnO has a cubic crystal structure when produced by electrodeposition. It was also discussed the dark current–voltage (I–V) characteristic of PSi and PSi/Cu_2O/ZnO structures. The I–V measurements of PSi/Cu_2O/ZnO structures showed a rectifying effect with increasing deposition time as compared with those relative to PSi.

INTRODUCTION

Metal oxide nanostructures are of great interest today as functional materials that offer numerous applications in several fields, due to unusual properties, such as the versatile electronic band structure, electrical, optical and mechanical properties (1). Among these metal oxide materials, the cupros oxide-zinc oxide (Cu_2O / ZnO) stands out with its interesting properties, low cost and environmentally friendly device applications. In this structure, p-type metal oxide semiconductor Cu_2O has a band gap of 2 eV, while, n-type metal oxide semiconductor ZnO has a 3.3 eV band gap (2). Furthermore, cuprous oxide-zinc oxide (Cu_2O/ZnO) binary compound, produced on transparent electrodes such as indium tin oxide (ITO), have shown very promising results in solar cell and photodetector applications (3). However, the using of the transparent electrodes as substrates in silicon and germanium-based technology is a difficult and costly process. However, Cu_2O and ZnO structures have high lattice mismatch with silicon, this is the most important disadvantages in terms of growing these structures on silicon (4). On the other hand, porous silicon (PSi) layer is a promising substrate material to produce these metal oxides due to the important properties of (PSi) such as a large surface area, direct band structure and low lattice mismatch with Cu_2O and ZnO (4,5).

The growth and characterization of ZnO nanostructures in the PSi matrix have been studied for many years (4). On the other hand, the production and characterization of Cu_2O nanoparticles on p-type PSi have attracted less attention and the production of Cu_2O nanostructures using n-type PSi substrates has not been investigated up to date (5). Sol-gel, radio-frequency sputtering, thermal evaporation and electrochemical deposition methods are frequently used to produce nanostructures on different substrates (2). Compared to other production methods, the electrochemical deposition method is at the forefront because of its advantages such as being fast and controlled, requiring no vacuum, performing at room temperature, being much cheaper than other systems and being environmentally friendly (1,2). To achieve good junction quality, increasing the quality of the lattice matching and low defect density, the deposition method and parameters for the Cu_2O/ZnO must be investigated in detailed. It is also important to analyze that how the substrate and growth conditions affect the structural and electrical properties of the PSi/Cu_2O/ZnO nanostructures.

ISBN:978-605-83516-6-0

Thus, the aim of the reported work is to investigate effect of the deposition time on structural, morphological and electrical properties of PSi/Cu_2O/ZnO nanostructures, produced by using the electrochemical deposition technique.

MATERIALS AND METHODS

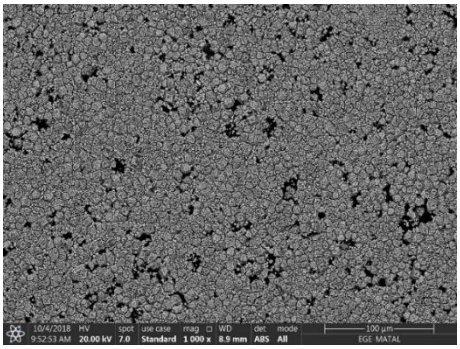
Porous silicon layer was produced by phosphorous doped, double-sided polished n-type Si wafer with (100) orientation and 1–10 Ω cm resistivity via electrochemical etching in HF solution (40%)/Ethanol (99.8%) (1:1) with backside illumination. The etching process was carried out with a constant current density of 60 mA/cm^2 for 20 min. Silicon wafer and platinum wire were selected as anode and cathode, respectively.

The electrodeposition was carried out at 65 ^{0}C in an aqueous solution of 0.4 M copper sulfate ($CuSO_4$) (Merck, 99.995%), 0.08 M Zinc nitrate hexahydrate [$Zn(NO_3)_2.6H_2O$] (Merck, 98%) and 0.5 M Boric acid (H_3BO_3) (Merck, EMSURE). The pH value of solution was adjusted to 12 by adding 4 M potassium hydroxide (KOH) (Merck) solution. PSi/Cu_2O/ZnO nanostructures were obtained under the constant current density of 0.8 mA/cm_2 after reversing the polarization direction. The electrodeposition time were varied from 15 to 90 min.

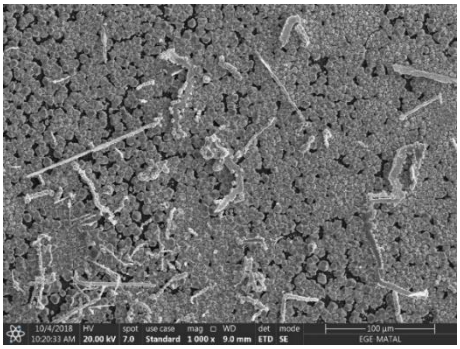
Surface morphologies of Cu_2O/ZnO nanostructures were analyzed using a field emission scanning electron microscopy system (FE-SEM, Thermo Scientific Apreo S). X-ray diffraction (XRD) patterns of Cu_2O/ZnO samples were obtained using a Philips X'Pert Pro X-Ray Diffraction system employing a CuKα radiation (λ=0.15418 nm). The dark I-V characteristics of the Cu_2O/ZnO nanostructures was also investigated by 4-probe method at room temperature.

RESULTS AND DISCUSSION

The surface morphology of PSi/Cu_2O/ZnO samples, deposited in 15, 30, 60 and 90 min, was obtained by using top-view FE-SEM imaging, as shown in Fig. 1. When electrochemical reactions were performed at 0.8 mA/cm_2 for 15 min, Cu_2O/ZnO nanoparticles agglomerated and formed clusters on the surface of PSi. When the deposition time increases to 30 and 60 min, it is clearly seen in Fig. 2b,c that Cu_2O/ZnO nanowire grow on nanoparticle clusters on the PSi surface. Increasing the deposition time to 90 min, the Cu_2O/ZnO nanowire became thicker, denser and spread out over the larger areas on the PSi surface. It is also found that the thickness of nanowires are several hundred nanometers, while their lengths reach several micrometers. Figure 2 shows EDAX mapping analysis providing precise information of the concentration of elements in PSi/Cu_2O/ZnO sample deposited in 30 and 90 min. The distribution of the components in the PSi/Cu_2O/ZnO samples indicate that deposition of Cu_2O ratio is higher than ZnO ratio due to probably the low concentration of Zinc nitrate hexahydrate. It is also found that as seen in Fig. 2, the FE-SEM image of Cu_2O/ZnO samples, prepared in 30 min, shows typical hollow polyhedron-like structures with relatively good dispersibility, and it displays the porous shell of the hollow polyhedron structure, which composed of many nanoparticles. The results of the FE-SEM analyses suggest that deposition of Cu_2O/ZnO structures occurred in the stages, i) nucleation and agglomeration of primary nanoparticles, ii) nanoparticle clusters coalescence into continuous film and formation of nanowire on this film.

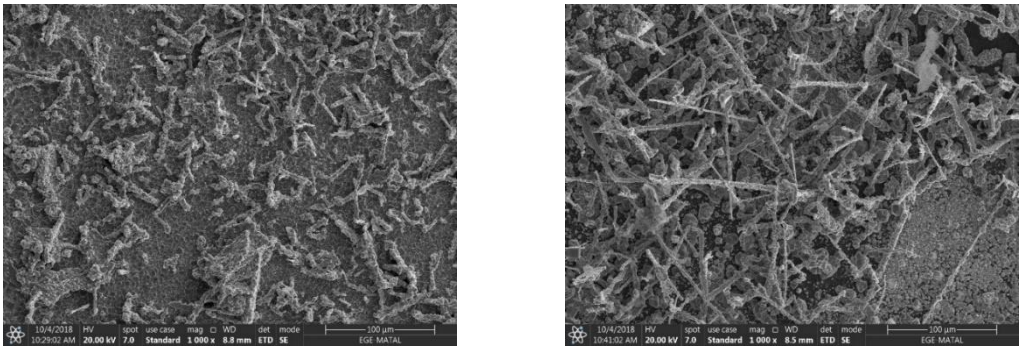


(a)



(b)

ISBN:978-605-83516-6-0



(c) (d)

FIGURE 1. FE-SEM images of PSi/Cu_2O/ZnO samples deposited at 0.8 mA/cm^2 in a) 15 min, b) 30 min, c) 60 min, and d) 90 min.

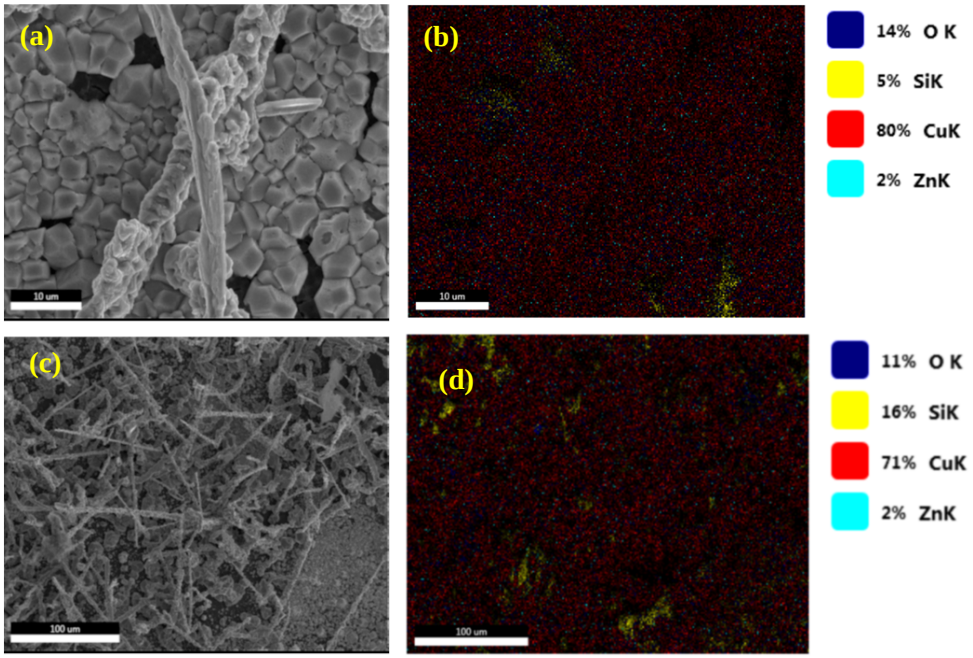


FIGURE 2. FE-SEM imaging by EDAX mapping showing the elemental analysis of PSi/Cu_2O/ZnO sample via electrochemical deposition, a,b) 30 min, and c,d) 90 min.

The XRD patterns of n type Si wafer, PSi and PSi/Cu_2O/ZnO samples, obtained for 15, 30, 60 and 90 min at 0.8 mA/cm^2, are shown in Fig. 2. As for the XRD pattersn of Cu_2O/ZnO structures, it can be clearly seen that there are five main peaks with 2θ values for 29.5, 36.5, 42.4, 50.5, 73.6 corresponding to the (110), (111), (200), (211), (311) crystal planes of cubic Cu_2O, respectively (1,6). Because of the low lattice mismatch among ZnO, Cu_2O and PSi, it is expected that the Cu_2O phase were crystallized with the preferred orientation along the (111) direction, as shown in Fig. 2 (5). The other weaker peaks can be indexed to ZnO structures (7). We also think that ZnO (101) peak with 2θ value for 36.3 is very close to the Cu_2O (111) peak with 2θ value for 36.5, they are probably overlapped in the XRD pattern. Apart from Cu_2O and ZnO diffraction peaks, the Si (400) peak seen at $2\theta=70^0$ is the main peak of the n-type Si substrate (8). The higher peak intensity is attributed to an increase in the grain size of the Cu_2O particles in the (111) plane on PSi, with increasing deposition time. As seen in Figure 3, small crystallite size causes broader reflections, whereas large crystallite size leads to sharp reflections, which is consistent with the SEM analysis (9).

ISBN:978-605-83516-6-0

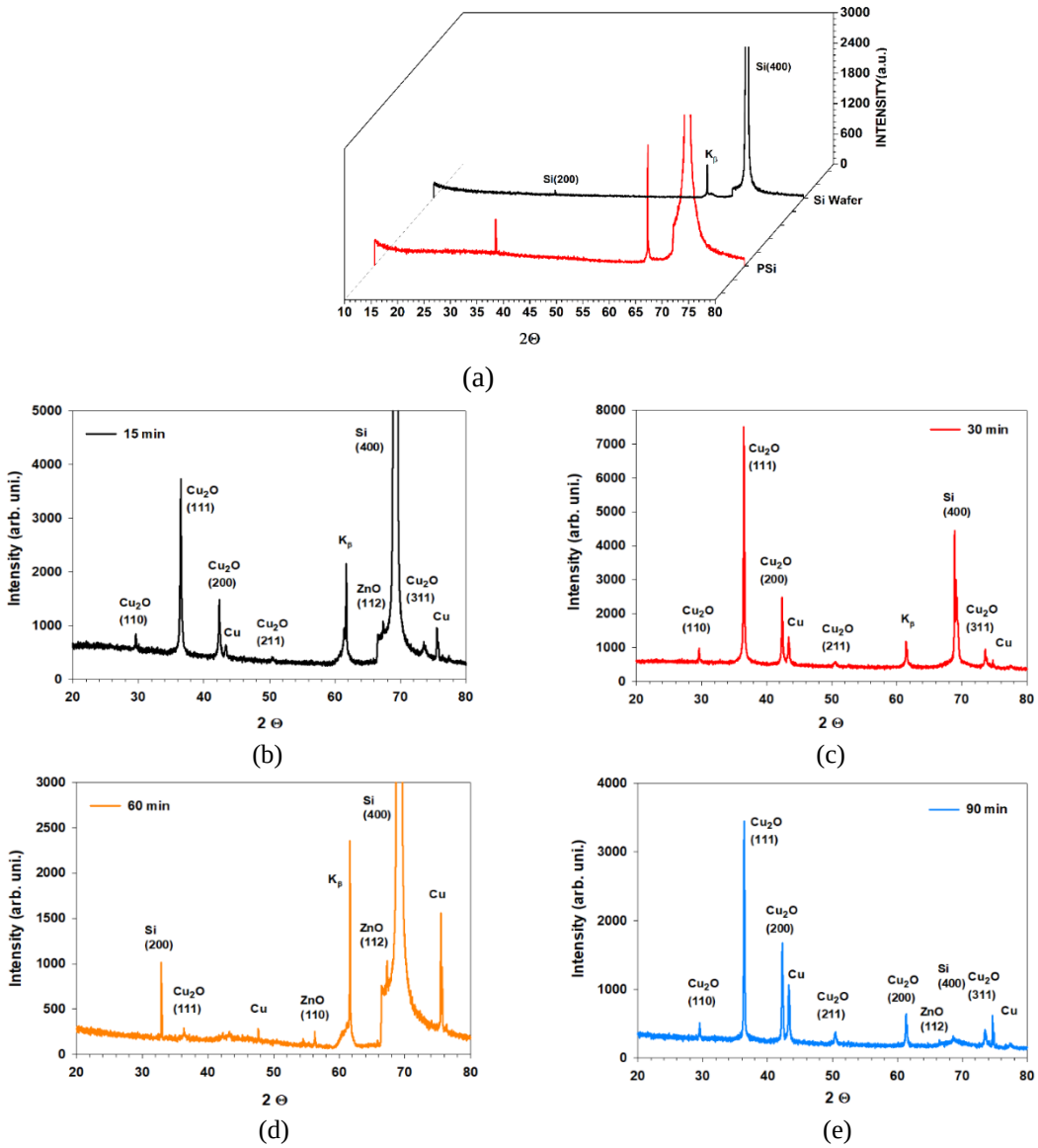


FIGURE 3. (a) TheXRD patterns of n-type Si wafer and reference as prepared PSi are drawn for comparison. The XRD patterns of PSi/Cu_2O/ZnO nanostructures prepared at current density of 0.8 mA/cm^2 with varying deposition times, b) 15 min, c) 30 min, d) 60 min, and e) 90 min.

We present in Fig. 4 the room temperature dark current-voltage (I-V) characteristics of PSi and PSi/Cu_2O/ZnO samples for 15, 30, 60 and 90 min. When the Cu_2O/ZnO samples are obtained with 15 and 30 min deposition times, an ohmic behavior observed due to the presence of carrier traps created by the association of copper vacancy and oxygen interstitials (10,11). For 60 and 90 min deposition times, Cu_2O/ZnO samples display p-n junction behavior, confirmed by the non-linear I-V characteristics, as seen in Fig. 4. Increasing rectifying behavior with increasing deposition time can be attributed that Cu_2O/ZnO layer deposited on PSi prevents the formation of SiO layer and enhances the formation of Schottky barrier between Cu_2O/ZnO and PSi layer (11,12). It is thought that such samples have diode characteristic, but further studies could be carried out to clarify the temperature dependent current-voltage (I-V) characteristics providing detailed information about the structures.

ISBN:978-605-83516-6-0

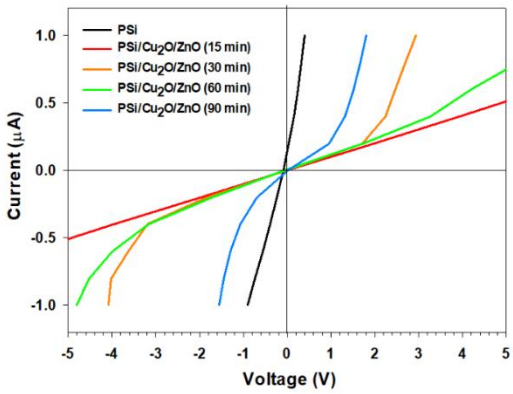


FIGURE 4. Current–voltage (I-V) characteristics of the PSi and PSi/Cu_2O/ZnO samples with different deposition times.

CONCLUSION

In this study, we have synthesized Cu_2O/ZnO nanostructures on the surface of PSi with deposition time of 15, 30, 60 and 90 min by using an electrochemical deposition method. Then, we studied the effect of deposition time on the morphological and electrical characteristics of the PSi/Cu_2O/ZnO nanostructures. SEM analysis revealed that the hollow polyhedron-like structures agglomerated and formed clusters on the PSi surface. It was also found that Nanowire-like structures grow on these clusters. XRD analysis confirmed the presence of Cu_2O and ZnO on the PSi matrix. XRD analysis also revealed that Cu_2O phase were crystallized along the (111) direction. The room temperature dark I-V characteristics of PSi/Cu_2O/ZnO samples displayed from ohmic to p-n junction behavior with a good rectification.

ACKNOWLEDGMENTS

This work was supported by the Ege University, Research Project Foundation (Project no.: FGA-2019-20860).

REFERENCES

1. S. Zoolfakar, R. A. Rani, A. J. Morfa, S. Balendhran, A. P. O'Mullane, S. Zhuiykov and K. Kalantar-zadeh, J. Mater. Chem., **22**, 21767 (2012).
2. M. H. Tran, J. Y. Cho, S. Sinha, M. G. Gang and J. Heo, Thin Solid Films **661**, 132-136 (2018).
3. N. G. Elfadill, M. R. Hashim, K. M. A. Saron, K. M. Chahrour, M. A. Qaeed and M. Bououdina, Materials Chemistry and Physics **156**, 54-60 (2015).
4. H. Cai, H. Shen, Y. Yin, L. Lu, J. Shen and Z. Tang, Journal of Physics and Chemistry of Solids **70**, 967-971 (2009).
5. D. Yan, S. Li, M. Hu, S. Liu, Y. Zhu and M. Cao, Sensors and Actuators B **223**, 626-633 (2016).
6. J. Cui and U. J. Gibson, J. Phys. Chem. C **114**, 6408-6412 (2010).
7. Y. H. Ok, K. R. Lee, B. O. Jung, Y. H. Kwon and H. K. Cho, Thin Solid Films **570**, 282-287 (2014).
a. Çetinel, N. Artunç and E. Tarhan, Materials Science & Engineering B **243**, 131-140 (2019).
8. Çetinel, N. Artunç and E. Tarhan, Eur. Phys. J. Appl. Phys. **86**, 11301 (2019).
9. Kathalingam, D. Vikraman, H. S. Kim and H. J. Park, Optical Materials **66**, 122-130 (2017).
10. S. Brandt, M. A. Tumelero, S. Pelegrini, G. Zangari and A. A. Pasa, J Solid State Electrochem **21**, 1999-2020 (2017).
11. P. Ghamgosar, F. Rigoni, S. You, I. Dobryden, M. G. Kohan, A. L. Pellegrino, I. Concina, N. Almqvist, G. Malandrino and A. Vomiero, Nano Energy **51**, 308-316 (2018).

BOOK OF FULL TEXT PROCEEDINGS TURKISH PHYSICAL SOCIETY 35th INTERNATIONAL PHYSICS CONGRESS
(TPS35) TPS35, Vol.01, No.04, pp.285-292.
ISBN:978-605-83516-6-0

15 December 2019

Investigation of Some Physical Properties of Tungsten Trioxide Thin Films Deposited via Thermionic Vacuum Arc Technique

Uğur Demirkol,[a)] Suat Pat,[b)] Nihan Akkurt,[c)] Mustafa Özgür,[d)] Reza Mohammadigharehbagh,[e)] Ali Olkun,[f)] and Şadan Korkmaz[g)]

Department of Physics, Eskişehir Osmangazi University, Eskisehir, Turkey

[a)] *Correspondingauthor:udemirkol@ogu.edu.tr*
[b)] *suatpat@ogu.edu.tr*
[c)] *akkurtnihan@gmail.com*
[d)] *ozgurm@ogu.edu.tr*
[e)] *rezagha@ogu.edu.tr*
[f)] *aliolkun30@gmail.com*
[g)] *skorkmaz@ogu.edu.tr*

Abstract. Tungsten Trioxide WO_3 thin films deposited onto microscope glass and Indium Tin Oxide (ITO) substrate with thermionic vacuum arc (TVA) system. TVA technique provides thin films that have high homogeneity, low roughness and high adhesiveness to the substrate. In high vacuum medium, plasma of deposited material is generated and accelerated to the substrate. The deposited thin films are investigated by X-Ray Diffraction (XRD), Raman Spectrometer, Atomic Force Microscope (AFM), Field Emission Scanning Electron Microscopy (FE-SEM), UV-Vis Spectrophotometer, Photoluminescence Spectrometer, Thin Film Measurement System and Potentiostat System. WO_3 is used in many electrochromic applications. The produced WO_3 thin films with TVA method are proven to be usable in electrochromic devices.

INTRODUCTION

Tungsten Trioxide, as a thin film, one of the pillars of electrochromic materials. WO_3 is the most studied and well- known material [1]. The electrochromic, structural and optical properties of WO_3, is highly related with its preparation method. WO_3 thin films generally prepared with thermal evaporation [2], chemical vapor deposition (CVD) [3], sputtering [4], electrodeposition [5] and sol-gel methods [6]. Tungsten Trioxide is a semiconductor with wide band gap between 2.6 eV to 3.0 eV [7]. WO_3 thin films are used in many applications such as smart windows [8], displays [9], gas sensors [10], field emission devices [11] and photo-catalysts [12].

Thermionic Vacuum Arc (TVA) technique has lot of advantages over other thin film deposition methods; since the particles of coating material is highly energetic, while substrate can be kept at room temperature. The thin films deposited with TVA technique shows desirable properties such as high homogeneity, low roughness, less impurity and good adhesiveness to the substrate [13].

In this study; the structural, morphological, optical and electrochromic properties of WO_3 thin films which pre- pared by TVA technique are investigated. The aim of this study is to create an alternative method for desired WO_3 applications.

EXPERIMENTAL SETUP

In this study, firstly WO_3 powder with >99.9% purity was compressed into pellet form to prevent to be vacuumed in the chamber. Microscope glass slide and Indium Tin Oxide (ITO) coated glass were used as substrates. Also the substrates were cleaned and dried and placed onto holders in the vacuum chamber.

Thermionic vacuum arc system can be described as a plasma generator. Desired materials for coating can be in solid, liquid or gas state. Various materials can be deposited at the same time and in the same vacuum chamber. Coating process begins with electron release from electron gun. Electron gun consists of tungsten filament and Wehnelt cylinder which helps to focus electrons released by thermionic emission mechanism from tungsten filament. The electron beam accelerated to the anode crucible, which holds the materials to be coated, by applying DC voltage. Highly energetic electrons evaporate the material into plasma state which can be deposited onto substrates. The system can only work in high vacuum conditions in order to prevent tungsten filament being oxidized; however, this necessity also enables evaporation process of materials to be coated can be done without any precursor gas. The illustration of TVA setup is shown in the Figure 1.

TABLE I. Working parameters for WO_3 deposition with TVA technique

Parameter (unit)	Value
Discharge Current (A)	0.3
Deposition Time (s)	120
Working Pressure (torr)	$9x10^{-5} \rightarrow 1x10^{-4}$
Applied Voltage (V)	100
Filament Current (A)	20.5

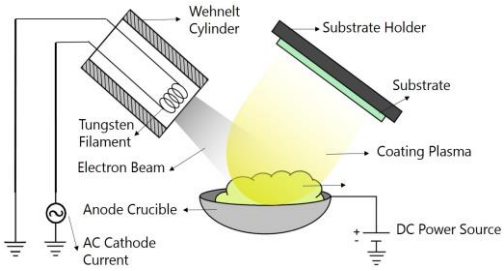


FIGURE 1. The illustration of a TVA setup

The main advantage of thermionic vacuum arc technique is the high energy of the deposited material. The deposited thin films with TVA technique near room temperature can obtain similar properties with annealed thin films or the thin films deposited onto heated substrate via other deposition techniques. Also for some materials, being able to keep the temperature near room temperature can prevent additional stress caused by thermal expansion. Secondly, precursor is not required. This prevents common defects and impurities to be formed during deposition and increases the homogeneity across the thin film. Finally, it is a fast deposition technique and can reach 10 nm per second deposition rate. The working parameters for WO_3 deposition with TVA technique is presented in Table I.

EXPERIMENTAL RESULTS

The structural, morphological, optical and electrochromic properties were investigated. Structural properties were defined by X-Ray Diffraction (XRD) and Raman spectroscopy. XRD patterns is acquired with Panalytical Empyrean X-Ray Diffractometer with CuKα (λ = 0.154056 nm) monochromatic radiation, in the range of 20° - 80° for 2θ diffraction angles, using Panalytical PIXcel3D detector. XRD patterns are shown in Figure 2.

WO_3 thin film deposited onto glass substrate shows only one visible peak at 28.24° which is attributed to hexagonal WO_3 crystallites [14]. WO_3 thin film deposited onto ITO coated glass substrate shows many peaks which are attributed to different crystallite formations. The peaks at 30.80°, 40.06°, 62.30° and 76.36° are attributed to Tin (Sn) crystallites [15, 16]. The peak at 33.33° shows Tin Oxide (SnO) crystallite formation [17]. Also, there is a peak at 37.98° which is related to another Tin Oxide form, Cassiterite (SnO_2) crystallites [18]. There are several peaks, which are attributed to Tungsten Trioxide WO_3, at 35.77°, 41.88°, 42.02°, 49.50° and 60.73° [19, 20, 21, 22]. There are two peaks at 45.84° and 75.00° which are related to Indium Tungsten Oxide [$In_2(WO_4)_3$] crystallites [23, 24]. Similarly, there are peaks at 56.10°, 58.75° and 59.05° which are attributed to Tin Tungsten Oxide crystallites [25]. Finally, there is a peak at 51.09° which is related to Indium Oxide (In_2O_3) crystallites [26].

Using Scherrer's formula crystallite size (CS), dislocation density (δ) and microstrain (ε) values were calculated [27, 28]. In this equation, λ is wavelength used in the measurement, which is CuKα radiation that has a value of 0.154056 nm. K is the shape factor which is a dimensionless value and it is selected as 0.94 β is the full-width at half-maximum (FWHM) value in radians of the peak and lastly, θ is the half of the diffraction angle 2θ.

$$\text{Crystallite Size (CS)} = \frac{K\lambda}{\beta cos\theta} \quad (1)$$

ISBN:978-605-83516-6-0

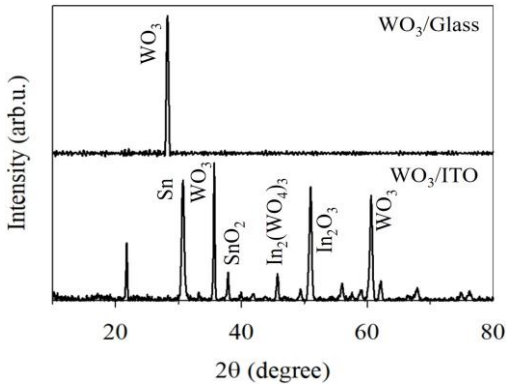


FIGURE 2. XRD pattern of WO_3 thin films, deposited onto glass and ITO coated glass substrates

$$\varepsilon = \frac{\beta cos\theta}{4} \tag{2}$$

$$\delta = \frac{1}{CS^2} \tag{3}$$

The more information about peak center positions, crystal structures, miller indices, crystallite sizes, microstrain values, dislocation density values and Crystallography Open Database ID (COD ID) numbers are listed in the Table II.

The structural properties of the thin films were also investigated using Raman spectroscopy. The measurements were taken with Renishaw inVia Raman Microscope using 532 nm laser light source. The Raman studies show similar peaks with variation in intensities between thin films deposited onto different substrates. The peaks between 300 – 500 cm^{-1} are related to O – W – O stretching and bending vibrations [28]. The expected peaks near 725 cm^{-1} and 800 cm^{-1} related to WO3 vibrations were masked behind the peaks comes from glass substrates which at 765 cm^{-1}, 950 cm^{-1} and 1100 cm^{-1} [29]. The Raman spectra of thin films are shown in Figure 3.

TABLE II. XRD peaks of WO_3 thin films, a) deposited onto glass substrate, b) deposited onto ITO coated glass substrate

	$2\theta^{\circ}$	Diffraction Plane	Miller Indices	Crystal Structure	Crystallite Size (nm)	Microstrain $\varepsilon x10^{-3}$	Dislocation Density, δ (pm^{-2})	COD ID
a)	28.24	WO_3	(200)	hexagonal	22	6.8	0.21	1004057
b)	30.80	Sn	(020)	tetragonal	19	7.1	0.27	9008570
	33.33	SnO	(110)	tetragonal	35	3.6	0.08	1100021
	35.77	WO_3	(121)	triclinic	39	3.0	0.06	1010618
	37.98	Cassiterite (SnO_2)	(200)	tetragonal	32	3.5	0.10	9009082
	40.06	Sn	(110)	tetragonal	42	2.5	0.06	1540069
	41.88	WO_3	(22$\underline{2}$)	monoclinic	41	2.5	0.06	2106382
	42.02	WO_3	(222)	triclinic	41	2.4	0.06	2106293
	45.84	$In_2(WO_4)_3$	(414)	monoclinic	27	3.4	0.14	1533055
	49.50	WO_3	(014)	tetragonal	25	3.5	0.16	1521532
	51.09	In_2O_3	(440)	cubic	21	4.1	0.23	2310009
	56.10	Tin Tungsten Oxide	(361)	tetragonal	22	3.4	0.20	1526683
	57.69	W	(200)	cubic	47	1.6	0.05	1512550
	58.75	Tin Tungsten Oxide	(711)	tetragonal	49	1.5	0.04	1526683
	59.05	Tin Tungsten Oxide	(560)	tetragonal	32	2.3	0.10	1526683
	60.73	WO_3	(241)	triclinic	22	3.3	0.21	1010618
	62.30	Tin (Sn)	(313)	cubic	24	2.9	0.17	9008568
	75.00	$In_2(WO_4)_3$	(233)	hexagonal	24	2.4	0.17	1001039
	76.36	Tin (Sn)	(151)	cubic	28	2.1	0.12	9008568

ISBN:978-605-83516-6-0

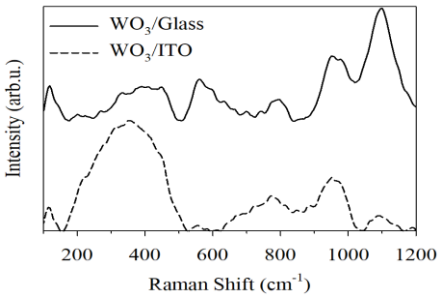


FIGURE 3. Raman Spectra of WO_3 thin films

The morphological properties of the deposited WO_3 thin films were investigated by field emission scanning electron microscopy (FE-SEM) and atomic force microscopy (AFM) techniques. Ambios Q-Scope Atomic Force Microscope in non-contact mode were used to obtain surface images. Surface roughness, which is 3.5 nm for the WO_3 thin film deposited onto glass substrate and 2.5 nm for the WO_3 thin film deposited onto ITO coated glass substrate, is relatively low. AFM images of thin films, as well as height distribution are shown in Figure 4.

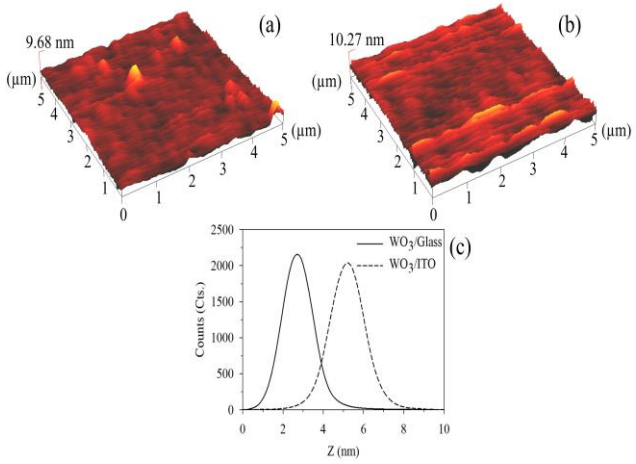


FIGURE 4. AFM images of the WO_3 thin films: a) onto glass substrate, b) onto ITO coated glass substrate and c) heigh distribution of the thin films

Field Emission Scanning Electron Microscope (FE-SEM) images were captured with HITACHI REGULUS 8230 FESEM with $25x10^3$ magnification. WO_3 thin films show homogeneity and low roughness all around the samples. FE-SEM images were shown in Figure 5.

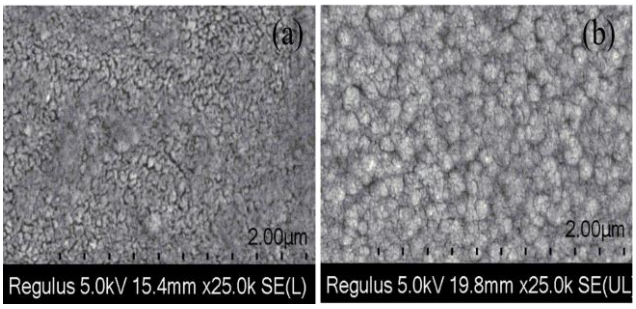


FIGURE 5. FE-SEM images of the deposited thin films a) onto glass substrate and b) onto ITO coated glass substrate at $25x10^3$magnification

ISBN:978-605-83516-6-0

Electrochromic properties of WO_3 thin film deposited by thermionic vacuum arc technique were investigated using GAMRY Instruments Reference 3000 Device potentiostat only for the thin film deposited onto ITO coated glass substrate, since conductive layer is required. The measurements were taken using three-electrode arrangement in 0.1 M $LiClO_4$ propylene carbonate solution. Silver (Ag/AgCl) electrode was used as a reference. Cyclic voltammetry measurements were obtained in the range of -1.8V to +1.2V and at 50 mV/s scan rate. Electrochemical impedance spectrum measurements were conducted and Nyquist plot have been plotted. According to the Nyquist plot, diffusion processes were occurring in the sample. Also chronoamperometric (CA) and repeated chronoamperometric (RCA) measurements were conducted. The voltage was applied as square signal between -0.5 V to 1.2 V. Both CA and RCA measurements were taken 80 s for coloration and 80 s for bleaching. Current densities were higher in coloration processes than bleaching process. This can be explained as lithium ions intercalated more than de-intercalated in the sample. Electrochromic measurements were shown in Figure 6.

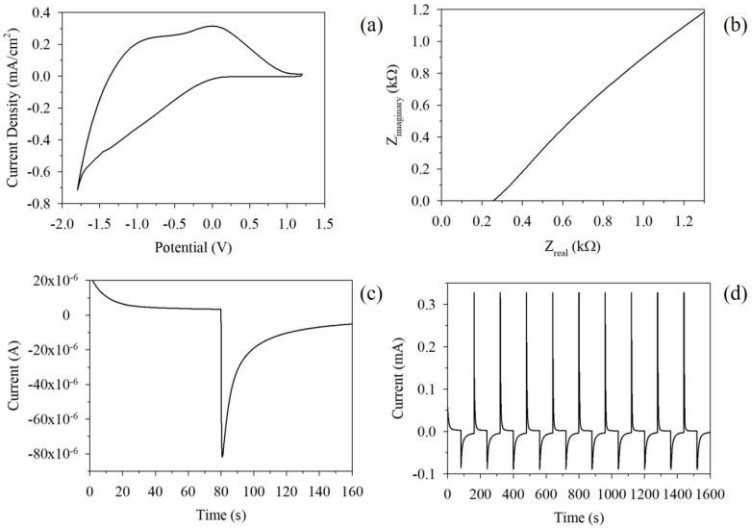


FIGURE 6. Graphs of electrochromic measurements a) cyclic voltammetry, b) Nyquist plot, c) Chronoamperometric data and d) repeated chronoamperometric data

Additionally, chronocoulometry (CC) measurement was taken in the range of -0.5 V to 1.2 V; which is used for estimating reversibility and coloration efficiency by measuring the amount of Li^+ ions extracted or inserted during a certain time period. Reduction of tungsten states from W^{+6} to W^{+5}, results in coloration from intercalation of charges into the film by diffusion process during the cathodic scan. Also, during the anodic scan reverse processes occurs and results in bleaching of the film. Residual charge (ΔQ) is calculated by subtracting de-intercalated charge value (Q_{di}) from intercalated charge value (Q_i), obtained by chronocoulometry measurement [30]. Electrochromic reversibility is also calculated by using dividing same values respectively.

$$\Delta Q = Q_i - Q_{di} \tag{4}$$

$$\text{Reversibility} = Q_{di}/Q_i \tag{5}$$

Using UNICO SQ4802 UV-Vis Double Beam Spectrophotometer, transmittance (T) were measured for both col- ored and bleached states and optical density changes (ΔOD) were calculated with given equation below for 550 nm wavelength [31].

$$\Delta OD = \ln \frac{T_{\text{Bleached}}}{T_{\text{Colored}}} \tag{6}$$

At 550 nm wavelength, transmittance values are found as 54% for colored state and 57% for bleached state. Trans- mittance for both states are illustrated in Figure 7. Coloration efficiency (η), which is generally used for comparing

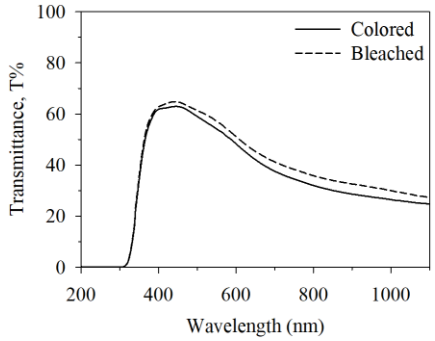


FIGURE 7. Optical transmittance of WO_3 thin film deposited onto ITO coated glass substrate a) for colored state, b) for bleached state

TABLE III. Electrochromic properties of deposited WO_3 thin film

Sample	Q_i (mC/cm^2)	Q_{di} (mC/cm^2)	Reversibility (Q_{di}/Q_i)	Transmittance (%)		Optical Density Changes ΔOD	Coloration Efficiency (cm^2/C)
			%	T_b	T_c		
WO_3/ITO	1.136	0.185	16.3	57	54	0.054	47.80

electrochromic devices overall performance with other electrochromic devices, is given by following equation.

$$\eta(\lambda) = \frac{\Delta OD(\lambda)}{Q_i} = \frac{\ln \frac{T_{Bleached}}{T_{Colored}}}{Q_i} \tag{7}$$

Calculated electrochromic parameters of WO_3 thin film deposited onto ITO coated glass sample is given in Table III. Optical properties of WO_3 thin films were measured by using Filmetrics F20 Thin Film Thickness Measurement System, UNICO SQ4802 UV-Vis Double Beam Spectrophotometer and PerkinElmer LS 55 Florescence Spectrometer. Thicknesses were measured as 262 nm for WO_3 thin film deposited onto glass and 312 nm for WO_3 thin film deposited onto ITO coated glass. Optical properties are shown in Figure 8.

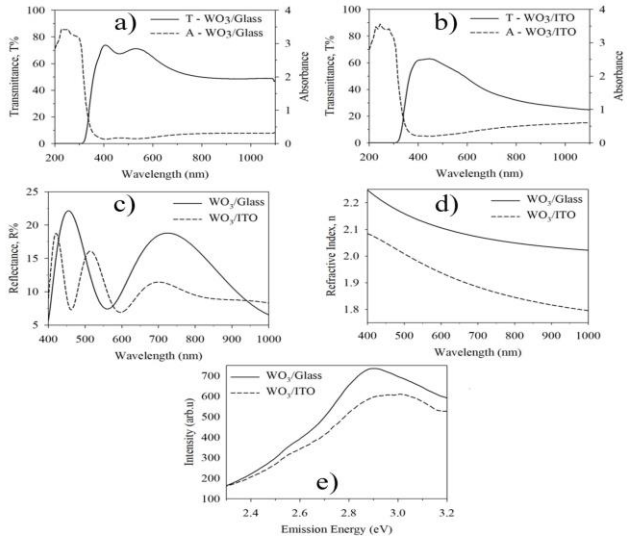


FIGURE 8. Optical Properties of deposited WO_3 thin films, Transmittance (T) and Absorbance (A) spectra of WO_3 thin film deposited a) onto glass, b) onto ITO coated glass, c) Reflectance spectra, d) Refractive Index spectra and e) Photoluminescence spectra of deposited thin films

CONCLUSION

In this study, WO_3 thin films deposited onto glass and ITO coated glass substrates using thermionic vacuum arc (TVA) technique and their structural, morphological, electrochromic and optical properties were observed. As XRD results show, WO_3 thin film deposited onto glass have only hexagonal structured crystallites, whereas WO_3 thin film deposited onto ITO coated glass have various structured crystallites. Raman spectroscopy confirms presence of WO_3. The morphological properties were investigated by AFM and FE-SEM techniques. The deposited thin films have low roughness and high homogeneity across all surface of the films. Coloration efficiency for the thin film deposited onto ITO coated glass was found as 47.80 cm^2/C which is similar to literature but reversibility was found as 16.3% which is poorer compared to WO_3 thin films deposited with other techniques. This is due to thickness and low roughness of the films which limits surface area for intercalation/de-intercalation processes. In order to create efficient electrochromic device using thermionic vacuum arc, the thickness of WO_3 layer should be around 30 nm. The band gap values are measured as wide band around 2.90 eV for the deposited thin film onto glass substrate and wide band around 2.97 eV for the thin film deposited onto ITO coated glass substrate, which is consistent with literature.

REFERENCES

1. P. Monk, R. Mortimer, and D. Rosseinsky, *Electrochromism and electrochromic devices* (Cambridge University Press, 2007).
2. K. Patel, C. Panchal, V. Kheraj, and M. Desai, "Growth, structural, electrical and optical properties of the thermally evaporated tungsten trioxide (wo3) thin films," Materials Chemistry and Physics **114**, 475–478 (2009).
3. T. Maruyama and S. Arai, "Electrochromic properties of tungsten trioxide thin films prepared by chemical vapor deposition," Journal of the Electrochemical Society **141**, 1021–1024 (1994).
4. G. Sberveglieri, L. Depero, S. Groppelli, and P. Nelli, "Wo3 sputtered thin films for nox monitoring," Sensors and Actuators B: Chemical **26**, 89–92 (1995).
5. P. KangáShen and C. Alfred, "Study of electrodeposited tungsten trioxide thin films," Journal of Materials Chemistry **2**, 1141–1147 (1992).
6. M. Breedon, P. Spizzirri, M. Taylor, J. du Plessis, D. McCulloch, J. Zhu, L. Yu, Z. Hu, C. Rix, W. Wlodarski, *et al*., "Synthesis of nanostructured tungsten oxide thin films: a simple, controllable, inexpensive, aqueous sol- gel method," Crystal Growth & Design **10**, 430–439 (2009).
7. P. González-Borrero, F. Sato, A. Medina, M. Baesso, A. Bento, G. Baldissera, C. Persson, G. A. Niklasson, C. G. Granqvist, and A. Ferreira da Silva, "Optical band-gap determination of nanostructured wo 3 film," Applied Physics Letters **96**, 061909 (2010).
8. J. Svensson and C. Granqvist, "Electrochromic coatings for smart windows: crystalline and amorphous wo3 films," Thin Solid Films **126**, 31–36 (1985).
9. H. Kawasaki, T. Matsunaga, W. Guan, T. Ohshima, Y. Yagyu, and Y. Suda, "Preparation of wo3 thin films for electrochromic display by plasma process," J Plasma Fusion Res Series **8**, 1431 (2009).
10. X.-L. Li, T.-J. Lou, X.-M. Sun, and Y.-D. Li, "Highly sensitive wo3 hollow-sphere gas sensors," Inorganic chemistry **43**, 5442–5449 (2004).
11. F. Liu, L. Li, F. Mo, J. Chen, S. Deng, and N. Xu, "A catalyzed-growth route to directly form micropatterned wo2 and wo3 nanowire arrays with excellent field emission behaviors at low temperature," Crystal Growth & Design **10**, 5193–5199 (2010).
12. J. A. Seabold and K.-S. Choi, "Effect of a cobalt-based oxygen evolution catalyst on the stability and the selectivity of photo-oxidation reactions of a wo3 photoanode," Chemistry of Materials **23**, 1105–1112 (2011).
13. U. Demirkol, S. Pat, R. Mohammadigharehbagh, C. Musaoğlu, M. Özgür, S. Elmas, S. Özen, and Ş. Korkmaz, "Determination of the structural, morphological and optical properties of graphene doped sno thin films deposited by using thermionic vacuum arc technique," Physica B: Condensed Matter **569**, 14–19 (2019).
14. B. Gerand, G. Nowogrocki, J. Guenot, and M. Figlarz, "Structural study of a new hexagonal form of tungsten trioxide," Journal of Solid State Chemistry **29**, 429–434 (1979).
15. R. W. Wyckoff, "Cubic closest packed, ccp," Structure, Cryst. Struct **1**, 33 (1963).
16. W. Helfrich and R. Dodd, "Densities and lattice parameters of tin (indium) solid solutions," Tech. Rep. (Wisconsin. Univ., Madison, 1963).
17. F. Izumi, "Pattern-fitting structure refinement of tin (ii) oxide," Journal of Solid State Chemistry **38**, 381–385 (1981).
18. H. Bräkken, "Die kristallstrukturen der trioxyde von chrom, molybdän und wolfram," Zeitschrift für Kristallographie-Crystalline Materials **78**, 484–488 (1931).
19. B. Loopstra and H. Rietveld, "Further refinement of the structure of wo3," Acta Crystallographica Section B: Structural Crystallography and Crystal Chemistry **25**, 1420–1421 (1969).
20. R. Diehl, G. Brandt, and E. Salje, "The crystal structure of triclinic wo3," Acta Crystallographica Section B: Structural Crystallography and Crystal Chemistry **34**, 1105–1111 (1978).
21. K. Locherer, I. Swainson, and E. Salje, "Transition to a new tetragonal phase of wo3: crystal structure and distortion parameters," Journal of Physics: Condensed Matter **11**, 4143 (1999).
22. A. P. Richard and D. D. Edwards, "Subsolidus phase relations and crystal structures of the mixed-oxide phases in the in2o3–wo3 system," Journal of Solid State Chemistry **177**, 2740–2748 (2004).
23. P. Labbe, M. Goreaud, B. Raveau, and J. Monier, "Etude comparative des structures mx wo3 de type bronze hexagonal. ii. evolution structurale dans la série des bronzes inx wo3 (0, 12< x< 0, 33)," Acta Crystallographica Section B: Structural Crystallography and Crystal Chemistry **35**, 1557–1564 (1979).
24. R. Steadman, "On the structure of tetragonal tin-tungsten bronzes," Materials Research Bulletin **7**, 1143–1150 (1972).
25. M. Marezio, "Refinement of the crystal structure of in2o3 at two wavelengths," Acta Crystallographica **20**, 723–728 (1966).
26. A. Patterson, "The scherrer formula for x-ray particle size determination," Physical review **56**, 978 (1939).

27. A. Monshi, M. R. Foroughi, and M. R. Monshi, "Modified scherrer equation to estimate more accurately nano-crystallite size using xrd," World journal of nano science and engineering **2**, 154–160 (2012).
28. J. Díaz-Reyes, R. Castillo-Ojeda, M. Galván-Arellano, and O. Zaca-Moran, "Characterization of wo3 thin films grown on silicon by hfmod," Advances in Condensed Matter Physics **2013** (2013).
29. R. Hemley, H. Mao, P. Bell, and B. Mysen, "Raman spectroscopy of si o 2 glass at high pressure," Physical Review Letters **57**, 747 (1986).
30. M. Meenakshi, R. Sivakumar, P. Perumal, and C. Sanjeeviraja, "Studies on electrochromic properties of rf sputtered vanadium oxide: Tungsten oxide thin films," Materials Today: Proceedings **3**, S30–S39 (2016).
31. X. An, C. Y. Jimmy, Y. Wang, Y. Hu, X. Yu, and G. Zhang, "Wo 3 nanorods/graphene nanocomposites for high-efficiency visible-light-driven photocatalysis and no2 gas sensing," Journal of Materials Chemistry **22**, 8525–8531 (2012).

BOOK OF FULL TEXT PROCEEDINGS TURKISH PHYSICAL
SOCIETY 35th INTERNATIONAL PHYSICS CONGRESS (TPS35)
TPS35, Vol.01, No.04, pp.293-297.
ISBN:978-605-83516-6-0

15 December 2019

Electrical and Morphological Properties of CuO:In Thin Films

Barbaros Demirselcuk[1, a)] and Vildan Bilgin[2, b)]

[1]*Çanakkale Onsekiz Mart Üniversitesi, Vocational School Of Technical Sciences, Electrical and Energy, Canakkale,TURKEY*
[2] *Çanakkale Onsekiz Mart Üniversitesi, Faculty of Arts and Sciences, Physics Department, Canakkale,TURKEY*

[a)]Corresponding author: b.demirselcuk@comu.edu.tr
[b)]vbilgin@comu.edu.tr

Abstract. In this study, undoped and different proportions of Indium (In) doped CuO (4, 8 and 12 at. %) thin films were deposited onto microscope glass substrates at 300±5 oC by using ultrasonic spray pyrolysis technique. In order to improve the physical properties of CuO thin films for photovoltaic applications, In elements are preferred as doping elements and we have investigated the effect of In doping on the electrical and morphological properties of copper oxide (CuO) thin films. Electrical resistivity values were calculated using a four-probe technique to investigate the electrical properties of produced all films. Electrical analyses have revealed that, electrical resistivity of CuO:In thin films which have p-type conductivity increased as a consequence of In doping. The surface properties of the films were determined by using atomic force microscopy (AFM). Morphological analysis show that all the films have almost homogeneous surface morphologies.

INTRODUCTION

In studies on nanostructures and solar cells, CuO thin films doped and undoped are often used. Cu is a widely preferred compound due to its simple chemical structure, inexpensive and high electrical conductivity values. $CuInSe_2$ (CIS) and $CuInGaSe_2$ (CIGS) are used in semiconductor nano materials [1]. CIS and CIGS structures are increasingly used in recent years especially in solar cell and photovoltaic applications. CuO, which is one of the simplest compounds of Cu atom, has very important physical properties such as superconductivity and spin Dynamics at high temperatures [2]. CuO can also be used as a thermal conductor in machine part due to its high thermal conductivity [3]. CuO based material are of interest on account of their potential uses in many technological fields. CuO and Cu_2O materials are known to be p-type semiconductors in general and hence potentially useful for constructing junction devices such as pn junction diodes [4]. Copper forms two different oxides Cu_2O having direct band gap of 2,1 eV and is, therefore, strongly absorbing only at wavelengths below 600 nm, whereas CuO with an band gap of 1.21-1.51 eV [5-6]. Several techniques have been used to deposit CuO thin films namely: thermal oxidation, dip coating, chemical vapor deposition, plasma evaporation, electrodeposition, spray pyrolysis and reactive sputtering [7-15]. In this study, undoped and In-doped CuO films with (4, 8 and 12 at %) were obtained by ultrasonic spray pyrolysis technique. The electrical, morphological properties and elemental analyses of the films were characterized by Hall Effect measurements, scanning electron microscope (SEM) and atomic force microscope (AFM) respectively.

Türk Fizik Derneği
1950
Turkish Physical Society

EXPERIMENTAL DETAILS

In this study, undoped and In doped CuO films (at 4, 8 and 12 %) were deposited onto microscope glass (1cmx1cm) by ultrasonic spray pyrolysis technique (USP) at the substrate temperature of 350±5°C controlled by using an iron-constantan thermocouple. A photograph of the ultrasonic spray pyrolysis system is given in Figure 1. The spraying solution was prepared by mixing the 1:1 volumes of copper acetate [$Cu(CH_3COO)_2$] and indium chloride [$InCl_3$] at solution molarity (0.01M) and dissolved in deionized water. Totally, 150 ml of solution was used and sprayed for 30 min. The solution flow rate was kept at 5 $ml.min^{-1}$and controlled by a flowmeter. The compressed air was used to as a carrier gas with a pressure of 10^5 Pa.



FIGURE 1. An image of the ultrasonic spray pyrolysis system.

The electrical resistivities were measured at the room temperature by using Keitley 2601 A System Sourcemeter and the surface characterization of the films analyzed by using atomic force microscope (AFM, Park-System XE-70 Model). SEM analysis of thin films was used scanning electron microscopy (SEM, JEOL JSM-7100F). PHE 102 Spectroscopic Elipsometer was used to determine the thicknesses of the films. The amounts of spray solution prepared for the films and the thicknesses of the films are given in Table 1.

RESULTS AND DISCUSSION

Electrical Properties

When the resistivity values of CuO and CuO:In doped films were examined, it was found that the resistivity values increased up to %8 In doped. However, this increase then declined again with a %12 contribution and decreased to almost the same level with undoped thin films. However, when the changes in carrier densities from the table 2 are examined, it is observed that the carrier density of In doped films decreased significantly compared to undoped CuO films. We believe that the main reason for this decrease is the defects in the structure along with the In doped. We used hot probe technique to determine the conductivity types and it was seen that all the films have p-type electrical conductivity.

TABLE 2. The resistivity, mobility, carrier density values and conductivity types of CuO:In films.

Sample Code	Resistivity (Ω·cm)	Mobility μ ($cm^2 V^{-1} s^{-1}$)	Carrier Density n (cm^{-3})	Conductivity Type
CuO	$1,62\times10^1$	$4,3\times10^{-3}$	$4,08\times10^{19}$	p
CuO:In (%4)	$4,35\times10^2$	$7,89\times10^1$	$4,39\times10^{13}$	p
CuO:In (%8)	$2,72\times10^2$	$1,35\times10^1$	$1,54\times10^{15}$	p
CuO:In (%12)	$3,26\times10^1$	$4,18\times10^1$	$1,17\times10^{14}$	p

ISBN:978-605-83516-6-0

MORPHOLOGICAL PROPERTIES

When the AFM images and data's given in Figure 2,3 and Table 3 were examined, it was observed that undoped CuO thin films had a smooth surface shape and surface images gradually deteriorated with increasing In contribution ratio.. When the roughness values of the undoped and In doped CuO thin films were examined, the defects observed in the images were confirmed. Roughness values of around 5nm for undoped CuO films increased to 25nm for 12% In doped films. However, if the white dots seen on the surface are considered as defects in the structure, the growing white dots became more prominent with the In contribution. When AFM analysis is considered together with electrical and structural analyzes, the defected structure and decreasing carrier concentration values together with the In contribution are the result of the same reason as the defects seen in surface topography.

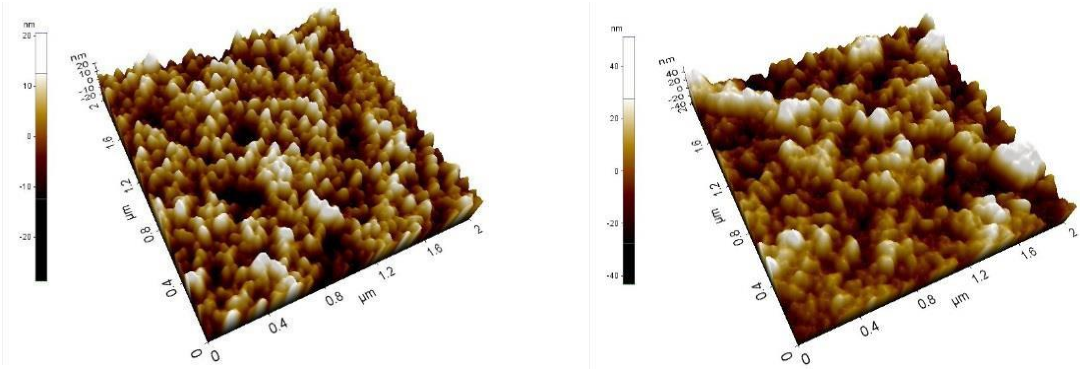


FIGURE 2. (a) undoped CuO, (b) %4 In doped CuO thin film's AFM

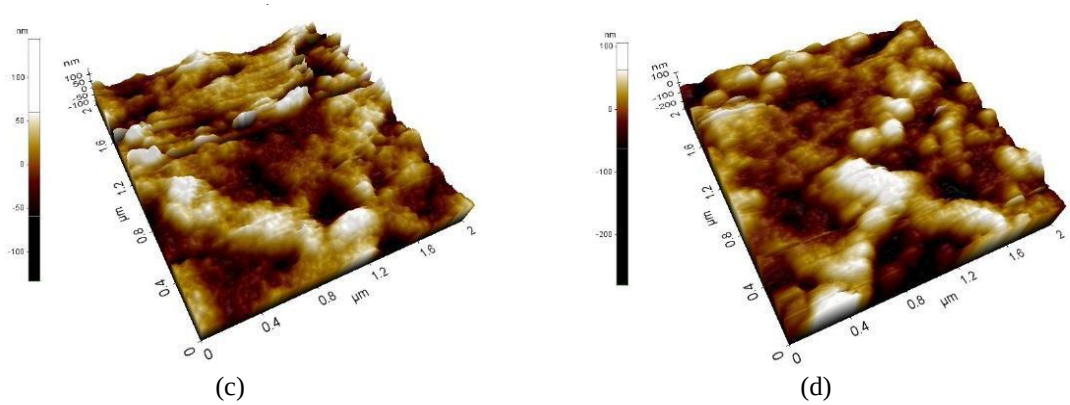
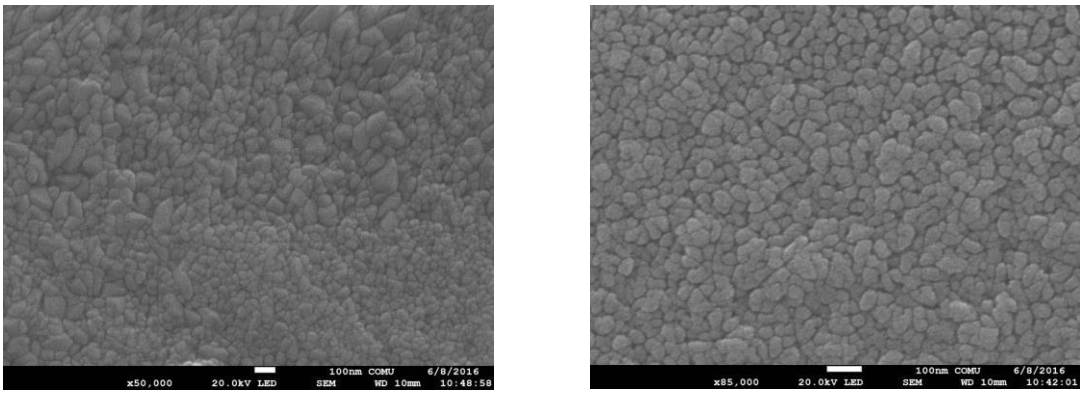


FIGURE 3. (c) %8 In doped CuO, (d) %12 In doped CuO thin film's AFM images.

TABLE 3. The roughness values of CuO:In Films.

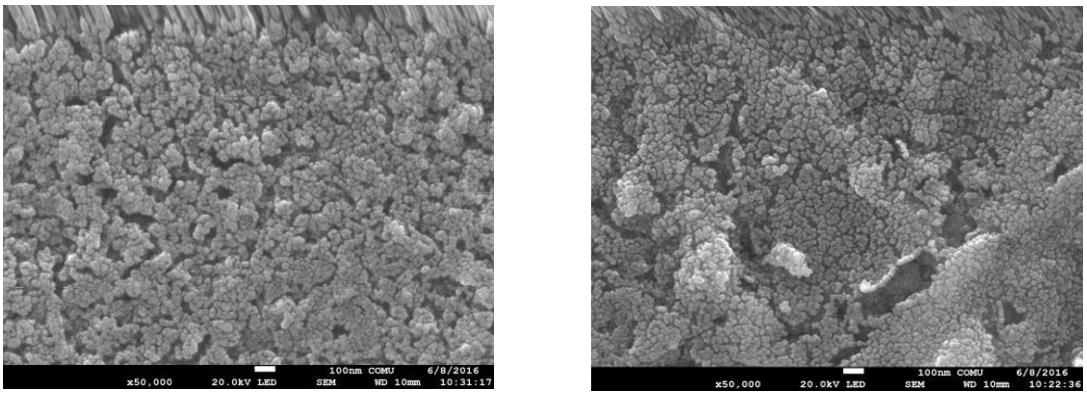
Sample	Roughness (Ra)(nm)
CuO	5.037
CuO: In (%4)	11.045
CuO: In (%8)	24.654
CuO:In (%12)	25.262

Surface images of 50.000 magnification of CuO and CuO:In (4-8-12%) thin films are given in Figure 4 and 5. SEM studies confirmed that all films had an almost homogeneous surface morphology. When the surface images of CuO and CuO: In (4-8-12%) thin films were examined, significant changes was observed that the surface with the addition of In. We were seen different structures on their surfaces especially after 4% In doped films. It is seen that the homogeneous structure with the contribution of In is broken down and some threadlike structures are formed. It is thought that the the most important reason for the formation of filamentous structures is that the doped atoms enter the structure completely and created different forms. . In the structural analyzes, which can obtain more comprehensive results from surface analysis, significant changes and defects were observed in the structure of CuO thin films with the addition of In.



(a) (b)

FIGURE 4. (a) undoped CuO, (b) %4 In doped CuO thin film's SEM images.



(c) (d)

FIGURE 5. (c) %8 In doped CuO, (d) %12 In doped CuO thin film's SEM images.

CONCLUSIONS

In this study, undoped and In doped CuO films were deposited onto glass substrates by ultrasonic spray pyroylsis at the substrate temperature of 350±5°C and the effect of In doping on electrical and morphological properties of CuO films was investigated. Electrical investigations showed that the resistivity values of the all films were changed between $1.62x10^{1}$-$4.35x10^{2}$ (Ωcm) and for the CuO:In thin films has also been found that the resistivity values increase with increasing In doping. It was determined that all the films have p-type electrical conductivity. SEM and AFM studies confirmed that all films had an almost homogeneous surface morphology with a fine microstructure without holes and cracks.

REFERENCES

1. Tang J. Hinds S., Kelley S.O., Sargent E.H., 2008. Chem. Mater., 20:690.
2. Asbrink S., Norrby L.J., 1953. A refinement of the crystal structure of copper (II) oxide with a discussion of some exceptional e.s.d.'s. Acta Cryst., 26, 8-15.
3. Chang H., Jwo C.S., Lo C.H., Tsung T.T., Kao M.J., Lin H.M., 2005. Rheology of CuO nanoparticle suspension prepared by ASNSS. Rev. Adv. Mater. Sci. 10:128-132.
4. Morales J., Sanchez L., Martin F., Ramos-Barrada J.R., Sanchez M., 2005. Use of low-temperature nanostructured CuO thin films deposited by spray-pyrolysis in lithium cells. Thin Solid Films, 133-140
5. Marabelli F., Parraviciny G.B., Drioli F.S., Phys. Rev. B. 1995. 52:1433.
6. Ghijsen J., Tjeng L.H., Elp J.V., Eskes H., Westerink J., Sawatsky G.A., Czyzk M.T. Phy. Rev. B. 1988. 38: 11322.
7. Y.S. Gong, C. Lee, C.K. Yang, J. Appl. Phys. 77 (1995) 5422.
8. E.R. Kari, K.S. Brown, C. Choi, Chem. Commun. (2006) 3311.
9. T. Maruyama, Jpn. J. Appl. Phys. 37 (1998) 4099.
10. K. Santra, C.K. Sarkar, M.K. Mukherjee, B. Ghosh. Thin Solid Films 213 (1992) 226.
11. S.Kose, E. Ketenci , V. Bilgin, F. Atay, I. Akyuz. Curr. Appl. Phys. 12 (2012) 890.
12. J. Morales, L. Sanchez, F. 13. Martın, J.R. Ramos-Barrado, Miguel Sanchez, Electrochim. Acha 49 (2004) 4589.
13. V.F. Drobny, D.L. Pulfrey, Thin Solid Films 61 (1979) 89.
14. Mosbah, M.S. Aida, J. Alloys Compd. 515 (2012) 149.
15. F. Ynineb, A. Hafdallah,M.S. Aida, N. Attaf, J. Bougdşra, H. Rinnert, S. Rahman, Mater. Sci. Semicond. Process. 16 (2013) 2021.

BOOK OF FULL TEXT PROCEEDINGS TURKISH PHYSICAL
SOCIETY 35th INTERNATIONAL PHYSICS CONGRESS (TPS35)
TPS35, Vol.01, No.04, pp.298-303.
ISBN:978-605-83516-6-0

15 December 2019

Characterization of DLC Thin Films Deposited on Glass and Si Substrates under The Influence of Electric Field with ECR-MP Method

Mehmet ESEN[1, a)] and Mustafa ESEN[2, b)]

[1]*Cukurova University, Adana Vocational School of Higher Education, Adana, Turkey*
[2]*Isparta University of Applied Sciences, Technical Sciences Vocational School of Higher Education, Isparta, Turkey*

[a)]Corresponding author: mehesen@cu.edu.tr
[b)] mustafaesen@isparta.edu.tr

Abstract. In this study, we searched the influence of electric field on DLC thin films. We used Electron Cyclotron Resonance Chemical Vapor Deposition (ECR-CVD) method for forming DLC thin films. Electric field (applied voltage range 150-200 volts) and bias voltage (800-1200 V) were applied in thin film production stage and the films produced under these conditions were examined. XRD, AFM, optical, Raman techniques were used in characterization. It is observed that the crystallization increases and the optical properties of the films absorption and transmission spectra change under the effect of electric field.

INTRODUCTION

Carbon-based thin films have very unique properties as high thermal conductivity, high stability, high mechanical strength near room temperature. For this reasons, they are very suitable for electro-optical devices, solar cells, carbon wear coatings etc. First ion beam method was used for carbon film deposition by Aisenberg and Chabot in 1971. They have noticed that these carbon films they produced had similar properties like diamond so they named it “Diamond-Like Carbon” (DLC) [1]. Deep interest has been paid for experiments using carbon based material coatings such as DLC and amorphous carbon forms. DLC carbon based coatings have smooth surface, low friction coefficient of friction, high hardness, wear resistance, thermal conductivity, good adhesion, chemical inertness, long wavelength transparency. DLC films can be grown at room temperature [2]. DLC films has several advantages such as coating metal parts, cutting tools, reflective layer for sun glasses, motor parts such as piston rings. DLC is biocompatible and can be used in implants, in-body metal parts such as orthopedic DLC coated screw and orthodontic treatment parts [4].

METHODOLOGY

The growth of thin films are obtained using various methods, one of which is the Electron Cyclotron Resonance Chemical Vapor Deposition method (Fig. 1). This technique is very attractive for coating due to high electron temperature and high ionization rate. ECR-CVD method has advantages such as high power ionization and ions can be accelerated in both the grid and the substrate via bias voltages [3].

Türk Fizik Derneği
1950
Turkish Physical Society

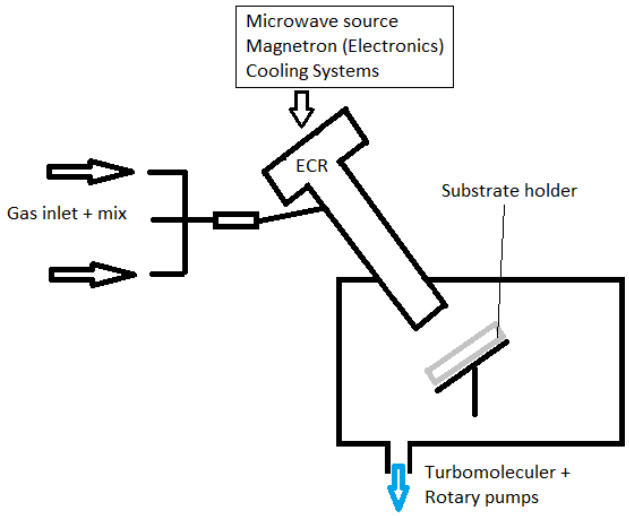


FIGURE 1. ECR-CVD and reaction chamber used for coating.

Electric field was used for deposition Carbon films with ECR-CVD.

In this work, we deposited carbon based DLC thin films with ECR-CVD method on glass and silicon substrates. We investigated the structural and optical properties of grown films optic spectrometer, atomic force microscopy (AFM), X-ray diffractometer (XRD).

.

RESULTS AND DISCUSSION

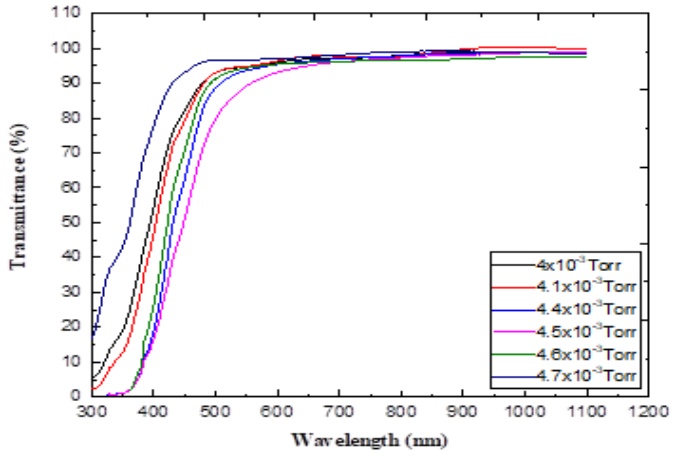
In this work, ECR-MP CVD plasma system was used for depositing DLC films. The substrates were cleaned in de-ionized water, methanol and dried with nitrogen gas. ECR system applies 875 Gauss onto the coils with microwave frequency of 2.45 GHz. Plasma chamber pressure was set at 1.3×10^{-3} Torr at room temperature.

TABLE 1. Parameters for films deposited on glass substrate (a) with electric field (b) without electric field.

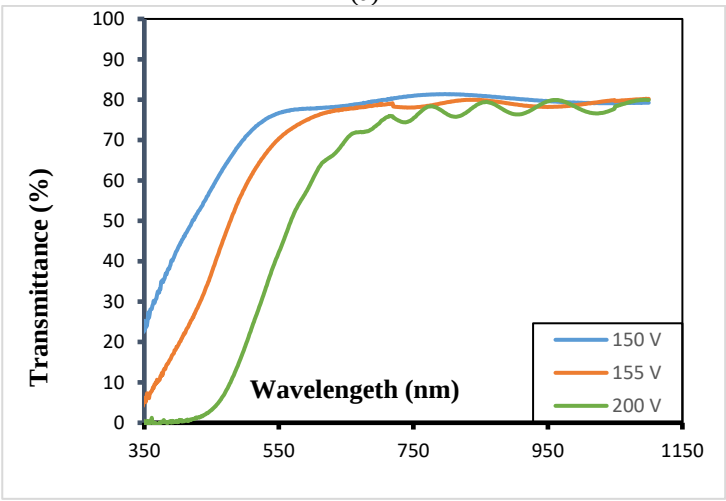
(a) Working pressure = 4.5×10^{-3} Torr Deposition time = 30 min, Temperature = 25 ◦C on Glass substrate with electric field						
Sample Name	**Deposited Film**	**Distance (cm)**	**Applied Voltage (V)**	**CH_4 Gas Flow (sccm)**	**Microwave power (Watt)**	**Ion Energy (keV)**
S-11	DLC	3.7	150	8.87	45	0.3
S-8	DLC	3	155	9.12	47.5	0.2
S-9	DLC	1.26	200	8.93	50	0.2

(b) Microwave power = 45W Deposition time = 30 min, Temperature = 25 ◦C On Glass substrade without Electric Field			
Sample name	**Film type**	**Working Pressure (Torr)**	**CH_4 Gas Flow (sccm)**
S-2	Amorphous	$4x10^{-3}$	6.41
S-6	DLC	$4.5x10^{-3}$	8.93
S-7	DLC	$4.6x10^{-3}$	8.97
S-10	Amorphous	$4.7x10^{-3}$	8.99

Fig. 2 demonstrates the effects of applied voltages onto thin films and working pressures on optical reflectance properties at 350-1150nm.



(a)



(b)

FIGURE 2. (a) Optical Properties of carbon films without Electric Field, (b) Optical Properties of carbon films with Electric Field

ISBN:978-605-83516-6-0

Peak position, half-widths, intensity and I_D/I_G ratios of 0.472, 0.485, 0.535 were obtained from Raman measurements for samples S-9 (200V), S-10 (unbiased) and S-11 (150V), respectively. (Fig. 3).

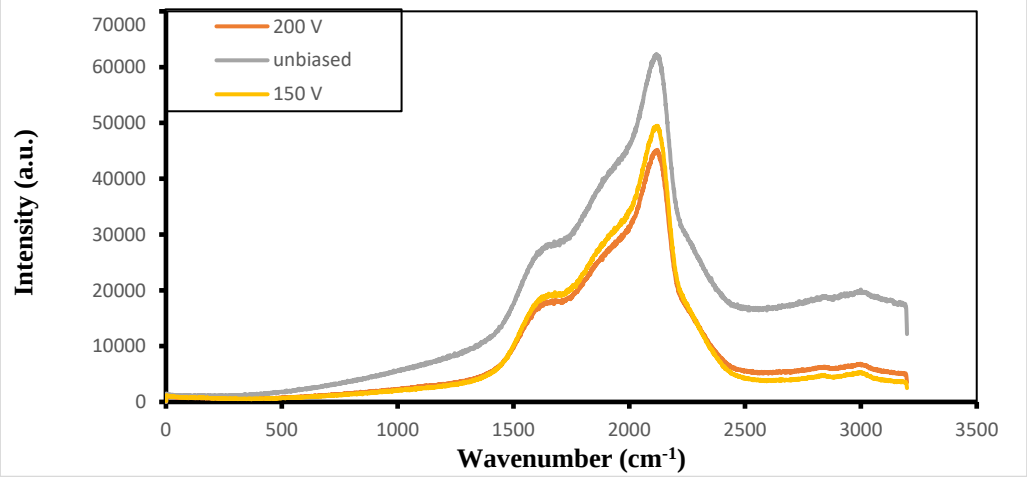


FIGURE 3. Raman spectra of carbon thin films fabricated on the glass substrates at different bias voltages

As shown in Fig. 4, XRD results show no difference between biased and unbiased samples that formed on silicon wafer.

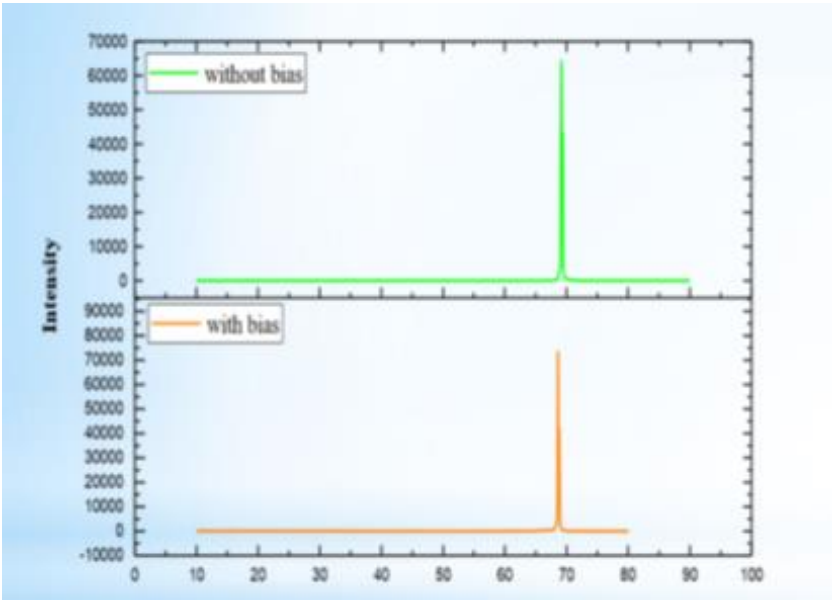


FIGURE 4. XRD results of biased and unbiased (150 V) films.

AFM images of the biased and unbiased films show that if bias voltage is applied onto the surface, roughness increases and surface islands rise.

ISBN:978-605-83516-6-0

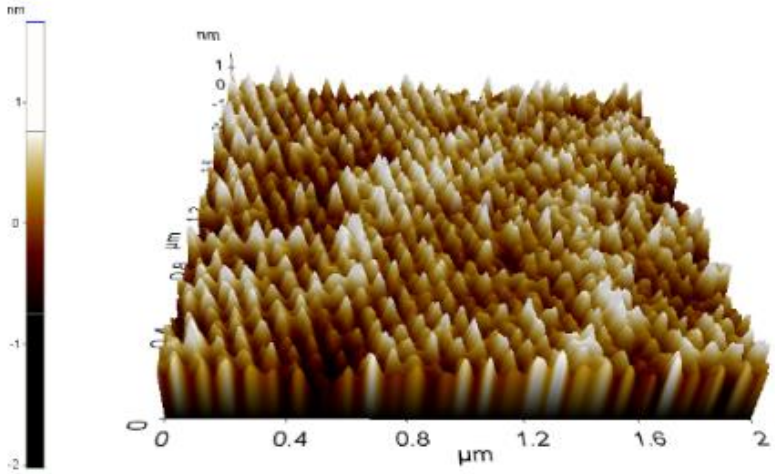


FIGURE 5. AFM images of unbiased film (1-3nm).

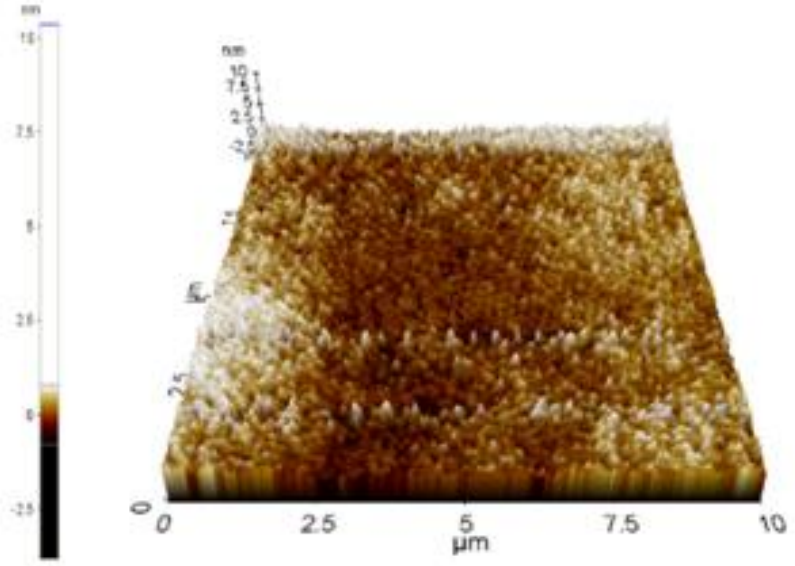


FIGURE 6. AFM images of biased film (3-10nm).

CONCLUSION

This experimental study investigates the effects of biased voltage on optical and structural characteristics of DLC films. For optical characteristics; the applied voltage reduces the transmission ratio and absorption zones on transmission (550-1150 nm) region. Depositing C and H ions with different q/m ratios at 150V and 200V results different C/H regions which narrows optical energy gaps of the films from 2.16eV to 1.97eV. Raman and XRD studies show that applying a bias voltage results in more crystalline film formation. The deposited film shows a more regular structure. From AFM results, it was observed that the unbiased deposited films were relatively smoother and more uniform as compared to those of the biased film.

ACKNOWLEDGMENTS

The authors would like to present their sincere thanks to staff of Cukurova University, Department of Physics, Plasma Laboratory for providing opportunity in conducting this study. This work was financially supported by Cukurova University, Scientific Research Projects under Grant Number: FBA-2018-10899.

REFERENCES

1. Aisenberg, S., & Chabot, R. Ion-beam deposition of thin films of diamondlike carbon. Journal of applied physics, 42(7), 2953-2958(1971).
2. Bewilogua, K., & Hofmann, D. History of diamond-like carbon films—from first experiments to worldwide applications. Surface and Coatings Technology, 242, 214-225 (2014).
3. Cui, J., Rusli, Yoon, S. F., Teo, E. J., Yu, M. B., Chew, K., ... & Watt, F. Effect of radio-frequency bias voltage on the optical and structural properties of hydrogenated amorphous silicon carbide. Journal of Applied Physics, 89(11), 6153-6158 (2001).
4. Roy, R. K., & Lee, K. R. Biomedical applications of diamond-like carbon coatings: A review. Journal of Biomedical Materials Research Part B: Applied Biomaterials: An Official Journal of The Society for Biomaterials, The Japanese Society for Biomaterials, and The Australian Society for Biomaterials and the Korean Society for Biomaterials, 83(1), 72-84(2007).

BOOK OF FULL TEXT PROCEEDINGS TURKISH PHYSICAL
SOCIETY 35th INTERNATIONAL PHYSICS CONGRESS (TPS35)
TPS35, Vol.01, No.04, pp.304-306.
ISBN:978-605-83516-6-0

15 December 2019

Enhancing Tribological Characteristics of Piston Rings of Internal Combustion Engines Using ECR-CVD Coating Method

Mustafa ESEN[1, a)], Mehmet ESEN[2, b)] and Ali Can YILMAZ[2, c)]

[1]*Isparta University of Applied Sciences, Technical Sciences Vocational School, Isparta, Turkey*
[2]*Cukurova University, Adana Vocational School, Adana, Turkey*

[a)]Corresponding author: mustafaesen@isparta.edu.tr
[b)]mehesen@cu.edu.tr
[c)]acyilmaz@cu.edu.tr

Abstract. In this study, it is aimed to improve the friction and abrasion resistance of steel piston rings of internal combustion engines. The piston rings are the parts most subjected to friction during operation. Carbon and carbon nitride coatings are known to improve anti-friction and durability of the coated surface. Thanks to ECR-CVD technique, smooth and durable carbon/nitride surface coatings can be obtained. In this study, bias voltage was applied during coating process (600V-800V) within specified nitrogen/methane gas ratio. The coated steel rings were examined with SEM, EDX, hardness and abrasion analyses. The results depicted that the tribological characteristics of the piston rings were improved when the rings were coated along with the applied bias voltage and nitrogen gas addition. Coating of the surfaces provided diminished roughness and increased hardness which led to reduced friction and wear.

INTRODUCTION

The key role of automotive manufacturers has been producing high efficiency and long life fired engines to meet emission restrictions and reduce fuel consumption. Internal combustion engines consist of several moving parts which are responsible for power transmission. In order to reduce energy consumption of a reciprocating engine, diminishing friction forces between piston rings and liner is of great importance hence the piston is the main part of the combustion chamber which transmits the power formed by the explosion of the fuel-air mixture. Friction between piston and cylinder lining of an internal combustion engine causes approximately 50% of the total power loss [1,2]. Piston rings are used for isolating the combustion chamber from the oil sump region of the engine to prevent leakage of unburned or burned gases towards the oil sump or oil vapors towards the combustion chamber. These rings should depict robust endurance against the tremendous pressure and temperature conditions as well as resisting to high-level friction and wear. Due to problems mentioned above, this study focuses on reducing frictional losses and wear rates between piston rings and liner by Electron Cyclotron Resonance Chemical Vapor Deposition (ECR-CVD) coating on the contact zones of the piston ring. ECR-CVD coating also provided elevated hardness of the ring material which led to improved strength. This phenomenon will also yield more efficient and low maintenance cost engine to be built.

METHODOLOGY

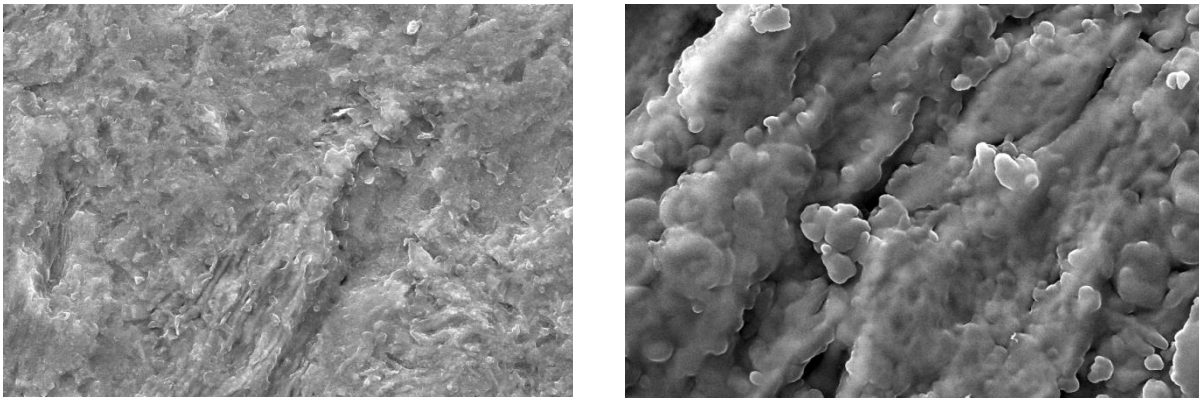
Carbon-based coating was deposited using ECR-CVD plasma technique. This technique comprises of a gun in which the plasma forms to ionize gas or gas mixture (accelerated) within a magnetic field. Accelerated gases bombard the surface to be coated and other non-participating elements are expelled from the reaction chamber. The plasma possesses high electron temperature and ionization characteristics. The substrate to be coated is bombarded by well-ionized and accelerated ions in case of applying high voltage to the substrate or grid [3].

Türk Fizik Derneği
1950
Turkish Physical Society

The piston ring surface was first pre-treated in a low-concentration HCl bath to facilitate the adherence of the coating and then rinsed with pure water and dried using nitrogen gas. 5.76 sscm of methane along with 8 sscm of nitrogen gas was sent onto the steel surface to form layers comprising of carbon-nitrogen diamond-like coating (DLC) under the vacuum of $4.5*10^{-3}$ Torr. Methane and nitrogen gases were introduced into the reaction chamber through two separate control valves and then into the ECR plasma gun under plasma ionization power of 60 W and voltage of 600-800 V (for accelerating) via an antenna. The piston ring surface was placed 2-3 cm away from the plasma gun grid to ensure utilizing most of the plasma without scattering and convey adherence on the substrate.

RESULTS AND DISCUSSION

Fig. 1 demonstrates the SEM images of the uncoated and DLC coated surfaces. As can be seen from the images, the coated surface possesses colossal carbon clusters/islands (in order of μm) which, in the first place, develop by preserving the original structure of the metal surface but in the subsequent stage, circular clusters specified the coating characteristics. The diameter of these circular clusters range between 0.5-1.5 μm.



(a) (b)

FIGURE 1. SEM images of (a) Uncoated piston ring surface, (b) DLC coated piston ring surface *(both 20 μm in horizontal direction, 5000x magnification)*

Elemental compositions of two surfaces (EDAX) are shown in **Table 1**. Nitrogen-doped carbon coated surface consists of considerable amount of carbon and nitrogen percentages compared to those of uncoated surface. The results of the coated surface in **Table 1** belong to the coating thickness of 2 μm. Elemental analysis proves that carbon and nitrogen atoms were included in the surface composition in which carbon was the dominant element.

TABLE 1. EDAX results of the uncoated and coated surfaces

	Uncoated				DLC coated		
	Weight %	**Atomic %**	**Net Int.**		**Weight %**	**Atomic %**	**Net Int.**
C	9.34	30.79	129.6	***C***	***30.45***	***62.23***	***623.36***
O	2.81	6.95	124.52	***N***	***2.36***	***4.13***	***22.47***
Mn	1.51	1.08	29.98	Mn	3.75	5.76	123.96
Fe	86.34	61.18	3571.9	Fe	63.44	27.88	3089.2

Macrohardness tests were performed (Qness/Q250 Ms) under the normal load of 10 kg and the results (**Table 2**) show that hardness of the specimen surface depicted a considerable increment when coated with nitrogen-doped carbon (DLC). A hardness increment of 32.3% was obtained when the surface was DLC coated and this increment facilitates the strength and resistance to friction improvement.

TABLE 2. Macrohardness test results

Surface	**HRC**
Uncoated	34
DLC coated	45

The surface roughness is a crucial parameter in terms of defining wear characteristics. The measurements were conducted via MarSurf M 300 roughness device and referring to results (**Table 3**), maximum roughness (R_z) reduced from 4.260 μm to 3.645 μm (14.4% reduction) when the surface is deposited with DLC coating (smoother surface).

TABLE 3. Surface roughness test results

Surface	R_a (μm)	R_z (μm)
Uncoated	0.643	4.260
DLC coated	0.668	3.645

The measurement results (Nanovea) related to wear rate of the surfaces are shown in **TABLE 4**. The mass loss of the coated surface after abrasion test was lower than that of the uncoated surface. Reduced mass loss can be attributed to the higher smoothness (low roughness) and higher hardness of the DLC coated surface.

TABLE 4. Wear rates of the surfaces exposed to abrasion tests

Surface	Mass (before abrasion test)	Mass (after abrasion test)	Mass loss
Uncoated	1.5823 gr	1.5816 gr	0.0442%
DLC coated	1.8820 gr	1.8813 gr	0.0371%

CONCLUSION

This experimental study investigates the effects of DLC coating (using ECR-CVD technique) on tribological characteristics of a piston ring of an internal combustion engine. DLC coating of the piston ring depicted high tribological performance in terms of friction, wear rate and hardness with comparison to those of uncoated surface. Compared to the uncoated surface, 2 μm of coating thickness deposited on the piston ring surface provided 32.3% increment in hardness, 14.4% reduction in roughness and lower wear rate. This coating method represents a promising technique in the context of producing more efficient fired engines.

ACKNOWLEDGMENTS

The authors would like to present their sincere thanks to staff of Cukurova University, Department of Physics, Plasma Laboratory for providing opportunity in conducting this study. This work was financially supported by Cukurova University, Scientific Research Projects under Grant Number: FBA-2018-10899.

REFERENCES

1. M. Kennedy, S. Hoppe and J. Esser, J. MTZ Worldwide 73, 40-41 (2012).
2. M.K.A. Ali, H. Xianjun, L. Mai, C. Bicheng, R.F. Turkson, C. Qingping, Wear 365, 270–281 (2016).
3. J. Cui, S.F. Yoon, M.B. Yu, K. Chew, J. Ahn, and Q. Zhang, J. of Appl. Physics 89, 2699 (2001).

BOOK OF FULL TEXT PROCEEDINGS TURKISH PHYSICAL
SOCIETY 35th INTERNATIONAL PHYSICS CONGRESS (TPS35)
TPS35, Vol.01, No.04, pp.307-316.
ISBN:978-605-83516-6-0

15 December 2019

Graphene Oxide Assembled Au-based Nanocomposite for Temperature Dependent InP Heterojunction Devices

İmran KANMAZ[1], Ali BALTAKESMEZ[2], Cengiz AYKAÇ[3], Betül GÜZELDİR[3,a)] and Mustafa SAĞLAM[3]

[1]*Department of Renewable Energy Sources/Teknologies, Faculty of Arts and Sciences, Karadeniz Technical University, 61080 Trabzon, Turkey*
[2]*Department of Electricity and Energy, Technical Scientific Vocational School, Ardahan University, 75000 Ardahan, Turkey*
[3]*Department of Physics, Faculty of Sciences, Atatürk University, 25240 Erzurum, Turkey*

a)Corresponding author: bguzeldir@atauni.edu.tr

Abstract. The graphene oxide (GO) nanocomposite samples decorated by Au nanoparticles (NPs) were successfully synthesized using a modified Hummer's method and the effect of the barrier height modifacition of InP heterojunction devices were investigated. The samples were characterized by Raman spectroscopy, UV-vis spectroscopy, TEM and SEM measurements. The current-voltage (I-V) characteristics of the AuNPs-GO /n-InP junction were studied in the temperature range of 80-320 K in the steps of 20 K. The forward-bias I-V-T characteristics of AuNPs-GO/n-InP junctions were successfully explained in terms of the thermionic-emission (TE) mechanism with a double Gaussian Distribution of barrier heights. The better I-V characteristics of the AuNPs-GO/n-InP junction may be attributed to the combined effect of the conductivity of GO and Au nanoparticles, and the presence of some surface states or recombination centers near the surface of n-InP.

INTRODUCTION

The lnP heterostructure system is potentially useful for optoelectronic, high-speed digital, and high-frequency microwave device applications. They have become a promising candidate for the light source of an optical fiber communication system because of the recent development of low-loss, low-dispersion optical fibers. Also, they are necessary for the efficient operation of a number of optoelectronic and transport devices, such as photodetectors, light-emitting diodes, Gunn diodes, and high-speed heterojunction transistors [1-4].

Nanoparticles of different materials such as gold, platinum, copper and silver have been widely studied due to their important properties. Graphene, a two dimensional atomically thin material has caught the attention of researchers due to its remarkably high carrier mobility and radically distinctive band structure. The discovery of graphene and graphene based nanocomposites in this regard is a breakthrough and plays a vital role in earth with remarkable potential applications such as high speed and radio frequency logic devices, thermally and electrically active nanocomposites, sensors, electronic circuits, elastic and transparent electrodes for displays and photovoltaic cells [5-8].

In this study, we report the AuNPs-GO nanocomposites were characterized by Raman spectroscopy, UV-vis spectroscopy, transmission electron microscopy (TEM) and scanning electron microscopy (SEM). After well characterization of the AuNPs-GO nanocomposites, they were used as an interface layer over an n-type InP wafer, contacted by Au to fabricate a heterojunction. Finally, the forward bias I-V-T characteristics of this junction have been systematically analyzed over the temperature range 80-320 K with steps in 20 K.

EXPERIMENTAL PROCEDURE

The Au nanoparticles were synthesized according to a procedure described in the literature [9]. The, $AuNO_3$ (3×10^{-2} M) and 11-mercaptoundecanoic acid (MUA) (1.3×10^{-4} M) were dissolved in 10 mL of ethanol under stirring at room temperature. Then, a saturated solution of $NaBH_4$ in ethanol was added drop-wise to this solution, and the mixture was stirred at room temperature for 2 h. The excess of unbound thiol was removed by a centrifuge, and the nanoparticles were washed three times with a mixture of hexane and ethanol.

Graphene oxide (GO) was synthesized from graphite powder by a modified Hummer's method [10]. Firstly, graphite powder (10 g) was gradually added into a hot solution of concentrated H_2SO_4 (50 mL) containing $K_2S_2O_8$ (5 g) and P_2O_5 (5 g). The mixture was kept at 80 ^{0}C for 6 h, and then the resulting dark blue mixture was slowly cooled to room temperature. The mixture was diluted and filtered. The filtered product was dried under overnight at 60 ^{0}C. After this preoxidizitation process, the graphite powder (1 g) was put into 50 mL of concentrated H_2SO_4 at 0 ^{0}C, then $NaNO_3$ (1 g) and $KMnO_4$ (6 g) were added slowly into the mixture within 1 h to avoid a sudden increase in temperature. The solution was stirred at 35 ^{0}C for 3 h, followed by adding 50 mL of distilled water. After being stirred for 15 min, the reaction was terminated by addition a large amount of water (500 mL) and 30% H_2O_2 solution (8 mL). The product was filtered and washed with HCl and water. Finally, the resulting purified GO powders were collected by centrifugation and dried at 60°C for 36 h in an air-dry oven.

The n-type InP wafers were used in this study. The wafers were cleaned in standard organic solutions (trichloroethylene, acetone and methanol) and the acid solution (H_2SO_4:H_2O_2:H_2O=3:1:1) for 60 s, (HF:H_2O=1:10) for another 60 s. Between each polishing step the samples were rinsed in de-ionized water and dried nitrogen gas. Ohmic contacts on the back side were formed an Au-Ge alloy; followed by a temperature treatment at 465°C during 5 min. AuNPs-GO nanocomposites has been deposited on the other face of n-type InP wafer with spin coating technique. Circular dots of Au were then evaporated at pressure of 10^{-7} Torr to form the Schottky diodes and the fabrication of the Au/AuNPs-GO/n-InP junction were completed.

Raman spectrum were recorded on a WITec Alpha300 Micro Raman instrument. UV-Vis electronic absorption spectra were recorded on a Shimadzu UV-3600 Plus UV-VIS-NIR instrument. TEM images were obtained on a FEI Technai G2 Spirit BiO (TWIN) instrument working at 120 kV. SEM images were acquired on a Zeiss Sigma 300 field emission SEM instrument. The I-V measurements of the junction were carried out in the temperature range of 80-320 K using Leybold Heraeus closed-cycle helium cryostat with KEITHLEY 487 Picoammeter/Voltage Source.

RESULTS AND DISCUSSION

GO film and AuNPs-GO nano-composite film coated on the glass and the InP substrates by spin coating were analyzed by the Raman spectroscopy due to it give reliable information about the vibration of the atoms and the chemical composition of material, as seen in Fig. 1. There are two characteristic peaks located at 1331 cm^{-1} (D peak) and 1595 cm^{-1} (G peak) in the Raman spectra of the GO film. The D peak is assigned to the breathing mode of k-point phonons of A_{1g} symmetry, while the G peak is ascribed to the plane vibrations with E_{2g} symmetry which is sensitive to the configuration of sp^2 sites [10]. As for the AuNPs-GO nano-composite film, the measured signal intensity of both D and G peaks is more than one order of magnitude enhanced from GO film while the peak position shift is not observed. It has been widely acknowledged that effect of surface-enhanced Raman scattering (SERS) is owing to electromagnetic and chemical enhancement. The electromagnetic enhancement may cause a high enhancement factor as high as 10^{12}, while the chemical enhancement results in a one to two order of magnitude enhancement. Therefore, it can be attributed that increased signal intensity is mainly due to chemical enhancement because the enhancement factor is about one order of magnitude in our study.

ISBN:978-605-83516-6-0

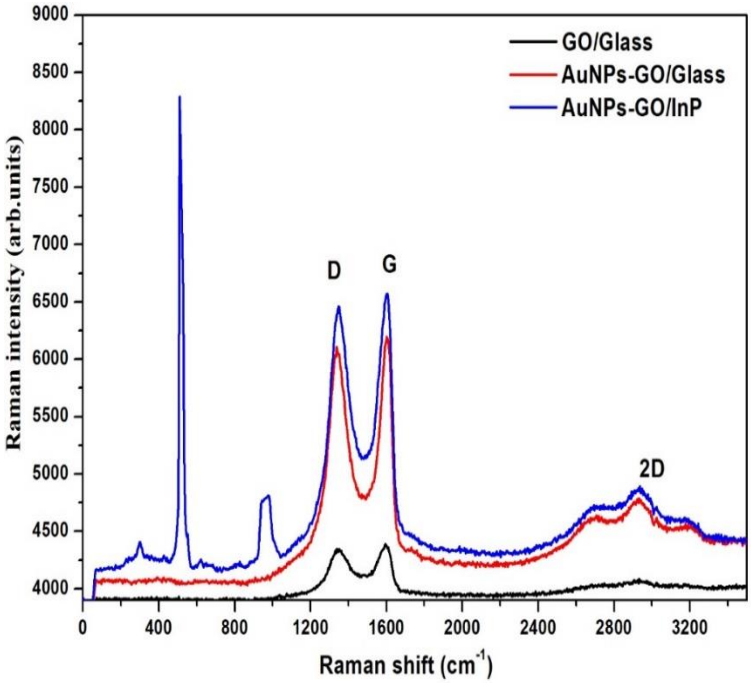


FIGURE 1. Raman spectrum of as-prepared AuNPs-GO nanocomposites.

UV-Vis spectroscopy is one of the most practical and suitable instrument for the characterization of metal NPs. The AuNPs, GO and AuNPs attached on the graphene was confirmed by UV-visible spectra in Fig.2 [11].

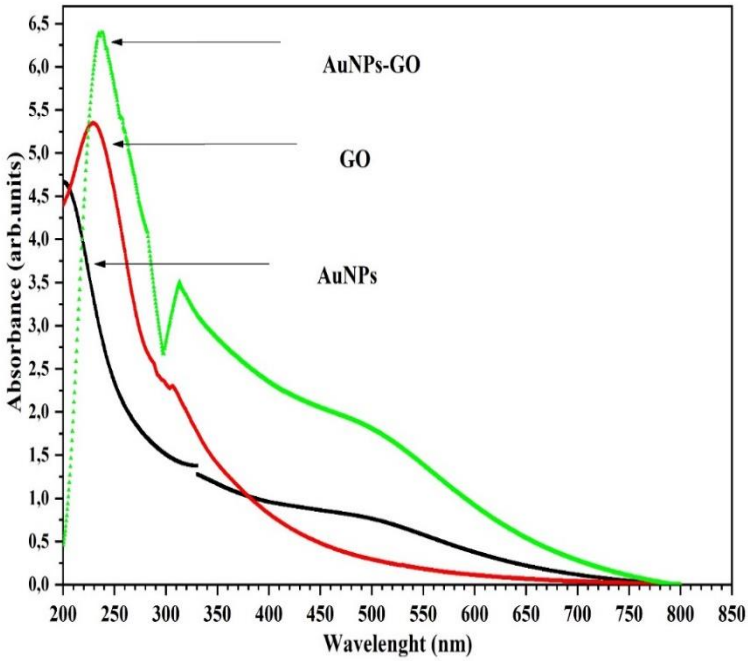


FIGURE 2. UV-Vis electronic absorption spectra of AuNPs, GO and AuNPs-GO nanocomposites.

ISBN:978-605-83516-6-0

The TEM images of AuNPs-GO composite are shown in Fig.3 taken at different magnifications. In Fig.3, different sizes and forms of AuNPs well distributed on the GO surface and it has been caused to the nature and amount of oxidized defects present on the GO surface. It is expected that NP nucleation take place at these defects [11].

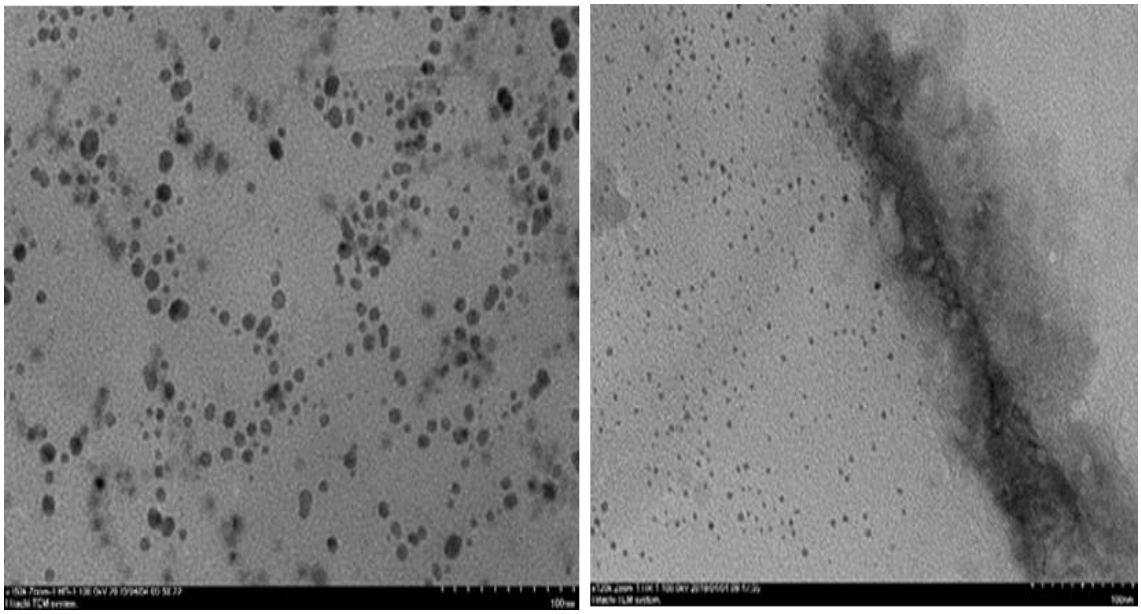


FIGURE 3. TEM images of as-synthesized AuNPs-GO nanocomposites taken at different magnifications.

To understand the more about the structure and surface properties of AuNPs-GO composite, we studied the SEM images were showed in Fig. 4a and 4b. As seen these figures, high density of AuNPs preventing the accumulation of GO sheets and allowing good coverage of the glass and InP surface, respectively. The nanoparticles are on the surface of the film and clearly observed in the SEM.

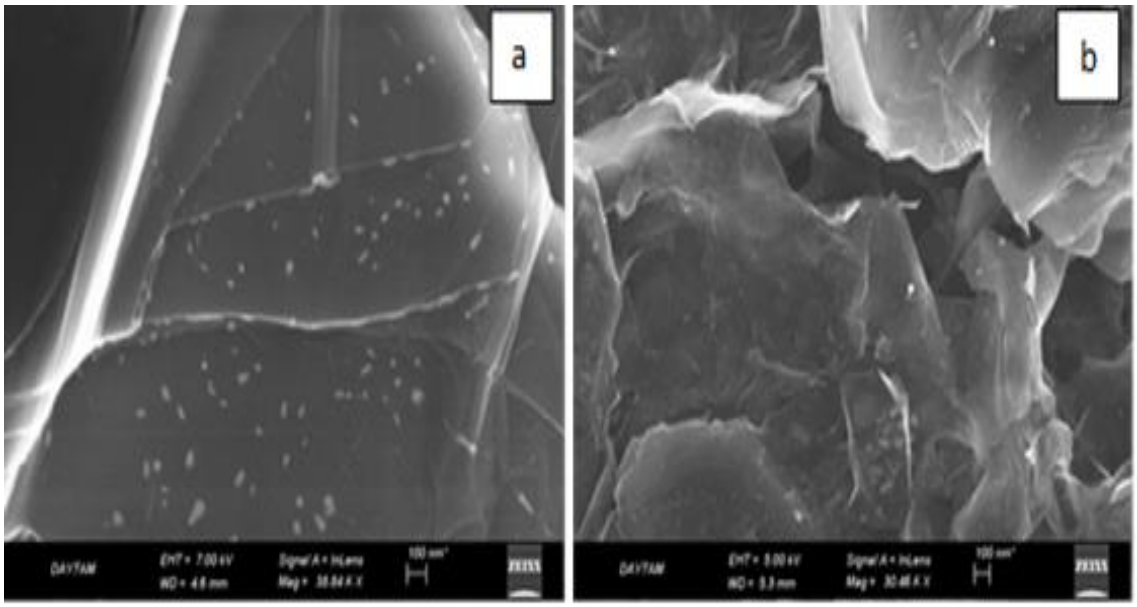


FIGURE 4. A representative SEM image of as-synthesized AuNPs-GO nanocomposites at different scale bars.

The experimental I-V data are analyzed by the well-known equation at forward bias [12],

$$I = I_0 exp\left(\frac{eV}{nkT}\right)\left[1 - exp\left(-\frac{e(V-IR_S)}{kT}\right)\right] \quad (1)$$

where *n* is the ideality factor, *k* is the Boltzmann constant, *e* is the electron charge, *V* is the forward bias voltage, *T* is the temperature, R_s the series resistance and I_0 is the saturation current and is given by

$$I_0 = AA^*T^2 exp\left(-\frac{e\phi_b}{kT}\right) \quad (2)$$

A*, A, Φb are the effective Richardson constant of 9,4 A/cm2K2 for n type InP, the area of the rectifier contact, the experimental zero bias barrier height, respectively. The value of ideality factor n is can be obtained from Eq. (1) as,

$$n = \frac{e}{kT}\frac{dV}{d(lnI)} \quad (3)$$

Typical semi-logarithmic forward bias I-V characteristics of one of the AuNPs-GO/n-InP junctions at various temperatures ranging from 80 to 320K are shown in Fig. 5. As can be seen in Fig. 5, the semi-logarithmic I-V plots of AuNPs-GO/n-InP structure are linear at low forward bias voltage but deviate considerably from linearity at high voltages.

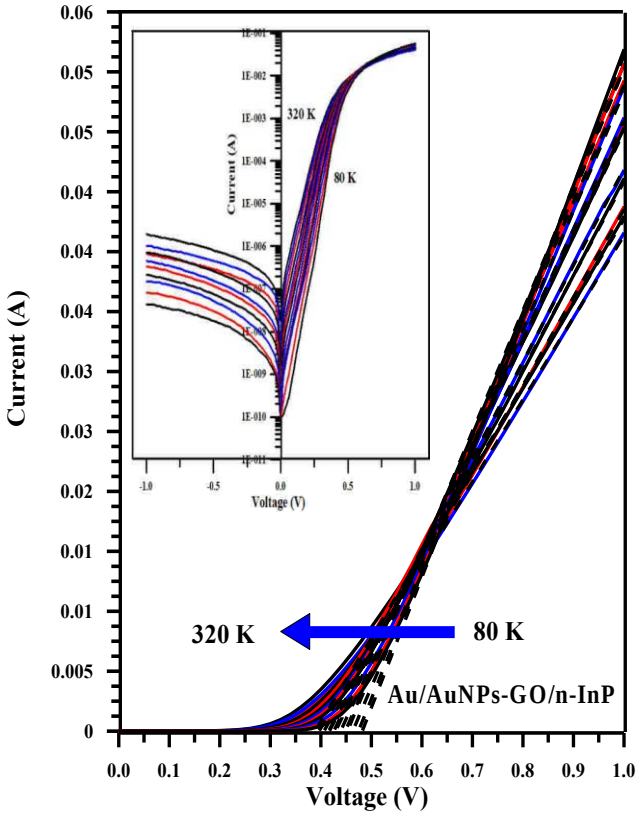


FIGURE 5. The I-V characteristics of the AuNPs-GO /n-InP heterojunction device as a function of temperature.

The saturation current I_0 obtained by extrapolating the linear intermediate voltage region part of linear curve to zero applied bias voltage and the forward current increases with increasing temperature owing to the activation of carriers in Figure 6. The turn on voltage is limited owing to the increase in leakage current, which might be flowing through defects or an AuNPs-GO [13]

ISBN:978-605-83516-6-0

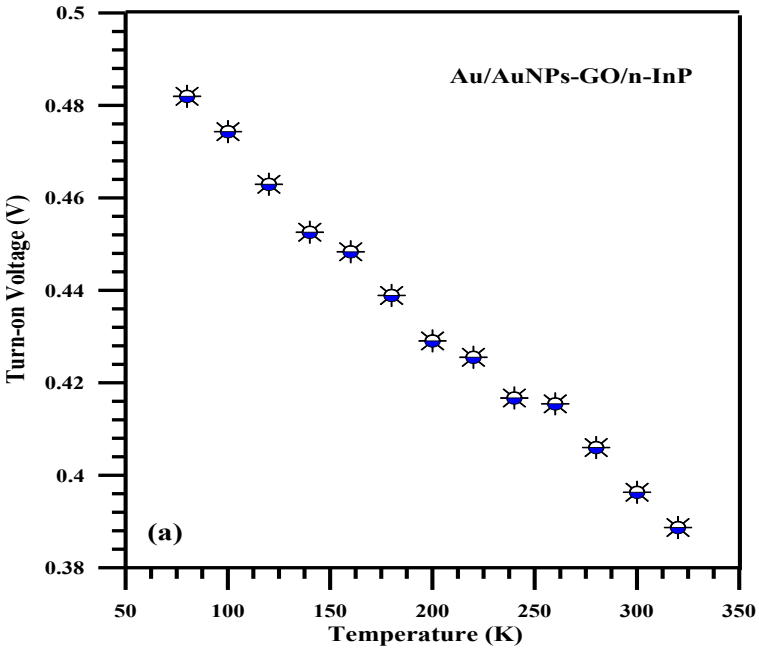


FIGURE 6. The turn-on voltage of the AuNPs-GO/n-InP heterojunction device as a function of temperature.

Fig. 7 shows a linear correlation between the experimental effective barrier heights and the ideality factors and it has also two linear regions with different slopes. From the extrapolation, the homogeneous barrier height has been calculated as 0,740 eV (in the range of 320-180 K) and 0.513 eV (in the range of 160-80 K). We account for the barrier inhomogeneity as a source of the decrease of the effective BH and increase of the n, especially at low temperatures [14]. S

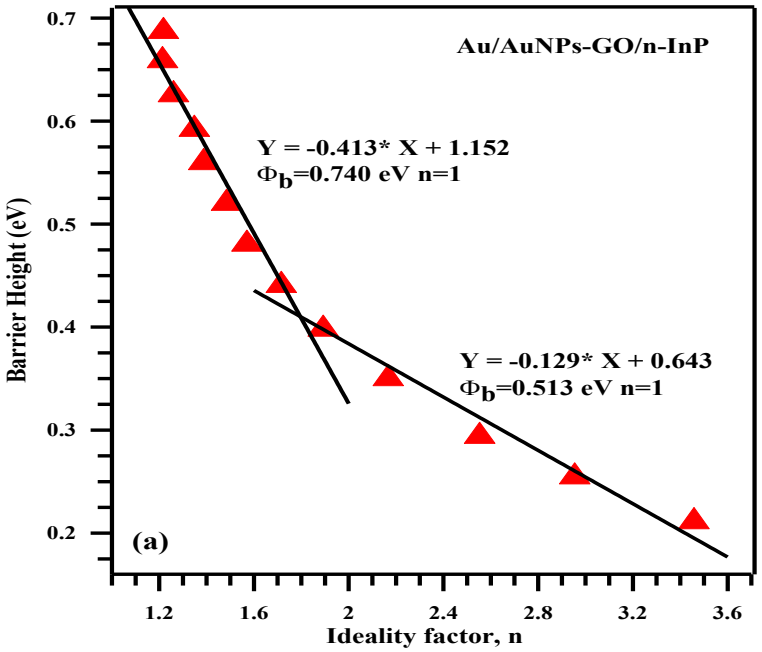


FIGURE 7. Temperature dependence of the zero-bias apparent barrier height and experimental ideality factor for the AuNPs-GO /n-InP heterojunction device.

The nature and origin of the temperature dependence for the Φb and n in metal-semiconductors contacts have been successfully explained on the basis of a TE mechanism with Gaussian distribution of the metal-semiconductors [15]. The current transport across the metal-semiconductor interface is a temperature-activated process, electrons at low temperatures are able to surmount the lower barriers. Therefore, the current transport will be dominated by the current flowing through the patches of lower barrier height. Thus, the value of the ideality factor increases, and the value of the barrier height decreases with decreasing temperature [16-18].

For determining the BH, the $\ln(I_0/T^2)$ versus $(kT)^{-1}$ or $(nkT)^{-1}$ plots of AuNPs-GO/n-InP junction have been given in Fig. 8 and Eq. (2) can be written as [19]

$$ln\left(\frac{I_0}{T^2}\right) = ln(AA^*) - \frac{q\Phi_b}{kT} \tag{4}$$

The activation energy $\ln (I_0/T^2)$ vs. 1/nkT plot (open triangles) with the ideality factors was drawn and this plot yielded 0.569 eV value for effective barrier height. The deviation in graphic at low temperatures was typically an indication of recombination in the depletion region and the presence of the spatially inhomogeneous barrier height and potential of the AuNPs-GO/n-InP device. Namely, current prefentially flow through lower barriers in the potential distribution.

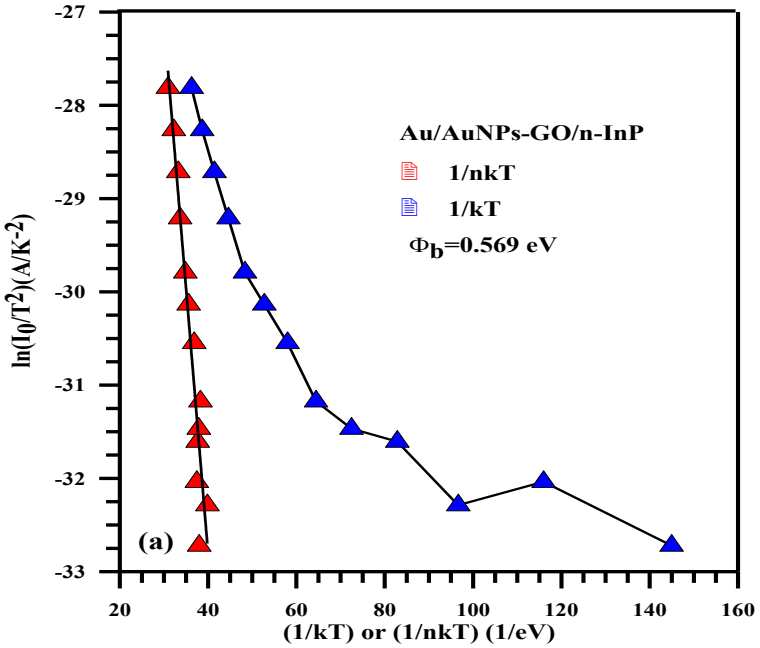


FIGURE 8. Richardson plot (ln(I0/T2) vs 1/kT or 1/nkT) of AuNPs-GO /n-InP heterojunction device.

The appearent barrier height and appearent ideality factor [19], respectively, are given by

$$\Phi_{ap} = \bar{\Phi}_b - \frac{q\sigma_s^2}{2kT} \tag{5}$$

$$\left(\frac{1}{n_{ap}} - 1\right) = -\rho_2 + \frac{q\rho_3}{2kT} \tag{6}$$

where $\bar{\Phi}_{b_0}$ is the mean SBH at zero bias (V = 0) and extrapolated towards zero T, σ_s is the standard deviation at zero bias and $\bar{\Phi}_b = \bar{\Phi}_{b0} + \rho_2 V$ and standard deviation $\sigma_s = \rho_{s0} + \rho_3 V$, where ρ_2, ρ_3 are voltage coefficients that may depend on T. The experimental Φap versus 1/T and nap versus 1/T plots drawn by means of experimental data

obtained from Fig. 9 respond to two lines instead of single line. The values of ρ_2 are 0.336 in 180-320 K and 0.115 in 80-160 K range. The intercept and slope of straight line have given two sets of values of $\bar{\Phi}_{b0}$ and σ_0 as 0.512eV and 64.3 mV in the temperature range of 80-160 K and as 0.959 eV and 126.5mV in the temperature range of 180-320 K. The value is not insignificant even though it is low when compared to the Schottky barrier inhomogeneity.

In general, the low value of $\bar{\Phi}_{b0}$ signifies lower barrier inhomogeneity [19]. Furthermore, considering the barrier height inhomogeneities, the effective Richardson plot is modified as follows:

$$\ln\left(\frac{I_0}{T^2}\right) - \left(\frac{q^2\sigma_s^2}{2kT^2}\right) = \ln(AA^*) - \frac{q\bar{\Phi}_b}{kT} \tag{7}$$

Figure 10 shows the modified In(I0/T2)-(q2σs2/2k2T2) versus 1/T plot. The calculations yielded zero bias mean barrier height Φb0 of 0.541 eV (in the range of 80-160 K) and 0.913 eV (in the range of 180-320 K). The intercepts at the ordinate give the Richardson constant A* as 7.57A/cm2K2 (in 80-160 K range) and 4.21 A/cm2K2 (in 180-320 K), which is very close to the theoretical value of n-Inp of 9.4 Acm2 k2. Hence, the barrier inhomogeneities at the metal-semiconductor interface for AuNPs-GO/n-InP can be explained by thermionic emission with the Gaussian distribution of barrier over the Schottky barrier heights.

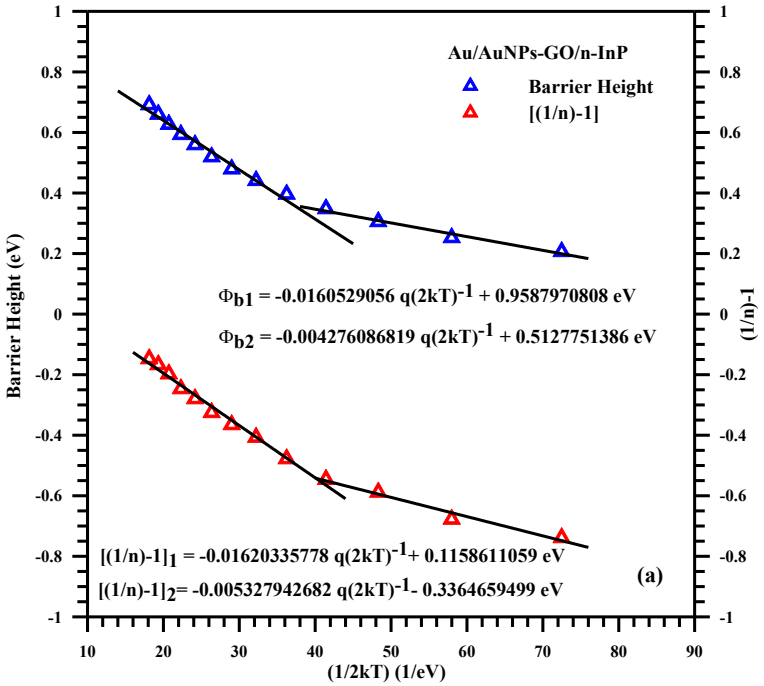


FIGURE 9. Zero-bias ideality factor (opentriangles) and apparent barrier height (opentriangles) versus 1/(2kT) curves of AuNPs-GO/n-InP heterojunction device according to two Gaussian distributions.

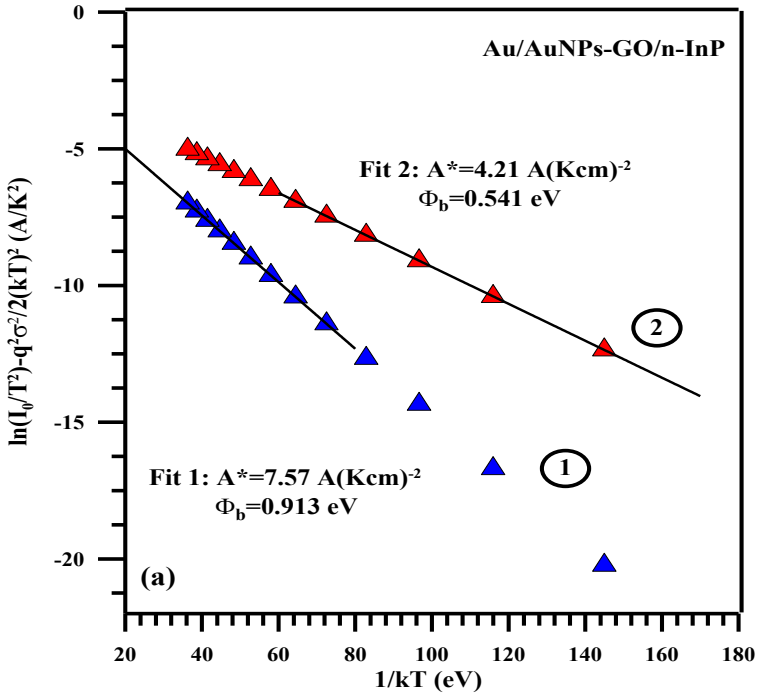


FIGURE 10. Modified Richardson $\ln(I_0/T^2) - q^2\sigma_s^2/2k^2T^2$ vs. 1/T plots for the AuNPs-GO /n-InP heterojunction device according to two Gaussian distributions.

CONCLUSIONS

In this paper, the I-V characteristics of Au/n-InP junction modified with uniform AuNPs-GO nanocomposites interfacial layer have been studied at the temperature range (80-320 K). Firstly; the Raman, Uv-vis, TEM and SEM methods were used for investigation of structural and morphological properties of AuNPs-GO nanocomposites. Secondly, we discussed the adaption of the thermionic emission theory to the Au/AuNPs-GO/n-InP junction with the Gaussian distribution at the changing temperature range. The barrier height, from the I-V characteristics, decreases while the ideality factor n increases with a decrease in temperature due to the barrier inhomogeneity or to local enhancement of electric field which can also yield a local reduction of the barrier height. According to these results, it was shown that AuNPs-GO nanocomposites interface layer can be confidently used in the Au/n-InP metal-semiconductor contacts.

REFERENCES

1. V. R. Reddy, M. S. P. Reddy, A.A. Kumar, C.J. Choi, Thin Solid Films 520 (2012) 5715-5721.
2. H. Umezawa, S. Shikata and T. Funaki, Diamond Schottky barrier diode for high temperature, high-power, and fast switching applications, Japanese Journal of Applied Physics 53 (2014) 1-11.
3. S. Pellegrino, L. Tarricone, MOVPE growth and study of InP-based materials: opportunities and challenges, Materials Chemistry and Physics 66 (2000) 189-196.
4. Y. Wang, J. Chen, J. Xu and X. Li, Modeling of frequency-dependent negative differential capacitance in InGaAs/InP photodiode, Infrared Physics & Technology 89 (2018) 41-45.
5. S. Stankovich, D.A. Dikin, G.H. Dommett, K.M. Kohlhaas, E.J. Zimney, E.A. Stach, R.D. Piner, S.T. Nguyen, R.S. Ruoff, Graphene-based composite materials, Nature 442 (2006) 282-286.
6. A.K. Geim, K.S. Novoselov, The rise of graphene, Nat. Mater. 6 (2007) 183-191.
7. A.K. Bodenmann, A.H. MacDonald, Graphene: exploring carbon flatland, Phys. Today 60 (2007) 35-41.
8. W. Liu, H. Li, C. Xu, Y. Khatami, K. Banerjee, Synthesis of high-quality monolayer and bilayer graphene on copper using chemical vapor deposition, Carbon 49 (2011) 4122-4130.

9. I. Karaduman, E. Er, H. Çelikkan, N. Erk, S. Acar, Room-temperature ammonia gas sensor based on reduced graphene oxide nanocomposites decorated by Ag, Au and Pt nanoparticles, Journal of Alloys and Compounds 722 (2017) 569-578.
10. Z. Li, S. Jiang, Y. Huo, T. Ning, A. Liu, C. Zhang, Y. He, M. Wang, C. Li and B. Man, 3D silver nanoparticles with multilayer graphene oxide as a spacer for surface enhanced Raman spectroscopy analysis, Nanoscale 10 (2018) 5897-5905.
11. Ö. Metin, H. Can, K. Şendil, and M. S. Gültekin, J. Colloid Interface Sci. 498, 378 (2017).
12. E. H. Rhoderick and R. H. Williams, Metal-Semiconductor Contacts, (Oxford: University Press, 1988).
13. A. Baltakesmez, A. Taşer, Z. Kudaş, B. Güzeldir, D. Ekinciand M. Sağlam, Barrier height modification of n-InP using a silver nanoparticles loaded graphene oxide as an interlayer in a wide temperature range, Journal Of Electronic Materials 48 (2019) 3169-3182.
14. T. Çakıcı, B. Güzeldir and M. Sağlam, Temperature dependent of electrical characteristics of Au/n-GaAs/In Schottky diode with In2S3 interfacial layer obtained by using spray pyrolysis method, Journal of Alloys and Compounds 646 (2015) 954-965.
15. S. M. Sze, Physics of Semiconductor Device, (New York: Wiley 1981).
16. F. E. Cimilli, H. Efeoğlu, M. Sağlam and A. Türüt, J Mater Sci: Mater Electron 20 (2009) 105-111
17. H. Korkut, N. Yildirim and A. Türüt, Microelectron. Engineer., 86 (1) (2009) 111-120.
18. P. Kaushal, S. Chand and J. Osvald, Int. Journal Of Electronics, 100 (2012) 686-691
19. B. Güzeldir, M. Sağlam and A. Ateş, Analysis of the electrical characteristics of Zn/ZnSe/n-Si/Au–Sb structure fabricated using SILAR method as a function of temperature, Journal of Alloys and Compounds 506 (2010) 388-394

BOOK OF FULL TEXT PROCEEDINGS TURKISH PHYSICAL
SOCIETY 35th INTERNATIONAL PHYSICS CONGRESS (TPS35)
TPS35, Vol.01, No.04, pp.317-321.
ISBN:978-605-83516-6-0

15 December 2019

Preparation and Characterization of Fe Doping CoO Thin Films

Esra Kus[1, a)], Ayse Kucukarslan[2], Vildan Bilgin[2,b)], Erhan Tiryaki[3] and Idris Akyuz[4]

[1]*Department of Physics, Graduate School of Natural and Applied Sciences, Uludag University, Bursa, Turkey*
[2]*Department of Physics, Faculty of Arts and Sciences, Canakkale Onsekiz Mart University, Canakkale, Turkey*
[3]*Department of Physics, Graduate School of Natural and Applied Sciences, Canakkale Onsekiz Mart University, Canakkale, Turkey*
[4]*Department of Physics, Faculty of Arts and Sciences, Eskisehir Osmangazi University, Eskisehir, Turkey*

[a)] esraakus@hotmail.com
[b)] vbilgin@comu.edu.tr

Abstract. In this work, undoped and Fe doped cobalt oxide (CoO) thin films were deposited on microscope glass substrates at substrate temperature of $300 \pm 5°C$ by using Ultrasonic Spray Pyrolysis (USP) technique. The influence of Fe doping on the optical and structural properties of the CoO films was investigated. Structural properties of the films were examined by using x-ray diffraction (XRD) technique. Some structural parameters such as the average grain size, lattice constant and volume of unit cell for all films were calculated by XRD patterns. Optical transmittance, absorbance and reflectance spectra of the deposited films were taken in the wavelength range of 300-900 nm and optical parameters such as absorption coefficients, energy band gaps and Urbach parameters of the films were determined by using these spectra. All analysis revealed that incorporation of Fe has a significant effect on some physical properties of CoO thin films.

1. INTRODUCTION

Among the transition metal oxides, cobalt oxide is one of the most attracted attention oxide due to it importance for many industrial applications [1]. Cobalt oxide films are interest in thin film electronics and optoelectronic applications as they can be produced on large areas using economical glass and flexible plastic bases. This material is suitable for use in ceramics and glass, electrochemical devices, gas sensors, electrochromic devices [2-3]. The cobalt oxide thin films are several deposited by methods such as laser deposition, RF sputtering, electrodeposition, dip coating, spray pyrolysis and chemical bath deposition [4-6].

In this study, the ultrasonic spray pyrolysis was chosen for its simplicity and easy experiment setup. Undoped and Fe doped CoO thin films with (at 2, 4 and 6 %) were obtained by ultrasonic spray pyrolysis technique. Structural and optical properties of these films were characterized by X-ray diffraction (XRD) and UV-Visible spectrophotometer, respectively.

2. EXPERIMENTAL DETAILS

The undoped and Fe doped cobalt oxide (at the Fe percentages of 2, 4 and 6) thin films were produced onto microscope glass substrates (1cm×1cm) by using a ultrasonic spray pyrolysis (USP) technique at a substrate temperature of 300±5°C. The spray solution was prepared by mixing the appropriate volumes of $CoCl_2.6H_2O$ (0.025 M) and $FeCl_3.6H_2O$ (0.025 M) dissolved in deionized water for cobalt and iron source, respectively. The total solution

Türk Fizik Derneği
1950
Turkish Physical Society

of 100 cc was sprayed during 20 min. The solution flow rate was kept constant at 5 ccmin^{-1} and controlled by a flowmeter during deposition process. Compressed purified air was used as the carrier gas with a pressure of 10^5 Pa. The substrates temperature 300 °C were heated by an electrical heater and the substrate temperature was controlled by using an iron-constantan thermocouple. The amounts of spray solution prepared for the films and the thickness are given in Table 1. The produced films were named as F0 (undoped), F2, F4 and F6 depending on the increasing Fe incorporation. PHE 102 Spectroscopic Elipsometer was used to determine the thickness of the films and presented in Table 1. The structural properties of all the films were analyzed by using X-ray diffractometer with CuK_α radiation (PANalytical Empyrean Model, λ=1.5405 Å). A continuous scan mode was used to collect 2θ data from 20° to 80 ° with a step of size 0.013°, acceleration voltage 45 kV and emission current 30 mA. The optical properties of all the films were studied by a Shimadzu UV-2550 (double beam, 190-900 nm) spectrophotometer.

TABLE 1. The amounts of spray solution prepared for the films and the thickness.

Sample	Sample Code	$CoCl_2.6H_2O$ (ml)	$FeCl_3.6H_2O$ (ml)	Totally (ml)	Thickness (nm)
CoO	F0	100	-	100	349
CoO:Fe (%2)	F2	98	2		471
CoO:Fe (%4)	F4	96	4		527
CoO:Fe (%6)	F6	94	6		590

3. RESULTS AND DISCUSSION

3.1. Optical Properties

The absorbance and transmittance spectra of the undoped and iron doped cobalt oxide films are shown in Figure 1 (a) and (b), respectively. Also, transmission and absorbance values at some different wavelength listed in Table 2. When the Figure 1 (a) is examined, it is observed that optical transmittance values of the films decrease slightly due to the increase in Fe concentration. The low transmittance of the films is may be due to the high thickness of the films and the poor crystal structure as seen from a XRD patterns. As seen in Figure 1 (b), undoped and Fe doped CoO thin films were found to have low absorption value in the visible region.

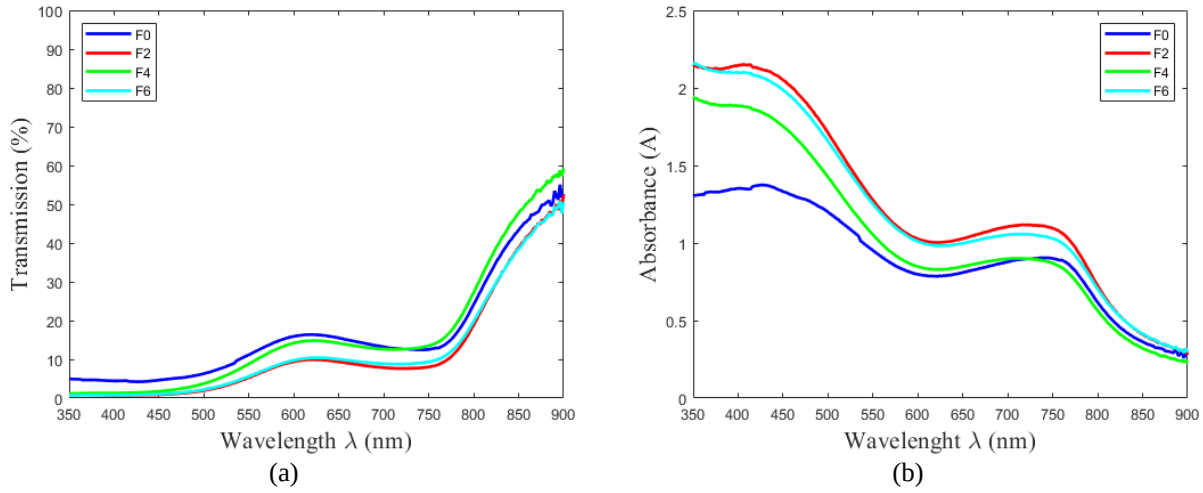


FIGURE 1. (a) Transmittance, (b) Absorbance spectra for the CoO:Fe thin films.

TABLE 2. The absorbance and transmittance values for CoO:Fe thin films for different wavelength.

Sample	Sample Code	λ= 350 nm			λ= 600 nm			λ= 850nm		
		A	T (%)	n	A	T (%)	n	A	T (%)	n
CoO	F0	1.30	4.95	7.21	0.79	15.90	4.50	0.36	43.35	2.69
CoO:Fe	F2	2.14	0.70	14.40	1.02	9.40	5.62	0.41	38.77	2.88
	F4	1.94	1.14	12.07	0.84	14.20	4.73	0.32	47.76	2.53
	F6	2.15	0.69	14.23	1.01	9.77	5.54	0.42	38.49	2.89

The relation between the absorption coefficient α and the photon energy $h\nu$ of the semiconductor material was given by $\alpha h\nu = A(h\nu - E_g)^n$. Where α is absorption coefficient, A is constant, n is constant with n=1/2 for direct transition and n=2 for indirect transition [7]. Figure 2 shows plots of $(\alpha h\nu)^2$ as a function of photon energy $(h\nu)$ for CoO:Fe thin films. As shown in Figure 2, two straight line portions have been identified, indicating that the CoO:Fe films have two direct band gaps. The values of the two direct band gaps are defined E_{g1} and E_{g2}, and these values are listed in Table 3. The values E_{g1} and E_{g2} are in the range 1.48-1.50 and 1.98-2.12 eV, respectively, and these values agree with the others results in literature. Here, E_{g1} corresponds to the onset of O (−II) → Co (III) excitations, while E_{g2} is the energy band gap corresponding to inter-band transitions [8].

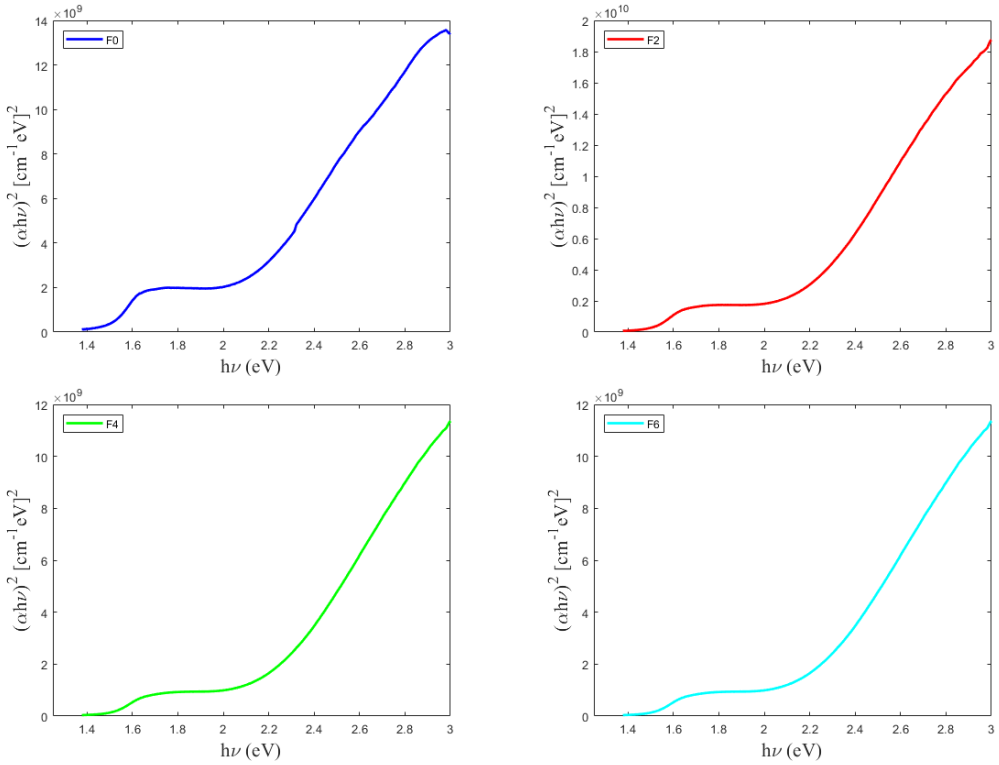


FIGURE 2. The $(\alpha h\nu)^2$ versus photon energy $(h\nu)$ for CoO:Fe thin films.

TABLE 3. The optical band gap energies (E_g) for CoO:Fe thin films.

Sample	Sample Code	E_g (eV)
CoO	F0	1.48 1.98
CoO:Fe	F2	1.49 2.08
	F4	1.50 2.12
	F6	1.49 2.10

3.2. Structural Properties

X-ray diffraction (XRD) measurements were performed to investigate the structural properties of undoped and Fe doped CoO thin films. XRD patterns of CoO:Fe films are shown in Figure 3. The 2θ values were varied from 20° to 80°. All peaks observed in XRD patterns were indexed by comparing with the data file of the Joint Committee on Powder Diffraction Standards (JCPDS) [9]. As seen from XRD patterns, all the films have polycrystalline cubic crystal structure. No secondary phases related to Fe elements or compounds were detected for the doped thin films and doping atoms did not alter the crystalline structure of CoO. It is determined from XRD data's that there is a slightly shift in 2θ to the lower diffraction angle by increasing Fe doping. This is mainly because the lattice constant has change with the increasing amount of Fe [10]. The radius values of Fe and Co atoms are 0.126 nm and 0.125 nm, respectively. Lattice parameters and lattice spacing values vary due to difference may cause shifts. Or this effect can occur when the parameters change as a result of detects in the crystal structure [11].

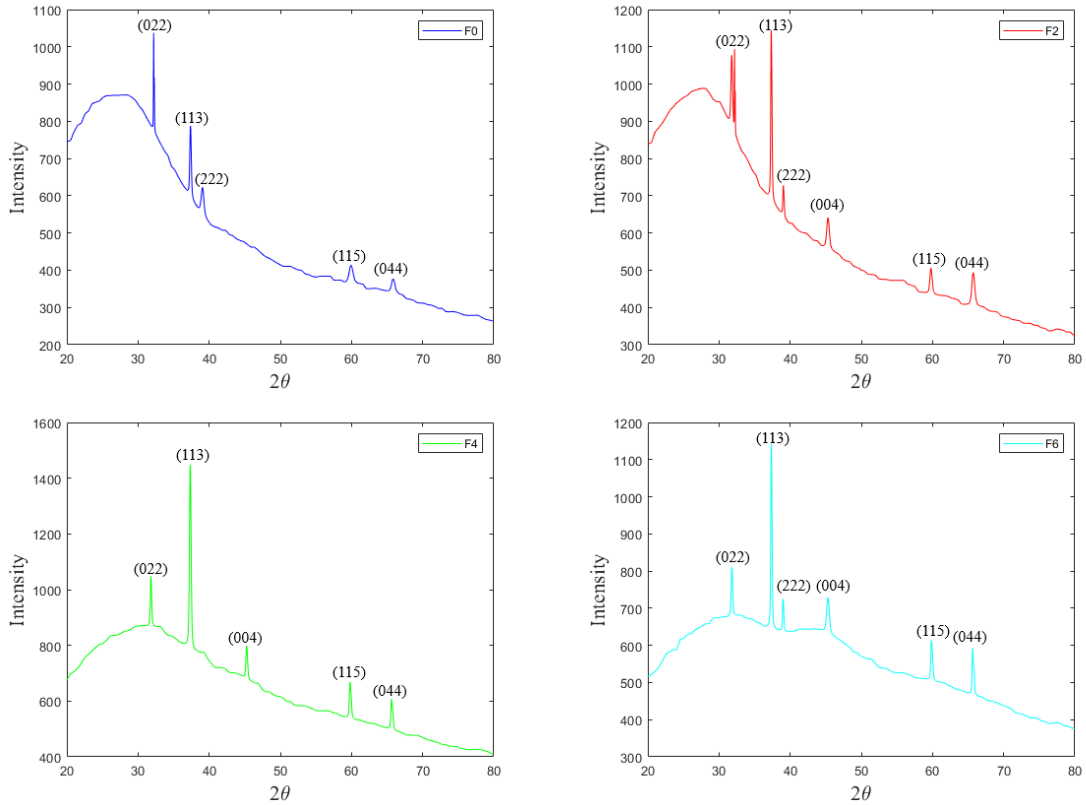


FIGURE 3. The XRD patterns of the undoped and Fe doped CoO thin films.

4. CONCLUSIONS

In summary, undoped and iron doped cobalt oxide thin films were deposited onto a glass substrate using ultrasonic spray pyrolysis technique. The effect of Fe doping on optical and structural properties of the films were studied. The thicknesses of the films were determined to be between 349-590 nm. As a result of examining the optical properties of all the films, it has been found that the optical transmittances values of CoO films are about 50-60 %. The band gaps of CoO:Fe films were determined by using absorption edge. It was determined that optical band gap energies of all films were between 1.48-1.50 eV and 1.98-2.12 eV. From XRD patterns, it was determined that all films had a polycrystalline cubic crystal structure.

REFERENCES

1. V.R. Shinde, S.B. MAhadik, T.P. Gujar, C.D. Lokhande, "Supercapacitive cobalt oxide (Co_3O_4) thin films by spray pyrolysis", Apllied Surface Science **252**: 7487-7492 (2006).
2. Y. Li, K. Huang, Z., Yao, S. Liu, X. Qing, "Co_3O_4 thin film prepared by a chemical bath deposition for electrochemical capacitors", Electrochimica Acta, **56**, 2140-2144 (2011).
3. X.H. Xia, J.P: Tu, J. Zhang, J.Y. Xiang, X.I. Wang, X.B. Zhao, "Fast electrochromic properies of self-supported Co_3O_4 nanowire array film", Solar Energy Materials & Solar Cells, **96**, 386-389 (2010).
4. B. Pejova, A. Isahi, M. Najdoski, I. Grozdanov, "Fabrication and characterization of nanocrystalline cobalt oxide thin film", Materials Research Bulletin **36**: 161-170 (2001).
5. L.D. Kadam, S.H. Pawar, P.S. Patil, "Studies on ionic interaction properties of cobalt oxide thin films prepared by spray pyrolysis technique", Materials Chemistry and Physics **68**: 280-282 (2001).
6. V. Helen and J.J. Prince, "Influence of annealing on the structural, optical and magnetic properties of CoO thin films", Materials Research Innovations **23**: 200-206 (2019).
7. K. Chansaengsri, K. Onlaor, T. Thiwawong and B. Tunhoo, "Effect of annealing temperature on structural and optical properties of cobalt oxide thin films prepared by electrostatic spray deposition technique", Key Engineering Materials **675**: 229-232.
8. D. Barreca, C. Massignan, S. Daolin, M. Fabrizio, C. Piccirillo, L. Armelao, E. Tondello, "Composition and microstructure of cobalt oxide thin films obtained from a novel cobalt (II) precursor by chemical vapor deposition", Chem. Mater. **13**: 588-593 (2001).
9. Strada, M.;Natta, G., Gazzetta Chimica Italiana, **58**: 419 - 433, (1928).
10. Y. Yuan, X. Xia, J. Wu, J. Gui, Y. Chen, S. Guo, Electrochromism in mesoporousnanowall cobalt oxide thin films prepared via lyotropic liquid crystal mediawith electrodeposition, J. Membr. Sci. **364**: 298–303 (2010).
11. J. Zhang, X. Wang, D. Qin, Z. Xue and X. Lu, "Fabricaiton of iron-doped cobalt oxide nanocomposite films by electrodeposition and application as electrocatalyst for oxygen reduction reaction", Apllied Surface Science **320**: 73-82 (2014).

BOOK OF FULL TEXT PROCEEDINGS TURKISH PHYSICAL
SOCIETY 35th INTERNATIONAL PHYSICS CONGRESS (TPS35)
TPS35, Vol.01, No.04, pp.322-326.
ISBN:978-605-83516-6-0

15 December 2019

Optical and Morphological Studies of CoO:Ni Thin Films Grown by Ultrasonic Spray Pyrolysis

Esra Kus[1, a)], Ayse Kucukarslan[2,], Vildan Bilgin[2, b)], Barbaros Demirselcuk[3] and Idris Akyuz[4]

[1][1]*Department of Physics, Graduate School of Natural and Applied Sciences, Uludag University, Bursa, Turkey*
[2]*Department of Physics, Faculty of Arts and Sciences, Canakkale Onsekiz Mart University, Canakkale, Turkey*
[3]*Department of Electricity and Energy, Voc. School of Techn. Sciences, Canakkale Onsekiz Mart University, Canakkale, Turkey*
[4]*Department of Physics, Faculty of Arts and Sciences, Eskisehir Osmangazi University, Eskisehir, Turkey*

[a)] esraakus@hotmail.com
[b)] vbilgin@comu.edu.tr

Abstract. Undoped and nickel (Ni) doped CoO (3, 6 and 9 at. %) thin films were deposited by Ultrasonic Spray Pyrolysis method at substrate temperature of 300±5°C. By examining some physical properties of the produced films, the effect of Ni doping on the optical and morphological properties of CoO thin films was investigated. The optical properties of the films such as reflectance, band gap energy, refractive index, extinction coefficients and Urbach parameters were calculated by using the transmittance and absorption spectra taken by using UV-VIS spectrophotometer to examine the optical properties of films. The surface morphologies and roughness of the films were determined by atomic force microscope (AFM). As a result of all these analyzes, it has been determined that the Ni doping have influences on the optical and surfaces properties of CoO thin films.

1. INTRODUCTION

In recent studies, transition metal oxide materials have attracted attention in technological and scientific applications due to their physical and chemical properties. Cobalt oxide (CoO) materials are popular in the chemical and industrial sectors for production of the energy storage devices [1-2]. Cobalt oxide generally has three different structures such as cobalt (II) oxide, cobalt (III) oxide and cobalt (II), (III) oxide and all three structure are used in devices [3]. Cobalt oxide electrical resistivity values range from 10^2 to 10^4 Ωcm at room temperature [4]. In the literature, refractive index values of cobalt oxide thin films are given between 1.6-2.8 [5]. CoO thin films have been prepared by several deposition methods such as chemical bath deposition [6], chemical vapor deposition [7], atomic layer deposition [8], sol-gel processes [9-10], spray pyrolysis [11-12].

In this study, CoO:Ni thin films were deposited onto glass substrates by using Ultrasonic Spray Pyrolysis technique. The influence of Ni doping on the optical and morphological of undoped CoO thin films was reported. The optical and morphological analyses of the all films were characterized by UV-VIS spectrophotometer and atomic force microscope (AFM), respectively.

Türk Fizik Derneği
1950
Turkish Physical Society

2. EXPERIMENTAL DETAILS

Ultrasonic spray pyrolysis (USP) technique was used to produce undoped and nickel (Ni) doped CoO thin films. $CoCl_2.6H_2O$ (0.01 M) and $NiCl_2.6H_2O$ (0.025 M) for cobalt and iron source, respectively. Deionized water used as a solvent. Totally 150 ml of solution was sprayed during 30 min. Flow rate was controlled with a flowmeter as to 5 $ccmin^{-1}$ during deposition process. All thin films were deposited onto microscope glass substrates (1cm×1cm) using air as carrier gas with a pressure of at a substrate temperature of 300±5°C. The spray solution was prepared by1:1 mixing the appropriate volumes. The distance between the nozzle and substrate was kept constant at 35 cm. Also substrates temperature heated by an electrical heater and the substrate temperature was controlled within ±5°C using an iron-constantan thermocouple. The experimental details of spray solution prepared for the films and the thickness are given in Table 1.

The thickness of the films were measured by PHE 102 Spectroscopic Elipsometer System. The optical transmittance and absorbance spectra for the all films were determined by a Shimadzu UV-2550 (double beam, 190-900 nm) spectrophotometer. The surface morphologies and roughness measurement were determined by Park-System XE-70 Model (AFM) microscope.

TABLE 1. The amounts of spray solution ,and the thicknesses of the films.

Sample	Sample Code	$CoCl_2.6H_2O$ (ml)	$NiCl_2.6H_2O$ (ml)	Totally (ml)	Thickness (nm)
CoO	N0	150	-	150	349
CoO:Ni (%3)	N3	145.5	4.5		374
CoO:Ni (%6)	N6	141	9		388
CoO:Ni (%9)	N9	136.5	13.5		338

3. RESULTS AND DISCUSSION

3.1. Optical Properties

In order to obtain information about the optical properties of undoped and Ni doped CoO films, transmittance and absorbance spectra for all the films were obtained and some optical parameters such as refractive index (n) and band gap energy (E_g) were determined by using these spectra. The variation of the transmittance and absorbance spectra with wavelength for undoped and Ni doped CoO thin films in the range of 350-900 nm are presented in Figure 1(a) and Figure 1(b), measured at room temperature in air. Also, transmission and absorbance values at some different wavelength listed in Table 2.

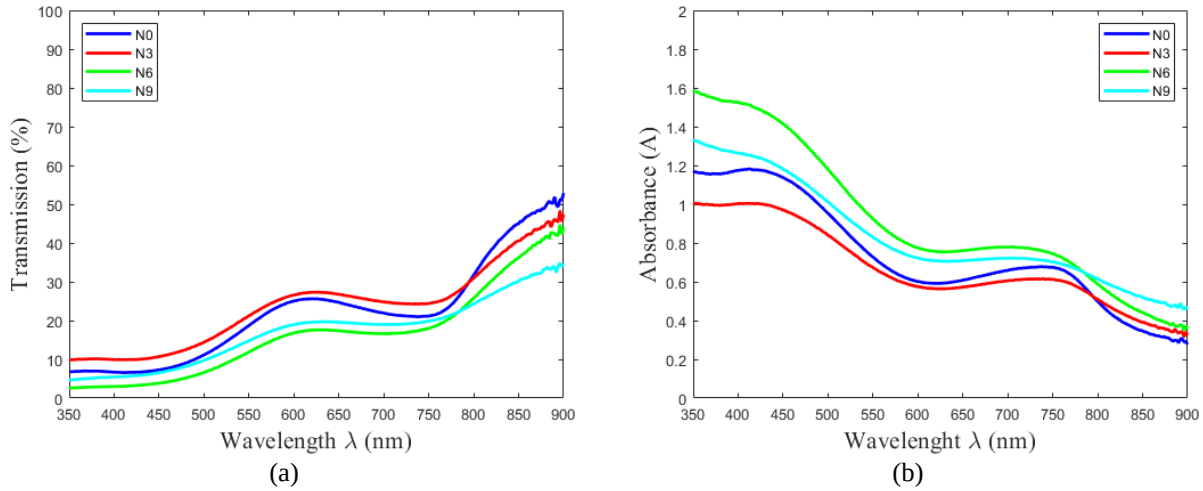


FIGURE 1. (a) Transmittance, (b) Absorbance spectra for the undoped and Ni doped CoO thin films.

As it can be seen from Figure 1, all films have low transmission and relatively high absorption in the visible region. Also, it was identified from these spectra that the optical transmittance of the CoO films decreases while their absorption increases depending on the Ni doping. The effect of Ni doping on the transmission of CoO films may be due to the structural, surface effects or thickness. The effects such as better crystallization, surface homogeneity or less thickness can increase the transmission.

TABLE 2. The absorbance and transmittance values for CoO:Ni thin films for different wavelength.

Sample	Sample Code	λ= 350 nm			λ= 600 nm			λ= 850nm		
		A	T (%)	n	A	T (%)	n	A	T (%)	n
CoO	N0	1.17	6.75	6.41	0.60	25.04	3.64	0.34	45.01	2.63
	N3	1.00	9.83	5.52	0.57	26.58	3.53	0.39	40.55	2.80
CoO:Ni	N6	1.58	2.58	9.13	0.77	16.80	4.39	0.44	36.14	2.99
	N9	1.33	4.66	7.37	0.72	18.93	4.16	0.52	30.18	3.30

The optical band gap (E_g) of the all films can be determined from the absorption spectra using the formula $(\alpha h\upsilon)^2 = A(h\upsilon - E_g)$ for allowed direct transitions, E_g is the optical band gap, α is the absorption coefficient, A is a constant, h is the Planck's constant, υ is the frequency of the incident photon [13]. The energy band gap of the semiconductor material is determined from the graph $(\alpha h\upsilon)^2 \sim h\upsilon$ plotted using the absorption spectrum. The optical band gap values obtained by extrapolating the linear region of the plots of $(\alpha h\upsilon)^2$ versus $h\upsilon$ to $\alpha = 0$. The curves of $(\alpha h\upsilon)^2$ versus $h\upsilon$ for all the films are shown in Figure 2. It gives two energy band gaps from two edges of absorption on the all films. In the cobalt oxide band structure, besides the valence and transmission band, there is a subband within the forbidden band gap energy. For these optical transitions, two energy levels have been found in different studies in the literature [14]. Energy band gap is calculated using the relationship between the absorption and the photon energy [15]. It was determined that the optical band gap (E_g) values listed in Table 3 were between 1.35-1.46 eV and 2.03-2.08 eV.

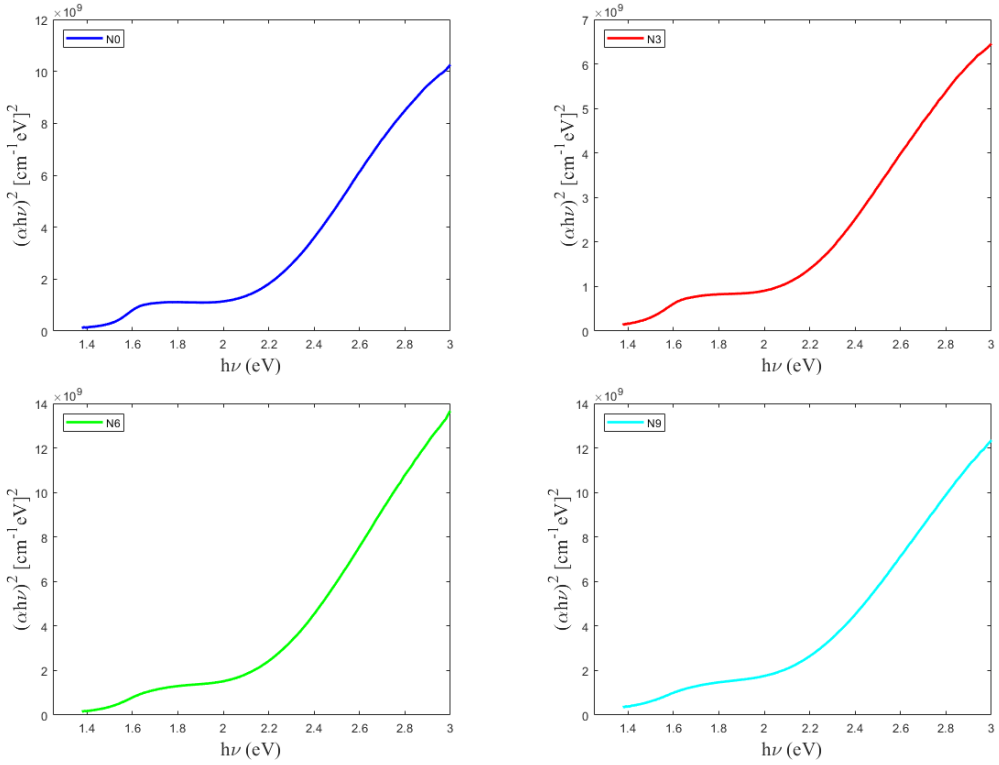


FIGURE 2. The $(\alpha h\upsilon)^2$ versus photon energy $(h\upsilon)$ for the undoped and Ni doped CoO thin films

TABLE 3. The optical band gap energies (E_g) for CoO:Ni thin films.

Sample	Sample Code	E_g (eV)
CoO	N0	1.46 2.08
CoO:Ni	N3	1.41 2.03
	N6	1.40 2.08
	N9	1.35 2.06

3.2. Morphological Properties

The morphological properties of undoped and Ni doping CoO films were confirmed by using atomic force microscope (AFM). Three-dimensional AFM images of all films are given in Figure 3. When the AFM images were investigated, dark and bright regions which represent different size hole and hill formation on the film surface respectively were observed for all deposited films. The surface roughness values were determined for undoped and Ni doped CoO films by AFM measurements. It was found that the films have the porosity surface. It can be seen that Ni incorporation has effect on the surface morphology of the undoped CoO films. The average surface roughness was determined at 85 nm, 84.30 nm, 339 nm and 149 nm for the undoped, 3, 6 and 9% Ni doped CoO thin film, respectively.

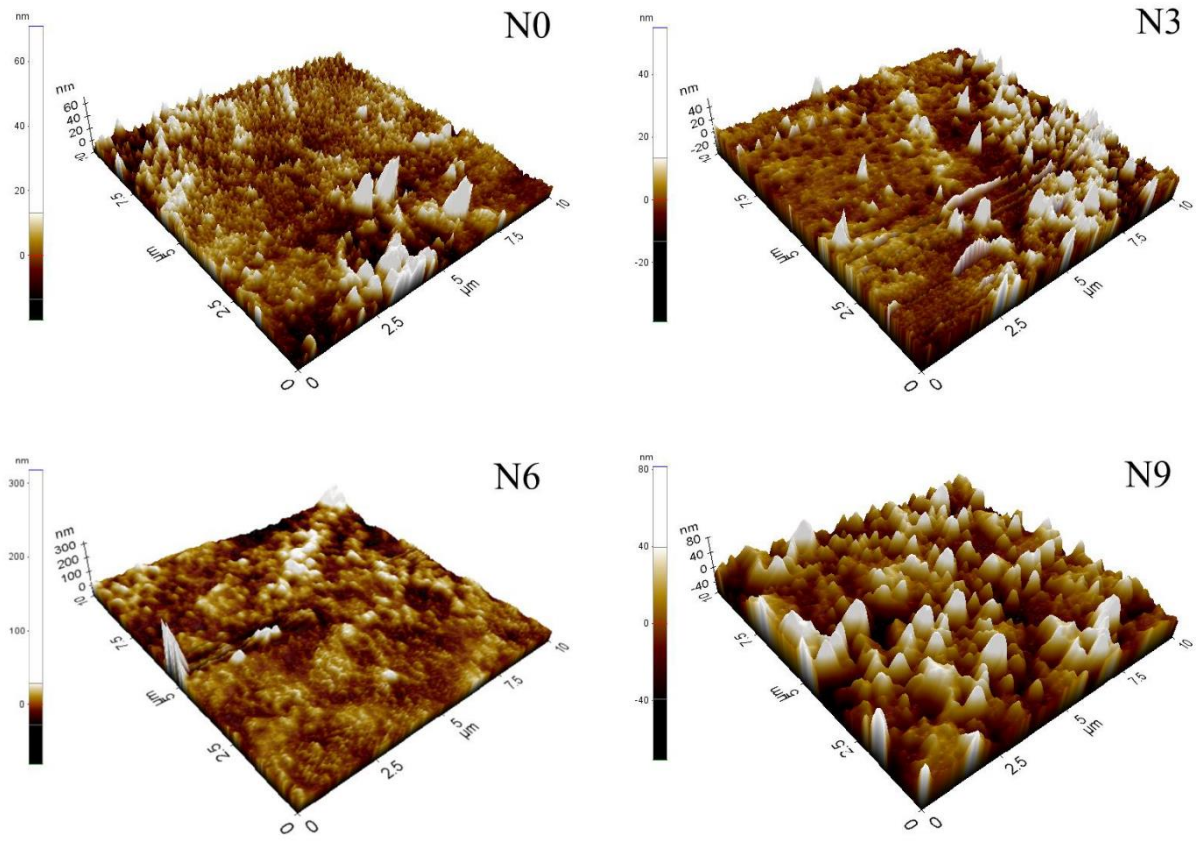


FIGURE 3. The AFM images of the undoped and Ni doped CoO thin films.

4. CONCLUSIONS

Undoped and Ni doped CoO (3, 6 and 9 at. %) thin films were deposited by Ultrasonic Spray Pyrolysis method at substrate temperature of 300±5°C. The effect of Ni doping on the optical and morphological properties of the CoO films was investigated. by using UV-VIS spectrophotometer and AFM, respectively. Optical transmittance values of CoO films were decreased with Ni doping, which may be attributed to the structural and morphological effects. It was calculated two optical band gap energies from two edges of absorption on the all films. AFM images show that all the films have almost homogenous surface morphologies but surface homogeneous decreased with increase of Ni doping. Consequently, it was determined that the Ni doping has important effects on the optical and morphological properties of CoO thin films.

REFERENCES

1. L.D. Kadam, S.H. Pawar and P.S. Patil, "Studies on ionic intercalation properties of cobalt oxide thin films prepared by spray technique", Materials Chemistry and Physics **68**: 280-282 (2001).
2. V. Helen and J.J. Price, "Influence of annealing on the structural, optical and magnetic properties of CoO thin films", Materials Reserch Innovation **23**(4): 200-206.
3. K. Chansaengsri, K. Onlaor, T. Thiwawong and B. Tunhoo, "Effect of annealing temperature on structural and optical properties of cobalt oxide thin films prepared by electrostatic spray deposition technique", Key Engineering Materials **675**: 229-232.
4. V. Patil, P. Joshi, M. Chougule, S. Sen, "Synthesis and characterization of Co3O4 thin film", Soft Nanoscience Letters **2**: 1-7 (2012).
5. E. Barrera-Calva, J.C. Martinez-Flores, L. Huerta, A. Avila and M. Ortega-Lopez, "Ellipsometric spectroscopy study of cobalt oxide thin films deposited by sol-gel". Solar Energy Materials and Solar Cells **90**: 2523-2531 (2006).
6. F.C. Eze, "Electroless deposition of CoO thin films", Journal of Physics D: Applied Physics **32**: 533-540 (1999).
7. N. Bahlawane, E. Fischher Rivera, K. Kohse-Höinghaus, A. Brechling and U. Kleineberg, "Characterization and tests of planar Co_3O_4 model catalysts prepared by chemical vapor deposition", Applied Catalysis B: Enviromental **53**: 245-255 (2004).
8. S. Jung, D.K. Nandi, S. Yeo, H. Kim, Y. Jang, J.S. Bae, T.E. Hong, S.H. Kim, "Phase-contralled growth of cobalt oxide thin films by atomic layer deposition", Surface and Coatings Technology **337**: 404-410 (2018).
9. M. El Baydi, G. Poillerat, J. Rehspringer, J.L. Gautier, J.F. Koenig and P. Chartier, "A sol-gel route for the preparation of Co_3O_4 catalys for oxygen electrocatalysis in alkaline medium", Journal of solid state chemistry **109**: 281-288 (1994).
10. Z.N. Kayani, S. Arshad, S. Riaz, R. Zia and S. Naseem, "Structural characterization and optical properties of cobalt oxide thin films", The 2014 World Congress on Advances in Civil, Enviranmental, and Materails Research (ACEM14) Busan, Korea, August 24-28, (2014).
11. S.Z. Abbas, A.A. Aboud, A. Irfan and S. Alam, "Effect of substrate temperature on structure and optical properties of Co_3O_4 films prepared by spray pyrolysis technique", IOP Conf. Series: Materials Science and Engineering 60 (2014).
12. A. Elsakhi S. M. Hamed, M.A. Siddig, A.A. Elbadawi, A.I. Mohamed, M. Elhadi, "Preperation of Cobalt oxide thin film using chemical spray pyrolysis method and the effect of annealing temperature in its optical properties", International Journal of Scientific Research and Innovative Technology **2**(5): 112-116 (2015).
13. B. Demirselcuk and V. Bilgin, "Ultrasonically sprayed ZnO:Co thin films: Growth and characterization", Applied Surface Science **273**, 478-483 (2013).
14. V.R. Shinde, S.B.Mahadik, T.P. Gujar, C.D. Lokhande, "Supercapacitive cobalt oxide (Co_3O_4) thin films by spray pyrolysis", Applied Surface Science **252**: 7487-7492 (2006).
15. R. Drasovean, R. Monteiro, E. Fortunato, V. Musat, Optical properties of cobalt oxide films by a dipping sol-gel process, Journal of Non-Crystalline Solids. **352**:1479-1485 (2006).

BOOK OF FULL TEXT PROCEEDINGS TURKISH PHYSICAL
SOCIETY 35th INTERNATIONAL PHYSICS CONGRESS (TPS35)
TPS35, Vol.01, No.04, pp.327-331.
ISBN:978-605-83516-6-0

15 December 2019

Experimental Investigation of Some Thermal Properties of Al-1,9Sc Alloy

*Gencer S.[1, a)] and Hamza Y. O.[1]

[1]*Kütahya Dumlupınar University, Faculty of Science, Department of Physics, Kütahya*

[a)]Corresponding author: * *gencer.sarioglu@dpu.edu.tr*

Abstract. Al-Sc alloys have an important place in the industrial sector in terms of their mechanical properties. In this respect, the thermal properties of Al-Sc alloys are of great interest. The Al-1,9Sc alloy was obtained by a special technique. Thermal properties were investigated using different experimental systems. This study was carried out in Kütahya Dumlupınar University Advanced Technology Center laboratory in the range of room temperature to 600 °C. As a result of the analysis, thermal expansion constant, Young constant, shear constant, enthalpy change, Gibbs energy change and entropy change of Al-1,9Sc alloy were obtained. As a result of the analysis, it was concluded that there was no phase transition in the alloy but there was recrystallization at some temperatures. In addition, it was found that the results obtained were consistent with the results of Al-Sc alloy.

INTRODUCTION

Al-base alloys are one of the important raw materials of the industry in terms of cost and energy efficiency and experimental and theoretical studies on these alloys are continuing intensively [1]. Al-Sc alloys are used at different temperatures in the aerospace and automobile industry due to their lightness and flexibility [2]. Although its solubility in aluminum is very low, scandium makes a significant contribution to improving the mechanical properties of aluminum alloys. The scandium element provides benefits such as increased strength of the alloy, reduced particle size, increased recrystallization temperature, and improved resistance to hot cracking. These two elements form four intermetallic phases: Al_3Sc, Al_2Sc, AlSc and $AlSc_2$. At low scandium rates, the effect of high strength and high temperature recrystallization of the material is due to the Al_3Sc precipitations in the material [3,4]. In this study, Al-1,9Sc alloy has been thermally measured and its physical parameters have been investigated.

METHODS

Differential scanning calorimetry (TG/DSC) and Thermomechanical analysis (TMA) measurements of Al-1,9Sc alloy samples were performed in thermal analysis experiments.

For the TG / DSC, SETARAM Labsys Evo model Simultaneous Thermal Analyzer is used which can work at temperatures between 30 - 1600 °C. For the TMA experiments, SETARAM brand Setsys Evo model Thermo-Mechanical Analyzer which can work at temperatures between 30-1750 °C was used.

For TG / DSC analyzes, samples weighing 55 mg were placed in platinum crucibles. Heat treatment was applied to the samples between 30 - 600 °C using argon atmosphere with 10 °C/min heating rate. Simultaneous weight and energy changes on the material during the heat treatment were measured. Enthalpy, Gibbs free energy and entropy values were derived from the measured values.

For TMA analysis, 2.36 mm high samples were placed on the alumina holder and 5 g load was applied. Heat treatment was applied to the samples between 30 - 600 °C using argon atmosphere with 10 °C/min heating rate. The size change and thermal expansion and Young modulus coefficient on the material during the heat treatment were obtained.

SENSYS EVO TG-DSC for differential scanning calorimetry (TG/DSC) analysis and SETSYS EVOLUTION TMA for thermomechanical analysis (TMA) are shown in Figure 1 and Figure 2, respectively. The measuring devices are located in Kütahya Dumlupınar University İLTEM research center.

ISBN:978-605-83516-6-0



FIGURE 1. SENSYS EVO TG-DSC



FIGURE 2. SETSYS EVOLUTION TMA

Recrystallization temperatures and enthalpy were determined from the peaks formed in the obtained TG/DSC curve. The entropy of recrystallization was also calculated using temperature and temperature data. Using Equation 1, Gibbs energy of the recrystallization peak was calculated. Here, ΔG; Gibbs energy, ΔH; Enthalpy, T; recrystallization temperature and ΔS; It shows entropy values.

$$\Delta G = \Delta H - T\Delta S \quad (1)$$

TMA ölçümleri ile elde edilen eğrilerden faydalanarak birim yer değişimi (ϵ), termal genleşme katsayısı (α) ve Young modülü (E) sırasıyla denklem 2, 3 ve 4 kullanılarak hesaplanmıştır. Burada Δl; genleşme miktarı, l_0; malzemenin ilk uzunluğu ve ΔT; sıcaklık değişimini göstermektedir [5].

$$\epsilon = \frac{\Delta l}{l_0} \tag{2}$$

$$\alpha = \frac{\Delta l}{l_0 \Delta T} (°C)^{-1} \tag{3}$$

$$E = \frac{G}{\epsilon} (N/m^2) \tag{4}$$

DISCUSSION AND CONCLUSION

The maximum peak at 276.55 °C in the DSC graph of the Al-1,9Sc alloy in Figure 3 is the recrystallization temperature and shows the Al3Sc interface. -14.61 J / g obtained from the peak area gives the enthalpy value of the alloy. Entropy and Gibbs energy obtained from the enthalpy value are given in Table 1.

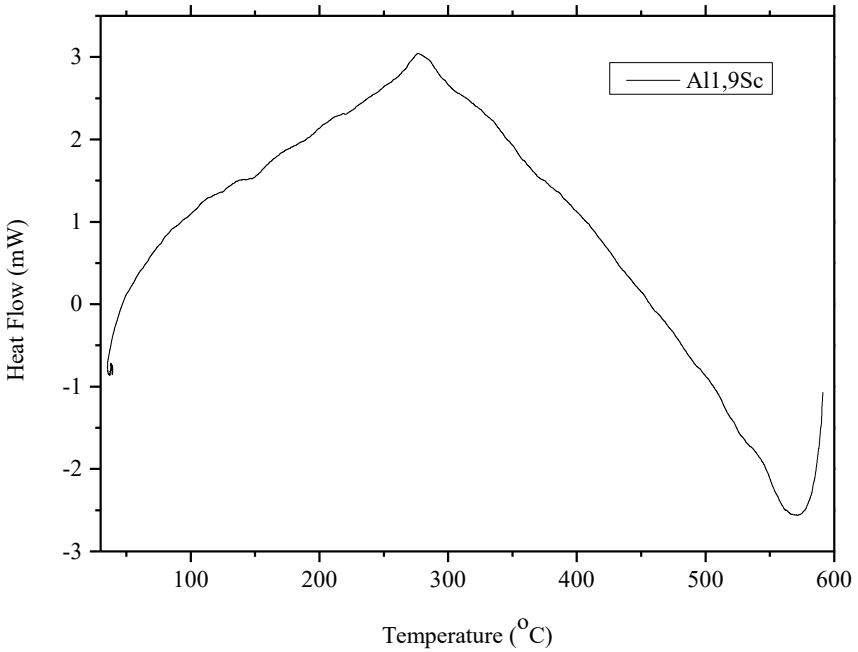


FIGURE 3. DSC graph of the Al-1,9Sc alloy

Recrystallization temperature, enthalpy change, entropy change and Gibbs energy change were obtained from DSC data. Addition of scandium has been shown to recrystallize this alloy. Accordingly, it can be said that the strength of Al-1.9Sc alloy at this temperature is good. It was seen from the thermal graphs and results that the material had exothermic reaction and consequently there was a slight increase in the amount of material. A negative Gibbs energy change means that the reaction tends to be voluntary, that is, if the entropy change is too small, the crystal regularity of the material is good. As a result of the very small change in entropy of the Al-1,9Sc alloy, it can be explained that the strength increases due to the crystallization being more uniform.

TABLE 1. Some thermal parameters of Al-1.9Sc alloy.

	Recrystallization Temperature	**ΔH (J/g)**	**ΔS (J/g°C)**	**ΔG (J/g)**
Al1,9Sc	276,55	-5,116	0,0092	-7,664

ISBN:978-605-83516-6-0

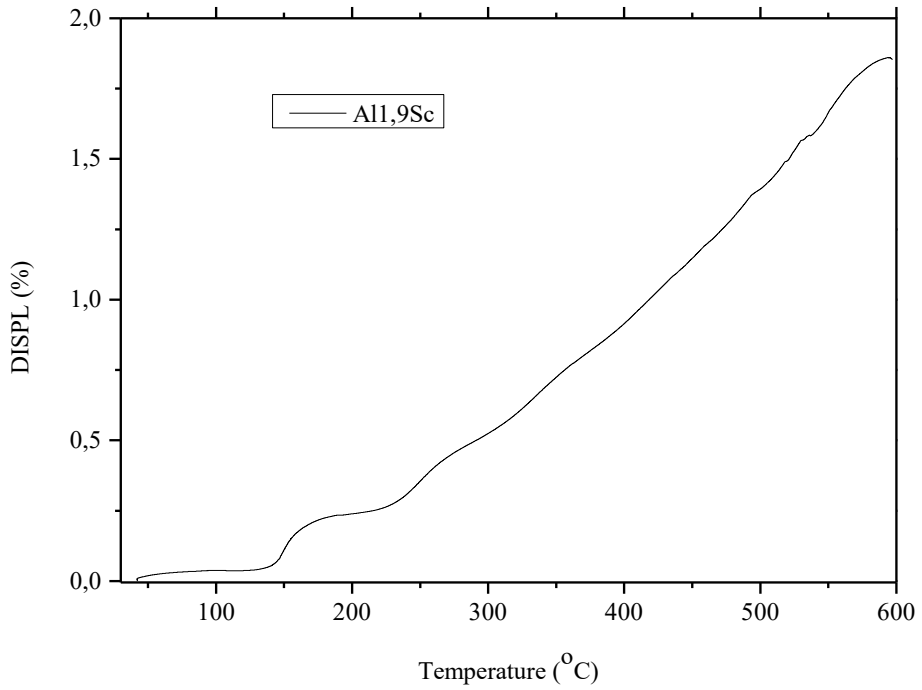


FIGURE 4. TMA graph of Al-1,9Sc alloy

Figure 4 shows the TMA graph of Al-1,9Sc alloy. In the graph, it was seen that the amount of elongation in the material increased in direct proportion with the increase in temperature. Depending on the increase in temperature, it was observed that the slope of the graph was slightly altered. Therefore, the coefficient of thermal expansion also showed a different change in different temperature ranges. Furthermore, the variation of the coefficient of expansion with temperature is interpreted as the recrystallization of the material.

In Table 2, the change in size (ϵ), thermal expansion (α) and Young Constant (E) values of Al-1,9Sc alloy were calculated with temperature. The mean value of thermal expansion coefficient was calculated as 27.84 (* 10^{-6}) $(°C)^{-1}$ and it was observed that the thermal expansion coefficient was directly proportional to the temperature. Young constant was calculated as 61,71 GPa and it was observed that it is inversely proportional to temperature.

TABLE 2. Al-1.9Sc Alloy Size change (ϵ), thermal expansion (α) and Young's Constant (E)

Temperature Range **(°C)**	**α (*10^{-6}) $(°C)^{-1}$**	**ϵ (*10^{-5})**	**E (GPa)**
42,86 – 122,89	3,34	26,77	64,78
122,89– 141,77	10,74	20,28	85,54
141,77 – 171,06	51,39	150,54	11,52
171,06 – 229,23	11,03	64,16	27,03
229,23 – 277,54	39,44	190,56	9,10
277,54 – 532,55	43,44	1107,93	1,56
532,55 – 593,37	47,47	288,75	6,00
593,37 – 597,15	15,92	6,02	288,17
Arithmetic Average	27,84	231,87	61,71
42,58 – 597,15	33,23	1842,99	0,33

If the results are compared with pure aluminum results; The theoretical thermal expansion coefficient of aluminum is 24 (* 10^{-6}) (°C) $^{-1}$, and the average value of Al-1,9Sc alloy is 27.84 (* 10^{-6}) (°C) $^{-1}$. It can be seen that the addition of Sc increases the coefficient of thermal expansion, albeit very small. The Young constant is 69 GPa for pure aluminum. Considering the Young's constant at low temperature values of this alloy, it is evident that the element Sc adds strength to the material. At high temperatures, it is thought that Young's constant may decrease due to partial dissolution in the material.

We would like to thank Kütahya Dumlupınar University BAP Program for supporting this study.

REFERENCES

1. Nembach E., "Order strengthening: recent developments, with special reference to aluminum-lithium alloys ", Prog. Mater. Sci. 45, 275 (2000).
2. Willey L.A., Patent, US (1971).
3. Cacciamani G., Riani P., Borzone G., Parodi N., Saccone A., Ferro R., Pisch A., Schmid-Fetzer R. (1999) *Intermetallics* 7, 101-108.
4. Xuan L., Jilai X., Zhichao G., Cheng Z. (2019) Journal of Materials Science & Technology, 35, 1422–1431.
5. W. D. Callister and D. G. Rethwisch, Materials Science and Engineering, (Nobel publishing, Wiley, 2014), pp. 992.

BOOK OF FULL TEXT PROCEEDINGS TURKISH PHYSICAL
SOCIETY 35th INTERNATIONAL PHYSICS CONGRESS (TPS35)
TPS35, Vol.01, No.04, pp.332-336.
ISBN:978-605-83516-6-0

15 December 2019

Experimental Investigation of Some Thermal Properties of Al-6Mg-1,9Sc Alloy

Gencer S.[1, a)] and Hamza Y. O.[2]

[1]*Kütahya Dumlupınar University, Faculty of Science, Department of Physics, Kütahya*

[a)]Corresponding author: *gencer.sarioglu@dpu.edu.tr*

Abstract. Al-Sc-Mg alloys have an important place in the industrial sector in terms of mechanical properties and thermal properties are also of great interest. For this purpose, thermal properties of Al-1,9Sc-6Mg alloy obtained by special technique were investigated using experimental techniques. This study was carried out at Kütahya Dumlupınar University Advanced Technology Center laboratory from room temperature to 600 ℃. As a result of the analysis, thermal expansion constant, Young constant, shear constant, enthalpy change, Gibbs energy change and entropy change of Al-1,9Sc-6Mg alloy were obtained. As a result of the analysis, it is concluded that there is no phase transition from the alloy but there is recrystallization at some temperatures. In addition, it was found that the results obtained were compatible with the results of closely proportional Al-Mg-Sc alloy results.

INTRODUCTION

Al-base alloys are one of the important raw materials of the industry in terms of cost and energy efficiency and experimental and theoretical studies on these alloys are continuing intensively [1]. Al-Mg alloys, sea water resistance, ductility resistance, corrosion resistance, has a wide range of applications in the industry because of the characteristics of good weldability [2,3]. The addition of Sc to Al-Mg alloys results in an extremely thin and homogeneously dispersed sequence of Al_3Sc precipitates [4,5]. The scandium element provides benefits such as increased strength of the alloy, reduced particle size, increased recrystallization temperature, and improved high resistance to hot cracking [6,7]. At low scandium rates, the effect of high strength and high temperature recrystallization of the material is due to the Al_3Sc precipitations in the material [8]. In this study, thermal measurements of Al-1.9Sc-6Mg alloy were investigated and the effect of temperature change and physical parameters and Mg contribution were investigated.

METHODS

Differential scanning calorimetry (TG/DSC) and Thermomechanical analysis (TMA) measurements of Al-1.9Sc-6Mg alloy samples were performed in thermal analysis experiments.

For the TG / DSC, SETARAM Labsys Evo model Simultaneous Thermal Analyzer is used which can work at temperatures between 30 - 1600 °C. For the TMA experiments, SETARAM brand Setsys Evo model Thermo-Mechanical Analyzer which can work at temperatures between 30-1750 °C was used.

For TG/DSC analyzes, samples weighing 55 mg were placed in platinum crucibles. Heat treatment was applied to the samples between 30 - 600 °C using argon atmosphere with 10 °C/min heating rate. Simultaneous weight and energy changes on the material during the heat treatment were measured. Enthalpy, Gibbs free energy and entropy values were derived from the measured values.

For TMA analysis, samples of 2.36 mm height were placed on the alumina holder and 5 g. load applied. Heat treatment was applied to the samples between 30 - 600 °C using argon atmosphere with 10 °C/min heating rate. The size change and thermal expansion and Young modulus coefficient on the material during the heat treatment were obtained.

SENSYS EVO TG-DSC for differential scanning calorimetry (TG/DSC) analysis and SETSYS EVOLUTION TMA for thermomechanical analysis (TMA) are shown in Figure 1 and Figure 2, respectively. The measuring devices are located in Kütahya Dumlupınar University İLTEM research center.

ISBN:978-605-83516-6-0



FIGURE 1. SENSYS EVO TG-DSC



FIGURE 2. SETSYS EVOLUTION TMA

Recrystallization temperatures and enthalpy were determined from the peaks formed in the obtained TG / DSC curve. The entropy of recrystallization was also calculated using temperature and temperature data. Using Equation 1, Gibbs energy of the recrystallization peak was calculated. Here, ΔG; Gibbs energy, ΔH; Enthalpy, T; recrystallization temperature and ΔS; It shows entropy values.

$$\Delta G = \Delta H - T\Delta S \quad (1)$$

Unit displacement (ϵ), thermal expansion coefficient (α) and Young's modulus (E) were calculated using equations 2, 3 and 4, respectively, using the curves obtained by TMA measurements. Here Δl; the amount of expansion, 10; the first length of the material and ΔT; temperature changes [9].

$$\epsilon = \frac{\Delta l}{l_0} \tag{2}$$

$$\alpha = \frac{\Delta l}{l_0 \Delta T}(℃)^{-1} \tag{3}$$

$$E = \frac{G}{\epsilon}(N/m^2) \tag{4}$$

DISCUSSION AND CONCLUSION

Figure 3 shows the DSC graph of the Al-6Mg-1.9Sc alloy. The graph shows the maximum peak recrystallization zone at a temperature of 491.93 ℃. -30,128 J/g obtained from the peak area gives the enthalpy change of the alloy. Entropy and Gibbs energy changes obtained from enthalpy changes are also given in Table 1.

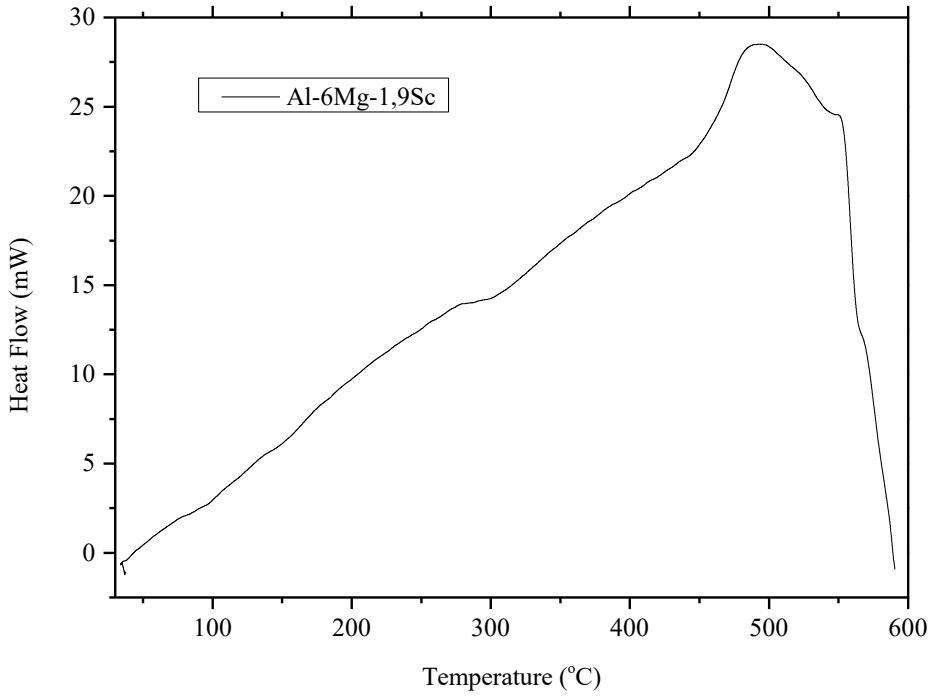


FIGURE 3. DSC graph of the Al-6Mg-1,9Sc alloy

Recrystallization temperature, enthalpy change, entropy change and Gibbs energy change were obtained from DSC data. The addition of Sc and Mg was found to increase the recrystallization temperature in this alloy. In this case, the alloy can be considered to have good strength at high temperatures. Thermal data indicate that the internal reaction of the material is exothermic; enthalpy and Gibbs energy changes are understood to be negative. These energies are negative, the reaction is voluntary, and the entropy magnitude gives an idea of disorder. In this study, it is seen that the entropy change is not very small. According to this result, it is concluded that there is a small irregularity in the crystal structure of Al-6Mg-1,9Sc alloy. The reason for this is the high Mg content in the alloy.

TABLE 1: Some thermal parameters of Al-1.1Sc alloy

	Recrystallization Temperature	**ΔH (J/g)**	**ΔS (J/G℃)**	**ΔG (J/g)**
Al-1,9Sc-6Mg	491,93	-30,128	0,0470	-53,264

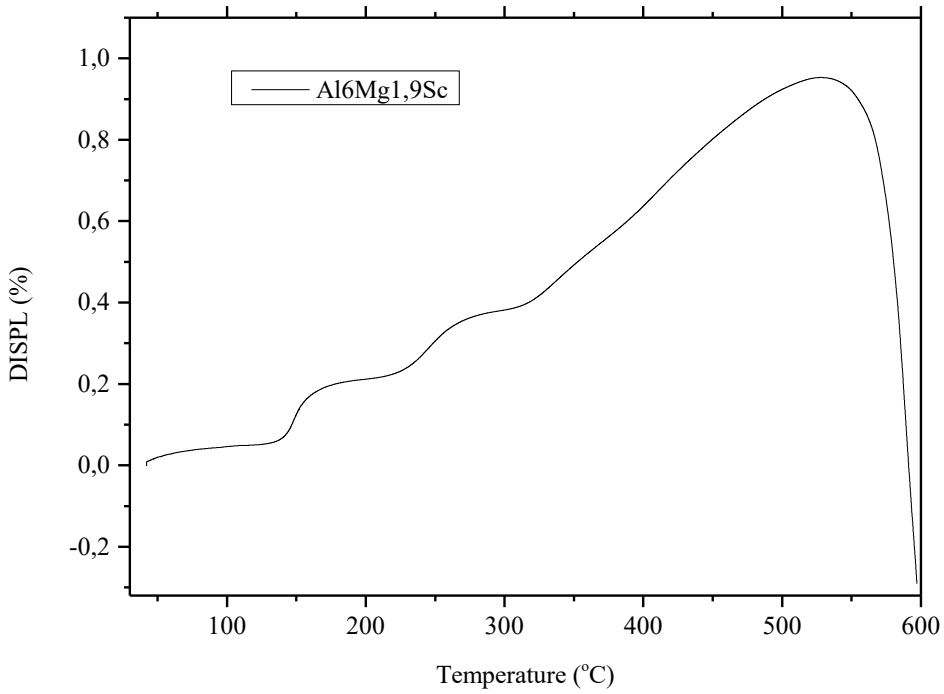


FIGURE 4. TMA graph of Al-1,9Sc alloy

Figure 4 shows the TMA graph of Al-6Mg-1.9Sc alloy. In the graph, it was seen that the amount of elongation in the material increased in direct proportion with the increase in temperature. With the increase in temperature, it was observed that there were small changes in the slope of the graph. Therefore, the coefficient of thermal expansion showed different variations in different temperature ranges. Recrystallization in the material can also be understood from the differences in temperature variation of the expansion constant.

In Table 2, the change in size (ϵ), thermal expansion (α) and Young Constant (E) values of Al-6Mg-1.9Sc alloy were calculated with temperature. The mean value of the thermal expansion coefficient was calculated as 35,54 $(*10^{-6})$ $(℃)^{-1}$ and it was found that the thermal expansion coefficient was directly proportional to the temperature. Young constant was calculated as 21.78 GPa and it was observed to be inversely proportional to temperature.

TABLE 2. Al1,9Sc size change (ϵ), Thermal expansion (α) and Young's Constant (E)

Temperature Range (℃	**α (*10-6) $(℃)^{-1}$**	**ϵ $(*10^{-5})$**	**E (GPa)**
43,33 – 136,76	5,48	51,22	33,86
136,76 – 161,67	45,99	114,57	15,14
161,67 – 229,26	9,44	63,83	27,17
229,26 – 278,94	25,71	127,74	13,58
278,94 – 315,2	8,23	29,86	58,08
315,2 – 539,25	24,51	549,19	3,15
539,25 – 595,62	129,43	729,61	1,49
Arithmetic Average	35,54	238,01	21,78
43,33 – 597,12	5,40	300,03	5,78

If the results are compared with pure aluminum results; The theoretical coefficient of thermal expansion of aluminum 24 (* 10-6) (℃) -1, the average value of Al-6Mg-1.9Sc alloy was found to be 35.54 (* 10-6) (℃) -1. It can be seen that the addition of Sc increases the coefficient of thermal expansion, albeit very small. The Young

constant is 69 GPa for pure aluminum. The Young constant of the Al-6Mg-1,1Sc alloy suddenly decreased after 140 ℃ (Table 2). Considering the Young's constant (26,55GPa) at the initial temperature of this alloy, it is clear that the high content of Mg adds negatively to the strength, since Sc is known to add strength to the material. At high temperatures, it is thought that partial dissolution in the material accelerates due to Mg element and therefore Young's constant decreases.

We would like to thank Kütahya Dumlupınar University BAP Program for supporting this study.

REFERENCES

1. E. Nembach, “Order strengthening: recent developments, with special reference to aluminum-lithium alloys ”, Prog. Mater. Sci. 45, 275 (2000).
2. Z. Shi'ang, Z. Zhen, L. Ming, P. Dejiang, S. Hailin, D. Xiaodong, L. Ping, W. Yucheng, Materials and Design 90 1077–1084 (2016).

1. 3. K. Seong-jong, L. Seung-jun, J. Jae-yong, K. Yu-hwan, Transactions of Nonferrous Metals Society of China 22 (3) 881-886 (2012).
3. X. Pian, J. Feng, T. Zhongqin, Y. Ning, J. Jingyu, X. Xuda, P. Yongyi, Journal of Alloys and Compounds 781 209-215 (2019).
4. Z. Shi'ang, Z. Zhen, L. Ming, P. Dejiang, S. Hailin, D. Xiaodong, L. Ping, W. Yucheng, Materials Characterization 118 85–91 (2016).
5. M. Kaiser, S., Datta S., Roychowdhury A., and M. K. Banerjee, Materials and Manufacturing Processes, 23: 74–81 (2008).
6. V. V. Zakharov, Metal Science and Heat Treatment 45 7-15 (2003).
7. G. Cacciamani, P. Riani, G. Borzone, N. Parodi, A. Saccone, R. Ferro, A. Pisch, and R. Schmid-Fetzer, Intermetallics, 7, pp. 101-109, (1999).
8. W. D. Callister and D. G. Rethwisch, Materials Science and Engineering, (Nobel publishing, Wiley, 2014), pp. 992.

BOOK OF FULL TEXT PROCEEDINGS TURKISH PHYSICAL
SOCIETY 35th INTERNATIONAL PHYSICS CONGRESS (TPS35)
TPS35, Vol.01, No.04, pp.337-344.
ISBN:978-605-83516-6-0

15 December 2019

The Theorical Investigation of Antiperovskite $ANTi_3$ (A=A1l, In, Tl) Compounds with DFT Calculations

İnanç Yılmaz[1], Ülkü Bayhan[1, a)] and Yasemin Öztekin Çiftçi[2]

[1] *Burdur Mehmet Akif University, Department of Physics, 15100, Burdur, Turkey*
[2]*Gazi University, Department of Physics, Teknikokullar, Ankara, Turkey*

[a)]Corrensponding author: ubayhan@mehmetakif.edu.tr

Abstract. The structural, elastic, electronic and thermodynamic properties of $ANTi_3$ (A = Al, In, Tl) compound are investigated using the methods of density functional theory within the generalized gradient approximation (GGA). The results on the basic physical parameters, such as the lattice constant, bulk modulus, second-order elastic constants, Zener anisotropy factor, Poisson's ratio, Young's modulus and isotropic shear modulus are presented. In addition, the anisotropic properties of the material group were examined and 3D graphs were drawn and interpreted.

INTRODUCTION

The triple compounds of carbides and nitrites with the general presentation of cubic type matrials AXM_3, known as antiperovskite, are worth investigating as promising compounds used in different technological applications. In general notation, A (IIIA - VA) is the element, X is C or N elements and M is the transition metal (s - d) [1]. Interesting properties of these materials include high magneto resistances [2], low temperature near-zero resistance coefficients [3], and a wide range of properties from superconductor to insulator [4 - 5]. Crystallizing matterial in $Pm\bar{3}m$ (# 221) space group. A atoms are located in the Wyckoff positions of 1a (0, 0, 0), X atoms 1b (0.5, 0.5, 0.5) and M atoms 3c (0, 0.5, 0.5).

Chern et al. [6] Ca_3N_2 powders VA group elements N_2 gas at 1000 °C $ANCa_3$ synthesis as a result of the semiconductor properties were observed. When the electronic structure and bonding properties of $BiNCa_3$ and $PbNCa_3$ compounds were examined by Papaconstantopoulos and Pickett [7] local density approach and using Vansant et al [8], the band spacing of these compounds was determined to be very narrow bandgap. In the superconducting antiperovskite search studies by Schaak et al [9], the intermetallic AXM_3 have a broad stoichiometry that can critically affect superconductivity properties. New intermetallic antiperovskite type triple nitrides were synthesized by Cao et al. Experimental and theoretical studies have been conducted to understand the nature of superconductivity and high magneto resistance [6, 9–12].

In this study, mechanical properties (lattice constant, elastic properties, Bulk, Young, and Shear modulus, anisotropic properties Debye temperature), electronic properties (band structure and state density) and vibration properties of $ANTi_3$ determined fort he first time. . In addition to the study results compared with those of $ACTi_3$ compounds in the literature. The data obtained were consistent with other theoretical studies.

COMPUTATIONAL METHODS

The first principles methods are currently used to identified the features of materials and are highly accepted by researchers because of the high sensitivity of the various physical and chemical properties to be examined [13]. In this study, Generalized Gradient Approach [14-15] (GGA) was developed by Perdew et al. Electron-ion interactions were represented by the Vanderbilt type ultrasoft pseudopotential [16]. Cut - off energy was determined as 400 eV. Convergence was determined according to the Monkhorst - Pack scheme taking into account the 8 x 8 x 8 k - points in the Brillouin region [17-18].

ISBN:978-605-83516-6-0

By applying a given set of homogeneous deformation calculated elastic coefficients and by calculating the stress associated with optimizing internal atomic degrees of freedom [19]. The total energy in the atom was chosen $5x10^{-6}$ eV / atom, ionic Hellmann - Feynman force 10^{-2} eV/Å was chosen for optimization of atomic internal freedoms ($4x10^{-4}$ Å for max ionic displacements). A tensile pattern with non-zero first and fourth components using two positive and two negative stresses for all three independent elastic constants for the cubic system.

RESULTS AND DISCUSSION

Structural Properties

Lattice parameter was calculated for $ANTi_3$ (A = Al, In, T1) compounds and compared the parameters with other availale theoretical and experimental studies,

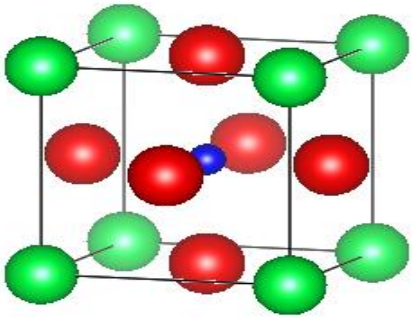


FIGURE 1. Structure of Antiperovskite $ANTi_3$ (A= Al, In, Tl). The green atoms (corner located) represent by *A (A= Al, In, Tl)*, the red atoms (primitive cell surface bottom) represent by *Titanium* and the blue atom (bottom of primitive cell) represent by *Nitrogen*.

Bulk modulus, eigenvalue and enthalpy of formation are presented in Table.1. The lattice constants from results increased in the order of $AlNTi_3$> $InNTi_3$> $TlNTi_3$. This can be easily understood from the fact that the atomic radius of Al and In is smaller than the atomic radius of T1 [20]. This is true for the calculated eigenvalue (ρ) values. The negative formation enthalpy calculated for $ANTi_3$ (A = Al, In, Tl) compounds is a criterion indicating that these compounds can be synthesized in laboratory.

TABLE 1. Lattice parameter (a_0 in Å), density (ρ in g/cm^3), bulk modulus (B in GPa) and formation energy (ΔH_f in eV/atom) for $ANTi_3$ compounds

Compounds	Reference	a_0	ρ	B_0	ΔH_f
$AlNTi_3$	This Work	4.0375	4.65965	189.22	-2.5580
	[21]	4.1123	4.410	162.88 ± 0.13	-
	[22]	4.112	-	-	-
$InNTi_3$	This Work	4.1092	6.5219	173.93	-2.5111
	[21]	4.195	6.129	152.961 ± 0.14	-
	[23]	4.190	-	-	-
$TlNTi_3$	This Work	4,1135	8.6381	186.36	-2.4331
	[21]	4.204	8.091	152.557 ± 0.5	-
	[23]	4.191	-	-	-

Elastic Properties

In this study, the calculated elastic constants of the materials are given in Table.2. Elastic constants (C_{ij}) are the cornerstones of a material that determine the mechanical and dynamic behavior. It is very important to calculate the elastic constants in order to have information about the hardness and stability of the material and to determine the technological application area according to the need. A cubic symmetry has three elastic parameters (C_{11}, C_{12} and C_{44}). In this study, elastic constants of $ANTi_3$ (A = Al, In, T1) compounds were obtained by forced - forcing technique.

ISBN:978-605-83516-6-0

These constants, also called mechanical stability of crystals, are very important for the follow-up of the usability and sustainability of materials in technological applications (Eq 1). The elastic constants calculated for all compounds are positive and mechanically stable [24]. All calculated compounds in $ANTi_3$ (A = Al, In, T1) comply with this criterions are below:

$$C_{44} > 0 \quad ; \quad C_{11} - C_{12} > 0 \quad ; \quad C_{11} + C_{12} > 0 \quad ; \quad B > 0 \tag{1}$$

TABLE 2. Calculated elastic constants (C_{ij} in GPa) of $ANTi_3$ compounds

Compounds	Ref	C_{11}	C_{12}	C_{44}
$AlNTi_3$	This Work	240.34905	163.64855	65.61895
	[21]	199.42 ± 3.4	146.86 ± 1.1	50.72 ± 0.4
$InNTi_3$	This Work	178.72095	171.53670	46.05105
	[21]	137.69 ± 2.1	161.35 ± 0.5	38.54 ± 0.04
$TlNTi_3$	This Work	264.92260	147.08330	64.86525
	[21]	198.00 ± 1.9	128.31 ± 1.1	52.62 ± 0.3

The other data obtained from the calculated elastic constants (Bulk modulus, Shear modulus and Young modulus etc.) given in Table 2 are presented in Table.3.

TABLE 3. Calculated bulk modulus (B in GPa), Young's modulus (E in GPa), shear modulus (G in GPa), Poisson's ratio (σ) and hardness (H_v in GPa) for $ANTi_3$ compounds

Compounds	Ref	B	E	G	σ	H_v
$AlNTi_3$	This Work	189.22	145.17	52.9	0.37213	14.032
	[21]	164.38 ± 1.4	108.311	38.956	0.3901	-
$InNTi_3$	This Work	173.93	53.749	18.554	0.4485	12.8880
	[21]	153.47 ± 0.7	−56.880	−18.21	0.5617	-
$TlNTi_3$	This Work	186.36	168.45	62.418	0.34936	12.7843
	[21]	−151.54 ± 0.9	121.862	44.606	0.3659	-

The ratios obtained from these data (B/G and G/B) anisotropy factor (A) *Lamé* coefficients (λ and μ) are presented in Table.4.

TABLE 4. Calculated B/G ratio, G/B ratio, B/C_{44} ratio, anizotropy factor(A) and *Lamé* coefficients (λ and μ) for $ANTi_3$ compounds

Compounds	Ref	B/G	G/B	B/C_{44}	A	λ	μ
$AlNTi_3$	This Work	3.576	0.2795	2.8836	1.7110	153.9494	52.8995
	[21]	-	-	3.81	1.9299	138.409	38.956
$InNTi_3$	This Work	9.374	0.1066	3.7769	12.8200	161.5760	18.5533
	[21]	-	-	3.57	−3.2578	165.603	−18.210
$TlNTi_3$	This Work	2.985	0.3349	2.8730	1.1009	144.7592	62.4184
	[21]	-	-	2.78	1.5101	121.802	44.6063

Bulk modulus (B), Young modulus (E), Shear modulus (G), Poisson's ratio (σ) and hardness (H_v) given in Table 3 were calculated with the help of the following expressions [25, 26, 27]:

$$B = \frac{(C_{11}+2C_{12})}{3} \tag{2}$$

$$E = \frac{9BG}{3B+G} \tag{3}$$

$$G = \frac{G_V+G_R}{2} = \frac{1}{2}\left[\frac{C_{11}-C_{12}+3C_{44}}{5} + \frac{5C_{44}C_{11}-5C_{44}C_{12}}{4C_{44}+3C_{11}-3C_{12}}\right] \tag{4}$$

$$H_v = 2(k^2G)^{0.585} - 3; (k = G/B) \tag{5}$$

$$\sigma = \frac{3B-E}{6B} \tag{6}$$

The bulk modulus (B) is a measure of the hardness of solids. The Bulk modulus of a material is defined as a measure of the resistance of a material to volume change under hydrostatic pressure(Eq. 2). The quantity defined as another measure of hardness is the Shear (G) modulus. Shear modulus (G) or moduus of rigidity (Eq. 4) can be defined as the material's resistance to shear stress of a material and shows the material's resistance to reversible deformations. The maximum value of Bulk modulus calculated according to Table 3 belongs to $AlNTi_3$ (189.22 GPa). The lowest

ISBN:978-605-83516-6-0

Bulk modulus value belongs to $InNTi_3$ (173.93 GPa). According to Table 3, the highest Shear modulus value belongs to $TlNTi_3$ (62.418 GPa) and the lowest calculated value belongs to $InNTi_3$ (18.554 GPa). Since materials with bulk modulus greater than 100 GPa are considered rigid, all calculated compounds have low compressibility.

Young's modulus (E) is defined as the relationship between stress (force per unit area) and strain (proportional deformation) in a material in the linear elasticity conditions of a uniaxial deformation (Eq. 3**)**. Young's modulus is higher if the materials are harder properties. Among the compounds calculated according to Table 3, the highest Young modulus value belongs to $TlNTi_3$ (168.45 GPa) and the lowest value belongs to $InNTi_3$ (53.749 GPa).

In the hardness expression, k parameter is the ratio of Pugh's modulus [28]. If we use the hardness expression calculated in Table.3, we see that the hardest material calculated is $AlNTi_3$ (14.032 GPa). We see that the lowest hardness material belongs to $TlNTi_3$ (12.7843 GPa) compound. All calculated hardness values ($H_v \geq 40$ GPa) are below the super hardness limit. Among these compounds, $AlNTi_3$ (14.032 GPa) is relatively harder than others.

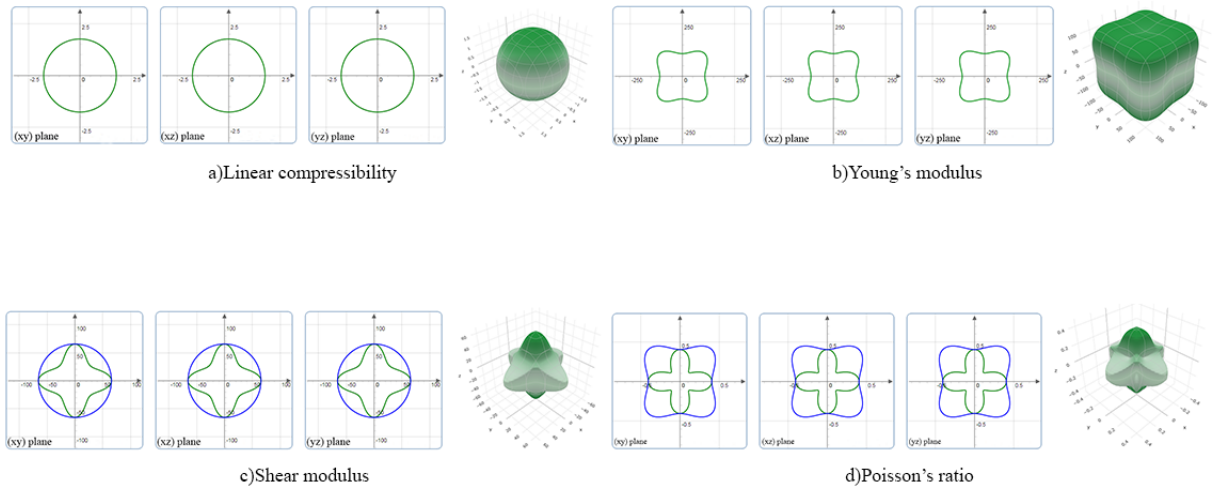


FIGURE 2. The 2D and 3D results (a)linear compressibility, (b)Young's modulus, (c)Shear modulus and (d) Poisson's ratio for $ANTi_3$ compounds (such as Mo_2Pb)

Poisson's ratio(σ) gives information about intraatomic bonds (Eq. 6). It is generally around 0.1 for materials with covalent bonds and about 0.25 for materials with ionic bonds. For metallic materials, the Poisson ratio is around 0.33. Poisson ratios given in Table 3 are around 0.33 except for the value of $InNTi_3$ compound. The two compounds other than the $InNTl_3$ compound are typically thought to be metallic materials [29].

In Table 4, B/G ratio, G/B ratio, anisotropy factor (A) and Lame coefficients (λ and μ) were calculated with the help of the following statements (Eq. 8-9).

$$A = \frac{2C_{44}}{C_{11}-C_{12}} \tag{7}$$

$$\mu = \frac{E}{2+2\sigma} \tag{8}$$

$$\lambda = \frac{E\sigma}{1-\sigma-2\sigma^2} \tag{9}$$

Cracks in crystals are directly related to the anisotropy of thermal and elastic properties [25]. For materials with cubic symmetry, the anisotropy factor A in Table 4 was calculated using the following statement. If the anisotropy values given in Table 4 are examined, the compound with the highest anisotropy is $InNTi_3$. The lowest compound is $TlNTi_3$.

The B/G ratio is a very important criterion for hardness. When this value is less than 1.75, it is concluded that the material is fragile and in case it is high, the material is ductile. Since all B/G ratios calculated in Table 4 are greater than 1.75, all compounds are ductile.

ISBN:978-605-83516-6-0

The *G*/*B* ratio (*Pugh's modulus*) is used to find the bonding characteristics of atoms in crystals. If the value of the Pugh modulus is about 1.1, the covalent bond is more dominant than the ionic bond. Otherwise, the value of the Pugh modulus is approximately 0.6. As this value decreases, the ionic bonds in the atom gain more dominance against covalent bonds [28].

Lamé coefficients are λ which are related to the material shown in stress - strain relations. It is related to the hardness of the materials [25, 27]. Table 3 shows the calculated *Lamé* coefficients. The calculated B/C_{44} ratios also indicate that the materials subject to this study are ductile.

TABLE 5. Calculated longitudinal sound velocity(V_l in m/s), transverse sound velocity (V_t in m/s), average sound velocity (V_m in m/s) and *Debye* temperature (θ_D in °K) for $ANTi_3$ compounds

Compounds	Ref	V_l	V_t	V_m	θ_D
$AlNTi_3$	This Work	3369.4	7466.3	4593,7	579.45
	[21]	6849	2906	3285	407
$InNTi_3$	This Work	1686.7	5601.9	2389.9	296.18
	[21]	5867	2697	3039	369
$TlNTi_3$	This Work	2688.1	5586.5	3625.5	448.83
	[21]	5106	2697	3015	365

Debye temperature, elastic constants and specific heat are related to many physical characteristics are basic parameters in solids [30]. Debye temperature was calculated for $ANTi_3$ (A = Al, In, Tl) compounds and average sound velocity [30]

$$\theta_D = \frac{h}{k_B}\left[\frac{3q}{4\pi}.\frac{N\rho}{M}\right]^{1/3} v_m \tag{10}$$

In this equation, h Planck Constant, k_B Boltzmann Constant, N Avogadro number, ρ density, M is the crystalline molecular weight and q is the number of atoms in the molecule. The remaining v_m the average sound velocity in the crystal [30].

$$v_m = \left[\frac{1}{3}\left(\frac{2}{{v_t}^3} + \frac{1}{{v_l}^3}\right)\right]^{-1/3} \tag{11}$$

The variables v_t and v_l in this equation are the transverse / longitudinal sound velocities. These variables are calculated by *Navier* equations [30]. Navier equations are given below.

$$v_t = \left(\frac{3B+4G}{3\rho}\right)^{1/2} \qquad \text{and} \qquad v_l = \left(\frac{G}{\rho}\right)^{1/2} \tag{12}$$

The calculated parameters of the compounds are given in Table 5 above. Comparing with the other theoretical data available, there is no experimental studies on these compounds in the literature.

Electronic Properties

For $ANTi_3$ (A = Al, In, T1) compounds in equilibrium lattice constants, band structure calculations give almost identical electronic band structures around the Fermi energy level E_f .

Band structure (tDOS), state densities (pDOS) predicted by atomic region were calculated in equilibrium geometry for $ANTi_3$ (A = Al, In, T1) compounds. The absence of a gap at the Fermi level in the band structure graphs visualized along the high symmetry points for $ANTi_3$ (A = Al, In, T1) compounds indicates that these compounds are of metallic properties (Figure3-a,b,c).

ISBN:978-605-83516-6-0

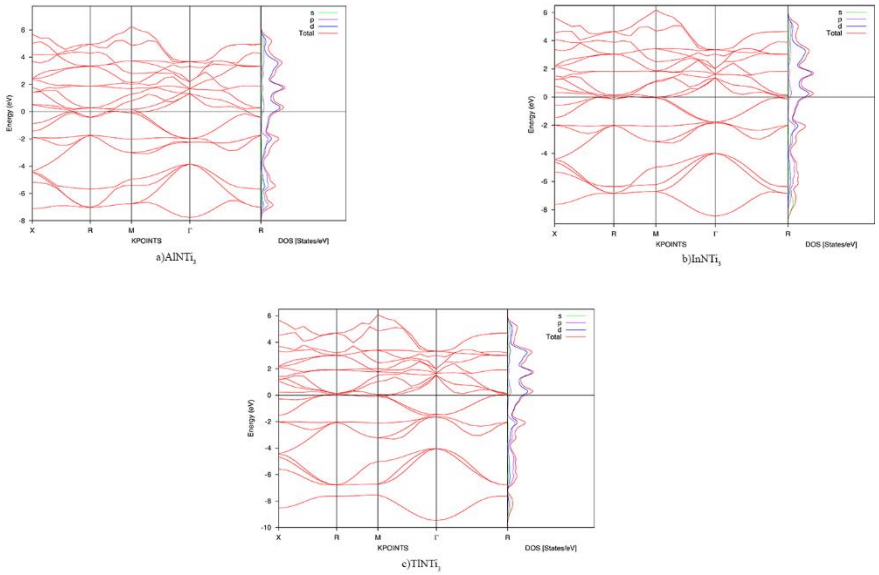


FIGURE 3. Band structure for (a) $AlNTi_3$, (b) $InNTi_3$ and (c)$TlNTi_3$ compounds

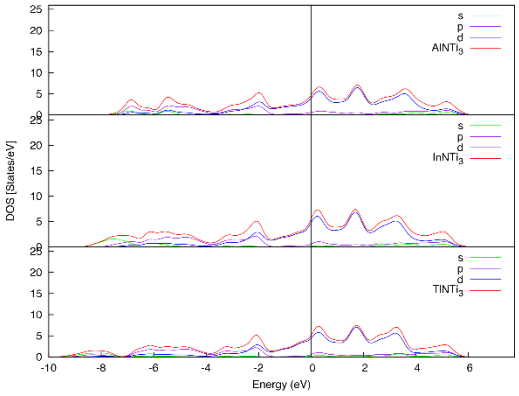


FIGURE 4. Partial density of states of $ANTi_3$ compounds

Figure 4. presented partial density of states of $ANTi_3$ compounds. The interaction is caused by Ti 3d and N 2p states electrons can be seen the graphs indicated.

ISBN:978-605-83516-6-0

Vibrational Properties

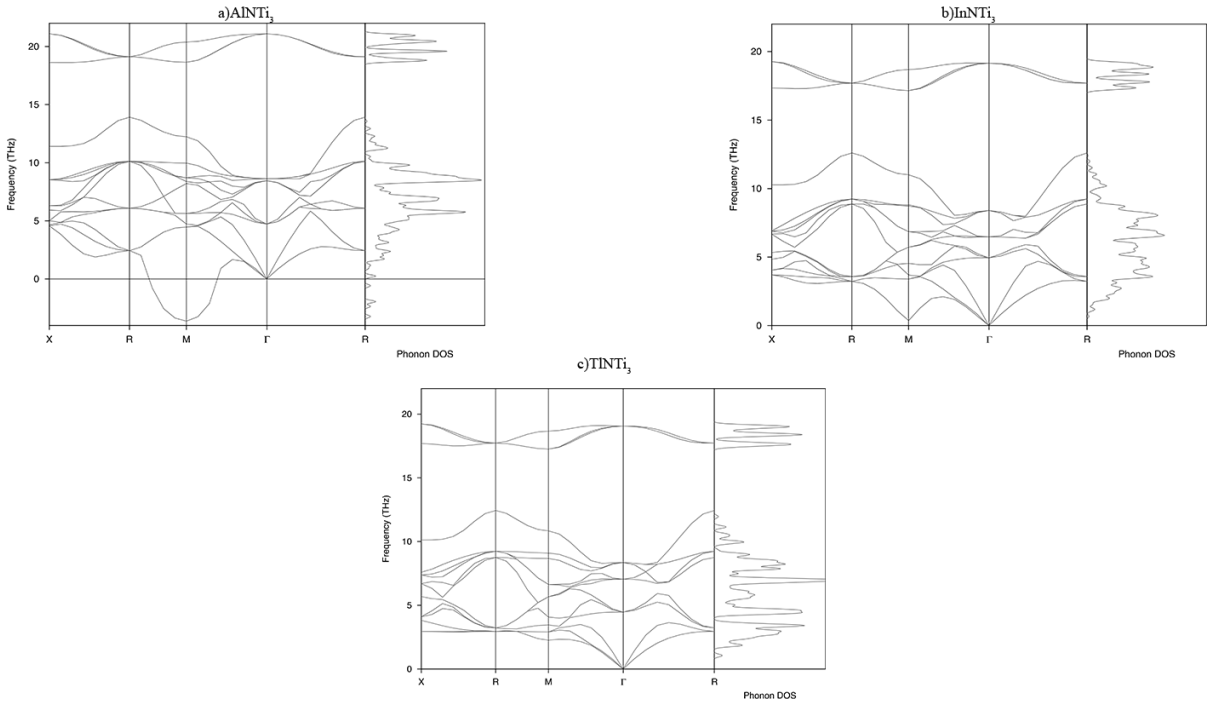


FIGURE 5. Phonon dispersion curves and PDOS for (a) $AlNTi_3$, (b) $InNTi_3$ and (c) $TlNTi_3$

Phonon dispersion and PDOS calculations have been using CASTEP [13-14] finite displacement method. This method implements schemes based on numerical differentiation of forces when atoms are displaced by a small amount from their equilibrium positions. In addition, in cases where ultrasoft pseudopotentials are used in a DFPT calculation, it gives a good result compared to the linear response method. There are 15 branches in the Figure 5. where 3 branches acoustic and the odhers are optic branches. $InNTi_3$ and $TlNTi_3$ are stable while $AlNTi_3$ is unstable (Figure 5a). The negative mode seen in the phonon graph of $AlNTi_3$ is thought to be caused by the transition of this material from the ferromagnetic phase (FM) to the antiferromagnetic phase.

CONCLUSION

We have studied the structural, elastic and electronic properties of $ANTi_3$ compounds. The conclusions can be summarized as follows: • The B/G values of $ANTi_3$ compounds show that these materials behave as ductile. • The band structure calculations show that our compounds are ionic charecter and only one $AlNTi_3$ exhibit magnetism at their equilibrium lattice constants. • The elastic properties of the studied compounds showed $InNTi_3$ and $TlNTi_3$ are stable while $AlNTi_3$ is unstable. The phonon graph drawn for the first time for this material showed that phase transitions can also be studied.

ACKNOWLEDGMENTS

This work was partly supported by NanoSimLab and The Scientific Research Unit of Burdur Mehmet Akif Ersoy University under Grant No. 0362-NAP16 and 0147-NAP12. Some of the calculations were performed in the HPCC (High Performance Computing Center) at Gazi University. The researchers have gratefully acknowledged this support.

REFERENCES

1. S. Goodenough, J.B., Gräper, W., Holtzberg, F., Huber, D.L., Lefever, R.A., Longo, J.M., McGuire, T.R., Methfessel, “Magnetic and Other Properties of Oxides and Related Compounds Part B,” *Landolt–Bornstein, New Ser. Gr. III*, vol. 4a, pp. 126-275 Springer-Verlag; Berlin, 1970.
2. N. H. H. W.S. Kim, E.O. Chi, J.C. Kim, H.S. Choi, “Close correlation among lattice, spin, and charge in the

ISBN:978-605-83516-6-0 15 December 2019

manganese-based antiperovskite material," *Solid State Commun.*, vol. 119, no. 8–9, pp. 507–510, 2001.
3. E. O. Chi, W. S. Kim, and N. H. Hur, "Nearly zero temperature coefficient of resistivity in antiperovskite compound CuNMn3," *Solid State Commun.*, vol. 120, no. 7–8, pp. 307–310, 2001.
4. A. Bouhemadou, R. Khenata, M. Chegaar, and S. Maabed, "First-principles calculations of structural, elastic, electronic and optical properties of the antiperovskite AsNMg3," *Phys. Lett. Sect. A Gen. At. Solid State Phys.*, vol. 371, no. 4, pp. 337–343, 2007.
5. C. M. I. Okoye, "Theoretical investigation of electronic structure and optical properties of paramagnetic non-oxide perovskite $AlCNi_3$," *Solid State Commun.*, vol. 136, no. 11–12, pp. 605–610, 2005.
6. M. Y. Chern, D. A. Vennos, and F. J. Disalvo, "Synthesis, structure, and properties of anti-perovskite nitrides Ca_3MN, M=P, As, Sb, Bi, Ge, Sn, and Pb," *J. Solid State Chem.*, vol. 96, no. 2, pp. 415–425, 1992.
7. D. A. Papaconstantopoulos and W. E. Pickett, "Ternary nitrides BiNCa3 and PbNCa3: Unusual ionic bonding in the antiperovskite structure," *Phys. Rev. B*, vol. 45, no. 8, pp. 4008–4012, 1992.
8. P. Vansant, P. Van Camp, V. Van Doren, and J. Martins, "Variable-cell-shape-based structural optimization applied to calcium nitrides," *Phys. Rev. B - Condens. Matter Mater. Phys.*, vol. 57, no. 13, pp. 7615–7620, 1998.
9. R. E. Schaak *et al.*, "Formation of transition metal boride and carbide perovskites related to superconducting $MgCNi_3$," *J. Solid State Chem.*, vol. 177, no. 4–5, pp. 1244–1251, 2004.
10. W. H. Cao, B. He, C. Z. Liao, L. H. Yang, L. M. Zeng, and C. Dong, "Preparation and properties of antiperovskite-type nitrides: $InNNi_3$ and $InNCo_3$," *J. Solid State Chem.*, vol. 182, no. 12, pp. 3353–3357, 2009.
11. J. H. Shim, S. K. Kwon, and B. I. Min, " Electronic structures of antiperovskite superconductors MgXNi3 (X=B, C, and N) ," *Phys. Rev. B*, vol. 64, no. 18, pp. 3–6, 2001.
12. S. Q. Wu, Z. F. Hou, and Z. Z. Zhu, "Elastic properties and electronic structures of CdCNi3: A comparative study with MgCNi3," *Solid State Sci.*, vol. 11, no. 1, pp. 251–258, 2009.
13. W. Rose *et al.*, "Universities of Leeds , Sheffield and York First principles methods using CASTEP," *Transition*, vol. 220, pp. 567–570, 2005.
14. M. D. Segall *et al.*, "First-principles simulation: Ideas, illustrations and the CASTEP code," *J. Phys. Condens. Matter*, vol. 14, no. 11, pp. 2717–2744, 2002.
15. J. P. Perdew, K. Burke, and M. Ernzerhof, "Generalized Gradient Approximation Made Simple [Phys. Rev. Lett. 77, 3865 (1996)]," *Phys. Rev. Lett.*, 1997.
16. D. Vanderbilt, "Soft self-consistent pseudopotentials in a generalized eigenvalue formalism," *Physical Review B*, vol. 41, no. 11. p. 7892, 1990.
17. J. D. Pack and H. J. Monkhorst, ""Special points for Brillouin-zone integrations"—a reply," *Phys. Rev. B*, vol. 16, no. 4, pp. 1748–1749, Aug. 1977.
18. T. H. Fischer and J. Almlöf, "General methods for geometry and wave function optimization," *J. Phys. Chem.*, vol. 96, no. 24, pp. 9768–9774, 1992.
19. M. C. Milman, V., Warren, "Elasticity of hexagonal BeO," *J. Phys. Condens. Matter*, vol. 13, no. 2, pp. 241–251, 2001.
20. A. S. Verma and V. K. Jindal, "Lattice constant of cubic perovskites," *J. Alloys Compd.*, vol. 485, no. 1–2, pp. 514–518, 2009.
21. D. Cherrad, L. Selmani, D. Maouche, and M. Maamache, "First principles calculations on elasticity, electronic structure and bonding properties of antiperovskites ANTi3 (A = Al, in and Tl)," *J. Alloys Compd.*, vol. 509, no. 12, pp. 4357–4362, 2011.
22. J. C. Schuster and J. Bauer, "The ternary system titanium-aluminum-nitrogen," *J. Solid State Chem.*, vol. 53, no. 2, pp. 260–265, 1984.
23. W. Jeitschko, H. Nowotny, and F. Benesovsky, "Die Kristallstruktur von Ti3InC, Ti3InN, Ti3TIC und Ti3TIN," *Monatshefte für Chemie*, vol. 95, no. 2, pp. 436–438, 1964.
24. K. Born, M., Huang, "Dynamical Theory of Crystal Lattices." Oxford:At the Clarendon press, 1954.
25. D. J. Green, "An Introduction to the Mechanical Properties of Ceramics," *An Introd. to Mech. Prop. Ceram.*, 2010.
26. E. Schreiber, O. L. Anderson, N. Soga, and J. F. Bell, "Elastic constants and their measurement," *J. Appl. Mech.*, vol. 42, p. 747, 1975.
27. J. F. Nye, *Propriétés physiques des cristaux*. Dunod, 1961.
28. S. F. Pugh, "XCII. Relations between the elastic moduli and the plastic properties of polycrystalline pure metals," *London, Edinburgh, Dublin Philos. Mag. J. Sci.*, vol. 45, no. 367, pp. 823–843, 1954.
29. J. Haines, J. M. Léger, and G. Bocquillon, "Synthesis and design of superhard materials," *Annu. Rev. Mater. Sci.*, 2001.
30. O. L. Anderson, "a Simplified Method for Calculating the," *J. Phys. Chem. Solids*, vol. 24, pp. 909–917, 1963.

BOOK OF FULL TEXT PROCEEDINGS TURKISH PHYSICAL
SOCIETY 35th INTERNATIONAL PHYSICS CONGRESS (TPS35)
TPS35, Vol.01, No.04, pp.345-353.
ISBN:978-605-83516-6-0

15 December 2019

Anisotropic, Elastic and Lattice Dynamical Properties of Mo_2AB (A=Al, P, Si) MAX Phase Compounds

İnanç Yılmaz[1], Ülkü Bayhan[1, a)], Ayşenur Gencer[2] and Gökhan Sürücü[2,3,4]

[1] *Burdur Mehmet Akif University, Department of Physics, 15100, Burdur, Turkey*
[2]*Middle East Technical University, Department of Physics, 06800, Ankara, Turkey*
[3]*Ahi Evran University, Department of Electric and Energy, 40100, Kirsehir, Turkey*
[4]*Gazi University, Photonics Application and Research Center, 06500, Ankara, Turkey*

[a)]Corrensponding author: ubayhan@mehmetakif.edu.tr

Abstract. The structural, electronic, elastic, anisotropic elastic, lattice dynamical and thermodynamical properties of the MAX Phase borides compounds Mo_2AB (A=Al, P, Si) were made using the first principle calculations. These calculations were calculated using VASP code which has been included generalized gradient approximation based on density functional theory. Fundamental parameters for example lattice constant(a), elastic constants(C_{ij}), Shear Modulus(G), Young's Modulus(E), Bulk Modulus(B) and Poisson's Ratio(v) have been calculated by VASP code. The negative formation enthalpies calculated for compounds Mo_2AB (A=Al, P, Si) MAX Phase borides compounds have been shown to be stable and synthesizable materials. In the terms of calculation data it was determined that *Mo_2AlB* compound showed brittle character and the other compounds showed a ductile character. In addition to these properties, Mo_2AB (A = Al, P, Si) MAX Phase Boron compounds linear compressibility, Poisson's ratio, Young and Shear modules were determined to have anisotropic properties and direction dependence graphs were drawn and visualized in two and three dimensions. These compounds for the obtained electronic band structures and density of states found to show metallic character. The phonon dispersion and the density of states were plotted for Mo_2AB (A = Al, P, Si) MAX Phase compounds All compounds were stable.

INTRODUCTION

MAX Phase compounds are worth examining because they can be used as a high temperature material with ceramic-like hardness due to their layered crystal structures, high thermal shock resistance, friction life, thermal fatigue strength and oxidation resistance.

The general form of MAX Phase compounds $M_{(n+1)}AX_n$ (n = 1,2,3) has superior properties due to structurally ionic covalent and metallic bonds [1]. MAX Phase cystal structure is hexagonal (Space Group = 194), where M is a transition metal (such as Titanium, Tungsten, Zirconium) A is a group of elements A (Aluminum, Silicon, Gallium, etc.). X is Carbon or Nitrogen. Due to both the metallic and ceramic properties of the MAX Phase compounds, it is used in areas requiring high technology such as abrasion and coating against corrosion [2], superconducting materials[3] and the Boron's high neutron cross section due to its nuclear industry [4].

MAX Phase compounds consist of three atoms, these atoms have a large number of forms and these compounds have about 60 phases known today [5]. The common form of the MAX Phase compounds is the (211) phase with n = 1, and *Ti_2AlC* and *Ti_3SiC_2* are the most well known compounds [6–10]. Recently, research has been investigating new combinations of MAX Phase compounds. The most interesting of the researches is the use of Boron instead of Nitride and Carbide which are the components representing this group [11–13].

COMPUTATIONAL METHODS

In the DFT calculations using VASP (Vienna Ab - inito Simulation Package) [14–22], the cut - off energy of 550 eV [15, 16] PAW (Projector Augmented - wave Method) was used for electron - ion interaction. For the terms of change and correlation in electron - electron interaction, GGA and Perdew - Burke - Enzerhof [18] functionals were used. Convergence was performed according to the Brillouin region sampling, taking into account the Gamma (Γ)

ISBN:978-605-83516-6-0

centered 16 x 16 x 4 k points [19]. Stress and Hellman - Feynman forces were minimized by conjugated gradient [19, 20] algorithm with a force convergence lower than 10^{-8} eVÅ^{-1} to determine the ground state geometries. Energy tolerance was chosen to be less than 10^{-9} eV in the iterative solution of Kohn - Sham equations. Methfessel - Paxton [20] method was used for convergence calculations. To calculate the energy values more accurately, Blöchl corrections [21] and tetrahedron method were used.

In the DFT calculations using VASP (Vienna Ab - inito Simulation Package) [14–22], the cut - off energy of 550 eV [15, 16] PAW (Projector Augmented - wave Method) was used for electron - ion interaction. For the calculation of elastic constants in electron - electron VASP, the forced - strain method was used [14–18, 21–23]. The anisotropic elastic properties were plotted with the ELATE program using the calculated elastic constants. ELATE [26] is an open source elastic tensor software compiled from EIAM code [27]. Phonon band structure and state density were obtained using PHONOPY [28]. Force constants matrix density was obtained by the application of functional perturbation theory (DFPT). The unit cell used was expanded by 2 x 2 x 1 to form a 32-atoms supercell.

RESULTS AND DISCUSSION

Structural Properties

MAX Phase compounds crystallize in Mo_2AB hexagonal ($P6_3/mmc$: Space Group: 194) structure. Here, *M* atom *4f* (1/3, 2/3, z), *A* atom *2d* (1/3, 2/3, 3/4) and *2a* (0, 0, 0) *B* atom in Figure 1. It is found in the Wyckoff positions shown in Table 1. In addition to the information presented in Table 1, the formation energies of the calculated compounds are also indicated. Formation energies were calculated as in equation (1).

$$\Delta H_f = E_{Formation}^{Mo_2AB} = E_{Total}^{Mo_2AB} - (2E_{Solid}^{Mo} + E_{Solid}^{A} + E_{Solid}^{B}) \quad (1)$$

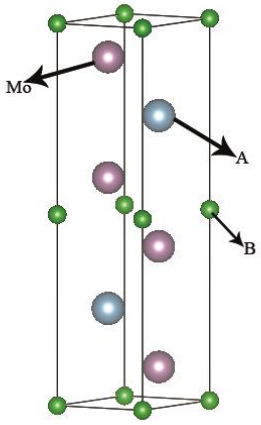


FIGURE 1. The crystal structure of Mo_2AB coumpounds shows the pink atoms M (Mo), the blue atoms A (A = Al, P, Si), the green atoms B (B).

Initial data for Mo_2AB (A = Al, P, Si) MAX Phase compounds optimized in hexagonal structure are given in the table below (Table 1. – 2.).

TABLE 1. Parameters (*a* and *c* in Å), Wyckoff Positions, and formation energy (ΔH_f in *eV/atom)*

Compounds	*a*	*c*	Atomic positions	ΔH_f
Mo_2AlB	3,086	13,285	Mo 4f (1/3, 2/3, 0,0922) 2d (1/3, 2/3, 3/4) B 2a (0, 0, 0)	-0,023
Mo_2PB	3,254	11,274	Mo 4f (1/3, 2/3, 0,105) P (1/3, 2/3, 3/4) B 2a (0, 0, 0)	-0,401
Mo_2SiB	3,219	11,709	Mo 4f (1/3, 2/3, 0,101) Si (1/3, 2/3, 3/4) B 2a (0, 0, 0)	-0,314

ISBN:978-605-83516-6-0

TABLE 2. Compounds parameters (*a* and *c* in Å),*c*/*a* ratio, density (ρ in g/cm^3), *z* parameter of the Wyckoff Positions, and formation energy (ΔH_f in *eV*/*atom)*

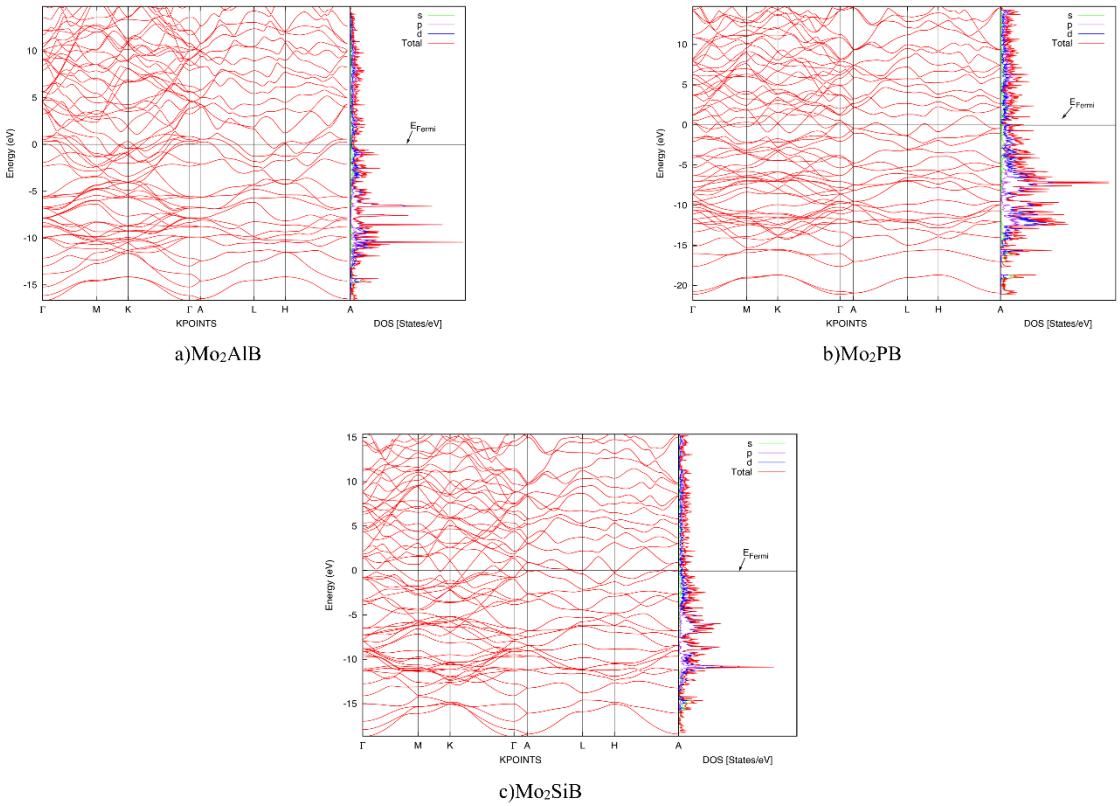
Compounds	Reference	*a*	*c*	*c/a*	ρ	*z*	ΔH_f
Mo_2AlB	Present	3,086	13,285	4,304	4,304	0,0922	-0,023
	[12]	3,088	13,262	-	6,963	-	-
Mo_2AlC	[12]	3,029	13,448	-	-	-	-
Mo_2PB	Present	3,254	11,274	3,464	3,464	0,105	-0,401
Mo_2PC	[12]	3,185	11,603	-	-	-	-
Mo_2SiB	Present	3,219	11,709	3,637	3,637	0,101	-0,314
Mo_2SiC	[12]	3,103	12,401	-	-	-	-

Due to the limited number of studies in the literature, the calculated properties of *Mo_2AB* MAX Phase compounds were compared with the results of the MAX Phase compounds with X = C. The calculated formation enthalpy of the *Mo_2AB* compounds are presented in the table above (Table 2.). The enthalpy of negative formation is a criterion that these compounds can be synthesized in the laboratory. When the table cel is examined, it is seen that low formation enthalpy is found in *Mo_2PB* (-0,401 eV/atom) Compound and it can be said that it is the most stable compound compared to other investigated compounds.

Electronic Properties

The band structure for *Mo_2AB* (A = Al, P, Si) MAX Phase compounds was calculated from the calculated equilibrium lattice parameters along the high symmetry points in the first Brillouin region. The MAX phase compounds examined from the band structures and the partial and total state densities (DOS) corresponding to the band structures were highly likely to have metallic character. The band structures of *Mo_2AB* compounds and corresponding partial density of states (PDOS) shown in Figure 2 and Figure 3.

ISBN:978-605-83516-6-0



a)Mo_2AlB b)Mo_2PB

c)Mo_2SiB

FIGURE 2. Band structure of (a) Mo_2AlB, (b) Mo_2PB, and (c) Mo_2SiB

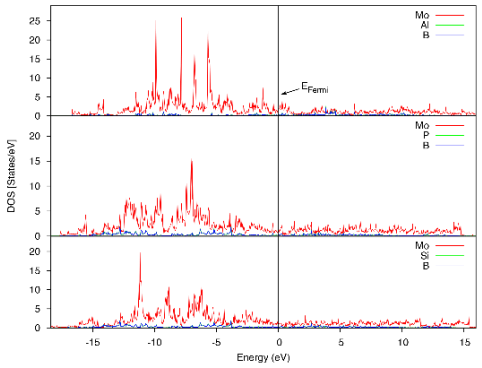


FIGURE 3. Partial density of states of Mo_2AB compounds

Elastic Properties

The mechanical behavior of materials during mechanical design and manufacturing is very important to know. Elastic constants (C_{ij}) are one of the key determinants of the understanding of the properties of the mechanical and dynamic behavior of a material. It is very important to calculate the elastic constants in order to have information about the hardness and stability of the material and to determine the technological application area according to the need. The elastic constants C_{11}, C_{12}, C_{13}, C_{33} and C_{44} of the hexagonal structure of the MAX phase material group were obtained by forcing method. The mechanical stability of the material can be checked according to the Born - Huang criteria [9].

ISBN:978-605-83516-6-0

TABLE 3. Calculated elastic constants (C_{ij} in GPa) of *Mo_2AB* compounds

Coumpounds	Reference	C_{11}	C_{12}	C_{13}	C_{33}	C_{44}
Mo_2AlB	Present	312,251	96,457	158,245	281,035	107,897
	[12]	316,560	105,436	151,713	268,716	161,082
Mo_2AlC	[12]	354,4	98,0	146,7	358,9	144,4
Mo_2PB	Present	353,266	137,306	218,524	354,404	107,978
Mo_2PC	[12]	266,4	139,2	228,9	331,0	106,4
Mo_2SiB	Present	325,610	147,620	208,990	312,245	88,995

Table 4. Calculated Bulk Modulus (*B* in GPa), Young's Modulus (*E* in GPa), Shear Modulus (*G* in GPa), Poisson's ratio (*v*), *B*/*G* ratio, *G*/*B* ratio and Hardness (H_v in GPa) of *Mo_2AB* Compounds

Compounc	Referenc	*B*	*E*	*G*	*v*	*B/G*	*G/E*	H_v
Mo_2AlB	Present	192,07	278,71	110,76	0,2581	1,730	0,577	17.859
	[12]	191,06	278,721	110,87	0,257	-	-	-
Mo_2PB	Present	243,2	308,33	119,63	0,2887	2,033	0,492	21.578
Mo_2SiB	Present	231,76	287,51	111,16	0,2932	2,085	0,480	12.820

A measure of hardness in solids are the bulk modulus and the isotropic shear modulus. Bulk Module (*B*) is a measure of the resistance of a material to volume change under hydrostatic pressure. The shear modulus is defined as the reaction of the material to shear stress and shows the material's resistance to reversible deformations. The highest value of the Bulk modulus calculated according to Table 4. belongs to *Mo_2PB* (243.2 GPa) compound. The lowest value of the Bulk modulus is observed in *Mo_2AlB* (192.07) in Table 4. Bulk modulus Since materials larger than 100 GPa are hard materials, they have low compressibility. According to equation (2) were calculated Bulk modulus and Shear modulus. In this equation B_V and B_R are Voigt – Reuss – Hill (VRH) approximations[28].

$$B = \frac{B_v + B_R}{2} \qquad G = \frac{G_V + G_R}{2} \tag{2}$$

Elasticity Module; It is obtained by the ratio of the stress applied to the material to the unit deformation caused by the applied stress. The higher the modulus of elasticity of a material, the higher the force that a material can withstand without permanent deformation, or the lower the elastic elongation rate. Young's modulus is high if the material is hard. The highest Young's modulus value calculated according to the Table 4. belongs to *Mo_2PB* (308.33 GPa). The lowest Young's modulus value was *Mo_2SiB* (287,51 GPa). Young's modulus were calculated according to equation (3). In this equation *B* and *G* are bulk modulus and shear modulus respectively.

$$E = \frac{9BG}{3B + G} \qquad v = \frac{3B - 2G}{2(3B + G)} \tag{3}$$

The Poisson ratio gives information about intraatomic bonds and is generally around 0.1 for covalently bonded material and about 0.25 for ionic bonded material. . Since the Poisson ratios of the compounds calculated according to the Table 4. are around 0.25, it can be said that all compounds have ionic bonds. Poisson's ratio were calculated according to equation (3). In this equation *B* and *G* are bulk modulus and shear modulus respectively.

B/G ratio is one of the important criteria for hardness. It is concluded that when these values are less than 1.75, the material is fragile and in case it is high, it is ductile. Since the B/G ratios of the compounds calculated according to the Table 4. are greater than 1.75, it is likely that all compounds are ductile.

The G/B ratio is also known as Pugh's modulus. Pugh's modulus allows the exploration of the bonding nature of a material. Pugh's modulus value is around 1.1 material has dominantly covalent bonding. But this value is around 0.6 if the material has dominantly ionic bonding. Pugh's modulus value is around 0.6, these compounds have dominantly ionic bonding. In addition, Chen et al. [31] developed the semi-empirical method using Pugh's modulus ratio and was used to calculate the hardness of the compounds. This is given in equation (4).

$$H_v = 2(k^2G)^{0.585} - 3; \quad \left(k = \frac{G}{B}\right) \tag{4}$$

Anisotropic Elastic Properties

Unusual phonon modes in the material, linear defects, anisotropic plastic deformation and some other physical or mechanical properties may result from the anisotropy of the elasticity of the material. In addition, in any technological application, it is necessary to understand whether micro-cracks caused by elastic anisotropy are formed to increase the mechanical strength of the material. Therefore, it is useful to make anisotropy calculations and these servers support the results of elastic analysis.

In this study, open source ELATE [26] elastic tensor software compiled from EIAM [27] software was used to calculate and visualize maximum and minimum values of Young modulus, shear modulus, linear compressibility and

ISBN:978-605-83516-6-0

Poisson ratio of MAX phase material. The green curves show the minimum points. The blue curves show the maximum points for the examined parameters. The maximum and minimum values of Young's modulus, shear modulus, Poisson's ratio and linear compressibility are given in Table 5.

TABLE 5. Maximum and minium values of Young's Modulus (E_{min} and E_{max} in GPa), linear compressibility (β_{min} and β_{max} in GPa), Shear modulus (G_{min} and G_{max} in GPa) and Poisson's ratio (ν_{min} and ν_{max}) for Mo_2AB compounds

Compound	Young modulus		Linear Compressibility		Shear Modulus		Poisson's Ratio	
	E_{min}	E_{max}	β_{min}	β_{max}	G_{min}	G_{max}	ν_{min}	ν_{max}
Mo_2AlB	158.49	345.15	1.4236	1.8955	63.77	161.36	-0.16669	0.65694
Mo_2PB	159.72	404.66	0.6831	1.7342	60.918	199.15	-0.28611	0.79301
Mo_2SiB	127.66	390.25	0.91455	1.7093	49.639	216.91	-0.38316	0.92575

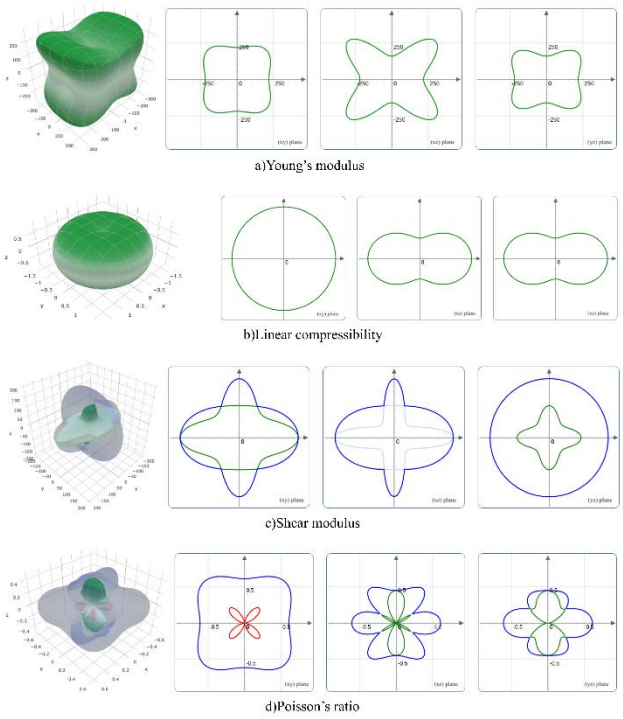


FIGURE 4. The calculated directional dependence of the mechanical properties (a) Young's modulus, (b)linear compressibility, (c)Shear modulus and (d)Poisson's ratio for Mo_2AB compounds

Vibrational Properties

The phonon dispersion curves of the Mo_2AB MAX Phase compounds were calculated using the VASP derived density functional perturbation theory (DFPT) [28, 29] Linear Response method. In the calculations, PHONOPY software was used to expand the unit cell hexagonal structure by 2 x 2 x 1 to create super cells containing 32 atoms, and the phonon dispersion curves and phonon state density curves were plotted. The phonon dispersion curves corresponding to the high symmetry points for the calculated compounds and the phonon state densities corresponding to the phonon dispersion curves (Figure 5).

ISBN:978-605-83516-6-0

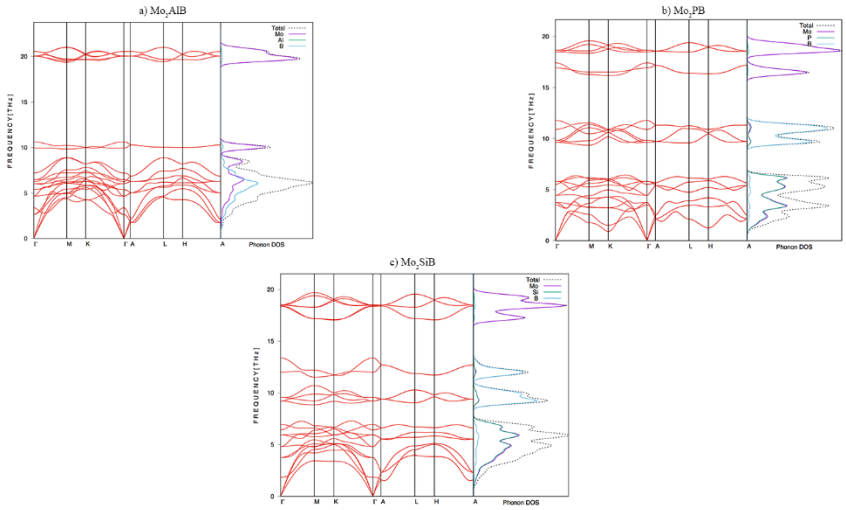


FIGURE 5. Phonon dispersion curves and PDOS of (a)Mo_2AlB, (b)Mo_2PB and (c)Mo_2SiB

The number of atoms in the unit cell determines the number of acoustic and optical branches. *Mo_2AB* MAX There are 8 atoms in the unit cells of phase compounds. Accordingly, 3 acoustic 21 optical branches are observed for each compound. When the phonon dispersion curves of the calculated *Mo_2AB* MAX Phase compounds are examined, it is seen that the contribution from Mo atom is dominant at high frequencies and the contribution from A atom is dominant at low frequencies. This is thought to be due to the mass difference between atoms.

Thermodynamic Properties

Using PHONOPY software, thermodynamic properties such as Helmholtz free energy, enthalpy, entropy, constant heat capacity (Cv) in the range of 0K to 2000K calculated for *Mo_2AB* MAX Phase compounds were calculated using phonon results and semi-harmonic approach. *Mo_2AB* MAX It is seen that free energy decreases as entropy increases for phase compounds. It is seen that the temperature increases linearly at 300K. It is also seen that the heat capacity reaches a fixed value known as Dulong - Petit limit for temperatures higher than 700K. Thermodynamic properties of *Mo_2AB* compounds shown in Figure 6.

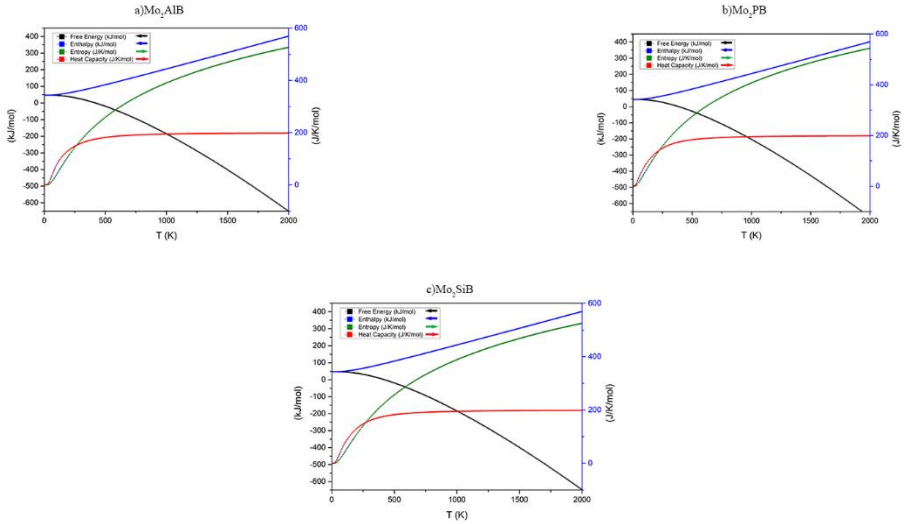


FIGURE 6. Free energy, enthalpy, entropy and heat capacity as a function of temperature of (a)Mo_2AlB, (b)Mo_2PB and (c)Mo_2SiB

CONCLUSION

In this study, structural, electronic, anisotropic - elastic, lattice dynamics and thermodynamic properties of *Mo_2AB* (A = Al, P, Si) MAX Phase compounds were investigated. Structural parameters, formation enthalpies, electronic band structures and phonon dispersion curves were calculated for all compounds. As a result of the calculations in this theoretical study, *Mo_2AB* (A = Al, P, Si) MAX Phase compounds which are the subject of the study showed that they can be synthesized in laboratory. In addition, load density, electronic tape structure and DOS curves were shown to have metallic character.

In order to determine the mechanical properties depending on the orientation, the elastic constants were obtained by the forced - strain technique. Numerically estimated *Mo_2AB* (A = Al, P, Si) MAX Phase compounds were found to be stable and hard, with low thermal conductivity. *Mo_2AB* (A = Al, P, Si) MAX Phonon dispersion curves and the corresponding phonon DOS curves were plotted to determine the vibration properties of the phase compounds. There was no negative mode in phonon dispersion curves. It was found that all the calculated compounds were stable.

Mo_2AB (A = Al, P, Si) is the *Mo_2PB* compound with the lowest formation enthalpy of MAX Phase compounds which is more stable in structure than the others.

Mo_2AB (A = Al, P, Si) MAX Phase compounds were found to meet the Born - Huang stability criteria. Bulk modulus is the highest *Mo_2PB* compound is the hardest compound. Because the Bulk modulus of *Mo_2AlB* is lower than the others, it is softer than the other compounds.

Since the Bulk modulus does not detect compounds smaller than 100 GPa, all compounds examined fall into the hard material group and these compounds are considered to have low compressibility under laboratory conditions.

Young's modulus of *Mo_2PB* compound was found to be the best predicted.

Since the Poisson ratio for all calculated compounds is around 0.25, it can be said that the ionic bonds are dominant in *Mo_2AB* (A = Al, P, Si) MAX Phase compounds compared to covalent bonds.

When the calculated B/G ratio values are compared, the ductile *Mo_2AlB* compound is brittle since the others except *Mo_2AlB* are larger than 1.75.

Poisson's ratio, Young's modulus and Shear's modulus have skewed shapes, while linear compressibility is spherical for all compounds in the xy plane.

When looking at the DOS graphs versus the phonon dispersion curves and the phonon dispersion curves, all calculated compounds are stable. 3 acoustics and 21 optical branches were observed.

When the phonon dispersion curves of all compounds are examined, it is seen that the contributions from M atoms are dominant at high frequencies and the contributions from A atoms are dominant at low frequencies.

When the graphs of the compounds whose thermodynamic properties are calculated are examined, it is seen that they reach a constant value called Dulong-Petit limit for temperatures higher than 700 K.

After 300 K, it is observed that the temperature increases linearly for all compounds.

As a result of the calculations, *Mo_2PB*, which has more hardness properties than other compounds at high temperature, has attracted attention as the most stable and hardest material which attracts attention to the properties of MAX Phase family.

Exploring the results of the new calculation will be an important development. MAX phase compounds with Boron doped, which have important superior properties at high temperature, are considered as a reliable source for experimental researchers. Therefore, the use of these compounds in the future is expected to become widespread.

ACKNOWLEDGMENTS

This project has been supported by 0362-NAP16 and 0147-NAP12 projects of Burdur Mehmet Akif Ersoy Unıversity. The author would like express our gratitude to the Ahilab HPC from Ahi Evran University for using the computer cluster to perform the first – principles calculations. The author would like express our gratitude to the NanoSim Laboratory from Burdur Mehmet Akif Ersoy University for using the computer cluster to perform the first – principles calculations.

REFERENCES

1. A. Gencer, I. Yılmaz, U. Bayhan, and G. Surucu, “Anisotropic Elastic and Lattice Dynamical Properties of Cr2AB MAX Phases Compounds,” *Eur. J. Sci. Technol.*, no. 15, pp. 351–359, 2019.
2. C. Lange, M. W. Barsoum, and P. Schaaf, “Towards the synthesis of MAX-phase functional coatings by pulsed laser deposition,” vol. 254, pp. 1232–1235, 2007.
3. I. R. Shein, A. L. Ivanovskii, I. The, F. Scs, and T. Wyckoff, “solidi,” vol. 232, no. 1, pp. 228–232, 2011.
4. A. Gencer and G. Surucu, “Electronic and lattice dynamical properties of *Ti_2SiB* MAX phase,” *Mater. Res. Express*, vol. 5, no. 7, p. 076303, Jul. 2018.
5. Z. Sun, D. Music, R. Ahuja, and J. M. Schneider, “Ab initio study of M2AlN (M = Ti , V , Cr),” no. June 2014, 2005.

ISBN:978-605-83516-6-0

6. T. Liao, J. Wang, and Y. Zhou, "Chemical bonding and mechanical properties of M 2 A C (M = Ti , V , Cr , A = Al , Si , P , S) ceramics from first-principles investigations," 2009.
7. M. A. Ghebouli, B. Ghebouli, M. Fatmi, and A. Bouhemadou, "Theoretical prediction of the structural, elastic, electronic and thermal properties of the MAX phases X2SiC (X = Ti and Cr)," *Intermetallics*, 2011.
8. B. Ghebouli, M. A. Ghebouli, M. Fatmi, L. Louail, T. Chihi, and A. Bouhemadou, "First-principles calculations of structural, electronic, elastic and thermal properties of phase M<inf>2</inf>SiC (M=Ti, V, Cr, Zr, Nb, Mo, Hf, Ta and W)," *Trans. Nonferrous Met. Soc. China (English Ed.*, 2015.
9. Z. Wu, E. Zhao, H. Xiang, X. Hao, X. Liu, and J. Meng, " Publisher's Note: Crystal structures and elastic properties of superhard IrN2 and IrN3 from first principles [Phys. Rev. B 76 , 054115 (2007)] ," *Phys. Rev. B*, 2007.
10. J. Wang and Y. Zhou, "Dependence of elastic stiffness on electronic band structure of nanolaminate M2A1C (M = Ti , V , Nb , and Cr) ceramics," no. September 2015, 2004.
11. S. Aydin, "Spin-Polarized Ground State Properties of Cr 2 AlX (X = C , N and B) Ceramics," vol. 28, no. 2, pp. 185–193, 2015.
12. M. Khazaei, M. Arai, T. Sasaki, and M. Estili, "Trends in electronic structures and structural properties of MAX phases : a first-principles study on M 2 AlC (M = Sc , Ti , Cr , Zr , Nb , Mo , Hf , or Ta), M 2 AlN , and hypothetical M 2 AlB phases," vol. 505503.
13. G. Sürücü, "Bor ' lu Max Faz Bileşiklerin Yapısal , Elektronik , Anizotropik Elastik Ve," vol. 433003, no. 2016, p. 433003, 2018.
14. G. Kresse and J. Furthmüller, "Efficient iterative schemes for ab initio total-energy calculations using a plane-wave basis set," *Phys. Rev. B - Condens. Matter Mater. Phys.*, vol. 54, no. 16, pp. 11169–11186, 1996.
15. G. Kresse, "From ultrasoft pseudopotentials to the projector augmented-wave method," *Phys. Rev. B - Condens. Matter Mater. Phys.*, 1999.
16. G. Kresse and D. Joubert, "Kresse, Joubert - Unknown - From ultrasoft pseudopotentials to the projector augmented-wave method," vol. 59, no. 3, pp. 11–19, 1999.
17. P. E. Blöchl, "Projector augmented-wave method," *Phys. Rev. B*, vol. 50, no. 24, pp. 17953–17979, Dec. 1994.
18. J. P. Perdew, K. Burke, and M. Ernzerhof, "Generalized Gradient Approximation Made Simple [Phys. Rev. Lett. 77, 3865 (1996)]," *Phys. Rev. Lett.*, 1997.
19. J. D. Pack and H. J. Monkhorst, ""Special points for Brillouin-zone integrations"—a reply," *Phys. Rev. B*, vol. 16, no. 4, pp. 1748–1749, Aug. 1977.
20. M. Methfessel and A. T. Paxton, "High-precision sampling for Brillouin-zone integration in metals," *Phys. Rev. B*, vol. 40, no. 6, pp. 3616–3621, Aug. 1989.
21. P. E. Blöchl, O. Jepsen, and O. K. Andersen, "Improved tetrahedron method for Brillouin-zone integrations," *Phys. Rev. B*, vol. 49, no. 23, pp. 16223–16233, Jun. 1994.
22. Y. Le Page and P. Saxe, "Symmetry-general least-squares extraction of elastic data for strained materials from *ab initio* calculations of stress," *Phys. Rev. B*, vol. 65, no. 10, p. 104104, 2002.
23. M. P. Teter, M. C. Payne, and D. C. Allan, "equation for large systems," vol. 40, no. 18, pp. 255–263, 1989.
24. D. M. Bylander, L. Kleinman, and S. Lee, "Self-consistent calculations," vol. 42, no. 2, 1990.
25. Y. Le Page and P. Saxe, "Symmetry-general least-squares extraction of elastic data for strained materials from *ab initio* calculations of stress," *Phys. Rev. B*, vol. 65, no. 10, p. 104104, Feb. 2002.
26. R. Gaillac, P. Pullumbi, and F. Coudert, "ELATE : an open-source online application for analysis and visualization of elastic tensors," vol. 275201.
27. A. Marmier, Z. A. D. Lethbridge, R. I. Walton, C. W. Smith, S. C. Parker, and K. E. Evans, "ElAM: A computer program for the analysis and representation of anisotropic elastic properties," *Comput. Phys. Commun.*, vol. 181, no. 12, pp. 2102–2115, Dec. 2010.
28. A. Togo, F. Oba, and I. Tanaka, "First-principles calculations of the ferroelastic transition between rutile-type and CaCl2-type SiO2 at high pressures," *Phys. Rev. B - Condens. Matter Mater. Phys.*, vol. 78, no. 13, pp. 1–9, 2008.
29. X. Gonze and C. Lee, "Dynamical matrices, Born effective charges, dielectric permittivity tensors, and interatomic force constants from density-functional perturbation theory," *Phys. Rev. B - Condens. Matter Mater. Phys.*, 1997.
30. K. Momma and F. Izumi, "VESTA 3 for three-dimensional visualization of crystal, volumetric and morphology data," *J. Appl. Crystallogr.*, 2011.
31. Chen X. Q., Niu H., Li D. & Li Y. 2011. Modeling hardness of polycrystalline materials and bulk metallic glasses Intermetallics 19, 1275-1281.

05. Energy



BOOK OF FULL TEXT PROCEEDINGS TURKISH PHYSICAL
SOCIETY 35th INTERNATIONAL PHYSICS CONGRESS (TPS35)
TPS35, Vol.01, No.05, pp.355-363.
ISBN:978-605-83516-6-0

15 December 2019

Comparative Performance Analysis of Two-Bed Adsorption Cooling System Using Water Vapor Adsorption on Different Types of Silica Gel

Mustafa Anjrini[1, a)] and Muhsin Kılıç [2,b)]

[1,2] *Bursa Uludağ University, Engineering Faculty, Mechanical Engineering Department, Bursa, Turkey*

[a)] Corresponding author: most-ar388@hotmail.com
[b)] mkilic@uludag.edu.tr

Abstract. The aim of this paper is to analyze comparatively the performance of an adsorption cooling system. One of the widely used adsorbate-adsorbent pair is the water-silica gel pair. However, there are many types of silica gel as well as several kinds of composite adsorbents that utilize silica gel as a major component. Therefore, in this comparative study, analysis is conducted for the cooling system performance by employing water as adsorbate and four types of adsorbents (RD silica gel, RD silica gel 2060, Silica gel-$CaCl_2$, and silica gel-LiCl). The Dubinin-Astakhov (D-A) equation and linear driving force (LDF) model are used to compute the adsorption isotherms and kinetics; as a result, comparing among the aforementioned adsorbents through the coefficient of performance COP of the system. The calculations are implemented in MATLAB platform that we correlated it with coolProp library in order to compute the thermodynamic properties of the process during the operating of the system.
Keywords: silica gel, composite adsorbent, sorption cooling system, COP

INTRODUCTION

Recently, it is obvious that energy is one of the essential keys for the continuous in our earth. To ensure the continuity of the evolution in the world, it is important to search for alternative ways to reduce the consumption of traditional energy. In the refrigeration sector, the adsorption system is considered among these alternative ways. The desorption cooling system uses low-grade temperature from renewable energies or waste heat that may come from different thermal processes in several applications. The adsorption chiller has four primary components; evaporator, condenser, expansion valve, and the core part of the system which is the thermal compressor that contains the working pairs (adsorbent/adsorbate). Schematic of the adsorption refrigeration system is illustrated in Fig .1. The adsorption process is a physical phenomenon takes place between the adsorbent and adsorbate where the molecules of the adsorbate settle or release within the surface and pores of the solid adsorbent which depending on heating or cooling process in the bed [1].

The adsorbate concentration in adsorbent not only depends on the pressure and temperature variations but also on the system operating conditions [2]. Utilizing the correct working pair has also a major impact on the performance; therefore, several studies have been done in a wide range of working pairs in the bed such as refs [3–6]. The commonly utilized working pairs are (Silica gel/water, zeolite/ water, Activated carbon/ (methanol, ethanol, ammonia, R134a). One of the available and preferred adsorbate/adsorbent pair is silica gel/water for many reasons; steady through the wide span of adsorption/desorption temperatures, non-toxic, widely available, friendly to the environment. Additionally, it requires a relatively moderate temperature to operate. There are different types of silica gel. Each kind has only one type of pore diameters that create narrow channels inside the adsorbent structure. The distribution of the pore size is a remarkable property to characterize the absorptivity of the adsorbents[3].

Türk Fizik Derneği
1950
Turkish Physical Society

ISBN:978-605-83516-6-0

Composite sorbents have been presented recently for adsorption cooling systems. One of the inorganic salt such as (LiBr, LiCl, $CaCl_2$, $MgCl_2$, $MgSO_4$, etc) is added to silica gel to form the composite adsorbent[7]. The inorganic salt is impregnated inside the pores of silica gel to form the composite sorbent. The disadvantage of this kind of sorbents is that some salt stuck on the surface of the silica gel; it would form a salt solution that would fall down and harm the component of the chiller as a result. Therefore, there are some methods to remove the extra salt that you can find them in the literature[8]. Researchers have found that the hygroscopic capability of LiCl and $CaCl_2$ is better than the aforementioned inorganic salts [9]. Choosing a suitable working pair (adsorbent/adsorbate) is a crucial and vital factor which has to satisfy the important requirements that differ depending on the application. The physical, thermo-physical properties and surface characteristics of the adsorbent are important factors through calculating the adsorption isotherms and adsorption kinetics of the adsorbate which they are key parameters in determining the performance and making the choice.

Several studies have been submitted such as refs [4,6,10] about employing silica gel/ water as a working pair in the adsorption cooling system. Lots of them have studied the effects of changing the adsorption/desorption temperature on the performance of the system. Only a few of them have studied the effect of evaporation temperature on the system. Therefore, the present study aims to investigate the performance of two-bed adsorption refrigeration system by employing water as adsorbate and four types of adsorbents (RD silica gel, RD silica gel 2060, Silica gel-$CaCl_2$, and silica gel-LiCl). The calculations have been done through a simulation program that developed according to an introduced mathematical model in this study.

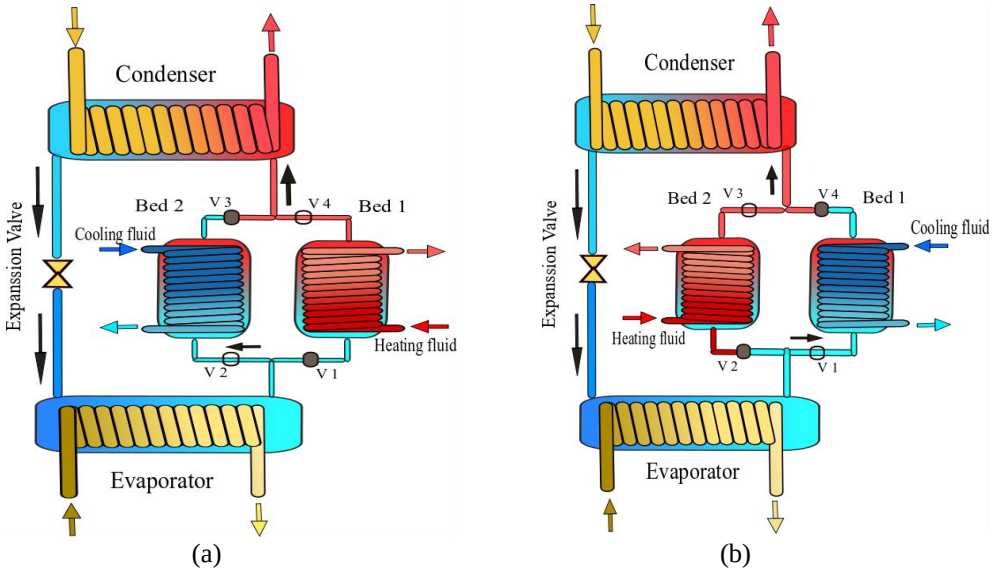


FIGURE 1. Schematic of two-bed adsorption refrigeration system: (a) Bed 1 in desorption phase, Bed 2 in adsorption phase; (b) Bed 1 in adsorption phase, Bed 2 in the adsorption phase

MATHEMATICAL MODELING

The adsorption refrigeration system and the mechanical compression refrigeration system are nearly the same in the components such as the condenser, evaporator, and the expansion valve. However, instead of using the mechanical compressor as in the traditional cooling system thermal compressor is used. To study the system, it is more understandable to divide the processes into two main cycles. The first cycle is the same as the traditional one, while the second cycle takes place in the thermal compressor. The thermal compressor cycle consists of two main processes called heating and cooling processes. Each process is divided into two processes; isosteric heating and isosteric cooling, where changing the mass is not observed between the working pair. The other two processes, on contrary, where changing the mass is observed, are desorption process (during the heating stage) and adsorption process (during the cooling process) under constant pressure. The thermodynamic cycle of the aforementioned processes is given in the lnp -1/T diagram in Fig.2.

ISBN:978-605-83516-6-0

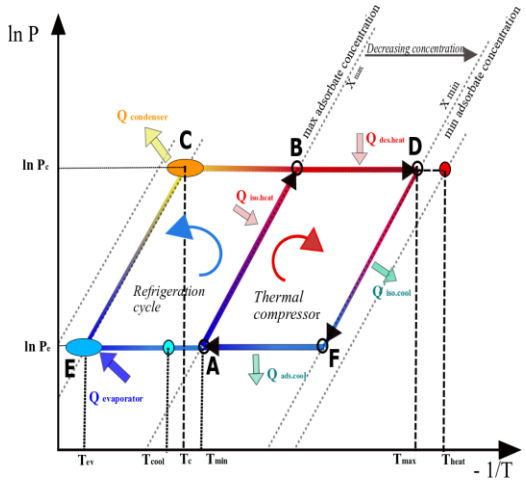


FIGURE 2. Basic adsorption thermodynamic cycle for adsorption cooling system

The cooling effect occurs in the isobaric adsorption process. However. This cooling effect is intermittent in the bed. To provide continues cooling effect it is common to utilize multiple thermal compressor (two, four, or six) beds in the system. During operating the cycle, one bed is in the desorption mode while the other one in the adsorption mode. In other words, the function of each room is interchanged in the other cycle. The two modes of operating the system are illustrated in Fig.1.

Adsorption Isotherms

There are many equations that are compatible with the test measurements of adsorption isotherms. Such as the Freundlich, Tòth, and Dubinin-Astakhov (D-A) correlations. However, it becomes common to use Dubinin-Astakhov (D-A) model to compute the adsorption uptake of the adsorbate into the adsorbent. The D-A equation has different forms where the uptake value may be a function of operating temperature or operating pressure in addition to the temperature of adsorbent as the following equations [3,6,11]:

$$W = W_m . exp\left\{ - \left[\frac{R.T}{E} ln\left(\frac{P_S}{P} \right) \right]^n \right\} \tag{1}$$

$$W = W_m . exp\left\{ - k \left[ln\left(\frac{P_S}{P} \right) \right]^n \right\} \tag{2}$$

With

$$W = X . v_a , W_m = X_m . v_o \tag{3}$$

$$v_a = v_b . exp\left(\Omega \left(T - T_b \right) \right) \tag{4}$$

Where k and n are constants and their values can be determined by a fitting process to the test data. E is the specific characteristic energy of the adsorbent-adsorbate pair that is also determined from experimental measurements. R is the gas constant. T and P are the temperature and pressure of the bed, respectively, suffix s refers to the state of saturation. v_a and v_b are the specific volume of the adsorbate phase and boiling phase, respectively. The values of these parameters can be found in the literature for water [6].

Tòth model is also used to calculate the adsorption isotherms for specific kinds of composite adsorbents where the uptake value fit the experimental measurements more than D-A equation. Tòth equation can be written in the following form [7]:

ISBN:978-605-83516-6-0

$$X = \frac{X_m \cdot K_O \cdot exp\left(\frac{\Delta h_{ads}}{R.T}\right).P}{\left[1+\left\{k_O \cdot exp\left(\frac{\Delta h_{ads}}{R.T}\right)P\right\}^n\right]^{1/n}} \quad (5)$$

Where k_o and n are constants and their values can be determined by a fitting process to the test data.

The isosteric heat of adsorption Δh_{ads} may be determined by the experimental measurements and can be also defined as the following equation [6]:

$$\Delta h_{ads} = h_{fg} + E\left[ln\left(\frac{W_m}{W}\right)\right]^{1/n} + E.T.\Omega\left[ln\left(\frac{W_m}{W}\right)\right]^{(1-n)/n} \quad (6)$$

Adsorption Kinetics

It is common to use Linear Driving Force (LDF) approach in order to describe the amount of the adsorbate concentration in the solid bed with time. LDF equation is given as the following:

$$\frac{dX}{dt} = \frac{15 D_O}{r_p^2} . exp\left(\frac{E_a}{R.T}\right).\left(X_{eq} - X\right) \quad (7)$$

X_{eq} is the adsorbate/adsorbent concentration at the equilibrium conditions. E_a, D_o, and r_p are the activation energy, pre-exponent constant, and average radius of the particles in the adsorbent, respectively, which they are related to the type of adsorbent used in the system like the. The values of the previous parameters for the adsorbents used in our study are given in table.1.

System Performance Parameters and Indicators

As we already know that the purpose of cooling systems generally is to absorb undesirable heat through the evaporator by consuming energy. The cooler's efficiency is generally expressed in terms of coefficient of performance COP. For adsorption cooling system COP can be written as the following expression:

$$COP = \frac{Q_e}{Q_{is,h} + Q_{des,h}} \quad (8)$$

Where $Q_{is,h}$ and $Q_{des,h}$ are the amount of needed heat for isosteric and desorption processes, respectively. They are defined as the following equations:

$$Q_{is,h} = \int_{T_A}^{T_B} \left[m_{ads} \cdot C_{P,ads} + C_{P,ref} \cdot m_{ads} + m_{m,b} \cdot C_{m,b}\right] dT \quad (9)$$

$$Q_{de,h} = \int_{T_B}^{T_D} \left[m_{ads} \cdot C_{P,ads} + h_{fg@T_e} \cdot m_{ads} + m_{m,b} \cdot C_{m,b}\right] dT + \int_{X_{max}}^{X_{min}} \left[m_{ads} \cdot \Delta h_{ads}\right] dT \quad (10)$$

The absorbed heat in the evaporator can be written as the following expression:

$$Q_e = m_{ads} . \Delta X . \left[h_{fg@T_e} - C_{P,ref}\left(T_{con} - T_e\right)\right] \quad (11)$$

Another indicator that also describes the system performance in this kind of systems is the specific cooling power (SCP) in kW/kg_{ads}. SCP is expressed by the following equation:

ISBN:978-605-83516-6-0

$$SCP = \frac{Q_e}{t_{cycle} \cdot m_{ads}} \quad (12)$$

The previous equations have been used and validated with experimental results such as in the refs[3,6,12]. Here in this article, in order to analyze comparatively the performance of two-bed adoption system using water as an adsorbate into the forenamed adsorbents, we set some assumptions and operating conditions such as; $T_{b,min} = T_{cool\ in}$ +2ºC, $T_{b,max} = T_{heat\ in}$ +2ºC, and $T_{cond} = T_{cool\ in}$ +2ºC. The mass of solid adsorbents for all used types in the current study ($m_{ads.}$ =47 kg). For the bed materials, the heat capacity is taken as ($m_{m,b}.C_{m,b}$ = 78 kJ/K) [6]. Besides that, Table.1 shows the physical properties and parameters of adsorbents used in the current study.

TABLE 1. Properties and parameters of different types of adsorbents used in the present study [3,6,7,11,13].

Property	**RD Silica gel**	**RD Silica gel 2060**	**Silica gel-$CaCl_2$**	**Silica gel-LiCl**
Chemical formula	SiO_2.n(H_2O)	SiO_2.n(H_2O)	SiO_2.n(H_2O)+ $CaCl_2$	SiO_2.n(H_2O) + LiCl
D (mm)	0.8-0.89	0.5-0.59	0.25-0.5	0.5-1
A ($\mathbf{m^2}$/g)	827.5	686.3	350	300
$\mathbf{V_{Po}}$(cc/g)	0.462	0.335	1	1
$\mathbf{D_{Po}}$ (nm)	3.24	3.19	15	15
Inorganic salt content %	0	0	33.7	20
$\mathbf{C_P}$ (kJ/kg.K)	0.92	0.92	0.85	0.85
$\Delta\ \mathbf{h_{ads}}$ (kJ/kg)	Eq.(7)	Eq.(7)	2760	2376
E (kJ/kg) Eq (1)	129.29	242.79	-	-
n	*RP<0.4; n=1.1 RP>0.4; n=1.6 Eq.(1)	RP<0.4; n=1.1 RP>0.4; n=1.6 Eq.(1)	1.1 (Eq.(6))	1.604 (Eq. (2))
$\mathbf{D_O}$ ($\mathbf{m^2}$/s)	2.9 E^{-4}	2.9 E^{-4}	2.54 E^{-4}	2.54 E^{-4}
$\mathbf{E_a}$ (kJ/kg)	2330	2330	2330.7	2020
$\mathbf{r_P}$ (m)	3.75 E^{-4}	2.7 E^{-4}	1.74 E^{-4}	4.5 E^{-4}
$\mathbf{X_m}$($\mathbf{kg_{ref}/kg_{ads}}$)	0.48	0.38	0.8	0.489

RP = $\frac{P_e}{P_{b,min}}$;

RESULT AND DISCUSSION

The aim of the present study is to introduce a comparative analysis of the adsorption refrigeration system using water as adsorbate and different types of silica gel (RD Silica gel, RD Silica gel 2060, Silica gel-$CaCl_2$, and Silica gel-LiCl). The results are computed by utilizing home-made-software written in MATLAB platform. The thermophysical properties of the coolant (water) used in the model are obtained by including the CoolProp library, which provides a property package for fluids. More details about the CoolProp library can be obtained from Bell et al [14]. Moreover. We executed first-order ordinary differential equations (ODEs) and solved by ode45 which provides an accurate solution. In the computations, the first case study was done by changing evaporation temperature at the evaporator between 5 to 20 ºC. The heating inlet temperature and cooling inlet temperature used for the desorption and adsorption processes are considered 90 ºC and 30 ºC, respectively. The second case study was done by changing the heating inlet temperature to the thermal compressor between 65 to 95 ºC, while 10ºC and 30ºC are set for evaporation and cooling inlet temperatures, respectively. Furthermore, Isosteric heating/cooling time is taken as 50 seconds. While the desorption time has been calculated through the LDF method assuming that adsorption to desorption time ratio is 1.0. The same working conditions for the studied four different silica gels are performed through the computations.

ISBN:978-605-83516-6-0

Effect of Variation in the Evaporation Temperature

Fig.3. shows the calculated results of COP and SCP indictors for all the selected adsorbents at different evaporation temperatures. It can be observed that, for COP indicator, all the curves go up by increasing T_e. The explanation of this behavior is that increasing T_e leads to an increase in the maximum concentration of the adsorbate into the adsorbent X_{max}; increasing in the evaporation heat and COP occur as a result. We can also notice from the Fig.3.a. That the composite adsorbents have the best values of COP because these adsorbents provide higher values of the maximum concentration of the water into their materials. For SCP indicator, on contrary, we can notice from Fig.3.b that the curves are slightly increased. In fact, even though the values of evaporation heat in the evaporator rise by increasingT_e, the necessary time to desorb the water particles also increased; a minor increase of SCP values is observed as a result. By comparing the performance indicators for different adsorbents used in the studied system, it can be noticed that the highest values are obtained for the composite materials at different evaporation temperature and especially for Silica gel-$CaCl_2$ reach up to 1.905 (kW/kg) and 0.71 for SCP and COP, respectively.

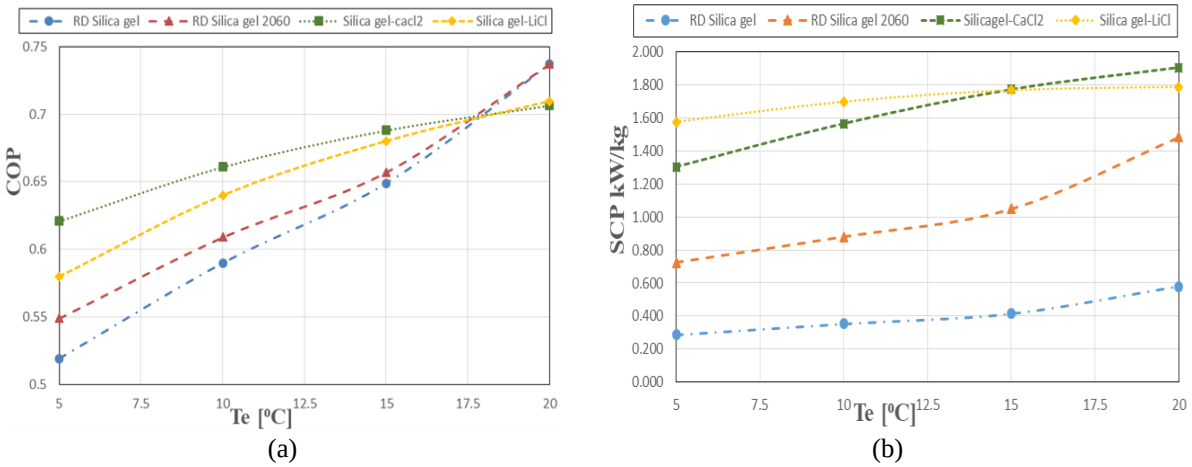


FIGURE 3. Comparison of the two performance indicators for different types of adsorbents at different evaporation temperatures (a) COP; (b) SCP

Fig..4. states the computed results of the required time to desorb the particles of water when the adsorbents are subjected to the same outside heat source. Results show that the required time to desorb the adsorbate when using RD silica gel and RD silica gel 2060 is more than that when using composite adsorbents.

ISBN:978-605-83516-6-0

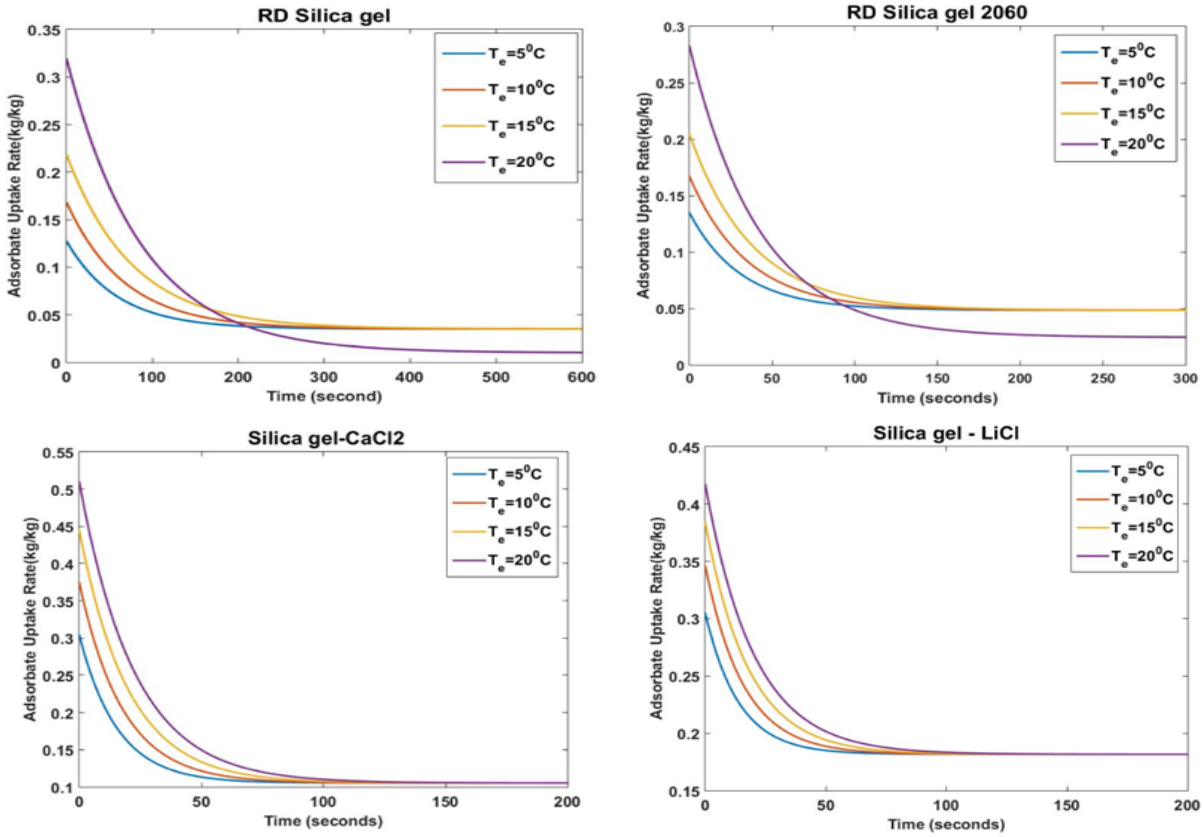
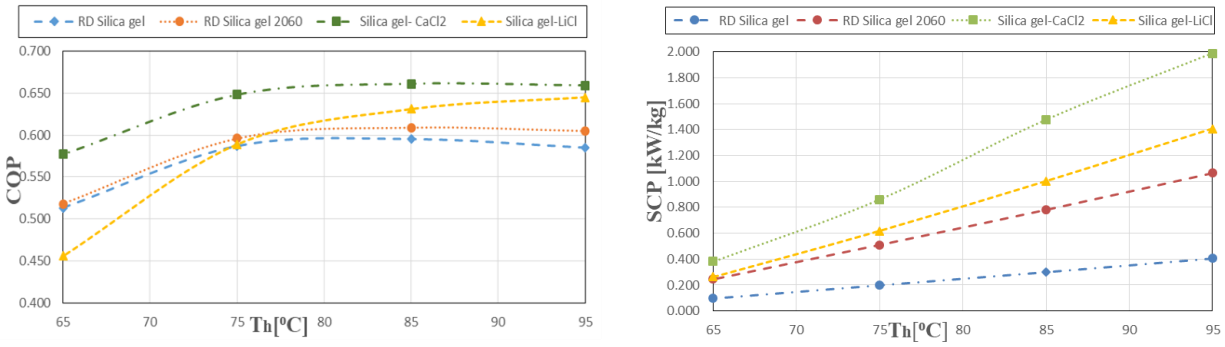


FIGURE 4. Comparison between adsorption uptake rate against desorption time for different types of adsorbents at different evaporation temperatures

Effect of Variation Heating Inlet Temperature



(a) (b)

FIGURE 5. Comparison of the two performance indicators for different types of adsorbents at different heating inlet temperatures (a) COP; (b) SCP

Fig.5. clarifies the computed outcomes of COP and SCP indictors for all adsorbents at different heating inlet temperatures. The results show that there is an increase in the efficiencies by rising the heating inlet temperature. In fact, as the value of T_h goes up, the difference between the maximum and minimum concentration of water into adsorbent increases; this increasing not only effects on desorption heating but also on the evaporation heat in the evaporator. Therefore, an increase in COP and SCP values occurs.

ISBN:978-605-83516-6-0

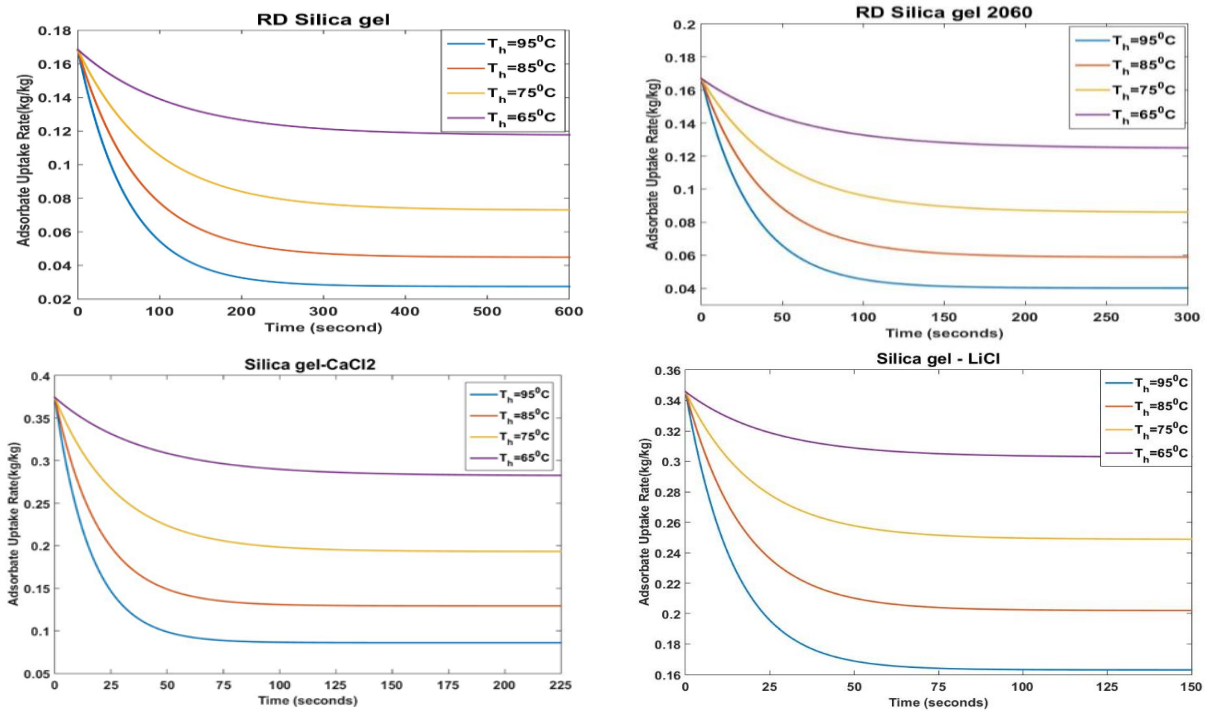


FIGURE 6. Comparison between adsorption uptake rate against desorption time for different types of adsorbents at different heating inlet temperatures

From the Fig.5, The composite adsorbents present higher performance values reach up to 0.66 and 0.64 for silica gel- $CaCl_2$ and Silica gel-LiCl, respectively. On the other hands. The computed results also show a slight increase in the SCP values for RD silica gel, RD silica gel 2060. Whereas the advance in the SCP values for composite adsorbents is obviously noticeable reach up to 1.99 and 1.4 (kW/kg) for silica gel- $CaCl_2$ and Silica gel-LiCl, respectively. In fact, SCP values are related to desorption time which varies depending on the adsorption uptake rate and heating inlet temperature as it is illustrated in Fig.6. The desorption time values at the lowest heating inlet temperature 65 ºC can reach up to 220 and 145 (seconds) for silica gel- $CaCl_2$ and Silica gel-LiCl, respectively.

CONCLUSION

The current study introduces a comparative analysis of the adsorption cooling system that has two-bed with different types of silica gels (RD Silica gel, RD Silica gel 2060, Silica gel-$CaCl_2$, and Silica gel-LiCl) as adsorbent and water as the adsorbate. To predict the performance of the system filled with mentioned adsorbents, a mathematical model has been built in MATLAB platform. These four types of adsorbents with water and several operating conditions are investigated at the evaporation temperature range from 5 to 20 ºC, as a first case study. It is noteworthy to mention that evaporation temperature setting depends on the type of application. The COP and SCP indicators are the performance measurements that we have made our study on. Among the above-mentioned adsorbents, composite ones have higher performance values reached up to 20% compared with pure silica gels.

This article also studied the effect of heating inlet temperature range from 65 to 95ºC on the performance indicators as a second case study. The computed results show that by rising this temperature, an increasing appears on both indicators for all adsorbents. The composite adsorbents, indeed, show better performance results reached up to 13% compared with the pure adsorbents.

This paper also shows that desorption time plays an important role in calculating SCP indictor. We observed that the required time to desorb the adsorbate when using RD silica gel and RD silica gel 2060 is more than that when using composite adsorbents. From our results, composite silica gel shows outstanding comparative results especially the one supported with $CaCl_2$ due to its large water sorption amount.

This technology has considerable potential in the application that uses low-grade energy sources. Besides, it is one of the promising technologies to lessen the huge consumption of energy.

ISBN:978-605-83516-6-0

REFERENCES

1. Wang LW, Wang RZ, Oliveira RG. A review on adsorption working pairs for refrigeration. Renew Sustain Energy Rev. 2009;13(3):518–34.
2. Wang DC, Li YH, Li D, Xia YZ, Zhang JP. A review on adsorption refrigeration technology and adsorption deterioration in physical adsorption systems. Renew Sustain Energy Rev. 2010;14(1):344–53.
3. Mohammed RH, Mesalhy O, Elsayed ML, Hou S, Su M, Chow LC. Physical properties and adsorption kinetics of silica-gel/water for adsorption chillers. Appl Therm Eng. 2018;137(October 2017):368–76.
4. Mohammed RH, Mesalhy O, Elsayed ML, Su M, C. Chow L. Revisiting the adsorption equilibrium equations of silica-gel/water for adsorption cooling applications. Int J Refrig. 2018;86:40–7.
5. Askalany AA, Saha BB, Habib K. Adsorption Cooling System Employing Activated Carbon/R32 Adsorption Pair. MATEC Web Conf. 2014;13(May):06001.
6. Kılıç M. Comparative performance analysis of a two-bed adsorption cooling system with adsorption of different adsorbates on silica-gel. Bulg Chem Commun. 2018;50(G):102–10.
7. Saha BB, Chakraborty A, Koyama S, Aristov YI. A new generation cooling device employing CaCl2-in-silica gel-water system. Int J Heat Mass Transf. 2009;52(1–2):516–24.
8. Gong LX, Wang RZ, Xia ZZ, Chen CJ. Adsorption equilibrium of water on a composite adsorbent employing lithium chloride in silica gel. J Chem Eng Data. 2010;55(8):2920–3.
9. Li X, Li H, Huo S, Li Z. Dynamics and isotherms of water vapor sorption on mesoporous silica gels modified by different salts. Kinet Catal. 2010;51(5):754–61.
10. Pan QW, Wang RZ, Wang LW, Liu D. Design and experimental study of a silica gel-water adsorption chiller with modular adsorbers. Int J Refrig. 2016;67:336–44.
11. Gong LX, Wang RZ, Xia ZZ, Chen CJ. Design and performance prediction of a new generation adsorption chiller using composite adsorbent. Energy Convers Manag. 2011;52(6):2345–50.
12. Sharafian A, Bahrami M. Critical analysis of thermodynamic cycle modeling of adsorption cooling systems for light-duty vehicle air conditioning applications. Renew Sustain Energy Rev. 2015;48:857–69.
13. Islam MA, Thu K, Saha BB. Specific heat capacity of mesoporous silica gel for adsorption heat pump applications. Nov Carbon Sci Green Asia Strateg. 2017;19.
14. Bell IH, Wronski J, Quoilin S, Lemort V. Pure and pseudo-pure fluid thermophysical property evaluation and the open-source thermophysical property library coolprop. Ind Eng Chem Res. 2014;53(6):2498–508.

06. High Energy and Plasma Physics



BOOK OF FULL TEXT PROCEEDINGS TURKISH PHYSICAL
SOCIETY 35th INTERNATIONAL PHYSICS CONGRESS (TPS35)
TPS35, Vol.01, No.06, pp.365-368.
ISBN:978-605-83516-6-0

15 December 2019

Demirci-Pro: A Single Software Interface for RFQ, Ion Source and LEBT Line Design

O. Çakır[a], E. Çelebi[b], H. Çetinkaya[b, c], H. Kolenoğlu[d], G. Türemen[a], Z. Uysal[e], G. Ünel[f]

[a] *Ankara University, Department of Physics, Ankara, Turkey;* [b] *Bogazici University, Department of Physics, Istanbul, Turkey;* [c] *Dumlupinar University, Department of Physics, Kutahya, Turkey;* [d] *Eskisehir Technical University, Department of Physics, Eskisehir, Turkey;*
[e] *Gaziantep University, Department of Physics Engineering, Gaziantep, Turkey;*
[f] *University of California UCI, Department of Physics and Astronomy, Irvine, USA.*

[a)] Corresponding author: ocakir@science.ankara.edu.tr
[b)] hilal.kolenoglu@gmail.com

Abstract. Demirci-Pro is the natural evolution of Demirci software, aiming to provide a single integrated graphical user interface for designing an ion source, a radio frequency quadrupole (RFQ) and a Low Energy Beam Transport (LEBT) system. With this addition, the usage of the Demirci-Pro software can now extend even after the production of the RFQ vanes. LEBT calculations and simulations are implemented in Demirci-Pro together with a GUI for a realistic design of the associated magnets using the industry standard Superfish / Poisson package. The ion source design and simulations are provided via a graphical interface to the well-known IBSimu package. In this study, after presenting the novelties, we focus on the comparison of design results from Demirci-Pro to the already available software packages. Furthermore, the updated finite element method (FEM) solver for the RFQ designer can now be extended even after the effects of production errors on the electric field and provide more realistic beam dynamics simulations.

INTRODUCTION

Demirci-Pro software allows to design the radio frequency quadrupole (RFQ) easy, fast and accurate. It aims to provide a single integrated graphical user interface for the whole system, as seen in Fig. 1. The RFQ is a compact, low velocity, high current and multi-purpose linear accelerator for protons and low-charge ions, accelerating from few keV to MeV energy [1]. Study includes eight term potential, Ion source calculation, LEBT calculation, matching beam emittance and geometry.

DESIGNING RFQ

The RFQs perform three tasks: bunching a continuous beam, focusing and accelerating the beam. We can adjust the main parameters from the graphical user interface (GUI) and use the “Interpolate” and “Run” buttons to launch the calculations in the background, however the results can be read from this panel [2]. It is also important to watch out for warnings like KP limit violations from the main window.

ISBN:978-605-83516-6-0

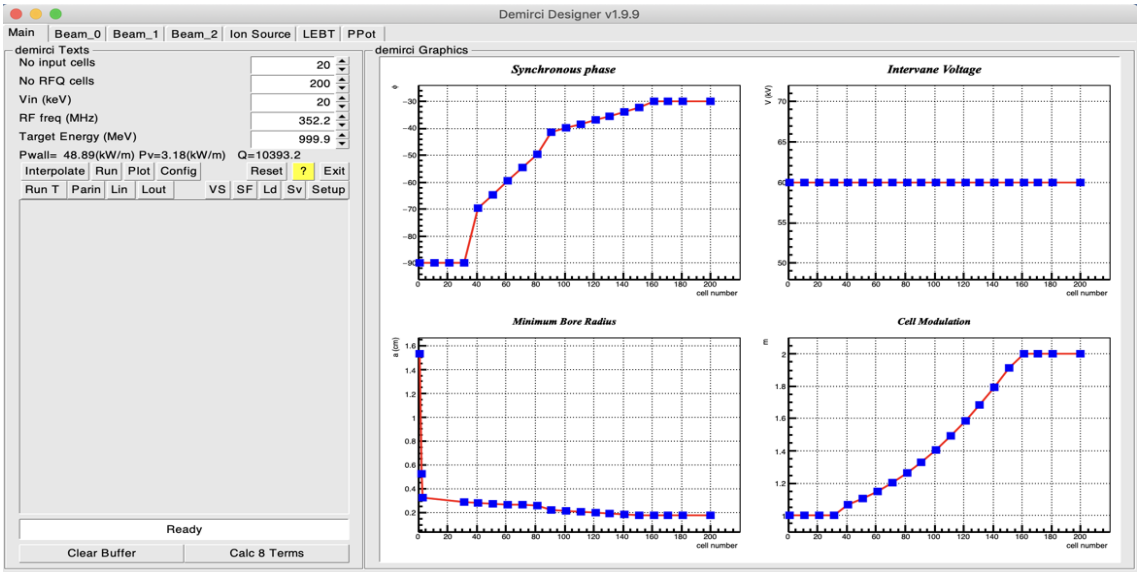


FIGURE 1. Demirci-Pro GUI

ION SOURCE DESIGN

IBSimu package is integrated into Demirci-Pro. It is one of the most known software of this field to design an ion source extraction electrodes. The main part is a plasma chamber, where the gas injected for required ion species and simultaneously evacuated constantly by pumping. The gas inside the plasma chamber is heated by using different methods so energetic electrons ionize the neutral particles and thus form a plasma. The ions can be pulled from the plasma chamber by applying high voltage to the extraction region to form the ion beam. The program uses the IBSimu library to read DXF electrode drawings, automatically create and execute an ion source simulation defined by the user parameters, as shown in Fig. 2. The resulting beam profile is saved in DST format and can be used later in LEBT part of the program.

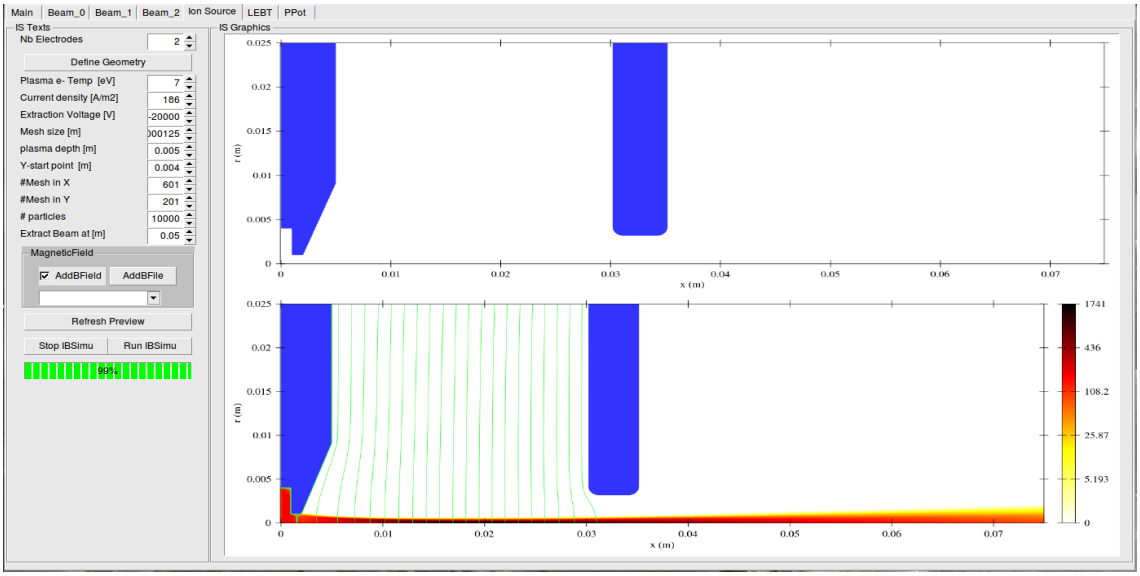


FIGURE 2. Ion source design

ISBN:978-605-83516-6-0

LEBT LINE DESIGN

The LEBT line consists mainly of beam measuring devices and magnets. The ability to simulate the result of the LEBT section for a specific magnet configuration has been added to the Demirci-Pro program [3]. With the Run button, the particles are advanced in these magnets and drift spaces. As shown in Fig. 3, the distributions are refreshed to reflect the final situation. In this way, the distribution at the bottom right always shows the first beam section, and the two-sigma distribution areas are indicated by purple frame [4]. We have compared the LEBT section of Demirci-Pro with the Travel program and the results are in good agreement.

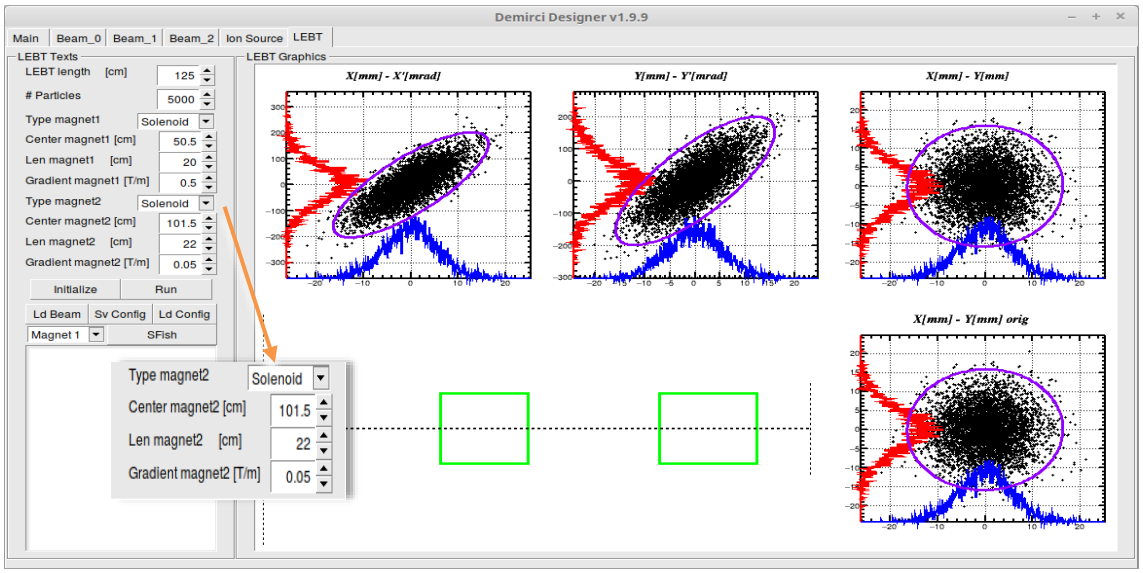


FIGURE 3. LEBT line design panel

MAGNET DESIGN

Demirci-Pro provides an interface to the related programs for the design of LEBT magnets. These magnets can be designed as a solenoid magnet or a quadrupole magnet, which is indicated by the green frame in Fig. 3. With the quadrupole or solenoid magnets placed in this line, the beam emitted from the ion source can be brought to the input parameters of the RFQ cavity. In this menu, input file for Poisson / Superfish can also be prepared with SFish button.

CONCLUSIONS

Demirci-Pro has been developed to match the requirements from both national and international RFQ designer communities. It provides the interaction mechanisms with other tools to design the ion chamber and the low energy beam transport magnets via the graphical user interface. With the addition of these modules the scope of Demirci-Pro is increased to whole RFQ beam line design.

ACKNOWLEDGMENTS

This study was supported by TUBITAK project number 117F143 and 114F106.

ISBN:978-605-83516-6-0

REFERENCES

1. J.W. Staples, AIP Conference Proceedings 249, 1483 (1992).
2. B. Yasatekin, G. Turemen and G. Unel, Computer Physics Communications, Volume 192, 108-113, (2015).
3. E. Celebi, B. Yasatekin, G. Turemen, G. Unel, O. Cakir, IPAC'17, Copenhagen, (2017).
4. E. Celebi, G. Turemen, O. Cakir, G. Unel, IPAC'18, Vancouver, (2018).

BOOK OF FULL TEXT PROCEEDINGS TURKISH PHYSICAL
SOCIETY 35th INTERNATIONAL PHYSICS CONGRESS (TPS35)
TPS35, Vol.01, No.06, pp.369-371.
ISBN:978-605-83516-6-0

15 December 2019

Investigating Magnetic Properties of YIG Thin Film Grown on Si Substrates

Zürbiye ÇAPKU [1,2, a)] and *Fikret YILDIZ* [1, b)]

[1]*Gebze Technical University, Kocaeli, Turkey*
[2]*Boğaziçi University, İstanbul, Turkey*

[a)] z.capku@gtu.edu.tr

the magnetic properties of the Yttrium Iron Garnet (YIG-Y3Fe5O12) ferromagnetic insulator, which is widely used in microwave, [b)] fyildiz@gtu.edu.tr

Abstract. We have investigated magneto optic and spintronic applications due to the low spin wave damping[1]. In literature, static and dynamical magnetic properties of bulk or micron-thickness YIG material were investigated in detail. In our study, we introduced YIG thin film grown on silicon (Si) substrates by PLD technique. The structural analysis showed that the lattice mismatch between the substrate and the film led to the crystal structure distortion. For this reason, film was annealed. The crystal structure improved as the annealing temperature. We observed the polycrystalline YIG phase in the structural analysis. The magnetic properties were measured by FMR technique at a constant frequency of 9.1 GHz.

Keywords: YIG, FMR, Magnetic Anisotropy.

INTRODUCTION

YIG is one of the most important ferromagnetic insulator materials for microwave devices, acoustic, optical and magnetooptical applications[2]. It has the narrowest known linewidth of ferromagnetic resonance (FMR) in microwave region[3]. Intrinsically low magnetic spin wave damping (10^{-5}) gives rise to extremely low losses as a resonant element in filtering[4] and other essential electromagnetic properties; including tunable saturation magnetization, good temperature and chemical resistance have attracted much interest in spin-related phenomena such as spin pumping and Spin Seebeck effect and especially in microwave device applications (tunabling, isolators, phase shifters, etc.) [1]. Thus, it is important to have an accurate structural and magnetic characterization of YIG thin films. We prepared YIG thin film on Si-100 substrate by PLD technique and studied the effect of annealing temperature after deposition on the crystallization of the film. The magnetic properties of the annealed films were studied at room temperature by FMR technique.

EXPERIMENT

PLD (a KrF excimer laser 248nm) was used to obtain the desired YIG film stoichiometry in that adjustment of the oxygen vacancy, deposition temperature and epitaxial growth were systematically controlled. Films were fabricated using laser energy 170 mJ at 10 Hz in oxygen atmosphere of 10^{-5} mbar at the substrate temperatures of 400°C. After deposition, the oxygen partial pressure was raised to near atmosphere and the films were cooled to the room temperature. The as-grown film was ex situ annealed in air atmosphere at 800°C for 1 hour.

Türk Fizik Derneği
1950
Turkish Physical Society

ISBN:978-605-83516-6-0

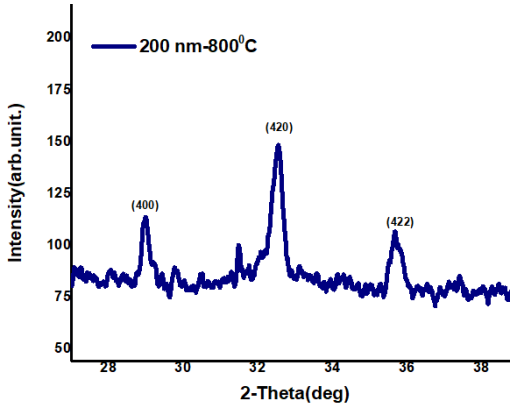
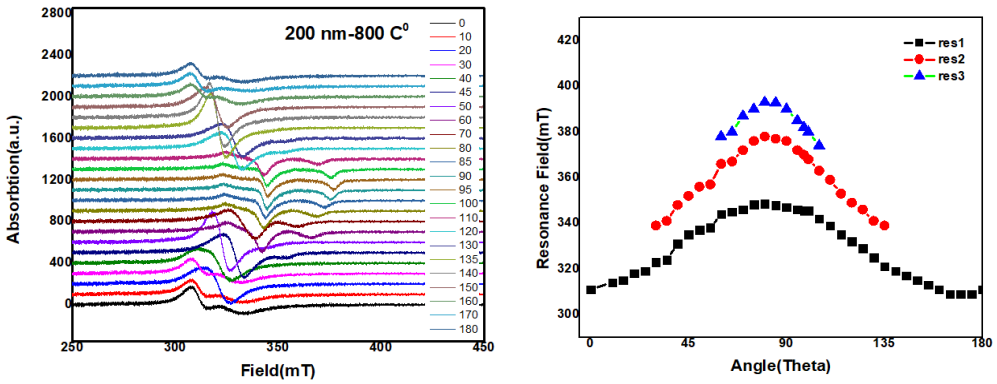


FIGURE 1. XRD pattern of 200 nm YIG film before and after annealing.

RESULTS

The film thickness was measured by a DEKTAK profilometer (200 nm). The crystal structures of the as-prepared and annealed YIG films were studied using X-ray diffraction (XRD). Although as grown film showed almost no peak, we observed characteristic YIG peaks when the film was ex-situ annealed in air as seen in fig.1. XRD patterns of the annealed films reveals that annealing leads to high quality crystallization of YIG films. FMR was performed at 9.1 GHz with magnetic field (H) applied in parallel and perpendicular directions to the film plane. Ferromagnetic resonance mode and spin wave modes were observed in the out of plane geometry where the magnetic field was applied from the sample plane (0^o) to the normal of the sample (90^0). At the perpendicular direction (90^o) the main peak shifted towards the higher applied magnetic field in fig.2. An apparent in-plane magnetic anisotropy existed due to the demagnetization field. However, there is no measurable anisotropy in in-plane geometry where the magnetic field is always in the sample plane.



(a) (b)

FIGURE 2. FMR measurement.(a) FMR spectra in out of plane geometry (b) Angular variation of resonance field for 200 nm YIG film.

ISBN:978-605-83516-6-0

CONCLUSION

We investigated the phase formation, crystallization and magnetic properties of YIG thin films deposited by PLD. Growth of YIG on a silicon substrate is considerably challenging due to the lattice mismatch between substrate and the film. We conclude that a post deposition annealing process is required to obtain proper crystal structure of the YIG film. We acquired polycrystalline YIG thin film after annealing. FMR spectrum showed an in plane magnetic anisotropy and magneto-static spin waves propagating in the sample plane along the main resonance peak.

REFERENCES

1. A. Serga, A V Chumak and B Hillebrands, YIG magnonics, Journal of Physics D: Applied Physics 43, 26 (2010)
2. B. Bhoi et al. FMR and Magnetic Studies on Polycrystalline YIG Thin Films Deposited Using Pulsed Laser. IEEE Transactions on Magnetics, Vol. 49, No.3 (2013)
3. A.J. Princep et al. The full magnon spectrum of yttrium iron garnet, Nature 63 (2017)
4. Carter P.S. Magnetically Tunable Microwave Filters Using Single Crystal Yttrium Iron Garnet Resonators, IEEE Transactions on Microwave Theory and Applications 252-260 (1961)

BOOK OF FULL TEXT PROCEEDINGS TURKISH PHYSICAL
SOCIETY 35th INTERNATIONAL PHYSICS CONGRESS (TPS35)
TPS35, Vol.01, No.06, pp.372-375.
ISBN:978-605-83516-6-0

15 December 2019

Investigating Magnetic Properties of NiFe Dot/Antidot Structure

Zürbiye ÇAPKU [1,2, a)] and *Fikret YILDIZ* [1, b)]

[1]*Gebze Technical University, Kocaeli, Turkey*
[2]*Boğaziçi University, İstanbul, Turkey*

[a)] z.capku@gtu.edu.tr
[b)] fyildiz@gtu.edu.tr

Abstract. Dot / Antidot structures control magnetic properties in nanoscale thin films such as reversing magnetization, magnetic domain structure and magnetic anisotropy tuning[1]. They provide applications such as magnonic crystal, microwave filters and high-density magnetic data storage in technology[2]. First, a lithography process was applied to obtain dot/antidot structures. Permalloy (Ni_{80} Fe $_{20}$) film was deposited on Si substrates with dot/antidot lithographic structures by sputtering. After a lift off process, array structures were imaged by an optic microscope. Ferromagnetic resonance measurement was used to explore magnetic properties. Demagnetization was related to the shape factor. They modified magnetic anisotropy locally.

Keywords: Permalloy (Ni_{80} Fe $_{20}$), Dot / Antidot, **FMR, Magnetic Anisotropy.**

INTRODUCTION

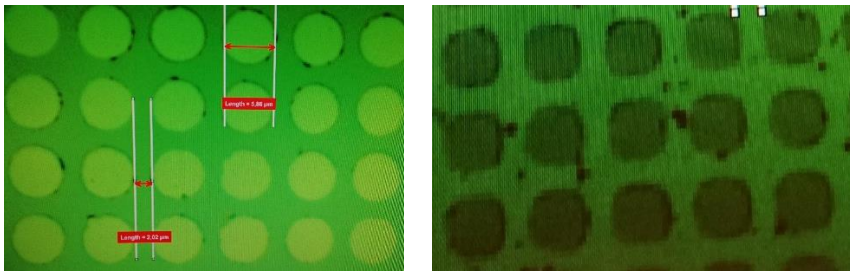
Antidot structure is a periodic arrangement of nano/microscale defects introduced to the continuous film. Structures as such allow for a control of magnetic properties in nanoscale thin films such as tuning the magnetization reversal, magnetic domain structure and magnetic anisotropy[2]. These defects provide applications as magnonic crystal waveguides, spin wave emitters, microwave filters and high density magnetic data storage in technology. We investigate the effect of dot/antidot geometry on the magnetic anisotropy of Permalloy thin films.

EXPERİMENT

RF sputtering technique was used for NiFe thin film deposition on a photoresist coated Si substrate with dot and antidot array structure. Subsequently, a lift off process was done. Figure1 shows the array of dot and antidot structure with 5,8 μm diameter and 2,8 μm interspacing. A reference uniform NiFe film was also grown for a comparision of shape effect. All the film thicknesses were the same. The film thickness was measured by X Ray Reflection (XRR) method (20 nm). The FMR measurements were performed at 9,1 GHz at room temperature at both in sample plane and out of sample plane geometry.

Türk Fizik Derneği
1950
Turkish Physical Society

ISBN:978-605-83516-6-0



(a) (b)

FIGURE 1. NiFe antidot and dot array structure.

RESULTS

The effects of dot/antidot array on the magnetic anisotropy were investigated by FMR technique. We observed that FMR spectra of NiFe films with dot/antidot array was different from the pure film. Spin wave modes appeared beside main resonance mode which results from shape anisotropy in fig.2. Geometrical parameters affect ferromagnetic resonance behavior due to the competition between shape and intrinsic anisotropies.

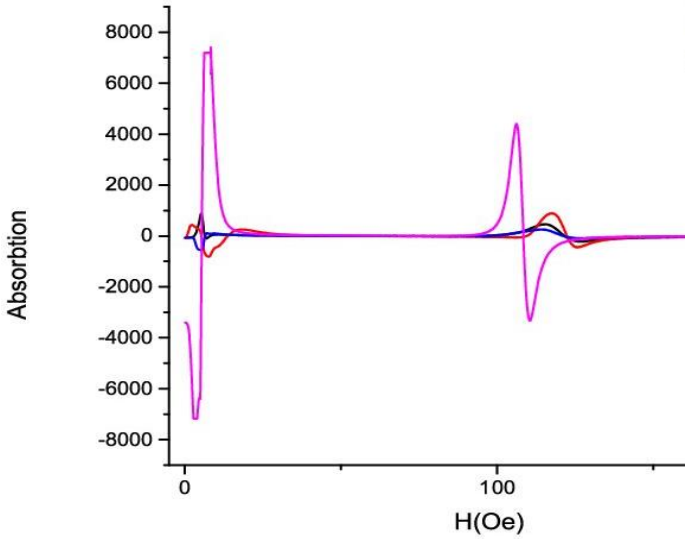
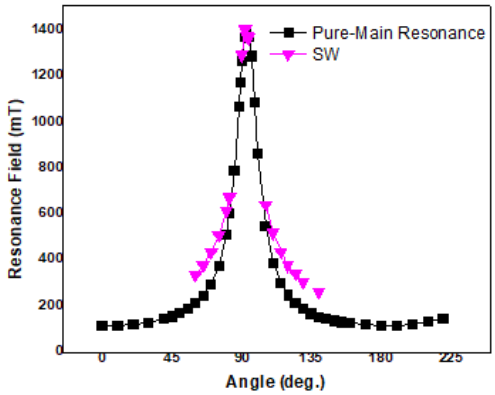


FIGURE 2. FMR spectrum for different structures. Pink is the pure film, blue is the dot and red is the antidot array.

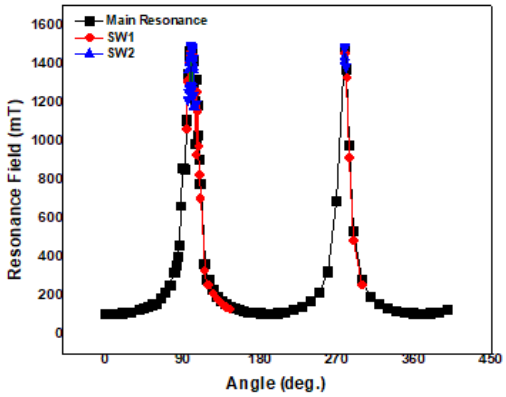
Figure 3 shows the angular variation of resonance fields of three NiFe films. FMR modes were the same for three of them. However, spin waves located at different angles and mostly at perpendicular direction. Magnetization reversal mechanism was influenced by variation of antidot/dot structure.

ISBN:978-605-83516-6-0

(a)



(b)



(c)

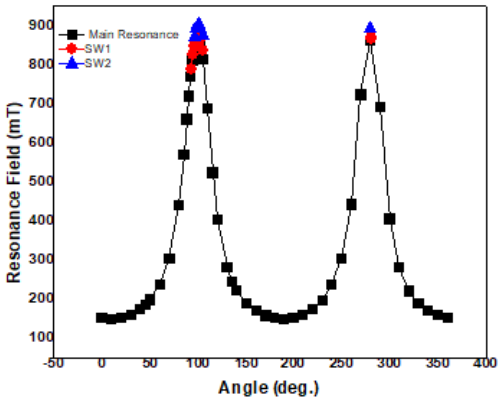


FIGURE 3. Angular variation of resonance field in out of plane geometry for (a) pure Permalloy,(b) dot array,(c) antidot array.

ISBN:978-605-83516-6-0

CONCLUSION

Antidots behave as pinning center for domain wall propagation and modify intrinsic magnetic anisotropy locally. We conclude that antidots and dots in magnetic thin films can control magnetic reversal, domain wall pinning and spin wave mode structure.

REFERENCES

1. Deger, C., M. Ozdemir, and F. Yildiz, Magnetostatic spin wave resonance in square-patterned Ni 0.77 Fe 0.16 Cu 0.05 Cr 0.02 (Mu-metal) thinfilms. Journal of Magnetism and Magnetic Materials, 2016. 408: p. 13-17.
2. Zivieri, R., Metamaterial properties of one-dimensional and two-dimensional magnonic crystals. Solid State Physics, 2012. 63(151): p. 4.

BOOK OF FULL TEXT PROCEEDINGS TURKISH PHYSICAL
SOCIETY 35th INTERNATIONAL PHYSICS CONGRESS (TPS35)
TPS35, Vol.01, No.06, pp.376-380.
ISBN:978-605-83516-6-0

15 December 2019

Associated Production of Higgs Boson at an Electron-Photon Collision in The Two Higgs Doublet Model

Mehmet Demirci

Karadeniz Technical University, Depertmant of Physics, 61080, Trabzon, Turkey

mehmetdemirci@ktu.edu.tr

Abstract. In the framework of two Higgs doublet model (2HDM), the associated production of neutral Higgs boson with a γ via an e^-e^+ collision is investigated at the one-loop level. On the other hand, the process at the tree level is suppressed by the electron mass. For numerical evaluation, a few benchmark points, which are compatible with theoretical and current experimental constraints, are chosen in the type-I of 2HDM. The dependence of the cross section on the center-of-mass energy is also presented at the various polarization configurations of the initial beams. It is shown that depending selected BPs, there is a deviation from the predictions of SM where the production rate is significantly enhanced. The cross section is enhanced up to about four times by the completely polarized right-handed positron and left-handed electron. At $\sqrt{s}$ = 250 GeV, $\sigma^{2HDM}(e^-_L e^+_R \to h^0\gamma)$ reaches to a value of 0.27 fb.

INTRODUCTION

After the discovery of the Higgs boson [1, 2], the search for new scalars by the experimental groups at the LHC, further motivated the study of physics beyond Standard Model (SM), particularly for models with extended Higgs sector. The simplest extensions of the Higgs sector of the SM provide a perfect framework for the interpretation of many searches. Besides, there are many motivations to offer extra Higgs doublets such as to explain the electroweak baryogenesis, neutrino mass generation, top-bottom mass hierarchy and so on.

The two Higgs doublet model (2HDM) [3, 4] is one of the simplest such extensions, which contains one extra Higgs doublet compared to the SM. After electroweak symmetry breaking (EWSB), 2HDM will generate 5 mass eigenstates, a pair of charged Higgs boson $H^{\pm}$, one *CP*-odd Higgs boson *A* and two *CP*-even Higgs bosons, *h*, *H*. The additional Higgs states can provide window into the underlying physics of EWSB. Here we take the lighter h as the observed SM-like Higgs.

The future e^-e^+ colliders, such as the International Linear Collider (ILC), Compact Linear Collider (CLIC), Future Circular Collider (FCC) and Circular Electron-Positron Collider (CEPC), are expected to yield a high precision picture of the Higgs boson and its couplings. The precise measurement programs of Higgs properties at the e^-e^+ colliders and LHC are complementary to each other in many aspects. At the e^-e^+ colliders, the one loop mediated process $e^+e^- \to \gamma h^0$ if measured could also shed some light on $h^0\gamma\gamma$ and $h^0\gamma Z$ couplings. Such a process has been investigated in the SM [5,6], and also in many Beyond SM (BSM) scenarios, like extended Higgs sector [7], in the Inert Higgs Model [8] and MSSM [9, 10, 11].

In this study, the associated production of $h^0\gamma$ via e^-e^+ collisions is investigated in the framework the type-I of 2HDM with an alignment limit, taking into account a full set of one-loop Feynman diagrams contributing to process. For numerical evaluation, we select 4 benchmark points (BPs), which are compatible with current experimental and theoretical constraints. We investigate ability of selected BPs to increase the $h^0\gamma$ signal at the future e^-e^+ colliders. The present work reveals the potential of exploring the process interested in the 2HDM.

Türk Fizik Derneği
1950
Turkish Physical Society

ISBN:978-605-83516-6-0

ANALYTICAL EXPRESIONS FOR THE PRODUCTION CROSS SECTION

The associated production of $h^0\gamma$ via an e^-e^+ collision is expressed by

$$e^+(p_1)e^-(p_2) \to h^0(k_1)\gamma(k_2) \tag{1}$$

where p_1, p_2, k_1 and k_2 represent to the four momenta of the relevant particles. The Mandelstam variables are defined by

$$s=(p_1+p_2)^2,\ t=(p_1-k_1)^2,\ u=(p_1-k_2)^2. \tag{2}$$

At tree level, the process $e^-e^+\to\gamma h^0$ occurs through *t*-channel *e*-exchange diagram and it is suppressed by the electron mass. Therefore, tree-level amplitude can be safely neglected. Consequently, it receives main contributions from one-loop level diagrams. Hence, this process is sensitive to all virtual particles (fermions, gauge bosons and charged Higgs bosons as well as ghost particles $u^{\pm}$ and Goldstone $G^{\pm}$) inside the loop.

The one-loop level Feynman diagrams of the process $e^-e^+\to\gamma h^0$ could be grouped into three different types: box-type, triangle-type and self-energy diagrams. Figure 1 shows some representative Feynman diagrams. Box-type diagrams are necessary for gauge invariance. For the particles inside the *s*-channel triangle-type diagrams, we have all possible charged particles. The contributions of self-energy γ–Z mixing diagram, which come from all SM particles and charged Higgs boson, are necessary in order to get the finite results. For *t*-channel triangle-type diagrams with *e*-exchange, *F* denotes electron or neutrino, while *V* denotes *Z*-boson or *W*–boson.

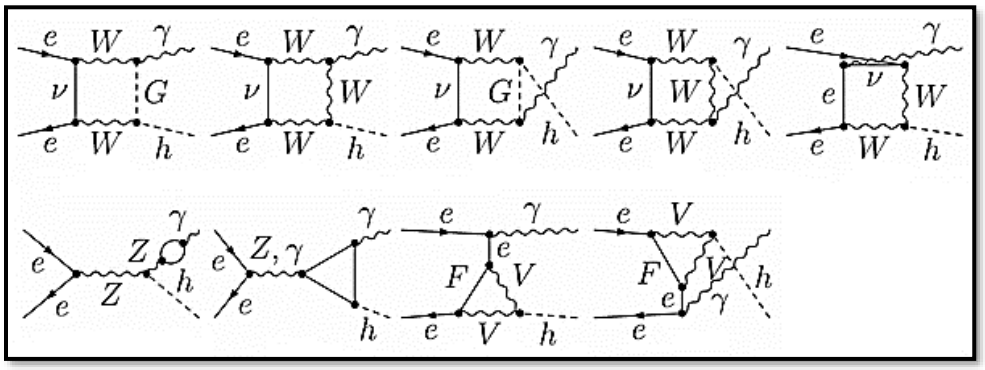


FIGURE 1. Generic one-loop diagrams contributing to $e^-e^+ \to h^0\gamma$.

In the present study, a full set of one-loop Feynman diagrams which contribute to process is taken into account. The total amplitude can be written in the form

$$M_{\text{total}} = M_{\square} + M_{\Delta} + M_{\circ} \tag{3}$$

as a sum over box-type, triangle-type, and self-energy contributions. The differential cross section is given by

$$\frac{d\sigma}{d\cos\theta} = \frac{s-m_h^2}{32\pi s^2}\sum_{pol}|M_{total}|^2 \tag{4}$$

summing over the polarization of the photon, where $\sqrt{s}$ is the center-of-mass energy of e^+e^- collisions. The integrated cross section over all scattering angles is calculated by

$$\sigma(e^+e^-\to h^0\gamma) = \int_{-1}^{+1} d\cos\theta \frac{d\sigma}{d\cos\theta}. \tag{5}$$

Our calculations are carried in the 't Hooft-Feynman gauge by using *FeynArts* and *FormCalc* packages [12,13]. The total amplitude is provided by *FeynArts*. The squared amplitude is obtained via *FormCalc*. The scalar-loop integrals are evaluated by *LoopTools* [14]. It has been checked both analytically and numerically that the total amplitude is ultraviolet finite. Our results are consistent with those of SM obtained at the previous studies (see, e.g. Refs.[7,8]). Using the tools described above, we have previously carried out several works and found significant results [11, 15, 16].

ISBN:978-605-83516-6-0

PARAMETER SETTINGS

The parameter space of 2HDM is subjected to both the bounds coming from experimental searches as well as theoretical constraints that come from the theory itself. The theoretical constraints are known as potential stability, perturbativity and unitarity. We will work with a CP-conserving vacuum and a scalar potential which is CP-conserving, in which the quartic terms obeys Z_2 symmetry. Depending on the Z_2 assignment, there appear four types of 2HDMs, which are named as type-I, type-II, type-X, and type-Y 2HDMs. Working in the "physical basis", the 2HDM can be determined by seven independent parameters: a soft Z_2 symmetry breaking term m_{12}^2, tanβ, sin(β-α) (mixing-angle α) and m_h, m_H, m_A, $m_{H^\pm}$.

During numerical evaluations, the procedure used in our previous paper [16] is followed for parameter settings. In this study, 4 benchmark point (BP) scenarios are selected from the type-I of 2HDM with an alignment limit sin($\beta-\alpha$) $\rightarrow$1 and hence the CP-even Higgs h^0 is a SM-like Higgs. The selected BPs are given in Table 1. By using *2HDMC* 1.7.0 [17], they have been checked to comply with theoretical constraints. They are also consistent with the limits derived from different works on additional Higgs bosons at the LHC, provided that h^0 ought to provide the properties of the discovered Higgs boson.

TABLE 1. Selected benchmark points in type-I of 2HDM with alignment limit.

BPs	m_h (GeV)	m_A (GeV)	m_H (GeV)	$m_{H^\pm}$ (GeV)	m_{12}^2 (GeV^2)	tanβ	sin($\beta-\alpha$)
BP1	125.09	150	150	150	2000	10	1
BP2		200		250			
BP3		250					
BP4			250	300	6000		

NUMERICAL RESULTS AND DISCUSSION

In this section, both polarized and unpolarized cross sections of the process $e^+e^- \rightarrow \gamma h^0$ are numerically evaluated as a function of center of mass energy for representative BPs given in Table 1.

For both 2HDM-BPs and SM[1], in Fig. 2, total cross section is presented as a function of $\sqrt{s}$ from 100 GeV to 1500 GeV. To see deviations from the values predicted by SM, the ratio of the total cross sections $\Delta R=(\sigma_{2HDM}-\sigma_{SM})/\sigma_{SM}$ is also plotted. It is clearly seen that the total cross section $\sigma(e^+e^- \rightarrow \gamma h^0)$ increases rapidly with the opening of the phase-space and then decreases near $\sqrt{s} \sim 2m_t$, with increments of $\sqrt{s}$. It has a dip at $\sqrt{s} \approx 340$ GeV for all BPs due to the top-antitop threshold. The destructive interference between the $W^\pm$ and t-quark contributions is maximum near the top-antitop threshold, hence a dip appears in the Fig. 2.. Two peaks also appear as follows: the first peak near $\sqrt{s}$ =250 GeV, and other one near $\sqrt{s}$ = 0.5 TeV. The cross section $\sigma(e^+e^- \rightarrow \gamma h^0)$ reaches to its maximum value of 0.07 fb around $\sqrt{s}$ =250 GeV. According to our BPs, total cross sections are sorted in descending order as $\sigma(BP1)>\sigma(BP2)\approx\sigma(BP3)>\sigma(BP4)$. For BP2 and BP3, total cross sections overlap because the only input parameter m_A is different; other parameters are the same in both BPs. It can conclude that cross-section is almost independent of the pseduscalar boson mass m_A. For BP1, unpolarized cross section is around 0.07 fb ($\sqrt{s}$ = 240), 0.025 fb ($\sqrt{s}$ = 350 GeV), 0.027 fb ($\sqrt{s}$ = 380 GeV) and 0.038 fb ($\sqrt{s}$ = 500 GeV) for the proposed CEPC, FCC_{ee}, CLIC-380 and ILC-500 projects, respectively.

In BP1, a remarkable deviation from the predictions of SM, which reaches a value of ΔR=4%, is seen after $\sqrt{s}\sim$700 GeV. Accordingly, it could be a sensitive probe of 2HDM. In other BPs, a favorable deviation occurs at higher energies compared to BP1 as follows: $\sqrt{s}\sim$1100 GeV for BP2 and BP3 and $\sqrt{s}\sim$1360 GeV for BP4. However, in our previous work [11], there appear more significant deviations for the same process in framework of MSSM.

[1] A more detailed explanations of the SM results can be found in Ref.[11].

ISBN:978-605-83516-6-0

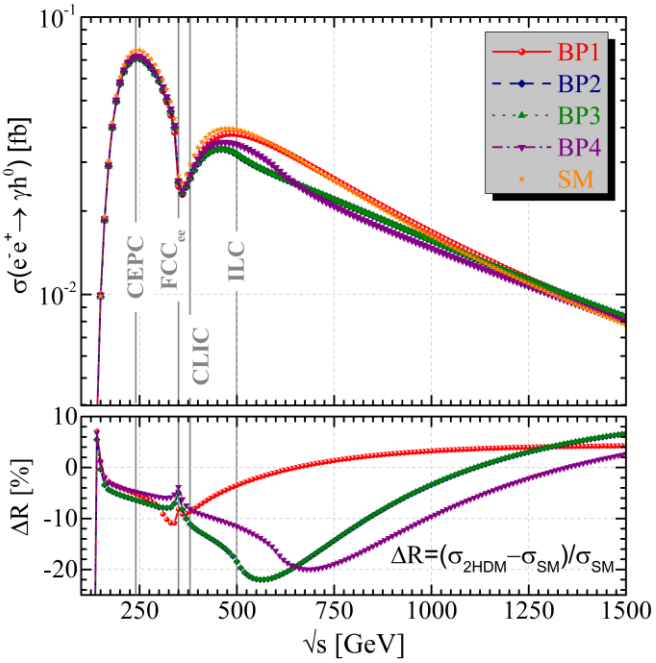


FIGURE 2. Total cross section of process $e^-e^+\to h^0\gamma$ vs center of mass energy. The vertical solid-lines represent to the proposed energy of e^-e^+ colliders. The deviations from the predictions of SM, the ΔR ratio, is also shown in lower panel of this figure.

In Fig.3, focusing on various polarizations of the electron and positron-beams, polarized cross section is presented as a function of $\sqrt{s}$ in the two BP1 and BP2. Compared to unpolarized case, the total cross section with completely polarized right-handed positron and left-handed electron, $\sigma^{2HDM}(e^-_Le^+_R\to h^0\gamma)$, is amplified by about a factor 4. It can be seen that the longitudinal polarization of initial beams increases the production rate of $h^0\gamma$ signal. At $\sqrt{s}$ = 250 GeV, $\sigma^{2HDM}(e^-_Le^+_R\to h^0\gamma)$ reaches to a value of 0.27 fb. One can see that cross sections are sorted as $\sigma(LR)>\sigma(-0.8,\ 0.3)>\sigma(-0.8,\ 0)>\sigma(UU)>\sigma(RL)$ according to polarization cases of initial beams. For example, $\sigma(LR)=0.27$, $\sigma(-0.8,\ 0.3)=0.16$ fb, $\sigma(-0.8,\ 0)=0.12$ fb and $\sigma(RL)=0.013$ fb for $\sqrt{s}$ = 250 GeV. The left-right asymmetry A_{LR} has a dip at the region of $\sqrt{s}$ = 340 GeV.After crossing the top-antitop-threshold, A_{LR} remains almost

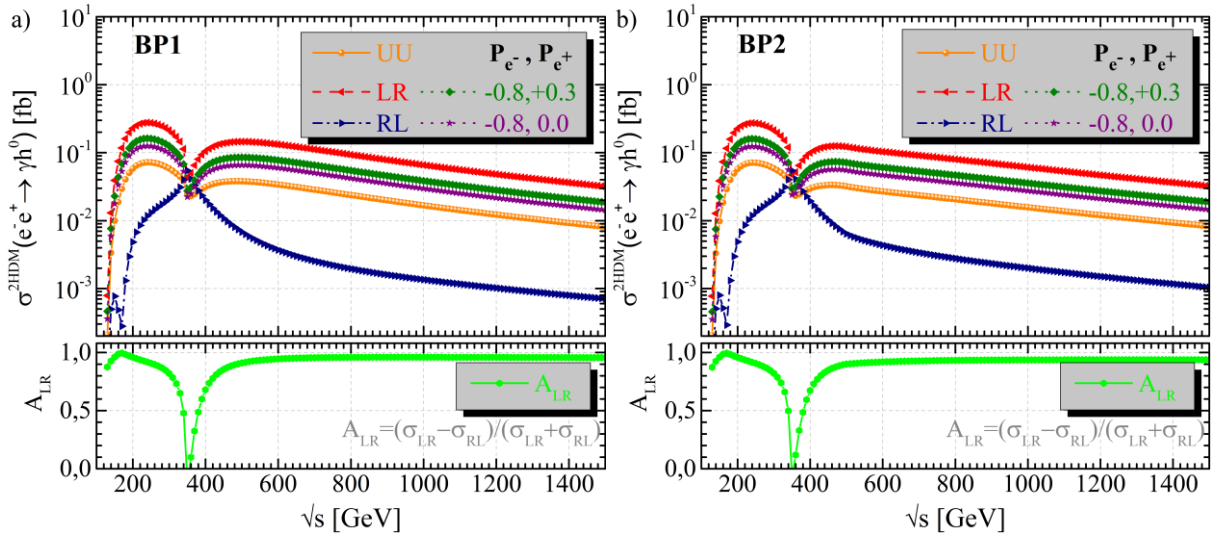


FIGURE 3. For various polarizations of the initial beams, cross section of process $e^-e^+\to h^0\gamma$ as a function of $\sqrt{s}$ for two BPs. Here, $P_{e^\pm}$ represents to the longitudinal polarization of the initial electron/positron beams. The lower panels show the left-right asymmetry A_{LR}.

Türk Fizik Derneği
1950
Turkish Physical Society

ISBN:978-605-83516-6-0

constant which is about 0.96 and 0.94 for BP1 and BP2, respectively. Note that the polarized cross sections for the other two BPs are not given here since these are almost similar to those of the BP1 or BP2.

CONCLUSION

In this paper we have presented and discussed the effects of 2HDM on the associated production of Higgs boson with a photon at e^-e^+-colliders. The total cross-section can be increased in the 2HDM, compared to the prediction of SM. Particularly, for selected BP1 in 2HDM, a remarkable deviation, which reaches a value of $\Delta R=4\%$, is seen after $\sqrt{s}\sim700$ GeV. Depending on model parameters, in other BPs, the favorable deviations are seen at higher energies. Thus, the considered process can be used to probe 2HDM. It is seen that with the polarization of the initial state of e^-_L and e^+_R the total cross section is enhanced by about a factor 4, compared with the unpolarized case.

REFERENCES

1. G. Aad et al. (ATLAS Collaboration), Phys. Lett. B **716**, 1–29 (2012).
2. S. Chatrchyan et al. (CMS Collaboration), Phys. Lett. B **716**, 30–61 (2012).
3. J. F. Gunion, H. E. Haber, G. L. Kane and S. Dawson, *The Higgs Hunters Guide*, Front. Phys. 80, 1404, (2000).
4. G. C. Branco, P. M. Ferreira, L. Lavoura, M. N. Rebelo, M. Sher and J. P. Silva, Phys. Rept. **516**, 1 (2012).
5. A. Barroso, J. Pulido and J. C. Romao, Nucl. Phys. B **267** (1986) 509.
6. A. Abbasabadi, D. Bowser-Chao, D. A. Dicus, and W. W. Repko, Phys. Rev. D **52**, 3919 (1995).
7. S. Kanemura, K. Mawatari, and K. Sakurai, Phys. Rev. D **99**, 035023 (2019).
8. A. Arhrib, R. Benbrik, and T.-C. Yuan, Eur. Phys. J. C **74**, 2892 (2014).
9. A. Djouadi, V. Driesen, W. Hollik and J. Rosiek, Nucl. Phys. B **491** (1997) 68
10. G. J. Gounaris and F. M. Renard, Phys. Rev. D **91**, 093002 (2015).
11. M. Demirci, Phys. Rev. D 100, 075006 (2019).
12. J. Küblbeck, M. Böhm, and A. Denner, Comput. Phys. Commun. **60**, 165 (1990); T. Hahn, Comput. Phys. Commun. **140**, 418 (2001).
13. T. Hahn and C. Schappacher, Comput. Phys. Commun. **143**, 54 (2002).
14. T. Hahn and M. Perez-Victoria, Comput. Phys. Commun. **118**, 153 (1999).
15. M. Demirci and A. I. Ahmadov, Phys. Rev. D **94**, 075025 (2016).
16. M. Demirci, Turk J Phys **43**, pp.1-17 (2019).
17. D. Eriksson, J. Rathsman, and O. Stal, Comput. Phys. Commun. **181**, 189 (2010); **181**, 833 (2010).

BOOK OF FULL TEXT PROCEEDINGS TURKISH PHYSICAL
SOCIETY 35th INTERNATIONAL PHYSICS CONGRESS (TPS35)
TPS35, Vol.01, No.06, pp.381-386.
ISBN:978-605-83516-6-0

15 December 2019

Neutral Higgs Boson Pair Production via Photon-Photon Collision in The Two Higgs Doublet Model

Mehmet Demirci

Karadeniz Technical University, Depertmant of Physics, 61080, Trabzon, Turkey

mehmetdemirci@ktu.edu.tr

Abstract. In the framework of two Higgs doublet model (2HDM), the direct pair production of the neutral Higgs boson is evaluated at a $\gamma\gamma$–collider, considering the full one-loop diagrams. To show the effect of the new physics, four benchmark points are selected in the type-I 2HDM, and they are compatible with current experimental and theoretical constraints. The total cross section is calculated as a function of the c. m. energy for both the opposite and the same polarization of the initial photons. The differential cross section is also presented in both 2HDM and SM for $\sqrt{s}$ = 500 GeV. The total cross section can be enhanced by the oppositely polarized photons as well as threshold effects. It is shown that depending on model parameters, the production rate is significantly enhanced in 2HDM, compared to the predictions of SM.

INTRODUCTION

The future electron-positron colliders can provide the high resolution profile determination of the Higgs boson discovered at the LHC [1, 2] (couplings, self-couplings, etc.). In these colliders, the clear signals of Higgs events, which have a manageable background, are expected. This is exactly the case of neutral Higgs pair production via photon-photon collisions $\gamma\gamma \rightarrow h^0h^0$. This process can produce the Higgs boson of the Standard Model (SM) or one predicted by the various extensions of the SM, such as two Higgs doublet model (2HDM) or the Minimal Supersymmetric Standard Model (MSSM).

The extensions of the SM provide a perfect framework for the interpretation of many searches. The 2HDM [3, 4], which extend beyond the SM Higgs sector to include two complex Higgs Doublets, is one of the simplest such extensions. The 2HDM contains five physical Higgs states as follows: one *CP*-odd Higgs boson *A*, a pair of charged Higgs boson $H^{\pm}$ and two *CP*-even Higgs bosons, *h*, *H*. Hence, it provides a rich phenomenology.

The basic production mechanism of neutral Higgs boson in $\gamma\gamma$ collisions is $\gamma\gamma \rightarrow h^0$ [5,6]; however, in order to probe the triple/quartic couplings of Higgs boson at future e^+e^- colliders, the process of pair production of Higgs should be considered. Such process has been studied in the SM [7, 8], and also in many Beyond SM (BSM) scenarios, like extended Higgs sector: 2HDM with decoupling limit [9, 10] and the fermiophobic limit [11], the type-III of 2HDM [12] and MSSM [13]. However, due to the most recent experimental constraints on the parameter space of the 2HDM, it would be useful to review the effect of the 2HDM contributions to $\gamma\gamma \rightarrow h^0h^0$ in the allowed parameter space.

In this paper, we study the one loop mediated process $\gamma\gamma \rightarrow h^0h^0$ in the framework the type-I of 2HDM with an alignment limit, taking into account a full set of one-loop Feynman diagrams contributing to process. For numerical evaluation, four benchmark points (BPs), which are compatible with current experimental and theoretical constraints, are selected. We investigate ability of selected BPs to increase the h^0h^0 signal at the $\gamma\gamma$-collider. The present work reveals the potential of exploring the process interested in the 2HDM.

Türk Fizik Derneği
1950
Turkish Physical Society

BOOK OF FULL TEXT PROCEEDINGS TURKISH PHYSICAL
SOCIETY 35th INTERNATIONAL PHYSICS CONGRESS (TPS35)
ISBN:978-605-83516-6-0 15 December 2019

NEUTRAL HIGGS BOSON PAIR PRODUCTION VIA PHOTON-PHOTON COLLISION

The pair production of higgs boson h^0 via gamma-gamma collision is expressed by

$$\gamma(p_1)\gamma(p_2) \to h^0(k_1)h^0(k_2) \tag{1}$$

where p_1, p_2, k_1 and k_2 represent to the four momenta of the relevant particles. The Mandelstam variables are defined by

$$s=(p_1+p_2)^2,\ t=(p_1-k_1)^2,\ u=(p_1-k_2)^2. \tag{2}$$

The process $\gamma\gamma\to h^0h^0$ has no amplitude at tree level, and it has one-loop level amplitude in the lowest order. Hence, this process is sensitive to all virtual particles (fermions, gauge bosons and charged Higgs bosons) inside the loop. The one-loop level Feynman diagrams of the process $\gamma\gamma\to h^0h^0$ could be classified into three different types: box-type, triangle-type and quartic-type diagrams. We show the generic box-type, triangle-type and quartic-type Feynman diagrams with charged scalar particles exchanges, in Fig. 1, Fig. 2 and Fig. 3, respectively. Note that the SM contribution with exchanging of fermions and gauge bosons is not shown in these figures. In loop diagrams, the dashed lines represent to charged Higgs bosons and Goldstone bosons, and the wavy lines denote to W boson.

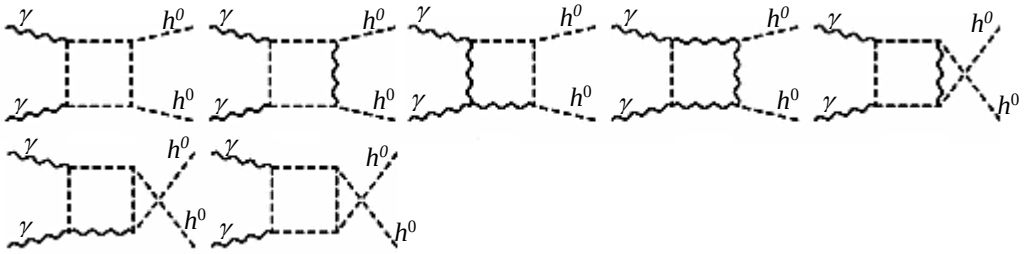


FIGURE 1. Generic box-type Feynman diagrams contributing to $\gamma\gamma\to h^0h^0$.

The box-type diagrams with intermediated virtual charged Higgs boson are sensitive to the triple coupling $h^0H^+H^-$. Box-type diagrams are t- or u-channel contributions. The triangle-type diagrams and quartic-type diagrams in top line of Fig.3 are s-channel contributions.

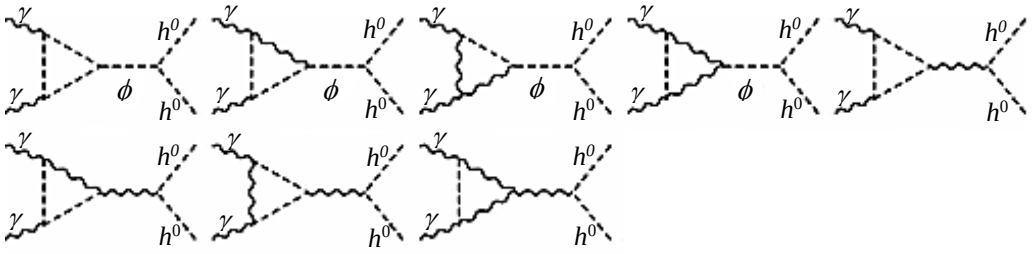


FIGURE 2. Generic triangle-type Feynman diagrams contributing to $\gamma\gamma\to h^0h^0$. Here ϕ indicates to h^0 or H^0.

Türk Fizik Derneği
1950
Turkish Physical Society

ISBN:978-605-83516-6-0

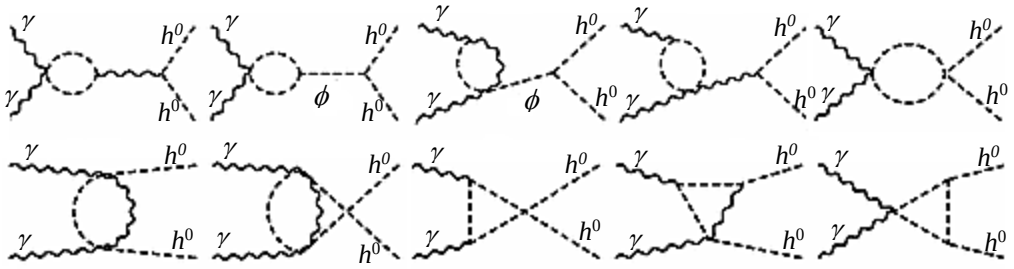


FIGURE 3. Generic quartic-interaction type Feynman diagrams contributing to $\gamma\gamma \to h^0 h^0$. Here ϕ indicates to h^0 or H^0.

In the present study, a full set of one-loop Feynman diagrams contributing to process is taken into account. The one-loop amplitude of the process $\gamma\gamma \to h^0 h^0$ can be calculated by summing all unrenormalized reducible and irreducible contributions. Hence, renormalization is not required for ultraviolet divergence. The results are obtained as finite and gauge invariant. The total amplitude can be written in the form

$$M_{\text{total}} = M_{\text{box}} + M_{\text{triangle}} + M_{\text{quartic}} \tag{3}$$

as a sum over of box-type, triangle-type, and quartic-type contributions. The total cross section is given by

$$\sigma(\gamma\gamma \to h^0 h^0) = \frac{1}{32\pi s_{\gamma\gamma}^2} \int_{t^-}^{t^+} dt \overline{\sum} \left| M_{total} \right|^2 \tag{4}$$

with

$$t^{\pm} = (\mathrm{m}_h^2 - \frac{\mathrm{s}_{\gamma\gamma}}{2}) \pm \frac{\sqrt{(\mathrm{s}_{\gamma\gamma} - \mathrm{m}_h^2)^2 - 4\mathrm{m}_h^4}}{2} \tag{5}$$

where $\sqrt{s_{\gamma\gamma}}$ is the center-of-mass energy of $\gamma\gamma$ collisions and the bar over the summation stands for average over initial spins. The collision can be performed at the facility of the next generation of TeV-class linear colliders such as the CLIC and the ILC.

Our calculations are carried in the 't Hooft-Feynman gauge by using *FeynArts* and *FormCalc* packages [14, 15]. The relevant amplitudes are provided by *FeynArts*. The squared amplitude is obtained via *FormCalc*. The scalar-loop integrals are evaluated by *LoopTools* [16]. It has been checked both analytically and numerically that the total amplitude is ultraviolet finite. Using the tools described above, we have previously carried out several works and found significant results [17, 18, 19].

PARAMETER SETTINGS

The 2HDM parameter space is subjected to both the bounds coming from experimental searches as well as theoretical constraints that come from the theory itself. The theoretical constraints are known as potential stability, perturbativity and unitarity. We will work with a CP-conserving vacuum and a scalar potential which is CP-conserving, in which the quartic terms obeys Z_2 symmetry. Depending on the Z_2 assignment, there appear four types of 2HDMs, which are named as type-I, type-II, type-X, and type-Y 2HDMs. Working in the "physical basis", the 2HDM can be determined by seven independent parameters: m_{12}^2, $\tan\beta$, $\sin(\beta-\alpha)$ (mixing-angle α) and m_h, m_H, m_A, $m_{H^\pm}$.

In this study, 4 benchmark point (BP) scenarios[1] are selected from the type-I of 2HDM with an alignment limit $\sin(\beta-\alpha) \to 1$ and hence the CP-even Higgs h^0 is a SM-like Higgs. The selected BPs are given in Table 1. By using *2HDMC* 1.7.0 [20], they have been checked to comply with theoretical constraints. They are also consistent with the limits derived from different works on additional Higgs bosons at the LHC, provided that h^0 ought to provide the properties of the discovered Higgs boson.

[1] During numerical evaluations, the procedure used in our previous paper [18] is followed for parameter settings.

Türk Fizik Derneği
1950
Turkish Physical Society

ISBN:978-605-83516-6-0

TABLE 1. Selected benchmark points in type-I of 2HDM with alignment limit [18].

BPs	m_h (GeV)	m_A (GeV)	m_H (GeV)	$m_{H^\pm}$ (GeV)	m_{12}^2 (GeV^2)	tanβ	sin($\beta-\alpha$)
BP1	125.09	150	150	150	2000	10	1
BP2		200		250			
BP3		250					
BP4			250	300	6000		

NUMERICAL RESULTS AND DISCUSSION

In this section, for representative BPs given in Table 1, the numerical predictions for the neutral Higgs boson pair production at a $\gamma\gamma$ collision are presented in detail, taking into account a full set of one-loop level Feynman diagrams.

In Fig. 2a, the total cross section is presented as a function of center of mass energy for both 2HDM-BPs and SM. The ratio of the cross sections $\Delta R=(\sigma_{2HDM}-\sigma_{SM})/\sigma_{SM}$ is also plotted, in order to make a comparison with the values predicted by SM. The total cross section $\sigma(\gamma\gamma\to h^0h^0)$ increases rapidly with the opening of the phase-space and next slowly decreases with increments of $\sqrt{s}$. In particular, $\sigma(\gamma\gamma\to h^0h^0)$ is increased by the threshold effect when $\sqrt{s}\sim 2m_{H^\pm}$, corresponding to the opening of the pair production process $\gamma\gamma\to H^+H^-$. Note that for large values of $\sqrt{s}$, the contribution from *s*-channel triangle-type and quartic-type diagrams is suppressed because of the *s*-channel propagator. At high energies, the total cross section is dominated by box-type diagrams.

The maximum values of $\sigma(\gamma\gamma\to h^0h^0)$ are 0.34 fb for BP2 and BP3 while 0.27 fb for BP1 and BP4. However, the SM cross section reaches to its maximum value of 0.28 fb. These maximum values appear around $\sqrt{s}$ =500 GeV. According to our BPs, total cross sections are sorted in descending order as σ(BP2)~σ(BP3)>σ(BP1)~σ(BP4). For BP2 and BP3, total cross sections overlap because the only input parameter m_A is different; other parameters are the same in both BPs. It can conclude that cross-section is almost independent of the pseduscalar boson mass m_A. In BP2 or BP3, a remarkable deviation from the predictions of SM, which reaches a value of ΔR=%24, is seen at $\sqrt{s}\sim$500 GeV. In other BPs, the positive deviation appears at higher energies compared with BP2 or BP3 as follows: $\sqrt{s}\sim$1270 GeV for BP4 and $\sqrt{s}\sim$1600 GeV for BP1.

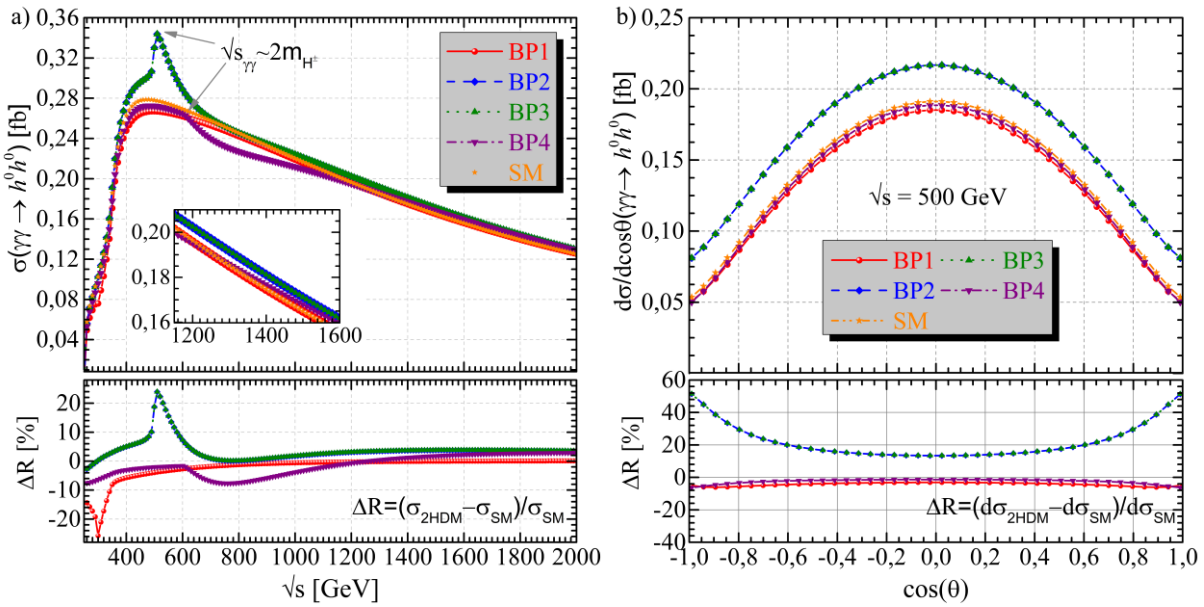


FIGURE 2. a) Total cross section of process $\gamma\gamma\to h^0h^0$ vs center of mass energy, and b) differential cross section of process $\gamma\gamma\to h^0h^0$ vs cos(θ) for $\sqrt{s}$ = 500 GeV. The deviations from the predictions of SM are also shown.

Türk Fizik Derneği
1950
Turkish Physical Society

ISBN:978-605-83516-6-0

In Fig. 2b, the corresponding angular distribution $d\sigma/d\cos\theta$ at $\sqrt{s}$=500 GeV is presented for each BPs. It is seen that all distributions are rather symmetric and the differential cross section of BP2 and BP3 are larger than those of the SM. The differential cross-section in the 2HDM has the same shape as in the SM and is shifted up due to the charged Higgs bosons effects. In BP2-3, the deviation from the predictions of SM increase from 14% to 50%, when cos(θ) runs from 0 to -1 or 1. However, there is no positive deviation for BP1 and BP4.

In Fig.3, focusing on various polarizations of incoming photons, cross section is presented as a function of $\sqrt{s}$. At high energies, the total cross section with oppositely polarized photons (−+) or (+−) is amplified by more than a factor 2 as compared to the unpolarized case. In case of both photons with right-handed or left-handed polarized (++) or (−−), the cross section is suppressed at high energies. Note that in the case of the following polarization configurations of the initial photons, the total cross sections are equal to each other: σ(++)=σ(−−), σ(−+)=σ(+−). However, at low energies, there appear the vice versa of the cases mentioned above. It can be seen that the longitudinal polarization of initial beams increases the production rate of h^0h^0 signal. When $\sqrt{s}$~900 GeV, $\sigma(\gamma\gamma\rightarrow h^0h^0)$ with the opposite polarizations of photons reaches a value of 0.42 fb.

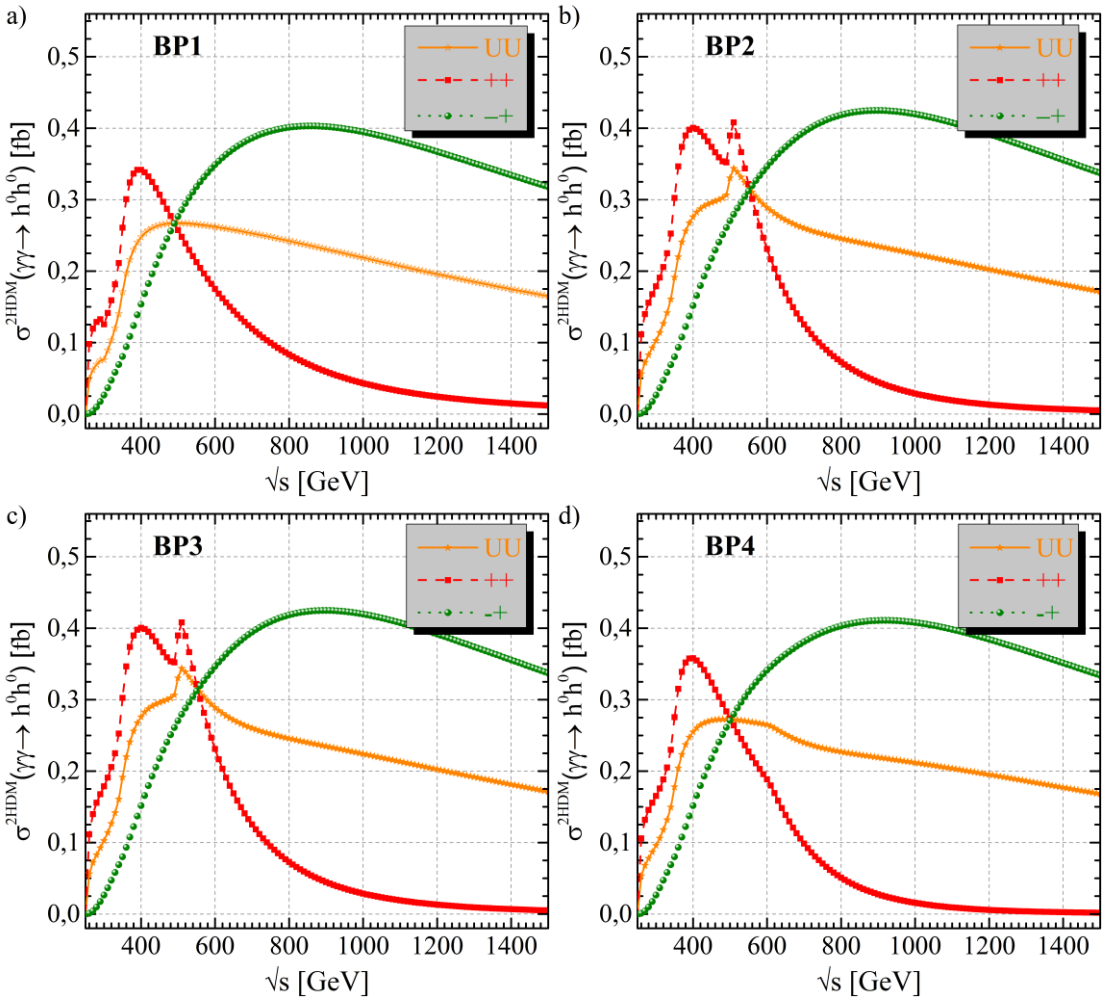


FIGURE 3. For both beams with right polarization or opposite polarization, polarized cross section of process $\gamma\gamma\rightarrow h^0h^0$ as a function of $\sqrt{s}$.

Türk Fizik Derneği
1950
Turkish Physical Society

ISBN:978-605-83516-6-0 15 December 2019

CONCLUSION

In this paper the effects of 2HDM on pair production of Higgs boson via γγ-collisions have been presented and discussed. This production occurs with a process for which the lowest order contribution in both the SM and 2HDM, appears at one loop. We have shown how the total cross section in 2HDM deviates from the prediction of SM. Particularly, for selected BP2 and BP3 in 2HDM, a remarkable deviation, which reaches a value of ΔR=24%, is seen after $\sqrt{s}$~500 GeV. Accordingly, it could be a sensitive probe of 2HDM. In other BPs, the favorable deviation is seen at higher energies. The total cross section is enhanced by the threshold effect when $\sqrt{s}\sim 2m_{H^{\pm}}$. It is seen that with the opposite polarization of the initial state of photons, the total cross section is enhanced by about a factor 2, compared with the unpolarized case. At the e^-e^+ colliders, the one loop mediated process $\gamma\gamma \rightarrow h^0h^0$ if measured can also shed some light on triple Higgs couplings.

REFERENCES

1. G. Aad et al. (ATLAS Collaboration), Phys. Lett. B **716**, 1–29 (2012).
2. S. Chatrchyan et al. (CMS Collaboration), Phys. Lett. B **716**, 30–61 (2012).
3. J. F. Gunion, H. E. Haber, G. L. Kane and S. Dawson, *The Higgs Hunters Guide*, Front. Phys. 80, 1404, (2000).
4. G. C. Branco, P. M. Ferreira, L. Lavoura, M. N. Rebelo, M. Sher and J. P. Silva, Phys. Rept. **516**, 1 (2012).
5. J. F. Gunion and H. E. Haber, Phys. Rev. D **48**, 5109 (1993).
6. D. L. Borden, D. A. Bauer, and D. O. Caldwell, Phys. Rev. D **48**, 4018 (1993).
7. G.V. Jikia and Yu. F. Pirogov, Phys. Lett. B **283**, 135 (1992); G.V. Jikia, Nucl. Phys. B **412**, 57 (1994).
8. R. Belusevic and G. Jikia, Phys. Rev. D **70**, 073017 (2004).
9. F. Cornet and W. Hollik, Phys. Lett. B **669**, 58 (2008).
10. E. Asakawa, D. Harada, S. Kanemura, Y. Okada, and K. Tsumura, Phys. Lett. B **672**, 354 (2009).
11. A. Arhrib, R. Benbrik, C.-H. Chen, and R. Santos Phys. Rev. D **80**, 015010 (2009).
12. J. Hernandez-Sanchez, C. G. Honorato, M. A. P´erez, J. J. Toscano, Phys. Rev. D **85**, 015020 (2012).
13. S. H. Zhu, C. S. Li, and C. S. Gao, Phys. Rev. D **58**, 015006 (1998).
14. J. Küblbeck, M. Böhm, and A. Denner, Comput. Phys. Commun. **60**, 165 (1990); T. Hahn, Comput. Phys. Commun. **140**, 418 (2001).
15. T. Hahn and C. Schappacher, Comput. Phys. Commun. **143**, 54 (2002).
16. T. Hahn and M. Perez-Victoria, Comput. Phys. Commun. **118**, 153 (1999).
17. M. Demirci and A. I. Ahmadov, Phys. Rev. D **94**, 075025 (2016).
18. M. Demirci, Turk J Phys **43**, pp.1-17 (2019).
19. M. Demirci, Phys. Rev. D 100, 075006 (2019).
20. D. Eriksson, J. Rathsman, and O. Stal, Comput. Phys. Commun. **181**, 189 (2010); **181**, 833 (2010).

BOOK OF FULL TEXT PROCEEDINGS TURKISH PHYSICAL
SOCIETY 35th INTERNATIONAL PHYSICS CONGRESS (TPS35)
TPS35, Vol.01, No.06, pp.387-394.
ISBN:978-605-83516-6-0

15 December 2019

Searching for the Dark Photon with the PADME Experiment

Simeon Ivanov[a)]

Faculty of Physics, Sofia University, 5 James Bourchier Blvd., 1164 Sofia, Bulgaria.

Abstract. The PADME experiment, at the Laboratori Nazionali di Frascati (LNF) of INFN, is designed to be sensitive to the production of a low mass gauge boson A' of a new U(1) symmetry holding for dark matter particles. The DAΦNE Beam-Test Facility of LNF provides a high intensity, mono-energetic positron beam impacting on a diamond active target. The PADME detectors measure with high precision the momentum of a photon, produced along with A' in e^+e^- annihilation in the target, thus allowing to measure the A' mass as the missing mass in the final state – a technique adopted for a first time in a fixed target experiment. Simulation studies predict a sensitivity on the A' interaction strength down to 10^{-6}, in the mass region $M_{A'} <$ 23.7 MeV, for one year of data taking with a 550 MeV beam. In winter 2018-2019 the first run took place, providing useful data to study the detector performance, along with the beam and background conditions. The status of the experiment and the prospects are reviewed.

DARK MATTER PHENOMENON OVERVIEW

A large body of evidence accumulated since the beginning of the 20th century points at the existence of a physical phenomenon that is detectable only through its gravitational action, while otherwise invisible to existing methods of observation [1], [3]. The nature of this phenomenon, tentatively named "Dark Matter" (DM), is one of the important unsolved problems of modern physics.

To explain this evidence, many models have been developed over the years, which can be roughly grouped into three large categories: hypotheses that deal with baryonic and non-baryonic Standard Model (SM) matter in various forms [1]; models that modify the laws of classical mechanics to produce a description that fits the observations [2]; and models, which employ new physics beyond the SM [3].

There are strong indications that only the class of hypotheses from the first group that involve SM weakly interacting particles, and new physics from the third group can currently provide satisfactory theoretical treatment of all observed phenomena that involve DM [3].

Unfortunately, while the Standard Model has been very successful otherwise, no weakly interacting particles with properties that could explain the observed DM phenomena have been discovered as of today, despite a number of experiments worldwide [3].

In the light of these negative results, a range of "new physics" models of exotic forms of matter beyond the Standard Model have been proposed. One group of these hypotheses, which has become a topic of intensive theoretical and experimental research in the past two decades considers the existence of "dark sectors" (DS), that is of particles, which while neutral to the SM interact among themselves through "hidden" modes of interaction [3].

One of the simplest available DS models assumes that while DM does not interact directly with SM gauge fields, it can do so via the mechanism of "portals", that is low-probability and difficult to observe windows of interaction. The "portals" are mediator particles of different forms (scalars, fermions, vectors, axions, etc.) that may exist and interact weakly with both the SM and the DS. [3]. Their detection requires the accumulation of a large statistical database of precise measurements, and a subsequent search for small effects that could originate in them.

Some of the DS models can also naturally explain other unsolved physics problems [3], which make them useful candiates for testing.

[a)]Corresponding author: simeonvi@uni-sofia.bg, for the PADME collaboration: P. Albicocco, F. Bossi, B. Buonomo, R. De Sangro, D. Domenici, G. Finocchiaro, L.G. Foggetta, A. Ghigo, P. Gianotti, G. Piperno, I. Sarra, B. Sciascia, T. Spadaro, E. Spiriti, E. Vilucchi (INFN Laboratori Nazionali di Frascati), A.P. Caricato, F. Gontad, M. Martino, I. Oceano, F. Oliva, S. Spagnolo (INFN Sezione di Lecce and Dip. di Matematica e Fisica, Universitá del Salento), C. Cesarotti, A. Frankenthal, J. Alexander (Department of Physics, Cornell University), G. Chiodini (INFN Sezione di Lecce), F. Ferrarotto, E. Leonardi, F. Safai Tehrani, P. Valente (INFN Sezione di Roma), S. Fiore (INFN Sezione di Roma and ENEA), G. Georgiev, V. Kozhuharov (University of Sofia St. Kl. Ohridski, INFN Laboratori Nazionali di Frascati), B. Liberti, C. Taruggi (INFN Laboratori Nazionali di Frascati and Universitá degli Studi di Roma Tor Vergata), G.C.Organtini, M.Raggi (INFN Sezione di Roma e Dip. di Fisica, Sapienza Università di Roma), S. Ivanov, L. Tsankov (University of Sofia St. Kl. Ohridski)

Türk Fizik Derneği
1950
Turkish Physical Society

ISBN:978-605-83516-6-0

THE PADME EXPERIMENT

Theoretical Model

One of the simplest DS models of ”portal“ interaction adds a U(1) symmetry and its corresponding vector particle A' (a "dark photon", or DP). Under this symmetry, the SM particles are neutral to the new field, which is expected to couple to the SM with an effective charge of εe [4], where ε is a small parameter. There are also indications that a vector boson of this kind with a mass in the range of 1 MeV to 1 GeV and a constant $\varepsilon \approx 10^{-3}$ may explain the anomalous muon magnetic moment [5]. Depending on the specific assumptions of the particular model of this type being studied, the DM mediator may decay into SM ("visible channel") or DS ("invisible channel") particles [3].

The PADME experiment is the first experiment to look for a DP produced by annihilation and decaying into the invisible channel. The experiment will attempt to detect the missing mass of the hypothesised DP mediator from known initial and final states of a $e^+e^- \rightarrow \gamma A'$ annihilation process in positron-on-target collisions. The missing mass of the DP can then be determined in a straightforward manner:

$$M^2_{missing} = (\mathbf{P}_{e^-} + \mathbf{P}_{e^+} - \mathbf{P}_{\gamma})^2$$

where the right side terms are the 4-momenta of the initial and final state [6].

Experiment Design

In the experiment (shown in figure 1), a thin active diamond target is bombarded with positrons from the linear accelerator of DAΦNE (LINAC). Some positrons annihilate with target electrons, generating gamma photons and, if the DP hypothesis is valid, in some of these annihilations A' particles are created.

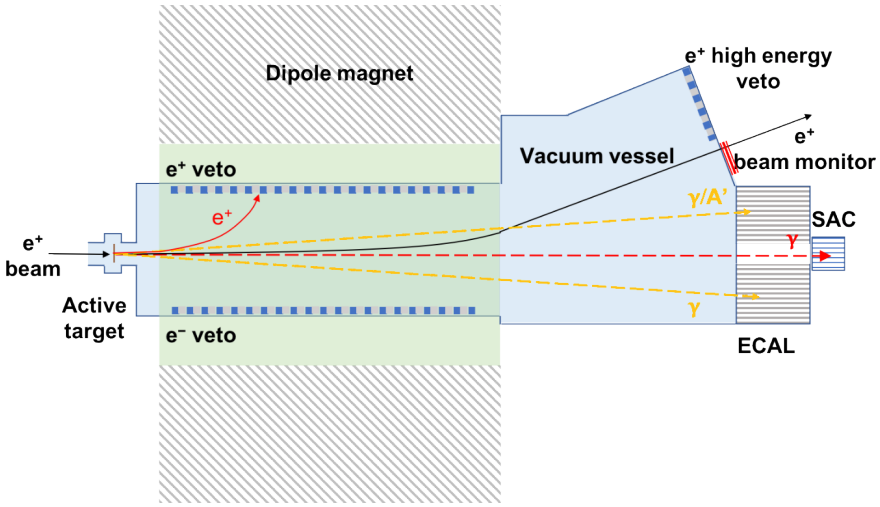


FIGURE 1. The PADME experiment concept.

Magnetic field deflects the charged reaction products onto the charged particle detectors, and the gamma rays produced by the processes of annihilation and Bremsstrahlung are captured by the two calorimeters (SAC and ECAL), shown on the far right side of figure 1. This design allows to filter the events of interest and to establish the final state of each process. The initial state is established from the beam properties and the active target measurements.

The experiment will attempt to detect the $e^+e^- \rightarrow \gamma A'$ process (figure 2). Since the cross-section is extremely low, the detector is constructed so that the operation of all elements allow for maximum discrimination of the sources of background and for accumulating sufficient number of annihilation events to test the hypothesis of A' existence [6].

The dominant background sources are summarized in figure 3. The most intesive is the Bremsstrahlung emission from positrons, and the process of SM annihilation into multiple photons.

Türk Fizik Derneği
1950
Turkish Physical Society

ISBN:978-605-83516-6-0

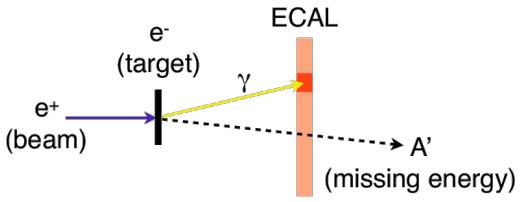


FIGURE 2. The PADME experiment concept.



FIGURE 3. Dominant background sources: Bremsstrahlung (left) and SM multiphoton annihilations (right)

FACILITIES, COMPONENTS AND CHARACTERISTICS

Positron Source

The PADME experiment is taking place at the LNF of INFN in Frascati. The positrons move to the target via a dedicated line from the LINAC. The nominal beam parameters are summarized in table I.

TABLE I. Parameters of the BTF@DAΦNE's positron source

Item	Value	Units	Comment
Energy	550	MeV	Energy dispersion under 1%
Rate	49	Bunches/s	50 Hz, with one bunch used for testing.
Multiplicity	$\sim 25 * 10^3$	Positrons/bunch	
Pulse Length	10~200	ns	Optimized for PADME
Beam σ_{xy}	~1	mm	
Beam divergence	~1	mrad	

The LINAC is able to provide sufficient rate to accumulate the number of $4 * 10^{13}$ positrons on target (PoT), required for testing the DP hypothesis.

The Active Target (AT)

This device performs several functions. It is the annihilation target for the positron beam and its low Z-number improves the signal to background ratio. It also provides real-time measurements of the position, quality and multiplicity of the incoming beam [7]. The target has an area of 20×20 mm^2 and thickness of 100 μm. The sensor of the AT is made from polycrystalline diamond film with carbon strip electrodes prepared by laser-writing them directly on the film at the University of Salento and INFN Lecce [7].

Readout is performed by two IDEA boards placed on the two sides of the sensor film, which are in turn read out via a 16-channel AMADEUS chips, providing data for 16X + 16Y strips.

The module has its own housing, which provides movement, power and control as well as mechanical interfaces to the vacuum chamber and the beam exit.

Figure 4 shows the complete sensor. Single channel gain can be measured in-situ, which allows to obtain the charge collected by the target by waveform integration and estimate beam multiplicity.

ISBN:978-605-83516-6-0

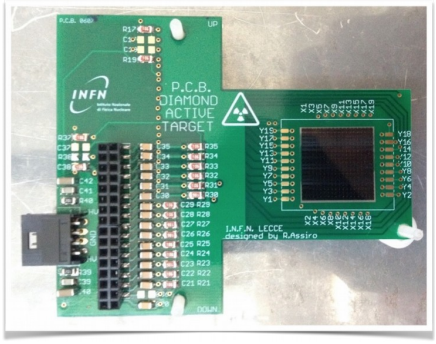


FIGURE 4. The Active Target.

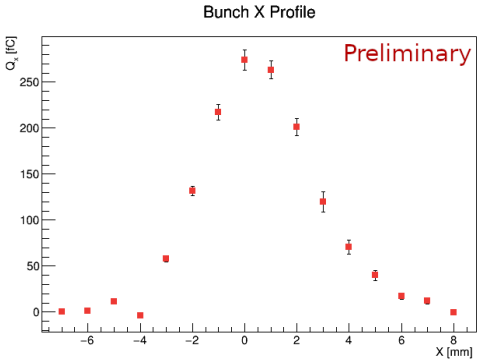


FIGURE 5. Active Target: X Profile.

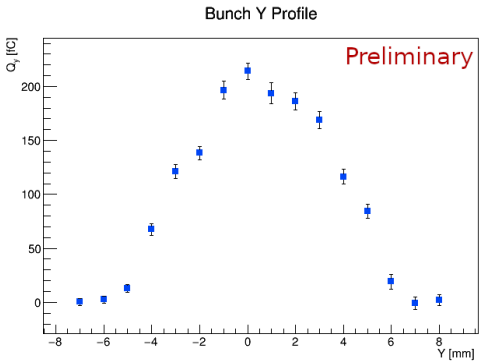


FIGURE 6. Active Target: Y Profile.

Figures 5 and 6 show beam profiles obtained during data taking. The AT has operated continuously within its design parameters during the full first run of the experiment. It also measured the average beam multiplicity to be ~25×10^3 positrons.

The Charged Particle Vetos

There are three charged particle detectors (CPD) in the vacuum chamber of the PADME experiment - the P-Veto, the E-veto and the HEP veto. The P-veto's main function is to filter out calorimeter events that are due to strong Bremsstrahlung interactions which produce high-energy gammas; the HEP veto is filtering out the positrons which have emited low-energy gammas as a result of Bremsstrahlung, and the E-veto is responsible for detecting e^+/e^- pair creation and possible decays in the visible channel.

The detectors are placed in a magnetic field, which deflects the positrons into different positions onto the CPD depending on their momenta, allowing computation of particle energies from the impact positions. Timings of detector hits are matched offline with hits of the calorimeters, vetoing Bremsstrahlung events effectively.

The vetos are build with the same general design, shown in figure 7. A photograph of the E- and P-vetos (on the right) mounted inside the vacuum chamber is shown in figure 8. They are each made from a line of plastic scintillators with dimensions $10 \times 10 \times 178$ mm^3, placed vertically along the direction of beam propagation and rotated to overlap to ensure capture of all charged particles of interest crossing the detector. Matching the light output to the sensitive range of the detector is ensured by using a glued-in wavelength-shifting fiber. The P-Veto and the E-veto consist of 96 scintillator rods each; the HEP veto counts 16 scintillators.

Readout of the scintillators is performed with Hamamatsu 13360 silicon photomultipliers, fitted on custom developed preamplifier front-end boards, which manage 4 sensors each. The cards are in turn managed and powered by custom controller modules; signal digitalization is performed with CAEN V1742 modules.

During operation, the charged particle detectors have shown that they work well within the expected design param-

ISBN:978-605-83516-6-0

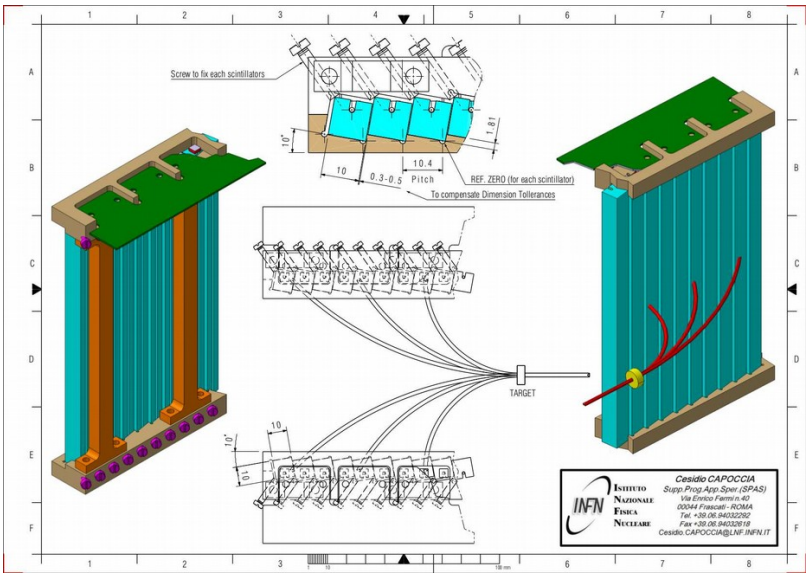


FIGURE 7. CPD Design.

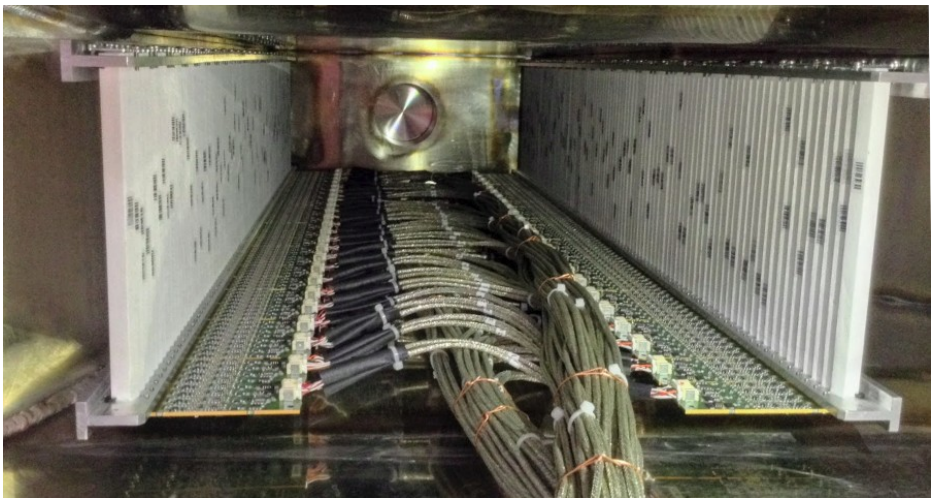


FIGURE 8. CPD Inside the Vacuum Chamber.

eters. Positron position resolution measurements provide momentum resolution better than the 5 MeV required by the simulation.

Timing resolution is estimated at about 750 ps and the distribution of differences between the time of the hits between neighboring scintillating rods is shown in figure 9.

The EM Calorimeters

The function of the EM Calorimeters is to measure the energy deposition from the gamma photons produced in the various processes of the experiment. They are the main detectors for annihilation events, information from them will be analyzed to test the DP hypothesis of the PADME Experiment. Operated in coincidence with the P-vetos, they will allow to filter out the major source of background, the Bremsstrahlung emissions, as depicted in figure 2.

The structure of the EM calorimeters is shown in figure 10, and a photograph of the completed device - in figure 11. The full detector is assembled from two parts.

ISBN:978-605-83516-6-0

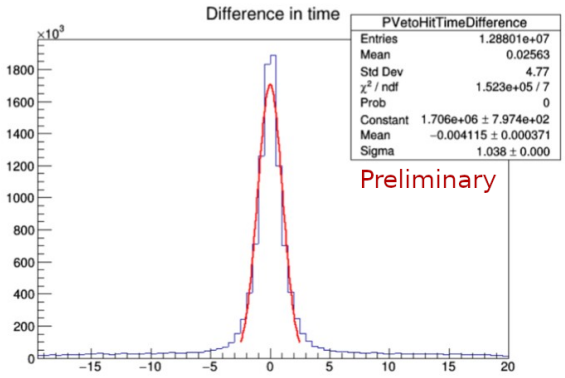


FIGURE 9. Time difference between adjacent channels of CPDs (in nanoseconds).

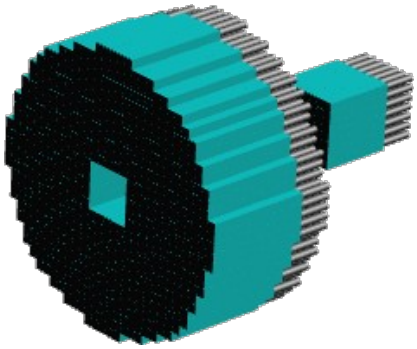


FIGURE 10. The structure of the electromagnetic calorimeters.

The front component is the high energy resolution electromagnetic calorimeter, ECAL, whose main function is to register most of the missing mass events. These are expected to be single-photon events with no registration of a corresponding positron arriving onto the charged particle detectors.

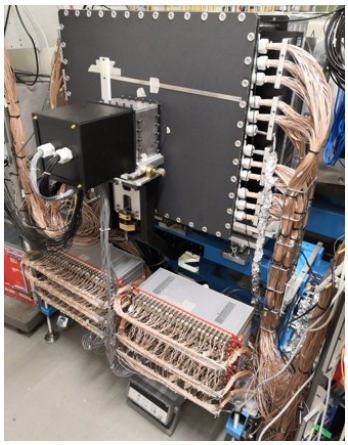


FIGURE 11. Completed Calorimeter Module.

The ECAL is placed at a distance of about 3 m from the target. It is built from 616 bismuth germanate (BGO) scintillating crystals measuring $21 \times 21 \times 230$ mm^3. The time, spacial and energy resolutions are, respectively 700 ps, 5 mm and $2\%/\sqrt{E}$ [8], where E is measured in GeV. The scintillator bars form a cylinder with radius of 29 cm with a

ISBN:978-605-83516-6-0

central hole. The readout of the BGO scintillators is performed with HZC XP1911 photomultiplier tubes.

Behind the central hole of the ECAL is the SAC, a fast Cherenkov light detector for the high-energy Bremsstrahlung photons (Small Angle Calorimeter, or SAC), which is constructed from 25 PbF_2 crystals with dimensions of $30 \times 30 \times 140$ mm^3. Its readout is implemented with fast Hamamatsu R13478UV photomultiplier tubes. It is positioned 50 cm behind the ECAL, with angular coverage from 0 to 20 mrad.

The calorimeter design allows most of the background Bremsstrahlung photons to arrive at the fast small-angle calorimeter (SAC), leaving the count rate in the more precise, but slower ECAL, at levels allowing to isolate the events of interest.

Triggers and DAQ

The processing of all analog signals, generated by the readout electronics of all components, is performed by CAEN V1742 VME digitizers, with a total of 29 VME boards used. The sampling speeds chosen for the different detectors vary from 1 to 5 Gs/s with 12-bit ADC range. This provides a data volume of approximately 900 kB per bunch, or approximately 60 MB/s of sustained data throughput for the operating system.

A custom-developed trigger board is distributing 2×32 channels.

FIRST RUN PERFORMANCE

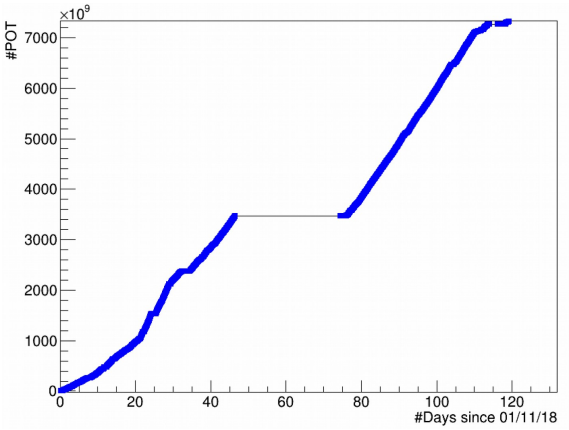


FIGURE 12. First run timeline

The first run of the PADME experiment took place between November and February 2018, with a maintenance break of two weeks at the end of 2018. During most of that time the expriment ran on secondary positrons generated and selected after the LINAC, which was a noisier source than expected. Since mid-February 2019, the experiment has began operating with the calibrated primary positron beam compatible with the design parameters.

During the first run interval, approximately 7×10^{12} positrons on target were collected as shown in fig 12, totalling approximately 270 TB of data. This dataset is being used to confirm and complete the detector calibration and functionality, and refine the analysis framework to deal with event pile-ups and "catastrophic" showers, generated by non-gaussian beam tail positrons interacting with beam pipe.

Several other tasks are being worked on based on the first run data sets, the most important are the absolute calibration of the ECAL and SAC with 1 positron per bunch, the veto calibration for the momentum of Bremsstrahlung positrons, the improvement in the correlation of events between the different detector modules, the determination of the production environment background and development of mitigation measures.

ISBN:978-605-83516-6-0

CONCLUSION

The PADME experiment, at the Laboratori Nazionali di Frascati (LNF) of INFN, the first experiment to study the production of a low mass gauge boson A' of a new U(1) symmetry holding for dark matter particles, has been operated since November 2018. The first run took place providing useful data to perform calibrations, studies of the detector performance, along with the beam and background conditions and the refinement of the analysis software. Detectors and DAQ have reached expected performance, and the experiment is preparing for a second run aiming to collect 4×10^{13} PoT from the primary source.

ACKNOWLEDGMENTS

The work is partly supported by BG-NSF DN-08/14 from 14.12.2016 and MoU SU – LNF-INFN 70-06-497/07-10-2014.

REFERENCES

1. Trimble V., Ann. Rev. Astron. Astrophys. 425-72 (1987).
2. Clifton T., Ferreira P., Padilla A., Skordis C., Physics Reports 513, 1-189, 1 (2012).
3. Raggi M., Kozhuharov V., Riv.Nuovo Cim. 38 449-505, 10 (2015).
4. Holdom B., Phys. Lett. B 166-196 (1986).
5. Pospelov M., Phys. Rev. D 80 095002 (2009).
6. M. Raggi, V. Kozhuharov, "Proposal To Search for a Dark Photon in Positron on Target Collisions at DAΦNE Linac" Advances in High Energy Physics 959802 (2014).
7. F. Oliva [PADME Collaboration], "Operation and performance of the active target of PADME," Nucl. Instrum. Meth. A , 162354. (2019).
8. G. Piperno [PADME Collaboration], J. Phys. Conf. Ser. **1162**, no. 1, 012031 (2019).

BOOK OF FULL TEXT PROCEEDINGS TURKISH PHYSICAL
SOCIETY 35th INTERNATIONAL PHYSICS CONGRESS (TPS35)
TPS35, Vol.01, No.06, pp.395-398.
ISBN:978-605-83516-6-0

15 December 2019

Review of The Nucleon to Delta Transition Axial Form Factors

Ayşe Küçükarslan[1, a)] and Yasemin Ünal[1, 2, b)]

[1]*Canakkale Onsekiz Mart University, Department of Physics, Terzioglu Campus, 17100, Canakkale, Turkey*
[2]*Universitat Bonn, Helmholtz-Institut für Strahlen-und Kernphysik, Nussallee 14-16, D-53115, Bonn, Germany.*
[a)]*akucukarslan@comu.edu.tr*
[b)]*yaseminunal@comu.edu.tr*

Abstract. We present the calculation on the nucleon to delta transition axial form factors to third chiral order in relativistic chiral effective field theory. Especially, we focus on the dominant axial form factors C_5 and C_6. And, in order to have a consistent power counting we consider the complex-mass scheme (CMS). Among the axial form factors the most important contribution comes from C_5. The form factor C_6 can be related to C_5 thanks to the partial conservation of the axial current. Then, we also analyze the ratio of two form factors. The expected value in chiral limit for this ratio is one assuming partial conservation of axial current (PCAC) and pion dominance. Thus, this ratio is plotted as a function of Q^2, and we discuss the shape of the data depending on the Q^2. The results for the axial form factors C_5 and C_6 are compared to previous findings in the framework of other approaches.

INTRODUCTION

Form factors are fundamental probes of hadron structure. The Δ(1232) resonance is the most important nucleon excitation. In this study, we use the relativistic baryon chiral perturbation theory, including explicitly the delta resonance, to compute the axial Nucleon-Delta transition form factors up to order 3. The most general effective Lagrangian which is relevant for the calculation of the axial C_5^A and C_6^A form factors at order three is given as

$$\mathcal{L}_{eff} = \mathcal{L}_2 + \mathcal{L}_4 + \mathcal{L}_{\pi N}^{(1)} + \mathcal{L}_{\pi N\Delta}^{(1)} + \mathcal{L}_{\pi N\Delta}^{(2)} + \mathcal{L}_{\pi N\Delta}^{(3)} + \mathcal{L}_{\pi\Delta}^{(1)} + \mathcal{L}_{\pi\Delta}^{(2)} + \cdots \tag{1}$$

where the ellipsis denotes terms of higher order than order three. The effective Lagrangian has purely mesonic, baryonic and meson-baryon interaction Lagrangians which are organized in a chiral derivative and quark-mass expansion. The locally invariant Lagrangians at chiral order $\mathcal{O}(q^2)$ and $\mathcal{O}(q^4)$ are given by [1,2]

$$\mathcal{L}_2 = \frac{F^2}{4}\left(Tr\left[D_\mu U(D^\mu)^\dagger\right] + Tr[\chi U^\dagger + U\chi^\dagger]\right) ,$$

$$\mathcal{L}_4 = \frac{L_1}{4}\left(Tr\left[D_\mu U(D^\mu U)^\dagger\right]\right)^2 + \frac{L_2}{4}Tr\left[D_\mu U(D_\upsilon U)^\dagger\right]Tr[D^\mu U(D^\upsilon U)^\dagger] + \frac{L_3}{16}(Tr[\chi U^\dagger + U\chi^\dagger])^2 + \frac{L_4}{4}[Tr\left[D_\mu U(D^\mu\chi)^\dagger\right] + D_\mu\chi(D^\mu U)^\dagger] + \cdots \tag{2}$$

Respectively with $\chi = 2B(s + ip)$, s and p denote the scalar and pseudoscalar external sources. The leading and next to leading order Lagrangians for π and Δ baryon interactions are given in the following fashion [3]

Türk Fizik Derneği
1950
Turkish Physical Society

ISBN:978-605-83516-6-0

$$\mathcal{L}_{\pi\Delta}^{(1)} = -\bar{\psi}^{\mu}\xi^{\frac{3}{2}}\Big[(i\gamma^{\alpha}D_{\alpha} - m_{\Delta^0})g^{\mu\nu} - i(\gamma^{\mu}D^{\nu} + \gamma^{\nu}D^{\mu}) + i\gamma_{\mu}\gamma^{\alpha}D_{\alpha}\gamma_{\nu} + m_{\Delta^0}\gamma_{\mu}\gamma_{\nu} + \frac{g_1}{2}\left(\gamma^{\alpha}u_{\alpha}\gamma_5 g_{\mu\nu} - \gamma_{\mu}u_{\nu}\gamma_5 - u_{\mu}\gamma_{\nu}\gamma_5 - \gamma_{\mu}\gamma^{\alpha}u_{\alpha}\gamma_5\gamma_{\nu}\right)\Big]\xi^{\frac{3}{2}}\psi^{\nu}$$

$$\mathcal{L}_{\pi\Delta}^{(2)} = -4c_1^{\Delta}M^2\bar{\psi}^{\mu}\xi^{\frac{3}{2}}g^{\mu\nu}\psi^{\nu} \tag{3}$$

In the following the pion-nucleon-delta Lagrangians up to chiral order three are given as [3,4]

$$\mathcal{L}_{\pi N\Delta}^{(1)} = g_{\pi N\Delta}\bar{\psi}_{\mu}^{i}\xi_{ij}^{\frac{3}{2}}(g^{\mu\nu} + \tilde{z}_1\gamma^{\mu}\gamma^{\nu})u_{\nu}^{j}\psi + h.c\ ,$$

$$\mathcal{L}_{\pi N\Delta}^{(2)} = \bar{\psi}_{\mu}^{i}\xi_{ij}^{\frac{3}{2}}(g^{\mu\nu} + \tilde{z}_2\gamma^{\mu}\gamma^{\nu})\left[ib_3u_{\nu\beta}^{j}\gamma^{\beta} + i\frac{b_8}{m}u_{\nu\beta}^{j}iD^{\beta}\right]\psi + h.c\ , \tag{4}$$

$$\mathcal{L}_{\pi N\Delta}^{(3)} = \bar{\psi}_{\mu}^{i}\xi_{ij}^{\frac{3}{2}}(g^{\mu\nu} + \tilde{z}_3\gamma^{\mu}\gamma^{\nu})\left[\frac{f_1}{m}\left[D_{\alpha},u_{\nu\beta}^{j}\right]\gamma^{\nu}iD^{\beta} - \frac{f_2}{2m^2}\left[D_{\alpha},u_{\nu\beta}^{j}\right]\{D^{\nu},D^{\beta}\} + f_4u_{\alpha}^{j}Tr(\chi_+) + f_5[D_{\alpha},i\chi_-^{j}]\right]\psi + h.c$$

CMS is realized by splitting the bare parameters of the Lagrangians (3) and (4) into complex renormalized parameters and counterterms as follow

$$m_{\Delta^0} = z_{\Delta} + \delta z_{\Delta}\ ,$$
$$m_0 = m + \delta m\ ,$$
$$c_{1,0}^{\Delta} = c_1^{\Delta} + \delta c_1^{\Delta}\ , \ldots$$

z_Δ is the complex pole of the delta propagator and m is the mass of the nucleon in the chiral limit. We write renormalized masses as the complex poles of the dressed propagators in the chiral limit and use the renormalized mass parameters in the free propagators and improve the counter terms perturbatively. We choose the renormalized couplings such that the corresponding counter terms exactly cancel the power counting violating parts of the loop diagrams. Nucleon-delta matrix element of the isovector axial vector current is expressed in the following [5]

$$\langle\Delta(p_f)|A_{\mu}^{3}|N(p_i)\rangle = \bar{u}^{\lambda}(p_f)\left[\left(\frac{C_3^A(Q^2)}{m_N}\gamma^{\nu} + \frac{C_4^A(Q^2)}{m_N^2}p_f^{\nu}\right)(g_{\lambda\mu}g_{\rho\nu} - g_{\lambda\rho}g_{\mu\nu})q^{\rho} + C_5^A(Q^2)g_{\lambda\mu} + \frac{C_6^A(Q^2)}{m_N^2}q_{\lambda}q_{\nu}\right]u(p_i) \tag{5}$$

where A_{μ}^{3} and $q^{\mu} = p_f^{\mu} - p_i^{\mu}$ are the physically relevant axial-vector current and momentum transfer and $Q^2 = -q^2$. $\Delta(p_f)$ is the Rarita-Schwinger spinor of delta baryon and $N(p_i)$ is the nucleon spinor. The flavor-isovector axial-vector current operator is defined as $A^{\mu}(x) = \bar{\psi}(x)\gamma^{\mu}\gamma_5\frac{\tau^3}{2}\psi(x)$.

$S^{\mu\nu}$ denotes the result of the diagrams with two Lorentz indices.

$$S^{\mu\nu}(p_f,q) = k_1p_f^{\mu}q^{\nu} + k_2q^{\mu}q^{\nu} + k_3\gamma^{\mu}q^{\nu} + k_4g^{\mu\nu}$$

while k_1, k_2, k_3 and k_4 represents the coefficients of the result corresponding to the related Lorentz structure. We extract the form factors matching the result of the diagrams $S^{\mu\nu}$ with the structure of Eq. (5).

RESULT AND DISCUSSIONS

The calculation of the tree level diagrams gives the following contributions to the form factors of C_5^A and C_6^A,

$$C_5(Q^2) = g_{\pi N\Delta} - \frac{(m_N - m_{\Delta})[2b_3m_N + b_8(m_N + m_{\Delta})]}{2m_N} + \frac{b_8q^2}{m_N}$$
$$+\frac{1}{4m_N^2}\left[32f_4M^2m_N^2 + (m_N^2 - m_{\Delta})^2(m_N + m_{\Delta})\left(2f_1m_N - f_2(m_N + m_{\Delta})\right) + 2f_1m_N(m_{\Delta} - m_N)q^2 + f_2q^4\right]$$

ISBN:978-605-83516-6-0

$$C_6(Q^2) = -b_3 m_N + \frac{(m_N - m_\Delta)[(2f_1 - f_2)m_N - f_2 m_\Delta]}{2} - \frac{f_2 q^2}{2} - \frac{g_{\pi N\Delta} m_N^2 + b_3 m_N^2 (m_N - m_\Delta)}{(q^2 - M^2)}$$
$$- \frac{2 g_{\pi N\Delta} M^2 m_N^2 L_4}{F^2 (q^2 - M^2)} - \frac{2 f_1 m_N (m_N^3 - m_N^2 m_\Delta)}{4(q^2 - M^2)} + \frac{2 f_1 m_N (m_\Delta^2 m_N - m_\Delta^3) - f_2 (m_N^4 - 2 m_N^2 m_\Delta^2 + m_\Delta^4)}{4(q^2 - M^2)} \quad (6)$$

Where the unknown low energy constants (LECs) f_1, f_2, f_4, f_5 and b_3, b_8 are in units of GeV^{-2} and GeV^{-1}, respectively. The unknown LECs are fitted to model-dependent data collected by weak neutrino interaction events [6]. We show the one-loop contributions to the real and imaginary parts to the form factors C_5^A and C_6^A in Fig.1. One can calculate the axial charges where the momentum transfer squared is equal to zero. Results are shown in Table 1.

TABLE 1. Axial charges for the axial vector nucleon to delta transition form factors together with comparison of some other works.

	This work	**[7]**	**[8]**
C_5^A	1.19	0.9	0.93
C_6^A	15.13	3.5	5.0

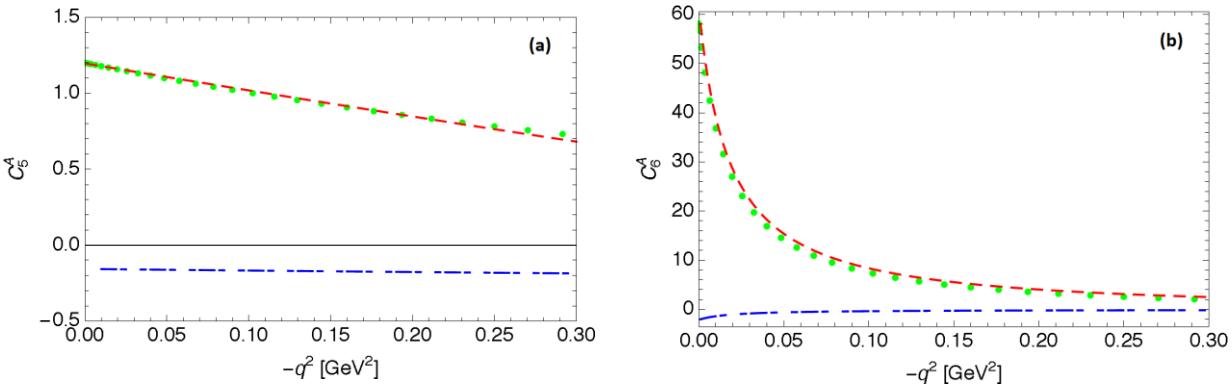
Partial conservation of axial vector current (PCAC) and pion pole dominance leads to the relation,

$$C_6(Q^2) = \frac{m_N^2}{Q^2 + M^2} C_5(Q^2) \quad (7)$$

One can define the function R(Q^2) as

$$R(Q^2) = \frac{C_6^A(Q^2) Q^2 + M^2}{C_5^A(Q^2) + m_N^2} \quad (8)$$

to test PCAC and pion meson dominance. If PCAC and pion pole dominance is assumed then the function R(Q^2) should be equal to 1. From Fig. 2 it is seen that PCAC and pion pole dominance approximations work well up to $Q^2 = 0.3$ GeV^2. However, R(Q^2) deviates considerably from unity for larger values of momentum transfer squared meaning that PCAC and pion dominance assumptions break down.



(a) (b)

FIGURE 1. Q^2 dependence of (a) C_5^A and (b) C_6^A form factors. Red, blue and green lines correspond to real, imaginary parts and fitted results.

ISBN:978-605-83516-6-0

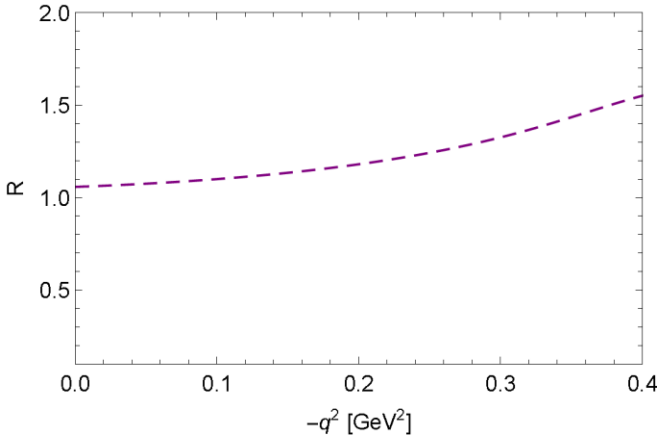


FIGURE 2. The dependence of R(Q^2) as a function of transfer momentum squared.

SUMMARY AND CONCLUSIONS

Despite the fact that there are two more axial form factors to the nucleon to delta transition the dominant contributions come from $C_5^A(Q^2)$ and $C_6^A(Q^2)$. In this study we analyze these two form factors. And we also predict the ratio of two form factors. Fitting the results to model-dependent data [6] we obtain the Q^2 dependence of the form factors which is given in Fig.1. One can see from the figures energy dependence of the form factoırs are compatible with the data. Q^2 dependence of C_6^A mainly comes from pion pole dominance. We also see that C_5^A shows a rich contribution to the matrix element because of large dependence of Q^2 . One may also test PCAC and pole dominance of pion and see that it works well in the limit of ChPT.

REFERENCES

1. J. Gasser and H. Leutwyler, Annals of Physics **158**, 142 (1984).
2. S. Bellucci, J. Gasser and M. E. Sainio, Nucl. Phys. B **423**, 80 (1994).
3. T. R. Hemmert, B. R. Holstein and J. Kambor, Journal of Phys. G **24**, 1831 (1998).
4. De-L. Yao, D. Siemens, V. Bernard, E. Epelbaum, J. Gegelia, H. Krebs and Ulf-G. Meissner, Journal of High Energy Physics **1605**, 038 (2016).
5. S. L. Adler, Annals of Physics **50**, 189 (1968).
6. T. Kitagaki, M. Higuchi and S. A. Kahn et al., Phys. Rev D **42**, 1331 (1990).
7. C. Alexandrou, G. Koutsou, Th. Leontiou, J. W. Negele and A. Tsapalis, Phys. Rev. D **76**, 094511 (2007).
8. D. Barquilla-Cano, A. J. Buchmann and E. Hernandez, Phys. Rev. C **75**, 065203 (2007).

07. Mathematical Physics



BOOK OF FULL TEXT PROCEEDINGS TURKISH PHYSICAL
SOCIETY 35th INTERNATIONAL PHYSICS CONGRESS (TPS35)
TPS35, Vol.01, No.07, pp.400-405.
ISBN:978-605-83516-6-0 15 December 2019

LRS Bianchi-Type I Space-Time in *κ(R,T)* Gravity

Nazım Ümit ERDEN [1] and Değer SOFUOĞLU [2, a)]

[1]*YÖK Fundamental Sciences Program, Faculty of Science, Istanbul University, 34134, Vezneciler, Fatih, Istanbul, TURKEY*
[2]*Department of Physics, Faculty of Science, Istanbul University, 34134, Vezneciler, Fatih, Istanbul, TURKEY*

[a)] Corresponding author: degers@istanbul.edu.tr

Abstract In this study, we have investigated locally rotationally symmetric (LRS) Bianchi-type I universe model filled with a perfect fluid in *κ(R,T)* modified gravity theory, where *κ* is the generalized gravitational constant, *R* is Ricci curvature scalar and *T* is trace of the energy-momentum tensor. We have derived the field equations of this modified theory for LRS Bianchi-type I model and obtained the solution of the field equations. We have also discussed what the matter-energy content of such a universe model is. Finally, we have calculated the kinematic properties of the model.

1. INTRODUCTION

Einstein's General Relativity (GR) theory is very compatible with some observations in our solar system. However, it is not useful enough to explain the accelerating expansion of our universe at the late time. The late time accelerating expansion has been supported by several observations since 1997 [1-11]. To explain the accelerating expansion of the universe, cosmologists have turned to modified gravity theories. The most common method to build a modified gravity theory is the Lagrangian formalism, that includes some terms corresponding to curvature or matter or to curvature-matter coupling to the gravitational action of GR. There are several modified gravity theories based on the Lagrangian formalism as such. One of the most popular modified gravity theory is *f(R)* gravity theory. *f(R)* gravity has been built by writing an arbitrary function of scalar curvature *R* instead of itself of the curvature scalar which appears in the original Einstein-Hilbert action of GR [12-16]. Another one is *f(R,T)* gravity theory that has become very popular in the last decade since it has been imposed. *f(R,T)* theory is a generalization of *f(R)* theory by taking the function of scalar curvature *R* and also trace *T* of the energy-momentum tensor in the gravitational action [17].

On the other hand, the Lagrangian formalism is not the only way to build a modified theory. Some theories have, modified field equations, which do not start from the Lagrangian formalism. Recently it has been introduced a new modified gravity theory, called *κ(R,T)* gravity, by adding new possible source terms, such as curvature scalar *R* and the trace *T* of the energy-momentum tensor, directly in the Einstein field equations [18]. Since this theory is taking Einstein gravitational constant as a function of *R* and *T*, it can be considered as a natural generalization of General Relativity.

Since *κ(R,T)* gravity is a new theory, it is not known whether the field equations of this theory consistent with some well-known metrics yet, except for the Friedmann-Lemaître-Robertson-Walker metric [18], even though some cosmological implications of the *κ(R,T)* theory has been considered in the study mentioned above and it has been compared with the *f(R,T)* theory.

Inspired by this situation, in the present study, locally rotationally symmetric (LRS) Bianchi-type I universe is taken into account in this modified gravity theory in order to investigate whether the field equations of *κ(R,T)* gravity theory is consistent with the model when the matter source is perfect fluid.

ISBN:978-605-83516-6-0 15 December 2019

The outline of this paper is as follows: A brief description of the field equations of Einstein's General Relativity and of *κ(R,T)* gravity are presented. By assuming the matter content of the universe is perfect fluid, the field equations for LRS Bianchi-type I universe model and their solutions are obtained and the kinematic properties of the model are calculated. Finally, the results are summarized and concluded.

2. EINSTEIN FIELD EQUATIONS

As it is well known, the standard gravitational field equations of the Einstein's General Relativity are

$$G_{ab} \equiv R_{ab} - \frac{1}{2}Rg_{ab} = \kappa^2 T^m_{ab}, \tag{1}$$

which relate to the geometrical part and the matter content of the universe. The field equations (1) can be derived from the following Einstein-Hilbert action

$$S_{EH} = \frac{1}{2\kappa^2}\int d^4x\sqrt{-g}R + S_m. \tag{2}$$

Here G_{ab} is Einstein Tensor, g_{ab} is the metric tensor of the 4-dimensional space-time, R_{ab} is Ricci tensor, $R \equiv g^{ab}R_{ab}$ is Ricci curvature scalar, S_m is matter-energy action, T^m_{ab} is energy-momentum tensor of the matter, and G being Newtonian gravitational constant, $\kappa^2 = \frac{8\pi G}{c^4}$ is Einstein gravitational constant.

3. FIELD EQUATIONS OF *κ(R,T)* GRAVITY THEORY

To use Lagrangian formalism is not only way to build a modified theory. Recently, the field equations of GR have been modified without starting from the Lagrangian formalism, rather it has been introduced the new modified gravity theory, so-called *κ(R,T)* gravity, by adding new possible source terms, such as curvature scalar *R* and the trace *T* of the energy-momentum tensor, directly in the field equations [18]. This theory can be considered as a natural generalization of GR, because the modification is based on taking the Einstein gravitational constant as a function of *R* and *T*.

The field equations of *κ(R,T)* gravity are

$$R_{ab} - \frac{1}{2}Rg_{ab} + \Lambda g_{ab} = \kappa(R,T)T_{ab}, \tag{3}$$

where $g^{ab}T_{ab} \equiv T$ is trace of the energy-momentum tensor, and *κ(R,T)* is an arbitrary function of *R* and *T* which corresponds to the Einstein gravitational constant in the original Einstein field equations.

The author of Ref. [18] analyzed following two different $\kappa(R,T)$ models namely, matter-matter coupling and matter-curvature coupling

- matter-matter coupling: $\kappa(R,T) = \kappa(T)$
- matter-curvature coupling: $\kappa(R,T) = \kappa(R)$

In this study we consider the first model, i.e., matter-matter coupling. By taking

$$\kappa(R,T) = \kappa(T) = 8\pi G - \lambda T, \tag{4}$$

the field equations become

$$G_{ab} = (8\pi G - \lambda T)T_{ab}\,, \tag{5}$$

where λ is a constant, and we assume that c=1.

We assume that the universe filled with a perfect fluid with linear barotropic equation of state. The energy-momentum tensor of perfect fluid is

$$T_{ab} = (\mu + p)u_a u_b + p g_{ab}, \tag{6}$$

ISBN:978-605-83516-6-0 15 December 2019

where μ is the matter-energy density of the fluid, p is the pressure, **u** is the 4-velocity of the fluid (normalized as $u^a u_a = -1$) and trace T is trace of the energy momentum tensor. One can easily see from Eq. (6) that the trace T of the energy-momentum tensor is

$$g^{ab}T_{ab} \equiv T_a^a \equiv T = -\mu + 3p \, . \tag{7}$$

By using $p = w\mu$ (w is a constant state parameter, $-1 \leq w \leq 1$) linear barotropic equation of state, we can write the energy-momentum tensor and its trace as, respectively,

$$T_{ab} = [(1+w)\mu]u_a u_b + w\mu g_{ab} \, , \tag{8}$$

and

$$T = (-1+3w)\mu. \tag{9}$$

Then using Eqs. (8) and (9) in Eq. (5), the field equations which we deal with become

$$G_{ab} = [8\pi G - \lambda(-1+3w)\mu][(1+w)\mu u_a u_b + w\mu g_{ab}] \, . \tag{10}$$

4. BIANCHI-TYPE I MODEL

The LRS Bianchi-type I model which is a spatially homogeneous and anisotropic model, is given by the line element

$$ds^2 = -dt^2 + A^2(t)dx^2 + B^2(t)dy^2 + B^2(t)dz^2 \, , \tag{11}$$

where A and B are time dependent scale factors.

Now, we have calculated the field equations of the model in $\kappa(R,T)$-gravity as

$$\text{(00)-component} \quad : \frac{2\dot{A}\dot{B}}{AB} + \frac{\dot{B}^2}{B^2} = [k + \lambda(-1+3w)\mu)]\mu \, , \tag{12}$$

$$\text{(11)-component} \quad : -\frac{2\ddot{B}}{B} - \frac{\dot{B}^2}{B^2} = [k + \lambda(1+3w)\mu]w\mu \, , \tag{13}$$

$$\text{(22)=(33)-components:} \quad -\frac{\ddot{A}}{A} - \frac{\ddot{B}}{B} - \frac{\dot{A}\dot{B}}{AB} = [k + \lambda(1+3w)\mu]w\mu \, , \tag{14}$$

where dot represents derivative with respect to time t and k=8πG. In order to solve this system of differential equations we take

$$A = B^n. \tag{15}$$

In that case the field equations (12)-(14) become

$$\text{(00):} \quad (2n+1)\frac{\dot{B}^2}{B^2} = [k + \lambda(-1+3w)\mu)]\mu, \tag{16}$$

$$\text{(11):} \quad -\frac{2\ddot{B}}{B} - \frac{\dot{B}^2}{B^2} = [k + \lambda(-1+3w)\mu)]w\mu, \tag{17}$$

$$\text{(22):} \quad -(n+1)\frac{\ddot{B}}{B} - n^2\frac{\dot{B}^2}{B^2} = [k + \lambda(-1+3w)\mu)]w\mu. \tag{18}$$

Subtracting Eq. (18) from Eq. (19) we get

ISBN:978-605-83516-6-0

$$\frac{\ddot{B}}{B} + (n+1)\frac{\dot{B}^2}{B^2} = 0\,. \tag{19}$$

Integration of the differential equation Eq. (18) yields *B(t)* as

$$B(t) = ((n+2)(c_1 t + c_2))^{\frac{1}{n+2}}\,, \tag{20}$$

where c_1 and c_2 are constants of integration. Using this solution in Eq. (15) we have obtained *A(t)* as

$$A(t) = [((n+2)(c_1 t + c_2))^{\frac{n}{n+2}}]\,. \tag{21}$$

Thus we have found the exact solution of the LRS Bianchi-type I universe filled with perfect fluid. Then one may obtain the matter-energy content of the universe model. To do that by substituting these *A(t)* and *B(t)* solutions given by Eqs. (20) and (21) into the (00)-component of field equations given by Eq. (16), we have found the following energy density of the model

$$\mu_{(00)} = \pm\frac{1}{2}\frac{1}{(3w-1)\lambda(c_1 t+c_2)(n+2)}[c_1 knt + 2c_1 kt + c_2 kn + 2c_2 k + (c_1{}^2k^2n^2t^2 + 4c_1{}^2k^2nt^2 + 2c_1c_2k^2n^2t + 4c_1{}^2k^2t^2 + 8c_1c_2k^2nt + c_2{}^2k^2n^2 - 24c_1{}^2\lambda nw + 8c_1c_2k^2t + 4c_2{}^2k^2n + 8c_1{}^2\lambda n - 12c_1{}^2\lambda w + 4c_2{}^2k^2 + 4c_1{}^2\lambda)^{\frac{1}{2}}]\,. \tag{22}$$

Using again Eq. (19) for *B(t)* on the Eq. (16), μ can be found as

$$\mu_{(11)} = \pm\frac{1}{2}\frac{1}{(3w-1)\lambda w(c_1 t+c_2)(n+2)}[c_1 kntw + 2c_1 ktw + c_2 knw + 2c_2 kw + (w(c_1{}^2k^2n^2t^2w + 4c_1{}^2k^2nt^2w + 2c_1c_2k^2n^2tw + 4c_1{}^2k^2t^2w + 8c_1c_2k^2ntw + c_2{}^2k^2n^2w + 8c_1c_2k^2tw + 4c_2{}^2k^2nw - 24c_1{}^2\lambda nw + 4c_2{}^2k^2nw + 8c_1{}^2\lambda n - 12c_1{}^2\lambda w + 4c_1{}^2\lambda))^{\frac{1}{2}}]\,. \tag{23}$$

In order to be consistent our results with the system of equations (16)-(18), $\mu_{(11)}$ and $\mu_{(00)}$ must be equal. When using these two results to form an equation, either *w*=1, in that case the fluid is called stiff fluid, or n=-1/2 can be found as conditions of consistency. Note that both (+) and (–) values of the μ*s* are used for equations, and same conditions are obtained. Now, let us reconsider above equations under the consistency conditions which we hold above.

Case i: *w*=1

In the case of *w*=,1 i.e., p=μ, the matter-energy density from Eq: (22) or (23) become

$$\mu = \pm\frac{1}{4}\frac{1}{\lambda(c_1 t+c_2)(n+2)}[-c_1 knt - 2c_1 kt - c_2 kn - 2c_2 k + (c_1{}^2k^2n^2t^2 + 4c_1{}^2k^2nt^2 + 2c_1c_2k^2n^2t + 4c_1{}^2k^2t^2 + 8c_1c_2k^2nt + c_2{}^2k^2n^2 + 8c_1c_2k^2t + 4c_2{}^2k^2n - 16c_1{}^2\lambda n + 4c_2{}^2k^2n - 8c_1{}^2\lambda)^{\frac{1}{2}}]\,. \tag{24}$$

By using the Eqs. (20) and (21), we calculate some kinematic quantities of the model for that case and we find expansion scalar θ as

$$\theta = \nabla_a u^a = \frac{\dot{A}}{A} + 2\frac{\dot{B}}{B} = \frac{c_1}{c_1 t+c_2}\,, \tag{25}$$

and shear scalar as

$$\sigma^2 = \frac{1}{2}\sigma_{ab}\sigma^{ab} = \frac{1}{3}\left(\frac{\dot{A}^2}{A^2} + \frac{\dot{B}^2}{B^2}\right) - \frac{2}{3}\frac{\dot{A}\dot{B}}{AB} = \frac{1}{3}\frac{c_1{}^2(n-1)^2}{(n+2)^2(c_1 t+c_2)^2}\,, \tag{26}$$

where σ_{ab} is shear tensor defined by

ISBN:978-605-83516-6-0

$$\sigma_{ab} \equiv \frac{1}{2}(\nabla_a u_b + \nabla_b u_a) - \frac{1}{3}\theta(g_{ab} + u_a u_b). \quad (27)$$

In that point we have to consider also the conservation equation. The energy-momentum tensor of *κ(R,T)* gravity is not conserved, thus the non-conservation of the energy-momentum tensor, ∇_a being the covariant derivative operator, is given by [18]

$$\nabla^a T_{ab} = -\frac{\nabla^a(\kappa(R,T))}{\kappa(R,T)} T_{ab}. \quad (28)$$

One can write this equation in more convenient form in terms of time derivatives [19,20]. Here we calculate conservation equation of matter-matter coupling case in that form for perfect fluid with barotropic equation of state as

$$-[\dot{\mu} + (1+w)\mu\theta][\kappa - \lambda(-1+3w)\mu] = \lambda(1-3w)\dot{\mu}\mu. \quad (29)$$

Using Eq. (24) and (25) we show that this conservation equation always satisfied when *w=1* is used on. Thus the matter-energy density (24) and the kinematic quantities (25) and (27) of the model remain valid.

Case ii: n=-1/2

When the second condition *n*= -1/2 is used on the equations, we obtain the energy density, expansion scalar and shear scalar, respectively, as follows:

$$\mu = \pm\frac{k}{\lambda(3w-1)}, \quad (30)$$

$$\theta = \frac{c_1}{c_1 t + c_2}, \quad (31)$$

$$\sigma^2 = \frac{1}{3}\frac{{c_1}^2}{(c_1 t + c_2)^2}, \quad (32)$$

We see that the energy density is constant and the conservation equation given by Eq. (29) is always satisfied in the case of *n=-1/2.*

5. SUMMARY and CONCLUSIONS

We have considered LRS Bianchi-type I universe in *κ(R,T)* gravity for matter-mater coupling case. We have dealt with the perfect fluid solution of the model with linear barotropic equation of state. We have found exact solution of the field equations of LRS Bianchi-type I model in *κ(R,T)* gravity. For the solution obtained we have calculated the matter-energy density of the model. In order to hold consistency between the energy density and the other equations of the model, we get two conditions. One of them is the state parameter *w=1*, that is stiff fluid case, and the second one is *n=-1/2*, that give $A = 1/\sqrt{B}$. Under both of the first and the second conditions, we have calculated kinematic properties expansion and shear scalars.

On the other hand, we write the conservation equation of *κ(R,T)* gravity in more convenient form including only time derivatives, not covariant derivatives. Then by using the matter conservation equation, we have verified our results. Consequently, we have shown that the field equations of *κ(R,T)* gravity theory is consistent with the LRS Bianchi-type I model filled with a perfect fluid.

6. REFERENCES

1. S. Perlmutter et al., Astrophys. J. 483 (1997) 565.
2. S. Perlmutter et al., Nature 391 (1998) 51.
3. A. G. Riess et al., Astron. J. 116 (1998) 1009.
4. S. Perlmutter et al., Astrophys. J. 517 (1999) 565.
5. C. Bennett et al., Astrophys. J. Suppl. 148 (2003) 1.

ISBN:978-605-83516-6-0

6. D. N. Spergel et al., Astrophys. J. Suppl. 148 (2003) 175.
7. E. Hawkins et al., Mon. Not. R. Astron. Soc. 346 (2003) 78.
8. A. G. Riess et al., Astrophys. J. 607 (2004) 665.
9. M. Tegmark et al., Phys. Rev. D 69 (2004) 103501.
10. S. Cole et al., Mon. Not. R. Astron. Soc. 362 (2005) 505.
11. D. N. Spergel et al., Astrophys. J. Suppl. 170 (2007) 377.
12. S. Rippl, H. V. Elst, R. Tavakol and D. Taylor, Gen. Relativ. Gravit. 28 (1996) 193.
13. S. Nojiri and S. D. Odintsov, Int. J. Geom. Methods Mod. Phys. 4 (2007) 115.
14. S. Capozziello and M. Francaviglia, Gen. Relativ. Gravit. 40 (2008) 357.
15. T. P. Sotiriou, J. Phys. Conf. Ser. 189 (2009) 012039.
16. A. Felice and S. Tsujikawa, Living Rev. Rel. 13 (2010) 3.
17. T. Harko, F. S. N. Lobo, S. Nojiri and S. D. Odintsov, Phys. Rev. D 84 (2011) 024020.
18. G. R. P. Teruel, Eur. Phys. J. C (2018) 78: 660.
19. G. F. R. Ellis, H. van Elst, NATO Series C: Math. Phys. Sci., vol. 541, pp. 1–116
20. D. Sofuoğlu, PhD Thesis, Istanbul University, 2014.

BOOK OF FULL TEXT PROCEEDINGS TURKISH PHYSICAL
SOCIETY 35th INTERNATIONAL PHYSICS CONGRESS (TPS35)
TPS35, Vol.01, No.07, pp.406-410.
ISBN:978-605-83516-6-0 15 December 2019

Bianchi-Type I Universe With Dust Matter in $\kappa(R,T)$ Gravity

Nazım Ümit ERDEN[1,] and Değer SOFUOĞLU[2,a)]

[1]*YÖK Fundamental Sciences Program, Faculty of Science, Istanbul University, 34134, Vezneciler, Fatih, Istanbul,TURKEY*
[2]*Department of Physics, Faculty of Science, Istanbul University, 34134, Vezneciler, Fatih, Istanbul, TURKEY*

[a)] Corresponding author: degers@istanbul.edu.tr

Abstract. In this study, Bianchi-type I space-time filled with dust matter is investigated in the framework of $\kappa(R,T)$ gravity theory which is based on a kind of generalization of the original Einstein's field equations by assuming that the gravitational constant κ is a function of Ricci curvature scalar R and trace T of the energy momentum tensor**.** The field equations of the model and the exact solution of the field equations are obtained. It is shown that Bianchi-type I model in the framework of $\kappa(R,T)$ gravity theory permit to dust as a matter source.

1. INTRODUCTION

Even though Albert Einstein's General Relativity (GR) is verified its compatibility with some of the observations of our Solar System years ago, the theory cannot explain the accelerated expansion of the universe at the late time, which is supported by several observations since 1997 [1-11]. To explain the accelerated expansion of the universe, cosmologists preferred modified gravity theories. In order to build a modified gravity theory, the most common method is the Lagrangian formalism, that includes some terms corresponding to curvature or matter or to curvature and/or matter coupling to the gravitational action GR. For example, *f(R)* gravity theory has been built by writing an arbitrary function of scalar curvature *R* instead of itself of the curvature scalar in the original Einstein-Hilbert action of GR [12-16]. There are several modified gravity theories based on the Lagrangian formalism as such. One of the most popular modified gravity theory based on Lagrangian formalism is *f(R,T)* gravity theory that is a generalization of *f(R)* theory by taking the function of scalar curvature *R* and also trace *T* of the energy-momentum tensor in the gravitational action [17]. It is also known that the Lagrangian formalism is not the only way to build a modified theory. Later theories have, modified field equations of General Relativity, which do not start from the Lagrangian formalism. Rather it has been introduced the new modified gravity theory, called $\kappa(R,T)$ gravity, by adding new possible source terms, such as curvature scalar *R* and the trace *T* of the energy-momentum tensor, directly in the field equations [18]. Since this theory is taking Einstein's gravitational constant as a function of *R* and *T*, it can be considered as a natural generalization of GR.

Since it is a new theory, it is not known whether the field equations of this theory consistent with some well-known metrics yet, except for the Friedmann-Lemaître-Robertson-Walker metric [18], even though some cosmological implications of the $\kappa(R,T)$ theory has been considered in the study mentioned above and it has been compared with the *f(R,T)* theory.

In the present study, a dust filled universe is taken into account, the field equations are derived for Bianchi-type-I space time in the framework of $\kappa(R,T)$ gravity theory, and an exact solution has been obtained. The energy content of the model is also calculated.

The outline of this paper is as follows: We present a brief description of the field equations of Einstein's General Relativity (GR) and of $\kappa(R,T)$ gravity. We derive the field equations for Bianchi-type I universe model by assuming the matter content of the universe is dust. And then, we summarize and we conclude the results.

Türk Fizik Derneği
1950
Turkish Physical Society

ISBN:978-605-83516-6-0 15 December 2019

2. EINSTEIN FIELD EQUATIONS

As it is well known, the standard gravitational field equations of the Einstein's General Relativity is

$$G_{ab} \equiv R_{ab} - \frac{1}{2} R g_{ab} = \kappa^2 T^m_{ab}, \tag{1}$$

which relate to the geometrical part and the matter content of the universe. The field equations (1) can be derived from the following Einstein-Hilbert action

$$S_{EH} = \frac{1}{2\kappa^2} \int d^4x \sqrt{-g} R + S_m. \tag{2}$$

Here G_{ab} is Einstein Tensor, g_{ab} is the metric tensor of the 4-dimensional space-time, R_{ab} is Ricci tensor, $R \equiv g^{ab} R_{ab}$ is Ricci curvature scalar, S_m is matter-energy action, T^m_{ab} is energy-momentum tensor of the matter, and G being Newtonian gravitational constant, $\kappa^2 = \frac{8\pi G}{c^4}$ is Einstein gravitational constant.

3. FIELD EQUATIONS OF $\kappa(R,T)$ GRAVITY THEORY

To use Lagrangian formalism is not only way to build a modified theory. Recently, the field equations of GR have been modified without starting from the Lagrangian formalism, rather it has been introduced the new modified gravity theory, so-called *κ(R,T)* gravity, by adding new possible source terms, such as curvature scalar R and the trace T of the energy-momentum tensor, directly in the field equations [18].

This theory can be considered as a natural generalization of GR, because the modification is based on taking the Einstein gravitational constant as a function of R and T.
The field equations of *κ(R,T)* gravity are

$$R_{ab} - \frac{1}{2} R g_{ab} + \Lambda g_{ab} = \kappa(R,T) T_{ab}, \tag{3}$$

where $g^{ab} T_{ab} \equiv T$ is trace of the energy-momentum tensor, and κ(R,T) is a function of R and T which corresponds to the Einstein gravitational constant in the original Einstein field equations.

The author of Ref. [18] analyzed two different $\kappa(R,T)$ models as matter-matter coupling and matter-curvature coupling as

- matter-matter coupling: $\kappa(R,T) = \kappa(T)$
- matter-curvature coupling: $\kappa(R,T) = \kappa(R)$

In this study we consider the first model, namely matter-matter coupling. By taking

$$\kappa(R,T) = \kappa(T) = 8\pi G - \lambda T, \tag{4}$$

the field equations become

$$G_{ab} = (8\pi G - \lambda T) T_{ab}\ , \tag{5}$$

where λ is a constant, and we assume that c=1.

We assume that the universe filled with a dust fluid i.e., pressureless (*p=0*) fluid. The energy-momentum tensor of dust is

$$T_{ab} = \mu u_a u_b\ , \tag{6}$$

where μ is the matter-energy density of the fluid, **u** is the 4-velocity of the fluid (normalized as $u^a u_a = -1$) and trace $g^{ab} T_{ab} \equiv T^a_a \equiv T$ of the energy-momentum tensor is

ISBN:978-605-83516-6-0

$$T = -\mu\,. \tag{7}$$

Then using Eqs. (6) and (7) in Eq. (5), the field equations which we deal with become

$$G_{ab} = (8\pi G + \lambda\mu)(\mu u_a u_b)\,. \tag{8}$$

4. BIANCHI-TYPE I MODEL IN $\kappa(R,T)$-GRAVITY

The Locally Rotationally Symmetric (LRS) Bianchi-type I model, a spatially homogeneous and anisotropic model, is given by the line element

$$ds^2 = -dt^2 + A^2(t)dx^2 + B^2(t)dy^2 + C^2(t)dz^2\,, \tag{9}$$

where A and B are time dependent scale factors.

Now, we have calculated the field equations of the model in *κ(R,T)*-gravity as

$$\text{(00)-component} \quad : \frac{2\dot{A}\dot{B}}{AB} + \frac{\dot{B}^2}{B^2} = [k+\mu]\mu, \tag{10}$$

$$\text{(11)-component} \quad : -\frac{2\ddot{B}}{B} - \frac{\dot{B}^2}{B^2} = 0, \tag{11}$$

$$\text{(22)=(33)-components} : -\frac{\ddot{A}}{A} - \frac{\ddot{B}}{B} - \frac{\dot{A}\dot{B}}{AB} = 0, \tag{12}$$

where dot represents derivative with respect to time *t* and k=8πG.

Integration of the (11)-component of the field equations given by Eq. (11) gives the following solution for *B(t)*

$$B(t) = \left(\frac{2}{3}c_1 t + \frac{3}{2}c_2\right)^{\frac{2}{3}}. \tag{13}$$

Using this solution in Eq. (12) we have obtained *A(t)* as

$$A(t) = \frac{-c_1c_4t + c_1c_3 - c_2c_4}{\left(\frac{c_1t+c_2}{c_1}\right)^{\frac{1}{3}} + c_1}\,. \tag{14}$$

Thus we have obtained the exact solution of the LRS Bianchi-type I universe filled with dust. Then one may obtain the matter-energy content of the universe model. To do that by substituting these *A(t)* and *B(t)* solutions given by Eqs. (13) and (14) into the (00)-component of field equations given by Eq. (10), we have found the following energy density of the model

$$\mu = \pm\frac{1}{6}(3{c_1}^2c_4kt^2 - 3{c_1}^2c_3kt + 6c_1c_2c_4kt - 3c_1c_2c_3k + 3{c_2}^2c_4k + \sqrt{3}((c_1t+c_2)(-c_1c_4t + c_1c_3 - c_2c_4)(-3{c_1}^2c_4k^2t^2 + 3{c_1}^2c_3k^2t - 6c_1c_2c_4k^2t + 3c_1c_2c_3k^2 - 3{c_2}^2c_4k^2 - 16{c_1}^2c_4\lambda))^{\frac{1}{2}})/(\lambda(c_1t+c_2)(-c_1c_4t + c_1c_3 - c_2c_4)). \tag{15}$$

We need to consider also conservation equation for our model. The energy-momentum tensor is not conserved in *κ(R,T)* gravity unlike General Theory of Relativity. The conservation equation of *κ(R,T)* gravity is given by [18] in terms of covariant derivative. In this study we have converted it into the more convenient form in terms of ordinary derivatives with respect to time. By using the 1+3 covariant decomposition method [19-20], for a dust fluid we obtain the following conservation equation

ISBN:978-605-83516-6-0

$$-(\dot{\mu}+\mu\theta)\,(k+\lambda\mu)\;=\lambda\dot{\mu}\mu, \tag{16}$$

where, ∇_a being the covariant derive operator , θ is expansion scalar defined as

$$\theta=\nabla_a u^a. \tag{17}$$

The expansion scalar of LRS Bianchi-type I model is

$$\theta=\frac{\dot{A}}{A}+2\frac{\dot{B}}{B}. \tag{18}$$

In order to investigate consistency of the model, using Eqs. (18) and (19) in Eq. (16) we get the reduced form of the conservation equation

$$\frac{8}{3}\frac{{c_1}^2c_4(-2c_1c_4t+c_1c_3-2c_2c_4)}{(c_1t+c_2)^2(-c_1c_4t+c_1c_3-c_2c_4)^2}=0 \tag{19}$$

As it can easily be seen this equation is satisfied when c_4=0, in other words LRS Bianchi-type I model filled with a dust is consistent with the field equations of *κ(R,T)* gravity if c_4=0. This restriction make the scale factor *A(t)* and the energy density μ simplify. Now for the sake of completeness we write the scale factors *A(t), B(t)* and the energy density μ, respectively,

$$A(t)=\frac{c_3}{(t+\frac{c_2}{c_1})^{1/3}}, \tag{20}$$

$$B(t)=(\frac{3}{2}c_1t+\frac{3}{2}c_2)^{2/3}, \tag{21}$$

$$\mu=(0,-\frac{k}{\lambda}). \tag{22}$$

5. SUMMARY AND CONCLUSIONS

In this study we have considered LRS Bianchi-type I universe in *κ(R,T)* gravity and dealt with the pressureless fluid i.e., dust solution of the model. We have found an exact solution of the field equations of LRS Bianchi-type I model for dust in *κ(R,T)* gravity. For the solution obtained we have calculated the matter-energy density of the model. By using the matter conservation equation, we have reconsider our results and we have shown that matter energy density of the universe is constant.

Consequently we have shown that LRS Bianchi-type I model filled with a dust fluid allowed in *κ(R,T)* gravity theory and the model has constant energy density.

6. REFERENCES

1. S. Perlmutter et al., Astrophys. J. 483 (1997) 565.
2. S. Perlmutter et al., Nature 391 (1998) 51.
3. A. G. Riess et al., Astron. J. 116 (1998) 1009.
4. S. Perlmutter et al., Astrophys. J. 517 (1999) 565.
5. C. Bennett et al., Astrophys. J. Suppl. 148 (2003) 1.
6. D. N. Spergel et al., Astrophys. J. Suppl. 148 (2003) 175.
7. E. Hawkins et al., Mon. Not. R. Astron. Soc. 346 (2003) 78.
8. A. G. Riess et al., Astrophys. J. 607 (2004) 665.
9. M. Tegmark et al., Phys. Rev. D 69 (2004) 103501.
10. S. Cole et al., Mon. Not. R. Astron. Soc. 362 (2005) 505.
11. D. N. Spergel et al., Astrophys. J. Suppl. 170 (2007) 377.

ISBN:978-605-83516-6-0

12. S. Rippl, H. V. Elst, R. Tavakol and D. Taylor, Gen. Relativ. Gravit. 28 (1996) 193.
13. S. Nojiri and S. D. Odintsov, Int. J. Geom. Methods Mod. Phys. 4 (2007) 115.
14. S. Capozziello and M. Francaviglia, Gen. Relativ. Gravit. 40 (2008) 357.
15. T. P. Sotiriou, J. Phys. Conf. Ser. 189 (2009) 012039.
16. A. Felice and S. Tsujikawa, Living Rev. Rel. 13 (2010) 3.
17. T. Harko, F. S. N. Lobo, S. Nojiri and S. D. Odintsov, Phys. Rev. D 84 (2011) 024020.
18. G. R. P. Teruel, Eur. Phys. J. C (2018) 78: 660.
19. G. F. R. Ellis, H. van Elst, NATO Series C: Math. Phys. Sci., vol. 541, pp. 1–116
20. D. Sofuoğlu, PhD Thesis, Istanbul University, 2014.

BOOK OF FULL TEXT PROCEEDINGS TURKISH PHYSICAL
SOCIETY 35th INTERNATIONAL PHYSICS CONGRESS (TPS35)
TPS35, Vol.01, No.07, pp.411-419.
ISBN:978-605-83516-6-0 15 December 2019

Cosmological Evolution and Constraint Equations in *f(G,T)* Gravity Theory

Değer SOFUOĞLU[1, a)] and Ertan GÜDEKLİ[1]

[1]*Department of Physics, Faculty of Science, Istanbul University, 34134, Vezneciler, Fatih, Istanbul, TURKEY*

[a)] Corresponding author: degers@istanbul.edu.tr

Abstract. In this study, we have considered *f(G,T)* gravity field equations where *G* is the Gauss-Bonnet invariant and *T* is the trace of the energy-momentum tensor of ordinary matter. We have decomposed the field equations to their irreducible forms and by using the effective fluid approach we have calculated the expressions of effective dynamical quantities of this modified theory. Through these dynamical quantities, we have written the cosmological evolution and constraint equations which are equivalent to the field equations.

1. INTRODUCTION

One of the most popular problem of theoretical cosmology is current accelerated expansion of the universe which has been indicated by several observations since the late 1990s. Mainly there are two ways based on modifying the original Einstein-Hilbert (EH) action to explain the late time acceleration. The first one is to add some scalar terms to EH action such as Chaplygin gas, quintessence, phantom, tachyon, K-essence [1-11]. The second one is to change the form of the geometrical part of EH action. This second approach is called modified gravity theories. In the modified gravity approaches some theories introduced by taking only curvature scalars to modify the EH action such as *f(R)*, *f(G)*, *f(R,G)* [12-21], while others by taking not only curvature scalars, but also matter-curvature coupling terms such as *f(R,T)* gravity theory [22]. The *f(R,T)* theory has been studied by many authors in the context of various cosmological models [23-36]. Recently, in that context, i.e., by coupling matter and quadratic curvature invariant, a new modified gravity theory, namely *f(G,T)* gravity, has been proposed [37]. The *f(G,T)* gravity theory has become one of the most prominent theories of recent times and various problems of contemporary cosmology have been considered in this theory [38-41].

Although the cosmological evolution and constraint equations are equivalent to the field equations, studying with the evolution and constraint equation is more convenient, since they make integrability conditions directly take into accounts. The 1+3 covariant decomposition method was applied to field equations of Einstein's General Relativity (GR) by [42], to the *f(R)* gravity field equations by Leach et al. [43] and Carloni et al. [44,45], to *f(R,T)* gravity field equations by Sofuoğlu [28]. The perturbation equations in *f(G)* gravity were obtained by Li et al. [46] making use of the covariant approach. Fully covariant decomposition of the field equations of *f(R,G)* gravity was represented in [47,48]. On the other hand, tetrad versions of these splittings in *f(R)*, *f(R,T)* and *f(R,G)* theories had also been derived in [28,47-49].

In the present study we aim to hold evolution and constraint equations of *f(G,T)* gravity theory. To express the equations in this modified gravity theory, we use effective fluid approach. In the effective fluid approach, the field equations are written in the form of Einstein field equations, then one can write the evolution and constraint

Türk Fizik Derneği
1950
Turkish Physical Society

ISBN:978-605-83516-6-0

equations also in their GR forms, but this time the dynamic quantities which appear in these equations are the quantities of the effective curvature fluid, not of the ordinary matter.

This paper is organized as follows: We give a brief description of the field equations of *f(G,T)* gravity, decompose the field equations in covariant forms and obtain the effective dynamical quantities and then we summarize our results.

Thorough this paper we use natural units $8\pi G = c = 1, \kappa^2 = 1$; round brackets indices denote symmetrization, square brackets indices denote anti-symmetrization and angled brackets indices spatially projected, symmetric and trace-free parts; and the Latin indices $a, b, c, ...$ run from 0 to 3; the dot " $\cdot$ " represents the derivative with respect to time *t*.

2. FIELD EQUATIONS OF *f(G,T)* GRAVITY

The action of *f(G,T)* modified theory of gravity is given by [37]

$$S = \frac{1}{2}\int d^4x\sqrt{-g}[R + f(G,T)] + \int d^4x\sqrt{-g}\,L_m, \tag{1}$$

where *R* is the Ricci curvature scalar, L_m is the matter Lagrangian density, *f(G,T)* is an arbitrary function of the trace T of the T^m_{ab} energy-momentum tensor of standard matter, defined by $T = g^{ab}T^m_{ab}$, and of the Gauss-Bonnet invariant Gdefined as

$$G = R^2 - 4R_{ab}R^{ab} + R_{abcd}R^{abcd}. \tag{2}$$

Here R_{ab} and R_{abcd} are the Ricci and Riemann tensors, respectively. The energy momentum tensor of matter is defined in terms of the matter Lagrangian as

$$T^m_{ab} = -\frac{2}{\sqrt{-g}}\frac{\delta(\sqrt{-g}L_m)}{\delta g^{ab}}. \tag{3}$$

If it is assumed that the matter Lagrangian density L_m only depends on the metric tensor components g_{ab}, then the energy-momentum of matter becomes

$$T^m_{ab} = g_{ab}L_m - 2\frac{\partial L_m}{\partial g^{ab}}. \tag{4}$$

The variation of the action (1) with respect to the metric g^{ab} gives

$$\begin{aligned} G_{ab} = {} & T^m_{ab} + \frac{1}{2}g_{ab}f - (T^m_{ab} + \Theta_{ab})f_T - (2RR_{ab} - 4R_a{}^cR_{cb} - 4R_{acbd}R^{cd} + 2R_a{}^{cde}R_{bcde})f_G \\ & - (2Rg_{ab}\Box - 2R\nabla_a\nabla_b - 4g_{ab}R^{cd}\nabla_c\nabla_d - 4R_{ab}\Box + 4R^c{}_a\nabla_b\nabla_c + 4R^c{}_b\nabla_a\nabla_c - 4R_a{}^{cd}{}_b\nabla_d\nabla_c)f_G, \end{aligned} \tag{5}$$

where $G_{ab} = R_{ab} - \frac{1}{2}g_{ab}R$ is Einstein tensor, $\Box = g^{ab}\nabla_a\nabla_b$, ∇_a is the covariant derivative,

$$\Theta_{ab} \equiv g^{mn}\frac{\delta T_{mn}}{\delta g^{ab}} = -2T_{ab} + g_{ab}L_m - 2g^{mn}\frac{\partial^2 L_m}{\partial g^{ab}\partial g^{mn}}, \tag{6}$$

f=f(G,T) and, f_G and f_T denote the partial derivatives of the *f=f(G,T)* function with respect to *G* and *T*, respectively.

Because of the Gauss-Bonnet term *G* is topologically invariant in four dimensions, if $f(G,T) = G - 2\Lambda$, Λ is the cosmological constant, the field equations reduced to the original Einstein field equations, Eqs. (5) give

$$\frac{1}{2}g_{ab}G - (2RR_{ab} - 4R_a{}^cR_{cb} - 4R_{acbd}R^{cd} + 2R_a{}^{cde}R_{bcde}) = 0, \tag{7}$$

ISBN:978-605-83516-6-0

which on using Eqs. (5) one can get the field equations of *f(G,T)* gravity as

$$G_{ab} = T^m_{ab} - (T^m_{ab} + \Theta_{ab})f_T + \frac{1}{2}g_{ab}(f - Gf_G) - (2Rg_{ab}\Box - 2R\nabla_a\nabla_b - 4g_{ab}R^{cd}\nabla_c\nabla_d - 4R_{ab}\Box + 4R^c{}_a\nabla_b\nabla_c + 4R^c{}_b\nabla_a\nabla_c - 4R_a{}^{cd}{}_b\nabla_d\nabla_c)f_G \quad (8)$$

3. 1+3 COVARIANT DECOMPOSITION OF *f(G,T)* GRAVITY FIELD EQUATIONS

The 1+3 covariant decomposition method aims to make space-time splits of geometrical and physical quantities with respect to the 4-velocity of an observer u^a which is normalized as $u_a u^a = -1$. By means of this preferred vector field one may define two unique projection tensors: $U_{ab} = -u_a u_b$ and $h_{ab} = g_{ab} + u_a u_b$. The first one of these tensors splits any space-time quantity into parts parallel to u^a and the second one splits parts orthogonal to u^a. One may also define two derivatives, namely, fully orthogonally projected covariant derivative onto the instantaneous rest space of the observer and covariant time derivative along the flow of the observer. For any $T^{m\ldots}{}_{p\ldots}$ tensor, the former derivative is

$$D_a T^{m\ldots}{}_{p\ldots} = h^m{}_n \ldots h^q{}_p h^r{}_a \nabla_r T^{n\ldots}{}_{q\ldots}, \quad (9)$$

and the latter is

$$\dot{T}^{m\ldots}{}_{p\ldots} = u^a \nabla_a T^{m\ldots}{}_{p\ldots}, \quad (10)$$

The covariant derivative of u_a, in particular, can be split uniquely in terms of the kinematic quantities of the observer as

$$\nabla_a u_b = -u_a \dot{u}_b + D_a u_b = -u_a \dot{u}_b + \theta_{ab} + \omega_{ab} = -u_a \dot{u}_b + \sigma_{ab} + \frac{1}{3}\theta h_{ab} + \eta_{abc}\omega^c, \quad (11)$$

where $\dot{u}_a = u^b \nabla_b u_a$ is acceleration; $\theta_{ab} = D_{(a}u_{b)}$ is expansion tensor, $\theta = D_a u^a$ is expansion scalar,$\sigma_{ab} = D_{\langle a}u_{b\rangle}$ is shear tensor, $\sigma^2 = \frac{1}{2}\sigma_{ab}\sigma^{ab}$ is shear scalar, $\omega_{ab} = D_{[a}u_{b]}$ is vorticity tensor, $\omega_a = \eta_{abc}\omega^{bc}$ is vorticity vector,$\omega^2 = \omega_a \omega^a$ is vorticity scalar; and $\eta_{abc} = \eta_{abcd}u^d$ is 3-dimensional permutation tensor, η_{abcd} being the 4-dimensional volume element [42,47,50].

The unique splitting of any energy-momentum tensor is

$$T_{ab} = \mu u_a u_b + p h_{ab} + 2q_{(a}u_{b)} + \pi_{ab}, \quad (12)$$

where μ is the energy density, p is the pressure, q_a is the heat flux and π_{ab} is the anisotropic stress tensor. The dynamic quantities are defined as

$$\mu = T_{ab}u^a u^b, \quad p = \frac{1}{3}h^{ab}T_{ab}, \quad q_a = -h^b{}_a T_{bc}u^c, \quad \pi_{ab} = h^c{}_{\langle a}h^d{}_{b\rangle}T_{cd}. \quad (13)$$

One may also decompose the Riemann and the Weyl tensors as

$$R_{abcd} = C_{abcd} + R_{a[c}g_{d]b} - R_{b[c}g_{d]a} - \frac{1}{3}R g_{a[c}g_{d]b}, \quad (14)$$

$$C^{ab}{}_{cd} = 4u^{[a}u_{[c}E^{b]}{}_{d]} + 4h^{[a}{}_{[c}E^{b]}{}_{d]} + 2\eta^{abe}u_{[c}H_{d]e} + 2\eta_{cde}u^{[a}H^{b]e}, \quad (15)$$

where $E_{ab} = C_{aebd}u^e u^d$ is the electric and $H_{ab} = \frac{1}{2}\eta_{ae}{}^{gh}C_{ghbd}u^e u^d$ is the magnetic parts of the Weyl tensor.

ISBN:978-605-83516-6-0

Now, it would be better to return the field equations of *f(G,T)* theory in order to express them in the form of Einstein field equations. In the present study we assume that the universe filled with a perfect fluid whose energy-momentum tensor is

$$T_{ab}^{m} = \mu^{m} u_a u_b + p^{m} h_{ab}, \tag{16}$$

where μ^m and p^m are energy density and pressure of the matter, respectively. The matter Lagrangian may be taken as $L_m = p^m$ [22, 37], then Eq. (6) becomes

$$\Theta_{ab} = -2T_{ab}^{m} + p^{m} g_{ab}. \tag{17}$$

By using Eqs. (16) and (17), and adopting the effective energy-momentum tensor approach one can define the following effective energy-momentum tensors from Eq. (8)

$$\begin{aligned} T_{ab}^{GT} = {} & \frac{1}{2} g_{ab}(f - G f_G) + (\mu^m + p^m) u_a u_b f_T - (2R g_{ab}\Box - 2R\nabla_a\nabla_b \\ & - 4 g_{ab} R^{cd}\nabla_c\nabla_d - 4R_{ab}\Box + 4R^{c}{}_{a}\nabla_b\nabla_c + 4R^{c}{}_{b}\nabla_a\nabla_c - 4R_{a}{}^{cd}{}_{b}\nabla_d\nabla_c) f_G, \end{aligned} \tag{18}$$

in which the superscript *GT* corresponds to the Gauss-Bonnet term and the trace of the energy-momentum tensor corrections. Then using Eq. (18), the field equations of modified *f(G,T)* gravity given by Eq. (8) reduce the standard Einstein form

$$G_{ab} = T_{ab}, \tag{19}$$

where

$$T_{ab} = T_{ab}^{m} + T_{ab}^{GT}, \tag{20}$$

is the effective total energy-momentum tensor. Definitions (13), according to Eq. (20), give the following effective total dynamic quantities

$$\mu = \mu^m + \mu^{GT}, \quad p = p^m + p^{GT}, \quad q_a = q_a^{GT}, \quad \pi_{ab} = \pi_{ab}^{GT}. \tag{21}$$

We need also the expressions of R_{ab} and R_{abcd} in terms of effective total dynamic and kinematic quantities of the fluid in order to calculate μ^{GT}, p^{GT}, q_a^{GT} and π_{ab}^{GT}. For getting explicit expressions R_{ab} and R_{abcd}, we can decompose the Ricci tensor R_{ab} with respect to u^a [46] as

$$R_{ab} = \Delta u_a u_b + \Xi h_{ab} + 2u_{(a}\Upsilon_{b)} + \Sigma_{ab}, \tag{22}$$

where Δ, Ξ, Υ_a and Σ_{ab} defined by

$$\Delta = R_{ab}u^a u^b, \quad \Xi = \tfrac{1}{3} R_{ab} h^{ab}, \quad \Upsilon_c = -R_{ab} h_c^a u^b, \quad \Sigma_{ab} = h_{\langle a}^{c} h_{b\rangle}^{d} R_{cd}, \tag{23}$$

and, Υ_a is a spatial vector and Σ_{ab} is a symmetric trace free spatial tensor. Using Eqs. (22) and (23), one can easily obtain the following relations:

$$\Delta = \tfrac{1}{2}(\mu + 3p), \quad \Xi = \tfrac{1}{2}(\mu - p), \quad \Upsilon_a = q_a, \quad \Sigma_{ab} = \pi_{ab}, \tag{24}$$

$$\mu = \tfrac{1}{2}(\Delta + 3\Xi), \quad p = \tfrac{1}{2}(\Delta - \Xi), \quad q_a = \Upsilon_a, \quad \pi_{ab} = \Sigma_{ab}. \tag{25}$$

Then by using Eqs. (13) in order to apply Eq. (18), we find the dynamical quantities of effective fluid as

ISBN:978-605-83516-6-0

$$\mu^{GT} = -\frac{1}{2}(f - Gf_G) + (\mu^m + p^m)f_T + f_{GT}[\frac{2}{3}(\Delta + 3\Xi)M^T - 4(E^{ab} + \frac{1}{2}\Sigma^{ab})M^T_{ab}$$
$$+ f_{GG}\left[\frac{2}{3}(\Delta + 3\Xi)M^G - 4\left(E^{ab} + \frac{1}{2}\Sigma^{ab}\right)M^G_{ab}\right]$$
$$+f_{GTT}[\tfrac{4}{3}(\Delta + 3\Xi)D^aTD_aT - 8(E^{ab} + \tfrac{1}{2}\Sigma^{ab})D_aTD_bT]$$
$$+ f_{GGT}[\frac{4}{3}(\Delta + 3\Xi)D^aGD_aT - 8(E^{ab} + \frac{1}{2}\Sigma^{ab})D_aGD_bT]$$
$$+f_{GGG}[\tfrac{2}{3}(\Delta + 3\Xi)D^aGD_aG - 4(E^{ab} + \tfrac{1}{2}\Sigma^{ab})D_aGD_bG], \quad (26)$$

$$p^{GT} = \frac{1}{2}(f - Gf_G) + f_{GT}[\frac{2}{3}(\Delta + 3\Xi)L^T + \frac{8}{9}\Delta M^T + \frac{8}{3}\Upsilon^aN^T_a - \frac{4}{3}(E^{ab} - \frac{1}{2}\Sigma^{ab})M^T_{ab}]$$
$$+ f_{GG}[\frac{2}{3}(\Delta + 3\Xi)L^G + \frac{8}{9}\Delta M^G + \frac{8}{3}\Upsilon^aN^G_a - \frac{4}{3}(E^{ab} - \frac{1}{2}\Sigma^{ab})M^G_{ab}]$$
$$+ f_{GTT}[\frac{2}{3}(\Delta + 3\Xi)\dot{T}^2 + \frac{8}{9}\Delta D^aTD_aT + \frac{8}{3}\dot{T}\Upsilon^aD_aT - \frac{4}{3}(E^{ab} - \frac{1}{2}\Sigma^{ab})D_aTD_bT]$$
$$+ f_{GGT}[\frac{4}{3}(\Delta + 3\Xi)\dot{G}\dot{T} + \frac{16}{9}\Delta D^aGD_aT + \frac{8}{3}\Upsilon^a(\dot{G}D_aG + \dot{T}D_aT) - \frac{8}{3}(E^{ab} - \frac{1}{2}\Sigma^{ab})D_aGD_bT]$$
$$+ f_{GGG}[\tfrac{2}{3}(\Delta + 3\Xi)\dot{G}^2 + \tfrac{8}{9}\Delta D^aGD_aG + \tfrac{8}{3}\dot{G}\Upsilon^aD_aG - \tfrac{4}{3}(E^{ab} - \tfrac{1}{2}\Sigma^{ab})D_aGD_bG], \quad (27)$$

$$q^{GT}_a = f_{GT}[-\frac{2}{3}(\Delta + 3\Xi)N^T_a - 2\Upsilon^bM^T_{ab} + 2\Upsilon_aM^T + 4\eta_a{}^{bc}H_b{}^dM^T_{cd} + 4(E_a{}^b + \frac{1}{2}\Sigma_a{}^b)N^T_b]$$
$$+ f_{GG}[-\frac{2}{3}(\Delta + 3\Xi)N^G_a + 2\Upsilon_aM^G - 2\Upsilon^bM^G_{ab} + 4\eta_a{}^{bc}H_b{}^dM^G_{cd} + 4(E_a{}^b + \frac{1}{2}\Sigma_a{}^b)N^G_b]$$
$$+ f_{GTT}[-\frac{2}{3}(\Delta + 3\Xi)\dot{T}D_aT + 2\Upsilon_aD^bTD_bT - 2\Upsilon^bD_bTD_aT + 4(E_a{}^b + \frac{1}{2}\Sigma_a{}^b)\dot{T}D_bT + 4\eta_a{}^{bc}H_b{}^dD_cTD_dT]$$
$$+ f_{GGT}[-\frac{2}{3}(\Delta + 3\Xi)(\dot{G}D_aG + \dot{T}D_aT) + 4\Upsilon_aD^bGD_bT - 4\Upsilon^bD_{(a}GD_{b)}T$$
$$+ 4(E_a{}^b + \frac{1}{2}\Sigma_a{}^b)(\dot{G}D_bG + \dot{T}D_bT) + 8\eta_a{}^{bc}H_b{}^dD_{(c}GD_{d)}T]$$
$$+f_{GGG}[-\tfrac{2}{3}(\Delta + 3\Xi)\dot{G}D_aG + 2\Upsilon_aD^bGD_bG - 2\Upsilon^bD_bGD_aG$$
$$+4(E_a{}^b + \tfrac{1}{2}\Sigma_a{}^b)\dot{G}D_bG + 4\eta_a{}^{bc}H_b{}^dD_cGD_dG], \quad (28)$$

$$\pi^{GT}_{ab} = f_{GT}[-\tfrac{4}{3}\Delta M^T_{<ab>} - 4\Upsilon_{<a}N^T_{b>} + 8\left(E_{<a}{}^c - \tfrac{1}{2}\Sigma_{<a}{}^c\right)M^T_{b>c}$$
$$-4\left(E_{ab} - \tfrac{1}{2}\Sigma_{ab}\right)M^T - 4\left(E_{ab} + \tfrac{1}{2}\Sigma_{ab}\right)L^T + 8\eta_{<a}{}^{cd}H_{b>d}N^T_c]$$
$$+f_{GG}[-\tfrac{4}{3}\Delta M^G_{<ab>} - 4\Upsilon_{<a}N^G_{b>} + 8\left(E_{<a}{}^c - \tfrac{1}{2}\Sigma_{<a}{}^c\right)M^G_{b>c}$$
$$-4\left(E_{ab} - \tfrac{1}{2}\Sigma_{ab}\right)M^G - 4\left(E_{ab} + \tfrac{1}{2}\Sigma_{ab}\right)L^G + 8\eta_{<a}{}^{cd}H_{b>d}N^G_c]$$
$$+f_{GTT}[-\tfrac{4}{3}\Delta D_{<a}TD_{b>}T - 4\dot{T}\Upsilon_{<a}D_{b>}T + 8\left(E_{<a}{}^c - \tfrac{1}{2}\Sigma_{<a}{}^c\right)D_{b>}D_cT$$
$$-4\left(E_{ab} - \tfrac{1}{2}\Sigma_{ab}\right)D^cTD_cT - 4\left(E_{ab} + \tfrac{1}{2}\Sigma_{ab}\right)\dot{G}^2 + 8\eta_{<a}{}^{cd}H_{b>d}\dot{T}D_cT]$$
$$+f_{GGT}[-\frac{4}{3}\Delta D_{<a}GD_{b>}T - 4\Upsilon_{<a}(\dot{G}D_{b>}G + \dot{T}D_{b>}T) + 8\left(E_{<a}{}^c - \frac{1}{2}\Sigma_{<a}{}^c\right)(D_{b>}GD_cT + D_{b>}TD_cG)$$
$$-8\left(E_{ab} - \tfrac{1}{2}\Sigma_{ab}\right)D^cGD_cT - 8\left(E_{ab} + \tfrac{1}{2}\Sigma_{ab}\right)\dot{G}\dot{T} + 8\eta_{<a}{}^{cd}H_{b>d}(\dot{G}D_cT + \dot{T}D_cG)]$$
$$+f_{GGG}[-\tfrac{4}{3}\Delta D_{<a}GD_{b>}G - 4\dot{G}\Upsilon_{<a}D_{b>}G + 8\left(E_{<a}{}^c - \tfrac{1}{2}\Sigma_{<a}{}^c\right)D_{b>}GD_cG$$
$$-4\left(E_{ab} - \tfrac{1}{2}\Sigma_{ab}\right)D^cGD_cG - 4\left(E_{ab} + \tfrac{1}{2}\Sigma_{ab}\right)\dot{G}^2 + 8\eta_{<a}{}^{cd}H_{b>d}\dot{G}D_cG] \quad (29)$$

where

$$M^G_{ab} = -(\sigma_{ab} + \tfrac{1}{3}\theta h_{ab} + \eta_{abc}\omega^c)\dot{G} + D_aD_bG \quad , \quad M^G = g^{ab}M^G_{ab},$$

ISBN:978-605-83516-6-0

$$M^T_{ab} = -(\sigma_{ab} + \frac{1}{3}\theta h_{ab} + \eta_{abc}\omega^c)\dot{T} + D_a D_b T \quad , \quad M^T = g^{ab}M^T_{ab},$$
$$N^G_a = -(\sigma_a{}^b + \frac{1}{3}\theta h_a{}^b + \eta_a{}^{bc}\omega_c)D_b G + D_a\dot{G} \quad , \quad L^G = -\dot{u}^a D_a G + \ddot{G},$$
$$N^T_a = -(\sigma_a{}^b + \frac{1}{3}\theta h_a{}^b + \eta_a{}^{bc}\omega_c)D_b T + D_a\dot{T} \quad , \quad L^T = -\dot{u}^a D_a T + \ddot{T}.$$

One may also express the Ricci scalar *R* and the Gauss-Bonnet term *G* in terms of Δ, Ξ, Υ_a and Σ_{ab} as

$$G = -\frac{4}{3}\Delta^2 - 4\Delta\Xi + 4\Upsilon_a\Upsilon^a - 2\Sigma_{ab}\Sigma^{ab} + C^2, \tag{30}$$

where

$$C^2 = C_{abcd}C^{abcd} = 8(E_{ab}E^{ab} - H_{ab}H^{ab}). \tag{31}$$

4. EVOLUTION AND CONSTRAINT EQUATIONS IN *f(G,T)* GRAVITY

In 1+3 covariant approach to GR, there are two sets of equations which are equivalent to the field equations. The evolution equations include only time derivatives and the constraint equations include orthogonally projected covariant derivatives of the quantities. These equations are derived from Ricci and Bianchi identities, where the Einstein field equations are used as an algebraic substitution for R_{ab} in terms of the energy-momentum tensor T^m_{ab} [42, 47, 50]. The advantage of the effective energy-momentum tensor approach is that the evolution and constraint equations of the standard cosmology retain their forms, except from the conservation equations since the standard conservation law of the matter does not hold in *f(G,T)* gravity theory, but the dynamic quantities of standard matter replace with effective total dynamic quantities.

Before we list all the equations, let us consider the conservation equations of *f(G,T)* gravity. Using Eq. (8) one can calculate the covariant derivative of the effective total energy-momentum tensor,

$$\nabla^a T_{ab} = \nabla^a(T^m_{ab} + T^{GT}_{ab}) = 0, \tag{32}$$

and obtain the following general conservation equation of *f(G,T)* gravity [38]

$$(1 - f_T)\nabla^a T^m_{ab} = f_T(\nabla^a\Theta_{ab} - \frac{1}{2}g_{ab}\nabla^a T) + (T^m_{ab} + \Theta_{ab})\nabla^a f_T. \tag{33}$$

Now, applying the 1+3 projection techniques to the last equation and using Eq. (17) for Θ_{ab}, we find the following matter and conservation equations, respectively:

$$\dot{\mu}^m + f_T(\dot{\mu}^m + \dot{p}^m - \frac{1}{2}\dot{T}) + (f_{GT}\dot{G} + f_{TT}\dot{T})(\mu^m + p^m) = -(1 + f_T)(\mu^m + p^m)\theta, \tag{34}$$

$$D_a p^m + \frac{1}{2}f_T D_a T = -(1 + f_T)(\mu^m + p^m)\dot{u}_a, \tag{35}$$

Notice that when *f(G,T) =0*, Eqs. (34) and (35) reduce to the matter and the momentum conservation equations for a perfect fluid in GR, respectively.

Now, we list the 1+3 covariant evolution and the constraint equations of *f(G,T)* gravity theory in terms of effective total dynamical quantities in the following:

4.1. Evolution Equations

$$\dot{\theta} = D_a\dot{u}^a - \frac{1}{3}\theta^2 + \dot{u}_a\dot{u}^a - 2\sigma^2 + 2\omega^2 - \frac{1}{2}(\mu + 3p)\ , \tag{36}$$

ISBN:978-605-83516-6-0

$$\dot{\omega}^a = \tfrac{1}{2}\eta^{abc}D_b\dot{u}_c - \tfrac{2}{3}\theta\omega^a + \sigma^a{}_b\omega^b + u^a\dot{u}_b\omega^b, \tag{37}$$

$$\begin{aligned}\dot{\sigma}_{ab} = {} & (u_a\sigma_{bc} + u_b\sigma_{ac})\dot{u}^c + \frac{1}{2}(D_a\dot{u}_b + D_b\dot{u}_a) - \sigma_{ac}\sigma^c{}_b - \frac{2}{3}\theta\sigma_{ab} + \dot{u}_a\dot{u}_b \\ & - \omega_a\omega_b - \tfrac{1}{3}(D_c\dot{u}^c + \dot{u}_c\dot{u}^c - 2\sigma^2 - \omega^2)h_{ab} - (E_{ab} - \tfrac{1}{2}\pi_{ab}),\end{aligned} \tag{38}$$

$$\begin{aligned}\dot{E}_{ab} + \frac{1}{2}\dot{\pi}_{ab} = {} & (E_{ae} + \frac{1}{2}\pi_{ae})\dot{u}^e u_b + (E_{be} + \frac{1}{2}\pi_{be})\dot{u}^e u_a + \frac{1}{2}(\eta_{aef}D^e H^f{}_b + \eta_{bef}D^e H^f{}_a) \\ & - \frac{1}{4}(D_a q_b + D_b q_a) + \frac{1}{6}h_{ab}D^e q_e - \frac{1}{2}(\mu + p)\sigma_{ab} - \frac{1}{2}(q_a\dot{u}_b + q_b\dot{u}_a) + \frac{1}{3}h_{ab}q^e\dot{u}_e \\ & - \theta(E_{ab} + \frac{1}{6}\pi_{ab}) + \frac{3}{2}\sigma^e{}_a(E_{be} - \frac{1}{6}\pi_{be}) + \frac{3}{2}\sigma^e{}_b(E_{ae} - \frac{1}{6}\pi_{ae}) - h_{ab}\sigma^{ef}(E_{fe} - \frac{1}{6}\pi_{fe}) \\ & - \tfrac{1}{2}\eta_{aef}[(E^e{}_b + \tfrac{1}{2}\pi^e{}_b)\omega^f + 2H^e{}_b\dot{u}^f] - \tfrac{1}{2}\eta_{bef}[(E^e{}_a + \tfrac{1}{2}\pi^e{}_a)\omega^f + 2H^e{}_a\dot{u}^f],\end{aligned} \tag{39}$$

$$\begin{aligned}\dot{H}_{ab} = {} & (u_a H_{bc} + u_b H_{ac})\dot{u}^c - \frac{1}{2}\eta_{aef}D^e(E^f{}_b - \frac{1}{2}\pi^f{}_b) - \frac{1}{2}\eta_{bef}D^e(E^f{}_a - \frac{1}{2}\pi^f{}_a) \\ & - \theta H_{ab} + \frac{3}{2}(H_{ac}\sigma^c{}_b + H_{bc}\sigma^c{}_a) - H_{ef}\sigma^{ef}h_{ab} + \frac{3}{4}(\omega_a q_b + \omega_b q_a) - \frac{1}{2}\omega_c q^c h_{ab} \\ & + (\eta_{aef}E^e{}_b + \eta_{bef}E^e{}_a)\dot{u}^f - \tfrac{1}{2}(\eta_{aef}H^e{}_b + \eta_{bef}H^e{}_a)\omega^f + \tfrac{1}{4}(\eta_{aef}\sigma^e{}_b + \eta_{bef}\sigma^e{}_a)q^f,\end{aligned} \tag{40}$$

The evolution equations also include the conservation equations which are given by Eqs. (34) and (35).

4.2. Constraint Equations

$$0 = D_b\sigma^{ab} - \tfrac{2}{3}D^a\theta + \eta^{abc}D_b\omega_c + 2\eta^{abc}\dot{u}_b\omega_c + q^a, \tag{41}$$

$$0 = D_a\omega^a - \dot{u}_a\omega^a, \tag{42}$$

$$0 = H_{ab} + (\omega_a\dot{u}_b + \omega_b\dot{u}_a) - \omega^e\dot{u}_e h_{ab} - \tfrac{1}{2}(\eta_{aef}D^e\sigma^f{}_b + \eta_{bef}D^e\sigma^f{}_a) + \tfrac{1}{2}(D_a\omega_b + D_b\omega_a) \tag{43}$$

$$0 = D_b(E^b{}_a + \tfrac{1}{2}\pi^b{}_a) - \tfrac{1}{3}D_a\mu - \tfrac{1}{2}\sigma^b{}_a q_b + \tfrac{1}{3}\theta q_a - \eta_{aef}(\sigma^{eb}H^f{}_b - \tfrac{3}{2}\omega^e q^f) - 3H^b{}_a\omega_b, \tag{44}$$

$$0 = D_b H^b{}_a + \tfrac{1}{2}\eta_{aef}D^e q^f + (\mu + p)\omega_a + 3(E^b{}_a - \tfrac{1}{6}\pi^b{}_a)\omega_b + \eta_{aef}\sigma^e{}_b(E^{fb} + \tfrac{1}{2}\pi^{fb}), \tag{45}$$

5. SUMMARY AND CONCLUSIONS

In the present study we have decomposed the field equations of *f(G,T)* gravity by using 1+3 covariant decomposition method. We have started from the effective fluid approach that is allow us to use the formalism of the general relativistic cosmology in order to express the evolution and constraint equations. In that formalism we have defined an effective curvature fluid which correspond to modifications of Gauss-Bonnet and matter coupling terms. By applying the 1+3 covariant decomposition method to the energy momentum tensor of the effective fluid we have obtained effective dynamic quantities of the fluid. By writing these effective dynamic quantities instead of dynamic quantities of ordinary matter's in the evolution and constraint equations of GR, we have get the evolution and constraint equations of *f(G,T)* gravity theory except from the conservation equations. Since the energy momentum tensor is not conserved in this modified gravity, unlike GR, the conservations is not the same form with general relativistic ones. Thus we also apply the technique to conservation equations and obtained the matter and momentum conservation equations of *f(G,T)* gravity.

To study with the evolution and the constraint equations instead of directly field equations may be more favorable, since the integrability conditions occur spontaneously. In other words, the evolution and constraint equations give us all the equations and also conditions.

In light of this fact, in order to be an application of this study, it will be the subject of upcoming study to investigate the solution of a cosmological model by using evolution and constraint equations in *f(G,T)* gravity theory.

6. ACKNOWLEDGMENTS

D.S. is supported by Istanbul University Scientific Research Projects (BAP) under Project No. BYP-2019-34605.

7. REFERENCES

[1] S. Chaplygin, Sci. Mem. Mosc. Univ. Math. Phys. 21 (1904).
[2] P. Ratra and L. Peebles, Phys. Rev. D 37 (1988) 3406.
[3] R. Dave and P.J. Steinhardt, Phys. Rev. Lett. 80 (1998) 1582.
[4] T. Padmanabhan, Phys. Rev. D 66, (2002) 021301.
[5] M. Bento, O. Bertolami. and A. Sen, Phys. Rev. D 66 (2002) 043507.
[6] R. Caldwell, Phys. Lett. B 545 (2002) 23.
[7] S. Nojiri, S.D. Odintsov, Phys. Lett. B 562 (2003) 147.
[8] B. Feng, X.-L. Wang and X.-M. Zhang, Phys. Lett. B 607 (2005) 35.
[9] N. Afshordi, D.J.H. Chung, and G. Geshnizjani, Phys. Rev. D 75 (2007) 083513.
[10] M.R. Setare, Phys. Lett. B 648 (2007) 329.
[11] T. Padmanabhan, Gen. Relativ. Gravit. 40 (2008) 529.
[12] R. Maartens and D. R. Taylor, Gen. Relativ. Gravit. 26 (1994) 6.
[13] S. Rippl, H. V. Elst, R. Tavakol and D. Taylor, Gen. Relativ. Gravit. 28 (1996) 193.
[14] S. Nojiri and S. D. Odintsov, Int. J. Geom. Methods Mod. Phys. 4 (2007) 115.
[15] S. Capozziello and M. Francaviglia, Gen. Relativ. Gravit. 40 (2008) 357.
[16] T. P. Sotiriou, J. Phys. Conf. Ser. 189 (2009) 012039.
[17] A. Felice and S. Tsujikawa, Living Rev. Rel. 13 (2010) 3.
[18] S. Nojiri, and S. D. Odintsov, S.D.: Phys. Rep. 505 (2011) 59.
[19] S. Nojiri and S.D. Odintsov, Phys. Lett. B 631 (2005) 1.
[20] A. De Felice and T. Tanaka, Prog. Theor. Phys. 124 (2010) 503.
[21] A. De Felice, J.-M. Gerard and T. Suyama, Phys.Rev.D 82 (2010) 063526.
[22] T. Harko, F.S.N. Lobo, S. Nojiri, S.D. Odintsov, Phys. Rev. D 84 (2011) 024020.
[23] A. F. Santos, Mod. Phys. Lett. A 28 (2013) 32.
[24] D. R. K. Reddy, R. Santikumar and R. L. Naidu, Astrophys. Space Sci. 342 (2012) 249.
[25] D. R. K. Reddy, R. B. Vijaya, T. V. Sagar and R. L. Naidu, Astrophys. Space Sci. 350 (2014) 375.
[26] P. K. Sahoo and M. Sivakumar, Astrophys. Space Sci. 357 (2015) 60
[27] D. Momeni, R. Myrzakulov and E. Güdekli, Int. J. Geom. Methods Mod. Phys. 12 (2015) 1550101.
[28] D. Sofuoğlu, Astrophys. Space Sci. 361 (2016) 12.
[29] A. Alhamzawi and R. Alhamzawi, Int. J. Mod. Phys. D 25 (2016) 1650020.
[30] C. Aktaş and S. Aygün, Chin. J. Phys.55 (2017) 71.
[31] S. Aygün, C. Aktaş and İ.Yılmaz, Arch. Curr. Res. Int. 11 (2017) 1, No: ACRI.37868.
[32] P. K. Sahoo, P. Sahoo and B. K. Bishi, Int. J. Geom. Methods Mod. Phys. 14 (2017) 1750097.
[33] B. K. Bishi, S. K. J. Pacif, P. K. Sahoo and C. P. Singh, Int. J. Geom. Methods Mod. Phys. 14 (2017) 11.
[34] E. Güdekli and A. Çalışkan, AIP Conf. Proc. 2042 (2018) 1.
[35] P. K. Sahoo, S. K. Tripathy and P. Sahoo, Mod. Phys. Lett. A 33 (2018) 33.
[36] D. Sofuoğlu, Int. J. Mod. Phys. D 28 (2019) 1950089.
[37] M. Sharif and A. Ikram, Eur. Phys. J. C 76 (2016) 640.
[38] M. Sharif and A. Ikram, Int. J. Mod. Phys. D 26 (2017) 1750084.
[39] M. Sharif and A. Ikram, Eur. Phys. J. Plus 132 (2017) 526.
[40] M.F. Shamir and M. Ahmad, Eur. Phys. J. C 77 (2017) 55.
[41] M. Sharif and A. Ikram, Ad. High Energy Phys. 2019 (2019) 1873804.
[42] G. F. R. Ellis, H. van Elst, NATO Series C: Math. Phys. Sci., vol. 541, pp. 1–116. Kluwer, Dordrecht (1999).
[43] J. A. Leach, S. Carloni and P. K. S. Dunsby, Class. Quant. Grav. 23 (2006) 4915-4937.
[44] S. Carloni, P. K. S. Dunsby, A. Troisi, Phys. Rev. D 77 (2008) 024024.

ISBN:978-605-83516-6-0

[45] K.N. Ananda, S. Carloni, P. K. S. Dunsby, Phys. Rev. D 77, 024033 (2008) 1-14.
[46] B. Li, J. D. Barrow, D. F. Mota, Phys. Rev. D76 (2007) 044027.
[47] D. Sofuoğlu, PhD Thesis, İstanbul University, 2014.
[48] M. Erman, D. Sofuoğlu and E. Güdekli, Turkish Physical Society 29th Intern. Physics Congress, Turkey, 2012.
[49] D. Sofuoğlu, and H. Mutuş, Gen. Relativ. Gravit. 46 (2014) 1831.
[50] E. Güdekli, PhD Thesis, İstanbul University, 2004.

BOOK OF FULL TEXT PROCEEDINGS TURKISH PHYSICAL
SOCIETY 35th INTERNATIONAL PHYSICS CONGRESS (TPS35)
TPS35, Vol.01, No.07, pp.420-426.
ISBN:978-605-83516-6-0 15 December 2019

Power-Law Solution in *f(G,T)* Gravity

Değer SOFUOĞLU[1, a)] and Ertan GÜDEKLİ[1]

[1] *Istanbul University, Faculty of Science, Department of Physics, 34134, Vezneciler, Fatih, Istanbul, TURKEY*

[a)] Corresponding author: degers@istanbul.edu.tr

Abstract. Spatially homogeneous and anisotropic Bianchi type I cosmological model has been considered in the context of *f(G,T)* modified gravity theory. The field equations have been derived for power-law scale factors. By assuming that the energy-momentum tensor of matter is conserved and the matter source of the universe is a perfect fluid, we have investigated the power-law solution is consistent with the field equations of the *f(G,T)* gravity theory. We have shown that this model is a solution provided that there are some relationships between metric parameters through the new condition arising from our conserved matter assumption. We have also shown that if the matter energy content of this universe is a stiff fluid, the power law scale factors can be the solution of the field equations of *f (G,T)* theory.

1. INTRODUCTION

As now it is well known, the modified gravity theories, that theories aim to explain the accelerated expansion of last era of our universe [1-11], in general, are introduced by modifying the Einstein-Hilbert (EH) action. The action is modified by writing some arbitrary functions of the curvature scalars or curvature-matter coupling terms instead of the Ricci curvature scalar *R*. The *f(R)* gravity theory has been the most studied modified gravity theory for the last two decades. Another most popular theories of these years, *G* being Gauss-Bonnet invariant, have been *f(G)* and *f(R,G)* theories [12-21]. After that a new modified gravity theory containing matter-curvature coupling term in the action has been proposed by Harko et al. [22]. The theory, namely *f(R,T)* theory, where *T* is the trace of the energy momentum-tensor of the ordinary matter, has attracted the attention of many cosmologists [23-34]. One of the latest modified gravity theories is *f(G,T)* gravity theory which can be considered as some kind of generalization of these theories, has been proposed by [35]. In this theory, Sharif and Ikram have dealt with the stability of Einstein Universe and get results [36,37]; Shamir and Ahmad, using Noether symmetry approach, have constructed some cosmological viable *f(G,T)* model for spatially homogeneous and isotropic universe [38]; Sharif and Ikram have studied to analyze the cosmological evolution of holographic dark energy [39].

In this paper, we consider the spatially homogeneous Bianchi-type I universe model in *f(G,T)* gravity theory and aim to investigate whether the Kasner-type scale factors is a solution of the field equations of *f(G,T)* gravity theory. For this task, once we derive the field equations of *f(G,T)* gravity. By assuming that the universe filled with a perfect fluid and the energy-momentum tensor of matter is conserved, we consider the Bianchi-type I model in this modified theory. Then we deal with the power-law solution of the model. And we summarize our results.

Thorough this paper we use natural units $8\pi G = c = 1\ \kappa^2 = 1$; the indices $a, b, c,$ ... run from 0 to 3; the dot " $\cdot$ " represents the derivative with respect to cosmic time *t*.

2. FIELD EQUATIONS OF *f(G,T)* GRAVITY

The field equations of *f(G,T)* gravity theory is based on the following action [35]

Türk Fizik Derneği
1950
Turkish Physical Society

ISBN:978-605-83516-6-0 15 December 2019

$$S = \frac{1}{2}\int d^4x\sqrt{-g}[R + f(G,T)] + \int d^4x\sqrt{-g}\,L_m. \quad (1)$$

Here g is the determinant of the metric tensor g_{ab}, R is the Ricci curvature scalar, *f(G,T)* is an arbitrary function of the trace T of the matter energy-momentum tensor T^m_{ab}, L_m is Lagrangian density of the matter, and G

$$G = R^2 - 4R_{ab}R^{ab} + R_{abcd}R^{abcd}, \quad (2)$$

is the Gauss-Bonnet term where R_{ab} is the Ricci tensor and R_{abcd} is the Riemann tensor. The energy momentum tensor of matter is defined as

$$T^m_{ab} = -\frac{2}{\sqrt{-g}}\frac{\delta(\sqrt{-g}L_m)}{\delta g^{ab}}. \quad (3)$$

If it is assumed that the matter Lagrangian density L_m only depends on the metric tensor components g_{ab}, then the energy-momentum tensor of matter becomes

$$T^m_{ab} = g_{ab}L_m - 2\frac{\partial L_m}{\partial g^{ab}}. \quad (4)$$

The variation of Eq. (1) with respect to the metric g^{ab} yields the following field equations

$$\begin{aligned} G_{ab} = {} & T^m_{ab} + \frac{1}{2}g_{ab}f - (T^m_{ab} + \Theta_{ab})f_T - (2RR_{ab} - 4R_a{}^cR_{cb} - 4R_{acbd}R^{cd} + 2R_a{}^{cde}R_{bcde})f_G \\ & - (2Rg_{ab}\Box - 2R\nabla_a\nabla_b - 4g_{ab}R^{cd}\nabla_c\nabla_d - 4R_{ab}\Box + 4R^c{}_a\nabla_b\nabla_c + 4R^c{}_b\nabla_a\nabla_c - 4R_a{}^{cd}{}_b\nabla_d\nabla_c)f_G, \end{aligned} \quad (5)$$

where $G_{ab} = R_{ab} - \frac{1}{2}g_{ab}R$ is Einstein tensor, $\Box = g^{ab}\nabla_a\nabla_b$ is 4-dimensional D'Alembert operator, f denotes the *f(G,T)* function, f_G and f_T are symbolized the partial derivatives of the *f(G,T)* function with respect to G and T, respectively and

$$\Theta_{ab} \equiv g^{mn}\frac{\delta T_{mn}}{\delta g^{ab}} = -2T_{ab} + g_{ab}L_m - 2g^{mn}\frac{\partial^2 L_m}{\partial g^{ab}\partial g^{mn}}. \quad (6)$$

Since G is topologically invariant in four dimensions, if f function is selected as $f(G,T) = G - 2\Lambda$, Λ being cosmological constant, the field equations (5) reads

$$\frac{1}{2}g_{ab}G - (2RR_{ab} - 4R_a{}^cR_{cb} - 4R_{acbd}R^{cd} + 2R_a{}^{cde}R_{bcde}) = 0. \quad (7)$$

Eqs. (5) with Eq. (7) give the field equations of *f(G,T)* gravity as

$$\begin{aligned} G_{ab} = {} & T^m_{ab} - (T^m_{ab} + \Theta_{ab})f_T + \frac{1}{2}g_{ab}(f - Gf_G) \\ & - (2Rg_{ab}\Box - 2R\nabla_a\nabla_b - 4g_{ab}R^{cd}\nabla_c\nabla_d - 4R_{ab}\Box + 4R^c{}_a\nabla_b\nabla_c + 4R^c{}_b\nabla_a\nabla_c - 4R_a{}^{cd}{}_b\nabla_d\nabla_c)f_G. \end{aligned} \quad (8)$$

In this study we assume that the matter source of the universe is perfect fluid. The energy-momentum tensor of perfect fluid is defined as

$$T^m_{ab} = \mu^m u_a u_b + p^m h_{ab}, \quad (9)$$

where μ^m is the matter-energy density and p^m is the pressure of the fluid. If the Lagrangian of matter can be taken as $L_m = p^m$ [22, 35], then Eq. (6) becomes

$$\Theta_{ab} = -2T^m_{ab} + p^m g_{ab}. \quad (10)$$

By using Eqs. (9) and (10) in Eq. (8), we get the following field equations of *f(G,T)* gravity

ISBN:978-605-83516-6-0

$$G_{ab} = T^{m}_{ab} + \frac{1}{2}g_{ab}(f - Gf_G) + (\mu^m + p^m)u_a u_b f_T - (2Rg_{ab}\Box - 2R\nabla_a\nabla_b - 4g_{ab}R^{cd}\nabla_c\nabla_d - 4R_{ab}\Box + 4R^{c}{}_{a}\nabla_b\nabla_c + 4R^{c}{}_{b}\nabla_a\nabla_c - 4R_{a}{}^{cd}{}_{b}\nabla_d\nabla_c)f_G. \quad (11)$$

Here the superscript *GT* denotes the Gauss-Bonnet term and the trace of the energy-momentum tensor corrections.

3. BIANCHI-TYPE I UNIVERSE IN *f(G,T)* GRAVITY

In the present study we have considered Bianchi-type I universe model in *f(G,T)* gravity, by choosing the *f(G,T)* function as

$$f(G,T) = f_1(G) + f_2(T). \quad (12)$$

Spatially homogeneous and anisotropic Bianchi-type I model is given by the line element

$$ds^2 = -dt^2 + A^2(t)dx^2 + B^2(t)dy^2 + C^2(t)dz^2, \quad (13)$$

where *A*, *B* and *C* are time dependent scale factors. For this line element, by using the field equations (11) and the *f* function given Eq. by (12) we find the following equations

$$\frac{\dot{a}}{a}\frac{\dot{b}}{b} + \frac{\dot{b}}{b}\frac{\dot{c}}{c} + \frac{\dot{c}}{c}\frac{\dot{a}}{a} = \mu^m + f_T(\mu^m + p^m) - \frac{1}{2}(f - Gf_G) - 12\frac{\dot{a}}{a}\frac{\dot{b}}{b}\frac{\dot{c}}{c}f_{GG}\dot{G}, \quad (14)$$

$$-\frac{1}{3}\left(\frac{\dot{a}}{a}\frac{\dot{b}}{b} + \frac{\dot{b}}{b}\frac{\dot{c}}{c} + \frac{\dot{c}}{c}\frac{\dot{a}}{a}\right) - \frac{2}{3}\left(\frac{\ddot{a}}{a} + \frac{\ddot{b}}{b} + \frac{\ddot{c}}{c}\right) = p^m + \frac{1}{2}(f - Gf_G) + \frac{4}{3}\left[\frac{\ddot{a}}{a}\left(\frac{\dot{b}}{b} + \frac{\dot{c}}{c}\right) + \frac{\ddot{b}}{b}\left(\frac{\dot{c}}{c} + \frac{\dot{a}}{a}\right) + \frac{\ddot{c}}{c}\left(\frac{\dot{a}}{a} + \frac{\dot{b}}{b}\right)\right]f_{GG}\dot{G} + \frac{4}{3}\left(\frac{\dot{a}}{a}\frac{\dot{b}}{b} + \frac{\dot{b}}{b}\frac{\dot{c}}{c} + \frac{\dot{c}}{c}\frac{\dot{a}}{a}\right)(f_{GG}\ddot{G} + f_{GGG}\dot{G}^2), \quad (15)$$

$$\frac{1}{3}\left(\frac{\dot{a}}{a}\frac{\dot{b}}{b} - 2\frac{\dot{b}}{b}\frac{\dot{c}}{c} + \frac{\dot{c}}{c}\frac{\dot{a}}{a}\right) + \frac{1}{3}\left(2\frac{\ddot{a}}{a} - \frac{\ddot{b}}{b} - \frac{\ddot{c}}{c}\right) = -\frac{4}{3}\left[\frac{\ddot{a}}{a}\left(\frac{\dot{b}}{b} + \frac{\dot{c}}{c}\right) + \frac{\ddot{b}}{b}\left(-2\frac{\dot{c}}{c} + \frac{\dot{a}}{a}\right) + \frac{\ddot{c}}{c}\left(\frac{\dot{a}}{a} - 2\frac{\dot{b}}{b}\right)\right]f_{GG}\dot{G} - \frac{4}{3}\left(\frac{\dot{a}}{a}\frac{\dot{b}}{b} - 2\frac{\dot{b}}{b}\frac{\dot{c}}{c} + \frac{\dot{c}}{c}\frac{\dot{a}}{a}\right)(f_{GG}\ddot{G} + f_{GGG}\dot{G}^2) \quad (16)$$

$$\frac{1}{3}\left(\frac{\dot{a}}{a}\frac{\dot{b}}{b} + \frac{\dot{b}}{b}\frac{\dot{c}}{c} - 2\frac{\dot{c}}{c}\frac{\dot{a}}{a}\right) + \frac{1}{3}\left(-\frac{\ddot{a}}{a} + 2\frac{\ddot{b}}{b} - \frac{\ddot{c}}{c}\right) = -\frac{4}{3}\left[\frac{\ddot{a}}{a}\left(\frac{\dot{b}}{b} - 2\frac{\dot{c}}{c}\right) + \frac{\ddot{b}}{b}\left(\frac{\dot{c}}{c} + \frac{\dot{a}}{a}\right) + \frac{\ddot{c}}{c}\left(-2\frac{\dot{a}}{a} + \frac{\dot{b}}{b}\right)\right]f_{GG}\dot{G} - \frac{4}{3}\left(\frac{\dot{a}}{a}\frac{\dot{b}}{b} + \frac{\dot{b}}{b}\frac{\dot{c}}{c} - 2\frac{\dot{c}}{c}\frac{\dot{a}}{a}\right)(f_{GG}\ddot{G} + f_{GGG}\dot{G}^2), \quad (17)$$

$$\frac{1}{3}\left(-2\frac{\dot{a}}{a}\frac{\dot{b}}{b} + \frac{\dot{b}}{b}\frac{\dot{c}}{c} + \frac{\dot{c}}{c}\frac{\dot{a}}{a}\right) + \frac{1}{3}\left(-\frac{\ddot{a}}{a} - \frac{\ddot{b}}{b} + 2\frac{\ddot{c}}{c}\right) = -\frac{4}{3}\left[\frac{\ddot{a}}{a}\left(-2\frac{\dot{b}}{b} + \frac{\dot{c}}{c}\right) + \frac{\ddot{b}}{b}\left(\frac{\dot{c}}{c} - 2\frac{\dot{a}}{a}\right) + \frac{\ddot{c}}{c}\left(\frac{\dot{a}}{a} + \frac{\dot{b}}{b}\right)\right]f_{GG}\dot{G} - \frac{4}{3}\left(-2\frac{\dot{a}}{a}\frac{\dot{b}}{b} + \frac{\dot{b}}{b}\frac{\dot{c}}{c} + \frac{\dot{c}}{c}\frac{\dot{a}}{a}\right)(f_{GG}\ddot{G} + f_{GGG}\dot{G}^2). \quad (18)$$

On the other hand for the Bianchi-type I model, Gauss-Bonnet term Ggiven by Eq. (2), become

$$G = 8\left(\frac{\ddot{a}}{a}\frac{\dot{b}}{b}\frac{\dot{c}}{c} + \frac{\ddot{b}}{b}\frac{\dot{c}}{c}\frac{\dot{a}}{a} + \frac{\ddot{c}}{c}\frac{\dot{a}}{a}\frac{\dot{b}}{b}\right). \quad (19)$$

Now we deal with the Kasner type solution described by means of the following scale factors [49]

$$a(t) = a_0 t^{p_1}, \quad b(t) = b_0 t^{p_2}, \quad c(t) = c_0 t^{p_3}, \quad (20)$$

where a_0, b_0 and c_0 are constants. By using Eq. (20) in Eq. (19) we obtain the Gauss-Bonnet term as

ISBN:978-605-83516-6-0

$$G = \frac{8P}{t^4}, \tag{21}$$

where $P = p_1 p_2 p_3 (p_1 + p_2 + p_3 - 3)$. As it is immediately seen, the last equation leads to

$$t = (\frac{8P}{G})^{1/4}. \tag{22}$$

Eqs. (21) and (22) allow us to express the following first and the second derivatives of the Gauss-Bonnet term with respect to *t*

$$\dot{G} = -2(\frac{2}{P})^{1/4} G^{5/4}, \quad \ddot{G} = 5\sqrt{\frac{2}{P}} G^{3/2}. \tag{23}$$

By using Eqs. (20), (22) and (23), Eqs. (14)-(18) become

$$\frac{\sqrt{2}}{4}\frac{(p_1p_2+p_2p_3+p_3p_1)}{\sqrt{P}}\sqrt{G} = \mu^m + f_T(\mu^m + p^m) - \frac{1}{2}(f - Gf_G) + 6\frac{p_1p_2p_3}{P} f_{GG} G^2, \tag{24}$$

$$-\frac{\sqrt{2}}{12\sqrt{P}}[2({p_1}^2 + {p_2}^2 + {p_3}^2) + (p_1p_2 + p_2p_3 + p_3p_1) - 2(p_1 + p_2 + p_3)]\sqrt{G}p^m + \frac{1}{2}(f - Gf_G)$$
$$-\frac{2}{3P}[{p_1}^2(p_2 + p_3) + {p_2}^2(p_3 + p_1) + {p_3}^2(p_1 + p_2) - 7(p_1p_2 + p_2p_3 + p_3p_1)] f_{GG} G^2$$
$$+\frac{8}{3P}(p_1p_2 + p_2p_3 + p_3p_1) f_{GGG} G^3 \tag{25}$$

$$\frac{\sqrt{2}}{12\sqrt{P}}(p_1 + p_2 + p_3 - 1)(2p_1 - p_2 - p_3)\sqrt{G}$$
$$= \frac{2}{3P}(p_1 + p_2 + p_3 - 7)(p_1p_2 - 2p_2p_3 + p_3p_1) f_{GG} G^2 - \frac{8}{3P}(p_1p_2 - 2p_2p_3 + p_3p_1) f_{GGG} G^3, \tag{26}$$

$$\frac{\sqrt{2}}{12\sqrt{P}}(p_1 + p_2 + p_3 - 1)(-p_1 + 2p_2 - p_3)\sqrt{G}$$
$$= \frac{2}{3P}(p_1 + p_2 + p_3 - 7)(p_1p_2 + p_2p_3 - 2p_3p_1) f_{GG} G^2 - \frac{8}{3P}(p_1p_2 + p_2p_3 - 2p_3p_1) f_{GGG} G^3, \tag{27}$$

$$\frac{\sqrt{2}}{12\sqrt{P}}(p_1 + p_2 + p_3 - 1)(-p_1 - p_2 + 2p_3)\sqrt{G}$$
$$= \frac{2}{3P}(p_1 + p_2 + p_3 - 7)(-2p_1p_2 + p_2p_3 + p_3p_1) f_{GG} G^2 - \frac{8}{3P}(-2p_1p_2 + p_2p_3 + p_3p_1) f_{GGG} G^3. \tag{28}$$

Note that now we have expressed these equations in terms of only *G*, *f(G,T)* and derivatives of *f(G,T)*. The differential equations (26) – (28) may be easily integrated, however before integrating, we examine whether these equations are consistent with each other. Thus, first, we consider the Eq. (26) to obtain

$$f_{GGG} = \frac{\sqrt{2P}}{32}\frac{(p_1+p_2+p_3-1)(2p_1-p_2-p_3)}{p_1p_2-2p_2p_3+p_3p_1} G^{-5/2} + \frac{1}{4}(p_1 + p_2 + p_3 - 7) f_{GG} G^{-1}, \tag{29}$$

which using with Eq. (27) and (28) we find the consistency condition as follows

$$p_1 + p_2 + p_3 = 1. \tag{30}$$

The condition is the same condition of general relativistic Kasner type solution [40]. By substituting that condition into Eqs. (26)-(28), we obtain the following single equation

$$3f_{GG} + 2f_{GGG} G = 0. \tag{31}$$

ISBN:978-605-83516-6-0

Integration of Eq. (31) gives

$$f_1(G) = c_1\sqrt{G} + c_2 G + c_3, \tag{32}$$

where c_1, c_2 and c_3 are constants of integration. Without any loss of generality, we may assume that $c_3 = 0$ and since G is topologically invariant in 4-dimensional, $f_1(G)$ may be written as

$$f_1(G) = c_1\sqrt{G}. \tag{33}$$

Now, under the condition (30), summation of Eqs. (24) and (25) with Eq. (33) yields

$$\sqrt{\frac{G}{2P}}(-p_1p_2 + p_1 - {p_1}^2 + p_2 - {p_2}^2) = (1 + f_T)(\mu^m + p^m) + c_1\sqrt{G}. \tag{34}$$

By using Eq. (21) in the last equation, we get

$$(1 + f_T)(\mu^m + p^m) = 2(-p_1p_2 + p_1 - {p_1}^2 + p_2 - {p_2}^2 - \sqrt{2P}c_1)\frac{1}{t^2}. \tag{35}$$

Now, we consider the matter conservation equation. The matter conservation equation of *f(G,T)* gravity theory is

$$\dot{\mu}^m + (\mu^m + p^m)\theta = \frac{1}{2}f_T(\dot{\mu}^m - \dot{p}^m) + \dot{f}_T(\mu^m + p^m), \tag{36}$$

where θ is the expansion scalar defined by $\theta = \nabla_a u^a$. For our model we obtain the expansion scalar as

$$\theta = \frac{1}{3}\left(\frac{\dot{a}}{a} + \frac{\dot{b}}{b} + \frac{\dot{c}}{c}\right) = \frac{1}{t}. \tag{37}$$

If we assume that the energy-momentum tensor is conserved, then we get the following two equations

$$\dot{\mu}^m + (\mu^m + p^m)\theta = 0, \tag{38}$$

$$\frac{1}{2}f_T(\dot{\mu}^m - \dot{p}^m) + \dot{f}_T(\mu^m + p^m) = 0, \tag{39}$$

in which the first equation is the conservation equation of GR and the second one is an additional condition. At this stage we hold barotropic equation of state with the state equation

$$p^m = w\mu^m, \tag{40}$$

where $-1 \leq w \leq 1$ is constant state parameter. Using Eq. (9) together with Eq. (40) the trace of energy-momentum tensor reads

$$T = (-1 + 3w)\mu^m\ . \tag{41}$$

We use the last equation in order to express the matter-energy density in terms of trace T as

$$\mu^m = \frac{T}{(-1+3w)} \quad (w \neq 1/3). \tag{42}$$

On the other hand, using Eqs. (37) and (40) the integration of Eq. (38) gives,

$$\mu^m = \mu_0 t^{-(1+w)} \quad (w \neq -1). \tag{43}$$

One may easily solve Eq. (43) for *t* as

ISBN:978-605-83516-6-0

$$t = (\frac{\mu_0}{\mu^m})^{1/(1+w)}. \tag{44}$$

Eq. (39), on using Eqs. (40), (42) and (44), becomes

$$(1 + f_T)T^{(w-1)/(w+1)} = C. \tag{45}$$

The integration of the last equation gives

$$f_2(T) = \frac{1}{2}C(w + 1)T^{2/(w+1)} - T + c_4, \tag{46}$$

where c_4 is an integration constant and

$$C = \frac{2(-1+3w)^{w-1}(-p_1p_2+p_1-{p_1}^2+p_2-{p_2}^2-\sqrt{2P}c_1)}{(1+w){\mu_0}^{2/1+w}}. \tag{47}$$

Now, again we may assume that $c_4 = 0$. The solution (47) must be consistent with Eq. (39). To examine the consistency, we use Eqs. (39), (47), (41) and (43) and we get a specific value for state parameter that *w*=1 which corresponds to a stiff fluid. Then the *f(G,T)* function becomes

$$f(G, T) = c_1\sqrt{G} + (C - 1)T. \tag{48}$$

Finally, we use Eqs. (19), (30), (40), (41) and (43) in Eq. (24) or (25), for *w*=1, we find the following relation between the metric parameters

$$p_2 = \frac{1\mp\sqrt{2}}{2p_1}. \tag{49}$$

4. SUMMARY AND CONCLUSIONS

In this study we have consider the spatially homogeneous and anisotropic Bianchi type I cosmological model in the context of *f(G,T)* modified gravity theory. We have obtained the field equations for power-law scale factors. We assume that the energy-momentum tensor of matter is conserved, thus we have had one more equation besides the field equations and the well-known conservation equation of the conserved matter. We have shown that all of these equations are consistent if some relationships between the metric parameters given by the Eqs. (30) and (49) are hold, moreover if the matter energy content of this universe is a stiff fluid, i.,e., $p = \mu$. In other word, we have shown that the Kasner-type solution is allowed in the modified *f(G,T)* gravity theory under the abovementioned conditions for stiff fluid.

5. ACKNOWLEDGMENTS

D.S. is supported by Istanbul University Scientific Research Projects (BAP) under Project No. BYP-2019-34605.

6. REFERENCES

[1] Perlmutter S. et al., Astrophys. J. 483 (1997) 565.
[2] Perlmutter S. et al., Nature 391 (1998) 51.
[3] Perlmutter S. et al., Astrophys. J. 517 (1999) 565.
[4] Riess A.G., et al., Astron. J.116 (1998) 1009.
[5] Riess A.G. et al., Astrophys. J. 607 (2004) 665.
[6] Bennett C. et al., Astrophys. J. Suppl. 148, (2003) 1.
[7] Spergel D.N. et al., Astrophys. J. Suppl. 148 (2003) 175.
[8] Spergel D.N. et al., Astrophys. J. Suppl. 170 (2007) 377.

[9] Hawkins E. et al., Mon. Not. Roy. Astron. Soc. 346 (2003) 78.
[10] Tegmark M. et al., Phys. Rev. D 69, (2004) 103501.
[11] Cole S. et al., Mon. Not. Roy. Astron. Soc. 362 (2005) 505.
[12] R. Maartens and D. R. Taylor, Gen. Relativ. Gravit. 26 (1994) 6.
[13] S. Rippl, H. V. Elst, R. Tavakol and D. Taylor, Gen. Relativ. Gravit. 28 (1996) 193.
[14] S. Nojiri and S. D. Odintsov, Int. J. Geom. Methods Mod. Phys. 4 (2007) 115.
[15] S. Capozziello and M. Francaviglia, Gen. Relativ. Gravit. 40 (2008) 357.
[16] T. P. Sotiriou, J. Phys. Conf. Ser. 189 (2009) 012039.
[17] A. Felice and S. Tsujikawa, Living Rev. Rel. 13 (2010) 3.
[18] S. Nojiri, and S. D. Odintsov, S.D.: Phys. Rep. 505 (2011) 59.
[19] S. Nojiri and S.D. Odintsov, Phys. Lett. B 631 (2005) 1.
[20] A. De Felice and T. Tanaka, Prog. Theor. Phys. 124 (2010) 503.
[21] A. De Felice, J.-M. Gerard and T. Suyama, Phys.Rev.D 82 (2010) 063526.
[22] T. Harko, F.S.N. Lobo, S. Nojiri, S.D. Odintsov, Phys. Rev. D 84 (2011) 024020.
[23] A. F. Santos, Mod. Phys. Lett. A 28 (2013) 32.
[24] D. R. K. Reddy, R. Santikumar and R. L. Naidu, Astrophys. Space Sci. 342 (2012) 249.
[25] D. R. K. Reddy, R. B. Vijaya, T. V. Sagar and R. L. Naidu, Astrophys. Space Sci. 350 (2014) 375.
[26] P. K. Sahoo and M. Sivakumar, Astrophys. Space Sci. 357 (2015) 60
[27] D. Momeni, R. Myrzakulov and E. Güdekli, Int. J. Geom. Methods Mod. Phys. 12 (2015) 1550101.
[28] D. Sofuoğlu, Astrophys. Space Sci. 361 (2016) 12.
[29] A. Alhamzawi and R. Alhamzawi, Int. J. Mod. Phys. D 25 (2016) 1650020.
[30] C. Aktaş and S. Aygün, Chin. J. Phys.55 (2017) 71.
[31] S. Aygün, C. Aktaş and İ.Yılmaz, Arch. Curr. Res. Int. 11 (2017) 1, No: ACRI.37868.
[32] B. K. Bishi, S. K. J. Pacif, P. K. Sahoo and C. P. Singh, Int. J. Geom. Methods Mod. Phys. 14 (2017) 11.
[33] E. Güdekli and A. Çalışkan, AIP Conf. Proc. 2042 (2018) 1.
[34] D. Sofuoğlu, Int. J. Mod. Phys. D 28 (2019) 1950089.
[35] M. Sharif and A. Ikram, Eur. Phys. J. C 76 (2016) 640.
[36] M. Sharif and A. Ikram, Int. J. Mod. Phys. D 26 (2017) 1750084.
[37] M. Sharif and A. Ikram, Eur. Phys. J. Plus 132 (2017) 526.
[38] M.F. Shamir and M. Ahmad, Eur. Phys. J. C 77 (2017) 55.
[39] M. Sharif and A. Ikram, Ad. High Energy Phys. 2019 (2019) 1873804.
[40] E. Kasner, Am. J. Math. 43 (4) (1921), 217–221.

BOOK OF FULL TEXT PROCEEDINGS TURKISH PHYSICAL
SOCIETY 35th INTERNATIONAL PHYSICS CONGRESS (TPS35)
TPS35, Vol.01, No.07, pp.427-431.
ISBN:978-605-83516-6-0 15 December 2019

Bianchi Type-V Cosmology with Gamma Law EoS in F(R,T) Gravity

G. D. AÇAN YILDIZ[1,a)], E. GUDEKLİ[2,b)], D. SOFUOĞLU[3,c)]

1,2,3 Istanbul University, Faculty of Science, Department of Mathematical Physics, Istanbul, Turkey

a)gizemdilaraacan@gmail.com , b) gudekli@istanbul.edu.tr , c) degers@istanbul.edu.tr

Abstract. We take into account, in the presence of the EoS parameter, Bianchi Type-V in f (R, T) (R Ricci scalar and T trace of energy momentum tensor) gravity theory. At the beginning of the universe, the "Gamma-Law" state equation are considered to explore the role of particle formation. Exact solutions of field equations are obtained using scalar expansion proportional to shear. The physical and kinematic properties of the model were examined.

Keywords: Bianchi type-V spacetime, f(R,T) gravity, EoS parameter, gamma law, cosmological model, scalar model, scalar expantion, shear scalar.

EXAMINATION OF F (R, T) GRAVITATION

The equation of motion of the modified gravitation theory f (R, T) is expressed as follows, [2-3]

$$S = \frac{1}{16\pi}\int f(R,T)\sqrt{-g}\,d^4x + \int \mathcal{L}_m\sqrt{-g}\,d^4x, \tag{1}$$

T is the trace of the energy momentum tensor T_{ij} of matter, $\mathcal{L}_m$ corresponds to the matter Lagrangian. Energy momentum tensor T_{ij} defined as

$$T_{ij} = -\frac{2}{\sqrt{-g}}\frac{\delta(\sqrt{-g}\mathcal{L}_m)}{\delta g^{ij}} \tag{2}$$

İt is trace is $T = g^{ij}T_{ij}$. Here the matter Lagrangian $\mathcal{L}_m$, depends only on metric tensor g_{ij}. Therefore, we can write;

$$T_{ij} = g_{ij}\mathcal{L}_m - \frac{\partial \mathcal{L}_m}{\partial g_{ij}} \tag{3}$$

The equation of motion of f(R, T) are obtained by changing S, depending on g_{ij}. [2]

$$f_R(R,T)R_{ij} - \frac{1}{2}f(R,T)g_{ij} + \left(g_{ij}\Box - \nabla_i\nabla_j\right)f_R(R,T) = 8\pi T_{ij} - f_T(R,T)T_{ij} - f_T(R,T)\Theta_{ij} \tag{4}$$

$$\Theta_{ij} = -2T_{ij} + g_{ij}\mathcal{L}_m - 2g^{lm}\frac{\partial^2 L_m}{\partial g^{ij}\partial g^{lm}} \tag{5}$$

Here,

$$f_R(R,T) = \frac{\partial f(R,T)}{\partial R}, \qquad f_T(R,T) = \frac{\partial f(R,T)}{\partial T}$$

D'Alambert operator $\Box \equiv \nabla^j\nabla_i$, ∇_i means covariant derivative. It is used for index contraction in equation (4).

$$f_R(R,T)R - 3\Box f_R(R,T) - 2f(R,T) = (8\pi - f_T(R,T)T - f_T(R,T)\Theta, \tag{6}$$

Here we consider $f(R,T) = R + 2f(T)$ is the arbitrary function of the trace of matter source. It represents the interaction between curvature and matter. Suppose that

f (T) = λT, λ is constant, and then take a look at the field equation. [3]

Türk Fizik Derneği
1950
Turkish Physical Society

ISBN:978-605-83516-6-0

$$R_{ij} - \frac{1}{2}Rg_{ij} + \left(g_{ij}\square - \nabla_i\nabla_j\right)\lambda = 8\pi T_{ij} - 2\left(T_{ij} + \Theta_{ij}\right)f_T(R,T) + f(T)g_{ij}. \quad (7)$$

Assuming $\left(g_{ij}\square - \nabla_i\nabla_j\right)\lambda = 0$, we get

$$R_{ij} - \frac{1}{2}Rg_{ij} = 8\pi T_{ij} - 2\left(T_{ij} + \Theta_{ij}\right)f_T(R,T) + f(T)g_{ij}. \quad (8)$$

METRIC AND FIELD EQUATIONS

Bianchi type-V metric, homogeneous and anisotropic symmetric [1-4],

$$dS^2 = c^2dt^2 - A^2(t)dx^2 - B^2(t).e^{-2x}dy^2 - C^2(t).e^{-2x}dz^2 \quad (9)$$

A,B and C are functions of cosmic time t. The average scale multiplier, spatial volume and scalar expansion are as follows for the metric ;

$$a = (ABC)^{\frac{1}{3}}, \quad V = a^3 = ABC, \quad \theta = u^i_{;i} = \frac{\dot{A}}{A} + \frac{\dot{B}}{B} + \frac{\dot{C}}{C}, \quad (10)$$

(') represents an ordinary derivative according to cosmic time t. H_1, $H_2 and\ H_3$ are Hubble parameters. Hubble parameter H can be written as [4];

$$H_1 = \frac{\dot{A}}{A}, \quad H_2 = \frac{\dot{B}}{B}, \quad H_3 = \frac{\dot{C}}{C}$$

$$H = \frac{1}{3}(H_1 + H_2 + H_3) \quad (11)$$

In the presence of particle formation, energy momentum tensor is given by.

$$T_{ij} = (\rho_{m+}p_m + p_c)u_iu_j - (p_m + p_c)g_{ij} \quad (12)$$

ρ_m, p_m, p_c are energy density, thermodynamic pressure and supplementary pressure respectively. Supplementary pressure p_c is creation pressure of the particles and supplementary pressure is considered as part of the cosmological pressure within the Einstein field equations

$$p_c = -\frac{(\rho_{m+}p_m)}{n}\frac{dN}{dV} \quad (13)$$

N particle number, V is volume, and $n = \frac{N}{V}$ is the particle number density. The value of p_c is either negative or zero depending on the presence of particle creation. $u^i = (0,0,0,1)$ is the four velocity vector, $u^iu_i = 1$ and $u^i\nabla_ju_i = 0$. The particle flux vector is

$$N^\alpha = nu^\alpha \quad (14)$$

and this provides the balance equation.

$$N^\alpha_{;\alpha} = \psi \quad (15)$$

ψ is a particle source term that can be positive or negative due to the generation or disappearance of particles. In cosmology, ψ is generally considered to be 0. Here we consider the relationship between particle number n and V as the particle formation process. For metric (9), the equation (15) is as follows;

$$\dot{n} + 3nH = \psi. \quad (16)$$

Equation (14) takes the following to form matter;

$$p_c = -\frac{(\rho_{m+}p_m)}{3nH}\psi \quad (17)$$

The energy-momentum tensor for perfect fluid in presence particle creation is given by

$$T = \rho_m - 3(p_{m+}p_c). \quad (18)$$

ISBN:978-605-83516-6-0

Matter Lagrangia can be assumed as $\mathcal{L}_{m=} - (p_m + p_c)$. With the help of the energy-momentum tensor and the material Lagrangian, the equation (5) can be written as [1],

$$\Theta_{ij} = -2T_{ij} - (p_m + p_c)g_{ij} \tag{19}$$

using this expression, the field equation (9) can be written as follows;

$$G_{ij} = 8\pi T_{ij} + 2[T_{ij} + (p_m + p_c)g_{ij}]f_T(R,T) + f(T)g_{ij} \tag{20}$$

thus, the space equation (9) and the energy momentum tensor (12) for space-time are as follows;

$$H_1H_2 + H_1H_3 + H_2H_3 - \frac{3}{A^2} = -8\pi\rho_m - \big(3\rho_m - (p_m + p_c)\big)\lambda \tag{21}$$

$$H_3^2 + H_3' + H_2^2 + H_2' + H_2H_3 - \frac{1}{A^2} = 8\pi(p_m + p_c) - \big(\rho_m - 3(p_m + p_c)\big)\lambda \tag{22}$$

$$H_3^2 + H_3' + H_1^2 + H_1' + H_1H_3 - \frac{1}{A^2} = 8\pi(p_m + p_c) - \big(\rho_m - 3(p_m + p_c)\big)\lambda \tag{23}$$

$$H_2^2 + H_2' + H_1^2 + H_1' + H_1H_2 - \frac{1}{A^2} = 8\pi(p_m + p_c) - \big(\rho_m - 3(p_m + p_c)\big)\lambda \tag{24}$$

$$2H_1 = H_3 + H_2 \tag{25}$$

SOLUTION OF FIELD EQUATIONS

Two further assumptions are necessary to solve field equations. On the other hand equation (17) gives the value of p_c from p_m and ρ_m and this means we need only one equation. [3-4]

For the solution of the field equations group, we thought that the shear scalar is proportional to the expansion scalar. [4]

This yield;

$$H_{3=}lH_1 \tag{26}$$

Where $\ell \neq 1$ is constant. For $\ell = 1$, the model is isotropic, in other cases it is anisotropic. From equations (22) and (23) we obtain;

$$H_1 = \frac{1}{3t+k_1}\ , \tag{27}$$

k_1 is the integration constant. When equation (26) is used in equation (25), we get

$$H_2 = \frac{(2-l)}{3t+k_1} \qquad (28),\ H_3 = \frac{l}{3t+k_1}. \tag{29}$$

A(t), B(t) and C(t) are the metric potential. [3]

$$A(t) = k_2[3t + k_1]^{\frac{1}{3}} \tag{30}$$

$$B(t) = k_3[3t + k_1]^{\frac{2-l}{3}} \tag{31}$$

$$C(t) = k_4[3t + k_1]^{\frac{l}{3}} \tag{32}$$

k_2, k_3 are integration constants. The metric is like this;

$$dS^2 = c^2dt^2 - k_2^2[3t + k_1]^{\frac{2}{3}}dx^2 - k_3^2[3t + k_1]^{\frac{4-2l}{3}}.e^{-2x}dy^2 - k_4^2[3t + k_1]^{\frac{2l}{3}}.e^{-2x}dz^2 \tag{33}$$

Here we evaluate the EoS parameter of the fluid known as gamma law in the cosmological field as follows:

ISBN:978-605-83516-6-0

$$p_m = (\gamma - 1)\rho_m \tag{34}$$

γ is constant lies in [0,2]. We have restricted γ between [0,2], so that the energy density behavior for both the positive and negative can be studied. In the set (22) - (24), energy density of matter, particle creation pressure and the pressure of the matter are given using (26), (27) and (31).

$$\rho_m = \frac{1}{4(3t+k_1)^2(\lambda^2+3\lambda+4\pi^2)}\left((\lambda+2\pi)(l^2+2l-2)+\frac{\lambda+3\pi}{{k_2}^2(3t+k_1)^{\frac{1}{3}}}\right) \tag{35}$$

$$p_m = \frac{(\gamma-1)}{4(3t+k_1)^2(\lambda^2+3\lambda+4\pi^2)}\left((\lambda+2\pi)(l^2+2l-2)+\frac{\lambda+3\pi}{{k_2}^2(3t+k_1)^{\frac{1}{3}}}\right) \tag{36}$$

$$p_c = \frac{(2-\gamma)}{4(3t+k_1)^2(\lambda^2+3\lambda+4\pi^2)}\left((\lambda+2\pi)(l^2+2l-2)+\frac{\lambda+3\pi}{{k_2}^2(3t+k_1)^{\frac{1}{3}}}\right) \tag{37}$$

We can write the Hubble parameter as follows from (12) [4];

$$H = \frac{l}{3t+k_1} \tag{38}$$

The volume is

$$V = k_2k_3k_4[3t+k_1] \tag{39}$$

It is seen that the Hubble parameter decreases with time as the spatial volume increases. The values scale factor, scalar expansion and the shear scalar are obtained as

$$a = [\,k_2k_3k_4(3t+k_1)]^{\frac{1}{3}} \;,\; k_4 = [k_1k_2k_3]^{\frac{1}{3}} \tag{40}$$

$$\theta = \frac{3}{3t+k_1} \tag{39}$$

$$\sigma^2 = \frac{(l-1)^2}{(3t+k_1)^2} \tag{40}$$

The anisotropy parameter $\Delta = 6\left(\frac{\sigma}{\theta}\right)^2$ is

$$\Delta = \frac{2(l-1)^2}{3} \tag{41}$$

CONCLUSIONS

In the presence of the EoS parameter, we created the Bianchi type-V state equation for f (R, T) gravitation and examined its time-dependent behavior. As a result, we observed that scalar expansion decreased with time in the case of l>0. If the anisotropy parameter is constant, it means deviation from isotropic, indicating that the universe is not isotropic. However, we can observe an isotropic behavior for l=1.

This work supported by İstanbul University Scientific Research Projects unit under Project 17347

ISBN:978-605-83516-6-0

REFERENCES

1.Momeni D., Myrzakulov R., Güdekli E., "Cosmological viable mimetic f(R) and f(R,T) theories via Noether symmetry", INTERNATİONAL JOURNAL OF GEOMETRİC METHODS IN MODERN PHYSICS, vol.12, 2015

2.Güdekli E., "Conformal Invariance in f(R,T) Gravity", ICLT 2015 : 17th International Conference on Law and Trade, ISTANBUL, TURKEY, 16-17 February 2015, pp.1-3

3.Güdekli E., Demir E., "Conformal Invariance in Mimetic f(R,T) Gravity" TURKISH PYHSICS SOCIETY 32ND INTERNATIONAL PHYSICS CONGRESS, MUGLA, TURKEY, 5-9 September 2016, pp.21

4.Shukla P. and Jayadev A. "LRS Bianchi Type-I Cosmology with Gamma Law EoS in f(R, T) Gravity" Department of Mathematics Birla Institute of Technology and Science-Pilani Hyderabad Campus, HYDERABAD-500078, INDIA, March 28, 2016

5. Myrzakulov, R.(2012). FRW Cosmology in F(R,T) gravity, Eur. Phys. J.C, Vol.72, p.2203.

BOOK OF FULL TEXT PROCEEDINGS TURKISH PHYSICAL
SOCIETY 35th INTERNATIONAL PHYSICS CONGRESS (TPS35)
TPS35, Vol.01, No.07, pp.432-436.
ISBN:978-605-83516-6-0 15 December 2019

The Purity and Entropy of a Multi-Site Dissipative System Driven by Random Telegraph Noise

Arzu Kurt[1,a)], Matteo A. C. Rossi[2,b)] and Jyrki Piilo[2,c)]

[1]*Department of Physics, Bolu Abant İzzet Baysal University, 14030-Bolu, Turkey*
[2]*QTF Centre of Excellence, Turku Centre for Quantum Physics, Department of Physics and Astronomy, University of Turku, FI-20014 Turun Yliopisto, Finland*

[a)]Corresponding author: arzukurt@ibu.edu.tr
[b)]matteo.rossi@utu.fi
[c)]jyrki.piilo@utu.fi

Abstract. We consider a three site system that is in contact with a thermal bath and driven by a classical noise and investigate the dynamics of the purity and entropy of the system by using the variational polaron master equation approach. The driving classical noise modulates the system site energies and can be described as a two-state random telegraph noise. We have found that purity and entropy dynamics exhibit qualitatively very rich structure as a result of the interplay between the classical noise and the quantum bath.

INTRODUCTION

In open-quantum systems, maintaining the quantumness of the relevant system is a crucial problem that needs to be dealt with in various areas of the physics ranging from quantum computation [1, 2, 3] to quantum biology [4, 5]. Two of the important quantumness measures are the purity and the entropy of the state of the system in contact with a bath, which are indicators of the mixedness and disorder of the quantum state. In order to study the dynamics of the purity and entropy, authors has considered the description of the environment as either an external classical noise [1, 4] or a thermal bath [2, 5, 3] and found that those quantities show either monotonic decay or slightly damped oscillations depending on the environmental temperature, decoherence strength as well as noise strength. For instance, Gillard et. al. [3] considered a qubit in contact with a thermal bath at arbitrary temperature in order to study informational quantities including the entropy and reported that there are three different entropy tendencies depending on the extreme noise temperatures. Cheng and Silbey [1] study a model where the coupling to the bath is treated as stochastic fluctuations-delta correlated Gaussian noise- to investigate the influence of the noise in quantum computations and show that the purity monotonically reaches to its maximum possible value (1) with the increasing noise strength.

In the present study, we consider a three sites system and investigate the dynamics of the site purity and entropy dynamics. In the model, each site is assumed to have its independent quantum bath and the fluctuation of the site energies can be described by random telegraph noise. Our aim is to study the effect of external noise on the dynamical behavior of the quantumness/entanglement measures purity and entropy. The details of the noisy variational polaron frame master equation approach is given in Ref. [6].

We organise the article as follows. In Section 1, we describe the model and present the variational master equation. Then in Sec. 2, we report the results for the dynamics of purity and entropy of a three site dissipative system. Finally, we discuss the obtained results in Sec. 3.

ISBN:978-605-83516-6-0

MODEL

We consider a system of which site energy levels are driven by RTN and interact also with their own environment. The system total Hamiltonian is given by

$$H = H_S(t) + H_E + H_I, \tag{1}$$

where $H_S(t)$ (H_E) is the Hamiltonian of the system (the bath modeled by an ensemble of harmonic oscillators) and H_I is the interaction between the system and the bath. Each term can be given the following:

$$\begin{aligned} H_S(t) &= \sum_n \epsilon_n(t)|n\rangle\langle n| + \sum_{n\neq m} V_{nm}|n\rangle\langle m|, \\ H_E &= \sum_{n,k} \omega_{n,k}\, b^\dagger_{n,k} b_{n,k}, \\ H_I &= \sum_{n,k} |n\rangle\langle n|(g_{n,k} b^\dagger_{n,k} + g^*_{n,k} b_{n,k}), \end{aligned}$$

where $b_{n,k}(b^\dagger_{n,k})$ is the annihilation (creation) operator for the kth oscillator on the nth site, $|n\rangle$ is the state of the system in which we consider that there exists a single electronic excitation, V_{nm} is the electronic coupling between nth and mth sites, and $g_{n,k}$ is the coupling strength between the excitation on the nth site and the kth harmonic mode of its bath. Also, $\epsilon_n(t) = \epsilon_n + \Omega_n\alpha_n(t)$ are the time-dependent site energies of the system. Here, ϵ_n are the static site energies while $\alpha(t)$ describes the external noise which is a two state telegraph process with zero average $\langle\alpha(t)\rangle = 0$ and the exponentially decreasing correlations $\langle\alpha(t)\alpha(t')\rangle = e^{-\nu|t-t'|}$. The correlation time of the noise is $\tau = 1/\nu$ where ν can be considered as the noise frequency which is a measure of the average number of noise flippings in unit time. Ω is the amplitude of the noise signal.

The coupling to the bosonic environment can modeled as a spectral density function $J_n(\omega)$ describing the coupling strength between the system and the bath as function of environmental modes, and defined by $J_n(\omega) = \sum_k |g_{n,k}|^2\delta(\omega-\omega_k)$. The reorganization energy (E^r_n) that is a good measure of the strength of the interaction to the bath is characterized by $E^r_n = \int_0^\infty d\omega\, J_n(\omega)/\omega$ in the continuum regime. In the present work, we use the spectral density $J_n(\omega)$ containing both overdamped and a discrete underdamped vibrational modes. We present the behavior of spectral density and variational transform function in terms of environmental frequency ω in Fig.1. For more information about the expression of the spectral density function see Ref [6].

In this study, in order to describe the dynamics of the reduced density matrix $\rho_S(t) = \mathrm{Tr}_E(\rho)$, we transform $\rho_S(t)$ into the variational polaron frame, which makes $\tilde{\rho}_S(t)$ presented by [6]:

$$\frac{\partial\tilde{\rho}_S(t)}{\partial t} = -i\left[\tilde{H}_S(t), \tilde{\rho}_S(t)\right] - \sum_{i,j=1}^{N^2}\int_0^t ds\langle E_i(s)E_j(0)\rangle\left(\{S_i\, S_j(s)\,\tilde{\rho}_S(t) - S_j(s)\tilde{\rho}_S(t)S_i\} + hc\right), \tag{2}$$

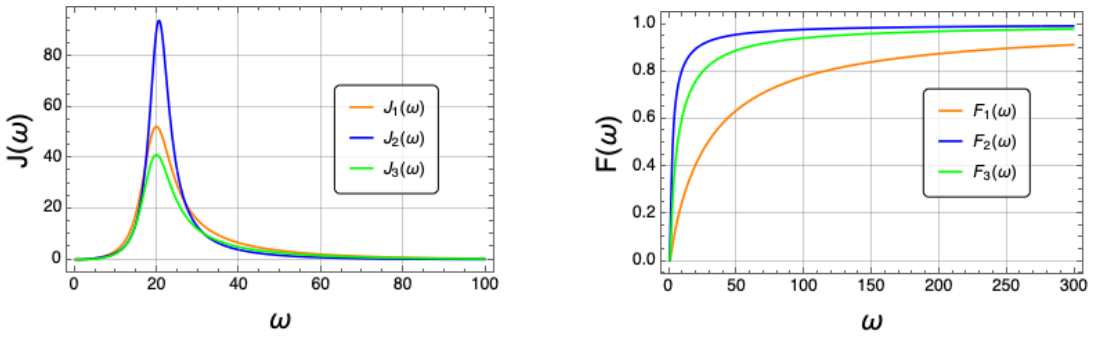
where $\langle E_i(s)E_j(0)\rangle$ are the bath correlation functions (see Eqs. (17)-(21) in [7]) and $S_j(t) = U(t)S_jU^\dagger(t)$ is the jth system operator in the Schrödinger picture by means of the time evolution operator $U(t) = \mathcal{T}\exp\left(-i\int_0^t \tilde{H}_S(t')dt'\right)$ where $\mathcal{T}$ is the time-ordering operator which determines how the system changes in time. Since $\tilde{H}_S(t)$ is time-dependent because of the RTN on the site energies, it does not commute with itself at different times. Obtaining $U(t)$ requires time ordering, which is not practical. So we establish the procedure to calculate it for each noise realization. Let us assume the RTN flipping times be $\{0, t_1, t_2, \ldots, t_F\}$ in the time interval $[0, t_F]$. $\tilde{H}_S(t)$ would be time-independent because of the character of $\alpha(t)$ that becomes either 1 or -1 in the consecutive times, that results in $U(t)$ easily calculated as $\exp(-i\,\tilde{H}_S\,t)$. In this case, $U(t)$ in the interval $[0, t_1]$ is formed by either $U_+(t)$ or $U_-(t)$ depending on RTN being in state $+1$ or -1. Basically, if $t_n < t < t_{n+1}$, $U(t)$ would be to $U_+(t-t_n)\,U_-(t_n-t_{n-1})\,U_+(t_{n-1}-t_{n-2})\ldots U_+(t_2-t_1)\,U_-(t_1)$ providing that the $\alpha(t)$ starts from negative values and the number of noise flippings in $(0, t_{n+1}]$ is odd. It is noted that above procedure is valid when the site energies are driven by the same noise with different amplitude, i.e., collective noise affects those energy levels. When the noises affecting the site energies are independent, the method above would be cumbersome to implement. One could use either an approximate method such as Magnus expansion to obtain $U(t)$ or can built it as the solution of Schrödinger equation for different initial conditions as follows: Let $|\psi(t)\rangle = \sum_{i=1}^N a_i(t)|i\rangle$ be the state vector of the system with N-sites and the Shrödinger equation for $|\psi(t)\rangle$ is:

$$i\frac{d}{dt}|\psi(t)\rangle = \tilde{H}_S(t)|\psi(t)\rangle. \tag{3}$$

ISBN:978-605-83516-6-0

Since the state vector $|\psi(t)\rangle$ can be written as $|\psi(t)\rangle = U(t)|\psi(0)\rangle$, the solutions of Eq. (3) for different initial conditions can be used to build columns of time evolution operator $U(t)$.

In the present study, we will examine the dependence of the noise amplitude on the purity and the entropy for the 3-site noisy dissipative system based on different bath descriptions-RTN only and bath+RTN. Let us introduce those quantities: (i) the purity of a quantum system whose state is described by $\rho_S(t)$ is defined as $P(t) = \mathrm{Tr}(\rho_S(t)^2)$ and is a measure of degree of mixedness of the state, (ii) the von-Neumann entropy $S(t) = -\mathrm{Tr}(\rho_S(t)\ln\rho_S(t))$ of the state is a measure of the disorder of the quantum state.



(a) (b)

FIGURE 1. (a) The spectral density and (b) variational transform function as a function of environmental frequencies ω for the 3-site system calculated by the following parameters: $\omega_{c,1,3} = 10, \omega_{c,2} = 20/3$, $\sigma_{1,2,3} = 0.7$, $S_1 = 0.06$, $S_2 = 0.04$, $S_3 = 0.02$, $\xi_{1,2,3} = 0.5$, $\Lambda_{1,3} = 20, \Lambda_2 = 15$, $\zeta_{1,2,3} = 20$, $X_1 = 0.5$, $X_2 = 0.6$, and $X_3 = 0.4$. Here the spectral density (reorganization energy) obtained by those values would be in the intermediate system-bath interaction regime. In order to get weak system-bath coupling for 3-site system, S_i and X_i need to be multiplied by $1/6$.

RESULTS

We study the dynamics of entropy and purity of the 3-site system as function of the noise amplitude for various configurations of the system and noise descriptions. The system we consider has static site energies ($\epsilon_1 = 20$, $\epsilon_2 = 10$, $\epsilon_3 = 0$). The electronic coupling network is assumed to be linear with two different sets of tunneling matrix elements as ($V_{12} = V_{23} = 10$) and ($V_{12} = V_{23} = 1$) which would be examples of strong and weak electronic coupling settings. The environment is assumed to be at low temperature ($k_BT = 1$ ps^{-1}). Concerning the properties of the external noise; we assume two different noise motifs of the form $\Omega = \{1, 0, 0\}$ and $\Omega = \{1, -1, 0\}$. The first motif describes a system for which only the site 1 is driven by a noise while the last one describes a system whose first and second sites are driven at opposite polarities. We, also, consider two different noise models called independent and collective. For the independent model, each site has its independent noise signal while for the collective model, $\alpha_n(t)$ are same for each n but Ω_n might be different. The results presented in this section are obtained by ensemble averaging approach for the noise averaging. In this approach, one numerically solves the master equation in Eq. (2) for N_n realizations of the noise and average the resulting ρ_S which is used to calculate purity ($P(t) = \mathrm{Tr}(\rho_S(t)^2)$) and entropy ($S(t) = -\mathrm{Tr}(\rho_S(t)\ln\rho_S(t))$). We will report the findings for two different noise frequencies $\nu = 0.001$ and 5ps^{-1} which correspond to static and high frequency limits. The number of noise realizations N_n for $\nu = 0.001$ is only two (eight), because in the time interval considered in the present study ($t \in [0, 3]$ps) the $\alpha_n(t)$ can take only ± 1 values for the collective (independent) noise models. For the high frequency noise, $N_n = 100$ is found to be adequate for reasonably converged purity and entropy values.

Figs. 2 (a)-(c) present the dynamics of the purity $P(t)$ of the system as function of noise amplitude Ω for three different combinations of noise frequency and site motifs. In each subfigure, we display the dynamics for a pure noise model called RTN only for which the effect of the thermal environment is ignored and dynamics for the bath+RTN model which considers the effects of both the quantum bath and the external classical noise. Figs. 2 (a)-(c) give an indication of possibilities for manipulating the purity dynamics by using different driving noise parameters: Fig. 2(a) is an example of the system approaching maximally mixed state with increasing noise amplitude while Fig. 2(b) presents a situation where increasing the noise amplitude drives the system to a pure state. Furthermore, Fig. 2(c) shows that

ISBN:978-605-83516-6-0

one can induce purity oscillations with carefully chosen noise parameters. In Fig. 2(a), we present $P(t)$ as function of noise amplitude for a system with strong electronic and intermediate bath coupling. For this example, only the site 1 is driven by high frequency RTN. One can see from Fig. 2(a) that increasing noise strength drives the system to the maximally mixed state which is the most expected behaviour in such dissipative systems where increasing noise akin to increasing temperature. As is well known, the RTN only model corresponds to an infinite temperature bath, which would lead to $P(t \to \infty) = 1/3$ for the present system which is achieved even in relatively short $t = 3$ps. $P(t)$ curve in Fig. 2(a) for the bath+RTN model shows that as the strength of the driving noise is increased, RTN overcomes the effect of the quantum bath and dynamics of both models become qualitatively similar.

In Fig. 2(b), system has weak electronic (intermediate bath) coupling and a collective RTN with high frequency drives the sites 1 and 2 at opposite polarities. Interestingly, it is found that the system approaches the pure state as the noise strength is increased for both the RTN only and bath+RTN models for this setting which can be understood as the noise induced suppression of the tunneling at high noise strength. One can, also, observe that when the noise amplitude is comparable to the site energy difference (10 ps^{-1}), purity is minimum for both models. In Fig. 2(c), we present $P(t)$ dynamics as function of Ω for a system with strong-electronic and weak-bath coupling which is driven by an independent static RTN with $\Omega = \{1, -1, 0\}$ noise motif. Contrary to two cases we have considered above, $P(t)$s for the RTN only and bath+RTN models are found to be qualitatively different here: While purity of the RTN only model oscillates with increasing Ω, that of bath+RTN model approaches to the value of the maximally mixed state. We should note that at the long time limit, which is not shown here, $P(t)$ of RTN only model would be equal to 1/3. Considering the fact that the system-bath interaction is weak for this set of problem parameters, one would expect the difference between $P(t)$s for the RTN only and bath+RTN models to be smaller compared to the differences for the two other set of parameters discussed above. The difference stems mainly from the way very low frequency noise averaging: for the independent noise model with $\Omega = \{1, -1, 0\}$ motif, we have only four distinct noise realizations to consider averaging. Each one of those realizations would create coherent dynamics with different periods for the RTN only model and their average would produce the dynamics seen in Fig. 2(c). Dynamics for the bath+RTN model would be exponential decay for each noise realization. Averaging over those decays would lead to the observed behaviour.

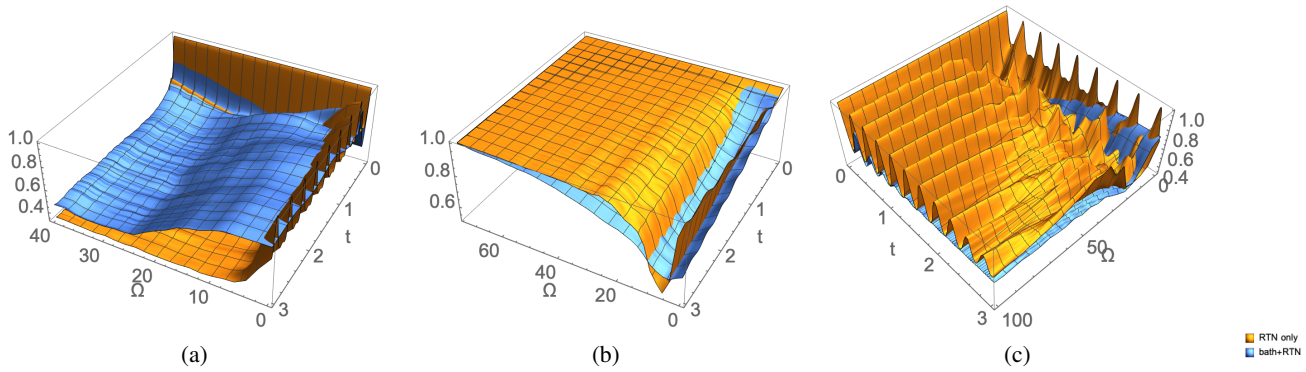
Fig. 3 shows the time evolution of the entropy $S(t)$ of the system for the same conditions as in Fig. 2. Purity and entropy are two types of measures that describe the mixedness of the system in time; for pure states $P = 1$ and $S = 0$, while for the maximally mixed states, those values would be $1/N$ and $\log N$, respectively. So, it is expected that these quantities might have inversely proportional behaviors, that can be seen from Figs. 2 and 3 where the results indicate that entropy $S(t)$ behaves in a inversion fashion to purity $P(t)$. That is, it is clearly seen that wherever the purity of the system increases, the entropy starts to decrease. For instance, we observe that as increasing noise amplitude Ω, $S(t)$ tends to increase due to the fact that the system in a strong-electronic and intermediate-bath coupling regime is in the maximally mixed state (see Figs. 2 and 3(a)). Fig.3(b) displays the similar dependence of the $S(t)$ on the increasing noise amplitude for two models, which results in the entropy being zero. It means that the system that may not find a chance to tunnel between sites due to the weak-electronic coupling will maintain its purity (see Fig.2(b)) and naturally its entropy will end up with zero (see Fig.3). Also, we observe that there is a oscillation behavior of the entropy of the system with very low independent noise in the strong-electronic and weak-bath coupling regime, which is expected due to the fact that purity and entropy measures may be inversely interconnected with respect to the mixedness of the system in Fig.3(c). We can conclude that the behavior of the quantities we consider in the present study strongly depends on different bath models, noise parameters as well as the magnitude of the system-bath coupling.

CONCLUSIONS

In this work, we have studied the evolution of purity and entropy for a dissipative three-site system whose site energies fluctuate as random telegraph noise, by using a variational polaron master equation.

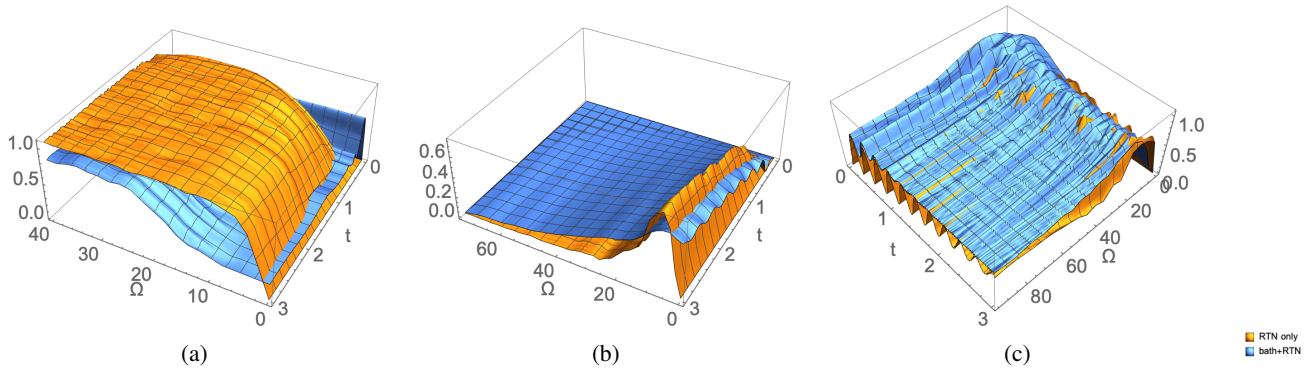
Our main aim was to investigate the dependence of the quantumness measures of the system for two different bath models (RTN only and bath+RTN) on the noise parameters (frequency and amplitude) as well as the noise configurations. We observed that mixedness of the three-site system has prominent dependence on both environmental and system parameters. The results for the weak-electronic coupling under high frequency noise driving clearly shows that the simultaneous action of stochastic noise and a quantum bath preserves to the quantumness of the system as the noise amplitude increases.

ISBN:978-605-83516-6-0



(a) (b) (c)

FIGURE 2. The time evolution of purity of the three-site system as a function of noise amplitude (a) in strong-electronic and intermediate-bath coupling regime at high frequency ($\nu = 5\text{ps}^{-1}$) and its noise motif: $\Omega = \{1, 0, 0\}$, (b) in weak-electronic and intermediate-bath coupling regime at collective high frequency and its noise motif: $\Omega = \{1, -1, 0\}$, (c) in strong-electronic and weak-bath coupling regime at independent low noise ($\nu = 0.001\text{ps}^{-1}$) and its noise motif: $\Omega = \{1, -1, 0\}$.



(a) (b) (c)

FIGURE 3. The dynamics of entropy of the 3-site system versus noise amplitude for the same conditions as in Fig.2.

ACKNOWLEDGMENTS

We acknowledge fruitful discussions with Resul Eryiğit. AK acknowledges financial support from The Scientific and Technological research Council of Turkey (TUBITAK) Project no. 1059B191700098. MR and JP acknowledge financial support from the Academy of Finland via the Centre of Excellence program (Project no. 312058 as well as Project no. 287750). MR acknowledges support from the Turku Collegium for Science and Medicine.

REFERENCES

[1] Y. C. Cheng and R. J. Silbey, Phys. Rev. A **69**, p. 052325 (2004).
[2] K. L. Hur, Annals of Physics **323**, 2208–2240 (2018).
[3] N. Gillard, E. Belin, and F. Chapeau-Blondeau, Physica A **507**, 219–230 (2018).
[4] B. C. Smyth, F. Fassioli, and G. D. Scholes, Phil. Trans. R. Soc. A **370**, 3728–3749 (2012).
[5] A. W. Chin, E. Mangaud, O. Atabek, and M. Desouter-Lecomte, Phys. Rev. A **97**, p. 063823 (2018).
[6] A. Kurt, M. A. C. Rossi, and J. Piilo, arXiv:1909.00167 (2019).
[7] F. A. Pollock, D. P. S. McCutcheon, B. W. Lovett, E. M. Gauger, and A. Nazir, New J. Phys. **15**, p. 075018 (2013).

BOOK OF FULL TEXT PROCEEDINGS TURKISH PHYSICAL
SOCIETY 35th INTERNATIONAL PHYSICS CONGRESS (TPS35)
TPS35, Vol.01, No.07, pp.437-446. 15 December 2019
ISBN:978-605-83516-6-0

String Cloud with Perfect Fluid Matter Distribution for Homogenous and Anisotropic Space-Time in $f(R,T)$ Gravity

Cihan KÖMÜRCÜ [1, a)] and Can AKTAŞ [2, b)]

[1]*Graduate School of Natural and Applied Sciences, Çanakkale Onsekiz Mart University, Terzioğlu Campus 17020, Turkey*
[2]*Department of Mathematics, Arts and Sciences Faculty, Çanakkale Onsekiz Mart University, Terzioğlu Campus 17020, Turkey*

[a)] Corresponding author: cihan_komurcu@hotmail.com
[b)] canaktas@comu.edu.tr

Abstract. In this study, we have investigated string cloud with perfect fluid solutions for homogenous and anisotropic space-time models in $f(R,T)$ theory, which plays an important role in the solution of the acceleration problem of the universe. In addition, we have obtained specifically Kasner's space-time solutions. Their counterparts in the General Relativity Theory were also calculated. We have analyzed the physical results of our solutions with graphs.

INTRODUCTION

Our universe is approximately 13.8 billion years old and is homogeneous, isotropic and almost flat when viewed at large scale (> 100Mpc), although locally solar, milky way galaxy and other galaxies are inhomogeneous and anisotropic (Caroll, 2004; Hobson et al., 2006). This assumption CMB, Planck, WMAP and so on observations (Caroll, 2004; Hobson et al., 2006). According to current observations, the model that best describes the universe is straight FRW space (Caroll, 2004; Hobson et al., 2006). However, this model fails to explain the content of the universe (Caroll, 2004; Hobson et al., 2006). Therefore, the content of the universe is explained better by taking various space-time models. General Relativity theory explains the structure of the universe on a large scale (Aktaş et al., 2012). However, it cannot fully explain issues such as dark energy and dark matter that are thought to cause the universe to accelerate (Aktaş et al., 2012). General The theory of relativity was insufficient to explain dark energy and dark matter, which led to the emergence of other alternative gravitation theories (Aktaş et al., 2012). The most well-known of these theories are Lyra theory, Brans-Dicke theory, $f(T)$, $f(G)$ and $f(R,T)$ theory etc. (Aktaş et al., 2012). In this study, we have examined the homogeneous anisotropic Bianchi type I universe model for perfect fluid matter distribution in $f(R,T)$ gravitation theory.

In 2011, Harko et al. have put forward an alternative gravitation theory namely $f(R,T)$ theory. In this study, Harko et al. have suggested three $f(R,T)$ function as $f(R,T)=T+2f(T)$, $f(R,T)=f_1(R)+f_2(T)$, $f(R,T)=f_1(R)+f_2(R)f_3(T)$. They used the flat Robertson-Walker metric for space-time. After the study of Harko et al., this theory has been studied for different space-time metrics. Sharif and Zubair $f(R,T)$ discussed the thermodynamics of the theory in detail (Sharif and Zubair, 2012). A study of $f(R,T)$ theory and cosmic expansion was conducted by Ahmed and Pradhan (Ahmed and Pradhan, 2014). $f(R,T)$ in the theory of solutions containing perfect fluid and scalar field are also examined by Sharif and Zubair (Sharif and Zubair, 2012). Sofuoğlu has investigated the $f(R,T)$ theory for the Bianchi IX universe model (Sofuoğlu, 2016). Singh and Bishi have considered the Bianchi I universe model using the quadratic equation of state in $f(R,T)$ theory (Singh and Bishi, 2015). Shamir has investigated $f(R,T)$ theory for the LRS Bianchi type universe model (Shamir, 2015). Reddy and Umadevi have solved bulk viscous fluid for Kantowski Sachs universe model in the $f(R,T)$ theory (Reddy and Umadevi, 2014). Zubair et al. have investigated $f(R,T)$ theory the compatibility of the theory of killing vector field (Zubair et al, 2016). Momeni

et al. have obtained the second law of thermodynamics in $f(R,T)$ gravity (Momeni et al., 2016). Singh and Kumar have researched modified holographic dark energy model in $f(R,T)$ theory (Singh and Kumar, 2016). Singh et al. have investigated various universe models with cosmological constants in $f(R,T)$ theory (Singh et al., 2015-2016). Reddy et al. have studied the bulk viscous cosmological model in $f(R,T)$ theory (Reddy et al., 2014). Also, Ramesh and Umadevi (2016), Amani and Dehneshin (2015), Chattopadhyay (2014) have studied the FRW universe model in $f(R,T)$ theory. Aktaş and Aygün have examined the magnetized strange quark matter distribution for the FRW universe model in $f(R,T)$ theory (Aktaş and Aygün, 2017). Aygün et al. have studied strange quark matter solutions with the cosmological constant in the Marder universe within the framework of $f(R,T)$ theory (Aygün et al., 2016).

FIELD EQUATIONS IN $f(R,T)$ GRAVITY

The action integral is given by,

$$S=\int\left(\frac{1}{16\pi G}f(R,T)+L_m\right)\sqrt{-g}d^4x \tag{1}$$

In the form of Einstein-Hilbert axiom R Ricci scalar curvature instead of R and T is the trace of the stress-energy tensor of T dependent $f(R,T)$ taking an arbitrary function (Harko et al., 2011). Here is L_m the Lagrange density of matter. The stress-energy tensor of matter (T_{ik}),

$$T_{ik}=-\frac{2}{\sqrt{-g}}\frac{\delta\left(\sqrt{-g}L_m\right)}{\delta g^{ik}}=g_{ik}L_m-2\frac{\partial L_m}{\partial g^{ik}} \tag{2}$$

is provided with (Harko et al., 2011). Now, if the variation of equation (2) is taken to obtain the geometric part of Einstein field equations $(G=c=1)$, we get

$$f_T(R,T)R_{ik}-\frac{1}{2}f(R,T)g_{ik}+(g_{ik}\Box-\nabla_i\nabla_k)f_R(R,T)=[8\pi-f_T(R,T)]T_{ik}-T_{ik}\Theta_{ik} \tag{3}$$

here, $f_R(R,T)$ shows the derivative of $f(R,T)$ with respect to R and $f_T(R,T)$ shows the derivative of $f(R,T)$ with respect to T, $\Box$ D'Alembert operator $\Box=\nabla^i\nabla_i=g^{ik}\nabla_i\nabla_k$ and ∇_i covariant derivative (Harko et al., 2011). Also, Θ_{ij} are defined as follows

$$\Theta_{ik}=g^{\alpha\beta}\frac{\delta T_{\alpha\beta}}{\delta g^{ik}}=-2T_{ik}+g_{ik}L_m-2g^{\alpha\beta}\frac{\partial^2 L_m}{\partial g^{\alpha\beta}\partial g^{ik}}=-2T_{ik}-pg_{ik} \tag{4}$$

where the Lagrange density of matter. If the perfect fluid is taken as the material distribution, the Lagrange density is $L_m=-p$ (Harko et al., 2011). In 2011, Harko et al. described Einstein's field equations with the help of a $f(R,T)$ function, which would change both the geometry and the material.

METRIC, FIELD EQUATIONS AND SOLUTIONS

In the $(x^0,x^1,x^2,x^3)=(t,x,y,z)$ coordinate, the Bianchi type I metric is as follows.

$$ds^2=dt^2-A^2(t)dx^2-B^2(t)dy^2-C^2(t)dz^2 \tag{5}$$

In equation (6), specially we can take $A(t)=t^{n_1}$, $B(t)=t^{n_2}$ and $C(t)=t^{n_3}$. In this case, our metric is as fallows

$$ds^2=dt^2-t^{2n_1}dx^2-t^{2n_2}dy^2-t^{2n_3}dz^2 \tag{6}$$

where t cosmic time, and n_1,n_2 and n_3 are constants.

ISBN:978-605-83516-6-0

The string cloud with perfect fluid for the stress-energy tensor (T_{ik}) is given by

$$T_{ik} = (\rho + p)u_i u_k - p g_{ik} - \lambda x_i x_k \tag{7}$$

where p, ρ and λ are, respectively, the pressure, energy density for perfect fluid and tension energy density for string cloud (Tiwari et al., 2019). Also where u^i 4 −velocity vector $u^i = \left(\frac{1}{\sqrt{g_{00}}}, 0,0,0\right) = (1,0,0,0)$ and x^i is the vector that determines the direction of the anisotropy and the direction of the string is taken parallel to the x-axis $x^i = \left(0, \frac{1}{\sqrt{-g_{11}}}, 0,0\right) = (0, t^{-n_1}, 0,0)$. Also, there are $u^i u_k = -x^i x_k = 1$ and $u^i x_k = 0$ relation between them.

The particle energy density (ρ_p) attached to the cords and the trace of the stress-energy tensor (T) are as follows

$$\rho_p = \rho - \lambda \tag{8}$$

$$T = \rho - 3p + \lambda \tag{9}$$

The physical and kinematical parameters such as directional expansion scalar (θ), shear scalar (σ^2), average scale factor (a), volume (V), the components of Hubble parameter in the directions of x, y and z axes, respectively, (H_x), (H_y) and (H_z), Hubble parameter (H), anisotropy parameter $(\bar{A})$ and deceleration parameter (q) are given by

$$\theta = \frac{n_1 + n_2 + n_3}{t} \tag{10}$$

$$\sigma_1^1 = \frac{2n_1 - n_2 - n_3}{3t} \tag{11}$$

$$\sigma_2^2 = \frac{2n_2 - n_1 - n_3}{3t} \tag{12}$$

$$\sigma_3^3 = \frac{2n_3 - n_1 - n_2}{3t} \tag{13}$$

$$\sigma^2 = \frac{n_1^2 + n_2^2 + n_3^2 - n_1 n_2 - n_1 n_3 - n_2 n_3}{3t^2} \tag{14}$$

$$V = a^3 = t^{n_1 + n_2 + n_3} \tag{15}$$

$$H_x = \frac{n_1}{t} \tag{16}$$

$$H_y = \frac{n_2}{t} \tag{17}$$

$$H_z = \frac{n_3}{t} \tag{18}$$

$$H = \frac{1}{3}\left(\frac{n_1 + n_2 + n_3}{t}\right) \tag{19}$$

$$\bar{A} = \frac{2(n_1^2 + n_2^2 + n_3^2 - n_1 n_2 - n_1 n_3 - n_2 n_3)}{(n_1 + n_2 + n_3)^2} \tag{20}$$

$$q = -1 + \frac{3}{n_1 + n_2 + n_3} \tag{21}$$

and

$$\frac{\sigma}{\theta} = \frac{\sigma}{3H} = \frac{1}{\sqrt{3}} \frac{(n_1^2 + n_2^2 + n_3^2 - n_1 n_2 - n_1 n_3 - n_2 n_3)^{\frac{1}{2}}}{n_1 + n_2 + n_3} \tag{22}$$

From equations (3), (6) and (7), we obtain field equations in $f(R,T)$ gravity for $f(R,T) = R + f_2(R) f_3(T)$

$$n_1 n_2 + n_1 n_3 + n_2 n_3 = \frac{t}{2[1 + f_3(T) f_2'(R)]} [16\pi t\rho + t f_2(R)\Big(f_3(T) + 2(p+\rho) f_3'(T)\Big) - \\ - f_3(T)(t R f_2'(R) + 2(n_1 + n_2 + n_3)\dot{R} f_2''(R))] \tag{23}$$

$$n_2^2 + n_3^2 + n_2 n_3 - n_2 - n_3 = \frac{t}{2[1 + f_3(T) f_2'(R)]} [16\pi t(-p + \lambda) + t f_2(R)(f_3(T) + \\ + 2\lambda f_3'(T)) - f_3(T)(t R f_2'(R) + 2 f_2''(R)\left((n_2 + n_3)\dot{R} + t\ddot{R}\right) + 2t\dot{R}^2 f_2'''(R))] \tag{24}$$

$$n_1^2 + n_3^2 + n_1 n_3 - n_1 - n_3 = \frac{t}{2[1 + f_3(T) f_2'(R)]} [-16p\pi t + t f_2(R) f_3(T) - \\ - f_3(T)(t R f_2'(R) + 2 f_2''(R)((n_1 + n_3)\dot{R} + t\ddot{R}) + 2t\dot{R}^2 f_2'''(R))] \tag{25}$$

$$n_1^2 + n_2^2 + n_1 n_2 - n_1 - n_2 = \frac{t}{2[1 + f_3(T) f_2'(R)]} [-16p\pi t + t f_2(R) f_3(T) - \\ - f_3(T)(t R f_2'(R) + 2 f_2''(R)\left((n_1 + n_2)\dot{R} + t\ddot{R}\right) + 2t\dot{R}^2 f_2'''(R))] \tag{26}$$

We can investigate for the solutions of field equations $(23) - (26)$ for some $f(R,T)$ functions.

The $f(R,T) = R + 2\mu T$ Model

In the field equations $(23) - (26)$, if we take $f_2(R) = 1$, $f_3(T) = 2\mu T$ and eliminating these equations according to p, ρ and λ, $(n_2 - n_3)(n_1 + n_2 + n_3 - 1) = 0$ is obtained. There are two situations; for $(n_1 + n_2 + n_3 - 1) = 0$ we get $\lambda = 0$. In order to examine the string situation, we must take $n_2 - n_3 = 0$. For $n_2 = n_3$, our metric is reduced to the LRS Bianchi type I form and p the pressure, ρ the energy density, λ the tension energy density and ω the equation of state parameter are as follows

$$p = -\frac{2(2\pi + \mu)(-1 + n_1)n_1 + (4\pi + \mu)(-1 + n_1)n_2 + 4\pi n_2^2}{4(2\pi + \mu)(4\pi + \mu)t^2} \tag{27}$$

$$\rho = \frac{n_2(\mu + (8\pi + 3\mu)n_1 + 4\pi n_2)}{4(2\pi + \mu)(4\pi + \mu)t^2} \tag{28}$$

$$\lambda = -\frac{(n_1 - n_2)(-1 + n_1 + 2n_2)}{2(4\pi + \mu)t^2} \tag{29}$$

$$\omega = -\frac{2(2\pi + \mu)(-1 + n_1)n_1 + (4\pi + \mu)(-1 + n_1)n_2 + 4\pi n_2^2}{n_2(\mu + (8\pi + 3\mu)n_1 + 4\pi n_2)} \tag{30}$$

The $f(R,T) = R + \mu RT$ Model

In the field equations $(23)-(26)$, if we take $f_2(R) = R$ and $f_3(T) = \mu T$ and eliminating these equations according to p, ρ and λ, $(n_2 - n_3)(n_1 + n_2 + n_3 - 1) = 0$ is obtained. There are two situations; for $(n_1 + n_2 + n_3 - 1) = 0$ we get $\lambda = 0$. In order to examine the string situation, we must take $n_2 - n_3 = 0$. For $n_2 = n_3$, our metric is reduced to the LRS Bianchi type I form and p the pressure, ρ the energy density, λ the tension energy density and ω the equation of state parameter are as follows

$$p = \frac{(-4\pi t^2 + \mu((-1+n_1)(n_1+2n_2)+3n_2^2))K_{11}}{4(8\pi^2 t^4 + \mu((-1+n_1)(n_1+2n_2)+3n_2^2)(-4\pi t^2 + \mu K_{11}))} \tag{31}$$

$$\rho = -\frac{\mu(-1+n_1)^2 n_1^2 + n_1(-8\pi t^2 + 3\mu + 3\mu(-2+n_1)n_1)n_2 + K_{12}}{4(8\pi^2 t^4 + \mu((-1+n_1)(n_1+2n_2)+3n_2^2)(-4\pi t^2 + \mu K_{11}))} \tag{32}$$

$$\lambda = -\frac{\pi t^2 (n_1 - n_2)(-1+n_1+2n_2)}{8\pi^2 t^4 + \mu((-1+n_1)n_1 + 2(-1+n_1)n_2 + 3n_2^2)(-4\pi t^2 + \mu K_{11})} \tag{33}$$

$$\omega = -\frac{(-4\pi t^2 + \mu((-1+n_1)n_1 + 2(-1+n_1)n_2 + 3n_2^2))K_{11}}{\mu(-1+n_1)^2 n_1^2 + n_1(-8\pi t^2 + 3\mu + 3\mu(-2+n_1)n_1)n_2 + K_{12}} \tag{34}$$

where K_{11} and K_{12} are as follows

$$K_{11} = n_1^2 + (-1+n_2)(n_1+n_2) \tag{35}$$

$$K_{12} = 2\big(-2\pi t^2 + \mu + \mu n_1(-4+3n_1)\big)n_2^2 + 5\mu(-1+n_1)n_2^3 + 3\mu n_2^4 \tag{36}$$

The General Theory of Relativity for $f(R,T) = R$ Model

For $n_2 = n_3$, p the pressure, ρ the energy density, λ the tension energy density and ω the equation of state parameter are as follows

$$p = -\frac{4\pi(-1+n_1)n_1 + 4\pi(-1+n_1)n_2 + 4\pi n_2^2}{32\pi^2 t^2} \tag{37}$$

$$\rho = \frac{n_2(8\pi n_1 + 4\pi n_2)}{32\pi^2 t^2} \tag{38}$$

$$\lambda = -\frac{(n_1 - n_2)(-1+n_1+2n_2)}{8\pi t^2} \tag{39}$$

$$\omega = -\frac{4\pi(-1+n_1)n_1 + 4\pi(-1+n_1)n_2 + 4\pi n_2^2}{n_2(8\pi n_1 + 4\pi n_2)} \tag{40}$$

Specific Cases of Gravitational Field Equations in the $f(R,T)$ Models

Case I. When $n_1 = 3$, $n_2 = 4.1$ *and* $n_3 = 4.1$ the deceleration parameter is $q = -0.73$.
Case II. When $n_1 = 1.9$, $n_2 = 1.3$ *and* $n_3 = 1.3$ the deceleration parameter is $q = -0.33$.
Case III. The general LRS Kasner for $n_1 = -\frac{1}{3}$, $n_2 = \frac{2}{3}$ and $n_3 = \frac{2}{3}$ the deceleration parameter is $q = 2$ (Schuecker et al., 1998) also n_1, n_2 and n_3 relationship between $n_1 + n_2 + n_3 = 1$ and ${n_1}^2 + {n_2}^2 + {n_3}^2 = 1$.

The deceleration parameters corresponding to some n_1, n_2 and n_3 values except for the above conditions are as follows.

TABLE 1. The deceleration parameter (q) versus n_1,n_2 and n_3 values.

n_1	$n_2 = n_3$	q	Reference	n_1	$n_2 = n_3$	q	Reference
1.1	1.7	-0.33	Ghaffari et al., 2014	1.5	5.8	-0.77	Pradhan et al., 2019
1.1	2.8	-0.55	Li et al., 2019	1.6	3.5	-0.65	Xu et al, 2007
1.1	6	-0.77	Pradhan et al., 2019	1.6	4.8	-0.73	Cunha et al., 2009
1.2	3.7	-0.65	Xu et al, 2007	1.7	1.4	-0.33	Ghaffari et al., 2014
1.2	5	-0.73	Cunha et al., 2009	1.7	5.7	-0.77	Pradhan et al., 2019
1.3	1.6	-0.33	Ghaffari et al., 2014	1.7	2.5	-0.55	Li et al., 2019
1.3	5.9	-0.77	Pradhan et al., 2019	1.8	3.4	-0.65	Xu et al, 2007
1.4	3.6	-0.65	Xu et al, 2007	1.8	4.7	-0.73	Cunha et al., 2009
1.4	4.9	-0.73	Cunha et al., 2009	1.9	5.6	-0.77	Pradhan et al., 2019
1.5	1.5	-0.33	Ghaffari et al., 2014	2	3.3	-0.65	Xu et al, 2007

From the relation $1 + z = \frac{a_0}{a} = \frac{1}{a}$, with z being the redshift and the present scale factor $a_0 = 1$, we obtain the following time-redshift relation (Capozziello et al., 2015; Sahoo et al., 2018).

$$t = (1+z)^{-\frac{3}{n_1+n_2+n_3}} \tag{41}$$

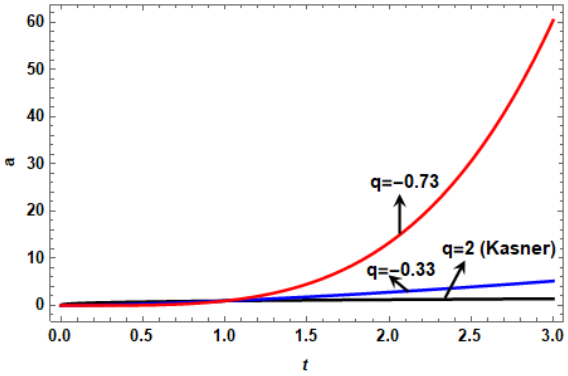


FIGURE 1. The plot of the average scale factor a versus cosmic time t for Case I-II-III and $\mu = -6/\pi$.

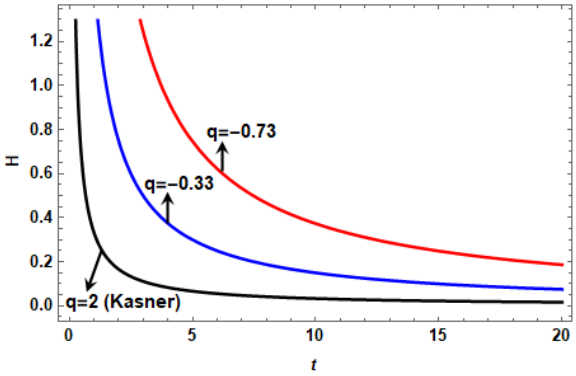


FIGURE 2. The plot of the Hubble parameter H versus cosmic time t for Case I-II-III and $\mu = -6/\pi$.

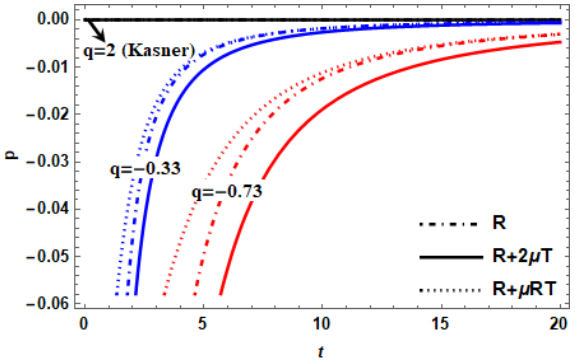


FIGURE 3. The plot of the pressure p versus cosmic time t for Case I-II-III and $\mu = -6/\pi$.

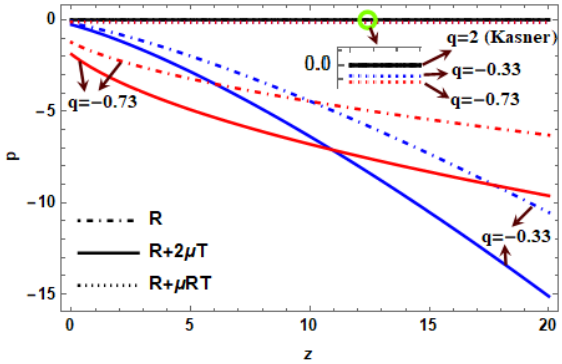


FIGURE 4. The plot of the pressure p versus red-shift z for Case I-II-III and $\mu = -6/\pi$.

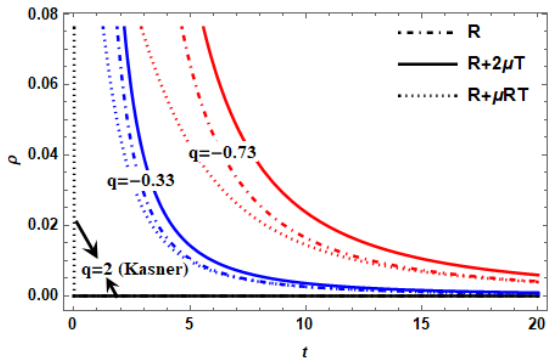


FIGURE 5. The plot of the energy density ρ versus cosmic time t for Case I-II-III and $\mu = -6/\pi$.

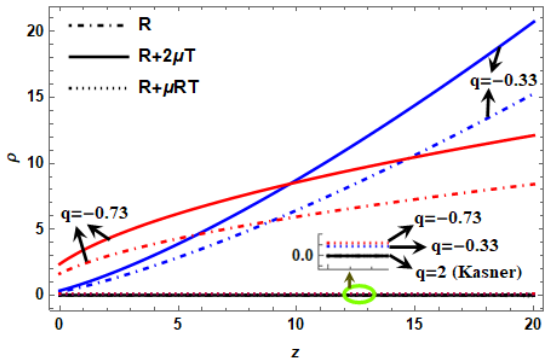


FIGURE 6. The plot of the energy density ρ versus red-shift z for Case I-II-III and $\mu = -6/\pi$.

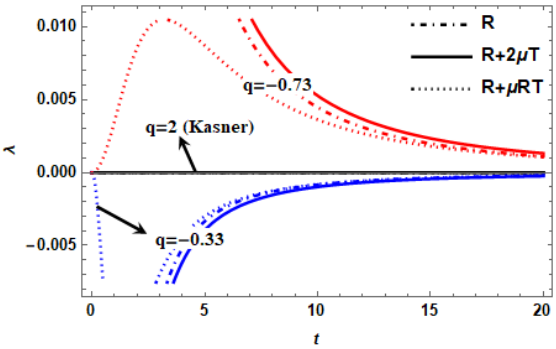


FIGURE 7. The plot of the tension energy density λ versus cosmic time t for Case I-II-III and $\mu = -6/\pi$.

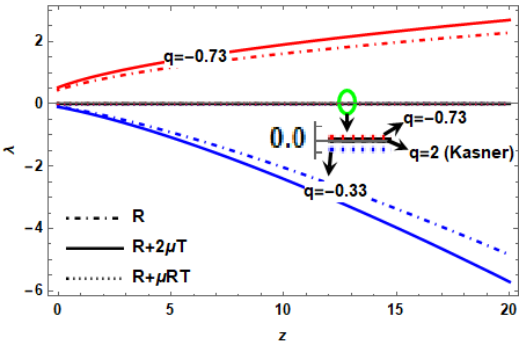


FIGURE 8. The plot of the tension energy density λ versus red-shift z for Case I-II-III and $\mu = -6/\pi$.

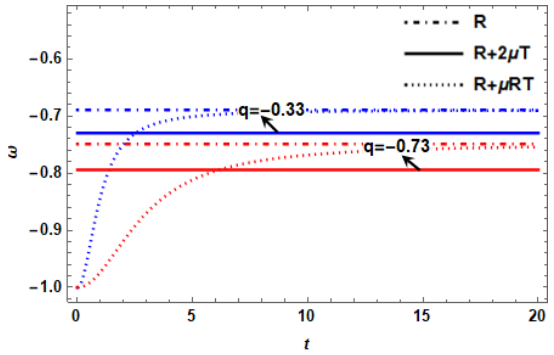


FIGURE 9. The plot of the equation of state parameter ω versus cosmic time t for Case I-II-III and $\mu = -6/\pi$.

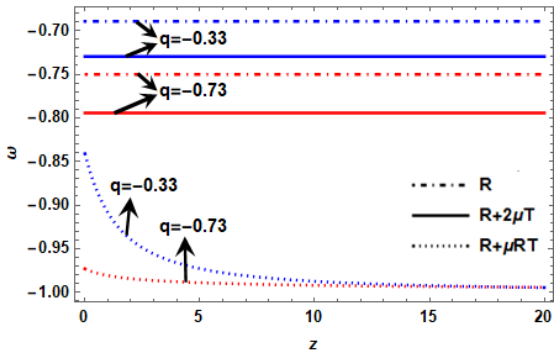


FIGURE 10. The plot of the equation of state parameter ω versus red-shift z for Case I-II-III and $\mu = -6/\pi$.

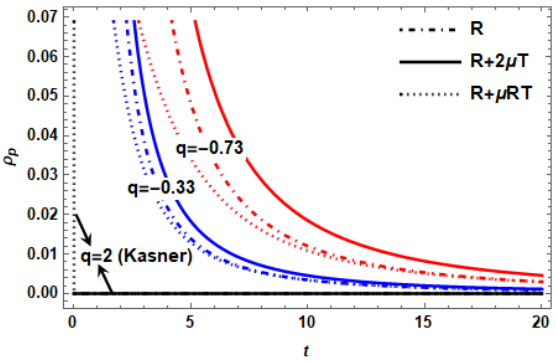


FIGURE 11. The plot of the particle energy density ρ_p versus cosmic time t for Case I-II-III and $\mu = -6/\pi$.

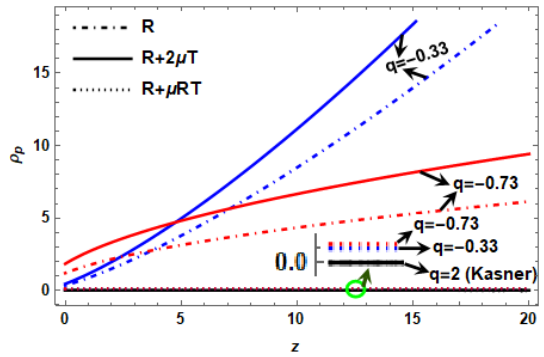


FIGURE 12. The plot of the particle energy density ρ_p versus red-shift z for Case I-II-III and $\mu = -6/\pi$.

Recent observations in cosmology show that the deceleration parameter of the universe is in the range $-1 \leq q \leq 0$ i.e. $q_0 \approx -0.77$ (Pradhan et al., 2019).

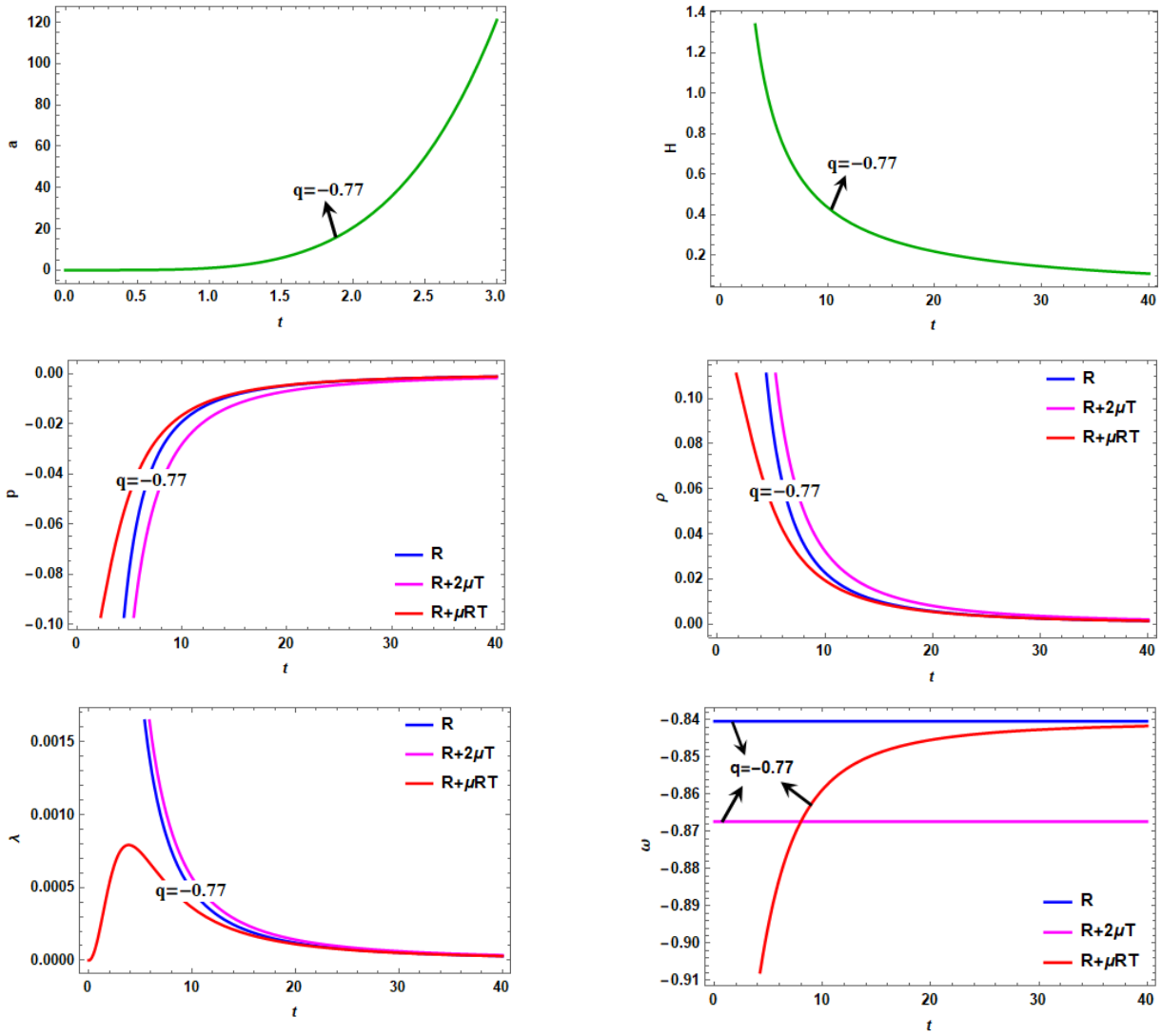


FIGURE 13. The plot of the average scale factor a, the Hubble parameter H, pressure p, the energy density ρ, the tension energy density λ and the equation of state parameter ω versus cosmic time t. Here $n_1 = 4.3$, $n_2 = n_3 = 4.4$ and $\mu = -6/\pi$.

CONCLUSION

In this study we have researched string cloud with perfect fluid matter distribution for the special case of the Bianchi I metric within the framework of $f(R,T)$ gravitation theory. For $t \to 0$, the average scale factor (a) and the spatial volume (V) are tends to zero, the Hubble parameter (H), expansion scalar (θ) and shear scalar (σ^2) are tends to infinite and the anisotropy $(\bar{A})$ and deceleration parameter (q) are constant. Also for models $f(R,T) = R$ and $f(R,T) = R + 2\mu T$, pressure (p) is in Case III tends to zero and in other cases negative infinity, energy density (ρ) is in Case III tends to zero and in other cases tends to infinite and tension energy density (λ) is in Case III tends to zero and in Case I tends to negative infinite and in other cases tends to infinite and $f(R,T) = R + \mu RT$ for model pressure is in Case III tends to zero and in other cases tends to -0.13, energy density is in Case III tends to zero and in other cases tends to 0.13 and tension energy density in all cases tends to zero at $t \to 0$. When $t \to \infty$, the average scale factor (a) and the spatial volume (V) are tends to infinite, the Hubble parameter (H), expansion scalar (θ) and shear scalar (σ^2) are tends to zero and the anisotropy $(\bar{A})$ is constant. In addition, in our $f(R,T)$ models, p, ρ and λ

ISBN:978-605-83516-6-0

are tends to zero for all cases become infinite as $t \to \infty$. To put more precisely, redshift studies the limit $\frac{\sigma}{H} \leq 0.3$ in the nearest of our galaxy today (Tiwari et al., 2019). Hence, the ratio $\frac{\sigma}{H}$ is time independent and is compatible $\left(\frac{\sigma}{H} \leq 0.3\right)$ in other cases except in Case III. The ratio $\frac{\sigma^2}{\theta^2}$ is time-independent and $\frac{\sigma^2}{\theta^2} \neq 0$ for our cases, and therefore our cases are anisotropic throughout the evolution of the universe. For all cases, $\left(-1 < \omega < -\frac{1}{3}\right)$ is the fluidity of dark energy throughout the evolution of the universe (Ha et al., 2012). For $f(R,T) = R + \mu RT$ only, $\omega = -1$ at the beginning of the universe, the fluid has its (Λ) cosmological constant form (Ha et al., 2012). Here, $\mu = -\frac{6}{\pi}$ is taken.

TABLE 2. Limit states of some physical and kinematic quantities.

		Case I						**Case II**			**Case III**		
		$q = -0.77$ $\{n_1 = 4.3,\ n_2 = 4.4$ $and\ n_3 = 4.4\}$			$q = -0.73$ $\{n_1 = 3,\ n_2 = 4.1$ $and\ n_3 = 4.1\}$			$q = -0.33$ $\{n_1 = 1.9,\ n_2 = 1.3$ $and\ n_3 = 1.3\}$			$q = 2$ $\{n_1 = -1/3,\ n_2 = 2/3$ $and\ n_3 = 2/3\}$		
$f(R,T)$		p	ρ	λ	p	ρ	λ	p	ρ	λ	p	ρ	λ
R	$t \to 0$	$-\infty$	∞	∞	$-\infty$	∞	$-\infty$	$-\infty$	∞	∞	0	0	0
	$t \to \infty$	0	0	0	0	0	0	0	0	0	0	0	0
$R + 2\mu T$	$t \to 0$	$-\infty$	∞	∞	$-\infty$	∞	$-\infty$	$-\infty$	∞	∞	0	0	0
	$t \to \infty$	0	0	0	0	0	0	0	0	0	0	0	0
$R + \mu RT$	$t \to 0$	-0.13	0.13	0	-0.13	0.13	0	-0.13	0.13	0	0	0	0
	$t \to \infty$	0	0	0	0	0	0	0	0	0	0	0	0
	σ/H	$0.01 \leq 0.3$			$0.23 \leq 0.3$			$0.17 \leq 0.3$			$1.73 \not\leq 0.3$		
	σ^2/θ^2	$0.00002 \neq 0$			$0.006 \neq 0$			$0.003 \neq 0$			$0.33 \neq 0$		
	$\bar{A}$	$0.0001 \neq 0$			$0.035 \neq 0$			$0.019 \neq 0$			$2 \neq 0$		
H, θ and σ^2	$t \to 0$	∞			∞			∞			∞		
	$t \to \infty$	0			0			0			0		
a and V	$t \to 0$	0			0			0			0		
	$t \to \infty$	∞			∞			∞			∞		

ACKNOWLEDGMENTS

This study was produced from the master thesis of the first author.

REFERENCES

1. A. Pradhan, R. K. Tiwari, A. Beesham and R. Zia, Eur. Phys. J. Plus **134**, 229 (2019).
2. A. R. Amani and S. L. Dehneshin, Can. J. Phys. **93**, 1453-1459 (2015).
3. C. Aktaş and S. Aygün, Chinese Journal of Physics **55**, 71-78 (2017).
4. C. Aktaş, S. Aygün and İ. Yilmaz, Physics Letters B **707**, 237-242 (2012).
5. C. P. Singh and P. Kumar, Astrophys. Space Sci. **361**, 157 (2016).
6. D. Momeni, P. H. R. S. Moraes and R. Myrzakulov, Astrophys. Space Sci. **361**, 228 (2016).
7. D. R. K. Reddy and S. Umadevi, Eur. J. Plus **129**, 96 (2014).
8. D. R. K. Reddy, S. Anitha and S. Umadevi, European Physical Journal Plus **129**, 96 (2014).
9. D. Sofuoğlu, Astrophysics and Space Science **361**, 12 (2016).
10. E.-K. Li, M. Du and L. Xu, arXiv:1903.11433, (2019).
11. G. Ramesh and S. Umadevi, Astrophys. Space Sci. **361**, 2 (2016).
12. G. P. Singh and B.K. Bishi, Astrophys Space Sci **360**, 34 (2015).
13. G. P. Singh, B. K. Bishi and P. K. Sahoo, Astrophys. Space Sci. **360**, 34 (2015).
14. G. P. Singh, B. K. Bishi and P. K. Sahoo, Chin. J. Phys. **54**, 244-255 (2016).
15. G. P. Singh, B. K Bishi and P. K. Sahoo, J. Geom. Methods Mod. Phys. **13**, 1650058 (2016).
16. J. V. Cunha, Phys. Rev. D **79**, 047301 (2009).
17. L. Xu, C. Zhang, B. Chang and H. Liu, arXiv:astro-ph/0701519v2 (2007).

18. M. F. Shamir, European Physical Journal C **75**, 354 (2015).
19. M. P. Hobson, G. P. Efstathiou and A. N. Lasenby, General Relativity (2006).
20. M. Sharif and M. Zubair, Journal of Cosmology and Astroparticle Physics **3**, 028 (2012).
21. M. Sharif and M. Zubair, Journal of the Physical Society of Japan **81**, 114005 (2012).
22. M. Zubair, I. H. Sardar, F. Rahman and G. Abbas, Astrophys. Space Sci. **361**, 238 (2016).
23. N. Ahmed and A. Pradhan, International Journal of Theoretical Physics **53**, 289 (2014).
24. P. Schuecker, H. Ott, W. C Seitter, R. Ungruhe, H. W. Duerbeck, B. Cunow and R. Duemmler, The Astrophysical Journal **496**, 635–647 (1998).
25. P. K. Sahoo, P. H. R. S. Moraes, P. Sahoo and B. K. Bishi, Eur. Phys. J. C **78**, 736 (2018).
26. R. K. Tiwari, B. K. Shukla and S. Mishra, Prespacetime Journal **10**, 306-315 (2019).
27. S. Aygün, C. Aktaş and İ. Yılmaz, İ. Astrophys. Space Sci. **361**, 380 (2016).
28. S. Chattopadhyay, Proc. Natl. Acad. Sci., India, Sect. A Phys. Sci. **84**, 87–93 (2014).
29. S. Capozziello, O. Luongo and E. N. Saridakis, Phys. Review D **91**, 124037 (2015).
30. S. Caroll, Spacetime and Geometry, An Introduction to General Relativity (2004).
31. S. Ghaffari, M. H. Dehghani and A. Sheykhi, Physical Review D **89**, 123009 (2014).
32. T. Harko, F. S. N. Lobo, S. Nojiri and S. D. Odintsov, Phys. Rev. D **84**, 024020 (2011).
33. T. Ha, Y. Huang, Q. Ma, K. D. Pechan, T. J. Renner, Z. Wu, G. A. Benesh and A. Wang, Gen. Relativ. Gravit. **44**, 1433–1458 (2012).

BOOK OF FULL TEXT PROCEEDINGS TURKISH PHYSICAL
SOCIETY 35th INTERNATIONAL PHYSICS CONGRESS (TPS35)
TPS35, Vol.01, No.07, pp.447-455.
ISBN:978-605-83516-6-0

15 December 2019

Space-Time Geometry of Perfect Fluid Distribution in $f(R,T)$ Gravitation Theory

Cihan KÖMÜRCÜ [1, a)] and Hüsnü BAYSAL [2, b)]

[1]*Graduate School of Natural and Applied Sciences, Çanakkale Onsekiz Mart University, Terzioğlu Campus 17020, Turkey*
[2]*Department of Mathematics, Arts and Sciences Faculty, Çanakkale Onsekiz Mart University, Terzioğlu Campus 17020, Turkey*

[a)] Corresponding author: cihan_komurcu@hotmail.com
[b)] hbaysal@comu.edu.tr

Abstract. In this study, we have researched perfect fluid solutions in $f(R,T)$ theory for Bianchi V universe model. In addition, all of our solutions in the General Theory of Relativity were calculated. Finally, we have discussed the physical results of our solutions and gave their graphs.

INTRODUCTION

Models in cosmology deal with the large-scale structure of the universe. Our universe is approximately 13.8 billion years old and is homogeneous, isotropic and almost flat when viewed at large scale (> 100Mpc), although locally solar, milky way galaxy and other galaxies are inhomogeneous and anisotropic [1,2]. This assumption CMB, Planck, WMAP and so on observations [1,2]. According to current observations, the model that best describes the universe is straight FRW space [1,2]. However, this model fails to explain the content of the universe. Therefore, the content of the universe is explained better by taking various space-time models. General Relativity theory explains the structure of the universe on a large scale [3]. However, it cannot fully explain issues such as dark energy and dark matter that are thought to cause the universe to accelerate [3]. General relativity theory was insufficient to explain dark energy and dark matter, which led to the emergence of other alternative gravitation theories [3]. The most well-known of these theories are Lyra theory, Brans-Dicke theory, $f(T)$, $f(G)$, $f(R,T)$ theory etc. [3]. In this study, we have examined the homogeneous anisotropic Bianchi type V universe model for perfect fluid matter distribution in $f(R,T)$ gravitation theory.

In 2011, Harko et al. [4] expressed Einstein field equations with the help of a $f(R,T)$ function that would change both the geometry and the material part of the field equations as follows

$$f_T(R,T)R_{ik} - \frac{1}{2}f(R,T)g_{ik} + (g_{ik}\Box - \nabla_i\nabla_k)f_R(R,T) = \big(8\pi - f_T(R,T)\big)T_{ik} - T_{ik}\Theta_{ik} \tag{1}$$

where, $f_R(R,T) = \frac{\partial f(R,T)}{\partial R}$, $f_T(R,T) = \frac{\partial f(R,T)}{\partial T}$, ($\Box$) D'Alembert operator $\Box = \nabla^i\nabla_i = g^{ik}\nabla_i\nabla_k$ and (∇_i) covariant derivative [4].

Türk Fizik Derneği
1950
Turkish Physical Society

If $f(R,T) = R + 2\mu T$, the Eqn. (1) is as follows

$$R_{ik} - \frac{1}{2}Rg_{ik} = (8\pi - 4\mu)T_{ik} - 4\mu\Theta_{ik} + 2\mu T g_{ik} \tag{2}$$

Also if the matter source is a perfect fluid for (Θ_{ik}) and the stress-energy tensor (T_{ik}) as follows [4]

$$\Theta_{ik} = -2T_{ik} - pg_{ik} \tag{3}$$

$$T_{ik} = (\rho + p)u_i u_k - pg_{ik} \tag{4}$$

here (p) pressure, (ρ) the energy density for perfect fluid and (u_i) four-velocity vector.

After the study of Harko et al. [4] this theory has been studied for different space time metrics. Shamir, has investigated the perfect fluid solutions for the Bianchi type V universe model in $f(R,T)$ theory [5]. Rao and Rao have studied Bianchi type V string cosmological models in $f(R,T)$ gravity [6]. Rao et al. have studied the perfect fluid solutions for the Bianchi type III, V and VI_0 universe models in $f(R,T)$ theory [7]. Ram and Chandel have studied Bianchi type V universe model for solutions containing perfect fluid, one dimensional cosmic string with magnetic field in $f(R,T)$ gravity [8]. Ahmed et al. have investigated Bianchi type V universe model for solutions containing perfect fluid together with $\Lambda(T)$ in $f(R,T)$ gravity [9]. Kanakavalli et al. have studied Bianchi type V scalar field cosmological model in $f(R,T)$ theory [10]. Zubair et al. have investigated the perfect fluid solutions for the Bianchi type V universe model in $f(R,T)$ gravity [11]. Singh and Bishi have studied Bianchi type V universe model for solutions containing domain walls and quark matter with cosmological constant Λ in $f(R,T)$ theory [12]. Tiwari and Mishra have investigated perfect fluid matter distribution for Bianchi type V universe model with cosmological constant Λ in $f(R,T)$ gravity [13]. Bhardwaj has investigated the non-minimal matter-geometry coupling for the Bianchi type V universe model in $f(R,T)$ theory [14]. Nath et al. have studied perfect fluid solutions for the LRS Bianchi type V universe model in $f(R,T)$ gravity [15]. Pawar et al. have investigated a modified holographic Ricci dark energy model solutions for the Bianchi type V space-time in $f(R,T)$ theory [16]. Sharma have studied the coupling of non-minimal matter solutions for the Bianchi type V universe models in $f(R,T)$ gravity [17]. Also, Yılmaz et al. have studied quark and strange quark matter solutions for the Bianchi type I and V universe models in $f(R)$ theory [18].

METRIC, FIELD EQUATIONS AND SOLUTIONS

In the $(x^1, x^2, x^3, x^4) = (x, y, z, t)$ coordinate, we consider the spatially homogeneous and anisotropic Bianchi type V metric of the form

$$ds^2 = dt^2 - A^2(t)dx^2 - e^{-2x}(B^2(t)dy^2 + C^2(t)dz^2) \tag{5}$$

where t cosmic time, $A(t)$, $B(t)$ and $C(t)$ metric potentials. The trace of the stress-energy tensor (T) as follows

$$T = \rho - 3p \tag{6}$$

The physical and kinematical parameters such as directional expansion scalar (θ), average scale factor (a), volume (V), are the Hubble parameter in the directions of x, y and z axes, respectively, (H_x), (H_y) and (H_z), Hubble parameter (H), anisotropy parameter $(\bar{A})$ and shear scalar (σ^2) are given by

$$V = a^3 = ABC \tag{7}$$

$$H_x = \frac{\dot{A}}{A} \tag{8}$$

$$H_y = \frac{\dot{B}}{B} \tag{9}$$

$$H_z = \frac{\dot{C}}{C} \tag{10}$$

$$H = \frac{1}{3}(H_x + H_y + H_z) \tag{11}$$

$$\theta = H_x + H_y + H_z \tag{12}$$

$$\sigma_1^1 = \frac{1}{3}(2H_x - H_y - H_z) \tag{13}$$

$$\sigma_2^2 = \frac{1}{3}(2H_y - H_x - H_z) \tag{14}$$

$$\sigma_3^3 = \frac{1}{3}(2H_z - H_x - H_y) \tag{15}$$

$$\bar{A} = \frac{2}{9}\left(\frac{{H_x}^2 + {H_y}^2 + {H_z}^2 - H_yH_z - H_x(H_y + H_z)}{H^2}\right) \tag{16}$$

$$\sigma^2 = \frac{1}{3}\left[{H_x}^2 + {H_y}^2 + {H_z}^2 - H_yH_z - H_x(H_y + H_z)\right] \tag{17}$$

and the Ricci scalar (R) given by

$$R = \frac{6}{A^2} - 2\left[\dot{H}_x + \dot{H}_y + \dot{H}_z - {H_x}^2 - {H_y}^2 - {H_z}^2 + H_yH_z + H_x(H_y + H_z)\right] \tag{18}$$

Now with the help of Eqn. (4) the field equations in $f(R,T)$ gravity Eqn. (2) for the metric in Eqn. (5) can be written as.

$$\dot{H}_y + \dot{H}_z + H_yH_z + {H_y}^2 + {H_z}^2 - \frac{1}{A^2} = \mu\rho - p(8\pi + 3\mu) \tag{19}$$

$$\dot{H}_x + \dot{H}_z + H_xH_z + {H_x}^2 + {H_z}^2 - \frac{1}{A^2} = \mu\rho - p(8\pi + 3\mu) \tag{20}$$

$$\dot{H}_x + \dot{H}_y + H_xH_y + {H_x}^2 + {H_y}^2 - \frac{1}{A^2} = \mu\rho - p(8\pi + 3\mu) \tag{21}$$

$$H_xH_y + H_xH_z + H_yH_z - \frac{3}{A^2} = \rho(8\pi + 3\mu) - \mu p \tag{22}$$

$$2H_x - H_y - H_z = 0 \tag{23}$$

From Eqn. (23), we get

$$A^2 = \gamma BC \tag{24}$$

without loss of generality, by taking, $\gamma = 1$ we get

ISBN:978-605-83516-6-0

$$A^2 = BC \tag{25}$$

and if the Eqn. (25) is taken into account in the Eqn. (20) and Eqn. (21)

$$\ddot{C} = \frac{C^2\dot{B}^2 - B^2\dot{C}^2 + 2B\ddot{B}C^2}{2CB^2} \tag{26}$$

equation is obtained. In the $(19) - (22)$ equations, if Eqn. (25) first and then Eqn. (26) are taken into account, we obtain p, ρ and $\left(\omega = \frac{p}{\rho}\right)$ as follows

$$p = -\frac{[(8\pi+\mu)H_yH_z + (20\pi+7\mu){H_y}^2 - 2(2\pi+\mu){H_z}^2 + 2(8\pi+3\mu)\dot{H}_y]BC - 8\pi}{8(2\pi+\mu)(4\pi+\mu)BC} \tag{27}$$

$$\rho = \frac{[(16\pi+5\mu)H_yH_z + (4\pi-\mu){H_y}^2 + 2(2\pi+\mu){H_z}^2 - 2\mu\dot{H}_y]BC - 8(3\pi+\mu)}{8(2\pi+\mu)(4\pi+\mu)BC} \tag{28}$$

$$\omega = -\frac{[(8\pi+\mu)H_yH_z + (20\pi+7\mu){H_y}^2 - 2(2\pi+\mu){H_z}^2 + 2(8\pi+3\mu)\dot{H}_y]BC - 8\pi}{[(16\pi+5\mu)H_yH_z + (4\pi-\mu){H_y}^2 + 2(2\pi+\mu){H_z}^2 - 2\mu\dot{H}_y]BC - 8(3\pi+\mu)} \tag{29}$$

Considering the model average scale factor $a = \mathrm{c}_1 e^{2\beta\sqrt{t+\alpha}}$ [19] in equations (7), (25) and (26)

$$A = a \tag{30}$$

$$B = c_1\sqrt{c_2}\,e^{2\beta\sqrt{t+\alpha} - \frac{c_3 e^{-6\beta\sqrt{t+\alpha}}(1+6\beta\sqrt{t+\alpha})}{36{c_1}^3\beta^2}} \tag{31}$$

$$C = \frac{\sqrt{c_2}}{c_2}c_1 e^{2\beta\sqrt{t+\alpha} + \frac{c_3 e^{-6\beta\sqrt{t+\alpha}}(1+6\beta\sqrt{t+\alpha})}{36{c_1}^3\beta^2}} \tag{32}$$

$$H = \frac{\beta}{\sqrt{t+\alpha}} \tag{33}$$

$$q = -1 + \frac{1}{2\beta\sqrt{t+\alpha}} \tag{34}$$

$$\sigma^2 = \frac{{c_3}^2 e^{-12\beta\sqrt{t+\alpha}}}{4{c_1}^6} \tag{35}$$

$$\bar{A} = \frac{{c_3}^2 e^{-12\beta\sqrt{t+\alpha}}(t+\alpha)}{6{c_1}^6\beta^2} \tag{36}$$

obtained. Here c_1, c_2, c_3, α and β are constant.

From the relation $1 + z = \frac{a_0}{a} = \frac{1}{a}$, with z being the redshift and the present scale factor $a_0 = 1$, we obtain the following time-redshift relation [20, 21]

$$t = -\alpha + \frac{ln(c_1(1+z))^2}{4\beta^2} \tag{37}$$

$\{\beta = 0.8,\ \alpha = 0.125\}$, $\{\beta = 1,\ \alpha = 0.125\}$ and $\{\beta = 1.2,\ \alpha = 0.125\}$ values were used to plot the graphs. They are the values that provide $\alpha, \beta > 0$ and $\beta\sqrt{\alpha} < 0.5$ conditions for the universe model from deceleration to acceleration [19].

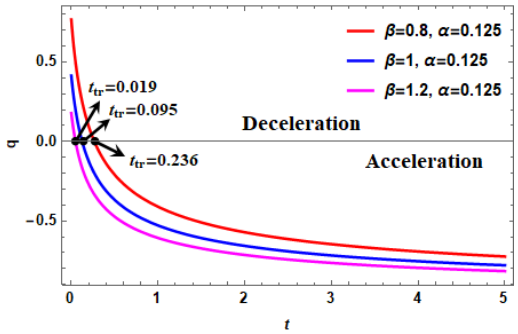


FIGURE 1. The plot of the deceleration parameter q versus cosmic time t for $c_1 = 1.9$, $c_2 = 1$, $c_3 = 0.1$ and $\mu = -6/\pi$.

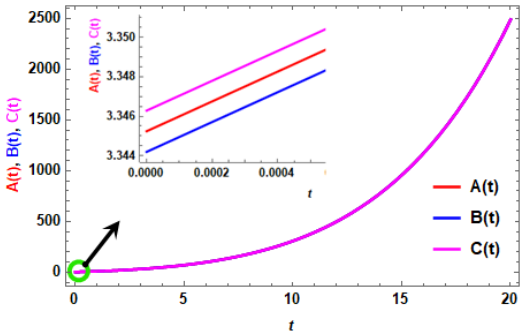


FIGURE 2. The plot of the metric potentials $A(t)$, $B(t)$ and $C(t)$ versus cosmic time t for $c_1 = 1.9$, $c_2 = 1$, $c_3 = 0.1$ and $\mu = -6/\pi$.

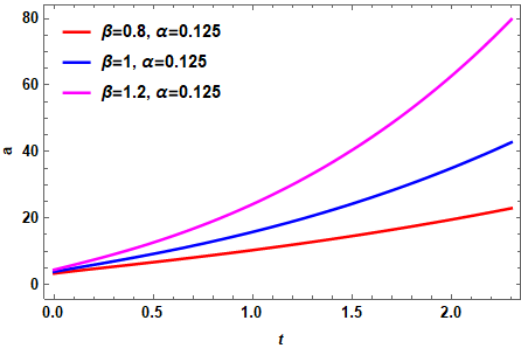


FIGURE 3. The plot of the average scale factor a versus cosmic time t for $c_1 = 1.9$, $c_2 = 1$, $c_3 = 0.1$ and $\mu = -6/\pi$.

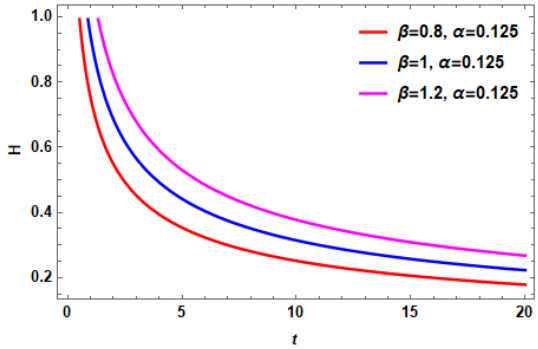


FIGURE 4. The plot of the Hubble parameter H versus cosmic time t for $c_1 = 1.9$, $c_2 = 1$, $c_3 = 0.1$ and $\mu = -6/\pi$.

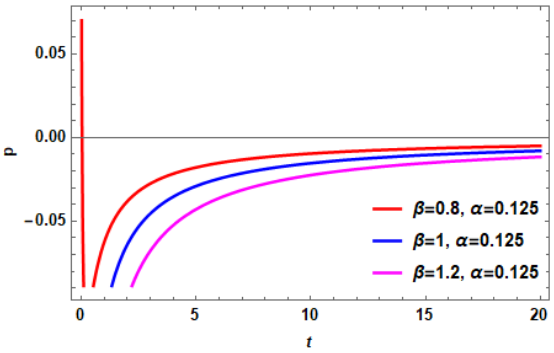


FIGURE 5. The plot of the pressure p versus cosmic time t for $c_1 = 1.9$, $c_2 = 1$, $c_3 = 0.1$ and $\mu = -6/\pi$.

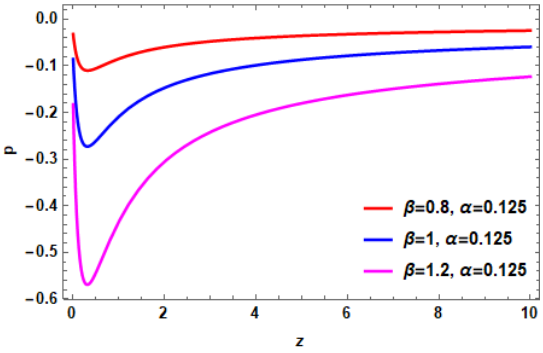


FIGURE 6. The plot of the pressure p versus red-shift z for $c_1 = 1.9$, $c_2 = 1$, $c_3 = 0.1$ and $\mu = -6/\pi$.

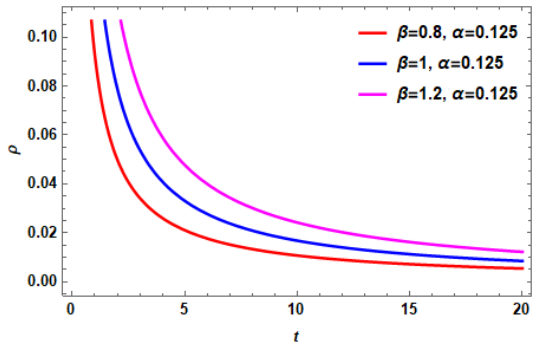


FIGURE 7. The plot of the energy density ρ versus cosmic time t for $c_1 = 1.9$, $c_2 = 1$, $c_3 = 0.1$ and $\mu = -6/\pi$.

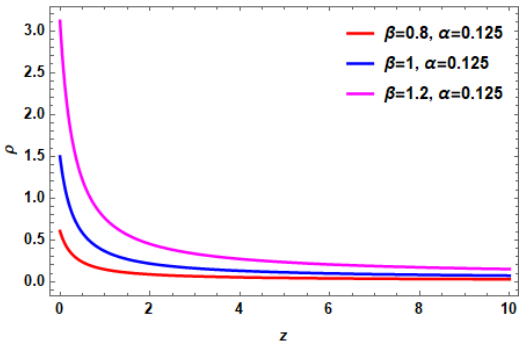


FIGURE 8. The plot of the energy density ρ versus red-shift z for $c_1 = 1.9$, $c_2 = 1$, $c_3 = 0.1$ and $\mu = -6/\pi$.

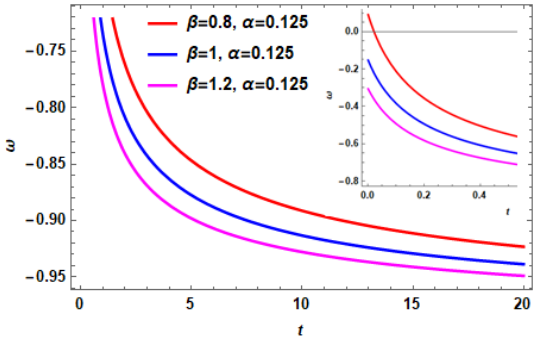


FIGURE 9. The plot of the equation of state parameter ω versus cosmic time t for $c_1 = 1.9$, $c_2 = 1$, $c_3 = 0.1$ and $\mu = -6/\pi$.

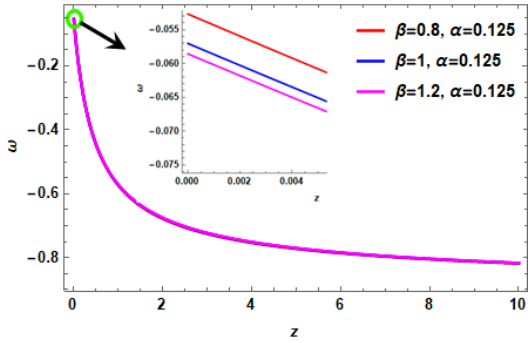


FIGURE 10. The plot of the equation of state parameter ω versus red-shift z for $c_1 = 1.9$, $c_2 = 1$, $c_3 = 0.1$ and $\mu = -6/\pi$.

ENERGY CONDITIONS

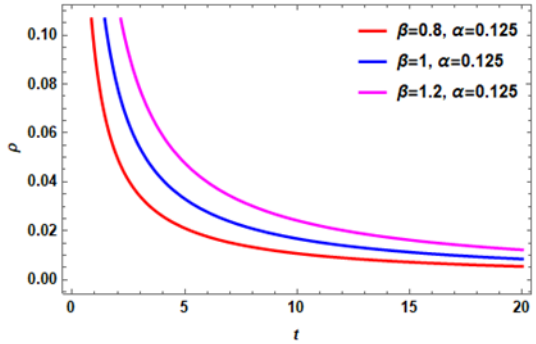


FIGURE 11. Validation of the weak energy conditions WEC ($\rho \geq 0$, $\rho + p \geq 0$) for. Here $c_1 = 1.9$, $c_2 = 1$, $c_3 = 0.1$ and $\mu = -6/\pi$.

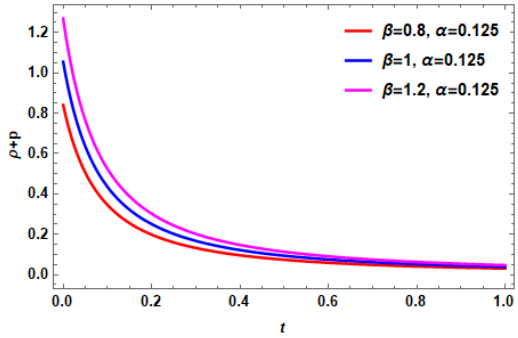


FIGURE 12. Validation of the null energy conditions NEC ($\rho + p \geq 0$) for. Here $c_1 = 1.9$, $c_2 = 1$, $c_3 = 0.1$ and $\mu = -6/\pi$.

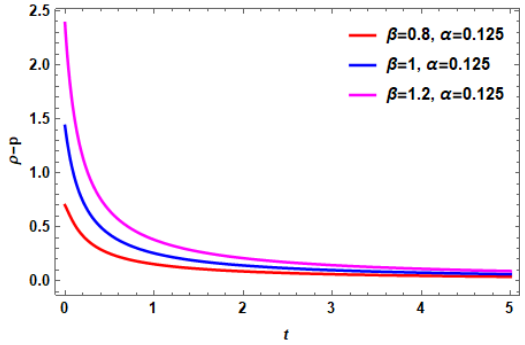


FIGURE 13. Validation of the dominant energy conditions DEC ($\rho \geq |p|$) for. Here $c_1 = 1.9$, $c_2 = 1$, $c_3 = 0.1$ and $\mu = -6/\pi$.

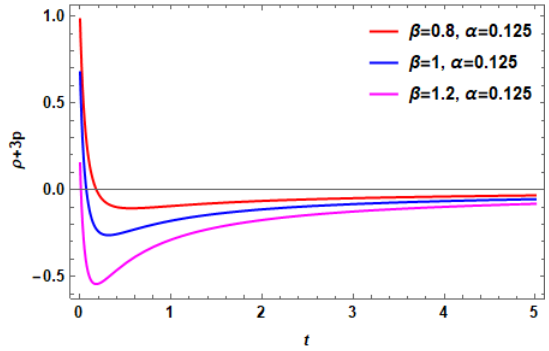


FIGURE 14. Violation of the strong energy conditions SEC ($\rho + p \geq 0$, $\rho + 3p \geq 0$) for. Here $c_1 = 1.9$, $c_2 = 1$, $c_3 = 0.1$ and $\mu = -6/\pi$.

COSMOGRAPHIC PARAMETERS

The (H) Hubble, (q) deceleration, (j) jerk ($j = r, [22]$), (s) snap, (l) lerk and (m) paremeters are defined as $[22, 23, 24]$.

$$H = \frac{1}{a}\dot{a} = \frac{\beta}{\sqrt{t+\alpha}} \tag{38}$$

$$q = -\frac{1}{a}\frac{\ddot{a}}{H^2} = -1 + \frac{1}{2\beta\sqrt{t+\alpha}} \tag{39}$$

$$j = \frac{1}{a}\frac{\dddot{a}}{H^3} = q + 2q^2 - \frac{\dot{q}}{H} = 1 + 3\frac{\dot{H}}{H^2} + \frac{\ddot{H}}{H^3} = 1 + \frac{3\left(1 - 2\beta\sqrt{t+\alpha}\right)}{4\beta^2(t+\alpha)} \tag{40}$$

$$s = \frac{1}{a}\frac{a^{(4)}}{H^4} = 1 + \frac{3(-5 + 10\beta\sqrt{t+\alpha} - 8(t+\alpha)\beta^2)}{8\beta^3(t+\alpha)^{3/2}} \tag{41}$$

$$l = \frac{1}{a}\frac{a^{(5)}}{H^5} = \frac{105 + 2\beta(-105\sqrt{t+\alpha} + 2(t+\alpha)\beta(45 + 4\beta(-5\sqrt{t+\alpha} + (t+\alpha)\beta)))}{16\beta^4(t+\alpha)^2} \tag{42}$$

$$m = \frac{1}{a}\frac{a^{(6)}}{H^6} = \frac{1}{32\beta^5(t+\alpha)^{5/2}}[-945 + 2\beta(945\sqrt{t+\alpha} + 4(t+\alpha)\beta(-210 + \\ +105\beta\sqrt{t+\alpha} - 30(t+\alpha)\beta^2 + 4(t+\alpha)^{3/2}] \tag{43}$$

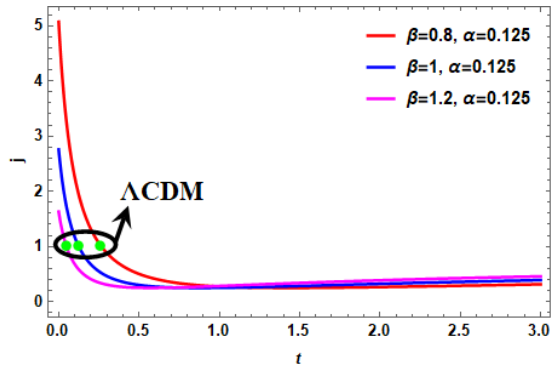


FIGURE 15. The Jerk parameter j versus cosmic time t for a flat ΛCDM model, jerk parameter has the value $j = 1$. Here $c_1 = 1.9$, $c_2 = 1$, $c_3 = 0.1$ and $\mu = -6/\pi$.

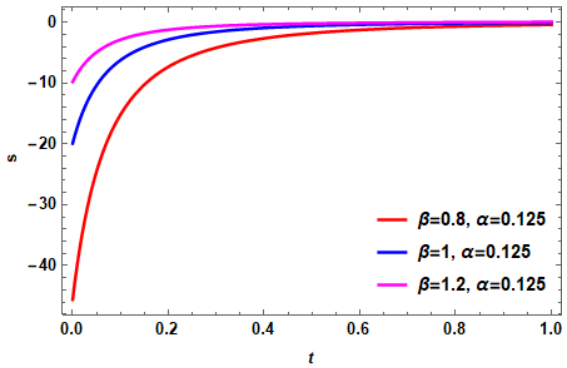


FIGURE 16. The snap parameter s versus cosmic time t. Here $c_1 = 1.9$, $c_2 = 1$, $c_3 = 0.1$ and $\mu = -6/\pi$.

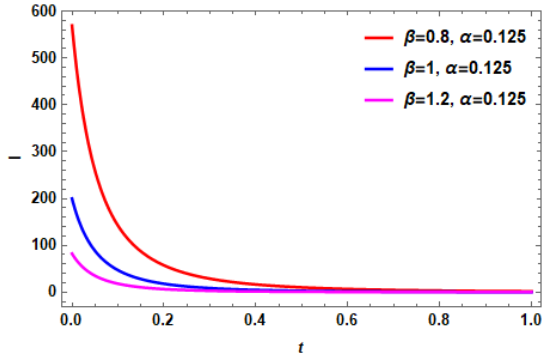


FIGURE 17. The lerk parameter l versus cosmic time t. Here $c_1 = 1.9$, $c_2 = 1$, $c_3 = 0.1$ and $\mu = -6/\pi$.

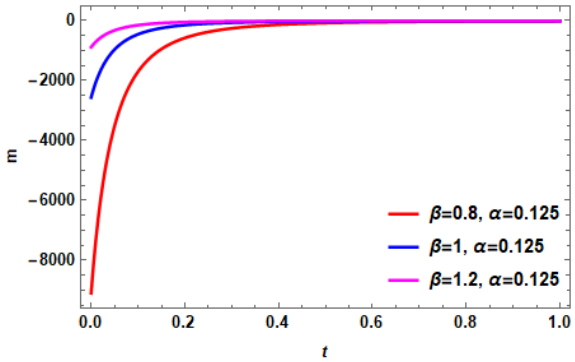


FIGURE 18. The m parameter versus cosmic time t. Here $c_1 = 1.9$, $c_2 = 1$, $c_3 = 0.1$ and $\mu = -6/\pi$.

CONCLUSION

In this study we have researched perfect fluid matter distribution for the special case of the Bianchi type V metric within the framework of $f(R,T)$ gravitation theory. For $t \to 0$, the spatial volume (V), expansion scalar (θ), anisotropy $(\bar{A})$, pressure (p) and energy density (ρ) are tends to constant. When $t \to \infty$, the spatial volume (V) tends to infinite, expansion scalar (θ), anisotropy $(\bar{A})$, pressure (p) and energy density (ρ) are tends to zero. Therefore, since $\bar{A} = 0$ towards the end of the universe, our model switches to isotropy and since $\theta = 0$, the universe closes on itself. Also, the Hubble parameter has a singularity at $t = -\alpha$. The deceleration parameter changes from deceleration to acceleration and is compatible with the current universe. Energy conditions are provided in conditions other than SEC. In addition, jerk (j), snap (s), lerk (l) and (m) parameters are tends to one as $t \to \infty$. In three cases at the beginning of the universe, $\left(\omega \geq -\frac{1}{3}\right)$ is a fluid normal substance [25]. This situation continues for a very short time, $t \cong 0.2$ from the moment of $\left(\omega < -\frac{1}{3}\right)$ is fluid dark energy features [25].

TABLE 1. Limit states of some physical and kinematic quantities for $c_1 = 1.9$, $c_2 = 1$, $c_3 = 0.1$, $\alpha = 0.125$ and $\mu = -6/\pi$.

β		V	θ	$\bar{A}$	p	ρ	q	j	s	l	m
0.8	$t \to 0$	37.4	6.8	2.32×10^{-7}	0.07	0.77	0.77	5	-45	569	-9102
	$t \to \infty$	∞	0	0	0	0	-1	1	1	1	1
1	$t \to 0$	57.2	8.5	6.36×10^{-8}	-0.19	1.25	0.41	2	-19	199	-2563
	$t \to \infty$	∞	0	0	0	0	-1	1	1	1	1
1.2	$t \to 0$	87.5	10.2	1.89×10^{-8}	-0.56	1.83	0.18	1	-9	82	-883
	$t \to \infty$	∞	0	0	0	0	-1	1	1	1	1

ACKNOWLEDGMENTS

This study was produced from the master thesis of the first author.

REFERENCES

1. S. Caroll, Spacetime and Geometry: An Introduction to General Relativity **(2004)**.
2. M. P. Hobson, G. P. Efstathiou and A. N. Lasenby, General Relativity **(2006).**
3. C. Aktaş, S. Aygün and İ. Yilmaz, Physics Letters B **707**, 237-242 (2012).
4. T. Harko, F. S. N. Lobo, S. Nojiri and S. D. Odintsov, Phys. Rev. D **84**, 024020 (2011).
5. M. F. Shamir, Int. J. Theor. Phys. **54**, 1304-1315 (2014).
6. V. U. M. Rao and D. C. P. Rao, Astrophys Space Sci **357**, 77 (2015).
7. V. U. M. Rao, T. Vinutha, D. Neelima and G. S. Narayana, The African Review of Physics **10**, 0017 (2015).
8. S. Ram and S. Chandel, Astrophys Space Sci **355**, 195–202 (2015).
9. N. Ahmed, A. Pradhan, M. Fekry and S. Z. Alamri, NRIAG Journal of Astronomy and Geophysics **5**, 35-47 (2016).
10. T. Kanakavalli, G. A. Rao and D. R. K. Reddy, Prespacetime Journal **7**, 1722-1728 (2016).
11. M. Zubair, S. M. A. Hassan and G. Abbas, Canadian. J. of Phys. **94**, 1289-1296 (2016).
12. G. P. Singh and B. K. Bishi, Iran J Sci Technol Trans Sci **41**, 33-43 (2017).
13. R. K. Tiwari and S. Mishra, Prespacetime Journal **8**, 818-833 (2017).
14. V. K. Bhardwaj, Modern Physics Letters A **33**, 1850234 (2018).
15. Nath and S. K. Sahu, Canadian. J. of Phys. **97**, 443-449 (2018).
16. D. D. Pawar, R. V. Maparı and P. K. Agrawal, J. Astrophys. Astr. **40**, 13 (2019).
17. L. K. Sharma and B. K. Singh, arXiv:1907.03552 (2019).
18. İ. Yılmaz, H. Baysal, and C. Aktaş, General Relativity and Gravitation **44**, 2313–2328 (2012).
19. S. K. J. Pacif, R. Myrzakulov and S. Myrzakul, International Journal of Geometric Methods in Modern Physics **14**, 1750111 (2017).
20. S. Capozziello, O. Luongo and E. N. Saridakis, Phys. Review D **91**, 124037 (2015).
21. P. K. Sahoo, P. H. R. S. Moraes, P. Sahoo and B. K. Bishi, Eur. Phys. J. C **78**, 736 (2018).
22. S. Pan, S. Bhattacharya and S. Chakraborty, M. N. Royal Astronomical Society **452**, 3038–3046 (2015).
23. M. Visser, Gen. Relativ. Gravit. **37**, 1541–1548 (2005).
24. E.-K. Li, M. Du and L. Xu, arXiv:1903.11433 (2019).
25. T. Ha, Y. Huang, Q. Ma, K. D. Pechan, T. J. Renner, Z. Wu, G. A. Benesh and A. Wang, Gen. Relativ. Gravit. **44**, 1433–1458 (2012).

BOOK OF FULL TEXT PROCEEDINGS TURKISH PHYSICAL
SOCIETY 35th INTERNATIONAL PHYSICS CONGRESS (TPS35)
TPS35, Vol.01, No.07, pp.456-462.
ISBN:978-605-83516-6-0 15 December 2019

Bianchi V Universe Model for String Cloud with Perfect Fluid in Lyra Manifold

Elif KAPLAN[1, a)] and Can AKTAŞ[2, b)]

[1]Graduate School of Natural and Applied Sciences, Çanakkale Onsekiz Mart University, Terzioğlu Campus 17020, Çanakkale, Turkey
[2]Department of Mathematics, Çanakkale Onsekiz Mart University, Arts and Sciences Faculty, Terzioğlu Campus, 17020, Turkey

[a)]eliffkaplann17@gmail.com
[b)]canaktas@comu.edu.tr

Abstract. In this study, we have investigated homogeneous and anisotropic Bianchi V universe model for string cloud with perfect fluid matter distribution in Lyra geometry. In order to obtain the exact solutions of the field equations in Lyra geometry, which is proposed as an alternative to the general theory of relativity, we have used the deceleration parameter. At the same time, the physical and geometrical structure of the model is examined and graphs are given.

Keywords: Bianchi type-V · Lyra theory · string cloud · perfect fluid ·Hubble parameter.

INTRODUCTION

Observations made in recent years show that the universe is expanding with acceleration [1, 2]. Albert Einstein published General Relativity theory in 1916, which explains the relationship between matter and space-time geometry. In 1926, a scientist named Edwin Hubble proved that the universe was accelerating and expanding. After this proof, other theories have been proposed that could be an alternative to Albert Einstein's General Relativity theory. Scientists have put forward various theories to explain the reasons for acceleration and expansion. This acceleration and expansion is explained by some alternative gravitation theories such as Lyra, f (R), f (R, T), Creation Field, Brans-Dicke. One of these alternative theories was Lyra's theory in 1951. In Lyra theory, Einstein is a modified theory created by adding the term containing scalar field to the left side of field equations. There are many studies in Lyra theory for various matter distributions and various metrics.

In 1991, Singh and Singh have studied perfect fluid solutions for Bianchi-type V and Bianchi-type VI0 in Lyra geometry [3]. In 1992, Ram and Singh have obtained the full solution for Bianchi-type III and Bianchi type V in Lyra geometry [4]. In 1997, Singh and Desikan studied the solutions of equations by taking the displacement vector for the Robertson-Walker space-time with the ideal fluid in time and using the braking parameter in Lyra geometry [5]. In 2011, Sahu investigated the solutions of Einstein field equations for Bianchi Type-I space-time in the context of general relativity [6]. In 2012, Chaubey obtained Kantowski-Sachs for ideal fluid and space-time as a material and obtained solutions in Lyra geometry [7]. In 2012, Baysal and Aktaş studied Bianchi type I and V for f-time (R) have worked on [8]. In 2013 Sahu and Kumar studied the Bianchi-I cosmological model with ideal fluid and heat flux in Lyra geometry [9]. In 2015, Sahu et al. studied the Tilted Bianchi-III cosmological model with ideal fluid and heat flux in Lyra geometry [10]. In 2016, Santhi et al. He studied the scalar tensor theory and the scalar tensor theory for the LRS Bianchi V metric [11]. In 2016, Santhi et al. studied the scalar tensor theory for Bianchi V

Türk Fizik Derneği
1950
Turkish Physical Society

ISBN:978-605-83516-6-0

metric [12]. In 2012, Aygün et al. studied a massive scalar field for a Marder type universe in the context of Lyra and Riemannian geometries [13].

In 2015, Aygun et al. investigated the higher dimensional flat Friedmann-Robertson-Walker (FRW) universe for a cloud of string with perfect fluid attached quark and strange quark matter (SQM) in Lyra geometry [14].

Field equations in Lyra geometry are given by,

$$R_{ik}-\frac{1}{2}Rg_{ik}+\frac{3}{2}\left(\Phi_{;i}\Phi_{;k}-\frac{1}{2}g_{ik}\Phi_{;l}\Phi^{;l}\right)=-8\pi GT_{ik} \tag{1}$$

where Φ is the displacement field vector according to time defined by $\Phi_i=(0,0,0,\beta(t))$. Other symbols contain the meaning of Riemannian geometry.

THE METRIC AND FIELD EQUATIONS

We consider homogeneous anisotropic Bianchi type-V metric is as follows,

$$ds^2=-dt^2+A^2dx^2+e^{-2x}(B^2dy^2+C^2dz^2) \tag{2}$$

here A,B,C are functions of cosmic time t. The energy-momentum tensor for string cloud with perfect fluid matter distribution is given by,

$$T_{ik}=(\rho+p)u_iu_k+pg_{ik}-\lambda x_ix_k \tag{3}$$

here ρ is energy density, p is pressure, λ is string tension, u^i is four velocity vector and x_i is direction of the string. In addition, there are $u^iu_i=1$, $x^ix_i=-1$ and $u^ix_i=0$ correlations between u_i and x_i. Therefore, the direction of the string is taken in the x direction. The kinematical quantities for the metric which is given by equation (2) are as follows

$$\theta=\frac{\dot{A}}{A}+\frac{\dot{B}}{B}+\frac{\dot{C}}{C} \tag{4}$$

$$\sigma^2=\frac{1}{3}\left[\left(\frac{\dot{A}}{A}\right)^2+\left(\frac{\dot{B}}{B}\right)^2+\left(\frac{\dot{C}}{C}\right)^2\right]-\frac{1}{3}\left[\frac{\dot{A}\dot{B}}{AB}+\frac{\dot{A}\dot{C}}{AC}+\frac{\dot{B}\dot{C}}{BC}\right] \tag{5}$$

$$V=a^3=ABC \tag{6}$$

$$H=\frac{\dot{a}}{a}=\frac{1}{3}(H_1+H_2+H_3) \tag{7}$$

θ scalar expansion, σ shear tensor, V volume, H Hubble's parameters. Where $H_1=\dot{A}/A$, $H_2=\dot{B}/B$ and $H_3=\dot{C}/C$ are the directional Hubble's parameters in the directions of x,y and z respectively. Also, the deceleration parameter (q) is defined as

$$q=\frac{d}{dt}\left(\frac{1}{H}\right)-1=-\frac{a\ddot{a}}{\dot{a}^2} \tag{8}$$

From equations (1) – (3), the field equations for Lyra manifold is as follows,

$$\frac{\ddot{B}}{B}+\frac{\dot{B}\dot{C}}{BC}+\frac{\ddot{C}}{C}-\frac{1}{A^2}+\frac{3\beta^2}{4}=-p+\lambda \tag{9}$$

$$\frac{\ddot{A}}{A}+\frac{\dot{A}\dot{C}}{AC}+\frac{\ddot{C}}{C}-\frac{1}{A^2}+\frac{3\beta^2}{4}=-p \tag{10}$$

$$\frac{\ddot{A}}{A}+\frac{\dot{A}\dot{B}}{AB}+\frac{\ddot{B}}{B}-\frac{1}{A^2}+\frac{3\beta^2}{4}=-p \tag{11}$$

$$\frac{\dot{A}\dot{B}}{AB}+\frac{\dot{A}\dot{C}}{AC}+\frac{\dot{B}\dot{C}}{BC}-\frac{3}{A^2}-\frac{3\beta^2}{4}=\rho \tag{12}$$

ISBN:978-605-83516-6-0

$$\frac{2\dot{A}}{A}-\frac{\dot{B}}{B}-\frac{\dot{C}}{C}=0 \tag{13}$$

here the dot indicates derivative w.r.t time. As can be seen from equations (9) – (13), there are five equations with seven unknowns (A, B, C, p ρ, λ, β). To solve these equations, we need two additional equations. For this aim, we can use Hubble equation and equation of state parameter. If we solve equation (13), we get

$$A^2 = c_1 BC \tag{14}$$

here c_1 is an arbitrary constant. We can take $c_1 = 1$ without loss of generality. From equations (6) and (15), we obtain

$$A = a \tag{15}$$

Pacif et al. [15] In an article published in 2017, they examined various Hubble parameters to explain the cosmic acceleration of time. Some of the Hubble parameters they examined showed that they were compatible with both observations and theory. We can also use one of the Hubble parameters proposed by Pacif et al.[15]. Therefore, we can take the Hubble parameter as follows [15].

$$H = \frac{\gamma t^m}{(t^n + \alpha)^p} \tag{16}$$

here m, n, p, α and γ are constants. If we take $m = 0, p = \frac{1}{2}, n = 1$, we obtain

$$H = \frac{\gamma}{\sqrt{t+\alpha}} \tag{17}$$

From equations (8) and (18), we obtain volume scale factor is as follows,

$$a = c_2 e^{2\gamma\sqrt{t+\alpha}} \tag{18}$$

here c_2 is an integral constant. From equations (8) and (18), we get the deceleration parameter

$$q = -1 + \frac{1}{2\gamma}\frac{1}{\sqrt{t+\alpha}} \tag{19}$$

From equations (10), (11) and (15), the metric functions can be written respectively as

$$A = a \tag{20}$$

$$B = \sqrt{c_3}\, a\, exp\left(\frac{c_4}{2}\int \frac{dt}{a^3}\right) \tag{21}$$

$$C = \frac{a}{\sqrt{c_3}}\, exp\left(-\frac{c_4}{2}\int \frac{dt}{a^3}\right) \tag{22}$$

c_3 and c_4 are constants. If the equations (20) - (22) are substitute equation (5), we have shear scalar is as follows,

$$\sigma^2 = \frac{c_4^2}{4c_2^6} exp\left(-12\beta\sqrt{t+\alpha}\right) \tag{23}$$

Second, we can use the equation known as the equation of state that gives the relationship between pressure and energy density. The equation of state is defined by

ISBN:978-605-83516-6-0

$$p = \omega\rho \tag{24}$$

where ρ is the energy density, p is the pressure and ω is constant. If the equations (20) - (22) are written in the field equations (9) - (12), the energy density, pressure and string tension are obtained as follows.

$$\rho = \frac{\left(\frac{4\exp\left(-4\sqrt{t+\alpha}\gamma\right)}{c_2^2} + \gamma\left(\frac{1}{(t+\alpha)^{3/2}} - \frac{6\gamma}{t+\alpha}\right)\right)}{\omega - 1} \tag{24}$$

$$p = \frac{\omega\left(\frac{4\exp\left(-4\sqrt{t+\alpha}\gamma\right)}{c_2^2} + \gamma\left(\frac{1}{(t+\alpha)^{3/2}} - \frac{6\gamma}{t+\alpha}\right)\right)}{\omega - 1} \tag{25}$$

$$\lambda = 0 \tag{26}$$

The component of the displacement vector is,

$$\beta^2 = \frac{4\gamma(-1+3\gamma(1+\omega)\sqrt{t+\alpha})}{3(\omega-1)(t+\alpha)^{\frac{3}{2}}} - \frac{\exp\left(-4\gamma\sqrt{t+\alpha}\right)}{3c_2^2}\left[\frac{c_4^2\exp\left(-8\gamma\sqrt{t+\alpha}\right)}{c_2^4} + \frac{4(1+3\omega)}{\omega-1}\right] \tag{27}$$

CONCLUSION AND DISCUSSION

In this study, we have researched string cloud with perfect fluid matter distribution for Bianchi type V universe model in Lyra manifold. To solve exact solutions of modified field equations we have used equation of state and Hubble equation. As can be seen from equation (26), string tension is zero. This shows us that in Lyra theory the Bianchi V universe model does not allow string formation. In our solutions, the point $t = -\alpha$ is the singular point. As it is known, singular points are points where gravitation theories do not apply. Therefore, it must be $t \neq -\alpha$ for our solutions to be continuous. We can write the pressure and energy density in terms of deceleration parameter, shear scalar, Hubble parameter and displacement vector component as follows.

$$\rho = 3H^2 - \sigma^2 - \frac{3}{a^2} - \frac{3\beta^2}{4} \tag{28}$$

$$p = -H^2(1+2q) - \sigma^2 + \frac{1}{a^2} - \frac{3\beta^2}{4} \tag{29}$$

$\alpha = 0.1, 0.2, 0.3$ and $\beta = 0.6$ values were used to plot the graphs. They are the values in the article of Pacif et al. that provide $\alpha > 0$, $\beta > 0$ and $\beta\sqrt{\alpha} < \frac{1}{2}$ conditions for the universe model from deceleration to acceleration. Kinematic quantities Hubble parameter and deceleration parameter decrease with time (see figs. 1 and 2).

ISBN:978-605-83516-6-0

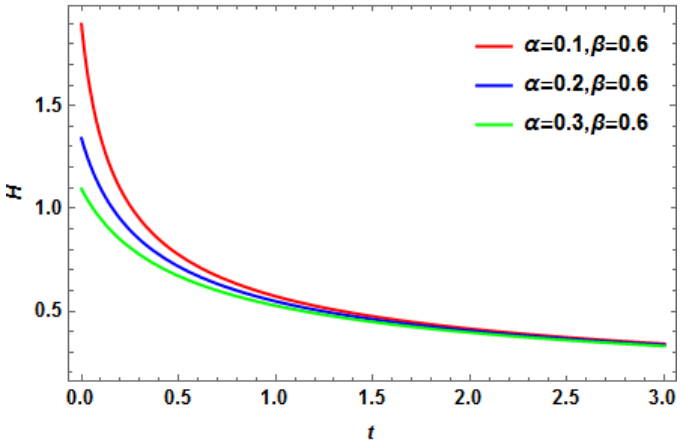


FIGURE 1. Variation of Hubble parameter against time with $\alpha = 0.1,0.2,0.3$, $\beta = 0.6$

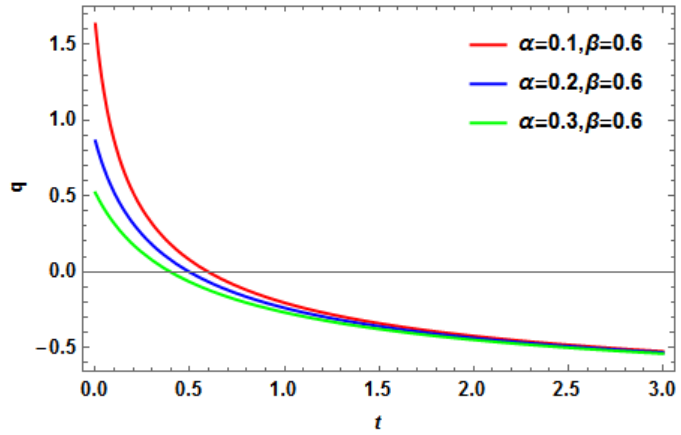


FIGURE 2. Variation of deceleration parameter against time with α=0.1,0.2,0.3,$\beta = 0.6$

As can be seen from figures (3) and (4), energy density and pressure also decrease with time. As can be seen from equation (30), string tension is zero. For $t \to 0$, the metric potentials A, B and C are constant, while for $t \to \infty$ the metric potentials A, B and C approach infinity (see fig.5). Also, component of the displacement field vector (β^2) decreases with time.

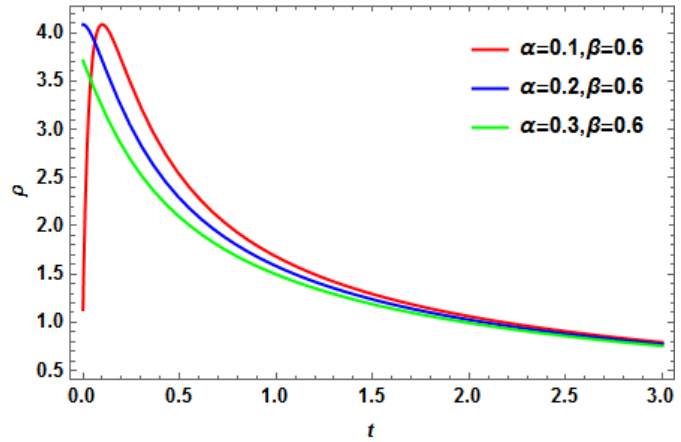


FIGURE 3. Variation of energy density against time with α=0.1,0.2,0.3,$\beta = 0.6$

ISBN:978-605-83516-6-0

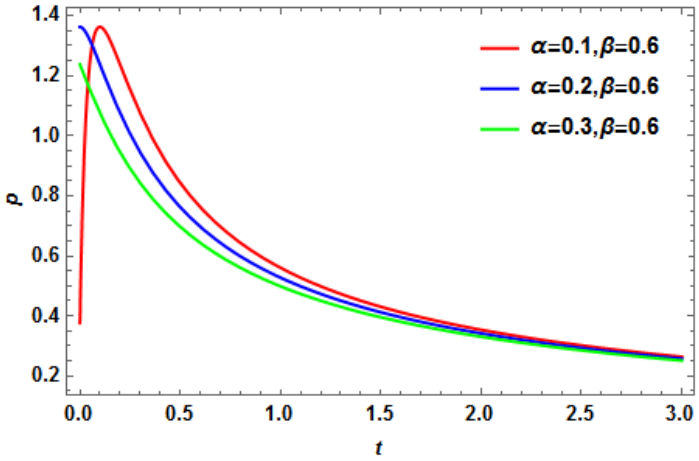


FIGURE 4. Variation of pressure versus time α=0.1, 0.2, 0.3, $\beta = 0.6$

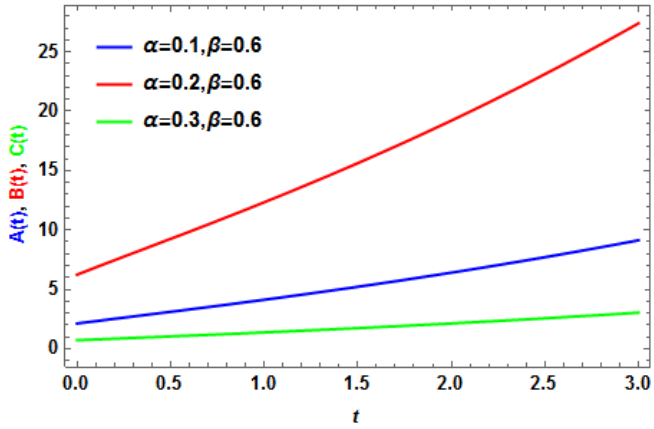


FIGURE 5. Variation of metric potentials against time with $\alpha = 0.1,0.2,0.3$, $\beta = 0.6$

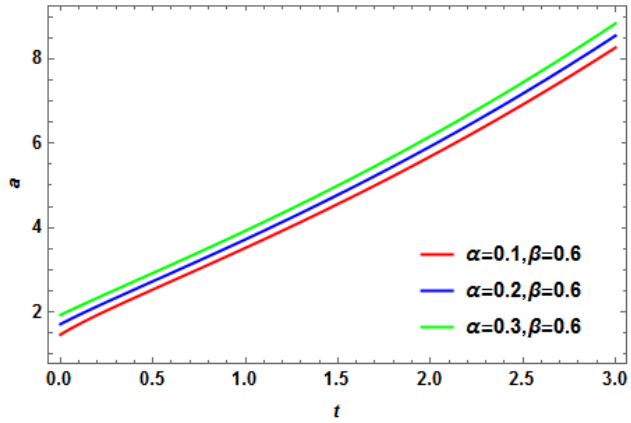


FIGURE 6. "a" change over time $\alpha = 0.2,0.3,\beta = 0.6$

ISBN:978-605-83516-6-0

ACKNOWLEDGMENTS

This study was produced from the master thesis of the first author.

REFERENCES

1. S. Perlmutter, G. Aldering, G. Goldhaber, R.A. Knop, P. Nugent, P.G. Castro, S. Deustua, S. Fabbro, A. Goobar, D.E. Groom, I. M. Hook, A.G. Kim, M.Y. Kim, J.C. Lee, N.J. Nunes, R. Pain, C.R. Pennypacker, R. Quimby, C. Lidman, R.S. Ellis, M. Irwin, R.G. McMahon, P. Ruiz-Lapuente, N. Walton, B. Schaefer, B.J. Boyle, A.V. Filippenko, T. Matheson, A.S. Fruchter, N. Panagia, H.J.M. Newberg, W.J. Couch Astrophys.J., 517,565-586, (1998).
2. A.G. Riess, A.V. Filippenko, P. Challis, A. Clocchiatti, A. Diercks, P. M. Garnavich, R. L. Gilliland, C. J. Hogan, S. Jha, R. P. Kirshner, B. Leibundgut, M. M. Phillips, D. Reiss, B. P. Schmidt, R. A. Schommer, R. C. Smith, J. Spyromilio, C. Stubbs, N. B. Suntzeff and J. Tonry, The Astronomical Journal, **116**, 1009 (1998).
3. Singh T., Sing P., Astrophysics and Space Science, **181**, 89-101,(1991)
4. Ram S. ,Singh P., International Journal of Theoretical Physics, **31**, 2095–2102, (1992).
5. Singh G. P. ,Desikan K., Pramana Journal of Physics, **49**, 205–212, (1997).
6. Sahu S.K., Int J Theor Phys, **50**, 3368, (2011)
7. Chaubey R., Int J Theor Phys, **51**, 3933-3940, (2012).
8. Baysal H., Aktas C., Gen. Relativ. Gravit., **44**, 2313-2328, (2012).
9. Sahu S.K. , Kumar T., Int J Theor Phys, **52**, 793-797, (2013).
10. Sahu S.K., Dalecha T. T.,Welay K., Int J Theor Phys, **54**, 807-811, (2015).
11. Santhi Vijaya M., Rao V.U.M., Aditya Y., Canadian Journal of Physics, **94**, 578-582, (2016).
12. Santhi Vijaya M.,. Rao V.U.M, Aditya Y., Canadian Journal of Physics, **95**, 179-183, (2016).
13. Aygün S., Aktaş C. , Yılmaz I., Journal of Geometry and Physics, **62**, 100-106, (2012).
14. Aygün S., Çaglar H., Taşer D., Aktaş C., The European Physical Journal Plus, **130**, 12, (2015).
15. Pacif S.K.J., Myrzakulov R.,Myrzakulov S., **14**, 7, (2017).

BOOK OF FULL TEXT PROCEEDINGS TURKISH PHYSICAL
SOCIETY 35th INTERNATIONAL PHYSICS CONGRESS (TPS35)
TPS35, Vol.01, No.07, pp.463-468.
ISBN:978-605-83516-6-0

15 December 2019

Solutions for Some Dark Energy Models in Kaluza-Klein Space-time

Elif Ece Demir[1, 2] and Can Aktaş[3]

[1)] *Graduate School of Natural and Applied Sciences*
Çanakkale Onsekiz Mart University, Terzioğlu Campus
17020, Çanakkale, Turkey

[2)] *Department of Mathematics, Gazi University, Faculty of Science, Teknikokullar, 06500 Ankara, Turkey*
elifecedemir@gazi.edu.tr

[3)] *Department of Mathematics, Çanakkale Onsekiz Mart University*
Arts and Sciences Faculty, Terzioğlu Campus
17020, Çanakkale, Turkey
canaktas@comu.edu.tr

Abstract. In this work, we have studied homogeneous anisotropic Kaluza-Klein space-time for some of the dark energy candidates in Lyra manifold. To achieve these solutions, we used the deceleration parameter. In addition to, we have illustrate graphic for various physical quantities.

INTRODUCTION

Observations in 1998 revealed that the universe was expand by accelerating [1, 2, 3, 4]. However, the source of this accelerating still maintains its mystery. Many ideas have been put forward to explain the reason for this expansion. One of these is the cosmological term that Einstein added to his equation and then take out. However, this term has two problems such as fine tuning and cosmic coincidence. Therefore, other candidates have been proposed as alternatives to the cosmological term. One of them is the dark energy that is thought to constitute seventy-three percent of the universe, although its existence is still unproven [5]. However, observations provide us information about the existence of dark energy. Scalar field models such as quintessence, dilaton and k-essence which is an accelerated expansion caused by changes in scalar fields are some of the dark energy candidates.

In 1916 Einstein published the field equation showing that matter and geometry were equivalent. This equation explains that the universe is expanding, but it cannot explain that it is expand by accelerating. Therefore, scientists have modified this equation and put forward various theories. One of these modified theories is Lyra theory which is formed by adding measure function to field equations. The function could not be integrated if a vector was parallel transported, but this was eliminated thanks to the added measure function. Therefore, it has been an interesting theory. Our aim in this study is to obtain solutions in the presence of k-essence scalar field within the framework of Lyra geometry.

Shikha , Umesh Kumar et al. obtained the solutions of Einstein's field equations by using deceleration parameter that shows universe transition from early decelerating to the current accelerating phase [6]. Myrzakulov made a thorough analysis to determine the equivalent conditions of the $F(T)$ and k-essence models [7]. Aktaş studied scalar field models with diverse space-times [8] [9, 10].Putter and Linder studied the limits to dynamical degeneracy between quintessence and k-essence [11] .Socoro et al. obtained solutions at k-essence for a perfect barotropic fluid $(p = \gamma\rho)$ and used the cosmological constant to obtain these solutions [12]. Borkar and Gayakwad studied the quintessence scalar field in the bimetric gravity theory when there was in the absence of the K magnetic field [13] . Our purpose in this study is to obtain exact solutions for k-essence and quintessence which are dark energy candidates, in Kaluza Klein space time in Lyra geometry.

BOOK OF FULL TEXT PROCEEDINGS TURKISH PHYSICAL
SOCIETY 35th INTERNATIONAL PHYSICS CONGRESS (TPS35)
ISBN:978-605-83516-6-0

MODIFIED FIELD EQUATIONS IN LYRA GEOMETRY

Field equation for Lyra Geometry which is formed by modifying Einstein Field equations by adding gauge function as follows:

$$R_{ij} - \frac{1}{2}g_{ij}R + \frac{3}{2} + \Phi_i\Phi_j - \frac{3}{4}g_{ij}\Phi_k\Phi^k = -T_{ij} \tag{1}$$

where $\Phi_i = (0,0,0,0,\beta)$ and β are the displacement vector and gauge function respectively.

Kaluza and Klein accomplished to unify gravity and electromagnetism. Adding extra dimensions to the standard (4D) spacetime has been found to be a good idea for combining electromagnetism and gravity. Besides, models such as supersymmetry [14] and string theory [15] include the idea of high dimension. Kaluza Klein theory was formed by the addition of a spacial dimension. Kaluza metric consisting of (x,y,z,u,t) coordinates is as follows:,

$$ds^2 = A^2(dx^2 + dy^2 + dz^2) + B^2du^2 - dt^2 \tag{2}$$

here, u_i that the fourth coordinate is space-like.

$$T_{ik} = (\rho + p)u_iu_k + pg_{ik} \tag{3}$$

where $u_i = (0,0,0,1)$ is 4-velocity of the co-moving observer, ρ is the energy density and p denotes the cosmic pressure also providing $u_iu^i = 1$. From equations (1)-(3), modified field equations in Lyra geometry as follows,

$$\frac{\ddot{B}}{B} + \frac{2\ddot{A}}{A} + \frac{2\dot{A}\dot{B}}{AB} + \frac{\dot{A}^2}{A^2} + \frac{3\beta^2}{4} = -p \tag{4}$$

$$\frac{3\dot{A}^2}{A^2} + \frac{3\ddot{A}}{A} + \frac{3\beta^2}{4} = -p \tag{5}$$

$$\frac{3\dot{A}\dot{B}}{AB} + \frac{3\ddot{A}}{A} - \frac{3\beta^2}{4} = \rho \tag{6}$$

where the dot denotes derivative with respect to t.

As you have seen that, we have three equations with five unknowns (A,B,p,ρ,β). To obtain exact solutions of field equations, we need more equality for this reason we take the deceleration parameter q and the conservation.

The conservation of the left side of equation (1) leads to the following equation.

$$(R_i^j - \frac{1}{2}Rg_i^j)_{;j} + \frac{3}{2}(\Phi_i\Phi^j)_{;j} - \frac{3}{4}(\Phi_k\Phi^k g_i^j)_{;j} = 0 \tag{7}$$

and from equation (7), we obtain

$$\left(3\frac{\dot{A}}{A} + \frac{\dot{B}}{B}\right)\beta^2 + \beta\dot{\beta} \tag{8}$$

As Berman points out, the constant deceleration parameter gives the power law for the scale factor at different phases of the universe. Deceleration parameter as follows,

$$q = \frac{d}{dt}\left(\frac{1}{H}\right) - 1 \tag{9}$$

In this study, we take the deceleration parameter as the constant deceleration parameter $q = m - 1$ proposed by Berman and m is constant [16].

From (q=m-1) we find B as follows;

$$B = \frac{(m(at+b))^{\frac{4}{m}}}{A^3} \tag{10}$$

If we solve Eqs.(4,5,6,8), we find metric potential A, gauge function, pressure and energy density as follows,

$$A = e^{\frac{-mc_2 a^{\frac{4}{m}}(at+b)^{\frac{m-4}{m}}+mc_3+a}{a(m-4)}}(at+b)^{\frac{1}{m}} \tag{11}$$

If we write equation (11) in equation (10);

$$B = (m^4(at+b))^{\frac{1}{m}} e^{\frac{3mc_2 a^{\frac{4}{m}}(at+b)^{\frac{m-4}{m}}-3mc_3-3a}{a(m-4)}} \tag{12}$$

$$\beta = c_3(at+b)^{\frac{-4}{m}} \tag{13}$$

$$p = \frac{12a^2(m-2)-24m^2c_2^2(at+b)^{\frac{2m-8}{m}}a^{\frac{8}{m}}-3m^2c_1^2(at+b)^{\frac{2m-8}{m}}}{4m^2(at+b)^2} \tag{14}$$

$$\rho = \frac{24a^2-24m^2c_2^2(at+b)^{\frac{2m-8}{m}}a^{\frac{8}{m}}-3m^2c_1^2(at+b)^{\frac{2m-8}{m}}}{4m^2(at+b)^2} \tag{15}$$

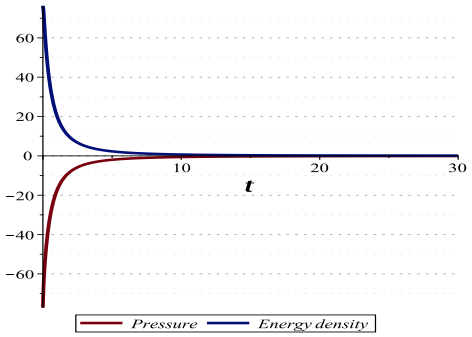


FIGURE 1. Variations of pressure and energy density against time.

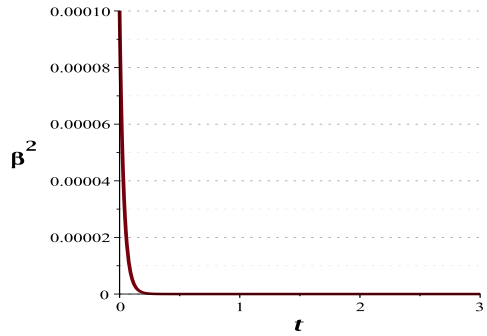


FIGURE 2. Variation of displacement vector against time.

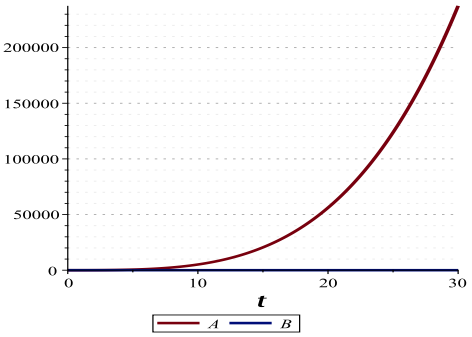


FIGURE 3. Variations of metric potential against time.

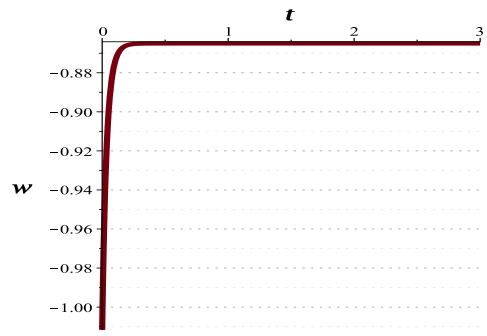


FIGURE 4. Variation of equation of state against time.

We obtained equation of state as a result of the ratio of energy density to pressure as follows:

$$w = \frac{m^2(c_1^2 a^{\frac{-8}{m}}+8c_2^2)(at+b)^2-4a^{\frac{2m-8}{m}}(m-2)(at+b)^{\frac{8}{m}}}{m^2(at+b)^2(c_1^2 a^{\frac{-8}{m}}+8c_2^2)-8a^{\frac{2m-8}{m}}(at+b)^{\frac{8}{m}}} \tag{16}$$

SCALAR FIELD SOLUTIONS IN LYRA GEOMETRY

In this work, we took the matter as dark energy that we needed to solve field equations. Although the existence of dark energy, which is thought to constitute approximately %73 of the universe, has not yet been proved, several candidates have been proposed for it. Some of them are k-essence [17], quintessence [17], tachyon [18] etc. In the following section, we assumed some of these scalar fields using the deceleration parameter and conservation equation.

k-essence Solutions in Lyra Geometry

In this paper, we represent k-essence that based on scalar fields with non-linear kinetic energy terms in the action. The aim of introducing the K-essence is to supply a non-anthropic dynamic explanation. In some situations, the k-essence component may behaves as a negative pressure component, thereby this componenet can cause cosmic accelerated [19].

The energy density ρ and pressure for the k-essence are given as follow;

$$\rho = V(\psi)\left(3\frac{\dot{\psi}^4}{4} - \frac{\dot{\psi}^2}{2}\right) \tag{17}$$

$$p = V(\psi)\left(\frac{\dot{\psi}^4}{4} - \frac{\dot{\psi}^2}{2}\right) \tag{18}$$

ψ is k-essence scalar field and $V(\psi)$ is k-essence potential.
We find from Eq. (20) that, when $w < -\frac{1}{3}$, the universe accelerates for $\dot{\psi}^2 < V(\psi)$.
From Eqs. (17),(18)

$$\dot{\psi}^2 = \frac{2a^2(m-4)}{8m^2c_2^2(at+b)^{\frac{2m-8}{m}}a^{\frac{-8}{m}} + m^2c_1^2(at+b)^{\frac{2m-8}{m}} - 2a^2(3m-8)} \tag{19}$$

$$V(t) = \frac{-3(8m^2c_2^2a^{\frac{-8}{m}}(at+b)^{\frac{2m-8}{m}} + m^2c_1^2(at+b)^{\frac{2m-8}{m}} - 2a^2(3m-8))^2}{8a^2m^2(m-4)(at+b)^2} \tag{20}$$

quintessence Solutions in Lyra Geometry

In the case w is -1, quintessence acts as a positive cosmological term. The acceleration of this scalar field that defined in range of $(-1, \frac{-1}{3})$ is also provided by the motivation of potential energy [20, 21]. The energy density and pressure for the quintessence are given as follows [22]

$$\rho = T_4^4 = \frac{\dot{\psi}^2}{2} + V(\psi) \tag{21}$$

$$p = -T_i^i = \frac{\dot{\psi}^2}{2} - V(\psi) \tag{22}$$

if we use eq. ($w = \frac{p}{\rho}$) for $w < -\frac{1}{3}$, we find that the universe accelerates when $\dot{\psi}^2 < V(\psi)$ [23] .

$$\dot{\psi}^2 = \frac{6a^2 - 24mc_2^2a^{\frac{8}{m}}(at+b)^{\frac{2m-8}{m}} - 3mc_1^2(at+b)^{\frac{2m-8}{m}}}{m(at+b)^2} \tag{23}$$

$$V(t) = \frac{3a^2(4-m)}{2m^2(at+b)^2} \tag{24}$$

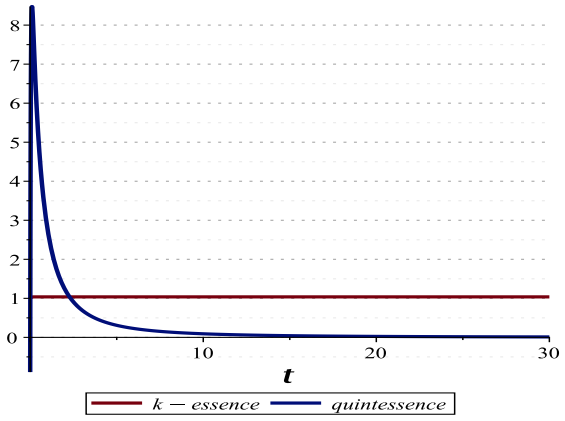


FIGURE 5. Variations of kinetic energy against time.

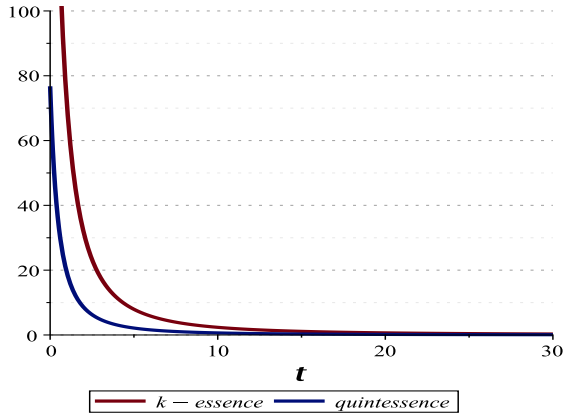


FIGURE 6. Variation of scalar potential against time.

CONCLUSION

In this study, we assumed that the matter that fill the universe is dark energy. For this reason, we have discussed the k-essence and quintessence scalar field in order to obtain exact solutions. We also used the Kaluza Klein metric in Lyra geometry. Since our unknown functions were more than our equations, we needed another equations. Therefore, we used the deceleration parameter and conservation equation.

We know that the deceleration parameter is in the range of -1 to 0. According to our results, our solutions comply with the observations since the parameter is in this range. In our model, t goes to infinity, metric potentials A and B both increase. However, if we compare the increase of B with the increase of A, it is quite small. When β equals zero, the Lyra geometry convert to general relativity. This is obtained if we take c_1 to zero. While the scalar potential decreases for both k-essence and quintessence, kinetic energy decreases for quintessence and increases for k-essence. For the dark energy candidates that we consider negative pressure and positive energy density, the pressure and energy density goes to 0 over time. In addition, the displacement vector resulting from lyra geometry decreases with time.

REFERENCES

1. S. Perlmutter, G. Aldering, G. Goldhaber, R. A. Knop, P. Nugent, P. G. Castro, S. Deustua, S. Fabbro, A. Goobar, D. E. Groom, I. M. Hook, A. G. Kim, M. Y. Kim, J. C. Lee, N. J. Nunes, R. Pain, C. R. Pennypacker, R. Quimby, C. Lidman, R. S. Ellis, M. Irwin, R. G. McMahon, P. Ruiz-Lapuente, N. Walton, B. Schaefer, B. J. Boyle, A. V. Filippenko, T. Matheson, A. S. Fruchter, N. Panagia, H. J. M. Newberg, W. J. Couch, and T. S. C. Project, "Measurements of Ω and Λ from 42 High-Redshift Supernovae," Astrophys. J. **517**, 565–586 (1999), arXiv:astro-ph/9812133 [astro-ph].
2. P. M. Garnavich, R. P. Kirshner, P. Challis, J. Tonry, R. L. Gilliland, R. C. Smith, A. Clocchiatti, A. Diercks, A. V. Filippenko, M. Hamuy, C. J. Hogan, B. Leibundgut, M. M. Phillips, D. Reiss, A. G. Riess, B. P. Schmidt, R. A. Schommer, J. Spyromilio, C. Stubbs, N. B. Suntzeff, and L. Wells, "Constraints on Cosmological Models from Hubble Space Telescope Observations of High-z Supernovae," **493**, L53–L57 (1998), arXiv:astro-ph/9710123 [astro-ph].
3. A. G. Riess, A. V. Filippenko, P. Challis, A. Clocchiatti, A. Diercks, P. M. Garnavich, R. L. Gilliland, C. J. Hogan, S. Jha, R. P. Kirshner, B. Leibundgut, M. M. Phillips, D. Reiss, B. P. Schmidt, R. A. Schommer, R. C. Smith, J. Spyromilio, C. Stubbs, N. B. Suntzeff, and J. Tonry, "Observational Evidence from Supernovae for an Accelerating Universe and a Cosmological Constant," **116**, 1009–1038 (1998), arXiv:astro-ph/9805201 [astro-ph].
4. R. Scranton, A. J. Connolly, R. C. Nichol, A. Stebbins, I. Szapudi, D. J. Eisenstein, N. Afshordi, T. Budavari, I. Csabai, J. A. Frieman, J. E. Gunn, D. Johnston, Y. Loh, R. H. Lupton, C. J. Miller, E. S. Sheldon, R. S. Sheth, A. S. Szalay, M. Tegmark, and Y. Xu, "Physical Evidence for Dark Energy," arXiv e-prints , astro-ph/0307335 (2003), arXiv:astro-ph/0307335 [astro-ph].
5. A. G. Riess, A. V. Filippenko, P. Challis, A. Clocchiatti, A. Diercks, P. M. Garnavich, R. L. Gilliland, C. J. Hogan, S. Jha, R. P. Kirshner, B. Leibundgut, M. M. Phillips, D. Reiss, B. P. Schmidt, R. A. Schommer, R. C. Smith, J. Spyromilio, C. Stubbs, N. B. Suntzeff, and J. Tonry, "Observational Evidence from Supernovae for an Accelerating Universe and a Cosmological Constant," The Astronomical Journal **116**, 1009–1038 (1998).
6. S. Srivastava, U. K. Sharma, and A. Pradhan, "New holographic dark energy in bianchi- III universe with k-essence," **68**, 57–64 (2019).
7. R. Myrzakulov, "Cosmology of F(T) Gravity and k-Essence," Entropy **14**, 1627–1651 (2012), arXiv:1212.2155 [gr-qc].
8. C. Aktaş, "Massive and massless scalar field models for Kaluza-Klein universe in f(R, T) gravity," Modern Physics Letters A **34**, 1950066 (2019).
9. C. Aktaş, S. Aygün, and İ. Yılmaz, "Behaviors of dark energy and mesonic scalar field for anisotropic universe in f(R) gravity," Physics Letters B **707**, 237–242 (2012).

10. S. Aygün, C. Aktaş, P. K. Sahoo, and B. K. Bishi, "Scalar Field Cosmology in f(R, T) Gravity with Λ," Gravitation and Cosmology **24**, 302–307 (2018).
11. R. de Putter and E. V. Linder, "Kinetic k-essence and quintessence," Astroparticle Physics **28**, 263–272 (2007), arXiv:0705.0400 [astro-ph].
12. J. Socorro, L. O. Pimentel, and A. Espinoza-García, "Classical Bianchi type I cosmology in K-essence theory," arXiv e-prints , arXiv:1409.3163 (2014), arXiv:1409.3163 [gr-qc].
13. M. S. Borkar and P. V. Gayakwad, "LRS Bianchi type I magnetized cosmological model with perfect fluid and with quintessence, Chaplygin gas dark energy in bimetric theory of gravitation," International Journal of Modern Physics D **26**, 1750061 (2017).
14. D. Z. Freedman and A. Van Proeyen, *Supergravity* (2012).
15. M. B. Green, J. H. Schwarz, and E. Witten, *Superstring Theory* (1988).
16. M. S. Berman, "A special law of variation for Hubble's parameter." Nuovo Cimento B Serie **74**, 182–186 (1983).
17. E. J. Copeland, M. Sami, and S. Tsujikawa, "Dynamics of Dark Energy," International Journal of Modern Physics D **15**, 1753–1935 (2006), arXiv:hep-th/0603057 [hep-th].
18. E. J. Copeland, "Dynamics of Dark Energy," in *Particles, Strings, and Cosmology-PASCOS 2007*, American Institute of Physics Conference Series, Vol. 957, edited by A. Rajantie, C. Contaldi, P. Dauncey, and H. Stoica (2007) pp. 21–29.
19. C. Armendariz-Picon, V. Mukhanov, and P. J. Steinhardt, "Essentials of k-essence," Phys. Rev. D **63**, 103510 (2001), arXiv:astro-ph/0006373 [astro-ph].
20. G.-B. Zhao, J.-Q. Xia, X.-M. Zhang, and B. Feng, "Probing Dynamics of Dark Energy with Supernova, Galaxy Clustering and the Three-Year Wilkinson Microwave Anisotropy Probe (wmap) Observations," International Journal of Modern Physics D **16**, 1229–1242 (2007), arXiv:astro-ph/0603621 [astro-ph].
21. J.-Q. Xia, H. Li, G.-B. Zhao, and X. Zhang, "Determining cosmological parameters with the latest observational data," Physical Review D **78** (2008), 10.1103/physrevd.78.083524.
22. E. J. Copeland, "Dynamics of Dark Energy," in *Particles, Strings, and Cosmology-PASCOS 2007*, American Institute of Physics Conference Series, Vol. 957, edited by A. Rajantie, C. Contaldi, P. Dauncey, and H. Stoica (2007) pp. 21–29.
23. M. S. J. M. Karami, K; Khaledian, "Reconstructing interacting entropy-corrected holographic scalar field models of dark energy in the non-flat universe," Physica Scripta **83** (2011).

BOOK OF FULL TEXT PROCEEDINGS TURKISH PHYSICAL
SOCIETY 35th INTERNATIONAL PHYSICS CONGRESS (TPS35)
TPS35, Vol.01, No.07, pp.469-473.
ISBN:978-605-83516-6-0 15 December 2019

Examination of Bianchi Type -VI0- for Dark Energy in Ƒ(R,T)=R+Λt Gravity

B.CIL[1], E.KARA[2], E. GUDEKLI[3], D.SOFUOGLU[4]

Istanbul University, Faculty of Science, Department of Mathematical Physics, Istanbul, Turkey

[1)]batuhan.cil@ogr.iu.edu.tr

[2)] erhan.kara@ogr.iu.edu.tr

[3)]gudekli@istanbul.edu.tr

[4)]degers@istanbul.edu.tr

Abstract. In this study, we considered the find dark energy situations with Einstein field equations in F(R,T)=R+λf(t) for Bianchi Type -VI$_0$- . After the analysis and interpretation of the Einstein field equations status and effects of the outcome were discussed. Then we examined the results within the framework of F(R,T) gravity. The results are finalized by performing physical and kinematic functions and their discussions.

Keywords. Dark Energy, Bianchi Type -VI$_0$-, F(R,T)=R+λf(t) Gravity

INTRODUCTION

We will examine dark energy situations with framework at F(R,T) gravity and builded from the Einstein-Hilbert variation principle. Principle gives us [1]

$$S = \frac{1}{16\pi G}\ [\int f(R,T)\sqrt{-g}\,d^4x + \int L_m\sqrt{-g}\,d^4x\,] \tag{1}$$

In axiom (1), f(R,T) is function of Ricci scalar R which express the curvature of the space-time and T energy-momentum scalar. L_m represents the lagragian of matter. Finding the energy-momentum tensor T_{uv} gives

$$T_{uv} = -\frac{2}{\sqrt{-g}}\frac{\partial\sqrt{-g}}{\partial g^{uv}}L_m \quad , \quad \theta_{\mu v} = -2T_{\mu v} - pg_{\mu v} \tag{2}$$

and we can find the F(R,T) field equation what we are looking to with varying the (1) respect to g_{uv} and we can obtain

$$f_R(R,T)R_{\mu v} - \frac{1}{2}f(R,T)g_{\mu v} + (g_{\mu v}\nabla^k\nabla_k - \nabla_\mu\nabla_v)$$

$$f_R(R,T) = 8\pi T_{\mu v} - f_T(R,T)T_{\mu v} - f_T(R,T)\theta_{\mu v} \tag{3}$$

∇ represents to covariant derivative.

Finding the f_R and f_T gives

$$f_R = \frac{\partial f(R,T)}{\partial R} \quad , \quad f_T = \frac{\partial f(R,T)}{\partial T} \quad , \quad \theta_{\mu v} = g^{\alpha\beta}\frac{\delta T_{\alpha\beta}}{\delta g^{\mu v}} \tag{4}$$

We assume the f(R,T) as

$$f(R,T) = f_1(R) + f_2(T) \tag{5}$$

Perfect fluid assumption gives us

$$f_1'(R)R_{ij} - \frac{1}{2}f_1(R)g_{ij} = 8\pi T_{ij} + f_2'(T)T_{ij} + [f_2'(T)p + \frac{1}{2}\,f_2(T)]g_{ij} \tag{6}$$

In the above equation,

ISBN:978-605-83516-6-0

finding a matter tensor from (6) gives

$$\theta_j^i \equiv -2T_{ij} - \delta_j^i p = (\rho, -p, -p, -p) \ , \tag{7}$$

for

$$T_j^i = (\rho + p)u_i u^j - \delta_j^i p$$

If we consider the $f_1 = R$ and $f_2 = \lambda T$, λ is an arbitrary constant [3], we can write our F(R,T) equation as F(R,T)= R+Λt and we can write our equation simplier.[2]

$$R_{ij} - \frac{1}{2}Rg_{ij} - \left(p + \frac{T}{2}\right)\lambda g_{ij} = \frac{8\pi+\lambda}{\lambda}T_{ij} \tag{8}$$

and [1]

$$G_j^i \equiv R_{ij} - \frac{1}{2}g_{ij}R = (8\pi + \lambda)T_{ij} + \lambda(p + \frac{T}{2})g_{ij} \tag{9}$$

That is worth to note that our energy-momentum tensor

$$T_{ij} = (\rho + p)u_i u_j - pg_{ij} \tag{10}$$

EXAMINATION OF METRIC AND FIELD EQUATIONS

In this paper, we will examine the homogeneus Bianchi Type-VI_0 space-time model below.

$$ds^2 = -c^2dt^2 + A^2dx^2 + B^2e^{-2mx}dy^2 + C^2e^{2mx}dz^2 \tag{11}$$

In this metric, A,B and C are functions which dependent of the cosmic time t and m is a constant.

Assuming the comoving coordinate system as u^u=(0,0,0,1) and solving the Einstein's field equation (9) with (10), our metric (11) gives

$$-\frac{\dot{A}}{A}\frac{\dot{B}}{B} - \frac{\dot{A}}{A}\frac{\dot{C}}{C} - \frac{\dot{B}}{B}\frac{\dot{C}}{C} + \frac{\dot{m}^2}{A^2} = (8\pi + \lambda)\rho + \lambda(\tfrac{\rho-p}{2}) \tag{12}$$

$$A^2(\frac{\ddot{B}}{B} + \frac{\ddot{C}}{C} + \frac{\dot{B}}{B}\frac{\dot{C}}{C} - \frac{m^2}{A^2}) = (8\pi + \lambda)A^2p - A^2\lambda(\tfrac{\rho-p}{2}) \tag{13}$$

$$\frac{B^2}{e^{2mx}}(\frac{\ddot{A}}{A} + \frac{\ddot{C}}{C} + \frac{\dot{A}}{A}\frac{\dot{C}}{C} - \frac{m^2}{A^2}) = (8\pi + \lambda)\frac{B^2}{e^{2mx}}p - \lambda\frac{B^2}{e^{2mx}}(\tfrac{\rho-p}{2}) \tag{14}$$

$$C^2e^{2mx}\left(\frac{\ddot{A}}{A} + \frac{\ddot{B}}{B} + \frac{\dot{A}}{A}\frac{\dot{B}}{B} - \frac{m^2}{A^2}\right) = (8\pi + \lambda)(C^2e^{2mx}) - (C^2e^{2mx})\lambda(\tfrac{\rho-p}{2}) \tag{15}$$

$$m\left(\frac{\dot{C}}{C} - \frac{\dot{B}}{B}\right) = 0 \tag{16}$$

And a dot head in equations denotes differentiation of functions for cosmic time t.

We relate the energy density of the universe ρ and pressure of the universe p as

$$p = w\rho \tag{17}$$

w is the EoS parameter.

Unit scalar factor a and volüme scalar V defining as

$$a^3 = V = ABC \tag{18}$$

ISBN:978-605-83516-6-0 15 December 2019

Hubble parameter H gives

$$H = \frac{\dot{a}}{a} = \frac{1}{3}(H_1 + H_2 + H_3) \tag{19}$$

Considering the directional Hubble parameters gives

$$H_1 = \frac{\dot{A}}{A} \quad , \quad H_2 = \frac{\dot{B}}{B} \quad , \quad H_3 = \frac{\dot{C}}{C} \tag{20}$$

$H_1, H_2\ and\ H_3$ representing the $H_x, H_y\ and\ H_z$

Expansion scalar θ and shear scalar σ defines as

$$\theta = 3H = 3\left[\frac{1}{3}(H_1 + H_2 + H_3)\right] = \frac{\dot{A}}{A} + \frac{\dot{B}}{B} + \frac{\dot{C}}{C} \tag{21}$$

$$3\sigma^2 = (\theta_{11} + \theta_{22} + \theta_{33})^2 - 3(\theta_{11}\theta_{22} + \theta_{22}\theta_{33} + \theta_{11}\theta_{33)} \tag{22}$$

Deceleration parameter of the universe q is

$$q = \frac{d}{dt}(H) - 1 \tag{23}$$

We can understand from that is the inflation happening or not so positive sign of q means to standart universe but negative sign means inflation.

SOLUTION OF THE EQUATIONS

Integration of (16) gives

$$B=C \tag{24}$$

In (24) neglecting the integration constant becomes our operations easier. Considering (24) gives us equation below from (12), (13), (14) and (15)

$$-2\frac{\dot{A}}{A}\frac{\dot{B}}{B} - \frac{\dot{B}^2}{B^2} + \frac{m^2}{A^2} = (8\pi + \lambda)\rho + \lambda\left(\frac{\rho - p}{2}\right) \tag{25}$$

$$2\frac{\ddot{B}}{B} + \frac{\dot{B}^2}{B^2} - \frac{m^2}{A^2} = (8\pi + \lambda)p - \lambda\left(\frac{\rho - p}{2}\right) \tag{26}$$

$$\frac{\ddot{A}}{A} + \frac{\ddot{B}}{B} + \frac{\dot{A}}{A}\frac{\dot{B}}{B} - \frac{m^2}{A^2} = (8\pi + \lambda)p - \lambda\left(\frac{\rho - p}{2}\right) \tag{27}$$

We will establish the following equality because of expansion scalar and shear scalar supposed to be proportional.

$$A = B^n \tag{28}$$

n is an arbitrary constant.

Finding the functions of A and B in terms of value scalar gives us

$$A = V^{\frac{n}{n+2}} \quad , \quad B = V^{\frac{1}{n+2}} \tag{29}$$

We can understand the left side of equations (26) and (27) are equal. It gives us

$$\frac{\ddot{B}}{B} - \frac{\ddot{A}}{A} + \frac{\dot{B}^2}{B^2} - \frac{\dot{A}}{A}\frac{\dot{B}}{B} + 2\frac{q^1}{A^2} = 0 \tag{30}$$

We have the functions of A and B in terms of volüme scalar V, so we can find their differential for cosmic time t.

Finding the differentials and puts to (30) given by

$$\ddot{V} = \frac{2m^2(n+2)}{(n-1)} V^{\frac{2-n}{n+2}} \tag{31}$$

ISBN:978-605-83516-6-0

integrating for V gives

$$\int \frac{dV}{V^{\frac{2}{N+2}}+C} = \int \frac{m(n+2)}{\sqrt{n-1}} dt \tag{32}$$

C is an integration costant.As a necessity from the right-hand side of the equation (32), the costant n must be grerater than 1. Otherwise the equation will become undefined with a negative expression on the root.In addition, in order to get the integral easier, we will assume the C=0 as we have bounded to the n element.

So our integral gives

$$V = (\frac{mn}{\sqrt{n-1}})^{\frac{n}{n+2}}(t + k_1) \tag{33}$$

k_1 is an costant from second integration.

We find a volüme scalar function so we can find the function of A and B

$$A = \frac{mn}{\sqrt{n-1}}(t + k_1) \tag{34}$$

$$B = (\frac{mn}{\sqrt{n-1}})^{\frac{1}{n}}(t + k_1)^{\frac{1}{n}} \tag{35}$$

Now we found A and B functions so we can write the metric like following form.

$$ds^2 = -dT^2 + \left(\frac{mn}{\sqrt{n-1}}\right)^2 dx^2 + \left(\frac{mn}{\sqrt{n-1}}\right)^{\frac{2}{n}} T^{\frac{2}{n}}(e^{-2mx}dy^2 + e^{2mx}dz^2) \tag{36}$$

In (36), we define the T= t+k.

Now we can find the energy density ρ and pressure p with analysing our equations and datas we found.

$$\rho = \frac{1-2n}{n^2T^2(8\pi+\lambda)} - \frac{1}{n^2T^2(4\pi+\lambda)} \tag{37}$$

$$p = \frac{2}{n^2T^2(4\pi+\lambda)} \tag{38}$$

Other physical and kinematic equations gives us equations below.

$$\frac{H_1}{n} = H_2 = H_3 = \frac{1}{T} \tag{39}$$

$$\theta = 3H = \frac{n+2}{nT} \tag{40}$$

$$\sigma = \frac{1}{\sqrt{3}}\frac{n-1}{nT} \tag{41}$$

$$q = -\frac{2}{n+2} \tag{42}$$

ISBN:978-605-83516-6-0

CONCLUSION

We have examined the physical and kinematic parameters for analysing dark energy and dark matter situations. That's worth to note that we studied in F(R,T)=R+Λt framework.

I- Hubble parameter and its dimentional Hubble parameters are inversely proportional with cosmic time t. Velocity of expansion is decreasing by the time running and also expansion parameter θ behave like that.

II- Shear scalar σ is also inversely proportional to cosmic time t and when n=1, shear scalar tends to zero.

III- Deceleration parameter q have a constant value. It doesn't depending any parameter. Never have a positive value so we can say the universe expansion velocity is decreasing with increasing the cosmic time t.

IV- All parameters tends to be zero when cosmic time t goes to infinity instead of deceleration parameter q.

V- At t=0, all parameters tends to infinite and that shows the singularity.

REFERENCES

[1] V.U.M. Rao, K.V.S. Sireesha and G. Suryanarayana, Perfect Fluid Bianchi Universes in a Modified Theory of Gravity (The African Review of Physics, 2016) 11:0040

[2] Chandel, P.S., Singh, M.K. and Ram, S. (2012) Bianchi Type-VI Dark Energy Cosmological Model in General Relativity. Global Journal of Science Frontier Research Mathematics and Decision Sciences, 12, 83A05.

[3] V.U.M. Rao, D. Neelima and K.V.S. Sireesha, Cosmological Models in a Modified Theory of Gravity (Prespacetime Journal, March 2013, Volume 4, Issue 3), pp.298-311

08. Medical Physics



BOOK OF FULL TEXT PROCEEDINGS TURKISH PHYSICAL
SOCIETY 35th INTERNATIONAL PHYSICS CONGRESS (TPS35)
TPS35, Vol.01, No.08, pp.475-480.
ISBN:978-605-83516-6-0

15 December 2019

CSDA Range Calculation of Proton Beam and Water Equivalent Ratio (WER) Value of Lucite ($C_5O_2H_8$)

Rıza Dilek

Istanbul Gedik University, Vocational High School, 34913 Pendik, Istanbul, Turkey

riza.dilek@gedik.edu.tr

Abstract. WER is known as the ratio of water equivalent thickness (WET) to radiological thickness of material thickness which commonly expressed in proton therapy. In this study, in order to calculate WER value of Lucite, measurements of the particle range were performed with a Water Phantom and Markus Chamber. The position of the Bragg-Peak was estimated by varying the Marcus Chamber's location inside water phantom and measuring the ratio of the charge deposited in the chamber for proton beam which has 58.7 MeV energy. On the other hand, an analytical CSDA range formula by basing on the definition of stopping power (SP) was developed for theoretically range calculation and effective SP formula was used to calculate SP values. Subsequently, both experimentally and theoretically WER results compared with NIST database. As a result, The analytical formula can be used to calculate WER values and WER value of Lucite can be used to range prediction without any range calculation for later researches

INTRODUCTION

In radiotherapy, the main purpose is to deliver maximum radiation dose to tumor while sparing adjacent healthy tissues or critical organs. The main advantage of proton therapy is the release of maximum energy in the area called Break Peak immediately before the end of the proton range. The position of the Bragg peak is determined by the proton SP ratios relative to water along the beam's path in each patient. Therefore, inaccurate stopping power measurements in human tissues would introduce range uncertainties for proton therapy (1). Thus, it is critical to measure stopping power for proton therapy patients with high accuracy and high confidence.

During quality assurance testing which is made for treatment planning, generally, water is used to characterize tissues. Besides water, WET or WER values are important to calculate absorbed dose, beam penetrations, the thickness of components that are in the proton beam path and etc. In clinical application, WER value could be measured by observing the range shift in water phantom associated with the introduction of a test object (2). The International Atomic Energy Agency (IAEA) used ratio of continuous-slowing-down approximation (CSDA) ranges in water and in the material wanted to predict WET (IAEA 2000) (3). Newhauser et al (2007a) revealed that WER calculations depend on proton energy and material thickness by studying on their numerical method (4). Afterward, Zhang et al (2009) tried to develop and validate analytical expressions using theoretical range-energy relations, with the goal of achieving 1 mm uncertainty in WET (5). Then they calculated WET of various materials exposed to beams of protons, helium, carbon and iron ions (6).

In this study, in order to calculate WER value of Lucite as clinically, measurements of the particle range were performed with Markus Chamber. The position of the Bragg-Peak was estimated by varying the Marcus Chamber's location inside water phantom and measuring the ratio of the charge deposited in the chamber for proton beam which has 58.7 MeV energy. On the other hand, to theoretical WER calculation, an analytical CSDA range formula by basing on the definition of stopping power (SP) was developed. For his purpose, effective SP that suggested by Gunes at all was used. In this formula Gunes et al. (2015) used effective charge of proton, z*, atomic number of target, Z*, and ionization potential of target, I* in the stopping power equation proposed by Bethe-Bloch (1930-1933) and later modified by Tsoulfanidis (1995) for proton (7)

Türk Fizik Derneği
1950
Turkish Physical Society

ISBN:978-605-83516-6-0

METODOLOGY

Stopping Power

Proton's mass stopping power was calculated using new approach. The novelty of the approach was to introduce the values of effective charge, z*, atomic numer, Z* and ionization potential, I* respectively instead of z, Z and I. This formula is:

$$\frac{1}{\rho}\frac{dE}{dx} = 4\pi r_0^{\,2}(z^*)^2\frac{mc^2}{\beta^2}\frac{N_0}{A}(Z^*)\left[\ln\left(\frac{2mc^2}{(I^*)}\beta^2\gamma^2\right)-\beta^2\right] \tag{1}$$

Here, $r_0 = 2.818\times10^{-15}\ m$ is classical electron radius, mc^2 is rest mass energy of electron and it's values is 0.511 MeV. mc^2 is rest mass energy of proton and it's values is 931.5 MeV. N_0 is number of atom in target material per m^3, A is atomic mass number of target material, Z is atomic number of target material and ρ is density of target.

The following equations were proposed, taking the values of z^*, Z^* and I^* respectively from publications (8), (9), (10), (11), (12),

$$z^* = 1-\exp(-2200\beta^{1.78}) \tag{2}$$

$$Z^* = Z\frac{b^2(3x+b)}{(x+b)^3} \tag{3}$$

$$I^* = 2(13,6)\gamma Z C_0^{-3/2} exp(\alpha) \tag{4}$$

$C_0 = 0.6064741718$

where b is the normalization constant,

$$b = \left(\frac{8}{\pi}\right)^{2/3} \tag{5}$$

$$a = \frac{b^2}{0,60647}\frac{V_0^2}{V^2}Z^{4/3} \qquad V_0 = 2.42x10^6\ m/s \tag{6}$$

$$\beta = \frac{V}{c} \tag{7}$$

$$x = -2\left(\frac{b}{3}\right)+\frac{\left(\frac{b}{3}\right)^3}{\left[\frac{a}{2}+\left(\frac{b}{3}\right)^3+\sqrt{\left(a/2\right)^2+a\left(b/3\right)^3}\right]^{1/3}}+ \left[\frac{a}{2}+\left(\frac{b}{3}\right)^3+\sqrt{\left(a/2\right)^2+a\left(b/3\right)^3}\right]^{1/3} \tag{8}$$

ISBN:978-605-83516-6-0

$$\alpha = \frac{Z}{2Z^*}\Big[x^2\left(x+3b\right)\ln x + x\left(x+b\right)b + x\left(\ln 6-2\right)3b^2 + b^3\left(\ln 6-10/3\right) + \left(3x+b\right)b^2\ln\frac{b^2}{\left(x+b\right)^4} - \left(x+b\right)^3\ln\left(x+b\right)\Big]/\left(x+b\right)^3 \quad (9)$$

$$I = 10,4621\,\gamma\,Z \quad (10)$$

CSDA and Range Calculation

Theoretically, CSDA ranges are calculated in the continuous-slowing-down approximation by integrating the reciprocal of the stopping power with respect to energy. But in this study in order to be practical, we have developed following analytical formula for CSDA calculation by basing on the definition of stopping power;

$$R_{CSDA} = ((E_{i+1} - E_i)(2/(S_{i+1} + S_i)))\rho \quad (11)$$

Here; R_{CSDA} is continuous-slowing-down approximation range, E_i and E_{i+1} are respectively first and further energy, S_i and S_{i+1} are respectively first and further stopping power and ρ is target density. The relative difference of the calculated and measured range is quantified by the following expression:

$$\text{Re}\,lative\ \text{Difference}(\%) = \frac{\left|R_{Teo} - R_{NIST}\right|}{R_{NIST}} x100(\%) \quad (12)$$

Water Equivalent Ratio (WER)

Experimental WER Value

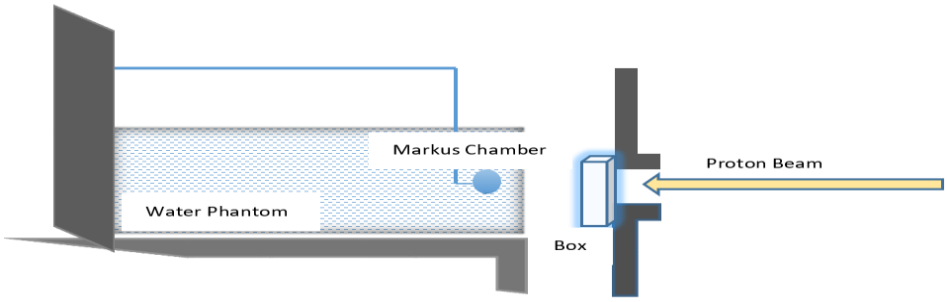


Figure 1. Schematic view on the Lucite range measurement setup

Proton beam which has 58.7 MeV energy and Lucite which has 1,74 cm thickness were used to measure experimental WER. The measurements of the particle range in Lucite were performed with a Water Phantom and Markus Chamber. The sample was positioned upstream to a Water Phantom, as it is schematically drawn in Figure 1. The position of the Bragg-Peak was estimated by varying the Marcus Chamber's location inside water phantom and measuring the ratio of the charge deposited in the chamber.
Then the formula below was used for the experimental measurement of WER by taking values from sample's Bragg Peak graphic.

ISBN:978-605-83516-6-0

$$WER_{Exp} = \frac{R_{w,\%90} - R_{l,\%90}}{l_l} \tag{13}$$

Here, $R_{w,\%90}$ is protons range in water, $R_{l,\%90}$ is protons range in lucite and l_l is Lucite thickness. (Range is measured at Bragg Peak's %90 position as experimentally)

Theoretically WER Calculation

For theoretical calculations, ranges were calculated analytically by using R_{CSDA} (Equation 11). Then WET values were obtained by using the formula below for each sample. For these calculations, E_i was taken as 55.7 MeV and E_{i+1} taken as 58.7 MeV

$$WER_{Teo} = \frac{R_{w,i+1} - R_{w,i}}{R_{s,i+1} - R_{s,i}} \tag{14}$$

RESULTS

We used Equation 1 to calculate mass SP that is necessary to calculate RCSDA for Lucite. Besides NIST mass SP values were taken from NIST DATA to compare with our results.

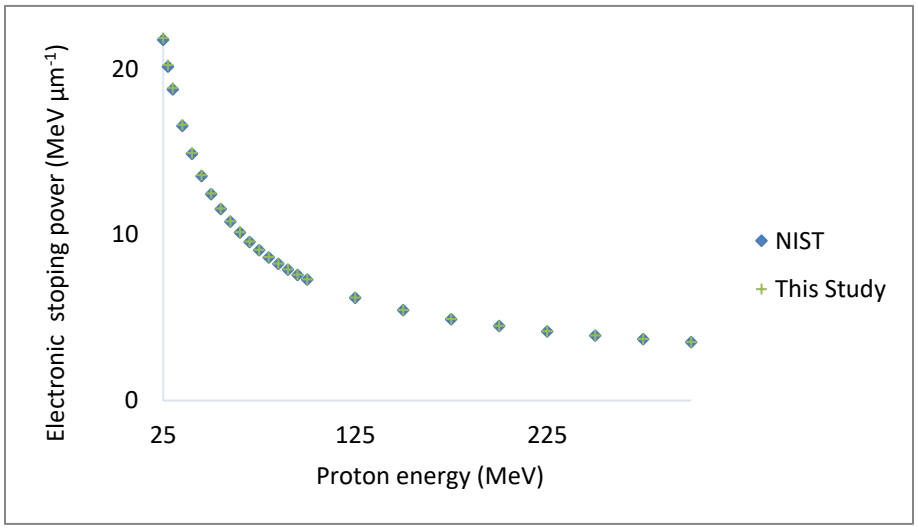


Figure 2. Lucite's mass stopping power versus proton energy

Figure 2 shows the concordance of the NIST data and the results obtained using Eq 1 in the treatment energies.

The experimental measurements of the particle range in Lucite were performed at the proton therapy eye treatment room using 58 MeV protons generated from AIC_144 cyclotron The measurements was performed by Markus type ionization chamber moving along the water phantom.

ISBN:978-605-83516-6-0

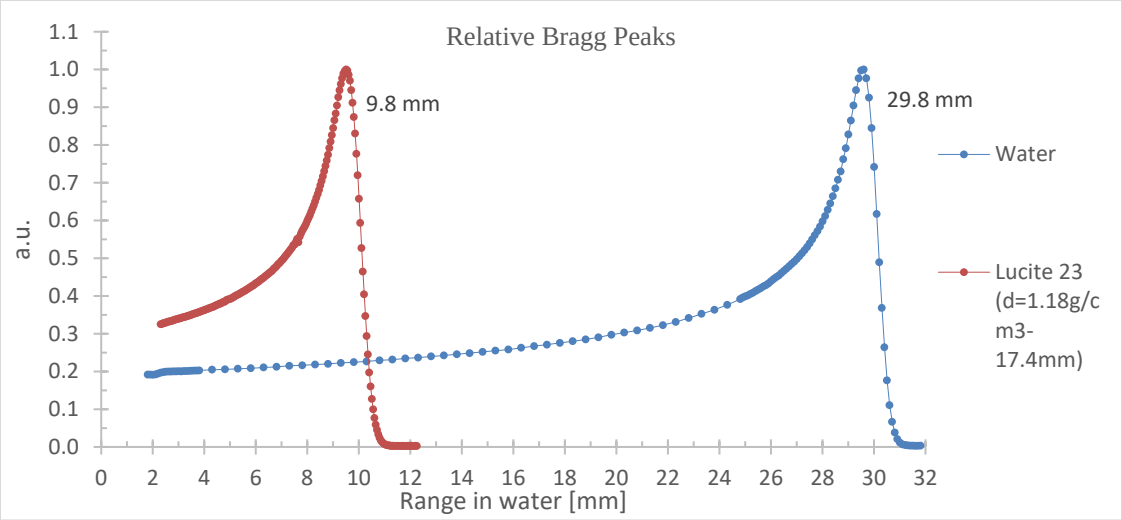


Figure 3. Relative Bragg Peaks in water and water with Lucite ($C_5O_2H_8$)

As seen in figure xx, while range of proton beam in water that has 58.7 MeV energy is 29.8 mm, when Lucite with 1.74 cm thickness is used, range is 9.8 mm.

In this study, the relative differences between WER values were made by using equation 3 considering NIST values.

TABLE 1. WER and relative difference values of Lucite

	WER_{EXP}	WER_{TEO}	WER_{NIST}	Relative $Dif._{EXP}$	Relative $Dif._{TEO}$
Lucite ($C_5O_2H_8$)	1.16	1.17	1.16	% 0.00	% 0.43

Table 1 illustrates that experimental WER value in full compliance with NIST WER value. In addition relative difference of theoretical WER value is below of %1.

DISCUSSION

We evaluated experimental and theoretical methods to calculate WER values for Lucite that is using commonly as tissue-like phantom material. While experimental values gave the most accurate results for WER, Relative difference of result of SP-based analytical formula used for theoretical calculations were less than 1%.

Because of the fact that clinical requirement on range accuracy is 1.5 mm, WET calculation must be less than 1.5 mm. Accordingly selecting an appropriate approach to determine WET is critical. According to our theoretical results, in order to perform WER calculations correctly by using analytical formula, SP calculations must be accurate. However, WER calculation findings of Lucite and the recommended formula are not sufficient for practical application in the clinical setting. Because there are studies in the literature indicate that WER values could vary with material thickness and energy of the beam (2).

Therefore, this study demonstrates that the necessity of expanding the study as well as a simple method can be used to calculate WET values.

ISBN:978-605-83516-6-0

ACKNOWLEDGMENTS

This Project was supported by The Scientific and Technological Research Council of Turkey (TUBITAK) 2214-A, 2015/2 Fellowship Programme and experimental studies were made in Institute of Nuclear Physics PAN,KRAKOW/POLAND. Thank you for all their supports.

The reference section will follow the "Acknowledgment" section. References should be numbered using Arabic numerals followed by a period (.) as shown below, and should follow the format in the below examples.

REFERENCES

1. Yang M, Virshup G, Clayton J, Zhu XR, Mohan R, Dong L. Theoretical variance analysis of single- and dual-energy computed tomography methods for calculating proton stopping power ratios of biological tissues. Phys Med Biol. 2010;55(5):1343–62.
2. Zhang R, Newhauser WD. Calculation of water equivalent thickness of materials of arbitrary density , elemental composition and ... 2009;(February).
3. Mather SJ, Mansi L. IAEA Technical Report Series. Eur J Nucl Med Mol Imaging. 2008;35(5):1030–1.
4. Newhauser W, Fontenot J, Koch N, Dong L, Lee A, Zheng Y, et al. Monte Carlo simulations of the dosimetric impact of radiopaque fiducial markers for proton radiotherapy of the prostate. Phys Med Biol. 2007;52(11):2937–52.
5. Zhang R, Newhauser WD. Calculation of water equivalent thickness of materials of arbitrary density, elemental composition and thickness in proton beam irradiation. Phys Med Biol [Internet]. 2009;54(6):1383–95. Available from: http://stacks.iop.org/0031-9155/54/i=6/a=001?key=crossref.ab9ef6eb3cf7329de71382ef9e5c761d
6. Zhang R, Taddei PJ, Fitzek MM, Newhauser WD. Water equivalent thickness values of materials used in beams of protons, helium, carbon and iron ions. Phys Med Biol [Internet]. 2010;55(9):2481–93. Available from: http://stacks.iop.org/0031-9155/55/i=9/a=004?key=crossref.5458d08dd994e473f3590c69a2fa57d6
7. Tanır G, Dilek R, Hicabi Bölükdemir M, Feng Z. The Stopping Powers of Water and Lung for Protons in Radiotherapy. J Sci Res Reports JSRR [Internet]. 2015;6(64):287–93. Available from: www.sciencedomain.org
8. Salvat F, Martinez JD, Mayol R. Stopping power formula for intermediate energy electrons Related content A simple model for electron scattering: inelastic collisions. Phys Med Biol H Sugiyama Phys Med Biol [Internet]. 1985 [cited 2018 Apr 6];30. Available from: http://iopscience.iop.org/article/10.1088/0031-9155/30/4/006/pdf
9. Tufan MÇ, Gümüş H. A study on the calculation of stopping power and CSDA Range for incident positrons. J Nucl Mater [Internet]. 2011 May 31 [cited 2018 Apr 7];412(3):308–14. Available from: https://www.sciencedirect.com/science/article/pii/S0022311511002741
10. Cabrera-Trujillo R, Cruz SA, Oddershede J, Sabin JR. Bethe theory of stopping incorporating electronic excitations of partially stripped projectiles. Phys Rev A [Internet]. 1997 Apr 1 [cited 2018 Apr 8];55(4):2864–72. Available from: https://link.aps.org/doi/10.1103/PhysRevA.55.2864
11. Tufan MÇ, Gümüs H. Stopping Power Calculations of Compounds by Using Thomas–Fermi–Dirac–Weizsäcker Density Functional. 2008 [cited 2018 Apr 7];114. Available from: http://przyrbwn.icm.edu.pl/APP/PDF/114/a114z406.pdf

09. Nuclear Physics



BOOK OF FULL TEXT PROCEEDINGS TURKISH PHYSICAL
SOCIETY 35th INTERNATIONAL PHYSICS CONGRESS (TPS35)
TPS35, Vol.01, No.09, pp.482-490.
ISBN:978-605-83516-6-0 15 December 2019

A Study on TL Properties of Natural Dolomite Mineral Irradiated with Beta Particles

S. Akça[1, a)]

[1]*Çukurova University, Faculty of Arts and Sciences, Department of Physics, Adana, Turkey*

[a)]*Corresponding author: sblakca@gmail.com*

Abstract. The present study aims to reveal thermoluminescence (TL) features of natural dolomite mineral. In the first stage, the proper filter was selected as WBB with HR of 2 $^{o}Cs^{-1}$ from RT to 450 °C. The results obtained from TL glow curves showed that the curves were composed of two peak maxima (pm) located at 102 and 252 °C at doses between 0.11-10 Gy. When examined the dose dependence of each peak maxima, each of them exhibited a good linear response. The mineral was found to be reusable within 8% and 16% for peak 1 and 2, respectively. The effects of the HRs in the range of 0.5-10 $°Cs^{-1}$ on TL were researched taking into account the change of the FWHM, T_m, I_m and peak area vs HR for each pm and observed an anomalous case increasing TL intensity with HR. The T_m-T_{stop} experiment and CGCD analyses performed showed that the curves consist of at least 8 superposition peaks. The E_a values are in good agreement at both methods and found to be 0.65-1.08 (p1) and 1.4-1.71 eV (p2) applying CGCD method.

INTRODUCTION

Dolomite ($CaMg(CO_3)_2$) is a common mineral consisting of alternate layers of calcite $CaCO_3$ and magnesite $MgCO_3$ used mostly in industrial fields. One of the most important application areas of dolomite mineral is to use in the production of fire-resistant materials, used in metallurgy, chemical and ceramic industries [1–2]. In recent years, besides, several studies on thermoluminescence (TL) characteristic of this mineral have been performed by the irradiation with gamma rays in general [3-6].

In a study on TL of natural dolomite, Soliman et al. observed that the glow curve of the blue emission band in TL in the range from room temperature (RT) to 400 °C had peaks at 240 and 270 °C with a heating rate (HR) 4 °C/s. The laboratory induced glow curve had 10 peaks between 145 and 355 °C for a gamma dose of 10^4 Gy and the TL response to gamma-rays was found to be linear over the dose range 500–10^4 Gy [3]. Ramasamy et al. studied on features of TL glow curve of ten dolomitic crystals. Two peaks at 270 °C and 335 °C were observed in the natural thermoluminescence (NTL) measurements whereas an extra peak at 180 °C appeared when the sample had been exposed to a gamma dose of 200 Gy. Annealing experiments of the samples were carried out at the temperatures in the range of 200-950 °C for all three TL peaks and annealing temperature of 700 °C for 4 h followed by quenching in air was found to be in the optimum condition for TL. They also evaluated the kinetic parameters of dolomite crystal using peak shape (PS) and initial rise (IR) method and concluded that the trapping centers were not influenced by the annealing process [4]. A theoretical study on concentration quenching (CQ) of TL in dolomite was also performed by Mostefa el al. It was carried out using the model of 5TOR. The simulated results achieved using their model were found in harmony with the experimental results put submitted previously in the literature [5]. Soliman et al. studied again on natural dolomite and observed that their natural dolomite sample gave two peaks at 240 °C and 325 °C in the green region and four peaks at 225, 240, 270 and 325 °C in the red region. They also obtained sublinearity for both bands in the range of 1-100 Gy and linearity in the region 200-10^4Gy at the dose response curves [6].

In the present study, dose-response, reusability, heating rate (HR) effect and kinetic parameters (activation energy (E_a), frequency factor (s) and order of kinetic (b)) of natural dolomite samples were investigated to determine the TL properties of the mineral. To evaluate the kinetic parameters, T_m-T_{stop} experiment and CGCD (Computed Glow Curve Deconvolution) analyses were carried out.

Türk Fizik Derneği
1950
Turkish Physical Society

ISBN:978-605-83516-6-0

MATERIAL AND METHODS

The natural dolomite samples were supplied from Mersin province in Turkey. The samples were ground to a powder with an agate mortar, and the powdered samples were sieved at the size of 90 µm then placed in Eppendorf tubes. The powder samples of 25 mg pressed with pressure of 2 tons/cm^2 during 20 minutes were converted to thin pellet form before being analyzed and measured.

All TL measurements of the pellets were performed using an automated Lexsyg Smart TL/OSL reader system having different filter combinations. The reader system has an internal $^{90}Sr/^{90}Y$ source with 1.95 GBq emitting beta particles with a maximum energy of 2.2 MeV and a dose rate of 0.11 Gys^{-1}.

The pellet samples of 25 mg were heated from RT to 450 °C to eliminate the previous history of any geological information prior to irradiation. In the first stage of the experiment, TL glow curves of the filter test performed using different band filters were recorded with a constant HR of 2 ^{o}Cs^{-1} from RT to 450 °C after a dose of 5 Gy. The TL glow curves to observe dose-response were also recorded at the dose in the range of 0.11–10 Gy with beta irradiation. In addition, the TL curves of the HRs in the range of 0.5-10 °Cs^{-1} and reusability test were performed with beta dose of 5 Gy.

RESULTS AND DISCUSSION

Optimum Filter

The selection of the best suitable filter is of great importance to observe the TL signal more efficiently. The automated Lexsyg Smart TL/OSL reader used in this study provides the opportunity to choose the desired one among various types of band pass filters inserted between the sample and the photomultiplier tube (PMT). The pellet samples were exposed to a constant beta dose of 5 Gy for suitable filter selection. Fig. 1 displays a comparison of IRSL wideband blue (WBB), BSL 365 nm, IRSL 410 nm, and IRSL 565 filters. It can be easily seen from Fig. 1, the highest TL intensity has been obtained using WBB filter and there are two peak maxima centered at 102 and 252 °C. In the lights of these results, TL measurements in the present study were carried out using the WBB filter.

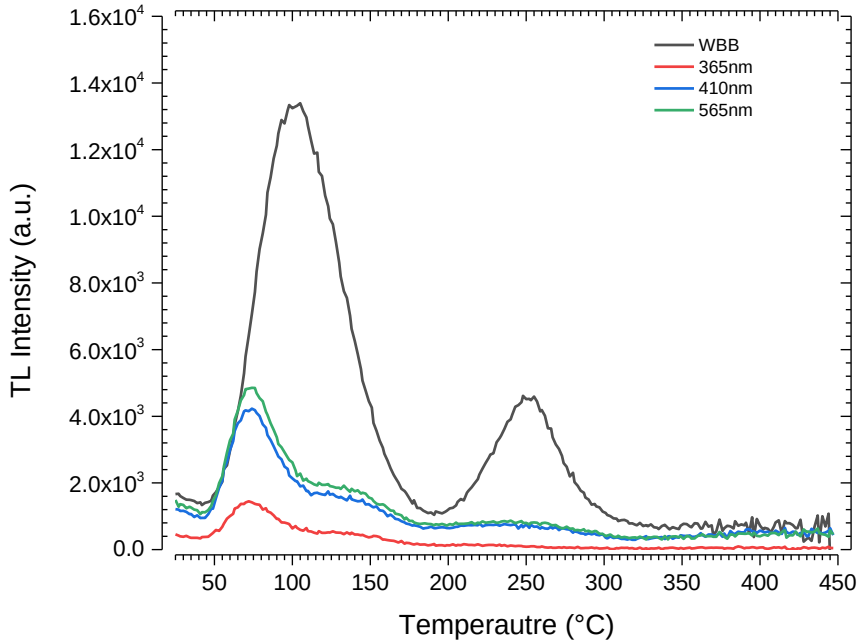


FIGURE 1. The results of filter test of natural dolomite mineral at dose of 5 Gy with heating rate of 2 ^{o}Cs^{-1}

ISBN:978-605-83516-6-0

Dose-Response

A good TL material is expected to respond to different dose levels with the same precision. To evaluate dose-response of the dolomite pellets TL glow curves were recorded at low beta doses in the range of 0.11 – 10 Gy. Fig. 2 shows TL glow curves of the pellets at the dose of 0.11, 1, 3, 5, 8 and 10 Gy. As seen in Fig. 2, the curves compose of two peak maxima up to 10 Gy and the TL intensity increased with the increasing beta doses.

In addition, to see the relation between TL intensity and irradiation dose more clearly, a figure (Fig. 3) that shows the change of peak area versus beta dose is plotted using an equation of the form; $TL = aD^b$. When examined the dose dependence of each peak maxima, according to area under each peak maxima, each of them exhibits a good linear response with linearity parameters of b=1.03 and b=1.17 for peak-1 and peak 2, respectively.

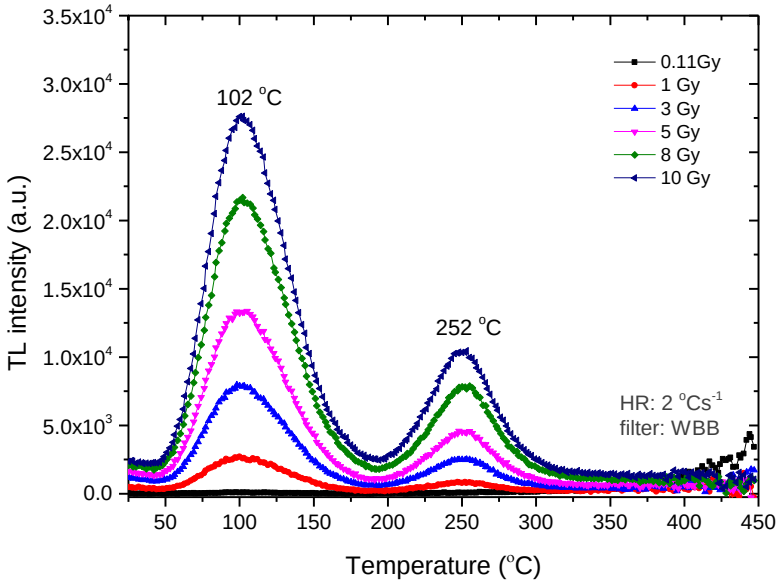


FIGURE 2. TL responses versus doses between 0.11-10 Gy of natural dolomite mineral

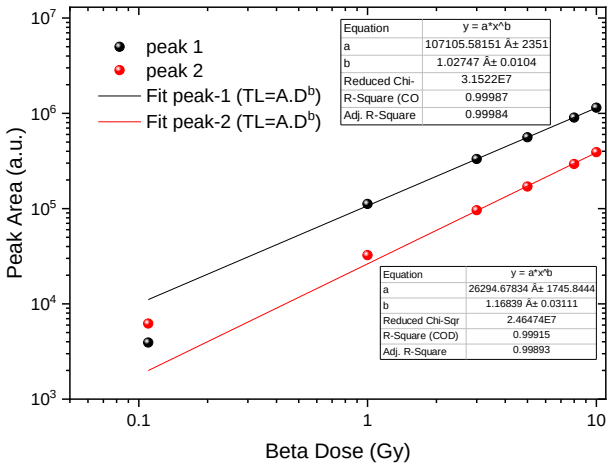


FIGURE 3. The change of peak area versus the dose of natural dolomite mineral for peak 1 and peak 2

ISBN:978-605-83516-6-0

Heating Rate

TL peak shape and position show changes depending on the heating rate (HR). Thus, the influences of the HRs in the range of 0.5-10 °Cs^{-1} on TL glow peak of natural dolomite pellet were examined with beta irradiation of 5 Gy. The effects of the HRs are presented in Fig.4. One can see in Fig.4 that (the unit of TL intensity is given as count/ °C) the peak maxima temperatures of the glow curve shift to higher temperatures with increasing HR. Besides, it is seen in the figure that behavior of TL intensity of the glow peaks does not exhibit the expected result in the TL theory [7]. The intensity of TL glow peak maxima increases with an increase at HR, which is known as anomalous heating rate effect. Such an anomalous effect can be resulted from an increase in the probability of radiative transitions compared to that of the non-radiative transitions [8].

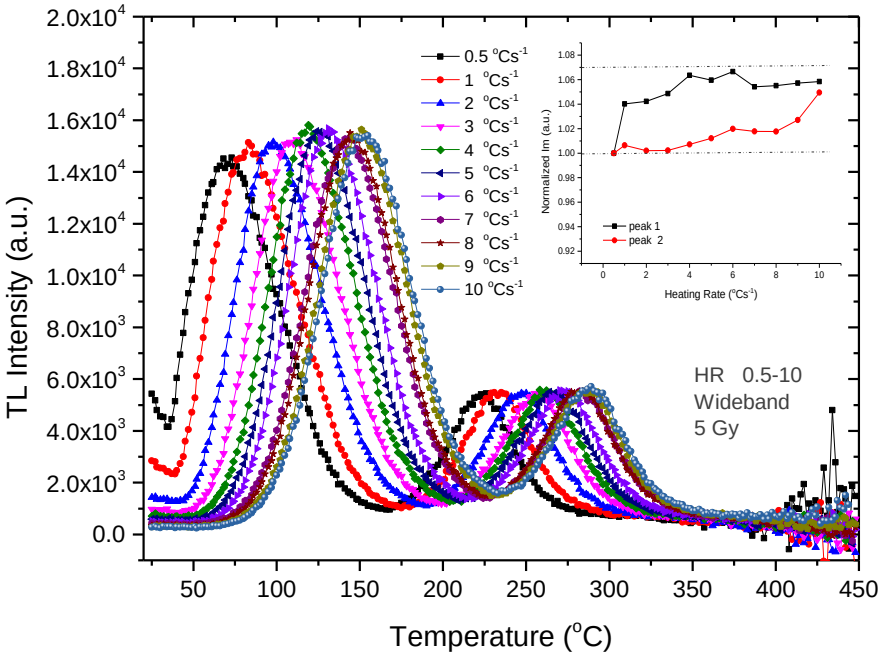


FIGURE 4. TL glow curves of natural dolomite mineral measured at various heating rates from 0.5 to 10 °Cs^{-1}. Inset Figure shows the normalized maximum intensity (I_m) versus heating rate for peak 1 and 2.

To examine the influence of HR in detail, the graphs of the change of the normalized peak area, peak maxima temperature (T_m) and the full width at the half maximum (FWHM) versus HR for each peak maxima were plotted (Fig. 5 (a), (b), (c)). The area under the TL peak maxima increases in the rate of about 15% by the increase of HR for peak 1 and 2 (Fig. 5(a)). The T_m shifts to the higher temperatures with increasing HR (Fig. 5(b)). Besides, when examined the behavior of the FWHM of natural dolomite pellets versus HR (Fig. 5(c)), it is observed that the glow peak comparatively becomes much wider for both peak maxima.

ISBN:978-605-83516-6-0

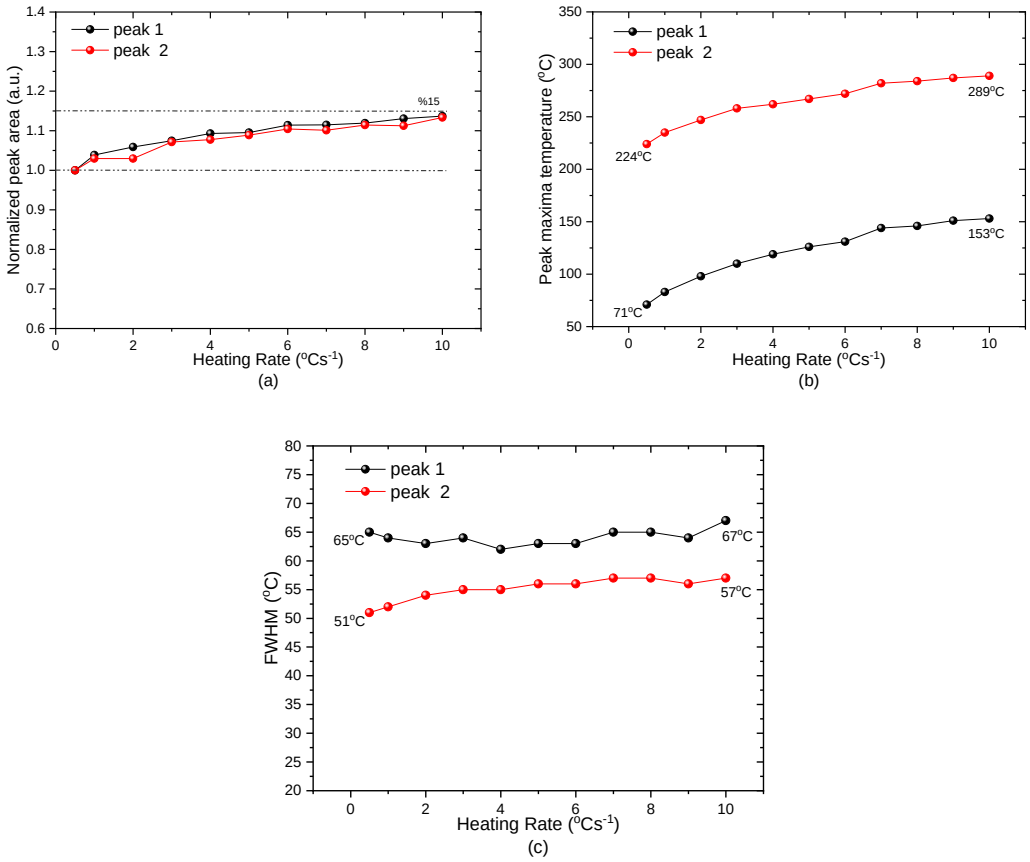


FIGURE 5. The change of **(a)** the normalized peak area **(b)** the peak maxima temperature **(c)** FWHM versus heating rate for peak 1 and peak 2 of natural dolomite mineral

Reusability

The reusability test determines if TL signal from material exhibits any changes when exposed to the same conditions. In this experiment, the readouts of the glow curve were carried out for 9 sequential measurements with dose of 5 Gy at a linear HR of 2 $^{o}Cs^{-1}$ and the results revealed that the mineral is reusable within 8% and 16% for peak 1 and 2, respectively (Fig. 6). Actually, reusability of a good TL material should have less than 5% for sequential measurements under the same dose and readout conditions [9]. However, natural materials can give higher value than 5% at reusability test due to impurities in natural mineral or new traps that occur depending on the radiation exposure at each cycle [10-12].

ISBN:978-605-83516-6-0

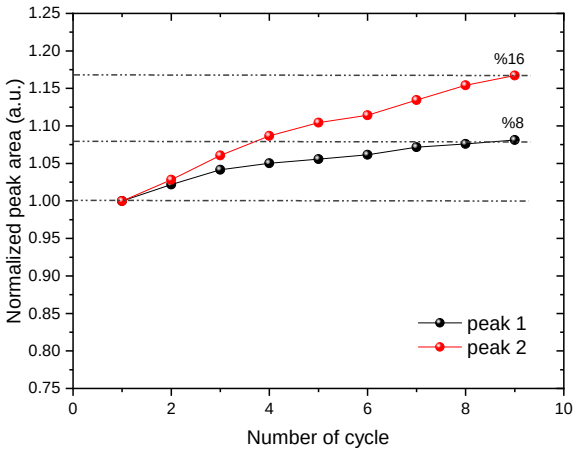


FIGURE 6. The behavior of normalized peak area for peak 1 and peak 2 through 9 consecutive cycles of natural dolomite mineral

The Evaluation of Kinetic Parameters

$T_m - T_{stop}$ experiment

$T_m - T_{stop}$ experiment has been performed in the literature to decompose TL glow curves consisting of overlapping peaks [13]. In this study, $T_m - T_{stop}$ experiment was carried out to deconvolve the overlapping peaks and determine the order of kinetics (b), activation energy (E_a) and frequency factor (s). The natural dolomite pellet irradiated with a beta dose of 5 Gy was heated up to a T_{stop} at HR of 2 °Cs^{-1} and cooled to RT. Then TL readouts were performed up to 450 °C. The sample irradiated with the same dose was reheated to a new T_{stop} with the increment of 5 °C and the cycles were repeated in the complete interval T_{stop}= 45-320 °C. Thus, clean peaks for each curve were obtained in order to apply the initial rise (IR) method after $T_m - T_{stop}$ experiment and the activation energies and frequency factors given in Table 1 were estimated for probable deconvolved peaks. In addition, a plot of the calculated activation energy (Ea) versus Tstop is shown as Fig. 7. The figure indicates that the main peaks consist of at least eight superposition peaks.

TABLE 1 The values of activation energy *E* (eV) and frequency factor *s* (s^{-1}) obtained using the initial rise (IR) method after $T_m - T_{stop}$ experiment.

The obtained peaks	T_{stop} range (°C)	E (eV)	s (s^{-1})
1st Peak	45-90	0.55-0.64	8.2E+07-1.4E+08
2nd Peak	95-135	0.78-0.80	3.6E+08-1.4E+10
3rd Peak	140-165	0.81-0.83	7.4E+07-5.6E+08
4th Peak	170-185	1.13-1.16	1.7E+11-4.1E+11
5th Peak	190-215	1.42-1.44	8.7E+13-1.3E+14
6th Peak	220-250	1.54-1.56	9.9E+13-1.2E+15
7th Peak	255-285	1.63-1.66	1.4E+13-5.4E+14
8th Peak	290-320	1.70-1.84	6.3E+12-3.9E+14

ISBN:978-605-83516-6-0

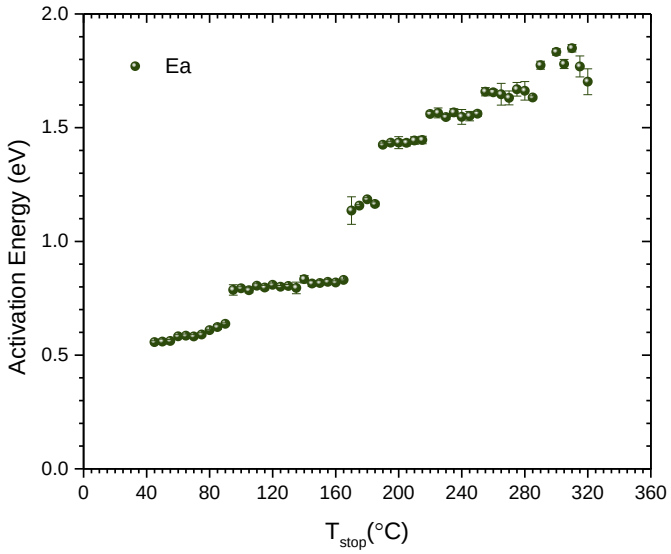


FIGURE 7. The change of the activation energy versus T_{stop} obtained after T_m-T_{stop} experiment with dose of 5 Gy at HR of 2 °Cs^{-1} of natural dolomite mineral.

CGCD Method

CGCD (Computerized Glow Curve Deconvolution Method) is a useful method for analysis of the main peaks that includes overlapping TL glow peaks. This method also allows to evaluate the kinetic parameters without the need of any further thermal annealing. The experimentally obtained glow curve with the readouts at a HR of 2 °Cs^{-1} after beta irradiation under 5 Gy dose was deconvolved applying general order kinetic equation which Chen, and Kitis et al. [14-16] have contributed using R-software package "tgcd" [17]. Fig. 8 shows the deconvolution results consisting of at least eight superposition peaks of natural dolomite pellet. Figure of merit (FOM) value which is a sign of agreement between experimental and theoretical data was found to be 1.67%. The FOM value should be less than 5% considering acceptable fit value.

The best estimates of kinetic parameters of the deconvolved peaks are given in Table 2. As seen in Table 2, the activation energy values were found to be 0.65-1.08 (Peak 1 maxima) and 1.4-1.71 eV (Peak 2 maxima). The orders of kinetic were determined to be in the range of 1.44-2. In addition, s values were found to be in the range of 10^8-10^{14}, as expected.

ISBN:978-605-83516-6-0

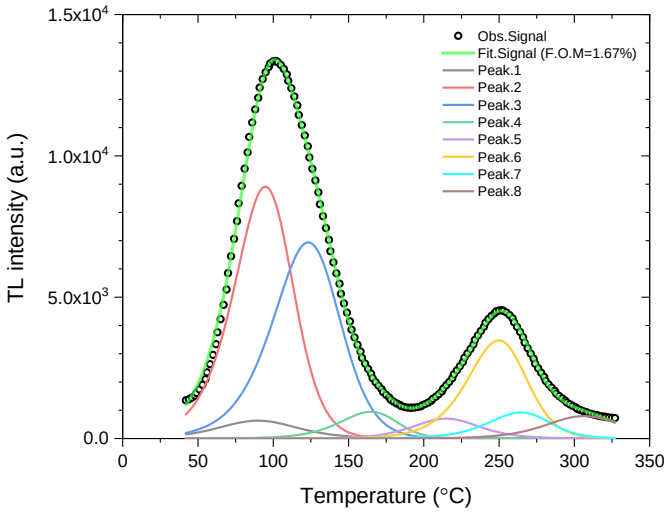


FIGURE 8. Deconvolution of the glow curve at 5 Gy dose of natural dolomite mineral.

TABLE 2 The values of maximum peak temperature T_m(°C), the activation energy E (eV), frequency factor s (s^{-1}) and kinetic order b of deconvolved peaks obtained by the deconvolution of the main peak of natural dolomite sample using CGCD method (HR: 2 °Cs^{-1}, irradiation dose: 5 Gy)

Deconvolved Peaks	T_m(°C)	E (eV)	s (s^{-1})	b
1st Peak	89.85	0.65	1.10E+08	2
2nd Peak	94.77	0.79	8.15E+09	1.6
3rd Peak	123.34	0.8	1.66E+09	1.6
4th Peak	164.85	1.08	3.39E+11	1.44
5th Peak	214.85	1.4	3.70E+13	2
6th Peak	249.85	1.58	2.18E+14	1.6
7th Peak	264.59	1.6	1.23E+14	1.6
8th Peak	306.37	1.71	8.30E+13	2

CONCLUSION

In the present study, dose-response, reusability, heating rate (HR) effect and kinetic parameters of natural dolomite mineral supplied from Mersin province were examined in order to determine the TL properties of the samples. The results of the measurements revealed that TL response at low beta doses between 0.11 and 10 Gy exhibited good linearity. Heating rate effect on TL signal showed an anomalous state that TL intensity enhances with increasing HR due to an increase in the probability of radiative transitions compared to that of the non-radiative transitions. The reproducibility results of the natural dolomite samples were examined and the obtained results were found to be in the acceptable limits when compared with the reproducibility results of natural materials. To find the kinetic parameters of TL glow curves of the mineral, $T_m - T_{stop}$ and CGCD Methods were used, and the results obtained using these methods were found to be in good agreement.

These experiments and calculations performed up to now is a preliminary study to learn TL properties of dolomite mineral. For future studies, dolomite mineral samples will be annealed to make them more stable and the measurements and calculations will be performed again for the annealed samples to compare both results and to learn whether the mineral can be used as a dosimetric material.

ISBN:978-605-83516-6-0

ACKNOWLEDGMENTS

This work was supported by the Research Fund of the Çukurova University, Turkey (Project Number: FBA-2018-10828).

REFERENCES

1. G.S. Gai, Y.F. Yang, S.M. Fan, Z.F. Cai, Powder Technol. **153**, 153–158 (2005).
2. M. Rabah, E.M.M. Ewais, Ceram. Int. **35**, 813–819 (2009).
3. C. Soliman , A.M. Massoud, M.A. Hussein, Nucl. Instrum. Meth. B **222**, 163–168 (2004).
4. V. Ramasamy, V. Ponnusamy, S.S. Gomathi, M.T. Jose. Radiat. Meas. **44**, 351–358 (2009).
5. R. Mostefa, A. Kadari, S. Hiadsi, D. Kadria. Optik **127**, 368–370 (2016).
6. C. Soliman, S.M. Metwally, F.F. Alharbi, K.M. Elshokrofy. Journal of Taibah University for Science **11**, 534–539 (2017).
7. J.T. Randall, M.H.F. Wilkins, and M.L.E, Proc. R. Soc. Lond. A **184**, 366-389 (1945).
8. S. Delice, E. Bulur, and N.M. Gasanly, J. Mat. Sci. **49**, 8294-8300 (2014).
9. Furetta C. Handbook of thermoluminescence, World Scientific, Singapore, 2003.
10. H. Tugay, Z. Yegingil, T. Dogan, N. Nur, N. Yazici, Nucl. Instr. Meth. Phys. Res. B **267**, 3640–3651(2009).
11. M. Sardar, M. Tufail, Nucl. Instr. Meth. Phys. Res. B **269**, 284–287 (2011).
12. N. Nur, Z. Yegingil, M. Topaksu, K. Kurt, T. Dogan, N. Sarıgül, M. Yüksel, V. Altunal, A. Özdemir, V. Güçkan, I. Günay. Nucl. Instr. Meth. Phys. Res. B **358**, 6–15 (2015).
13. K.H. Nicholas and J. Woods, British Journal of Applied Physics. **15**, 783–795 (1964).
14. R. Chen, J. Electrochem. Soc. **116** (9), 1254–1257 (1969a).
15. R. Chen, J. Appl. Phys. **40**, 570–585 (1969b).
16. G. Kitis, J.M. Gomez-Ros, J.W.N. Tuyn, J. Phys. D. Appl. Phys. **31**, 2636–2641 (1998).
17. J. Peng, Z. Donga and F. Han, SoftwareX **5**, 112–120 (2016).

BOOK OF FULL TEXT PROCEEDINGS TURKISH PHYSICAL
SOCIETY 35th INTERNATIONAL PHYSICS CONGRESS (TPS35)
TPS35, Vol.01, No.09, pp.491-496.
ISBN:978-605-83516-6-0 15 December 2019

Nucleon Densities of Chrome Isotopes Calculation by Skyrme Interactions

Ferhan Akdeniz[1,a], Ismail Hakki Sarpun [1,2,b], Eyyup Tel [3,c], Abdullah Aydin [4,d]

[1] *Akdeniz University, Physics Dept., Antalya, Turkey.*
[2] *Akdeniz University, Nuclear Sciences Res. and App. Center, Antalya, Turkey.*
[3] *Osmaniye Korkut Ata University, Physics Dept., Osmaniye, Turkey.*
[4] *Kirikkale University, Physics Dept., Kirikkale, Turkey.*

[a)] *ferhanakdeniz@gmail.com*
[b)] *sarpun@akdeniz.edu.tr*
[c)] *eyuptel@osmaniye.edu.tr*
[b)] *aaydin@kastamonu.edu.tr*

Abstract. Proton and neutron densities of the Chrome isotopes, namely 50, 52, 53, 54Cr are calculated with HF and HFB approximation. Skyrme interaction was used in HF and HFB models, while Gogny force was used in HFB approximation. Woods-Saxon and Harmonic Oscillator potentials were used in Skyrme-Hartree-Fock method with various Skyrme set parameters. Theoretical calculated charge density compared with experimental data of Angeli and Marinova works to determine which is the best parameter set in the calculations for Skyrme interactions.

INTRODUCTION

The ground state properties of the nucleus contain a lot of information about the nuclei. Skyrme force [1,2]is a phenomenological force that defines the ground state properties of the nucleus. In addition, both two-body and three-body interaction form;

$$\vec{V}_{Skyrme} = \sum_{i<j} \vec{V}_{ij} + \sum_{i<j<k} \vec{V}_{ijk}$$

Refers to,

$$\vec{V}(i,j) = t_0(1 + x_0P_x)\delta(\vec{r}_i - \vec{r}_j) + \frac{1}{2}t_1(1 + x_1P_x)\left[\vec{P}_{12}^{\,\prime\,2}\,\delta(\vec{r}_i - \vec{r}_j) + \delta(\vec{r}_i - \vec{r}_j)\vec{P}_{12}^{\,2}\right] + t_2(1 + x_2P_x)\vec{P}_{12}^{\,\prime}\delta(\vec{r}_i - \vec{r}_j)\vec{P}_{12} + i\,t_4\vec{P}_{12}^{\,\prime}.\delta(\vec{r}_i - \vec{r}_j)(\sigma_i + \sigma_j) \times \vec{P}_{12}$$

ISBN:978-605-83516-6-0

$$\vec{V}(i,j,k) = \frac{1}{6}t_3(1+x_3P_x)\rho\left(\frac{\vec{r}_i+\vec{r}_j}{2}\right)\delta(\vec{r}_i-\vec{r}_j)$$

In this equation, δ is delta function, $\vec{p}_{12} = \mp i(\vec{\nabla}_1 - \vec{\nabla}_2)$ is relative momentum operator acting on the wave functions moving to the right / left, P_x is spin exchange operator and σ is Pauli spin matrices. The interaction of two objects depends on seven parameters ($t_0 t_1 t_2 x_0 x_1 x_2$ and t_4).

Skyrme interaction, which is suitable for the calculation of nucleon-nucleon interaction, has a simple structure and allows us to write the Hamiltonian of the system. This interaction can be calculated by using Hartree-Fock method. the densities depend on φ_i single particle states. For the $\varphi_i^{(0)}$ radial single particle wave function, the Harmonic Oscillator (HO) or Woods-Saxon (WS) [3] wave function is selected. ρ, the diagonal part of a total body density operator in the coordinate space and t_3 represent a parameter that characterizes the density dependence of the interaction

The HF method [3-5] allows us to examine a multi-body system acting under a potential effect as a single particle and is written as a function of the three basic intensities;

$$\rho_q(\vec{r}) = \sum_{i,\sigma} w_i \, |\varphi_i(\vec{r},\sigma,q)|^2$$

$$\tau_q(\vec{r}) = \sum_{i,\sigma} w_i \left|\vec{\nabla}\varphi_i(\vec{r},\sigma,q)\right|^2$$

$$\vec{J}_q(\vec{r}) = (-i)\sum_{i,\sigma,\sigma'} w_i\varphi_i^*(\vec{r},\sigma,q)\left[\vec{\nabla}\varphi_i(\vec{r},\sigma',q)\times\langle\sigma|\vec{\sigma}|\sigma'\rangle\right]|\varphi_i(\vec{r},\sigma,q)|^2$$

In that event ρ_q proton densities, τ_q kinetic energy, $\vec{J}_q$ spin - orbital densities (wherein q = n and p represent protons and neurons). Also, w_i denotes the occupation probability of the states i and σ is Pauli spin matrice. The SHF method is a self-compatible field method.

Bardeen-Cooper-Schrieffer (BCS) [7] is a model that examines the correlation between complete shells and particles as a single particle. The Hartree-Fock-Bogolyubov (HFB) [8] theory was formed by combining and generalizing the HF and BCS model. The HFB method is applied to the zero-range Skyrme force and reduces the system to set of differential equations.

Another self-compatible field method is the Gogny model [9-11] using Gogny interaction. Gogny force is the interaction of two non-divergent of particles and its parameters are arranged according to experimental data.

CALCULATION METHOD

It was used to HAFOMN [12] and TALYS[13] codes to calculate the theoretical data of proton and neutron densities of ^{50,52,53,54}Cr isotopes. For HO and WS potentials separately by SHF method the nucleon density calculation was performed by using HAFOMN computer program. TALYS nuclear reaction code was used for Skyrme and Gogny interactions by SHB method. Using SkA [14], GS6 [15], SKM* [16], SGII [17], Sly4, Sly5, SLy6, SLy7 [18], SLy8, SLy9 and SLy10 [19] parameters, proton and neutron densities were obtained for each. Theoretical calculated charge density compared with experimental data of Angeli and Marinova [20] works to determine which is the best parameter set in the calculations for Skyrme and Gogny interactions and were plotted in a graphic drawn software.

ISBN:978-605-83516-6-0

RESULT

In this study 11 different parameter sets of Skyrme interactions were used in nucleon density calculation for HAFOMN code using HO and WS potentials. The parameters of these sets were given in **"TABLE 1".**

TABLE 1. Various Skyrme Parameter Sets and coefficients.

Parameters	$\mathbf{t_0}$	$\mathbf{t_1}$	$\mathbf{t_2}$	$\mathbf{t_3}$	$\mathbf{x_0}$	$\mathbf{x_1}$	$\mathbf{x_2}$	$\mathbf{x_3}$	$\mathbf{W_0}$	**alpha**
SkA	-1602.78	570.88	-67.7	8000	-0.02	0	0	-0.28	125	1/3
GS6	-1012	209	-76.3	10619	0.139	0	0	1	105	1
SkM*	-2645	410	-135	15595	0.09	0	0	0	130	1/6
SGII	-2645	340	-41.9	15595	0.09	-0.0588	1.425	0.06044	105	1/6
SLy4	-2488.913	486.818	-546.395	13777	0.834	-0.3438	-1	1.354	123	1/6
SLy5	-2483.45	484.23	-556.69	13757	0.776	-0.317	-1	1.263	125	1/6
SLy6	-2479.5	462.18	-448.61	13673	0.825	-0.465	-1	1.355	122	1/6
SLy7	-2480.8	461.29	-433.93	13669	0.848	-0.492	-1	1.393	126	1/6
SLy8	-2481.41	480.78	-538.34	13731	0.8024	-0.3424	-1	1.3061	122.425	1/6
SLy9	-2511.13	510.6	-429.8	13716	0.7998	-0.6213	-1	1.3727	119	1/6
SLy10	-2506.77	430.98	-304.95	13826.41	1.0398	-0.6745	-1	1.6833	90.685	1/6

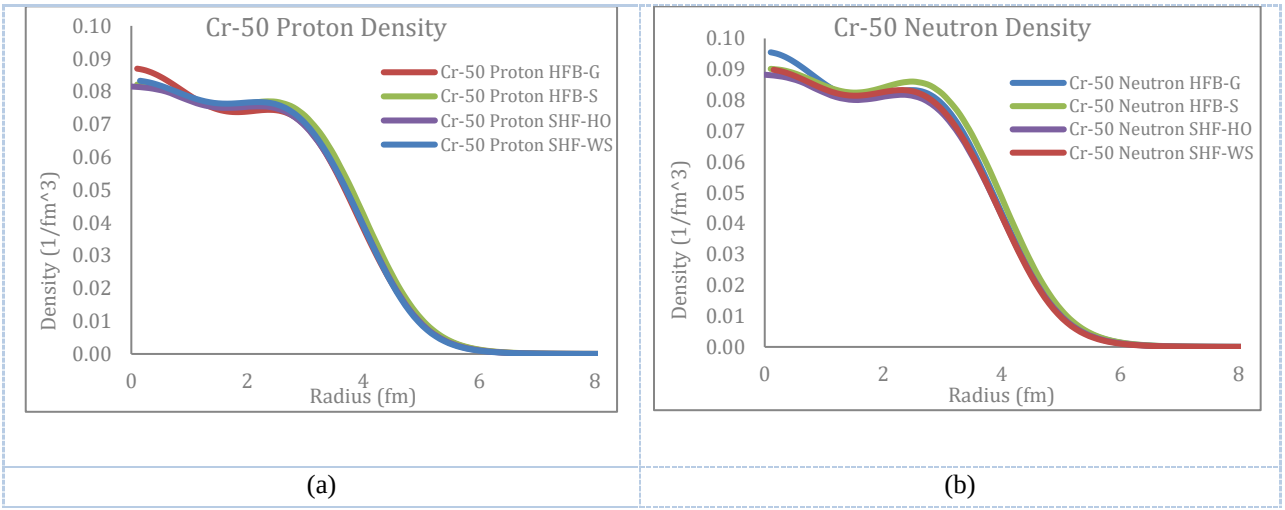
Charge radius of ^{50,52,53,54}Cr isotopes were calculated with HAFOMN code using Skyrme-Hartree-Fock (SHF) methods via harmonic oscillator (SHF-HO) and Woods-Saxon (SHF-WS) potentials given in **"TABLE 2".**

TABLE 2. Charge radius of ^{50,52,53,54}Cr isotopes were calculated by different parameter sets using SHF-WS and SHF-HO methods. Comparison of calculated Charge radii of investigated isotopes with experimental values of [21].

R_{charge}	**Z=24 N=26** ^{50}Cr		**Z=24 N=28** ^{52}Cr		**Z=24 N=29** ^{53}Cr		**Z=24 N=30** ^{54}Cr	
Method	SHF-WS	SHF-HO	SHF-WS	SHF-HO	SHF-WS	SHF-HO	SHF-WS	SHF-HO
EXP	3.6588		3.6452		3.6511		3.6885	
SkA	3.6702	3.6598	3.6762	3.6688	3.6845	3.6823	3.6928	3.6948
GS6	3.3140	3.3124	3.3371	3.3308	3.3550	3.3473	3.3733	3.3635
SkM*	3.6603	3.6705	3.6649	3.6716	3.6730	3.6921	3.6813	3.6989
SGII	3.6332	3.6437	3.6423	3.6492	3.6519	3.6731	3.6616	3.6819
SLy4	3.6703	3.6759	3.6772	3.6787	3.6859	3.6982	3.6944	3.7060
SLy5	3.6631	3.6694	3.6694	3.6723	3.6778	3.6903	3.6861	3.6978
SLy6	3.6508	3.6588	3.6582	3.6618	3.6674	3.6818	3.6765	3.6903
SLy7	**3.6495**	**3.6577**	**3.6568**	**3.6608**	**3.6661**	**3.6805**	**3.6755**	**3.6892**
SLy8	3.6636	3.6692	3.6702	3.6723	3.6788	3.6911	3.6872	3.6988
SLy9	3.7107	3.7116	3.7189	3.7270	3.7282	3.7508	3.7375	3.7589
SLy10	3.6593	3.6689	3.6709	3.6771	3.6811	3.7037	3.6913	3.7132

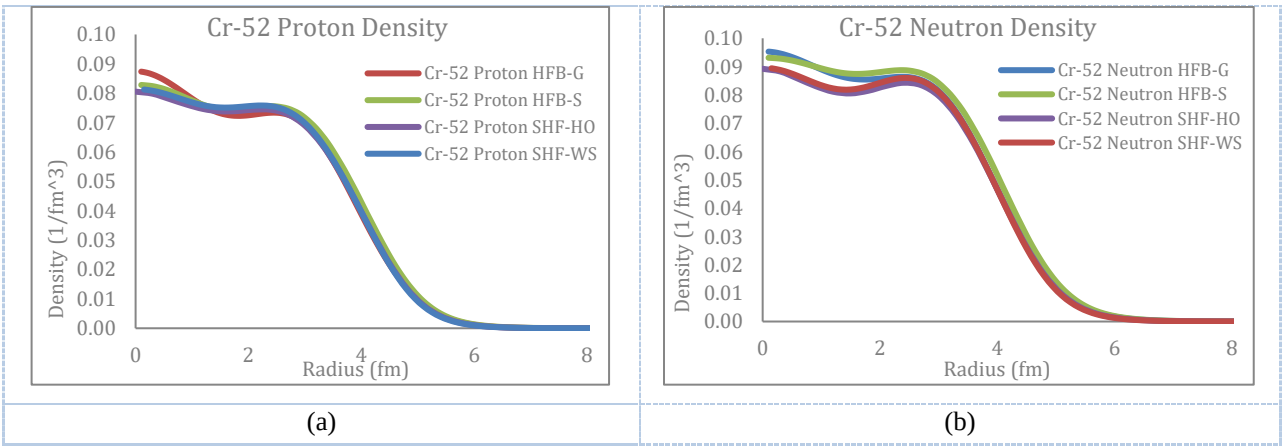
According to "**TABLE 2**", Sly7 [17] parameter set has the best harmony with experimental values of Angeli and Marinova [20] among the used sets in this study. Therefore, in the nucleon density graphs, Sly4 parameter set was used in SHF-WS and SHF-HO methods. TALYS 1.9 nuclear reaction code was used for HFB-G and HFB-S method calculations. Calculated proton and neutron densities of ^{50,52,53,54}Cr isotopes were given in **"FIGURES 1-4",** respectively.

ISBN:978-605-83516-6-0



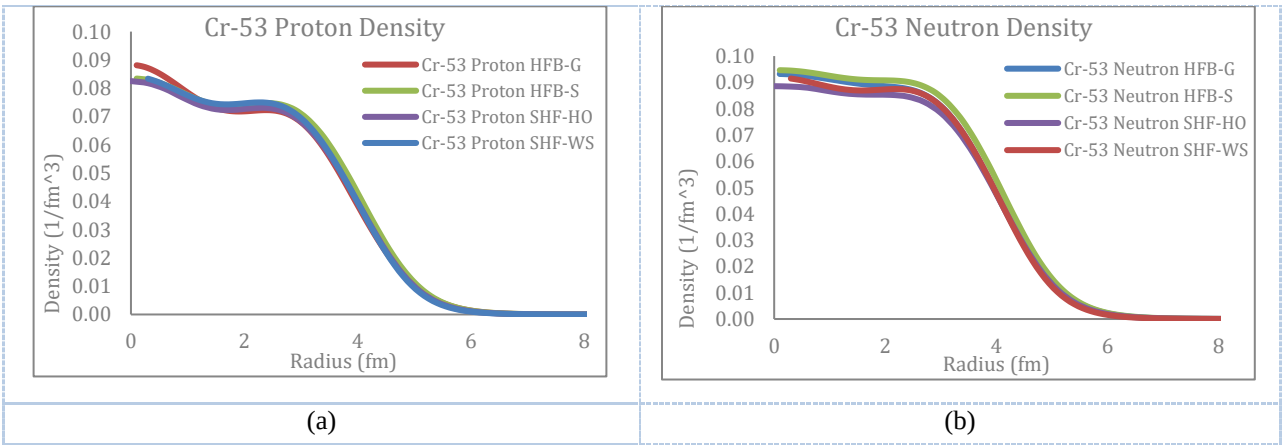
(a) (b)

FIGURE 1. (a) Proton and (b) Neutron densities of ^{50}Cr



(a) (b)

FIGURE 2. (a) Proton and (b) Neutron densities of ^{52}Cr



(a) (b)

FIGURE 3. (a) Proton and (b) Neutron densities of ^{53}Cr

ISBN:978-605-83516-6-0

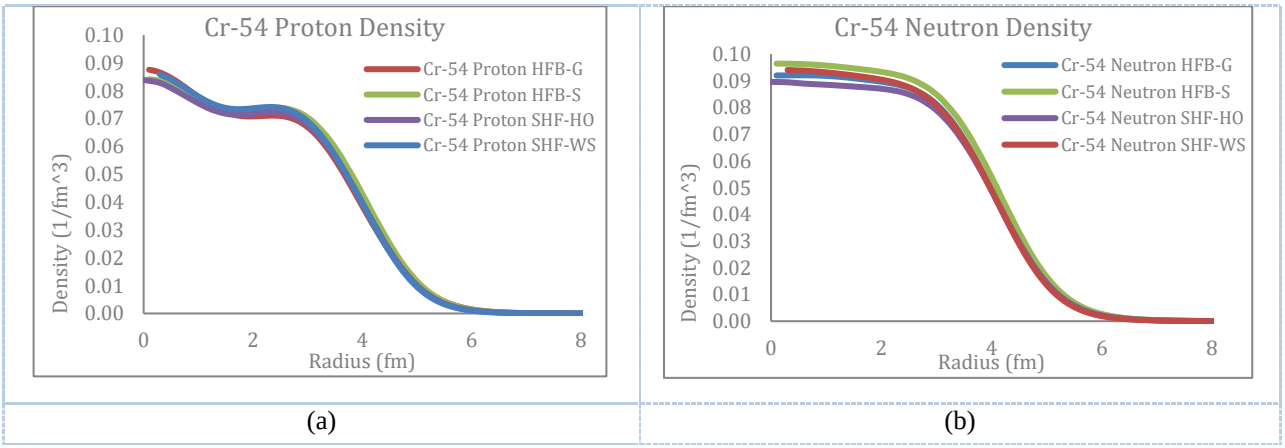


FIGURE 4. (a) Proton and (b) Neutron densities of ^{54}Cr

According to "**FIGURE 1-4"**, all density calculations with four different methods have a harmony each other. In the proton density calculations, HFB-G method has slightly higher values than other methods in the 0-2 fm radius region. In the neutron density calculations, HFB-G method has slightly higher values than other methods for ^{50}Cr target nucleus, while HFB-S and SHF-WS methods have slightly higher values than other methods for ^{53}Cr and ^{54}Cr nuclei, in the same radius region.

REFERENCES

1. T.H.R. Skyrme, The Nuclear Surface. Phil. Mag. 1: 1043-1054 (1956).
2. T.H.R. Skyrme, The effective nuclear potential. Nucl. Phys. 9(2): 615-634 (1959).
3. R.D. Woods and D.S. Saxon, Phys.Rev. 95 577 (1954).
4. D.R. Hartree, The wave mechanics of an atom with a non-Coulomb central field.part I. theory and methods. Proc. Camb. Phil. Soc. 24(1): 89-110 (1928).
5. V. Fock, Näherungsmethode zur lösung des quantenmechanischen Mehrkörperproblems. Z. Physik., 61: 126-148 (1930).
6. R.D. Adamson, Novel Methods for Large Molecules in Quantum Chemistry.Ph.D. Thesis, University of Cambridge, Cambridgeshire, England, 141 p (1998).
7. J. Bardeen, L.N. Cooper and J.R. Schrieffer, Theory of Superconductivity. Phys. Rev., 108(5):1175-1204 (1957).
8. N.N. Bogolyubov, On a Variational Principle in the Many Body Problem. Sov. Phys. Dokl., 3: 292-294(1958).
9. D. Gogny, Simple separable expansions for calculating matrix elements of two- body local interactions with harmonic oscillator functions. Nucl. Phys. A, 237(3): 399-418 (1975).
10. J.R. Stone and P.G. Reinhard, The Skyrme interaction in finite nuclei and nuclear matter. Prog. Part. Nucl. Phys., 58:587-657 (2007).
11. J. Déchargé and D. Gogny, Hartree-Fock-Bogoliubov calculations with the D1effective interaction on spherical nuclei. Phys. Rev. C, 21(4):1568-1593(1980).
12. P.G. Reinhard and H. Flocard, Nuclear effective forces and isotope shifts. Nucl. Phys.A, 584(3): 467-488 (1995).
13. A.J.Koning and D.Rochman, Modern Nuclear Data Evaluation with the TALYS Code System, Nuc. Dat. She., 113(12): 2841-2934 (2012).

14. H.S.Kohler, Skyrme force and the mass formula. Nucl. Phys. A, 258 (2): 301-316 (1976).
15. S. Krewald, V. Klemt, J. Speth and A. Faessler, On the use of Skyrme forces in self-consistent RPA calculations. Nucl. Phys. A, 281(2) 166–206 (1977).
16. J. Bartel, P. Quentin, M. Brack, C. Guet and H.B. Håkansson, Nucl. Phys. A386, 79 (1982).
17. N. Van Giai, H. Sagawa, Spin isospin and pairing properties of modified Skyrme interactions, Phys. Lett. B, 106, 379 (1981).
18. E. Chabanat, P.Bonche, P.Haensel, J. Meyer and R. Schaeffer, Nucl. Phys. A635, 231 (1998).
19. E. Chabanat, Ph. D. thesis, Lyon (1995).
20. I. Angeli, K.P. Marinova, Table of experimental nuclear ground state charge radii: An update, Atomic Data and Nuclear Data Tables 99 ,69–95 (2013).
21. R. Baldık, Skyrme etkileşmesi kullanılarak bazı egzotik çekirdeklerin taban durum özelliklerinin incelenmesi, Ph.D. Thesis, Zonguldak Karaelmas University (2010).

BOOK OF FULL TEXT PROCEEDINGS TURKISH PHYSICAL
SOCIETY 35th INTERNATIONAL PHYSICS CONGRESS (TPS35)
TPS35, Vol.01, No.09, pp.497-502.
ISBN:978-605-83516-6-0 15 December 2019

Calculation of The Photomultiplier Output Voltage by FLUKA Monte Carlo Program

Elif Ebru Ermis[1, a)] and Cuneyt Celiktas[1,b)]

[1] *Ege University, Faculty of Science, Physics Department., 35100, Bornova, Izmir, Turkey*
[a)]*Corresponding author:elermis@hotmail.com*
[b)]*Electronic mail: cceliktas@yahoo.com*

Abstract. Revealing the output signal characteristics of the photomultiplier tubes (PMTs) with NaI(Tl) and BC420 type scintillation crystals using FLUKA Monte Carlo (MC) program aimed in the present work. For this purpose, the numbers of scintillation photons produced in these scintillation crystals were taken from the literature and additionally calculated by means of this program. Results were given in a table and compared, and the conclusion from these results was included in the final section.

INTRODUCTION

Scintillation is a general term referring to the process of giving off light; it is used both literally and figuratively. More specifically in the sciences, a scintillator is any material that can release a photon in the UV or visible-light range, when an excited electron in the scintillator returns to its ground state. These scintillation photons are detected by a photomultiplier tube (PMT) and converted into an electronic signal [1].

Most of the inorganic scintillators are crystals of the alkali metals, in particular alkali iodides, that contain a small concentration of an impurity. One of the example is NaI(Tl). The element in parentheses is the impurity or activator. NaI(Tl) is the most commonly used scintillator for gamma rays [2].

Light yield is defined as an amount of photons produced by a scintillator per unit of absorbed energy. It is often expressed in photons/MeV (ph/MeV) [3]. Scintillation efficiency is a term that is used to characterize the efficiency with which the energy lost by the incident particle is converted into scintillation photons. The light output of a scintillator is directly related to its scintillation efficiency [4]. In the following expression, the definition of scintillator efficiency is given by

$$\eta_{max} = \frac{hc}{\gamma E_g \lambda_{max}} \quad (1)$$

where E_g, γ, λ_{max}, h and c are scintillator band gap energy, a factor that depends on the scintillator material, the wavelength of the photons corresponding to the peak of the scintillation spectrum, Planck constant and speed of light, respectively [4].

Among the photosensitive devices in use today, the PMT is a versatile device that provides extremely high sensitivity and ultra-fast response. A typical photomultiplier tube consists of a photoemissive cathode (photocathode) followed by focusing electrodes, an electron multiplier and an electron collector (anode) in a vacuum tube, as shown in Figure 1 [5].

Türk Fizik Derneği
1950
Turkish Physical Society

ISBN:978-605-83516-6-0

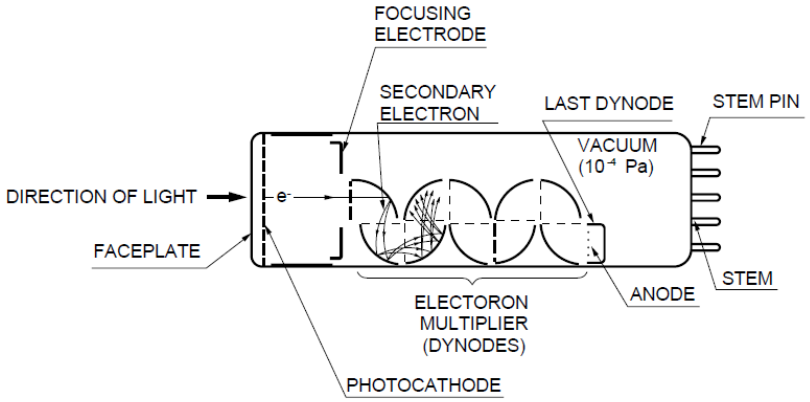


FIGURE 1. A schematic of a PMT [5].

When light enters the photocathode, the photocathode emits photoelectrons into the vacuum. These photoelectrons are then directed by the focusing electrode voltages towards the electron multiplier where electrons are multiplied by the process of secondary emission. The multiplied electrons are collected by the anode as an output signal. Because of secondary-emission multiplication, photomultiplier tubes provide extremely high sensitivity and exceptionally low noise among the photosensitive devices currently used to detect radiant energy in the ultraviolet, visible, and near infrared regions. The photomultiplier tube also features fast time response, low noise and a choice of large photosensitive areas [5].

The PMT is coupled to a scintillator which emits light pulses in response to alpha, beta and gamma radiation, the average quantity of light per pulse being proportional to the radiation energy dissipated in the scintillator. The mean anode charge per pulse is proportional to the quantity of light and, hence, also to the energy dissipated [6].

Spectral response is usually expressed in terms of radiant sensitivity or quantum efficiency as a function of wavelength. Radiant sensitivity is the photoelectric current from the photocathode, divided by the incident radiant power at a given wavelength, expressed in A/W (amperes per watt). QE is the number of photoelectrons emitted from the photocathode divided by the number of incident photons. It is customary to present quantum efficiency in a percentage. Quantum efficiency and radiant sensitivity have the following relationship at a given wavelength

$$QE(\%) = \frac{124}{\lambda(nm)} x Radiant\ sensitivity\ (\frac{mA}{W}) \qquad (2)$$

where λ is the wavelength in nm [5].

The number of electrons produced by the photocathode (N_e) per unit time can be estimated from

$$N_e = N_s \eta_{max} QE \qquad (3)$$

where N_s represents the number of scintillation photons produced per unit time, η_{max} is the efficiency of the process of transfer of photons to the photocathode, and QE is the quantum efficiency of the photocathode [4].

In many research areas in physics, Monte Carlo (MC) calculations are a standard tool for any simulation. In this calculation technique, sequential random examples are generated to evaluate complex models. After various iterations, the results are interpreted by statistically. The essential application area of this technique is simulation of the particle transport and interactions in particle physics. It has advantageous to make different configurations in this technique [7]. One of the general purpose tools for calculations of particle transport and interactions is FLUKA (FLUktuirende KAskade) [8, 9]. FLUKA obtains a simple input file rather than other MC particle codes. FLUKA presents many options to score quantities and to apply numerous variance reduction techniques; thus, the users do not write a single line of code. FLUKA input files consist in ASCII file with extension .inp. Instructions (named cards) are given in each line of this file. Title, geometry description, material, particle and requested card definitions, material assignments together with the random number sequence are given in these cards [8].

In this work, some output signal characteristics of the PMTs (Burle 8575 and Hamamatsu R1828-01 type) with two different types of scintillator (NaI(Tl) inorganic and BC420 organic scintillator) were determined by using

ISBN:978-605-83516-6-0

FLUKA MC program. To determine these characteristic values, the numbers of scintillation photons produced in the scintillation crystals were obtained in two ways: (1) literature, (2) the calculation by the program.

MATERIALS AND METHODS

In this section, some characteristics of the output signals generated by the PMTs with NaI(Tl) and BC420 type scintillation crystals were examined. Firstly, efficiency values of the used scintillation crystals were calculated by using Eq. (1). Secondly, QE values of the used PMTs were obtained through Eq. (2). Then, produced electron numbers in the photocathodes of the PMTs (N_e) were calculated by means of Eq. (3). As can be seen in Eq. (3), the number of scintillation photons produced per unit time (N_s) was taken into account to calculate the produced electron number in the photocathode (N_e). In this calculation, N_e values were acquired from both literature and FLUKA MC program. The program (ver. 2011.2c) was installed on an Ubuntu operating system (ver. 13.10). The transport of gamma photons in FLUKA (EMF, for Electro Magnetic FLUKA) handles all interactions and scattering processes. DEFAULTS card sets FLUKA defaults suitable for a specified kind of problems [8]. In this study, PRECISIOn was selected. PRECISIOn defaults for precision simulations. In this selection, EMF is on, that is, gamma photons are transported. And also, FLUKA provides a BEAM card by which it is possible to choose the particle kind and its energy. BEAMPOS card defines the starting point of beam particles and the beam direction. Materials can be defined by the option; MATERIAL, by assigning a density, a name, a code number, in the case of single elements, an atomic number and atomic weight [8]. Then, current values in the final dynodes of the PMTs were calculated by multiplying N_e values by PMT gains and unit charge ($1.6x10^{-19}$ C). Finally, the amplitudes of output signals of the PMTs were obtained using Ohm's law for two different N_e values. Constants used in the equations are listed in Table 1.

ISBN:978-605-83516-6-0

TABLE 1. Constants used in the calculations of the characteristics of the PMTs.

Constant		
Planck constant (h)	$6.63x10^{-34}$J. s [4]	
Speed of light (c)	$2.99x10^{8}$ m/s [4]	
Factor (γ)	3 [4]	
Scintillator band gap energy (E_g)	5.9 eV for NaI(Tl) crystal [4]	3 eV for BC420 crystal [4]
Wavelength of the photons (λ_{max})	410 nm for NaI(Tl) crystal [4]	391 nm for BC420 crystal [4]
Wavelength of PMT (λ)	400 nm for Burle 8575 PMT [10]	420 nm for Hamamatsu R1828-01 PMT [5]
Radiant sensitivity (mA/W)	81 for Burle 8575 PMT [10]	85 for Hamamatsu R1828-01 PMT [5]
PMT gain	$2.7x10^{7}$ for Burle 8575 PMT [10]	$2x10^{7}$ for Hamamatsu R1828-01 PMT [5]
Resistance of PMT (MΩ)	1.5 for ORTEC 266 PMT Base [11]	4.31 for Hamamatsu R1828-01 PMT [5]

ISBN:978-605-83516-6-0

RESULTS

Calculated characteristics of the used PMTs through Eqs. (1)-(3) are listed in Table 2.

TABLE 2. Calculated characteristics of the used PMTs.

Results	NaI(Tl) crystal with Burle 8575 PMT		BC420 crystal with Hamamatsu R1828-01 PMT	
η_{max}	0.17		0.6	
QE (%)	25		25	
	Literature	**FLUKA MC**	**Literature**	**FLUKA MC**
N_s (photon/MeV)	38,000 [12]	39,096	12,800 [13]	15,563
N_e (s^{-1})	1,615	1,661	832	1,011
I (nA)	6.976	7.175	2.662	3.235
V (mV)	10.464	10.762	11.473	13.942

CONCLUSION AND DISCUSSION

The characteristics of the PMTs with NaI(Tl) and BC420 type scintillation crystals were calculated. The number of scintillation photons produced in the scintillation crystals were used in this calculation. They were acquired from both literature and FLUKA MC program. In this way, amplitude values were compared with each other, and the validity of the FLUKA MC program in the calculation was investigated.

One of the important differences between inorganic and organic scintillators is in the response time, which is less than 10 ns for the latter and makes them suitable for fast timing measurements [2]. Therefore, two different types of scintillators were chosen to test the success of FLUKA MC program in the determination of PMT characteristics.

In Table 2, both literature values and FLUKA MC program results for the number of the produced scintillation photons (N_s) in the crystals were indicated for comparison. Gamma photons were sent to the crystals in vacuum medium in the program. This means that their energy losses and scatterings in the medium were omitted. Therefore, calculated N_s values via the program were slightly higher than the literature ones. Since N_e depends on N_s result as can be seen in Eq. (3), I and V values in FLUKA MC columns were normally higher than the literature ones as well.

It was concluded from the results above that the characteristic values of PMTs can be determined using FLUKA MC program.

ISBN:978-605-83516-6-0

REFERENCES

1. J. Prekeges, *Nuclear Medicine Instrumentation* (Jones and Barlett Publishers, United States, 2013).
2. N. Tsoulfanidis, *Measurements and Detection Radiation* (Taylor&Francis, USA, 1995).
3. K. Iniewski, *Radiation Detectors for Medical Imaging, Devices, Circuit, and Systems* (Taylor&Francis, New York, 2016).
4. S.N. Ahmed, *Physics and Engineering of Radiation Detection* (Elsevier, Netherlands, 2015).
5. Hamamatsu Photomultiplier Tube, *Opening the future with photonis*, https://www.hamamatsu.com/resources/pdf/etd/PMT_TPMZ0002E.pdf (Accessed 21 September 2019).
6. S.O. Flyckt and C. Marmonier, *Photomultiplier Tubes Principles & Applications* (Photonis, France, 2002).
7. F. Collamati, *An Intraoperative Beta-Probe for Cancer Surgery* (Springer, Switzerland, 2016).
8. A. Ferrari, P.R. Sala, A. Fasso, J. Ranft, *Fluka: A multi-particle Transport Code* (CERN INFN/T_05/11 SLAC-R-773, Geneva, 2005).
9. G. Battistoni, F. Cerutti, A. Fasso, A., et al., AIP Conference Proceeding, **86**, 31-49 (2007).
10. Burle Electron Tubes, http://123.physics.ucdavis.edu/shot_files/Burle_8575PMT.pdf (Accessed 21 September 2019).
11. ORTEC 266 PMT Catalogue, https://www.ortec-online.com/-/media/ametekortec/manuals/266-mnl.pdf (Accessed 21 September 2019).
12. International Atomic Energy Agency, *Quality Assurance for PET and PET/CT Systems* (IAEA Human Health Series No.1, Vienna, 2009).
13. G.F. Knoll, *Radiation Detection and Measurement* (John Wiley & Sons. Inc, New York, 2000).

BOOK OF FULL TEXT PROCEEDINGS TURKISH PHYSICAL
SOCIETY 35th INTERNATIONAL PHYSICS CONGRESS (TPS35)
TPS35, Vol.01, No.09, pp.503-510.
ISBN:978-605-83516-6-0 15 December 2019

Energy Resolution Improvement Using Timing Method

Elif Ebru Ermis[1, a)] and Cuneyt Celiktas[1,b)]

[1] *Ege University, Faculty of Science, Physics Department., 35100, Bornova, Izmir, Turkey*
[a)]Corresponding author:elermis@hotmail.com
[b)]Electronic mail: cceliktas@yahoo.com

Abstract. In this work, whether constant fraction discrimination timing method was succesful to obtain neat source spectrum was aimed. For this aim, this timing method was implemented to a gamma energy spectrometer. Therefore, ^{137}Cs and ^{60}Co gamma energy spectra were first acquired through a spectrometer consisted of NaI(Tl) scintillation detector. Secondly, energy signals were gated by the timing signals using this method. Energy resolution of the spectrometer was enhanced for ^{137}Cs and ^{60}Co from 8.97% to 6.41%, from 6.43% to 5.66% for 1.17 MeV energy-peak and from 6.06% to 5.70% for 1.33 MeV energy-peak through the method, respectively. Obtained results showed that the neat gamma energy spectra of the radioisotopes can be achieved by means of the constant fraction timing method.

INTRODUCTION

Scintillators are the materials that emit visible light or ultraviolet radiation after the interaction of ionizing radiation with the material [1]. The inorganic scintillators are mainly crystals of alkali halides containing a small activator impurity [2]. One of the most commonly used inorganic scintillation detectors for gamma ray detection is NaI(Tl) (sodium iodide activated with thallium). The most notable property of NaI(Tl) is its excellent light output [3]. Scintillators are main components of radiation detectors [1]. In nuclear and particle physics research studies, scintillation detectors are currently used to detect the particles. When a nuclear particle or radiation struck the materials, they emit a small flash of light, i.e. scintillation [2]. This type of detectors is also used in many different areas. These are industry, medicine, government research, and academic research [4].

In scintillation counting, the combination of a scintillator and a PMT (Photomultiplier tube) is one of the most commonly used detectors for practical applications [5]. For more than sixty years, photomultipliers have been used to detect low-energy photons in the UV to visible range, high-energy photons (X-rays and gamma rays) and ionizing particles using scintillators [6].

In many applications of radiation detectors, the object is to measure the energy distribution of the incident radiation. These efforts are classified under the general term radiation spectroscopy [3]. A particle energy spectrum is a function giving the distribution of particles in terms of their energies [7]. Energy resolution evaluates how well a given detector distinguishes between gamma rays of closely spaced energies [8]. The energy resolution is usually given in terms of the full width at half maximum of a peak (FWHM) in the energy spectrum. ΔE is this width and the relative resolution at the energy E is can be defined as follows [2].

$$\text{Resolution}=\Delta E/E \quad (1)$$

The energy resolution parameter is usually expressed in percent [2].

The measurement of the time relationship between two events is carried out by means of timing spectroscopy. A signal which is related to these events is accurately achieved in timing spectroscopy [9]. Timing in nuclear physics refers to the measurements of very small time intervals. Accurate measurements of very small time

Türk Fizik Derneği
1950
Turkish Physical Society

ISBN:978-605-83516-6-0

intervals require special techniques. Probably the most efficient and versatile method available today is the constant fraction timing method [2].

Moszynski et al. determined energy resolution values of NaI(Tl) scintillation detectors which have different dimensions [10]. The energy resolution values of NaI(Tl) detector were achieved at different gamma-ray energies by Akkurt et al. [11]. Ackermann et al. investigated the energy resolution value of different types of scintillation detectors [12].

In this work, a spectrometer composed of NaI(Tl) inorganic scintillation detector was used. Improvement of energy resolution value of the introduced spectrometer in the next chapter was carried out by means of constant fraction timing method.

MATERIALS AND METHODS

In the first part of the experimental study, ^{137}Cs and ^{60}Co energy spectra were achieved by using a NaI(Tl) scintillation detector. In the second section, energy spectra were separately gated via constant fraction timing method in the MCA (Multichannel analyzer).

The half-lives and activities of ^{137}Cs and ^{60}Co are 30.07 and 5.27 years, 5 μCi and 0.1 μCi, respectively. The dimensions of the used NaI(Tl) scintillation detector (Rexon Inc.) were 3 inch x 3 inch. The distances between detector surface and ^{137}Cs radioactive source and ^{60}Co were 4.5 cm and 3 cm respectively during the measurements.

In the constant-fraction timing method, the input signal to the circuit is delayed and a fraction of the undelayed pulse is subtracted from it. A bipolar pulse is generated and its zero crossing is detected and used to produce an output logic pulse [9].

Introduced spectrometer is shown in Fig. 1.

As can be seen in Fig. 1, the detector output (DT, Rexon Inc.) was connected to a photomultiplier tube (PMT, ORTEC 266). Its dynode (D) output was forwarded to preamplifier (PA, ORTEC 113) and delay line amplifier (DLA, ORTEC 460), respectively. Bipolar output of DLA was divided into two. One of the output DLA was sent to delay amplifier (DA, ORTEC 427A). DA output was connected to multichannel analyzer (MCA, ORTEC Trump 8K) input. The other output of the DLA was forwarded to timing single channel analyzer (TSCA, ORTEC 420A). Its output was sent to strobe input of time to amplitude converter (TAC, ORTEC 566). TAC can be used to measure the time relationship between correlated or coincident events [9]. The anode output (A) of the PMT was connected to fast preamplifier (FPA, ORTEC VT120A). The output of FPA was forwarded to constant fraction discriminator (CFD, ORTEC 584) for timing signal. One of its outputs was sent directly to start input of TAC. The other output of CFD was connected to delay (DL, ORTEC 425) in order to generate time difference between start and stop input of TAC. DL output was sent to stop input of TAC. The output of TAC was directed to gate input of MCA. The reason why the energy signals were gated by signals obtained using timing measurement method in the spectrometer was to achieve spectra with better energy resolution value.

Signal shapes of CFD and TAC are shown in Figs. 2 and 3, respectively.

ISBN:978-605-83516-6-0

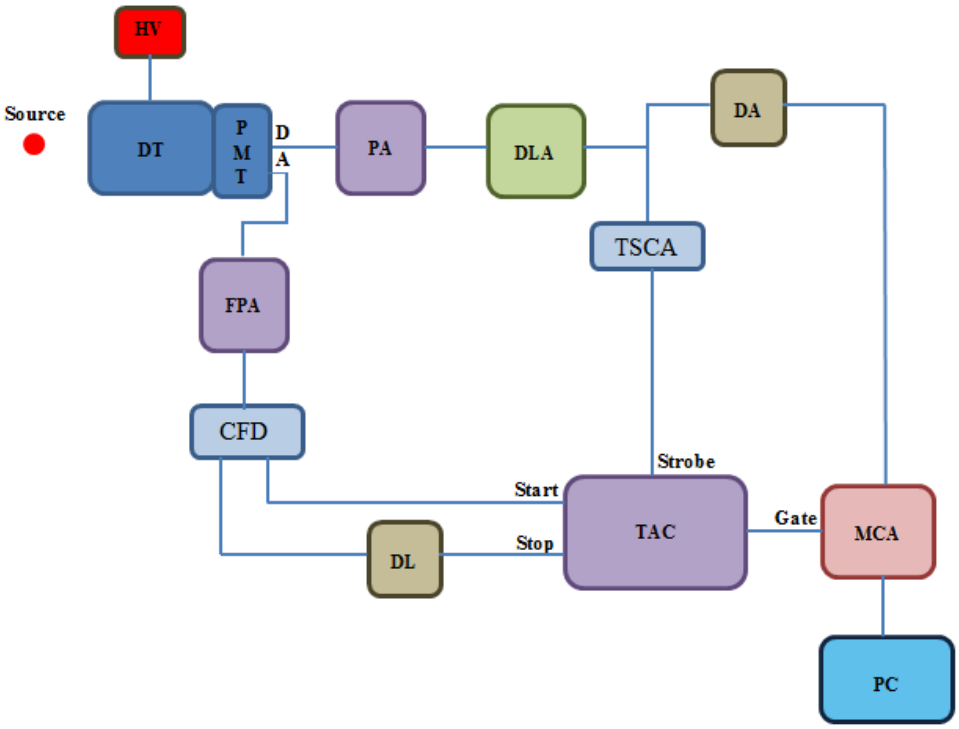


FIGURE 1. Block diagram of the used spectrometer. HV: power supplier, DT: detector, PMT: photomultiplier tube, PA: preamplifier, DLA: delay line amplifier, DA: delay amplifier, TSCA: timing single channel analyzer, FPA: fast preamplifier, CFD: constant fraction discriminator, DL: delay, TAC: time to amplitude converter, MCA: multichannel analyzer, PC: computer.

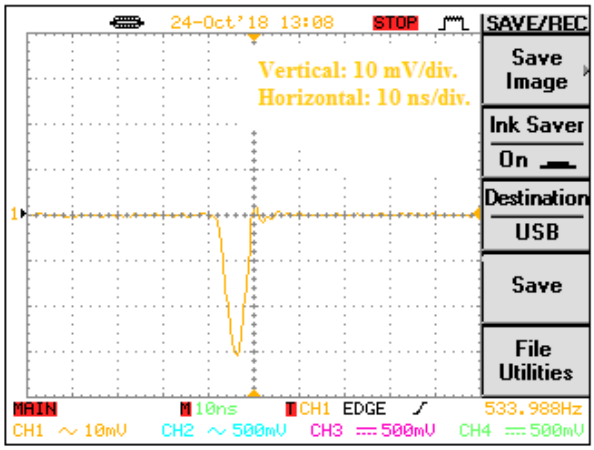


FIGURE 2. Signal shape of CFD output.

ISBN:978-605-83516-6-0

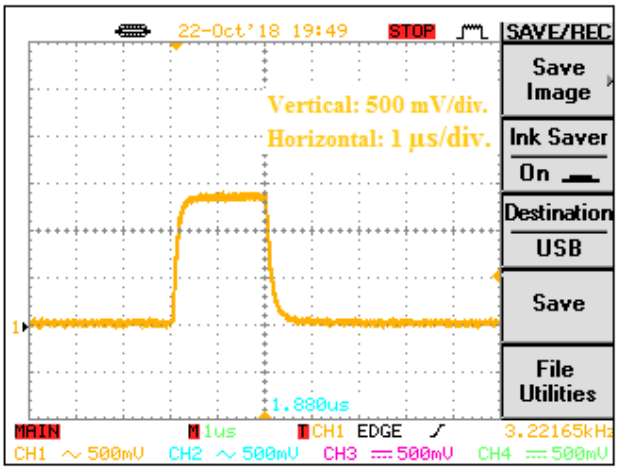


FIGURE 3. Signal shape of TAC output.

RESULTS AND DISCUSSION

^{137}Cs gamma energy spectrum without timing method is shown in Fig. 4.

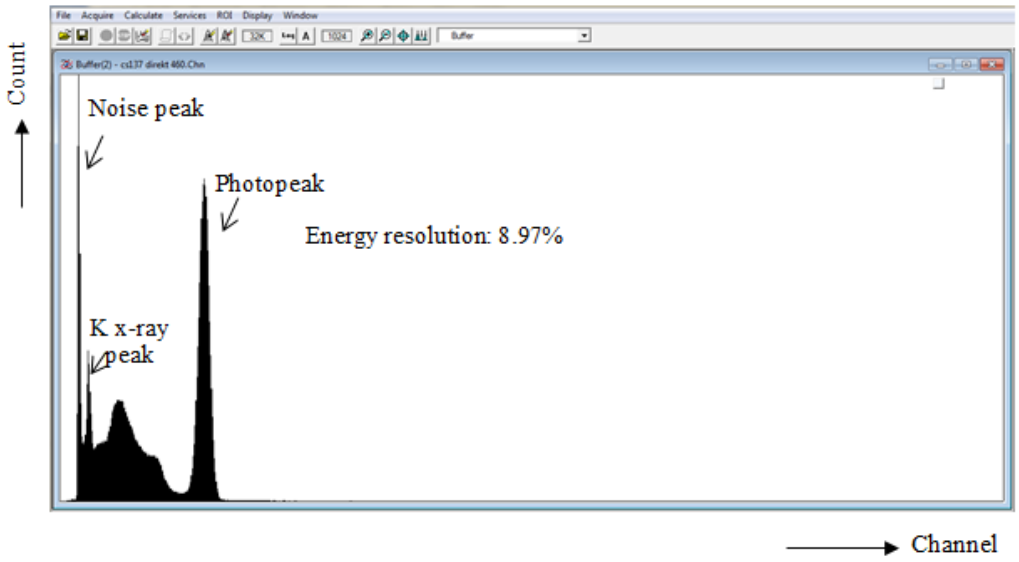


FIGURE 4. ^{137}Cs gamma energy spectrum without timing method.

The reason why the energy signals from the amplifier was gated by the timing signals was to acquire the neat energy spectrum of source particles only, connecting the energy and timing signals coincidentally in the MCA. In this way, energy resolution improvement can be achieved. Resultant ^{137}Cs gamma energy spectrum together with constant fraction timing method is shown in Fig. 5. In this figure, only photopeak was chosen for comparison of energy resolution.

ISBN:978-605-83516-6-0

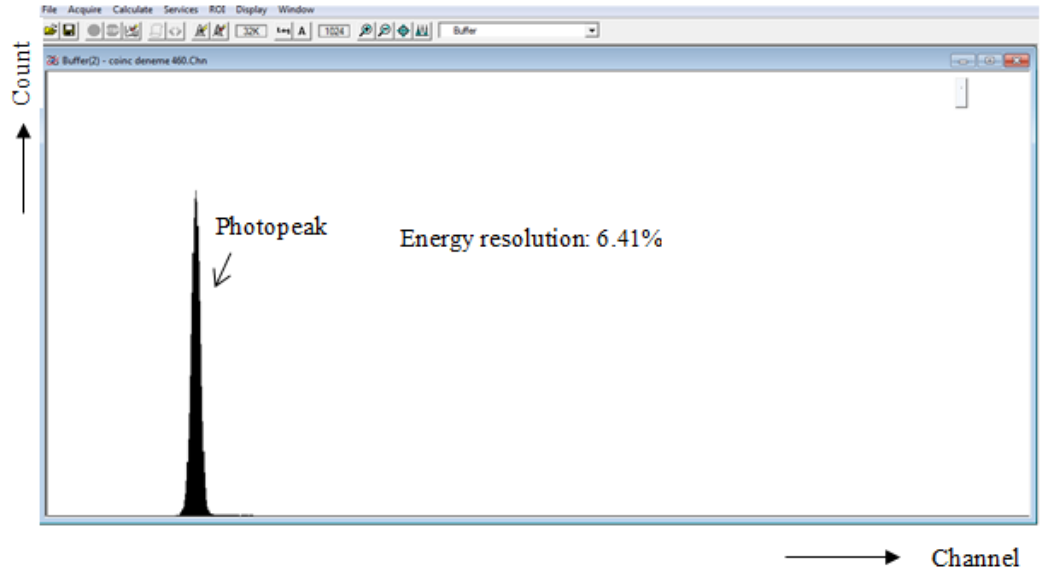


FIGURE 5. ^{137}Cs energy spectrum after constant fraction timing method.

As can be seen in Fig. 4, the energy resolution value without timing method was determined as 8.97%. After timing process, it was found as 6.41% (Fig. 5). In Fig. 6, the energy spectra which were acquired with and without timing method were compared.

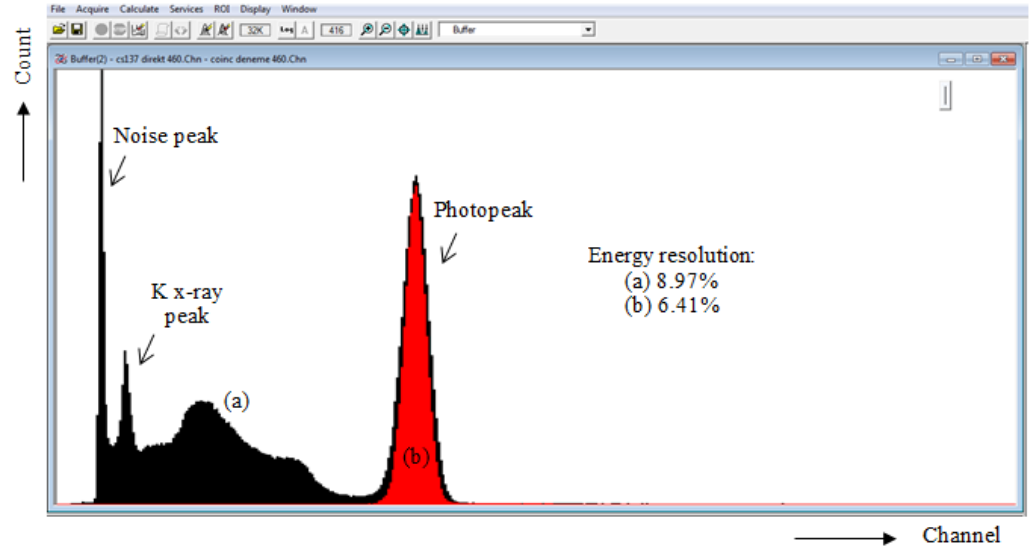


FIGURE 6. Comparison of energy spectra of ^{137}Cs (a) without (b) with constant fraction timing method.

Gamma energy spectra of ^{60}Co without and with constant fraction timing method are shown in Figs. 7 and 8, respectively.

ISBN:978-605-83516-6-0

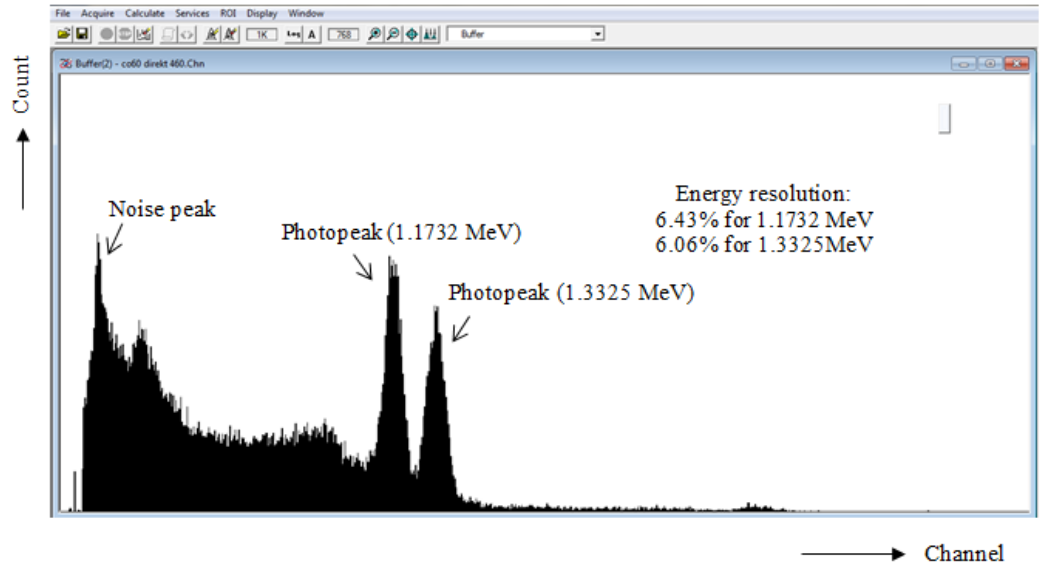


FIGURE 7. ^{60}Co gamma energy spectrum without timing method.

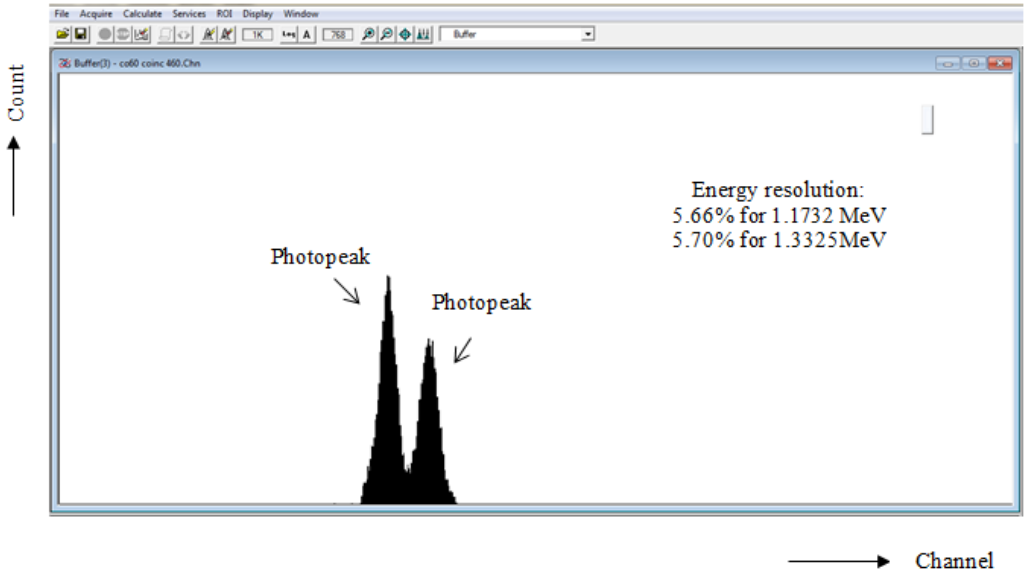


FIGURE 8. ^{60}Co energy spectrum after constant fraction timing method.

The energy resolution values of 1.1732 MeV and 1.3325 MeV energy-peaks without timing method were determined as 6.43% and 6.06% as can be seen in Fig. 7, respectively. After timing process, the results were found as 5.66% and 5.70% (Fig. 8). The energy spectra which were acquired with and without timing method were compared in Fig. 9.

ISBN:978-605-83516-6-0

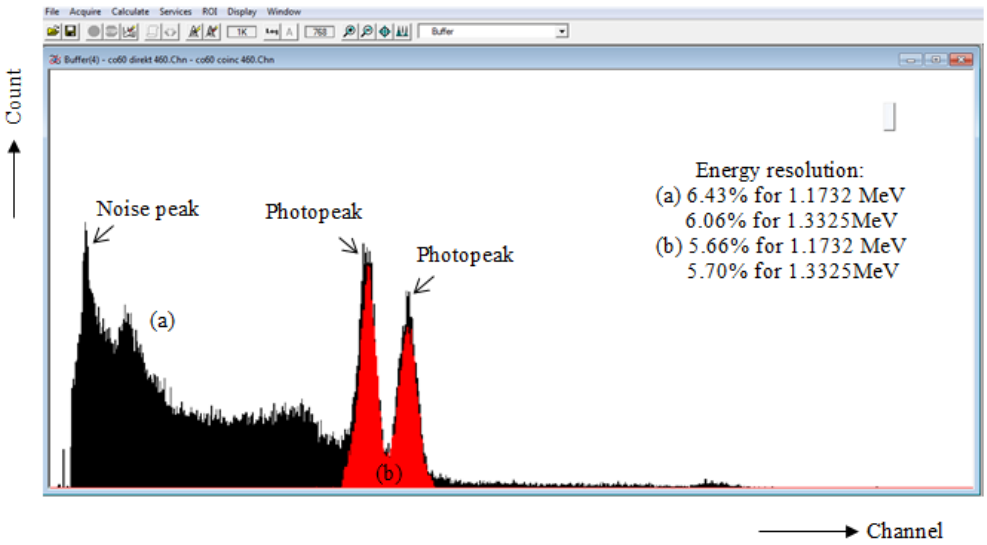


FIGURE 9. Comparison of energy spectra of ^{60}Cs (a) without (b) with constant fraction timing method.

CONCLUSION AND COMMENT

^{137}Cs and ^{60}Co gamma energy spectra were achieved through a spectrometer consisted of NaI(Tl) scintillation detector. The energy spectrum was gated by means of constant fraction timing method in order to improve the energy resolution value of the spectrometer. The energy resolution value of ^{137}Cs was enhanced after using constant fraction timing method. It can be concluded that the constant fraction timing method was successful to improve the energy resolution. Comparisons of the achieved energy spectra with and without constant fraction timing method was shown in Figs. 6 and 9.

It can be concluded from the obtained results that constant fraction timing method is successful in the discrimination of the source particle signals from the other deteriorating effects such as electronic noise, background, scattering, backscattering, etc. By this way, this timing method can successfully be used to obtain neat energy spectrum of the source particles.

In our previous work, constant fraction timing method was used to enhance energy resolution of the spectrometer like in the present study [13-15]. However, the difference of this study from the other ones [13-15] is that the energy resolution values here were obtained better than those. Because, the spectrometer was consisted of new generation electronic modules (Ortec VT120A fast preamplifier and Ortec 584 constant fraction discriminator). It is believed that the fast preamplifier was quite effective on the discrimination of undesired pulses according to the conventional timing methods. For this reason, it is suggested to use it in timing spectroscopy for optimum performance.

Additionally, this timing method was only applied to gamma particles here. This method can be implemented not only to gamma particles but also alpha, beta, neutron and proton particles for the elimination of any undesirable effects, and the particle discrimination.

ACKNOWLEDGEMENTS

This work was supported by EBILTEM, Center of Science and Technology, Ege University under Project No. 18 BIL 004.

ISBN:978-605-83516-6-0

REFERENCES

1. J.T. Bushberg, *The Essential Physics of Medical Imaging* (William-Wilkins, USA, 2001).
2. R.W. Leo, *Techniques for Nuclear and Particle Physics Experiments* (Springer-Verlag, Germany, 1987).
3. G.F. Knoll, *Radiation Detection and Measurement* (John Wiley & Sons. Inc, New York, 2000).
4. M.N. Wernick and J.N. Aarsvold, *Emission Tomography: The Fundamentals of PET and SPECT* (Elsevier Academic Press, USA, 2004).
5. Hamamatsu Photonics K. K., *Photomultiplier Tubes Basics and Applications* https://www.hamamatsu.com/resources/pdf/etd/PMT_handbook_v3aE.pdf. (Accessed 21 September 2019).
6. Hamamatsu Photomultiplier Tube, *Opening the future with photonis*, https://www.hamamatsu.com/resources/pdf/etd/PMT_TPMZ0002E.pdf (Accessed 21 September 2019).
7. N. Tsoulfanidis, *Measurements and Detection Radiation* (Taylor&Francis, USA, 1995).
8. J. Prekeges, *Nuclear Medicine Instrumentation* (Jones and Barlett Publishers, United States, 2013).
9. Ortec AN42 Application Note, *Principles and Applications of Timing Spectroscopy* https://www.ortec-online.com/-/media/ametekortec/application%20notes/an42.pdf (Accessed 21 September 2019).
10. M. Moszynski, J. Zalipska, M. Balcerzyk, M. Kapusta, W. Mengesha, J.D. Valentine, Nucl. Instrum. Meth., **484**, 259-269 (2002).
11. I. Akkurt, K. Gunoglu, S.S. Arda, Sci. Tech. Nucl. Installations **186798**, 1-5 (2014).
12. U. Ackermann, W.Egger, P. Sperr, G. Dollinger, Nucl. Instrum. Meth. **786,** 5-11 (2015).
13. C. Celiktas, E.E. Ermis, M. Bayburt, J. Radioanal. Nucl. Chem. **293**, 377-382 (2012).
14. E.E. Ermis, C. Celiktas, Int. J. Instrum. Sci. **1**, 54-62 (2012).
15. E.E. Ermis, C. Celiktas, AIP Conference Proceedings, **1815**, 060009 (2017).

BOOK OF FULL TEXT PROCEEDINGS TURKISH PHYSICAL
SOCIETY 35th INTERNATIONAL PHYSICS CONGRESS (TPS35)
TPS35, Vol.01, No.09, pp.511-514.
ISBN:978-605-83516-6-0 15 December 2019

Radiogenic Heat Productions Caused by Volcanic Tuffs Collected from Quarries in Turkey

Onur METİN[1, a)], Şeref TURHAN[2], Aslı KURNAZ [2] and Aybaba HANÇERLİOĞULLARI [2]

[1]*Kastamonu University, Taşköprü Vocational School, Department of Electric and Energy Kastamonu-TURKEY*
[2] *Kastamonu University, Faculty of Science and Letters, Department of Physics Kastamonu-TURKEY*

[a)]ometin@kastamonu.edu.tr

Abstract. All building raw materials and products derived from rock and soil contain various amounts of naturally occurring radionuclides of the uranium, thorium, and the radioactive potassium. Volcanic tuff stones are widely used to coat the interior and exterior surfaces of the buildings for ornamental purposes in the construction industry in Turkey and also used as structural material in the construction of masonry buildings. In this study, the concentrations of uranium, thorium and potassium in seventy-six volcanic tuff samples collected from different quarries located in different geographical regions were analyzed to estimate radiogenic heat production of these tuff samples using a wavelength dispersive X-ray fluorescence (WDXRF) spectrometry. The values of the radiogenic heat productions varied from 0.5 to 13.4 μW/m3 with an average of 3.7 μW/m3. The average the radiogenic heat production is approximately four times higher than the average continental crust of 0.9 μW/m3.

Key Words: Radiogenic heat productions, Volcanic tuff, Heat generation, Quarries, WDXRF

INTRODUCTION

The radiogenic heat production was generated when the planet is collected and formed (which has been cooled to date), and the frictional heating arising from the dense outer core, which sinks to the inner core are the three heat sources arising from the earth's interior [1,2].The heat present in the earth's crust consists of the decomposition of radiogenic elements by mantle heat. By radiogenic welding, heat is generated by short and long half-life isotopes in the earth's crust. Short half-life radiogenic isotopes (^{26}Al, ^{26}Cl and ^{60}Fe) are effective in the heat production of the earth's early periods, while long-life isotopes (^{238}U, ^{235}U, ^{232}Th and ^{40}K) are involved in the generation of radiogenic heat from the first periods of the earth to the present [3].

Radiogenic heat production from the decay series of long-lived radioactive isotopes is one of the major heat sources of the planet. Surface heat flow values determined in deep boreholes are essentially affected by the radiogenic heat generated in the crust as well as heat transported from deeper levels of the Earth [4].

Radiogenic heat production which is dependent on the uranium (U), thorium (Th) and potassium (K) concentrations of rocks is one of the most important thermal parameters of the lithosphere. U and Th concentrate in melts, and the upward transport and emplacement of melts results in a vertical differentiation of heat production in the crust. The differentiation is one of the main factors contributing to the thermal stability of the continental lithosphere. Under oxidizing conditions, U is relatively easily mobilized, whereas Th is more conservative. The

Türk Fizik Derneği
1950
Turkish Physical Society

ISBN:978-605-83516-6-0

geochemical characteristics of K are somewhat different, and its concentration histogram is not log-normal. In crustal rocks it is typically a major component and present in most of the major rock forming minerals [5,6,7,8].

In this study, the concentrations of uranium, thorium and potassium in seventy-six volcanic tuff samples collected from different quarries located in different geographical regions were analyzed to estimate radiogenic heat production of these tuff samples using a wavelength dispersive X-ray fluorescence (WDXRF) spectrometry.

MATERIALS AND METHODS

For analyses, 76 volcanic tuff samples were collected from different quarries located in different geographical regions in Turkey. The concentrations of uranium, thorium and potassium in the volcanic tuff samples were determined by using a WDXRF spectrometer (PANalytical Axios advanced model) to estimate the radiogenic heat generation. WDXRF determines the amount of X-rays obtained from the sample by first reflecting them in special crystals and then counting the elements and rays by determining the reflection angles. . In general, the sensitivity of EDXRF systems depends on the resolution of the detector used, and on WDXRF systems the sensitivity varies with the power of the X-ray tube used [9]. For the analysis of major elements, the spectrometer used Super IQ- Analysis Software was calibrated using advanced fundamental parameters algorithm. For the accurate analysis of trace elements Pro-Trace software was used

The radiogenic heat generation (A) was estimated using Rybach empirical formula as follows [10]:

$$A[\mu W/m^3] = 10^{-5} * \rho[kg/m^3] * (9.52 * C_u[ppm] + 2.56 * C_{Th}[ppm] + 3.48 * C_k[\%]) \quad (1)$$

where C_U, C_{Th} and C_K are the concentrations of uranium (in mg/kg or ppm), thorium (in ppm) and potassium (%), respectively and ρ is the density of the volcanic tuff sample.

RESULTS AND DISCUSSION

The values of the radiogenic heat productions estimated for the volcanic tuff samples are given in Table 1. The values of the radiogenic heat productions varied from 0.2 to 10,3 μW/m3 with an average of 2.7 μW/m3. The average the radiogenic heat production is higher than the average continental crust of 0.9 μW/m3.

CONCLUSION

Since there is no previously calculated data on radiogenic heat generation in the studied regions and samples, we cannot make a comparative analysis. The values we obtained are important for the separation of mantle and radiogenic heat in geothermal energy research and for providing a data infrastructure for geologists on radiogenic heat production.

ISBN:978-605-83516-6-0

Table 1. Radiogenic heat production of volcanic tuff samples

Sample Code	A (μW/m^3)	Sample Code	A(μW/m3)
S1	2.5	**S39**	0.6
S2	1.3	**S40**	2.1
S3	1.0	**S41**	2.1
S4	0.2	**S42**	2.2
S5	1.5	**S43**	2.1
S6	2.2	**S44**	1.9
S7	2.3	**S45**	1.3
S8	1.3	**S46**	1.4
S9	1.4	**S47**	2.3
S10	1.2	**S48**	1.8
S11	3.1	**S49**	1.7
S12	1.4	**S50**	1.4
S13	1.2	**S51**	1.4
S14	1.3	**S52**	1.7
S15	1.8	**S53**	1.5
S16	2.5	**S54**	1.9
S17	2.1	**S55**	1.6
S18	1.6	**S56**	1.7
S19	1.7	**S57**	1.5
S20	0.9	**S58**	1.5
S21	0.8	**S59**	3.0
S22	1.0	**S60**	10.3
S23	1.2	**S61**	10.2
S24	2.8	**S62**	7.9
S25	2.5	**S63**	9.7
S26	1.3	**S64**	10.0
S27	3.2	**S65**	8.9
S28	5.7	**S66**	6.2
S29	3.5	**S67**	4.7
S30	4.3	**S68**	4.8
S31	2.1	**S69**	4.8
S32	3.4	**S70**	3.9
S33	1.6	**S71**	6.0
S34	1.9	**S72**	1.2
S35	1.5	**S73**	1.2
S36	1.3	**S74**	2.4
S37	0.6	**S75**	3.1
S38	0.8	**S76**	0.9

REFERENCES

1. K. Strivastava, R.N. Singh, *A model for temperature variations in sedimentary basins due to random radiogenic heat sources*, Geophys. J. Int. 135 (1998) 727.

2. T.A Adagunodoa, O.G. Bayowab, M.R. Usikalua, A.I. Ojoawoc, *Radiogenic heat production in the Coastal Plain Sands of Ipokia, Dahomey Basin, Nigeria.* MethodsX 6 (2019) 1608–1616, doi: https://doi.org/10.1016/j.mex.2019.07.006.
3. G. Göktürkler, *Yer bilimlerinde, Isı Transferi Modellemesi: Kararlı-Hal Kondüktif Isı İletimi*, Dokuz Eylül Üniversitesi Mühendislik Fakültesi, Fen ve Mühendislik Dergisi, 4(3): (2002) 67-80.
4. L. Rybach, *Wärmeproduktionsbestimmungen an Gesteinen der Schweizer Alpen*, Beiträge zur Geologie der Schweiz: Geotechnische Serie. 51 (1973) (43pp).
5. I.T. Kukkonen, R. Lahtinen, *Variation of radiogenic heat production rate in 2.8–1.8 Ga oldrocks in the central Fennoscandian shield*, Physics of the Earth and Planetary Interiors 126 (2001) 279–294, doi: https://doi.org/10.1016/S0031-9201(01)00261-8.
6. M. Sandiford, S. McLaren, N. Neumann, *Long-term thermal consequences of the redistribution of heat-producing elements associated with large-scale granitic complexes*, J. Metamorph. Geol. 20 (2002) 87–98.
7. S. McLaren, R. Powell, *Magmatism, orogeny and the origin of high-heat-producing granites in Australian Proterozoic terranes*, J. Geol. Soc. 171 (2014) 149–152.
8. T. Veikkolainen, I.T. Kukkonen, *Highly varying radiogenic heat production in Finland, Fennoscandian Shield Tectonophysics*, 750 (2019) 93–116.
9. G.B. Arkalı, WD-XRF *Spektrometresiyle Jeolojik numunelerdeki Ana Oksitler Üzerine Matris Etkisinin Belirlenmesi*, Gazi Üniversitesi Fen Bilimleri Enstitüsü, Yüksek Lisans Tezi (2010).
10. L. Rybach, G. Buntebarth, *Relationships between the petrophysical properties density, seismic velocity, heat generation, and mineralogical constitution*, Earth and Planetary Science Letters, 57 (1982) 367-376.
11. A. Bubu, C. P. Ononugbo, *Radiogenic Heat Production Due to Natural Radionuclides in the Sediments of Bonny River, Nigeria*. Journal of Scientific Research & Reports, 17(6): (2017) 1-9.

BOOK OF FULL TEXT PROCEEDINGS TURKISH PHYSICAL
SOCIETY 35th INTERNATIONAL PHYSICS CONGRESS (TPS35)
TPS35, Vol.01, No.09, pp.515-518.
ISBN:978-605-83516-6-0 15 December 2019

The Excess Lifetime Cancer Risk Caused by Ingestion of Some Bottled Waters Consumed in Turkey

Onur METİN[1,a)], Şeref TURHAN[2], Aslı KURNAZ[2] and Aybaba HANÇERLİOĞULLARI[2]

[1]*Kastamonu University, Taşköprü Vocational School, Department of Electric and Energy Kastamonu-TURKEY*
[2] *Kastamonu University, Faculty of Science and Letters, Department of Physics Kastamonu-TURKEY*

[a)]ometin@kastamonu.edu.tr

Abstract. Drinking waters may contain natural radionuclides which may pose a risks (or hazards) to human health. Radionuclides with long half-life that can be entered into human body by the digestion of drinking water may cause internal irradiation of kidney, liver, bladder, bones and bone marrow so individuals may receive radiation dose to the extent of threat to their health. In addition, radon gas in drinking water entering into the body through the respiratory tract may increase the risk of lung cancer over time. In this study, the excess lifetime cancer risk was estimated for adult who consume some bottled waters commercially sold in Turkey based on the contents of gross alpha and gross beta in bottled water samples. The values of the excess lifetime cancer risk varied 3.8×10^{-5} to 2.8×10^{-4} with an average of 1.1×10^{-4}. Consequently, the excess life time cancer risks values via bottled water consumption were found below the acceptable limit of 10^{-3} for radiological risk.

Key Words: Bottled water, Lifetime cancer risk, Annual efficient radiation dose, Radionuclides

INTRODUCTION

As it is known, water is the most important foodstuff which is essential for human survival. Without water, human life ends in a short time. Groundwater and surface waters (rivers, streams, dams, lakes, ponds, etc.) are the sources of drinking water. Although about 80% of the world is covered with water, it is known that only 2.5% of these waters are fresh water suitable for human consumption. Turkey's freshwater potential is 112 billion m^3. In Turkey, of freshwater 10% domestic, 25% industrial, and 65% to is used for agricultural activities [1].

The commercially packaged drinking water sector (including bottled and sachet water) includes recycled/non-recycled water and mineral water. Bottled water sector which is a very dynamic and competitive market in Turkey uses natural mineral waters, groundwater extracted from drilled wells and free flowing spring waters. Surface water which is obtained from the lake, river, and stream in Turkey is prohibited to be commercially bottled and sold for human consumption. Turkey bottled waters; natural spring water, natural mineral water, drinking water and treated drinking water [2].

Water pollution occurs when unwanted substances enter the water, change the quality of the water, and are harmful to the environment and human health. Water pollution means poor quality water of poor quality which is not good for human health. Enough safe drinking water is a prerequisite for a healthy life. Waterborne diseases, which account for 80% of global diseases, are a major cause of death in many parts of the world, important in children [3]. Diseases due to pollution of drinking water create serious problems and burdens on human health. Therefore, interventions to improve the quality of drinking water provide significant health benefits. Drinking water contains in particular natural pollutants originating from the geological layers where water flows and unnatural pollutants from human activities.

Radioactivity in drinking water comes from natural and artificial sources. Some of the naturally occurring chemical elements in the environment (uranium, thorium and actinium of the radioactive series, radioactive potassium, etc.) are radioactive. Natural radionuclides exist in rocks and soils that vary from region to region [4]. As a result, these radionuclides carried by groundwater can enter the food chain directly by the groundwater used by people as drinking water and indirectly through the groundwater or surface water used for irrigating field

Türk Fizik Derneği
1950
Turkish Physical Society

ISBN:978-605-83516-6-0

crops. The amount of radioactive components dissolved and released as a result of the interaction of groundwater with soil and rocks is the geochemical component of the soil, the mineralogical structure of the rocks, the chemical structure of the water, the degree of erosion of the rocks, the redox conditions and may vary depending on the residence time of groundwater in soil and rocks [5].

Drinking water may contain natural radionuclides which may pose a risk to human health. Radionuclides, which have a long half-life that can enter the human body through the digestion of drinking water, can cause internal irradiation of the kidney, liver, bladder, bones and bone marrow. Lifetime cancer risk is related to the possibility of exposure time lifetime cancer in a particular subject. In this study, lifetime cancer risk for adults who consume bottled water sold commercially in Turkey, in bottled water samples depending on the content total alpha and total radioactivity was calculated.

MATERIALS AND METHODS

In this study, the excess lifetime cancer risk was estimated for adult who consume some bottled waters commercially sold in Turkey based on the activity concentrations of gross alpha and gross beta measured in bottled water samples. It is important to determine the annual effective radiation dose that can be taken by the individual who is exposed to ionizing radiation (internal radiation) such as alpha and beta released from radionuclides due to entry of drinking water into the digestive system.

The annual effective radiation dose (AERD) is calculated by the following formula, taking into account the dose conversion coefficient and annual water consumption, taking into account the gross alpha/beta activity concentrations measured in bottled water samples as follows [5-6]:

$$AERD\left(\mu Sv/y\right) = AC_{\alpha,\beta} \cdot DCC \cdot ACW \tag{1}$$

where $AC_{\alpha,\beta}$ is the gross alpha or gross beta activity concentration (mBq/L) taken from study performed by Turhan et al. [7] , DCC is dose conversion coefficient (mSv/Bq) and ACW is the annual amount of water consumed (L/y). ACW was taken as 730 L for adults [6].

Excess lifetime cancer risk (LTCR) is considered a value that represents the maximum number of cancer cases among individuals exposed to a certain level of ionizing radiation dose. Lifetime cancer risk was estimated by the following equation [8]:

$$LTCR = AERD \cdot AL \cdot RF \tag{2}$$

where, AERD is the annual effective radiation dose values taken from study performed by Turhan et al. [7], AL is the average life (accepted as 78 years) and the RF is the risk factor regarded as 0.057/Sv risk factor [9].

RESULTS AND DISCUSSION

The values of the excess lifetime cancer risk estimated for adults consumed the bottled drinking water samples commercially sold in Turkey are given in Table 1. As seen from Table 1 that the values of LTCR varied 3.8×10^{-5} to 2.8×10^{-4} with an average of 1.1×10^{-4}. It has been found that the lifetime risk of cancer varies from 3.8×10^{-5} to 2.8×10^{-4}. The highest value of LTCR is estimated for the water sample of BD15 while the lowest vale of LTCR is estimated for the water sample of BD4.

ISBN:978-605-83516-6-0

Table 1. The values of the excess lifetime cancer risk estimated for adult person

Sample code	LTCR
BW1	7.6×10^{-5}
BW2	4.8×10^{-5}
BW3	$4. \times 10^{-5}$
BW4	3.8×10^{-5}
BW5	6.1×10^{-5}
BW6	4.7×10^{-5}
BW7	9.7×10^{-5}
BW8	8.1×10^{-5}
BW9	5.2×10^{-5}
BW10	2.4×10^{-4}
BW11	1.2×10^{-4}
BW12	6.9×10^{-5}
BW13	7.0×10^{-5}
BW14	4.3×10^{-5}
BW15	2.8×10^{-4}
BW16	2.6×10^{-4}
BW17	2.1×10^{-4}
BW18	1.4×10^{-4}
BW19	1.5×10^{-4}
Average	1.1×10^{-4}
Standard deviation	8.0×10^{-5}
Standard error	1.8×10^{-5}
Min	3.8×10^{-5}
Max	2.8×10^{-4}

CONCLUSION

All values of the excess lifetime cancer risk are below the acceptable limit of 10^{-3} for radiological risk. Radiological results indicate that the consumption of bottled drinking water samples examined does not pose any risk from the radiological point of view and that these water samples are of sufficient quality to be consumed as drinking water. The data obtained as a result of this study can be used as a guide for the control of drinking water.

ISBN:978-605-83516-6-0

REFERENCES

1. C. Kınacı, *Su yönetiminde temel kavramlar ve bileşenler;Türkiye'de su yönetimi*, İstanbul, (2017).
2. Güler, C., Alpaslan, M., *Mineral content of 70 bottled water brands sold on the Turkish market: Assessment of their compliance with current regulations.* Journal of Food Composition and Analysis, 22 (2009) 728-737.
3. Haseena, M., Malik, M.F. *Water pollution and human health.* Environmental Risk Assessment and Remediation, 1(3): (2017) 16-19.
4. Unscear (United Nations Scientific Committee on the Effects of Atomic Radiation), *Sources and effects of ionizing radiation*. United Nations Publication, New York, USA, (2000).
5. Özçıtak, E. *Nevşehir ili ve ilçelerinde tüketilen içme ve kaplıca sularındaki radyoaktivitenin ölçülmesi.* Yüksek Lisans Tezi. Nevşehir Üniversitesi Fen Bilimleri Enstitüsü. Nevşehir (2012).
6. Who (World Health Organization). *Guidelines for Drinking-water Quality*. 4th edition, WHO Library Cataloguing-in-Publication Data NLM classification: WA 675, Geneva. (2011).
7. Turhan, Ş., EM Zriba, N.A., Taşkın, H., Yılmaz, Z., Bayülken, S., Hançerlioğulları, A., Kurnaz, A., *Radiochemical analysis of bottled drinking waters consumed in Turkey and a risk assessment study*. Microchemical Journal 149, (2019) 1-7.
8. Atıcı, E. *Kapadokya Bölgesinde Yapı Taşı Olarak Üretilen Tüflerdeki Doğal Radyoaktivitenin Gama Spektrometrik Yöntemle Ölçülmesi.* Yayınlanmış Yüksek Lisans Tezi, Nevşehir Hacı Bektaş Veli Üniversitesi Fen Bilimleri Enstitüsü. Nevşehir. (2016).
9. ICRP (International Commission on Radiological Protection), *Age-dependent doses to members of the public from intake of radionuclides*. ICRP Publication, 20 (3): (1990).

BOOK OF FULL TEXT PROCEEDINGS TURKISH PHYSICAL
SOCIETY 35th INTERNATIONAL PHYSICS CONGRESS (TPS35)
TPS35, Vol.01, No.09, pp.519-523.
ISBN:978-605-83516-6-0 15 December 2019

Electric Dipole ($E1$) Strength in ^{139}La Nucleus below The Neutron-Separation Energy

Emre Tabar[1, 2, a)] and Gamze Hoşgör[1, b)]

[1]*Sakarya University, Faculty of Science and Arts, Physics Department, Sakarya, Turkey*
[2]*2Biomedical, Magnetic and Semiconductor Materials Research Center (BIMAS-RC), Sakarya University, Sakarya, Turkey*

[a)] Corresponding author: etabar@sakarya.edu.tr
[b)] hosgorgamze@yahoo.com

Abstract. The electric dipole ($E1$) strength below the particle separation energy, which is commonly denoted as Pygmy Dipole Resonance (PDR), is one of the characteristic features of the nuclei in both spherical and deformed region of the periodic table. In the present study, PDR in ^{139}La, of which the photo-absorption cross section has been measured in a recent experiment, has been investigated in the framework of the Translation and Galilean Invariant Quasiparticle Phonon Nuclear Model (TGI-QPNM) for the first time. The comparison between the experimentally determined $B(E1)$ strength distributions and the results of the TGI-QPNM calculations shows a good agreement. The gross features of the experimental $E1$ strength in the energy range from 6 to 10 MeV and the two major peaks at about 6.5 and 9 MeV observed in the experiment have been also well reproduced in the TGI-QPNM calculations.

INTRODUCTION

Electric dipole ($E1$) mode occurring as a result of the collective motion of the nucleons is one of the universal features of the atomic nucleus. A large fraction of the $E1$ strength in atomic nuclei is exhausted by the Giant Dipole Resonance (GDR), lying at the energies between 10-18 MeV. However, strong $E1$ transitions concentrated around the neutron separation energy, so-called Pygmy Dipole Resonance (PDR), have been observed over the last few decades [1]. As the energy ranges from 5 to 8 MeV, where the PDR mode occurs, became accessible with the new technology Nuclear Resonance Fluorescence (NRF) experiments, the $E1$ response of the atomic nuclei in these energies has taken considerable attention in recent years [2].

Especially the gross features of PDR in many doubly-even mass nuclei have been successfully reproduced in different theoretical approaches. [3,4]. The Quasiparticle Random Phase Approximation (QRPA) with a phenomenological mean-field is one of the most successful methods for studying the electric and magnetic dipole strength in both even- and odd-mass deformed nuclei, see e.g. [7-15]. However, in QRPA several symmetries of the single-quasiparticle Hamiltonian are violated because of the mean-field potential. In the case of $E1$ transitions, theoretical $E1$ spectra contain spurious admixtures as a result of the broken translation and Galilean symmetry of the Hamiltonian. Therefore, for a realistic description of the $E1$ transitions, one has to restore broken translation and Galilean symmetry of the QRPA Hamiltonian. [14,15]. For such a treatment, Pyatov prescription [12] offers an easy and efficient way, which has been successfully applied to restore the violated Galilean and translational symmetry of the QRPA Hamiltonian of both spherical [13] and deformed nuclei [14,15]. In the present work, in order to study the

Türk Fizik Derneği
1950
Turkish Physical Society

ISBN:978-605-83516-6-0

PDR mode, observed recently in ^{139}La [16], Pyatov's restoration method has been applied to the QPNM (Quasiparticle Phonon Nuclear Model) Hamiltonian of an odd-mass nucleus for the restoration of the broken Galilean and translational symmetry of it for the first time.

THEORY

In the TGI- QPNM, the starting Hamiltonian is written in the following form [14,15]:

$$H = H_{sqp} + W_1 + h_0 + h_\Delta \tag{1}$$

Here $H_{sqp.}=\sum_{q,\tau}\varepsilon_q(\tau)\alpha^+_{qp}(\tau)\alpha_{qp}(\tau)$ is the single quasiparticle Hamiltonian consisting of a Woods-Saxon mean field. $\alpha^+_q(\alpha_q)$ creates (annihilates) a quasiparticle and ε_q is quasiparticle-energy. $W_1 = \frac{3}{2\pi}\chi_1\left(\frac{NZ}{A}\right)^2 (R_N - R_Z)^2$ is the isovector part of the dipole-dipole (λ=1) interaction where χ_1 are the strength of it [14,15]. h_0 and h_Δ are separable effective residual interactions and if they are added to system Hamiltonian [7-15], the broken symmetry of it has been restored. These terms are:

$$h_0 = -\frac{1}{2\gamma}\sum_{\mu=0,\pm1}\left[H_{sqp}, P_\mu\right]^+\left[H_{sqp}, P_\mu\right] \tag{2}$$

$$h_\Delta = -\frac{1}{2\beta}\sum_{\mu=0,\pm1}\left[U_\Delta, R_\mu\right]^+\left[U_\Delta, R_\mu\right] \tag{3}$$

where

$$\gamma_\mu = \left\langle\psi_0\middle|\left[P^+_\mu,\left[H_{sqp}, P^+_\mu\right]\right]\middle|\psi_0\right\rangle \quad , \quad \beta_\mu = \left\langle\psi_0\middle|\left[R^+_\mu,\left[U_{\Delta.}, R^+_\mu\right]\right]\middle|\psi_0\right\rangle \tag{4}$$

In Eqs. (2,3) U_Δ is the pairing potential, P_μ is the linear momentum operator of the nucleus, R_μ is the center of mass (c.m.) coordinate vector of the nucleus and γ_μ, β_μ are the strength of h_0 and h_Δ residual forces, respectively [14,15].

In QPNM the wave function for an odd-mass deformed nucleus consists of the single-quasiparticle and quasiparticle⊗phonon terms [7-11]:

$$\psi^j_K(\tau) = \left\{N^j_{\varsigma_q}(\tau)\alpha^+_\varsigma(\tau) + \sum_{i\mu}\sum_\nu G^{i\mu\nu}_j\alpha^+_\nu(\tau)Q^+_{i\mu}\right\}\left|\psi_0\right\rangle \qquad \mu = 0,\pm1 \tag{5}$$

with normalization

$$\left\langle\psi^j_K(\tau)\middle|\psi^j_K(\tau)\right\rangle = \left(N^j_{\varsigma_q}\right)^2 + \sum_{i\mu}\sum_\nu\left(G^{i\mu\nu}_j\right)^2 = 1 \tag{6}$$

N^j_K and $G^{i\mu\nu}_j$ are the amplitudes of the one-quasiparticle and the quasiparticle⊗phonon component in the wave function, respectively. Employing the variation principle [7-11]:

$$\delta\left\{\left\langle\psi^j_K(\tau)\middle|H\middle|\psi^j_K(\tau)\right\rangle - \left\langle\psi_{K_0}(\tau)\middle|H\middle|\psi_{K_0}(\tau)\right\rangle - \eta_K\left[\left(N^j_{\varsigma_q}\right)^2 + \sum_{i\mu}\sum_\nu\left(G^{i\mu\nu}_j\right)^2 - 1\right]\right\} = 0 \tag{7}$$

one can obtain the secular equation in the following analytical form which determines the excitation energies (η_K) in odd-mass deformed nuclei:

ISBN:978-605-83516-6-0

$$P(\eta_K) \equiv \varepsilon_\varsigma - \eta_K - \sum_{i\mu}\sum_{\nu} \frac{\left(\kappa_1 \frac{2}{N_\tau} r^\tau_{\varsigma_q\nu} V_{\varsigma_q\nu} \overline{L_i} - \varepsilon^{(-)}_{\varsigma_q\nu} p^\tau_{\varsigma_q\nu} M_{\varsigma_q\nu} + \Delta_\tau r_{\varsigma_q\nu} L_{\varsigma_q\nu} L_i\right)^2}{4\omega_i Y(\omega_i)\left(w_i + \varepsilon_\nu - \eta_K\right)} = 0 \tag{8}$$

where;

$$L_i = \frac{\gamma}{\beta} \frac{\sum_\tau \Delta_\tau \sum_{qq'} r_{qq'} M_{qq'} w^i_{qq'}}{\sum_\tau \sum_{qq'} \varepsilon_{qq'} p_{qq'} L_{qq'} g^i_{qq'}} \qquad \overline{L_i} = \gamma \frac{\sum_\tau \frac{1}{N_\tau} \sum_{qq'} r_{qq'} u_{qq'} g^i_{qq'}}{\sum_\tau \sum_{qq'} \varepsilon_{qq'} p_{qq'} L_{qq'} g^i_{qq'}} \tag{9}$$

Here, $p^\mu_{qq'} = \langle q | p_\mu | q' \rangle$ is the single particle matrix elements of the linear momentum and $r^\mu_{qq'} = \langle q | r_\mu | q' \rangle$ is the center of mass coordinate vector. Further, the quantities $v_{qq'} = u_q u_{q'} - v_q v_{q'}$, $u_{qq'} = u_q v_{q'} + u_{q'} v_q$, $L_{qq'} = u_q v_{q'} - u_{q'} v_q$ and $M_{qq'} = u_q u_{q'} - v_{q'} v_q$ are expressed the Bogolyubov canonical transformation parameters (u_q and v_q) [17]. $\psi^i_{qq'}$ and $\varphi^i_{qq'}$ are forward and backward amplitudes of two-quasiparticles and $\varepsilon_{qq'} = \varepsilon_q + \varepsilon_{q'}$ and $\varepsilon^{(-)}_{qq'} = \varepsilon_q - \varepsilon_{q'}$ are terms are two-quasiparticle energies, also $g^i_{qq'} = \psi^i_{qq'} + \varphi^i_{qq'}$ and $w^j_{qq'} = \psi^i_{qq'} - \varphi^i_{qq'}$ as well.

The formula for the reduced probabilities of *E*1 transitions from the ground-states to the excited-states of odd-mass deformed nuclei can be written in the form:

$$B(E1, I_i K_i \to I_f K_f) = \sum_\mu \left\langle I_i 1 K_i \mu | I_f K_f \right\rangle^2 \left| -\frac{1}{2} e^n_{eff.} \sum_q N^j_{\varsigma_q} N^j_{\varsigma_q\varsigma_{q_0}} r^\tau_{\varsigma_q\varsigma_{q_0}} V_{\varsigma_q\varsigma_{q_0}} + N^j_{\varsigma_{q_0}} \sum_{i\mu} G^{i\mu\varsigma_{q_0}}_j \frac{\kappa_1(1-L_i)}{\sqrt{\omega_i Y(\omega_i)}} \left[e^{eff.}_n \frac{F_n}{N} - e^{eff.}_p \frac{F_p}{Z} \right] \right|^2 \tag{10}$$

where

$$F_\tau = \sum_{qq',\tau} \frac{\varepsilon_{qq'} r^2_{qq'} u^2_{qq'}}{\left(\varepsilon^2_{qq'} - \omega^2_i\right)} \tag{11}$$

The neutron and proton effective charges are $e^{eff}_n = -(Z/A)$ and $e^{eff}_p = (N/A)$, respectively.

RESULTS AND DISCUSSIONS

The *TGI-QPNM* calculations have been performed for odd-proton ^{139}La nuclei. The experimental value for ground-state spin-parity of ^{139}La is $7/2^+$ and its Nilsson configuration assigned to be [404]. The pairing gap parameters, Δ_n=1.213 MeV for neutrons and Δ_p=1.277 MeV for protons, have been taken from ref [18] and the chemical potentials are found to be λ_n=-6.850 MeV and λ_p=-9.073 MeV for neutrons and protons, respectively. β_2= 0.0933 quadrupole deformation parameter taken from the work of Pritychenko et al. has been used in calculations [19]. The strength parameter for the isovector dipole–dipole interaction has been chosen to be χ_1=300 $A^{-5/3}$ MeV/fm^2 according to ref [12].

In Figure 1 theoretical results for *E*1 and magnetic dipole (*M*1) radiation widths in ^{139}La along with the experimental data have been given. *M*1 radiation widths have been calculated in the framework of rotational invariant (RI)-QPNM. Details of these calculations can be found in Ref. [7-11]). The experiment data have been taken from the work of *Makinaga et al*. [16].

ISBN:978-605-83516-6-0

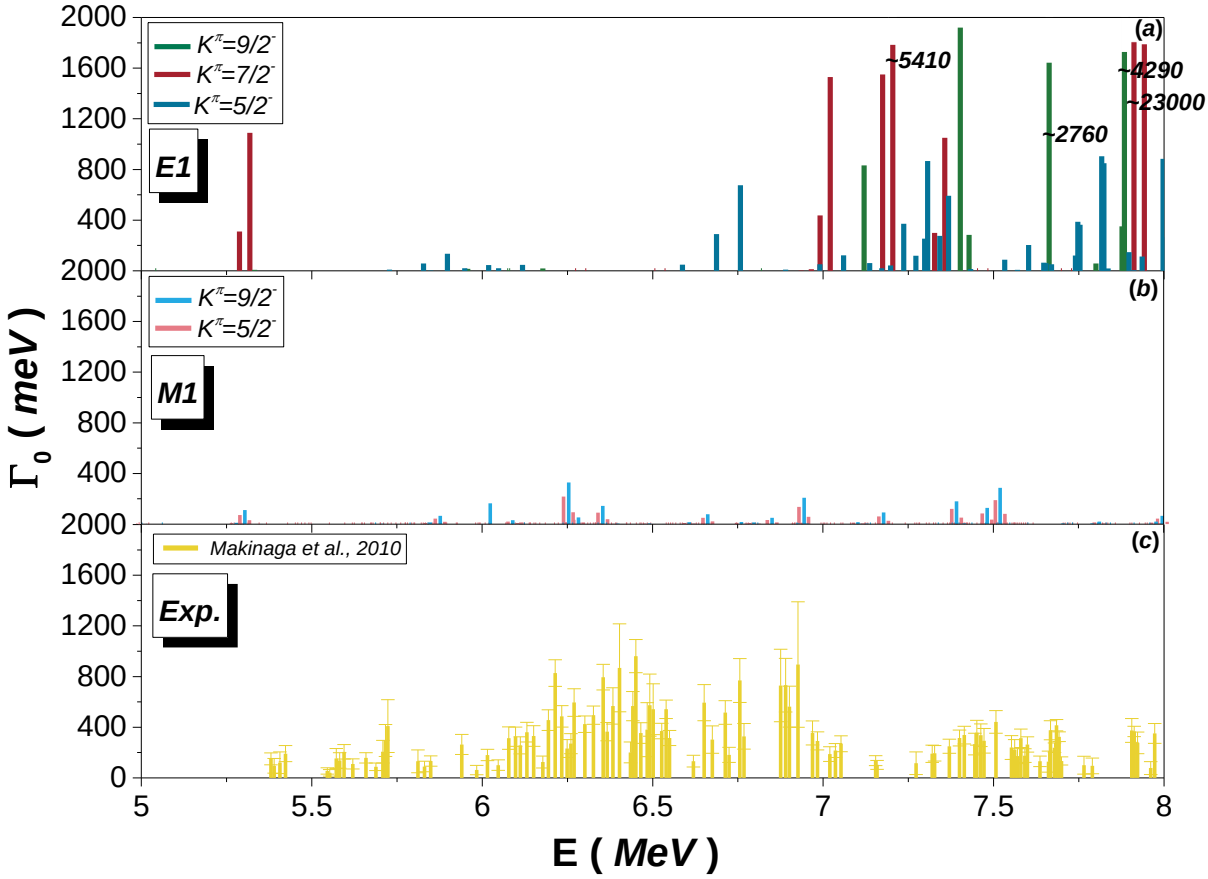


FIGURE 1. (a) The *E*1 radiation width, **(b)** the *M*1 radiation width, **(c)** and correspounding experimental data [16] in ^{139}La.

As can be seen, *E*1 strength is more dominant than the *M*1 strength in the 5-8 MeV energy range and the TGI-QPNM does not satisfactorily reproduce the fragmentation of the experimental dipole strength especially in 5.5-6.5 MeV energy range. This is possibly due to fact that in the present model complex configurations such as two- and three-phonon components in wave function have not been considered, which is known to play an essential role in the fragmentation of the *E*1 strength especially in the energies above 4 MeV. However, most of the *E*1 strength, as a rule, is carried by the one-phonon components. Therefore, it may be more sufficient to compare experimental and theoretical gross features rather than the fine structures. Such a comparison is given in Table 1.

TABLE 1. Comparison of theoretical and experimental gross features of the dipole transitions in 5-8 MeV in ^{139}La.

	Theory (*M*1)	**Theory (*E*1)**	**Theory (*M*1+*E*1)**	**Experiment** [16]
$\sum\Gamma_0$ [*meV*]	3845.85	29510.58	33356.43	31468±88.52

As can be seen in Table 1, there is a satisfactory agreement between the theoretical results of the gross features for dipole strength in ^{139}La and experimental data.

The structure of the *E*1 states has been also determined and the results have been presented in Table 2 for 5-9 MeV energy range. As can be seen in Table 2, the contribution of the quasiparticle⊗one-phonon ($G_j^{i\mu\nu}$) components are ~100%, while the contribution of one-quasiparticle (N_K^j) components is less than 2%. From this results it can be say that the *E*1 transition states in ^{139}La has predominantly quasiparticle⊗one-phonon structure.

ISBN:978-605-83516-6-0

TABLE 2. The structure of $E1$ states in ^{139}La in the energy range 5-8 MeV.

E [MeV]	K^{π}	$\left(N_K^j\right)^2$	$\sum_{i\mu}\sum_{\nu}\left(G_j^{i\mu\nu}\right)^2$	Structure
5.0106	9/2$^-$	0.006		100%[404]↓ $\otimes Q_4$
5.9277	5/2$^-$	0.007		100%[404]↓ $\otimes Q_8$
6.0430	9/2$^-$	0.003		100%[404]↓ $\otimes Q_9$
6.0487	5/2$^-$	0.003		100%[404]↓ $\otimes Q_{10}$
6.7874	5/2$^-$	0.007	-0.999	100%[404]↓ $\otimes Q_{12}$
7.0903	9/2$^-$	0.019		100%[404]↓ $\otimes Q_{13}$
7.3365	5/2$^-$	0.006		100%[404]↓ $\otimes Q_{14}$
7.6330	9/2$^-$	0.030		100%[404]↓ $\otimes Q_{17}$
7.8533	5/2$^-$	0.011		100%[404]↓ $\otimes Q_{20}$

CONCULUSIONS

In the present paper, we have investigated $E1$ response of the odd-proton ^{139}La nucleus around the neutron separation energy. The results show that $E1$ strength is more dominant than the $M1$ strength in the 5-8 MeV energy range. The experimental dipole spectra are much more fragmented than the theoretical one. This may be due to considering only one-phonon states in the present model and not taking into account the complex configurations. The agreement between the experimental and theoretical results for gross features also supports this idea.

ACKNOWLEDGMENTS

We are grateful to Prof A.A. Kuliev and Assoc Prof H. Yakut for their valuable comments. This research was supported by the Scientific and Technological Research Council of Turkey (TUBITAK) (Project No.118F094).

REFERENCES

1. A. P. Tonchev *et al.*, Physical Review Letters, **104**, 072501, 2010.
2. D. Savran et al., Nuclear Physics A, **788**, 165c-170c.
3. V. Derya *et al*., Physical Review C, **93**, 034311 (1-10), 2016.
4. G. A. Bartholomez, Annual Review of Nuclear Science, **11**, 259-302, 1961.
5. A. Zilges and D. Savran, EPJ Web of Conferences, **93**, 01028 (1-4), 2015.
6. D. Savran, T. Aumann and A. Zilges, Progress in Particle and Nuclear Physics, **70**, 210-245, 2013.
7. E. Tabar, Nuclear Physics A, **987**, 202-221, 2019.
8. E. Tabar, Turkish Journal of Physics, **41(2)**, 133-142, 2017.
9. E. Tabar and A. A. Kuliev, Nuclear Physics A, **964**, 1-17, 2017.
10. E. Tabar, H. Yakut and A. A. Kuliev, Nuclear Physics A, **979**, 143-164, 2018.
11. E. Tabar, H. Yakut and A. A. Kuliev, Nuclear Physics A, **981**, 130-146, 2019.
12. N. I. Pyatov and D. I. Salamov, Nucleonica **22**, 127, 1977.
13. N. Cakmak, S. Cakmak, C. Selam and S. Unlu, Pramana, **90 (2)**, 7, 2018.
14. E. Guliyev, A. A. Kuliev and H. Quliyev, AIP Conference Proceedings, **1815**, 060010, 2017.
15. E. Guliyev, A. A. Kuliev and M. Güner, Central European Journal of Physics, **8(6)**, 961-969, 2010.
16. A. Makinaga *et al.*, Physical Review C, **82**, 024314, 2010.
17. V. G. Soloviev, Theory of Complex Nuclei, Pergamon Press, 1976.
18. P. Moller *et al.*, Atomic Data and Nuclear Data Tables **59**, 185, 1995.
19. B. Pritychenko *et al.*, Atomic Data and Nuclear Data Tables **107**, 1-139, 2016.

BOOK OF FULL TEXT PROCEEDINGS TURKISH PHYSICAL
SOCIETY 35th INTERNATIONAL PHYSICS CONGRESS (TPS35)
TPS35, Vol.01, No.09, pp.524-531.
ISBN:978-605-83516-6-0 15 December 2019

Radon Exhalation Rate and Effective Radium Content of the Soil Samples Collected from Orhaneli District of Bursa,Turkey

Hakan Yakut[1,2 a)], Emre Tabar[1,2 b)] and Yunus Emre Yaşar[1, c)]

[1] *Sakarya University, Physics Department, Sakarya, Turkey*
[2] *Sakarya University,Biyomed. Manyet.&Yarıiletken Malz. Araş. ve Uyg. Merkezi, Sakarya, Turkey*

[a)] hyakut@sakarya.edu.tr
[b)] etabar@sakarya.edu.tr
[c)] *Corresponding author: yunusyasar56@hotmail.com*

Abstract. Exhalation briefly refers to radon escape from a material to the atmosphere. Radon gas produced by alpha-decay of ^{226}Ra in soil grains can escape from the soil grains by diffusion or recoil to the pores of soil, which is called emanation. The number of radon atoms released per unit surface area (or mass) per unit of time from a material is called the exhalation rate. This study aims to determine the radon exhalation rates in terms of mass and surface and the effective radium contents of soil samples collected from the study area via the sealed can technique and LR-115 Type II plastic track detectors. Compared to similar active experimental measurement methods, this technique is a cheaper and more efficient method in determining the radon exhalation rate and effective radium content of samples. Mass and surface radon exhalation rates in soil samples vary from 101.12 ±5.0 to 1132.75±16.8 mBq kg^{-1} h^{-1} with an average value of 620.49±12.5 mBq kg^{-1} h^{-1} and 1.63±0.6 to 22.97±2.4 Bq m^{-2} h^{-1} with an average value of 13.00±1.8 Bq m^{-2} h^{-1}, respectively. The effective radium content has been found to vary in the range 1.26±0.6-14.23±1.9 Bq kg^{-1} with an average value of 7.80±1.4 Bq kg^{-1}. The results obtained in this study will be compared with the data of similar studies in the literature and radiological evaluations will be made.

INTRODUCTION

Exposure to the background radiation from naturally occurring radionuclides is always a part of the human's life since the world exists. The estimated value of worldwide average annual exposure to the various components of natural radiation shows that the contribution of radon represents about 52 % of the total radiation dose [1,2].

^{222}Rn (radon) is a naturally occurring radioactive gas and is produced in the Earth's crust by the alpha-decay of ^{226}Ra which is a member of ^{238}U decay series [3,4]. Since the parent radionuclide, ^{226}Ra, occurs in trace amounts thorough out the earth, radon is present in both indoor and outdoor air. However, the radon concentration in soil may vary over a wide range depending on weather conditions, climatic factors and soil types [5].

Radon atoms transport within the soil, until they are undergoing radioactive decay or are released into the atmosphere. This is called as the exhalation process and the amount of activity of releasing radon per unit surface area per unit time is termed the radon exhalation rate. Radon exhalation depends on a number of variables such as the ^{226}Ra activity concentration and its distribution in soil, porosity, soil temperature, soil water saturation, atmospheric

Türk Fizik Derneği
1950
Turkish Physical Society

ISBN:978-605-83516-6-0

pressure, rainfall, geology of the area, surface wind, emanation coefficient and associated uranium mineralization [6-8]. The radon exhalation rate is one of the most important quantities for estimating local radon level, since the outdoor and indoor radon concentration mainly depends on the radon exhalation from surrounding soil [8]. Building material and tap water if it is supplied from groundwater in radium bearing aquifers also contribute towards the indoor radon concentration. However, several studies on the exhalation rate of ^{222}Rn from building materials and tap water show that these two sources normally contribute only a small fraction of the total amount of measured ^{222}Rn. Hence the underlying soil is usually the primary source of radon [8-10].

Over the past several years, investigations of radon exhalation rates from soil have received particular attention Worldwide [11-29] and also led to some surveys in Turkey [30,31]. However, no investigation has been carried out regarding radon exhalation from soil in Bursa. In this regard, an attempt has been made for the first time in Orhaneli district of Bursa in order to determine the radon exhalation rate (in terms of both mass and areal) in soil samples collected from different counties. In addition to the radon exhalation rates, the effective radium content of soil samples and the radon activity contributing to indoor air have been determined. The annual effective doses based on radon concentration contributing to indoor air have been also estimated to assess the health hazard due to ^{222}Rn in this region.

MATERIALS AND METHODS

Measurement Technique

The sealed can technique was used to measure radon exhalation rate, radon concentration and radium content of soil samples. The schematic diagram of the experimental set up is shown in Fig. 3. In such system, the exhalation rate depends on the amount of the sample as well as on the geometry and dimension of the Can. A total of 14 representative soil samples were collected by grab sampling from Orhaneli district of Bursa. In the laboratory, soil samples were pulverized, homogenized and sieved through 2 mm mesh. The samples were dried in an oven at a temperature of 80 ^{0}C for 24h to remove all the moisture content. 100 g of each sample was placed in a plastic cylindrical container (diameter 8.0 cm and height 10 cm) of volume 503 cm^{-3}. The mouth of the container was sealed with a cover and LR-115 type-II plastic track detectors (2 cm x 2 cm) was fixed at the top inner surface [32-34] (The containers were then sealed tightly with silicone to prevent the escape of radon and the detectors were exposed for a period of about 3 months . In order to obtain good statistics such period of time is needed for the accumulation of sufficient amount of nuclear tracks [34]. In this period the detectors recorded the tracks of α-particles emitted by radon gas produced through the decay of radium in the soil samples. After exposure, the detectors were retrieved and etched in 2.5 N NaOH solution at a temperature of 60±1 ^{0}C for 90 minutes in a constant temperature water bath for revelation of tracks. Then, the detectors were stand in distilled water for 20 minutes and dried with fresh air. Resulting alpha tracks on sensitive surface of the detectors were scanned under an optical microscope at a magnification of 400x to determine the track density per cm^2.

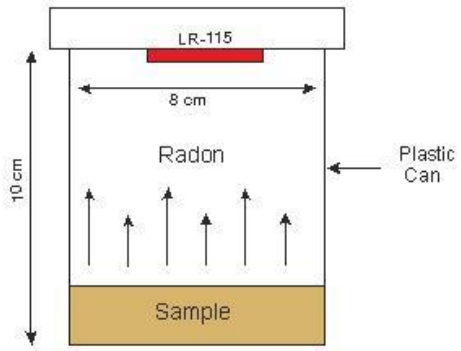


FIGURE 1. Experimental setup for measuring radon exhalation rate, radium content and radon concentration in soil samples.

ISBN:978-605-83516-6-0

The backgrounds of the detectors were determined by using unexposed films. The detectors calibrated with a radium standard in Turkish Atomic Energy Authority Çekmece Nuclear Research and Training Center (TAEK-CNAEM) and the calibration factor found to be 0.051 track.cm^{-2}.Bq^{-1}.m^3.d^{-1} [35]. After background correction, track densities were related to the radon concentrations (Bqm^{-3}) using the above calibration factor. After closing of the can, the radon activity in it is increased with time (*T*), according to the relation:

$$C_{Rn}\,(Bqm^{-3}) = \frac{\rho}{kT_e} \tag{1}$$

where ρ (*track cm*$^{-2}$) the track density, *k* (*track.cm*$^{-2}$*.h*$^{-1}$*. Bq*$^{-1}$*.m*$^{-3}$) is the calibration factor, T_e is effective exposure time in units hour (h). The detectors in cans record the ^{222}Rn concentration starting from zero activity to equilibrium activity. Therefore, it is needed to determine the effective exposure time [12]. The effective exposure time (T_e) is calculated using the following equation:

$$T_e = \left[T - \tau(1 - e^{-\lambda_{Rn}T})\right] \tag{2}$$

where λ_{Rn} is the decay constant of ^{222}Rn, τ is the average life of ^{222}Rn and ($\tau=1/\lambda_{Rn}$) and *T* refers to the total actual time of exposure. Once the radioactive equilibrium is established in sealed can, the alpha particles released from the radon can be used to determine the ^{226}Ra content (*Bqkg*$^{-1}$) of soil samples [36]. The radium concentration in soil samples was computed using the relation [23],

$$C_{Ra} = \frac{C_{Rn}hA}{M} \tag{3}$$

where *h* (c*m*) is the distance between soil sample and the detector, *A* (*cm*^{2}) is the area of cross section of the can and *M* (*kg*) refers to the mass of soil sample. Can technique can be also used to determine the radon exhalation rate from the soil using the following equations [37-39]:

$$E_M = \frac{C\lambda_{Rn}V}{T_eM} \tag{4}$$

$$E_S = \frac{C\lambda_{Rn}V}{T_eA} \tag{5}$$

here C is radon exposure as measured by Lr-115 solid state nuclear track detectors (Bqm^{-3}h), *V* (*cm*$^{-3}$) is the volume of the can. E_M and E_S refers to the radon exhalation rate in terms of mass and surface, respectively. The areal ^{222}Rn exhalation rate represents the radon gas that is released from the soil sample [34]. It should be noted that the radon exhalation rate is constant, whereas the radon concentration reaches a maximum value that depends on the exhalation rate.

For being a simple and low cost technique, the sealed can technique is widely used to determine radon exhalation rates. However, leakage and back diffusion may underestimate the true exhalation rate in can [39]. The sample is sealed inside the can for a long period. As the radon concentration around the sample grow, radon atom diffusing back to the material due to porous nature of the materials. As a result of this, the equilibrium radon concentration inside the can decreases. This phenomenon was known as back diffusion which causes an underestimate of true radon exhalation rate [39, 40]. On the other hand, due to its tightening, the leakage rate is neglected in can method [39]. It is well known that there is a satisfactory positive correlation between soil gas radon and indoor radon activities. Based on the radon exhalation rate of soil samples, the radon concentration in soil contributing to indoor radon can be calculated from the following formula [33,34,41]:

$$C_{Rn}^{ind.} = \frac{E_S S_r}{V_r \varphi} \tag{6}$$

here φ=0.5 h^{-1} is the air exchange rate. In these calculations, the room assuming to be a cavity with the ratio S_r/V_r=2 m^{-1}, where S_r and V_r are the internal surface area and volume of the room, respectively [34].

ISBN:978-605-83516-6-0

The radiation hazards due to radon can be estimated from the effective doses. Several methods have been reported to calculate the effective dose of radon received by a person in an environment. In the present paper the effective radiation doses due to radon and its products were calculated according to the ICRP 65 [42]. The exposure is defined simply as the product of the progeny concentration in air and the time a person has breathed in this air. Here, the progeny concentration is expressed in working level (WL) units instead of Bq m^{-3}. If a person is exposed for 170 h (1 month) to a 1 WL progeny concentration the exposure is 1 working level month (WLM) [43]. In order to calculate the annual Working Level Month (WLM), a method proposed by Nazaroff and Nero is used [41]:

$$(\mathrm{WLM})\mathrm{y}^{-1} = \frac{\mathrm{t.n.F.C_{Rn}^{ind.}}}{(170).(3700)} \tag{7}$$

where $C_{Rn}^{ind.}$ is the soil radon concentration indoor contributing to indoor radon activity (in Bqm^{-3}), t=8760 is number of hours per year, 1/3700 is a conversition factor (in WL/Bqm^{-3}), and 170 is the number of hours per month. While *n* refers to the fraction of time spending indoors (occupancy), *F* denotes an indoor equilibrium factor between radon and its decay products. The values of *n=0.8* and *F=0.4* were used [2]. The conversion factor of 6.3 mSv/WLM proposed by ICRP (1987) was used to estimate effective dose from radon [44].

RESULTS AND DISCUSSION

The effective radium content, mass and surface exhalation rates as well as the radon concentration contribute to indoor air in soil samples collected from the study region are shown in Fig. 2. The effective ^{226}Ra activity is found to vary from 1.26±0.6-14.23±1.9 Bq kg^{-1} with an mean value of 7.80±1.4 $Bq.kg^{-1}$. The mass and surface exhalation rates vary from 101.12 ±5.0 to 1132.75±16.8 mBq kg^{-1} h^{-1} and 1.63±0.6 to 22.97±2.4 Bq m^{-2} h^{-1} with an average value of 620.49±12.5 mBq kg^{-1} h^{-1} and 13.00±1.8 $mBqkg^{-1}h^{-1}$, respectively. The radon contribute to indoor air ranges from 6.53±1.3 to 91.88±4.8 Bqm^{-3} with an average value of 52.01±3.6 Bqm^{-3}. As may be seen in Fig. 2, maximum effective radium content, mass and surface exhalation rates and the radon concentration contribute to indoor air have been observed in the same soil sample (sample no:6). Also, the minimum effective radium content, mass and surface exhalation rates and the radon concentration contribute to indoor air have been recorded in the same soil sample (sample no:14).

As can be seen from Fig. 2, the results exhibit large variation. The variation in effective radium content may be due to the fact that uranium content in the earth crust is different at different locations. The results of other studies suggest that surface geology could be one of the influential factors for natural radioactivity [45]. The variation in mass and areal radon exhalation rates could be caused by many factors, such as differences in radium concentration in the samples, radium distribution within mineral grains of sample, the texture and size of the grains, and the permeability of the grains. Soil samples from different formations have different geometries and grain sizes.

The effective radium content, surface and mass radon exhalation rate in soil samples shows approximately similar distributions. Especially in the sample 6, the effective radium content, areal and mass radon exhalation rates levels are slightly higher. As can be seen from Figs. 2, It is noteworthy that the pattern of the effective radium content, areal and mass radon exhalation rate distributions around the sampling stations 5, 6, 7 and 9 are somewhat different from that around other stations.

ISBN:978-605-83516-6-0

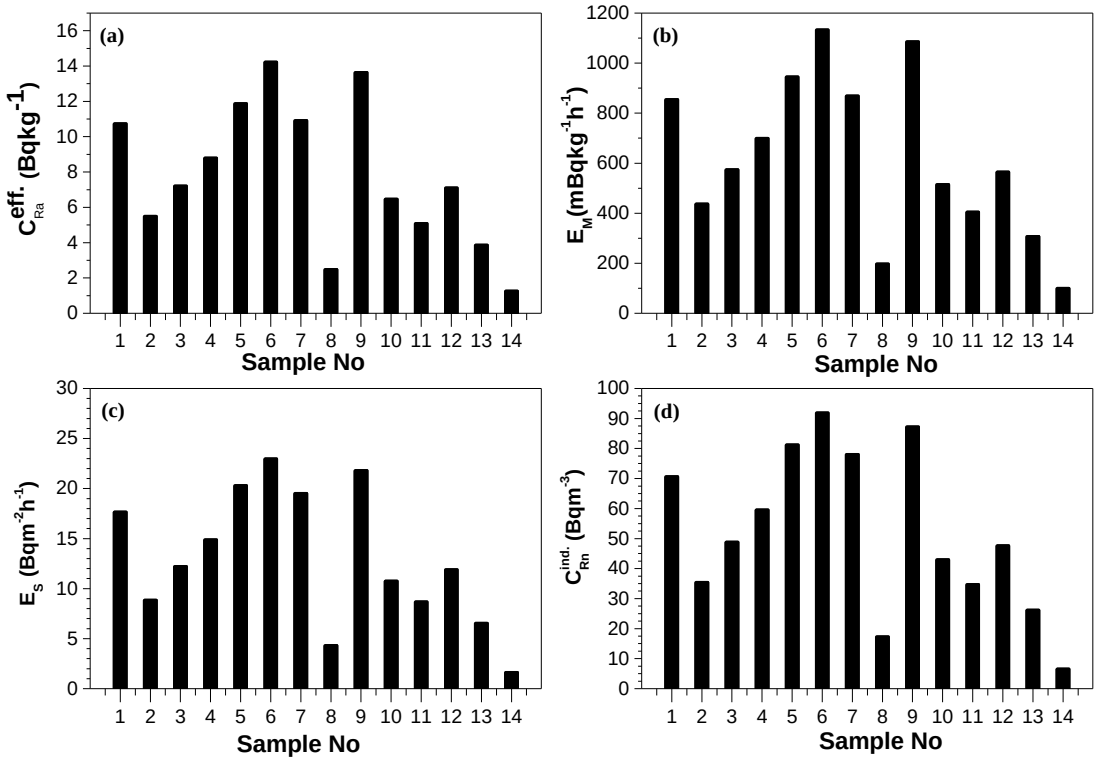


FIGURE 2. The results of effective radium content (a), mass exhalation rate (b), areal exhalation rate (c) and radon contribute to indoor air (d)

Considering the studies conducted in different countries it is obviously seen that the results obtained for effective radium content in Punjab area of India [47] and North and East Fault Systems in Turkey [30] are lower while the ones reported from India and Egypt are considerably higher than those measured in the present study (Table 1). However, the result of the effective radium content in present study is comparable with that of Libya [32] and Sakarya [31]. In Egypt, El-Zaher et al. reported mass radon exhalation rates of soil in the range of 3.14-233.70 mBqkg^{-1}h^{-1} [12] which are comparable to the results of the present study. However, the values of mass radon exhalation rate in are quite higher as compared to values of the other studies reported [12,17,19, 34, 47, 48, 30, 31] in Table 1.

ISBN:978-605-83516-6-0

TABLE 1. Comparison of the effective radium content, areal and mass radon exhalation rate values in soil samples from Bursa with those reported from different countries.

$C_{Ra}^{eff.}$ (Bqkg^{-1})	E_M (mBqkg^{-1}h^{-1})	E_S (Bqm^{-2}h^{-1})	Study, Country
1.5-25.3	1.16-19.13	0.031-0.507	Saad et al.(2013) [34], Libya
13.8-298.9	0.0039-0.082	-	Prasad et al.(2008) [19], India
5.72-157.99	8.31-233.70	0.48-15.37	El-Zaher (2013)[12], Egypt
5.70 - 25.45	7.17-31.98	0.246-1.100	Singh et al.(2005) [17], India
-	0.31-2.31	7.78-57.70	Singh et al.(2019) [28], India
7.01-55.26	0.014-0.112	0.361-2.890	Kumari et al. (2018) [29], India
45.6-226.1	10.0-50.0	0.27-1.33	Zubair and Shafiqullah (2018) [24], India
1.5-44.1	0.26-7.84	0.007-0.207	Thabayneh (2018) [25], Palestine
0.026-0.394	23.45-359.49	0.064-0.973	Kaliprasad et al. (2017) [26] India
18-33	135-251	4.58-8.40	Farid (2016) [27], SaudiArabia
1.39-5.31	1.62-6.55	0.053-0.217	Kumar and Narang (2014) [47], Punjab-India
10.54-49.67	-	0.502-2.063	Kakati et al.(2013) [48], Assam-India
0.02-0.80	-	0.0013-0.4	Baykara et al.(2005) [30], North and East Fault Systems, Turkey
3.77 - 26.69	35.76 - 253.15	0.73 - 5.18	Sakarya-Turkey [31]
1.26 – 14.23	101.12 -1132.75	1.63 – 22.97	This study, Bursa-Turkey

The result of the present study regarding the areal radon exhalation rates are higher than those reported for India, Pakistan and Turkey. On the other hand, it is important to state that the mean areal radon exhalation rates observed in the present study are well below the world average of 57.6 Bqm^{-2} h^{-1} [2] and hence do not pose any health hazards to the residents.

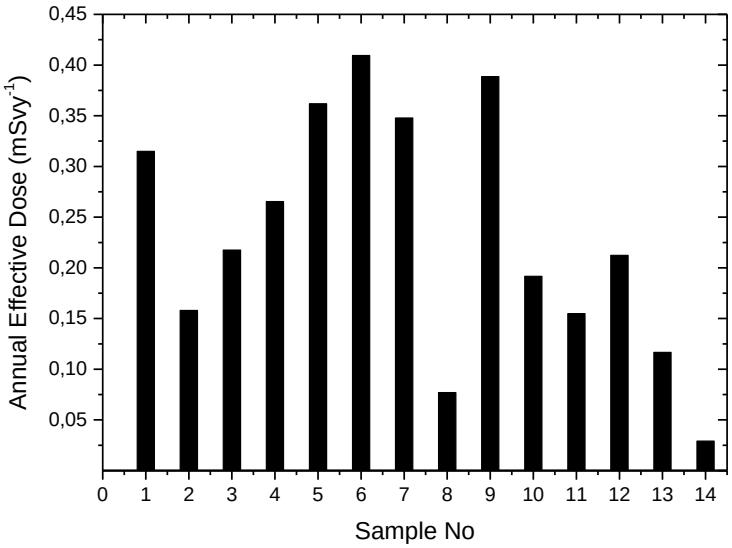


FIGURE 3. The calculated values of the annual effective dose equivalents in indoor air

In order to estimate the annual effective doses in indoor air, the contribution of radon from soil to indoor radon determined by using the measured areal radon exhalation rates have been used. Calculated values of the annual effective dose equivalents are presented in Fig 10 which varies from 0.09 to 0.61 mSvy^{-1} with an average value of 0.27 mSvy^{-1}. In all the areas surveyed, the estimated annual effective dose is less than the lower limit of the recommended action level (3–10 mSvy^{-1}) [42].

The effective radium content, areal and mass radon exhalation rates and their distribution have been determined by using closing can technique for the 23 soil samples collected from Orhaneli district of Bursa. The radiation hazards due to radon and its daughters can be calculated from the radon exhalation rate of soil samples. To do this the contribution of indoor radon concentration from soil has been computed directly from the measures areal radon exhalation rates. From the evaluation of the data presented in the current study, the following knowledge is acquired:

- The results show that the effective radium content, areal and mass radon exhalation rates vary significantly among samples.
- Statistical calculations on the effective radium content, areal and mass radon exhalation rates, and radon activity contribute to indoor air values give normal distributions.
- The results for the effective radium content, areal and mass radon exhalation rates presented in this paper are generally comparable to the values from different countries.
- To the best of our knowledge, this is the first study in which the effective radium content, areal and mass radon exhalation rates in soils of studying region have been determined.

REFERENCES

[1] S.B. Sundar, N. Chitra, I. Vijayalakshmi, B. Danalakshmi, S. Chandrasekaran, M.T. Jose, B. Venkatraman, Radiat. Prot. Dos. 164(4), 569–574 (2015).
[2] United Nations Scientific Committee on the Effects of Atomic Radiation Sources and effects of ionizing radiation, UNSCEAR 2000 Report, United Nations Publication, 2000.
[3] R. Catalano, G. Imme, G. Mangano, D. Morelli, M. Aranzulla, S. Giammanco, L.Thinova, J. Radioanal. Nucl. Chem. 306, 673–684 (2015).
[4] M. Faheem, Matiullah. Radiat. Meas. 43, 1458–1462 (2008).
[5] T. Nasir, N. Ahmad, J. Basic & Appl. Sci. 8, 430-436 (2012).
[6] G. Prasad, T. Ishikawa, M. Hosoda, A. Sorimachi, S.K. Sahoo, N. Kavasi, S. Tokonami, M. Sugino, S. Uchida, J. Radioanal. Nucl. Chem. 292, 1385–1390 (2012).
[7] B.M. Moharram, M.N. Suliman, N.F. Zahran, S.E. Shennawy, A.R. El Sayed, Ann. Nucl. Energy 45, 138–143 (2012).
[8] S. Rahman, Matiullah, B. Ghauri, Radiat. Prot. Dos. 130(2), 172–177 (2008).
[9] S. Rehman, Matiullah, S. Rehman, S. Rahman, Radiat. Meas. 41, 708–713 (2006).
[10] A.L. Kerry, Health Phys. 43(1), 65-71 (1982).
[11] S. Kumar, S. Singh, B.S. Bajwa, A.D. Sabharwal, Isot. Environ. Health S 47(4), 446-455 (2011).
[12] M.A. El-Zaher, Radiat. Prot. Dosim. 154(4), 490-496 (2013).
[13] D. Verma, M.S. Khan, M. Zubair, J. Radioanal. Nucl. Chem. 294, 267–270 (2012).
[14] S.R. Matiullah, B. Ghauri, Radiat. Prot. Dosim. 130(2), 172–177 (2008).
[15] G. Prasad, T. Ishikawa, M. Hosoda, A. Sorimachi, S.K. Sahoo, N. Kavasi, S.Tokonami, M. Sugino, S. Uchida, J. Radioanal. Nucl. Chem. 292, 1385–1390 (2012).
[16] M. Zubair, M.S. Khan, D. Verma, Iran. J. Radiat. Res. 10(2), 83-87 (2012).
[17] S. Singh, M. Kumar, M.R. Kumar, Radiat. Meas. 39, 535–542 (2005).
[18] M. Rafique, S. Rahman, T. Mahmood, S. Rahman, Matiullah, S. Rehman, Russian Geology and Geophys 52, 450–457 (2011).
[19] Y. Prasad, G. Prasad, G.S. Gusain, V.M . Choubey, R.C. Ramola, Radiat. Meas. 43, 369–374 (2008).
[20] M. Hosoda, A. Sorimachi, Y. Yasuoka, T. Ishikawa, S.K. Sahoo, M. Furukawa, N.M. Hassan, S. Tokonami, S. Uchida, J. Radiat. Res. 50, 333–343 (2009).
[21] D. Mazur, M. Janik, J. Loskiewicz, P. Olko, J. Swakon, Radiat. Meas. 31, 295–300 (1999).
[22] R.C. Ramola, V.M. Choubey, J. Radioanal. Nucl. Chem. 256, 219–223 (2003).
[23] D.K. Sharma, A. Kumar, M. Kumar, S. Singh, Radiat. Meas. 36, 363–366 (2003).
[24] M. Zubair and Shafiqullah, Radon Exhalation Rate Study of Sand Samples Collected from Sea Coast of Tirur, Kerala, India Using Track Etch Technique, MAPAN-Journal of Metrology Society of India (2018) 33(4):441–448, https://doi.org/10.1007/s12647-018-0268-2.

[25] K. M. Thabayneh, Determination of radon exhalation rates in soil samples using sealed can technique and CR-39 detectors, Journal of Environmental Health Science and Engineering, https://doi.org/10.1007/s40201-018-0298-2 (2018).
[26] CS Kaliprasad, PR Vinutha and Y Narayana ,Natural Radionuclides and Radon Exhalation Rate in the Soils of Cauvery River Basin, Air, Soil and Water Researc,hVolume 10: 1–7 (2017).
[27] S.M. Farid, Indoor radon in dwellings of Jeddah city, Saudi Arabia and its correlations with the radium and radon exhalation rates from soil ,Indoor and Built Environment, 2016, Vol. 25(1) 269–278.
[28] L.M. Singh et al., Measurement of radon exhalation rate using solid state nuclear track detector,AIP Conference Proceedings 2142, 120009 (2019); https://doi.org/10.1063/1.5122505
[29] P. Kumari et al., Radon exhalation rates in the soil samples of Dharamshala region of Himachal Pradesh NW Himalaya, India and their comparison with developing a theoretical model, AIP Conference Proceedings 2050, 020016 (2018); https://doi.org/10.1063/1.5083603
[30] O. Baykara, M. Doğru, M. Inceoz, E. Aksoy, Radiat. Meas. 39, 209–212 (2005).
[31] Emre Tabar, Hakan Yakut and Adem Kuş, Measurement of the radon exhalation rate and effective radium concentration in soil samples of southern Sakarya, Turkey, INDOOR AND BUILT ENVIRONMENT, 27, 2, 278–288, FEB 2018 (DOI: 10.1177/1420326X16672510)
[32] F. Abu-Jarad, J.H. Fremlin, R. Bull, Phys. Med. Biol. 25, 483–694 (1980).
[33] A.K. Mahur, R. Kumar, D. Sengupta, R. Prasad, Appl. Radiat. Isot. 66 (3), 401–406 (2008).
[34] A.F. Saad, R.M. Abdallah, N.A. Hussein, Appl. Radiat. Isotopes 72, 163–168 (2013).
[35] H. Yakut, E. Tabar, E. Yıldırım, Z. Zenginerler, F. Ertugral, N. Demirci, Radiat. Prot. Dosim. DOI 10.1093/rpd/NCW009 (*accepted*)
[36] G. Somogyi, ATOMKI Preprint E/25 (1986).
[37] R. Kumar, A.K. Mahur, N.S. Rao, D. Sengupta, R. Prasad, Radiat. Meas. 43, S508–S511 (2008).
[38] H. Singh, J. Singh, S. Singh, B.S. Bajwa, Radiat. Meas. 43, 459–462 (2008).
[39] M. J. Abo-Elmagd, Radiat. Res. Appl. Sci. 7, 390-398 (2014).
[40] B.K. Sahoo, Y.S. Mayya, Agric. Forest Meteo. 150, 1211-1224 (2010).
[41] W.W. Nazaroff, A.V. Nero, *Radon and its Decay Products in Indoor Air*. A Wiley-Interscience Publication, New York, 1988.
[42] International Commission on Radiological Protection (ICRP) 65, New York (1993)
[43] R.M. Amin, M.F. Eissa, Environ. Monit. Assess. 143, 59–65 (2008).
[44] International Commission on Radiological Protection (ICRP) 50, 17, New York (1987).
[45] A.A.M. Abadi, M. Rahimi, L.J. Koopaei, J. Radioanal. Nucl. Chem. DOI 10.1007/s10967-015-4581-8 (2015).
[46] TAEK (Turkish Atomic Energy Authority), *Türkiye Çevresel Radyoaktivite Atlası* (in Turkish). http://www.taek.gov.tr/radyasyon-izleme/turkiye-çevresel-radyasyon-atlasi.html (Accessed 31 Jan 2014).
[47] A. Kumar, S. Narang, Inter. J. Educ. Appl. Res. 4, 23-25 (2014).
[48] R.Kr. Kakati, L. Kakati, T.V. Ramachandran, APCBEE Procedia 5, 186-191 (2013).

BOOK OF FULL TEXT PROCEEDINGS TURKISH PHYSICAL
SOCIETY 35th INTERNATIONAL PHYSICS CONGRESS (TPS35)
TPS35, Vol.01, No.09, pp.532-538.
ISBN:978-605-83516-6-0 15 December 2019

The Investigation of the Giant Dipole Resonance (GDR) Characteristics for ^{141}Pr Nucleus*

H. YAKUT[1,2], E. TABAR[1,2] and E. KEMAH[1,2]

[1]Physics Department, Sakarya University, 54187 Sakarya, Turkey
[2]Biomedical, magnetic and semiconductor materials research center (BIMAYAM), Sakarya University, 54187 Sakarya, Turkey

Abstract Electric dipole (*E*1) response of ^{141}Pr nucleus in 8-20 MeV energy range, so-called Giant Dipole Resonance (GDR), is studied within the microscopic Translational Galilean Invariant Quasiparticle Phonon Nuclear Model (TGI-QPNM) which includes a Woods-Saxon potential as a mean field, an isovector dipole interaction term and the restoration forces as well. The TGI-QPNM calculations reveal several collective states in this energy region, whose wave function are dominated by quasiparticle⊗one-phonon components. The fragmentation of the $B(E1)$ strength is also influenced by quasiparticle⊗one-phonon admixtures. A fairly good agreement between the TGI-QPNM results of the photoabsorption cross-section folded using the Lorentz weight function with the experimental one in the energy range from 8 to 20 MeV is obtained. Besides, TGI-QPNM calculations well reproduce the cross section (σ_0) and its minus-first (σ_{-1}) and minus-second (σ_{-2}) moments determined in the experiment.

Keywords: *TGI-QPNM, E1, ^{141}Pr, GDR*

*This work was supported by the Scientific and Technological Research Council of Turkey (TUBITAK) (Project No.118F094).

INTRODUCTION

The history of the giant dipole resonances (GDR) in atomic nuclei started in 1947 when Baldwin and Klaibber observed high-energy excitations in their experimental study. In 1948 Goldhaber and Teller described this observation as nuclear vibrations of protons against to neutrons. Today GDR is known to be universal phenomena for all nuclei in the periodic table [1].

To the best of author's knowledge, up to now, there has been no theoretical study on the GDR mode in ^{141}Pr, although the experimental photoneutron cross section data for this nucleus have been available for a long time [2]. Therefore, the present study aims to investigate theoretically the *E*1 strength distribution in the GDR region in odd-proton ^{141}Pr nucleus. The theoretical model in this study is the Quasiparticle Phonon Nuclear Model (QPNM), which is a powerful tool to explain the collective dipole modes observed in odd-mass deformed nuclei [3]. The broken Translation and Galileo symmetry of the QPNM Hamiltonian, violated due to the mean-field approach, has been restored by using the Pyatov prescription [4]. The *E*1 excitations in both spherical [5] and deformed [6] even-even nuclei were successfully investigated in the frame work of the Pyatov's method before.

^{141}Pr is located N=82 shell closure and its core is stable. Therefore, it is assumed to be spherical from a theoretical point of view. However, because of its proton number, it has a small deformation and may be studied in a deformed basis as well. In a recent work of *Yakut et al.* [7] magnetic moments of the odd-mass Ce isotopes, which are generally studied in the spherical basis, have been investigated in the framework of QPNM, including a deformed Woods-Saxon potential as a mean field, and a satisfactory description of the experimental data have been obtained. Besides, the fine structure and gross features of the scissors mode in the even-even Ce isotopes have been successfully reproduced by *Kuliev et al.* [8] using a deformed basis in their QRPA formalism.

THEORY

The TGI-QRPA Hamiltonian for an odd-proton nucleus can be written as follows:

$$H = H_{sqp} + W_1 + h_0 + h_\Delta \tag{1}$$

Türk Fizik Derneği
1950
Turkish Physical Society

ISBN:978-605-83516-6-0

$$H_{sqp} = \sum_{q,\tau} \varepsilon_q(\tau) B_{qq}(\tau) \tag{2}$$

The H_{sqp} term is the single quasiparticle Hamiltonian including deformed Woods-Saxon potential as mean a field, and

$$W_1 = \frac{3}{2\pi} \chi_1 \left(\frac{NZ}{A} \right)^2 \left(\vec{R}_N - \vec{R}_Z \right)^2 \tag{3}$$

is the isovector part of the dipole-dipole (λ=1) interaction where χ_1 is the strength of it. In Eq. (2) ε_q represent the one-quasiparticle energies, where $\alpha^+(\alpha)$ are the quasiparticle creation (annihilation) operators. $R\mu$ are the center of mass (c.m.) coordinate vectors of the nucleons.

h_0 and h_Δ in the Hamiltonian (1) are the restoring forces chosen according to Pyatov's method in the following form [4]:

$$h_0 = -\frac{1}{2\gamma} \sum_\mu \left[H_{sqp}, P_\mu \right]^+ \left[H_{sqp}, P_\mu \right] \quad \text{and} \quad h_\Delta = -\frac{1}{2\beta} \sum_\mu \left[U_\Delta, R_\mu \right]^+ \left[U_\Delta, R_\mu \right] \tag{4}$$

where U_Δ is the pairing potential, P_μ is the linear momentum operator of the nucleus, R_μ is the center of mass (c.m.) coordinate vector of the nucleons in the quasiparticle-phonon representation, and

$$\gamma_\mu = \left\langle \psi_0 \left| \left[P_\mu^+, \left[H_{sqp}, P_\mu^+ \right] \right] \right| \psi_0 \right\rangle \quad \text{and} \quad \beta_\mu = \left\langle \psi_0 \left| \left[R_\mu^+, \left[U_{\Delta.}, R_\mu^+ \right] \right] \right| \psi_0 \right\rangle \tag{5}$$

are the strength of h_0 and h_Δ residual forces, respectively.

The wave function of the odd-mass deformed nuclei can be written in the following form

$$\psi_K^j(\tau) = \left\{ N_K^j(\tau) \alpha_K^+(\tau) + \sum_{i\mu} \sum_\nu G_j^{i\mu\nu} \alpha_\nu^+(\tau) Q_{i\mu}^+ \right\} \left| \psi_0 \right\rangle \qquad \mu = 0, \pm 1 \tag{6}$$

with the normalization condition,

$$\left\langle \psi_K^j(\tau) \middle| \psi_K^j(\tau) \right\rangle = \left(N_K^j \right)^2 + \sum_{i\mu} \sum_\nu \left(G_j^{i\mu\nu} \right)^2 = 1 \tag{7}$$

The one quasiparticle and the quasiparticle⊗phonon amplitudes of the wave function are defined by N_K^j and $G_j^{i\mu\nu}$, respectively. By using the variation principle, i.e.,

$$\delta \left\{ \left\langle \psi_K^j(\tau) \middle| H \middle| \psi_K^j(\tau) \right\rangle - \left\langle \psi_{K_0}(\tau) \middle| H \middle| \psi_{K_0}(\tau) \right\rangle - \eta_K \left[\left(N_K^j \right)^2 + \sum_{i\nu} \left(G_{ij}^{K\nu} \right)^2 - 1 \right] \right\} = 0 \tag{8}$$

the secular equation, giving the energies (η_K) of the odd-mass nucleus under investigation, can be obtained as follows:

ISBN:978-605-83516-6-0

$$P\left(\eta_K\right)\equiv\varepsilon_\varsigma-\eta_K-\sum_{i\mu}\sum_{\nu}\frac{\left(-\kappa_1\frac{2}{N}r^p_{\varsigma_q\nu}V_{\varsigma_q\nu}\overline{L_i}-\varepsilon^{(-)}_{\varsigma_q\nu}p^p_{\varsigma_q\nu}M_{\varsigma_q\nu}+\Delta_n r^p_{\varsigma_q\nu}L_{\varsigma_q\nu}L_i\right)^2}{4\omega_i Y\left(\omega_i\right)\left(\omega_i+\varepsilon_\nu-\eta_K\right)}=0 \qquad (9)$$

where

$$L_i=\frac{\gamma}{\beta}\frac{\sum_\tau\Delta_\tau\sum_{qq'}r_{qq'}M_{qq'}w^i_{qq'}}{\sum_\tau\sum_{qq'}\varepsilon_{qq'}p_{qq'}L_{qq'}g^i_{qq'}} \qquad \overline{L_i}=\gamma\frac{\sum_\tau\frac{1}{N_\tau}\sum_{qq'}r_{qq'}U_{qq'}g^i_{qq'}}{\sum_\tau\sum_{qq'}\varepsilon_{qq'}p_{qq'}L_{qq'}g^i_{qq'}} \qquad (10)$$

Here, $p^\mu_{qq'}=\langle q|p_\mu|q'\rangle$ and $r^\mu_{qq'}=\langle q|r_\mu|q'\rangle$ are the single particle matrix elements of the linear momentum and core mass center position operator, respectively. The Bogolyubov canonical transformation parameters (u_q and v_q) are also expressed in $V_{qq'}=u_qu_{q'}-v_qv_{q'}$, $U_{qq'}=u_qv_{q'}+u_{q'}v_q$, $L_{qq'}=u_qv_{q'}-u_{q'}v_q$ and $M_{qq'}=u_qu_{q'}-v_{q'}v_q$,respectively. $\psi^i_{qq'}$ and $\varphi^i_{qq'}$ terms are two quasiparticle amplitudes of the even-even core and given in the $g^i_{qq'}=\psi^i_{qq'}+\varphi^i_{qq'}$ and $w^i_{qq'}=\psi^i_{qq'}-\varphi^i_{qq'}$. Finally, the $Y(\omega_i)$ term is obtained from the normalization condition of the wave function of the core nucleus. $\varepsilon_{qq',\tau}=\varepsilon_q+\varepsilon_{q'}$ and $\varepsilon^-_{qq',\tau}=\varepsilon_q-\varepsilon_{q'}$ are terms of the two quasiparticle energies.

$$\left(N^j_K\right)^{-2}=1+\sum_{i\mu}\sum_{\nu}\left(\frac{-4\kappa_1\frac{1}{Z}r^p_{\varsigma_q\nu}V_{\varsigma_q\nu}\overline{L_i}-2\varepsilon^{(-)}_{\varsigma_q\nu}p^p_{\varsigma_q\nu}M_{\varsigma_q\nu}+2\Delta_n r^p_{\varsigma_q\nu}L_{\varsigma_q\nu}L_i}{4\omega_i Y\left(\omega_i\right)\left(\omega_i+\varepsilon_\nu-\eta_K\right)}\right)^2 \qquad (11)$$

$$G^{i\mu\nu}_j=-N^j_\varsigma\left\{\frac{-4\kappa_1\frac{1}{N}r^p_{\varsigma_q\nu}V_{\varsigma_q\nu}\overline{L_i}-2\varepsilon^{(-)}_{\varsigma_q\nu}p^p_{\varsigma_q\nu}M_{\varsigma_q\nu}+2\Delta_n r^p_{\varsigma_q\nu}L_{\varsigma_q\nu}L_i}{\sqrt{4\omega_i Y\left(\omega_i\right)}\left(\omega_i+\varepsilon_\nu-\eta_K\right)}\right\} \qquad (12)$$

The formula for the reduced probabilities of $E1$ transitions from the ground-states to the excited-states of odd-mass deformed nuclei can be written in the form:

$$B(E1,I_iK_i\to I_fK_f)=\sum_\mu\langle I_i1K_i\mu|I_fK_f\rangle^2\left|-\frac{1}{2}e^n_{eff.}\sum_q N^j_{\varsigma_q}N^j_{\varsigma_q\varsigma_{q_0}}r^\tau_{\varsigma_q\varsigma_{q_0}}V_{\varsigma_q\varsigma_{q_0}}+N^j_{\varsigma_{q_0}}\sum_{i\mu}G^{i\mu\varsigma_{q_0}}_j\frac{\kappa_1(1-L_i)}{\sqrt{\omega_iY(\omega_i)}}\left[e^{eff.}_n\frac{F_n}{N}-e^{eff.}_p\frac{F_p}{Z}\right]\right|^2 \qquad (13)$$

where

$$\mathrm{F}_\tau(\omega_i)=\sum_{qq'\tau}\frac{r^2_{qq'}\varepsilon_{qq'}u^2_{qq'}}{\varepsilon^2_{qq'}-\omega^2_i} \qquad (14)$$

ISBN:978-605-83516-6-0

The neutron and proton effective charges are $e_n^{eff} = -\frac{Z}{A}$ and $e_p^{eff} = \frac{N}{A}$, respectively. The dipole fotoabsorption cross-section of the odd mass deformed nuclei can be expressed in terms of the strength function [9]:

$$\sigma_{E_1}(E) = \frac{16\pi^3 e^2}{9\hbar c} E S_{E_1}(E) \tag{15}$$

The strength function with a Lorentzian weight is given by the formula [9].

$$S_{E_1}(E) = b(E_1,\eta) = \frac{1}{2\pi}\sum_i \frac{\Delta}{(\eta_i-\eta)^2 + \left(\frac{1}{2}\Delta\right)^2} B\left(E_1; I_i K_i \to I_f K_f\right) \tag{16}$$

RESULTS

In this work, numerical calculations have been performed for odd-proton ^{141}Pr nucleus. The method used in this work is based on the TGI-QRPA phonons of even-even core, ^{140}Ce. By using an axially symmetric Woods-Saxon code, the single-particle energies and wave functions were determined for both neutron and proton states [10]. The quadrupole deformation parameter (β_2) has been derived from the experimental quadrupole moment (Q_2) [11] value has been used in these calculations. The strength parameter of the isovector dipole-dipole interaction is chosen to be $\chi_1 = 300A^{-5/3}$ MeVfm^{-2} based on the previous calculations [4]. In Table 1 physical quantities used in the present calculations has been summarized.

TABLE 1. Pairing gaps (Δ), chemical potentials (λ) for both netron and protons, β_2 and δ_2 deformation parameters, and the ground-state Nilsson configuration of ^{141}Pr

[Nn$_z$ Λ]Σ	Δ_n [MeV]	Δ_p [MeV]	λ_n [MeV]	λ_p [MeV]	β_2	δ_2
[413]↓	1.218	1.297	-7.695	-7.262	0.1018(25)	0.151

The theoretical photoabsorption cross-section values of ^{141}Pr have been calculated using the TGI-QPNM method in the energy range from 8 to 20 MeV. Figure 1. is a comparison of the TGI-QPNM predictions for theoretical photoabsorption cross sections and the experimental data of Beljaev et al. (1991) in this energy range.

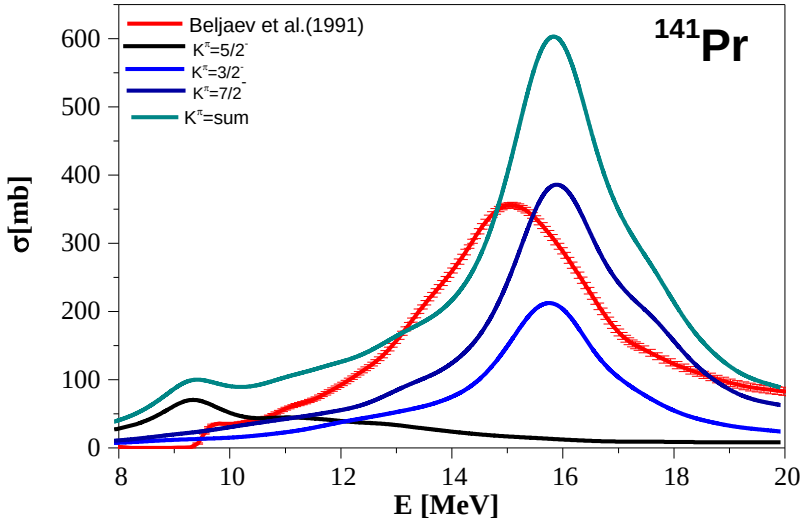


FIGURE 1. Comparison of the theoretical photoabsorption cross sections predicted in TGI-QPNM with the experimental data in the energy range 8-20 MeV for ^{141}Pr.

ISBN:978-605-83516-6-0

As seen from Figure 1. the trend of the TGI-QPNM values and experimental data are quite similar. But, theoretical spectrum has approximately two times larger than the experimental one. This may be related to the energy loss due to using of bremsstrahlung as the photon source in the experiment and the inaccurate calibration of the neutron detector [12].

The experimental spectrum of ^{141}Pr nucleus has a single-humped shape which is agree with TGI-QPNM predictions. As seen from the spectral peaks, TGI- QPNM approximations can be defined fairly well by Lorentzian shape. The position of the single-peak is also well reproduced in the theory. Besides, there are good agreement between the theoretical and experimental values of the resonance width and energy. The width of the experimental resonance equals to 7-7.5 MeV and the TGI- QPNM predictions is 7.9 MeV. The resonance energy of experiment and theory is 15.4 and 15.9, respectively.

In Table 2, the theoretical and the experimental datas of the integrated ^{141}Pr (γ, xn) cross sections and their minus-first and minus-second moments have been listed. As seen from the Table 2, there is a satisfactory agreement between the experimental and theoretical results.

TABLE 2. Comparison of the theoretical and experimental integrated ^{141}Pr (γ, xn) cross sections and their minus-first and minus-second moments

^{141}Pr	σ_0 **(bMeV)**	σ_{-1} **(mb)**	σ_{-2} **(mb/MeV)**
Experimental[13]	2.20 ± 0.3	141 ± 12	9.4 ± 0.7
Experimental[14]	2.51 ± 0.5	158 ± 30	10.4 ± 2
Theoretical	2.965	203.19	14.512

The distribution of the $E1$ strength calculated in the framework of TGI-QPNM for odd proton ^{141}Pr nucleus in the energy range 8-20 MeV is given in Figure 2. Although the experimental data for the fine structure of the $E1$ strength at the energies below 8 MeV is available for ^{141}Pr [15], there have not been yet any experimental data on the fine structure of E1 transitions in the higher energy regions of ^{141}Pr nucleus. Therefore, for the sake of comparison the distribution of $E1$ strength in the core nucleus (^{140}Ce) has been also illustrated in Figure 2. This comparison implies a strong fragmentation of the E1 strength in odd-mass nucleus with respect to even-even core. The strong fragmentation in $E1$ spectra of odd-mass nucleus is due to the coupling features of the $E1$ operator. On one hand, the ΔK=1 component of the $E1$ operator couples the (I_0, K_0) ground state to the excited-states with quantum numbers (I_0-1, K_0-1), (I_0, K_0-1), (I_0+1, K_0-1) and (I_0+1, K_0+1) thus distributing the strength of each $E1$ transition in core nucleus among four $E1$ levels in the odd-mass nucleus. On the other hand, the ΔK=0 component of the $E1$ operator couples the (I_0, K_0) ground state to the excited-states with quantum numbers (I_0, K_0) and (I_0+1, K_0) thus distributing the strength of each $E1$ transition in core nucleus among two $E1$ levels in the odd-mass nucleus [16].

ISBN:978-605-83516-6-0

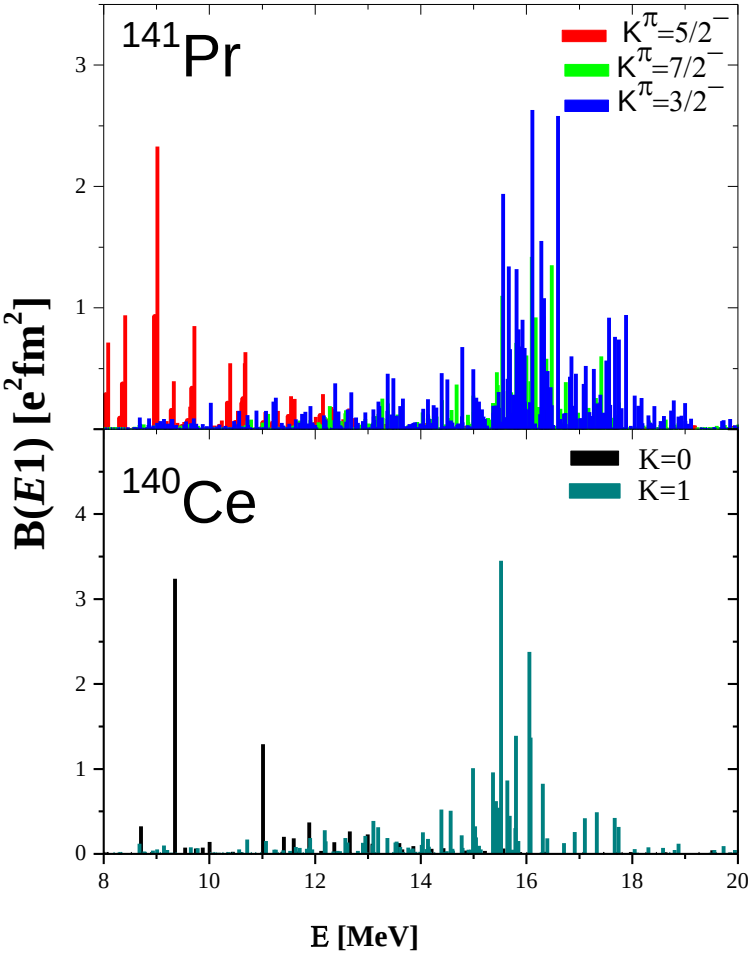


FIGURE 2. A comparison of theoretical $B(E1)$ values for ^{140}Ce and ^{141}Pr.

Figure 2 shows that ΔK=1 and ΔK=0 $E1$ transitions lie 8-10 MeV and 9-18 MeV, respectively in ^{141}Pr and the contribution of ΔK=0 branch to the summed strength is significantly lower than the ΔK =1 one.

Conclusion

We have investigated the GDR in odd proton ^{141}Pr using the TGI-QPNM methods. This method allows us to restore the broken symmetry of the Hamiltonian. The calculated integrated cross sections and their minus-first and minus-second moments by means of this theory agree well with the corresponding experimental data.

ACKNOWLEDGEMENTS

We are grateful to Prof A.A. Kuliev and Assoc Prof H. Yakut for their valuable comments. This research was supported by the Scientific and Technological Research Council of Turkey (TUBITAK) (Project No.118F094).

REFERENCES

1. H.Überall, Electron Scattering from Complex Nuclei, Part B, Academic Press, Newyork and London(1971),p.698.
2. S.N.Belyaev, V.A.Semenov, Izv.Akad.Nauk SSSR, Ser.Fiz. 55, 953 (1991); Bull.Acad.Sci.USSR, Phys.Ser. 55, No.5, 66 (1991).

ISBN:978-605-83516-6-0

3. E. Tabar, H. Yakut and A. A. Kuliev, Nuclear Physics A, 981, 130-146, 2019M.Arnould,S.Goriely,and K.Takahaski,Phy.Rep.450,97(2007).
4. N I Pyatov and D I Salamov, Nucleonica 22, 127(1977).
5. Necla Cakmak, Sadiye Cakmak, Cevad Selam and Serdar Unlu, Pramana – J. Phys. (2018) 90:15
6. E. Guliyev, A. A. Kuliev and M. Güner, Central European Journal of Physics, 8(6), 961-969, 2010.
7. H. Yakut, E. Tabar, G. Hoşgör, Canadian Journal of Physics, article in press,pp.1-8(2019)
8. A.A. Kuliev, E. Guliyev, and M. Gercekliogl u. J. Phys. G, 28, 407 (2002).
9. Ring P., Shuck P., The Nuclear Many Body Problem, (Printed in the United Statet of America, 2004), pp. 147-640.
10. J. Dudek, T. Werner, J. Phys. G, Nucl. Part. Phys. 4, 1453 (1978).
11. B. Pritychenko, M. Birch, B. Singh, M. Horoi, Tables of E2 transition probabilities from the first 2+ states in even–even nuclei, Atomic Data and Nuclear Data Tables,107(2016),pp.1-39.
12. R. L. Bramblett, J. T. Caldwell, B. L. Berman, R. R. Harvey, And S. C. Fultz, Physical Review,Vol.148,No.3,pp.1198-1205(1966)
13. R. Bergere, H. Beil and A. Veyssiere, Nucl. Phys. Al21 (1968),pp. 463.
14. T. K. Deague and R. J. J. Stewart, Nuclear Physics A191 (1972) 305-320.
15. M. Scheck, P. von Brentano, C. Fransen, U. Kneissl, C. Kohstall, A. Linnemann, D. M¨ucher, N. Pietralla, H. H. Pitz,C. Scholl, F. Stedile, S. Walter,V. Werner,and S. W. Yates, Physical Review C 75, 044313 (2007).
16. V.G. Soloviev et al, Nuclear Physics A 613,45 (1997).

10. Statistical Physics



BOOK OF FULL TEXT PROCEEDINGS TURKISH PHYSICAL
SOCIETY 35th INTERNATIONAL PHYSICS CONGRESS (TPS35)
TPS35, Vol.01, No.10, pp.540-546.
ISBN:978-605-83516-6-0 15 December 2019

Phase Diagrams of Generalized Spin-S Magnetic Binary Alloys

Gülşen Karakoyun[1, a)] and Ümit Akıncı[2, b)]

[1] *Dokuz Eylül University, The Graduate School of Natural and Applied Sciences, Nanoscience and Nanoengineering Department, Izmir, Turkey.*
[2] *Dokuz Eylül University, Faculty of Science, Physics Department, Buca, 35390 Izmir, Turkey*

[a)]*Corresponding author: umit.akinci@deu.edu.tr*
[b)]*gulsen.karakoyun@ogr.deu.edu.tr*

Abstract. The critical behavior of the generalized spin-S binary alloy represented by the formula A_cB_{1-c} has been investigated within the framework of effective field approximation. The binary magnetic alloy system consists of type A (spin-S) and type B (spin-S) atoms which are randomly distributed on a regular lattice. Both integer and half integer spin models of two atomic types are examined. The evolution of the phase diagrams is obtained for integer-integer, integer-half integer and half integer-integer spin values of the binary alloy. Order and disorder phase boundaries are presented in different planes. Variation of the critical temperature with crystal field parameter and concentration are inspected. By detailed investigation on behavior of the order parameter, multi-critical behaviors have been obtained about first and second order phase transitions with concentration.

INTRODUCTION

The disordered magnetic alloys represented by A_cB_{1-c} constitute a wide range of theoretical and experimental field of study due to their modifiable composition properties. More information on the magnetism of alloys can be found in the reference [1].

Although the spin-$1/2$ [2] and spin-1 [3,4] models are very basic models of magnetism, demand with high-order spin systems has increased for many systems day by day. Generalized spin-S models have been investigated by means of several methods such as mean field theory (MFT) [5], effective field theory (EFT) [6,7], Monte Carlo (MC) method [8], series expansion method [9,10]. Besides, a lot of mixed spin system systems are modeled where at least one of the components is generalized spin-S. For instance, mixed spin-$1/2$-spin-S system has examined with EFT [11,12], series expansion [13], exact recursion relations on the Bethe lattice [14] and exact results [15].

There are also many studies in literature for certain spin values of binary alloys. Binary alloy systems consisting of different spin values such as spin-$1/2$-spin-1 are investigated by the use of EFT [16,17,18,19,20], MFT [21], MC method [22]. Spin-$1/2$-spin-$3/2$ are also inspect by means of EFT [23,24] and MFT [25]. Besides, experimental implementation of magnetic alloy systems supported by experimental studies such as $FeAl_{1-x}Mn_x$ [26], $Gd_{1-x}C_x$ [27], $Mn_xSc_{1-x}N$ [28], $Mn_xZn_{1-x}F_2$[29], Ag_cAu_{1-c} and Ag_cPd_{1-c} [30].

Türk Fizik Derneği
1950
Turkish Physical Society

ISBN:978-605-83516-6-0

The main of this work to determine multi-critical behavior of the binary alloys by taking both generalized spin-S of type A and type B atoms consisting of different spin values. The outline of this paper as follow: the formulation of the generalized spin-S binary alloy has been constructed by effective field theory. In the following section, evolution of phase diagrams is presented in different planes. Results are presented at last section.

MODEL AND FORMULATION

Binary alloy system consists of type A atoms with concentration c and type B atoms with concentration 1-c which are represented by A_cB_{1-c}. The Hamiltonian of the generalized spin-S binary ferromagnetic alloy model can be given by

$$H = -J\sum_{<i,j>}(\xi_i\xi_j\sigma_i\sigma_j + \xi_i\xi_j\sigma_i S_j + \delta_i\xi_j S_i\sigma_j + \delta_i\delta_j S_i S_j) - D\sum_i \delta_i (S_i)^2 \tag{1}$$

where J is the ferromagnetic exchange interaction between nearest neighbor spins and D is the crystal field (single ion anisotropy) parameter. σ_i and S_i represents spin operator of type A atoms and type B atoms respectively. In our model both of A and B type atoms have spin-S values. They have $2\sigma+1$ and $2S+1$ different spin values such as $\sigma_i = -\sigma, -\sigma+1, ...\sigma-1, \sigma$ and $S_i = -S, -S+1, ...S-S, S$. ξ_i and δ_i are the site occupation numbers and $\xi_i + \delta_i = 1$. While $\xi_i = 1$ means that the site i has type A atom, $\xi_i = 0$ means that the site I has type B atom.

The magnetizations and quadrupole moments of the system is obtained via exact identities which are given by [31]

$$m_A = \frac{<< \xi_0\sigma_0 >>}{< \xi_0 >} = << \exp(E_0^A\nabla) >> F_A(x)\big|_{x=0} \tag{2}$$

$$m_B = \frac{<< \delta_0 S_0 >>}{< \delta_0 >} = << \exp(E_0^B\nabla) >> F_B(x)\big|_{x=0} \tag{3}$$

where m_A is the magnetization of A atom and m_B is the magnetization of the B atom.

$$q_A = \frac{<< \xi_0\sigma_0^2 >>}{< \xi_0 >} = << \exp(E_0^A\nabla) >> G_A(x)\big|_{x=0} \tag{4}$$

$$q_B = \frac{<< \delta_0 S_0^2 >>}{< \delta_0 >} = << \exp(E_0^B\nabla) >> G_B(x)\big|_{x=0} \tag{5}$$

where q_A is the quadrupole moment of A atom and q_B is the quadrupole moment of the B atom. E_0^A and E_0^B represent local fields. The explicit form of the functions,

$$F(x,D) = \frac{\sum_{k=-S}^{S} k\exp(\beta Dk^2)\sinh[\beta k(x)]}{\sum_{k=-S}^{S}\exp(\beta Dk^2)\cosh[\beta k(x)]} \tag{6}$$

ISBN:978-605-83516-6-0

$$G(x,D)=\frac{\sum_{k=-S}^{S}k^2\exp(\beta Dk^2)\cosh[\beta k(x)]}{\sum_{k=-S}^{S}\exp(\beta Dk^2)\cosh[\beta k(x)]} \tag{7}$$

Differential operator technique on functions can be given as

$$\exp(\alpha\nabla)F(x)=F(x+\alpha) \tag{8}$$

This expression can be used as approximated van der Waerden identities [32] for high order spins which is given by the formula

$$\exp(\alpha S_k)=\cosh(\alpha\eta)+\frac{S_k}{\eta}\sinh(\alpha\eta) \tag{9}$$

where η is the square root of the quadrupole moments.

Total magnetization of magnetic binary alloy system is calculated by

$$m=cm_A+(1-c)m_B \tag{10}$$

Linearization of this formula gives us second order critical temperatures of the binary alloy system.

RESULT AND DISCUSSION

Results have been obtained for $z=3$honeycomb lattice throughout this work. We will utilize scaled (dimensionless) quantities with the following

$$t=\frac{k_BT}{J},d=\frac{D}{J} \tag{11}$$

Phase Diagrams

The phase diagrams in (d,t) plane of the system can be seen in Fig. 1 with selected values of the concentrations $c=0.0, c=0.5$ and $c=1.0$. First we choose both of spin-A and spin-B atoms as half-integer- half-integer model. The concentration $c=1$ and $c=0$ means that full of lattice consists of type A atoms and type B atoms respectively. Spin values of type A and type B atoms chosen as $S_A=0.5$ and $S_B=1.5$ values. We emphasize that $S_A<S_B$ within this work. Phase diagram of the binary alloy system evolve according to this limiting cases. When c concentration values rises from 0 to 1, critical temperatures decrease to spin-A atoms so spin-1/2 model. When d takes negative large values, phase diagram evolve to parallel line to the crystal field axis. Ferromagnetic phase area holds for below this critical temperatures for negative large crystal field values. The system prefers spin-1/2 case in order to provide minimization of the free energy of the system.

The second case of phase diagram consist of both of spin-A and spin-B atoms as integer-integer model as seen in Fig 2. If we increase spin value of B atoms, then critical temperatures also increases as concentration of B atoms increases for larger crystal field parameter values. We examine only second order phase transition lines of phase diagram. We don't show first order transition curves. The system exhibits tricritical point TCP as it passes from the second order phase transition to the first order phase transition. TCP decreases as concentration of A type atoms

ISBN:978-605-83516-6-0

increases. When crystal field parameter takes negative large values, disordered phase appears for ground state for all concentrations.

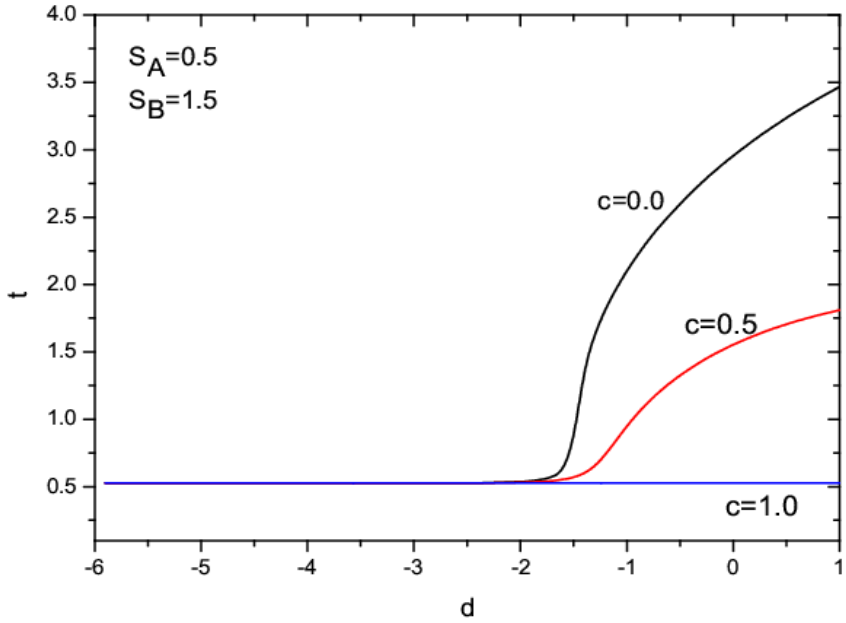


FIGURE 1. Variation of critical temperature with the crystal field parameter for selected values of concentration $c = 0.0, c = 0.5$ and $c = 1.0$ for $S_A = 0.5$ and $S_B = 1.5$ spin values. Solid lines represent to the second order transition

There are strike results for integer-half-integer model. If we choose spin value of A atoms integer and spin value of B atoms half-integer model, then we obtained different results from previous phase diagrams. Spin values of type A and type B atoms chosen as $S_A = 1.0$ and $S_B = 3.5$ values as seen in Fig 3. When c concentration value decreases from 1 to 0, first order portion of phase diagram disappear. After then, the phase diagram evolves to a parallel line to crystal field parameter axis. If we fixed spin of atom A and increase spin of atom B, also critical lines increases to

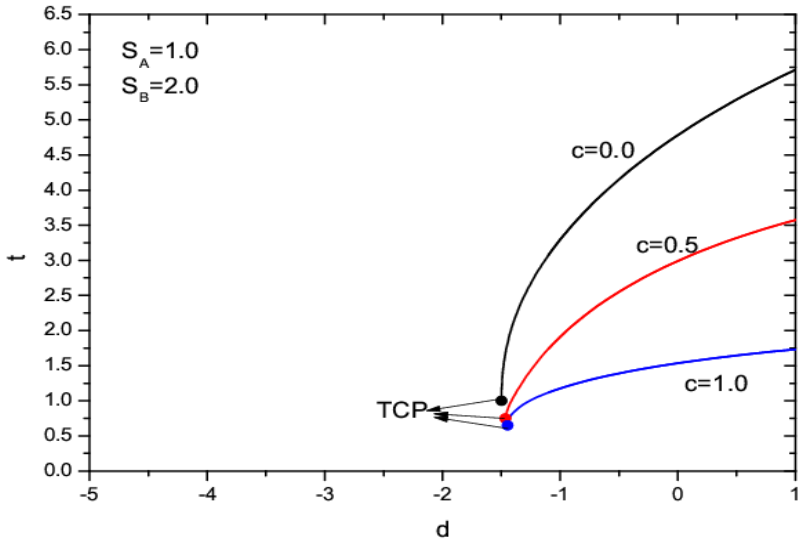


FIGURE 2. Variation of critical temperature with the crystal field parameter for selected values of concentration $c = 0.0, c = 0.5$ and $c = 1.0$ for $S_A = 1.0$ and $S_B = 2.0$ spin values. Solid lines represent to the second order transition. In figure, TCP stands for the tricritical point

ISBN:978-605-83516-6-0

critical lines of B atoms (compare with Fig 2). But unlike the second diagram, phase diagram in Fig 3 does not display TCP for $c = 0$, since the spin of A atom is half integer The system exhibits TCP for $c = 1$ concentration value.

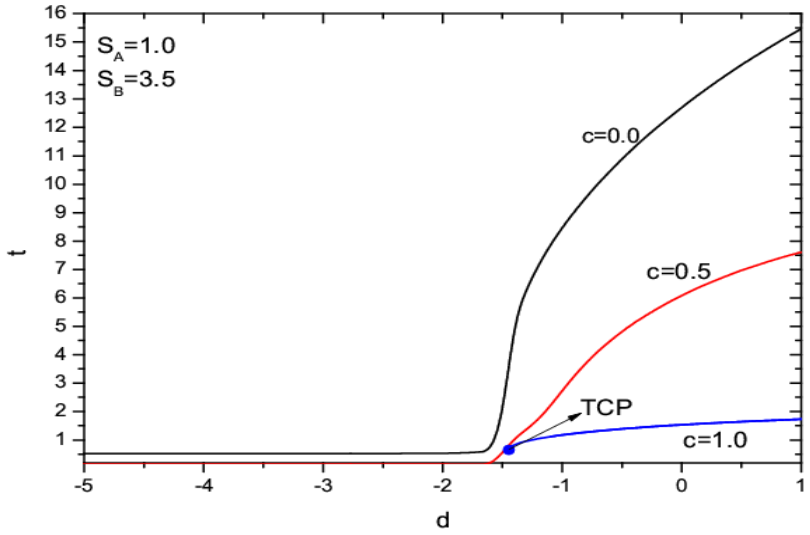


FIGURE 3. Variation of critical temperature with the crystal field parameter for selected values of concentration $c = 0.0, c = 0.5$ and $c = 1.0$ for $S_A = 1.0$ and $S_B = 3.5$ spin values. Solid lines represent to the second order transition. In figure,TCP stands for the tricritical point

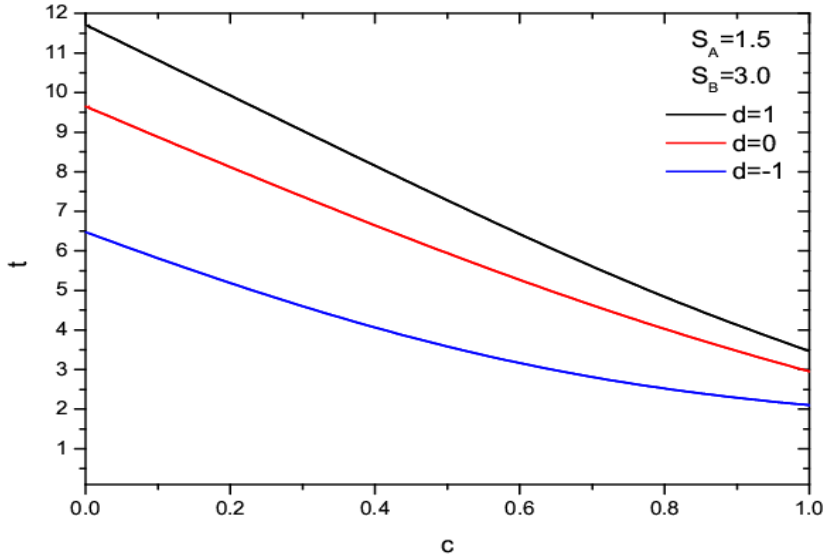


FIGURE 4. Variation of critical temperature with the concentration for selected values of crystal field parameters $d = 1.0, d = 0.0$ and $d = -1.0$ for $S_A = 1.5$ and $S_B = 3.0$ spin values. Solid lines represent to the second order transition

The phase diagram in (c,t) plane for selected values of crystal field parameter can be seen in Fig. 4. The variation of temperature with concentration is constructed for spin value of A atoms half-integer and spin value of B atoms integer model. Spin values of type A and type B atoms chosen as $S_A = 1.5$ and $S_B = 3.0$ values. The system exhibits ferromagnetic phase at low temperatures for all concentrations and exhibits paramagnetic phase at high temperatures. When c concentration value rises from 0 to 1, all critical temperatures decrease. If the crystal field

ISBN:978-605-83516-6-0

parameter takes lower values, also critical temperatures decrease. The system exhibits only second order phase transition lines for $d=1$, $d=0$ and $d=-1$.

CONCLUSION

In conclusion, critical properties of generalized spin-S magnetic binary alloy system represented by A_cB_{1-c} have been investigated within the framework of effective field theory. The system consists of type A atom and type B atom with the concentration c and $1-c$ respectively. Both of spin values of the system is chosen as generalized spin-S model. Results of generalized spin- S binary alloy model discussed as integer-integer, half integer-half integer and half integer-integer model.

The effect of concentration of the magnetic binary alloy model strongly depends on whether the spins of atoms are integer or half-integer. As consistently literature, first order transitions have been observed for integer spin model which is corresponding our limiting case since one of spin of atom consist of integer model. If the majority of concentration consists of half-integer spin model, system exhibit ordered phase at negative large crystal field parameter values. If the majority of concentration consists of integer spin model, system exhibit disordered phase at negative large crystal field values.

REFERENCES

1. Wohlfarth E. P. (Ed.), “Handbook of Magnetic Materials, vol.1, North-Holland Publishing Company, (1980)”
2. Ising E., Zeitschrift für Physik A Hadrons and Nuclei **31.1**, 253-258 (1925).
3. M. Blume, Phys. Rev. **141**, 517 (1966)
4. Capel, H. W, Physica **32.5** 966-988 (1966).
5. Ghatak, S. K. and D. Sherrington. , Journal of Physics C: Solid State Physics **10.16** 3149 (1977).
6. Tucker, J. W., M. Saber, and L. Peliti, Physica A: Statistical Mechanics and its Applications **206.3-4**, 497-507 (1994).
7. Costabile E. et al., Physica A: Statistical Mechanics and its Applications **393**, 297-303 (2014).
8. Nagai, O., Miyashita, S., & Horiguchi, T., Physical Review B **47.1**, 202 (1993).
9. Fox, P. F., and A. J. Guttmann, Journal of Physics C: Solid State Physics **6.5**, 913 (1973).
10. Camp W. J. and Van Dyke J. P., Physical Review B **11.7**, 2579 (1975).
11. Boughrara, M., M. Kerouad, and M. Saber, Journal of Magnetism and Magnetic Materials **316.2**, e287-e290 (2007).
12. Kaneyoshi T., Journal of Magnetism and Materials **151**, 45-53 (1995).
13. Yousif, B. Y., and R. G. Bowers., Journal of Physics A: Mathematical and General **17.17**, 3389 (1984).
14. Ekiz C., Physica A **353**, 286-296 (2005).
15. Strečka, Jozef., Physica A: Statistical Mechanics and its Applications **360.2**, 379-390 (2006).
16. Kaneyoshi, T., Physical Review B **33.11**, 7688 (1986).
17. Kaneyoshi, T., Journal of the Physical Society of Japan **55.5**, 1430-1433 (1986).
18. Kaneyoshi, T., Physical Review B **34.11**, 7866 (1986).
19. Akıncı Ü, and Karakoyun G, Physica B: Condensed Matter **521**, 365-370 (2017).
20. Karakoyun. G. and Akıncı Ü, Physica A: Statistical Mechanics and its Applications **510**, 407-414 (2018).
21. Plascak J.A., Physica A **198**, 655-665 (1993).
22. Cambui D.S., De Arruda A.S. and Godoy M., International Journal of Modern Physics C **23.8**, 1240015 (2012).
23. Kaneyoshi T. and Beyer H., Journal of Physical Society of Japan **49.4**, 1306 (1980).
24. Kaneyoshi T., Physica B **193**, 255-264 (1994).
25. Rancourt D.G., Dube M. and Heron P.R.L., Journal of Magnetism and Magnetic Materials **125**, 39-48 (1993.)
26. Kobeissi M.A., J. Phys. Condens. Matter **3**, 4983-4998 (1991).
27. Ma Y., Du A., Journal of Magnetism and Magnetic Materials **321**, L65-L68 (2009).
28. Alsaad A., Bani-Yassein M., Qattan I.A., Ahmad A.,, Malkawi S.R., Physica B **405**, 1408-1414 (2010).

ISBN:978-605-83516-6-0

29. Cowley R. A., Birgeneau R. J. and Shirane G., Physica **140A** (1986) 285-290.
30. Vilja I., Kokko K., Journal of Alloys and Compounds **614**, 408-414 (2014).
31. Sabarreto F.C., Fittipaldi I.P., Zeks B.,Ferroelectrics **39**, 1103 (1981).
32. Kaneyoshi T., Tucker J., Jascur M., Phys. A **393**, 297 (2013).

11. Condensed Matter Physics II



BOOK OF FULL TEXT PROCEEDINGS TURKISH PHYSICAL SOCIETY 35th INTERNATIONAL PHYSICS CONGRESS (TPS35)
TPS35, Vol.01, No.11, pp.548-552.
ISBN:978-605-83516-6-0

15 December 2019

Zinc Molar Concentration Induced Structural and Optical Properties of Chemically Derived ZnS Thin Films

İ. Boz[1, a)], A. Göktaş[2], A. Tumbul[2], A. Kilic[3]

1Mardin Vocational High School, Mardin Artuklu University, Mardin, Turkey
2 Department of Physics, Harran University, Sanliurfa, Turkey
3Department of Chemistry, Harran University, Sanliurfa, Turkey

[a)]Corresponding author: ibrahimboz@artuklu.edu.tr

ABSTRACT

Chemically derived polycrystalline ZnS thin films have a profound potantial for the optoelectronic and luminescent devices. Regarding this crucial fact that the chemically grown ZnS thin films, prepared at different Zn and S molar ratios, was investigated by X-ray diffraction (XRD), photoluminescence (PL), Fourier transmission infrared (FT-IR) spectrocopy and UV-Vis spectrocopy. The obtained results showed that the ZnS thin films had a hexagonal crystall structure. The crystalline quality of the films was changed depend on the molar ratios. The FT-IR analysis confirmed the formation of Zn-S binding. The PL measurements verified the presence of the main PL emissions of the ZnS structure. The UV-Vis analysis showed the transmittance and absorbance intensity was changed according to the molar ratios as well as the optical band gap of the ZnS thin films.

Key words: Chemical route, ZnS, Molar ratio, Photoluminescence, FT-IR, Band gap

1. INTRODUCTION

Recently, the demand for polycrystalline ZnS semiconductor, which is essential for the electronic circuit, optoelectronic and luminescent devices has been increased. This fact is because of the several reasons like its relatively wide band gap energy (3.6 eV), high exciton binding energy (40 eV), chemically stable at room temperature and environmentally friendly as well as having high refractive index [1-2]. It's structural and optical properties can be varied depend on the used thin film growth technique. Among the chemical film growth techniques, the solution based (sol-gel or chemical route) technique is one of the most preferred one due to it's easy handling and the inexpensive conditions. In chemically thin film growth technique, several parameters are very important to get realtively high crystalline quality and high optical quality for the prepared thin films. These parameters are followed as: pH (1); viscosity (2); the kind of used chemical precoursors (3); and molar ratio of the used premise chemicals (4). According to these facts, the ZnS thin films were synthesized by chemical route to investigate the effect of the molar ratio of the Zn and S on the structural and optical characteristics of the ZnS thin films [3-5].

2. EXPERIMENTAL DETAILS

To get ZnS thin films, the following chemical precoursors and method were used. Zinc acetate ($Zn(OOCCH_3)_2$) and thioure (CH_4N_2S) were dissolved in methanol with several drops of the triethanolamine by stirring on the magnetic stirrer. The different molar ratio (0.01, 0.03, 0.05 and 0.1 M) of the $Zn(OOCCH_3)_2$ and CH_4N_2S was used as Zn^{+2} and S^{-2} sources. In prepared solution the molar ratio of the Zn/S was fixed to 1:3. The pH of the solutions was

regulated by triethanolamine. The obtained solutions was stirred for 24 h by magnetic stirrer at room temperature to get desired homogeneouse and transparent solution as well as gelation. The obtained final solution were used for the coating of clean glass substrate with ZnS solution by dip coating process at 300 ºC. The coated films were sintered at 600 ºC for 30 min. under argon (Ar) atmosphere.

The crystal phase and structure of the prepared films was investigated by X-ray diffraction (XRD, Rigaku Ultima III (40 kV, 40 mA and 1.54 A◦). The fourier transform infrared (FT-IR spectra were obtained in the range of 4000-400 cm^{-1} using the ATR accessory with a resolution of 4 cm^{-1} and 32 scans using a Perkin-Elmer Two UATR-FT spectrophotometer) spectroscopy was used to confirm the existance of the chemical bondings within the film structure. Photoluminescence (PL, Perkin-Elmer model LS55 spectrometer) of the ZnS thin films was investigated for main PL emissions of the ZnS thin films at room temperature.

3. RESULTS AND DISCUSSIONS

3.1. Structural properties

The XRD spectrums of the ZnS thin films upon on molar concentration of the Zn were given in Fig.1. The diffraction peaks corresponding to the (100), (002), (101) and (112) planes, indicating ZnS hexagonal wurtzite structure (JCPSD No. 01-36-1450) in case of the 0.1 M. However, for the 0.03 and 0.01 M concentration of the Zn a mixed ZnS/Zn(S,O) hexagonal wurtzite, ZnS zinc blend and ZnS sphalerite syn structure has been detected [6]. Additionally, no evident peaks in case of the 0.05 M, showing amorphous ZnS structure. By using the Debye Shererr equation [7] the average crystalline size of the ZnS samples was calculated approximately as 32.1, 20.5, 9.8 nm for the molar concetration of 0.03, 0.01 and 0.1 M, respectively.

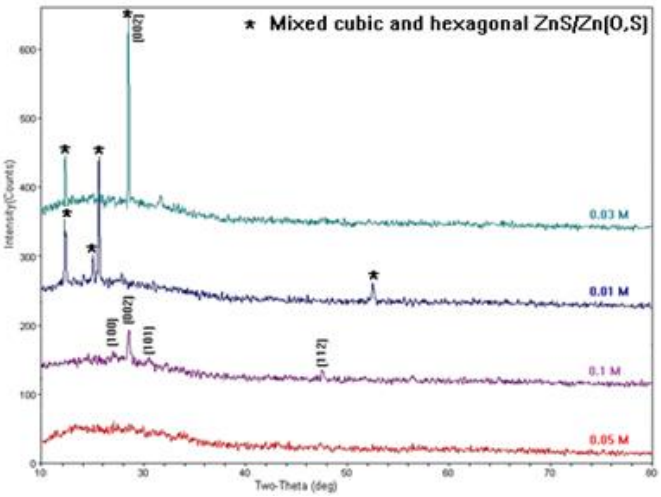


Fig.1. XRD spectra of the ZnS thin films at different molar ratio

3.2. FT-IR Analyses

To obtain information about the functional groups existance within the substances, the molecular geometry and inter/intra-molecular interactions, the FT-IR analyses were done. Fig. 2 shows the molar ratio depended FT-IR spectra of the ZnS thin films in the wavelength range of 400-4000 cm^{-1} wave numbers. The absorption peaks observed at 3749-3653cm^{-1} are possibly related to the stretching vibration mode of hydroxyl group (O-H). The certain absorption peak observed at 2973 and 2908 cm^{-1} are assigned for the alifatic C-H stretching vibration of organic compounds. The spectral band observed in the range of the 2010-2162 cm^{-1} is possibly related to the CO_2 stretching vibration. The peak at 1392 $cm^{-1}$is attributed to alkyl C–H deforming vibration. The distinguished C–O stretching frequency is observed at 1056 cm^{-1}. Generally, the spectral absorption bands belongs to the Zn-S stretching vibrations are between the 650 and 500 cm^{-1} as observed in the Fig. 2. The results are in good agreement with the previous studies on ZnS nanoparticles [8].

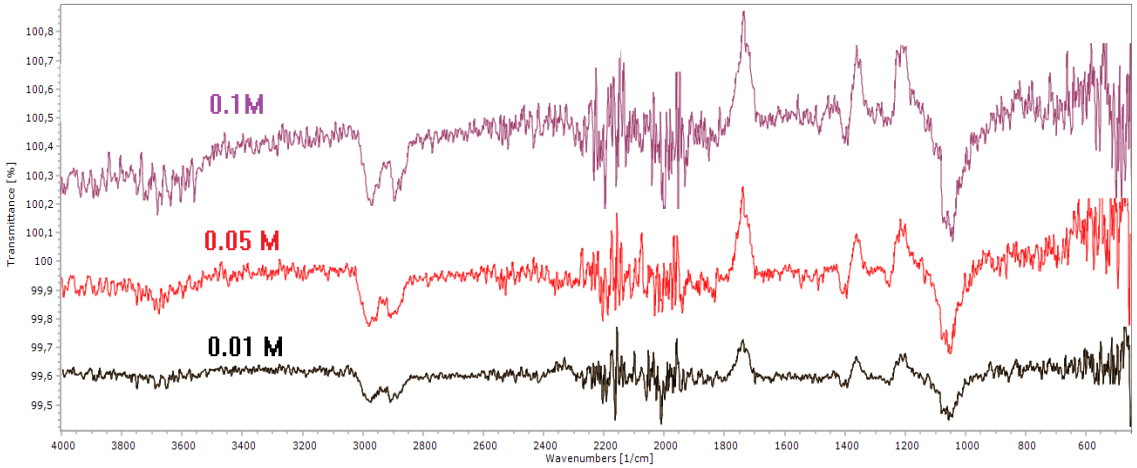


Fig. 2. FTIR spectra of the ZnS thin films at different molar ratio

3.3. Optical Properties

The absorbance spectra of the films was given in Fig. 3. It is observed that the absorption is higher at low Zn concentrations compared with the high Zn concentrations. It is also observed that the band edge of the ZnS thin films has shifted to the higher wavelengths as the Zn molar concentration decreased. Depend on this fact, the band gap energy (E_g) of the ZnS thin films has decreased by reduction of the Zn molar concentration (Fig. 4)

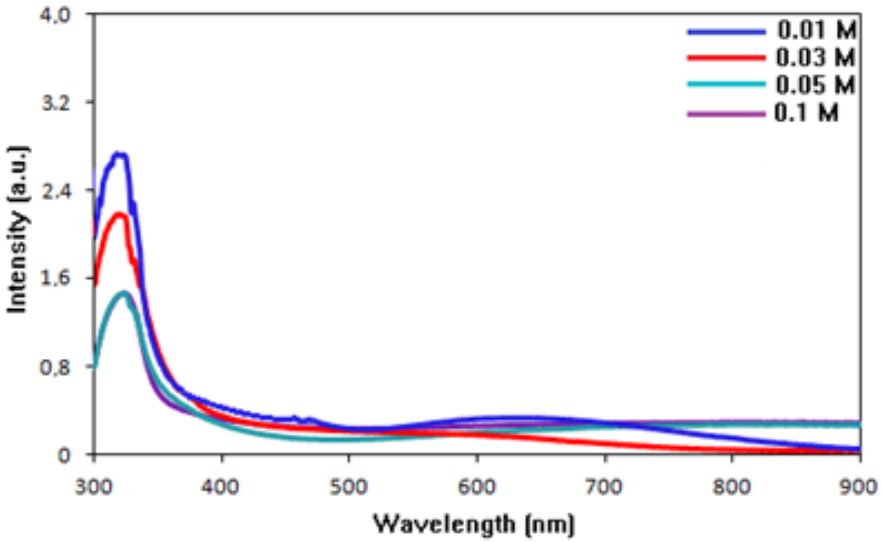


Fig. 3. Absorption spectra of the ZnS thin films at different molar ratio

The Eg of the ZnS thin films was estimated by using the Tauc's equation as Eq.1 [5].

$$\alpha h\nu = A\sqrt{h\nu - Eg} \tag{1}$$

This equation has been used to determine the E_g of the ZnS films. Where α represents the absorption coefficient, A is a constant and $h\nu$ indicates the incident photon energy. The E_g was generally obtained by extrapolation of the

linear part of $(\alpha hv)^2$ versus hv variation to $\alpha hv=0$. As seen from Fig. 4, the E_g was gradually decreased from 3.61 to 3.51 eV with reducing the Zn molar concentration from 0.1 to 0.01 M.

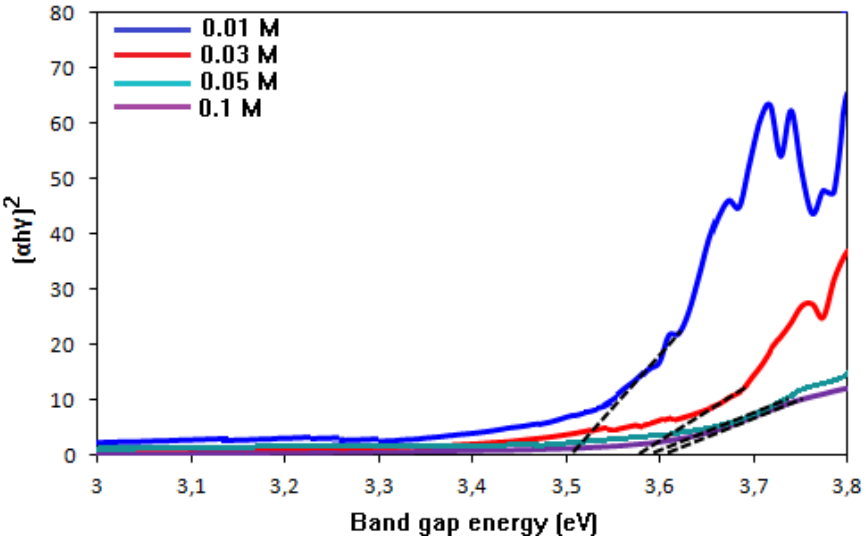


Fig. 4. Plots of $(\alpha h\nu)^2$ versus hν of the ZnS thin films at different molar ratio

Photoluminescence (PL) specterums of the ZnS thin films at room temperature were showed in Fig. 5. It exhibits that the presence of the four main PL emissions. PL_1 and PL_2 emissions at low wavelengths 369 nm and 398 nm have attributed to the surface defects of the ZnS thin films [9]. However, the observed PL_3 and PL_4 were assigned for the blue and green emissions due to the many defects such as Zn, S vacancies Zn interstitial defects likely related to the residual oxygen forming ZnO [10]. It is also observed that the intensity of the emissions has reduced as the zinc molar concetration increased.

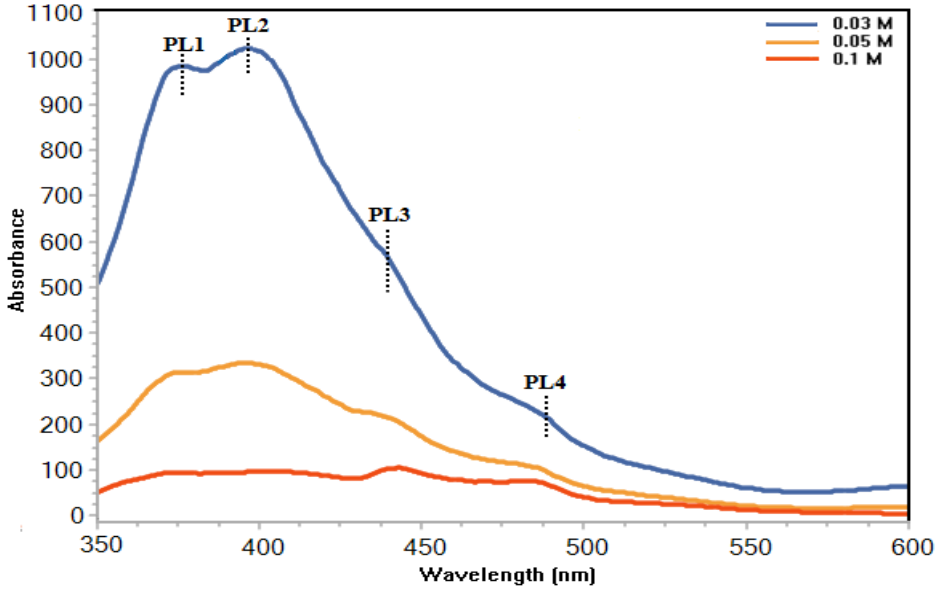


Fig. 5. Photoluminescence of the ZnS thin films at different molar ratio

ISBN:978-605-83516-6-0

4. CONCLUSION

Polycrystalline ZnS thin films was fabricated on glass substrate by the chemical route. The XRD spectra showed that the ZnS hexagonel structure with preferred orientation along the c axis. The best crystallization of ZnS thin films for the 0.03 Zn molar ratio. Accordingly, among all the thin films, the highest crystallization was also determined for it. The formation of the Zn-S and other hydroxyl, alkyl and organic bondings was observed by FT-IR analysis. Optical measurements showed that the optical band gap and the absorption intensity of the ZnS thin films were increased with decreasing the molar concentration of the Zn from 0.1 to 0.01 M. The PL analysis showed that the presence of the Zn, S vacancies and surface defects as well as the Zn interstitial defects. Among all the ZnS films the highest PL emissions were observed for the ZnS thin film with 0.01 M zinc concentration. It was also found that the intensity of the PL emissions was reduced as the zinc molar concentration increased. It is excepted that the observed results will find wide range applications in field of optoelectronic and luminescent devices.

5. ACKNOWLEDGEMENT

Financial support from the Scientific Research Project Commission of Harran University (HUBAK) under Project No. 18062 is gratefully acknowledged.

REFERENCES

1. Dietl T, Ohno H, Matsukura F, Cibert J, Ferrand D (2000) Science 287:1019.
2. Bartholomew DU, Furdyna JK, Ramdas AK (1986) Phys Rev B 34:6943.
3. A. Goktas, Appl. Surf. Sci. (2015) 340:151-159.
4. I. Polat, S. Aksu, M. Altunbas, S. Yılmaz, E. Bacaksız, J. Sol. Stat. Chem. (2011) 184:2683-2689.
5. A. Goktas, F. Aslan, E. Yasar, I. H. Mutlu, J. Mater. Sci.-Mater. Electron., (2012) 23:1361.
6. S. J. Pearton, W. H. Heo, M. Ivill, D. P. Norton, T. Steiner, Semicond. Sci. Technol. 19 (2004) R59-R74.
7. D Amaranatha Reddy, Chunli Liu, R. P. Vijayalakshmi, B. K. Reddy, J. Alloys Compd. 582 (2014) 257-264.
8. A. Goktas, İ. H. Mutlu, J. Electron. Mater., 45 (2016) 5709-5720.
9. T. Dedova, M. Krunks, I. Gromyko, V. Mikli, I. Sildos, K. Utt, and T. Unt,. Phys. Status
10. Solidi A 211, No. 2, (2014) 514-521.

12. Mathematical Physics II



BOOK OF FULL TEXT PROCEEDINGS TURKISH PHYSICAL
SOCIETY 35th INTERNATIONAL PHYSICS CONGRESS (TPS35)
TPS35, Vol.01, No.12, pp.554-558.
ISBN:978-605-83516-6-0

15 December 2019

Investigation of Bianchi Type-V Dark Energy Cosmological Models in F(R,T) Gravity

E. Kara[1, a)], B. Cil[2, b)], E. Gudekli[3, c)] and D. Sofuoglu[4, d)]

[1,2)]Student of High Performers Fundamental Sciences Programme in Istanbul University, Istanbul University Faculty of Science, Vezneciler, Fatih/Istanbul

[2,3)]Istanbul University Faculty of Science, Vezneciler, Fatih/Istanbul

[a)]erhan.kara@ogr.iu.edu.tr, [b)]batuhan.cil@ogr.iu.edu.tr, [c)]gudekli@istanbul.edu.tr, [d)]degers@istanbul.edu.tr

[c)]Corresponding author: gudekli@istanbul.edu.tr

Abstract. In this study, Bianchi type-V cosmological models of the universe filled dark energy with constant and time-dependent equation of state parameters are investigated in f(R,T) Gravity. We find exact solutions of Einstein's field equations using the condition that the shear scalar is proportional to expansion scalar, which represent singular and non-singular cosmological models of the universe. Then we examined the results within the framework of f(R,T) Gravity. The physical behavior of the models is discussed. We conclude that the universe models do not approach isotropy through the evolution of the universe.

1 – INTRODUCTION

We consider the homogeneous and anisotropic Bianchi type – V metric;

$$ds^2 = -c^2dt^2 + A^2dx^2 + B^2e^{2x}dy^2 + C^2e^{2x}dz^2 \tag{1}$$

Where A,B and C functions of the cosmic time (t).

We study in the f(R,T) gravity and we use field equations which obtained from the Hilbert-Einstein type variation principle in our operations is in the form below.

$$S = \frac{1}{16\pi G}\ [\int f(R,T)\sqrt{-g}\ d^4x + \int L_m\sqrt{-g}\ d^4x\ ] \tag{2}$$

In the above action, f(R,T) is function of Ricci scalar R and T energy-momentum scalar. L_m is the lagragian of matter. If we find the energy-momentum tensor T_{uv} we get,

$$T_{uv} = -\frac{2}{\sqrt{-g}}\frac{\partial\sqrt{-g}}{\partial g^{uv}}L_m \quad , \quad \theta_{\mu v} = -2T_{\mu v} - pg_{\mu v} \tag{3}$$

We can find the correspond F(R,T) field equation by varying the action principle (2) for g_{uv} and we obtained,

$$f_R(R,T)R_{\mu v} - \frac{1}{2}f(R,T)g_{\mu v} + (g_{\mu v}\nabla^k\nabla_k - \nabla_\mu\nabla_v)$$

$$f_R(R,T) = 8\pi T_{\mu v} - f_T(R,T)T_{\mu v} - f_T(R,T)\theta_{\mu v} \tag{4}$$

so we can find f_R and f_T

$$f_R = \frac{\partial f(R,T)}{\partial R} \quad , \quad f_T = \frac{\partial f(R,T)}{\partial T} \quad , \quad \theta_{\mu\nu} = g^{\alpha\beta}\frac{\delta T_{\alpha\beta}}{\delta g^{\mu\nu}} \tag{5}$$

In above form, ∇_i is the covariant derivation and T_{ij} is the energy-momentum tensor. Energy-momentum tensor becomes a derivation of matter lagragian L_m.

We assume the field equation of f(R,T) as form below **[1]**.

$$f(R,T) = f_1(R) + f_2(T) \tag{6}$$

If we assume the matter source is perfect fluid, we get

$$f_1'(R)R_{ij} - \frac{1}{2}f_1(R)g_{ij} = 8\pi T_{ij} + f_2'(T)T_{ij} + [f_2'(T)p + \frac{1}{2}f_2(T)]g_{ij} \tag{7}$$

In the above equation, finding a matter tensor for perfect fluid as

$$\theta_j^i \equiv -2T_{ij} - \delta_j^i p = (\rho, -p, -p, -p)$$

for

$$T_j^i = (\rho + p)u_i u^j - \delta_j^i p \tag{8}$$

After we think a spesific part of the functions f_1=R and f_2= λT and λ is an arbitrary constant. So our equation becomes f(R,T) =R+λT

The Einstein field equations are,

$$R_{ij} - \frac{1}{2}Rg_{ij} - \left(p + \frac{T}{2}\right)\lambda g_{ij} = \frac{8\pi+\lambda}{\lambda}T_{ij} \tag{9}$$

equation (7) can written as

$$G_j^i \equiv R_{ij} - \frac{1}{2}g_{ij}R = (8\pi + \lambda)T_{ij} + \lambda(p + \frac{T}{2})g_{ij} \tag{10}$$

Energy-momentum tensor is

$$T_{ij} = (\rho + p)u_i u_j - pg_{ij} \tag{11}$$

2 - APPLICATIONS OF EQUATIONS

In our coordinate system u^u=(0,0,0,1), the Einstein's field equation (10) with (11), for (1) gives **[3]**,

$$-\frac{\dot{A}}{A}\frac{\dot{B}}{B} - \frac{\dot{A}}{A}\frac{\dot{C}}{C} - \frac{\dot{B}}{B}\frac{\dot{C}}{C} + \frac{3}{A^2} = (8\pi + \lambda)\rho + \lambda\left(\frac{\rho - p}{2}\right) \tag{12}$$

$$A^2(\frac{\ddot{B}}{B} + \frac{\ddot{C}}{C} + \frac{\dot{B}}{B}\frac{\dot{C}}{C} - \frac{1^2}{A^2}) = (8\pi + \lambda)A^2 p - A^2\lambda(\frac{\rho - p}{2}) \tag{13}$$

$$B^2e^{2x}(\frac{\ddot{A}}{A} + \frac{\ddot{C}}{C} + \frac{\dot{A}}{A}\frac{\dot{C}}{C} - \frac{1}{A^2}) = (8\pi + \lambda)B^2e^{2x}p - (B^2e^{2x})\lambda(\frac{\rho - p}{2}) \tag{14}$$

$$C^2e^{2x}(\frac{\ddot{A}}{A} + \frac{\ddot{B}}{B} + \frac{\dot{A}}{A}\frac{\dot{B}}{B} - \frac{1}{A^2}) = (8\pi + \lambda)C^2e^{2x}p - (C^2e^{2x})\lambda(\frac{\rho - p}{2}) \tag{15}$$

$$\left(2\frac{\dot{A}}{A} - \frac{\dot{B}}{B} - \frac{\dot{C}}{C}\right) = 0 \tag{16}$$

Where w is the EOS parameter given by

$$p = w\rho \tag{17}$$

And a dot denotes ordinary differentiation with respect to (t).

The average scalar a and volume scalar V given by

$$a^3 = V = ABC \tag{18}$$

the Hubble parameter H is defined by

$$H = \frac{\dot{a}}{a} = \frac{1}{3}(H_1 + H_2 + H_3) \tag{19}$$

Where the directional Hubble parameters H_1, H_2 and H_3 are given by

$$H_1 = \frac{\dot{A}}{A} \quad , \quad H_2 = \frac{\dot{B}}{B} \quad , \quad H_3 = \frac{\dot{C}}{C} \tag{20}$$

The expansion scalar θ and shear scalar σ are given by

$$\theta = 3H = 3\left[\frac{1}{3}(H_1 + H_2 + H_3)\right] = \frac{\dot{A}}{A} + \frac{\dot{B}}{B} + \frac{\dot{C}}{C} \tag{21}$$

$$3\sigma^2 = (\theta_{11} + \theta_{22} + \theta_{33})^2 - 3(\theta_{11}\theta_{22} + \theta_{22}\theta_{33} + \theta_{11}\theta_{33)} \tag{22}$$

the deceleration parameter is defined by

$$q = \frac{d}{dt}(H) - 1 \tag{23}$$

q symbolizes the deceleration parameter of the universe. We can understand from that is the inflation happening or not so positive sign of q means to standart universe but negative sign means inflation **[1]-[2]**.

3 - SOLUTION OF FIELD EQUATIONS

The integration of (16), gives

$$A^2 = BC \tag{24}$$

equation. If we get (24), field equations defined by

$$-2\frac{\dot{B}}{B}\frac{\dot{C}}{C} - \frac{\dot{B}^2}{2B^2} - \frac{\dot{C}^2}{2C^2} + \frac{3}{BC} = (8\pi + \lambda)\rho + \lambda\left(\frac{\rho - p}{2}\right) \tag{25}$$

$$\frac{\ddot{B}}{B} + \frac{\ddot{C}}{C} + \frac{\dot{B}}{B}\frac{\dot{C}}{C} - \frac{1}{BC} = (8\pi + \lambda)p - \lambda\left(\frac{\rho - p}{2}\right) \tag{26}$$

$$\frac{\ddot{B}}{2B} + 3\frac{\ddot{C}}{2C} + \frac{\dot{C}^2}{4C^2} - \frac{\dot{B}^2}{4B^2} + \frac{\dot{B}}{B}\frac{\dot{C}}{C} - \frac{1}{BC} = (8\pi + \lambda)p - \lambda\left(\frac{\rho - p}{2}\right) \tag{27}$$

$$3\frac{\ddot{B}}{2B} + \frac{\ddot{C}}{2C} - \frac{\dot{C}^2}{4C^2} + \frac{\dot{B}^2}{4B^2} + \frac{\dot{B}}{B}\frac{\dot{C}}{C} - \frac{1}{BC} = (8\pi + \lambda)p - \lambda\left(\frac{\rho - p}{2}\right) \tag{28}$$

There are four equations connecting four unknown function.

$$B = C^n \tag{29}$$

In this equality, n is a constant (n≠1).

If we solve (25), (26), (27) and (28), we get A,B and C are

$$A = \left[\frac{3}{2}(n+1)(t + k_1)\right]^{\frac{1}{3}} \tag{30}$$

ISBN:978-605-83516-6-0

$$B = \left[\frac{3}{2}(n+1)(t+k_1)\right]^{\frac{2n}{3(n+1)}} \tag{31}$$

$$C = \left[\frac{3}{2}(n+1)(t+k_1)\right]^{\frac{2}{3(n+1)}} \tag{32}$$

Now, we can use (30), (31) and (32) forms in our metric (1)

$$ds^2 = -dT^2 + \left[\frac{3}{2}(n+1)T\right]^{\frac{2}{3}} dx^2 + \left[\frac{3}{2}(n+1)T\right]^{\frac{4n}{3(n+1)}} (e^{2x})dy^2 + \left[\frac{3}{2}(n+1)T\right]^{\frac{4}{3(n+1)}} e^{2x}dz^2) \tag{33}$$

In (33), we define the T = t+k.

Now, we can analysis field equations with using (30), (31) and (32). We can find energy densities ρ_1 and ρ_2 **[3]**.

$$\rho_1 = \frac{3^{\frac{1}{3}}2^{\frac{5}{3}}}{((n+1)T)^{\frac{2}{3}}(\lambda\omega+\lambda+16\pi)} \tag{34}$$

$$\rho_2 = -\frac{2}{3}\frac{3^{\frac{1}{3}}2^{\frac{2}{3}}}{((n+1)T)^{\frac{2}{3}}(3\lambda\omega+16\pi\omega-\lambda)} \tag{35}$$

We have two energy densities. If we solve ρ_1 and ρ_2 according to $\boldsymbol{\lambda}$ $(5\omega - 1 \neq 1)$,

$$\lambda = -\frac{8\pi(3\omega+1)}{5\omega-1} \tag{36}$$

and we get

$$\rho_1 = -\frac{1}{12}\frac{3^{\frac{1}{3}}2^{\frac{2}{3}}(5\omega-1)}{((n+1)T)^{\frac{2}{3}}\pi(\omega^2-2\omega+1)} \tag{37}$$

$$\rho_2 = -\frac{1}{12}\frac{3^{\frac{1}{3}}2^{\frac{2}{3}}(5\omega-1)}{((n+1)T)^{\frac{2}{3}}\pi(\omega^2-2\omega+1)} \tag{38}$$

and we can see $\rho_1=\rho_2=\rho$ in (37) and (38).

Other physical and kinematic equations defined by

$$H_1 = \frac{1}{3T} \tag{39}$$

$$\frac{H_2}{n} = H_3 = \frac{1}{\frac{3}{2}(n+1)T} \tag{40}$$

$$\theta = 3H = \frac{1}{T} \tag{41}$$

$$\sigma = \frac{1}{T}\sqrt{\frac{n+5}{n+1}} \tag{42}$$

$$q = -\frac{1}{3T^2} - 1 \tag{43}$$

4 - CONCLUSION

The energy densities of the our universe ρ_1, ρ_2 and state function ω inversely proportional to cosmic time t so that means, these parameters decreases in late time universe. Hubble parameters are inversely proportional to cosmic time t so we can say that, universe is expanding slower by the time. That's why the expansion scalar θ is inversely proportional to cosmic time t and that's what we expecting.Shear scalar σ is inversely proportional to

cosmic time t so we can say that universe is shearing slower by the time.Decelerated parameters q is negative and that's what we expecting because universe has accelerated expansion. It's the present universe.

5 – REFERENCES

1. Chandel, P.S., Singh, M.K. and Ram, S. (2012) Bianchi Type-VI Dark Energy Cosmological Model in General Relativity. Global Journal of Science Frontier Research Mathematics and Decision Sciences, 12, 83A05.

2. Ertan Güdekli, Yerlan Myrzakulov, Bekdaulet Meirbekov and Koblandy Yerzhanov, Myrzakulov gravity wıth f-essence and its FRW cosmology, (July 5, 2018)

3. Güdekli, A Çalışkan, Perfect fluid LRS Bianchi type -I- universe model n *F(R, T)* - AIP Conference Proceedings, 2018